The Institution of Engineering and Technology

Modeling, Simulation and Control of Electrical Drives

Edited by
Muhammed Fazlur Rahman and Sanjeet K. Dwivedi



IET CONTROL, ROBOTICS AND SENSORS SERIES 118

Modeling, Simulation and Control of Electrical Drives

www.TechnicalBooksPDF.com

Other volumes in this series:

Volume 8 **A History of Control Engineering, 1800–1930** S. Bennett
Volume 9 **Embedded Mechatronics System Design for Uncertain Environments: Linux®-based, Rasbpian®, ARDUINO® and MATLAB® xPC Target Approaches** C.S. Chin
Volume 18 **Applied Control Theory, 2nd Edition** J.R. Leigh
Volume 20 **Design of Modern Control Systems** D.J. Bell, P.A. Cook and N. Munro (Editors)
Volume 28 **Robots and Automated Manufacture** J. Billingsley (Editor)
Volume 33 **Temperature Measurement and Control** J.R. Leigh
Volume 34 **Singular Perturbation Methodology in Control Systems** D.S. Naidu
Volume 35 **Implementation of Self-tuning Controllers** K. Warwick (Editor)
Volume 37 **Industrial Digital Control Systems, 2nd Edition** K. Warwick and D. Rees (Editors)
Volume 39 **Continuous Time Controller Design** R. Balasubramanian
Volume 40 **Deterministic Control of Uncertain Systems** A.S.I. Zinober (Editor)
Volume 41 **Computer Control of Real-time Processes** S. Bennett and G.S. Virk (Editors)
Volume 42 **Digital Signal Processing: Principles, devices and applications** N.B. Jones and J.D. McK. Watson (Editors)
Volume 44 **Knowledge-based Systems for Industrial Control** J. McGhee, M.J. Grimble and A. Mowforth (Editors)
Volume 47 **A History of Control Engineering, 1930–1956** S. Bennett
Volume 49 **Polynomial Methods in Optimal Control and Filtering** K.J. Hunt (Editor)
Volume 50 **Programming Industrial Control Systems Using IEC 1131-3** R.W. Lewis
Volume 51 **Advanced Robotics and Intelligent Machines** J.O. Gray and D.G. Caldwell (Editors)
Volume 52 **Adaptive Prediction and Predictive Control** P.P. Kanjilal
Volume 53 **Neural Network Applications in Control** G.W. Irwin, K. Warwick and K.J. Hunt (Editors)
Volume 54 **Control Engineering Solutions: A practical approach** P. Albertos, R. Strietzel and N. Mort (Editors)
Volume 55 **Genetic Algorithms in Engineering Systems** A.M.S. Zalzala and P.J. Fleming (Editors)
Volume 56 **Symbolic Methods in Control System Analysis and Design** N. Munro (Editor)
Volume 57 **Flight Control Systems** R.W. Pratt (Editor)
Volume 58 **Power-plant Control and Instrumentation: The control of boilers and HRSG systems** D. Lindsley
Volume 59 **Modelling Control Systems Using IEC 61499** R. Lewis
Volume 60 **People in Control: Human factors in control room design** J. Noyes and M. Bransby (Editors)
Volume 61 **Nonlinear Predictive Control: Theory and practice** B. Kouvaritakis and M. Cannon (Editors)
Volume 62 **Active Sound and Vibration Control** M.O. Tokhi and S.M. Veres
Volume 63 **Stepping Motors, 4th Edition** P.P. Acarnley
Volume 64 **Control Theory, 2nd Edition** J.R. Leigh
Volume 65 **Modelling and Parameter Estimation of Dynamic Systems** J.R. Raol, G. Girija and J. Singh
Volume 66 **Variable Structure Systems: From principles to implementation** A. Sabanovic, L. Fridman and S. Spurgeon (Editors)
Volume 67 **Motion Vision: Design of compact motion sensing solution for autonomous systems** J. Kolodko and L. Vlacic
Volume 68 **Flexible Robot Manipulators: Modelling, simulation and control** M.O. Tokhi and A.K.M. Azad (Editors)
Volume 69 **Advances in Unmanned Marine Vehicles** G. Roberts and R. Sutton (Editors)
Volume 70 **Intelligent Control Systems Using Computational Intelligence Techniques** A. Ruano (Editor)
Volume 71 **Advances in Cognitive Systems** S. Nefti and J. Gray (Editors)
Volume 72 **Control Theory: A guided tour, 3rd Edition** J.R. Leigh

www.TechnicalBooksPDF.com

Volume 73 **Adaptive Sampling with Mobile WSN** K. Sreenath, M.F. Mysorewala, D.O. Popa and F.L. Lewis
Volume 74 **Eigenstructure Control Algorithms: Applications to aircraft/rotorcraft handling qualities design** S. Srinathkumar
Volume 75 **Advanced Control for Constrained Processes and Systems** F. Garelli, R.J. Mantz and H. De Battista
Volume 76 **Developments in Control Theory towards Glocal Control** L. Qiu, J. Chen, T. Iwasaki and H. Fujioka (Editors)
Volume 77 **Further Advances in Unmanned Marine Vehicles** G.N. Roberts and R. Sutton (Editors)
Volume 78 **Frequency-domain Control Design for High-performance Systems** J. O'Brien
Volume 80 **Control-oriented Modelling and Identification: Theory and practice** M. Lovera (Editor)
Volume 81 **Optimal Adaptive Control and Differential Games by Reinforcement Learning Principles** D. Vrabie, K. Vamvoudakis and F. Lewis
Volume 83 **Robust and Adaptive Model Predictive Control of Nonlinear Systems** M. Guay, V. Adetola and D. DeHaan
Volume 84 **Nonlinear and Adaptive Control Systems** Z. Ding
Volume 86 **Modeling and Control of Flexible Robot Manipulators, 2nd Edition** M.O. Tokhi and A.K.M. Azad
Volume 88 **Distributed Control and Filtering for Industrial Systems** M. Mahmoud
Volume 89 **Control-based Operating System Design** A. Leva *et al.*
Volume 90 **Application of Dimensional Analysis in Systems Modelling and Control Design** P. Balaguer
Volume 91 **An Introduction to Fractional Control** D. Valério and J. Costa
Volume 92 **Handbook of Vehicle Suspension Control Systems** H. Liu, H. Gao and P. Li
Volume 93 **Design and Development of Multi-lane Smart Electromechanical Actuators** F.Y. Annaz
Volume 94 **Analysis and Design of Reset Control Systems** Y. Guo, L. Xie and Y. Wang
Volume 95 **Modelling Control Systems Using IEC 61499, 2nd Edition** R. Lewis and A. Zoitl
Volume 96 **Cyber-Physical System Design with Sensor Networking Technologies** S. Zeadally and N. Jabeur (Editors)
Volume 99 **Practical Robotics and Mechatronics: Marine, space and medical applications** I. Yamamoto
Volume 100 **Organic Sensors: Materials and applications** E Garcia-Breijo and P Cosseddu (Editors)
Volume 102 **Recent Trends in Sliding Mode Control** L. Fridman J.P. Barbot and F. Plestan (Editors)
Volume 104 **Control of Mechatronic Systems** L. Guvenc, B.A. Guvenc, B. Demirel, M.T. Emirler
Volume 105 **Mechatronic Hands: Prosthetic and robotic design** P.H. Chappell
Volume 107 **Solved Problems in Dynamical Systems and Control** D. Valério, J.T. Machado, A.M. Lopes and A.M. Galhano
Volume 108 **Wearable Exoskeleton Systems: Design, control and applications** S. Bai, G.S. Virk and T.G. Sugar
Volume 111 **The Inverted Pendulum in Control Theory and Robotics: From theory to new innovations** O. Boubaker and R. Iriarte (Editors)
Volume 112 **RFID Protocol Design, Optimization, and Security for the Internet of Things** A.X. Liu, M. Shahzad, X. Liu and K. Li
Volume 113 **Design of Embedded Robust Control Systems Using MATLAB®/Simulink®** P.H. Petkov, T.N. Slavov and J.K. Kralev
Volume 114 **Signal Processing and Machine Learning for Brain-Machine Interfaces** T. Tanaka and M. Arvaneh (Editor)
Volume 117 **Data Fusion in Wireless Sensor Networks** D. Ciuonzo and P.S. Rossi (Editors)
Volume 119 **Swarm Intelligence Volumes 1–3** Y. Tan (Editor)
Volume 121 **Integrated Fault Diagnosis and Control Design of Linear Complex Systems** M. Davoodi, N. Meskin and K. Khorasani

www.TechnicalBooksPDF.com

This page intentionally left blank

www.TechnicalBooksPDF.com

Modeling, Simulation and Control of Electrical Drives

Edited by
Muhammed Fazlur Rahman and Sanjeet K. Dwivedi

The Institution of Engineering and Technology

www.TechnicalBooksPDF.com

Published by The Institution of Engineering and Technology, London, United Kingdom

The Institution of Engineering and Technology is registered as a Charity in England & Wales (no. 211014) and Scotland (no. SC038698).

© The Institution of Engineering and Technology 2019

First published 2019

This publication is copyright under the Berne Convention and the Universal Copyright Convention. All rights reserved. Apart from any fair dealing for the purposes of research or private study, or criticism or review, as permitted under the Copyright, Designs and Patents Act 1988, this publication may be reproduced, stored or transmitted, in any form or by any means, only with the prior permission in writing of the publishers, or in the case of reprographic reproduction in accordance with the terms of licences issued by the Copyright Licensing Agency. Enquiries concerning reproduction outside those terms should be sent to the publisher at the undermentioned address:

The Institution of Engineering and Technology
Michael Faraday House
Six Hills Way, Stevenage
Herts, SG1 2AY, United Kingdom

www.theiet.org

While the authors and publisher believe that the information and guidance given in this work are correct, all parties must rely upon their own skill and judgement when making use of them. Neither the authors nor publisher assumes any liability to anyone for any loss or damage caused by any error or omission in the work, whether such an error or omission is the result of negligence or any other cause. Any and all such liability is disclaimed.

The moral rights of the authors to be identified as authors of this work have been asserted by them in accordance with the Copyright, Designs and Patents Act 1988.

MATLAB® and Simulink® are trademarks of The MathWorks, Inc.

British Library Cataloguing in Publication Data
A catalogue record for this product is available from the British Library

ISBN 978-1-78561-587-0 (hardback)
ISBN 978-1-78561-588-7 (PDF)

Typeset in India by MPS Limited
Printed in the UK by CPI Group (UK) Ltd, Croydon

www.TechnicalBooksPDF.com

Contents

About the editors xix
Preface xxi
Foreword xxiii

1 Introduction to electric drives 1
Muhammed Fazlur Rahman

1.1 The role of motor drives in modern industry and energy usage 1
1.2 Controller hierarchy for electric drives 3
1.3 Quadrant operation of a drive and typical load torque 7
1.4 Power switch and integrated control devices for drive systems 8
1.5 Overview of chapters 9
List of symbols 12
Glossary of terms 13
Further reading 13

2 Electric machines, dynamic models and sensors in drive systems 15
Mohammad Fazlur Rahman, Rukmi Dutta and Dan Xiao

2.1 Introduction 15
2.2 Electric machines and torque–speed (T–ω) boundaries 15
2.3 T–ω characteristics within torque–speed boundaries 17
2.4 Dynamic models of machines and simulation 18
2.4.1 Dynamic model of DC machines 18
2.4.2 Dynamics model of synchronous machines in rotor reference frame [1] 19
2.4.3 Dynamic model of induction machines in synchronous reference frame 24
2.5 Simulation of drive systems 35
2.5.1 Tuning of an electric drive using a cascaded structure [4] 35
2.5.2 Voltage reference amplitude limitation 38
2.5.3 Pulse-width modulation block 38
2.6 Sensors in drive systems 39
2.6.1 Current sensors for electric drive systems 39
2.6.2 Speed sensors for electric drive systems 42
2.7 Recent developments in PM machines; with reference to developments of other types: DCM and IM 45
2.7.1 Developments in winding topologies 46
2.7.2 Emerging electric machine topologies 47

www.TechnicalBooksPDF.com

2.7.3 Permanent magnet synchronous machines (PMSMs) with deep flux weakening capability 53
2.7.4 Control of the PMSM at deep flux weakening 56
2.8 Summary 58
List of symbol 58
Glossary of terms 59
References 59

3 Converters for drives 63
Ramkrishan Maheshwari

3.1 Introduction 63
3.2 Three-phase two-level inverter 64
3.2.1 Sinusoidal PWM 66
3.2.2 Space Vector PWM 68
3.2.3 Carrier-based implementation of SVPWM 72
3.3 Three-phase multilevel inverter 76
3.3.1 Sinusoidal PWM 78
3.3.2 Space vector PWM 81
3.3.3 Carrier-based implementation of the three-level SVPWM [14] 86
3.3.4 Neutral-point voltage control 90
3.4 Summary 97
List of symbols 97
Glossary of terms 98
References 99

4 DC motor drives 101
Sanjeev Singh

4.1 Introduction 101
4.2 Modeling of DC motor 102
4.3 Classification of DC motor drives 104
4.4 Converters for DC motor drives 107
4.4.1 Single-phase controlled AC–DC converters 108
4.4.2 Three-phase controlled AC–DC converters 110
4.4.3 Single-phase uncontrolled AC–DC converters 110
4.4.4 Three-phase uncontrolled AC–DC converters 110
4.4.5 Choppers 110
4.4.6 DC–DC converters 114
4.5 Control schemes for DC motor drives 115
4.5.1 Controlled AC–DC converter-based DC motor drive 116
4.5.2 Uncontrolled AC–DC converter–chopper-based DC motor drive 117
4.5.3 Uncontrolled AC–DC converter-DC–DC converter-based DC motor drive 118

www.TechnicalBooksPDF.com

4.6 PI controller design 120
4.7 Power quality control and sensor reduction for DC motor drives 121
4.8 Modeling of controllers and PWM generators 123
4.8.1 Voltage controller 123
4.8.2 Reference current generator for power quality control 123
4.8.3 PWM current controller 124
4.8.4 PWM signal generator for voltage follower control 124
4.8.5 PWM signal generation for single switch converters 124
4.8.6 PWM signal generation for push–pull converter 124
4.8.7 PWM signal generation for half bridge converter 125
4.8.8 PWM signal generation for full-bridge converter 125
4.9 Performance simulation of DC motor drives 125
4.10 DC series motor control 131
4.11 Summary 131
List of symbols 132
Glossary of terms 134
References 134

5 Synchronous motor drives 137
Sanjeet K. Dwivedi

5.1 Introduction 137
5.2 Classification of synchronous motor drives 138
5.3 Magnet torque and reluctance torque-based classification 139
5.4 Comparison of IPMSM and PMaSynRM 140
5.5 Different control techniques for various synchronous speed motors 140
5.6 Operating principle of vector control technique 142
5.7 Mathematical model of vector-controlled PMSM drive 143
5.7.1 Modeling of speed controllers 143
5.7.2 Modeling of reference winding current generation 149
5.7.3 Modeling of PWM current controller 150
5.7.4 Modeling of PMSM 150
5.7.5 Modeling of voltage source inverter 151
5.8 MATLAB-based model of vector-controlled PMSM drive system 152
5.8.1 Modeling using power system blockset (PSB) toolbox 152
5.9 Description of DSP-based vector-controlled PMSM drive 156
5.9.1 Development of signal conditioning circuits 157
5.9.2 Development of power circuit of the drive 157
5.10 DSP-based software implementation of vector-controlled PMSM drive 157
5.10.1 Reference speed input 158
5.10.2 Sensing of rotor position signals 158
5.10.3 Speed sensing 158
5.10.4 Speed controller 158
5.10.5 Reference winding current generation 158

www.TechnicalBooksPDF.com

5.10.6 Switching signal generation for voltage source inverter 159
5.11 Testing of vector-controlled PMSM drive 159
5.11.1 Testing of control circuit 159
5.11.2 Testing of power circuit 160
5.12 Results and discussion 160
5.12.1 Starting dynamics of vector-controlled PMSM drive 160
5.12.2 Load perturbation performance of vector-controlled PMSM drive 166
5.12.3 Speed reversal dynamics of vector-controlled PMSM drive 174
5.12.4 Comparative study among different speed controllers 175
5.13 Sensor reduction in vector-controlled permanent magnet synchronous motor drive 175
5.13.1 Sensor requirements in vector-controlled PMSM drive system 175
5.13.2 Review of mechanical sensor reduction techniques in PMSM drive 176
5.13.3 Electrical sensor reduction in PMSM drive 179
5.14 Sensorless vector-controlled PMSM drive 179
5.14.1 Stator voltage estimation 180
5.14.2 Winding current estimation 180
5.14.3 Flux estimation 181
5.14.4 Position estimation 181
5.14.5 Speed estimation 181
5.15 MATLAB-based model of sensorless vector-controlled PMSM drive 182
5.15.1 Flux estimator 182
5.15.2 Position and speed estimation 183
5.15.3 Speed controller 183
5.15.4 Reference winding current generation 183
5.15.5 Current controlled pulse width modulator (CC-PWM) 184
5.16 DSP-based hardware implementation of sensorless vector-controlled PMSM drive 184
5.16.1 Development of signal conditioning circuits 185
5.16.2 Development of power circuit of the drive 185
5.17 DSP-based software implementation of sensorless vector-controlled PMSM drive 185
5.17.1 Reference speed input 185
5.17.2 Estimation of stator flux and position of rotor 185
5.17.3 Speed estimation 186
5.17.4 Speed controller 186
5.17.5 Reference winding current generation 186
5.17.6 Switching signal generation for voltage source inverter 186
5.18 Testing of sensorless vector-controlled PMSM drive 186
5.18.1 Testing of control circuit 187
5.18.2 Testing of power circuit 187

www.TechnicalBooksPDF.com

5.19 Results and discussion 187
5.19.1 Starting dynamics of sensorless PMSM drive 189
5.19.2 Load perturbation response of sensorless PMSM drive 192
5.19.3 Speed reversal dynamics of sensorless PMSM drive 193
5.19.4 Steady-state performance of sensorless PMSM drive 193
5.20 Summary 193
List of symbols 194
Glossary of terms 195
References 196

6 PM synchronous machine drives 201
Thomas M. Jahns

6.1 Introduction 201
6.2 PM machine equivalent circuit models 202
6.3 IPM machine torque production characteristics 206
6.3.1 Basics of torque production in IPM machines 206
6.3.2 PMSM torque production characteristics in *dq* current plane 207
6.3.3 Current limit circle 210
6.3.4 Impact of magnetic saturation on maximum torque-per-Amp trajectories 211
6.4 Vector control of PM machine 212
6.4.1 Review of basic vector control principles 212
6.4.2 Application of vector control to SPM and IPM machines 213
6.4.3 Introduction to self-sensing techniques for vector control drives 215
6.5 IPM machine capability curves 216
6.5.1 Basic principles 216
6.5.2 PMSM circle diagrams and capability curves 218
6.5.3 Three cases of PM machine capability curves 221
6.6 PM machine design space 227
6.7 Flux-weakening control of PM machines 230
6.7.1 Introduction to basic principles of flux-weakening control 230
6.7.2 Feedforward vs. closed-loop flux-weakening control algorithms 232
6.7.3 Six-step voltage operation for flux-weakening algorithms 239
6.8 Summary 240
List of symbols 241
Glossary of terms 241
References 242

7 Control of PM brushless DC motor drives 245
Ta Cao Minh

7.1 Introduction 245
7.1.1 Construction of BLDC motor 246

www.TechnicalBooksPDF.com

7.1.2 Operation principle of BLDC motor 247
7.1.3 Specific features of BLDC motor drives 249
7.2 Modeling of brushless DC motor 249
7.2.1 Dynamic model 250
7.2.2 Block diagram of BLDCM model 252
7.2.3 Torque-speed characteristic 252
7.3 Phase-current control of brushless DC motor 253
7.3.1 Control system configuration 253
7.3.2 Simulation results 254
7.4 Torque ripple analysis and reduction techniques 255
7.5 Pseudo-vector control of BLDC motor 258
7.5.1 System configuration 258
7.5.2 Principle of pseudo-vector control 258
7.5.3 Simulation results and performance comparison 260
7.6 Control of BLDCM in high-speed region 264
7.6.1 Operation in high-speed region 264
7.6.2 Phase-advance approach to expand the speed range of BLDCM 265
7.6.3 Pseudo-vector control for high-speed range of BLDCM 266
7.6.4 Simulation results for high-speed operation using PVC 267
7.7 Summary 271
List of symbols 271
Glossary of terms 272
References 273

8 Switched reluctance motor drives 275
Jin-Woo Ahn and Grace Firsta Lukman

8.1 Principle of switched reluctance motor 275
8.1.1 Operation of SRM 275
8.1.2 Characteristics of SRM 280
8.2 Design of switched reluctance motor 282
8.2.1 Selection of pole 283
8.2.2 Selection of phase number 285
8.2.3 Dimensions and parameters 286
8.3 Control of switched reluctance motor 288
8.3.1 Power converter 288
8.3.2 Switching angle control 290
8.3.3 Current control 294
8.3.4 Direct torque control 301
8.4 Modeling of switched reluctance motor 303
8.4.1 Equivalent circuit 303
8.4.2 Current waveform representation 304
8.4.3 Torque waveform representation 307
8.4.4 SRM control system 308

www.TechnicalBooksPDF.com

8.4.5 Example designs of control scheme 311
8.5 Emerging applications 313
8.5.1 Home appliances 314
8.5.2 Industrial applications 316
8.5.3 Electric vehicle application 319
8.6 Summary 321
List of symbols 321
Glossary of terms 323
References 323

9 Direct torque control of AC machines 325
Rahul Kanchan

9.1 Induction motor model 326
9.2 Two-level inverter voltage vector representation 328
9.3 DTC control principle 330
9.3.1 Flux and torque comparator 331
9.3.2 Optimum switching vector selection 332
9.3.3 Motor model 333
9.4 Flux estimation approaches 334
9.4.1 Use of low-pass filters 334
9.4.2 Flux estimation with feedback 335
9.4.3 Application of hybrid flux estimators 338
9.4.4 Other methods for estimation of stator flux 339
9.4.5 Speed-sensorless operation 340
9.5 Simulation of DTC control 341
9.6 Performance enhancement of classical DTC scheme 344
9.6.1 Reduction in torque and flux ripple using alternate switching tables 344
9.6.2 DTC-SVM control [11] 346
9.6.3 Predictive torque control 347
9.7 Direct torque control of synchronous motors 350
9.8 Industrial adaptation of DTC schemes 350
9.9 Summary 355
List of symbols 355
Glossary of terms 355
References 355

10 Direct torque control of PM synchronous motor drives 359
Muhammed Fazlur Rahman and Dan Xiao

10.1 Introduction 359
10.1.1 The PMSM model and RFOC 360
10.1.2 Current control trajectories for PMSM [8,9] 361
10.1.3 Field weakening under voltage limit 361
10.2 DTC for PMSM 363

www.TechnicalBooksPDF.com

10.2.1 Voltage space vector selection [10,11] 368
10.2.2 Stability criteria for DTC 370
10.2.3 Torque and flux linkage control of a PMSM by applying voltage vectors 371
10.3 DTC with fixed switching frequency and reduced torque and flux ripple 373
10.4 Closed-loop flux and torque estimation 378
10.5 Control trajectories with DTC [10,11] 381
10.5.1 The MTPA trajectory under DTC 383
10.5.2 Current and voltage trajectories in the T-λ_s plane 384
10.5.3 Performance of PMSM under DTC with trajectory following 385
10.6 Summary 385
List of symbols 387
Glossary of terms 387
References 387

11 Matrix converter-driven AC motor drives 389
Dan Xiao and Muhammed Fazlur Rahman

11.1 Matrix converter 390
11.1.1 Fundamentals of MC 390
11.1.2 Implementation of MC 391
11.1.3 Current commutation strategies 398
11.1.4 Modulation techniques 406
11.1.5 IPF compensation for MC 418
11.2 DTC for MC drive 422
11.2.1 DTC of MC drives using three hysteresis comparators 425
11.2.2 An improved DTC for MCs 427
11.2.3 Experimental results 429
11.2.4 DTFC for MC-fed PMSM drives by using ISVM 431
11.3 IMC-driven AC drives 439
11.3.1 Modulation scheme for IMC 439
11.3.2 Commutation issue for IMC 441
11.3.3 Rotor flux-oriented control of induction machine (IM)-driven by IMC 441
11.4 Summary 445
List of symbols 446
Glossary of term 446
References 447

12 An online parameter identification method for AC drives with induction motors 451
Dhirendran Munith Kumar, Hiye Krishan Mudaliar, Maurizio Cirrincione, and Marcello Pucci

12.1 Introduction 451

www.TechnicalBooksPDF.com

12.2 FOC design 453
12.2.1 Controller tuning 453
12.3 Description of the test bed 454
12.4 dSPACE AutoBox 455
12.4.1 DS1007 PPC processor board 456
12.4.2 DS5001 digital waveform capture board 456
12.4.3 DS4002 timing and digital I/O board 456
12.4.4 DS2004 high-speed A/D board 459
12.4.5 Hardware scheme and interface with dSPACE: I/O boards 459
12.5 IGBT inverter 461
12.6 Induction motor 462
12.7 Sensors of current, voltage and speed 463
12.7.1 Encoder configuration 463
12.7.2 Current sensor configuration 463
12.7.3 Voltage sensor configuration 463
12.8 Online estimation of the parameters: method and implementation 465
12.8.1 Description of the method 465
12.8.2 Description and realization of the signal processing system 466
12.8.3 Anti-aliasing filter 467
12.8.4 Digital processing 470
12.9 Experimental results 472
12.10 Summary 476
Appendix 476
List of symbols 478
Glossary of terms 478
References 478
Futher References 479

13 Sensorless control of IM drives 481
Lennart Harnefors

13.1 Introduction 481
13.2 Essentials of sensorless vector control 484
13.2.1 IM model and nomenclature 484
13.2.2 Dynamic model and principle for vector control 485
13.3 Flux estimation in DFO 487
13.3.1 Current model 487
13.3.2 Voltage model 489
13.3.3 Statically compensated VM 489
13.3.4 Combination of CM and VM 491
13.3.5 Reduced-order observer 491
13.3.6 Speed estimation 492
13.4 Flux estimation in IFO 493
13.4.1 Current model 493
13.4.2 Reduced-order observer 494

www.TechnicalBooksPDF.com

13.4.3 Voltage model 495
13.4.4 Statically compensated VM 496
13.4.5 Speed estimation 497
13.4.6 Inherently sensorless reduced-order observer 497
13.4.7 Speed estimation in an inherently sensorless scheme 500
13.5 Design for complete stability 500
13.6 Examples 503
13.6.1 Inherently sensorless reduced-order observer and SCVM 503
13.6.2 Sensorless CM 504
13.6.3 Simulations 505
13.7 Conclusion 508
List of symbols 508
Glossary of terms 508
References 509

14 Sensorless control of PMSM drives 513
Gilbert Foo, Zhang Xinan and Muhammed Fazlur Rahman

14.1 Introduction 513
14.2 Mathematical model of the PMSM 516
14.3 Open-loop back EMF estimator 518
14.4 Closed-loop speed-adaptive observer 520
14.5 Closed-loop speed non-adaptive observer 525
14.6 HF signal injection 528
14.7 Current slope measurement method 534
14.8 Summary 540
List of symbols 541
Glossary of terms 541
References 542

15 Predictive torque control of induction motor drive 545
Muhammed Habibullah, Dan Xiao, Muhammed Fazlur Rahman, and Dylan Dah-Chuan Lu

15.1 Introduction 545
15.2 Comparison between the PTC and classical control strategies (FOC and DTC) 546
15.3 PTC System modelling 547
15.3.1 State-space representation of three-phase systems 547
15.3.2 Modelling of the IM 549
15.3.3 Modelling of the inverter 551
15.4 Basic structure and working principle of PTC 552
15.4.1 Estimation 553
15.4.2 Prediction 553
15.4.3 Cost function optimisation 554
15.4.4 Limitations of the FS-PTC 555

www.TechnicalBooksPDF.com

15.5 SPVs-based FS-PTC 556
15.5.1 Selecting prediction vectors 556
15.5.2 Optimum voltage vector selection 559
15.5.3 Average switching frequency reduction 560
15.5.4 Overall control structure of SPVs-based FS-PTC 560
15.5.5 SPVs-based FS-PTC algorithm 561
15.6 Computational efficiency improvement in the SPVs-based FS-PTC 562
15.7 Performance of an IM drive under FS-PTC 563
15.7.1 Steady-state behaviour 564
15.7.2 Transient capability under rated-speed reversal 567
15.7.3 The average switching frequency 569
15.7.4 Investigation of robustness against rated-load torque disturbance 570
15.7.5 Step rated-torque-transient characteristics 571
15.7.6 Step rated-speed-transient characteristics 571
15.8 Summary 573
List of symbols 574
Glossary of terms 574
References 574

16 Multiphase machine drives 579
Radu Bojoi and Luca Zarri

16.1 Introduction 579
16.1.1 Definition of a multiphase drive 579
16.1.2 Advantages of multiphase drives 579
16.1.3 A brief history of multiphase motor drives 581
16.1.4 Applications 581
16.2 Multiphase electrical machines 583
16.2.1 VSD approach 584
16.2.2 Multi-stator approach 594
16.2.3 Summary on multiphase machines 596
16.3 Multiphase power converters 597
16.3.1 Modulation strategies for multiphase inverters 597
16.3.2 Pulse width modulation 598
16.3.3 Voltage limits 599
16.3.4 Space vector modulation 605
16.3.5 Analysis of the output current ripple 609
16.4 Control of multiphase drives 611
16.4.1 Field-oriented control 614
16.4.2 Direct torque control 617
16.4.3 Direct flux vector control 620
16.4.4 Model predictive control 623
16.5 Summary 628

www.TechnicalBooksPDF.com

List of symbols 629
Glossary of terms 629
References 629

17 Fractional-slot concentrated winding machines and drives 637
Ayman M. EL-Refaie

17.1 Definition of fractional-slot concentrated windings 637
17.2 Advantages of using concentrated windings 640
17.3 Challenges involved in using FSCW 644
17.4 Three-phase structures that can support FSCW 644
17.5 Comparison of SL and DL configurations 646
17.6 Criteria for choosing the optimum slot/pole combination 648
17.7 How to determine the winding layout 651
17.8 Calculation of the winding factor 656
17.8.1 EMF method 656
17.8.2 Winding function method 657
17.8.3 Closed-form expressions 657
17.8.4 Example of winding factor calculation using three methods 659
17.9 Design and analysis 662
17.10 Flux weakening 663
17.10.1 Same magnet flux linkage constraint 665
17.10.2 Inductance calculations 667
17.11 Losses in electrical machines equipped with FSCW 668
17.11.1 Rotor losses 668
17.11.2 End losses 670
17.11.3 AC losses in the windings 671
17.11.4 Loss reduction 671
17.12 Fault tolerance 673
17.13 Comparison of SPM versus IPM 677
17.14 Axial-flux, tubular, and flux-switching machines 681
17.15 Induction machines 682
17.16 Parasitic effects 682
17.17 Commercial applications and future evolution of research 683
17.18 Summary 686
List of symbols 686
Glossary of terms 688
References 688

Index 697

www.TechnicalBooksPDF.com

About the editors

Professor Faz Rahman obtained his B.Sc. Honours degree in Electrical Engineering from the Bangladesh University of Engineering and Technology in 1972 and his M.Sc and Ph.D degrees, also in Electrical Engineering, from the University of Manchester Institute of Science and Technology (UMIST), UK, in 1975 and 1978, respectively. He subsequently worked as a Systems Design Engineer in the General Electric Projects Co. at Rugby, UK, for two years and at the National University of Singapore as a Senior Lecturer for eight years. He is currently a Professor in Energy Systems at the University of New South Wales, Australia. His research interests are in power electronics, motor drives and design of electrical machines with permanent magnet excitation. His particular research contributions lie in the areas of design and control of permanent-magnet synchronous machines, in the direct torque control and sensorless control techniques of this motor, and in the development of concentrated-winding PMSMs for traction drive with high field weakening range. He was elevated to a Fellow of IEEE in 2014 for contributions to research and industry in these areas.

Dr. Sanjeet Kumar Dwivedi is Fellow of IET (UK), Senior Member of IEEE. He is working as senior R&D engineer in Drive Intelligence, Technology research group in Global R&D center of *Danfoss Drives A/S*, Gråsten, Denmark, where he is contributing for research of new control techniques in power electronics and motor drives since 2008.

Prior to this, Dr. Sanjeet was an electrical engineer in Larsen & Toubro India (1991–92) and a faculty member in the Department of Technical Education, MP, India (1993–2001). He worked as a research associate in power electronics, electrical machine and drives (PEEMD) research group at the Indian Institute of Technology Delhi (2002–06) toward his doctoral research. He worked as head of the Electrical Engineering department and dean academic at Indira Gandhi Engineering College, Sagar, MP, India (2007–08).

He was an adjunct professor at Curtin University, Perth, Australia (2016–18). Dr. Sanjeet has authored more than 40 technical papers and holds three international patents. He is a member of the Study Board of Innovation and Business Faculty at South Denmark University and Editorial Board of *International Journal of Power Electronics* (*IJPE*), associate editor of the *Transaction of Industrial Electronics of the IEEE*, technical editor of ASME/IEEE *Transaction of Mechatronics*, and European leader cum associate editor of IEEE online publication *Industrial Electronics Technology Transfer News* (*IETTN*). He has given invited

www.TechnicalBooksPDF.com

presentations, and organized and chaired special sessions in several IEEE and European Power Electronics conferences. Previously he worked as associate editor of IET (United Kingdom) *Power Electronics Journal* and associate editor of *Korean Journal of Power Electronics* (JPE).

Dr. Sanjeet was awarded *Gold Medal* for his Master of Engineering degree at the Indian Institute of Technology Roorkee (1999). He is a recipient of *Merit Award* from Institution of Engineers (India) IE(I) (2006) for his research publication on permanent magnet machines. He was also awarded with *9th Man on the Moon Global Innovation Award of Danfoss* (2015) and *IETE-Bimal Bose Award* (2017) for outstanding contributions in power electronics and drives.

www.TechnicalBooksPDF.com

Preface

The tremendous developments in power electronic switches, sensors and supporting embedded control products during the past 25 years have spurred many new control techniques and machine designs that are at the heart of modern electric drives. As a result, electric drive systems are being utilized in new applications that were once the bastions of other technologies. To mention just one, automotive traction drives in the form of electric vehicles is opening up a vast new area electric drive usage, which until now had been the domain of internal combustion engines. It has been reported that 50% of all electric power was utilized by electric drive until recently. This figure is poised go up further in future. This trend has been possible through the intense research and developments in many closely related areas, contributed by many individuals working on power electronics, motor design, magnetic materials, non-linear control and observer techniques, sensing techniques, embedded integrated circuits and so on. The research community involvement is enormous, as evidenced by the high growth of conference journal publications, led by many institutions, universities and industries. This book has tried to embody these recent works in a way that, hopefully, will be useful to new researchers in electric drive systems in universities and industries, in addition to those application engineers who may need to keep abreast of the present state-of-the-art in electric drives. The potential readership is also expected to be senior or postgraduate students at universities and engineers engaged in developing more advanced electric drive in the future.

The content of this book was selected with a view to not only describing the elements and subsystems of electric drive systems but also describing some of the developments in electric drives in recent years, such as mechanical sensorless control in order to remove a potentially weak link in a drive system, multiphase machines in order to improve the reliability of some critical applications, and concentrated winding machines which are displacing distributed winding machines where compact design, high power density, wide field-weakening or constant power-speed range and ease of manufacturing are important. A lot of content has been devoted to the control of the permanent-magnet synchronous machine, owing to the growing application of this type machine. Chapters of the book have been contributed by many renowned researchers/academics from Europe, USA, South Korea, India, Australasia and senior scientists from industries like ABB and Danfoss A/S.

We are grateful to my colleagues around the world for their hard work in writing the chapters and for going through many stages of checking the final

www.TechnicalBooksPDF.com

versions of their chapters and for their perseverance through these processes. This book would not have been possible without their participation. The team at the IET and the co-editor have done a tremendous job in keeping the authors meet certain deadlines and in proofreading the chapters thoroughly. I cannot thank them enough for pushing all preparations for the book along. We would also like to thank our respective families (Raihana Rahman and Alka Dwivedi) for their patience and support throughout our involvement with the book over the past two and a half years.

Faz Rahman
Sydney, Australia
Sanjeet Dwivedi
Graasten, Denmark
April 2019

www.TechnicalBooksPDF.com

Foreword

High-efficiency and high-performance electrical machine drives are widely used for applications in industrial, commercial, transportation, domestic, aerospace and military environments. Such applications are particularly important in the recent years for environmentally clean renewable wind energy generation systems and electric vehicles that help to solve climate change problems. This book, edited by Drs. M. Faz Rahman and Sanjeet Dwivedi, is an extremely important contribution and has appeared in right time. Dr. Rahman is well-known in the world for his research contributions in power electronics and motor drives. Dr. Dwivedi is an emerging scientist with tremendous amount of talent and industrial experience. This book is basically a state-of-the-art comprehensive review of electrical machines and drives, and covers practically all the aspects of modern technology in this area. The book has altogether seventeen chapters which are contributed by well-qualified contributors that include the editors. The dynamic modelling, simulation and control of all types of machines have been covered that include DC, induction, permanent magnet synchronous (PMSM) and switched reluctance machine (SRM) drives that are excited by modern two-level, three-level and matrix converters. The whole subject has been treated in a balanced way between the theory and practical applications which are extremely important for the readers. Both three-phase and multi-phase machines have been considered. All the advanced control techniques, such as vector control, DTC or direct torque and flux control (DTFC), and the recently emerging model predictive control (MPC) have been discussed. However, the classical scalar control methods which are getting obsolete have been excluded. The sensorless control with estimation of model-based signals, hardware and software for digital control implementation, and performances with simulation and experiment have also been included. The organization of the topics and presentation style are unique and extremely helpful for self-study of this complex subject. No such book is currently available in this area. Needless to say that the book is extremely important as a reference for researchers in motor drives and continuing education of industrial engineers. Selected materials of the book can also be taught in undergraduate and graduate courses.

Dr. Bimal K. Bose, IEEE Life Fellow
Emeritus Chair Professor of Electrical Engineering
(Formerly Condra Chair of Excellence in Power Electronics)
Member, U.S. National Academy of Engineering
Department of Electrical Engineering and Computer Science
The University of Tennessee, Knoxville
http://en.wikipedia.org/wiki/Bimal_Kumar_Bose

www.TechnicalBooksPDF.com

This page intentionally left blank

www.TechnicalBooksPDF.com

Chapter 1

Introduction to electric drives

Muhammed Fazlur Rahman[1]

1.1 The role of motor drives in modern industry and energy usage

Electric drives occupy a central role in many industrial processes and equipment. These continue to become ubiquitous every day, as more and more applications become highly automated, controlled precisely and efficient. There are many processes that benefit form continuously controllable drives. Material processing, handling, transportation, mining, rolling mills, machining centres and guidance systems are a few of the examples in which continuously variable speed is virtually indispensable nowadays. These processes also strive for higher control accuracy in order to deliver products the specifications of which are much tighter than before. The control accuracy must also overcome disturbances arising from supply conditions to the drive converter and load conditions applying on the drive shaft. Recently, electric drives are intruding into the main traction/motive element of vehicles, which for a long time has remained as the bastion of internal combustion engines. This may lead, potentially, to a huge expansion of application of electric drive systems. The use of drive systems for wind power conversion equipment is another application which is also opening up a new and large application area for electric drive systems.

It can be stated with confidence that the age of fixed speed motor drives is coming to an end in not too distant future. Continuously variable-speed drive systems allow the inflexible motor torque-speed characteristics of fixed speed drives to readily match with the characteristics of load. This is an attribute that is unmatched and unsurpassed by any other variable speed systems. The use of inverter-driven variable speed drives in air-conditioning systems, in household, offices, factories, pumping installations and in aircrafts has led to huge savings of energy. Many more applications are poised to benefit in terms of efficiency from the use of electric drives ranging in power from a few watts to a few megawatts, in speeds from a few revs/min to 100s of krevs/min. The vast application areas mentioned above require

[1]Energy Systems, School of Electrical Engineering and Telecommunications, The University of New South Wales Sydney, Australia

www.TechnicalBooksPDF.com

many different types of motors, associated appropriate power converters and controller designs. This book is an attempt to encompass the description of some of elements in electric drive systems.

The elements of an electric drive system are drawn from a number of disciplines as indicated in Figure 1.1. At the heart of an electric drive is the electric motor (AC, DC, switched reluctance and so on), the understanding and design of which stem from electromagnetic and machine theory. Design for certain steady-state performance in terms of cogging and developed torque, speed range and efficiency, and for meeting the requirements of an application are addressed increasingly through elaborate and very sophisticated design tools based on finite element analysis techniques. The dynamic performance of the machine and operating speed are addressed to some extent in this process; however, power electronic converters and control theory (real-time discrete control) have a large role to play in this. The representation of the load requires some basic understanding of mechanics for applications with fixed mass or moment of inertia. However, for more complex applications in robotics, multimachine drives with rotation in more than one axes requires deeper understanding of mechanics and mechanical system modelling.

The accuracy and bandwidth of sensors for sensing the applied voltages and currents to the motor, and the speed and position of the motor shaft also have important influence on the dynamics of the drive system. Isolated voltage and current sensors using the Hall and, recently, magneto resistive effects have delivered high voltage and current-sensing capabilities with galvanic isolation and high bandwidth. In some applications, speed and position sensors are a burden and a weak link in a drive system, not to mention their costs and requirement of secure and reliable housing. While voltage and current sensors can be located inside the converter cubicle, which is sometimes at a distance from the motor, cables from shaft sensors to the cubicle that houses the converter and controllers may be a serious issue for some applications. Often certain signals cannot be sensed, such as the air gap or rotor flux linkage and machine resistance. Elaborate model-based observers are used for obtaining these signals. Elimination of shaft position and

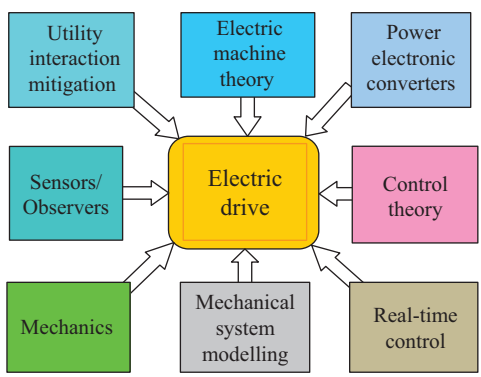


Figure 1.1 Elements of an electric drive system

www.TechnicalBooksPDF.com

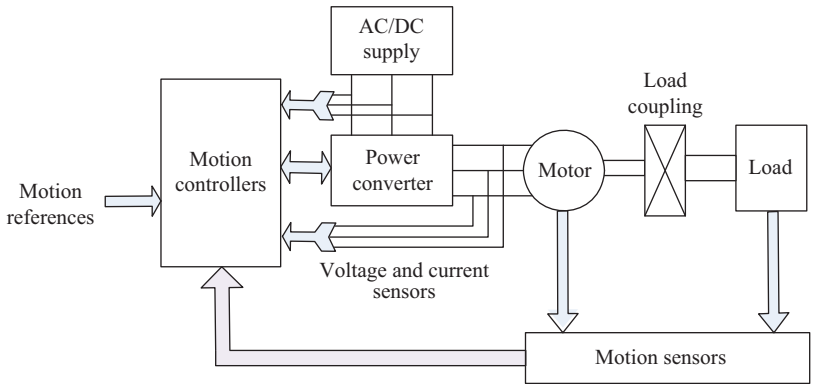


Figure 1.2 Typical structure of a variable-speed-drive system

speed sensors entirely and obtaining these signals using a variety of techniques which use analyses of the sensed voltages and currents to the motor are being aggressively developed.

Converter-driven drive systems which are connected to the AC grid for their power supply or inject power into the AC grid tend to inject harmonics into the grid, which in turn affects the performance of the motor drive. The topology and control of converter systems can mitigate this utility interaction to a large extent, at the cost its increased complexity of the converters and their controls. Figure 1.2 shows the typical arrangements of the elements of a drive system in which the motion references in terms of speed, position, torque and so on are available from a supervisory system that generates these references according to the requirements of the process that is driven by the drive system. In a machine-tool-drive system, often several machines with the drive structure of Figure 1.2 are simultaneously coordinated and driven with references that specify the motions of each drive. The accuracy and dynamics which the drives achieve determine the quality of the machined product and the productivity of the process.

1.2 Controller hierarchy for electric drives

From the fundamental laws of motion, the traditional structure of controller arrangements follows the hierarchical structure indicated in Figure 1.3. The acceleration (torque), speed and position controllers are embedded within progressively faster and decoupled control loops, whereby the controllers of each section can be designed and tuned to address the local indices and limitations of current (torque), speed and position without consideration of the other controllers. The innermost controller is for torque, the reference for which is the output of the speed controller. The reference for the speed controller is the output from the position controller, if any. The speed reference also specifies the rotor/air-gap flux; it is normally at the rated level for all speed below base speed and reduced (field weakening) for speed that are

www.TechnicalBooksPDF.com

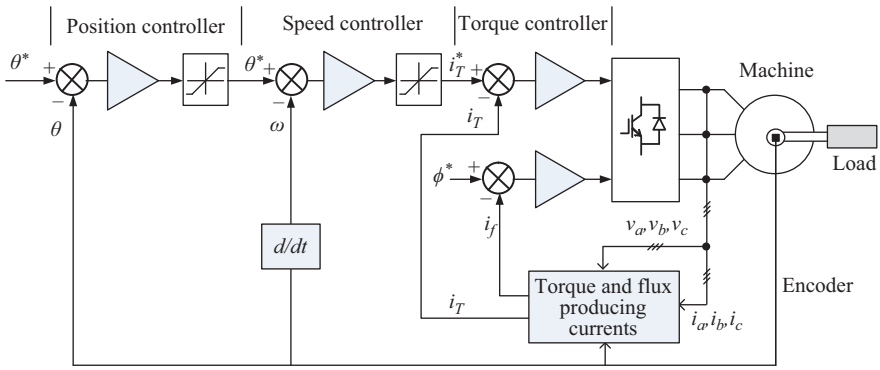


Figure 1.3 The hierarchical controller scheme from Newton's laws of motion

higher than base speed. The control bandwidth of each stage is six to ten times faster than the preceding stage, leading to decoupled control. This practice is advantageous to application engineers who install and maintain the drive in an application.

Figure 1.4(a) and (b) depicts the drive structure for DC motor drives with pulse-width modulated converters for the armature and field circuits. For motor drives up to a few kW, permanent magnets may be used for filed excitation, leading to considerable reduction of motor size and additional windings that allows better decoupling of the torque producing (armature) currents and the rotor field, resulting also in improved operational features. In this case, Converter 2 is not required, and the drive speed is limited to base speed that occurs for the rated armature voltage applied. Most DC servo motors have this structure. For larger power capacity DC drives, thyristor converters are used for both armature and field circuits. A mains-frequency (50 or 60 Hz) input transformer is often required to match the motor rated voltage with the utility AC input voltage for operation of such drives. In order to address the utility interaction, the AC–DC converter, which makes available the DC voltage source to the pulse width modulation (PWM) converter 1, is normally a PWM rectifier allowing unity power factor rectified DC supply for the PWM drive. This calls for an additional converter, unlike the case for naturally commutated thyristor converter-driven DC motor drive. Mitigation of utility interaction for thyristor converter-driven DC motor drive in larger capacity is often addressed through the use of multiphase converters with pulse number higher than 6.

The converter and controller structure for a three-phase AC motor drive is indicated by the concise Figure 1.5, which includes similar hierarchical speed and torque/current controllers of Figure 1.3 or 1.4. For such drives, the decoupled torque and rotor flux controls are exercised through the inverter by establishing torque and flux-producing current both supplied by the same inverter. This calls for motor voltages and currents to be transformed to quadrature synchronously rotating reference frame (for the AC induction motor) or the quadrature rotating frame that rotates as the same speed as the rotor. These transformations have an intermediate quadrature stage, called the $\alpha\beta$ reference frame which is stationary. The two stage

www.TechnicalBooksPDF.com

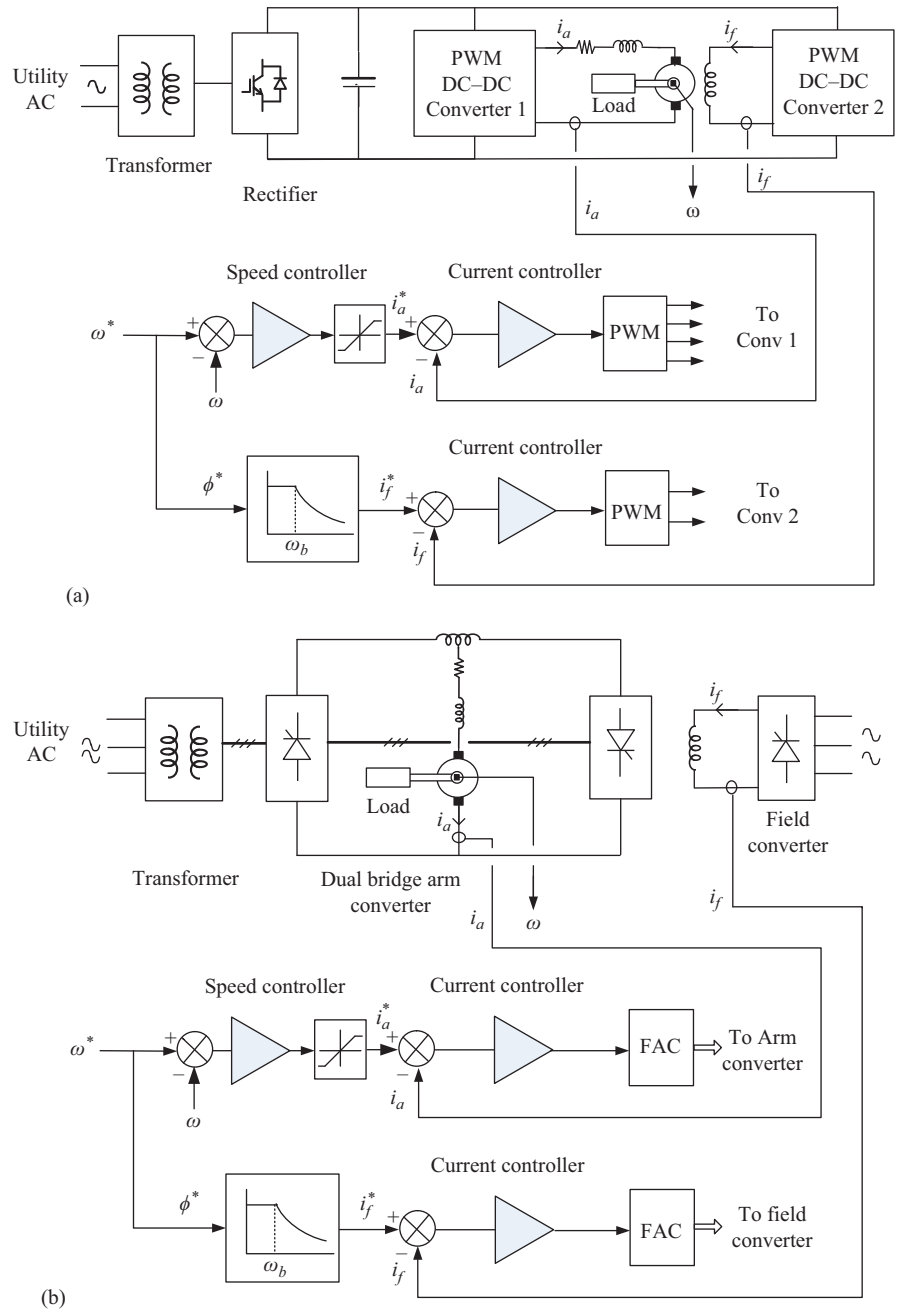


Figure 1.4 (a) PWM drive structure DC servo motor drives and (b) thyristor converter-driven DC motor drive with a field weakening converter

www.TechnicalBooksPDF.com

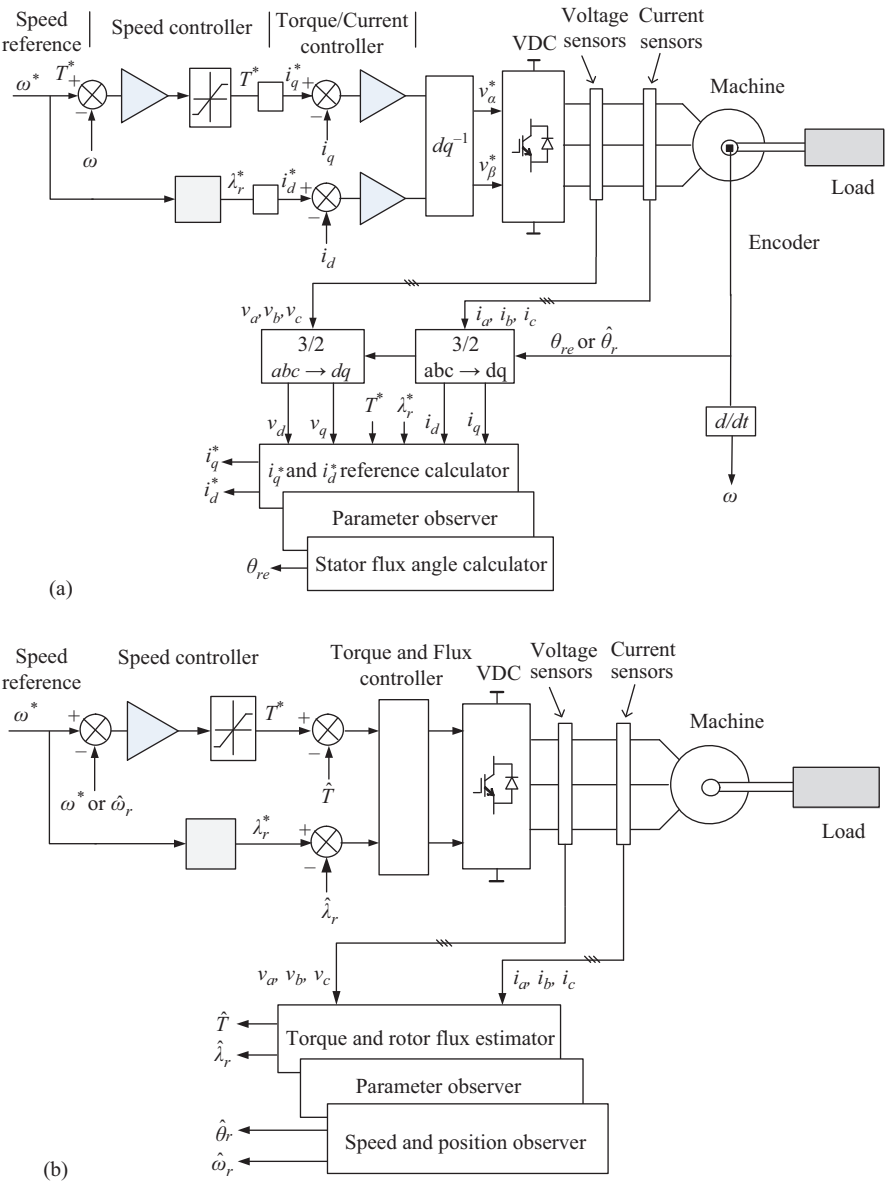


Figure 1.5 (a) The RFOC scheme of an AC motor drive and (b) the DTC/DTFC scheme of an AC motor drive

transformation leads to v_d, v_q, i_d and i_q variables that are DC quantities when the motor runs at a constant speed.

The torque and rotor flux references produced by the speed controller may be regulated in two ways. In one, the torque and flux references are converted into

www.TechnicalBooksPDF.com

current references for i_q and i_d, respectively, using machine parameters which may vary with operating condition, and these currents are then regulated in the synchronous (for AC Induction) or in the rotor reference frame (for AC Synchronous) machines. Control of torque and rotor flux via decoupled currents, i_d and i_q, is the so-called rotor flux oriented control (RFOC) of Figure 1.5(a). It requires low-noise digital rotor speed/position sensors that have far higher resolution, accurate and bandwidth than DC analogue tacho-generators and position sensors. The *dq* current controller outputs are then used with some feedforward speed-dependent compensation to produce the voltage references for the PWM inverter/motor. The delay due to the PWM current controllers and the requirement for the digital shaft position/speed sensor in this scheme is unavoidable. The variation of parameters, such as rotor time constant and *q*-axis inductance of an AC machine normally calls for parameter observer techniques to be employed, so that the current references can be computed correctly and accurately, online.

In another scheme, feedback signals of the torque and rotor flux are obtained from the machine model using only the measured voltages and currents of the AC machine, without requiring the sensor on the shaft. Variation of machine model parameters affect the accuracy of the torque and flux observers, calling for refined observers of machine parameters, torque and rotor flux. These observers also produce rotor speed and position information which may be used for sensorless control. This is the so-called direct torque control (DTC) and direct torque and flux controls (DTFC) of Figure 1.5(b). Because of no requirement of speed or position signals from the motor shaft, transformation of voltage and currents to the synchronous/rotor references are not necessary. Furthermore, torque and rotor flux can be controlled directly via closed loops using computed signals of feedback torque and flux.

1.3 Quadrant operation of a drive and typical load torque

The torque – speed characteristic of the load – largely determines the machine, converter, and controller selections for the drive system. Figure 1.6 indicated three typical load characteristics, namely viscous friction, traction and compressor loads indicated by 1, 2 and 3, respectively, in Figure 1.6. Applications requiring operation in both forward and reverse directions entail some simplifications for DC motor dives. For AC motor drives, a three-phase inverter will cover operation in all four quadrants.

Torque and speed characteristics for motor for asynchronous machines, such as AC induction and DC machines are also shown in all four quadrants in Figure 1.6. Motor and load characteristics for the types of loads 1–3 duplicate in quadrants 1 and 3. Machines are operated regenerative quadrants Q2 and Q4 for rapid dynamic response, which also results in energy savings if the input converter circuit permits it.

The load torque-speed characteristics are easily represented by a linear equation, such as $T_L = K\omega$ for load 1, a constant-power equation such $T_L = K/\omega$for load 2, and a parabolic equation like $T_L = K\omega^2$ for load 3. Load T–ω characteristics are normally available from the application, and these can be represented numerically using approximating equations. Unidirectional fixed load torque occurs in hoist and lift

www.TechnicalBooksPDF.com

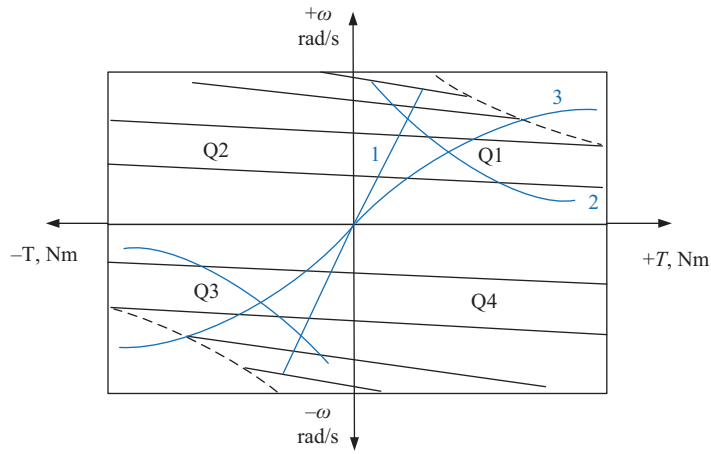


Figure 1.6 Torque-speed characteristics of asynchronous type motors and loads

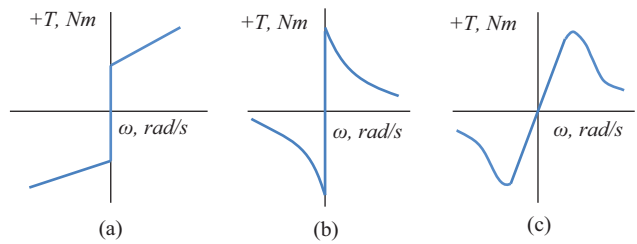


Figure 1.7 Loads with combinations of static and other frictions

loads, which are represented by a fixed term. Some loads have static friction, such as indicated in Figure 1.7(a) and (b). In general, a typical load may exhibit combinations some of the above simplified representations as indicated by Figure 1.7(c). For all types of loads, the motor T–ω characteristic must cover it in terms of their maximum values, in dynamic and steady states. Furthermore, the machine and load characteristics within the maximum operating boundary must have stable operating point. The converter must also have the required ratings in terms of voltage and current, and its T–ω characteristic should match closely with the load T–ω characteristic in order to optimize the machine size for the load that the motor is required to drive.

1.4 Power switch and integrated control devices for drive systems

There have been tremendous strides in the voltage and current capacities, switching frequency and many other characteristics of switching devices used in drive systems. This trend is spurred by the need to increase the efficiency and control

www.TechnicalBooksPDF.com

dynamics of drive systems at all power levels. Gate drives and interfacing circuits, modulators and sensors have followed this trend. Controller platforms in terms dedicated microcontrollers, digital signal processors and field programmable gate arrays have been evolving at a rapid pace. Recent developments and availability of wide band-gap switches such SiC and GAN devices indicate much improved drive performance in the near future. Many very powerful modelling platforms are also becoming available that allows drive system evaluations in many aspects at the design stage, before it is physically tested.

1.5 Overview of chapters

This book is a compilation 17 chapters, including this chapter, Introduction to Electric drives. Attempts have been made to cover the major types of motor drives widely used in industry and several aspects of new developments in machines, sensors drive control systems. Whenever possible, recent developments in converters, machines and control techniques have been sourced from eminent contributors to the topics. The main aim has been to cover motor drive technology for DC, AC and switched reluctance motors. The underlying effort is to combine the existing and recent developments in drive systems for the benefit of new researchers and engineers who aim to specialize in this area.

The basic elements of electric drive system are introduced in Chapter 1. The knowledge base comprising several disciplines that interact and encompass the selection of diverse components that go into a drive system for an application are brought out. Typical drive structures and control hierarchies that guide the designer to build an inherently reliable and well-protected drive system are discussed here. The multitudes of relay sequencing and outer protection mechanisms that surround a drive are not included however. These are application-specific issues best learned in application environments.

Chapter 2 gives an overview of machines for application over the full range of power spectrum. Steady-state torque-speed boundaries in all four quadrants within and above the base-speed for the major types of conventional DC and AC machines are introduced first, followed by the dynamic models of these machines. A limited, by no means complete, analysis of the two dominant types of AC machine (the AC induction and synchronous) dynamics is included with a view to guide the reader to appreciate the necessity for transformations of voltages and currents and flux linkages of a three-phase machine to one of the rotating axes, in order to appreciate how current controls are used for controlling the torque and flux linkages independently of each other. The logical control structures, the rotor flux-oriented control, for these machines then follow for each machine type. This is followed by a brief description of sensor technologies and associated hardware. Finally, an overview of recent developments in the AC induction and PM synchronous machines is included.

Chapter 3 presents the most popular DC–AC inverter topologies, namely, the two-level and three-level NPC inverter, used for the electric drives. It covers the

www.TechnicalBooksPDF.com

sinusoidal PWM (SPWM) and Space vector PWM (SVPWM) methods for the two-level and three-level NPC inverters. The emphasis is given to the implementation aspect of these PWM methods. It is shown that the SVPWM method can be implemented in the same way as the SPWM method with small modification in the sinusoidal reference signals. The neutral-point voltage balancing issue associated with the three-level NPC inverter is discussed. A popular method for balancing the neutral-point voltage is also discussed.

Chapter 4 covers DC motor drives. Steady-state and dynamic models are treated in detail first, before introducing single and three-phase thyristor and PWM DC–DC converters which are widely used for high and low-power DC motor drives, respectively, The inner current control loop design technique and its tuning using the Ziegler–Nichols step-response technique is introduced. Power quality issues are then addressed via control of front-end rectifier current shaping techniques. Several simulation results for thyristor and PWM DC–DC converter-driven DC motor with power factor corrected front end rectifier are included.

Control of the synchronous machine has been spread between Chapters 5 and 6 because of the enormous advances that has taken place in the analysis and control techniques associated with this motor. Chapter 5 covers several types of controllers which address issues of efficiency and controller design. This chapter also includes a suite of simulations on dynamic system modelling supported by experimental results.

Chapter 6 starts with a review of vector or RFOC control techniques for permanent magnet synchronous machines and then focuses on trajectory controls for high efficiency and field weakening while maintaining current voltage limits of the motor. The maximum torque per ampere and field-weakening control trajectories and their dependencies on machine parameters are described. Both Chapters 5 and 6 briefly introduce sensorless control, without including any analysis and performance evaluation of the several available techniques of sensorless control, leaving this to a latter Chapter 14.

The brushless DC motor has construction simplicity and reduced sensor cost compared to a PMSM. As a consequence, it is used in a wide range of applications. Chapter 7 includes full analysis and a dynamic model of this motor in the *dq* reference frame, taking into consideration the non-sinusoidal back-emf of the machine. A pseudo vector control (RFOC) is described which leads generation of current reference which leads to substantially reduced torque ripple compared to the conventional trapezoidal phase current control. It has also been shown that field-weakening operation can be easily adopted in this pseudo RFOC.

Chapter 8 gives a comprehensive analysis of the switched reluctance motor drive, starting with machine-inductance waveform, the required current waveform, its converter and shaft interfacing requirements for speed and current control. This chapter is supplemented with several examples of emerging application in drives for appliances and electric vehicles.

The treatment of the DTC technique for induction machines, which emerged after RFOC in the late 1990s for this machine, is included in Chapter 9. The basic of the DTC concept is presented first with representation of how stator voltage

www.TechnicalBooksPDF.com

vectors applied via an inverter controls the direction and amplitude of the stator flux vector with respect to the rotor flux vector. Several techniques of varying complexity for estimation of stator and rotor fluxes are also included, followed by simulation and experimental results of torque responses and accuracy.

This chapter describes the DTC technique for PM synchronous machines. It starts with a brief review of the context in which DTC stands, including the underlying theory (which had existed prior) and methods that have been used to apply DTC to permanent magnet synchronous machines. Some comparative evaluations are included with a view to help researchers and engineers to further develop the method and apply it to high-performance PMSM drives in various applications.

Chapter 11 is on DTC for matrix-converter-driven interior permanent magnet synchronous machine drive. It starts with a brief overview on the fundamentals of matrix converter followed by the implementation of bidirectional switches for matrix converter. Two current commutation strategies based on input voltage sign and output current direction, respectively, are presented in this chapter. Some other practical issues of matrix converter are also discussed in this chapter, in terms of input filter design and over-voltage protection. Different modulation strategies for matrix converter are briefly reviewed in this chapter. Among these methods, the indirect space vector modulation is demonstrated by considering the matrix converter as a two-stage converter, rectifier and inverter stages. The open-loop and closed-loop input power factor compensation schemes are presented followed by the DTC schemes for matrix converter drives.

Chapter 12 describes how to implement an online identification method for induction motors within a field oriented control by using least square (LS) methods. It first describes the development of an experimental rig by a step-by-step approach, where the different components of the set-up are described to enable readers to have a reference on their own. The LS online identification technique has been explained for its implementation. The LS permits easily the online parameter estimation by non-invasive real-time measurements of voltages and currents but requires a suitable signal processing, which has been fully described. Some experimental results have been shown to prove the flexibility of the experimental rig to estimate and validate the parameters under different magnetic conditions.

Chapter 13 reviews the available sensorless induction motor control techniques with focus on indirect rotor-flux-oriented control. It is pointed out that although sensorless induction motor control today is a mature field, there are still some openings for further research. The importance of obtaining complete stability with an estimator which eliminates the sensitivity to the stator resistance is discussed. The difficulty of achieving stability in the regeneration region of such estimators is also mentioned. It is noted that although the rotor resistance does not affect the field orientation in a sensorless drive, it does affect the accuracy of the speed estimation. Rotor-resistance adaptation for a sensorless drive is mentioned for future work.

Chapter 14 presents several key rotor position and speed-estimation methods used in sensorless permanent magnet synchronous motor drives. It bring out that open-loop back-emf estimation from impressed stator voltages and measured

www.TechnicalBooksPDF.com

currents leads to extreme sensitivity to machine parameters and inverter non-linearities, especially at low speed. Closed-loop observers built on machine models which do not take into account parameters are far better; however, these still suffer from the same factors. The chapter then describes the techniques based on high-frequency injection of currents on the fundamental input excitation, which covers wide speed range including zero speed. This is followed by some coverage on a new method which used current derivative measurements during PWM excitation. Several simulation results comparing the strengths of these techniques are included.

The application of model predictive control technique to a 2-level inverter-driven induction motor is described in Chapter 15. The state space model of the IM and inverter is discussed first. The basic principle of predictive torque control and its application on IM drive is presented in detail. The systematic process of finding the cost function is explained. This process can be used for incorporating other objectives in the cost function if required. The complexity of the PTC algorithm, in terms of computational burden and cost function design, is no longer an issue for a specific objective as shown in this chapter. Experimental results illustrating the finite-state predictive torque control algorithm and yielding good performance in terms of torque and flux ripple, stator current total harmonic distortion, robustness against load torque disturbance, step torque response and step speed response are presented.

Variable-speed AC drives are nowadays based on three-phase electrical machines fed by power electronic converters acting as power interface between the electrical machine and AC or DC power sources. Nevertheless, in the last two decades, the multiphase electrical drives have become an interesting alternative for particular applications. However, the application of multiphase drives is still limited, mainly due to their complexity and control that somehow make them more difficult to handle with respect to the conventional three-phase counterparts. The work presented in Chapter 16 intends to be a useful tool to disseminate the fundamental concepts of multiphase drives to students and application engineers.

Fractional-slot concentrated-wound AC machines have undergone intensive research and development recently due their compactness, ease of manufacturing and maintenance, and low cost compared to conventional AC machines. Many new applications in appliances, electric traction, and aerospace industries are already possible. These machines pose some control challenges due to the high number of poles, which can be taken advantage of in gearless drives, and the non-sinusoidal nature of its stator mmf. Chapter 17 is focused on the design and performance aspects of the fractional-slot concentrated-wound machines.

List of symbols

T	Torque in Nm
ω	Rotational speed in rad/s
θ	Position of rotor is rad
v_a, v_b, v_c	Stator voltages

www.TechnicalBooksPDF.com

i_t	Torque component of current
i_f	Flux component of current
Φ	Flux linkage
i_a, i_b, i_c	Stator currents
ω_r	Rotational speed

Glossary of terms

RFOC	Rotor-flux-oriented control
PWM	The pulse width modulation (PWM) technique which involves varying reference signal for generation of switching signals for inverter switches
Sinusoidal PWM (SPWM)	The pulse width modulation (PWM) technique which involves sinusoidal varying reference signal for generation of switching signals for inverter switches
SVM	Space vector modulation
SVPWM	Space vector pulse width modulation technique
IPMSM	Interior permanent magnet synchronous motor
Multi-level inverter	An inverter which has more than two levels of voltage in the output
Power electronic converters	AC–DC or DC–DC or AC–AC converters using power electronics switches, i.e. thyristors, IGBTs, MOSFETs
Inverter	A switching circuit used for generation of AC voltage waveforms
NPC	Neutral point clamp inverter
DTC	Direct torque control
DTFC	Direct torque and flux control
DSP	Digital signal processors
WBG	Wide bandgap devices
GaN	Gallium Nitride switch device
THD	Total harmonic distortion

Further reading

[1] Electric Drives – I. Boldea and S. A. Nasar, CRC Press, Boca Raton, FL, Third Edition, 2017.
[2] Control of Electric Machine Drive Systems – S.-K. Sul, Wiley and IEEE Press, Piscataway, NJ, 2011
[3] Advanced Electrical Drives – R. de Donker, Springer, New York, 2011.
[4] AC Electric Motors Control, Book edited by F. Giri, John Wiley, Chichester, 2013.
[5] Control of Electric Drives – W. Leonhard, Springer, Berlin, 2001.

www.TechnicalBooksPDF.com

[6] Electric Motor Drives, Modelling, Analysis and Control – R. Krishnan, Prentice Hall, Upper Saddle River, NJ, 2001.
[7] Power Electronics and Motor Drives – B. K. Bose, Academic Press, New York, 2006.
[8] Electric Drives: An Integrative Approach – N. Mohan, MNPREE, Hoboken, NJ, 2003.
[9] Vector Control and Dynamics of AC Drives – D. W. Novotny and T. A. Lipo, Oxford Science Publication, Oxford, 1997.
[10] Sensorless Vector and Direct Torque Control – P. Vas, Oxford Science Publications, Oxford, 1998.
[11] Electric machines and Drives – G. R. Slemon, Addison Wesley, Boston, MA, 1992.
[12] Power Electronic Control of AC Motors – JMD Murphy and FG Turnbull, Pergamon Press, Oxford, 1988.
[13] Power Electronics and AC Drives – B. K. Bose, Prentice Hall, Upper Saddle River, NJ, 1987.

www.TechnicalBooksPDF.com

Chapter 2

Electric machines, dynamic models and sensors in drive systems

Mohammad Fazlur Rahman[1], *Rukmi Dutta*[1] *and Dan Xiao*[1]

2.1 Introduction

This chapter is meant for researchers who may be looking for brief overview of electric machines, dynamic models and sensors that are used in electric drive systems. An attempt is made to point to new developments in machines and sensors and also to what is available currently in modeling techniques for drive systems. This may help the reader to appreciate the more elaborate and in-depth coverage of topics that subsequent chapters include.

2.2 Electric machines and torque–speed (T–ω) boundaries

From an application view point, the steady-state T–ω boundaries that prevailing electric machines offer is the first step in considering a drive motor for the application at hand. Issues of cost, controllability, dynamic performance, sensor bandwidth, maintenance, operating temperature, efficiency, expected drive system life and converter choices are then taken into consideration.

The T–ω boundaries of several types of electric machines that also lend themselves to highly dynamical control are indicated in Figure 2.1. For a long period of time prior to the development of fast power semiconductor switches in the form of MOSFETs and IGBTs since the 1980s, the DC machine (DCM) was the main type of machines applied to applications in the 160 kW to sub-kW power range covering speeds around 6,000 rev/min in the low power range to a few 100 rev/min in the high power range. Thyristor converters were the main available switches during this period, which meant that achievable control dynamics, especially at the higher power end, was modest. At the low power end however, the DC servo motor offered many design innovations in terms of very low inertia in the form printed armature and pancake type structures that offered very high dynamic

[1]Energy Systems, School of Electrical Engineering and Telecommunications, The University of New South Wales Sydney, Australia

www.TechnicalBooksPDF.com

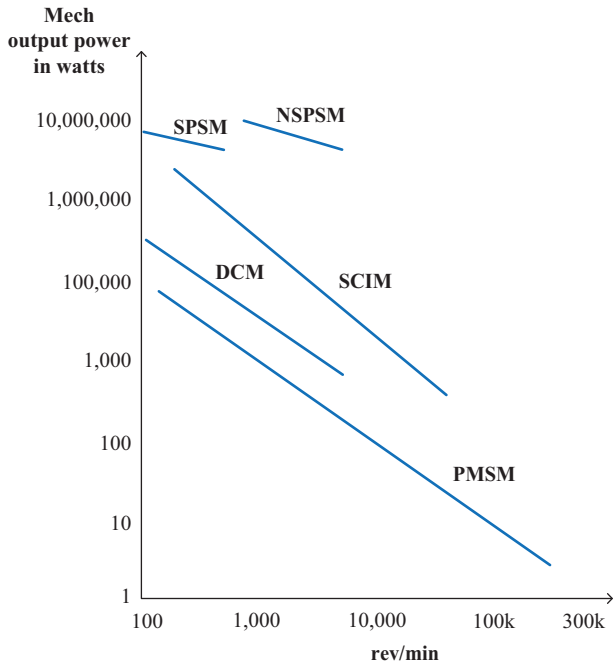


Figure 2.1 Power–speed boundaries of available electric machines

response at the low power end. With the advent of fast semiconductors of high power handling and high-speed signal processing capabilities, the squirrel-cage induction machine offered a wider torque and speed range with high dynamics. The last attribute, i.e., highly dynamic control, achievable with this rugged, cheap and ubiquitous motor became possible with two notable developments, namely, the rotor-flux-oriented (vector) control and the direct torque control techniques in the 1980s and 1990s. These developments allowed the scquirrel cage induction motor (SCIM) to increase its application areas and the terms "industrial workhorse" was, and still can be aptly, applied to SCIM drives. The lack of efficiency and low power-to-weight ratio of the SCIM were the main drawbacks that are being overcome with permanent magnet synchronous machines (PMSMs). This latter category of AC machines has rotor magnetic excitation via high energy-density permanent magnets which are not very expensive. As a result, PMSMs with various stator and rotor designs now offer highly efficient and high power-to-weight ratio machines with high dynamic capability at a reasonable cost. It is interesting to note virtually all electric vehicles and wind turbine-driven generators at multimegawatt power range are adopting this motor.

The high power range of applications covering multi-megawatt drives in large power applications, not including PMSMs of similar power capacity for wind energy systems, are still applications which are better served by the salient-pole and non-salient pole synchronous machine, SPSM and NSPSM, respectively. The cost of magnets vs. efficiency gain issues play important roles in this choice.

www.TechnicalBooksPDF.com

2.3 *T–ω* characteristics within torque–speed boundaries

For each of the motor types indicated in Figure 2.1, the torque–speed characteristics for each type are also of importance is some applications. Some applications, such as generators for wind turbines and machines for large pumps and compressors do not require significant speed range over the machine base speed. For other applications, especially in coilers and rolling mill applications, some speed range above base speed with constant power is required. This is normally arranged by weakening the air gap or rotor field via field weakening. The required *T–ω* characteristics of such drives are indicated in Figure 2.2.

Typical *T–ω* characteristics of asynchronous type machines (DCM and induction motor (IM)) indicated over several speed regions with and without field weakening in quadrant 1 are indicated in Figure 2.2. These characteristics are reversible in quadrant 3 and extend into the regenerative quadrants 2 and 4 with similar slopes. The more droopy characteristics at high and low speeds are due to weakened field and due to voltage drop in the stator/armature/rotor resistances, respectively. While the effect of field weakening on speed droop with shaft torque is an inherent machine characteristic, the latter can be compensated via estimation of parameters in DC and IM drives. It should be clear that the torque–speed

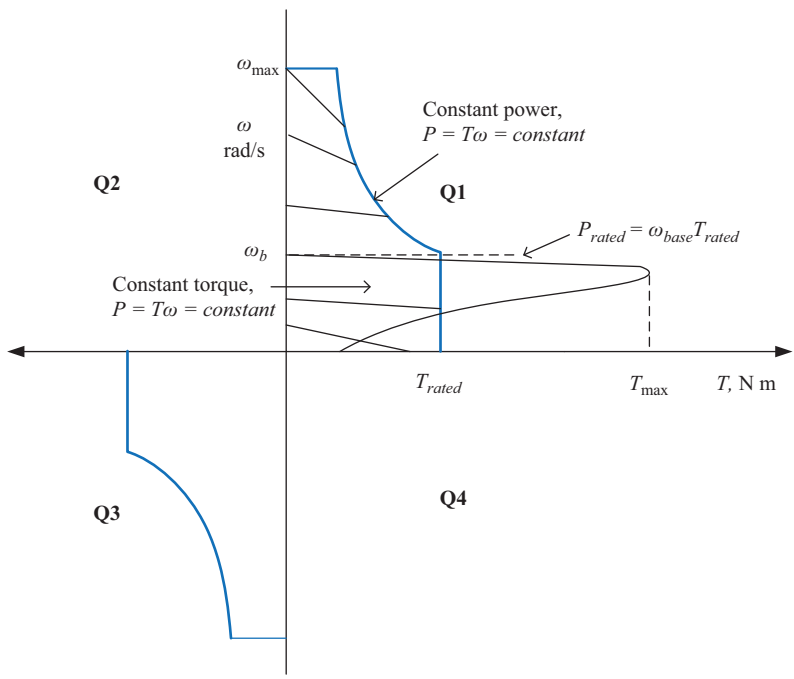


Figure 2.2 Torque speed and power requirements of typical traction drives (e.g., electric vehicles and trains) and coilers in paper, textile and other mill drives

www.TechnicalBooksPDF.com

characteristics of Figure 2.2 are normally found from steady-state representation of the machine. The reader is assumed to be familiar with this method of analysis.

For meeting the steady-state requirements of a drive, the superposition of load and machine torque–speed characteristics leads to appropriate selection of the motor, the converter and controller selections. For meeting the dynamic performance requirements, controller design has to be approached via the use of dynamic models of the drive.

2.4 Dynamic models of machines and simulation

This section presents dynamic models of DC, AC induction and synchronous machines, based on which controllers are designed.

2.4.1 Dynamic model of DC machines

The dynamic model of the separately excited DCM is rather simple, mainly owing to the commutator and brush assembly which leads orthogonal fields produced by field (in stator) and armature (in rotor) windings.

$$V_a = R_a i_a + L_a \frac{di_a}{dt} + K_f\, i_f \omega_m \tag{2.1}$$

$$v_f = R_f i_f + L_f \frac{di_f}{dt} \tag{2.2}$$

$$T = K_f i_f i_a \tag{2.3}$$

For machines with fixed excitation, such as with permanent magnet excitations, the developed torque T and back emf are determined by the speed and armature current i_a, respectively, and armature voltage to speed transfer characteristic is represented as in Figure 2.3. The motor is driven with an inner current (or torque) regulator as indicated in Figure 1.4(a) and (b) in Chapter 1, up to the base speed when the armature voltage v_a reaches the machine-rated voltage which is also determined by maximum the DC voltage which the converter can supply to the armature. Applications requiring operation at higher than the base speed reduces the field current i_f according to the speed reference. The inner current controller is designed to have a bandwidth significantly higher than the speed controller but lower than the bandwidth achievable with rated voltage applied to the machine with field excitation reduced to zero (stalled condition). Some compensation for the machine back emf

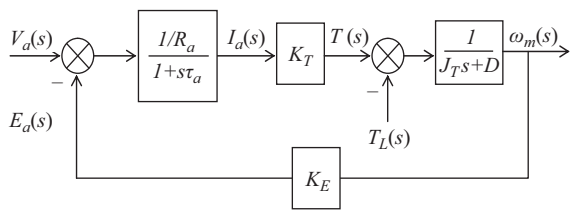


Figure 2.3 Voltage to speed transfer characteristic of a DC motor

www.TechnicalBooksPDF.com

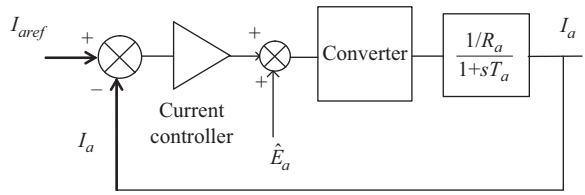


Figure 2.4 Armature current controller for a DC motor drive

as a feed forward signal to the voltage reference generator for the power converter during normal operation is normally used to enhance the transient response of the current control loop (see Figure 2.4).

Figure 2.5(a) and (b) illustrates the armature current dynamics of a DC motor under a unit step reference. The armature current settles at its reference value within the predefined settling time, 8 ms, in both of simulation and experiment.

2.4.2 Dynamics model of synchronous machines in rotor reference frame [1]

The synchronous machine model that allows the developed torque and air gap flux to be related to currents supplied from a converter is based on the representation of machine variables (voltages and currents) and machine fluxes in an orthogonal rotor *dq* frame. In this frame, the *d*-axis is aligned with the rotor *d*-axis indicated in Figure 2.5. The advantage of this representation is the fast and decoupled controls of torque and flux linkage via fictitious currents i_q and i_d in q and d axes, the so-called rotor flux-oriented (vector) control technique.

The general stator to rotor transformation is given by

$$\begin{bmatrix} f_d \\ f_q \\ f_o \end{bmatrix} = \frac{2}{3}\begin{bmatrix} \cos\theta & \cos(\theta-120^\circ) & \cos(\theta-240^\circ) \\ -\sin\theta & -\sin(\theta-120^\circ) & -\sin(\theta-240^\circ) \\ \frac{1}{2} & \frac{1}{2} & \frac{1}{2} \end{bmatrix}\begin{bmatrix} f_a \\ f_b \\ f_c \end{bmatrix} \tag{2.4}$$

in which f_a–f_b represent stator voltages, currents and flux linkages, f_d–f_q represent these variables in the rotor *dq* frame and θ is the rotor position in electrical radians.

2.4.2.1 Machine inductance and flux linkages

By referring to the geometry of the typical synchronous machine of Figure 2.6, the self-inductance of the phase windings can be assumed to vary sinusoidally with rotor angular position, as indicated in Figure 2.7 for phase "a" winding. It is assumed that these are similar for the other two phases, except for the phase shift of 120° electrical, from each.

Thus, the self-inductances are

$$\begin{aligned} L_{aas} &= L_A + L_B\cos 2\theta; \quad L_{bbs} = L_A + L_B\cos 2(\theta-120^\circ); \\ L_{ccs} &= L_A + L_B\cos 2(\theta+120^\circ) \end{aligned} \tag{2.5}$$

www.TechnicalBooksPDF.com

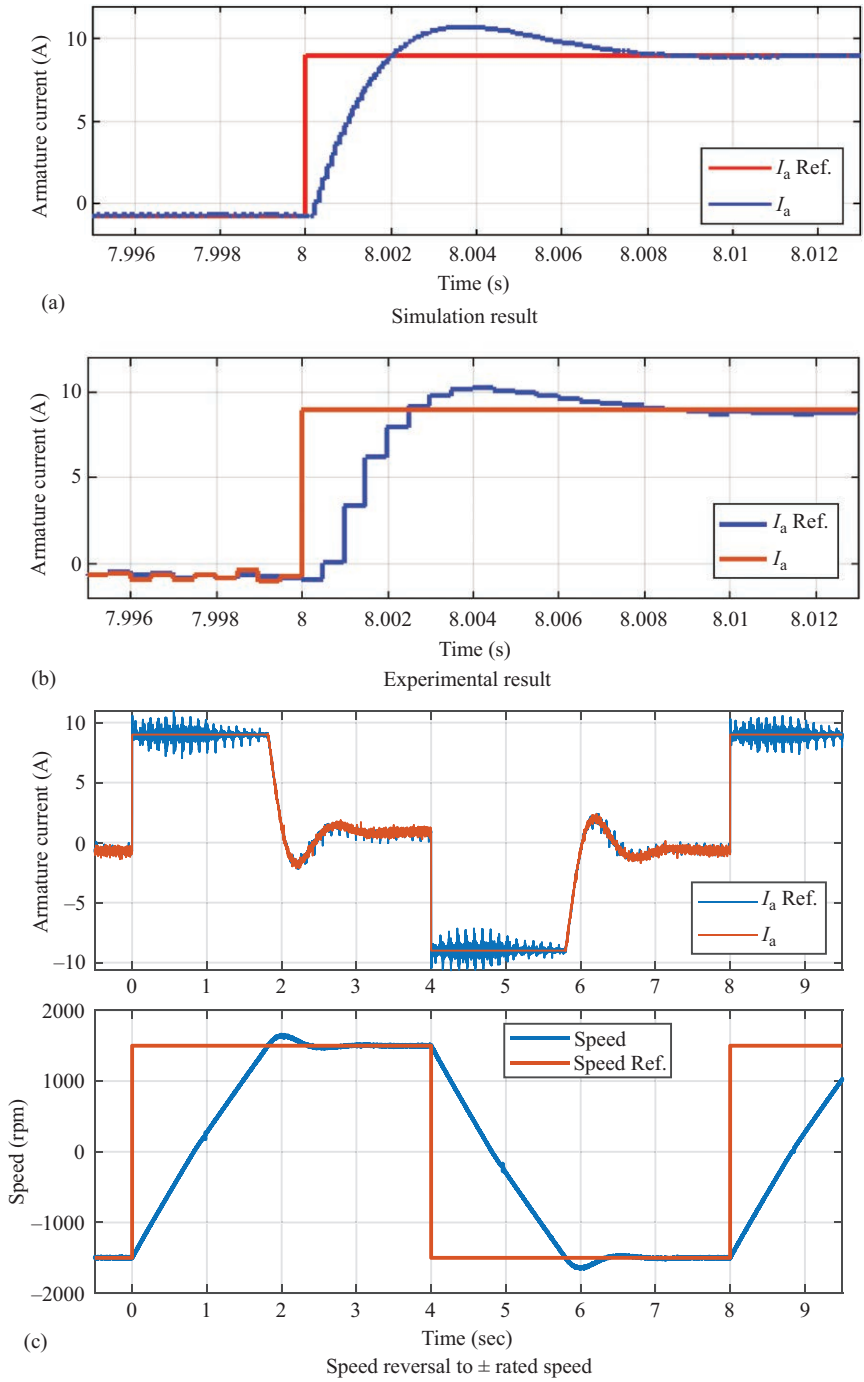


Figure 2.5 Step responses of armature current of DC motor (a) simulation, (b) experimental and (c) speed response under speed reversal, with PI controllers

www.TechnicalBooksPDF.com

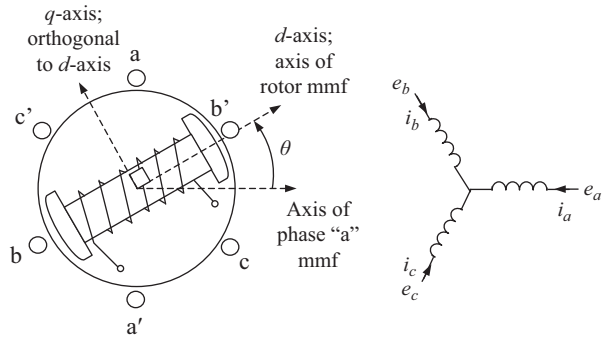


Figure 2.6 Synchronous machine geometry and stator and rotor windings

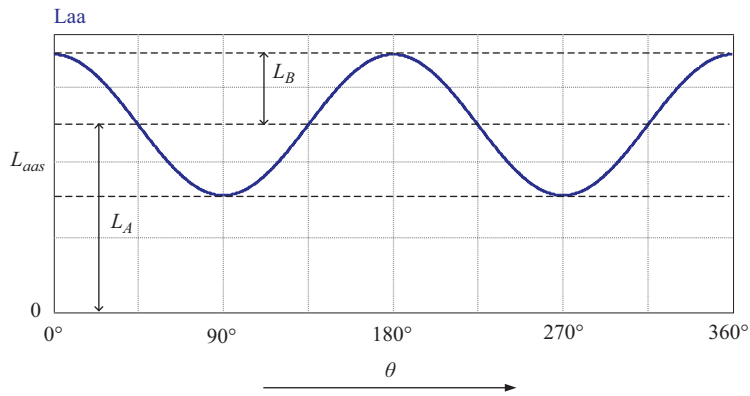


Figure 2.7 Stator winding inductance variation with angular position

where the maximum and minimum values of the inductance with the help of L_A and L_B are indicated in Figure 2.7.

The mutual inductances between the phase and the rotor windings can also be written as

$$L_{ab} = L_{ba} = -\left[\frac{1}{2}L_A + L_B \cos 2(\theta + 30^\circ)\right];\ L_{bc} = L_{cb} = -\left[\frac{1}{2}L_A + L_B \cos 2(\theta - 90^\circ)\right];$$
$$L_{ca} = L_{ac} = -\left[\frac{1}{2}L_A + L_B \cos 2(\theta + 150^\circ)\right] \tag{2.6}$$

$$L_{af} = L_{fa} = L_m \cos\theta;\quad L_{bf} = L_{fb} = L_m \cos(\theta - 120^\circ);\quad L_{cf} = L_{fc} = L_m \cos(\theta - 240^\circ) \tag{2.7}$$

www.TechnicalBooksPDF.com

The flux linkages of phase a, b and c windings, in terms of inductances, phase currents and rotor excitation, are given by

$$\lambda_a = \{L_A + L_B \cos 2\theta\} i_a - \left\{\frac{1}{2}L_A + L_B \cos 2(\theta + 30^\circ)\right\} i_b - \left\{\frac{1}{2}L_A + L_B \cos 2(\theta + 150^\circ)\right\} i_c + L_{af} i_f \tag{2.8}$$

$$\lambda_b = -\left\{\frac{1}{2}L_A + L_B \cos 2(\theta + 30^\circ)\right\} i_a + \left\{\frac{1}{2}L_A + L_B \cos 2(\theta - 120^\circ)\right\} i_b - \left\{\frac{1}{2}L_A + L_B \cos 2(\theta - 90^\circ)\right\} i_c + L_{bf} i_f \tag{2.9}$$

$$\lambda_c = -\left\{\frac{1}{2}L_A + L_B \cos 2(\theta + 150^\circ)\right\} i_a - \left\{\frac{1}{2}L_A + L_B \cos 2(\theta - 90^\circ)\right\} i_b + \left\{\frac{1}{2}L_A + L_B \cos 2(\theta - 240^\circ)\right\} i_c + L_{cf} i_f \tag{2.10}$$

By transforming flux linkages λ_a, λ_b and λ_c to rotor dq axes using the transformation of (2.4), stator flux linkages along the d and q axes are

$$\lambda_d = \left(L_A + \frac{1}{2}L_A + \frac{3}{2}L_B\right) i_d + L_{af} i_f = L_d i_d + L_m i_f = L_d i_d + \psi_f \tag{2.11}$$

$$\lambda_q = \left(L_A + \frac{1}{2}L_A - \frac{3}{2}L_B\right) i_q = L_q i_q \tag{2.12}$$

$$\lambda_s = \sqrt{\lambda_d^2 + \lambda_q^2} \tag{2.13}$$

where ψ_f represents the stator flux winding linkages due to rotor excitation, hereafter assumed to remain constant, as in a permanent magnet (PM)-excited machine. L_d and L_q are the inductances of fictitious stator windings in the rotor dq axes, i_d and i_q are stator currents represented in the rotor dq frame and ω is the rotor speed expressed in electrical rad/s.

2.4.2.2 Voltage equations

Voltage equations of phases a, b and c can be written as

$$v_a = Ri_a + \frac{d\lambda_a}{dt}; \quad v_b = Ri_b + \frac{d\lambda_b}{dt}; \quad v_c = Ri_c + \frac{d\lambda_c}{dt} \tag{2.14}$$

By transforming voltages v_a, v_b and v_c to rotor dq axes using the transformation of (2.4), stator voltages of the fictitious windings in d and q axes are

$$v_d = Ri_d + L_d \frac{di_d}{dt} - \omega L_q i_q \tag{2.15}$$

$$v_q = Ri_q + L_q \frac{di_q}{dt} + \omega\left(L_d i_d + \psi_f\right) \tag{2.16}$$

where $\omega = d\theta/dt$; and $\theta = p\theta_r$.

www.TechnicalBooksPDF.com

Finally, the developed power of the machine is given by

$$P = (v_a i_a + v_b i_b + v_c i_c) = \frac{3}{2}\left(v_d i_d + v_q i_q\right)$$
$$= \frac{3}{2}\left(i_d \frac{d\lambda_d}{dt} + i_q \frac{d\lambda_q}{dt} + 2i_0 \frac{d\lambda_0}{dt}\right) + \frac{3}{2}\left(i_q \lambda_d - i_d \lambda_q\right)\frac{d\theta}{dt} + \frac{3}{2}\left(i_d^2 + i_q^2 + 2i_0^2\right)R \tag{2.17}$$

The developed mechanical power is given by the second term on the right hand side. Thus, the developed torque of the machine is given by

$$T_{dev} = \frac{3p}{2}\left[\psi_f i_q + \left(L_d - L_q\right) i_q i_d\right] \text{ N m} \tag{2.18}$$

The inductance difference L_d–L_q is a measure of the saliency difference, saliency being defined as $\xi \equiv L_q/L_d$, of the rotor magnetic circuit. The second term in (2.18) is the reluctance torque which adds to the net developed torque with proper sign of the d-axis current. For synchronous machines with permanent magnets buried within the rotor, $L_q > L_d$, so that negative i_d, which leads to field weakening according to (2.11), results in net increase in the developed torque from exploitation of the reluctance torque derived from saliency.

2.4.2.3 Rotor flux-oriented control (RFOC) or vector control [2,3]

The torque equation (2.8) is nonlinear due to product to variables; however, incorporation of certain control and operational characteristics and boundaries, like maximum torque per ampere (MTPA) control and field weakening with current and voltage limits (see Chapter 7 for further explanation), can lead to separate control of torque and flux linkage using currents i_q and i_d, respectively, as indicated in Figure 2.8.

With rotor position feedback signal θ, via an encoder, for example, stator currents i_a–i_c can be transformed into i_q and i_d in the rotor reference frame using (2.4). The compensated speed error produces the torque references which in turn are separated into q and d axes current references, i_q^* and i_d^*, according to specified operating characteristics and control objectives mentioned above and in Chapter 7. Current reference i_d^* and takes into account the d-axis current as a function of speed when field weakening is included.

Regulations of i_q and i_d currents, which are obtained from measured currents i_a–i_c and transformed to their rotor value using transformation (2.4), are done by respective controllers *Gcq* and *Gcd* (usually proportional and integral (PI) controllers designed using stalled condition, as indicated in Figure 2.4) and back-emf compensation for each loop according to rotor speed. The compensated current errors are augmented with voltage compensations based on voltage equations (2.15) and (2.16) and as indicated in Figure 2.9 (the voltage drops in resistances and inductances L_d and L_q are normally ignored). The outputs of the current controllers are the voltage references v_q^* and v_d^* for the inverter. These voltage references are retransformed into stator voltage references v_a^*, v_b^* *and* v_c^* using inverse d–q transformation of (2.4), for the pulse-width modulation (PWM) inverter.

www.TechnicalBooksPDF.com

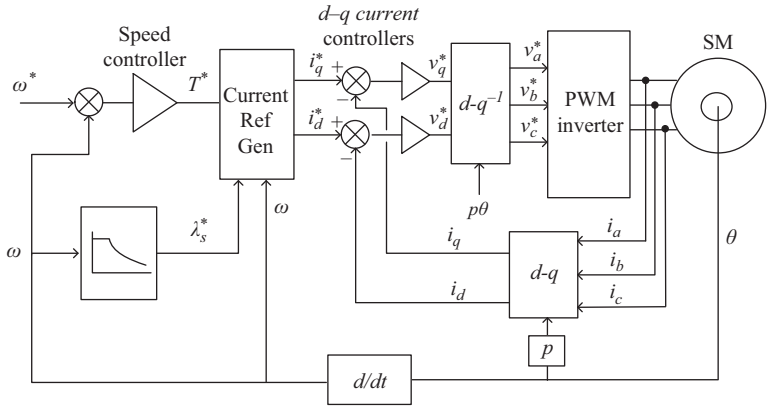


Figure 2.8 Control structure of a synchronous machine

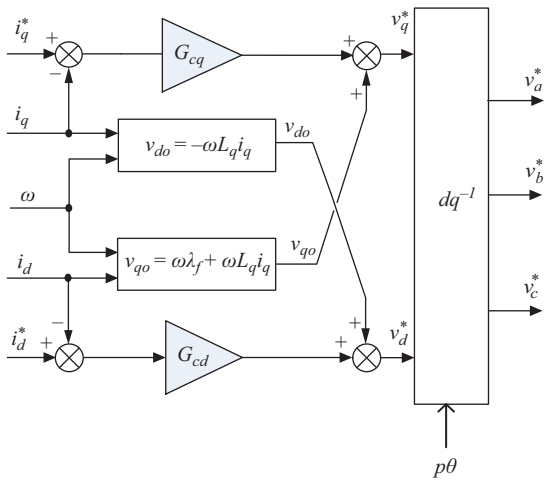


Figure 2.9 Current controllers for i_q and i_d, with speed-dependent back-emf compensations

The decoupling compensation results in faster dynamics of current and hence torque control. Figure 2.10(a) shows the simulation results with and without the decoupling compensation term included in the current control loop. In this simulation, all the parameters of the current controllers and operating conditions of the motor remain the same. It can be seen from Figure 2.10(a) and (b) that the errors of the *d*-axis and *q*-axis currents during the transient are greatly reduced, and the steady-state performance of the controllers is the same after the decoupling compensation.

2.4.3 *Dynamic model of induction machines in synchronous reference frame*

As for the synchronous machines, the induction machine can be controlled with dynamics and fast decoupled control of torque and rotor flux linkage via two

www.TechnicalBooksPDF.com

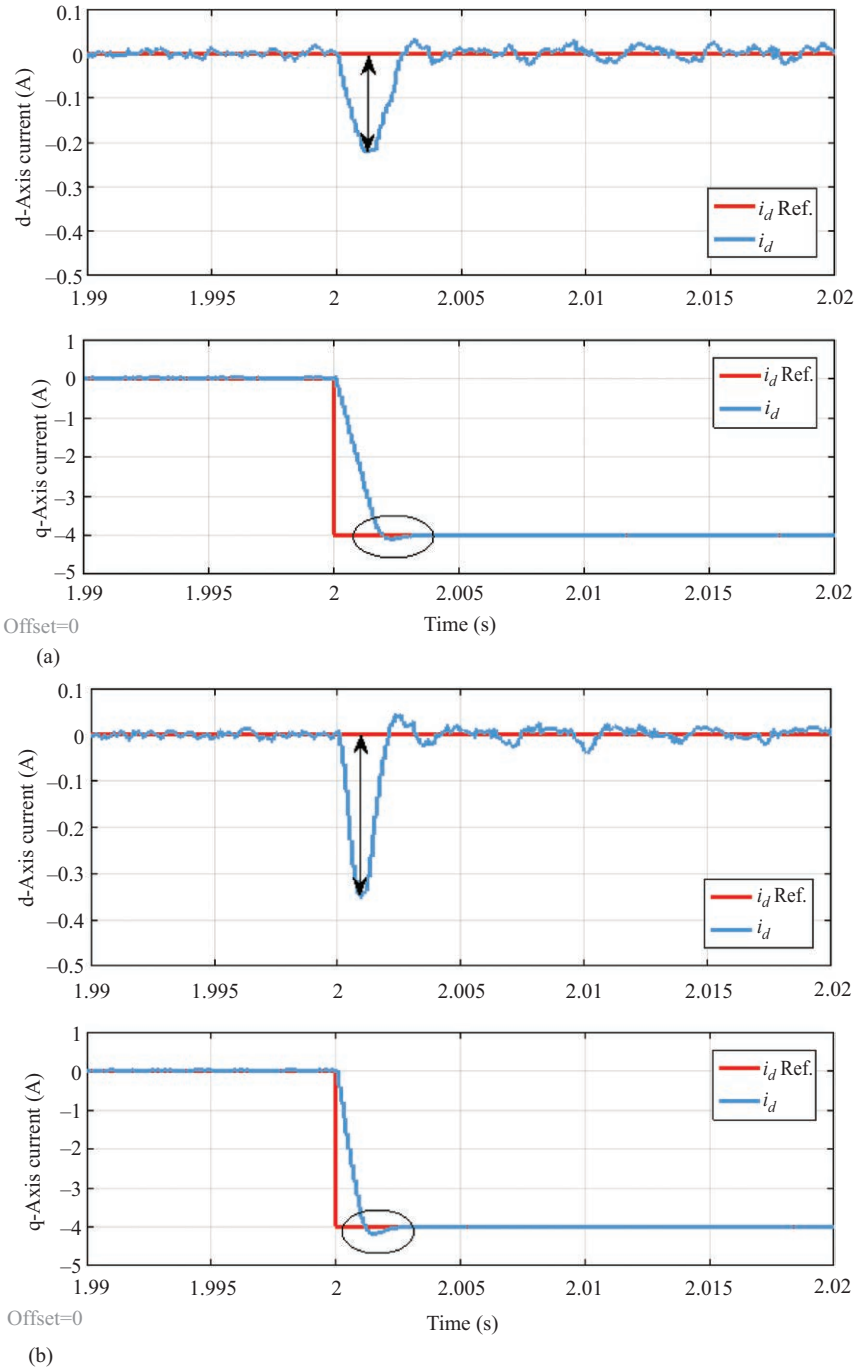
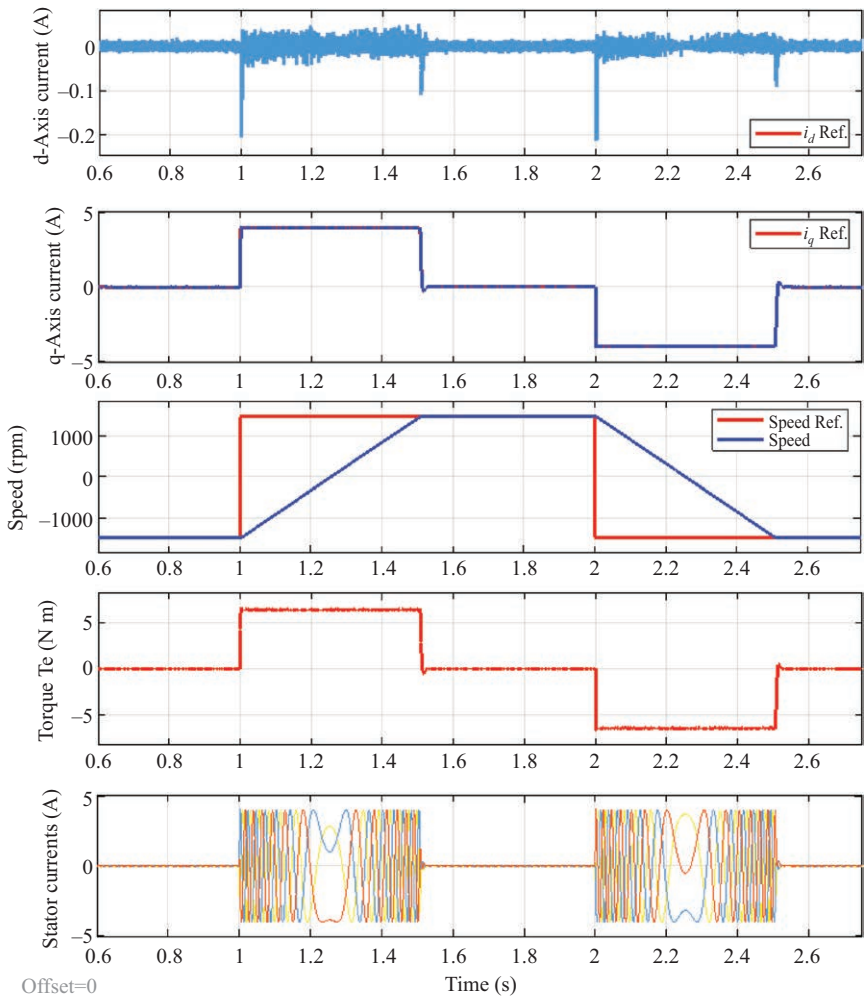


Figure 2.10 Dynamic performance of current control of a PMSM without decoupling: (a) with the decoupling compensation and (b) without the decoupling compensation

www.TechnicalBooksPDF.com

currents i_q and i_d, which are expressed in an orthogonal dq axes which rotate at synchronous speed. An induction machine has three stator windings and three rotor windings, real or equivalent, which rotate with a slip. It has been shown that transformation to the synchronously rotating orthogonal frame leads to the desired decoupling between d and q axes fluxes of the machine.

Consider the three-phase squirrel-cage IM representation of Figure 2.11. The three-stator (balanced and distributed) windings a–b–c may be represented by



(a)

Figure 2.11 (a) Dynamic performance of current and speed control of a PMSM (simulation) and (b) dynamic performance of current and speed control of a PMSM experiment

www.TechnicalBooksPDF.com

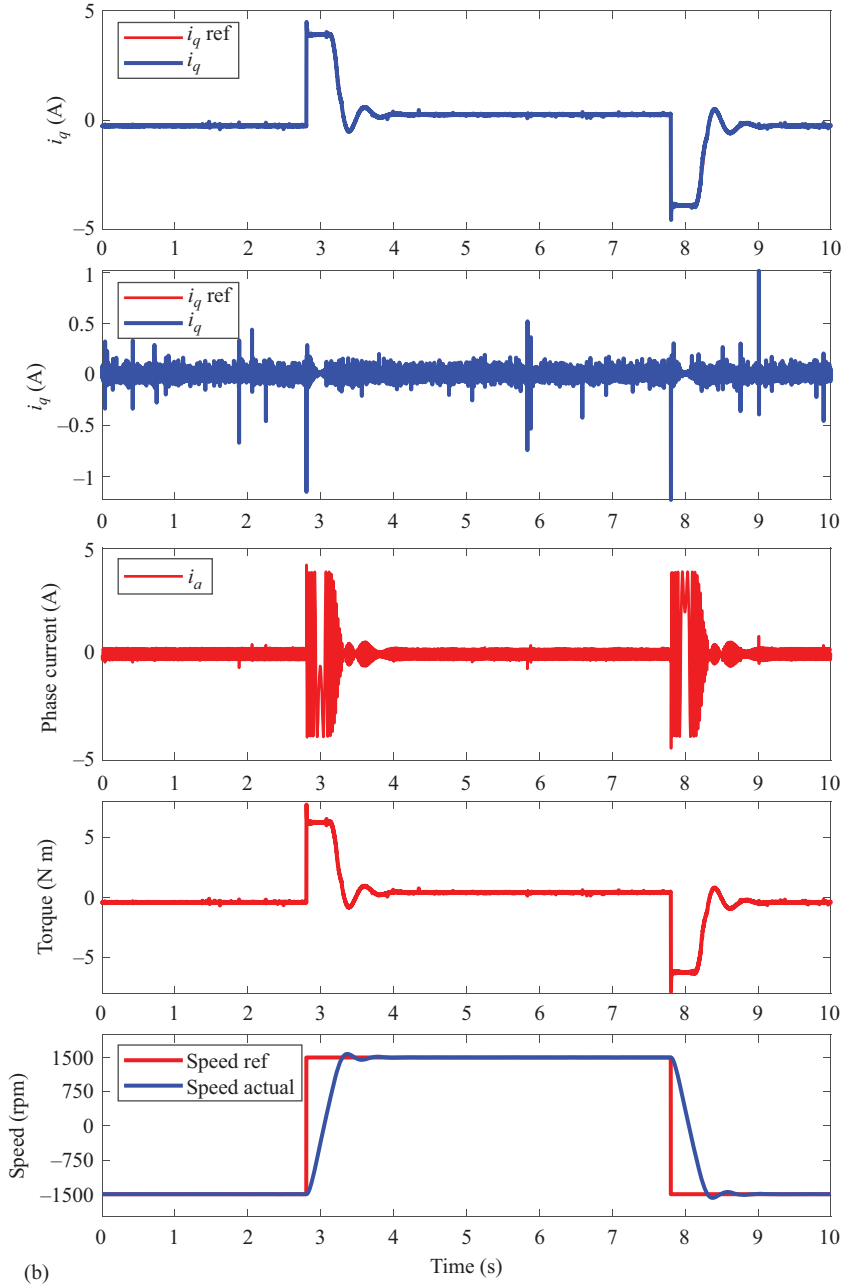


Figure 2.11 (*Continued*)

www.TechnicalBooksPDF.com

orthogonal *dq* axes windings (indicated in red) with currents i_{ds} and i_{qs}, respectively. Similarly, the rotor windings may also be represented by orthogonal *dq* axes windings (indicated in blue) with currents i_{dr} and i_{qr}, respectively. We will assume that both *dq* sets of windings rotate at synchronous speed. Note that we have assumed that the *d* and *q* axes of the stator and rotor are each colinear as shown in Figure 2.1 and that the rotor *a*-winding axis is at an arbitrary angle θ_r with respect to stator *a*-winding axis at $t = 0$.

If the orthogonal set of reference rotates at the synchronous speed ω_e, its angular position at any instant is given by

$$\theta = \int_0^t \omega_e t + \theta_o \tag{2.19}$$

Angle θ is the angular displacement of the *d*-axis with respect the *a* axis of the stator at time *t*. The orthogonal set is then referred to as *d*–*q*–0 axes in the synchronously rotating reference frame. Using θ from (2.19) into (2.4), stator variables *v*, *i* and λ can be expressed in the synchronously rotating axes *d*–*q*–0.

2.4.3.1 Machine inductance and flux linkages

Self-inductances of each stator winding an induction machine, assuming balanced and symmetrical windings are

$$L_{aas} = L_{bbs} = L_{ccs} = L_1 \tag{2.20}$$

Similarly for the rotor,

$$L_{aar} = L_{bbr} = L_{ccr} = L_2 \tag{2.21}$$

Mutual inductances between stator windings:

$$L_{abs} = L_{bcs} = L_{cas} = M_1 \tag{2.22}$$

Mutual inductances between rotor windings:

$$L_{abr} = L_{bcr} = L_{car} = M_2 \tag{2.23}$$

The mutual inductances *between* stator and rotor windings (*M*) have cosine variation with θ_r.

$$L_{absr} = M\cos q_r, \quad L_{bcsr} = M\cos(\theta_r - 120^\circ) \text{ and so on} \tag{2.24}$$

where θ_r is the angular displacement of the rotor *a*-axis with respect to stator *a*-axis at time *t*. Angle θ_r is given by

$$\theta_r = \int \omega_r dt = \int (1 - s)\omega_e dt \tag{2.25}$$

www.TechnicalBooksPDF.com

Flux linkages for stator windings are given by

$$\begin{aligned}
\lambda_{as} &= L_1 i_{as} + M_1(i_{bs} + i_{cs}) + M(i_{ar}\cos\theta_r + i_{br}\cos(\theta_r - 120^\circ) + i_{cr}\cos(\theta_r - 240^\circ)) \\
\lambda_{bs} &= L_1 i_{bs} + M_1(i_{as} + i_{cs}) + M(i_{ar}\cos(\theta_r - 120^\circ) + i_{br}\cos\theta_r + i_{cr}\cos(\theta_r - 240^\circ)) \\
\lambda_{cs} &= L_1 i_{cs} + M_1(i_{as} + i_{bs}) + M(i_{ar}\cos(\theta_r - 240^\circ) + i_{br}\cos(\theta_r - 120^\circ) + i_{cr}\cos\theta_r)
\end{aligned} \tag{2.26}$$

Similarly, flux linkages for rotor windings are

$$\begin{aligned}
\lambda_{ar} &= L_2 i_{ar} + M_2(i_{br} + i_{cr}) + M(i_{as}\cos\theta_r + i_{bs}\cos(\theta_r - 120^\circ) + i_{cs}\cos(\theta_r - 240^\circ)) \\
\lambda_{br} &= L_2 i_{br} + M_2(i_{ar} + i_{cr}) + M(i_{as}\cos(\theta_r + 120^\circ) + i_{bs}\cos\theta_r + i_{cs}\cos(\theta_r - 120^\circ)) \\
\lambda_{cr} &= L_2 i_{cr} + M_2(i_{ar} + i_{br}) + M(i_{as}\cos(\theta_r + 240^\circ) + i_{bs}\cos(\theta_r + 120^\circ) + i_{cs}\cos\theta_r)
\end{aligned} \tag{2.27}$$

The rotor windings rotate at the slip speed $s\omega_e$ with respect to the synchronously rotating axes. Let us assume that θ_{sl} is the angular displacement between the rotor "a" axis and the "d" axis of the synchronously rotating $dq0$ frame, which changes at a rate given by the slip speed $s\omega_e$. In terms of the slip s, we can write

$$\begin{aligned}
\frac{d\theta_{sl}}{dt} &= s\omega_e = \omega_e - \omega_r \\
\theta_{sl} &= \int s\omega_e dt = \int (\omega_e - \omega_r)dt + \theta_{slo}
\end{aligned} \tag{2.28}$$

By transforming stator flux linkages to the synchronously rotating frame with angle θ as defined in Figure 2.11 and by using (2.4) are given by

$$\begin{aligned}
\lambda_{ds} &= L_s i_{ds} + L_m i_{dr} \\
\lambda_{qs} &= L_s i_{qs} + L_m i_{qr} \\
\lambda_s &= \sqrt{\lambda_{ds}^2 + \lambda_{qs}^2}
\end{aligned} \tag{2.29}$$

where $L_m = (3/2)M$; $L_s = L_1 - M_1 = L_{ls} + L_m$; $L_r = L_2 - M_2 = L_{lr} + L_m$ and L_{ls} and L_{lr} are the stator and rotor leakage inductances.

Similarly, by transforming rotor flux linkages to the synchronously rotating frame with angle θ_{sl} as defined in Figure 2.11 and using (2.4) are given by

$$\begin{aligned}
\lambda_{dr} &= L_r i_{dr} + L_m i_{ds} \\
\lambda_{qr} &= L_r i_{qr} + L_m i_{qs} \\
\lambda_r &= \sqrt{\lambda_{dr}^2 + \lambda_{qr}^2}
\end{aligned} \tag{2.30}$$

www.TechnicalBooksPDF.com

2.4.3.2 Voltage, developed power and torque equations

The voltage equations for the winding are

$$v_{as} = R_s i_{as} + \frac{d}{dt}(\lambda_{as}) \tag{2.31}$$

and so on for v_{bs} and v_{cs} for the stator.

$$v_{ar} = R_r i_{ar} + \frac{d}{dt}(\lambda_{ar}) \tag{2.32}$$

and so on for v_{br} and v_{cr} for the rotor.

By transforming stator and rotor voltages, and currents and fluxes, the voltage equations in the synchronously rotating frame become

$$\begin{aligned} v_{ds} &= R_s i_{ds} + \frac{d}{dt}(\lambda_{ds}) - \omega_e \lambda_{qs} = R_s i_{ds} + \frac{d}{dt}(L_s i_{ds} + L_m i_{dr}) - \omega_e \left(L_s i_{qs} + L_m i_{qr}\right) \\ v_{qs} &= v_{qs} = R_s i_{qs} + \frac{d}{dt}\left(\lambda_{qs}\right) + \omega_e \lambda_{ds} = R_s i_{qs} + \frac{d}{dt}\left(L_s i_{qs} + L_m i_{qr}\right) + \omega_e (L_s i_{ds} + L_m i_{dr}) \end{aligned} \tag{2.33}$$

$$\begin{aligned} v_{dr} &= R_r i_{dr} + \frac{d}{dt}(\lambda_{dr}) - (\omega_e - \omega_r)\lambda_{qr} = R_r i_{dr} + \frac{d}{dt}(L_r i_{dr} + L_m i_{ds}) \\ &\quad -(\omega_e - \omega_r)\left(L_r i_{qr} + L_m i_{qs}\right) \\ v_{qr} &= R_r i_{qr} + \frac{d}{dt}\left(\lambda_{qr}\right) + (\omega_e - \omega_r)\lambda_{dr} = R_r i_{qr} + \frac{d}{dt}\left(L_r i_{qr} + L_m i_{qs}\right) \\ &\quad +(\omega_e - \omega_r)(L_r i_{dr} + L_m i_{ds}) \end{aligned} \tag{2.34}$$

Assuming the case of a squirrel-cage machine for which $v_{dr} = v_{qr} = 0$, the input power is given by

$$P_{input} = \frac{3}{2}\left(v_{ds} i_{ds} + v_{qs} i_{qs}\right) \text{W} \tag{2.35}$$

A part of this power is the mechanical developed power which is given by

$$p_{dev} = \frac{3}{2}\omega_r \left[\lambda_{qr} i_{dr} - \lambda_{dr} i_{qr}\right] \text{ in terms of rotor variables.} \tag{2.36}$$

The developed torque is thus given by

$$p_{dev} = \frac{3}{2} L_m \omega_r \left(i_{dr} i_{qs} - i_{qr} i_{ds}\right) = \frac{3}{2} p \frac{L_m}{L_r}\left(\lambda_{dr} i_{qs} - \lambda_{qr} i_{ds}\right) \text{ N m} \tag{2.37}$$

www.TechnicalBooksPDF.com

2.4.3.3 Conditions for rotor flux-oriented control

For rotor flux-oriented control (RFOC), in which the measurable stator currents i_{qs} and i_{ds} control the torque and rotor flux linkage independently, one of the obvious conditions is to ensure that

$$\lambda_{qr} = 0 \quad \text{and} \quad \frac{d\lambda_{qr}}{dt} = 0. \tag{2.38}$$

In other word, all of the rotor flux is along the d-axis and thus $\hat{\lambda}_r = \lambda_{dr}$. With these conditions satisfied, the developed torque is given by

$$T_{dev} = \frac{3P}{2}\frac{L_m}{L_r}\left(\lambda_{dr} i_{qs} - \lambda_{qr} i_{ds}\right) = \frac{3P}{2}\frac{L_m}{L_r}\hat{\lambda}_r i_{qs} \tag{2.39}$$

For a squirrel-cage motor, for which rotor voltage $v_{qr} = 0$, and conditions of (2.39) are satisfied when

$$\omega_e - \omega_r = \omega_{sl} = \frac{L_m}{\hat{\lambda}_r}\frac{R_r}{L_r} i_{qs} \tag{2.40}$$

Thus, the compensated speed error must be used to determine the current reference i_q^* according to (2.39), and the slip frequency reference ω_{sl}^* must be defined according to (2.40).

The other condition for RFOC is that λ_{dr} remains constant at all times. From rotor voltage (2.34) $v_{dr} = 0$,

$$\frac{d\hat{\lambda}_r}{dt} + \frac{R_r}{L_r}\hat{\lambda}_r - \frac{L_m}{L_r} R_r i_{ds} = 0 \quad \text{so that} \quad \frac{L_r}{R_r}\frac{d\hat{\lambda}_r}{dt} + \hat{\lambda}_r = L_m i_{ds} \tag{2.41}$$

Equation (2.41) implies that if i_{ds} is regulated to remain constant at a specified value for the required rotor flux linkage,

$$\hat{\lambda}_r = \lambda_{dr} = L_m i_{ds} \tag{2.42}$$

However, a change in reference i_{ds}^* is translated into rotor flux λ_{dr} subject to a time delay which is the rotor time electric circuit time constant L_r/R_r.

From the above, the required control structure for a squirrel-cage IM is indicated in Figure 2.12. The required developed torque for the drive is obtained by establishing i_{qs} while the rotor flux is established by i_{ds}, which follow their respective references given by (2.39) and (2.42), respectively. These feedback currents i_{qs} and i_{ds} are obtained from dq transformation of measured currents i_a–i_c using (2.4). The slip reference obtained from (2.40) and is added with the measured speed ω_m, which is integrated with respect to time according to (2.19) in order to obtain angle θ to be used for the transformations. The compensated current errors, with voltage compensations indicated by (2.33), are transformed back to stator *abc* reference

www.TechnicalBooksPDF.com

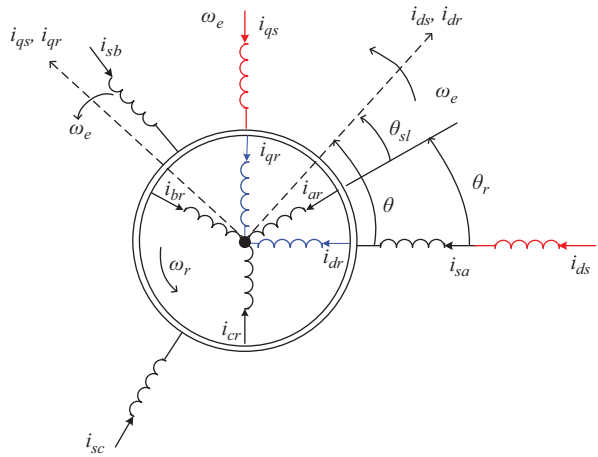


Figure 2.12 Stator, rotor and synchronous frame axes of an induction machine

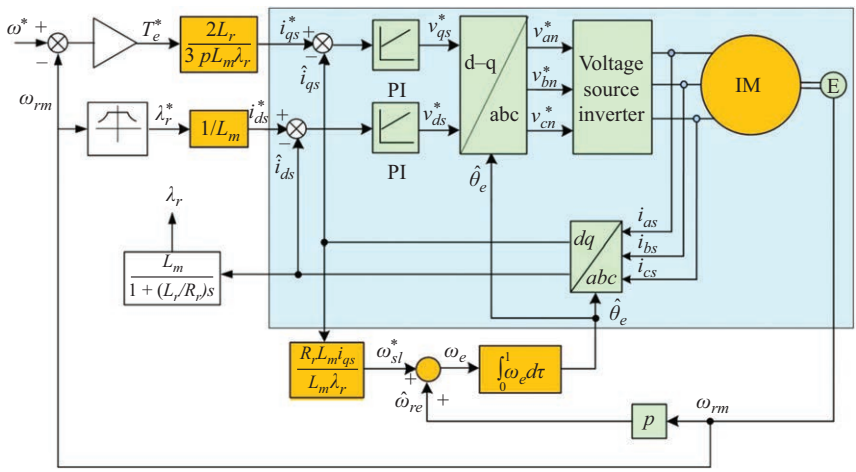


Figure 2.13 RFOC control structure of an induction motor drive

frame for producing and modulating the voltage reference signals for the inverter. The block diagram of RFOC based induction motor drive is shown in Figure 2.13.

Figures 2.14 and 2.15 illustrate the dynamic performance of the RFOC IM drive with simulation and experimental results, respectively. It can be observed that the IM accelerates under a constant and maximum torque set by the saturation point of the speed PI controller. The large overcurrent transients during acceleration are eliminated when the motor almost reaches the rated speed set point with a little

www.TechnicalBooksPDF.com

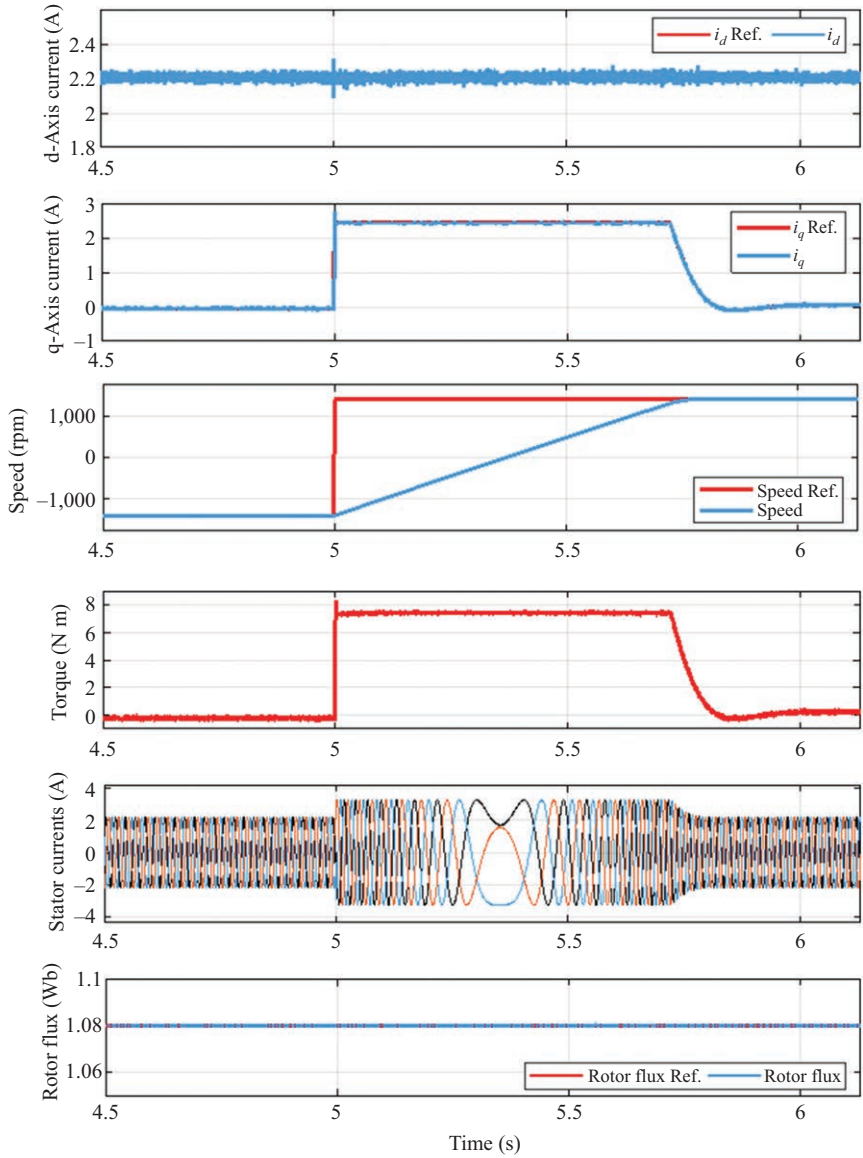


Figure 2.14 Dynamic responses of currents, torque, rotor flux and speed of an induction motor under RFOC (simulation results)

overshoot in speed. Obviously, rotor and air gap fluxes remain constant at all times. The *d*-axis current is regulated at a constant value, which produces the rated rotor flux linkage. The *q*-axis current is regulated at the desired values, which produces the torque to accelerate and decelerate the motor.

www.TechnicalBooksPDF.com

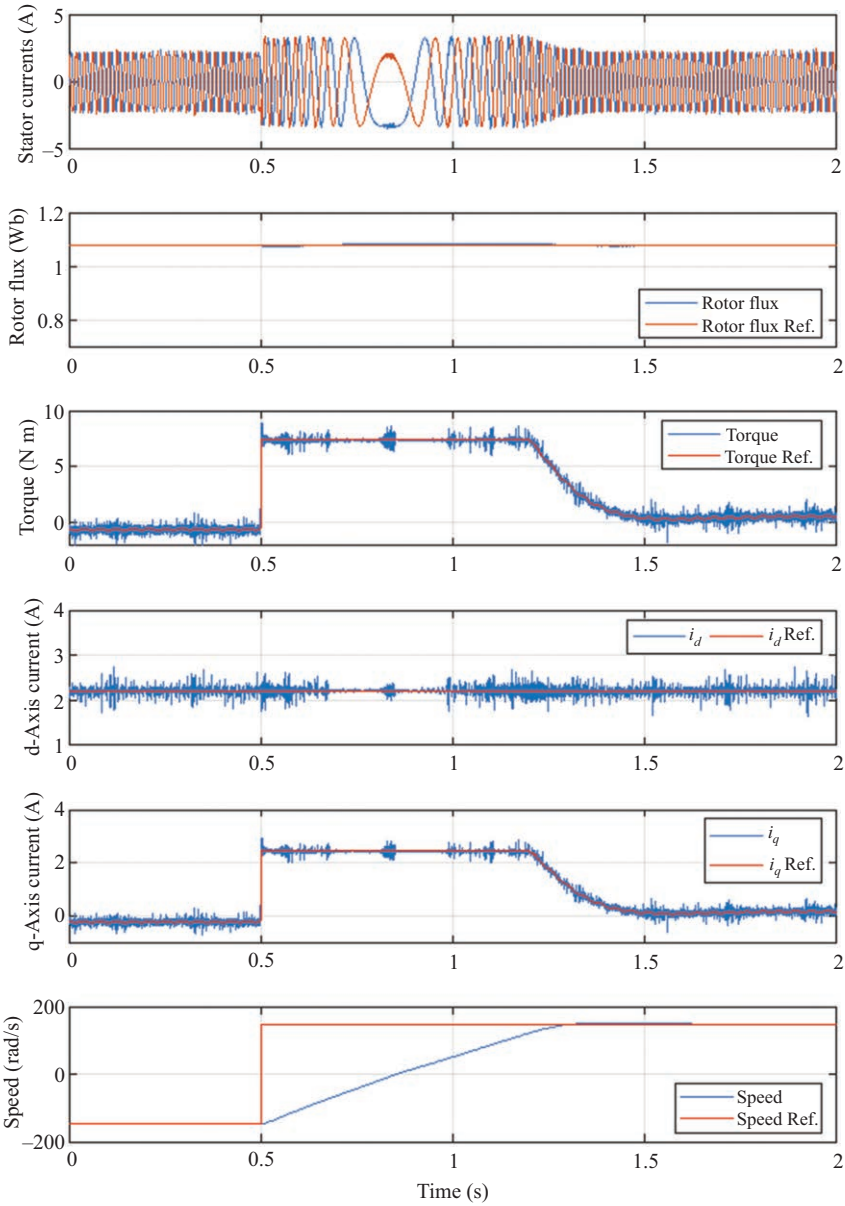


Figure 2.15 Dynamic responses of currents, torque, rotor flux and speed of an induction motor under RFOC (experimental results)

www.TechnicalBooksPDF.com

2.5 Simulation of drive systems

Several highly integrated and sophisticated simulation platforms like MATLAB®/Simulink® and PSIM exist that can simulate many steady-state and dynamic performances of a drive system. It generally means that many complex drive issues can be addressed at the design stage, without having to build a drive at the onset. Tuning of controllers for various control loops, effects of machine and load parameter variations and drive efficiency map can all be pre-assessed.

2.5.1 *Tuning of an electric drive using a cascaded structure [4]*

To achieve good dynamic performance and operational features, a cascaded structure of closed-loop controls is employed in the electric drive system. Figure 2.16 shows a cascaded control structure for electric drives, which includes speed control in the outer loop and current control in the inner loop. In DC drives, the current and voltage are the armature current and armature voltage, respectively. In AC drives, the current control loop contains *d*-axis and *q*-axis currents controllers in the inner loop. The control voltages are the three-phase stator voltage references.

As the inner current-control loop is acting much faster than the outer speed-control loop, the current controller should be tuned before the tuning of speed controller in the electric drive systems. To tune the current controller, assume that the model is linear, that is achieved by eliminating the decoupling terms. These terms can be considered as disturbance and are cancelled by applying feed-forward decoupling to the output of the current controller. This assumption allows for an approximation of the plant model using this first order Laplace equation.

$$G_i(s) = \frac{K_m}{T_m s + 1} \tag{2.43}$$

where K_m and T_m are the gain and time constant of the first-order system, respectively.

Steps for designing a PI controller for a first-order system are

1. Discretize the plant model with forward Euler discretization method. Substituting $s = (1 - z^{-1})/T_s z^{-1}$ into (2.43) yields the discrete plant model:

$$G_i(z^{-1}) = \frac{K_m(T_s/T_m)z^{-1}}{1 + ((T_s - T_m)/T_m)z^{-1}} = \frac{b_1 z^{-1}}{1 + a_1 z^{-1}} \tag{2.44}$$

where T_s is the sampling time for the discrete current controller.

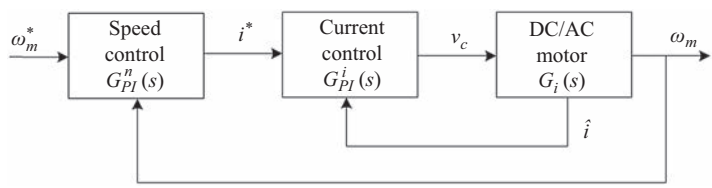


Figure 2.16 Cascaded feedback control loops for electric drives

www.TechnicalBooksPDF.com

2. Define a discrete PI controller using the same transform.

$$G_{PI}(z^{-1}) = K_P + K_I \frac{T_s z^{-1}}{1 - z^{-1}} = \frac{K_P + (K_I T_s - K_P) z^{-1}}{1 - z^{-1}} = \frac{q_0 + q_1 z^{-1}}{1 - z^{-1}} \tag{2.45}$$

Combining the discrete transfer function of the plant and PI controller, the closed-loop transfer function is given by

$$G_{CL}(z^{-1}) = \frac{q_0 b_1 z^{-1} + q_1 b_1 z^{-2}}{1 + (a_1 - 1 + q_0 b_1) z^{-1} + (-a_1 + q_1 b_1) z^{-2}} \tag{2.46}$$

where the denominator of the transfer function is the characteristic polynomial of the system.

$$P_{CL}(z^{-1}) = 1 + (a_1 - 1 + q_0 b_1) z^{-1} + (-a_1 + q_1 b_1) z^{-2} \tag{2.47}$$

3. The characteristic polynomial for achieving the required performance is defined as

$$P_{cd}(z^{-1}) = 1 + \alpha_1 z^{-1} + \alpha_2 z^{-2} \tag{2.48}$$

where $\alpha_1 = -2e^{-\xi\omega_n T_s} \cos\left(\omega_n T_s \sqrt{1 - \xi^2}\right)$ and $\alpha_1 = e^{-2\xi\omega_n T_s}$.

4. To determine the controller parameters, set the characteristic polynomial for the system equal to the characteristic polynomial for the required performance, i.e., $P_{CL}(z^{-1}) = P_{cd}(z^{-1})$. Solving for the proportional and integral gains of the controller for the first-order system yields

$$\begin{cases} K_P = \dfrac{\alpha_2 - a_1 + 1}{b_1} \\ K_I = \dfrac{\alpha_2 + a_1}{b_1 T_s} + \dfrac{K_P}{T_s} \end{cases} \tag{2.49}$$

The above general equations for the PI controller gains contain two coefficients, the damping factor ξ and natural frequency ω_n. These two coefficients determine two of the main step-response characteristics, overshoot σ and response time t_r.

$$\sigma = e^{-\pi\xi/\sqrt{1-\xi^2}} \tag{2.50}$$

$$t_r \cong \begin{cases} \dfrac{4}{\omega_n \xi}, & \text{if } (\xi < 0.7) \\ \dfrac{6\xi}{\omega_n}, & \text{if } (\xi \geq 0.7) \end{cases} \tag{2.51}$$

Given the system requirements such as overshoot and response time, you can now solve for the PI current controller gains.

www.TechnicalBooksPDF.com

It should be noted that the gain K_m and time constant T_m of the first-order system $G_i(s)$ will vary depending on the motor type. For a DCM,

$$\begin{cases} K_m = 1/R_a \\ T_m = L_a/R_a \end{cases} \tag{2.52}$$

where L_a and R_a are the armature inductance and resistance of the DCM.

For an NSPSM, such as PMSM,

$$\begin{cases} K_m = 1/R_s \\ T_m = L_s/R_s \end{cases} \tag{2.53}$$

where L_s and R_s are the synchronous inductance and stator resistance of the synchronous machine. Therefore, the PI gains are the same for the d and q current regulators.

An SPSM, such as interior-type PMSM (IPMSM), has two different gains and time constants for d and q axes current controllers. The proportional and integral gains of the controllers will be different and calculated separately.

$$\begin{cases} K_m^{d,q} = 1/R_s \\ T_m^{d,q} = L_{d,q}/R_s \end{cases} \tag{2.54}$$

The transfer function for the d–q current controllers of the vector-controlled IM drives is as follows:

$$G_i(s) = \frac{1/R_s}{(\sigma L_s/R_s)s + 1} = \frac{K_m}{T_m s + 1} \tag{2.55}$$

where $\sigma = 1 - L_m^2/(L_s L_r)$.

Once the current controller is properly tuned, the outer speed loop can be tuned. It can be assumed that the inner loop is much faster than the outer loop, and there is no steady-state error. These assumptions allow considering the inner current loop as a transfer function of "1." The resulting approximation for the outer loop plant model can be described by a first-order system with different gain and time constant.

$$G_n(s) = \frac{K_t/D}{(J/D)s + 1} \tag{2.56}$$

where K_t D and J are the torque constant, the viscous friction coefficient and the rotor moment of inertia, respectively.

The general workflow for designing the inner current controller is also applicable to outer speed loop tuning. But the response time is much slower than that of the current loop.

www.TechnicalBooksPDF.com

2.5.2 Voltage reference amplitude limitation

The space vector modulation (SVM) or sinusoidal PWM (SPWM) algorithm is normally used to synthesize the desired voltage vector at a constant switching frequency. During transients when current errors are too large, the amplitude of voltage vector reference may exceed the available maximum voltage of the inverter. In this case, the output of the PI controllers reaches the saturation limit $V_{\max}$. The limitation block ensures that the voltage reference satisfies the voltage constraint, namely, the voltage reference vector lies inside a circle with radius $V_{\max}$. $V_{\max} = 0.5 \times V_{DC}$ if SPWM strategy is employed to two-level voltage source inverter (VSI) drives and $V_{\max} = 0.577 \times V_{DC}$ for SVM strategy.

If the amplitude of the requested voltage vector by the current controllers is greater than $V_{\max}$, a proportional reduction of its magnitude is performed while the angular phase is preserved by the limitation block. The behavior of the limitation block is described by the following equation:

$$\bar{v}_s^* = \begin{cases} \bar{v}_s^{PI}, & \text{if } \left|\bar{v}_s^{PI}\right| \le V_{\max} \\ \dfrac{V_{\max}}{\left|\bar{v}_s^{PI}\right|}\bar{v}_s^{PI}, & \text{if } \left|\bar{v}_s^{PI}\right| \le V_{\max} \end{cases} \tag{2.57}$$

where $\bar{v}_s^{PI}$ is the requested stator voltage vector by PI current controllers and $\bar{v}_s^*$ is the reference voltage vector provided to the modulation block after the amplitude limitation.

2.5.3 Pulse-width modulation block

Control of the machine voltage is achieved using PWM. The duty cycle of the pulses is determined by the control voltage v_c in the closed-loop controlled motor drives. The control voltage is the required armature voltage reference in DC drives and the three-phase stator voltage reference in the AC drives. The maximum average voltage generated is limited by $V_{\max}$. In DC drives, $V_{\max}$ is determined by the DC bus voltage of the converter, while $V_{\max}$ is also determined by the modulation strategies employed in AC drives.

A typical PWM generator circuit for DC drives is given in Figure 2.17. The control voltage v_c is generated by the armature current controller and $V_{\max} = V_{DC}$. The switching transistors at the top and bottom of any leg of the converter must not conduct simultaneously. To prevent catastrophic short circuit of the DC source, an on-delay block is employed to generate a dead time for each of the gating signals. The duration of the dead time is determined by the turnoff times of the switching devices used. Typically, this is of the order of a few microseconds.

This PWM circuit can be extended to an SPWM or SVM modulator for AC drives. In three-phase AC drives, there will be three such PWM modulators, one for each of the phases. The control voltages for three phases are derived from *dq* current controllers output and *dq* to *abc* transformation block. $V_{\max}$ is determined by the modulation strategy and the topology of the converter used for the drives.

www.TechnicalBooksPDF.com

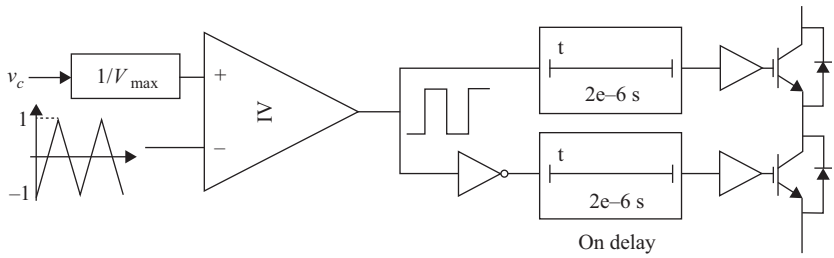


Figure 2.17 Pulse-width modulation block per phase including dead time generator

2.6 Sensors in drive systems

2.6.1 Current sensors for electric drive systems

Current sensors of high accuracy, resolution and bandwidth are required for both DC and AC drive systems. Additionally, galvanic isolation is required so that sensor outputs can be directly connected with controller hardware. These requirements are not easily and cost effectively met by resistive current-sensing resistors because of thermal effects on the resistive element for sensing, and the high common-mode voltage rejection required when AC currents have to be measured. Hall current sensors that are suitable for both DC and AC current measurements are now widely used in drive systems. Devices have sensing bandwidth higher than several hundred kHz at low current to about 5 kHz at kA levels.

In its simplest form of Figure 2.18(a), the Hall current sensor amplifies the voltage across the Hall element which carries a constant current. This being measured develops and confines the magnetic field to the dimension of the Hall device using a magnetic core. Due to the nonlinear *B–H* characteristic of the core, this Hall sensor does not generally have good precision and suffers from drift due to temperature variation and stray magnetic field in the environment.

A more advanced Hall sensor retains the basic structure of Figure 2.18(a) but additionally utilizes secondary coil that counteracts the field produced by the current being measured to zero as illustrated in Figure 2.18(b). The current in the secondary coil produces a voltage across a sensing resistor which is proportional to the current being measured. This Hall sensor produces excellent linearity, can measure current down to very low DC values, has very small DC offset over a wide temperature range and has bandwidth. Figure 2.19 shows a few commercial Hall sensors.

Rogowski coils measure AC currents by measuring the AC-induced voltage in an air-cored coil around the conductor carrying the current being sensed as indicated in Figure 2.20. The Rogowski coil measures the current derivative *dl*/*dt* of the current being measured; hence, its coil voltage must be integrated to develop an output voltage which is proportional to current. Since there is no magnetic core, large currents can be sensed without magnetic saturation and heating due to magnetic loss.

www.TechnicalBooksPDF.com

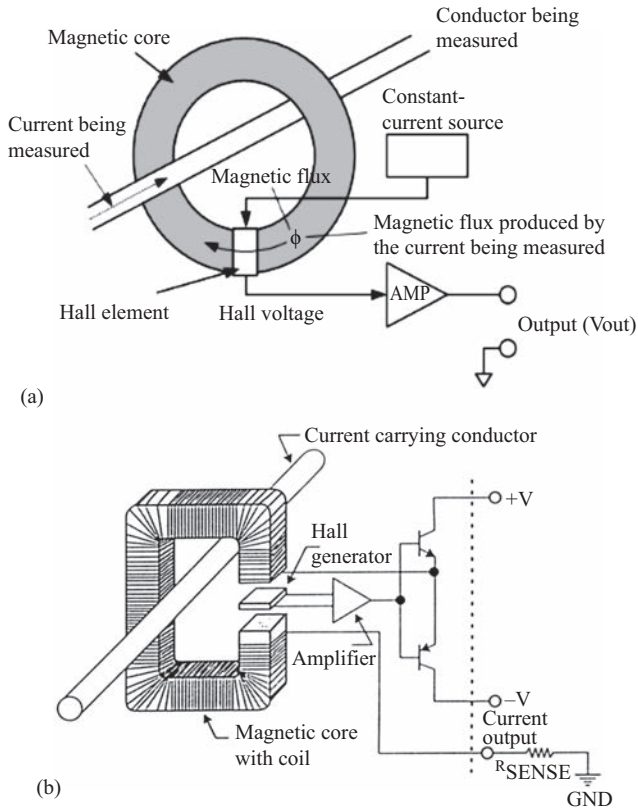


Figure 2.18 (a) The basic Hall sensor and (b) zero-flux type Hall sensor



DC – 400 kHz, up to 180 A

300 A, 100 kHz, to 8 KA, 5 kHz

Figure 2.19 Typical Hall sensors

A recently developed current-sensing technique utilizes the sensitivity of anisotropic magnetoresistive (AMR) effect to sense current. There is no need for any field guiding coil; hence these sensors require no magnetic core, hence free from remanence (see Figure 2.21). These sensors are very compact as a result. The thin film permalloy (Fe-Ni) material of the sensing resistor is linked by magnetic field alone and is isolated from the conductor carrying the current. A new type of current sensors are also developed which can be embedded directly to IGBT Power Module.

www.TechnicalBooksPDF.com

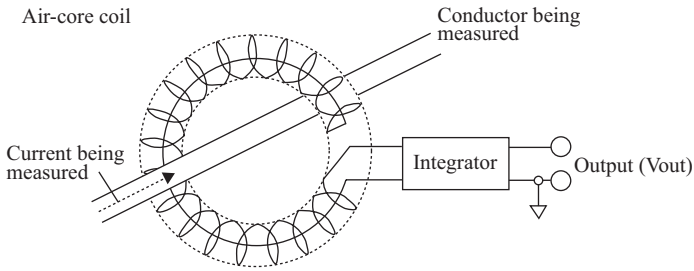


Figure 2.20 The Rogowski-coil-based current sensor

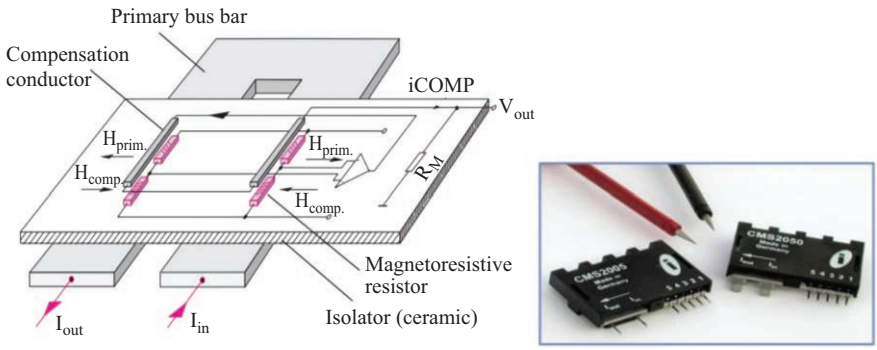


Figure 2.21 Structure of an AMR current sensor (Courtesy SENSITEC)

The thin film magnetoresistive resistors are placed on a silicon chip and are connected in a Wheatstone bridge. In order to obtain a high linearity (0.1%) and a low-temperature sensitivity, a current iComp is feedback to the sensor chip through a compensation conductor located above the magnetoresistive resistors. The resulting field Hcomp exactly compensates Hprim, so that the sensor always works around a single point. At the output of the sensors, the compensation current flows through the measurement resistor R_M. The output voltage, measured across that resistor, is Vout=±2.5 V at primary nominal current I_{in}. The nominal current is only determined by the geometry of the primary current conductor. High compactness, linearity and accuracy, low susceptibility with temperature of this sensor are very suitable for compact drive systems. AMR sensors with accuracy of 0.6% and bandwidth of 2 MHz, temperature range of −40°C to + 105°C are available.

The Rogowski coil because of its high bandwidth, isolation and temperature handling capabilities is also suitable for integration with inverter switch legs for both switch protection and inverter output current sensing. These dual functions require some additional hardware integrated with the switching of the inverter [5,6]. AMR sensors are also expected to be suitable for such integration for the same reasons.

www.TechnicalBooksPDF.com

2.6.2 Speed sensors for electric drive systems

Shaft-mounted speed sensors are nowadays mostly digital devices, because analogue DC tacho-generators suffer from noise and temperature variation and accuracy issues that are not acceptable in motor drives driven by current sources. Digital sensors can be magnetic or optical. The magnetic type, called resolvers, has three windings as indicated in Figure 2.22(a). Its reference winding is excited with a high-frequency signal in the range of 1–2 kHz. The rotor presents a variable reluctance coupling of the R winding with the other two S windings which are in quadrature (90° displaced). The S windings have multiple poles of appropriately high numbers. The amplitudes of the induced voltages in the S1–S2 and S3–S4 windings are sine and cosine modulated as shown in Figure 2.22(b).

The following signals for the resolver are available:

$$V_R = V_m \sin \omega t$$

$$V_{s1} = V_m K_1 \sin\ \theta \sin(\omega t + \alpha)$$

$$V_{s2} = V_m K_1 \cos\ \theta \sin(\omega t + \alpha)$$

where K_1 and K_2 are equal and angle α may be taken as zero.

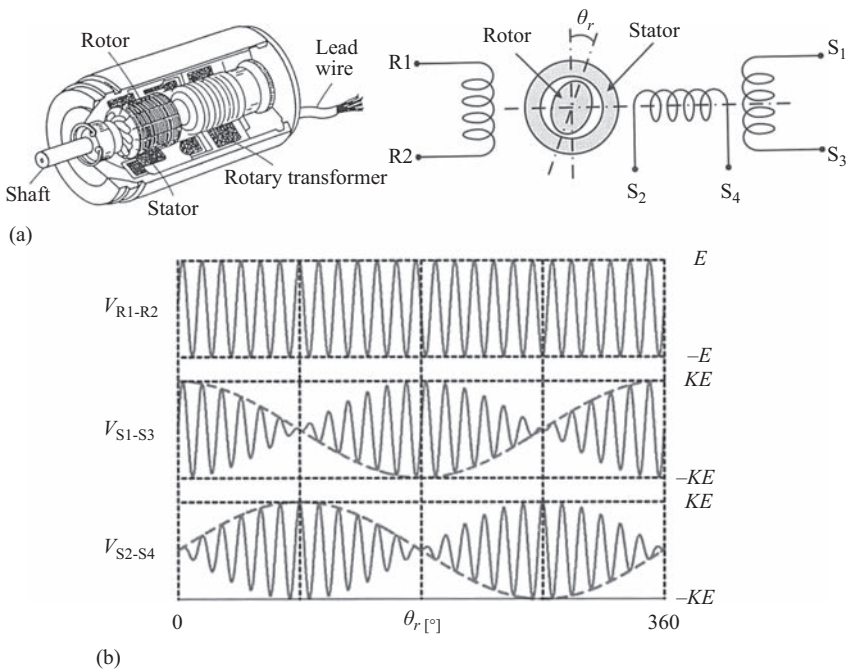


Figure 2.22 (a) Resolver cutout view and (b) reference and Synchro output waveforms

www.TechnicalBooksPDF.com

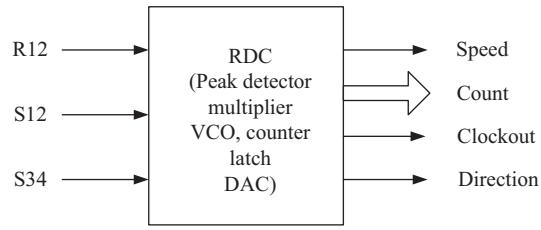


Figure 2.23 Resolver-to-digital converter (RDC)

These signals are passed through a resolver-to-digital converter in Figure 2.23 to extract the sine–cosine outputs using peak detectors, multiplication and digitization via analogue to digital converters (ADCs). Ratio of each signal relative to the reference V_R is used so that changes to absolute values of signals do not affect the accuracy of measurement.

The *Speed* output signal is an analog signal. However, the count signal is a pulse train the frequency of which is proportional to shaft speed. This signal, together with the direction signal, are counted up or down (according to direction) in a bidirectional counter, the output of which is read at a constant sampling frequency to determine shaft speed.

One of the strength of electromagnetic resolvers is the rugged mechanics, which can withstand shock and other adverse environmental condition, compared to optical encoders.

Shaft-mounted optical speed sensors use optically encoded disks to generate pulse trains, frequencies of which are proportional to speed. There are two types, the incremental and absolute encoders.

In the incremental type of Figure 2.24, collimated light beams from three suitably located light-emitting diodes (LEDs) are intersected by gratings on a moving disc mounted on the shaft. Three beams produce three digital pulse trains A, B and (see Figure 2.24(a)) Z at the outputs of three receiving optical sensors. The frequency of these pulses is proportional to the speed of the shaft which rotates the disc. The A and B pulses are in quadrature, i.e., 90° out of phase. These pulses can be used to obtain the direction of rotation and the speed. For speed sensing, the pulses are counted in an up–down counter (not shown in Figure 2.24) according to the direction of rotation, using up to four edges of the pulses in a cycle, giving a resolution of up to four times pulse number per rotation as indicated in Figure 2.25. Discs with a few hundred to several thousand pulses with bandwidth limited to around 300 kHz are available. The Z pulse occurs only once in a revolution and is used to reset the counter to zero. The content of the up–down counter after the reset gives the absolute position of the shaft. The counter output is normally Grey coded, so that its content can be read with error no more than ± 1 count.

The absolute encoder has Gray-coded tracks, as many as the number of bits of its resolution, on the disk as shown in Figure 2.26. It also uses as many collimated LED light sources and detectors as the number of tracks (bits) on the disc. The detectors provide Gray-coded absolute position of the shaft directly. This position signal is then differentiated to obtain shaft speed.

www.TechnicalBooksPDF.com

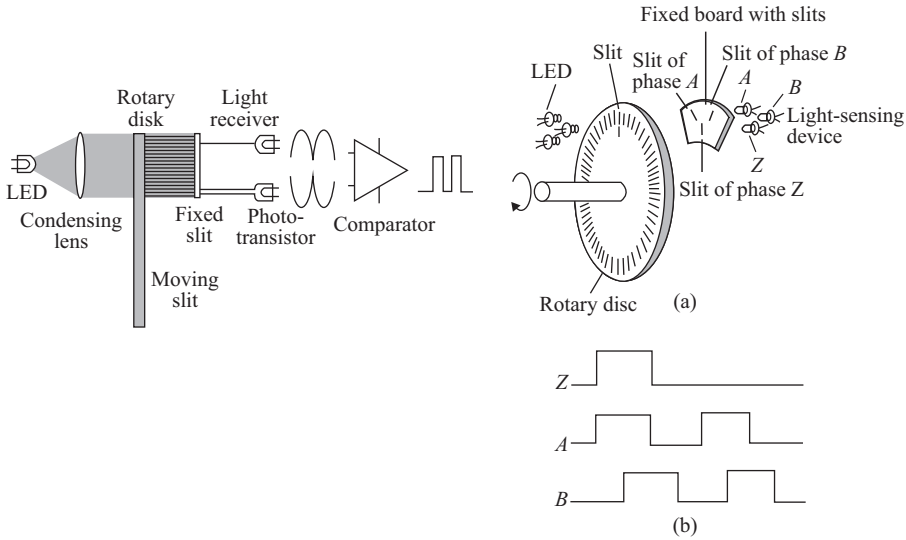


Figure 2.24 Incremental encoder schematic. (a) Schematic details of incremental encoder and (b) Timing of A, B and Z pulses

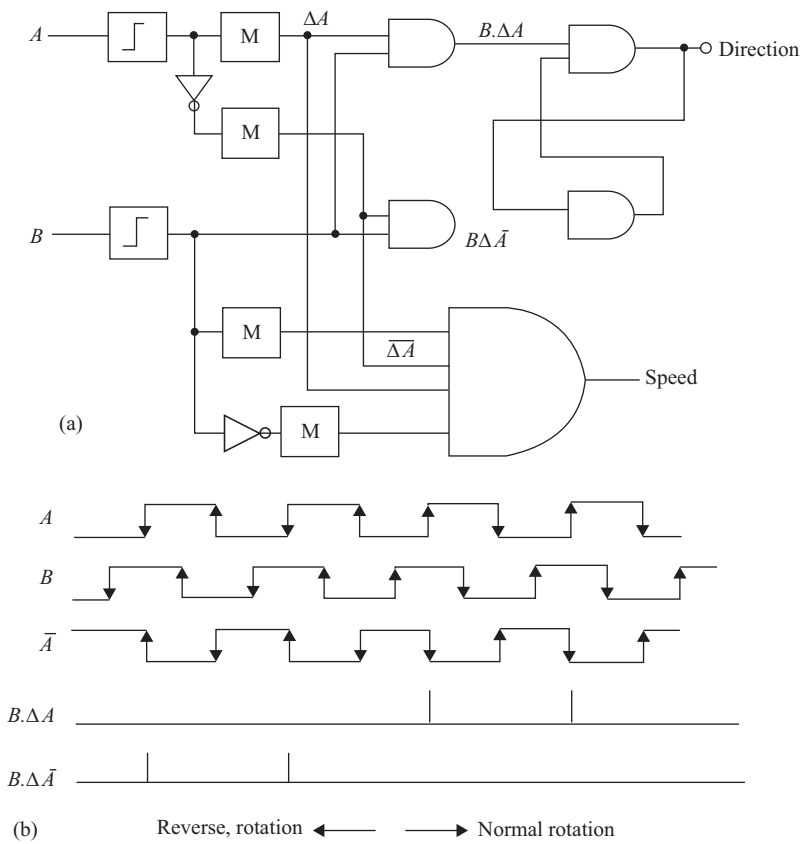


Figure 2.25 Encoder pulse multiplication and direction sensing. (a) Logic circuit of encoder for direction and speed and (b) Pulse multiplication of encoder

www.TechnicalBooksPDF.com

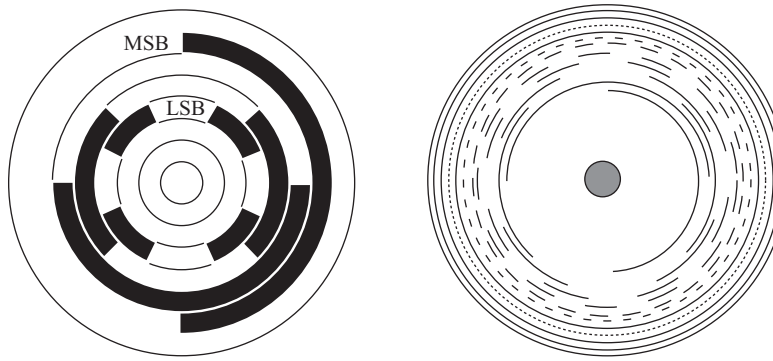


Figure 2.26 Gray-coded discs of absolute encoders

One of the weaknesses of optical encoders is the delicate optical systems with focusing lenses, which are vulnerable to mechanical shock, high temperature and other environmental factors. However, these are immune to stray magnetic fields.

In order to overcome the limitations of optical encoders and magnetic resolvers, a new class of encoders that use shaft-mounted PM poles alternate polarity. A combination of Hall sensors and complex signal-processing circuits mounted on the stator produce position and speed signals that are approaching the performance of optical encoders in terms of line density and high-speed capability.

2.7 Recent developments in PM machines; with reference to developments of other types: DCM and IM

Stringent energy-saving requirements, demands for improved performance-to-cost ratio, compact size and high reliability are some motivating factors behind many research activities that have led to development of novel electric machines. Permanent magnet type machines are at the forefront of these developments. However, conventional electric machines such as DC, induction and synchronous machines also have seen some developments pushed by the requirement of emerging applications. For example, advancement in the technology of doubly fed induction generator is being led solely by the requirements of wind energy conversion. Similarly, most of the current research related to the electrically excited synchronous machine has been spurred by the motivation to reduce size and cost by eliminating the slip rings and brushes. Developments of high torque density and high-performance electric machines are led by electrification of transport and various emerging industrial drive systems. Demands for direct-drive (gearless) technologies in many traditional applications are pushing the frontiers of both the low-speed and high-speed motors.

Many enabling technology contributes toward the recent advancements of electric motors, namely—novel materials, emergence of devices (GaN, SiC) with wide bandgap and high switching frequency, advanced control techniques (sensor-less control, model predictive control), advancement in numerical analysis

www.TechnicalBooksPDF.com

techniques such as finite element method and advanced optimization methods that use genetic algorithm, artificial neural network and particle swarm optimization.

Wide-spread use of permanent magnet machines was made possible by the emergence of high-energy permanent magnet materials—SmCo and NdFeB. Certain grades of sintered NdFeB can have remanence flux density as high as 1.45 T and coercivity 1,100 kA/m and operating temperature up to 230°C. Apart from three main ingredients—neodymium (Nd), iron (Fe) and boron (B), an NdFeB magnet also requires 3%–8% of Dysprosium to improve coercivity. Recent price fluctuation of NdFeB was blamed on the scarcity of Dysprosium (Dy), which is leading the research on Dy-free NdFeB and PM machines with the Dy-free magnet. Because of the same reason, research on reduction and elimination of rare-earth magnet in high-performance PM machine is also gaining momentum.

Apart from the magnet materials, other materials that are impacting on the electric machine design are soft magnetic composite with improved magnetic properties, ferromagnetic alloys with high saturation and temperature withstand capabilities, amorphous ferromagnetic alloy with considerably low core loss, high strength electrical steel, dual-phase material and the high-temperature superconductor.

2.7.1 Developments in winding topologies

The winding topologies of AC machines can be broadly categorized into two groups—(1) distributed winding (DW), also known as the overlapping type, and (2) concentrated winding (CW), also known as the nonoverlapping type and tooth-coil winding. Majority of the conventional AC machines use DW because of low harmonics in the magnetomotive force (MMF) waveform, relatively high winding factors. However, long end-windings of DW may result in longer non-active axial length.

The CW can have short end-winding, high slot-fill factor and easy winding automation. It was shown by Cros *et al.* [7] and Magnussen *et al.* [8] that high winding factors and lower harmonics in MMF could be achieved in CW by an appropriate choice of slot and pole combination. Since in such CW machines slot per-pole per-phase (SPP) is a fraction instead of an integer as in conventional DW, this type of CW is referred as fractional slot CW (FSCW). Based on the number of coil sides in a slot, the DW and CW can be further subdivided into the single and double layer as shown in Figure 2.27. Single layer windings are known to have higher MMF harmonics but negligible mutual inductance, which is useful for fault tolerance capability. It should be noted that MMF harmonics of the CW cause eddy current loss in the magnets of the PM machine, which can be minimized by segmenting the magnets in the axial direction. Higher leakage flux of FSCW increases the leakage inductance, which could be beneficial to reduce the characteristic current (also known as short circuit current) of the PM machines. Theoretically, optimum constant power speed operation is achieved in PM machine when the characteristic current (i.e., the ratio of magnet flux linkage to *d*-axis inductance) is equal to the rated current of the machine. FSCW can be optimized for this condition to achieve wide constant power speed range (CPSR), required by the traction drives of electric and hybrid electric vehicles in PM machines. Such a design process for a PM machine is described fully in Chapter 17.

www.TechnicalBooksPDF.com

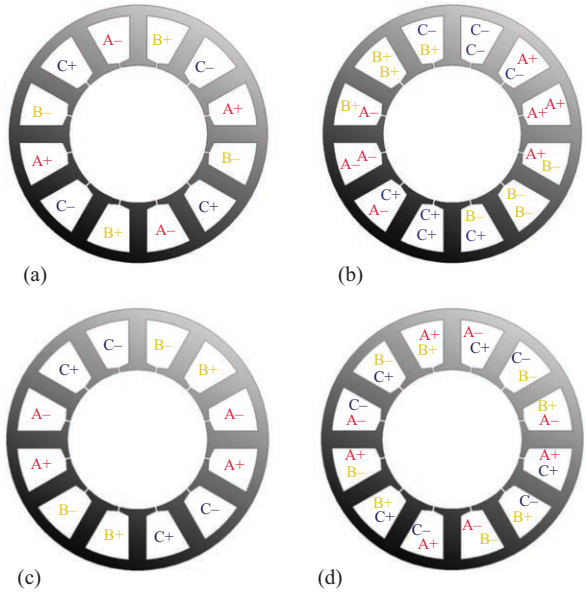


Figure 2.27 Single- and double-layer DW and CW: (a) single-layer distributed windings, (b) double-layer distributed windings, (c) Single-layer concentrated windings and (d) Double-layer concentrated windings

An alternative to DW and CW is the toroidal windings, in which winding is wrapped around the stator yoke, hence easier to manufacture. The toroidal winding is often used with axial flux machines and slot-less, high-speed machines [5–12]. The high slot-fill factor is desirable in electric machines for the efficient use of slot area. A higher slot-fill factor is possible in a toroidal winding than DW and CW, but the requirement of extra space between the toroidal coils increases the total volume of the machine. Quest of a high slot-fill factor has also led to use of rectangular windings of Figure 2.28 [13]. As a unique feature, the end regions of the rectangular winding stator are welded after the insertion of the preformed coils in the slots to ensure efficient use of the end regions. However, thick rectangular coils have higher AC resistance than the conventional stranded coils at high frequency. As a solution to the high loss at high frequency due to skin and proximity effects, Litz-wire winding has been suggested in [14].

2.7.2 *Emerging electric machine topologies*

A number of novel machine topologies, mostly in the space of the PM machine, have been proposed in recent years. Emergences of many of these topologies are driven by applications with challenging specifications. For example, a wave energy conversion system requires very high power density linear generators. Traverse-flux PM linear generator was developed keeping this application in mind [15]. In traverse flux machines, the flux path in the iron core could be made as short as

www.TechnicalBooksPDF.com

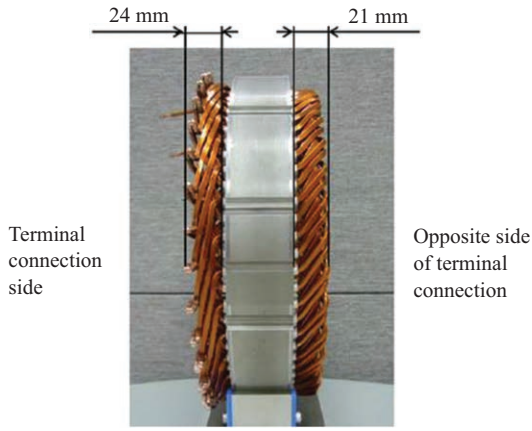


Figure 2.28 A prototype stator with rectangular winding [13]



Figure 2.29 (a) IPM rotor, (b) FSCW stator, (c) completed prototype generator

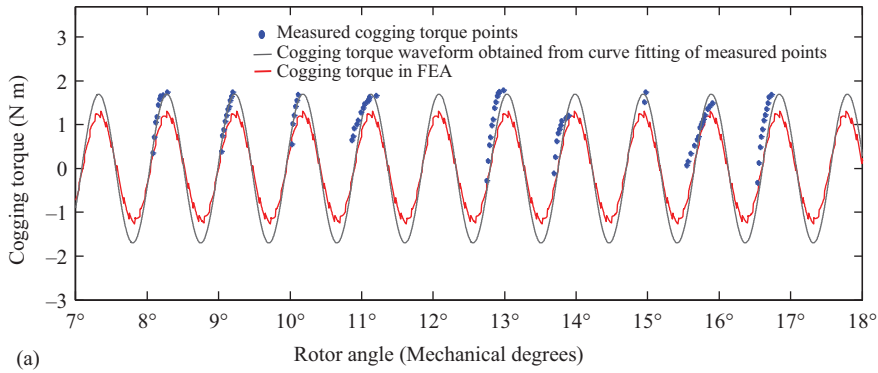
possible to maximize air gap flux density to achieve high power (or torque) per volume. Disc type axial flux PM machines also have considerably high power density. Iron coreless axial flux PM machine is also possible when Halbach magnet arrays are used.

For direct-drive applications that require lows speed, high torque, compact size and lightweight, axial flux PM machine, radial flux surface-type PM machine with Halbach array and FSCW interior permanent magnet (IPM) machines have been proposed [14–18].

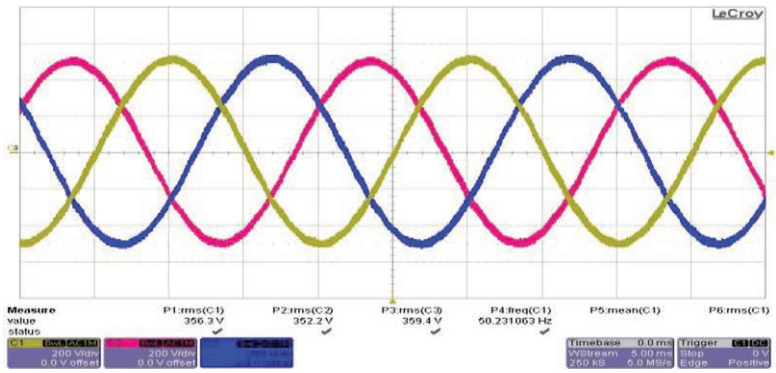
Figure 2.29(a)–(c) shows a prototype 4-kW, 42-pole/54-slot FSCW IPM machine designed at UNSW. This generator has less than 1% cogging torque sinusoidal induced emf shown in Figure 2.30(a) and (b), respectively.

Permanent magnet Vernier (PMV) machine of Figure 2.31(a) is another emerging candidate, which has very high torque density and suitable for direct-drive applications. The PMV machine shares its unique working principle with the magnetic gear machine of Figure 2.31(b). High torque density can be achieved because of the magnetic gear effect, i.e., a small movement of the rotor produces a

www.TechnicalBooksPDF.com

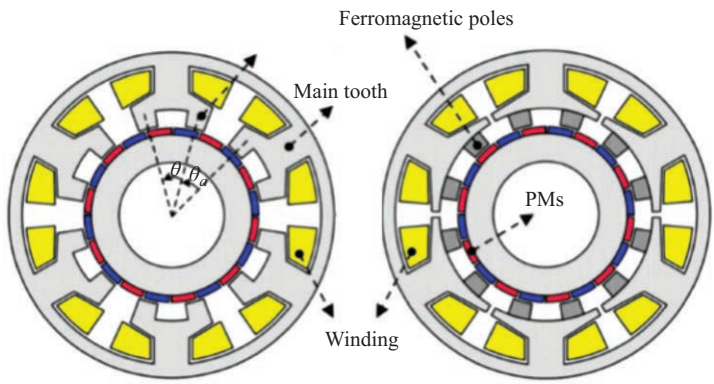


(a)



(b)

Figure 2.30 (a) Measured peak cogging torque of 1% of the rated torque and (b) induced back emf at rated speed



(a) (b)

Figure 2.31 (a) PM Vernier machine and (b) magnetic gear machine [20]

www.TechnicalBooksPDF.com

large change of the flux. In such machines, the stator pole pairs p_s, number of stator auxiliary teeth th_s and rotor pole pairs p_r share a unique relation ($p_r = p_s \pm th_s$). The stator auxiliary teeth modulate the stator flux by producing permeance harmonics of large magnitude in the air gap. The torque is produced by the interaction of the rotor and one component of the stator air gap flux harmonics that has the same pole number and rotational speed as the rotor flux. Dual stator, double rotor, axial flux and consequent pole type PMV topologies have been proposed. Non-overlapping CW and toroidal winding stator have also been proposed in bid to reduce the end-winding length of PMV topologies [19,20].

It is well known that rare-earth magnet losses its magnetic properties irreversibly, when operating temperature exceeds Curie's temperature. Heat dissipation by force cooling is relatively easier in a stator than a rotor, and based on this premise, the motor topologies with placement of PM on the stator have been suggested. Two such topologies that are gaining attention are Doubly salient PM (DSPM) motors and flux-switching PM (FSPM) motors. A DSPM in its simplest form is a switch reluctance motor, stator back iron of which contains permanent magnet poles as shown in Figure 2.32(a). DSPM has simple construction and requires minimum amount of magnet, hence cost-effective. But relatively low torque density due to unipolar flux linkage and large torque ripples is a concern for DSPM motors. Back emf is trapezoidal and requires square wave current for efficient operation. Sinusoidal back emf can be induced using rotor with skew [21,22]. The FSPM motors also have similar structure but capable to produce bipolar flux linkage because of equal number of magnets and stator poles in the stator. Figure 2.32(b) and (c) show a 5-pole/6-slot FSPM motor and a prototype stator, respectively. Usually CWs are used and sinusoidal back emf waveform can be obtained. The magnet volume in an FSPM motor is far larger than a DSPM motor.

Replacing of the magnets with DC excitation has been proposed, which albeit results in lower torque density [24]. Combination of DC and magnet excitation has also been proposed for both DSPM and FSPM motors. These types of motors are often referred to as hybrid excitation motors. The advantage of the presence of DC

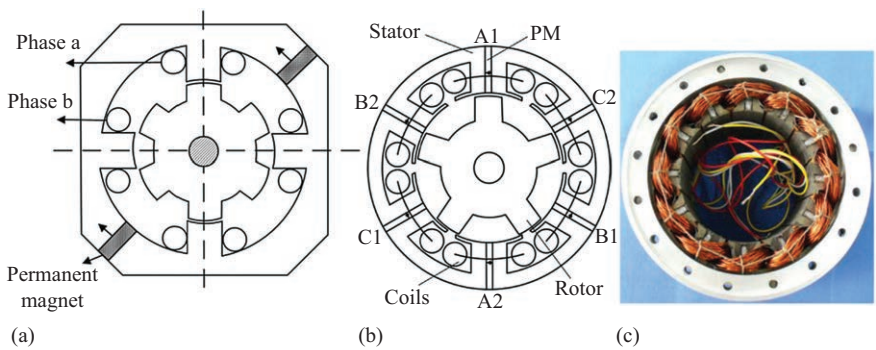


Figure 2.32 (a) Doubly salient PM motor, (b) flux-switching PM motors and (c) prototype of a flux-switching PM motor [23]

www.TechnicalBooksPDF.com

field winding (as shown in Figure 2.33) is that both the flux-weakening and strengthening can be achieved in the hybrid-excited PM motors [25]. However, the presence of additional field winding increases copper losses in the hybrid-excited PM motors.

Flux regulation similar to hybrid excitation motor but without the field winding losses can be achieved if AlNiCo magnets are used instead of ferrite or rare-earth magnets. AlNiCo has a high remanence flux density but low coercivity. By applying a current pulse, the magnetization state of AlNiCo can be adjusted. After removable of the current pulse, magnet can still hold on to the changed magnetization state. Because of this feature, flux-regulating PM motors with AlNiCo are also referred to as "flux memory motors." Even though the flux memory motors need a field winding to apply the current pulse to change magnetization state, the transient nature of the pulse makes the field winding losses negligible. Both AC and DC pulses have been proposed. The concept of variable flux has been applied to radial and axial flux PM motors and also to stator magnet motors like the FSPM motors. In recent times, hybrid variable flux PM motors are also being proposed for electric vehicle (EV) traction applications. This types of variable flux PM motors use a combination of low coercively magnet and NdFeB [26]. Figure 2.34(a) shows a single PM and hybrid-PM variable flux motors [26], and Figure 2.34(b) shows measured no-load back-emf waveforms at three different flux levels of a prototype variable-flux motor [21].

Direct-drive, high-speed applications such as more-electric aircraft and ships, flywheel energy storage, turbo-compressors in automotive, various high-performance industrial drives are gaining momentum in the recent years. Some of the advantages of high-speed motor drives are reduced cost and volume due to the compact size, increased overall system efficiency and reduced maintenance and risk of failure by the elimination of intermediate transmission gear, particularly in direct-drive, high-speed applications. Consequently, research of high-speed machines is gaining attention from both the industry and the academia. Induction machine, switch reluctance machine and PM machines are the three major contenders in the high-speed motor drive applications. Two performance indices—rpm$\sqrt{}$kW and tip speed—are often used to quantify the difficulty in simultaneously achieving both high speed and power. A comprehensive survey conducted in [28]

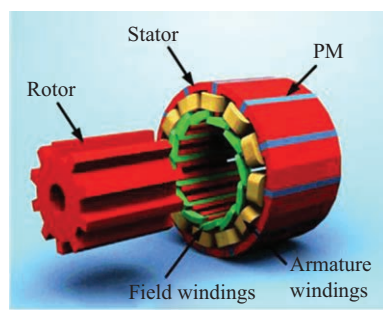
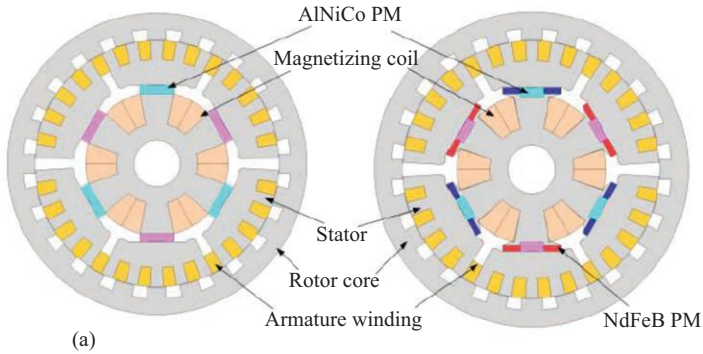


Figure 2.33 Hybrid-excited flux-switching PM motor

www.TechnicalBooksPDF.com



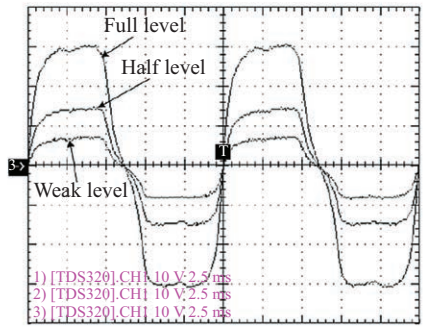


Figure 2.34 (a) Single PM and hybrid-PM variable flux motors and (b) no load back emfs of a variable-flux motor [26,27]

Table 2.1 Tip speed limits of high-speed machine technologies

Machine technologies	**rpm$\sqrt{}$kW**	**Tip speed (m/s)**
Solid rotor induction motor	1×10^6	400
Laminated rotor Induction motor with high strength steel	6×10^5	280
Laminated rotor-induction motor with normal silicon steel	2.5×10^5	185
Switch reluctance motor with high-strength steel laminations	3.5×10^5	210
Surface-PM motors with sleeve and without rotor laminations	8×10^5	300
Interior-PM motors with high-strength steel laminations	1.5×10^5	230

found that the current rpm$\sqrt{}$kW and tip speed limits of various motor technologies as listed in Table 2.1.

It is evident from Table 2.1 that high-strength steel materials play an essential role in the design of high-speed motors. Switch reluctance and surface-type motors may require an additional sleeve on the rotor to enhance mechanical robustness against the substantial centrifugal force generated during the high-speed operation. Titanium, Inconel, carbon and glass fiber are some commonly used materials for

www.TechnicalBooksPDF.com

the sleeve. These materials are nonmagnetic but conductive and hence, prone to eddy current losses. The eddy current losses of the sleeve must be considered carefully during the design of high-speed PM and switched reluctance motor (SRM) machines.

Inadequacy of mechanical bearings also plays a part on the rpm$\sqrt{}$kW limit of high-speed machines. Magnetic bearings resolve some the mechanical limits of common bearings but require long axial shaft to accommodate additional electromagnetic structure [29]. Long shaft reduces critical speed, which is unacceptable for some applications. Shaft length can be minimized if the magnetic bearings are combined with the motor structure. These types of motors are referred as bearingless motors. The bearingless motors requires additional stator windings to produce radial force to suspend the rotor. Similar to electromagnetic torque in an electric motor, the radial force is also the function of the rotor active length [30]. Bearingless concept has been applied to switch reluctance, induction and PM motors. Figure 2.35(a) shows a magnetic bearing of an induction motor, and Figure 2.35(b) shows the principle of production of radial force in a bearingless PM motor.

2.7.3 *Permanent magnet synchronous machines (PMSMs) with deep flux weakening capability*

At present, the PMSM dominates the field of traction application of electric and hybrid electric vehicles as shown in Table 2.2. Apart from high efficiency, the PMSM also offers wide CPSR. The advantage of wide CPSR in an electric motor that provides propulsion in an EV and hybrid electric vehicle (HEV) can be understood from the simple relation derived between motor power P_m and rated speed V_{rm} (m/s) in [32],

$$P_m = \frac{m}{2t_f}\left(V_{rm}^2 + V_{rv}^2\right) \tag{2.58}$$

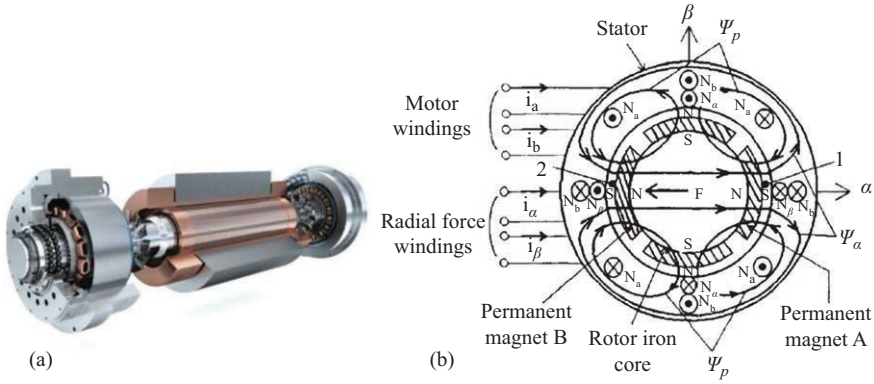


Figure 2.35 (a) Magnetic bearing of an induction motor [31] and (b) production of radial force in a bearingless PM motor [32]

www.TechnicalBooksPDF.com

Table 2.2 Electric motor technologies in EV and HEV

	Manufacturer	Electric motor		ECE data	Battery		
		Type	Power (kW)		Type	Capacity	Range (km)
Hybrid	Honda Insight, 2010	PMSM	9.7	1.3 L petrol	Li-ion	0.6 kW	
	Toyota Prius, 2017	PMSM	23, 53	1.8 L gasoline	Li-ion	8.8 kW h	40
	GM Volt hybrid, 2016	PMSM	55 (MG), 111 (M)	1.4 L petrol	Li-ion	18.4 kW h	85
	Hyundai Ioniq, 2017	PMSM	32	1.6 L petrol	Li-ion	1.56 kW h	
	BMW i3, 2014	PMSM	125	647 cm^3 petrol	Li-ion	33 kW h	290
Plug-in hybrid	Ford Fusion, 2015	PMSM	88	2.5 L petrol	Li-ion	7.6 kW	31
	Hyundai Sonata, 2016	PMSM	50	2.0 L Petrol	Li-ion	9.8 kW	43
All-electric	Tesla Model S, 2017	IM	581 (2 motors)	–	Li-ion	100 kW h	550
	Chevrolet Bolt, 2017	PMSM	150	–	Li-ion	60.0 kW h	380
	Ford Focus, 2017	PMSM	107	–	Li-ion	33.5 kW h	185
	Renault Fluence, 2014	PMSM	70	–	Li-ion	22 kW h	185

where m is the vehicle mass, t_f is the initial acceleration time and V_{rv} is the rated speed of the vehicle in m/s. The (2.59) in terms of rotational speeds of the motor ω_{rm} (rad/s) and the vehicle ω_{rv} (rad/s) can be expressed as

$$P_m = \frac{J}{2t_f}\left(\omega_{rm}^2 + \omega_{rv}^2\right) \tag{2.59}$$

where J is the moment of inertia of the vehicle.

By differentiating (2.59) with respect to ω_{rm} and equating to zero, condition for the minimum rated power of the motor can be found as $\omega_{rm} = 0$ and $P_{\min} = \left(J/2t_f\right)\omega_{rv}^2$. If CPSR is defined as the ratio of motor's rated speed over the maximum speed (CPSR $= \omega_{\max}/\omega_{rm}$), the condition of minimum motor power indicates an infinite CPSR. On the other hand, absence of any CPSR, i.e., $\omega_{rm} = \omega_{rv}$, would result in $P_m = \left(J/t_f\right)\omega_{rv}^2 = 2P_{\min}$, i.e., doubling of the minimum power. Thus, a large value of CPSR would result in a reduced required rated power of the motor of Figure 2.36 that shows an ideal torque- and power-speed characteristic of an electric motor in traction drive of EV. For the Freedom Car 2020, specifications released by US Department of Energy suggest a 5:1 CPSR for plug-in HEV. Majority of the conventional electric motors including PM motors achieving such a wide CPSR poses a challenge. A large body of research works has been dedicated to improve CPSR characteristic of PMSM. The surface-type PMSM with DW has very limited flux-weakening

www.TechnicalBooksPDF.com

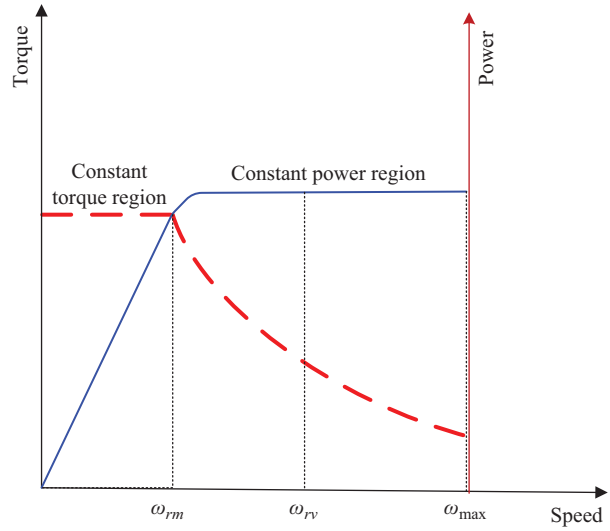


Figure 2.36 Ideal torque- and power-speed characteristic of an electric motor of traction drive in EV

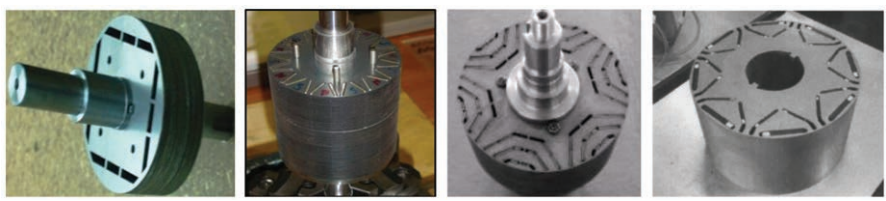


Figure 2.37 (a) Segmented-type, (b) V-type, (c) multilayer type and (d) ∇-type IPM rotors

capability and no useful CPSR. However, with FSCW stator, a much higher CPSR performance has been reported in the literature. Chapter 17 discusses design procedure of such PMSM in details. The IPMSM are capable of flux-weakening and fairly wide CPSR even with the conventional DW. In order to increase the CPSR of an IPMSM further, a number of different types of IPM rotor topologies have been proposed. Among them, the segmented-type, V-type, multilayer and ∇-type IPM rotors are shown in Figure 2.37(a)–(d).

CPSR obtained in a segmented-type IPMSM of Figure 2.37(a) was 3:1, whereas in a V-type IPMSM of Figure 2.37(b) with an FSCW stator was able to provide a CPSR range of 7:1. In the multilayer type IPMSM, an improved saliency ratio (ratio of *q*-axis inductance to *d*-axis inductances) and hence, a larger reluctance torque was achieved [33,34]. The concept of improved reluctance torque of

www.TechnicalBooksPDF.com

multilayer type IPMSM has also been applied in the design of multi-barrier synchronous reluctance and PM-assisted synchronous reluctance motors. It was found in [35] that the relation between the increased layers and increase in reluctance torque is not linear. In fact, more than two layers may not necessarily improve the reluctance torque any further. Design optimization of commonly used IPMSM rotor topologies with double layers has been carried out by the various researchers. Such a design optimization study of a double layer V-type IPMSM has led to a newer rotor topology ∇-type, as shown in Figure 2.37(d); ∇-type rotor has wide operating range with higher efficiency than other double layer types studied in [36].

2.7.4 Control of the PMSM at deep flux weakening

Many PMSM designed for wide CPSR enter into deep flux-weakening near its maximum speed. Conventionally, the PMSM is controlled along an MTPA trajectory in a *d*- and *q*-axes current plane during the constant torque operation. As the speed of the motor increases, the available voltage to provide for the growing back emf becomes limited. Once the voltage limit is reached, flux-weakening must be applied for a viable operation of the motor. At deep flux-weakening operation, motor can be operated along a maximum torque per voltage trajectory (MTPV) or maximum power per voltage trajectory. This trajectory is sometime also referred as minimum flux per torque trajectory. Figure 2.38 shows the typical trajectories. It should be noted that current and voltage limits at various speeds of a PMSM translate to a circle and a series of concentric ellipses in a *d*- and *q*-axes current plane. Shrinking of the ellipses with the increased speeds indicates limitation of the available voltage to support the growing back emf. The center of the concentric

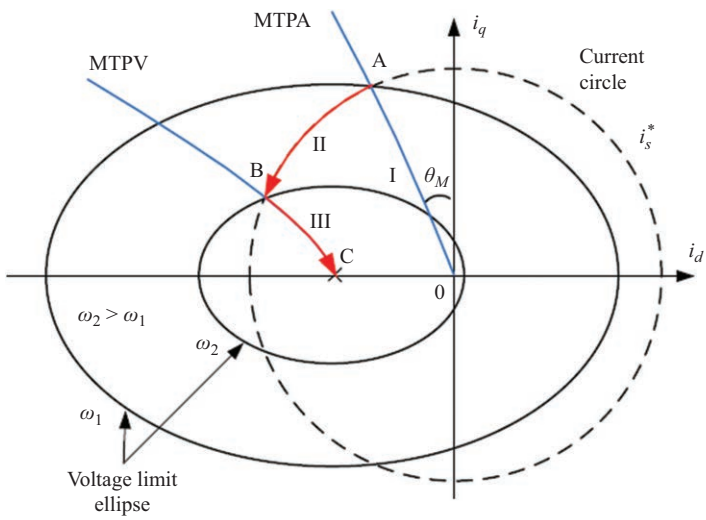


Figure 2.38 MTPA and MTPV trajectories of an IPMSM

www.TechnicalBooksPDF.com

ellipses lies on the negative axis of the *d*-axis current and its coordinate value is (-characteristic current, 0) at point C in Figure 2.38. MTPV trajectory is asymptotical to the ellipse center. If the characteristic current of a PMSM is greater than the rated current of the machine, MTPV trajectory lies outside of the current limit and hence, deep flux-weakening along MTPVtrajectory is not possible in such PMSMs. Similarly, if the characteristic current is equal to the rated current, theoretically, an infinite CPSR is possible, but MTPV trajectory still lies outside of the current limit. The operation along MTPV trajectory is possible only for those PMSM in which characteristic currents are less than the rated currents. For this class of PMSM, although CPSR is limited but theoretically, flux-weakening operation can be extended to the infinite speed. Operation along the MTPV trajectory can improve the performance at deep flux-weakening. Figure 2.39 shows experimentally measured improved performances of a PMSM using MTPV trajectory.

Implementation of the MTPV trajectory requires careful consideration. It is well known that during deep flux-weakening operation, *d*- and *q*-axes current controllers of field-oriented control (FOC) or flux and torque controllers of a direct torque and flux control scheme conflicts with each other. This strong coupling between the *d*- and *q*-axes during the deep flux-weakening also means that control of one of the currents (in case of FOC) should be sufficient. Because of the strong coupling, if one axis current is controlled, the other should automatically follow suit. The concept of the single current regulator (SCR) during deep flux has been proposed based on this premise in [37,38].

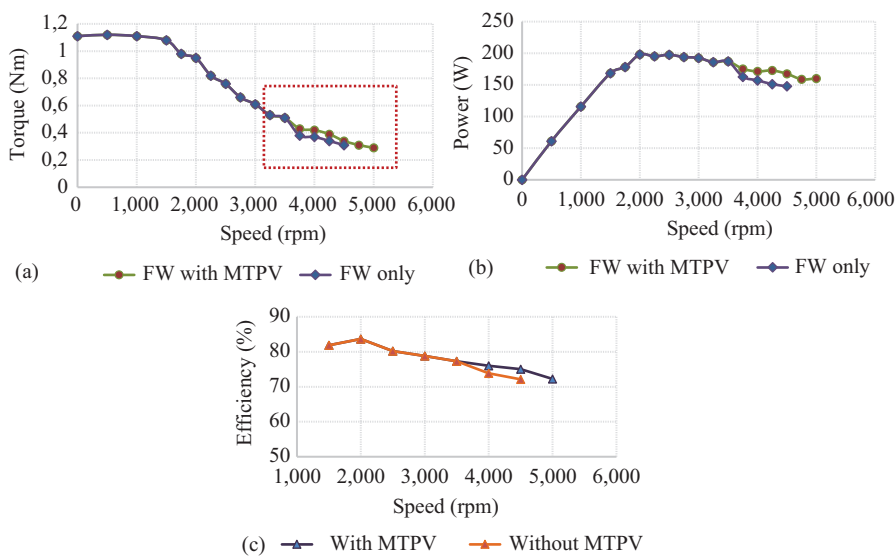


Figure 2.39 Measured (a) torque vs. speed, (b) power vs. speed and (c) efficiency vs. speed of a prototype PMSM with and without MTPV

www.TechnicalBooksPDF.com

2.8 Summary

This chapter gives an overview of three widely used machines of the full range of power spectrum. Steady-state torque–speed boundaries in all four quadrants within and above the base speed for the major types of conventional DC and AC machines are introduced first, followed by the dynamic models of these machines. A limited, by no means complete, analysis of the two dominant types of AC machine (the AC induction and the synchronous) dynamics is included with a view to guide the reader to appreciate the necessity for transformations of voltages and currents and flux linkages of a three-phase machine to one of the rotating axes, in order to appreciate how current controls are used for controlling the torque and flux linkages independently of each other. The logical control structures, the RFOC, for these machines then follow for each machine type. This is followed by a brief description of sensor technologies and associated hardware. Finally an overview of recent developments in the AC induction and PM synchronous machines is included.

List of symbol

φ_f	Rotor flux linkage
P	Number of pole pairs
r	Stator resistance
L_d	d-Axis inductance
L_q	q-Axis inductance
V	Phase voltage
I	Phase current
ω_b	Base speed
T_b	Rated torque
ω_c	Crossover speed
T^*	Torque reference
φ_s^*	Stator flux linkage reference
φ_s	Stator flux vector
φ_f	Rotor flux vector
$\delta.$	Load angle
T_b	Base torque
T_{rated}	Rated torque
$T_{\max}$	Maximum torque
ω_r	Rotational speed
ω_b	Base speed
$\omega_{\max}$	Maximum speed
R_a	Armature winding resistance
R_f	Field winding resistance
L_a	Armature winding inductance

www.TechnicalBooksPDF.com

L_f	Field winding inductance
E_b	Back emf generated across the armature
i_a	Current in armature winding
i_f	Current in field winding
v_a	Voltage across armature winding
v_f	Voltage across field winding
v_a–v_b	Stator voltages in a–b frame
i_a–i_b	Currents in a–b frame
φ_a–φ_b	Flux linkages in a–b frame
v_d–v_q	Stator voltages in d–q frame, θ is the rotor position in electrical radians
i_d–i_q	Currents in d–q frame
φ_d–φ_q	Flux linkages in d–q frame

Glossary of terms

Scalar control	The control of current or voltage in any application as a scalar quantity for control of other parameters
RFOC	Rotor flux-oriented control
IM	Induction motor
PMSM	Permanent magnet synchronous motor
IPMSM	Interior-type permanent magnet synchronous motor
CPSR	Constant power–speed ratio
Resolver	Resolver is an absolute position sensor based on the rotating transformer concept having two windings to generate two signals proportional to sine and cosine of angular displacement
RDC	Resolver to digital converter
LED	Light-emitting diode
PWM	Pulse width modulation
CW	Concentrated winding
DW	Distributed Winding
AMR	Anisotropic magnetoresistive
DSPM	Doubly salient permanent magnet
FSPM	Flux switching permanent magnet machines

References

[1] Control of Electric Machine Drive Systems – S.-K. Sul, Wiley and IEEE Press, Piscataway, NJ, 2011.
[2] Power Electronics and Motor Drives – B. K. Bose, Academic Press, New York, 2006.
[3] Vector Control and Dynamics of AC Drives – D. W. Novotny and T. A. Lipo, Oxford Science Publication, Oxford, 1997.

www.TechnicalBooksPDF.com

[4] https://au.mathworks.com/help/physmod/sps/ug/tune-an-electric-drive.html.
[5] S. Tabata, K. Hasegawa, M. Tsukuda, I. Omura, "New Power Module Integrating Output Current Measurement Function," Proceedings of 29th International Symposium on Power Semiconductor Devices and ICs, July 2017, pp. 267–270.
[6] K. Hasegawa, S. Takahara, S. Tabata, M. Tsukuda, and I. Omura, "A new output current measurement method with tiny PCB sensors capable of being embedded in an IGBT module," IEEE Transactions on Power Electronics, vol. 32, no. 3, pp. 1707–1712, 2017.
[7] J. Cros and P. Viarouge, "Synthesis of high performance PM motors with concentrated windings," IEEE Transactions on Energy Conversion, vol. 17, pp. 248–253, 2002.
[8] F. Magnussen and C. Sadarangani, "Winding factors and Joule losses of permanent magnet machines with concentrated windings," in Electric Machines and Drives Conference, 2003. IEMDC'03. IEEE International, 2003, p. 333.
[9] N. Bianchi, S. Bolognani, and F. Luise, "Analysis and design of a PM brushless motor for high-speed operations," IEEE Transactions on Energy Conversion, vol. 20, pp. 629–637, 2005.
[10] J. Seok-Myeong, J. Sang-Sub, R. Dong-Wan, and C. Sang-Kyu, "Design and analysis of high speed slotless PM machine with Halbach array," IEEE Transactions on Magnetics, vol. 37, pp. 2827–2830, 2001.
[11] E. Muljadi, C. P. Butterfield, and W. Yih-Huie, "Axial-flux modular permanent-magnet generator with a toroidal winding for wind-turbine applications," IEEE Transactions on Industry Applications, vol. 35, pp. 831–836, 1999.
[12] E. R. T. Goodier and C. Pollock, "Homopolar variable reluctance machine incorporating an axial field coil," IEEE Transactions on Industry Applications, vol. 38, pp. 1534–1541, 2002.
[13] T. Ishigami, Y. Tanaka, and H. Homma, "Motor stator with thick rectangular wire lap winding for HEVs," IEEE Transactions on Industry Applications, vol. 51, pp. 2917–2923, 2015.
[14] H. Hämäläinen, J. Pyrhönen, J. Nerg, and J. Talvitie, "AC resistance factor of Litz-wire windings used in low-voltage high-power generators," IEEE Transactions on Industrial Electronics, vol. 61, pp. 693–700, 2014.
[15] H. Polinder, B. C. Mecrow, A. G. Jack, P. G. Dickinson, and M. A. Mueller, "Conventional and TFPM linear generators for direct-drive wave energy conversion," IEEE Transactions on Energy Conversion, vol. 20, pp. 260–267, 2005.
[16] R. Wrobel and P. H. Mellor, "Design considerations of a direct drive brushless machine with concentrated windings," IEEE Transactions on Energy Conversion, vol. 23, pp. 1–8, 2008.
[17] A. D. Gerlando, G. Foglia, M. F. Iacchetti, and R. Perini, "Axial flux PM machines with concentrated armature windings: design analysis and test

www.TechnicalBooksPDF.com

validation of wind energy generators," IEEE Transactions on Industrial Electronics, vol. 58, pp. 3795–3805, 2011.
[18] B. Boazzo, G. Pellegrino, and A. Vagati, "Multipolar SPM machines for direct-drive application: a general design approach," IEEE Transactions on Industry Applications, vol. 50, pp. 327–337, 2014.
[19] Z. Q. Zhu and D. Evans, "Overview of recent advances in innovative electrical machines with particular reference to magnetically geared switched flux machines," in 2014 17th International Conference on Electrical Machines and Systems (ICEMS), 2014, pp. 1–10.
[20] T. Zou, D. Li, R. Qu, D. Jiang, and J. Li, "Advanced high torque density PM vernier machine with multiple working harmonics," IEEE Transactions on Industry Applications, vol. 53, pp. 5295–5304, 2017.
[21] L. Yuefeng, L. Feng, and T. A. Lipo, "A novel permanent magnet motor with doubly salient structure," IEEE Transactions on Industry Applications, vol. 31, pp. 1069–1078, 1995.
[22] M. Cheng, K. T. Chau, and C. C. Chan, "Design and analysis of a new doubly salient permanent magnet motor," IEEE Transactions on Magnetics, vol. 37, pp. 3012–3020, 2001.
[23] M. Cheng, W. Hua, J. Zhang, and W. Zhao, "Overview of stator-permanent magnet brushless machines," IEEE Transactions on Industrial Electronics, vol. 58, pp. 5087–5101, 2011.
[24] Z. Q. Zhu and J. T. Chen, "Advanced flux-switching permanent magnet brushless machines," IEEE Transactions on Magnetics, vol. 46, pp. 1447–1453, 2010.
[25] W. Hua, G. Zhang, and M. Cheng, "Flux-regulation theories and principles of hybrid-excited flux-switching machines," IEEE Transactions on Industrial Electronics, vol. 62, pp. 5359–5369, 2015.
[26] H. Yang, H. Lin, and Z. Q. Zhu, "Recent advances in variable flux memory machines for traction applications: A review," CES Transactions on Electrical Machines and Systems, vol. 2, pp. 34–50, 2018.
[27] C. Yu and K. T. Chau, "Design, analysis, and control of DC-excited memory motors," IEEE Transactions on Energy Conversion, vol. 26, pp. 479–489, 2011.
[28] D. Gerada, A. Mebarki, N. L. Brown, C. Gerada, A. Cavagnino, and A. Boglietti, "High-speed electrical machines: technologies, trends, and developments," IEEE Transactions on Industrial Electronics, vol. 61, pp. 2946–2959, 2014.
[29] X. Sun, L. Chen, and Z. Yang, "Overview of bearingless permanent-magnet synchronous motors," IEEE Transactions on Industrial Electronics, vol. 60, pp. 5528–5538, 2013.
[30] A. Chiba, T. Deido, T. Fukao, and M. A. Rahman, "An analysis of bearingless AC motors," IEEE Transactions on Energy Conversion, vol. 9, pp. 61–68, 1994.
[31] The Journal of Controlled Mechanical Power (2nd quarter, 2014). New standards in Magnetic Bearing Technology – Safra Official Publications, Safra Official Publications. Available: http://www.motioncontrol.co.za/8054a.

www.TechnicalBooksPDF.com

[32] M. Ooshima, A. Chiba, T. Fukao, and M. A. Rahman, "Design and analysis of permanent magnet-type bearingless motors," IEEE Transactions on Industrial Electronics, vol. 43, pp. 292–299, 1996.
[33] N. Bianchi and S. Bolognani, "Interior PM Synchronous Motor for High Performance Applications," Proceedings of the Power Conversion Conference-Osaka 2002, vol. 1, pp. 148–153, 2002.
[34] E. C. Lovelace, T. M. Jahns, J. Wai, *et al.*, "Design and experimental verification of a direct-drive interior PM synchronous machine using a saturable lumped-parameter model.," in Industry Applications Conference, 2002. 37th IAS Annual Meeting, 2002, pp. 2486–2492.
[35] C. Tang, W. L. Soong, T. M. Jahns, and N. Ertugrul, "Analysis of iron loss in interior PM machines with distributed windings under deep field weakening," IEEE Transactions on Industry Applications, vol. 51, pp. 3761–3772, 2015.
[36] K. Yamazaki and K. Kitayuguchi, "Investigation of magnet arrangements in double layer interior permanent-magnet motors," in 2010 IEEE Energy Conversion Congress and Exposition, 2010, pp. 1384–1391.
[37] Z. Zhang, C. Wang, M. Zhou, and X. You, "Flux-weakening in PMSM drives: analysis of voltage angle control and the single current controller design," IEEE Journal of Emerging and Selected Topics in Power Electronics, vol. 7, pp. 437–445, 2019.
[38] F. Xiaocun, H. Taiyuan, L. Fei, and Y. Zhongping, "A novel flux-weakening control method based on single current regulator for permanent magnet synchronous motor," in Power Electronics Conference (IPEC-Hiroshima 2014 – ECCE-ASIA), 2014 International, 2014, pp. 335–340.

www.TechnicalBooksPDF.com

Chapter 3

Converters for drives

Ramkrishan Maheshwari[1]

3.1 Introduction

Electric drives are extensively used in various industries like traction, process industry, aviation industry, etc. Typically, the electric drive consists of three parts: power converter, electric machine, and controller. The electric machines can be a dc machine or an ac machine. The dc machines were traditionally used in electric drives, because the control of the dc machine was very easy and simple. The control was done by using a variable resistance. However, this method is not efficient due to losses in the resistance. Thanks to the advent of the power semiconductor devices in the middle of twentieth century, the resistance is replaced with efficient power converters, which are made by the power semiconductors and convert a constant dc voltage to a variable dc voltage fed to the dc machine. Although the use of the power semiconductors increased the efficiency, the reliability and maintenance of the dc machine is a concern due to commutator and brushes [1].

Due to problems associated with the dc machine, the ac machine drives have become popular. A brief history of development of ac drives is given in [2]. Typically, the performance of the dc drives is superior as the flux and torque of the machine are separately controlled using the field and the armature current, respectively. This makes the magnetic flux and torque control decoupled. The same performance can also be achieved by modelling the three-phase ac machine in a synchronously rotating reference frame. If the reference frame is properly aligned, it can be shown that the ac machine current can be decomposed into torque and flux component which are not coupled with each other. This model can be used to design the controller for the ac machine, referred to as vector control drives, which can achieve the same dynamic performance as that of the dc machine-based drives [3].

High dynamic performance with vector control without the problem of mechanical commutation and maintenance of the dc drives has become the major driving force in replacing the dc drives with the vector controlled ac drives [3]. Conventionally, the three-phase squirrel-cage induction machine and permanent magnet synchronous machine are the most popular choice among several ac machines.

[1]Department of Electrical Engineering, Indian Institute of Technology, Delhi, India

www.TechnicalBooksPDF.com

They require controlled frequency and voltage magnitude of ac supply for easy control. However, the available power is the grid power which has ac supply of constant magnitude and frequency. Due to the power electronic converters, variable voltage and frequency ac supply can be achieved. Typically, the grid power is converted to controlled ac power using ac to ac converter for electric drive applications. These ac to ac converters can be single-stage power converter using matrix converter or a rectifier stage followed by a dc to ac inverters.

The main idea behind the usage of power converters for the drives is to create a controlled power supply from a fixed-frequency and fixed-voltage source with high efficiency. Therefore, these converters are not supposed to use any resistance. Only inductors, capacitors, transformers, and power semiconductor devices are supposed be used in power converters as these components have no losses if considered ideal. Ideal inductor, capacitor, and transformer have no resistance. Furthermore, an ideal power electronic semiconductor device is used as a switch which has

- zero voltage drop across the switch when turned on.
- zero leakage current through the switch when turned off.
- zero turn-on and turn-off time.

This ensures that the ideal power electronics devices have no conduction, blocking, and switching losses. Therefore, the power converters with ideal components are supposed to have 100% efficiency. However, it is not practical to get an ideal component, and the power converters are made with components whose characteristics are close to ideal to increase efficiency. As the cost of these devices and digital controller is decreasing, the usage of the power converters are increasing for the drives application.

There are several types of power converters which are used in the ac drives applications. In this chapter, the dc–ac three-phase voltage source inverters are discussed as they are the most commonly used power converters for the electric drive systems. First, the two-level inverters are discussed in Section 3.3 which are used for low-voltage drives. Then, the three-level inverters are discussed in Section 3.4 which are used for medium voltage drives. These inverters are a source of variable voltage variable frequency ac supply if the output of the inverters is pulse width modulated. Several discussions on the pulse width modulation (PWM) method are available in literature. In this chapter, the most popular PWM methods, the sinusoidal PWM and the space vector PWM, are discussed. The main focus is given on the simple implementation of these methods along with their relation with the theory. This makes this chapter useful for a practitioner engineer as well as academician.

3.2 Three-phase two-level inverter

For converting dc power to a controllable ac power, several dc–ac power inverters are available. Among them, two-level inverter is the most popular inverter. The two-level inverter is shown in Figure 3.1. A phase of the ac side can be connected

www.TechnicalBooksPDF.com

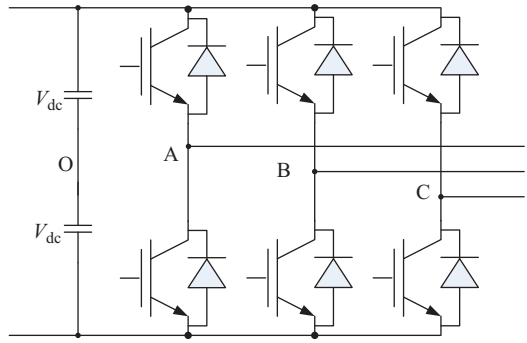


Figure 3.1 Two-level inverter

Table 3.1 Switching states of two-level inverter

	Pole voltage		
Switching state	**Phase A (v_{AO})**	**Phase B (v_{BO})**	**Phase C (v_{CO})**
$---$	$-V_{dc}$	$-V_{dc}$	$-V_{dc}$
$+--$	$+V_{dc}$	$-V_{dc}$	$-V_{dc}$
$++-$	$+V_{dc}$	$+V_{dc}$	$-V_{dc}$
$-+-$	$-V_{dc}$	$+V_{dc}$	$-V_{dc}$
$-++$	$-V_{dc}$	$+V_{dc}$	$+V_{dc}$
$--+$	$-V_{dc}$	$-V_{dc}$	$+V_{dc}$
$+-+$	$+V_{dc}$	$-V_{dc}$	$+V_{dc}$
$+++$	$+V_{dc}$	$+V_{dc}$	$+V_{dc}$

to either the positive dc-link terminal if the top device of that phase is turned on or the negative dc-link terminal if the bottom device of that phase is turned on. Therefore, the pole voltage of a phase is given by

$$v_{xO} = \begin{cases} V_{dc} & \text{if top device of phase } x \text{ is turned on} \\ -V_{dc} & \text{if bottom device of phase } x \text{ is turned on} \end{cases} \tag{3.1}$$

where $x = \{A, B, C\}$, and V_{dc} is equal to half of the total dc-link voltage.

As the pole of the ac side can have two levels, this inverter is called as the two-level inverter. Both devices in a phase should never be turned on simultaneously as it will short the dc power supply. Using this constraint, the two-level three-phase inverter can have $2^3 = 8$ different switching states as listed in Table 3.1. Each state is denoted by combination of plus (+) or minus (−) signs. The plus and minus signs denote that the pole voltage of that particular phase is $+V_{dc}$ and $-V_{dc}$, respectively.

www.TechnicalBooksPDF.com

These switching states are used to generate a set of required three-phase balanced output voltage as given by

$$\begin{aligned} v_{\mathrm{A}} &= V_m \cos(\omega t) \\ v_{\mathrm{B}} &= V_m \cos\left(\omega t - \frac{2\pi}{3}\right) \\ v_{\mathrm{C}} &= V_m \cos\left(\omega t + \frac{2\pi}{3}\right) \end{aligned} \tag{3.2}$$

where V_m is the peak of the desired phase voltage with fundamental frequency denoted by ω.

Although the converter is not able to generate the exact three-phase balanced output voltages, its output voltage can be modulated in a way that it approximates these balanced three-phase voltages. For that, several modulation techniques are used in literature. Among them, the most popular methods are sinusoidal PWM (SPWM) and space vector PWM (SVPWM) techniques [4].

3.2.1 Sinusoidal PWM

The SPWM technique is the most popular PWM technique due to its simplicity. In this method, the three-phase normalized sinusoidal reference signals are obtained by scaling the required ac output voltage as given by

$$\begin{aligned} v_{\mathrm{A,ref}} &= m_a \cos(\omega t) \\ v_{\mathrm{B,ref}} &= m_a \cos\left(\omega t - \frac{2\pi}{3}\right) \\ v_{\mathrm{C,ref}} &= m_a \cos\left(\omega t + \frac{2\pi}{3}\right) \end{aligned} \tag{3.3}$$

where $m_a = V_m/V_{\mathrm{dc}}$ is known as modulation index.

These reference signals are compared with a high-frequency triangular carrier signal, as shown in Figure 3.2. If the reference signal of a phase is higher or lower than the carrier signal, the top or bottom switch is turned on, respectively. Due to this arrangement of switching on/off, the pole voltages of the phases are obtained as shown in Figure 3.3, which is valid for $0<\omega t<\pi/3$. The resultant waveform is shown for one carrier cycle, also known as the switching period, where the reference signals are sampled and assumed to be constant. It can be seen that the applied sequence of the switching states in the carrier period is $(---)\rightarrow(+--)\rightarrow(++-)\rightarrow(+++)$ and reverse.

The pole voltage of phase A averaged over a switching period can be given by

$$\langle v_{\mathrm{AO}} \rangle_{T_s} = V_{\mathrm{dc}} \frac{(2t_a - T_s)}{T_s} \tag{3.4}$$

www.TechnicalBooksPDF.com

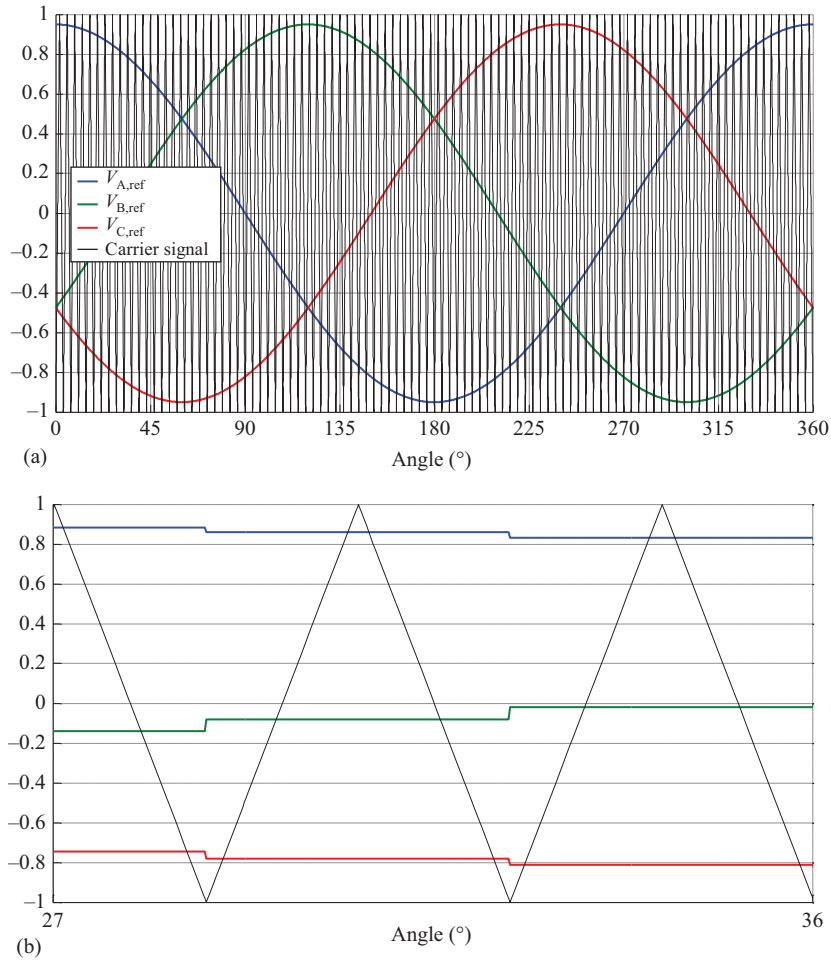


Figure 3.2 Reference and carrier signals for sinusoidal PWM for (a) a fundamental cycle and (b) few carrier cycle

where T_s is the switching period, and t_a can be given by

$$t_a = \frac{1 + v_{\mathrm{A,ref}}}{2} T_s \tag{3.5}$$

Using (3.4) and (3.5), the average value of phase A pole voltage is given by

$$\langle v_{\mathrm{AO}} \rangle_{T_s} = V_{\mathrm{dc}} v_{\mathrm{A,ref}} \tag{3.6}$$

The pole voltage of phase A averaged over a switching period is proportional to the normalized reference signal. Similarly, phases B and C pole voltages averaged over a switching period are proportional to their respective normalized reference

www.TechnicalBooksPDF.com

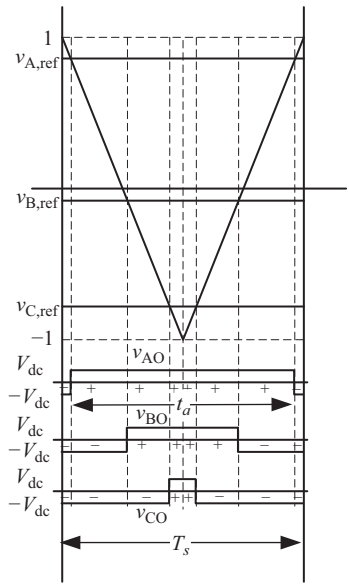


Figure 3.3 Reference signals, carrier signal, and corresponding pole voltage for sinusoidal PWM

signals. If the reference signal is sinusoidal varying, the average pole voltage will also have sinusoidal variation. If the switching period is very small compared to the fundamental cycle, $T_s \ll 2\pi/\omega$, the fundamental component of the three-phase pole voltage will be equal to the required three-phase balanced output voltage given by (3.2).

Equation (3.6) is valid for $m_a<1$. Therefore, the maximum value of the peak voltage V_m for the ac-side output voltage that can be obtained from this method is V_{dc}.

3.2.2 Space Vector PWM

The space vector finds its usage in explaining the rotating magnetic field due to three-phase balanced sinusoidal excitation current in the three-phase sinusoidal distributed winding in an ac machine [5]. The space vector, defined by its α- and β-components, describes the sinusoidal distribution of a variable in 'space'. For a three-phase variable (voltage, current, or any other electrical variable), the space vector is defined by

$$\begin{aligned} \mathbf{F} &= f_\alpha + jf_\alpha \\ f_\alpha &= f_A - \frac{f_B + f_C}{2} \\ f_\alpha &= \frac{\sqrt{3}}{2}(f_B - f_C) \end{aligned} \tag{3.7}$$

where α and β subscript describe the α- and β-components of the space vector.

www.TechnicalBooksPDF.com

The voltage space vector components of the desired three-phase output voltage can be obtained by replacing (3.2) in (3.7), as given by

$$v_\alpha = \frac{3}{2} V_m \cos(\omega t)$$
$$v_\beta = \frac{3}{2} V_m \sin(\omega t) \tag{3.8}$$

If the locus of the tip of the voltage space vector is plotted using (3.8) with respect to time, a circle is obtained. However, the two-level inverter cannot generate these voltage vectors. The space vectors that can be generated by the inverter can be obtained by replacing the voltage levels of the switching states of Table 3.1 in (3.8). The resultant space vectors form the space vector diagram (SVD), as shown in Figure 3.4 [6]. The space vectors $\mathbf{V_1}$–$\mathbf{V_6}$ have the magnitude of $2V_{dc}$, and their tips are located at the corner of a hexagon displaced by 60°. These vectors are called active vectors. The space vector corresponding to two remaining switching states $(+++)$ and $(---)$ has zero magnitude. Therefore, it is known as zero vector. In other words, the zero vector can be realized by two switching states (it has two redundancy), and the active vectors can be realizes by a unique switching state. The active vectors divide the SVD into six sectors identified by roman letters **I**–**VI** in Figure 3.4.

The vertices of a sector are the tip of the two active vectors and the zero vector. These vectors are used to approximate the desired voltage space vector, referred to as the reference vector. The reference vector can be obtained by sampling the reference signals of (3.3) in the switching period T_s and replacing the three-phase sampled reference signals in (3.7) after multiplying with V_{dc}. If the reference vector tip lies in sector I, the reference vector is approximated by applying the active vectors ($\mathbf{V_1}$ and $\mathbf{V_2}$) and zero vector ($\mathbf{V_0}$). The active vectors, $\mathbf{V_1}$ and $\mathbf{V_2}$, are realized by applying switching states $(+--)$ and $(++-)$, respectively, and the zero vector $\mathbf{V_0}$ is realized by applying a combination of switching states

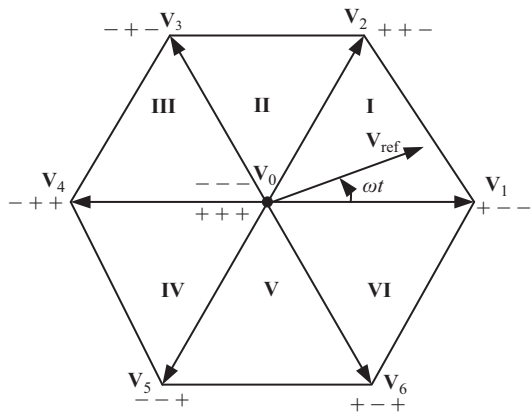


Figure 3.4 Space vector diagram of a two-level inverter

www.TechnicalBooksPDF.com

$(+++)$ and $(---)$. The time for which these switching states need to be applied depends on the magnitude and angle of the desired reference vector, and it is known as the dwell time for that particular switching state. The dwell times for the switching states $(+--)$ and $(++-)$ are given by

$$T_1 = \frac{V_{ref}\sin((\pi/3)-\theta)}{2V_{dc}\sin(\pi/3)}T_s$$
$$\text{and} \quad T_2 = \frac{V_{ref}\sin(\theta)}{2V_{dc}\sin(\pi/3)}T_s, \tag{3.9}$$

respectively. V_{ref} and θ are the magnitude and angle of the reference vector. The dwell time T_1 and T_2 are determined by equating the average of the α- and β-components of the active vectors, $\mathbf{V_1}$ and $\mathbf{V_2}$, to the α- and β-components of the desired reference vector, respectively. The remaining time in the switching period is used for the application of the switching states $(+++)$ and $(---)$ to realize the zero vector. In conventional SVPWM, the dwell time for state $(+++)$ (T_7) and for state $(---)$ (T_0) are equal, as given by

$$T_0 = T_7 = \frac{1}{2}(T_s - T_1 - T_2). \tag{3.10}$$

After the dwell time calculation, the sequence in which switching states need to be applied should be identified. The sequence of the application of the switching states is $(---)\rightarrow(+--)\rightarrow(++-)\rightarrow(+++)$ and reverse. This is same as the sequence for the SPWM as shown in Figure 3.3. For the reference vectors lying in different sector, different switching states will be used in conventional SVPWM which is shown in Table 3.2. The important points which are used to identify the sequence are

- *Three nearest vectors:* Each switching sequence has the three nearest vectors from the tip of the desired reference vector.
- *Single-phase transition:* In a switching sequence, each transition involves transition of only one phase, e.g. in the first row of Table 3.2, $(---)\rightarrow(+--)$ transition has only phase A transition from $-V_{\text{dc}}$ to $+V_{\text{dc}}$, $(+--)\rightarrow(++-)$ transition has only phase B transition from $-V_{\text{dc}}$ to $+V_{\text{dc}}$, and so on.

Table 3.2 Switching sequence for SVPWM

Sector	Switching sequence
I	$(---)\rightarrow(+--)\rightarrow(++-)\rightarrow(+++)$ and reverse
II	$(---)\rightarrow(-+-)\rightarrow(++-)\rightarrow(+++)$ and reverse
III	$(---)\rightarrow(-+-)\rightarrow(-++)\rightarrow(+++)$ and reverse
IV	$(---)\rightarrow(--+)\rightarrow(-++)\rightarrow(+++)$ and reverse
V	$(---)\rightarrow(--+)\rightarrow(+-+)\rightarrow(+++)$ and reverse
VI	$(---)\rightarrow(+--)\rightarrow(+-+)\rightarrow(+++)$ and reverse

www.TechnicalBooksPDF.com

After the switching states and their sequence to be applied are identified, the time for which each switch of the two-level inverter should be turned on can be calculated. For the reference vector in sector I, the times for which top switches of phase A, B, and C are turned on are given by

$$\begin{aligned} T_A &= T_1 + T_2 + T_7 \\ T_B &= T_2 + T_7 \\ T_C &= T_7, \end{aligned} \tag{3.11}$$

respectively. The times for which bottom switches of phase A, B, and C are turned on can be calculated by subtracting (3.11) from T_s.

Although (3.9) and (3.10) calculate the dwell times for the switching state for vectors in sector I, they can be used for other sectors as well, as the space vector diagram has 6-fold symmetry. To use (3.9) for other sectors, the reference vector angle, θ, should be replaced with the angle between the reference vector and the active vector which form the side of the subsector. As an example, if the reference vector lies in sector II, as shown in Figure 3.5, the dwell time of vector $\mathbf{V}_2$ and $\mathbf{V}_3$ is given by T_1 and T_2, respectively, if angle θ is replaced with θ' ($\theta' = \theta - \pi/3$) in (3.9). After finding the dwell times, the switching sequence need to be used is given by Table 3.2, and the duty cycle of each switch can be found using the approach of (3.11). Similarly, the dwell time of the active vectors for the reference vectors lying in other sectors can be found.

The maximum value of the reference vector amplitude that can be approximated using this method is equal to the radius of the circle that can be inscribed by the hexagon of the SVD, as shown in Figure 3.6, which is given by

$$V_{\text{ref, max}} = \sqrt{3} V_{\text{dc}} \tag{3.12}$$

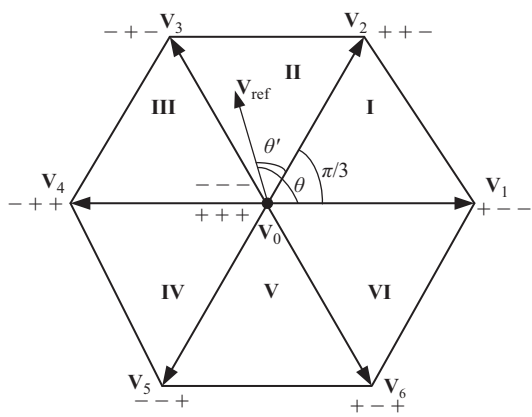


Figure 3.5 Angle calculation for dwell time calculation for the reference vectors lying in sector II

www.TechnicalBooksPDF.com

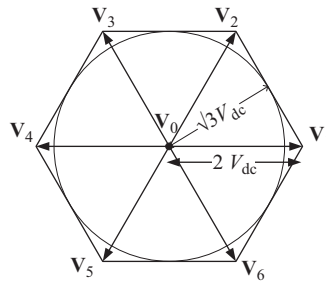


Figure 3.6 Maximum value of the reference vector amplitude for SVPWM method

Using (3.8) and (3.12), it can be said that the maximum value of the modulation index that can be used with the SVPWM is equal to

$$m_{a,\,\max} = \frac{2}{\sqrt{3}} V_{\mathrm{dc}} \tag{3.13}$$

Therefore, the maximum value of the peak voltage V_m for the ac-side output voltage that can be obtained from SVPWM method is 15.47% higher than that of the SPWM method. Therefore, the dc-link utilization of the two-level inverter is better in the SVPWM method compared to the SPWM method.

In summary, the following steps are required to implement the SVPWM method:

- Calculate the reference vector magnitude and angle.
- Identify the sector in which the reference vector lies.
- Find the corresponding value of θ.
- Calculate the dwell times using (3.9) and (3.10).
- Find the duty cycle of each switches of the two-level inverter.

The abovementioned steps require calculation of the magnitude, angle, dwell times, etc. These operations require multiplication, division, square root, etc., which are difficult to implement using analogue circuits and may take a lot of computation time in digital implementation. To simplify the implementation, a carrier-based implementation method is described in the following subsection.

3.2.3 Carrier-based implementation of SVPWM

This method is similar to the SPWM method of comparison where the reference signals are compared with the carrier signal. However, the reference signals are modified by adding a common-mode offset [7] in a way that fundamental component of the line-line voltage remains unchanged. In addition, the modified reference signals ensure the equal dwell time of the switching states to realize the zero vector, as given by (3.10). To find the required common-mode offset, it is required to analyse the switching states applied in the SPWM method. For that, the pole

www.TechnicalBooksPDF.com

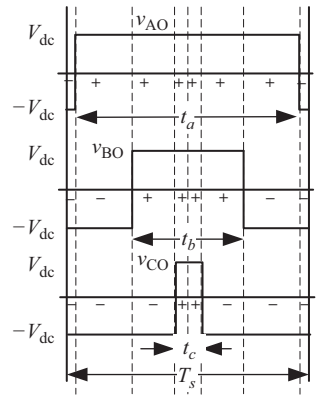


Figure 3.7 Pole voltage and corresponding switching states

voltage and switching state diagram of the SPWM method is repeated again in Figure 3.7. According to this, the dwell time for the switching state $(+--)$ is given by

$$T_1 = t_a - t_b \tag{3.14}$$

t_a is given by (3.5). Similarly, t_b can be calculated. Replacing t_a and t_b in (3.14) yield

$$T_1 = \left(v_{\mathrm{A,ref}} - v_{\mathrm{B,ref}}\right)\frac{T_s}{2} \tag{3.15}$$

Similarly, the dwell time for the switching state $(++-)$ is given by

$$T_2 = \left(v_{\mathrm{B,ref}} - v_{\mathrm{C,ref}}\right)\frac{T_s}{2} \tag{3.16}$$

Although T_1 and T_2 from (3.9) and from (3.15) and (3.16) are derived using two different methods, it can be shown that both set of equations are same by replacing (3.3) in (3.15) and (3.16). However, the dwell times of $(---)$ and $(+++)$, T_0 and T_7, are not equal which was the case with the SVPWM method, but the sum of dwell times of $(---)$ and $(+++)$ can be given by

$$\begin{aligned} T_0 + T_7 &= T_s - T_1 - T_2 \\ T_0 + T_7 &= T_s - \left(v_{A,ref} - v_{C,ref}\right)\frac{T_s}{2} \end{aligned} \tag{3.17}$$

To make $T_0 = T_7$, the reference signals should be modified in two steps. The first step is addition of

$$v_{\mathrm{off1}} = 2 - \frac{2t_a}{T_s} = 1 - v_{\mathrm{A,ref}} \tag{3.18}$$

www.TechnicalBooksPDF.com

to the reference signals of (3.3) which will yield the reference signals and the pole voltages as shown in Figure 3.8(a). In other words, the three-phase reference signals are shifted up in a way that the phase A modified reference signal is equal to the positive peak value of the carrier signal. This step will make the dwell time of $(---)$ equal to zero without changing the dwell times of $(+--)$ and $(++-)$. After this, it is required to shift the reference signals down in way that the dwell times of $(---)$ and $(+++)$ are equal. This can be done by addition of

$$v_{\text{off2}} = -\left(\frac{T_0 + T_7}{T_s}\right) = -1 + \frac{v_{\text{A,ref}} - v_{\text{C,ref}}}{2} \tag{3.19}$$

to the reference signal obtained after addition of (3.18). The resultant reference signals and the switching states are shown in Figure 3.8(b). This step yields $T_0 = T_7$.

In summary, if a common-mode offset, which is calculated from the above-mentioned steps, is added to the reference signals of (3.3), the dwell times of $(---)$ and $(+++)$ can be made equal. The total common-mode offset to be added to the sinusoidal reference signals for implementing the SVPWM method is given by

$$v_{\text{off}} = v_{\text{off1}} + v_{\text{off2}} = -\frac{\left(v_{\text{A,ref}} + v_{\text{C,ref}}\right)}{2} \tag{3.20}$$

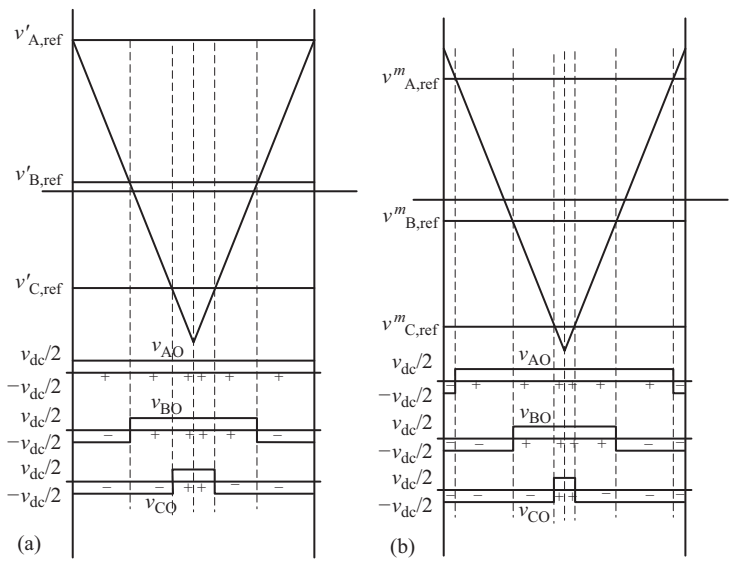


Figure 3.8 The reference signals and pole voltages after addition of (a) (3.18) and (b) (3.18) and (3.19)

www.TechnicalBooksPDF.com

The abovementioned common-mode offset is valid for the reference signals having the reference vector angle between 0° and 60°, for which phase A(C) reference signal has the maximum (minimum) value among the three-phase reference signals.

To find a general equation of the common-mode offset, the symmetry of the three-phase reference signals should be understood. If the reference signals are sampled at any instant, one of the reference signal value will have maximum value and one of the reference signals will have minimum value among the three signals. From the symmetry of the reference signals, as shown in Figure 3.2(a), it can be seen that the waveform of the maximum, middle, and minimum values of the reference signals for 0°–120° is same as that for 120°–240° and 240°–360°. In addition, if the reference signals from 0° to 120° is considered, it can be seen that the waveforms of the maximum, middle, and minimum values are the mirror image of itself around 60°. Therefore, the general equation of the common-mode offset can be found by replacing $v_{A,ref}$ and $v_{C,ref}$ with v_{max} and v_{min}, respectively, as given by

$$v_{off} = -\frac{v_{max} + v_{min}}{2} \tag{3.21}$$

where

$$\begin{aligned} v_{max} &= \max\left(v_{A,ref}, v_{B,ref}, v_{C,ref}\right) \\ v_{min} &= \min\left(v_{A,ref}, v_{B,ref}, v_{C,ref}\right) \end{aligned} \tag{3.22}$$

In summary, the SVPWM method can be carrier-based implemented by using the following steps:

- Sample the three-phase reference signal given by (3.3).
- Sort the sampled signals and find v_{max} and v_{min}. using (3.22).
- Find the common-mode offset using (3.21).
- Add the common-mode offset to the reference signals which yield the modified reference signals as given by

$$v^{m}_{x,ref} = v_{x,ref} + v_{off} \tag{3.23}$$

where $x = \{A, B, C\}$.

Using the abovementioned approach, the modified reference signals and the common-mode offset are shown in Figure 3.9 for $m_a = 1$. If compared with the implementation of the SVPWM method discussed in Section 3.2.2, this method requires sorting, addition, and comparison operations as compared to operations of multiplication, division, square root, etc. Therefore, this method is very simple and efficient to implement.

www.TechnicalBooksPDF.com

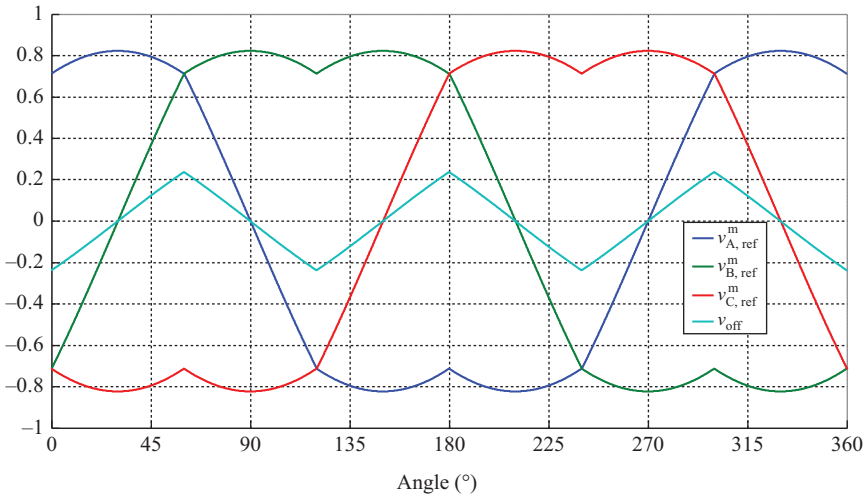


Figure 3.9 The reference signal for carrier-based implementation of the SVPWM method for $m_a = 1$

3.3 Three-phase multilevel inverter

The two-level inverter is the most common topology used for three-phase ac machine. However, this inverter topology is typically used for low power applications. For high-power applications, three-phase multilevel inverters are used. Several topologies are proposed for the multilevel inverter [8]. The most common topology among those topologies is the neutral-point-clamped (NPC) three-level inverter, as shown in Figure 3.10 [9]. This inverter consists of two capacitors connected in series as the dc-link, and the midpoint of the capacitors (O), also known as the neutral-point, is connected to the midpoint of the inverter legs. The main advantages of the NPC three-level inverter are

- Reduced voltage stress on the device.
- Reduced line current total harmonic distortion (THD).
- Reduced electromagnetic interference (EMI).
- Increased efficiency.
- Reduced ac side filter.

If a leg of the NPC three-level inverter is considered, as shown in Figure 3.11, the pole voltage can have three-levels: $+V_{dc}$, 0, and $-V_{dc}$. Different pole voltages and corresponding state of switches are listed in Table 3.3. It can be seen that when the switch S_{x1} (S_{x2}) is turned on, switch S_{x3} (S_{x4}) is turned off. Therefore, if the gate signals for S_{x1} and S_{x2} are known, the gate signals for S_{x3} and S_{x4} can be determined by inverting those signals. Therefore, only two signals are needed to apply a certain pole voltage level among three levels. At different voltage levels, the inverter should be capable to supply the current in both directions, out of and into the pole

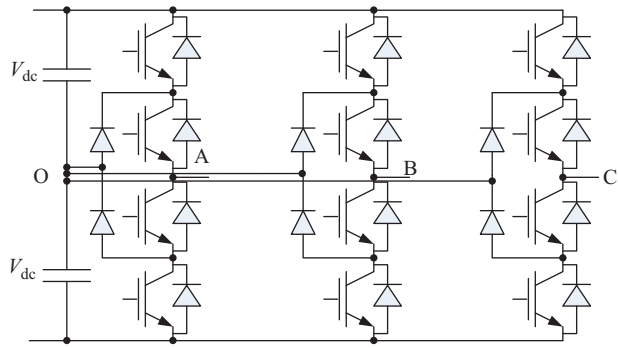


Figure 3.10 Neutral-point-clamped (NPC) three-level inverter

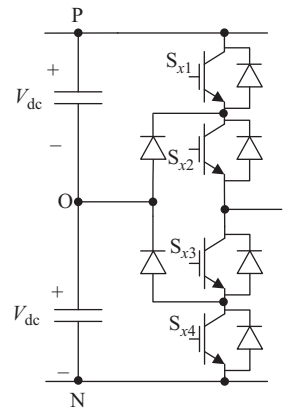


Figure 3.11 A leg of the three-level NPC inverter

Table 3.3 Pole voltage and corresponding state of the switches

Phase×output voltage	$\mathbf{S_{x1}}$	$\mathbf{S_{x2}}$	$\mathbf{S_{x3}}$	$\mathbf{S_{x4}}$
$+V_{dc}$	ON	ON	OFF	OFF
0	OFF	ON	ON	OFF
$-V_{dc}$	OFF	OFF	ON	ON

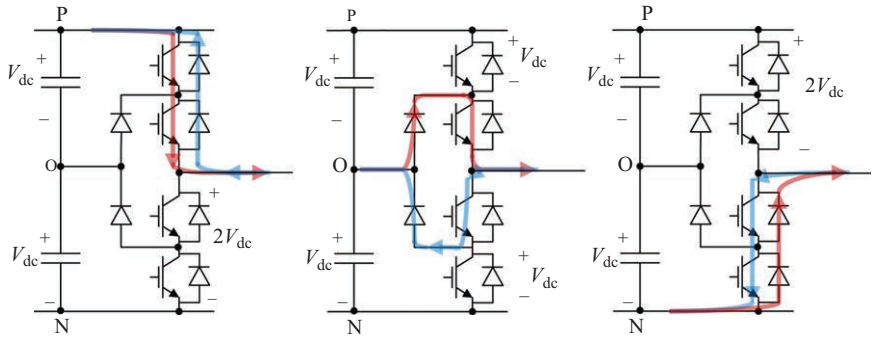


Figure 3.12 Different pole voltage level and current paths

terminal. The direction of the current and corresponding devices that are in conduction are shown in Figure 3.12. The red and blue lines show the current direction, respectively, out of and into the pole terminal. It should be noted that two devices are conducting at any point of time.

As the pole voltage can have three levels, there are $3^3 = 27$ switching states which can be obtained by all possible connection in the three-level inverter as compared to eight switching states in case of two-level inverters, as given in Table 3.4. Each switching state is denoted by a combination of 0, 1, and 2, where 0, 1, and 2 represent the voltage level $-V_{dc}$, 0, and $+V_{dc}$, respectively.

As compared to the two-level inverter, the three-level inverter have more number of switching states and voltage levels. Due to this, the three-phase output voltage of the three-level inverter is expected to have less harmonic distortion. However, the modulation of the three-level inverter is more complicated than that of the two-level inverter. Several PWM methods are available in the literature. Among them, the SPWM method and SVPWM method are the most popular method. These method are discussed in the following subsection.

3.3.1 Sinusoidal PWM

The SPWM for the three-level inverter is based on the comparison of sinusoidal reference signals, as given by (3.3), with two high-frequency carrier signals [10]. The reference signals are sampled and assumed to be constant for the carrier cycle, and the carrier signals are level-shifted as shown in Figure 3.13. The comparison between sampled phase x reference signal, and carrier 1 (carrier 2) decides the state of the switch S_{x1} (S_{x2}). If the reference signal is greater than the carrier 1 (carrier 2), S_{x1} (S_{x2}) is turned on. The gate signal of Sx_3 (S_{x4}) can be found by inverting the gate signal of S_{x1} (S_{x2}). A phase reference signal, carrier signals, corresponding gate signals, and corresponding pole voltage are given in Figure 3.13. The three-phase reference signals and high-frequency carrier signals for a fundamental cycle are shown in Figure 3.14. If the three-phase reference signals are sampled in a carrier

Table 3.4 Switching states and corresponding pole voltages of three-level inverter

	Voltage level		
Switching state	**Phase A**	**Phase B**	**Phase C**
0 0 0	$-V_{dc}$	$-V_{dc}$	$-V_{dc}$
0 0 1	$-V_{dc}$	$-V_{dc}$	0
0 0 2	$-V_{dc}$	$-V_{dc}$	$+V_{dc}$
0 1 0	$-V_{dc}$	0	$-V_{dc}$
0 1 1	$-V_{dc}$	0	0
0 1 2	$-V_{dc}$	0	$+V_{dc}$
0 2 0	$-V_{dc}$	$+V_{dc}$	$-V_{dc}$
0 2 1	$-V_{dc}$	$+V_{dc}$	0
0 2 2	$-V_{dc}$	$+V_{dc}$	$+V_{dc}$
1 0 0	0	$-V_{dc}$	$-V_{dc}$
1 0 1	0	$-V_{dc}$	0
1 0 2	0	$-V_{dc}$	$+V_{dc}$
1 1 0	0	0	$-V_{dc}$
1 1 1	0	0	0
1 1 2	0	0	$+V_{dc}$
1 2 0	0	$+V_{dc}$	$-V_{dc}$
1 2 1	0	$+V_{dc}$	0
1 2 2	0	$+V_{dc}$	$+V_{dc}$
2 0 0	$+V_{dc}$	$-V_{dc}$	$-V_{dc}$
2 0 1	$+V_{dc}$	$-V_{dc}$	0
2 0 2	$+V_{dc}$	$-V_{dc}$	$+V_{dc}$
2 1 0	$+V_{dc}$	0	$-V_{dc}$
2 1 1	$+V_{dc}$	0	0
2 1 2	$+V_{dc}$	0	$+V_{dc}$
2 2 0	$+V_{dc}$	$+V_{dc}$	$-V_{dc}$
2 2 1	$+V_{dc}$	$+V_{dc}$	0
2 2 2	$+V_{dc}$	$+V_{dc}$	$+V_{dc}$

cycle (switching period) and compared with the carrier signals which result in the gate signals as discussed above, the corresponding phase pole voltages are shown in Figure 3.15. The resultant switching sequence is (1 1 0)→(2 1 0)→(2 1 1)→(2 2 1) and reverse.

From Figure 3.15, the pole voltage of phase A averaged over a switching period is given by

$$\langle v_{AO} \rangle_{T_s} = V_{dc} v_{A,ref} \tag{3.24}$$

In general, the pole voltage for a phase averaged over a switching period is given by

$$\begin{aligned} &\langle v_{xO} \rangle_{T_s} = V_{dc} v_{x,ref} \\ &\text{where } x = \{A, B, C\} \end{aligned} \tag{3.25}$$

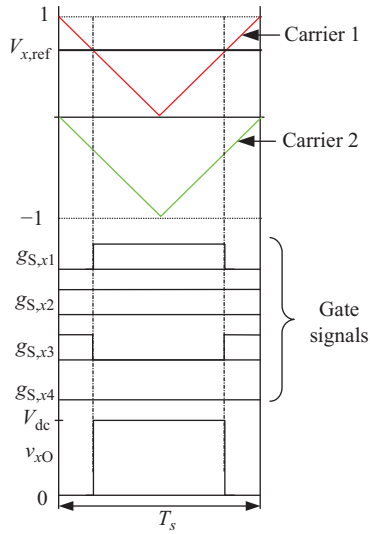


Figure 3.13 A reference signal, carrier signals, corresponding control signals, and the pole voltage for the switches of a phase for the three-level NPC inverter

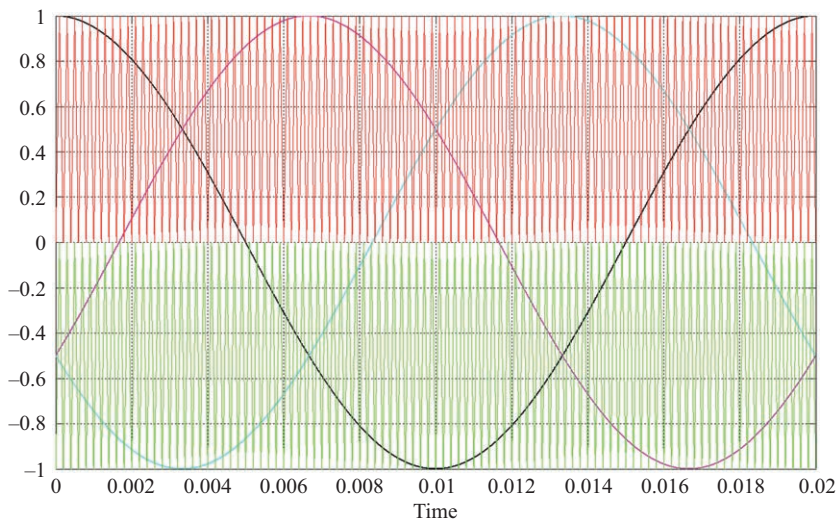


Figure 3.14 Three-phase reference signals and carrier signals for the three-level NPC inverter

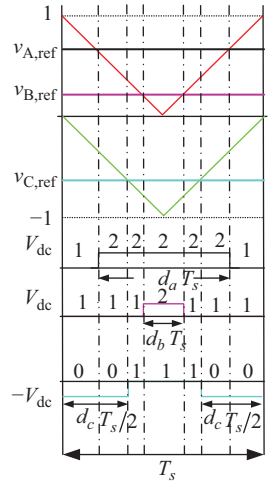


Figure 3.15 Carrier signals, reference signals, and corresponding pole voltage for the three-level NPC inverter

The pole voltages averaged over a switching period is proportional to the corresponding phase reference signals. The same results are obtained in the case of the two-level inverter. However, the instantaneous values of the pole voltages are not the same. The pole voltages in the two-level inverter have transition between $+V_{dc}$, and $-V_{dc}$. On the other hand, the pole voltages in the three-level inverter have transitions between either $+V_{dc}$ and 0 or 0 and $-V_{dc}$. Therefore, the harmonic distortions in the line voltage and line current are reduced. As the voltage transition in switching operation (turn-on or turn-off) is reduced, the switching losses are also reduced. However, as discussed in the previous section, two devices are conducting at any voltage level. This means that the conduction losses are higher than that of the two-level inverters. Therefore, the efficiency of the three-level inverter is expected to be higher than that of the two-level inverter at high switching frequency operation.

The maximum value of modulation index of the reference signals that can be used to generate the ac-side voltage is 1 for the SPWM as achieved in case of the two-level inverter.

3.3.2 Space vector PWM

Using the definition of the space vector in (3.7), the switching states and their corresponding voltage vectors are shown in Figure 3.16. The space vector diagram of the three-level inverter has six large vectors ($\mathbf{V}_{L1}$–$\mathbf{V}_{L6}$) (identical to that generated by the two-level inverter), six medium vectors ($\mathbf{V}_{M1}$–$\mathbf{V}_{M6}$) with no redundancy, six small vectors ($\mathbf{V}_{S1}$–$\mathbf{V}_{S6}$) with two redundancy whose tips are marked

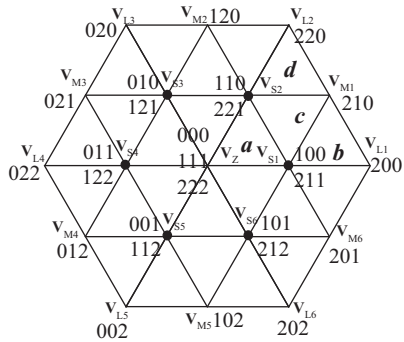


Figure 3.16 Space vector diagram for the three-level inverter

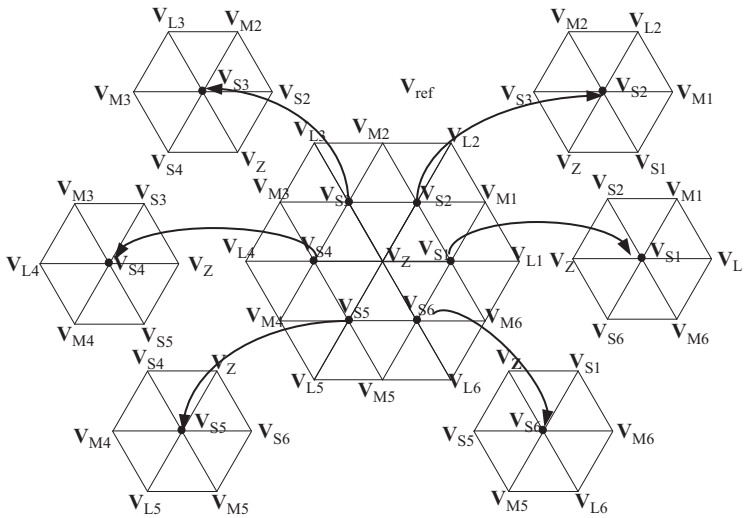


Figure 3.17 Visualization of the three-level space vector diagram as a combination of two-level space vector diagram with reduced dc-link voltage

with big solid dots, and a zero vector ($\mathbf{V}_Z$) with three redundancy. The space vector diagram can be divided into six sectors (identical to that of the two-level inverter). Furthermore, each sector can be divided into four subsectors, marked as ***a–d*** in sector I, whose corners are defined by the tip of the converter space vectors. Several methods to implement SVPWM are proposed [11–13].

To understand the space vector PWM method for the three-level inverter, the space vector diagram can be visualized as a combination of small hexagons, centred at the small vectors ($\mathbf{V}_{S1}$–$\mathbf{V}_{S6}$) with two redundant switching states, which are marked with big solid dots, as shown in Figure 3.17 [13]. Each small hexagon can be considered as the space vector diagram of a two-level inverter with reduced

dc-link voltage of V_{dc}. The small hexagon where the tip of the reference vector lies should be considered for the SVPWM method. After the identification of the small hexagon, a sector of the small hexagon, which is the reduced two-level space vector diagram, should be identified. If one small hexagon is considered, it can be seen that it has six small sectors which are the subsectors of the original three-level inverter space vector diagram. In addition, the centre of the small hexagon has two redundant switching states, which is analogous to two switching states to realize the zero vector in the two-level inverter.

For the SVPWM method, it is necessary to identify the centre with two redundant switching states for a given reference vector whose $\alpha\beta$-components are found from the reference signals and (3.7). For SVPWM, the vector with two redundant switching states is chosen as the centre which is closest to the reference vector. If a reference vector $\mathbf{V}_{ref}$, as shown in Figure 3.18, is considered, it lies in a subsector whose two corners are tip of $\mathbf{V}_{S1}$, $\mathbf{V}_{S2}$, and $\mathbf{V}_{M1}$. It can be seen that the reference vector is closest to $\mathbf{V}_{S2}$. Therefore, $\mathbf{V}_{S2}$ should be chosen as the centre, and the small hexagon with $\mathbf{V}_{S2}$ as the centre should be chosen for further calculation of SVPWM method. To identify the nearest centre in sector I, a line joining the tips of the zero vector and the middle vector ($\mathbf{V}_{M1}$) is drawn. If the tip of the reference vector lies in the triangle formed by tips of $\mathbf{V}_Z$, $\mathbf{V}_{M1}$, and $\mathbf{V}_{L2}$ ($\mathbf{V}_Z$, $\mathbf{V}_{M1}$, and $\mathbf{V}_{L1}$), the centre should be $\mathbf{V}_{S2}$ ($\mathbf{V}_{S1}$). In general, the space vector diagram of the three-level inverter can be divided into six sections by the lines joining the zero vector and middle vectors as shown in Figure 3.18 to identify the unique small vector whose tip can be considered as the centre of the two-level space vector diagram with reduced dc-link voltage. This unique small vector is referred to as the pivot vector.

After the pivot vector is identified, it is subtracted from the reference vector. The resultant vector is the modified reference vector of the two-level space vector diagram with reduced dc-link voltage. This modified reference vector can be used to identify the dwell time of the switching states which can be applied by the three-level inverter. As an example, the reference vector ($\mathbf{V}_{ref}$), as shown in Figure 3.19,

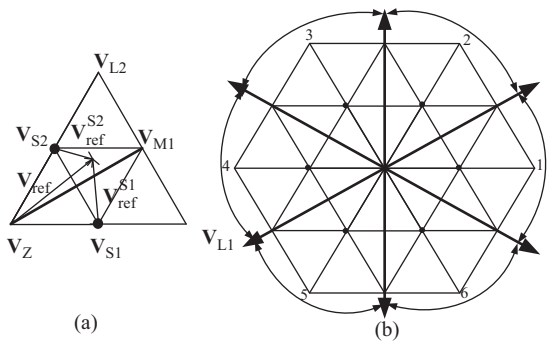


Figure 3.18 Pivot vector selection for the three-level SVPWM method (a) for Sector I (b) in SVD

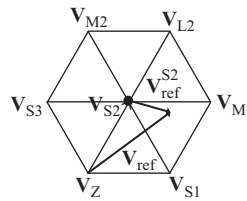


Figure 3.19 Reference vector, pivot vector, and modified reference vector

is considered. The pivot vector for the reference vector is $\mathbf{V}_{S2}$, which is subtracted from the reference vector to get the modified reference vector as given by

$$\mathbf{V}_{ref}^{S2} = \mathbf{V}_{ref} - \mathbf{V}_{S2} \tag{3.26}$$

After finding the modified vector, the switching states used to realize the reference vector are identified. The switching states are that of the three nearest vectors. For the reference vector $\mathbf{V}_{ref}$, the three nearest vectors are $\mathbf{V}_{S1}$, $\mathbf{V}_{M1}$, and $\mathbf{V}_{S2}$ among which $\mathbf{V}_{S1}$ and $\mathbf{V}_{S2}$ have two redundant switching states. To approximate $\mathbf{V}_{ref}$, both redundant switching states of $\mathbf{V}_{S2}$ are used as $\mathbf{V}_{S2}$ is the pivot vector. Besides these switching states, one of the redundant switching states of $\mathbf{V}_{S1}$ and the switching state to realize $\mathbf{V}_{M1}$ are used. To find the switching state to realize $\mathbf{V}_{S1}$, it is important to consider the possible switching sequences with both redundant switching states of $\mathbf{V}_{S1}$. For $\mathbf{V}_{ref}$, the possible switching sequences are

1. (110)→(210)→(211)→(221) and reverse if (211) is used to realize $\mathbf{V}_{S1}$.
2. (110)→(210)→(100)→(221) and reverse if (100) is used to realize $\mathbf{V}_{S1}$.

To find the switching sequences to be applied between the abovementioned possible sequences, the constraint of only one phase transition in each switching state transition should be met. Therefore, the switching sequence for approximating $\mathbf{V}_{ref}$ is the first one where (211) is used to realize $\mathbf{V}_{S1}$. The second switching sequence has two phase transitions for switching state transition of (210) to (100), phase A changes from 2→1 and phase B changes from 1→0. Therefore, this sequence is not recommended. Using similar analysis, the switching sequence for any reference vector can be found.

After the sequence is decided, it is required to calculate the dwell time of each switching state. For this, the magnitude and angle of the modified reference vector is required. If the angle between the modified reference vector and $\mathbf{V}_{M1}$ is given by θ_m, as shown in Figure 3.20, the dwell times of $\mathbf{V}_{M1}$, realized by (210), and $\mathbf{V}_{S1}$, realized by (211), can be given by

$$\begin{aligned} T_1 &= \frac{|\mathbf{V}_{ref}^{S2}|\sin((\pi/3) - \theta_m)}{V_{dc}\sin(\pi/3)} T_s \\ \text{and} \quad T_2 &= \frac{|\mathbf{V}_{ref}^{S2}|\sin(\theta_m)}{V_{dc}\sin(\pi/3)} T_s, \end{aligned} \tag{3.27}$$

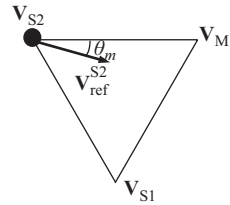


Figure 3.20 Modified reference vector magnitude and angle for dwell time calculation

respectively. Equation (3.27) is similar to (3.7) with denominator term of $2V_{dc}$ in (3.7) is changed to V_{dc} because (3.27) is for the two-level space vector diagram with reduce dc-link voltage of V_{dc}.

The dwell times of the switching states (110) and (221) are given by

$$T_{110} = T_{221} = \frac{1}{2}(T_s - T_1 - T_2) \tag{3.28}$$

The dwell times of (110) and (221) are kept equal as they correspond to the redundant switching states of the pivot vector whose tip is the centre of the two-level space vector diagram with reduced dc-link voltage. (Please note that the redundant switching states of the zero vector of the two-level space vector diagram have equal dwell times in the SVPWM method of the two-level inverter.) Using the dwell times given by (3.27) and (3.28), the duty cycles of individual switches can be found.

In summary, the implementation of the SVPWM for the three-level NPC inverter requires the following steps:

- Identification of the pivot vector.
- Find the modified reference vector, using (3.26), which corresponds to the space vector diagram of the two-level inverter with reduced dc-link voltage centred at the pivot vector.
- Find the switching sequence which meets the constraint of only one phase transition in each switching state transition.
- Find the dwell times of the switching states from (3.27) and (3.28).
- Using the dwell times, find the duty cycle of each switch.

As the large vectors of the three-level SVD are identical to the space vectors of the two-level SV diagram, the maximum value of the modulation index that can be realized by the three-level SVPWM method is same as that of the two-level inverter and given by (3.13).

The abovementioned steps to implement the SVPWM method require mathematical operations such square root and division. This operations are difficult to implement in analogue as well as discrete domain. Therefore, it is important to find a simplified implementation method of the SVPWM similar to the carrier-based implementation of the two-level SVPWM method. There are several methods proposed in the literature to carrier-based implement the three-level SVPWM method. One such method is discussed in the following subsection.

3.3.3 Carrier-based implementation of the three-level SVPWM [14]

As mentioned earlier, the first step for the SVPWM method is to identify the pivot vector with two redundancy which is nearest to the reference vector. To find the pivot vector, the reference vector in sector I is considered, as shown in Figure 3.18(a). The pivot vector can be found if the angle of the reference vector, θ, is known. If $\theta<30^\circ$, the pivot vector is $\mathbf{V}_{S1}$, otherwise it is $\mathbf{V}_{S2}$. However, this requires the calculation of the reference vector angle from the reference signals of (3.3) using (3.7). To reduce the computation complexity of calculating angle, a method to find the pivot vector without calculating the angle is described in the following. For that, the equation of the line joining the tip of the middle vector $\mathbf{V}_{M1}$ with coordinates $(3V_{dc}/2, \sqrt{3}V_{dc}/2)$ to the zero vector $\mathbf{V}_Z$ with coordinates (0,0) is found in terms of the $\alpha\beta$-components of the voltage space vector, v_α and v_β, and it is given by

$$v_\beta = \frac{v_\alpha}{\sqrt{3}} \tag{3.29}$$

Using (3.2), (3.3), (3.7), and (3.29), the tip of the reference vector will lie on the line joining the tip of $\mathbf{V}_{M1}$ and the zero vector $\mathbf{V}_Z$ if

$$v_{B,ref} = 0 \tag{3.30}$$

It can be deduced from (3.30) that the region of sector I which corresponds to $\theta<30^\circ$ can also be identified by

$$v_{B,ref} < 0, \tag{3.31}$$

and the region of $\theta>30^\circ$ of sector I can be identified by

$$v_{B,ref} > 0 \tag{3.32}$$

Therefore, if $v_{B,ref}<0$, the pivot vector is $\mathbf{V}_{S1}$, otherwise it is $\mathbf{V}_{S2}$. In this way, the pivot vector can be identified using the reference signal of phase B without calculating the angle of the reference vector.

As the reference vector under consideration corresponds to $v_{B,ref}>0$, the pivot vector is $\mathbf{V}_{S2}$. After identifying the pivot vector, the pivot vector is subtracted from the reference vector to get the modified reference vector as given by (3.26). The modified reference vector can be represented in terms of its $\alpha\beta$-components as given by

$$\begin{aligned} v^{S2}_{\alpha,ref} &= v_\alpha - v_{\alpha,S2} \\ v^{S2}_{\beta,ref} &= v_\beta - v_{\alpha,S2} \end{aligned} \tag{3.33}$$

To find the $\alpha\beta$-components of the modified reference vector, the $\alpha\beta$-components of the reference vector and $\mathbf{V}_{S2}$ are required. The reference vector $\alpha\beta$-components

can be found by replacing (3.2) in (3.7), and the $\alpha\beta$-components of $\mathbf{V}_{S2}$ can be given by

$$\begin{aligned} v_{\alpha,S2} &= \frac{V_{dc}}{2} = \left(\frac{V_{dc}}{2} - \frac{1}{2}\left(\frac{V_{dc}}{2} - \frac{V_{dc}}{2}\right)\right) \\ v_{\beta,S2} &= \frac{\sqrt{3}V_{dc}}{2} = \frac{\sqrt{3}}{2}\left(\frac{V_{dc}}{2} + \frac{V_{dc}}{2}\right) \end{aligned} \tag{3.34}$$

The $\alpha\beta$-components of $\mathbf{V}_{S2}$ can be obtained by applying (3.7) with the phase voltages $(v_A, v_B, v_C) = (V_{dc}/2, V_{dc}/2, -V_{dc}/2)$, as shown in (3.34). These phase voltages can be obtained by averaging the pole voltages, $(0, 0, -V_{dc})$ and $(V_{dc}, V_{dc}, 0)$, that is applied by the switching states which are required to realize the pivot vector $\mathbf{V}_{S2}$ (110) and (221), respectively.

From (3.2), (3.7), (3.33), and (3.34), the $\alpha\beta$-components of the modified reference vector is given by

$$\begin{aligned} v_{\alpha,\mathrm{ref}}^{S2} &= \left(v_A - \frac{V_{dc}}{2}\right) - \frac{1}{2}\left(v_B - \frac{V_{dc}}{2}\right) - \frac{1}{2}\left(v_C + \frac{V_{dc}}{2}\right) \\ v_{\beta,\mathrm{ref}}^{S2} &= \frac{\sqrt{3}}{2}\left(\left(v_B - \frac{V_{dc}}{2}\right) - \left(v_C + \frac{V_{dc}}{2}\right)\right) \end{aligned} \tag{3.35}$$

If (3.35) is compared with (3.7), the desired modified voltage signals corresponding to the modified reference vector ($\mathbf{V}_{\mathrm{ref}}^{S2}$) which corresponds to the two-level space vector diagram with reduced dc-link voltage of V_{dc} are given by

$$\begin{aligned} v_A^{S2} &= v_A - \frac{V_{dc}}{2} \\ v_B^{S2} &= v_B - \frac{V_{dc}}{2} \\ v_C^{S2} &= v_C + \frac{V_{dc}}{2} \end{aligned} \tag{3.36}$$

If the reference vector angle is less than 30°, $v_{B,\mathrm{ref}} < 0$. Therefore, the pivot vector will be $\mathbf{V}_{S1}$. This means that switching states (100) and (211) will be used to realize the pivot vector. The $\alpha\beta$-components of $\mathbf{V}_{S1}$ can be obtained if the phase voltages $(v_A, v_B, v_C) = (V_{dc}/2, -V_{dc}/2, -V_{dc}/2)$, which is the average of the pole voltages that can be achieved by (100) and (211). Using the abovementioned approach of calculating the $\alpha\beta$-components of the modified reference vector and comparing it with (3.7), the modified voltage signals corresponding to the modified reference vector ($\mathbf{V}_{\mathrm{ref}}^{S1}$) can be written as

$$\begin{aligned} v_A^{S1} &= v_A - \frac{V_{dc}}{2} \\ v_B^{S1} &= v_B + \frac{V_{dc}}{2} \\ v_C^{S1} &= v_C + \frac{V_{dc}}{2} \end{aligned} \tag{3.37}$$

From (3.36) and (3.37), it is clear that the equations of the modified voltage signals for phases A and C, which has maximum and minimum values, respectively, among the three-phase voltages during $0^\circ<\theta<60^\circ$, are same. However, phase-B-modified voltage signals in (3.36) and (3.37) are not same. From (3.36) and (3.37), it can be concluded that

$$\begin{aligned}
&v_{\mathrm{A}}^{PV} = v_{\mathrm{A}} - \frac{V_{\mathrm{dc}}}{2} \\
&v_{\mathrm{C}}^{PV} = v_{\mathrm{C}} + \frac{V_{\mathrm{dc}}}{2} \\
&\text{if}(v_{B,ref} < 0) \\
&\quad v_{\mathrm{B}}^{PV} = v_{\mathrm{B}} + \frac{V_{\mathrm{dc}}}{2} \\
&\text{else} \\
&\quad v_{\mathrm{B}}^{PV} = v_{\mathrm{B}} - \frac{V_{\mathrm{dc}}}{2}
\end{aligned} \tag{3.38}$$

These modified voltage signals can be considered as the desired voltage signals of a two-level inverter with reduced dc-link voltage of V_{dc}. If the symmetry of the three-phase reference signals, as discussed in Section 3.2.3, is considered, and the voltage signals are normalized, a general expression of the modified reference signals can be obtained by replacing $v_{\mathrm{A,ref}}$, $v_{\mathrm{B,ref}}$, and $v_{\mathrm{C,ref}}$ with $v_{\max}$, v_{mid}, and $v_{\min}$, respectively, in (3.38) which yield

$$\begin{aligned}
&v_{\max}^{PV} = v_{\max} - \frac{1}{2} \\
&v_{\min}^{PV} = v_{\min} + \frac{1}{2} \\
&\text{if}(v_{\mathrm{mid}} < 0) \\
&\quad v_{\mathrm{mid}}^{PV} = v_{\mathrm{mid}} + \frac{1}{2} \\
&\text{else} \\
&\quad v_{\mathrm{mid}}^{PV} = v_{\mathrm{mid}} - \frac{1}{2}
\end{aligned} \tag{3.39}$$

From (3.39), it can be said that 1/2 is subtracted from the positive reference signals and added to the negative reference signals to get the modified voltage signals. This modified reference signals correspond to a two-level inverter with reduced dc-link voltage of V_{dc}. Due to reduced dc-link voltage, the carrier signals should also be modified accordingly to get the same dwell time. If 0.5 is subtracted from the positive carrier signal (carrier 1) and 0.5 is added to the negative carrier signal (carrier 2), the resultant carrier signals will be identical with positive and negative peak of 0.5 and -0.5, respectively, as shown in Figure 3.21. The corresponding modified reference signals are also shown. These signals correspond to the original

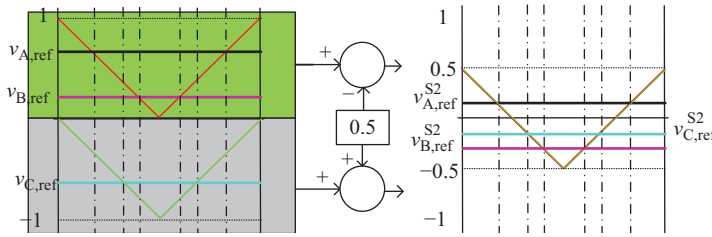


Figure 3.21 Carrier signals and reference signals for modified reference signals

reference signals of Figure 3.15(b) where phases A and C have maximum and minimum values, respectively, among the three signals. However, the modified reference signals do not follow the same trend. Among the modified reference signals, phase A has the maximum value, but phase B has the minimum value instead of phase C. Therefore, resorting of the reference signals is required to find the common-mode offset which is required to be added to the two-level reference signals for carrier-based implementation of the SVPWM method which is given by (3.21).

In this case, the common-mode offset is given by

$$v_{off} = -\frac{v''_{max} + v''_{min}}{2} \tag{3.40}$$

where

$$\begin{aligned} v''_{max} &= \max\left(v^{PV}_{max}, v^{PV}_{mid}, v^{PV}_{min}\right) \\ v''_{min} &= \min\left(v^{PV}_{max}, v^{PV}_{mid}, v^{PV}_{min}\right) \end{aligned} \tag{3.41}$$

The reference signals obtained after the common-mode offset is added to the modified reference signals are the reference signals which can be used to carrier based implement the SVPWM method for two-level inverter with reduced dc-link. To get the final reference signals for the three-level SVPWM method, 0.5 is added to (subtracted from) the modified reference signal from which it was subtracted from (added to) in (3.39). Therefore, in the above example, the final reference signals can be given by

$$\begin{aligned} v^{f}_{A,ref} &= v^{S2}_{A,ref} + v_{off} + \frac{1}{2} \\ v^{f}_{B,ref} &= v^{S2}_{B,ref} + v_{off} + \frac{1}{2} \\ v^{f}_{C,ref} &= v^{S2}_{C,ref} + v_{off} - \frac{1}{2} \end{aligned} \tag{3.42}$$

Replacing $v_{x,\text{ref}}^{\text{S2}}$ after normalizing (3.36) in (3.42)

$$\begin{aligned} v_{\text{A,ref}}^{f} &= v_{\text{A,ref}} + v_{\text{off}} \\ v_{\text{B,ref}}^{f} &= v_{\text{B,ref}} + v_{\text{off}} \\ v_{\text{C,ref}}^{f} &= v_{\text{C,ref}} + v_{\text{off}} \end{aligned} \tag{3.43}$$

Although (3.43) is derived for the reference signals as shown in Figure 3.15(b), it can be easily shown that (3.43) is valid for the reference signals sampled at any instant. In summary, the procedure for carrier based implementation of the SVPWM method for the three-level inverter is given in the following:

- Sample the three-phase reference signal given by (3.3).
- Sort the sampled signals and find v_{max} and v_{min} using (3.22). The remaining phase reference signal is v_{mid}.
- Find the modified reference signal using (3.39) which corresponds to the reference signals of the two-level inverter with reduced dc-link voltage V_{dc}.
- Sort the modified reference signals and find $v''_{\text{max}}$and v''_{min} using (3.41).
- Find the common-mode offset from (3.40).
- Add the common-mode offset to the original reference signals of step 1 to get the final reference signals, as given by (3.43).

It is clear from the above discussions that this implementation method requires the operations of sorting, averaging, and addition as compared to the operation of square root, division, etc., which are required by the SVPWM method discussed in Section 3.3.2. Therefore, the carrier-based implementation of SVPWM is simple, fast, and easy to implement. The original and final reference signals for phase A and the common-mode offset for the three-level inverter calculated from the abovementioned approach are shown in Figure 3.22 for $m_a = 0.9$ and 1.1547. The maximum modulation index that is possible with this method is 1.1547. If the reference signal modulation index is more than that, the final reference signals may have value more than 1 which is outside the range of the carrier signals and thus not feasible with this method.

3.3.4 Neutral-point voltage control

Typically, the inverters are fed by a single dc supply. The dc supply is connected between the positive and negative terminal of the dc-link. Therefore, the potential of those two points are decided by the dc supply. However, the neutral-point O is connected to the mid-points of the inverter legs, and its potential is affected by the pole voltages of the inverter legs and the ac side load. For proper operation of the three-level NPC inverter, it is necessary that the potential difference between the positive dc-link terminal and the neutral-point (v_{PO}) should be equal to that between the neutral-point and the negative dc-link terminal (v_{ON}). To maintain $v_{\text{PO}} = v_{\text{ON}} = V_{\text{dc}}$, the neutral-point current (i_{O}) which is defined as the sum of the currents flowing into the neutral-point from the mid-points of the inverter legs, as

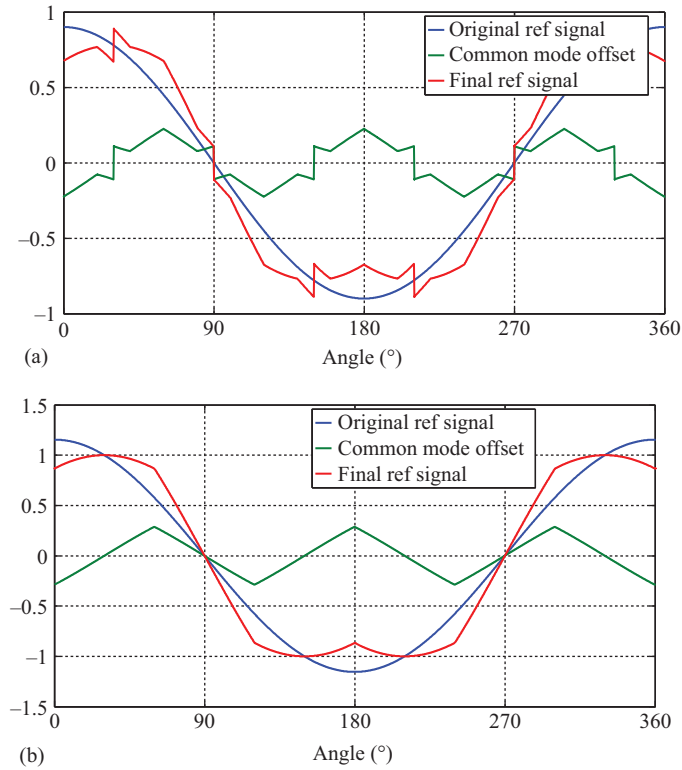


Figure 3.22 Phase A original reference signal, final reference signal, and common-mode offset for (a) $m_a = 0.9$ and (b) $m_a = 1.1547$

shown in Figure 3.23, should be zero. However, this may not be the case if switches S_{x2} and S_{x3} of a particular phase are turned on, and that particular phase current will contribute to the neutral-point current.

To find an expression of the neutral-point current, it is required to find the time for which a phase is connected to the neutral-point which can be found from Figure 3.15 [15]. Using that, the neutral-point current averaged over a switching period can be given by

$$\langle i_O \rangle_{T_s} = (1 - d_A) i_A + (1 - d_B) i_B + (1 - d_C) i_C \tag{3.44}$$

where i_A, i_B, and i_C are the ac-side phases A, B, and C currents, respectively, of the three-level NPC inverter flowing out of the poles. The phase currents are assumed to be constant during the switching period. The duty cycles d_A, d_B, and d_C are the duty cycle corresponding to the time for which phases A, B, and C are connected to positive or negative terminals of the dc-link which can be found in terms of the reference signals, as given by

$$d_x = \left| v_{x,\text{ref}} \right| \tag{3.45}$$

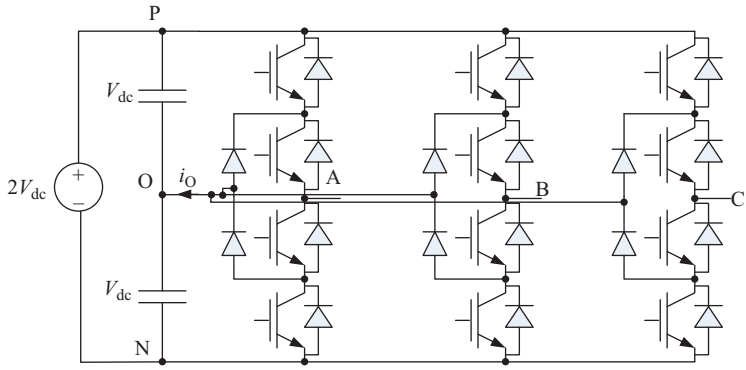


Figure 3.23 Neutral-point-clamped (NPC) three-level inverter

where $x = \{A, B, C\}$.

Equation (3.45) is derived for the SPWM method. However, this can be used for the SVPWM method if the reference signals are replaced with the final reference signals which can be obtained by the method discussed in Section 3.3.3. In general, (3.45) can be written as

$$d_x = \left| v^f_{x,\text{ref}} \right| \tag{3.46}$$

Using (3.44) and (3.46), the averaged neutral-point current is given by

$$\langle i_O \rangle_{T_s} = \sum_x \left(-\left| v^f_{x,\text{ref}} \right| \right) i_x \tag{3.47}$$

In steady state, the averaged neutral-point current depends on the modulation index, PWM method, phase current amplitude, and the power factor angle. The averaged neutral-point current for $m_a = 0.9$ with three-phase balanced load currents with rms amplitude of 15 A and power factor angle of 30° for SPWM and SVPWM method are given in Figure 3.24. It can be seen that the neutral-point averaged over a fundamental cycle is zero for both the SPWM and SVPWM methods. In addition, the neutral-point current averaged over a switching period has frequency equal to three times the fundamental frequency. This causes a voltage ripple at the neutral-point which also has the same frequency. To limit the voltage ripple under a given specification, the capacitance of the dc-link capacitor should be chosen accordingly.

For the neutral-point current of Figure 3.24, the capacitance value for the top and bottom dc-link capacitors is 560 μF for the SPWM method and 310 μF for the SPWM method for 30 V peak–peak voltage ripple at the neutral-point for $V_{dc} =$ 300 V dc-link voltage for $m_a = 0.9$.

In steady-state, as the neutral-point current averaged over a fundamental cycle is zero, the potential of the neutral-point will remain unchanged over the fundamental cycle. However, due to the nonidealities of the system, such as the dead-time, unbalanced loading conditions, or transients, the neutral-point voltage

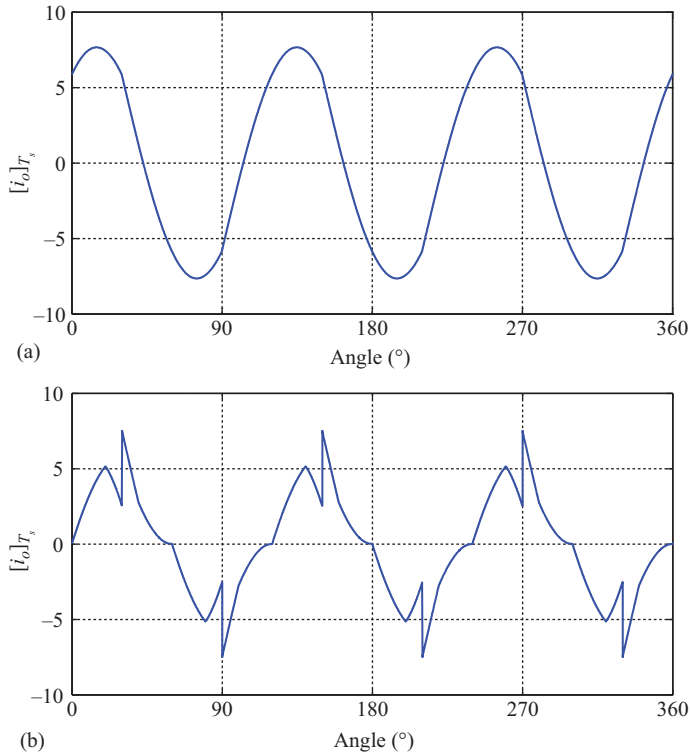


Figure 3.24 Neutral-point current averaged over a switching period for (a) SPWM and (b) SVPWM for $m_a = 0.9$

may change. Therefore, it is required to control the neutral-point voltage. Several neutral-point voltage controllers for this purpose are proposed in literature. Most of these methods use the common-mode offset as the control variable. The common-mode offset affects the neutral-point current which in turn affects the neutral-point voltage. Therefore, the neutral-point voltage controller output is considered as the common-mode offset and added to the reference signals. To design the controller which modifies the common-mode offset to control the neutral-point voltage, it is required to find a mathematical model which describes the dynamic behaviour of the neutral-point voltage. For this, the equation of the neutral-point current as a function of the common-mode offset is required which can be derived using (3.47). From (3.47), the neutral-point current is the sum of three components, and each component corresponds to the contribution of each phase to the neutral-point current. The neutral point current averaged over a switching period because of phase A is given by

$$\langle i_{\mathrm{O,A}} \rangle_{T_s} = -\left| v^{f}_{\mathrm{A,ref}} \right| i_{\mathrm{A}} = -\left| v_{\mathrm{A,ref}} + v_{\mathrm{off}} \right| i_{\mathrm{A}} \tag{3.48}$$

If the common-mode offset is a dc value, the final reference signals will be as given by Figure 3.25 [16]. The neutral point current averaged over a fundamental period can be given by

$$\langle i_{\mathrm{O,A}}\rangle_{T_f} = \frac{1}{2\pi}\int_0^{2\pi} \langle i_{\mathrm{O,A}}\rangle_{T_s} d\theta = \frac{-I_m\cos(\varphi)}{m_a\pi}\left[m_a^2 \sin^{-1}\left(\frac{v_{\mathrm{off}}^{\mathrm{dc}}}{m_a}\right) + v_{\mathrm{off}}^{\mathrm{dc}}\sqrt{m_a^2 - v_{\mathrm{off}}^{\mathrm{dc2}}}\right] \tag{3.49}$$

It can be seen that the neutral point current averaged over a fundamental period depends on the dc common-mode offset ($v_{\mathrm{off}}^{\mathrm{dc}}$), modulation index ($m_a$), ac current amplitude (I_m), and its power factor angle (ϕ). In addition, the constraint for which (3.49) is valid is given by

$$m_a + \left|v_{\mathrm{off}}^{\mathrm{dc}}\right| \leq 1 \tag{3.50}$$

If the abovementioned constraint is not met, the final reference signal will be more than the carrier signal, and the linear relation between average pole voltage and the reference signals will not be true.

The neutral-point current contribution due to phases B and C can be found by similar analysis. It can be derived easily that these current contributions will be same as that of phase A because the added common-mode offset, current amplitude, modulation index, and power factor angle are the same. These individual phase contribution towards the neutral point current should be added to find the total neutral-point current averaged over a fundamental cycle which is equal to three times of the current derived in (3.49), as given by

$$\langle i_{\mathrm{O}}\rangle_{T_f} = 3\langle i_{\mathrm{O,A}}\rangle_{T_f} = \frac{-3I_m\cos(\varphi)}{m_a\pi}\left[m_a^2 \sin^{-1}\left(\frac{v_{\mathrm{off}}^{\mathrm{dc}}}{m_a}\right) + v_{\mathrm{off}}^{\mathrm{dc}}\sqrt{m_a^2 - v_{\mathrm{off}}^{\mathrm{dc2}}}\right] \tag{3.51}$$

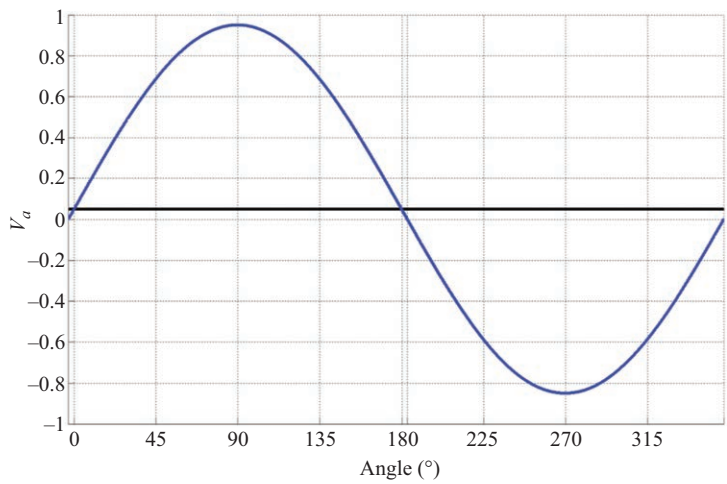


Figure 3.25 Final reference signal for a dc common-mode offset

Once the neutral-point current is derived, the neutral-point voltage can be found by considering the equivalent circuit of the dc-link side of the three-level NPC inverter, as shown in Figure 3.26. Using the circuit, the Kirchhoff's Current Law is applied to the neutral-point which results in

$$\langle i_{\mathrm{dc1}}\rangle_{T_f} - \langle i_{\mathrm{dc2}}\rangle_{T_f} = \langle i_{\mathrm{O}}\rangle_{T_f} \tag{3.52}$$

where i_{dc1} and i_{dc2} are the currents through the top and bottom dc-link capacitors, respectively. Replacing the average neutral-point current of (3.51) in (3.52) and expressing the capacitor currents as function of dc-link capacitor voltages yield

$$C_{\mathrm{dc}}\frac{d}{dt}\left(\langle v_{\mathrm{dc1}}\rangle_{T_f} - \langle v_{\mathrm{dc2}}\rangle_{T_f}\right) = \frac{-3I_m\cos(\varphi)}{m_a\pi}\left[m_a^2\sin^{-1}\left(\frac{v_{\mathrm{off}}^{\mathrm{dc}}}{m_a}\right) + v_{\mathrm{off}}^{\mathrm{dc}}\sqrt{m_a^2 - v_{\mathrm{off}}^{\mathrm{dc2}}}\right] \tag{3.53}$$

where v_{dc1} and v_{dc2} are the voltages across the top and bottom dc-link capacitors. The left-hand side of (3.53) consists of the difference of the top and bottom dc-link voltages which should be maintained to zero.

The dynamic equation of the neutral-point voltage difference, as given by (3.53), is a non-linear equation. Therefore, a linearized model describing the dynamic behaviour of the neutral-point voltage difference for small ac perturbations about a dc operating point should be derived. The model can be considered as a linear model, and linear control system theories can be used to design the controller. For deriving the linearized model, small ac perturbations denoted by '~' are added to the dc operating point values of variables which are denoted by capital letters, as given by

$$\begin{aligned} v_{\mathrm{off}}^{\mathrm{dc}} &= V_{\mathrm{off}}^{\mathrm{dc}} + \tilde{v}_{\mathrm{off}}^{\mathrm{dc}} \\ \langle v_{\mathrm{dc1}}\rangle_{T_f} - \langle v_{\mathrm{dc2}}\rangle_{T_f} &= \Delta V_{\mathrm{dc}} + \Delta\tilde{v}_{\mathrm{dc}} \end{aligned} \tag{3.54}$$

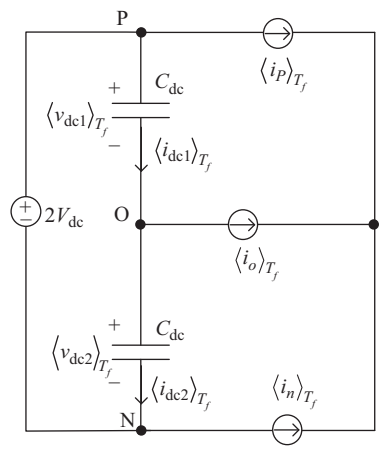


Figure 3.26 Equivalent circuit of the dc-link to find the neutral-point voltage deviation

The dc operating point value of the system governed by (3.53) has $V_{\text{off}}^{\text{dc}}=0$ as the system is expected to have balanced dc-link voltages inherently.

Replacing the variables of (3.54) and the dc operating point values in (3.53),

$$C_{\text{dc}}\frac{d}{dt}(\Delta\tilde{v}_{\text{dc}}) = \frac{-6I_m\cos(\varphi)}{\pi}\tilde{v}_{\text{off}}^{\text{dc}} \tag{3.55}$$

The second-order terms are neglected to find (3.55) which is the linearized small-signal model. It describes the dynamic small-signal behaviour of the neutral-point voltage deviation about the dc steady-state operating point. Equation (3.55) can be used as the plant model to design the controller using the linear control system principles which need the transfer function of the plant, i.e. the transfer function of the control variable ($\tilde{v}_{\text{off}}^{\text{dc}}$) to the output ($\Delta\tilde{v}_{\text{dc}}$). The transfer function of plant can be derived by taking the Laplace Transform of (3.55) and can be given by

$$\frac{\Delta\tilde{v}_{\text{dc}}(s)}{\tilde{v}_{\text{off}}^{\text{dc}}(s)} = \frac{-6I_m\cos(\varphi)}{\pi C_{\text{dc}}s} \tag{3.56}$$

The transfer function of (3.56) can be used to design the controller. To design the controller properly, a control system block diagram consisting the transfer function of the plant of (3.56) and the controller is shown in Figure 3.27. The plant transfer function is pure integral function. Therefore, a simple proportional–integral (PI) controller may be used as the neutral-point voltage controller.

The controller will make sure that both dc-link voltages are equal, and the neutral-point voltage is balanced. If the difference has become nonzero due to some disturbance, the controller will act on the error signal and output a common-mode offset which will change the neutral-point current that can be forced into or out of the neutral-point (O) depending on the error signal. This will charge or discharge the dc-link capacitors accordingly and maintain the neutral-point voltage.

The PI controller parameters are chosen based on the plant transfer function of (3.56). As the transfer function is a function of operating point values, I_m and power factor cosϕ, the PI controller parameters are designed for that particular operating point. To make the controller independent of operating point values, the output of the PI controller may be divided by $I_m\cdot\cos\phi$. The modified control block diagram is shown in Figure 3.28.

The output of the controller discussed above is a dc offset which is added to the sinusoidal reference signals with the SPWM method. Similar analysis can be done if the PWM method is changed. For that, the first step is to find the neutral-point

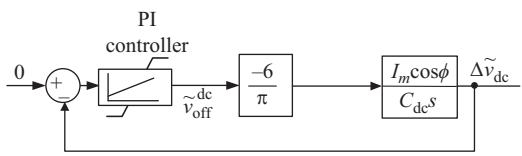


Figure 3.27 Neutral-point voltage control block diagram

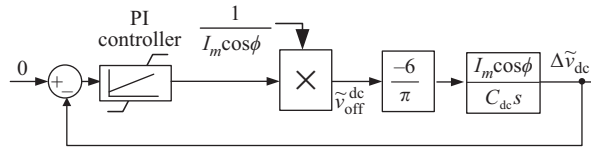


Figure 3.28 Modified neutral-point voltage control block diagram

current as a function of control variable. If the function is non-linear, it is linearized about an operating point in the second step. The linearized function can then be used to choose a controller and its parameters.

3.4 Summary

This chapter presents the most popular dc–ac inverter topologies, two-level and three-level NPC inverter, used for the electric drives. It focuses on the SPWM and SVPWM methods for the two-level and three-level NPC inverters. The emphasis is given to the implementation aspect of these PWM methods. It is shown that the SVPWM method can be implemented in the same way as the SPWM method with small modification in the sinusoidal reference signals. Furthermore, the problem of neutral-point voltage unbalance associated with the three-level NPC inverter is discussed. A popular method to balance the neutral-point voltage is also discussed.

List of symbols

v_{xo}	Pole voltage across phase x = A, B, C
v_A, v_B, v_C	Voltage across three-phases A, B, C
V_m	Peak value of the ac voltage waveform
ω	Angular frequency of ac voltage waveform
$v_{A,ref}$, $v_{B,ref}$, $v_{C,ref}$	Reference voltage across three-phases A, B, C
V_{dc}	Voltage at dc link
m_a	Modulation index
T_s	Switching period
t_a	On time of the switch
F	Space vector
$f_\alpha f_\beta$	α, β components of space vector
v_α v_β	α, β components of voltage space vector
V_{ref}	Magnitude of the reference vector
θ	Angle of the reference vector
T_1	Dwell time
T_A, T_B, T_C	Turn on time of top switches of phases A, B, C, respectively

$V_{\text{ref max}}$	Maximum value of the reference vector
$m_{a\ \max}$	Maximum value of modulation index
v_{off}	Offset voltage
$v_{\max}$	Maximum voltage among reference voltage across three-phases A, B, C
$v_{\min}$	Minimum voltage among reference voltage across three-phases A, B, C
$v^{m}_{x\text{ref}}$	Common-mode offset to the reference signals
S_{x1}, S_{x2}	Upper and lower switches respectively for one leg in phase $x = $ A, B, C
$v^{s}_{x\text{ref}}$	modified reference vector for a switch in phase $x = $ A, B, C
v^{f}_{Cref}	Final reference signals in phase $x = $ A, B, C
d_x	Duty cycles for phases $x = $ A, B, C
v^{dc}_{off}	dc common-mode offset
I_m	ac current amplitude
$\tilde{v}^{\text{dc}}_{\text{off}}$	Control variable
$\Delta\tilde{v}_{\text{dc}}$	Output of the controller

Glossary of terms

Vector control	The control of current or voltage in any application as a vector or sum of vectors
Power electronic converters	ac–dc or dc–dc or ac–ac converters using power electronics switches, i.e. thyristors, IGBTs, MOSFETs
Inverter	A switching circuit used for generation of ac voltage waveforms
Modulation index	The ratio of maximum value of the sinusoidal voltage output to the dc link voltage is referred as modulation index.
Two-level inverter	An inverter which connects the phase of the ac side to two levels of voltage, i.e. the positive dc-link terminal voltage, if the top device of that phase is turned on or the negative dc-link terminal voltage, if the bottom device of that phase is turned on
Sinusoidal PWM (SPWM)	The pulse width modulation (PWM) technique which involves sinusoidal varying reference signal for generation of switching signals for Inverter switches
Multilevel inverter	An inverter which has more than two levels of voltage in the output
Pivot vector	The unique small vector whose tip can be considered as the centre of the two-level space vector diagram with reduced dc-link voltage

References

[1] Wyk J. D. van Skudelny H. C., Müller-Hellmann A. 'Power electronics, control of the electromechanical energy conversion process and some applications'. *IEE Proceedings B – Electric Power Applications*. 1986; 133 (6): 369–399.

[2] Jahns T. M., Owen E. L. 'AC adjustable-speed drives at the millennium: how did we get here?'. *IEEE Transactions on Power Electronics*. 2001; 16(1): 17–25.

[3] Finch J. W., Giaouris D. 'Controlled AC electrical drives'. *IEEE Transactions on Industrial Electronics*. 2008; 55(2): 481–491.

[4] Holtz J. 'Pulsewidth modulation – a survey'. *IEEE Transactions on Industrial Electronics*. 1992; 39(5): 410–420.

[5] Fitzgerald A. E., Kingsley Jr. C., Umans S. D. *Electric Machinery*. 6th edn. New York: McGraw-Hill; 2003. p. 201.

[6] van der Broeck H. W., Skudelny H. C., Stanke G. V. 'Analysis and realization of a pulsewidth modulator based on voltage space vectors'. *IEEE Transactions on Industry Applications*. 1988; 24(1): 142–150.

[7] Blasko V. 'Analysis of a hybrid PWM based on modified space-vector and triangle-comparison methods'. *IEEE Transactions on Industry Applications*. 1997; 33(3): 756–764.

[8] Rodriguez J., Lai J.-S., Peng F. Z. 'Multilevel inverters: a survey of topologies, controls, and applications'. *IEEE Transactions on Industrial Electronics*. 2002; 49(4): 724–738.

[9] Nabae A., Takahashi I., Akagi H. 'A new neutral-point-clamped PWM inverter'. *IEEE Transactions on Industry Applications*. 1981; IA-17(5): 518–523.

[10] Tolbert L. M., Habetler T. G. 'Novel multilevel inverter carrier-based PWM method'. *IEEE Transactions on Industry Applications*. 1999; 35(5): 1098–1107.

[11] Gupta A. K., Khambadkone A. M. 'A space vector PWM scheme for multilevel inverters based on two-level space vector PWM'. *IEEE Transactions on Industrial Electronics*. 2006; 53(5): 1631–1639.

[12] Gupta A. K., Khambadkone A. M. 'A simple space vector PWM scheme to operate a three-level NPC inverter at high modulation index including overmodulation region, with neutral point balancing'. *IEEE Transactions on Industry Applications*. 2007; 43(3): 751–760.

[13] Seo J. H., Choi C. H., Hyun D. S. 'A new simplified space-vector PWM method for three-level inverters'. *IEEE Transactions on Power Electronic*. 2001; 16(4): 545–550.

[14] Maheshwari R., Busquets-Monge S., Nicolas-Apruzzese J. 'A novel approach to generate effective carrier-based pulsewidth modulation strategies for diode-clamped multilevel dc–ac converters'. *IEEE Transactions on Industrial Electronics*. 2016; 63(11): 7243–7252.

[15] Ogasawara S., Akagi H. 'Analysis of variation of neutral point potential in neutral-point-clamped voltage source PWM inverters'. *Proceedings of. IEEE*

Industry Applications Society (IAS) Annual Meeting; Toronto, ON, Canada, Oct 1993. 2, pp. 965–970.

[16] Newton C., Sumner N. 'Neutral point control for multi-level inverters: theory, design and operational limitations'. *Proceedings of. IEEE Industry Applications Society (IAS) Annual Meeting*; New Orleans, LA, Jul 1997. 2, pp. 1336–1343.

Chapter 4

DC motor drives

Sanjeev Singh[1]

This chapter is intended to provide insight on the design and development of controllers for DC motors, their classification and issues related to the control, power quality improvement and sensors reduction for various domestic, commercial and industrial applications.

4.1 Introduction

In most of the motive applications, the load has variable speed or torque and sometimes variable speed and torque, both. Usually, there exist three broad categories of motive applications, namely, variable speed, constant torque applications such as air or refrigerant compressors; variable torque, constant speed applications such as escalators and conveyor belts; and variable speed, variable torque applications such as fans and pumps [1]. The induction or synchronous motors, most commonly used motors, operated from conventional AC power sources, result in almost constant speed [2]. Therefore, to obtain variable speed operation, there are two choices: to operate induction or synchronous motors with appropriate drive [3–5] or to use DC motors with speed control [6–9].

The DC motors suffer from speed limit, noise, wear and electro-magnetic interference (EMI) problems due to the use of commutator and brushes [2]. However, with the advancements in power electronics and digital controllers [9,10], many applications are relooked from view point of energy efficiency improvement and ease of control. Different controller configurations are developed for new and advanced applications of DC motors while adding many convenience features to make them spread over the industrial installations [6–9].

Amongst various DC motors (shunt, series and compound), shunt motors and the separately excited motors are mostly preferred for variable speed applications [2,9]. The speed control of shunt or separately excited DC motor is controlled in two ranges, i.e., below base speed and above base speed. Below base speed, the control is said to be constant torque control because the flux is maintained at its

[1]On LIEN from EIE Department, Sant Longowal Institute of Engineering and Technology, Punjab, India, Working at Electrical Engineering Department, Maulana Azad National Institute of Technology, Bhopal, India

maximum value and the shaft power is directly proportional to the speed of the machine. On the other hand, speed control above the base speed requires the torque to be variable, because in this region, the motor has a constant power (i.e., maximum deliverable power). These controls are conventionally executed as Ward Leonard control [9], alternatively known as armature control (below base speed) and field control (above base speed), respectively. However, efficient and effective control is obtained using power electronic converters and digital signal controllers [10].

For such controls, the voltage and current of armature circuit and field circuit are controlled as per requirement of the load either in open loop (with visual observation) or in closed loop (with automated observation or sensors). When the sensors, actuators, controllers or decision makers and their configurations are combined together, it is known as a drive. This chapter discusses diverse options available with DC motors to operate them in variable speed mode for various applications.

4.2 Modeling of DC motor

For control of DC motor, it is essential to understand the basic model of the DC motor [6–9,11]. The basic model is obtained as mathematical equation from its equivalent circuit shown in Figure 4.1. The armature and field windings are represented as series combination of resistance (R_a and R_f, respectively) and inductance (L_a and L_f, respectively), whereas the back-emf of armature is considered as a voltage source (E_b) connected in series with R_a and L_a. The voltage equations for armature and field circuits (i_a and i_f, respectively), in terms of armature and field currents, are written as

$$V_a = R_a i_a + L_a \frac{di_a}{dt} + E_b \tag{4.1}$$

$$V_f = R_f i_f + L_f \frac{di_f}{dt} \tag{4.2}$$

The back-emf is an emf induced in the rotor windings of the DC motor due to rotation, measured across the brushes, represented as a function of flux linkage (φ) and rotor speed in rounds per minute (N).

$$E_b = K_b N \varphi \tag{4.3}$$

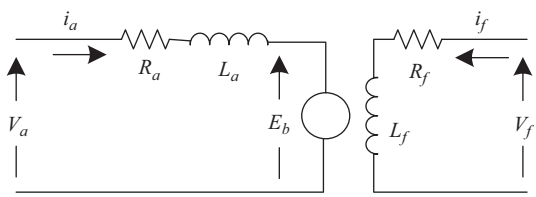


Figure 4.1 Equivalent circuit of a DC motor

where

$$K_b = \frac{pZ}{60a} \tag{4.4}$$

and

$$\varphi = B_{g\,\mathrm{av}}\tau l \tag{4.5}$$

for a given DC motor with p number of poles, a number of parallel paths in armature, N rpm armature (rotor) speed, Z number of armature conductors, $B_{g\ \mathrm{av}}$ average air gap flux density per pole, τ pole pitch and l pole stack length.

The spatial phase difference between the stator and rotor (armature) magnetic fields in a DC motor is observed as 90°; therefore, induced voltage due to transformer action shall be zero between stator field and armature windings in the absence of magnetic saturation. This phenomenon facilitates a decoupled control of field and armature currents (or torque) in a DC motor as an extraordinary built in feature.

The power across the rotor shall be the product of back-emf (E_b) and armature current (i_a). This power is utilized for generation of torque (T_e) in the shaft connected to rotor at ω radians per second angular speed. Therefore, the power (P_e) of the DC motor can be represented as

$$P_e = E_b i_a = T_e \omega \tag{4.6}$$

$$\omega = \frac{2\pi N}{60} \tag{4.7}$$

Using (4.3), (4.6) and (4.7), the relation for torque may be written as

$$T_e = \frac{30K_b}{\pi}\varphi i_a \tag{4.8}$$

During steady-state operation of DC motor, assuming that speed and torque are constant as a result of constant field and armature currents, (4.1) and (4.2) may be rewritten while using (4.3) as

$$V_a = R_a i_a + K_b N \varphi \tag{4.9}$$

$$V_f = R_f i_f \tag{4.10}$$

Using (4.8), the armature voltage represented in (4.9) is given as

$$V_a = R_a \frac{T_e \pi}{30\varphi K_b} + K_b N \varphi \tag{4.11}$$

The speed (N) of the DC motor can be represented as

$$N = \frac{1}{\varphi K_b}\left[V_a - R_a \frac{T_e \pi}{30\ \varphi K_b}\right] \tag{4.12}$$

Equation (4.12) presents that, for a constant torque operation, the speed of DC motor can be reduced efficiently by controlling the armature voltage (V_a), whereas increase in speed is obtained by flux (φ) control. The resistance (R_a) control shall

lead to inefficient operation of DC motor. However, for speed control above base speed using flux control, the constant power operation is observed which reduces the torque of the motor.

The inertia (J), frictional torque (B), rotor torque (T_e), rotor speed in round per second (n) and load torque (T_{load}) of the DC motor are related as

$$T_e - T_{\text{load}} - Bn = J\frac{d\omega}{dt} \tag{4.13}$$

For constant flux operation of DC motor, i.e., the field current is constant, (4.6) and (4.8) may be rewritten as

$$E_b = K_E\omega \tag{4.14}$$

$$T_e = K_T i_a \tag{4.15}$$

where $K_E = (K_b\varphi/2\pi)$ and $K_T = (30K_b\varphi/\pi)$

Accordingly, (4.1) and (4.13) can be rewritten as

$$\frac{di_a}{dt} = \frac{V_a}{L_a} - \frac{R_a}{L_a}i_a - \frac{K_E}{L_a}\omega \tag{4.16}$$

$$\frac{d\omega}{dt} = \frac{K_T}{J}i_a - \frac{B}{J}n - \frac{T_{\text{load}}}{J} \tag{4.17}$$

For variable flux operation, (4.1), (4.2) and (4.13) can be rewritten as

$$\frac{di_f}{dt} = \frac{V_f}{L_f} - \frac{R_f}{L_f}i_f \tag{4.18}$$

$$\frac{di_a}{dt} = \frac{V_a}{L_a} - \frac{R_a}{L_a}i_a - \frac{NK_b}{L_a}i_f \tag{4.19}$$

$$\frac{d\omega}{dt} = \frac{30\,K_b}{\pi J}i_f i_a - \frac{B}{J}n - \frac{T_{\text{load}}}{J} \tag{4.20}$$

These equations represent model of DC motor under different operation and used for obtaining simulated performance under variable load.

4.3 Classification of DC motor drives

The DC motor drives are classified on the basis of circuit topologies, converters and controllers used for different configurations. The DC power for these drives is derived from AC mains utility using various AC–DC converter configurations. Broadly, the DC motor drives have configurations with and without transformers as shown in Figure 4.2. For the drives with power rating less than 5 hp (3.7 kW), single phase AC supply is preferred. If the voltage rating of the DC motor is more than the average value of the AC mains supply voltage, step-up transformers are

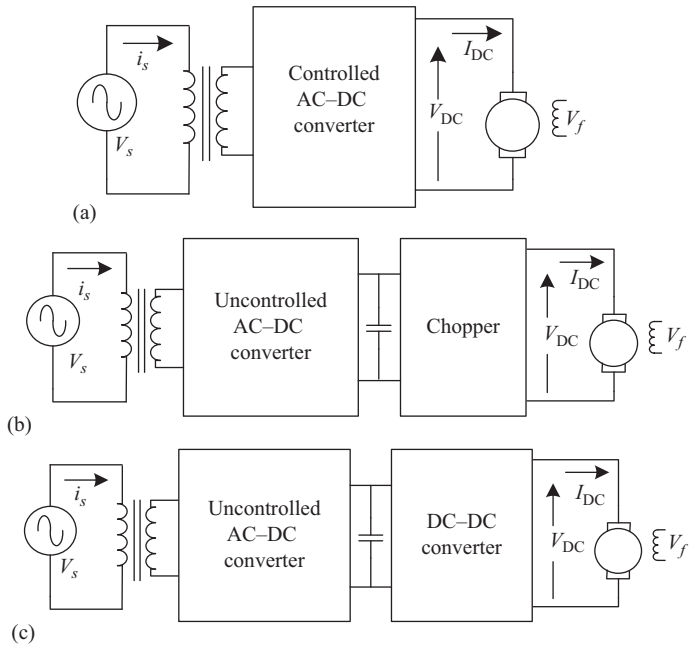


Figure 4.2 Configurations of DC motor drives with transformer: (a) controlled AC–DC converter-fed DC motor drive, (b) uncontrolled AC–DC converter – chopper-fed DC motor drive and (c) uncontrolled AC–DC converter – DC–DC converter-fed DC motor drive

used before the AC–DC converters to match the rated voltage of the DC motor. Further control of voltage is realized using controlled AC–DC converter as shown in Figure 4.2(a). Another configuration, as shown in Figure 4.2(b), uses uncontrolled AC–DC converter commonly known as diode bridge rectifier (DBR), which gives a constant value of DC voltage. This DC voltage is converted to a variable DC voltage using Chopper circuit for constant current application of DC motors.

The uncontrolled AC–DC converter or DBR-based circuits are also used with various DC–DC converters, to realize a voltage source converter for variable speed DC motor drives as shown in Figure 4.2(c).

Single-phase AC mains having 220 V, 50 Hz or 120 V, 60 Hz supply are used without transformers for low power DC motor applications as shown in Figure 4.3. Similar reasons, as discussed above, applies for choice of these configurations also. The uncontrolled AC–DC converter possesses advantages of reduced control requirements, which is an inevitable part for controlled AC–DC converters. For DC motors having power ratings higher than 5 hp or voltage ratings higher than 400 V, three-phase AC–DC converter configurations are used.

The classification of AC–DC (controlled and uncontrolled) converters, choppers and DC–DC converters which can be used for DC motor drives (Figures 4.2 and 4.3) are presented in Figures 4.4–4.7. In the case of choppers, regenerative

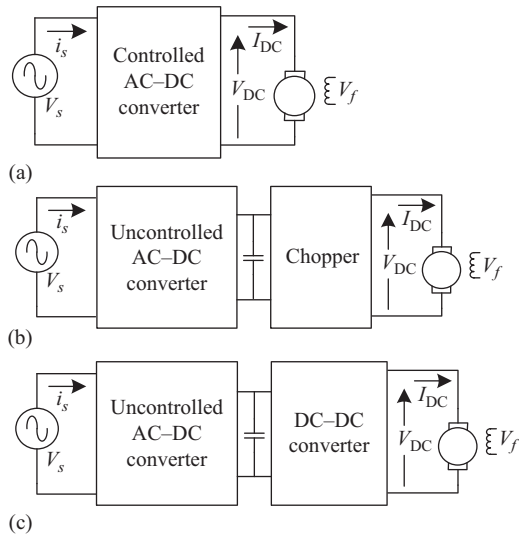


Figure 4.3 Configurations of DC motor drives without transformer: (a) controlled AC–DC converter-fed DC motor drive, (b) uncontrolled AC–DC converter – chopper-fed DC motor drive and (c) uncontrolled AC–DC converter – DC–DC converter-fed DC motor drive

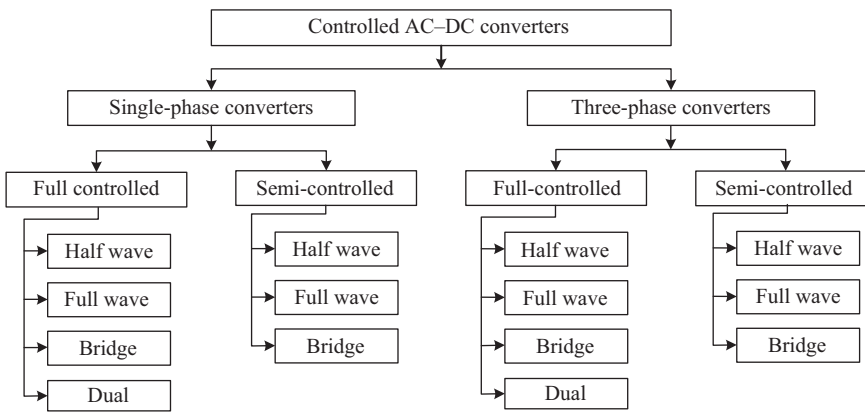


Figure 4.4 Classification of controlled AC–DC converters for DC motor drives

braking is one of the most desired phenomena for the traction control applications. It is realized using two or four quadrant choppers. Similar converter configurations are used for control of field winding voltage and currents, as and when required in any application. DC–DC converter-based configurations can also be used for power quality improvement at AC mains while applying appropriate controller in almost all applications.

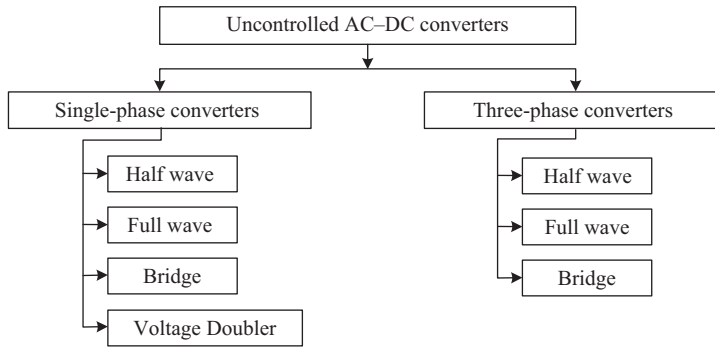


Figure 4.5 Classification of uncontrolled AC–DC converters for DC motor drives

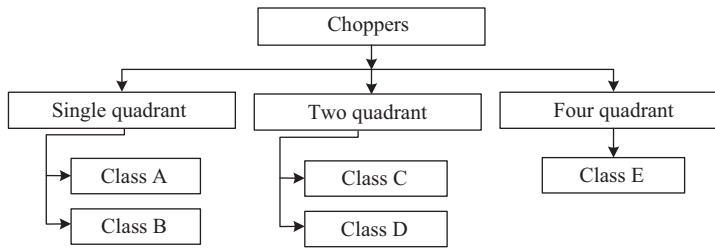


Figure 4.6 Classification of chopper configurations for DC motor drives

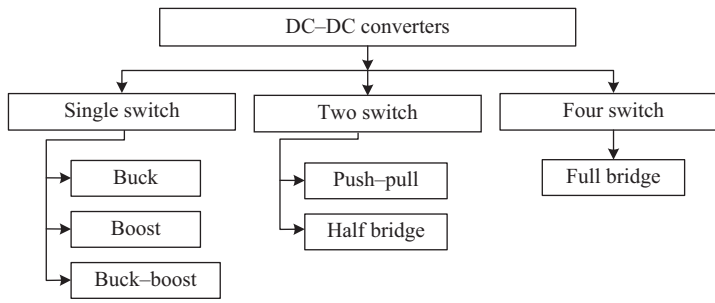


Figure 4.7 Classification of DC–DC Converter configurations for DC motor drives

4.4 Converters for DC motor drives

The circuit topologies of controlled AC–DC converters as per classification presented in Figure 4.4 segregates single-phase converters and three-phase converters. There are full-controlled and semi-controlled circuits specifically in the bridge topology which are based on the replacement of a pair of controlled switches

(thyristors) with uncontrolled switches (diodes). The full-controlled converter results in discontinuous current operation of the DC motor for some range of firing angle, whereas the semi-controlled converter results in a continuous current operation of DC motor in a broad range of firing angle. Similar continuous current operation of DC motor is obtained in the controlled converter topologies where a diode, known as free-wheeling diode, is used to provide local path for current across the motor circuit.

4.4.1 Single-phase controlled AC–DC converters

Single phase full-controlled AC–DC converter, shown in Figure 4.8, results in control of thyristors from α (the firing angle) to β (the extinction angle $= \pi + \alpha$). In this topology, the higher values of α (i.e., low speed operation) may result discontinuous DC motor currents leading to further decrease of speed. This condition may be improved by the use of free-wheeling diode across the DC motor, as discussed above in Section 4.4, to provide local circulating path for the motor current. Similar effect is obtained with the semi-controlled AC–DC converter shown in Figure 4.9 in a large range of firing angle [11].

The full-controlled bridge topology shown in Figure 4.10 with free-wheeling diode and similar circuits shown in Figure 4.11 is regarded as semi-controlled AC–DC converter topologies. These topologies are preferred for comparably better and smooth operation of DC motors. However, the design considerations should keep in mind the maximum speed and minimum torque requirements of the application.

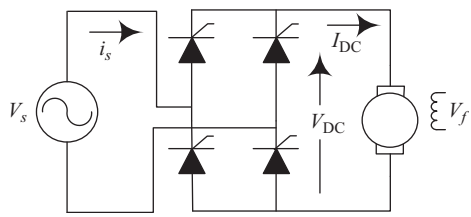


Figure 4.8 Single-phase full-controlled bridge AC–DC converter-fed DC motor drive

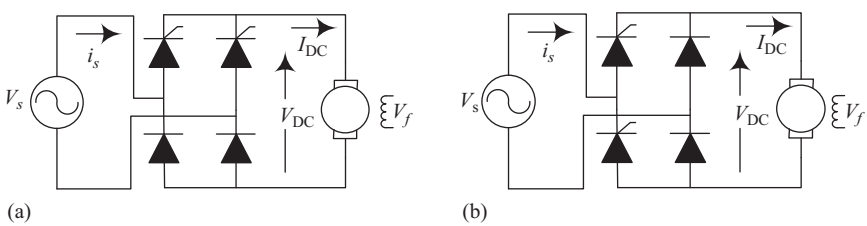


Figure 4.9 Single-phase semi-controlled bridge AC–DC converter-fed DC motor drives: (a) symmetrical configuration and (b) unsymmetrical configuration

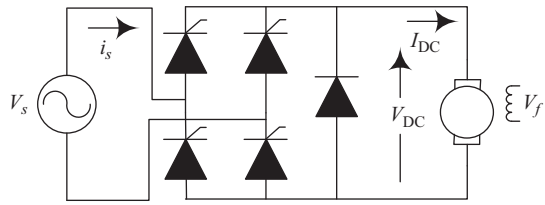


Figure 4.10 Single-phase semi-controlled bridge AC–DC converter-fed DC motor drive

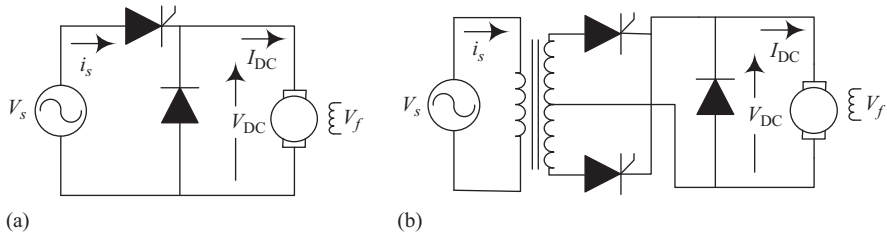


Figure 4.11 Single-phase semi-controlled AC–DC converter-fed DC motor drives: (a) half wave converter and (b) full wave converter

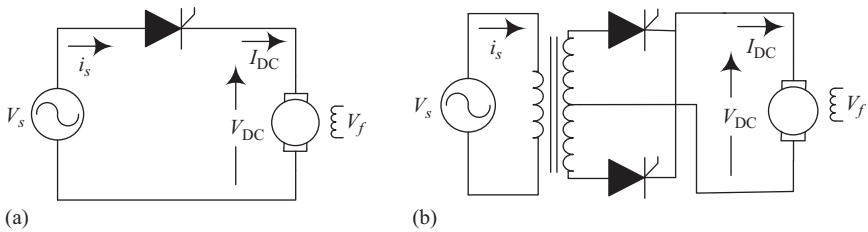


Figure 4.12 Single-phase full-controlled AC–DC converter-fed DC motor drives: (a) half wave converter and (b) full wave converter

The semi-controlled topologies shown in Figure 4.11 are converted to full-controlled AC–DC converter topologies when free-wheeling diode is removed, as shown in Figure 4.12. For low voltage DC motors operating at low speeds, the topologies shown in Figure 4.12 are preferred, because only one thyristor's voltage drop and switching loss shall be effective.

For smooth DC motor operation in all four quadrants, a specific AC–DC converter configuration known as dual converter as shown in Figure 4.13 is used. This configuration uses two full-controlled AC–DC bridge converters connected in such a way that the output voltages of these (positive (p) and negative (n)) converters are opposite to each other, i.e., $V_{op} = -V_{on}$. This requires the firing angle control such as $\alpha_p + \alpha_n = \pi$. An inductor ($L_c$) is used for connecting the load at the output of these converters to prevent the circulating current between the two bridge converters.

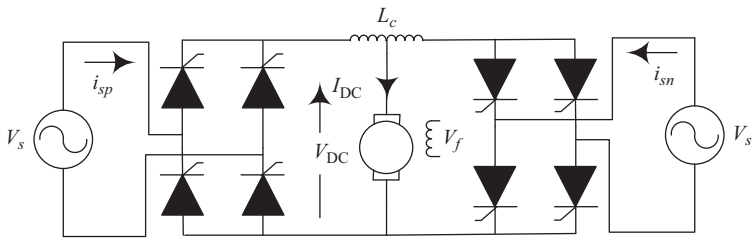


Figure 4.13 Single-phase full-controlled AC–DC dual-converter-fed DC motor drives

4.4.2 Three-phase controlled AC–DC converters

Three-phase controlled AC–DC converters are also having semi-controlled and full-controlled topologies. The topologies are shown as Figures 4.14–4.17 presenting a variety of circuit combinations to form semi-controlled and full-controlled converters. The behavior of three-phase full-controlled converters with free-wheeling diodes is similar to that of semi-controlled converters in terms of facilitating continuous flow of the DC motor current. Figure 4.18 shows a three-phase full-controlled AC–DC dual converter for four quadrant DC motor operation with almost ripple free DC voltage at the motor terminals.

4.4.3 Single-phase uncontrolled AC–DC converters

Single-phase uncontrolled AC–DC converters are having half wave, full wave and bridge topologies as shown in Figure 4.19. These topologies are similar to the controlled converter topologies while replacing the controlled switches (thyristors) with the uncontrolled switches (diodes). The voltage doubler shown in Figure 4.19(d) uses the transformer of the full wave converter (i.e., center-tapped transformer without using the center tapping) with the bridge converter topology to get double output voltage. The output voltage of uncontrolled converter shall be the input to the chopper or the DC–DC converters for control of DC motors.

4.4.4 Three-phase uncontrolled AC–DC converters

Three-phase uncontrolled AC–DC converters are also having half wave, full wave and bridge topologies as shown in Figure 4.20. These topologies are similar to the three-phase controlled converters while replacing the thyristors (controlled switches) with diodes (uncontrolled switches). The resultant voltage output is a fixed DC voltage used to feed the chopper or DC–DC converters for DC motor control.

4.4.5 Choppers

DC choppers usually convert constant DC voltage to variable DC voltages while realizing a DC current source. It is considered as a DC transformer which changes the output voltage level using a variable duty ratio. The chopper topologies used for DC motor control are shown in Figure 4.21 as per classification presented in

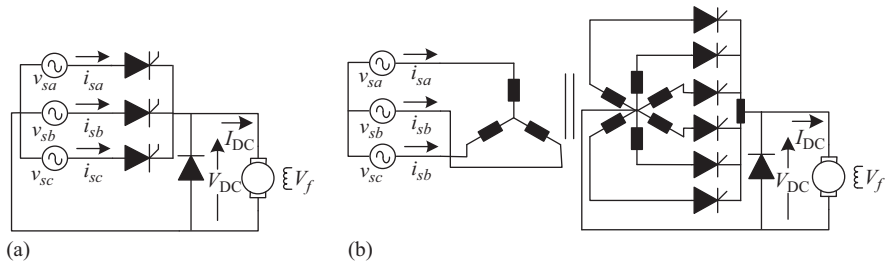


Figure 4.14 Three-phase semi-controlled AC–DC converter-fed DC motor drive: (a) half wave converter and (b) full wave converter

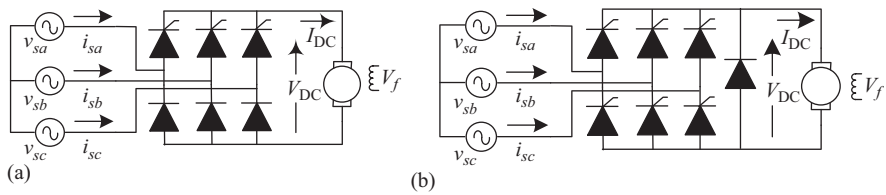


Figure 4.15 Three-phase semi-controlled bridge AC–DC converter-fed DC motor drive: (a) symmetrical converter and (b) bridge converter with free-wheeling diode

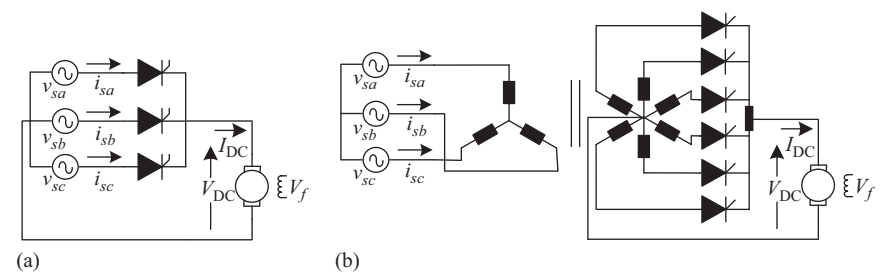


Figure 4.16 Three-phase full-controlled AC–DC converter-fed DC motor drives: (a) half wave converter and (b) full wave converter

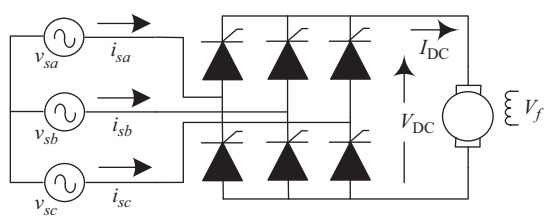


Figure 4.17 Three-phase full-controlled bridge AC–DC converter-fed DC motor drives

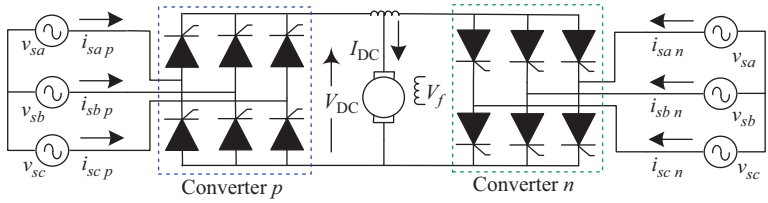


Figure 4.18 Three-phase full-controlled AC–DC dual-converter-fed DC motor drives

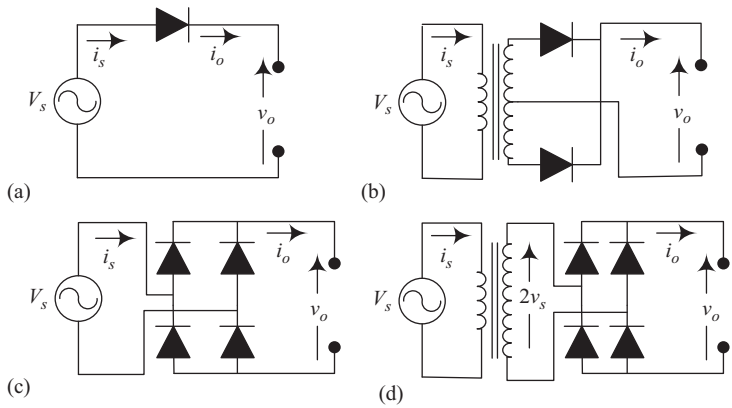


Figure 4.19 Single-phase uncontrolled AC–DC converters: (a) half wave converter, (b) full wave converter, (c) bridge converter and (d) voltage doubler

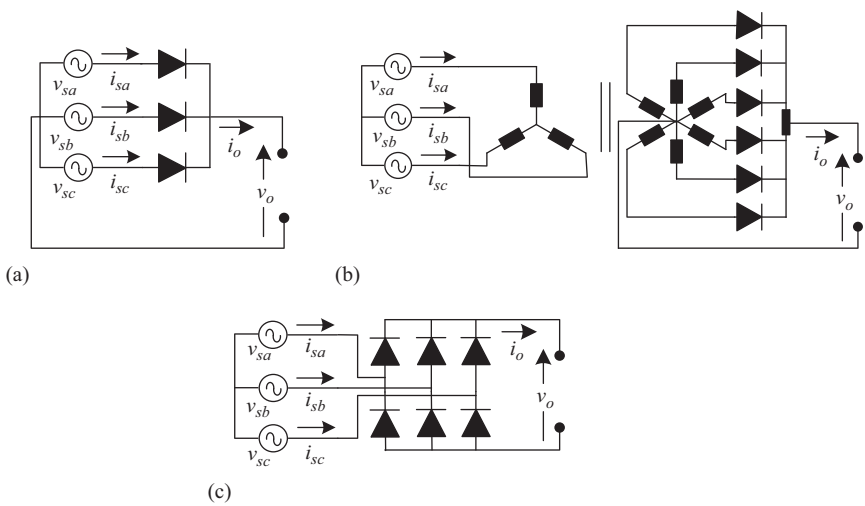


Figure 4.20 Three-phase uncontrolled AC–DC converters: (a) half wave converter, (b) full wave converter and (c) bridge converter

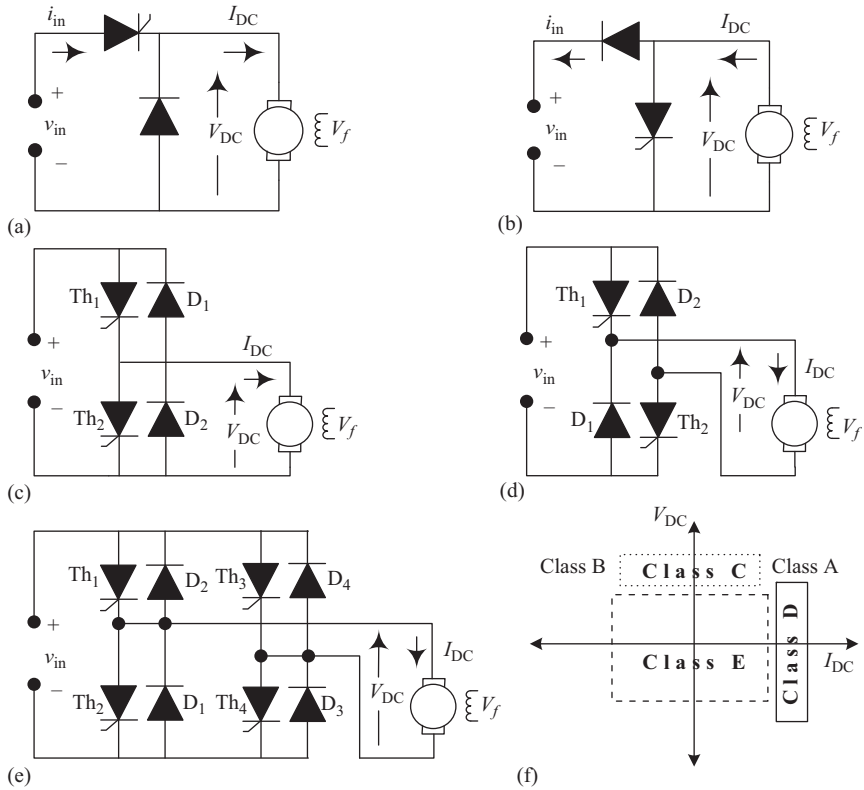


Figure 4.21 Chopper configurations for DC motor drives: (a) class A chopper, (b) class B chopper, (c) class C chopper, (d) class D chopper, (e) class E chopper and (f) the quadrants of chopper operation

Figure 4.6. The switches used in chopper circuits are thyristors with forced commutation and GTOs (i.e., gate turn off thyristors), operated below 1 kHz frequency [9–11].

Class A chopper is a step-down (buck) chopper and has circuit configuration as shown in Figure 4.21(a). It operates in first quadrant of the V_{DC}–I_{DC} graphical representation as shown in Figure 4.21(f). For continuous conduction, the chopper output voltage is independent of output current.

Class B chopper is a step-up (boost) chopper and has circuit configuration as shown in Figure 4.21(b). It is used to feed the energy stored in the motor inductors back to supply terminals during braking or deceleration, known as regenerative braking. It can also be used as boost chopper to supply high voltage to the DC Motor from a low voltage DC source. It operates in second quadrant of the V_{DC}–I_{DC} graph shown in Figure 4.21(f).

Class C chopper is a combination of step-down and step-up chopper with circuit configuration shown in Figure 4.21(c). The DC motor can be operated in first and second quadrant (Figure 4.21(f)) seamlessly using the thyristor switching.

When Th_1 is turned on, DC motor receives power from DC source and the current free wheels through D_2. To reverse the direction of the current Th_2 is turned on and stored energy is fed back to the DC supply through D_1 when Th_2 is turned off. This chopper is most useful for traction application, where it facilitates motoring and regenerative braking action of DC motor through single chopper configuration.

Class D chopper has circuit configuration as shown in Figure 4.21(d) and operates in first and fourth quadrants (Figure 4.21(f)). The operation of class D chopper has two scenarios – one overlapped operation of both the thyristors and the other alternative operation of thyristors. The first case increases the current through the load circuit, whereas the second case makes a short circuit across the load through thyristor-diode combination resulting in reduction of the current. This class of chopper is of less advantage for DC motor armature rather better for field circuit to control the field current.

Class E chopper shown in Figure 4.21(e) operates in all four quadrants as the circuit configuration has thyristor-diode combination in each leg of a bridge topology. This chopper configuration is best suited for fast reversal of DC motor and regenerative energy recovery.

4.4.6 DC–DC converters

DC–DC converters are fast switching voltage-source-based converters and available in buck, boost and buck–boost topologies [12–25] as shown in Figures 4.22–4.24. The two-switch and four-switch converter configurations use high frequency transformers for isolation between input and output circuits. Similar high frequency isolation is possible for single switch configurations but for low-power applications. Such configurations can be used for medium power applications if multiple units are connected in parallel.

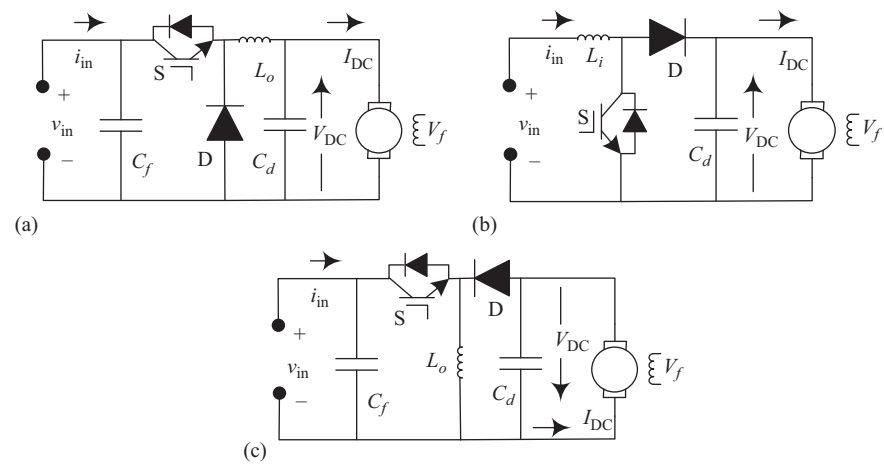


Figure 4.22 Single switch DC–DC converter configurations for DC motor drives: (a) buck converter, (b) boost converter and (c) buck–boost converter

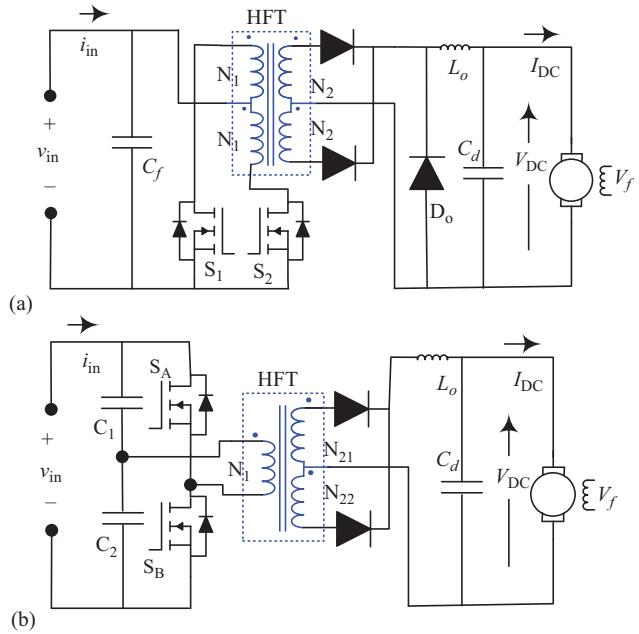


Figure 4.23 Two-switch DC–DC converter configurations for DC motor drives: (a) push–pull converter and (b) half-bridge converter

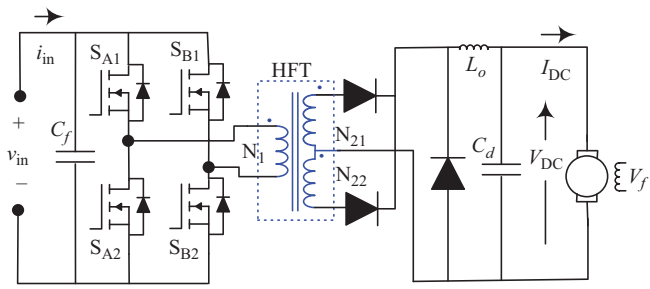


Figure 4.24 Four-switch (full bridge) DC–DC converter configuration for DC motor drives

These converter configurations can be used for improvement of power quality at AC mains supplying the power through the uncontrolled AC–DC converter [13,14]. Such configurations and their control are discussed in Section 4.5.

4.5 Control schemes for DC motor drives

There are three types of configurations discussed in previous section, namely, controlled AC–DC converter-based DC Motor drives, uncontrolled AC–DC

converter–chopper-based DC motor drives and uncontrolled AC–DC converter–DC–DC converter-based DC Motor drives. Accordingly, the control schemes shall be discussed separately for controlled AC–DC converter, chopper and DC–DC converters in this section.

4.5.1 Controlled AC–DC converter-based DC motor drive

The typical control scheme for a controlled AC–DC converter-based DC motor drive consists of voltage control of armature circuit with desired current limits as shown in Figure 4.25. The shown scheme also uses field voltage control loop for possible speed control above base speed of the DC motor known as field-weakening control.

The control scheme shown in Figure 4.25 is a simplest one which uses a tacho-generator for motor speed sensing, current sensors for armature and field current each. The control loop begins with speed error ω_e obtained between actual and reference speeds, ω and ω*, respectively. This speed error is used to generate desired torque through armature current control leading to firing angle control of the converter. The firing angle of the AC–DC converter is controlled to obtain desired speed and torque. The field weakening controller uses speed to field current conversion in the constant power zone of the DC motor characteristics. After obtaining the error between actual and desired field currents I_f and I_f^*, respectively, the controller generates desired firing angles for the control of field voltage AC–DC converter.

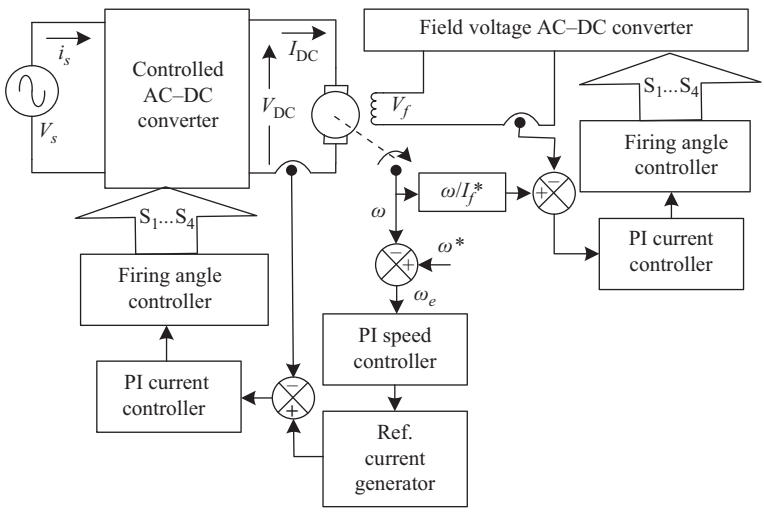


Figure 4.25 Control scheme for armature and field control of a DC motor using controlled AC–DC converter

4.5.2 Uncontrolled AC–DC converter–chopper-based DC motor drive

In a chopper-fed DC motor drive, the control varies according to the chopper configuration, because the uncontrolled DC–DC converter, i.e., diode rectifier provides almost constant voltage at the input of the chopper. A typical control scheme for diode rectifier-chopper-fed DC motor drive is shown as Figure 4.26. The main controller used is a proportional-integral (PI) controller owing to ease and simplicity of control.

The control scheme shown in Figure 4.26 is similar to that shown in Figure 4.25 with a difference of chopper duty cycle controller in armature as well as field control loops. This controller reduces control complexity of the processor used for duty cycle generation as well as the number of switching signals. This kind of controllers are best suited for constant torque variable speed applications. Use of regenerative braking is applicable with this control scheme, if a battery is used as input source to the chopper.

The duty cycle ($d = t_{on}/T$) of a chopper circuit is controlled by varying either the on time (t_{on}) of the chopper switch or the off time (t_{off}) to vary the time period (T). The on/off time control affects the current rise/fall in the connected circuit. Accordingly, the control techniques are divided into the following two broad categories:

1. Time ratio control (TRC)
2. Current limit control (CLC).

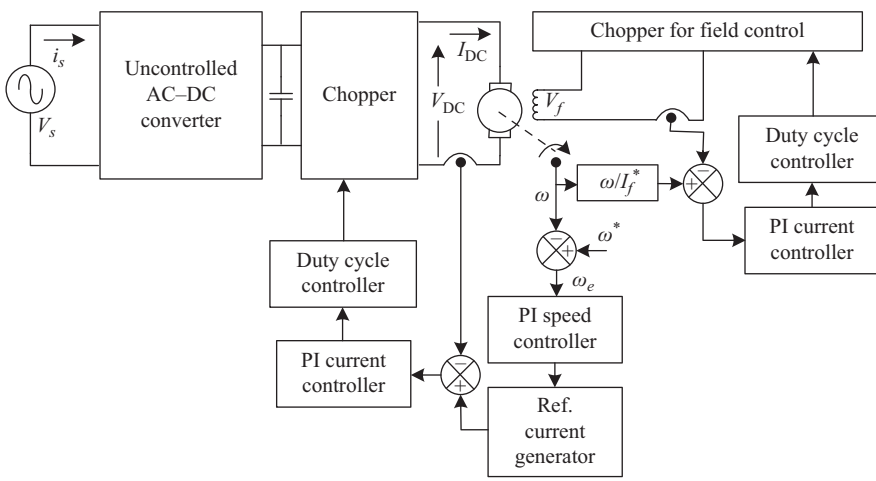


Figure 4.26 Control scheme for armature and field control of a DC motor using chopper

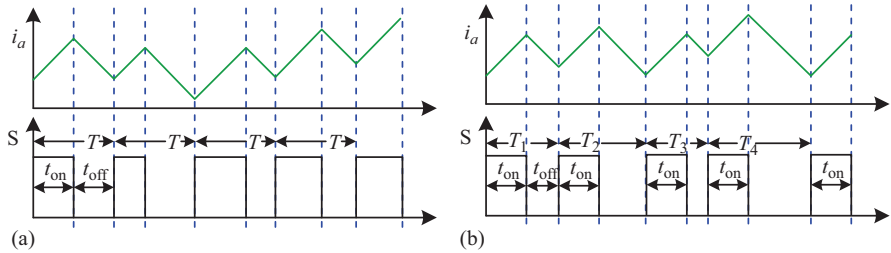


Figure 4.27 Switching signal (s) generated under time ratio control of chopper: (a) constant frequency TRC and (b) variable frequency TRC

The TRC is known as pulse-width control which can be executed in the following two ways:

(i) Constant frequency TRC, in which the chopping time period (T) is kept constant and the on time of switch (t_{on}) is varied to control the duty cycle (d). This variation of switching signal is shown in Figure 4.27(a) along with variation of armature current, while considering fixed slopes of current rise and decay during varying "on" and "off" times.

(ii) Variable frequency TRC, in which the duty cycle (d) is controlled either by varying the chopping time period (T) and keeping the on time of switch (t_{on}) constant or varying T and t_{on} both. This is depicted by variable time periods (T_1, T_2, T_3, T_4, etc.) in Figure 4.27(b).

In CLC, the chopper operates to control the armature current between the prescribed limits i_{min} and i_{max}. The chopper adjusts the value of d and T, such that the current fluctuates between these limits. This control is known as hysteresis control also. For fixed values of i_{min} and i_{max}, the average current and torque shall be nearly constant for all the speeds. Further, the on time (dT) and off time $\{(1-d)T\}$ of chopper shall be small as compared to the time constant of armature circuit; therefore, the rise and decay of armature current can be considered as straight line rather than exponential as shown in Figure 4.28(a). However, this control may have a large variation of switching frequency as depicted by variable time periods (T_1, T_2, T_3, T_4, etc.) in Figure 4.28(b) is the rise and decay of armature current has variable gradient.

4.5.3 Uncontrolled AC–DC converter-DC–DC converter-based DC motor drive

The operation of a DC–DC converter results in a precise control as high frequency pulse width modulation (PWM) is used for the control of switches. Figure 4.29 presents a typical control scheme for a DC–DC converter-fed DC motor drive. This scheme differs from earlier schemes presented in Figures 4.27 and 4.28, in the way

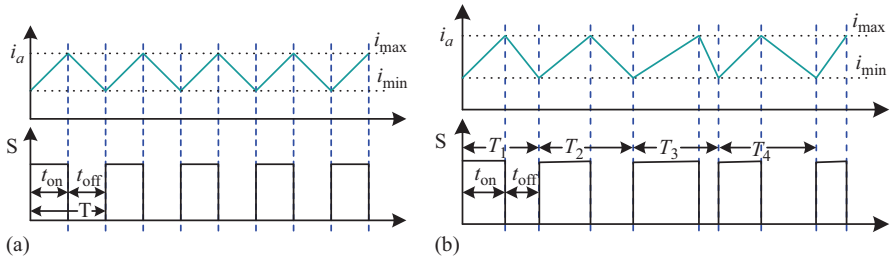


Figure 4.28 Switching signal(s) generated under current limit control of chopper: (a) constant slope of armature current rise and decay and (b) variable slope of armature current rise and decay

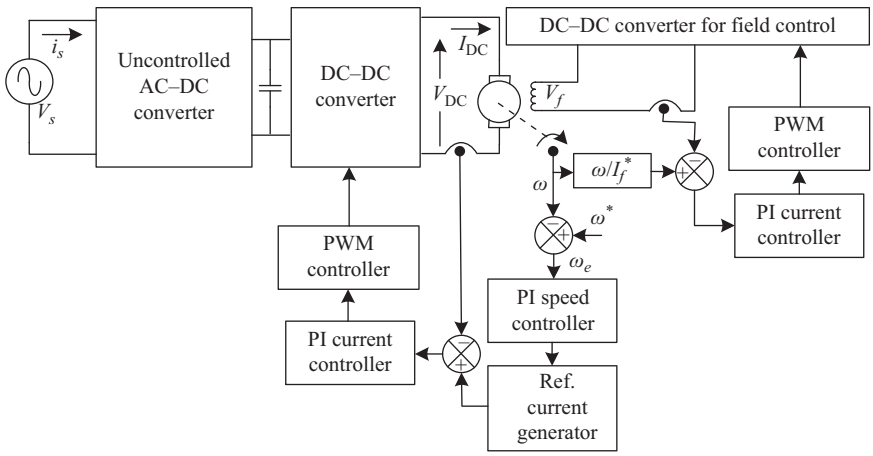


Figure 4.29 Control scheme for armature and field control of a DC motor using DC–DC converter

of switching signal generation for the DC–DC converter switches. The PWM switching signal generation is separately shown in Figure 4.30 for single switch, two-switch and four-switch DC–DC converters [12–25]. From Figure 4.30, it can be observed that the two-switch configurations have same switching losses as compared to single switch configurations, because only one switch operates at a time. However, the load sharing between switches shall reduce the temperature rise of the switches.

For precise control of speed and torque, sophisticated and advanced controllers such as sliding mode, fuzzy, neural network and adaptive control can be used in place of PI controllers in all the schemes shown in this chapter. Subsequent chapters have discussed the design of these controllers and their applications.

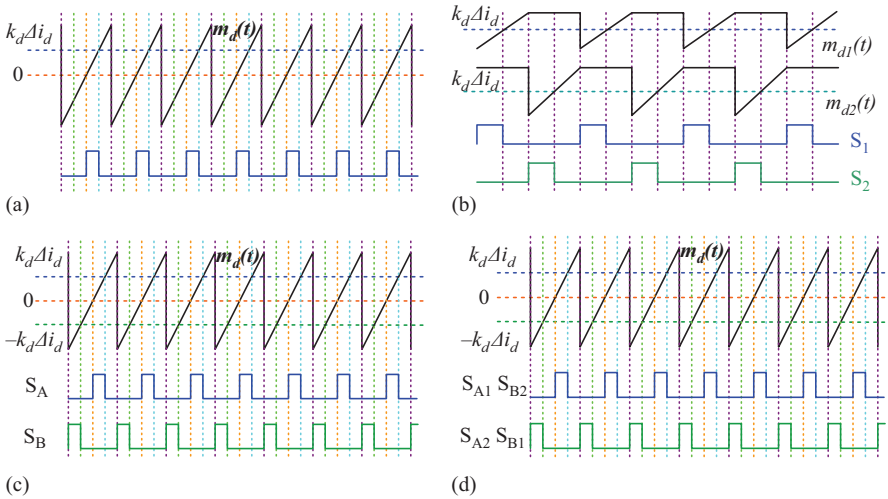


Figure 4.30 Switching signal generation for various DC–DC converters: (a) single switch converters, (b) push–pull converter, (c) half bridge converter and (d) full bridge converter

4.6 PI controller design

The closed loop speed control of DC motor requires speed sensor which is a tacho-generator coupled to the shaft of the motor (refer to Figures 4.25, 4.26 and 4.29). For effective speed control, the tacho-generator output is filtered to remove the ripples from equivalent speed signal ω. The reference speed command ω^* is compared with ω to get speed error ω_e, which is processed through a PI controller to get the control torque command. The torque command is restricted within a prescribed limit to keep the armature current within safe limits. The current reference command is obtained from the reference current generator by proper scaling of this torque command. The actual armature current is compared with the reference current command to get current error. This current error is processed through a PI current controller which generates control signal to minimize the current error. The control signal accordingly modifies the firing angle of the converter or the duty cycle of the chopper/DC–DC converter, feeding the DC motor. Therefore, for the accurate control of speed, the design of the gains and time constants of the speed and current controllers (PI controllers) is of paramount importance.

The PI controller is represented as $G(s) = K(1 + sT)/sT$ where K and T are the gain and time constant of the controller. The design of control loops starts from the inner most (fastest) loop and proceeds to the slowest loop. During the design, the gain and time constant of one controller at a time is solved, instead of solving for all controllers, simultaneously. As the performance of outer loop depends upon inner loop, the tuning and design of the inner loop has to precede the design of outer loop. In this case, speed loop is inside the current loop.

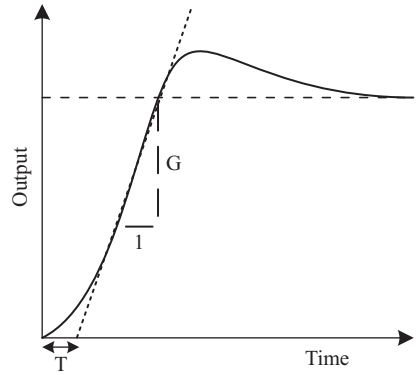


Figure 4.31 Step response of DC motor drive in open-loop speed control

To design the speed loop, the second-order current loop is replaced with an approximate first-order model. The input to any PI controller is the error between reference signal and the sensed signal (i.e., motor speed or current). The error is processed in the PI controller, and the output of the controller is given by the reference torque or the control signal for speed or current, respectively. K_p and K_i are the proportional and integral gains of the PI controller, respectively. For selection of K_p and K_i, the Ziegler–Nichols step-response technique is considered as base technique [26].

In the Ziegler–Nichols step response technique, the response of the system for step input is observed in open loop. From the step response (as shown in Figure 4.31), the maximum gradient (G) and the point at which the maximum gradient line crosses the time axis (T) are selected. The gains of the PI controller are calculated using the relations: $K_p = 1.2(U/GT)$ and $K_i = 0.6(U/GT^2)$, where U is the applied magnitude of step input. To achieve satisfactory response, the gains are further adjusted by trial and error method for the given system or any optimization technique to match the system requirement [1].

4.7 Power quality control and sensor reduction for DC motor drives

The AC–DC converter-based DC motor drives, whether controlled or uncontrolled, the power is drawn through AC mains. The uncontrolled topologies usually employ DBR and capacitive filters for getting constant DC voltage at the chopper or DC–DC converter inputs. These capacitors deteriorate the power quality at AC mains; specifically, the currents drawn from the AC mains have higher peaks and harmonic distortion. To mitigate these power quality problems, the DC–DC converters can be operated in power quality control mode which may give the desired speed control along with improved power quality at AC mains. Figure 4.32 shows the control scheme for power quality control of a boost converter-based DC motor drive. This scheme uses input AC voltage templates and forces the DC–DC converter current to follow the AC mains voltage. Another scheme shown in

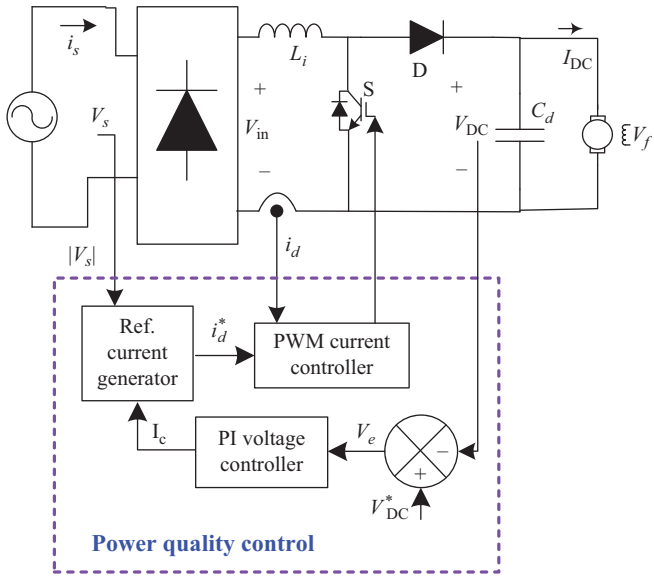


Figure 4.32 Power-quality-control scheme for boost converter-fed DC motor drive

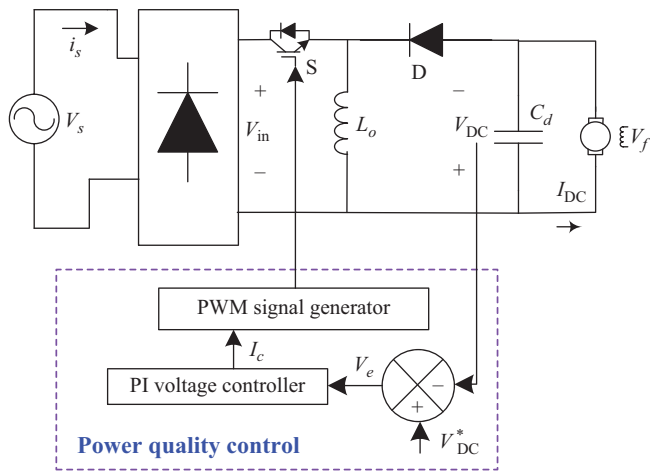


Figure 4.33 Power-quality control scheme with reduced sensor for buck–boost converter-fed DC motor drive

Figure 4.33 presents power quality control using voltage follower control for a buck–boost converter-based DC motor drive. This scheme operates the DC–DC converter in a discontinuous conduction mode of inductor current to get the improved power quality. The advantage of this scheme is the reduction of input voltage and current sensors with no compromise of the performance [27–30].

Many such schemes are available in the literature for application to these converters for power quality control and sensor reduction. Their selection is application specific and shall yield best results after rigorous research and implementation in real-time prototypes.

4.8 Modeling of controllers and PWM generators

The boost converter-fed DC motor drive as shown in Figure 4.32 employs various components for power quality control such as voltage controller, reference current generator and PWM current controller using current multiplier control. However, in the case of voltage follower control shown in Figure 4.33, the buck–boost converter employs only voltage controller and PWM signal generator. These components are modeled in the form of mathematical equation for performance simulation under various operating conditions.

4.8.1 Voltage controller

The voltage controller is a PI controller which generates a control signal (I_c) for minimization of voltage error. The error between reference DC voltage $V^*_{\rm DC}(k)$ and sensed DC voltage $V_{\rm DC}(k)$, at kth instant of time, is given by

$$V_e(k) = V^*_{\rm DC}(k) - V_{\rm DC}(k) \tag{4.21}$$

The PI voltage controller output $I_c(k-1)$ at $(k-1)$th instant is given as

$$I_c(k-1) = K_{pv}V_e(k-1) + K_{iv}\Sigma V_e(k-1) \tag{4.22}$$

where K_{pv} and K_{iv} are proportional and integral gains of the voltage controller.

Further, the PI voltage controller output $I_c(k)$ at kth instant is given as

$$I_c(k) = K_{pv}V_e(k) + K_{iv}\{V_e(k) + \Sigma V_e(k-1)\} \tag{4.23}$$

Subtraction of (4.22) from (4.23) results as

$$I_c(k) = I_c(k-1) + K_{pv}\{V_e(k) - V_e(k-1)\} + K_{iv}V_e(k) \tag{4.24}$$

This equation can be used as a generalized model for a PI controller in any simulation software while using the generalized error parameter between reference and actual commands as given in (4.21). The output of speed/current PI controller is limited to a maximum value depending on the rating of the DC motor.

4.8.2 Reference current generator for power quality control

The reference current of the power quality controlled converter (i^*_d) is given as

$$i^*_d = I_c(k)u_{vs} \tag{4.25}$$

where u_{vs} is the unit template of the input AC mains voltage, calculated as

$$u_{vs} = \frac{v_d}{V_{\rm sm}}; \quad v_d = |v_s|; \quad v_s = V_{\rm sm}\sin\omega t \tag{4.26}$$

where ω is frequency in rad/s at input AC mains.

4.8.3 PWM current controller

The reference input current of the power quality controlled converter (i_d^*) is compared with current (i_d) sensed just after the DBR to obtain the current error $\Delta i_d = \left(i_d^* - i_d\right)$. The amplified current error using gain k_d is compared with fixed frequency (f_s) sawtooth carrier waveform $m_d(t)$ to get the switching signals for the IGBT of the DC–DC converter as

$$\text{If} \quad k_d \Delta i_d > m_d(t) \quad \text{then S} = 1 \tag{4.27}$$

$$\text{If} \quad k_d \Delta i_d \leq m_d(t) \quad \text{then S} = 0 \tag{4.28}$$

where S represents "on" position of the switch with S = 1 and its "off" position with S = 0.

4.8.4 PWM signal generator for voltage follower control

The control signal (I_c) from voltage PI controller is compared with fixed frequency (f_s) sawtooth carrier waveform $m_d(t)$ to get the switching signals for the DC–DC converter as

$$\text{If} \quad I_c > m_d(t) \quad \text{then S} = 1 \quad (\text{switch "on"}) \tag{4.29}$$

$$\text{If} \quad I_c \leq m_d(t) \quad \text{then S} = 0 \quad (\text{switch "off"}) \tag{4.30}$$

4.8.5 PWM signal generation for single switch converters

The generation of pulses for single switch converters (buck, boost and buck–boost) is obtained by comparison of amplified current error with a high frequency sawtooth carrier waveform as shown in Figure 4.30(a).

$$\text{If} \quad k_d \Delta i_d > m_d(t) \quad \text{then S} = 1, \text{else } 0 \tag{4.31}$$

where S is the switch in any of the single switch DC–DC converters and the values "1" and "0" represent their "on" and "off" state.

4.8.6 PWM signal generation for push–pull converter

The push–pull converter requires a specific PWM generation scheme in which two separate carrier waveforms specifically designed as shown in Figure 4.30(b) are used. The PI controller output after processing the error is compared with these fixed frequency (f_s) signals $m_{d1}(t)$ and $m_{d2}(t)$ to get the pulses for switches S_1 and S_2 as follows:

$$\text{If } k_d \Delta i_d > m_{d1}(t) \quad \text{then } S_1 = 1, \text{else } S_1 = 0, \tag{4.32}$$

$$\text{If } k_d \Delta i_d > m_{d2}(t) \quad \text{then } S_2 = 1, \text{else } S_2 = 0. \tag{4.33}$$

4.8.7 PWM signal generation for half bridge converter

The half-bridge converter also requires two pulses for switches S_A and S_B as shown in Figure 4.30(c). However, it uses only one fixed frequency (f_s) carrier waveforms $m_d(t)$ and compares the amplified current error with it to get the PWM signal for the DC–DC converter switches as follows:

$$\text{If} \quad k_d \Delta i_d > m_d(t) \quad \text{then } S_A = 1, \text{else } 0 \tag{4.34}$$

$$\text{If} \quad -k_d \Delta i_d > m_d(t) \quad \text{then } S_B = 1, \text{else } 0 \tag{4.35}$$

where S_A and S_B are upper and lower switches of the half-bridge converter, and the values "1" and "0" represent their "on" and "off" state.

4.8.8 PWM signal generation for full-bridge converter

The generation of pulses for a full-bridge converter is similar to the half-bridge converter; however, pulses are given to two switches simultaneously. The PWM control and generation of pulses are shown in Figure 4.30(d) as follows:

$$\text{If } k_d \Delta i_d > m_d(t) \quad \text{then } S_{A1} = S_{B2} = 1, \text{else } 0 \tag{4.36}$$

$$\text{If } -k_d \Delta i_d > m_d(t) \quad \text{then } S_{A2} = S_{B1} = 1, \text{else } 0 \tag{4.37}$$

where S_{A1}, S_{A2} and S_{B1}, S_{B2} are upper and lower switches of two legs of the bridge converter, and the values "1" and "0" represent their "on" and "off" state.

4.9 Performance simulation of DC motor drives

The performance simulation of DC motor drives can be carried out in various software platforms. For realization of various control concepts discussed in preceding subsections, performance simulation of various DC motor drives, carried out in MATLAB®–Simulink®, is presented in Figures 4.34–4.40. The DC motor selected for these simulations has 5 hp, 400 V DC rating with 1,500 rpm speed. It is fed from 230 V, 50 Hz AC mains using controlled converter for control of speed and torque. The simulated performance for different loads, i.e., constant speed, variable torque; constant torque, variable speed; and variable speed variable torque loads are presented for various configurations of DC motor drives.

Figure 4.34 presents simulated performance of controlled converter-fed DC motor drive (as shown in Figure 4.25) with constant speed variable torque load. The transformer turns ratio is considered as 390/230 to match the voltage rating of the DC motor. The firing angle is adjusted in closed loop to meet the speed and torque requirements. For the variation of load, the torque reference is changed from 15 to 20 N m at 4 s and further it is changed to 10 N m at 5 s after starting, while keeping the speed constant at 1,500 rpm. The motor effectively follows the reference torque, and the speed remains constant at 1,500 rpm under all conditions. The same drive is subjected to speed variation from 1,500 to 2,000 rpm and then 1,000 rpm with constant

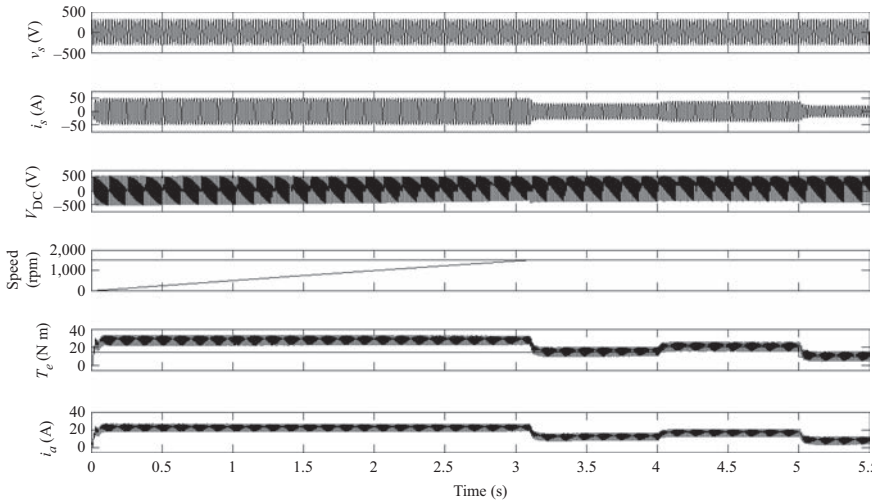


Figure 4.34 Simulated performance of controlled converter-fed DC motor drive (Figure 4.25) with constant speed variable torque load

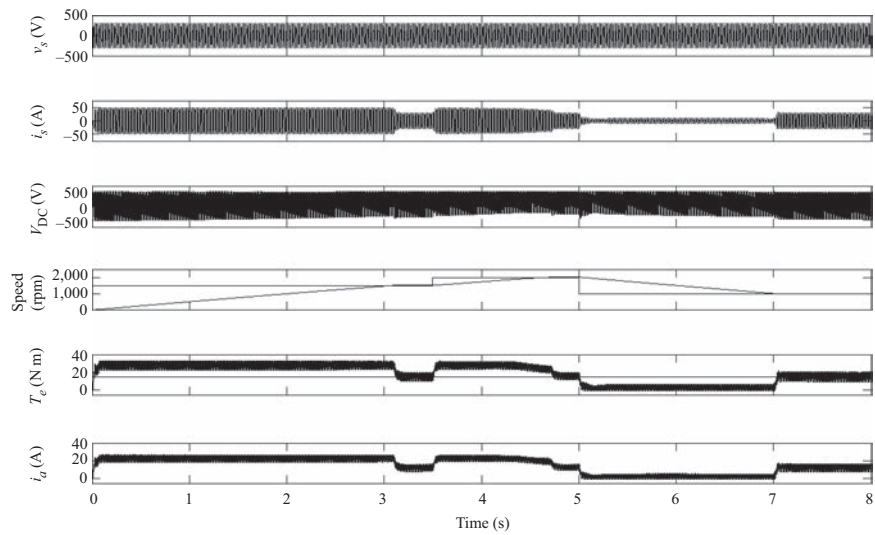


Figure 4.35 Simulated performance of controlled converter-fed DC motor drive (Figure 4.25) with constant torque variable speed load

torque of 15 N m. The simulated performance under this condition is shown in Figure 4.35. It is observed that the drive attains the desired speed in either direction effectively without any reduction in torque. Whenever, the speed is to be raised, additional torque is generated by the drive while increasing the current drawn from the

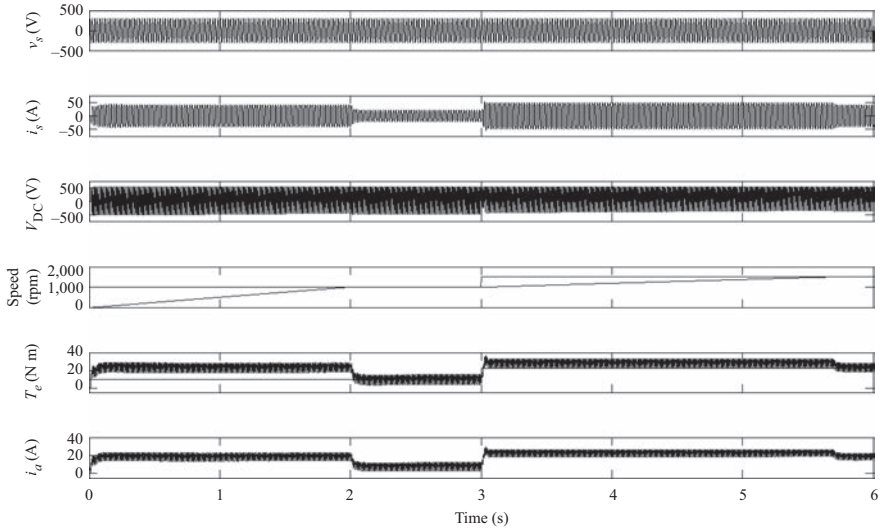


Figure 4.36 Simulated performance of controlled converter-fed DC motor drive (Figure 4.25) with variable speed variable torque load

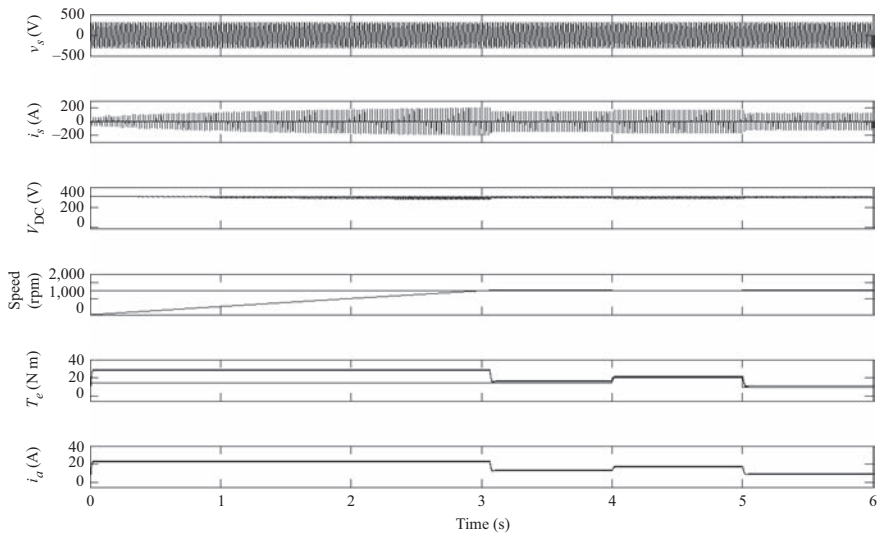


Figure 4.37 Simulated performance of uncontrolled converter – chopper-fed DC motor drive (Figure 4.26) with constant speed variable torque load

source. For verification of the controller, the variable speed and variable torque load is connected to the DC motor with requirement of torque in square proportion to the speed of the motor. As shown in the simulated performance of Figure 4.36, the torque varies as soon as the speed reference is varied. The drive closely tracks the speed as well as

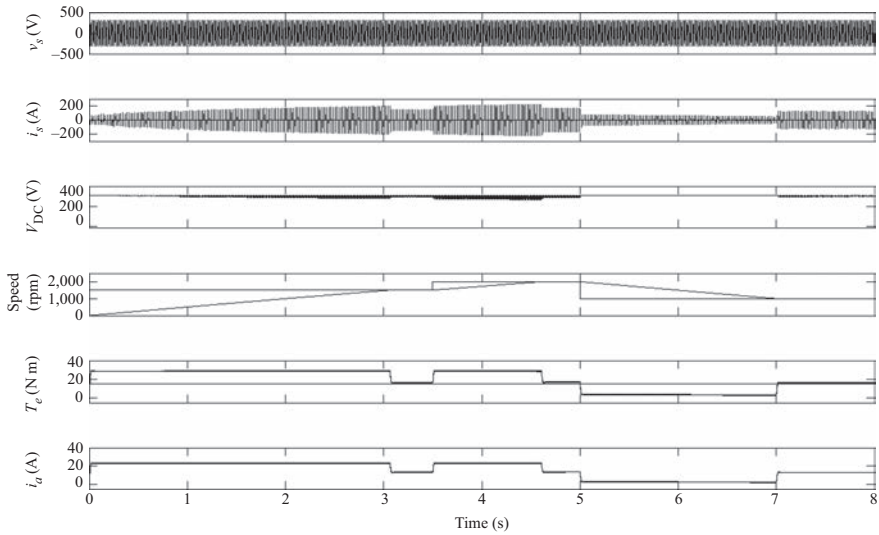


Figure 4.38 Simulated performance of uncontrolled converter – chopper-fed DC motor drive (Figure 4.26) with constant torque variable speed load

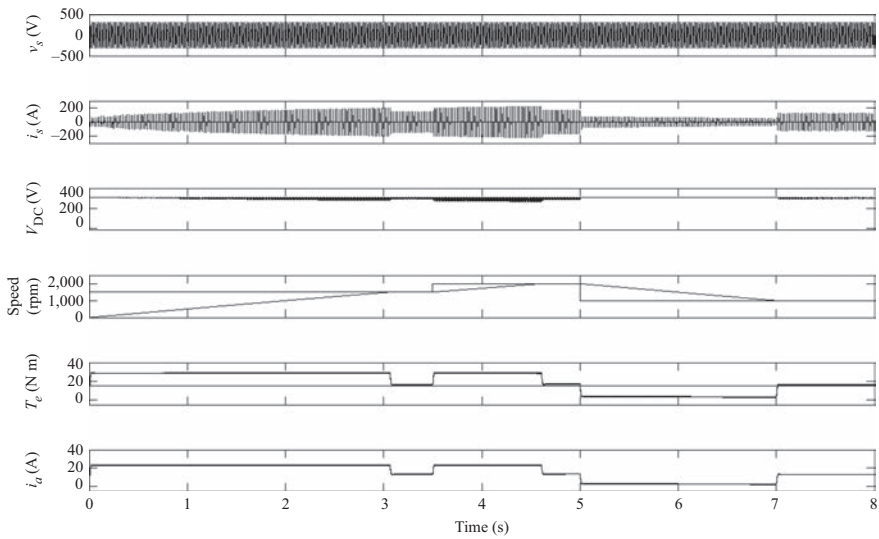


Figure 4.39 Simulated performance of uncontrolled converter – chopper-fed DC motor drive (Figure 4.26) with variable speed variable torque load

torque reference with increase and decrease in the current drawn from the supply. These simulated performances are shown in terms of supply voltage (V_s), supply current (I_s) at AC mains, DC voltage at converter output (V_{DC}), speed (N), torque (T_e) and armature current (I_a) of the DC motor, while assuming a constant field current.

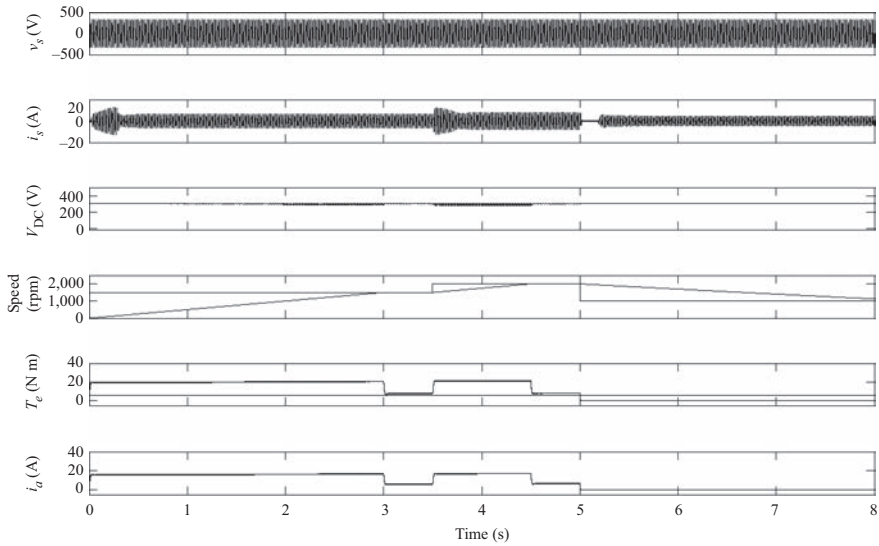


Figure 4.40 Simulated performance of uncontrolled converter (DBR) – boost DC–DC converter-fed DC motor drive for power quality control using current multiplier control (Figure 4.32) with constant torque variable speed load

For the realization of the uncontrolled converter chopper fed DC motor drives, same DC motor (rated at 5 hp, 400 V DC, 1,500 rpm fed from 230 V, 50 Hz AC mains) is considered and operated with a boost chopper. The simulated performance is shown in Figures 4.37–4.39 for specified loads, i.e., constant speed, variable torque; constant torque, variable speed; and variable speed variable torque loads, respectively. It can be observed from the simulation results that the torque ripples are reduced with this drive as compared to the controlled converter-based DC motor drive, whereas the source current (I_s) has larger peaks as compared to the controlled converter case. This is due to the capacitive filter used with uncontrolled converter (DBR). This can be controlled by using third kind of drives presented in Figure 4.29, where the DC–DC converter is used as power quality controller. There can be various configurations of power-quality converters including single and two-stage control [13,14].

Figure 4.40 shows the simulated performance of the same DC motor drive fed from DBR-boost DC–DC converter for power quality control using current multiplier control as depicted in Figure 4.32. The 5 hp DC motor drive is operated for a variable speed constant torque load under light load (6 N m torque) for similar speed variations at 3.5 and 5 s as shown in Figures 4.35 and 4.38. The power quality results for input AC mains current, obtained during steady state operation at 1,000, 1,500 and 2,000 rpm, without and with power quality control, are presented in Figure 4.41. It is observed that the DC–DC converter-fed drives improve the power quality at AC mains in terms of reduced total harmonic distortion in source

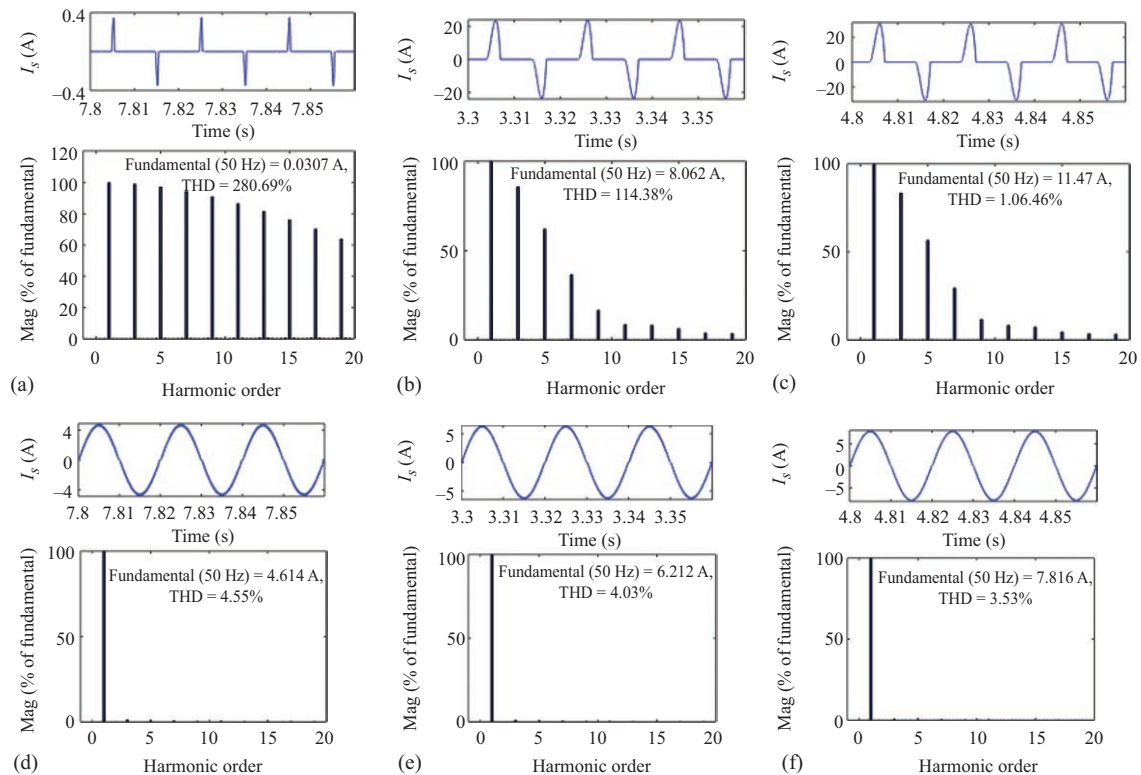
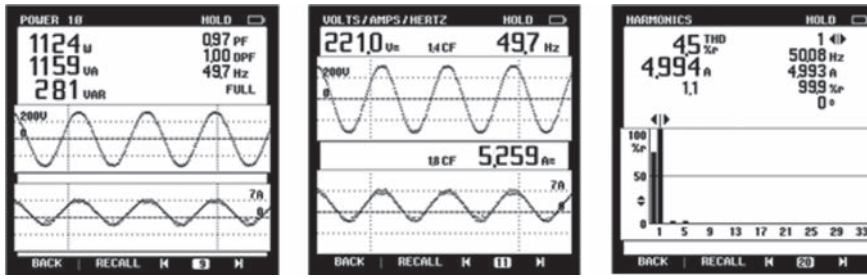


Figure 4.41 Simulated power quality performance at AC mains of an uncontrolled converter–boost DC–DC converter-fed DC motor drive at various speeds (Figure 4.29): (a) at 1,000 rpm without PQ control, (b) at 1,500 rpm without PQ control, (c) at 2,000 rpm without PQ control, (d) at 1,000 rpm with PQ control, (e) at 1,500 rpm with PQ control and (f) at 2,000 rpm with PQ control



(a) (b) (c)

Figure 4.42 Hardware results of power quality improvement using a boost DC–DC converter for a DC motor drive with current multiplier control: (a) AC mains voltage (V_s), current (I_s), power and power factor, (b) AC mains voltage (V_s) and current (I_s) waveforms and (c) harmonic spectra of AC mains current (I_s) at 1,000 rpm

current with perfect sinusoidal waveform and near unity power factor. The hardware results of the improved power quality at AC mains obtained for boost converter with current multiplier control feeding DC motor drive are presented in Figure 4.42 for validation of the discussed concepts. The other DC–DC converters may also be realized in a similar manner to obtain improvement in power quality at AC mains. The application of voltage follower control for the power quality control results in reduction of current and input voltage template sensors.

4.10 DC series motor control

There are some specific applications of DC series motors where a large value of torque is required at starting such as traction. From the basics of the DC motor, it can be said that in a series DC motor, the developed torque is proportional to the square of the armature current or the field current as both are same. At starting or low speeds, the back EMF of the motor shall be small, leading to large armature current, thereby large developed torque provided the field is not saturated. The required control action shall focus on the current limits from saturation view point and torque requirement at low speeds and starting. During usual running, maintaining the desired speed or torque level shall require only incremental control of voltage or current. Therefore, the controllers discussed for shunt or separately excited DC motors shall be applicable to DC series motors also with an essential CLC.

4.11 Summary

The DC motor drives are having very specific applications in present industrial scenario, owing to disadvantages of wear and tear due to brush–commutator arrangement. However, their advantages of easy control cannot be overlooked, in addition to quick and reliable operation in any direction with a wide speed range

(below as well as above the base speed). The quick control due to advanced power electronic switches and processors along with energy recovery during deceleration or braking has enhanced the application opportunities of these motors. The decoupled control of torque and speed makes this machine the best suited for cranes and hoists applications where maximum torque (holding torque) is required at zero speed. The AC–DC converters, choppers and DC–DC converters have offered a wide range of controllers to be used for any type of application. Use of bridge dual converters of four quadrant chopper for DC motor control allows maximum level of flexibility with a comparable affordable cost and ease of control. This deliberation shall open up new control applications of DC motor drives.

List of symbols

R_a	Armature winding resistance
R_f	Field winding resistance
L_a	Armature winding inductance
L_f	Field-winding inductance
E_b	Back EMF generated across the armature
i_a	Current in armature winding
i_f	Current in field winding
V_a	Voltage across armature winding
V_f	Voltage across field winding
Φ	Armature flux linkage
N	Rotor speed in rounds per minute
K_b	Back EMF constant
p	Number of field poles
a	Number of parallel paths in armature winding
Z	Number of armature conductors
$B_{g\ \mathrm{av}}$	Average air gap flux density per pole
τ	Pole pitch
l	Pole stack length
T_e	Torque generated at motor shaft
ω	Angular speed of the motor shaft in radians per second
P_e	Shaft power output of the DC motor
J	Motor inertia
B	Frictional torque
n	Rotor speed in round per second
T_{load}	Load torque
K_E	Modified back EMF constant
K_T	Torque constant

v_s	Supply voltage of AC source
i_s	Supply current of AC source
V_{DC}	Rectifier output voltage
I_{DC}	Rectifier output current
i_{sp}	Supply current of positive cycle conducting AC source in dual converter
i_{sn}	Supply current of negative cycle conducting AC source in dual converter
L_c	Inductor to restrict circulating current in dual converter
v_{sa}, v_{sb}, v_{sc}	Supply voltage of phases a, b and c, respectively, in three-phase AC source
i_{sa}, i_{sb}, i_{sc}	Supply current of phases a, b and c, respectively, in three-phase AC source
$i_{sa\ p}$, $i_{sb\ p}$, $i_{sc\ p}$	Supply current of phases a, b and c, respectively, conducting in positive cycle of three phase AC source dual converter
$i_{sa\ n}$, $i_{sb\ n}$, $i_{sc\ n}$	Supply current of phases a, b and c, respectively, conducting in negative cycle of three-phase AC source dual converter
v_o	Uncontrolled rectifier output voltage
i_o	Uncontrolled rectifier output current
v_{in}	Chopper input voltage
i_{in}	Chopper input current
C_f	Filter capacitor at input of DC–DC converter
S	Switch of DC–DC converter
D	Diode of DC–DC converter
C_d	Filter capacitor at output of DC–DC converter
L_o	Filter inductor at output of DC–DC converter
L_i	Filter inductor at input of DC–DC converter
ω_e	Error of angular speed of motor
T	Time period of switching signals
t_{on}	On time of the switch
t_{off}	Off time of the switch
d	Duty cycle of the switch
i_{min} and i_{max}	Minimum and maximum values of armature current
$V_{\mathrm{DC}}(k)$	Actual voltage at DC link at kth instant
$V^*_{\mathrm{DC}}(k)$	Reference voltage at DC link at kth instant
$V_e(k)$	Voltage error at kth instant
$I_c(k)$	PI voltage controller output $I_c(k)$ at kth instant
K_{pv}	Proportional gain of the voltage controller
K_{iv}	Integral gain of the voltage controller
u_{vs}	Unit template of the input AC voltage

v_d	Modulus of input AC supply voltage v_s
V_{sm}	Amplitude of input AC supply voltage v_s
i_d	Current sensed just after the diode bridge rectifier
i_d^*	Reference current for power quality-controlled converter
Δi_d	Current error
k_d	Current error amplification factor
m_d	Sawtooth waveform instantaneous value

Glossary of terms

Back-EMF	It is an emf induced in the rotor windings of a DC motor due to rotation in a magnetic field
Uncontrolled converter	The power electronic converter which uses uncontrolled switches, i.e., diodes.
Controlled converter	The power electronic converter which uses controlled switches, i.e., thyristors, IGBTs and MOSFETs
Chopper	The power electronic converter operated to get variable DC output from a constant DC input
DC–DC converter	The power electronic converter operated to get variable DC output from a constant DC input
Buck converter	The converter whose average output voltage is less than average input voltage
Boost converter	The converter whose average output voltage is more than average input voltage
Buck–boost converter	The converter whose average output voltage is less or more than average input voltage, depending on the duty cycle of converter
HFT	It is a high frequency transformer, used for electrical isolation between input and output circuits
Base speed	The speed at which the motor is designed to operate. It is also known as nominal or rated speed
Hysteresis control	It involves control of any quantity within a prespecified maximum and minimum values termed as hysteresis limit.
Power quality	It is a measure of various parameters of the supply voltage and current such as form factor, crest factor, total harmonic distortion and power factor

References

[1] Sanjeev Singh and Bhim Singh, "Optimized Passive Filter Design using Modified Particle Swarm Optimization Algorithm for a 12-Pulse Converter fed LCI-Synchronous Motor Drive," *IEEE Transactions on Industry Applications*, vol. 50, no. 4, pp. 2681–2689, 2014.

[2] A.E. Fitzgerald, Charles Kingsley, Jr. and Stephen D. Umans. *Electric Machinery*. Tata McGraw-Hill, New Delhi, 2002.
[3] John M. D. Murphy and Fred G. Turnbull. *Power Electronic Control of AC Motors*. Pergamon Press, Oxford, 1988.
[4] Bimal Kumar Bose. *Modern Power Electronics and AC Drives*. Pearson Education, New Delhi, 2002.
[5] David Finney. *Variable Frequency AC Motor Drive Systems*. Peter Peregrinus Ltd., London, 1988.
[6] Ion Boldea and Syed A. Nasar. *Electric Drives*. CRC Press, New York, 1998.
[7] Gopal K. Dubey. *Power Semiconductor Controlled Drives*. Prentice Hall, Upper Saddle River, NJ, 1989.
[8] Shashi B. Dewan, Gordon R. Slemon and Alan Straughen. *Power Semiconductor Drives*. Wiley Interscience, New York, 1984.
[9] Joseph Vithayathil. *Power Electronics: Principles and Applications*. McGraw Hill, East Windsor, NJ, 1994.
[10] Ned Mohan, Tore M. Undeland and William P. Robbins. *Power Electronics, Converter, Application and Design*. John Willey & Sons, New York, 1994.
[11] Muhammad H. Rashid. *Power Electronics*. Pearson Education, New Delhi, 2004.
[12] Sanjeev Singh and Bhim Singh, "A Voltage Controlled PFC Cuk Converter based PMBLDCM Drive for Air-Conditioners," *IEEE Transactions on Industry Applications*, vol. 48, no. 2, pp. 832–838, 2012.
[13] Bhim Singh, Sanjeev Singh, Ambrish Chandra and Kamal Al-Haddad, "Comprehensive Study of Single-Phase AC–DC Power Factor Corrected Converters with High Frequency Isolation," *IEEE Transactions on Industrial Informatics*, vol. 7, no. 4, pp. 540–556, 2011.
[14] Bhim Singh and Sanjeev Singh, "Single Phase PFC Topologies for Permanent Magnet Brushless DC Motor Drives," *IET Power Electronics*, vol. 3, no. 2, pp. 147–175, 2010.
[15] Sanjeev Singh and Bhim Singh, "A PFC Based PMBLDCM Drive for Air-Conditioner using Half-Bridge Buck Converter," *International Journal on Energy Technology and Policy (IJETP),* vol. 8, nos. 3/4/5/6, pp. 255–266, 2012.
[16] Sanjeev Singh and Bhim Singh, "A PFC Bridge Converter for Voltage Controlled Adjustable Speed PMBLDCM Drive," *Journal of Electrical Engineering and Technology (JEET)*, vol. 6, no. 2, pp. 215–225, 2011.
[17] Sanjeev Singh and Bhim Singh, "An Adjustable Speed PMBLDCM Drive for Air Conditioner using PFC Zeta Converter," *International Journal of Power Electronics (IJPElec)*, vol. 3, no. 2, pp. 171–188, 2011.
[18] Sanjeev Singh and BhimSingh, "PFC buck-boost Converter Based Voltage Controlled Adjustable Speed PMBLDCM Drive for Air-Conditioning," *European Transaction on Electric Power (ETEP)*, vol. 21, no. 1, pp. 424–438, 2010.
[19] Sanjeev Singh and Bhim Singh, "Single-Phase SEPIC Based PFC Converter for PMBLDCM Drive in Air-Conditioning System," *Asian Power Electronics Journal (APEJ)*, vol. 4, no. 1, pp. 16–21, 2010.

[20] Sanjeev Singh and Bhim Singh, "Modelling, Simulation and Design of Single-stage PFC Forward Boost Converter based Adjustable Speed PMBLDCM Drive for Small Air-conditioner," *Institution of Engineers (India) Journal – Electrical*, vol. 91, pp. 55–62, 2010.

[21] Sanjeev Singh and Bhim Singh, "A Voltage Controlled PFC Cuk Converter Based PMBLDCM Drive for Air-Conditioner," in *Proc. IEEE IAS 2010*, Houston, Texas (USA), 3–7 Oct. 2010, pp. 1–6.

[22] Sanjeev Singh and Bhim Singh, "A Power Factor Corrected PMBLDCM Drive for Air-conditioner Using Bridge Converter," in *Proc. IEEE PESGM 2010*, Minnesota (USA), 25–29 Jul. 2010, pp. 1–6.

[23] Sanjeev Singh and Bhim Singh, "A Voltage Controlled Adjustable Speed PMBLDCM Drive using A Single-Stage PFC Half-Bridge Converter," in *Proc. IEEE APEC 2010*, California (USA), 20–25 Feb. 2010, pp. 1976–1983.

[24] Sanjeev Singh and Bhim Singh, "Power Quality Improvement of PMBLDCM Driven Air-conditioner using a Single-Stage PFC Boost Bridge Converter," in *Proc. IEEE INDICON 2009*, Gandhinagar, Gujarat (India), 18–20 Dec. 2009, pp. 333–338.

[25] Bhim Singh and Sanjeev Singh, "Half Bridge Boost Converter for Power Quality Improvement in PMBLDCM Drive," in *Proc. IEEE Int. Conf. Emerging Trends in Engg. & Tech. (ICETET-09)*, Nagpur (India), 16–18 Dec. 2009, pp. 753–758.

[26] Katsuhiko Ogata. *Modern Control Engineering*. Prentice Hall of India, New Delhi, 1997.

[27] Saurabh Shukla and Sanjeev Singh, "Improved Power Quality PMBLDC Motor Drive for Constant Speed Variable Torque Load Using Non-Isolated SEPIC Converter," in *Proc. IEEE INDICON*, Pune (India), Dec. 2014, pp. 1–6.

[28] Sachin Singh, Kanwar Pal and Sanjeev Singh, "Single Current Sensor based Control Scheme for Position Sensor-less Starting and Running of PMBLDC Motor," in *Proc. IEEE ITEC*, Chennai (India), 27–29 Aug. 2015, pp. 1–4.

[29] Kanwar Pal, Saurabh Shukla and Sanjeev Singh, "Single Current Sensor PMBLDC Motor Drive with Power Quality Controller for Variable Speed Variable Torque Applications," in *Proc. IEEE ICEEI*, Bali, Indonesia, 10–11 Aug. 2015, pp. 1–6.

[30] Sanjeev Singh and Bhim Singh, "Power Quality Improved PMBLDCM Drive for Adjustable Speed Application with Reduced Sensor Buck-Boost PFC Converter," in *Proc. IEEE ICETET 2011*, Mauritius, 18–20 Nov. 2011, pp. 180–184.

Chapter 5

Synchronous motor drives

Sanjeet K. Dwivedi[1,2,3]

5.1 Introduction

The recent advances in power electronics and microelectronics have paved the way for the application of modern control techniques in motor control. Together, these developments have made a significant impact on operation and control of electric drives and, consequently, better options in application and/or control of drives are now available which effectively meet the diverse requirements of loads. A reasonable literature [1–54] is available to the efforts of researchers in bringing about notable improvements, not only in the performance of traditionally used induction motors [3,4] but also in the development of synchronous speed motors, such as permanent magnet synchronous motors (PMSMs) and synchronous reluctance motors (SynRMs). All along, the focus of development has been centered on attempts at meeting the ever-increasing demands of the load with required efficiency and ease of control. Earlier, the needs of the industry have been served mainly by its workhorse, the induction motor, which, on account of its physical ruggedness and cost-advantage, was the preferred choice for loads requiring operation at virtually constant speeds. Similarly, dc motors, due to their inherent flexibility, were used for variable speed loads. However, they suffered from the limitation of commutator and brushes and hence attempts were made in the past to provide ac drives with the speed control features of dc motors, avoiding at the same time the need to use the commutator and brushes. This culminated in the use of adjustable frequency induction and synchronous motors in the variable speed mode [6,7,10–15] as also of commutatorless motor [5,6,9–11].

The scalar control of key variables (voltage, frequency and slip) singly or jointly in an induction motor has given an excellent steady-state response but this was not found satisfactory in terms of transient-response. The advent of fast-acting solid-state devices and improved signal processors have, together, made it possible to implement the vector control of induction motor in applications requiring better dynamic response. For drives used in high-performance applications, such as aerospace, robotics and material handling systems, the demand of load has become

[1]Senior Research & Development Engineer, Motor Application Engineering, Danfoss Drives A/S, Gråsten, Denmark
[2]Fellow, IET, UK
[3]Electrical Engineering Department, Curtin University, Perth, Australia

more stringent requiring increased power density, compact machine size and faster dynamic performance. Similarly, the recent emphasis on energy conservation has made machine operation at higher efficiency a desirable feature in many applications. For achieving these objectives, it has become pertinent to consider the option of using the permanent magnet (PM) for the field excitation. The absence of field winding makes the PM motors more efficient and compact, aside from giving faster transient response and maintenance-free operation.

Earlier, the advantage of using PM motors was not fully exploited because of two important reasons, namely, the nonavailability of good quality PMs at a reasonable cost and the limitation imposed by the complexity and/or higher cost of available controllers. The situation has since been improved with the availability of improved magnetic materials [2,5,9,11] and high-power switching devices [16,17,19] as also of high-speed digital signal processors (DSPs) [6,15], all at reasonable costs. Together, these advances have made the PM brushless (PMBL) drives system flexible, compact, efficient and, most importantly, the overall cost of the system has been reduced comparatively. Consequently, these motors are emerging as competitors to the time-tested induction motors and are increasingly being used in many applications, such as pumps, fans and compressors in heating, ventilating and air-conditioning system, refrigerator and washing machines. Thus, the PMBL motors are suitable, not only for the top-end high-performance applications but also for small rating motors used in the low-end applications, such as home appliances owing to resulting gains in terms of cost, efficiency and compactness. In view of these attractive features, the brushless synchronous motor drive is included in this chapter with a view to improving its performance and identifying therefrom some aspects of the performance for further investigations by researchers.

This chapter deals with the development of model, simulation and hardware implementation of the synchronous motor (SM) drive under various operating conditions. In the modeling of vector-controlled PMSM drive, the complete model of the SM drive system is developed for different types of speed controllers with a view to improving the performance of the drive. The simulations of PMSM drive are carried out in MATLAB® environment with Power System Blockset (PSB) and fuzzy logic control (FLC) toolboxes. The hardware of vector-controlled PMSM drive system includes control circuit, interfacing circuit and the power circuit. The control circuit is implemented in DSP ADMC401 and the power circuit consists of the voltage source inverter (VSI) and the PMSM. The interfacing circuit is required for feedback signals in the form of motor winding currents and position as well as rotational speed of the rotor. The DSP-based software algorithm is used to obtain the performance of the drive for starting, speed reversal, load perturbation and steady-state response for different types of closed-loop speed controllers. The simulated results are presented in this chapter along with DSP-based implementation results of developed prototype of drive to validate both the model and the control algorithms.

5.2 Classification of synchronous motor drives

Variable speed ac motors can be classified into two main categories, i.e., asynchronous speed motors (induction motors) and synchronous motors.

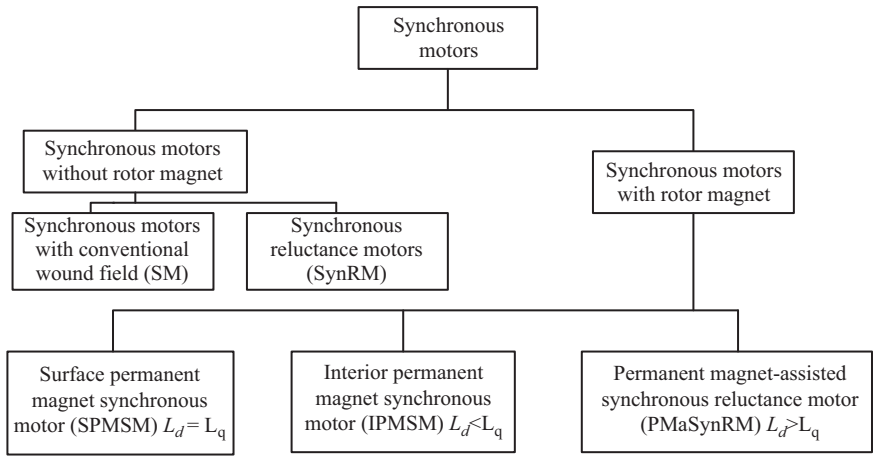


Figure 5.1 Classifications of synchronous motors

The synchronous motors can be further classified into two broad categories, i.e., motors without PM rotor and motor with PM rotor. The first category can be further named as conventional synchronous motors (wound field rotor) and SynRMs where iron core rotor is used without any field excitation.

A conventional synchronous machine is a rotating-field machine, where wound field rotor rotates synchronously with the rotating magnetic field of the armature winding of the machine placed in the stator. The stator winding provides three-phase distributed winding configuration and rotor field is wound on either cylindrical-rotor or salient-pole rotor structure, depending upon the maximum possible speed and application requirements.

The cylindrical-rotor configuration has the slots for holding the field winding and the salient-pole rotor is wound around the iron core of the rotor poles. In the outer surface of the rotor poles, a cage-like structure is provided for additional damper winding to improve the stability of the drive configuration.

Another type of synchronous machine is PMSMs. In this type of machine, excitation is based on PMs, and therefore, excitation cannot be controlled as in previously discussed wound field synchronous motors. The magnetization level of these PM synchronous machines is primarily dependent upon the back electro motive force (emf) generated due to rotor magnet. Synchronous motors categories are shown in Figure 5.1.

5.3 Magnet torque and reluctance torque-based classification

Synchronous motors can be classified on the basis of torque generated by PM placed in rotor. As we know, the developed torque of the PMSM or SynRM depends on the two factors—torque generated by the rotor magnet and torque generated by rotor *d* and *q*-axis reluctance difference. The magnet or reluctance-based classification of SMs is shown in Figure 5.2.

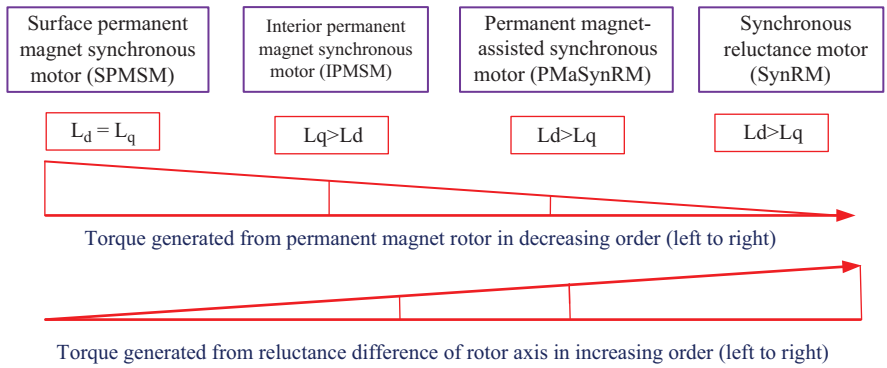


Figure 5.2 Magnet torque and reluctance torque-based classification of synchronous machines

5.4 Comparison of IPMSM and PMaSynRM

The interior permanent magnet synchronous motor (IPMSM) and permanent magnet-assisted synchronous reluctance motor (PMaSynRM) are essentially the same family of motors. Both motors generate torque from the PM and also from the reluctance difference between the *d*-axis and *q*-axis of the rotor circuit. The difference lies in the amount of torque generated by magnets, i.e., in IPMSM, the generated torque is a considerable part from the magnet; however, in the PMaSynRM, a considerable part of the torque is generated from the reluctance difference of the *d*-axis and *q*-axis of the rotor magnetic circuit. The magnet used in PMaSynRM is used to create difference between *d*-axis and *q*-axis inductances of rotor, i.e., L_d and L_q. To achieve it, magnet is placed in *q*-axis of the PMaSynRM in such a way as to reduce the total flux of the *q*-axis (the positive *q*-axis is aligned with the pole of the rotor magnet). Essentially, there is difference in the amount of magnet placed in the rotor circuit of IPMSM and PMaSynRM. The convention used to denote *d*-axis of the IPMSM can be compared with the *q*-axis of the PMaSynRM for showing direction of magnetic circuit of PM and synchronous reluctance class of motor as shown in Figure 5.3.

5.5 Different control techniques for various synchronous speed motors

There are various control strategies used for energy efficient and desired operation of synchronous motors with and without magnets. Operation of the synchronous motors at lower than base speed range can be obtained with fulfilling the following performance criteria for optimal operation of the drive.

The main control strategies for synchronous motors without magnet for lower than base speed operating range are as follows:

1. Maximum torque per ampere (MTPA) control
2. Maximum efficiency (ME) control

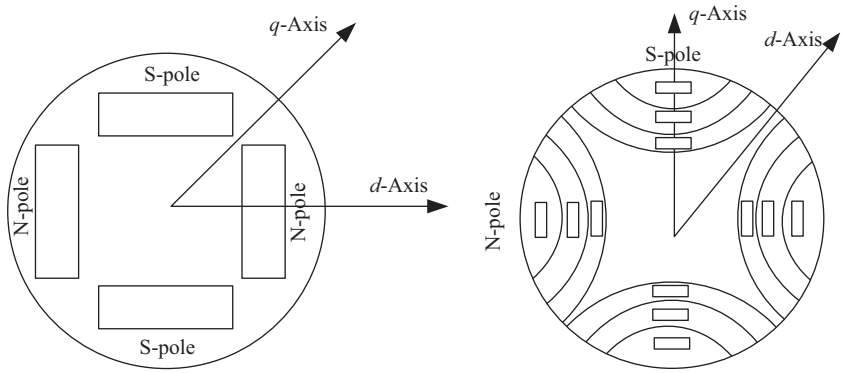


Figure 5.3 Orientation of d-axis and q-axis in the IPMSM and PMaSynRM

3. Unity power factor (UPF) control
4. Constant mutual flux linkages (CMFL) control
5. Zero *d*-axis current (ZDAC) control for the surface PM machine

The MTPA control strategy [18] provides maximum torque for a given amount of current. This, in turn, minimizes resistive losses for a given torque. This strategy is utilized in applications where efficiency is most important, and this control technique is most popular PMSMs. Another strategy, the UPF control strategy [18], optimizes the system's volt-amperes (VIs) requirement by maintaining the power factor at unity. The ME control strategy [18] minimizes the net loss of the motor at any operating point. This control strategy is particularly appealing in battery-operated motion control systems in order to extend the life of the battery. The CMFL strategy [18] limits the air gap flux linkage to a known value which is usually the magnet flux linkage. This is to avoid saturation of the core.

Each of the abovementioned control strategies has their own merits and demerits. A comparison between the ZDA, UPF and CMFL control strategies is provided in [18] from the point of view of torque per unit current ratio and power factor. The UPF control strategy results in the highest possible power factor in full range of speed. The ZDAC control strategy results in the lowest power factor among the five control strategies. The MTPAC control strategy is superior in both efficiency and torque per unit current as compared to the ZDAC control strategy. Torque is limited to rated value in all existing control techniques for the lower than base speed operating range. This operating range is referred to as the constant torque operating range.

The main control strategies for synchronous motors with magnet for operation above base speed:

1. Constant back emf (CBE) control
2. Six-step voltage (SSV) control

Performance criteria other than torque linearity cannot be enforced in this range due to the fact that a restriction on voltage is imposed. This range of operation is also

referred to as the flux weakening range. Two control strategies are possible depending on whether maximum phase voltage is applied, or the phase voltage is limited to a level lower than maximum possible. These control strategies are as follows:

The CBE control strategy [18] limits the back emf to a value that is lower than the maximum possible voltage to the phase. By doing this, a voltage margin is retained that can be used to implement instantaneous control over phase current. Applications that require high quality of control over torque in the higher than base speed operating range utilize the CBE control strategy. The SSV control strategy applies maximum possible voltage to the phase. In this case, only the average torque can be controlled, and a relatively higher magnitude of torque ripple is present.

Most of the control strategies for the flux weakening range of PMSM result in nonlinear control over torque. This happens either because of neglecting the impact of core losses or by erroneous implementation strategies. The SSV control strategy is widely utilized in many applications [18].

5.6 Operating principle of vector control technique

The vector control (VC) technique, which is also known as field-oriented control, is used to control the space vector of magnetic flux, current and voltage. In this technique, the stator current is decomposed into flux and torque producing components for obtaining the decoupled control of PMSM drive in a way similar to the separately excited dc motor. Figure 5.4 shows the basic building block of the vector-controlled PMSM drive. The drive consists of speed controller, resolver sine and cosine position signals, demodulation circuit, current sensors, current controlled pulse width modulator (CC-PWM), insulated gate bipolar transistor (IGBT)-based VSI and PMSM. The rotor speed (ω_r) is compared with the reference speed (ω_r^*). The error in

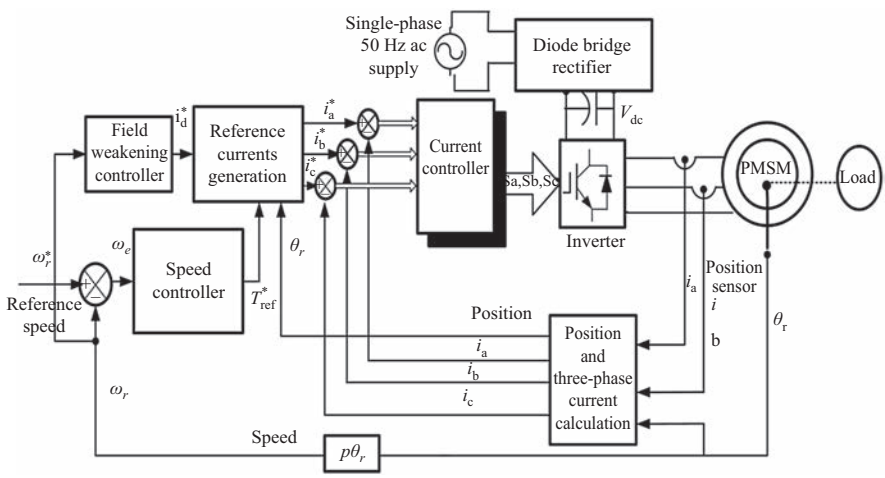


Figure 5.4 Block diagram of vector-controlled PMSM drive

speed (ω_e) is processed in the speed controller, which generates the reference torque (T_k^*). This reference torque is limited using a limiter and the limited reference torque (T_{ref}^*) is used to generate the q-axis reference current (i_q^*). Similarly, from the rotor speed of the motor, the d-axis current (i_d^*) is decided using the field weakening controller. Both these d-axis and q-axis stator currents generate three-phase reference currents (i_{a}^*, i_{b}^* and i_{c}^*), which are compared with the sensed winding currents (i_{a}, i_{b} and i_{c}) of the PMSM. The current errors are fed to the PWM current controller, which generates the switching signals for the VSI. These, in turn, control the winding currents of PMSM, thereby controlling the speed of the motor.

5.7 Mathematical model of vector-controlled PMSM drive

The vector-controlled PMSM drive consists of the various components including speed controller, filed weakening controller, reference current generator, PWM current controller, ac–dc converter, VSI and PMSM.

Each component of the vector-controlled PMSM drive is modeled by a set of mathematical equations. Such set of equations, when combined together, represents the mathematical model of the complete system. The modeling of different components of the drive system is as follows.

5.7.1 Modeling of speed controllers

The desired reference value of the speed signal is compared with the feedback speed signal and the speed error is processed in the speed controller. The output of the speed controller is the torque value and is fed to the limiter and the final reference torque is obtained from the limiter. The different types of speed controller, namely, the proportional integral (PI) controller, the sliding mode controller (SMC), fuzzy pre-compensated proportional-integral controller (FPPI) and hybrid fuzzy proportional integral (HFPI) controller are used in the vector-controlled PMSM drive.

The speed error at the kth instant of time is given as

$$\omega_{e(k)} = \omega_{r(k)}^* - \omega_{r(k)} \tag{5.1}$$

where $\omega_{r(k)}^*$ is the reference speed at kth instant, $\omega_{r(k)}$ is the rotor speed at the kth instant and $\omega_{e(k)}$ is the speed error at the kth instant

5.7.1.1 Proportional integral (PI) controller

The block diagram of the PI speed controller is shown in Figure 5.5. The output of the speed controller at kth instant is given as

$$T_{(k)} = T_{(k-1)} + K_P\left\{\omega_{e(k)} - \omega_{e(k-1)}\right\} + K_I\omega_{e(k)} \tag{5.2}$$

where K_P and K_I are the proportional and integral gain parameters of the PI speed controller. The gain parameters are appropriately selected by observing their effects on the response of the drive.

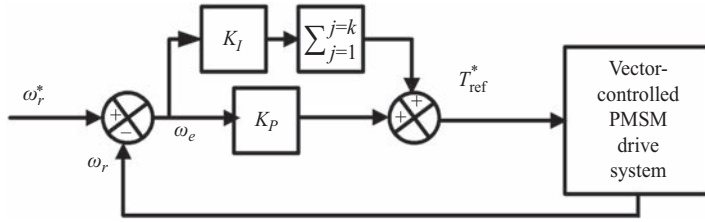


Figure 5.5 Schematic diagram of PI speed controller

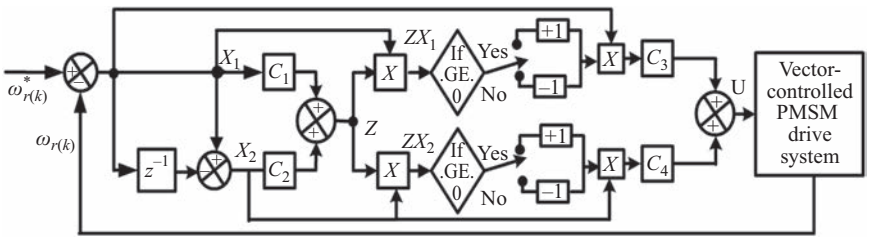


Figure 5.6 Schematic diagram of sliding mode speed controller

5.7.1.2 Sliding mode controller (SMC)

The block diagram of the SM speed controller is shown in Figure 5.6. This particular controller operates on the basis of switching functions [38]. The switching functions at the *k*th sampling instant are defined as follows:

$$X_1 = 1, \quad \text{if } zy_{1(k)} > 0 \quad \text{and} \quad X_1 = -1, \quad \text{if } zy_{1(k)} < 0 \tag{5.3a}$$

$$X_2 = 1, \quad \text{if } zy_{2(k)} > 0 \quad \text{and} \quad X_2 = -1, \quad \text{if } zy_{2(k)} < 0 \tag{5.3b}$$

wherein $Y_{1(k)} = \left\{\omega_{r(k)}^* - \omega_{r(k)}\right\}$ and $Y_{2(k)} = (d/dt)\{Y_{1(k)}\} = pY_{1(k)}$.

"Z" is switching hyperplane function on the speed locus of the drive and is given as

$$Z = C1Y1 + Y2 \tag{5.4}$$

where $C1$ is the parameter of the switching hyperplane function.

The output of the sliding mode speed controller at *k*th instant is given as

$$T_{(k)} = C_2 Y_{1(K)} X_{1(K)} + C_3 Y_{2(K)} X_{2(K)} \tag{5.5}$$

where C_2 and C_3 are the gains of the sliding mode controller.

5.7.1.3 Fuzzy pre-compensated PI controller

In the VC scheme, FPPI speed controller is used to generate the reference torque for the closed-loop operation of the PMSM drive system. The PI speed controller suffers from the problem of large overshoots and undershoots in its output response when some unknown nonlinearities are present in the drive system [43]. The fuzzy pre-compensator modifies the reference speed to compensate the undershoot and overshoot in the output response. The schematic block diagram of the fuzzy pre-compensated PI speed controller is shown in Figures 5.7 and 5.8, and it is described in the following equations.

Speed error can be given as

$$\omega_{e(k)} = \omega^*_{r(k)} - \omega_{r(k)} \tag{5.6}$$

The rate of change of speed error for a specified sampling period can be given as

$$\Delta\omega_{e(k)} = \omega_{e(k)} - \omega_{e(k-1)} \tag{5.7}$$

The reference speed $\omega^*_{r(k)}$ is modified based on the fuzzy intelligence to compensate the nonlinearities present in the model and modified reference input is given to

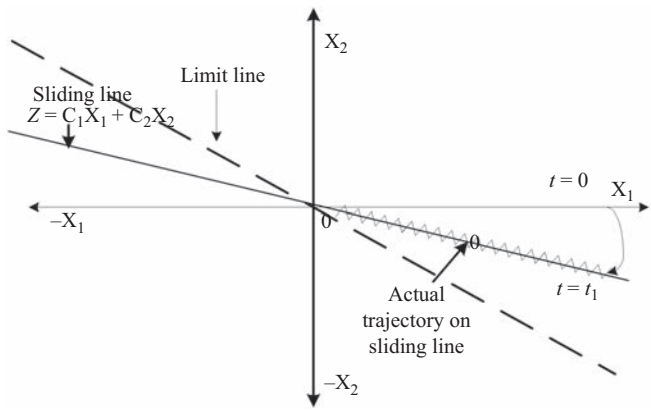


Figure 5.7 Sliding mode state trajectory in phase-plane

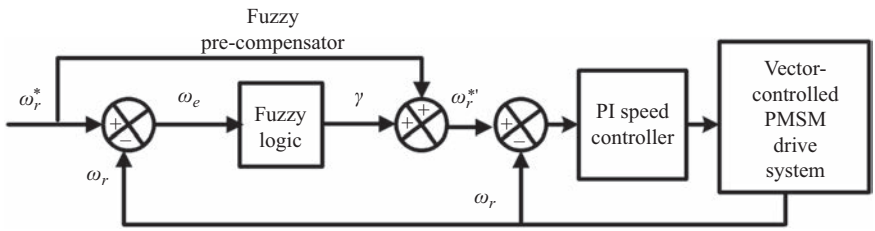


Figure 5.8 Fuzzy pre-compensated PI speed controller

PI speed controller as

$$\omega^{*'}_{r(k)} = \omega^{*}_{r(k)} + \gamma_{(k)} \tag{5.8}$$

where $\gamma_{(k)}$ is the output of the fuzzy logic (FL) controller and can be given as

$$\gamma_{(k)} = F\left(\omega_{e(k)}, \Delta\omega_{e(k)}\right) \tag{5.9}$$

The compensation term $F\left(\omega_{e(k)}, \Delta\omega_{e(k)}\right)$ is used to change the reference speed so that the transient response of the output speed is improved to reduce the effect of nonlinearities. The compensated reference signal $\left(\omega^{*'}_{r(k)}\right)$ is then applied to the conventional PI controller to obtain the modified torque reference $\left(T'_{\text{ref}(k)}\right)$ at that instant as follows:

$$\omega'_{e(k)} = \omega^{*'}_{r(k)} - \omega_{r(k)} \tag{5.10}$$

$$\Delta\omega'_{e(k)} = \omega'_{e(k)} - \omega'_{e(k-1)} \tag{5.11}$$

$$T'_{\text{ref}(k)} = T'_{\text{ref}(k-1)} + K_P\Delta\omega'_{e(k)} + K_I\omega'_{e(k)} \tag{5.12}$$

Fuzzy pre-compensator

As discussed in the preceding subsection, the compensation is shown in Figure 5.8. It is obtained by using an FL. The error $\omega_{e(k)}$ and change in error $\Delta\omega_{e(k)}$ are the inputs to the fuzzy mapping function F, and $\gamma_{(k)}$ is the output.

Fuzzy logic control

The schematic diagram of the FL speed controller is given in Figure 5.9. The input to the FL speed controller is the speed error and the change in speed error. These two inputs are normalized to obtain the error $\omega_{e(k)}$ and the change in error $\Delta\omega_{e(k)}$ in a desired range of -1 to 1. The FL controller then determines the compensation term $\gamma_{(k)}$ by the process given as follows:

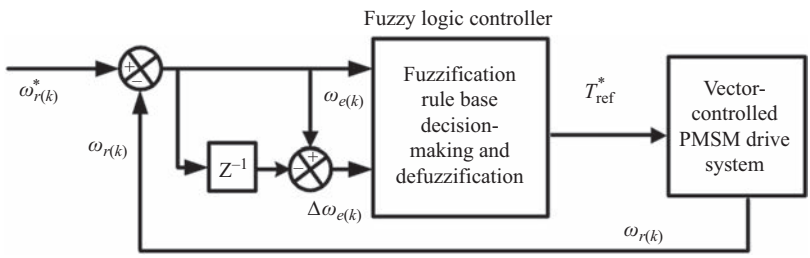


Figure 5.9 Schematic diagram of fuzzy logic controller for vector-controlled PMSM drive

Fuzzification

This step is used to convert the speed error and change in speed error to fuzzy variables. In this process of fuzzification, the membership functions are assigned in the universe of discourse "*U*" chosen in the interval of 1 to −1, namely, positive big (PB), positive medium (PM), positive small (PS), zero (ZE), negative small (NS), negative medium (NM) and negative big (NB) on the basis of normalized inputs of error and change in error. The membership function for the universe of discourse is given in Figure 5.10.

Decision-making

The decision-making process is associated with a set of FL rules. In accordance with the linguistic rules and the linguistic values of the inputs for the fuzzifier, the linguistic value of the output is computed. The first two linguistic values are associated with the input variables $\omega_{e(k)}$ and $\Delta\omega_{e(k)}$, while the third linguistic value is associated with the output $\gamma_{(k)}$. The decision-making rules of the fuzzy pre-compensator are given in Table 5.1.

Defuzzification

The output of the inference process gives degree of belonging of $\gamma_{(k)}$ to different fuzzy subsets. Defuzzification is the process of obtaining crisp output from these fuzzy values. To obtain $\gamma_{(k)}$, the method of center of gravity is used. The defuzzification process maps the results of the FL rule stage to a real number output $F\left(\omega_{e(k)}, \Delta\omega_{e(k)}\right)$. The output of defuzzification process can be given as

$$F\left(\omega_{e(k)}, \Delta\omega_{e(k)}\right) = \gamma_{(k)} = K_f \frac{\sum_i \mu_i \times \alpha_i}{\sum_i \mu_i} \tag{5.13}$$

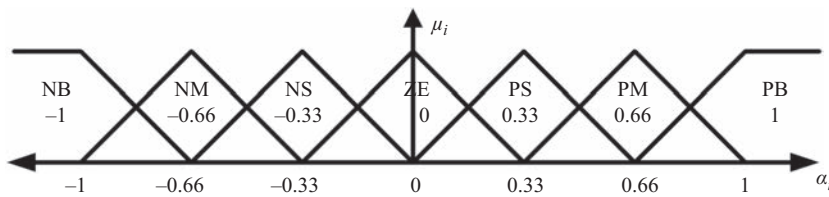


Figure 5.10 Membership function of fuzzy pre-compensated PI speed controller

Table 5.1 Logic rules for fuzzy pre-compensated controller

$\omega_{e(k)}$ / $\Delta\omega_{e(k)}$	**NB**	**NM**	**NS**	**ZE**	**PS**	**PM**	**PB**
NB	NB	NB	NM	NM	NS	NS	ZE
NM	NB	NM	NM	NS	NS	ZE	PS
NS	NB	NM	NS	NS	ZE	PS	PS
ZE	NM	NS	NS	ZE	PS	PS	PM
PS	NM	NS	ZE	PS	PS	PM	PM
PM	NS	ZE	PS	PS	PM	PM	PB
PB	NS	ZE	PS	PM	PM	PB	PB

where μ_i is output of fuzzy subset, α_i is the degree of belonging and K_f is the scaling factor of defuzzifier. The pre-compensated reference speed signal $\left(\omega^{*'}_{r(k)}\right)$ is used as the reference speed in PI speed controller.

5.7.1.4 Hybrid fuzzy PI controller

In the VC scheme, PI speed controller is normally used to achieve reference torque for the closed-loop operation of the PMSM drive system. The PI speed controller is most widely used in the drive system. It needs parameter tuning and as the operating condition of the drive changes, the performance of PI controller gets degraded and, therefore, retuning the gains of PI controller is essential, whereas FL controller is less sensitive to parameter tuning and change in operating conditions of the drive. However, it results in steady-state speed error. Therefore, to preserve the advantages of both the PI and FL controllers, a hybrid controller is used. The HFPI controller compensates undershoot or overshoot in the output response while retaining all the advantages of PI speed controller viz. zero steady-state error and no chattering at the set point [46]. The schematic block diagram of the HFPI speed controller is shown in Figures 5.11–5.13, and it is described by the following equations.

Speed error can be given as

$$\omega_{e(k)} = \omega^{*}_{r(k)} - \omega_{r(k)} \tag{5.14}$$

The rate of change of speed error for a specified sampling period can be given as

$$\Delta\omega_{e(k)} = \omega_{e(k)} - \omega_{e(k-1)} \tag{5.15}$$

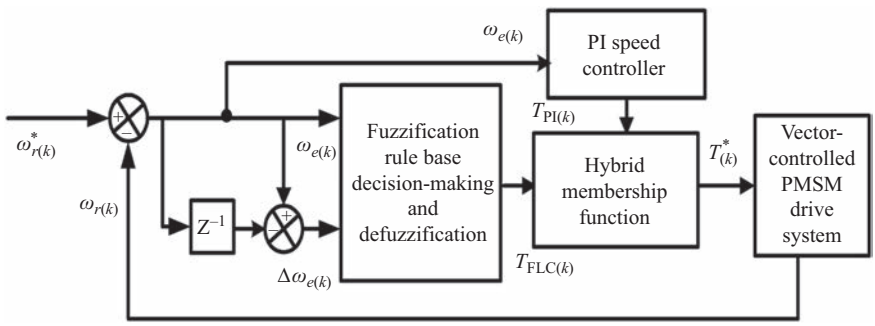


Figure 5.11 Schematic diagram of hybrid fuzzy PI speed controller for vector-controlled PMSM drive

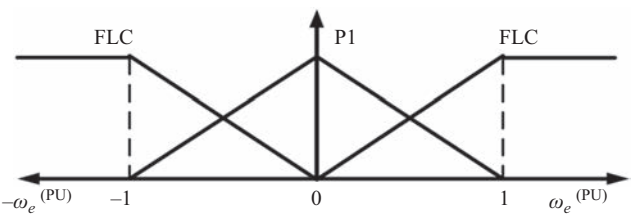


Figure 5.12 Membership function of hybrid fuzzy PI speed controller

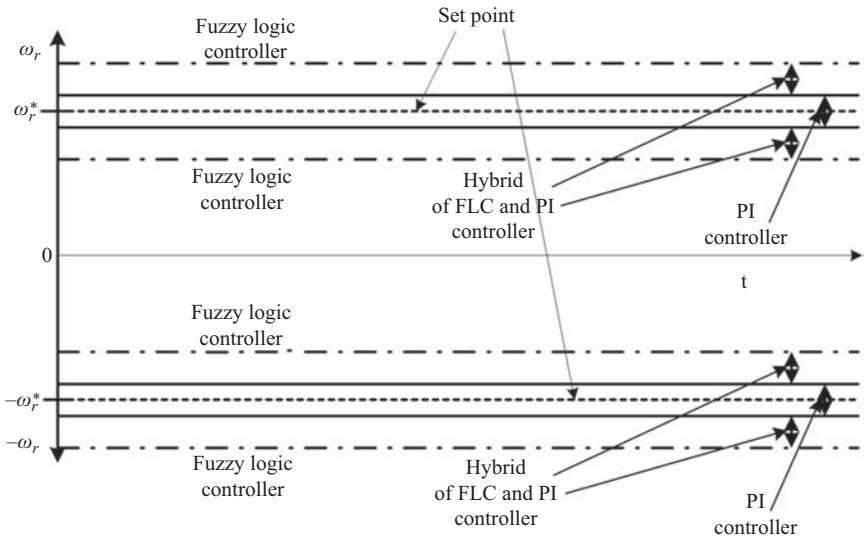


Figure 5.13 Operating zone of FLC and PI speed controller

The fuzzy intelligence is used to provide the fast control and to compensate the nonlinearities present in the model as

The output of the FL controller can be given as

$$T_{\mathrm{FLC}(k)} = F\left(\omega_{e(k)}, \Delta\omega_{e(k)}\right) \tag{5.16}$$

The FLC output term $F\left(\omega_{e(k)}, \Delta\omega_{e(k)}\right)$ is used to provide fast transient response and to reduce the effect of modeling error. The FLC output plus PI output is used to derive the reference torque in the hybrid form to obtain the modified reference torque $\left(T^*_{r(k)}\right)$ as follows:

$$T^*_{r(k)} = T^*_{r(k-1)} + K_{\mathrm{PI}} T_{\mathrm{PI}} + K_{\mathrm{FLC}} T_{\mathrm{FLC}} \tag{5.17}$$

where K_{PI} and K_{FLC} are membership functions for selection of hybrid proportion of the FLC controller as shown in Figure 5.13 and T_{PI} and T_{FLC} are the output of PI speed controller and FLC speed controller, respectively.

5.7.2 Modeling of reference winding current generation

Three-phase reference winding currents are generated using the output of the speed controller and the rotor position. The following are the equations for the reference currents [13]:

The flux component of reference stator current (i_d^*) can be defined as

$$i_d^* = 0 \quad \text{for} \quad \omega_r < \omega_{\mathrm{b}} \quad \text{and} \quad i_d^* = \varphi_f \left[\frac{\{\omega_r - \omega_{\mathrm{b}}\}}{\{\omega_r (L_d - L_q)\}}\right] \text{for} \quad \omega_r > \omega_{\mathrm{b}} \tag{5.18}$$

The torque component of the reference stator current (i_q^*) can be obtained from reference torque, T_{ref}^* as

$$i_q{}^* = \frac{T_{\text{ref}}^*}{\left\{K_t\left(\varphi_f + \left(L_d - L_q\right)i_d^*\right)\right\}} \tag{5.19}$$

where K_t is the motor torque constant.

Three-phase reference currents can be expressed as

$$i_{\text{a}}^* = i_d^* \text{Cos}\,\theta_r - i_q^*\,\text{Sin}\,\theta_r \tag{5.20}$$

$$i_{\text{b}}{}^* = i_d{}^*\,\text{Cos}(\theta_r - 2\pi/3) - i_q{}^*\,\text{Sin}(\theta_r - 2\pi/3) \tag{5.21}$$

$$i_{\text{c}}{}^* = i_d{}^*\,\text{Cos}(\theta_r + 2\pi/3) - i_q{}^*\,\text{Sin}(\theta_r + 2\pi/3) \tag{5.22}$$

where θ_r is the rotor angular position in electrical rad/s.

These reference currents (i_{a}^*, i_{b}^*, i_{c}^*) are compared with the sensed winding currents (i_{a}, i_{b}, i_{c}) and the resulting errors are fed to the PWM current controller.

5.7.3 Modeling of PWM current controller

In the PWM current controller, the instantaneous value of high-frequency triangular carrier wave (16 kHz) is compared with the amplified current errors. For the phase "A" if the amplified current error is more than the triangular carrier wave, then the gating signal for the upper switch of phase "A" leg of three-phase VSI (S_1 is on) is generated and the switching function "S_a" for phase "A" is set to one ($S_a = 1$), otherwise the gating signal is generated for the lower switch of the same phase "A" leg (S_2 is on) and the switching function "S_a" is set to zero ($S_a = 0$). Similar PWM controller outputs are generated for other two phases.

5.7.4 Modeling of PMSM

The stator of the PMSM consists of a balanced three-phase winding similar to the conventional synchronous motor. The mathematical model of PMSM is derived from the synchronous motor under the assumption that the armature emf is induced by the PMs in the place of dc excitation and there are no windings on the rotor. Considering the induced emf to be sinusoidal and eddy current and hysteresis losses to be negligible, the stator voltage equations in the rotor reference frame are given as [13]

$$v_q = R_s i_q + p\varphi_q + \omega_r \varphi_d \tag{5.23}$$

$$v_d = R_s i_d + p\varphi_d - \omega_r \varphi_q \tag{5.24}$$

where $\varphi_q = L_q i_q$ and $\varphi_d = L_d i_d + \varphi_f$. v_q and v_d are the d and q-axis stator voltages. i_q and i_d are the d and q-axis stator currents. L_q and L_d are the d and q-axis inductances. φ_f is stator flux linkages produced by PMs. R_s is stator-winding resistance per phase. ω_r is rotor speed in rad/s (electrical).

The developed electromagnetic torque is given as [4]

$$T_e = \left(\frac{3}{2}\right)\left(\frac{P}{2}\right)\left\{\varphi_f i_q + \left(L_d - L_q\right) i_d i_q\right\} \tag{5.25}$$

where P is the number of poles.

The electromagnetic torque is balanced by the load torque, accelerating torque and damping torque of the system and can be expressed in electromechanical equation as

$$T_e = T_L + B\omega_r + Jp\omega_r \tag{5.26}$$

where T_L is the load torque, B is the damping coefficient and J is the moment of inertia.

The model equations of PMSM can be rearranged in the form of following first-order differential equations as

$$pi_d = \frac{\left(v_d - R_s i_d + \omega_r L_q i_q\right)}{L_d} \tag{5.27}$$

$$pi_q = \frac{\left(v_q - R_s i_q - \omega_r L_d i_d - \omega_r \varphi_f\right)}{L_q} \tag{5.28}$$

$$p\omega_r = \frac{\left(T_e - T_L - B\omega_r\right)}{J} \tag{5.29}$$

$$p\theta_r = \omega_r \tag{5.30}$$

The phase currents of the motor can be reconstructed in terms of i_d and i_q by using the inverse Park's transformation as

$$i_{\mathrm{a}} = i_d \operatorname{Cos}\theta_r - i_q \operatorname{Sin}\theta_r \tag{5.31}$$

$$i_{\mathrm{b}} = i_d \operatorname{Cos}(\theta_r - 2\pi/3) - i_q \operatorname{Sin}(\theta_r - 2\pi/3) \tag{5.32}$$

$$i_{\mathrm{c}} = i_d \operatorname{Cos}(\theta_r - 4\pi/3) - i_q \operatorname{Sin}(\theta_r - 4\pi/3) \tag{5.33}$$

where θ_r is the position angle of the rotor.

5.7.5 Modeling of voltage source inverter

The VSI consists of IGBT-based three-phase VSI. The inverter voltage can be given by following equations in terms of switching signals $\mathrm{S_a}$, $\mathrm{S_b}$ and $\mathrm{S_c}$ and dc bus voltage, obtained from the CC-PWM as

$$v_{\mathrm{a}} = \left(\frac{V_{\mathrm{dc}}}{3}\right)\left(2\mathrm{S_a} - \mathrm{S_b} - \mathrm{S_c}\right) \tag{5.34}$$

$$v_b = \left(\frac{V_{dc}}{3}\right)(2S_b - S_a - S_c) \tag{5.35}$$

$$v_c = \left(\frac{V_{dc}}{3}\right)(2S_c - S_a - S_b) \tag{5.36}$$

where S_a, S_b and S_c are switching functions (which are either one or zero). v_a, v_b, v_c and V_{dc} are voltages of phase winding a, b, c and dc link, respectively.

These voltages can be expressed in the rotor reference frame as the forcing functions v_d and v_q by using the Park's transformation as

$$v_d = \left(\frac{2}{3}\right)(v_a \operatorname{Cos}\theta_r + v_b \operatorname{Cos}(\theta_r - 2\pi/3) + v_c \operatorname{Cos}(\theta_r - 4\pi/3)) \tag{5.37}$$

$$v_q = (-2/3)(v_a \operatorname{Sin}\theta_r + v_b \operatorname{Sin}(\theta_r - 2\pi/3) + v_c \operatorname{Sin}(\theta_r - 4\pi/3)) \tag{5.38}$$

These voltages v_d and v_q are forcing functions in the model of PMSM given in (5.27) and (5.28).

The set of first-order differential equations given in (5.27)–(5.30) defines the developed model in terms of dependent variables i_d, i_q, ω_r, θ_r and time as an independent variable.

5.8 MATLAB-based model of vector-controlled PMSM drive system

The simulation model is developed in MATLAB environment along with Simulink® and PSB toolboxes for simulating the response of vector-controlled PMSM drive under different operating conditions such as starting, speed reversal and load perturbation. The simulation environment in MATLAB/Simulink/PSB has become a standard tool in the research work. This section describes the model of vector-controlled PMSM drive developed in MATLAB environment using Simulink and PSB toolboxes. To test the versatility and accuracy of the developed model, the response of vector-controlled PMSM drive is initially simulated using a PI speed controller and afterward, the drive performance is simulated for other three speed controllers and finally these results are compared to examine their effectiveness.

5.8.1 Modeling using power system blockset (PSB) toolbox

The real-time simulation is performed in MATLAB environment along with Simulink and PSB toolboxes. The control structure is shown in Figure 5.14 in which the sampling period of 62.5 μs is used for simulation. The main parts of the block diagram are discussed in this subsection.

5.8.1.1 Speed controller

The model of speed controller is realized using the Simulink toolbox of the MATLAB software. The main function of speed controller block is to provide a reference torque for the vector-controlled drive. The output of the speed controller

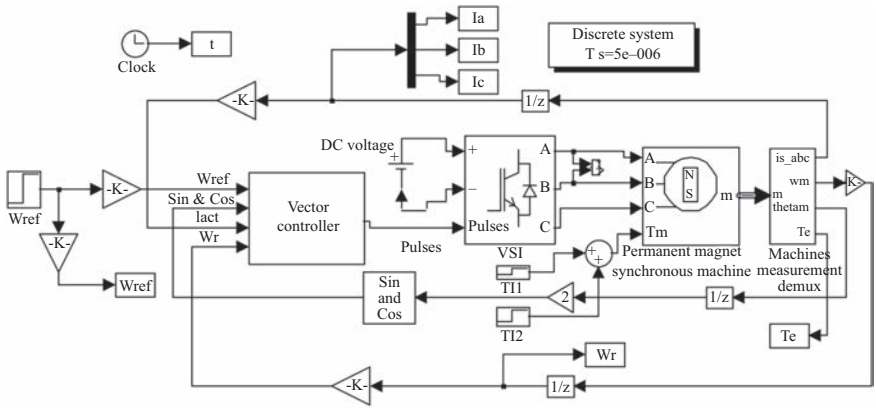


Figure 5.14 MATLAB simulation model of vector-controlled PMSM drive

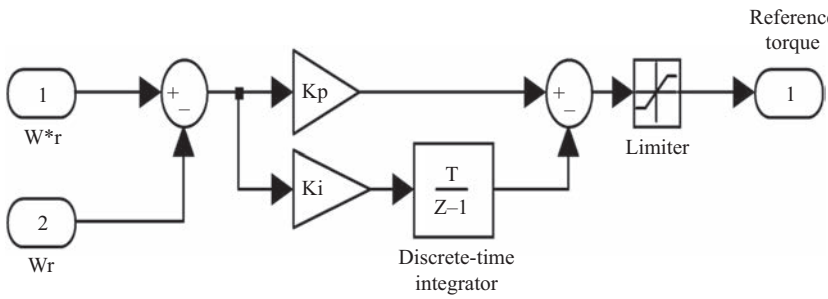


Figure 5.15 Simulink model of PI speed controller

is limited to a proper value in accordance with the motor rating to generate the reference torque for the vector controller. The speed controllers realized using the Simulink and PSB toolboxes are, namely, PI speed controller, sliding mode (SM) speed controller, FPPI speed controller and HFPI speed controller.

Figure 5.15 shows the Simulink model diagram of the PI speed controller in discrete time domain. The basic operating equations have been stated in the preceding section. The proportional and integral gain parameters, K_P and K_I, respectively, are used with limiter to generate the reference torque. The upper and lower limits for the limiter block are calculated as per the rating of the motor being used.

Figure 5.16 shows the Simulink model of the sliding mode (SM) speed controller. The mathematical equations describing the sliding mode controller action are shown in the previous section. The parameters C_1, C_2 and C_3 of the torque expression given in (5.5) are adjusted to give the reference torque to the required level, the torque obtained is limited according to the motor rating.

Figure 5.17 shows the Simulink model diagram for the FPPI speed controller. The two inputs, namely, speed error and change in speed error, are scaled and fed to the MATLAB FL block. The rescaled defuzzified output of the FL block produces the

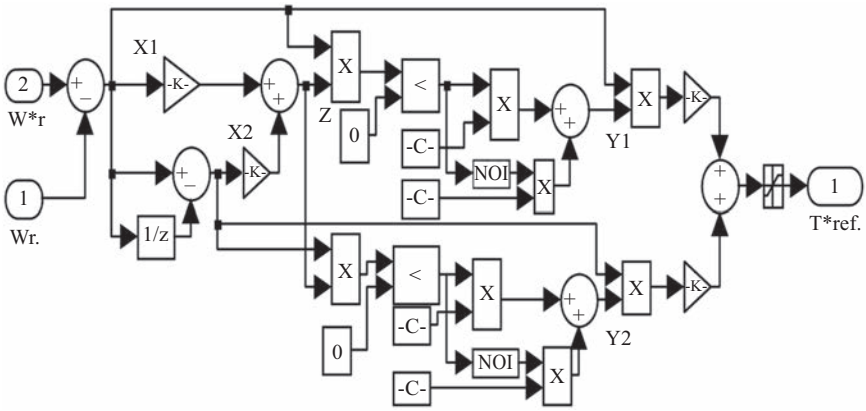


Figure 5.16 Simulink model of sliding mode-based speed controller

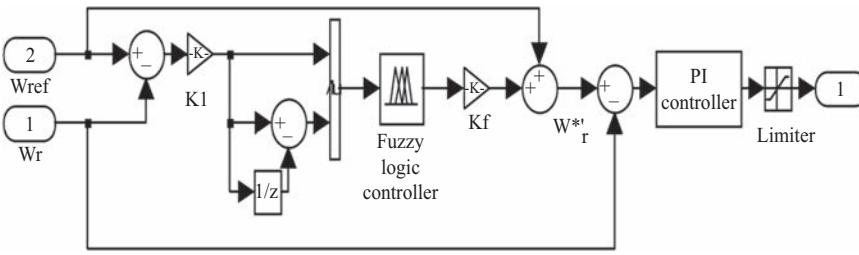


Figure 5.17 Simulink model of fuzzy pre-compensated PI speed controller

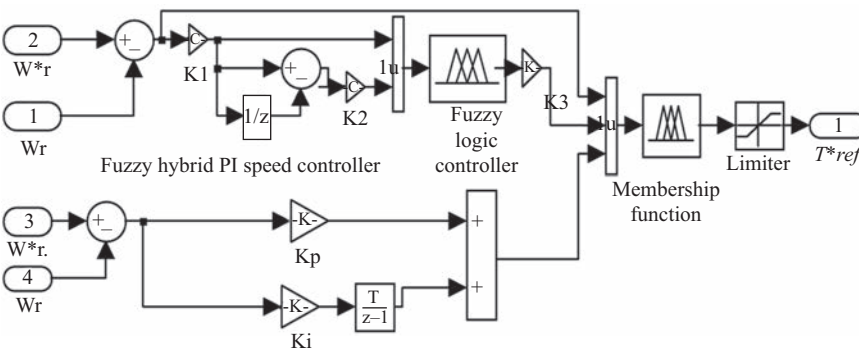


Figure 5.18 Simulink model of hybrid fuzzy PI speed controller

compensation term which is added to the reference speed signal to obtain the modified reference speed signal which is fed to the PI speed controller as described in (5.13).

Figure 5.18 shows the Simulink model diagram for the HFPI speed controller. The two inputs, namely, the speed error and change in speed error, are scaled and

fed to the MATLAB FL block. The rescaled defuzzified output of the FL block produces the reference torque term which is added according to a rule-based hybrid membership function shown in Figure 5.10(c) to obtain the reference torque term as described in (5.17).

5.8.1.2 Field weakening controller

The Simulink model diagram for the field weakening controller is shown in Figure 5.19. This block takes the rotor speed and reference toque as inputs and gives the *d*-axis reference stator current as output. This is reconstructed from the values of *q*-axis reference current and *d*-axis reference current, obtained from the controller output.

5.8.1.3 Reference winding current generation

The Simulink model diagram of reference winding current generator block is also shown in Figure 5.20. This block utilizes the limited value of speed controller and the output of field weakening controller along with the angular position of the rotor.

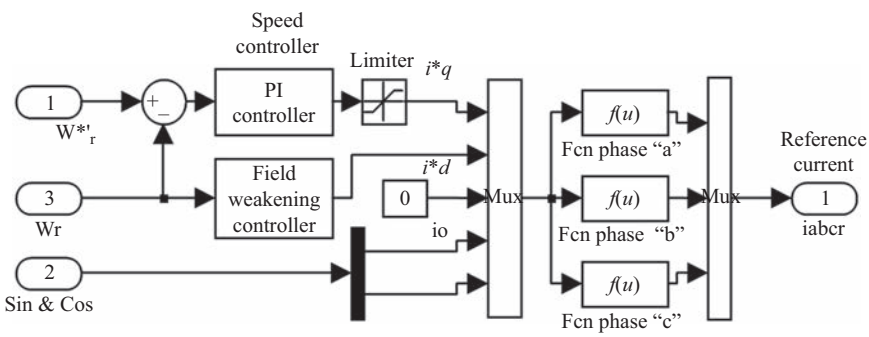


Figure 5.19 Simulink model of field weakening controller and reference current generator

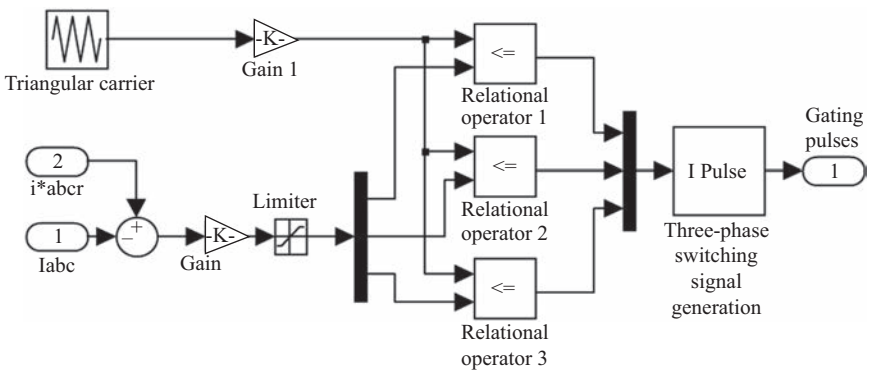


Figure 5.20 Simulink model of current controlled pulse width modulator

The inverse Park's transformation is used in the model for generating the reference winding currents of the PMSM.

5.8.1.4 Current controlled pulse width modulator (CC-PWM)

The Simulink model diagram of CC-PWM used for generation of switching signal for the VSI is shown in Figure 5.20. The inputs to this block are three-phase reference winding currents obtained from the reference winding current generator block and the sensed three-phase winding currents of the motor. For the corresponding phases "a", "b" and "c", switching signals are generated by current-controlled PWM technique.

5.9 Description of DSP-based vector-controlled PMSM drive

The proposed vector-controlled PMSM drive is implemented using the VC technique. Variable voltage and variable frequency (VVVF) source is realized with the VSI to feed the PMSM. The signals of winding currents and resolver position are the feedback signals for the closed-loop structure of the vector-controlled PMSM drive. The control algorithm is implemented in real time using Digital Motion Controller ADMC401 DSP developed by analog devices. Digital control eliminates the problem of drift and the use of programmable processors leads to the upgradation in the control scheme with the help of improved software. Fast speed and high accuracy features of DSPs like ADMC40 enable it to achieve a high-resolution control of the vector-controlled PMSM drive.

Figure 5.21 shows the block diagram of the vector-controlled PMSM drive system. The power circuit consists of single-phase 50 Hz ac supply, single-phase ac–dc diode bridge converter, dc-link inductance(L)-capacitance(C) filter, VSI and the PMSM.

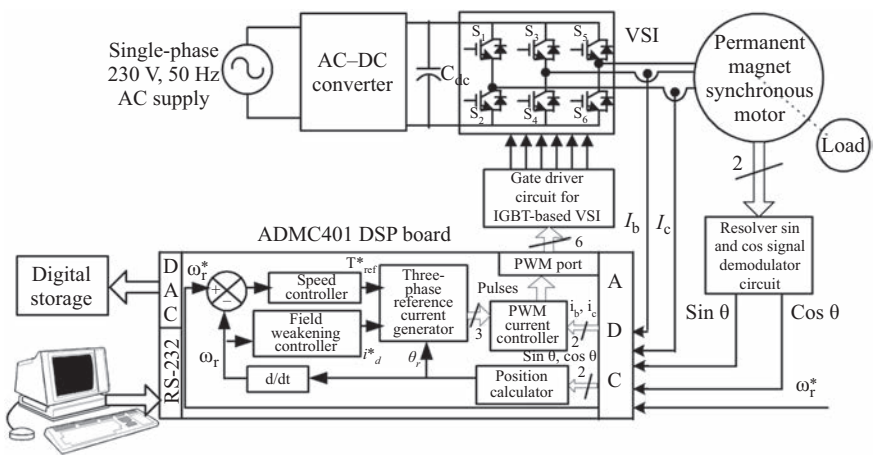


Figure 5.21 Experimental setup of vector-controlled PMSM drive

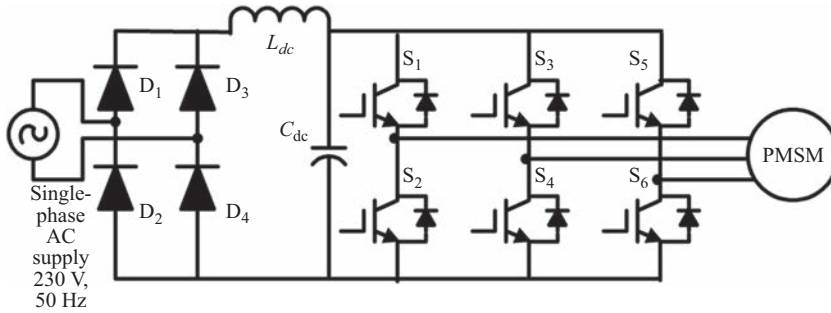


Figure 5.22 Power circuit diagram of single-phase rectifier and voltage source inverter feeding PMSM drive

The control circuit hardware consists of resolver demodulation circuit for sensing the rotor position, reference speed scaling circuits, sensed current scaling circuit using the Hall effect current sensors and gate driver circuit consisting of Semikron SKHI 22A driver. Each gate driver has an optical isolation in its initial stage to isolate the control circuit from the power circuit. Six gating signals obtained at the output of driver chips are applied between the gate and emitter of the IGBTs of VSI.

5.9.1 Development of signal conditioning circuits

The control circuit of the hardware implementation for the vector-controlled PMSM drive consists of the position sensing circuit and winding current sensing circuit. These circuits require respective signal conditioning circuits for proper scaling of the sensed position and current signals. These signal conditioning circuits for position sensing and winding current sensing are brought within the acceptable range of ± 2 V to feed the respective analog to digital converter (ADC) channels of the DSP. The reference speed signal is adjusted in the range of $+3{,}300$ to $-3{,}300$ rpm.

5.9.2 Development of power circuit of the drive

Figure 5.22 shows the diagram of the power circuit hardware of the drive system. This consists of a single-phase 230 V, 50 Hz ac supply, single-phase ac–dc diode bridge converter, dc-link LC filter, VSI and the PMSM. The VSI is fed from a diode bridge rectifier and an LC filter is used in the dc link, which filters the ripples in dc-link voltage. The VSI consists of the Semikron SKM 75 GB IGBTs. The thermal trip is provided in the VSI for the protection of the IGBTs devices. The switching pattern generated from the vector controller controls the ON/OFF time of the VSI switches.

5.10 DSP-based software implementation of vector-controlled PMSM drive

The control software consists of the reference speed input command, position sensing, speed estimation, speed controller, limiter, field-weakening controller, reference winding current generation and PWM current controller to produce switching signals

for vector-controlled VSI. The software used for implementation of vector-controlled PMSM drive is developed in assembly language of the analog devices DSP ADMC401. The main steps used in the control software modules are described in the following sub-section.

5.10.1 Reference speed input

The input voltage in the range of 0 to +2 V is applied to one of the ADC channel of the ADMC401. The corresponding digital value of the reference speed obtained from ADC channel is used in assembly language routine inside the DSP. The speed reversal command is applied through the digital input/output (I/O) port of the processor by inputting the +5 V command signal for the speed reversal. The algorithm checks if there is a speed reversal command given from the I/O port and, if so, then the reference speed is converted to the negative value for the motor motion in the reverse direction.

5.10.2 Sensing of rotor position signals

The sine and cosine amplitude modulated rotor position signals are obtained from the resolver unit fitted in the PMSM assembly. This resolver unit consists of one primary winding and two secondary windings both placed in the stator. The primary winding is excited by a high-frequency (5 V, 7 kHz) carrier signal, two secondary windings, which are placed in quadrature space to each other generate the Sin and Cos amplitude-modulated signals. The output of the resolver signal demodulation circuits is inputted to any two ADC channels of the DSP. These mechanical position signals are converted to corresponding electrical position signal by using the developed algorithm for resolver signals.

5.10.3 Speed sensing

The rotor position signals obtained from the resolver circuit are used for the calculation of the rotor speed of the PMSM. Two position signals are converted into speed signal by the algorithm used in the assembly language software of DSP.

5.10.4 Speed controller

The speed controller and limiter routines take the speed error between the reference speed and the estimated speed of the rotor and compute the reference torque. The maximum value of the reference torque is limited by the permissible winding currents of the motor. In this implementation of vector-controlled PMSM drive, all the four types of speed controllers are used in the drive. In the software corresponding assembly language, codes are developed for these speed controller routines.

5.10.5 Reference winding current generation

Three-phase reference winding current generation routine takes the digital value of *d*-axis stator current and *q*-axis stator current along with the digital value of Sin and Cos position signal of the rotor magnet as inputs and generates the three-phase

reference winding currents needed for the current controller routine as output. These reference currents ($i^*_{a(k)}$, $i^*_{b(k)}$, $i^*_{c(k)}$)which are compared with the sensed winding currents ($i_{a(k)}$, $i_{b(k)}$, $i_{c(k)}$) and the resulting errors are fed to the PWM current controller.

5.10.6 Switching signal generation for voltage source inverter

The generated three-phase reference currents and sensed three-phase currents from the PMSM winding are fed to the CC-PWM unit. The error between them is passed through the respective current controller unit and the limited output of the current controller unit is compared with a high-frequency (16 kHz) triangular carrier wave. If the error signal of corresponding phase is more than the carrier signal, then the switching signal for the upper switch of the same phase is turned on, otherwise, the lower switch of the same leg is turned on. Therefore, a total of six switching signals are generated, wherein two are meant for each leg of the three-phase VSI bridge, namely, leg "a", leg "b" and leg "c", respectively. Two paired complementary signals for respective legs are used for switching of the upper and the lower devices of the same leg of the VSI with proper dead band to avoid the shoot through fault in any of the VSI leg.

5.11 Testing of vector-controlled PMSM drive

The testing of the vector-controlled PMSM drive is carried out systematically. The drive consists of power circuit hardware and the control circuit consists of signal conditioning circuit for scaling of feedback current and position signals. After developing the complete drive system, the testing procedure is carried out for each part of the system and is described as follows:

5.11.1 Testing of control circuit

The control circuit of the drive consists of current feedback circuit, rotor position sensing circuit, the reference speed circuit and the gate driver circuit. The current and position feedback signals are tested for their defined range. The DSP is capable of receiving ± 2 V signals at its ADC channels. Therefore, all feedback signals are scaled by signal conditioning circuit so that the complete range of operation is covered with desirable accuracy in the predefined range.

The PMSM is run with the open loop voltage by frequency (V/F) control to test the current sensors for its calibration and accuracy. The converted digital current signals used for the DSP algorithm are converted back to the analog form with the help of digital-to-analog converters (DACs) and brought out on to a cathode ray oscilloscope (CRO), commonly known as oscilloscope, screen. Henceforth, the A to D and D to A conversions are checked by overlapping the sensed current signals from the Hall effect current sensors and current signals brought from the DSP DAC terminals. These two respective current signals must overlap each other on the CRO screen. The process verifies the A to D and D to A signal conversions.

The resolver demodulation circuit for obtaining the sinusoidal and cosinusoidal position signal of the rotor. The position signals obtained from the resolver demodulation circuit are scaled within ±2 V range and fed to the two ADC channels of DSP.

The gating signals obtained from the PWM unit of DSP are used for individual leg of the VSI. These gating signals are checked for complementary signal in each pair of the same leg with proper dead band. Three pairs of such PWM signals are checked to prove the correctness of the control circuit in all respect.

5.11.2 Testing of power circuit

The complete drive control system is connected, and the output of the VSI is connected across a three-phase star-connected resistive load. Reduced voltage (20%) is applied at the dc link of the inverter and the resistive load is tested from the open loop V/F control technique so that the equal amount of current flows in all three phases of resistive load. This test proves the correctness of the power circuit. The PMSM is now connected in place of the three-phase resistive load across the VSI. The vector-controlled PMSM drive is tested for its operation with a set reference speed. The closed-loop operation of the drive is tested for a set of reference speeds of the drive. The dc-link voltage is varied, but the rotor speed of the drive remains constant. Therefore, the correctness of the power circuit and closed-loop operation of the drive stand tested for varying the operating conditions of the drive system.

5.12 Results and discussion

The performance of the vector-controlled PMSM drive is simulated using the mathematical model in MATLAB environment along with Simulink and PSB toolboxes under different dynamic conditions, such as starting, speed reversal and load perturbation (load application and load removal). A set of response is obtained comprising reference speed, rotor speed in electrical rad/s and two of the three-phase winding currents in amperes. The VC algorithm is realized in discrete time domain with a sampling interval of 62.5 μs. The main system involving the vector-controlled VSI and the PMSM is taken as a discrete structure.

The simulated response of the VC PMSM drive is validated with test results obtained from the developed prototype of the vector-controlled PMSM drive system for a 1.93 kW, four-pole three-phase PMSM. Both the experimental and simulated responses of the drive system, with different speed controllers, are obtained under various operating conditions such as starting, speed reversal, load perturbation and steady-state conditions. Figures 5.23–5.35 depict these responses for the vector-controlled PMSM drive. While part (a) of the figure denotes the simulated results, the part (b) refers to experimental ones. The discussions on results for different operating conditions are made in the following sections.

5.12.1 Starting dynamics of vector-controlled PMSM drive

The PMSM is fed from the vector controller, which generates the controlled voltage and controlled frequency for the motor. The motor is started at a low frequency

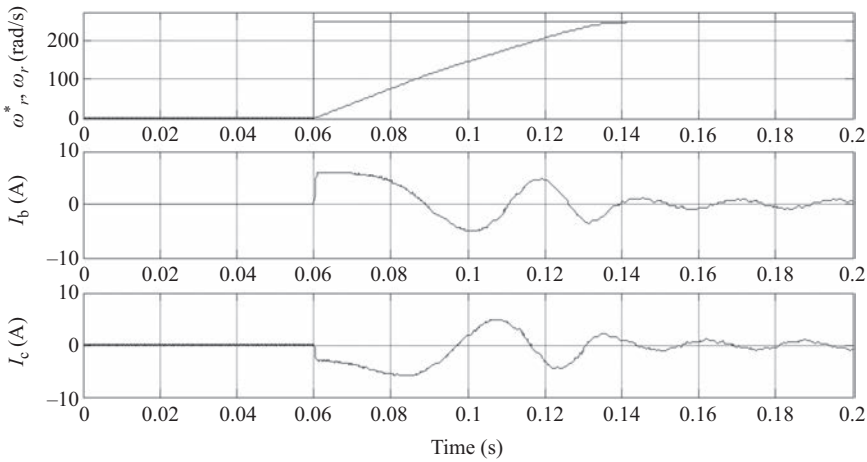


Figure 5.23 Simulated starting response of vector-controlled PMSM drive with PI speed controller at no load with reference speed of 251.32 rad/s (scale on X-axis 1 div = 20 ms, Y-axis channels 1 and 2, 1 div = 100 rad/s, on channels 3 and 4, 1 div = 10 A)

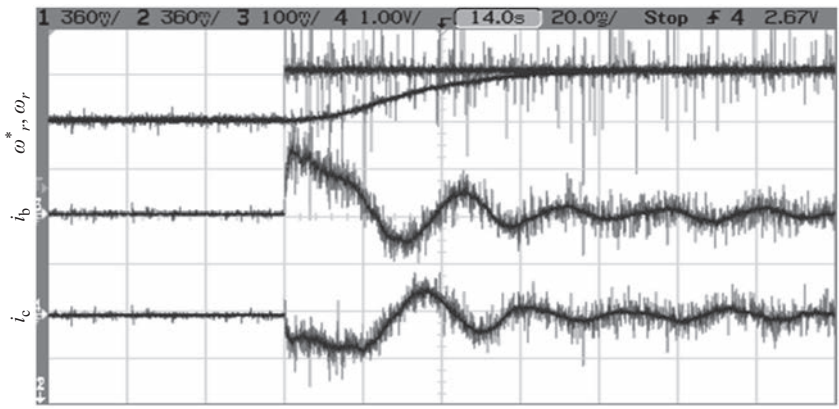


Figure 5.24 Experimental starting response of vector-controlled PMSM drive with PI speed controller at no load with reference speed of 251.32 rad/s (scale on X-axis 1 div = 20 ms, Y-axis channels 1 and 2, 1 div = 225 rad/s, on channels 3 and 4, 1 div = 5 A)

decided by the vector controller and finally the frequency is increased to run the motor in steady-state condition and to achieve the set reference value of speed. The starting time of the drive is defined as time needed for the drive to reach from standstill to 90% of reference speed. The reference speed is set to 251.32 electrical rad/s (1,200 rpm) with a torque limit set to one and half times of the rated value.

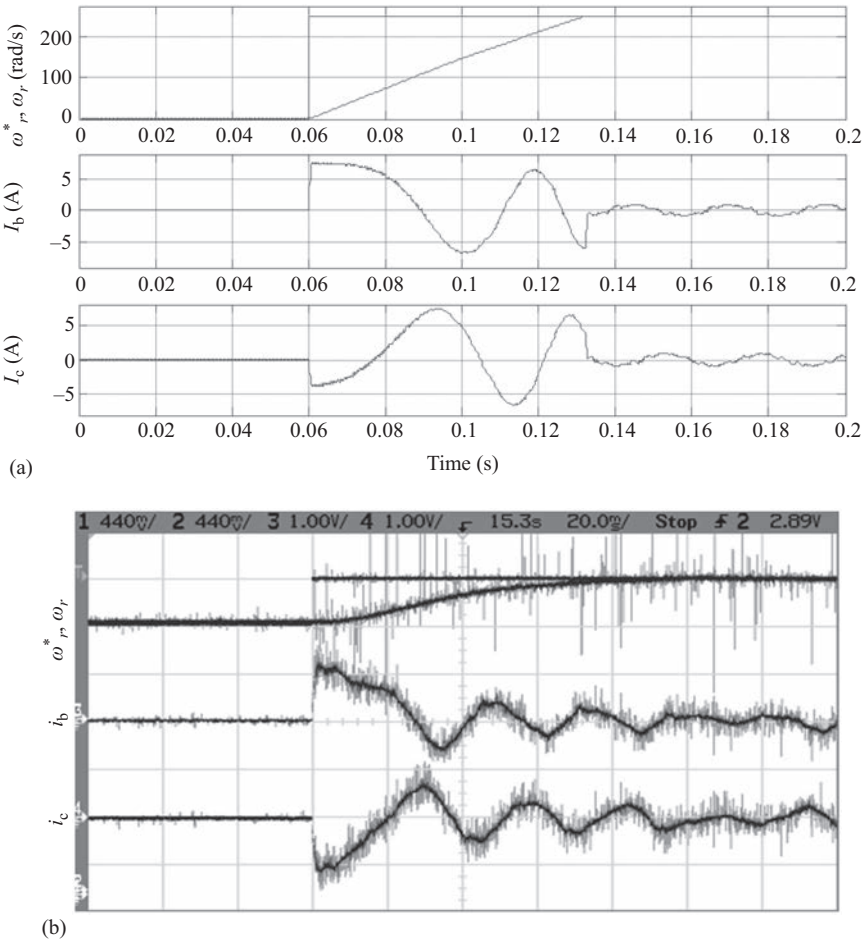


Figure 5.25 (a) Simulated starting response of vector-controlled PMSM drive for sliding mode speed controller at no load with reference speed of 251.32 rad/s (scale on X-axis 1 div = 20 ms, Y-axis channels 1 and 2, 1 div = 100 rad/s on channels 3 and 4, 1 div = 5 A); (b) experimental starting response of vector-controlled PMSM drive for sliding mode speed controller at no load with reference speed of 251.32 rad/s (scale on X-axis 1 div = 20 ms, Y-axis channels 1 and 2, 1 div = 250 rad/s on channels 3 and 4, 1 div = 5 A)

The starting current is inherently limited to one and half times of the rated current when the motor builds up the developed torque to reach the set reference speed. When the developed speed of the motor is almost equal to the reference speed, the winding currents get reduced to small values and the developed torque becomes equal to the load torque as observed in the starting response shown in

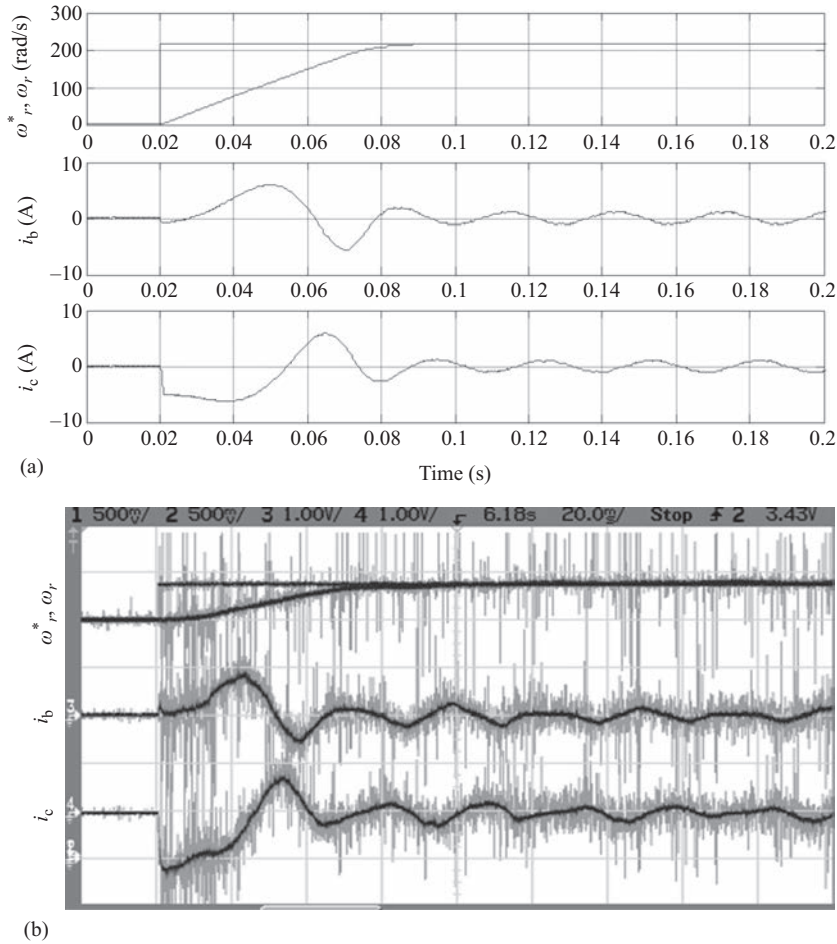


Figure 5.26 (a) Simulated starting response of vector-controlled PMSM drive for FPPI speed controller at no load with reference speed of 251.32 rad/s (scale on X-axis 1 div = 20 ms, Y-axis channels 1 and 2, 1 div = 100 rad/s, on channels 3 and 4, 1 div = 10 A); (b) experimental starting response of vector-controlled PMSM drive for fuzzy pre-compensated PI speed controller at no load with reference speed of 251.32 rad/s (scale on X-axis 1 div = 20 ms, Y-axis channels 1 and 2, 1 div = 325 rad/s, on channels 3 and 4, 1 div = 5 A)

Figures 5.24–5.27. Figure 5.24 shows both the experimental and simulated responses of the vector-controlled PMSM drive during starting with the PI controller in speed control loop. A step change in reference speed from 0 to 251.32 electrical rad/s (1,200 rpm) is applied at $t = 0.06$ s. The test results show that the motor attains the set speed of 1,200 rpm in 80 ms and it has close agreement with

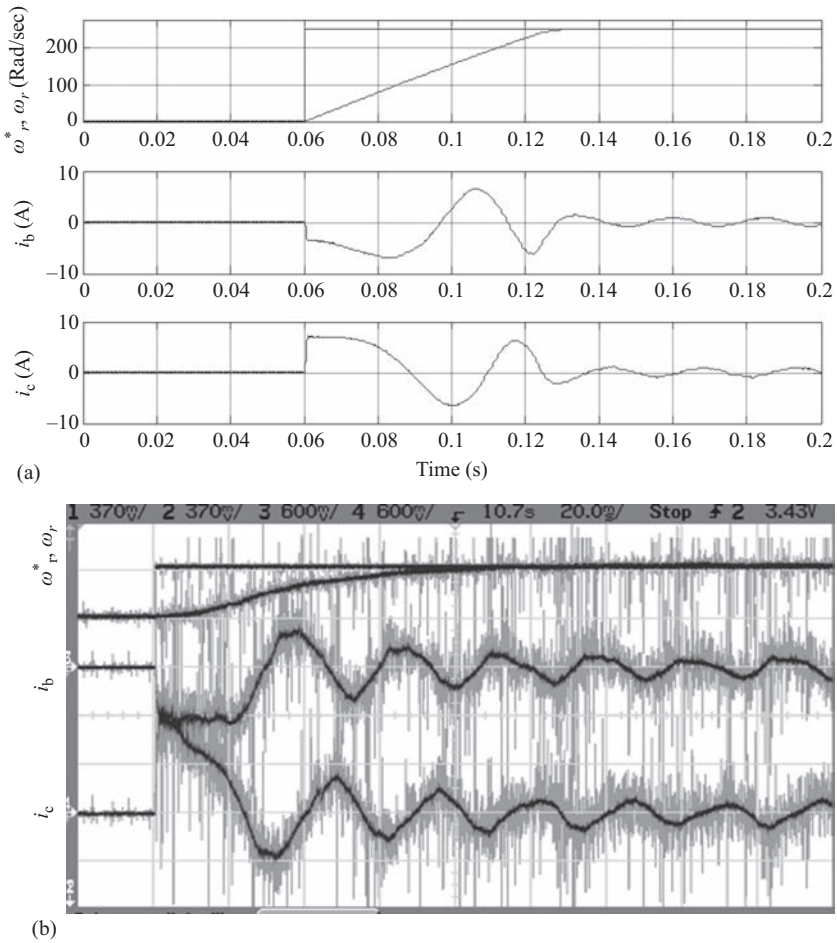


Figure 5.27 (a) Simulated starting response of vector-controlled PMSM drive for HFPI speed controller at no load with reference speed 251.32 rad/s (scale on X-axis 1 div = 10 ms, Y-axis channels 1 and 2, 1 div = 100 rad/s on channels 3 and 4, 1 div = 10 A); (b) experimental starting response of vector-controlled PMSM drive for HFPI speed controller at no load with reference speed of 251.32 rad/s (scale on X axis 1 div = 20 ms, Y-axis channels 1 and 2, 1 div = 225 rad/s on channels 3 and 4, 1 div = 3 A)

the simulated results of 78 ms for the starting of the drive for the same reference speed. The motor winding currents are found to increase to a high value at the time of starting decided by the torque limiter, which reduces to a small value under steady-state operating condition because the motor is running at no-load.

Figure 5.25 depicts the starting response of the vector-controlled PMSM drive with SMC speed controller. The reference speed is maintained at 251.32 electrical

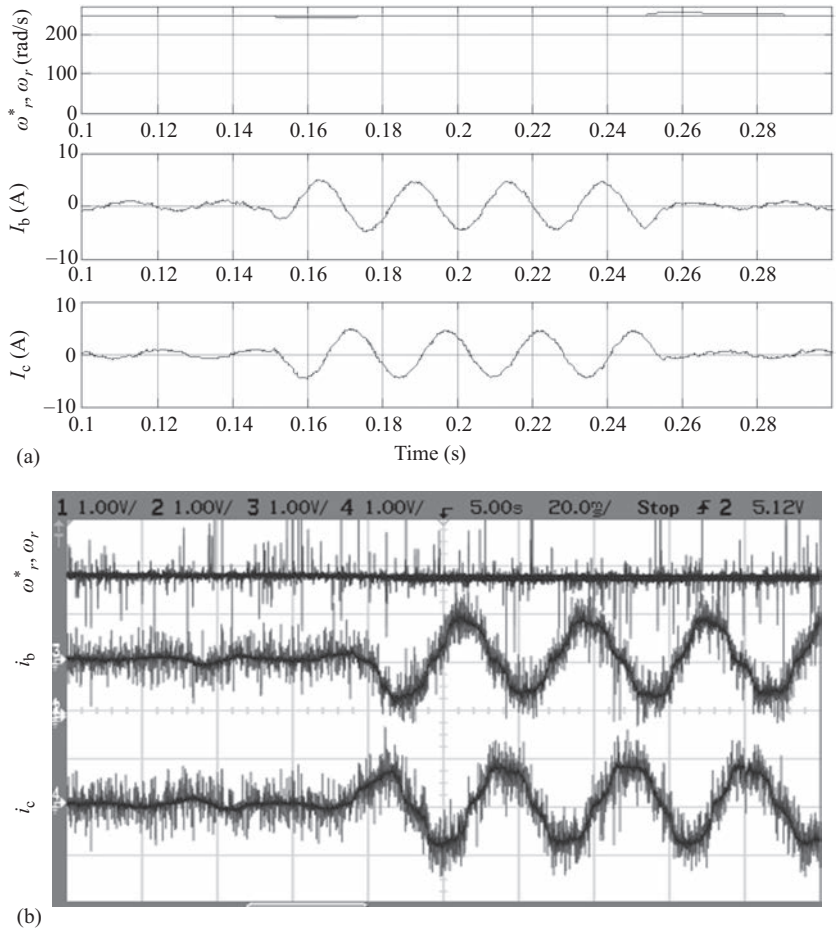
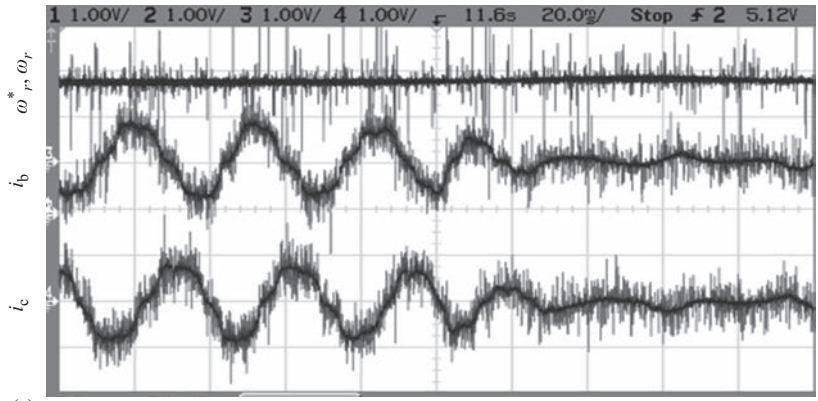


Figure 5.28 *(a) Simulated load perturbation response of vector-controlled PMSM drive with PI speed controller running at 251.32 rad/s load perturbation from no load to 2.5 N m to no load (scale on X-axis 1 div = 20 ms, Y-axis channels 1 and 2, 1 div = 100 rad/s, on channels 3 and 4, 1 div = 10 A); (b) experimental load application response of vector-controlled PMSM drive with PI speed controller running at 251.32 rad/s (scale on X-axis 1 div = 20 ms, Y-axis channels 1 and 2, 1 div = 200 rad/s, on channels 3 and 4, 1 div = 5 A); (c) experimental load removal response of vector-controlled PMSM drive with PI speed controller running at 251.32 rad/s (scale on X-axis 1 div = 20 ms, Y-axis channels 1 and 2, 1 div = 200 rad/s, on channels 3 and 4, 1 div = 5 A)*



(c)

Figure 5.28 (*Continued*)

rad/s for comparison of PMSM drive performance with different speed controllers. It is observed that in this case, the test results give the starting time of 75 ms, while the simulated result shows that a starting time of 72 ms is needed for the drive.

With FPPI speed controller, the performance of the vector-controlled PMSM drive is shown in Figure 5.26. It is observed from this figure that stating time required for the drive in test results is 70 ms, whereas it is 68 ms in simulation case.

The performance of HFPI speed controller for the VC PMSM drive is shown in Figure 5.27. It is observed from these results that the hybrid controller needs a starting time of 65 ms in test results and 62 ms in simulation results.

To facilitate comparison between the effectiveness of these controllers, the results pertaining to the starting time are given in Table 5.2. From these results, it is clear that the system needs least starting time with HFPI controller, and there is a close agreement between experimental and simulated results in each case.

5.12.2 Load perturbation performance of vector-controlled PMSM drive

The load perturbation response of the vector-controlled PMSM drive is shown in Figures 5.28–5.31. The motor is running at a steady-state speed of 251.32 electrical rad/s when suddenly a load torque equal to 2.5 N m (45.45% of rated torque) is applied on the motor shaft. Sudden application of the load causes an instantaneous fall in the speed of the motor. In response to the drop in speed, the output of the speed controller responds by increasing the value of reference torque. In response to this, the electromagnetic torque developed by the PMSM increases to quickly recover the loss in the motor speed and bring it to the reference value with the corresponding increase in winding currents. The load perturbation response of PMSM drive system is studied for the case of all four types of speed controllers viz., PI, SMC, FPPI and HFPI speed controllers and is analyzed separately for the load application and load removal.

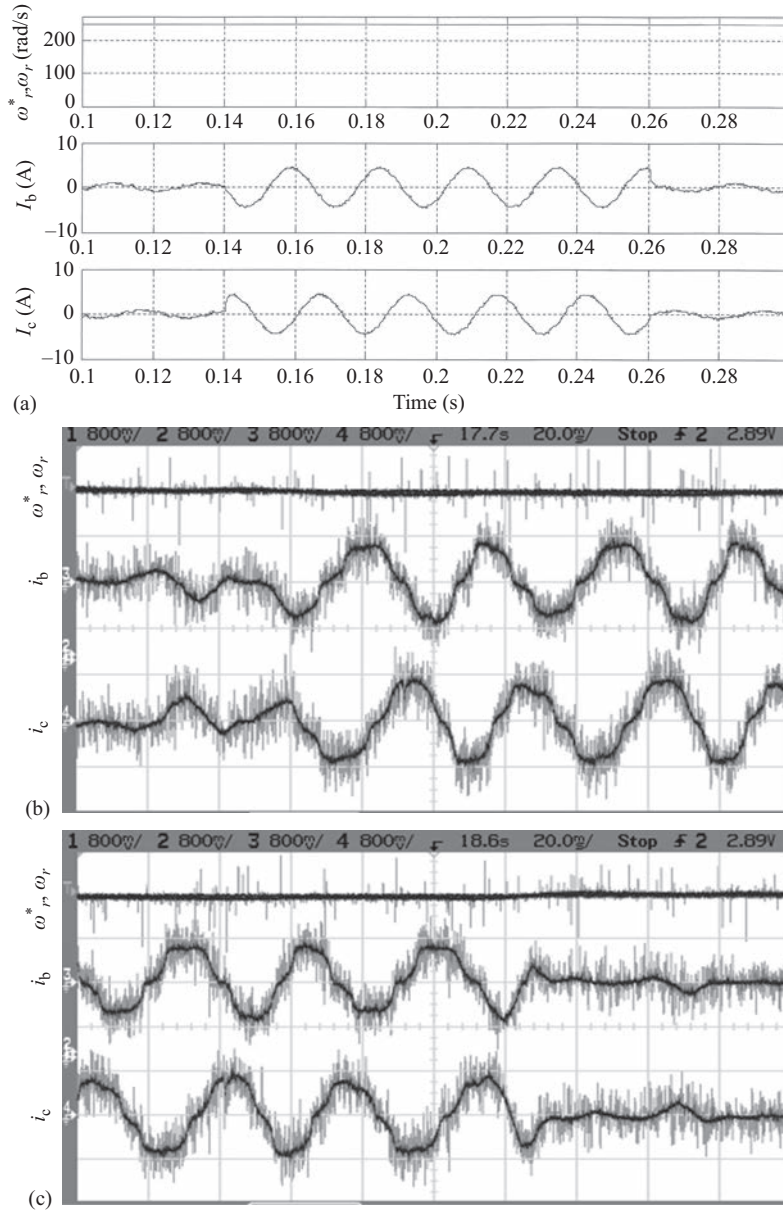


Figure 5.29 (a) Simulated load perturbation response of vector-controlled PMSM drive for sliding mode speed controller running at 251.32 rad/s, load perturbation from no load to 2.5 N m to no load (scale on X-axis 1 div = 200 rad/s on channels 3 and 4, 1 div = 10 A); (b) experimental load application response of vector-controlled PMSM drive for sliding mode speed controller running at 251.32 rad/s (scale on X-axis 1 div = 20 ms, Y-axis channels 1 and 2, 1 div = 300 rad/s, on channels 3 and 4, div = 4 A); (c) experimental load removal response of vector-controlled PMSM drive for sliding mode speed controller running at 251.32 rad/s (scale on X-axis 1 div = 20 ms, Y-axis channels 1 and 2, 1 div = 300 rad/s on channels 3 and 4, 1 div = 4 A)

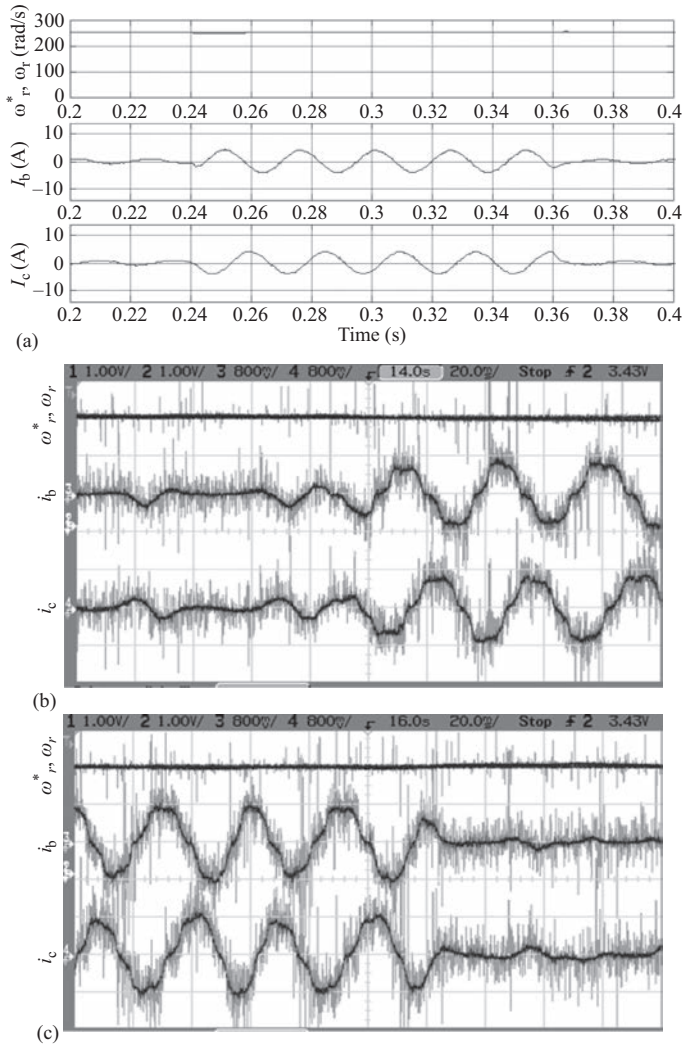


Figure 5.30 (a) Simulated load perturbation response of vector-controlled PMSM drive for fuzzy pre-compensated PI speed controller running at 251.32 rad/s load perturbation from no load to 2.5 N m to no load (scale on X-axis 1 div = 20 ms, Y-axis channels 1 and 2, 1 div = 100 rad/s, on channel); (b) experimental load application response of vector-controlled PMSM drive for fuzzy pre-compensated PI speed controller running at 251.32 rad/s (scale on X-axis 1 div = 20 ms, Y-axis channels 1 and 2, 1 div = 200 rad/s, on channels 3 and 4, 1 div = 4 A); (c) experimental load removal response of vector-controlled PMSM drive for fuzzy pre-compensated PI speed controller running at 251.32 rad/s (scale on X-axis 1 div = 20 ms, Y-axis channels 1 and 2, 1 div = 200 rad/s, on channels 3 and 4, 1 div = 4 A)

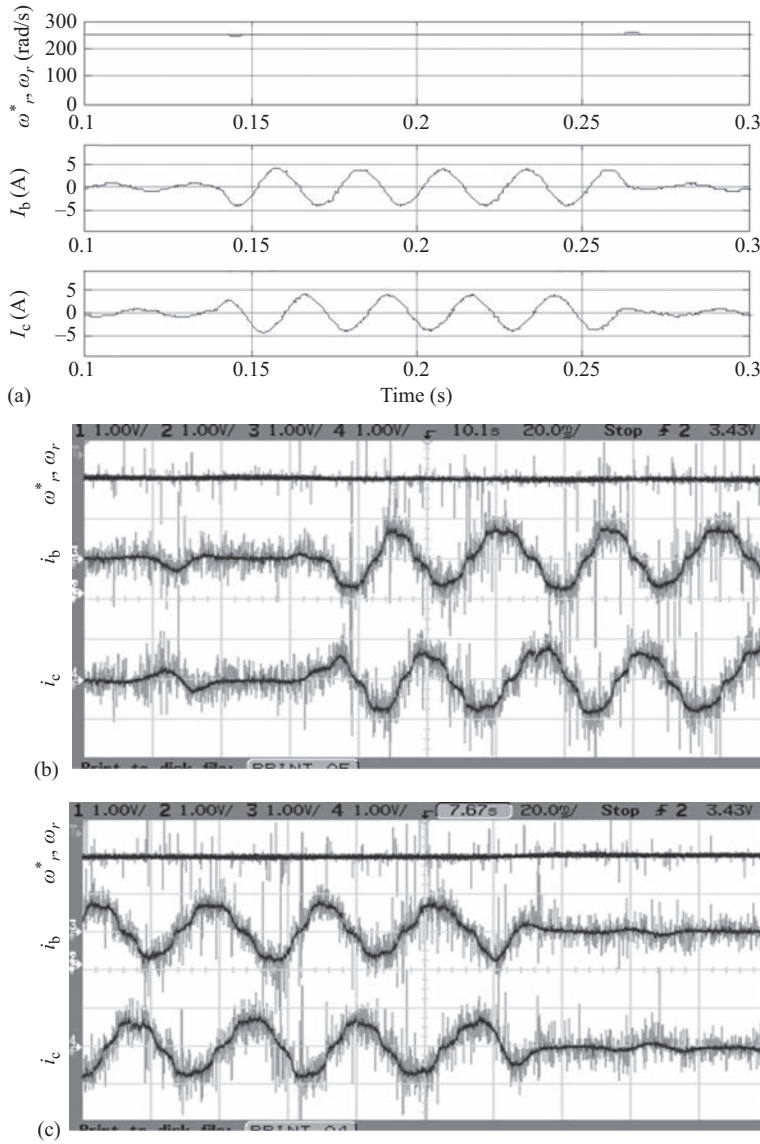


Figure 5.31 (a) Simulated load perturbation response of vector-controlled PMSM drive for HFPI speed controller from no load to 2.5 N m to no load with reference speed 251.32 rad/s (scale on X-axis 1 div = 20 ms, Y-axis channels 1 and 2, 1 div = 100 rad/s on channels 3 and 4, 1 div = 5 A); (b) experimental load application response of vector-controlled PMSM drive for HFPI speed controller with reference speed of 251.32 rad/s from no load to 2.5 N m load (scale on X-axis 1 div = 20 ms, Y-axis channels 1 and 2, 1 div = 600 rad/s on channels 3 and 4, 1 div = 5 A); (c) experimental load removal response of vector-controlled PMSM drive for HFPI speed controller with reference speed of 251.32 rad/s from 2.5 N m load to no load (scale on X-axis 1 div = 20 ms, Y-axis channels 1 and 2, 1 div = 600 rad/s on channels 3 and 4, 1 div = 5 A)

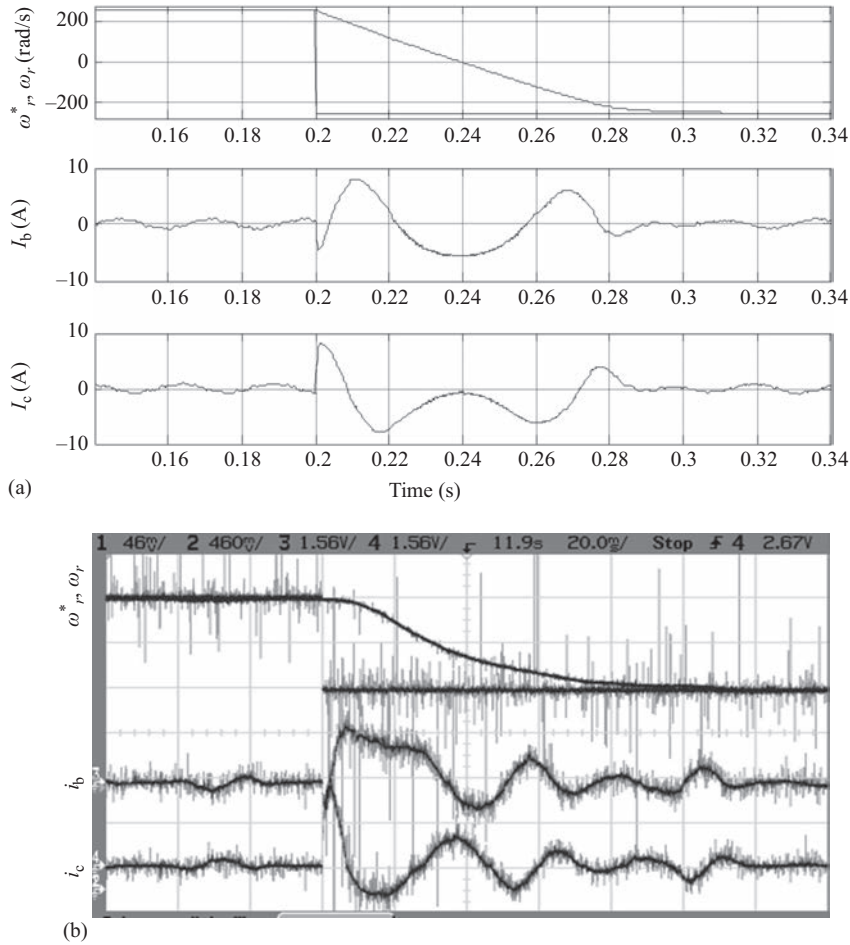


Figure 5.32 (a) Simulated speed reversal response of vector-controlled PMSM drive with PI speed controller at no load with reference speed from +251.32 to −251.32 rad/s (scale on X-axis 1 div = 20 ms, Y-axis channels 1 and 2, 1 div = 200 rad/s, on channels 3 and 4, 1 div = 10 A); (b) experimental speed reversal response of vector-controlled PMSM drive with PI speed controller at no load with reference speed from +251.32 to −251.32 rad/s (scale on X-axis 1 div = 20 ms, Y-axis channels 1 and 2, 1 div = 250 rad/s, on channels 3 and 4, 1 div = 7.8 A)

In Figure 5.28, load application response of the PMSM drive is shown with PI speed controller. The winding currents are found to increase as the load on the motor shaft is applied and a momentary dip of small magnitude is observed in the rotor speed, which is recovered in a very small time.

Similarly, Figures 5.29–5.31 show the load application response with the SMC, FPPI and HFPI speed controllers. On comparing these results, it is seen that

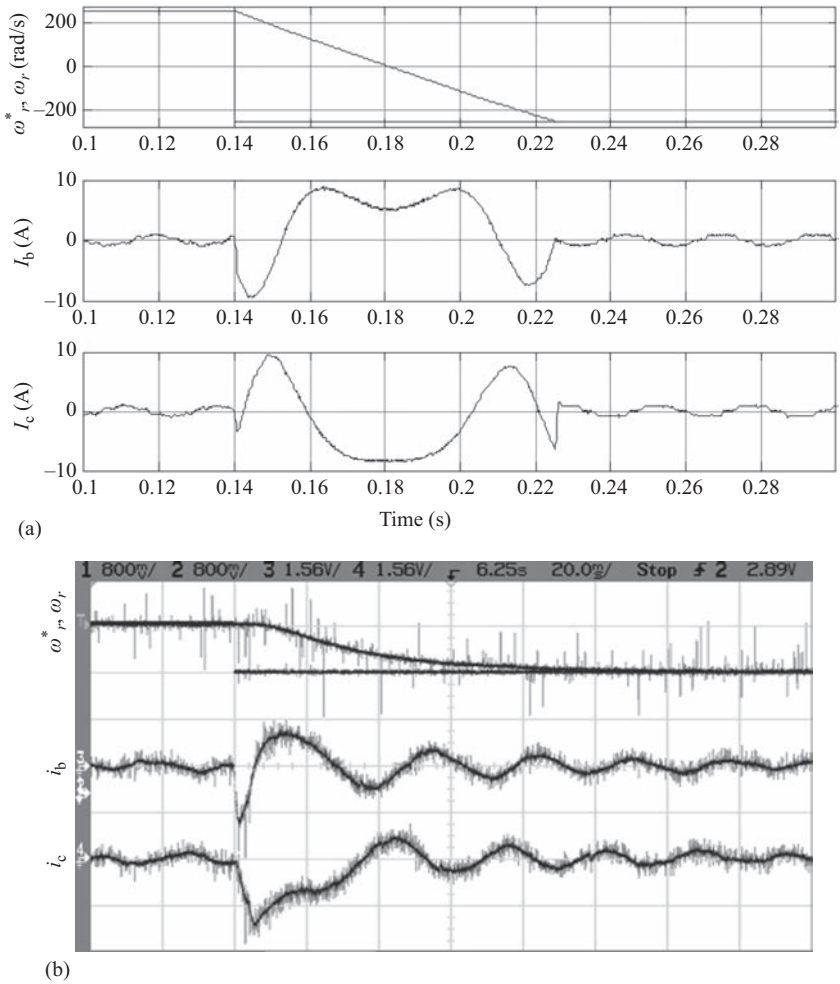
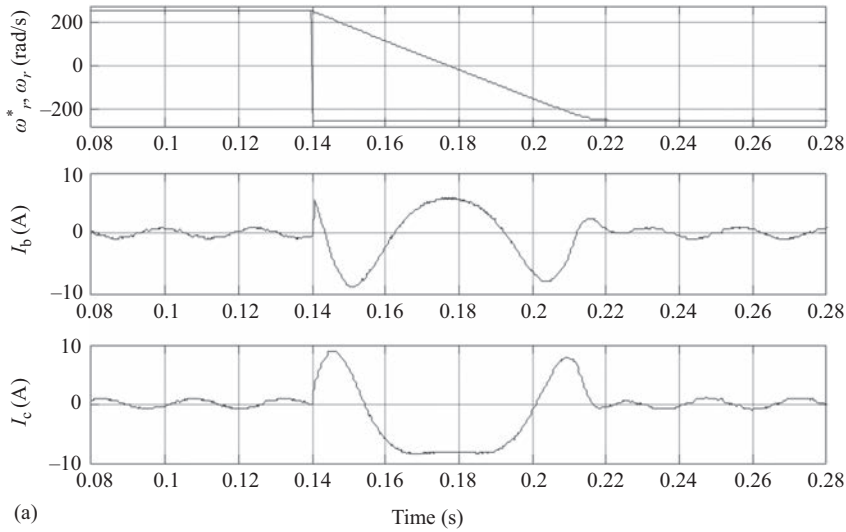


Figure 5.33 (a) Simulated speed reversal response of vector-controlled PMSM drive for sliding mode speed controller at no load with reference speed from 251.32 to −251.32 rad/s (scale on X-axis 1 div = 20 ms, Y-axis channels 1 and 2, 1 div = 200 rad/s on channels 3 and 4, 1 div = 10 A); (b) experimental speed reversal response of vector-controlled PMSM drive for sliding mode speed controller at no load with reference speed from 251.32 to −251.32 rad/s (scale on X-axis 1 div = 20 ms, Y-axis channels 1 and 2, 1 div = 500 rad/s on channels 3 and 4, 1 div = 7.8 A)

the response of the HFPI speed controller is least affected by the application of sudden load.

For studying the load removal response, the PMSM is run at 251.32 electrical rad/s (1,200 rpm) with a load of 2.5 N m, and this load is suddenly removed from the



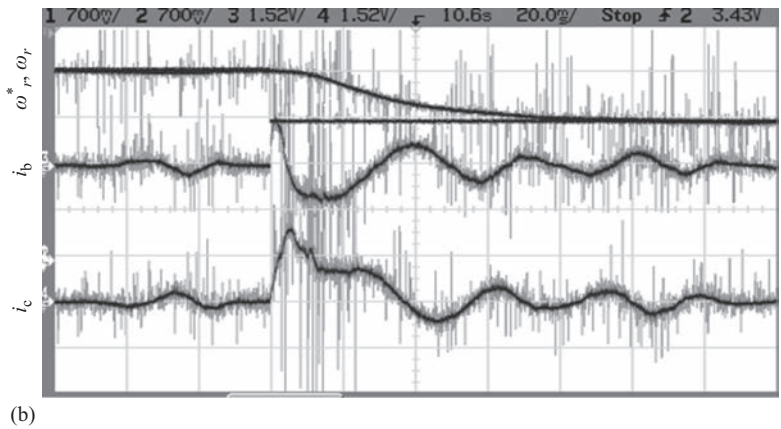


Figure 5.34 *(a) Simulated speed reversal response of vector-controlled PMSM drive for fuzzy pre-compensated PI speed controller at no load with reference speed from +251.32 to −251.32 rad/s (scale on X-axis 1 div = 20 ms, Y-axis channels 1 and 2, 1 div = 200 rad/s, on channels 3 and 4, 1 div = 10 A); (b) experimental speed reversal response of vector-controlled PMSM drive for fuzzy pre-compensated PI speed controller at no load with reference speed from +251.32 to −251.32 rad/s (scale on X-axis 1 div = 20 ms, Y-axis channels 1 and 2, 1 div = 400 rad/s, on channels 3 and 4, 1 div = 7.6 A)*

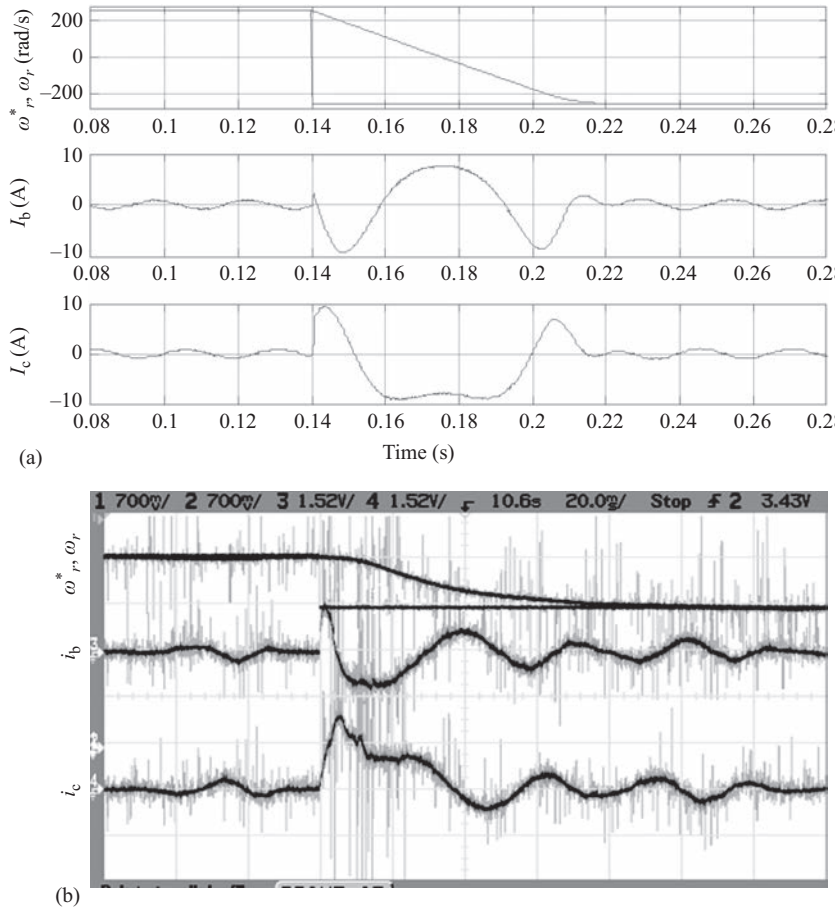


Figure 5.35 (a) Simulated starting response of vector-controlled PMSM drive for HFPI speed controller at no load with reference speed 251.32 rad/s (scale on X-axis 1 div = 10 ms, Y-axis channels 1 and 2, 1 div = 200 rad/s on channels 3 and 4, 1 div = 10 A); (b) experimental speed reversal response of vector-controlled PMSM drive for HFPI speed controller at no load with reference speed from 251.32 to −251.32 rad/s (scale on X-axis 1 div = 20 ms, Y-axis channels 1 and 2, 1 div = 425 rad/s, on channels 3 and 4, 1 div = 7.6 A)

motor shaft. The simulated and experimental responses for this case with all four types of speed controllers are obtained and shown in the same set of Figures 5.28–5.31. The HFPI speed controller is found to be the most suitable for maintaining the constant speed of PMSM and giving a good load removal response too. In all cases, the good correlation between simulated and test results is observed.

Table 5.2 Starting time for different types of speed controllers

Sr. no.	Type of speed controller	Starting time in ms	
		Simulated	Experimental
1	PI	78	80
2	SMC	72	75
3	FPPI	68	70
4	HFPI	62	65

Table 5.3 Reversal time for different types of speed controllers

Sr. no.	Name of speed controller	Reversal time in ms	
		Simulated	Experimental
1	PI	88	90
2	SMC	82	85
3	FPPI	77	80
4	HFPI	74	78

5.12.3 Speed reversal dynamics of vector-controlled PMSM drive

The speed reversal dynamics of the vector-controlled PMSM drive is observed for the sudden change of reference speed from +251.32 electrical rad/s (+1,200 rpm) to −251.32 electrical rad/s (−1,200 rpm) with all four different types of speed controllers. For the motor running previously at +251.32 electrical rad/s speed in forward direction, the reference speed command is suddenly changed to −251.32 electrical rad/s. The reversal time of the motor is measured between the instant of application of speed reversal command and the instant when the motor attained 95% of the speed in the set direction (reversed).

The drive speed reversal response with PI speed controller is shown in Figure 5.32. It is observed from this response that motor winding currents are increased to the maximum allowable value during the speed reversal time span and as soon as motor speed reaches the reference speed, the winding currents are settled to its normal value governed by the load on the motor shaft. Both the experimental and simulation results are shown in Figure 5.32 for the PMSM drive with PI controller in the speed loop.

The response of drive with SMC, FPPI and HFPI speed controllers for the speed reversal case is shown in Figures 5.33–5.35, respectively. The speed reversal time for different speed controllers is compared in Table 5.3. The reversal time for the PI speed controller and SMC speed controller is 90 and 85 ms, respectively, whereas the reversal time for FPPI speed controller is 80 ms and it further reduces to 78 ms with the HFPI speed controller.

A comparison of results confirms the earlier trend of response of drive with HFPI controller taking least time for reversal and of close agreement between simulated and test results in all cases.

5.12.4 Comparative study among different speed controllers

In the previous sections, simulated and experimental results of the vector-controlled PMSM drive for different operating conditions are given for four different types of speed controllers. Careful comparison of the performance of PMSM with different speed controllers reveals that HFPI speed controller results in giving the best response in terms of starting and speed reversal time. This particular controller combines the advantages of FL controller and conventional PI speed controller. The sliding mode controller, on the other hand, reflects the chattering problem. For the DSP-based implementation of these controllers, the fuzzy-based speed controllers need complex and long algorithms whereas PI and SMC speed controllers need simple and less lengthy code for their implementation.

5.13 Sensor reduction in vector-controlled permanent magnet synchronous motor drive

The method of analysis for both experiment and simulation developed earlier is now put to use by extending its use to include sensorless control of the PMSM drive. This chapter deals with the mechanical sensorless operation of the vector-controlled PMSM drive. It may be realized that a reduction in the sensor requirement of PMSM drive not only helps in giving greater reliability to the drive system but it also reduces the overall cost of the system. The vector-controlled PMSM drive system needs sensor for position/speed and current. The mechanical speed sensor has the disadvantages of increased cost, reduced reliability and is susceptible to noise. Estimation techniques for position/speed are required for the elimination of mechanical sensors in PMSM drives. The winding currents of PMSM are sensed using the Hall current sensors and for elimination/reduction of these electrical sensors, methods of estimation of motor winding current are needed which can help in reducing/eliminating with reduced/without current sensors. Similarly, for the elimination of voltage sensor, which is required for the sensing of PMSM stator winding applied voltages, methods are required to reconstruct the voltage waveforms with reduced/without using voltage sensors.

With these objectives in view, an attempt is made to develop a simple and robust technique to estimate the rotor speed using the sensed currents in two phases of PMSM and the dc-link voltage.

5.13.1 Sensor requirements in vector-controlled PMSM drive system

The vector-controlled PMSM drive requires feedback signal for its control algorithm, which includes the position of the rotor magnet, speed of the rotor and winding currents of PMSM. For providing feedback of these signals to the drive, the use of position/speed sensors and current sensors is needed in a drive system.

These sensors, both mechanical and electrical, add to the cost and complexity of the drive. In addition, they also suffer from the effect of drift, noise, nonlinearity and aging. It is, therefore, considered desirable to reduce/eliminate some of these sensors from the drive system so that cost and complexity of drive are reduced without compromising on the level of performance. For this purpose, the existing techniques of sensor reduction need to be examined with a view to identifying suitable technique for the given application.

5.13.2 Review of mechanical sensor reduction techniques in PMSM drive

The mechanical sensors used for speed/position feedback increase the drive system inertia, which is undesirable in high-performance drives. They also increase the maintenance requirement and have difficulties of mounting in very small motors and also in low power drive, the cost of such sensors is comparable to other costs. Moreover, in drives operating in hostile environments, or in the high-speed drives, speed sensors cannot be mounted.

Availability of high computing facility of DSP at reasonable cost has paved the way for the estimation of position and speed by using the software algorithm of state estimation techniques where observation of applied stator voltages and winding currents is required. Some of the available techniques for estimating the position and speed of the PMSMs include [13–15] the following:

1. Back emf-based position estimation technique.
2. Monitoring applied stator voltages and resulting winding current-based estimation technique.
3. Observer-based sensorless estimation of position and speed.
4. High-frequency carrier signal injection method for estimation of position and speed.
5. Stochastic filtering-based sensorless estimation of position and speed.
6. Current and voltage model-based sensorless algorithms.
7. Artificial intelligence (AI)-based position and speed estimators.

The basic features of these techniques are given as follows:

5.13.2.1 Back emf-based position estimation technique

The principle of this method is to compute the back emf vector in order to determine the rotor position angle and find from this the velocity of rotor. It can be seen that the PM flux vector of the rotor is aligned with the *d*-axis and, therefore, the back emf vector is aligned with the *q*-axis and together they indicate the rotor position angle θ_r.

5.13.2.2 Stator voltages and winding current-based techniques

In this method, the stator voltages and currents are sensed and by subtracting the ohmic drop from the terminal voltage, the induced back emf is calculated. The stator flux is obtained by simple integration of this back emf. However, this method suffers from integration drift and dc offset that lead to an offset in flux waveform

and consequently, it gives an incorrect value of motor speed. Special techniques are, therefore, required to compensate for the offset error of this method.

5.13.2.3 Observer-based sensorless estimation of position and speed

The observer-based position and speed estimation techniques are used to increase the overall ruggedness of the drive. This scheme is sensitive to the parameter of the plant and also to the external disturbance, such as load torque. The stability of this technique can be improved by proper choice of the location of the observer pole. The speed and position information can also be obtained from the reduced order observers. This allows both the simplification of the system and the reduction of the computational burden in implementation.

5.13.2.4 High-frequency carrier signal injection method for estimation of position and speed

In this method, a carrier signal is superimposed on the fundamental excitation to track the spatial saliency images to provide sensorless control of the PMSM drive down to very low or zero speed. When a rotor position or saturation-dependent variation in the stator transient inductance exists, its shape can be tracked by injecting a high-frequency carrier signal voltage. The resulting carrier signal current consists of a positive sequence component that contains no spatial information and a negative sequence component that contains the desired spatial saliency position information in its phase. The position information is extracted from the negative sequence component by a suitable decoder circuit and in this way, the mechanical position and speed sensors are totally eliminated. The advantage of this method lies in the fact that this method works satisfactorily even at zero speed.

5.13.2.5 Stochastic filtering-based sensorless estimation of position and speed

In the model-based adaptive system, linearization of the nonlinear equations describing the drive behavior along the nominal state trajectory does not guarantee the overall stability. Carrier signal injection-based method for sensorless estimation of position/speed works only if PMSM has anisotropic property. Extended Kalman filter (EKF) is a stochastic filter-based approach which performs the state estimation for nonlinear system and it can overcome the shortcoming of observer based and carrier signal injection methods. The EKF method is gaining wide application in position and speed estimation of ac drives including PMSM drive.

5.13.2.6 Current and voltage model-based sensorless algorithms

In the current and voltage model-based control for sensorless position and speed estimation of PMSM drive, two approaches are used. The basis of the proposed sensorless control algorithm is to use the difference between the sensed state variable and the estimated state variables, which are calculated from an equivalent motor model in the controller. The different approach is adopted depending upon the type of the motor

model, namely, voltage model and the current model. In the current and voltage model-based sensorless control methods, the initial rotor position detection in PMSM is difficult which can lead to a temporary reverse rotation or starting failure. Separate starting procedure is needed in this type of sensorless control approach of PMSM drive.

5.13.2.7 Artificial intelligence-based position and speed estimators

Intelligent sensorless control of PMSM drive is based on AI. The various AI-based methods used for estimation of position and speed of PMSM are based on expert system, FL, genetic algorithm and artificial neural network approach. This system is dependent on the exact model of the plant, which often works on the ill-defined model. For a nonlinear complex multivariable and parameter varying problem, the AI-based system can identify the model and predict the performance even with the variation in the parameter over a wide range.

The advantages and shortcomings of these methods of sensorless operation of the PMSM drive are summarized and given in Table 5.4.

Table 5.4 Comparison of sensorless position and speed estimation techniques of PMSM [11,13–15]

Sr. no.	Position and speed estimation method	Advantages	Shortcoming
1.	Back-emf-based technique	Simpler in real-time implementation	Initial rotor position is not detectable, error in the estimation at low speed
2.	Monitoring applied stator voltages and resulting winding currents technique	Good steady state response, fast response in transients	Sensitive to parameter variations, initial rotor position is not detectable
3.	Observer-based techniques	Possibility to estimate five unknown states of PMSM	Initial rotor position is not detectable
4.	High-frequency carrier signal injection techniques	Work satisfactory even at zero speed of the drive	Separate high-frequency source and signal conditioning circuit is needed, works only if PMSM has anisotropic property
5.	Stochastic-filtering-based techniques	Perform in better results even nonlinearities are present in system	Large computation is required, fast processors are required for real-time implementation
6.	Current and voltage-model-based techniques	Work satisfactory even if error in assumed initial position of rotor	Heavy computation is required, sensitive to parameter variations,
7.	Artificial-intelligence-based techniques	Work with ill-defined model, nonlinear and parameter varying system	Most demanding in computation, Very fast processors required for real-time implementation

5.13.3 Electrical sensor reduction in PMSM drive

Electrical sensors are used in the PMSM drive to measure the electrical quantities which include stator winding currents and applied voltage to stator winding. Drive complexity can be reduced as well as robustness of the drive is increased by reduction/elimination of these electrical sensors. Sensor reduction offers saving the overall cost of the drive. Voltage and current sensor reduction leads to greater reliability of drive. Increased computation burden can be met by DSPs or microcontrollers and software algorithms, which do not contribute toward increase of the overall cost. The electrical sensor reduction/elimination also results in increased noise immunity of the drive. The estimation technique for reducing/eliminating current and voltage sensors includes reconstruction of the three-phase winding currents and stator winding applied voltages by the use of dc-link current and dc-link voltage, along with the switching sequence applied to power semiconductor devices. In this work, the stator winding applied voltages are reconstructed by using the single voltage sensor at the dc-link terminal of the VSI and the applied switching pulse sequence to the inverter legs.

5.14 Sensorless vector-controlled PMSM drive

The schematic diagram of the sensorless vector-controlled PMSM drive system is shown in Figure 5.36. In this drive, a VC method is used to control the speed of PMSM. The estimated rotor speed (ω_{est}) is compared with the reference speed (ω_r^*). The error in speed (ω_e) is processed in the PI speed controller, which generates the reference torque (T^*). This reference torque is limited using a limiter and the limited reference torque (T_{ref}^*) is used to generate the q-axis component of reference current. The d-axis reference current is decided on the basis of rotor speed of the drive. If the rotor speed is above base speed, then field-weakening control decides the d-axis component of reference current, otherwise, if the rotor speed is less than the base speed, than the d-axis component of the reference current is considered zero. The rotor reference frame component of current is transformed in stationary reference frame using inverse Park's transformation. The reference winding currents are

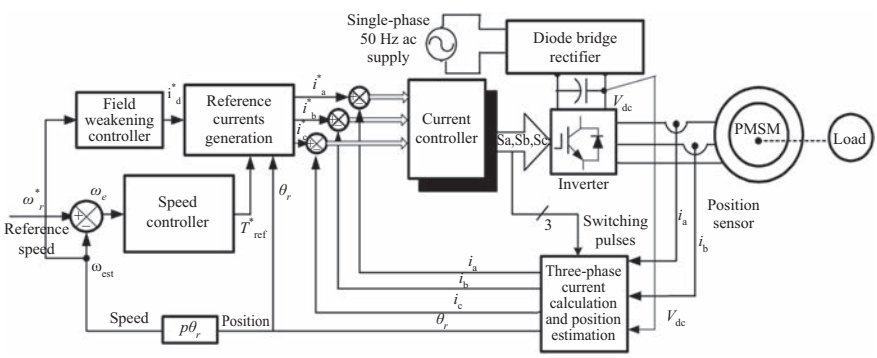


Figure 5.36 Block diagram of sensorless vector-controlled PMSM drive

compared with sensed winding currents of the motor and error is fed to the current controller unit for generation of switching signals of the CC-PWM VSI. The CC-PWM VSI controls the winding currents of PMSM in desired manner by switching on and off of appropriated IGBT in the bridge. For the mechanical sensorless VC of PMSM drive, the position and speed of the rotor are estimated from the applied stator voltages and sensed winding current of the motor. The estimator block estimates stator flux linkages in stationary reference frame, Sin and Cos position of rotor magnet and speed of the rotor of PMSM. The inputs to the estimator are the dc-link voltage, two phase currents of the stator winding of PMSM and switching status of the VSI obtained by CC-PWM unit of the drive. The phase voltages of the PMSM are obtained from the switching status of VSI and dc-link voltage.

The modeling of sensorless VC drive is similar to VC PMSM drive as given in previous section for the mathematical model of reference current generator, model of PMSM, model of VSI and model of CC-PWM unit. In the sensorless vector-controlled PMSM drive, the position and speed are estimated from the stator flux signals which are obtained from the integration and filtering of back emf signals of the drive. The mathematical equations for back emf, fluxes, position and speed estimator are given in the following subsections.

5.14.1 Stator voltage estimation

The three-phase voltage applied to the stator winding of the PMSM is estimated with a single voltage sensor connected to the dc link of the VSI. The instantaneous value of the stator voltage can be reconstructed from the sensed dc-link voltage and the switching sequence of inverter legs. The stator voltage is estimated in the stationary reference frame from the mathematical relation as

$$v_\alpha = \left(\frac{v_{\mathrm{dc}}}{3}\right)(2\mathrm{S_a} - \mathrm{S_b} - \mathrm{S_c}) \tag{5.39}$$

$$v_\beta = \left(\frac{v_{\mathrm{dc}}}{\sqrt{3}}\right)(\mathrm{S_b} - \mathrm{S_c}) \tag{5.40}$$

where v_{dc} is voltage of the dc link of inverter, S_{a} is switching function of leg of phase "a", S_{b} is switching function of leg of phase "b" and S_{c} is switching function of leg of phase "c".

5.14.2 Winding current estimation

The PMSM winding currents in stationary reference frame can be computed by sensing any of two phase currents out of three phases of the motor winding. The third phase current is derived from these two phase currents by considering the fact that stator winding is isolated star connected and there are balanced currents in the PMSM. The third phase current can be estimated from the application of Kirchhoff's law. The stationary reference frame current can be expressed as

$$i_\alpha = (-i_{\mathrm{b}} - i_{\mathrm{c}}) \tag{5.41}$$

$$i_\beta = \left(\frac{1}{\sqrt{3}}\right)(i_{\mathrm{b}} - i_{\mathrm{c}}) \tag{5.42}$$

where i_α is α-axis winding current of the motor in stationary reference frame and i_β is the β-axis winding current of the motor in stationary reference frame.

5.14.3 Flux estimation

The flux linkage in the stationary reference frame can be obtained by using the sensed winding currents (i_a and i_b), and stator voltage (v_a and v_b) which are computed from the sensed dc-link voltage (v_{dc}) and switching functions (S_a, S_b and S_c) as per the (5.39)–(5.42). The flux estimator provides the stator flux linkage in the stationary reference frame (α and β) coordinates as

$$\psi_\alpha = \int (v_\alpha - Ri_\alpha)dt \tag{5.43}$$

$$\psi_\beta = \int \left(v_\beta - Ri_\beta\right)dt \tag{5.44}$$

where v_α, v_β and i_α, i_β can be obtained from the stationary reference frame transformation from three-phase voltages and currents as follows:

The estimated stator flux-linkage modulus can be expressed as

$$|\psi_s| = \left(\psi_\alpha^2 + \psi_\beta^2\right)^{1/2} \tag{5.45}$$

5.14.4 Position estimation

The rotor position is estimated from the known values of stator fluxes in stationary reference frame, the rotor Sin and Cos positions are related to the stator fluxes. The α-axis component of flux gives sinusoidal position of the rotor magnet whereas the β-axis component of flux gives cosinusoidal position of the rotor magnet. The estimated Sin and Cos positions of the rotor are given as

$$\mathrm{Sin}(\theta) = \frac{\psi_\alpha}{\left(\psi_\alpha^2 + \psi_\beta^2\right)^{1/2}} \tag{5.46}$$

$$\mathrm{Cos}(\theta) = -\frac{\psi_\beta}{\left(\psi_\alpha^2 + \psi_\beta^2\right)^{1/2}} \tag{5.47}$$

5.14.5 Speed estimation

The rotor speed estimation is based on the accurate estimation of stator flux in the stationary (α and β) reference frame. The speed of the rotor is calculated based on the equation given as

$$\omega_{est} = \left(\frac{\left(\psi_\alpha p\psi_\beta\right) - \left(\psi_\beta p\psi_\alpha\right)}{\left(\psi^2{}_\alpha + \psi^2{}_\beta\right)}\right) \tag{5.48}$$

where ω_{est} is the estimated speed of the rotor of PMSM in electrical rad/s, p is derivative operator equal to d/dt.

5.15 MATLAB-based model of sensorless vector-controlled PMSM drive

The simulation model is developed in MATLAB environment along with Simulink and PSB toolboxes for simulating response of sensorless vector-controlled PMSM drive under different operating conditions such as starting, speed reversal and load perturbation. To test the effectiveness of the developed model, the response of sensorless vector-controlled PMSM drive is simulated using PI speed controller.

The real-time simulation is performed in MATLAB environment along with Simulink and PSB toolboxes. The control structure is shown in Figure 5.37 in which a sampling period of 100 μs is used for simulation. The main parts of this block diagram are discussed in this section.

5.15.1 Flux estimator

The Simulink model diagram of flux estimator is shown in Figure 5.38. This block takes the dc-link voltage and two of the three-phase winding current along with the

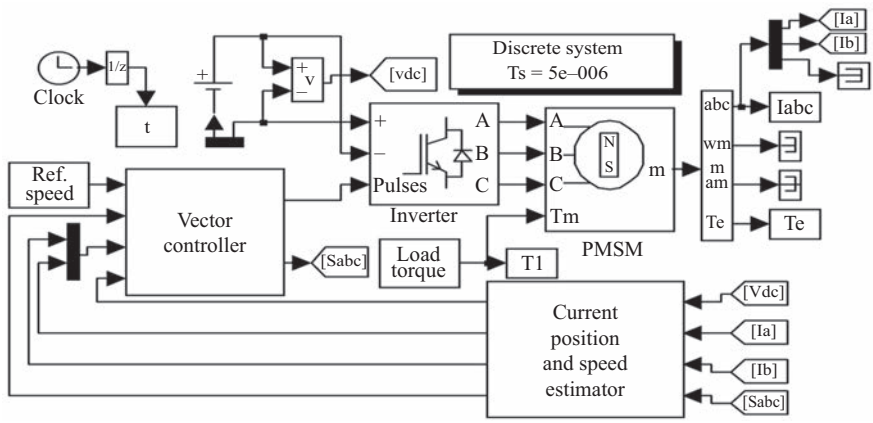


Figure 5.37 MATLAB model diagram of sensorless vector-controlled PMSM drive

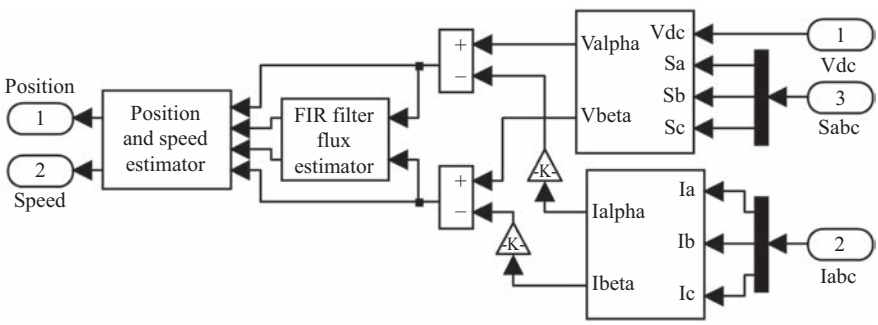


Figure 5.38 MATLAB subsystem model diagram of sensorless flux estimator

switching status of VSI as input and gives the stator fluxes in stationary reference frame as the output. The back emf is obtained by subtracting the ohmic drop from the voltage applied to the stator winding of the PMSM. This is filtered with the finite impulse response (FIR) filter used for estimating the stationary reference frame fluxes of the PMSM.

5.15.2 Position and speed estimation

The Simulink model diagram of position and speed estimator of vector-controlled PMSM drive is shown in Figure 5.38. The inputs to this block are fluxes in stationary reference frame voltage and current signals and the output is the position signals and the mechanical speed of rotor. The MATLAB-based model of PI speed controller is shown in Figure 5.39. The PI speed controller is used to provide a reference torque for the vector-controlled PMSM drive. The output of the speed controller is limited to a proper value in accordance with the motor rating to generate the reference torque for the load.

5.15.3 Speed controller

The model of speed controller is realized using the Simulink toolbox of the MATLAB software. In this part of the work, only PI speed controller is considered for brevity, although the analysis is applicable to speed and β-axis fluxes are directly used for the estimation of rotor position from which the speed is estimated.

5.15.4 Reference winding current generation

The Simulink model diagram of reference winding current generator block is shown in Figure 5.39. This block utilizes the output of limited value of the speed controller and the output of field weakening controller along with the estimated angular position of the rotor. The inverse Park's transformation is used in the model for generating the reference winding currents of the PMSM.

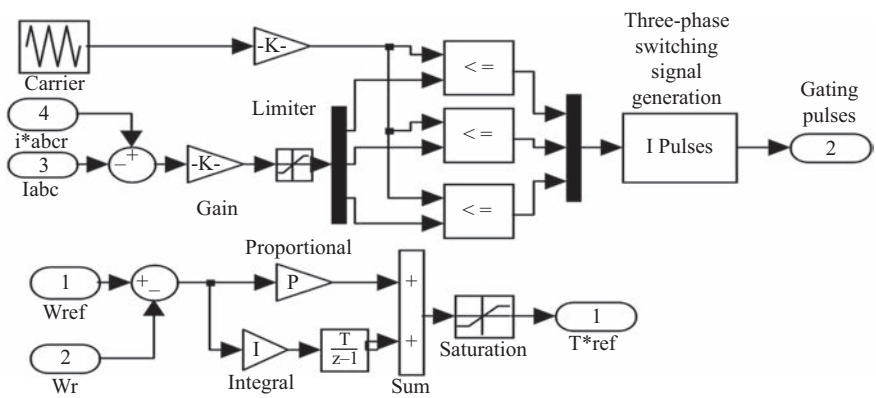


Figure 5.39 MATLAB subsystem model diagram of PI speed controller and PWM current controller

5.15.5 Current controlled pulse width modulator (CC-PWM)

The Simulink model diagram of CC-PWM used for generation of switching signal for the VSI is shown in Figure 5.39. The inputs to this block are the three-phase reference-winding currents obtained from the reference winding current generator block and the sensed winding currents of the motor. For the corresponding phases "a", "b" and "c", switching signals are generated by current controlled PWM technique.

5.16 DSP-based hardware implementation of sensorless vector-controlled PMSM drive

The sensorless vector-controlled PMSM drive is implemented using the DSP ADMC401. The VVVF source is realized using the VSI in sensorless control mode. The winding currents and dc-link voltage are the feedbacks for the closed-loop structure of the sensorless vector-controlled PMSM drive. The control algorithm is implemented in real time using a Digital Motion Controller ADMC401 DSP developed by analog devices.

Fast speed and high accuracy features of DSPs like ADMC401, which is used for the implementation of VC technique, enables a high-resolution control of the sensorless vector-controlled PMSM drive.

Figure 5.40 shows the block diagram of the sensorless vector-controlled PMSM drive system. The power circuit consists of single-phase 50 Hz ac supply, single-phase ac–dc diode bridge converter, dc-link LC filter, VSI and the PMSM. The control circuit hardware consists of reference speed scaling circuits, sensed current scaling circuit using the Hall effect current and voltage sensors. Gate driver circuit consists of Semikron make SKHI 22A driver. Six gating signals achieved at the output of driver chips are applied between the gate and emitter of the IGBTs of VSI.

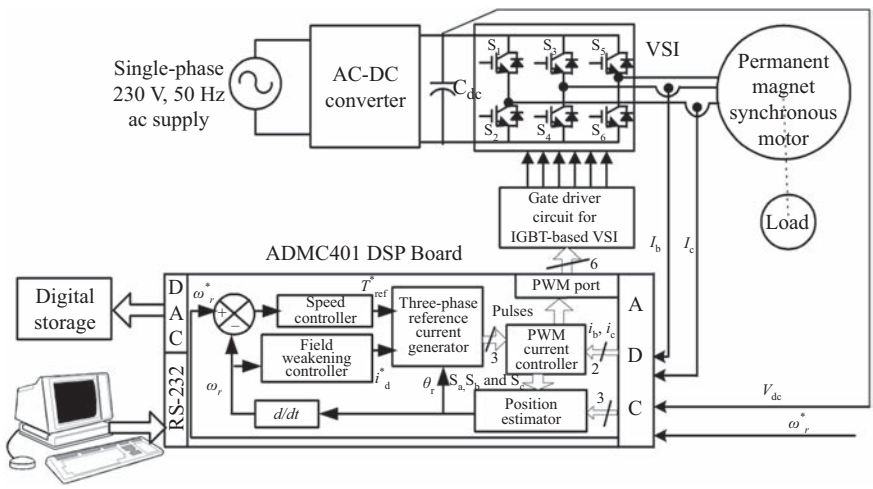


Figure 5.40 Experimental setup of sensorless vector-controlled PMSM drive

5.16.1 Development of signal conditioning circuits

The control circuit of the hardware implementation of the drive consists of the dc-link voltage sensing circuit and winding current sensing circuit. These circuits require their respective signal conditioning circuits for proper scaling of the sensed voltage and current signals. The outputs of these sensors are brought within the acceptable range of ± 2 V to be fed to respective ADC channels of the DSP. The reference speed needed for the closed-loop control is generated by analog voltage of ± 2 V for the entire speed range from $+3{,}300$ to $-3{,}300$ rpm of the drive.

5.16.2 Development of power circuit of the drive

The power circuit consists of a single-phase 230 V, 50 Hz ac supply, single-phase ac–dc diode bridge converter, dc-link LC filter, VSI and the PMSM. The VSI is fed from a diode bridge rectifier and an LC filter is used in the dc link, which filters the ripples of the dc-link voltage. The VSI consists of the Semikron make SKM 75 GB IGBTs module. The thermal trip is provided in the VSI for protection of the IGBT devices. The switching pattern generated from the vector controller controls the ON/OFF time of the VSI switches.

5.17 DSP-based software implementation of sensorless vector-controlled PMSM drive

The control software consists of the reference speed input command, flux estimation, position estimation, speed estimation, speed controller, limiter, field-weakening controller, reference winding current generation and PWM current controller to produce switching signals for VSI feeding PMSM. The software used for implementation of vector-controlled PMSM drive is developed in assembly language of the analog devices DSP ADMC401. The main equations used in the control software modules are given in the following section.

5.17.1 Reference speed input

The input voltage in the range of 0 to $+2$ V is applied to one of the ADC channel of the ADMC401. The corresponding digital value of the reference speed obtained from the ADC channel is used in assembly language routine inside the DSP. The speed reversal command is inputted through the digital I/O port of the processor by inputting the $+5$ V command signal for speed reversal. The algorithm checks if there is a speed reversal command given from the I/O port and if so, the reference speed is converted to the negative value for the reverse direction motion of the PMSM.

5.17.2 Estimation of stator flux and position of rotor

In this routine, the stator fluxes in stationary reference frame are computed from the applied dc-link voltage, switching status of VSI and winding currents of PMSM. For estimation of stator fluxes, an FIR filter algorithm is used. The rotor Sin and Cos position signals are computed by comparing the instantaneous value of α and β – axis components of stator fluxes.

5.17.3 Speed estimation

The stator fluxes estimated from the FIR filter algorithm are used for the calculation of the rotor speed of the PMSM. The stator flux signals are converted into speed signal by the algorithm used in the assembly language software of DSP.

5.17.4 Speed controller

The speed controller and limiter routines take the speed error between the reference speed and estimated speed of the rotor and compute the reference torque. The maximum value of the reference torque is limited by the permissible winding currents of the motor. In this, implementation of vector-controlled PMSM drive, the PI speed controller is used. In the software, corresponding assembly language codes are developed for PI speed controller routine.

5.17.5 Reference winding current generation

Three-phase reference winding current generation routine takes the digital value of *d*-axis stator current and *q*-axis stator current along with the estimated value of Sin and Cos position signals of the rotor magnet as inputs and it generates the three-phase reference winding currents needed for the current controller routine as output. These reference currents ($i^*_{a(k)}$, $i^*_{b(k)}$, $i^*_{c(k)}$) are compared with the sensed winding currents ($i_{a(k)}$, $i_{b(k)}$, $i_{c(k)}$) and the resulting errors are fed to the PWM current controller.

5.17.6 Switching signal generation for voltage source inverter

The three-phase generated reference currents and the three-phase sensed currents from the PMSM winding are fed to the CC-PWM unit. The error between the two sets of currents is passed through respective current controller unit and the limited output of the current controller unit is compared with a high-frequency (10 kHz) triangular carrier wave. If the amplified error signal of corresponding phase is more than the carrier signal, then the switching signal for the upper switch of the same phase is turned on, otherwise, the lower switch of the same leg is turned on. Thus, in total, six switching signals are generated, wherein these are meant for each leg of the three-phase VSI bridge, namely, leg "a", leg "b" and leg "c", respectively. Two paired complementary signals for respective legs are used for switching the upper and the lower devices of the same leg of the VSI with proper dead band to avoid the shoot through fault in any of the VSI leg.

5.18 Testing of sensorless vector-controlled PMSM drive

The testing of sensorless vector-controlled PMSM drive is carried out systematically. The drive consists of power circuit hardware and the control circuit consists of signal conditioning circuit for scaling of feedback current and position signals. After developing the complete drive system, the testing procedure is carried out for each part of the system and it is described as follows.

5.18.1 Testing of control circuit

The control circuit of the VC PMSM drive consists of current feedback circuit, dc-link voltage sensing circuit, reference speed circuit and the gate driver circuit. The current feedbacks and the dc-link voltage are tested for their defined range. The DSP is capable of receiving ± 2 V signals at its ADC channels. Therefore, all feedback signals are scaled by using a signal conditioning circuit so that the complete operating range is covered with the desired accuracy in the predefined range.

The PMSM is run with the open loop V/F control to test the current sensors for its calibration and accuracy. The converted digital current signals used for the DSP algorithm are converted back to analog signal using DACs and are brought out on to the CRO screen. The sensed voltage and current signals and the signals obtained from DAC terminals must overlap each other on the CRO screen. The process verifies the current signals A to D conversions and D to A conversions, respectively.

The gating signals obtained from the PWM unit of DSP are used for individual leg of the VSI. These gating signals are checked for the complementary signal in each pair of the same leg with proper dead band. Three pairs of such PWM signals are checked to prove the satisfactory operation of the control circuit in all respect.

5.18.2 Testing of power circuit

The complete drive control system is connected and the output of VSI is connected across a three-phase star-connected resistive load. A reduced voltage (20%) is applied at the dc link of the inverter. The resistive load is fed from the open loop V/F control technique so that the equal amount of current flows in all three phases of resistive load. This test proves the proper functioning of the power circuit. The PMSM is now connected in place of three-phase resistive load across the VSI. The sensorless vector-controlled PMSM drive is tested for its operation with a set reference speed. The closed-loop operation of the drive is tested for a set of reference speeds of the drive, with varying dc-link voltage and rotor speed of the drive remaining constant. Therefore, the satisfactory operation of the power circuit and closed-loop operation of the drive are tested for different operating conditions of the drive system.

5.19 Results and discussion

The performance of the sensorless vector-controlled PMSM drive is simulated using the developed mathematical model in MATLAB environment along with Simulink and PSB toolboxes under different dynamic conditions such as starting, speed reversal and load perturbation (load application and load removal). A set of response is obtained comprising reference speed, rotor speed in electrical rad/s, two of three-phase winding currents.

The simulated response of the VC PMSM drive is validated with test results obtained from the developed prototype of the vector-controlled PMSM drive system for a 1.93 kW, four-pole three-phase PMSM. The experimental and simulated responses of the PMSM drive system with PI speed controller are obtained under

various operating conditions such as starting, speed reversal, load perturbation and steady-state conditions. These responses are shown in Figures 5.41–5.45 and are discussed in the following sections. To facilitate comparison, the estimated position and speed along with sensed position and speed of the rotor are shown in Figure 5.41(a) and (b).

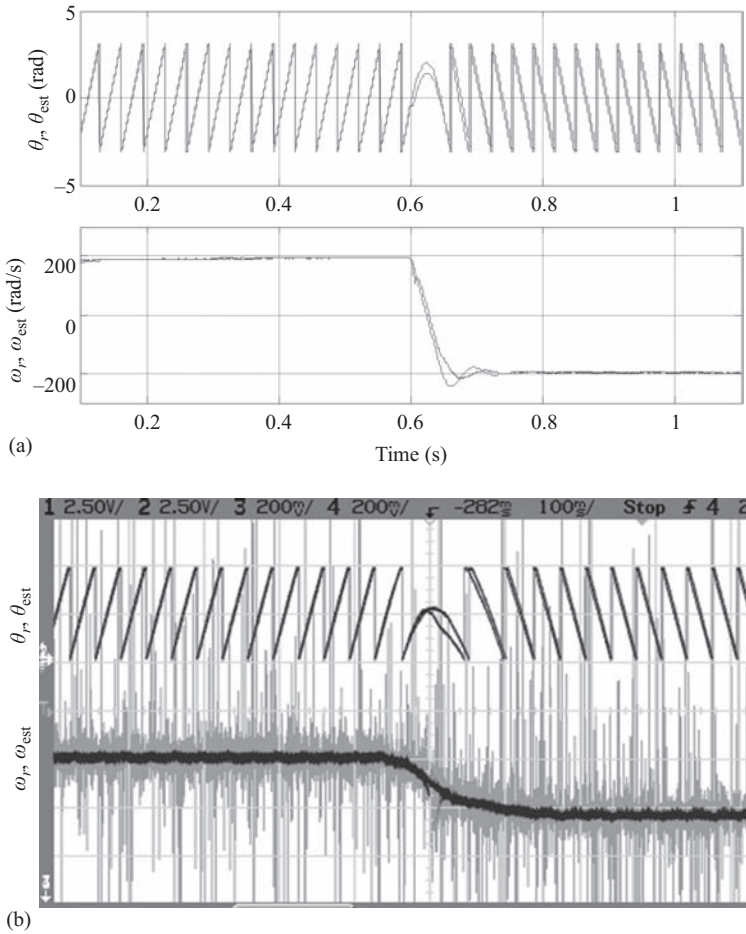


Figure 5.41 (a) Simulated position and speed estimation response of sensorless vector-controlled PMSM drive with PI speed controller with speed reversal from +188.49 to −188.49 rad/s (scale on X-axis 1 div = 0.2 s, Y-axis channels 1 and 2, 1 div = 5 rad, on channels 3 and 4, 1 div = 200 rad/s)r; (b) test results of position and speed estimation response of sensorless vector-controlled PMSM drive with PI speed controller at no load with speed reversal from +188.49 to −188.49 rad/s (scale on X-axis 1 div = 100 ms, Y-axis channels 1 and 2, 1 div = 3.14 rad, on channels 3 and 4, 1 div = 400 rad/s). r = reference value

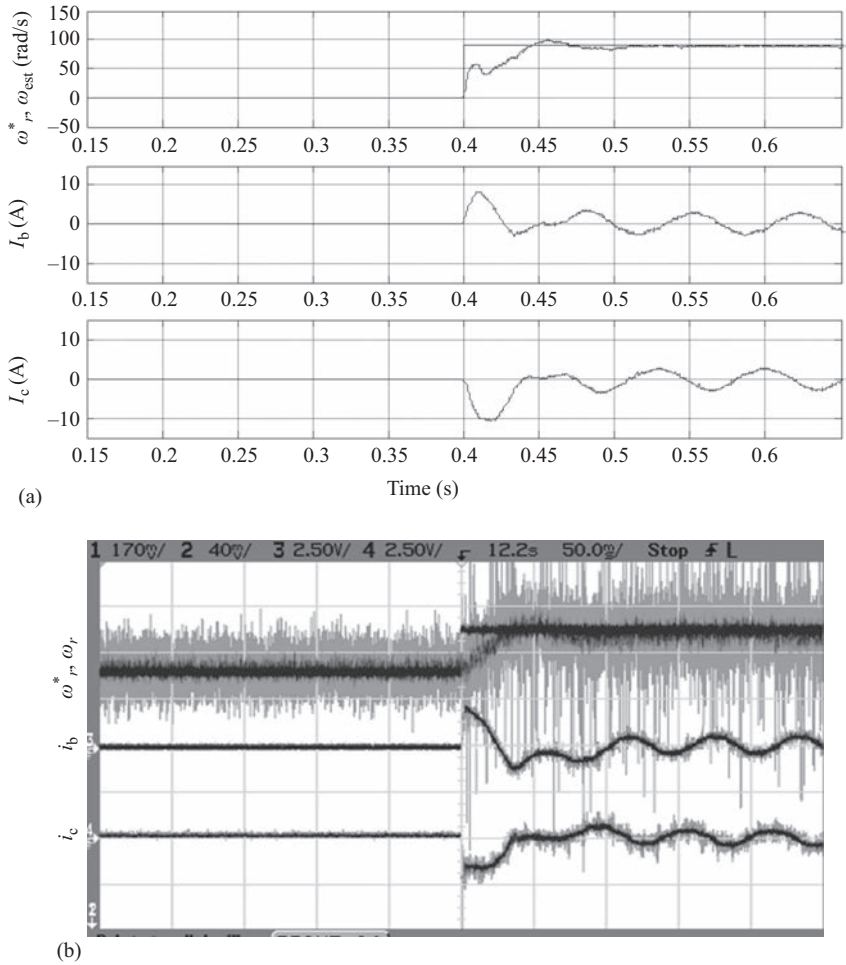


Figure 5.42 (a) Simulated starting response of sensorless vector-controlled PMSM drive with PI speed controller at no load with reference speed of 90 rad/s (scale on X-axis 1 div = 50 ms, Y-axis channels 1 and 2, 1 div = 50 rad/s, on channels 3 and 4, 1 div = 10 A); (b) test results of sensorless vector-controlled PMSM drive with PI speed controller at no load with reference speed of 90 rad/s (scale on X-axis 1 div = 50 ms, Y axis channels 1 and 2, 1 div = 100 rad/s, on channels 3 and 4, 1 div = 10 A)

5.19.1 Starting dynamics of sensorless PMSM drive

The PMSM is controlled using a vector controller, which generates controlled voltage and controlled frequency to the motor. The motor is started from the known position at a low frequency and by sensorless VC algorithm, the position and speed of the rotor

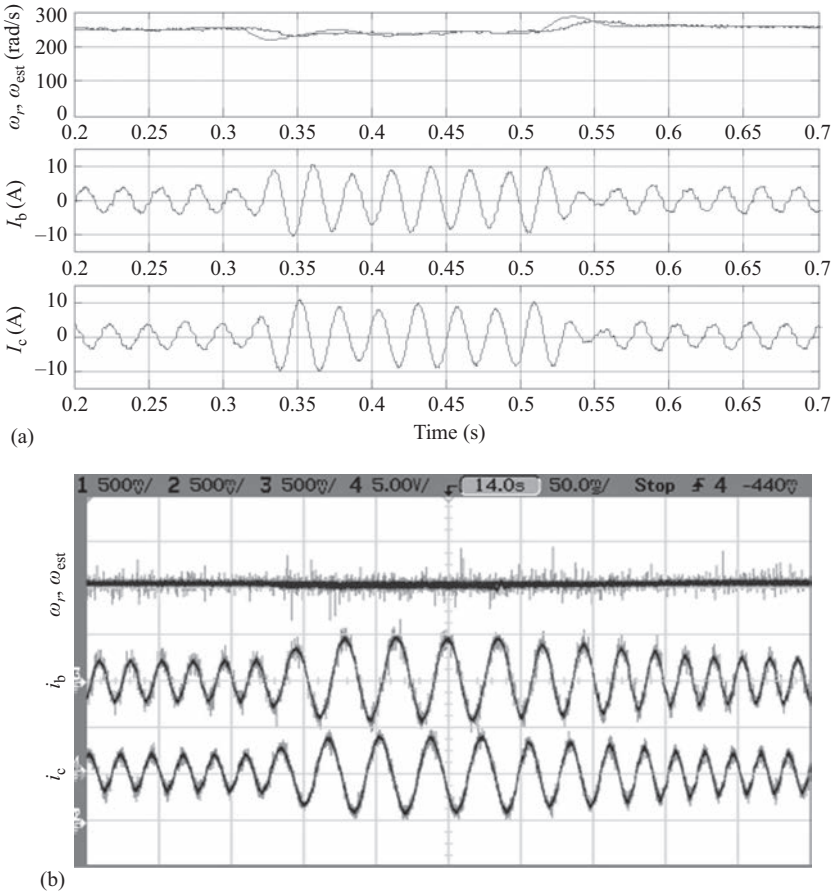


Figure 5.43 (a) Simulated load perturbation response of sensorless vector-controlled PMSM drive running at 251.32 rad/s load perturbation from 1.5 to 3 to 1.5 N m (scale on X-axis 1 div = 50 ms, Y-axis channels 1 and 2, 1 div = 100 rad/s, on channels 3 and 4, 1 div = 10 A); (b) experimental load perturbation response of sensorless vector-controlled PMSM drive running at 251.32 rad/s from 1.5 to 3 to 1.5 N m (scale on X axis 1 div = 50 ms, Y-axis channels 1 and 2, 1 div = 200 rad/s, on channels 3 and 4, 1 div = 10 A)

are estimated and the reference speed is increased to bring the motor in steady-state condition with set value of reference speed. In the test case, the reference speed is set to 90 electrical rad/s (430 rpm) with a torque limit set to one and half times of the rated value. The starting current is inherently limited to one and half times of the rated current when the motor builds up the developed torque to reach the set reference speed. When the developed speed of the motor is almost equal to the reference speed, the winding currents are reduced to their no-load values and the developed torque

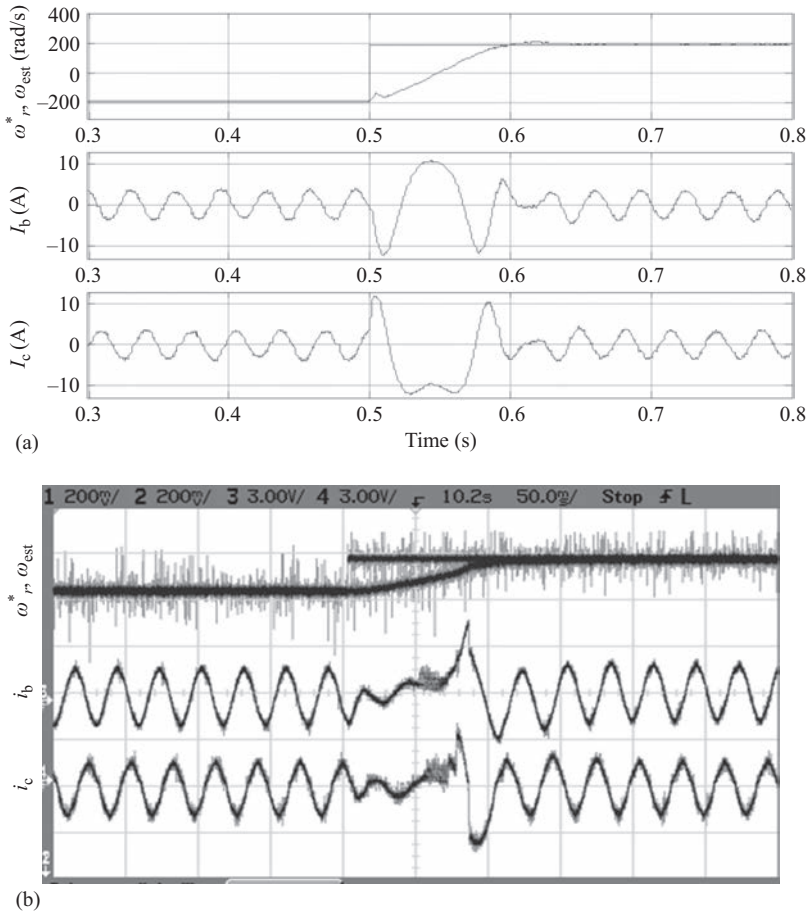


Figure 5.44 (a) Simulated speed reversal response of sensorless vector-controlled PMSM drive with PI speed controller at no load with reference speed from −188.49 to +188.49 rad/s (scale on X-axis 1 div = 100 ms, Y-axis channels 1 and 2, 1 div = 200 rad/s, on channels 3 and 4, 1 div = 10 A); (b) experimental speed reversal response of sensorless vector-controlled PMSM drive with PI speed controller at no load with reference speed from −188.49 to +188.49 rad/s (scale on X-axis 1 div = 50 ms, Y-axis channels 1 and 2, 1 div = 400 rad/s, on channels 3 and 4, 1 div = 10 A)

becomes equal to the load torque as observed in the starting response shown in Figure 5.42(a) and (b). A step change in reference speed from standstill to a reference speed of 90 electrical rad/s (430 rpm) is applied at $t = 0.4$ s. The test results show that the motor attains the reference speed of 460 rpm in 58 ms and it has close agreement with the simulated results which takes 50 ms for the starting of drive to the same

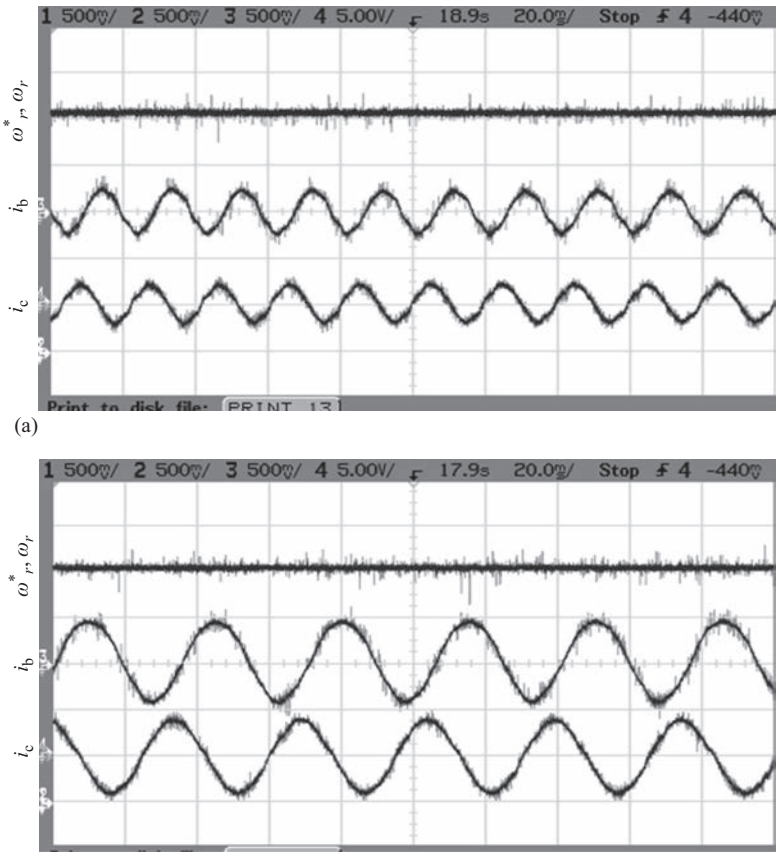


Figure 5.45 (a) Experimental steady-state response of vector-controlled PMSM drive running at 350 rad/s with 1.5 N m load (scale on X-axis 1 div = 20 ms, Y-axis channels 1 and 2, 1 div = 200 rad/s, on channels 3 and 4, 1 div = 10 A); (b) experimental steady-state response of vector-controlled PMSM drive running at 175 rad/s with 3 N m load (scale on X-axis 1 div = 20 ms, Y-axis channels 1 and 2, 1 div = 200 rad/s, on channels 3 and 4, 1 div = 10 A)

reference speed. The motor winding currents are increased to a high value which is decided by the torque limiter and it reduces to a small value under steady-state operating condition because the motor is running at no-load.

5.19.2 Load perturbation response of sensorless PMSM drive

The load perturbation response of the vector-controlled PMSM drive is shown in Figure 5.43(a) and (b). The motor is running at a steady-state speed of 251.32

electrical rad/s with a load torque of 1.5 N m. Suddenly, the load torque is increased to 3 N m (54.54% of rated torque). Sudden increase of the load causes an instantaneous fall in the speed of the motor. In response to the drop in speed, the output of the speed controller responds by increasing the reference torque value. Therefore, developed electromagnetic torque of the PMSM increases to recover back to fall in speed of the motor. The response is analyzed both for the load application and load removal. In Figure 5.43(a) and (b), load application and removal responses of the PMSM drive are shown. The winding currents are increased as the load on the motor shaft is applied upon which a momentary small dip in the rotor speed is observed, which is recovered within a very small time.

5.19.3 Speed reversal dynamics of sensorless PMSM drive

The speed reversal dynamics of the vector-controlled PMSM drive is observed for the sudden change of reference speed from −188.49 electrical rad/s (−900 rpm) to +188.49 electrical rad/s (+900 rpm) with a PI speed controller. The speed reversal response is shown in Figure 5.44(a) and (b). The motor is running at −188.49 electrical rad/s speed in the reverse direction and the reference speed command is suddenly changed to +188.49 electrical rad/s. The reversal time of the motor is measured between the instant of application of speed reversal command and the instant when the motor attained 95% of speed in the set direction. It is observed from this response that the motor takes 100 ms time for the speed reversal in simulation results while it takes 105 ms in test results. During speed reversal, the motor winding currents are increased to maximum allowable value during the speed reversal time and as soon as the motor speed reaches the reference speed, the winding currents are settled to its normal value dictated by the load on the motor shaft.

5.19.4 Steady-state performance of sensorless PMSM drive

The steady-state performance of vector-controlled PMSM drive with no-load and at loads of 1.5 N m at 251.32 electrical rad/s and 3 N m at 175 electrical rad/s is shown in Figure 5.44(a) and (b). It is observed from these responses that the PMSM operates satisfactorily under varying load torques. From the simulated and experimental results, it is evident that the sensorless vector-controlled PMSM gives acceptable steady-state performance.

5.20 Summary

The vector-controlled PMSM drive system has been mathematically modeled in MATLAB environment Simulink and PSB toolboxes. The response of the PMSM drive has been successfully simulated using the developed model under different operating conditions such as starting, load perturbation and speed reversal. The DSP-based implementation of PMSM drive has been carried out successfully. A comparative study of different speed controllers for variable speed operation of vector-controlled PMSM drive system has shown that they are quite effective in the control of drive, and the individual speed controllers have their own advantages

and disadvantages. Depending upon the application, the choice of a particular speed controller may be made. When the requirement is of simplicity in control and ease of application, the PI controller is considered to be a good choice. For achieving the fast response, the sliding mode controller may be selected. The main demerits of this selection are the steady-state error on the application of load. For eliminating the steady-state error as also for obtaining the fast response of the drive, it is concluded that the HFPI controller is a better choice when the requirement is of high-level accuracy and improved performance of vector-controlled PMSM drive system.

The sensorless vector-controlled PMSM drive system has been mathematically modeled in MATLAB environment along with Simulink and PSB toolboxes. The DSP-based implementation of sensorless vector-controlled PMSM drive has been achieved successfully. The FIR filter algorithm is developed and implemented for the real-time estimation of the stator fluxes of PMSM in stationary reference frame. From the estimated value of stator fluxes, the position and speed of rotor are obtained. However, near the zero speed operation of the drive, the accurate estimation of flux is not possible; therefore, the position of the rotor is required for the implementation of proposed algorithm. The sensorless vector-controlled PMSM drive has resulted in simple and robust control of the drive with improved noise immunity and greater reliability of drive system. It is concluded that sensorless vector-controlled PMSM drive is best suited for variable speed drive application.

List of symbols

$\omega_{r(k)}$	Measured rotor speed at kth instant
$\omega^*_{r(k)}$	Reference rotor speed at kth instant
$\omega_{e(k)}$	Speed error at kth instant
T^*_k	Reference torque at kth instant
$T^*_{\mathrm{ref}(k)}$	Limited reference torque at kth instant
i^*_q	q-Axis reference current
i^*_d	d-Axis reference current
i^*_a, i^*_b, i^*_c	Phase reference currents
i_a, i_b, i_c	Winding currents
K_P and K_I	Proportional and integral gain constants
Z	Switching hyperplane function
C_1	Constant of switching hyperplane function
C_2 C_3	Gains of the sliding mode controller
$\gamma_{(k)}$	Output of the fuzzy logic controller at kth instant
$T'_{\mathrm{ref}(k)}$	Modified torque reference at kth instant
$\Delta\omega_{e(k)}$	Rate of change in speed error at kth instant
F	Fuzzy mapping function
μ_i	Output of fuzzy subset
α_i	Degree of belonging

K_f	Scaling factor of defuzzifier
$\omega^{*'}_{r(k)}$	Pre-compensated reference speed signal
K_t	Motor torque constant
θ_r	Rotor angular position
L_q and L_d	Inductances along d and q-axis
φ_f	Stator flux linkages produced by permanent magnets
φ_d and φ_q	Stator flux linkages components along d and q-axis
R_s	Stator-winding resistance per phase
ω_{b}	Rotor base speed
i_d and i_q	Stator current components along d and q-axis
v_d and v_q	Stator voltage components along d and q-axis
P	Number of magnetic poles
T_L	Load torque
B	Damping coefficient
J	Moment of inertia
$\mathrm{S_a}$, $\mathrm{S_b}$ and $\mathrm{S_c}$	Switching functions for phases a, b, c
v_{a}, v_{b}, v_{c}	Voltage of phases a, b, c
V_{dc}	dc-Link voltage
i_α	α-Axis winding current of the motor in stationary reference frame
i_β	β-Axis winding current of the motor in stationary reference frame
v_α	α-Axis component of voltage in stationary reference frame
v_β	β-Axis component of voltage in stationary reference frame
ω_{est}	Estimated rotor speed
p	Derivative operator (d/dt)

Glossary of terms

Scalar control	The control of current or voltage in any application as a scalar quantity for control of other parameters
VC	Vector control
SMC	Sliding mode controller
FLC	Fuzzy logic controller
FP-PI	Fuzzy pre-compensated proportional plus integral controller
Resolver	Resolver is an absolute position sensor based on the rotating transformer concept having two windings to generate two signals proportional to sine and cosine of angular displacement
Sliding mode control	A control method which forces the system to slide along a plane of the system's normal behavior by continuously changing the control variables

Fuzzy control	It is based on a logic which can deal with situations that can neither be expressed as completely true nor false but can be said as partially true
Load perturbation	Sudden change of the load to any system such as increment, decrement, complete removal or full load application

References

[1] B.K Bose, *Modern Power Electronics and AC Drives*, Pearson Education, Delhi, 2003.

[2] T. Kenjo and S. Nagamori, *Permanent Magnet and Brushless DC Motors*, Clarendon Press, Oxford, 1985.

[3] P.C. Krause, *Analysis of Electric machinery*, McGraw-Hill Book Company, New York, 1986.

[4] C.-M. Ong, *Dynamic Simulation of Electric Machinery*, Prentice Hall, Upper Saddle River, NJ, 1998.

[5] T.J.E. Miller, *Brushless Permanent-Magnet and Reluctance Motor Drives*, Clarendon Press, Oxford, 1989.

[6] Y. Dote, *Servomotor and Motion Control Using Digital Signal Processors*, Texas Instruments, Warren, NJ, 1990.

[7] Y. Dote and S. Kinoshita, *Brush less Servomotors Fundamentals and Applications*, Clarendon Press, Oxford, 1990.

[8] P. Vas, *Parameter Estimation, Condition Monitoring and Diagnosis of Electrical Machines*, Clarendon Press, Oxford, 1993.

[9] J.F. Gieras and M. Wing, *Permanent Magnet Motor Technology*, Marcel Dekker Inc., New York, 1997.

[10] I. Boldea and S.A. Nasar, *Electric Drives*, CRC Press, Boca Raton, FL, 1998.

[11] B. Singh, "Recent Advances in Permanent Magnet Brushless DC Motors", *Sadhana*, Vol. 22, No. 6, pp. 837–853, 1997.

[12] P. Vas, *Sensorless Vector and Direct Torque Control*, Oxford University Press, Oxford, 1998.

[13] N. Mohan, *Advanced Electric Drives, Analysis, Control and Modeling Using Simulink®*, MNPERE, Minneapolis, USA, 2001.

[14] K. Rajashekara, A. Kawamura and K. Matsuse, *Sensorless Control of AC Motor Drives*, IEEE Press, New York, 1996.

[15] N. Mohan, T.M. Undeland and W.P. Robbins, *Power Electronics Converters, Applications and Design*, John Wiley and Sons (Asia) Pvt. Ltd., Singapore, 1998.

[16] B.K. Bose, "Power Electronics An Emerging Technology", *IEEE Transactions on Industrial Electronics*, Vol. 30, No. 3, pp. 403–412, 1989.

[17] M.P. Kazmierkowski, R. Krishnan and F. Blaabjerg, *Control in Power Electronics Selected Problem*, Academic Press, 2002.

[18] R.W. Erickson and D. Maksimovic, *Fundamentals of Power Electronics*, 2nd Edition, Kluwer Academic Publishers, Norwell, MA, 2004.

[19] F. Blaschke, "The Principle of Field-Orientation as Applied to the New Transvector Closed Loop Control System for Rotating Field Machines", *Siemens Review*, Vol. 39, pp. 217–220, 1972.

[20] W. Leonhard, "Field Orientation for Controlling AC Machines-Principle and Application", in *Proc. IEE-PEVSD'88*, 1988, pp. 277–282.

[21] P. Pillay and P. Freere, "Literature Survey of Permanent Magnet AC Motor and Drive", in *Proc. IEEE IAS'89*, 1989, Vol. 1, pp. 74–84.

[22] K.J. Binns and M.A. Jabbar, "Some Recent Developments in Permanent Magnet Alternating Current Machines" in *Proc. IEEE-ICEM'78*, 1978, pp. SP3/1–10.

[23] R. Dhaoudi and N. Mohan, "Analysis of Current Regulated Voltage Source Inverter for Permanent Magnet Synchronous Motor Drives in Normal and Extended Speed Ranges", *IEEE Transactions on Energy Conversion*, Vol. 5, No. 1, pp. 137–144, 1990.

[24] P. Pillay and R. Krishnan, "Modeling, Simulation, and Analysis of Permanent Magnet Motor Drives, Part I: the Permanent Magnet Synchronous Motor Drive", *IEEE Trans. on Industry Applications*, Vol. 25, No. 2, pp. 265–273, 1989.

[25] C. Mademlis and N. Margaris, "Loss Minimization in Vector Controlled Interior Permanent Magnet Synchronous Motor Drive", *IEEE Transactions on Industrial Electronics*, Vol. 49, No. 6, pp. 1344–1347, 1992.

[26] R. Samudio and P. Pillay, "DSP Controller for a Permanent Magnet Synchronous Motor Drive", in *Proc. IEEE Creative Technology Transfer – A Global Affair'94*, 1994, pp. 413–417.

[27] M.A. Rahman, "Permanent Magnet Synchronous Motors", in *IEEE ICEM'80*, 1980, pp. 313–319.

[28] S.K. Pal, "Comparative Study of the Design and Development of Direct Drive Brushed and Brushless DC motors with Samarium Cobalt, Neodymium-Iron-Boron and Ceramic Magnets", in *Proc. IEE Colloquium on Permanent Magnet Machines and Drives*, 1993, pp. 7/1–7/7.

[29] W. Chengyuan, L. Haodong and X. Jiakuan, "Study of Intelligent Vector Control System Based on TMS320F240", in *Proc. IEEE-ICEMS'01*, 2001, pp. 550–553.

[30] R. Fazai and M.J. Kharaajoo, "High Performance Speed Control of Interior Permanent Magnet Synchronous Motors With Maximum Power Factor Operation", in *Proc. IEEE-ICECS'03*, 2003, pp. 1125–1128.

[31] M. Konghirun, "A Resolver-Based Vector Control Drive of Permanent Magnet Synchronous Motor on a Fixed-Point Digital Signal Processor", in *Proc. IEEE-TENCON'04*, 2004, pp. 167–170.

[32] M. Konghirun and L. Xu, "A dq-Axis Current Control Technique for Fast Transient Response in Vector Control Drive of Permanent Magnet Synchronous Motor", in *Proc. IEEE-IPEMC'04*, 2004, pp. 1316–1320.

[33] C.C. Lee, "Fuzzy Logic in Control Systems: Fuzzy Logic Controller Part I and II", *IEEE Transactions on Systems, Man, and Cybernetics*, Vol. 20, No. 2, pp. 404–435, 1990.

[34] J.J. Yame, "Conventional Structure of a Simple Class of Takagi-Sugeno PI type Controllers", in *Proc. IEEE CDC'02*, 2002, pp. 185–190.
[35] V.I. Utkin, "Sliding Mode Control Design Principles and Application to Electric Drive", *IEEE Transactions on Industrial Electronics*, Vol. 40, No. 1, pp. 23–36, 1993.
[36] P.K. Nandam and P.C. Sen, "Accessible States Based Sliding Mode Control of a Variable Speed System", *IEEE Transactions on Industry Applications*, Vol. 3, No. 4, pp. 737–747, 1995.
[37] M. Kadjoudj, R. Abdessemed and N. Golea, "Adaptive Fuzzy Logic Control for High Performance PM Synchronous Drives", *Journal of Electrical Power Components and Systems*, Vol. 29, No. 9, pp. 780–807, 2001.
[38] Z. Ibrahim and E. Levi, "A Comparative Analysis of Fuzzy Logic and PI Speed Control in High-Performance AC Drives Using Experimental Approach", *IEEE Transactions on Industry Application*, Vol. 38, No. 5, pp. 1210–1218, 2002.
[39] M.N. Uddin, M.A. Abido and M.A. Rahman, "Development and Implementation of a Hybrid Intelligent Controller for Interior Permanent-Magnet Synchronous Motor Drives", *IEEE Transactions on Industry Application*, Vol. 40, No. 1, pp. 68–76, 2004.
[40] M.A. Rahman and M.A. Hoque, "On-line Adaptive Artificial Neural Network Based Vector Control of Permanent Magnet Synchronous Motors", *IEEE Transactions on Energy Conversion*, Vol. 13, No. 4, pp. 311–318, 1998.
[41] J. Zhou and Y. Wang, "Adaptive Backstepping Speed Controller Design for a Permanent Magnet Synchronous Motor", *IEE Proceedings—Electric Power Applications*, Vol. 149, No. 2, pp. 165–172, 2002.
[42] F.J. Lin and C.H. Lin, "A Permanent Magnet Synchronous Motor Servo Drive Using Self Constructing Fuzzy Neural Network Controller", *IEEE Transactions on Energy Conversion*, Vol. 19, No. 1, pp. 66–72, 2004.
[43] S.K. Dwivedi, M. Laursen and S. Hansen, "Voltage Vector Based Control for PMSM in Industry Applications", *2010 IEEE International Symposium on Industrial Electronics*, Bari, 2010, pp. 3845–3850.
[44] L. Harnefors, M. Jansson, R. Ottersten and K. Pietilainen, "Unified Sensorless Vector Control of Synchronous And Induction Motors", *IEEE Transactions on Industrial Electronics*, Vol. 50, No. 1, pp. 153–160, 2003.
[45] B. Bae, S. Sul, J. Kwon and J. Byeon, "Implementation of Sensorless Vector Control for Super-High-Speed PMSM of Turbo-Compressor", *IEEE Transactions on Industry Applications*, Vol. 39, No. 3, pp. 811–818, 2003.
[46] M. Konghirun, X. Longya and D. Figoli, "Implementation of Generic Sensorless Direct Field Oriented Control of AC Motors on a Low-Cost, Fixed-Point Digital Signal Processor", in *Proc. IEEE APEC'02*, 2002, pp. 304–309.
[47] J. Hu and B. Wu, "New Integration Algorithms for Estimating Motor Flux Over a Wide Speed Range", *IEEE Transactions on Power Electronics*, Vol. 13, No. 5, pp. 969–977, 1998.

[48] G. Xie, K. Lu, S.K. Dwivedi, J.R, Rosholm, F. Blaabjerg, "Minimum-Voltage Vector Injection Method for Sensorless Control of PMSM for Low-Speed Operations", *IEEE Transactions on Power Electronics "*, Vol. 31, No. 2, pp. 1785–1794, 2016.
[49] G. Xie, K. Lu, S.K. Dwivedi, J.R, Rosholm, W. Wu, "Permanent Magnet Flux Online Estimation Based on Zero-Voltage Vector Injection Method", *IEEE Transactions on Power Electronics*, Vol. 30, No. 12, pp. 6506–6509, 2015.
[50] S.K. Dwivedi, Method and Detection System for the State of the Rotor of an Electric Motor, 2012, WO Patent, WO2012136211.
[51] S.K. Dwivedi and N. Trolle, Automatic Identification of the Type of Motor, 2016, WO Patent WO2016005790.
[52] "PSIM User's Guide, Copyright©" Powersim Inc, 2003.
[53] "User's Guide of Simulink Toolbox of MATLAB®" Mathworks, 2000.
[54] "User's Guide of ADMC401 Motion Control DSP" of Analog Devices, 1999.

This page intentionally left blank

Chapter 6

PM synchronous machine drives

Thomas M. Jahns[1]

6.1 Introduction

The purpose of this chapter is to discuss techniques for analyzing and controlling the electrical performance characteristics of permanent magnet (PM) synchronous machines (PMSMs) based on electrical equivalent circuit models for the machine derived in the synchronously rotating reference frame. Representation of the *d*- and *q*-axes components of the key machine variables as complex vectors provides a powerful means of graphically illustrating the amplitudes and spatial orientations of these key variables in the machine. This complex-plane representation of the machine-phase currents will be used to investigate the performance limits of the machine at high speeds when operating from a source that is restricted by maximum voltage and current limits.

There are two major classes of PMSMs that will be addressed in this chapter, drawing on basic concepts introduced previously in Chapter 5. These two PMSM classes are distinguished by the configuration of their rotors, as illustrated in Figure 6.1. The rotor of the surface PM (SPM) synchronous machine in Figure 6.1(a) consists of alternating north- and south-pole magnet arcs mounted on the surface of a stack of round (non-salient) steel laminations. The magnets are secured in place using either a strong adhesive or some type of nonmagnetic containment shell surrounding the magnets to hold them in place at elevated speeds (not shown in the figure). The rotor of the interior PM (IPM) synchronous machine, the second major PMSM class, is shown in Figure 6.1(b). This type of PMSM rotor construction is distinguished by magnets mounted in internal cavities cut inside the stack of steel rotor laminations. The polarities of these magnets alternate around the periphery of the machine. While the differences between the construction details of the SPM and IPM machines may seem relatively minor at first, the act of burying the magnets inside the rotor creates a major difference between the torque production characteristics of the two types of PMSMs that can be of first-order importance when selecting the "best" PMSM design for specific applications. These differences must also be taken into account when designing the appropriate control algorithms.

[1]Department of Power Electronics and Electrical Machines, University of Wisconsin-Madison, United States

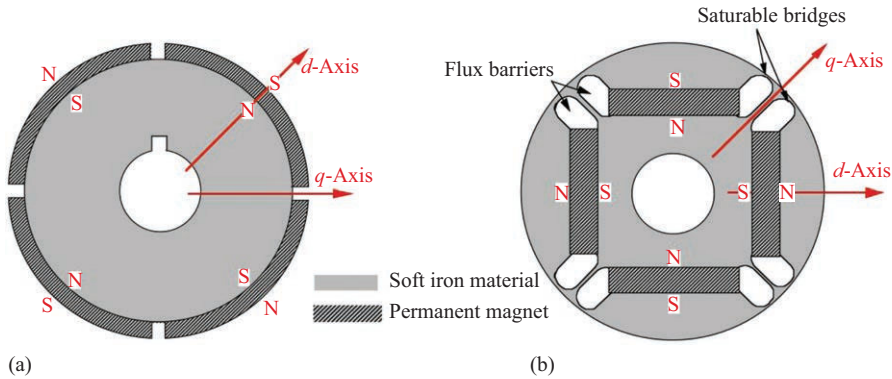


Figure 6.1 Rotors of two major classes of permanent magnet synchronous machines (PMSMs): (a) surface permanent magnet (SPM) and (b) interior permanent magnet (IPM)

Techniques for controlling the torque production in these two classes of PMSMs during both low-speed and high-speed operation are discussed in this chapter. Special attention is devoted to *vector control* algorithms that collectively represent the most widely adopted control technique used today for active torque control in medium- to high-performance PMSM drives. Modifications of vector control algorithms that have been developed for high-speed operation of PMSMs either to reduce eddy-current core (iron) losses or to achieve constant-power operation via flux weakening (FW) will also be addressed. Finally, alternative control algorithms that fundamentally differ from established vector control techniques and are either already used in some commercial PMSM drives or are under serious consideration for future drives will also be introduced.

6.2 PM machine equivalent circuit models

AC electric machines pose special challenges for analysis and control because of the significant nonlinearities that appear prominently in their differential equations, For three-phase synchronous machines (IPM or SPM), the governing differential equations can be expressed as follows:

$$\begin{aligned}
v_{as} &= R_s i_{as} + \frac{d}{dt}\psi_{as} \quad \psi_{as} = L_{as}(\theta_r) i_{as} + M_{ab}(\theta_r) i_{bs} + M_{ac}(\theta_r) i_{cs} + \psi_{pm}\cos(\theta_r) \\
v_{bs} &= R_s i_{bs} + \frac{d}{dt}\psi_{bs} \quad \psi_{bs} = M_{ab}(\theta_r) i_{as} + L_{bs}(\theta_r) i_{bs} + M_{bc}(\theta_r) i_{cs} + \psi_{pm}\cos\left(\theta_r - \frac{2\pi}{3}\right) \\
v_{cs} &= R_s i_{cs} + \frac{d}{dt}\psi_{cs} \quad \psi_{cs} = M_{ac}(\theta_r) i_{as} + M_{bc}(\theta_r) i_{bs} + L_{cs}(\theta_r) i_{cs} + \psi_{pm}\cos\left(\theta_r - \frac{4\pi}{3}\right)
\end{aligned} \tag{6.1}$$

where v_{as}, v_{bs}, v_{cs} is the instantaneous phase voltage (V), i_{as}, i_{bs}, i_{cs} is the instantaneous phase voltage (A), ψ_{as}, ψ_{bs}, ψ_{cs} is the instantaneous phase flux linkages (Wb),

R_s is the stator phase resistance (Ω), θ_r is the rotor angle (elec. rad), $L_{as}(\theta_r)$, $L_{bs}(\theta_r)$, $L_{cs}(\theta_r)$ is the stator phase self-inductances (H), $M_{ab}(\theta_r)$, $M_{bc}(\theta_r)$, $M_{ac}(\theta_r)$ is the stator mutual phase inductance (H), ψ_{pm} is the permanent magnet flux linkage (Wb).

While these same equations apply to both SPM and IPM machines, the key difference between them is that all of the self- and mutual-inductance values that appear in these equations do not vary as a function of the rotor angle θ_r for SPM machines because of their non-salient rotor magnetic structures. In contrast, these inductances all vary with rotor angle for the IPM machines because of the cavities in the rotor laminations that cause magnetic saliency. The nonlinearity of these differential equations is aggravated when the mechanical system differential equations (not shown here) are added, particularly in the case of the IPM machine.

The most convenient manner of analyzing sinusoidal PMSMs uses instantaneous current, voltage, and flux linkage phasors in a synchronously rotating reference frame locked to the rotor [1]. As indicated in Figure 6.2, the direct or d axis is aligned with the PM flux linkage phasor $\vec{\psi}_{pm}$, so that the orthogonal quadrature or q axis is aligned with the resulting back-emf phasor $\vec{E}$. The amplitude of the back-emf phasor can be expressed simply as

$$E = \omega_r \, \psi_{pm} \text{ (V)} \tag{6.2}$$

where ω_r is the rotor angular frequency in electrical radians per second, and E is the amplitude of the back-emf phasor in V-pk.

Although the full derivation of the transformation between the three-phase stationary reference frame and the two-phase synchronous rotor reference frame is not presented here, readers who are interested in more details regarding the transformation of electrical variables between actual phase values and dq-frame values are referred to [2]. To transform the stator phase voltages into their corresponding d- and q-axes voltage components in the synchronous rotor reference frame, the following equations are used:

$$\begin{aligned} v_d &= \frac{2}{3}\left[v_{as}\cos(\theta_r) + v_{bs}\cos\left(\theta_r - \frac{2\pi}{3}\right) + v_{cs}\cos\left(\theta_r - \frac{4\pi}{3}\right)\right] \\ v_q &= \frac{-2}{3}\left[v_{as}\sin(\theta_r) + v_{bs}\sin\left(\theta_r - \frac{2\pi}{3}\right) + v_{cs}\sin\left(\theta_r - \frac{4\pi}{3}\right)\right] \end{aligned} \tag{6.3}$$

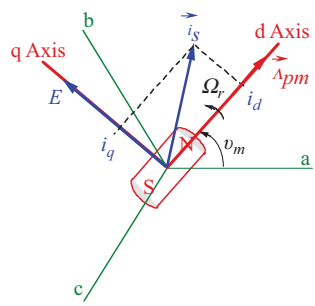


Figure 6.2 IPM machine synchronously rotating dq reference frame

These two equations were presented in the preceding chapter as (5.37) and (5.38) and are repeated hear for convenience. The same two equations can be used for transforming phase currents into their corresponding *d*- and *q*-axes components using the same two equations in (6.3) by replacing all of the *v* voltage variables with their *i* current counterparts. The sinusoidal three-phase current excitation can also be expressed in Figure 6.2 as an instantaneous current phasor $\vec{i}_s$ made up of the orthogonal *d*- and *q*-axes scalar components i_d and i_q, respectively, and the applied stator voltage phasor $\vec{v}_s$ can be similarly depicted. By convention, all of the electrical quantities including voltage, current, and flux linkage are represented by their *peak* sinusoidal values (not rms).

Applying these stator-to-rotor reference frame transformation equations to the three-phase PMSM voltage equations in (6.1), two coupled equivalent circuits can be derived for the direct and quadrature axes, as shown in Figure 6.3. The governing differential equations for these two equivalent circuits are

$$\begin{aligned} v_d &= R_s i_d + L_d \frac{di_d}{dt} - \omega_r L_q i_q \\ v_q &= R_s i_q + L_q \frac{di_q}{dt} + \omega_r \left(L_q i_q + \psi_{pm}\right) \end{aligned} \tag{6.4}$$

and the *d*- and *q*-axes flux linkage variables in Figure 6.3 are defined as

$$\begin{aligned} \psi_d &= L_d i_d + \psi_{pm} \\ \psi_q &= L_q i_q \end{aligned} \quad \text{Wb} \tag{6.5}$$

where L_d and L_q are the inductances in the *d*- and *q*-axes, respectively. It should be noted that the steady-state versions of these voltage equations can be easily extracted from (6.4) equations by setting the *di*/*dt* term in each of the equations to zero.

The magnet flux linkage source represented by the equivalent current source I_{ch} appears in the *d*-axis circuit, while the resulting back-emf appears as a dependent voltage source in the *q*-axis circuit as a component of $\omega_r \psi_d$. As defined in Figure 6.3, the equivalent magnet flux linkage source current I_{ch}, referred to

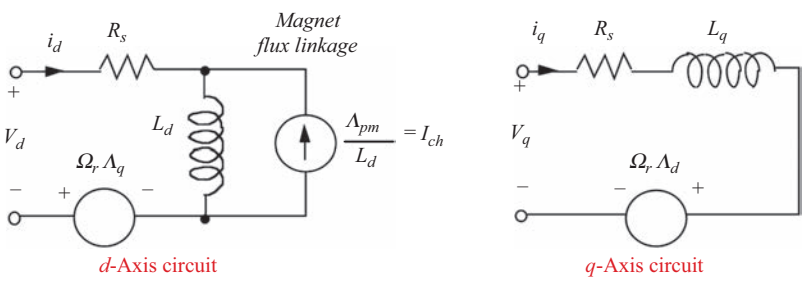


Figure 6.3 IPM machine dq-frame equivalent circuits in the synchronous rotor reference frame

henceforth, as the IPM machine characteristic current, equals the magnet flux linkage divided by the *d*-axis machine inductance:

$$I_{ch} \equiv \frac{\psi_{pm}}{L_d} \quad \text{(A)} \tag{6.6}$$

This characteristic current is an important parameter of the PM machine that influences several aspects of the PM machine's performance characteristics including extended high-speed operation and fault-mode performance. The significance of the characteristic current parameter will become clearer in later sections of this chapter.

The values of inductances along the two orthogonal axes L_d and L_q are equal (or nearly equal) in a non-salient PMSM (i.e., SPM machine). However, L_d will typically be smaller than L_q in salient-pole IPM synchronous machines using buried or inset magnets since the total magnet thickness appears as an incremental air gap length in the *d*-axis magnetic circuit (i.e., $\mu_r = 1$ for ceramic and rare-earth magnet materials) [1]. IPM machines with a single magnet barrier in each pole typically provide L_q/L_d ratios in the vicinity of 3, while novel axially laminated designs have been reported with elevated inductance saliency ratios of 7 or higher [3]. Because of the importance of the relative values of L_q and L_d, a machine parameter ξ known as the "saliency ratio" is defined as follows:

$$\xi \equiv \frac{L_q}{L_d} \tag{6.7}$$

Magnetic saturation typically has a significant impact on the performance characteristics of IPM machines. In particular, the *q*-axis inductance L_q tends to be particularly sensitive to magnetic saturation as the value of i_q increases because of the saturation characteristics of the rotor iron channels along the *q*-axis (i.e., parallel to the magnet faces) [4–6]. In comparison, the *d*-axis inductance L_d tends to be much less sensitive to magnetic saturation because this magnetic path is dominated by the thickness of the magnet cavity (or cavities) that behaves as a large air gap. These characteristics are illustrated in Figure 6.4 for a 6-kW IPM machine designed for a starter/alternator application [7] showing the significant drop in L_q as i_q is increased. Depending on the details of the rotor construction, the value of L_d may also some magnetic saturation effects to a lesser degree because of the impact of the saturating bridges at the end of the magnet cavities that hold the magnets in place.

Before closing this section, it is worth noting that the equivalent circuits shown in Figure 6.3 reflect some important assumptions and simplifications that deserve discussion. First, the assumption is made that the IPM machine does not include any rotor damper circuits that might be found in a classic salient-pole wound-field synchronous machine. As a result, neither the *d*- or *q*-axis equivalent circuits include *R*–*L* branches in the rotor circuit to model the damper windings. This is appropriate because the assumption is being made that the associated IPM machine controller is provided with information about the rotor's instantaneous position at all times. As long as this is the case, rotor damper windings are unnecessary for improving stability characteristics, and the losses they generate are undesirable.

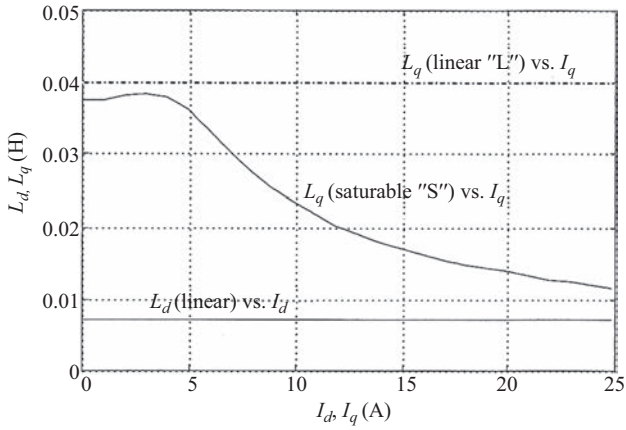


Figure 6.4 Impact of magnetic saturation on L_q as a function of i_q for a 6-kW IPM starter/alternator machine [7]

It is also worth noting that the equivalent circuits in Figure 6.3 ignore the presence of any hysteresis or eddy-current losses in either the machine lamination steel or the magnets themselves. The only machine losses that are explicitly modeled in Figure 6.3 circuits are the stator winding losses reflected in the stator resistance R_s that appears in both axes. Because the efficiency of IPM machines is typically quite high, the failure to model the iron and magnet losses is often acceptable for purposes of machine performance predictions. However, in those cases where higher accuracy is desired, the presence of these additional parasitic losses can be modeled by adding resistors in parallel with both L_d and L_q.

6.3 IPM machine torque production characteristics

6.3.1 Basics of torque production in IPM machines

The *dq*-frame representation discussed in the previous section leads to the following general expression for the instantaneous torque developed in a PMSM:

$$T_e = \frac{3p}{2}\left[\psi_{pm} i_q + i_q i_d (L_d - L_q)\right] = \frac{3pL_d}{2}\left[I_{ch} i_q - i_q i_d (\xi - 1)\right] \tag{6.8}$$

This torque expression applies to both SPM and IPM machines which becomes more apparent after studying the two terms in the torque expression more closely. Each of the two terms in (6.8) has a useful physical interpretation. The first "magnet" torque term is independent of i_d but is directly proportional to stator current component i_q which is in-phase with the back-emf $\vec{E}$. In contrast, the second "reluctance" torque term in (6.8) is proportional to the (i_d i_q) current component product and to the difference in the inductance values along the two axes (L_d–L_q). Since the SPM machine has no magnetic saliency (i.e., $L_d = L_q$), the reluctance

term vanishes, meaning that the SPM machine depends solely on the magnet torque term for it torque production. On the other hand, (6.8) emphasizes the hybrid nature of torque production in the salient-pole IPM machine because of the presence of both the magnet torque and reluctance torque terms. One important control-related implication of the presence of the reluctance torque component in the IPM machine torque expression is that, unlike the SPM machine, the IPM machine torque is no longer linearly proportional to the stator current amplitude in the presence of magnetic circuit saliency.

Please note that the presence of both magnet and reluctance torque components in the IPM machine does *not* imply its superiority in torque density over the SPM machine. The achievable torque density in any ac machine depends on other key machine design metrics, including the choice of lamination steel material and current density in the stator slots [8].

Since L_q is typically larger than L_d in IPM machines, it is worth noting that i_d and i_q must have opposite polarities in order for the second term to contribute a positive torque component. The rightmost expression for the torque in terms of the characteristic current I_{ch} and the saliency ratio ξ is another sign of the importance of these two parameters in determining the IPM machine's performance characteristics.

The relative amplitudes of the magnet and reluctance torque terms in (6.8) are set during the IPM machine design process by choosing the rotor topology and adjusting the magnet and rotor saliency dimensions in order to vary the relative amplitudes of ψ_{pm} and $(L_d–L_q)$. At one design extreme, the reluctance term entirely disappears in a non-salient surface-magnet machine when L_d equals L_q. At the other extreme, the machine design reverts to a pure synchronous reluctance machine if the magnets are removed, eliminating the magnet torque component. The effects of these design choices are particularly apparent in the high-speed regime as discussed later in this chapter.

6.3.2 *PMSM torque production characteristics in* dq *current plane*

In order to gain more insight into the torque production characteristics of the IPM machine, it is helpful to use the *dq* current plane in the synchronous rotor reference frame. That is, the observer is mounted firmly on the spinning rotor and oriented so that the magnet's north pole is directed along the positive (i.e., rightward) horizontal axis, corresponding to the positive *d*-axis. In this *dq* current plane, the *d*-axis current component i_d is plotted along the horizontal axis and the *q*-axis component i_q is plotted along the vertical axis, so that any current vector in this plane corresponds to a unique combination of i_d and i_q. This same *dq* current plane will be used repeatedly throughout the rest of this chapter because of its value for visualizing key machine parameter dependencies.

Figure 6.5 shows plots that include several constant-torque lines for both and SPM and IPM machine. Any current vector terminating on the same constant-torque line will deliver the same torque. To illustrate this concept, two vectors are drawn in Figure 6.5(a) for the SPM machine that delivers the same motoring

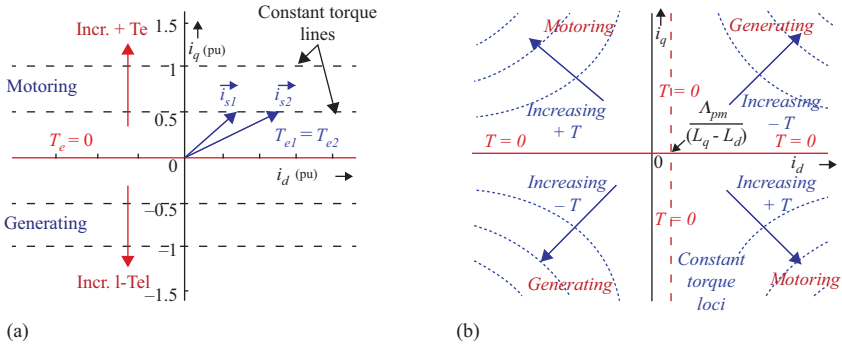


Figure 6.5 Constant-torque loci for an PMSMs in the dq current plane: (a) SPM matching and (b) IPM machine

torque. The constant-torque locus lines for the SPM machine are all parallel horizontal lines. This observation is consistent with the fact that the SPM machine produces torque that depends only on the value of i_q along the vertical axis. Any current vector that includes the same amplitude of i_q (i.e., vertical displacement in Figure 6.5(a)) will produce the same torque; the value of i_d does not matter since it does not contribute to the torque. It should be noted that the constant-torque locus line in the top half of this figure with $i_q > 0$ produce motoring torque with a positive polarity, while the locus lines in the lower half with $i_q < 0$ produce negative generating/braking torque.

The constant-torque locus lines for the IPM machine in Figure 6.5(b) have hyperbolic shapes because of the $i_d\ i_q$ product term that appears in the torque equation (6.8). The presence of the reluctance torque component in (6.8) is directly responsible for this important feature. To assist understanding, this plot and several others later in this chapter have been developed using the simplifying assumption that L_q is constant (i.e., no magnetic saturation).

The entire *dq* current plane for the IPM machine is broken into four quadrants with motoring torque in two of the diagonal quadrants and generating torque in the other diagonal pair. The differences between the SPM and IPM machines in this regard are clearly identified in Figure 6.5 via labeling of the motoring and generating regions. There are two orthogonal lines in the IPM *dq* current plane that represent the boundaries for the four torque-polarity quadrants, corresponding to the loci for zero torque. As can be seen in Figure 2.4, the horizontal axis ($i_q = 0$) serves as one of these boundaries, while the vertical line defined by $i_d = \Lambda_{pm}/(L_q - L_d)$ serves as the second zero-torque locus. Closer inspection reveals that this second zero-torque locus corresponds to the locus of all points where nonzero values of magnet torque are exactly canceled by the reluctance torque.

The PMSM drive designer is almost always challenged to achieve the highest possible drive efficiency during operation. Since the losses during low- and medium-speed operation are typically dominated by the stator current losses (i.e., magnet and iron core losses are secondary in these speed regimes), the resulting

control objective is to always develop the machine torque with the lowest possible stator current amplitude in order to minimize the stator I^2R resistive losses at all times. This control objective is almost universally referred to as maximum torque-per-Amp (MTPA) operation, and it is applied to both SPM and IPM machines.

Figure 6.7 shows the MTPA trajectories for both SPM and IPM machines side-by-side, simplifying comparisons. The MTPA trajectory for the SPM machine is particularly straightforward, consisting of a red locus line along the vertical q-axis. Figure 6.6 provides a visual definition of such a locus line for a more general case, indicating that each point along the locus line represents the terminus of a unique current vector corresponding to a particular value of torque. Looking back at the torque expression in (6.8), the magnet torque (the sole source of torque for the SPM machine) depends only on the q-axis current i_q. Applying any nonzero value of i_d does nothing to contribute to the torque, so if the objective is to generate each torque value with the least amount of current, one is quickly drawn to the conclusion that the best choice for i_d is zero for all torque values, whether motoring or generating.

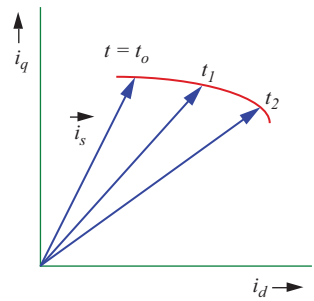


Figure 6.6 Illustration of current vector locus concept

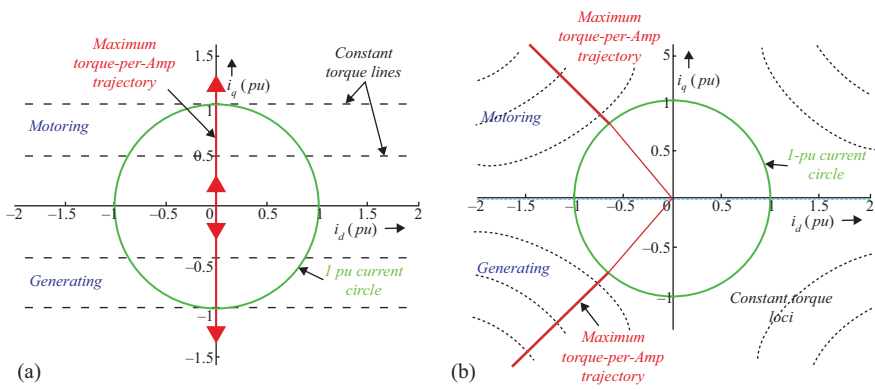


Figure 6.7 Plot of maximum torque-per-Amp (MTPA) trajectories in the dq current plane for motoring and generating operation of PMSM machines: (a) SPM machine and (b) IPM machine

As was the case for the IPM machines constant-torque locus lines in Figure 6.5, the MTPA trajectory for the IPM machine is more complicated than for the SPM machine. For the IPM machine in Figure 6.7(b), the torque increases monotonically as one moves along any of the four 45° trajectories away from the intersection of the two zero-torque loci, identified by arrows in Figure 6.7(b). Since the vertical zero-torque locus almost always occurs at a positive value of i_d for buried- or inset-magnet IPM machines (i.e., $L_q > L_d$), it can be shown that the achievable torque-per-Amp will always be higher in the second and third quadrants of Figure 2.4 (i.e., to the left of the q-axis at $i_d = 0$). As a result, IPM machine controllers for these machines are designed to operate in these two quadrants (i.e., with negative i_d) in order to maximize the efficiency of both the IPM machine and drive.

As noted above, the MTPA current vector locus, illustrated in Figure 6.6, consists of the curve traced out by the tip of the current vector $\vec{i}_s$ in the dq current plane as the torque is increased along the MTPA trajectory. This concept is used to plot the MTPA current trajectory for the IPM machine (Figure 6.7(b)), connecting all of the points in the dq current plane where each progressively higher torque amplitude is delivered using the minimum possible stator current amplitude. Two trajectories are shown emanating from the current plane origin, one corresponding to motoring operation in the second quadrant, and another for generating in the third quadrant. One helpful way to interpret the MTPA locus line is to inspect any one of the black constant-torque locus lines. The point along each locus line that is closest to the origin in the dq current plane represents the MTPA operating point for that particular value of torque. The red MTPA locus trajectory connects the MTPA operating points for each of the achievable torque values.

As a reminder, please recall that the effects of magnetic saturation are not included in this plot. Figure 6.7 and later plots in the dq current plane use normalized (per-unit) currents for both i_d and i_q. That is, all of the current values are normalized by the rated current of the IPM machine that flows when the machine is developing rated torque.

6.3.3 Current limit circle

Another feature illustrated in Figure 6.7 that will prove very useful later in the discussion of FW operation of the IPM machine at high rotor speeds is the current limit circle. Assuming that the available current from the source supplying the IPM machine is limited to 1 pu (rated current $= I_{\max}$), a locus can be conveniently drawn in the figure connecting all points that correspond exactly to this limiting condition. In fact, this current limit condition corresponds to a circle that can easily defined by the following equation:

$$i_s = \sqrt{i_d^2 + i_q^2} = 1 \qquad \text{(per unit)} \tag{6.9}$$

In order to satisfy this maximum current limit condition, the machine current vector $\vec{i}_s$ must always terminate either inside or on the current limit circle shown in Figure 6.6. Any point outside of this current limit circle corresponds to an

overcurrent condition for the source that is supplying electrical power to the machine. The ramifications of this current limit will be presented later in this chapter during the discussion of FW operation.

6.3.4 *Impact of magnetic saturation on maximum torque-per-Amp trajectories*

As noted above, the MTPA trajectories plotted in Figure 6.7 do not include the effects of magnetic saturation. However, IPM machines are almost always designed so that magnetic saturation *does* have a significant impact of the machine's electrical parameters (L_q, in particular, as shown in Figure 6.4).

One of the significant ways that the magnetic saturation is manifested in the IPM machine's performance is the developed torque and its specific dependence on the *d*- and *q*-axes current components. That is, the constant-torque locus curves in Figures 6.5(b) and 6.7(b) become distorted from their simple hyperbolic shapes because the value of L_q in the torque equation (6.8) is no longer a constant, but instead changing as a function of the *q*-axis current i_q, often with cross-coupled effects from i_d as well.

Of particular significance for purposes of operating the IPM machine at high efficiency, the MTPA trajectories shown in Figure 6.7(b) are also shifted as a result of magnetic saturation. Figure 6.8 shows an example of the change in the MTPA trajectory in the motoring regime (second quadrant) caused by including magnetic

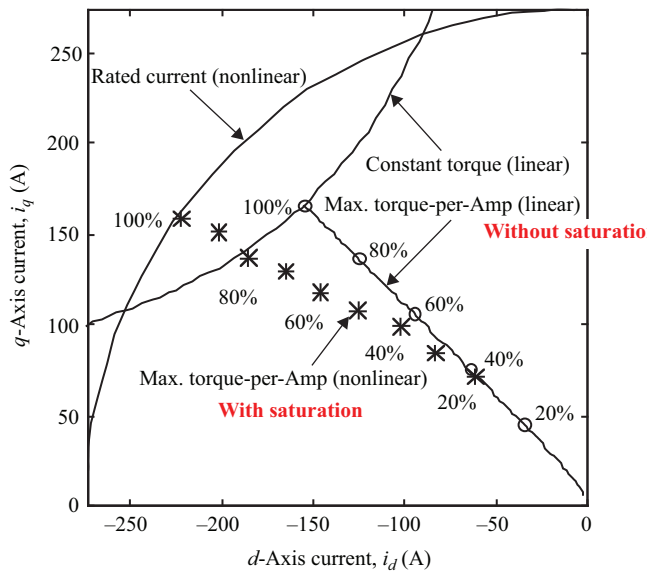


Figure 6.8 Maximum torque-per-Amp trajectories for 6-kW IPM starter/alternator machine in the motoring regime (second quadrant) both without and including the effects of magnetic saturation [7]

saturation effects for the same 6-kW IPM starter/alternator machine that provided the saturated *q*-axis inductance characteristics shown in Figure 6.4 [7].

First, it should be noted that the origin in the *dq* current plane of Figure 6.8 is located in the lower right corner. MTPA trajectories are plotted for the machine both with and without magnetic saturation, showing that the MTPA trajectory in the motoring regime swings counterclockwise in the direction of the negative *d*-axis as a result of saturation effects. It is typical for the angle of the trajectory with respect to the vertical *q*-axis (defined as angle γ) to increase from a value less than 45° to a value in the vicinity of 50°–60°. A symmetrical clockwise swing of the MTPA trajectory in the direction of the negative *d*-axis occurs for generating operation in the third quadrant.

The second major impact of magnetic saturation on torque production in the IPM machine is that a higher stator current amplitude is required to develop the same torque when saturation effects are included. For example, Figure 6.8 shows that approximately 15% higher stator current is required to develop rated torque (labeled 100%) when saturation effects are included than when they are ignored.

A natural question that arises when one first sees such comparisons is as follows: given the loss in torque-per-Amp, would it be better to design IPM machines that avoid magnetic saturation altogether? Unfortunately, so much volumetric and mass power density would be lost in the machine by designing it to avoid saturation that this approach is almost never practical to adopt. The situation is similar to that of switched reluctance machines with regard to magnetic saturation. In both cases, saturation is undesirable but unavoidable in order to achieve attractive machine power density and performance characteristics. The motor designer must simply learn to manage magnetic saturation as a fact of life in IPM machines.

6.4 Vector control of PM machine

6.4.1 Review of basic vector control principles

The basic concepts of vector control as a means of achieving high-performance torque control in PMSMs were introduced in the preceding chapter, Section 5.6. They will be reviewed briefly here and restated in a context that has been adjusted for the discussion in this chapter. More specifically, these principles will be addressed using the block diagram of a vector-controlled PMSM drive that is provided in Figure 6.9. This diagram is presented in a form that is sufficiently general to be applied to both SPM and IPM machines, but it is primarily intended to address operation at lower speeds where the drive operation is not limited by the available voltage. Extensions of this basic PMSM vector control diagram for operation in the high-speed constant-power range will be discussed later in this chapter.

The heart of this conventional vector control PMSM drive consists of a current-regulated voltage-source (VS) inverter that appears as a block on the right side of the figure. That is, the basic six-switch three-phase VS inverter incorporates pulse-width modulation (PWM) so that its three-output voltage waveforms can be

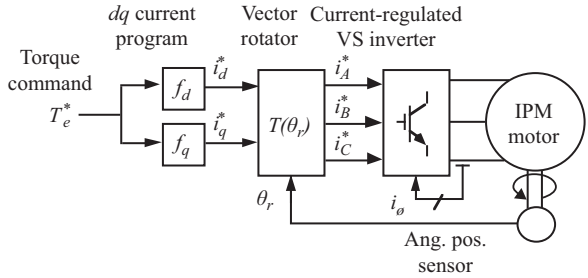


Figure 6.9 Block-diagram of vector control PMSM drive applicable to both SPM and IPM machines

conveniently modulated to adjust their amplitudes and wave shapes in addition to their fundamental frequency values. The instantaneous output phase currents are measured and closed-loop feedback control techniques are applied to control the instantaneous currents in the three machine phases (i_A, i_B, and i_C) using a high-bandwidth current regulation algorithm. It is assumed that the reader is already well acquainted with this key building block for the drive, and many suitable references are available for those who are not.

6.4.2 Application of vector control to SPM and IPM machines

In view of the nature of PMSM torque production discussion in this section, the vector control algorithm is configured to control the two current components in the synchronously rotating rotor reference frame, i_d and i_q. Accordingly, the instantaneous torque command T_e^* (commands are designated by the asterisk superscript (*)) are converted into the appropriate current commands in the rotor reference frame, i_d^* and i_q^*, based on the PMSM torque expression (6.8). In most cases, the MTPA trajectory for a given SPM or IPM machine (Figure 6.7) is used to provide the mapping of any motoring or generating/braking torque command into a unique combination of *d*- and *q*-axes current commands. This mapping is designated in Figure 6.9 by the "*dq* current program" functions f_d and f_q.

This MTPA current mapping is particularly straightforward for an SPM machine since the MTPA trajectory in Figure 6.7(a) calls for all of the stator current to be oriented along the *q*-axis with the amplitude of i_q being linearly proportional to the torque T_e. The corresponding f_d and f_q functions for the SPM machine are plotted in Figure 6.10(a) as a function of the torque command T_e^*. As shown, the value of f_d is always zero since no *d*-axis current is desired for MTPA operation, while the f_q function is a sloped straight line because of the linear proportionality feature.

In contrast, the f_d and f_q functions for the IPM machine plotted in Figure 6.10(b) are more complicated because of the presence of reluctance torque in addition to the magnet torque. Both f_d and f_q have square-root components because the reluctance torque is proportional to the *square* of the current amplitude (ignoring saturation

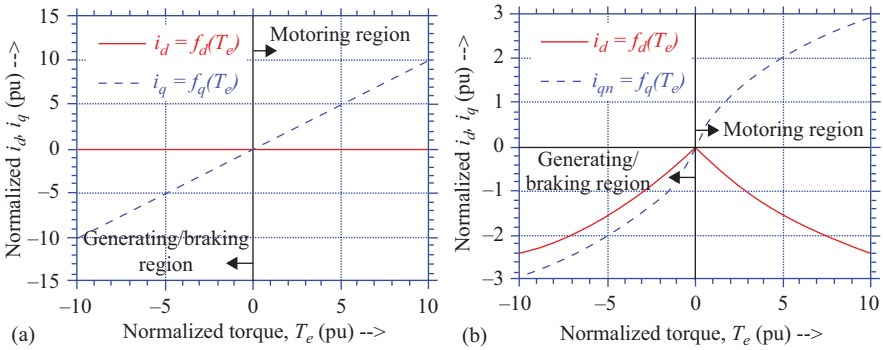


Figure 6.10 Plots of f_d and f_q functions for current command generation in vector control PMSM drive configuration shown in the figure using MTPA trajectories: (a) SPM machine and (b) IPM machine

effects), in contrast to the simpler linear proportionality of the magnet torque. It is interesting to note the contrasting symmetries of the two functions for the IPM machine, with f_d being an even function while f_q is an odd function. These characteristics are consistent with the MPTA current trajectory for the IPM machine in Figure 6.7(b), where the motoring and generating/braking segments of the MTPA trajectory are symmetrical with respect to the negative *d*-axis so that only the polarity of i_q determines the torque polarity, consistent with the features of f_d and f_q in Figure 6.10(b).

It is worth noting that the parameters defining the detailed shapes of the f_d and f_q functions must be adjusted to match those of the PMSM machine that is being controlled. That means that anything that causes the parameters of the actual machine to deviate from those programmed into the f_d and f_q functions will cause errors between the actual machine torque and the commanded value. Fortunately, this is not a major problem in many applications for a combination of reasons. First, the sensitivity of the machine torque T_e to modest or even moderate errors in the f_d and f_q functions is generally not very high, and second, any applications that close either speed or position loops around the innermost torque control loop will automatically compensate for typical errors in the gain or linearity of the torque loop. However, in those applications where high accuracy of the instantaneous torque produced the machine is required, special steps may be required to continually tune the machine parameters using techniques such as model reference adaptive control or temperature compensation algorithms.

Once the i_d^* and i_q^* current commands are generated, they have to be converted back to the stationary reference frame based on information available about the instantaneous rotor position angle θ_r. As indicated in Figure 6.9, it is assumed that this key feedback information is provided by a rotor shaft angle position sensor mounted on the shaft of the PMSM, typically taking the form of either an encoder or resolver. Unlike a squirrel-cage induction machine which does not have physically defined axes associated with the rotor because of its rotational symmetry, any

PMSM has well-defined rotor axes determined by the position and polarities of the rotor magnets. As a result, any rotor position sensor used in a PMSM vector control drive such as Figure 6.9 must be able to provide "absolute" rotor angular position to the controls so that the stator current vector can be properly oriented with respect to the instantaneous orientation of the magnet flux linkage ψ_{pm}.

The transformation of the i_d^* and i_q^* current commands from the synchronously rotating reference frame to the stationary frame is accomplished using the three equations provided previously in Chapter 5 as (5.20)–(5.22) and repeated here for convenience.

$$\begin{aligned} i_a^* &= i_d^* \cos\ \theta_r - i_q^* \sin\ \theta_r \\ i_b^* &= i_d^* \cos\left(\theta_r - \frac{2\pi}{3}\right) - i_q^* \sin\left(\theta_r - \frac{2\pi}{3}\right) \\ i_c^* &= i_d^* \cos\left(\theta_r + \frac{2\pi}{3}\right) - i_q^* \sin\left(\theta_r + \frac{2\pi}{3}\right) \end{aligned} \tag{6.10}$$

While these three equations are not particularly complicated, the fact that they include trigonometric functions and must be evaluated repeatedly in real-time means that appropriate computational resources must be allocated to perform these critical current command transformations very accurately and very quickly.

6.4.3 *Introduction to self-sensing techniques for vector control drives*

Although either shaft-mounted encoders and resolvers are standardly used in many PMSM applications, particularly in those requiring high-performance torque production for extended periods near zero speed, there is a rich and growing literature associated with self-sensing control technology that eliminates the shaft-mounted position sensors [9]. Although the term "sensorless control" is commonly used to describe this approach, "self-sensing" is a far more appropriate name since machine electrical variables including phase currents and terminal voltages are used as feedback signals to estimate the instantaneous rotor position in real time. Once the machine is spinning, the back-emf voltage generated by any PMSM is an appealing target for estimation since it provides so much information about the rotor position [10]. There are many commercial applications requiring little or no low-speed operation that use self-sensing control algorithms based on this approach, eliminating the need for expensive and fragile position sensors.

Self-sensing control algorithms that continue to work well down to machine standstill conditions depend on finding a source of rotor electromagnetic asymmetry that can be electrically sensed at zero speed. An excellent example is the magnetic saliency of IPM machines that makes it possible to accurately determine the rotor's angular position at very low speeds including standstill by detecting angular variations in the machine's phase inductance [11]. Unlike the back-emf voltage, the PMSM does not need to be spinning to measure the phase inductances, often using low levels of high-frequency voltage excitation to enable the

inductance measurements. There are many challenges associated with making these algorithms work under all of the operating conditions encountered in real-world applications. In fact, one of most powerful approaches to enhancing a drive's self-sensing capabilities is to custom design the PM machine itself to make it a better sensor [12]. As a result, research and development is continuing around the world on efforts to make this self-sensing technology sufficiently robust and low cost to qualify for demanding applications such as PM traction machines in commercially produced electric vehicles.

6.5 IPM machine capability curves

6.5.1 Basic principles

The available operating range of torque and speed values that can be delivered by any machine excited by a variable-speed drive is very important in determining the drive's suitability for specific applications. The torque and speed capabilities are ultimately determined by the machine type and parameter values combined with the limits on the voltage and current that can be supplied by the drive power electronics.

In many cases, the desired torque-speed operating envelope has features illustrated in Figure 6.11. This figure highlights the presence of the so-called constant-torque operating range at low speeds below the corner speed ω_o where the maximum torque is limited by the maximum available stator current $I_{\max}$. The voltage limit is not a factor in this low-speed operating range until the corner speed ω_o is reached at which point the envelope operating point is characterized by the machine operating simultaneously at the current and voltage limits ($V_{\max}$) simultaneously.

The drive operating regime above this corner speed is commonly referred to as the "constant-power" range even though the envelope for a particular machine

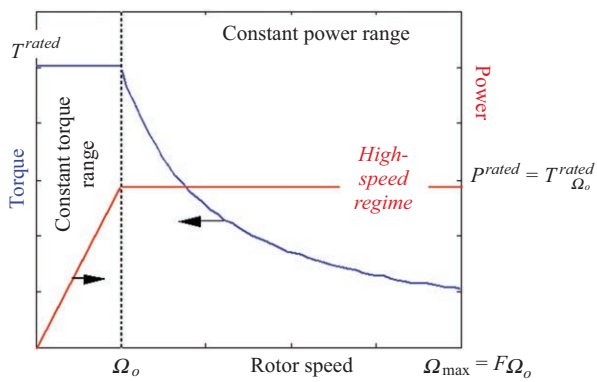


Figure 6.11 Idealized torque vs. speed and power vs. speed capability curves for variable-speed drive showing both constant-torque and constant-power ranges of operation

drive may not actually follow a constant-power trajectory. Throughout this operating range, the envelope operating points are determined by machine excitation by $I_{\max}$ and $V_{\max}$. Since the machine stator flux is determined by the ratio of the applied voltage to the excitation frequency, the fact that the voltage is constant at its limit while the speed increases means that this operating regime is characterized by reduced stator flux as the rotor speed increases. For the idealized conditions illustrated in Figure 6.11, the torque falls off as the reciprocal of the rotor speed (i.e., $1/\omega_r$) so that the delivered output power is exactly constant.

The maximum operating speed at which the machine drive can still deliver this same power is defined in Figure 6.11 as $F\omega_o$ which makes it convenient to define F as the constant-power–speed ratio (CPSR), a dimensionless parameter. In many cases, the value of F is determined by the machine parameters that cause the maximum achievable output power to drop below its rated value (P^{rated}) beyond the speed $F\omega_o$. The achievable values of CPSR vary widely among different types of machines and even among machines of the same type, depending on the details of the machine design. It should be pointed out that only certain classes of applications such as traction drives and spindle drives need wide ranges of constant-power operation, while other applications such as pumps and fans only make use of the constant-torque regime operation.

PMSMs suffer from an inherent disadvantage in applications that require a wide speed range of constant-power operation. More specifically, the magnet flux linkage ψ_{pm} is essentially fixed so that the resulting back-emf voltage E continues to increase linearly as the rotor speed is increased, despite the fact that the available terminal voltage is limited to $V_{\max}$. Unlike wound-field dc or synchronous machines, there is no direct way to reduce the field magnetic flux linkage. However, the important quantity that determines the stator terminal voltage is actually the d-axis flux linkage ψ_d that was defined in (6.5) and repeated here for convenience:

$$\psi_d = L_d i_d + \psi_{pm} \tag{6.11}$$

This equation suggests that the amplitude of ψ_d can be reduced despite the fixed nature of the magnet flux linkage ψ_{pm} by adding d-axis current with a negative polarity. This technique, referred to henceforth as FW, uses the d-axis "armature reaction" flux linkage ($L_d\, i_d$) to counteract the magnet flux linkage in order to reduce the total d-axis flux linkage ψ_d.

Although the concept of FW is not new, its usefulness is limited in many PMSMs because of machine parameter values. In particular, conventional SPM machines with distributed windings tend to be poor candidates for effective FW because the magnets behave as large air gaps in the magnetic circuit, leading to low values of d-axis inductance L_d [13–15]. Low values of L_d make it necessary to use unacceptably large values of negative d-axis current in order to achieve the desired FW at high speeds. As a result, the value of CPSR that can be achieved in many SPM machines with conventional distributed windings is 2 or less.

Before proceeding, it is worth noting that if (6.11) is solved to determine the value of *d*-axis current i_d needed to drive the *d*-axis magnetic flux linkage to zero, the answer is none other than the characteristic current with negative polarity:

$$i_d = -\frac{\psi_{pm}}{L_d} = -I_{ch} \qquad \text{for } \psi_d = 0 \tag{6.12}$$

IPM machines offer some advantages compared to SPM machines for extended ranges of constant-power operation (i.e., higher CPSR values). The underlying reason for this advantage is the fact that IPM machines inherently have an extra degree of freedom in their design that makes it possible to adjust the relative contributions of the magnet torque and the reluctance torque to the machine's total torque production. By reducing the magnet torque in favor of more reluctance torque, the value of the magnet flux linkage ψ_{pm} can be reduced significantly in comparison to its value in an SPM machine designed for the same application. As a result, the value of the IPM machine's characteristic current I_{ch} can be reduced, meaning that less *d*-axis current is needed to counteract the magnet flux linkage. This makes it significantly easier to achieve effective FW in an IPM machine, providing it a significant advantage when wide speed ranges of constant-power operation are desired. An additional value of lowering the value of the magnet flux linkage is reduction of the value of the back-emf ($E = \omega_r \psi_{pm}$) at high speeds which can otherwise reach values several times the inverter's dc link voltage in applications with high CPSR values.

More quantitative discussion of FW operation and its impact on the high-speed operating characteristics of IPM machines will be provided in the following subsections.

6.5.2 PMSM circle diagrams and capability curves

As described above, the available inverter source for an IPM machine imposes both a current limit and voltage limit that, in combination with the machine parameters, determine the machine's torque vs. speed and power vs. speed capability curves. The *dq* current plane provides the most convenient format for describing these effects [3,16]. As discussed in Section 6.3.3, the impact of the current limit is to define a circle in the *dq* current plane with a radius $I_{\max}$ such that the instantaneous current vector must always terminate either inside or on this circle in order to satisfy this constraint.

The impact of the voltage limit in the *dq* current plane takes a bit more effort to derive but yields some rich insights. Similar to the constraining current relationship expressed in (6.9), the voltage vector length cannot exceed the limiting value $V_{\max}$. If the voltages are normalized using $V_{\max}$ as the rated voltage and base voltage, the limiting equation is

$$V_{\max}^2 = 1 = v_d^2 + v_q^2 \quad \text{(pu)} \tag{6.13}$$

The steady-state equations for the *d*- and *q*-axes stator voltages expressed in terms of corresponding axis currents can then be substituted into (6.13) to derive the

desired constraint in the *dq* current plane. More specifically, the stator voltage equations in (6.5) can be evaluated for steady-state conditions by setting the *di*/*dt* terms to zero. In addition, the resistive voltage drop terms in the stator voltage equations will be deleted because they are invariably much smaller than the cross-coupled back-emf voltage terms at high speeds. The resulting *d*- and *q*-axes steady-state voltage equations in normalized form are

$$v_d = -\omega L_q i_q \quad (\text{V or pu}) \tag{6.14}$$

$$v_q = \omega(L_d i_d + \psi_{pm}) \quad (\text{V or pu}) \tag{6.15}$$

where ω is the per-unit excitation frequency (and rotor angular frequency) in per unit, normalized by the frequency at the corner operating point (Ω_0 in Figure 6.11).

The voltage limit equation in the *dq* current plane can then be derived by substituting (6.14) and (6.15) into (6.9) and dividing through by $\omega^2 L_d^2$, leading to

$$\left(i_d + \frac{\psi_{pm}}{L_d}\right)^2 + \left(\frac{L_q}{L_d}\right)^2 i_q^2 = \left(\frac{V_{\max}}{L_d}\right)^2 \frac{1}{\omega^2} \qquad (\text{V or pu}) \tag{6.16}$$

This expression can be simplified by applying the definitions for the characteristic current and saliency ratio in (6.6) and (6.7), leading to

$$(i_d + I_{ch})^2 + \xi^2 i_q^2 = \left(\frac{V_{\max}}{L_d}\right)^2 \frac{1}{\omega^2} \qquad (\text{V or pu}) \tag{6.17}$$

Depending on the value of the saliency ration, this voltage limit equation defines either a circle for an SPM machine ($\xi = 1$) or an ellipse for an IPM machine ($\xi \neq 1$) in the *dq* current plane. Figure 6.12 shows a family of voltage limit ellipses for an IPM machine, where each ellipse corresponds to a different value of ω. It should be noted that each ellipse is centered on the negative *d*-axis at $i_d = -I_{ch}$ with major and minor radii of $V_{\max}/(L_d\omega)$ and $V_{\max}/(L_q\omega)$ oriented in the *d*- and *q*-axes directions, respectively. The effects of magnetic saturation are ignored in

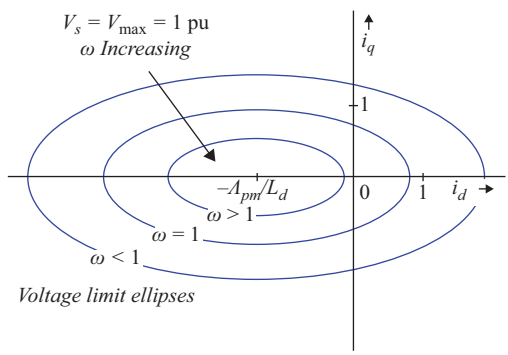


Figure 6.12 Voltage-limit ellipses in the dq current plane, with normalized rotor angular frequency ω as a parameter

this graphical representation of the voltage limit constraint. Similar to the case of the current limit constraint, all current vectors terminating either on or inside the ellipse satisfy the voltage constraint.

Unlike the current limit constraint in (6.9), the voltage limit constraint in (6.16) or (6.17) includes the rotor angular frequency (i.e., excitation frequency) ω so that that both the major and minor radii of the voltage limit ellipse are inversely proportional to this frequency. At any particular speed, the dimensions of the voltage ellipse are fixed. However, both radii of the ellipse gradually shrink as the rotor speed increases as shown in Figure 6.12, although the center of the ellipse never moves from $i_d = -I_{ch}$. This means that the available range of stator current vectors is increasingly limited as the speed increases. The equivalent diagram for an SPM machine would be identical to Figure 6.12 except that the ellipses would be circles.

In the actual drive, any PMSM must simultaneously satisfy the voltage and current limit constraints at all times. That is, the acceptable operating area in the *dq* current plane for the stator current vector at any particular rotor speed value is anywhere in the intersection of the current limit circle and the voltage limit ellipse (or circle) that applies for that particular speed. This concept is illustrated in Figure 6.13 for an IPM machine. The shaded area in the figure shows the acceptable region in the current *dq* plane for stator current vectors to terminate for the highest of these three speeds, ω_3, consisting of the interaction of the current limit circle and the voltage limit ellipse corresponding to ω_3. An example of a current vector i_s terminating in this region is included in the figure.

When the speed is low, the radii of the voltage limit ellipse are sufficiently large and the intersection area consists of the entire current limit circle. This is an illustration of the fact that only the current limit constraint is active in setting the capability curve envelope during constant-torque operation at low rotor speeds

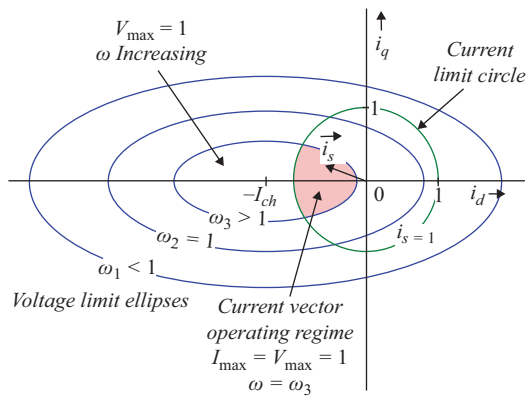


Figure 6.13 Interaction of current limit circle and voltage limit ellipses associated with an IPM machine for three increasing rotor speed values from ω_1 to ω_3, illustrating the current vector operating regime for rotor speed ω_3 as the shaded circle/ellipse intersection area

below the corner point speed (see Figure 6.11). In this regime, the maximum torque operating point on this envelope consists of the intersection of the MTPA trajectory and the current limit circle (i.e., the point identified 100% in Figure 6.8, including the effects of magnetic saturation).

When operating on the envelope of the capability curve, the operating point will stay at this intersection point of the MTPA trajectory and current limit circle as the speed gradually increases. This condition persists until the voltage limit ellipse shrinks sufficiently in size so that the ellipse intersects this same maximum torque operating point as well. This condition occurs at the corner point speed ω_o (see Figure 6.11) at which the drive transitions between the constant-torque and constant-power regimes. Under these conditions, the machine is delivering its maximum possible torque while simultaneously operating at its voltage and current limits ($V_{\max}$ and $I_{\max}$).

As soon as the rotor angular frequency increases above the corner point value ω_o, the machine can no longer operate at its maximum-torque point because the shrinkage of the voltage limit ellipse causes this point to lie outside it, making it inaccessible for steady-state operation. For this particular case, the best the drive can do to deliver the highest possible torque at each increasingly higher rotor speed is for the machine operating point to follow the intersection point of the shrinking voltage ellipse and the current limit circle.

As the speed increases so that the operating point moves counterclockwise along the current limit circle (assuming motoring operation), the amplitude of the negative *d*-axis current increases while the *q*-axis current decreases. This gradual increase in negative *d*-axis current corresponds to higher levels of FW as the rotor speed increases, consistent with the process described earlier in Section 6.4.1.

6.5.3 Three cases of PM machine capability curves

Based on the concepts introduced in the previous subsection, there are three distinct cases of PM FW operation that deserve discussion [4,16] differentiated by the values of the PM machine's characteristic current I_{ch}. These three cases will serve to highlight the importance of the characteristic current in determining the machine's high-speed performance capabilities.

An IPM machine is adopted for introducing these three cases, but the definitions are the same for an SPM machine. The only difference in the *dq* current plane figures is that voltage limit ellipses for the IPM machine are replaced by voltage limit *circles* for the SPM machine. The change in the shape of the resulting power vs. speed capability curve for each of the three cases is minor when drawn for the SPM machine, provided that the per-unit values of the *d*-axis inductance L_d and the characteristic current I_{ch} are the same in both machines.

6.5.3.1 Case 1: $I_{ch} > I_{\max}$

If the IPM machine characteristic current I_{ch} is greater than the current limit $I_{\max}$, it can be shown that there is a finite maximum rotor speed above which the IPM machine cannot operate and deliver any useful average torque. The reason for this

behavior becomes quite apparent by inspecting the migration of the machine's operating point at high speeds in the *dq* current plane, an example of which is provided in Figure 6.14(a). In this particular case, the value of the characteristic current is 30% higher than the maximum current limit.

As discussed in the preceding subsection, the machine operating point will migrate clockwise along the current limit circle at speeds above the corner point speed ω_o, tracking the intersection of the current limit circle and the voltage limit ellipse at each progressively higher value of rotor speed. Eventually, the rotor speed reaches a sufficiently high value that the intersection of the current limit circle and

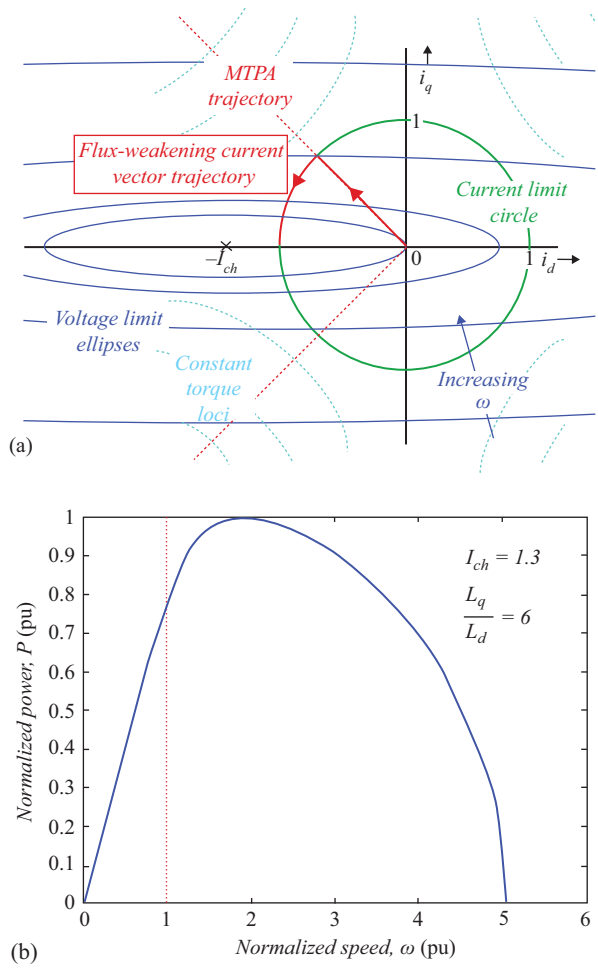


Figure 6.14 Case 1: (a) Flux-weakening current vector trajectory when $I_{ch}>I_{max}$ and (b) Case 1 power vs. speed capability curve (conditions: $\xi = 6$, $I_{ch} = 1.3$, $I_{max} = V_{max} = 1$)

the voltage limit consists of a single point with the rightmost edge of the voltage limit ellipse falling on the leftmost edge of the current limit circle ($i_d = -1,\ i_q = 0$).

Figure 6.14(b) provides the resulting power-vs.-speed capability for the Case 1 conditions, showing that the available power from the machine peaks at a rotor speed in the vicinity of 2 pu. The machine's available power falls sharply as the speed increases beyond 2 pu, dropping to zero in the vicinity of 5 pu. The CPSR for this particular set of machine parameters is approximately 3.5 based of the definition presented earlier in Section 6.4.1 (i.e., the output power falls to the same value as the output power at the corner point speed at approximately 3.5 pu rotor speed).

If $I_{\max} = V_{\max} = 1$, (6.17) can be readily solved for the case ($i_d = -1$, $i_q = 0$) to determine this maximum rotor speed at which the torque drops to zero:

$$\omega_{\max} = \frac{1}{L_d(I_{ch} - 1)} \qquad \text{(pu)} \tag{6.18}$$

This relationship indicates that the upper limit on the rotor speed range under Case 1 conditions drops inversely with the characteristic current. This observation is particularly important with respect to the SPM machines which obey this same relationship, since the value of the characteristic current in SPM machines can be significantly greater than 1 pu. This provides some insight into why the CPSR value for SPM machines with conventional distributed windings is often quite low, as discussed previously in Section 6.4.1.

6.5.3.2 Case 2: $I_{ch} = I_{\max}$

Equation (6.18) indicates that the maximum limit on the rotor speed will increase if the machine's characteristic current can be reduced. In fact, (6.18) suggests that the maximum rotor speed becomes infinite for the limiting case of equality between the machine's characteristic current and the current limit (i.e., rated current). This is a very important condition that can be considered optimum for FW operation, expressed for the general case as follows in terms of the rated current I_{rated} ($= I_{\max} = 1$, pu):

$$\textit{Optimum Flux Weakening Condition}: I_{ch} = \frac{\psi_{pm}}{L_d} = I_{rated} \qquad \text{(V or pu)} \tag{6.19}$$

Figure 6.15(a) shows the *dq* current plane for an example of Case 2 conditions with $I_{ch} = I_{\max} = 1$. For this special case, the center of the voltage limit ellipse lies right on the leftmost point of the current limit circle ($i_d = -1$, $i_q = 0$). As a result, the intersection of the current limit circle and the voltage limit ellipse never drops to the null set as the speed increases to any elevated value, despite the shrinkage in size of the ellipse. Thus, the operating point is able to follow the current limit circle clockwise at its intersection with the voltage limit ellipse all the way down to negative *d*-axis. As shown in Figure 6.15(b), the output power asymptotes to a constant value as the rotor speed continues to increase, reflecting the fact that the drop in torque is being exactly compensated by the increase in speed so that the output power is staying nearly constant. As a result, the CPSR for this optimal FW condition is infinite.

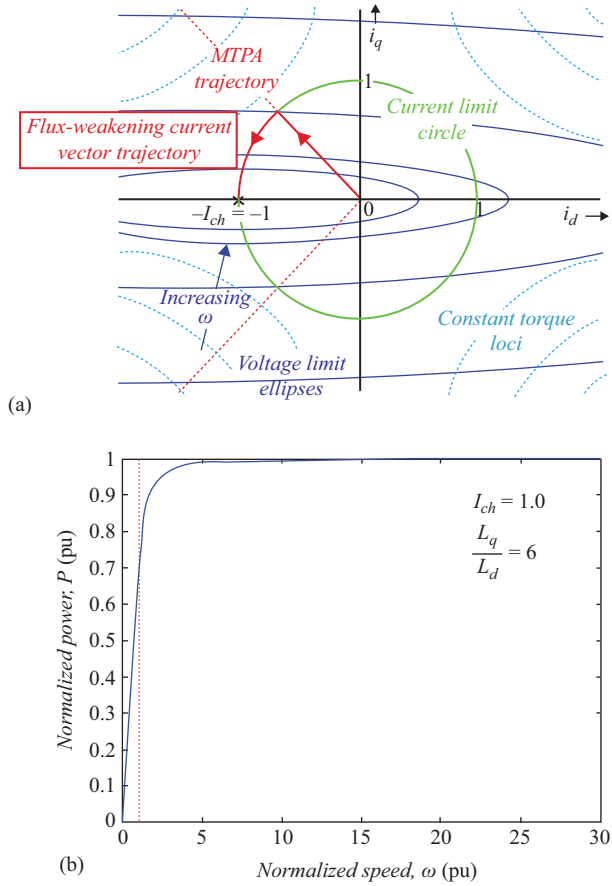


Figure 6.15 Case 2: (a) flux-weakening current vector trajectory when $I_{ch} = I_{max}$ and (b) Case 2 power vs. speed capability curve (conditions: $\xi = 6$, $I_{ch} = 1.0$, $I_{max} = V_{max} = 1$)

Another manifestation of the optimal nature of this FW condition is the fact that the machine power factor approaches 1 (unity power factor) at high speeds so that the per-unit power asymptote is also 1 per-unit. This is clearly desirable from the standpoint of achieving the highest possible inverter utilization as well as efficiency maximization.

Of course, the conditions described above are idealized because no losses are included, making the limiting case of infinite CPSR unrealizable. Nevertheless, it has been shown that it is possible to design PM machines (SPM and IPM) that can achieve high values of CPSR of 7 or higher [3] by closely matching the value of the machine's characteristic current to its rated current. Achieving this condition is a task for the machine designer, and some additional insights into the requirements for achieving optimal FW will be discussed in Section 6.5.

6.5.3.3 Case 3: $I_{ch} < I_{max}$

The final case that needs to be considered is associated with the conditions of characteristic current values that are less than the current limit value. This is a realistic condition that can be encountered in some PM machine designs. One example is an IPM machine that is dominated by reluctance torque production so that the magnet torque contribution is comparatively small. One example of application requirements that forces the machine design in this direction is tight limits on the maximum back-emf that the machine can generate at the maximum rotor speed. This case is less likely to occur in SPM machines because the absence of reluctance torque tends to bias SPM machine designs in the direction of higher values of characteristic current dominated by high values of magnet flux linkage ψ_{pm}.

Figure 6.16(a) shows the *dq* current plane for an example of Case 3 conditions with a relatively low value of characteristic current ($I_{ch} = 0.45$ pu). One similarity between this case and Case 2 discussed above is that the intersection of the current limit circle and the voltage limit ellipse never shrinks to the null set as the rotor speed increases to any finite value. This suggests that the deliverable output power will never drop to zero at any speed, unlike the characteristics observed in Case 1 with $I_{ch} > I_{max}$.

However, the fact that the center of the voltage limit ellipses lies inside the current limit circle means that there will be a finite rotor speed above which the voltage limit ellipse no longer intersects the current limit circle. As a result, it is impossible to follow the optimum FW trajectory for the current vector as shown previously in Figure 6.15(a). In fact, closer investigation shows that, under Case 3 conditions, there is a finite rotor speed above which it is best to move the stator current vector inside the current limit circle in order to extract the maximum machine torque in this speed regime. More specifically, the operating point resides at the point on the voltage limit ellipse where the torque is maximum in this high-speed regime.

This behavior can be observed in Figure 6.16(a) which shows that the amplitude of the stator current drops below the current limit value of 1 pu at sufficiently elevated speeds. In the limit of infinite speed, the current vector is oriented along the negative *d*-axis current with an amplitude equal to the characteristic current.

Figure 6.16(b) shows the resulting power vs. speed capability curve for this Case 3 condition. It is interesting to note that the maximum available output power peaks at a speed slightly above the corner point operating speed and then falls as the speed increases, asymptoting to a nonzero power level at high speeds. In fact, closer examination shows that the amplitude of this output power asymptote exactly equals the value of the characteristic current when both quantities are expressed as per-unit values. Thus, lowering the characteristic current below the current limit value has a detrimental effect on the output power that can be delivered at high speeds that is directly tied to the design value of the characteristic current itself.

6.5.3.4 High-speed capability curves for surface PM machines

Although the three cases identified in the preceding discussion of high-speed capability curves for PM machines were all introduced using IPM machine parameters, these case definitions apply equally well to SPM machines, as noted at the beginning of Section 6.5.3. For completeness, an example of Case 1 FW operation for an

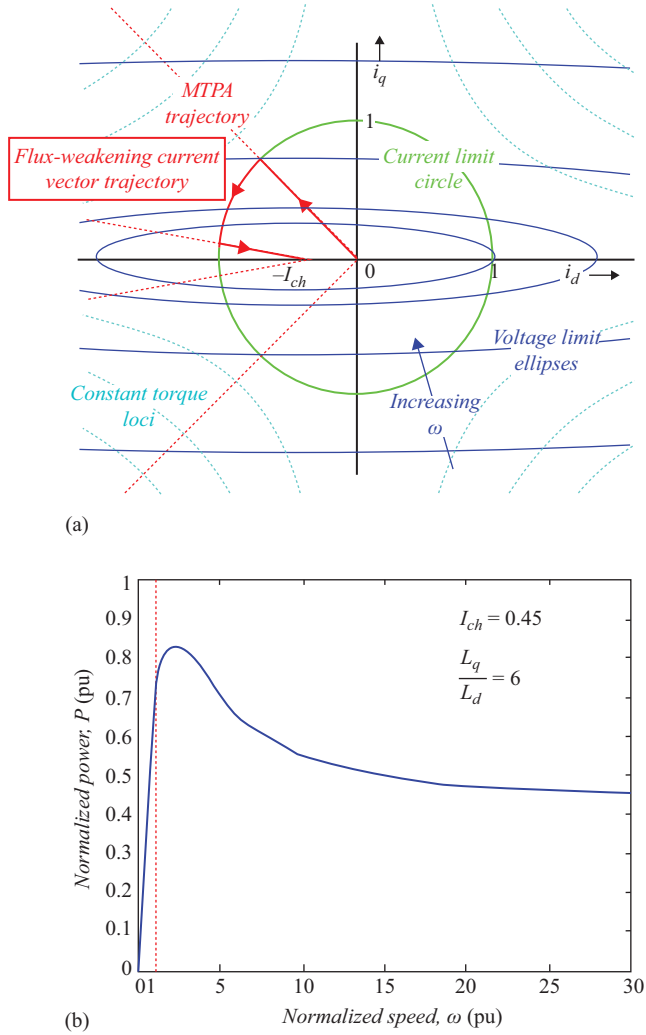


Figure 6.16 Case 3: (a) flux-weakening current vector trajectory when $I_{ch}<I_{max}$ and (b) Case 3 power vs. speed capability curve (conditions: $\xi = 6$, $I_{ch} = 0.45$, $I_{max} = V_{max} = 1$)

SPM machine with $I_{ch}>I_{\max}$ is provided in Figure 6.17 for comparison with the Case 1 operating characteristics for an IPM machine presented previously in Figure 6.14. In both cases, the value of the characteristic current I_{ch} is 1.3 pu, but the saliency ratio values ξ for the two machines are very different: ξ=6 for the IPM machine, compared to $\xi = 6$ for the SPM machine. This difference results in the voltage limit outlines taking the form of elongated ellipses for the IPM machine and circles for the SPM machine. Despite this significant difference, the resulting

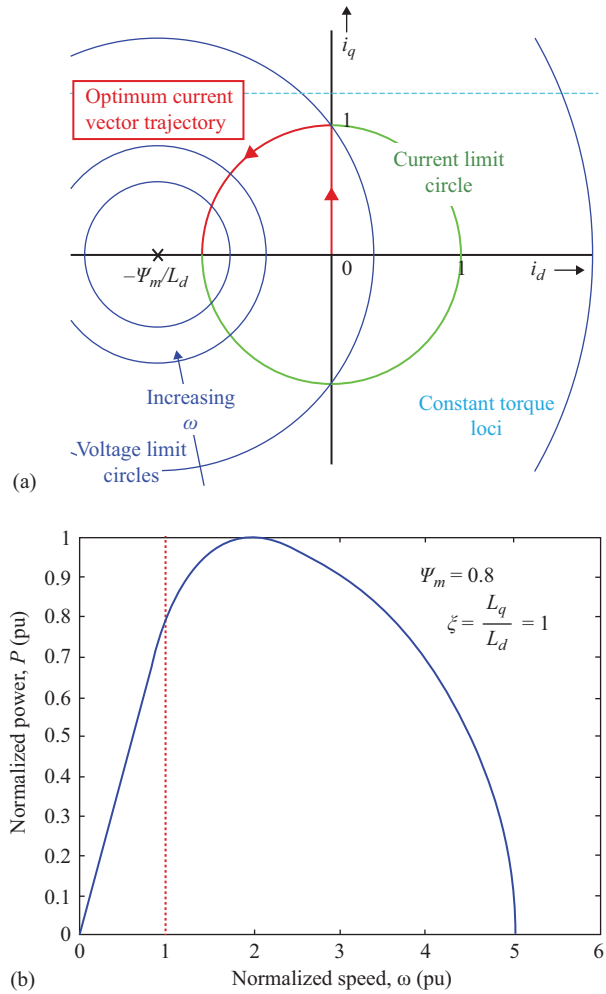


Figure 6.17 Case 1 (SPM): (a) flux-weakening current vector trajectory when $I_{ch} = I_{max}$ and (b) Case 1 power vs. speed capability curve (conditions: $\xi = 1$, $I_{ch} = 1.3$, $I_{max} = V_{max} = 1$)

power vs. speed capability curves in Figures 6.14(b) and 6.17(b) appear to be identical. This insensitivity of the shape of the high-speed power vs. speed capability curve to the value of the machine's saliency ratio (i.e., SPM vs. IPM machine) applies to cases 2 and 3 as well.

6.6 PM machine design space

Discussion in the preceding sections suggests that the PM machine's PM flux linkage and the inductance saliency ratio play key roles in determining the

machine's key operating characteristics, including its compatibility with FW to achieve extended high-speed operation. In fact, previous work [16] has shown that by normalizing the PM machine using corner point operation to define 1 pu voltage, 1 pu current, and 1 pu frequency, it is possible to reduce the number of independent IPM machine parameters to just the two parameters: normalized magnet flux linkage ψ_{pm} and the inductance saliency ratio ξ. Since high-speed operation is the principal focus of this discussion, the stator resistance is assumed to be negligible and ignored for the moment as a third independent machine design parameter.

If the number of free machine design parameters is reduced to two, it is convenient to develop a two-dimensional plot that captures all possible combinations with the normalized magnet flux linkage on the abscissa (x-axis), and the saliency ratio on the ordinate (y-axis). Actually, the ordinate axis in Figure 6.18 is shifted so that the plane covers all values of saliency ratio greater than one. PM machines with saliency ratios less than one represent a special class of machines that have been the subject of some recent investigations [17], but they are not reflected in this figure or this discussion.

When the design space in Figure 6.18 is explored to determine the FW capabilities of all possible combinations of ψ_{pm} and $\xi(>1)$, some very interesting insights emerge. In particular, there is a locus of machine designs that all exhibit nearly identical optimum FW (OFW) operating characteristics (refer to Figure 6.18). That is, any IPM machine designed using a combination of ψ_{pm} and ξ values that falls

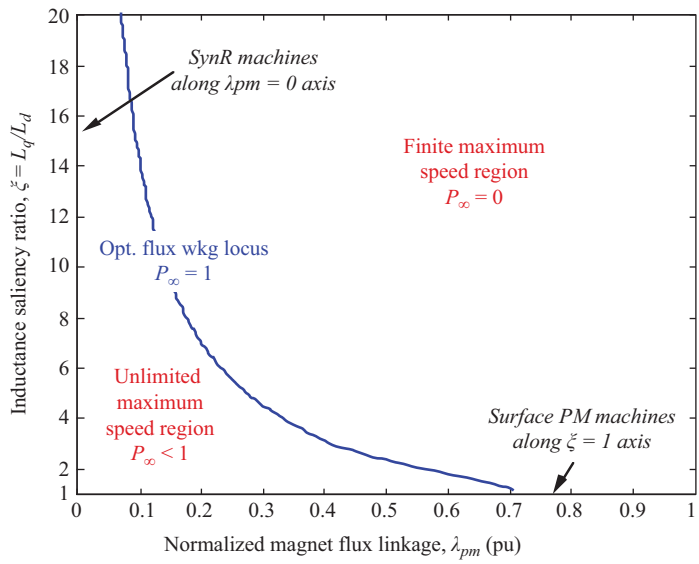


Figure 6.18 PM machine design space displayed as plane of magnet flux linkage vs. inductance saliency ratio, showing locus of designs exhibiting optimum flux weakening

on this locus line is capable of achieving wide speed ranges of constant-power operation with an output power that asymptotes to 1 pu as the speed increases above the corner point speed. Further investigation reveals that every point along this locus line corresponds to a PM machine having a characteristic current I_{ch} value of 1 pu.

The existence of this OFW locus is very important since it means that there is considerable flexibility available to the machine designer to develop a PM machine that meets the conditions for OFW. Unfortunately, other performance specifications and design constraints imposed in addition to the high-speed performance characteristics typically intrude to significantly constrain the range of acceptable ψ_{pm}–ξ combinations for a given application.

There are several other important insights that can be drawn from Figure 6.16. Machine designs falling to the right of the OFW locus have finite speed ranges with the output power falling to zero beyond a determinate maximum speed value. The farther one moves away from the OFW line, the lower the value of this maximum speed in per-unit.

Conversely, designs to the left of the OFW locus have (ideally) infinite speed ranges of nonzero power, although the value of this high-speed power (P_{∞} in Figure 6.18) is less than 1 pu. Similar to the trend described above to the right of the OFW locus, the farther one moves away from the locus to the left of the line, the lower the value of the available output power in pu.

It should be noted that the ψ_{pm}–ξ plane in Figure 6.18 covers a very wide range of synchronous machine designs. For example, machine designs along the ordinate axis (i.e., $\psi_{pm} = 0$) correspond to the family of synchronous reluctance machines with no magnets. The shape and position of the OFW locus line reflects the fact that synchronous reluctance machines always fall into the category of machines having infinite constant-power speed ranges, although the value of P_{∞} will always be less than 1 pu for finite values of ξ.

Machines falling along the abscissa axis ($\xi = 1$) in Figure 6.18 correspond to the family of non-salient SPM machines (i.e., $L_d = L_q$). Unlike the case of the synchronous reluctance machines discussed above, the OFW locus line intersects with the $\xi = 1$ axis, indicating that an SPM machine *can* be designed to achieve OFW conditions. This can be achieved by properly adjusting the value of the magnet flux linkage to approximately 0.71 pu.

Unfortunately, the value of the per-unit machine inductance needed to achieve this OFW condition in SPM machines is also 0.71 pu (i.e., the characteristic current corresponding to the ψ_{pm}/L_d ratio will be 1 pu). This is a high value of per-unit inductance for standard SPM machines that typically cannot be achieved using conventional distributed windings. The reason is that the magnets act as large air gaps in the machine's electromagnetic structure when the phase inductance is being calculated, acting to drive the inductance value downward. As a result, the majority of conventional SPM machines fall on the $\xi = 1$ axis to the right of the OFW intersection with ψ_{pm} value higher than 0.71 pu, meaning that they fall into the regime of machines with finite speed ranges of constant-power operation.

However, if the conventional distributed stator windings with integral slot-per-pole-per-phase values are replaced with concentrated tooth windings using low

fractional slot-per-phase-per pole values (<0.5), SPM machines can be designed to achieve the OFW condition of $I_{ch} = 1$ pu [18]. Leakage inductance components contributed by the spatial harmonic magnetic fields in the air gaps plus elevated slot leakage components are responsible for substantially raising the phase inductance values in these fractional slot, concentrated winding SPM machines. This approach makes it more practical to consider SPM machines for demanding applications that require wide speed ranges of constant power operation.

Finally, it critically important to note that there is no way to dodge the PM machine design issues associated with the characteristic current issue if wide speed ranges of constant-power operation are required for the PM machine drive. No amount of clever FW control algorithm design can make up for fundamental deficiencies in the PM machine's design that severely penalize the machine's torque and power vs. speed capability curves. This is a classic manifestation of the fact that designing high-performance machine drives requires a refined *systems engineering* perspective that requires integrated consideration of design issues involving the machine, power electronics, and controls.

6.7 Flux-weakening control of PM machines

6.7.1 Introduction to basic principles of flux-weakening control

The vector control principles introduced in Section 6.4 for operation at speeds below the corner speed ω_o are well established and widely adopted in PM machine drives around the world, despite many variations in implementation details. In contrast, the control algorithms that have been developed for FW operation of PM machines at high rotor speeds in the constant-power regime are more specialized and varied. A comprehensive treatment of this important topic would likely require a complete dedicated book by itself, making it necessary to limit the scope to an introduction of key features and alternatives in this chapter.

A reader new to this topic may wonder why this topic is so complicated since Section 6.5 lays out a roadmap identifying the desired current trajectory during FW operation for each of the three PM machine design cases (i.e., $I_{ch} > I_{\max}$, $I_{ch} = I_{\max}$, and $I_{ch} < I_{\max}$). Unfortunately, this view oversimplifies the challenges associated with FW control for a combination of reasons. For example, the current trajectories correspond only to operating points along the envelope of the machine's torque or power vs. speed capability curves in Figures 6.14(b), 6.15(b), and 6.16(b), and not to all of the valid operating points that lie *inside* these envelopes. This requires a seamless transition between normal vector control operation as discussed in Section 6.5 and FW operation.

Figure 6.19(a) illustrates the limitations imposed by not taking advantage of FW operation, using an IPM machine for this example. Three voltage ellipses are shown corresponding to three progressively higher speeds, causing the ellipses to shrink in size. The MTPA current trajectory for motoring operation is also drawn in the second quadrant of the *dq* plane. If the machine is being operated using only

MTPA-based vector control without FW, the *dq* current-operating point corresponding to maximum available torque for the lowest of the three speeds is shown at the intersection of the MTPA trajectory and the ellipse labeled $\omega<1$. If the speed is increased, the operating point for maximum torque would be forced to recede along the MTPA locus line, tracking the intersection of each progressively smaller voltage ellipse and the MTPA line. For example, the intersection of the MTPA line with the voltage ellipse $\omega = 1$ illustrates the migration of the maximum torque operating point back toward the origin. Eventually, the speed rises high enough so that the voltage ellipse no longer includes the origin (e.g., $\omega>1$), indicating the machine's torque and power vs. speed capabilities curves have dropped to zero.

By introducing FW operation, the machine's torque and power vs. speed capability curve can be significantly expanded beyond the one achieved using MTPA-based vector control alone. Figure 6.19(b) illustrates the basic concepts associated with FW control. Assume that the machine is operating at 1 pu speed ($\omega = 1$), imposing the voltage ellipse constraint shown in the figure. If the torque command is gradually increased from zero, the machine initially operates along the MTPA trajectory using MTPA-based vector control. Eventually the *dq* current-operating point moves far enough along the MTPA line to intersect the voltage ellipse. Rather that accepting this operating point as its maximum torque/power operating point for this speed, the control algorithm changes mode into FW control so that the *dq* current-operating point follows along the voltage ellipse in the counterclockwise direction. The torque (and power) developed by the machine will continue to monotonically increase as the operating point moves along the voltage limit ellipse, although not as rapidly as it would have for each increment of current amplitude (i.e., distance from the origin) as it would have along the MTPA trajectory line.

It should be noted that this motion along the voltage ellipse periphery requires *d*-axis current i_d to be increased in the negative polarity (i.e., $i_d<0$), while the *q*-axis current i_q changes very little. In fact, i_q actually begins to decrease modestly during FW operation as the torque command increases, causing the *dq* current-operating point to move further to the left in Figure 6.19(b) along the ellipse.

Eventually, the torque available from the machine during FW operation reaches its maximum value when the *dq* current-operating point intersects with the dashed maximum-torque-per-Volt (MTPV) line that is also plotted in Figure 6.19(b). Although the derivation of the MTPV line is not included here, it can be shown that the output torque and power will peak and actually start to drop again if the *dq* operating point moves too far along the voltage limit ellipse in the second quadrant. In fact, the output torque/power eventually drops to zero when the *dq* operating point reaches the negative *d*-axis (i.e., $i_q = 0$), consistent with the machine's torque equation (6.8).

In summary, the solid red line if in Figure 6.19(b) shows the complete *dq* current trajectory during motoring operation at $\omega = 1$ pu, clearly illustrating the transition from MTPA-mode operation for low torque commands to FW operating at high torque commands. When the speed changes in the high-speed regime, these general characteristics of transitioning between MTPA and FW control do not change, but the

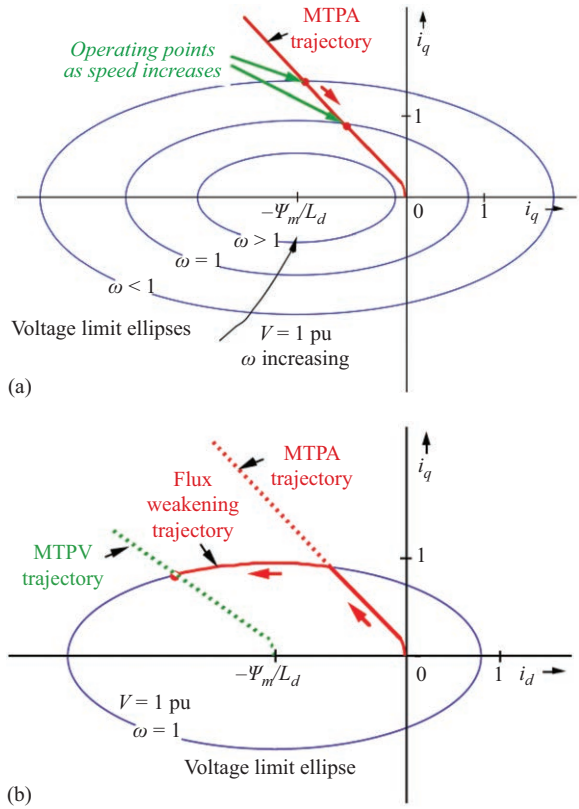


Figure 6.19 Plots of dq current plan introducing flux-weakening control concepts: (a) operation without flux-weakening control using only maximum-torque-per-Amp (MTPA) current trajectory (motoring) and (b) impact of flux-weakening control illustrating transition between MTPA and flux-weakening control regimes

details of the trajectory do change because of the changing ellipse dimensions. If the IPM machine used for these examples is replaced by an SPM machine, all of the same FW control features apply except that the voltage limit ellipses are replaced by circles. For generating operation, all of the same principles apply but the current trajectories are mirrored about the negative i_d axis from the second quadrant (upper left) of the *dq* current plane into the third quadrant (lower left). A generating mode example of FW mode operation will be discussed later in this section.

6.7.2 Feedforward vs. closed-loop flux-weakening control algorithms

As noted in the preceding subsection, there are many different version of FW control that have been developed for PM machines in a wide range of applications.

Although very few of them will be discussed in detail in this section, some of the key differences between major classes of these control algorithms will be identified in order to provide deeper insights into the most important FW control approaches.

One of the most important of these classifications that will be discussed here is the difference between feedforward (open-loop) and closed-loop FW control algorithms. First, it must be acknowledged that there are several other control applications in the field of electric machine control that are subject to this same type of feedforward vs. closed-loop algorithm classification, but FW control provides an excellent opportunity to explore this topic.

When approaching the task of developing an FW control algorithm, one of the key questions that arises is how to identify the proper conditions for transitioning the current trajectory in Figure 6.19(b) from MTPA-mode operation at low torque command levels to FW-mode operation at higher torque command levels. A closely related question is how to determine the FW control current trajectory to follow since it is highly sensitive to machine speed and other drive variables such as the inverter dc link voltage.

6.7.2.1 Feedforward flux-weakening control

One of the early generation of FW control algorithms that adopted the feedforward approach will be used here to illustrate this concept. Developed by Morimoto *et al.* [15], this algorithm uses the knowledge of the PM machine and drive parameters to precalculate the current trajectories and their transition points and then uses a minimum of sensor information, specifically the rotor speed, to implement the FW control over the complete high-speed operating regime. Figure 6.20 shows the block diagram of the resulting IPM machine speed control algorithm that includes a flowchart (in yellow) defining the series of steps used to determine both the instantaneous operating mode and the appropriate current trajectories for each mode. There are embedded decision blocks inside this flowchart that use the instantaneous measured rotor speed and, effectively, the torque command to determine whether the current trajectory for the FW operating mode (left half of flowchart) or the MTPA operating mode (right half) is activated for every operating point.

The flowchart also includes blocks for calculating the appropriate *d*-axis current command i_d^* for each of the operating modes based on closed-form machine equations found in the associated reference (not included here) to continually update their values in real time. One of the limitations of these closed-form equations is that they depend on using fixed machine parameters that do not include the impact of important nonlinearities such as magnetic saturation. Alternatively, it is possible to incorporate such nonlinearities by calculating these key current values numerically offline and then using fast look-up tables to evaluate them in real time.

Note: Equation numbers in the flowchart refer to equations found in [19] but not reproduced in this chapter.

Figure 6.21 shows a plot of the measured *dq* current values for this feedforward FW control algorithm in the synchronous rotor reference frame during operation at a high speed above the machine's corner speed, taken from the

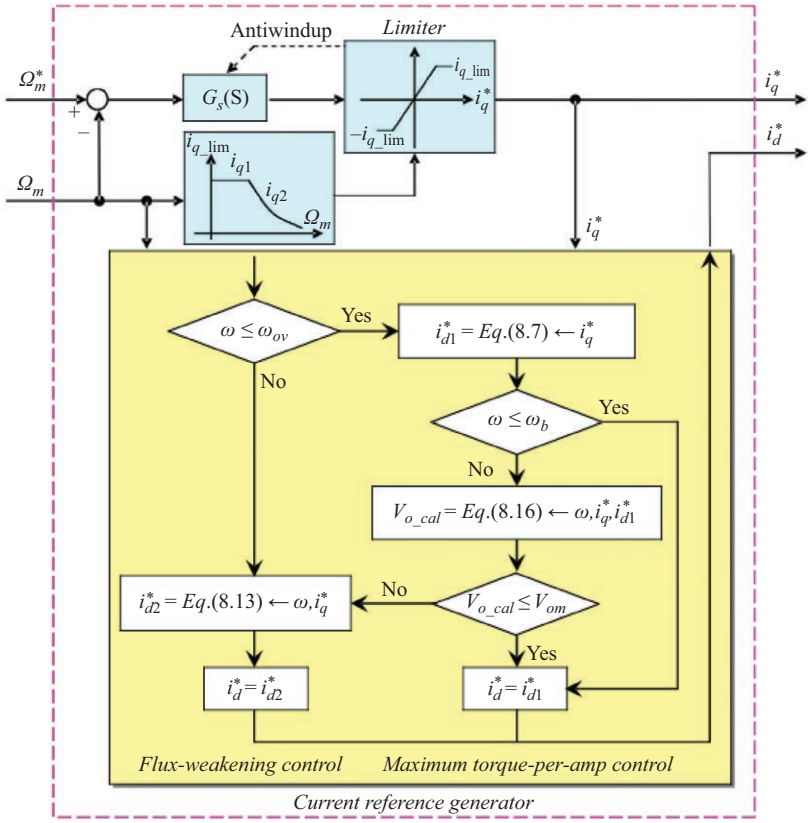


Figure 6.20 Block diagram of speed control algorithm for IPM machine incorporating a feedforward FW algorithm to accommodate high-speed operation above the machine's corner point speed. Image from [18] based on original paper by Morimoto et al. [15]

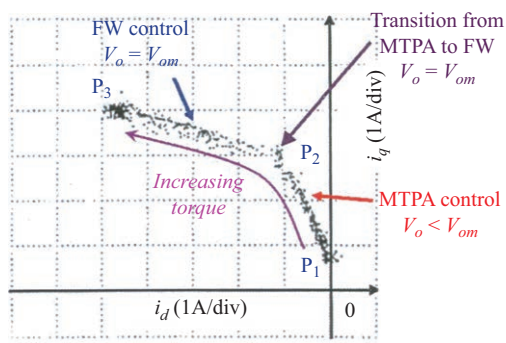


Figure 6.21 Measured dq plane current trajectory for feedforward flux-weakening control algorithm in Figure 6.20 [20, with additional labeling]

original reference [21]. The measured *dq* current values for a range of torque command values trace out a trajectory that looks very much like the theoretical current trajectory in Figure 6.19(b), clearly showing the expected transition from MTPA-mode operation at low torque values to FW-mode operation along the voltage limit ellipse for higher torque values.

6.7.2.2 Closed-loop flux-weakening control

Feedforward FW control algorithms of the type introduced in the preceding subsection suffer from the same deficiencies that virtually all feedforward control algorithms experience; their performance level is highly dependent on the accuracy of the parameters used to implement the algorithm. In the case of feedforward FW control algorithms, the sensitivity to parameter errors can be quite high. More specifically, the goal of the FW algorithm is to always keep the *dq* current-operating point inside the voltage ellipse to prevent complete saturation of the current regulator, which causes loss of current control with seriously negative consequences. On the other hand, another simultaneous objective is to allow the *dq* current-operating point to approach the voltage ellipse as closely as possible in order to take advantage of the inverter's full voltage capabilities. These two objectives directly compete with each other, particularly for feedforward control algorithms which depend critically on the accuracy of the parameters to make it possible for the *dq* current-operating point to approach the voltage limit envelope but not to inadvertently overstep it.

Closed-loop FW control algorithms use active feedback to detect that the *dq* current-operating point is approaching the voltage ellipse. By actively detecting its proximity to the voltage limit, the controller can immediately take action to move the current vector operating point a safe distance away from the ellipse, thereby avoiding saturation of the current regulator. This makes it possible for the controller to respond automatically to movements in the voltage ellipse caused by either changes in either the rotor speed or the inverter dc link voltage without the need to depend on equations programmed in the controller to constantly predict the ellipse's location.

An example of this type of closed-loop FW control algorithm will be briefly described that, unlike the preceding example, was primarily designed for generating mode operation of an IPM machine rather than motoring [22]. Figure 6.22(a) illustrates the basic concept of FW for an IPM machine during generating operation, including the transition from MTPA-mode of FW-mode operation, in contrast to the corresponding current trajectories during motoring operation presented earlier in this section in Figure 6.19(b). The basic principle of the FW control algorithm is illustrated in Figure 6.22(b). A key difference with all of the preceding discussion in this section is that the current vector is manipulated in terms of its polar coordinates, i.e., amplitude I_s and angle θ defined with respect to the negative *d*-axis, rather than in terms of its rectangular coordinates, i_d and i_q.

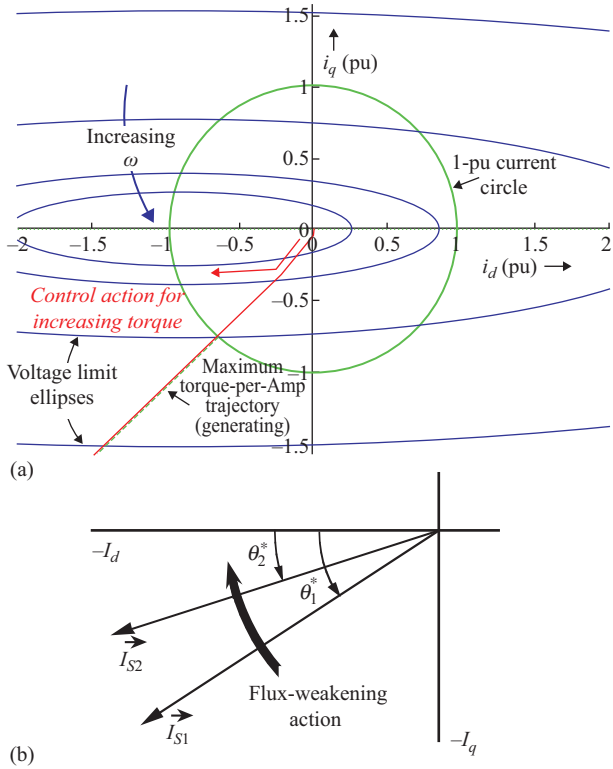


Figure 6.22 Closed-loop flux-weakening algorithm concepts: (a) flux-weakening dq-plane current trajectory for an IPM machine during generator operation and (b) flux-weakening actuation in polar coordinates, identifying clockwise rotation of current vector (reduction in θ) as the means of increasing flux weakening

During FW operation, the actuating variable is the angle θ which is reduced in order to rotate the current vector in the clockwise direction toward the negative *d*-axis. This action simultaneously increases the negative *d*-axis current amplitude, a critical feature of FW, while reducing the *q*-axis current amplitude by a commensurate amount to keep the current amplitude I_s constant. Another way of thinking about this action is that, if the voltage ellipse starts to shrink due to an increase in rotor speed, the FW action just described will act to keep the current vector terminus point inside the ellipse where it needs to remain in order to avoid saturation of the current regulator.

To implement a closed-loop FW control algorithm, it is critical to have a feedback variable that is sensitive to the proximity of the inverter's instantaneous operating point to its maximum output voltage limit. Fortunately, the basic operation of the PWM algorithm for a VS inverter generates a variable known as the modulation index *M* which is a normalized variable defined as the ratio of the

peak-to-peak amplitude of the line-to-line voltage's fundamental frequency component $V_{ll,pk-pk}$ to the inverter's dc-link voltage V_{dc}:

$$Modulation\ Index = M = \frac{V_{ll,pk-pk}}{V_{dc}}$$

For widely used PWM algorithms such as space-vector modulation, the inverter begins its transition into saturated operation whenever the value of the modulation index increases above approx. 1.15 [23]. The closed-loop current regulator automatically adjusts the value of m continuously in order to drive the error between the desired and actual phase current amplitudes to zero. As a result, monitoring the instantaneous value of the modulation index m provides a convenient variable for monitoring the inverter's proximity to saturation into six-step voltage operation. This modulation index variable represents an appealing candidate for use as an input variable for the closed-loop FW algorithm. As the speed increases for a fixed value of output current, the value of M naturally increases, eventually increasing beyond 1.15 at elevated speeds. Crossing that threshold signals the approach of the dq-plane current vector to its voltage limit ellipse and the impending current regulator saturation that it entails.

Figure 6.23(a) provides a block diagram showing the implementation of the closed-loop FW algorithm. The upper half of the diagram shows the baseline vector control algorithm including the f functions to generate the MTPA current trajectory in the synchronous rotor reference frame, and a closed-loop current regulator in the synchronous reference frame. The only thing different about this implementation of the MTPA current trajectory from the one discussed in Section 6.5 is that the f_1 and f_2 functions shown in Figure 6.23(a) are delivering the current commands in polar coordinates (amplitude and angle) rather than in rectangular coordinates, as discussed above.

The bottom half of the block diagram in Figure 6.23(a) shows the implementation of the closed-loop FW algorithm. Its inputs are the dq voltage commands in the synchronous reference frame $v_d^{e^*}$ and $v_q^{e^*}$ and the measured dc link voltage v_{dc}. These inputs are sufficient to calculate the instantaneous value of the modulation index M. During operation at low speeds, the modulation index value is low and the FW algorithm is dormant. Its output is a unitless scaling factor β ($0 \leq \beta \leq 1$) that multiplies the current angle θ^* command, and the value of β is constant at 1 during low-speed MTPA operation. When the speed and current command get sufficiently high for the modulation index value to exceed a preset threshold value M_{th}, the difference (error) value is integrated, causing the value of β and the resulting current angle $\theta^{*\prime}$ to decrease, initiating FW operation as described earlier in Figure 6.22(b). This FW action gradually reduces the modulation index M value as the dq current plane operating point moves further away from the voltage limit ellipse, causing the integrator to eventually cease its integration when the value of M drops back to M_{th}.

Experimental tests have verified that the closed-loop FW algorithm operates very well over a wide range of operating conditions. Figure 6.23(b) plots a collection of measured steady-state operating points for the IPM generator drive in the third quadrant over a range of speeds beyond the corner point speed from 1,000 to 3,500 rpm. The measured operating points correspond to two values of constant

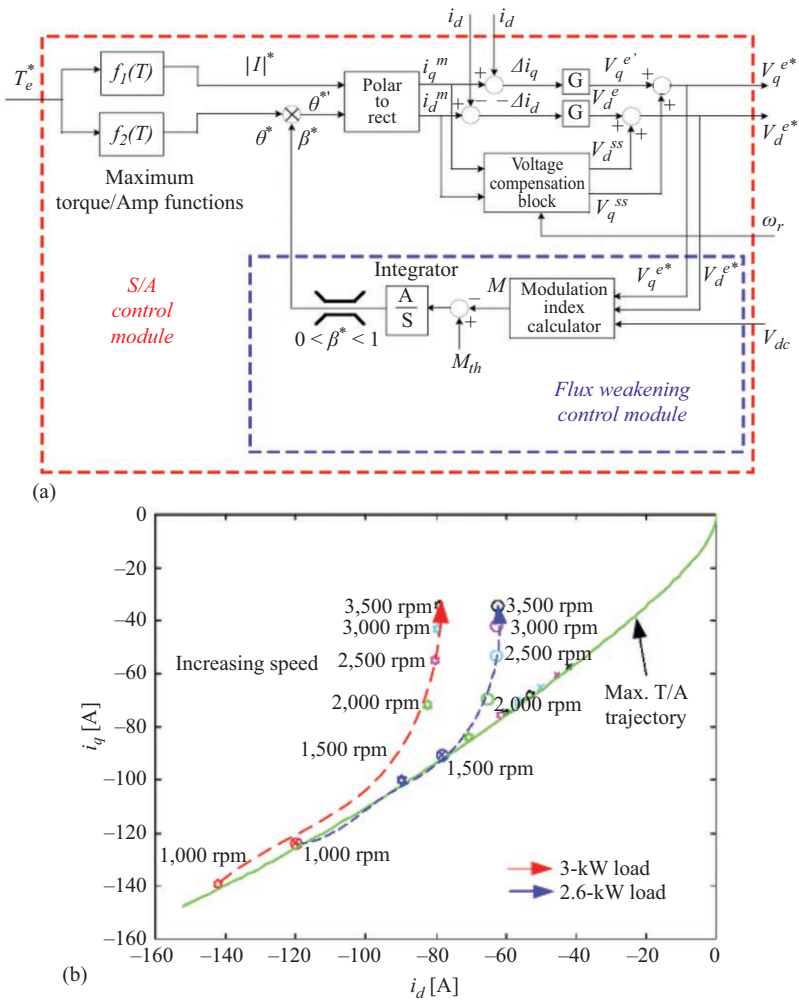


Figure 6.23 Details of closed-loop flux-weakening algorithm for an IPM generator machine: (a) implementation of closed-loop algorithm showing both baseline MTPA control functions and flux-weakening control module and (b) steady-state operating points of closed-loop flux-weakening algorithm in third quadrant of dq-current plane (i.e., origin is upper right corner) showing constant-power operating points for two power values over a speed range from 1,000 to 3,500 rpm

generator power, 2.6 and 3 kW. In both cases, the operating points gradually move away from the MTPA trajectory to new operating points with current angle θ values that monotonically decrease as the rotor speed increases, indicating progressively stronger FW. Test results for step changes in the generator load (not included here) confirm that the dynamics of the FW control loop are fast and well behaved.

6.7.3 Six-step voltage operation for flux-weakening algorithms

While the distinction between feedforward and closed-loop FW algorithms is an important one, it is not the only one of significance. One more differentiating factor that has practical importance will be briefly discussed here that is focused on the transition into six-step voltage operating mode.

To appreciate this additional factor, it must be noted that operating points lying on the voltage limit ellipses are, by definition, associated with applying the maximum available phase voltage V_{max} to the machine. For a VS inverter, maximum phase voltage is applied when the inverter is operating in its six-step mode without any PWM. This, in turn, corresponds to saturated operation of the closed-loop current regulator where current regulation is lost because the drive no longer has the ability to incrementally adjust its output voltage amplitude to maintain high-bandwidth regulation of the instantaneous phase current. Stated differently, the inverter reverts to its basic VS operating characteristics once it enters six-step voltage mode. As a result, the discussion in the preceding sections that referred to operation along the voltage limit ellipse during FW operation is only a simplifying approximation if the intention is to maintain current-regulated operation during this operating mode. In actuality, the operating points must lie inside the voltage ellipse with some margin for voltage headroom in order to be able to maintain closed-loop current regulation during FW operation.

This limitation imposed by the transition into six-step VS operating mode along the voltage ellipse presents a dilemma for the controls designer. If the control algorithm is designed to limit its maximum modulation index so that it never enters its six-step voltage operating mode, current regulation is maintained which makes it possible to continue using vector control with a modified current trajectory to implement FW for speeds above the corner speed. However, this approach effectively introduces a voltage buffer zone around V_{max} that prevents the inverter from ever delivering it maximum output voltage (i.e., six-step voltage operation). That is, the inverter is being purposely throttled back and prevented from delivering its maximum output power, thereby preventing the drive from ever reaching its maximum possible torque and power vs. speed capability curves. This strategy is a real disadvantage in cost-competitive commercial PM drive applications because of the inverter's effective over-rating for its application caused by the controller's special requirements for voltage headroom.

If, instead, the PM machine drive is designed to allow the inverter to operate in its six-step voltage mode, the control algorithm becomes more complicated because it is forced to transition back and forth between regulated-current mode and voltage angle control mode. In addition to the disadvantages associated with this transition, the dynamics of the voltage-angle control mode are significantly slower and less well behaved than those of the regulated-current mode. Despite these control disadvantages, the strong incentive to fully utilize the inverter's voltage and current capabilities has resulted in the successful development and commercial application of FW control algorithms that are designed to operate in six-step voltage mode.

6.8 Summary

This chapter has reviewed the electrical performance characteristics of PMSMs and their associated control principles. It has been shown that the *dq* equivalent circuit representation for PM machines provides a critical foundation for understanding the machine's performance characteristics. In particular, the accompanying torque equation expressed in terms of the machine equivalent circuit parameters and currents provides a valuable means for gaining an understanding of the torque production characteristics of PM machines. This includes insights into the key differences between the torque production characteristic of SPM and IPM machines. The current vector plane in the synchronous rotor reference frame plotted in terms of i_q vs. i_d is extremely helpful for identifying constant-torque contours for both of these PM machine types.

This discussion of torque production characteristics led to a discussion of vector control as a powerful means of achieving high-performance torque control in PM machines during operation in the "constant-torque" regime where the drive voltage limits are not influencing the machine's steady-state performance capabilities. By tightly regulating the machine's phase currents, the instantaneous current vector can be manipulated to achieve *MTPA* operation in both SPM and IPM machines at all reachable torque values in order to minimize the PM machine's stator resistive losses.

This chapter has also discussed the torque and power capability curves that can be achieved using IPM machines. Here again, the i_q vs. i_d plane proves to be very useful for exploring the interaction of the current limit and the voltage limit in determining the outer envelope of the torque vs. speed and power vs. speed characteristics. This discussion has revealed that the IPM machine is capable of achieving (ideally) infinite speed ranges of constant-power operation with output power levels up to 1 pu. However, achieving such optimal FW depends critically on the machine designer's capability to properly set the machine's parameters. In particular, setting the IPM machine's characteristic current I_{ch} $(= \psi_{pm}/L_d)$ equal to the machine's rated (1 pu) current has emerged as the key to achieving optimal FW.

Next, the observation was made that the IPM machine's high-speed performance capabilities can, with some simplifications, be reduced to setting two machine parameters: the machine's magnet flux linkage ψ_{pm} and the inductance saliency ratio ξ. This makes it possible to conveniently explore the IPM machine design space in a two-dimensional ψ_{pm}–ξ plane that is very helpful to identifying how the machine parameters must be set by the machine designer to achieve wide speed ranges of constant-power operation. The important point was made that there is nothing that a control engineer can do to recover high-speed performance capability if the machine is not designed with the required machine parameters to reach these operating regimes within the voltage and constraints imposed by the drive.

Finally, the basic control concepts associated with achieving FW torque control in the high-speed operating regime beyond the machine's corner point speed ω_o have been introduced. It has been shown that the wide variety of FW control algorithms that have been presented in the literature for PM machines can be

generally classified into two families: feedforward (open-loop) FW control algorithms that depend on having a significant amount of preknowledge about the machine's parameters in order to achieve high-performance torque control over a wide range of operating speeds in the FW regime, and closed-loop FW control algorithms that use feedback control concepts to implement FW control in a way that automatically adapts to changes in both the PM machine's electrical parameters and the drive's voltage and current limits.

List of symbols

v_{as}, v_{bs}, v_{cs}	Instantaneous phase voltages of stator
i_{as}, i_{bs}, i_{cs}	Instantaneous phase currents of stator
ψ_{as}, ψ_{bs}, ψ_{cs}	Instantaneous phase flux linkages of stator
R_s	Stator phase resistance
θ_r	Rotor angle in electrical radians
$L_{as}(\theta_r)$, $L_{bs}(\theta_r)$, $L_{cs}(\theta_r)$	Stator phase self-inductances
$M_{ab}(\theta_r)$, $M_{bc}(\theta_r)$, $M_{ac}(\theta_r)$	Stator mutual phase inductances
Ψ_{pm}	Permanent magnet flux linkage
ω_r	Rotor angular frequency
E	Amplitude of the back-emf phasor
L_d	Inductance in the d-axis
L_q	Inductance in the q-axis
ζ	Saliency ratio
$I_{\max}$	Rated maximum current
T_e^*	Instantaneous torque command
ω_o	Corner speed
ω	The rotor angular frequency (i.e., excitation frequency)
I_{ch}	Characteristic current
M	Modulation index
$V_{ll,pk-pk}$	Peak-to-peak amplitude of the line voltages
V_{dc}	DC link voltage
β	Scaling factor
$V_{\max}$	Maximum phase voltage

Glossary of terms

IPM	Interior permanent magnet motor has permanent magnets placed inside the rotor surface
SPM	Surface permanent magnet motor has permanent magnets placed on the rotor surface

Sensorless control	The motor control without using direct sensing of any parameter like rotor speed or rotor position
Flux-weakening control	The control used for speed control above base speed using reduction of PM flux

References

[1] T.M. Jahns, G.B. Kliman and T.W. Neumann, "Interior Permanent-Magnet Synchronous Motors for Adjustable-Speed Drives", *IEEE Transactions on Industry Applications*, vol. IA-22, no. 4, 1986, pp. 738–746.

[2] D.W. Novotny and T.A. Lipo, *Vector Control and Dynamics of AC Drives*, Oxford Press, Oxford, 1996.

[3] W. Soong, "Design and Modeling of Axially-Laminated Interior Permanent Magnet Motor Drives for Field-Weakening Applications", PhD Thesis, Department of Electronics and Electrical Engineering, University of Glasgow, 1993.

[4] E. Richter and T.W. Neumann, "Saturation Effects in Salient Pole Synchronous Motors with Permanent Magnet Excitation", in *Rec. 1984 International Conference on Electrical Machines (ICEM 1984)*, 1990, pp. 603–606.

[5] N. Bianchi and S. Bolognani, "Magnetic Models of Saturated Interior Permanent Magnet Motors Based on Finite Element Analysis", in *Rec. of 1998 IEEE Industry Applications Society Annual Meeting*, vol. 1, October 1998, pp. 27–34.

[6] E.C. Lovelace, T.M. Jahns and J.H. Lang, "A Saturating Lumped-Parameter Model For an Interior PM Synchronous Machine", *IEEE Transactions on Industry Applications*, vol. 38, 2002, pp. 645–650.

[7] E.C. Lovelace, "Optimization of a Magnetically Saturable Interior PM Synchronous Machine Drive", PhD Thesis, Dept. of Elec. Eng. & Comp. Sci., MIT, 2000.

[8] T.A. Lipo, "AC Machine Design", Wisconsin Power Electronics Research Center, University of Wisconsin, 1996.

[9] M. Corley and R.D. Lorenz, "Rotor Position and Velocity Estimation for a Salient-Pole Permanent Magnet Synchronous Machine at Standstill and High Speeds", *IEEE Transactions on Industry Applications*, vol. 43, no. 4, 1998, pp. 784–789.

[10] B.N.- Mobarakeh, F.M.- Tabar and F.-M. Sargos, "Back EMF Estimation-Based Sensorless Control of PMSM: Robustness with Respect to Measurement Errors and Inverter Irregularities", *IEEE Transactions on Industry Applications*, vol. 43, 2007, pp. 485–494.

[11] I. Boldea, M.C. Paicu, G.-D. Andreescu and F. Blaabjerg, "Active flux DTFC-SVM Sensorless Control of IPMSM", *IEEE Transactions on Energy Conversion*, vol. 24, 2009, pp. 314–322.

[12] K. Ide, M. Hisatsune, T. Shiota, S. Murakami, M. Ohto, "Encoderless Servo drive with Adequately Designed IPMSM for Saliency-Based Position Detection", *Proc of ICPE (ECCE Asia)*, Jeju, Korea, May 30–June 3, 2011, pp. 1257–1264.

[13] W. Soong and T.J.E. Miller, "Theoretical limitations to the Field-Weakening Performance of the Five Classes of Brushless Synchronous AC Motor Drives", in *Proc. IEE 6th International Conference on Electrical Machines and Drives (EMD 93)*, September 1993, pp. 127–132.

[14] W. Soong and T.J.E. Miller, "Practical Field-Weakening Performance of The Five Classes of Brushless Synchronous AC Motor Drive", in *Proc.* 5th *European Conference on Power Electronics and Applications (EPE 93)*, September 1993, pp. 303–310.

[15] S. Morimoto, Y. Takeda, T. Hirasa and K. Taniguchi, "Expansion of Operating Limits for Permanent Magnet Motor by Current vector Control Considering Inverter Capacity", *IEEE Transactions on Industry Applications*, vol. 26, 1990, pp. 866–871.

[16] A.K. Adnanes and T.M. Undeland, "Optimum Torque Performance in PMSM Drives Above Rated Speed", in *Rec. of 1991 IEEE Industry Applications Society Annual Meeting*, vol. 1, October 1991, pp. 169–175.

[17] N. Bianchi, S. Bolognani, B.J. Chalmers, "Salient-Rotor PM Synchronous Motors for an Extended Flux-Weakening Operation Range", *IEEE Transactions on Industry Applications*, vol. 36, 2000, pp. 1118–1125.

[18] A. EL-Refaie and T.M. Jahns, "Optimal Flux Weakening in Surface PM Machines using Concentrated Windings", in *Proc. 2004 IEEE Industry Applications Society Annual Meeting*, Seattle, October 2004.

[19] A. Fratta, A. Vagati and F. Villata, "Design Criteria of an IPM Machine Suitable for Field-Weakened Operation", in *Proc. of 1990 Intl. Conf. on Elec. Mach (ICEM)*, 1990, pp. 1059–1065.

[20] W. Soong, T.J.E. Miller, "Field Weakening Performance of Brushless Synchronous AC Motor Drives", *IEE Proceedings-Electric Power Applications*, vol. 141, no. 6, 1994, pp. 331–340.

[21] R.F. Schiferl and T.A. Lipo, "Power Capability of Salient Pole Permanent Magnet Synchronous Motor in Variable Speed Drive Applications", *IEEE Transactions on Industry Applications*, vol. 26, 1990, pp. 115–123.

[22] E.C. Lovelace, T.M. Jahns and J.H. Lang, "Impact of Saturation and Inverter Cost on Interior PM Synchronous Machine Drive Optimization", *IEEE Transactions on Industry Applications*, vol. 36, 2000, pp. 723–729.

[23] A. Consoli and G. Renna, "Interior Type Permanent Magnet Synchronous Motor Analysis by Equivalent Circuits", *IEEE Transactions on Energy Conversion*, vol. 4, 1989, pp. 681–689.

This page intentionally left blank

Chapter 7

Control of PM brushless DC motor drives

Ta Cao Minh[1]

7.1 Introduction

With the recent development of permanent magnet (PM) materials, PM (brushless) motors have become more and more popular and find their applications in a wide range of fields: industry, office use machines, house appliances and automotive space equipment. The use of PMs has a great advantage in that the created magnetic field is high-density, providing a high-efficiency operation of the whole drive. PM motors can be divided into two categories depending on their current waveform [1]:

- Sine-wave PM motor, which is also called PM synchronous motor (PMSM), is fed by sine-wave current.
- Square-wave PM motor that is fed by square-wave current and it is often called brushless DC motor (BLDCM).

The main difference between two kinds of motors from the construction viewpoint is the way of winding. In BLDCM, the stator winding is concentrated. Hence, the stator electromotrice force (EMF) waveform is trapezoidal. Whereas in PMSM, the stator winding is distributed winding, so the stator waveform is sinusoidal. The rotors in both types are made from PMs.

The torque produced in a sine-wave PM motor is smooth as the result of the interaction between the sinusoidal stator current and the sinusoidal rotor flux. High-performance PMSM drives are regulated by the well-known vector control method, in which motor currents are controlled in synchronously rotating d–q frame. Rotor position at any instant (measured by a high-resolution position sensor or estimated by an observer) is the mandatory requirement in the high-performance vector control method.

Vector control method cannot, however, be utilized for BLDCM because terminal variables (currents, voltages) and electromotive force (EMF) waveforms are not sinusoidal. Therefore, the phase current control technique is normally employed for this kind of motor. The control technique is relatively simple because the square-wave reference currents can be generated in a step manner, every $360/(m \cdot p)$ electrical degrees, where m is the number of phases and p is the pole-pair number. Hence, low-cost Hall-effect sensors served as position sensor are enough for the control purpose. Simplicity in control, BLDCMs suffer, however,

[1]Department of Industrial Automation, Hanoi University of Science and Technology, Vietnam

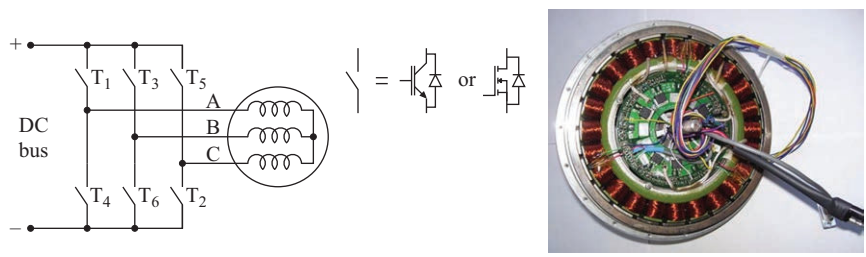
from a big drawback: because of phase commutations, the torque is not as smooth as that produced by their counterpart, sine-wave PM motors.

7.1.1 Construction of BLDC motor

A BLDCM is basically a non-salient pole surface PM machine with a full pitch-concentrated winding that generates trapezoidal EMF.

Figure 7.1(b) shows a photo of three-phase motor with concentrated winding and external rotor. Electronics commutator is integrated into the motor. In the photo, three Hall sensors are placed at 120° degrees, opposite the rotor magnets. BLDCMs can be constructed in different physical configurations. Depending on the stator windings, these can be configured as single-phase, two-phase, three-phase and multi-phase motors. However, three-phase BLDCMs with PM rotor are the most commonly used. A BLDCM has stator and rotor parts as all other motors. Stator of a BLDCM is made of stacked steel laminations to carry the windings. These windings are placed in slots which are axially cut along the inner periphery of the stator. These windings can be arranged in either star or delta. However, most BLDCMs have three stator windings connected in star pattern. The rotor is made of PMs. The number of poles in the rotor can vary from two to eight or even higher pole pairs with alternate south (S) and north (N) poles depending on the application requirement. The rotor can be constructed with different core configurations such as the circular core with PM on the periphery and a circular core with rectangular magnets. To achieve maximum torque, the PM material should should produce high flux density.

The basic configuration of a BLDCM system is shown in Figure 7.1(a), where there is a full-bridge driving circuit for a three-phase star-connected BLDCM. The DC supply at the input may be rectified DC or from an energy storage system, such as battery. In the diagram, power switches T1–T6 are used to turn on or turn off the currents of the windings according to the logic signals. The symbolical power switches in the figure may be insulated gate bipolar transistors (IGBTs) or metal-oxide semiconductor field-effect transistors (MOSFETs). As one can see, the power switches form a circuit which is the same as an inverter for three-phase AC motor. However, when the circuit is associated with a BLDCM, it is often called "electronics commutator" for emphasizing its specific role in the electronically commutated motor or "mechanically brushless" DC motor.



(a) (b)

Figure 7.1 (a) "Electronics commutator" and BLDC motor and (b) three-phase BLDC motor with concentrated winding and external rotor

7.1.2 Operation principle of BLDC motor

When the stator coils are electrically switched by a supply source, they become electromagnets and start producing the uniform field in the air gap. As we know, the rotor of a BLDCM is made of PMs. Due to the force of interaction between the electromagnet stator and PM rotor, the rotor rotates.

To rotate the BLDCM, the stator windings should be energized in a sequence. Thus, it is important to know the rotor position to determine which winding will be energized. Rotor position is sensed by using Hall-effect sensors (or Hall sensors) embedded into the stator. Whenever the rotor magnetic poles pass near the Hall sensors, they give a high or low signal, indicating that the N or S pole is passing near the sensors. Based on the combination of these three Hall sensors signals, the exact sequence of commutations can be determined [1,2].

The operation principle will be explained for two-phase mode. In this mode, for any given period, two of the motor windings are conducting all the time as well as suspending the third one. The states of the switches and machine rotor are shown in Figure 7.2, and the corresponding waveforms are illustrated in Figure 7.3.

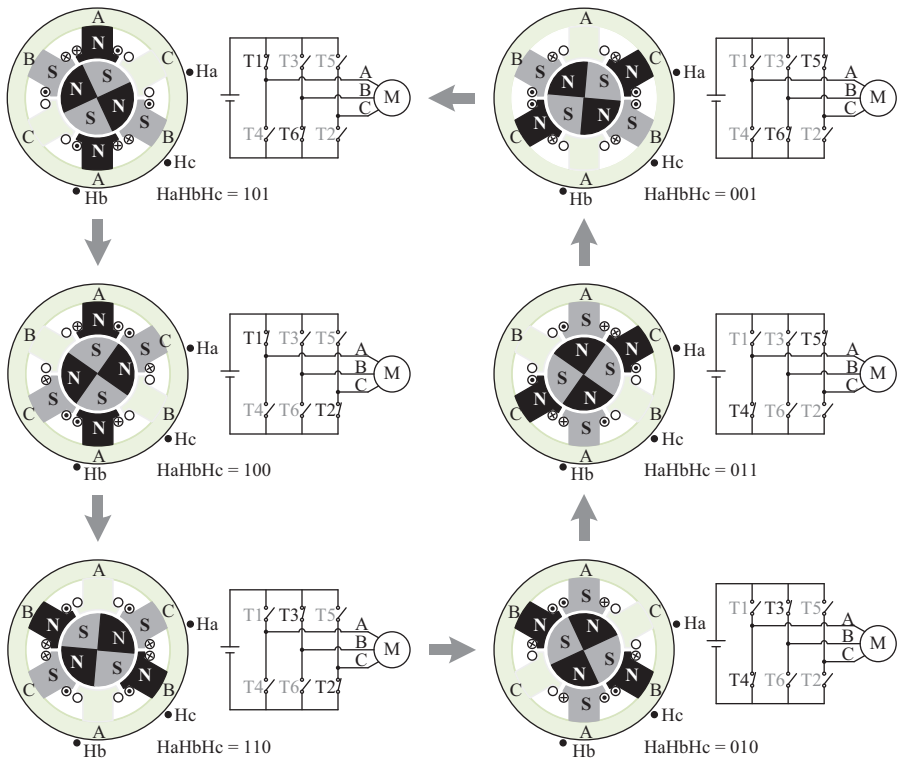


Figure 7.2 State of power switches and corresponding poles of stator and rotor in function of the sequences of Hall-effect sensors

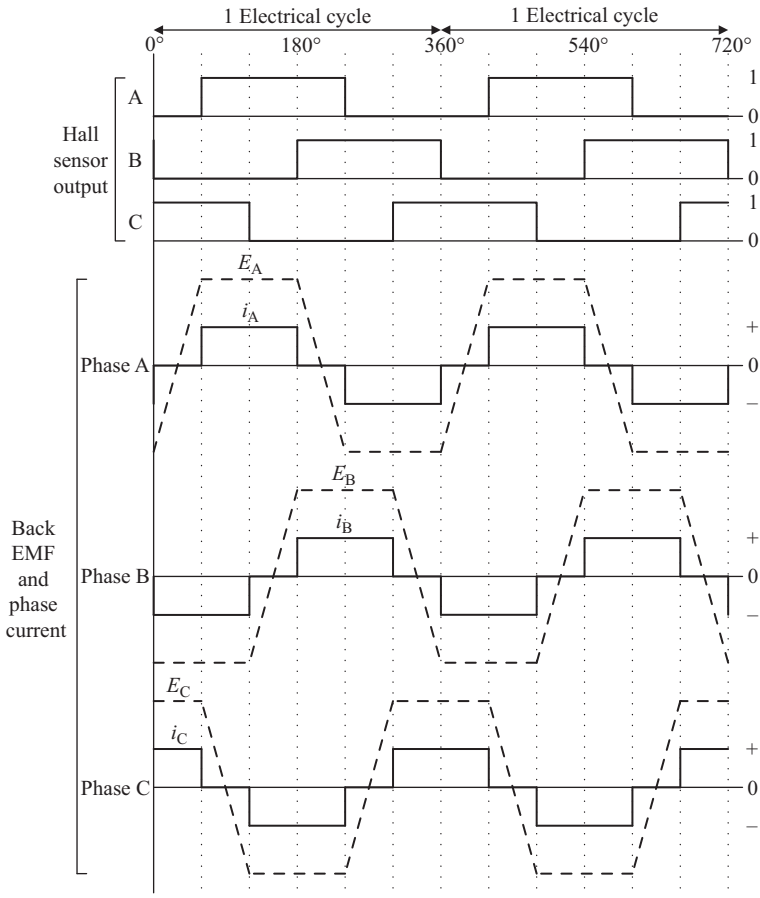


Figure 7.3 Waveforms of EMFs and currents of phase A, B, C with the signals from Hall-effect sensors

The conduction order and instant are determined by the rotor position information that is generated by the sensors. In this condition, the synthetic rotating magnetic field generated by the stator is a step field instead of a continuous one. The bridge converter commutates once the rotor rotates a 60° electrical angle, and the magnetic status is consequently changed. So, there are six magnetic status and two phase windings are conducting in each state. The time of current flowing continuously in each winding is 120° electrical angle.

In the two-phase mode, there is only one upper bridge switch conducted at a time, which produces the forward flowing current in the corresponding winding, resulting in a torque. Similarly, another torque is produced by the backward current because of the lower bridge switch conduction. The sum of these torques constitutes the synthetic torque, which rotates 60° electrical angle at each commutation period.

7.1.3 Specific features of BLDC motor drives

- *Compactness due to current of square-waveform.* The most distinguish feature of BLDCM resides in the waveform of current and EMF. As the current is in square (or quasi-square) form, its rms value is equal to the maximal value, whereas in sine-wave motor, the pick current is of $\sqrt{2}$ factor of the rms value. This fact is very important in sizing the motor winding. The BLDCM has, therefore, the highest power/volume ratio, i.e., is the smallest among the other types that have the same the power.
- *Torque ripple due to non-ideal commutations.* Unlike the sine-wave motor, where the commutations happen gradually, the commutations in BLDCM are executed at every 60° electrical. In the reality, the switch-on time and the switch-off one of power devices are not the same. As the consequence, the produced torque, as the interaction between the stator nonideal current and the rotor PM flux, content the ripples that impair the performance of the whole drive. Analysis of torque ripples and the techniques to reduce the ripples are presented in Section 7.4.
- *High-speed operation by conventional advance angle.* As well known, a motor attains its rated power in the rated operation point, where the speed and the developed torque are at rated values. Beyond the so-called base-speed region, it is common to use the flux-weakening techniques for sin-wave PM motors. For the BLDCM, we can advance the phase current before its EMF by an appropriate angle. The technique is treated in Section 7.6.

An alternative approach to minimize the torque ripples is the pseudo-vector control (PVC) technique that calculates the reference phase currents in $d-q$ frame, by taking the EMF information into consideration. The detailed PVC technique will be provided in Section 7.5. Beside the torque ripple elimination effect, the PVC can also enable the high-speed operation by acting on d-axis current.

In general, a BLDCM is recognized as having the highest torque and power capability for a given size and weight due to its (quasi-)square-wave current and trapezoidal form of EMF. In addition to that, a BLDCM also presents the cost advantage over the sine-wave PM motor, due to its construction and winding. Therefore, it seems to be evident that if the torque ripple in BLDCM can be overcome, this kind of motor would become a very attractive solution for many industrial and house-appliances applications.

7.2 Modeling of brushless DC motor

The equivalent circuit of a three-phase BLDCM is illustrated in Figure 7.4, where each coil is represented by an inductance, an internal resistor and an EMF. In the figure, the motor is in star connection. The fourth wire denoted N represents the neutral point, which is an option, as most motors in practice are provided with only three wires.

Although Figure 7.4 describes the motor in star connection, the equivalent circuit does not loss its generality and can be used for delta connection.

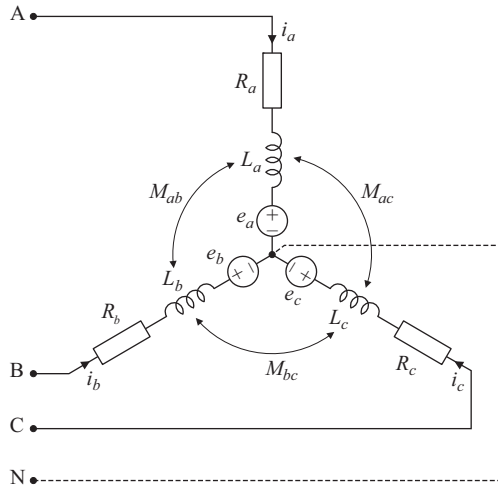


Figure 7.4 Equivalent circuit of three-phase BLDC motor

7.2.1 Dynamic model

Using the equivalent circuit, the set of voltage equations can be expressed as follows [3]:

$$\begin{aligned} u_a &= u_{AN} = R_a i_a + L_a \frac{di_a}{dt} + M_{ab} \frac{di_b}{dt} + M_{ca} \frac{di_c}{dt} + e_a \\ u_b &= u_{BN} = R_b i_b + L_b \frac{di_b}{dt} + M_{ab} \frac{di_a}{dt} + M_{bc} \frac{di_c}{dt} + e_b \\ u_c &= u_{CN} = R_c i_c + L_c \frac{di_c}{dt} + M_{ca} \frac{di_a}{dt} + M_{bc} \frac{di_b}{dt} + e_c \end{aligned} \tag{7.1}$$

where u_a, u_b, u_c are the phase voltages; i_a, i_b, i_c are the phase currents; e_a, e_b, e_c are the phase EMFs; R_a, R_b, R_c are the resistance of each phase; L_a, L_b, L_c are the inductance of each phase; and M_{ab}, M_{bc}, M_{ca} are the mutual inductance between two phases.

With the assumption that the motor is perfectly balanced, i.e., the three phases are identical, (7.1) can be simplified as (7.2), because all the parameters are equal, i.e., $R_a = R_b = R_c = R_s = R$, $L_a = L_b = L_c = L_s$, $M_{ab} = M_{bc} = M_{ca} = M$.

$$\begin{aligned} u_a &= R_s i_a + L_s \frac{di_a}{dt} + M \frac{di_b}{dt} + M \frac{di_c}{dt} + e_a \\ u_b &= R_s i_b + L_s \frac{di_b}{dt} + M \frac{di_a}{dt} + M \frac{di_c}{dt} + e_b \\ u_c &= R_s i_c + L_s \frac{di_c}{dt} + M \frac{di_a}{dt} + M \frac{di_b}{dt} + e_c \end{aligned} \tag{7.2}$$

According to Kirchhoff's first law, $i_a + i_b + i_c = 0$ and let the stator equivalent inductance be $L = L_s - M$, the following equations stand:

$$\begin{aligned} u_a &= Ri_a + L\frac{di_a}{dt} + e_a \\ u_b &= Ri_b + L\frac{di_b}{dt} + e_b \\ u_c &= Ri_c + L\frac{di_c}{dt} + e_c \end{aligned} \tag{7.3}$$

The electromechanical energy conversion is expressed as

$$P_e = e_a i_a + e_b i_b + e_c i_c = T_e \cdot \omega_m \tag{7.4}$$

where P_e is the electrical power, T_e is the electromechanical torque developed by motor, which is equal to the output torque on the shaft, and ω_m is the mechanical angular velocity (rad/s).

Equation (7.4) means that all the electrical power is transformed to the useful (mechanical) power if there is no mechanical rotating loss. The motor output torque can be then derived.

$$T_e = \frac{e_a i_a + e_b i_b + e_c i_c}{\omega_m} \tag{7.5}$$

The dynamics of mechanical part is represented as follows:

$$T_e = J\frac{d\omega_m}{dt} + T_L \tag{7.6}$$

where T_L is load torque, J is moment of inertia of rotor and coupled shaft.

Using Laplace transform for (7.3) and (7.6), we have dynamic model of BLDCM in form of transfer function:

$$\begin{aligned} i_a &= (u_a - e_a) \cdot \frac{1}{Ls + R} = (u_a - e_a) \cdot \frac{1/R}{\tau s + 1} \\ i_b &= (u_b - e_b) \cdot \frac{1}{Ls + R} = (u_b - e_b) \cdot \frac{1/R}{\tau s + 1} \\ i_c &= (u_c - e_c) \cdot \frac{1}{Ls + R} = (u_c - e_c) \cdot \frac{1/R}{\tau s + 1} \end{aligned} \tag{7.7}$$

$$\omega_m = (T_e - T_L)\frac{1}{J \cdot s} \tag{7.8}$$

where s denotes the differential operator and $\tau = L/R$ is the electrical time constant of the motor. The complete dynamic model of BLDC is therefore expressed by (7.5), (7.7) and (7.8).

7.2.2 Block diagram of BLDCM model

A direct use of dynamic model in the above equations for simulation of three-phase motor may not work, because the equations in (7.7) are independent. The practical motor model for simulation can be obtained as follows, considering the line-to-line voltages and currents (7.9) and the condition (7.10).

Equation (7.3) can be rearranged for the line-to-line voltages.

$$\begin{aligned} u_{ac} &= u_a - u_c = R(i_a - i_c) + sL(i_a - i_c) + e_a - e_c = Ri_{ac} + sLi_{ac} + e_{ac} \\ u_{bc} &= u_b - u_c = R(i_b - i_c) + sL(i_b - i_c) + e_b - e_c = Ri_{bc} + sLi_{bc} + e_{bc} \end{aligned} \tag{7.9}$$

Fundamental current equation for three-phase motor

$$i_a + i_b + i_c = 0 \tag{7.10}$$

After some manipulation, the phase currents can be obtained from the line currents

$$\begin{aligned} i_a &= \frac{2i_{ac} - i_{bc}}{3} \\ i_b &= \frac{2i_{bc} - i_{ac}}{3} \\ i_c &= \frac{-i_{ac} - i_{bc}}{3} \end{aligned} \tag{7.11}$$

In the block diagram model, the EMF is realized by look-up-table technique, where three-phase EMFs in per-unit-value (pu) are stored in a table in function of the electrical rotor position θ_e. The amplitude of the EMF is then calculated from the speed, by using the EMF constant k_e.

$$E = k_e \cdot \omega_m \tag{7.12}$$

Figure 7.5 shows the complete mathematical model of three-phase BLDCM, where (7.5), (7.8), (7.9), (7.11), (7.12) and EMF look-up tables are employed. The electrical angular velocity ω_e is related to the mechanical one by the pole pair number p ($\omega_e = p \cdot \omega_m$).

7.2.3 Torque-speed characteristic

In the two-phase conduction mode, when only two windings are on and the third phase is off, we have the steady-state voltage equation at constant speed directly from (7.3).

$$u_{ab} = U_{DC} = 2Ri_a + 2e_a = 2RI_m + 2E = 2RI_m + E_{LL} \tag{7.13}$$

where I_m is the current amplitude ($I_m = I_{DC}$) and E_{LL} is the line-to-line EMF.

$$U_{DC} = 2RI_m + E_{LL} = 2RI_m + 2k_e \cdot \omega_m \tag{7.14}$$

However, the torque developed by motor is related to current by the relation

$$T_e = k_T \cdot I_m \tag{7.15}$$

where k_T is the torque constant.

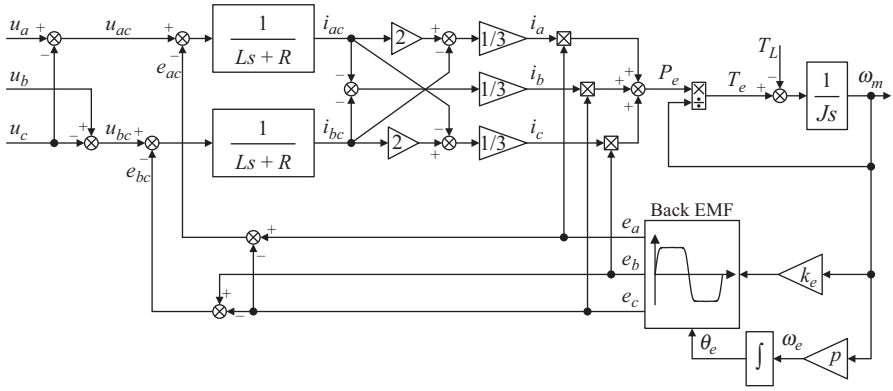


Figure 7.5 Block diagram of three-phase BLDCM model

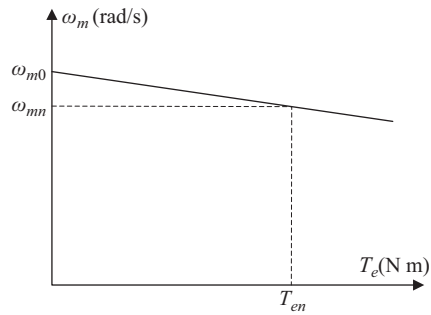


Figure 7.6 Torque-speed characteristics of BLDCM

Replacing (7.12) and (7.15) into (7.14), the angular motor speed is obtained in function of the torque.

$$\omega_m = \frac{U_{DC}}{k_e} - \frac{2 \cdot R}{k_e \cdot k_T} \cdot T_e = \omega_{m0} - \Delta\omega_m \tag{7.16}$$

where ω_{m0} is the no-load speed and $\Delta\omega_m$ is the speed drop for a given load torque. Figure 7.6 represents the torque-speed characteristic, which is similar to that of DC commutated motor.

7.3 Phase-current control of brushless DC motor

7.3.1 Control system configuration

Since the back electromotive force (BEMF) and current of BLDCM are not sinusoidal, the vector control principle cannot be readily applied. To control a BLDCM,

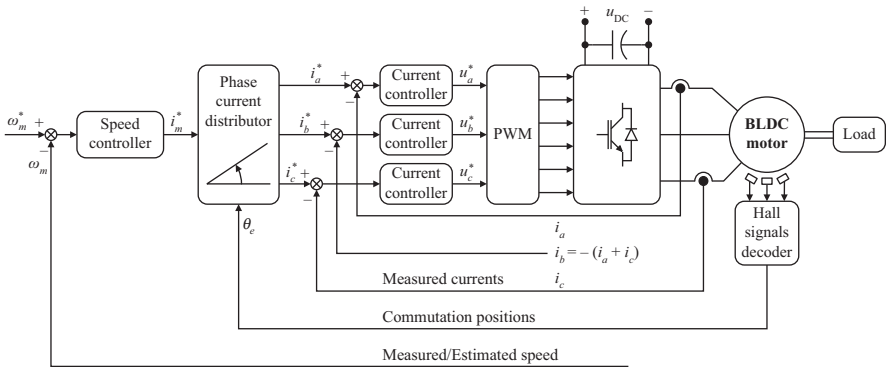


Figure 7.7 Conventional BLDCM drive system with current control loop and speed control loop

it is common to use the conventional phase-current control configuration as shown in Figure 7.7 with two closed loops for current and speed control. With this drive system, BLDCM can operate with rated torque at any speed under the rated speed. The motor is fed by a PWM-controlled MOSFET or IGBT inverter. The rotor position can be obtained from three Hall-effect sensors, which is integrated inside the motors. The reference signals are generated in the block "Phase current distributor" using the position information from the Hall-effect sensors. The reference current amplitude is readily shifted every 60° according to the communication positions yielded by Hall-effect sensors (see Figure 7.3). Phase division define conducted coil corresponding to the rotor position. The currents are then controlled by three current controllers, which calculate duty cycle for IGBT or MOSFET inverter. The simple hysteresis or proportional-integral (PI) feedback control law is wildly used in most applications.

If the speed control is required, the outer loop can be added. It is commonly known as the speed control loop with the speed regulator, which aims to stabilize speed and reject the load disturbance. The feedback signal for speed control loop is estimated from the Hall-effect sensors information or measured by a more sophisticated sensor, such as encoder or resolver, according to specific application requirement. The most common control law for the speed loop is the PI algorithm.

Nowadays, many control algorithms are applied to control BLDCM, like adaptive control, fuzzy control and genetic algorithms have been proposed. However, the PI control law and hysteresis control are still the most common and useful algorithms in BLDCM conventional control system because of their simplicity.

7.3.2 Simulation results

The operation and control performance of BLDCM drives are tested by numerical simulation in MATLAB®/Simulink® environment. The parameters of the laboratory prototype motor are shown in Table 7.1.

Table 7.1 Technical data of the motor

Parameters	Symbols	Value	Unit
Power (rated)	P	54	W
Speed (rated)	n	1,500	rpm
Voltage (rated)	V	36	V
Current (rated)	I	2	A
Torque (rated)	T_e	0.343	N m
Pole pair number	p	2	–
Resistance	R	0.8	Ω
Inductance	L	2.14	mH
EMF constant	k_e	0.1719	V s/rad
Torque constant	k_T	0.1715	N m/A
Flux	ψ	0.021486	Wb
Inertia	J	0.0002	kg m^2

Figure 7.8 shows the performance of the drive during starting up and load torque application. The motor is started up to nominal speed with no load, and a rated load torque is applied at $t = 0.15$ s when the speed is already at its constant value. A small speed drop can be seen in Figure 7.8(a), then it quickly comes back thanks to speed feedback control loop. The corresponding waveforms of currents and torque are reported Figure 7.8(b) and (c). The hysteresis control is employed for the current control loops.

The torque ripple is clearly detected in the instants of commutation due to the shape slop of the currents. Figure 7.9 shows a closer look at the EMF and current waveform, where they are plotted for one phase (phase a).

7.4 Torque ripple analysis and reduction techniques

In order to analyze the torque ripple, the currents of three phases and the produced torque at the instant of one commutation are examined. As it is shown in Figure 7.10, due to the difference in turn-on and turn-off time of power devices of two phases in commutation, the current of the third phase is perturbed (Figure 7.10(a)), resulting in a ripple in the torque (Figure 7.10(b)). The result is perfectly matched with theoritical analysis available the literature [4].

Torque ripple reduction is always an essential issue in BLDCM control system. The torque ripple would not only cause acoustics and vibration but severely limit the performance of the system, especially in high precision and high stabilization applications. There are three primary sources of torque production (and therefore of the torque ripple) in BLDCMs: cogging torque, reluctance torque and mutual torque [1].

The torque ripple can be reduced by motor design, control means or both of them. It is a great challenge to reduce cogging torque during machine design. If in a BLDCM either stator slots or rotor magnets are skewed by one slot pitch, the effect of the first two torque components is significantly reduced. Therefore, if the waveforms of phase EMFs and the phase currents are perfectly matched, torque

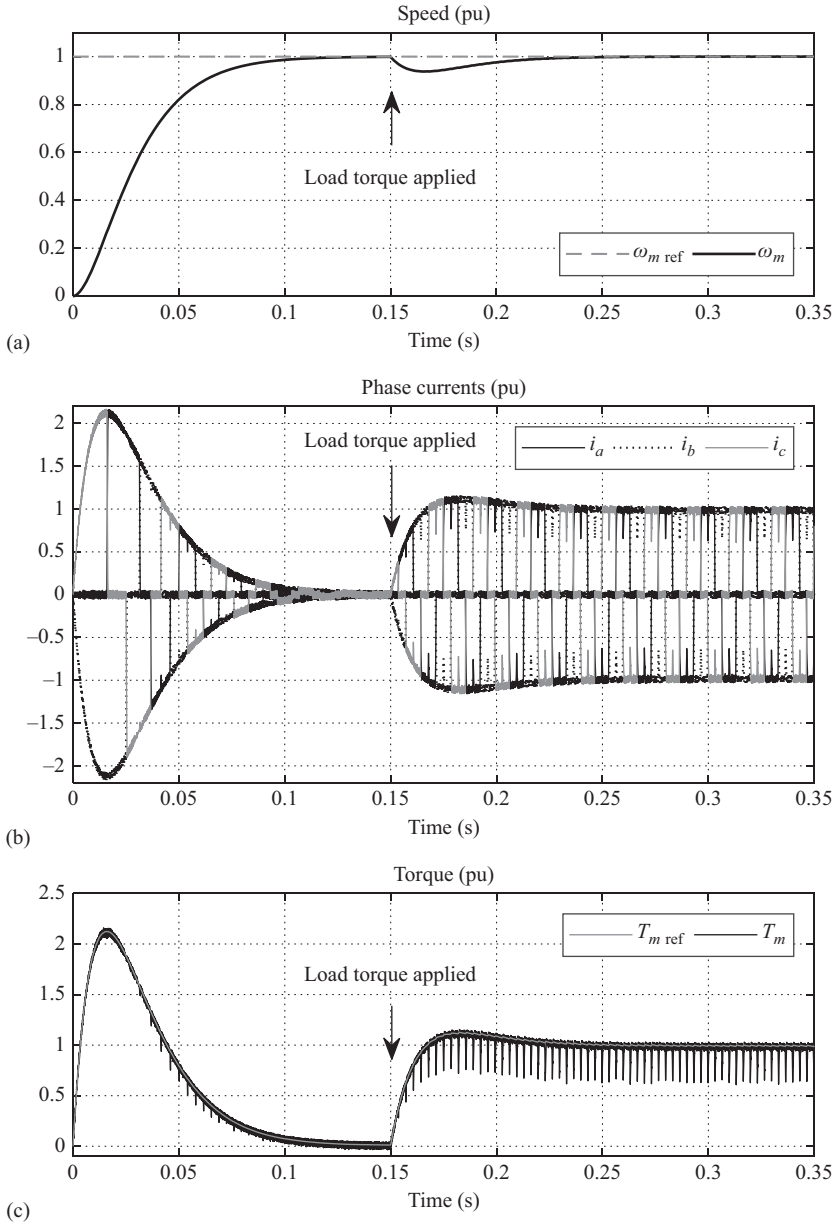


Figure 7.8 Performance of the BLDC motor drive during starting up and step load torque application: (a) speed, (b) three-phase currents, (c) torque

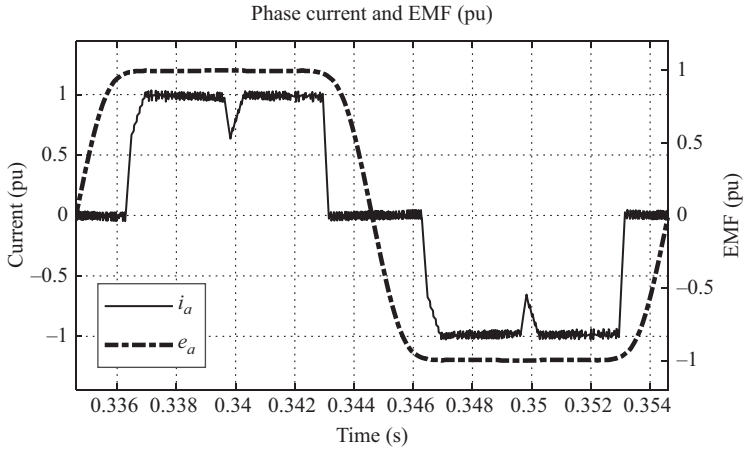


Figure 7.9 Current and EMF of one phase (phase a)

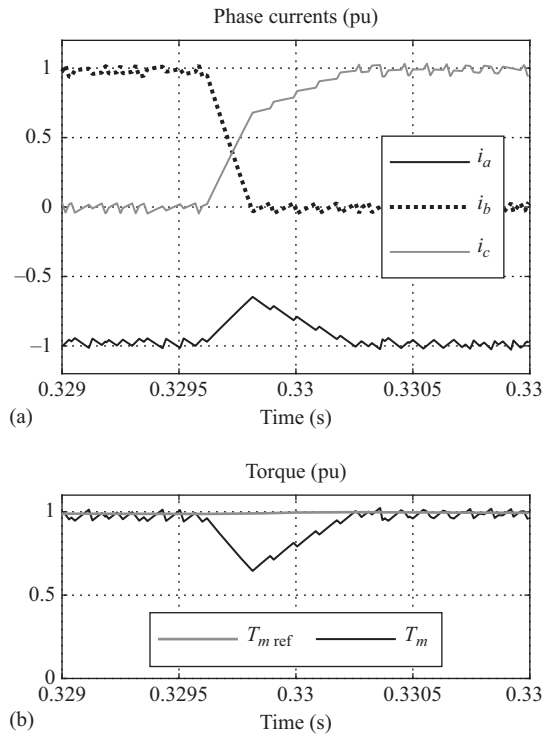


Figure 7.10 Current and torque during one commutation: (a) currents and (b) torque

ripple is minimized. However, perfect matching phase EMF and phase current are very difficult, considering unbalanced magnetization and/or imperfect windings [1]. Moreover, due to the finite cutoff frequency of the current control loop, the transient error of the controlled currents always occurs, especially in commutation instants, when the current profile changes drastically and also, the turn-on and turn-off characteristics of the power devices are not identical.

We can find in literature many efforts to reduce the torque ripple. References [5–10] are only some to name. Le-Huy, Perret and Feuillet [5] analyzed the torque by using Fourier series and showed that the torque ripple can be reduced by appropriately injecting selected current harmonics to eliminate the torque ripple components. Liu, Zhu and Howe [9] utilized direct torque control (DTC) to reduce torque ripple in addition to increasing torque dynamics. Lu, Zhang and Qu [10] calculated duty cycles in the torque controller considering unideal back EMFs. It can be noticed that the torque ripple cannot be completely removed despite computational effort.

7.5 Pseudo-vector control of BLDC motor

This section provides an alternative approach to reduce torque ripple in BLDCM drive. Instead of conventional square-waveform, the method uses the principle of vector control to optimally design the waveform of reference current in such a way that the torque ripple is minimal. The currents are however still controlled in the phase current control manner. For this reason, we have called the proposed approach PVC [11,12]. The proposed PVC has two major advantages: (a) the torque ripple is significantly reduced and (b) the flux weakening for constant power high-speed mode can be achieved by injecting a negative *d*-axis current into the control system, just like for the case of PMSMs (sine-wave machines).

7.5.1 System configuration

The configuration of the proposed control system is described in Figure 7.11, where the part generating current references are marked by the gray area.

It can be noted that except for the current reference generation part, the system in Figure 7.11 is the same as of the conventional control system for BLDCM (Figure 7.7). The motor is fed by a PWM-controlled MOSFET or IGBT inverter. As we can see in Figures 7.7 and 7.11, the currents are controlled by three controllers in the stationary frame. By convention, the suffix "*" refers to the reference variables and quantities.

The reference currents generating part of the PVC is described in the next subsection. To perform the direct transformation and the invert one, the rotor position will be needed. The instantaneous rotor position and speed can be obtained from the Hall-effect sensors information using an observer or measured by more sophisticated sensors.

7.5.2 Principle of pseudo-vector control

In the conventional square-wave phase current control (Figure 7.7), for a given torque command, the reference currents depend only on Hall-effect sensor signal showing the communication instants. The torque ripple is therefore inevitable.

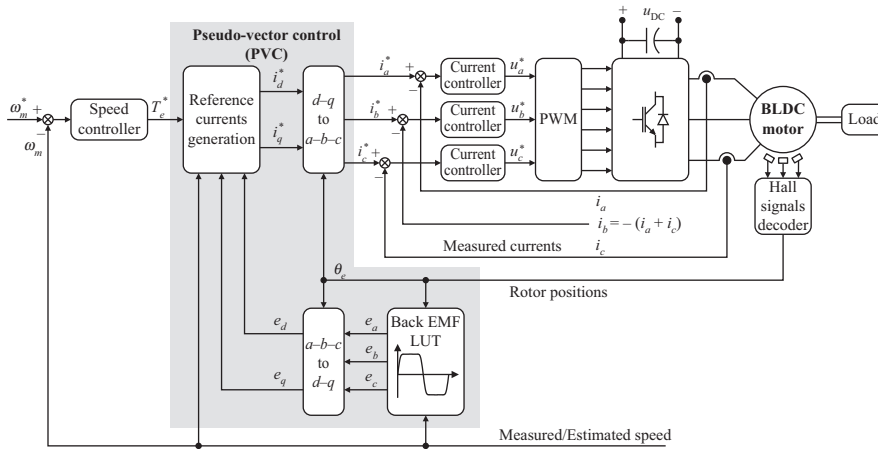


Figure 7.11 Block diagram of the proposed pseudo-vector control for BLDCM drives

Equation (7.4) shows the basic equation of the electromechanical torque, which is a result of the interaction between the motor currents and the EMF produced in the motor by the PMs. It also explains the fact that if the currents and EMF do not match each other, torque ripple occurs.

Rewriting (7.4) for the reference values, the reference torque is

$$T_e^* = \frac{i_a^* e_a + i_b^* e_b + i_c^* e_c}{\omega_m} \tag{7.17}$$

Because the torque reference is the ripple-free value, it is to note that if the reference currents i_a^*, i_b^*, i_c^* are chosen in the manner that (7.17) is respected, there would be no torque ripple.

We cannot directly obtain the reference currents i_a^*, i_b^*, i_c^* from a single equation (7.17), which has "three degree-of-freedom." Let us work in the synchronously rotating d–q frame instead of stationary a–b–c frame. The power equation can be rewritten in d–q frame

$$P_e = (i_a \cdot e_a + i_b \cdot e_b + i_c \cdot e_c) = \frac{3}{2} \cdot \left(i_d \cdot e_d + i_q \cdot e_q + i_0 \cdot e_0\right) \tag{7.18}$$

where the indexes d, q, 0 represent the variables in d-axis, q-axis and zero-sequence, respectively.

For a balanced system, it is desirable that the zero-sequence current i_0 is zero. Combining (7.17) and (7.18) gives for reference and desired values:

$$T_e^* \cdot \omega_m = \frac{3}{2}\left(i_d^* e_d + i_q^* e_q\right) \tag{7.19}$$

Equation (7.19) means that if we can *a priori* select the reference current i_d^*, we can calculate the reference current i_q^*, for a given speed and desired torque T_e^*.

$$i_q^* = \frac{(2/3)T_e^* \cdot \omega_m - i_d^* e_d}{e_q} \tag{7.20}$$

As the desired torque contains no torque ripple, the obtained torque is theoretically free of ripple if the current controllers work properly to yield currents perfectly equal to the reference ones.

The EMFs in *d–q* frame e_d, e_q in (7.19) and (7.20) are obtained from three-phase EMFs e_a, e_b, e_c by Park transformation. As previously mentioned, the zero-sequence current i_0 is forced to be zero in our system, so only e_d and e_q need to be calculated using simplified Park's transformation.

$$\mathscr{M} = \frac{2}{3}\begin{bmatrix} \cos(\theta_e) & \cos\left(\theta_e - \frac{2\pi}{3}\right) & \cos\left(\theta_e + \frac{2\pi}{3}\right) \\ -\sin(\theta_e) & -\sin\left(\theta_e - \frac{2\pi}{3}\right) & -\sin\left(\theta_e + \frac{2\pi}{3}\right) \end{bmatrix} \tag{7.21}$$

where θ_e is the rotor position: $\theta_e = \omega_e t$, with ω_e is the electrical angular speed ($\omega_e = \omega_m \cdot p$), ω_m is the motor (mechanical) angular speed and p is the pole pair number.

Having calculated i_d^*, i_q^*, the three-phase reference currents i_a^*, i_b^*, i_c^* are obtained by inverse Park transformation $\mathscr{M}^{-1}$.

$$\mathscr{M}^{-1} = \begin{bmatrix} \cos(\theta_e) & -\sin(\theta_e) \\ \cos\left(\theta_e - \frac{2\pi}{3}\right) & -\sin\left(\theta_e - \frac{2\pi}{3}\right) \\ \cos\left(\theta_e + \frac{2\pi}{3}\right) & -\sin\left(\theta_e + \frac{2\pi}{3}\right) \end{bmatrix} \tag{7.22}$$

It is worth to emphasis again here that by using the reference currents i_a^*, i_b^*, i_c^* to control the system, there would be theoretically no torque ripple, because the reference currents i_a^*, i_b^*, i_c^* were optimally designed taking EMFs into account. The *d–q* frame is utilized only for calculating these reference currents, while the phase current control principle is normally used in *a–b–c* frame.

7.5.3 Simulation results and performance comparison

The algorithm has been simulated in MATLAB/Simulink using the motor of which the parameters are shown in Table 7.1. The working condition in simulation is the same as that in Section 7.3.2: the motor is starting up with the conventional control to the rated speed without load, then a rated load is applied at $t = 0.15$ s when the system has been already in the steady state. The PVC is then applied at the instant $t = 0.355$ s. To emphasis the performance of the controlled system, the currents are controlled by hysteresis technique, the same as in the conventional control (Section 7.3.2).

Figure 7.12 shows the performance of the proposed PVC, in comparison with the conventional control. As we can see in Figure 7.12, the current is no longer in square-waveform, but rather in trapezoidal form when the PVC is applied. As the result, the torque ripple due to the 60° interval commutation is eliminated. It is noted that high-frequency noise in the current and the torque waveforms is the natural consequence of the hysteresis band in current control, but it does not harm the quality of produced torque.

The EMF and current of one phase (phase a) are shown in Figure 7.13. Special features should be noted for the operation under base speed:

- The current is in phase with the EMF
- The current amplitude is the same for both conventional control and PVC
- Only the shape of the current is different, quasi-square form in conventional control, but nearly trapezoidal form in PVC.

To further evaluate the performance of the system, the flux trajectory ($\Psi_\alpha - \Psi_\beta$) is examined. Figure 7.14 clearly shows the "cogs," which have originated from the commutations at every 60° in case of conventional control. The sharp change of current waveform in commutation instants is reflected in the flux. Again, the torque produced in the machine can also be considered as an interaction between rotor and stator flux. The torque ripple is therefore evident in this case.

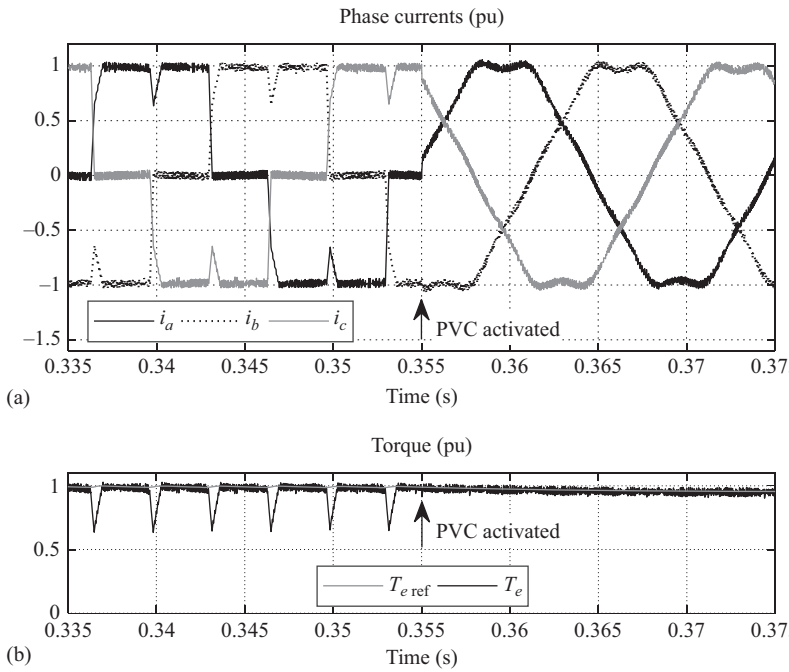


Figure 7.12 Performance of BLDCM drive with two control modes: conventional control and PVC (from 0.355 s): (a) currents and (b) torque

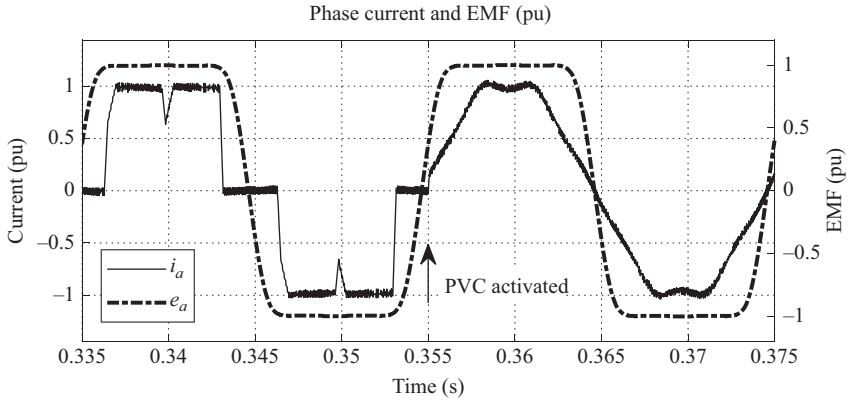


Figure 7.13 Current and EMF of one phase (phase a) with two control modes: conventional control and PVC (from 0.355 s)

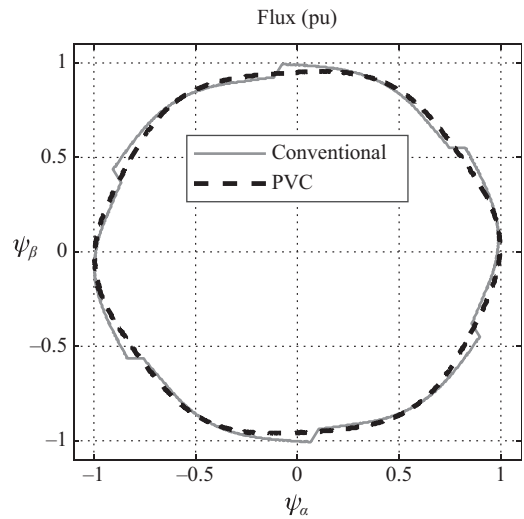


Figure 7.14 The flux trajectories (ψ_α–ψ_β) using conventional phase-current control and using PVC

On the contrary, the flux trajectory of the PVC method is nearly round, because the current waveform of PVC is smooth, as previously shown in Figures 7.12(a) and 7.13. This interesting feature gives another explanation of the superiority of the proposed PVC over the conventional phase-current control method.

Note that the simulation in Figures 7.11–7.14 was carried out in the based-speed region, with $i_d^* = 0$ in (7.20). The flux weakening for constant-power high-speed mode can be achieved by injecting a negative *d*-axis current ($i_d^* < 0$) into the control system, just like for the case of PMSMs (sine-wave machines).

Figure 7.15 shows the waveform of EMF and currents in *d–q* frame in the PVC block (Figure 7.11).

The waveforms of referent currents and the actual ones are illustrated in Figure 7.16, for monitoring purpose only, because these currents are not used directly in control.

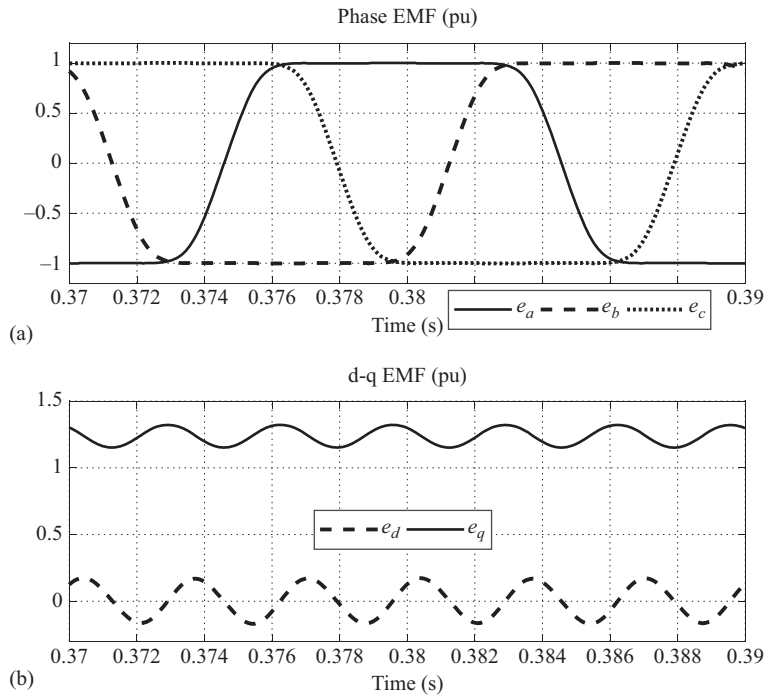


Figure 7.15 Waveforms of EMFs in a–b–c and d–q frames: (a) e_a, e_b, e_c and (b) e_d, e_q

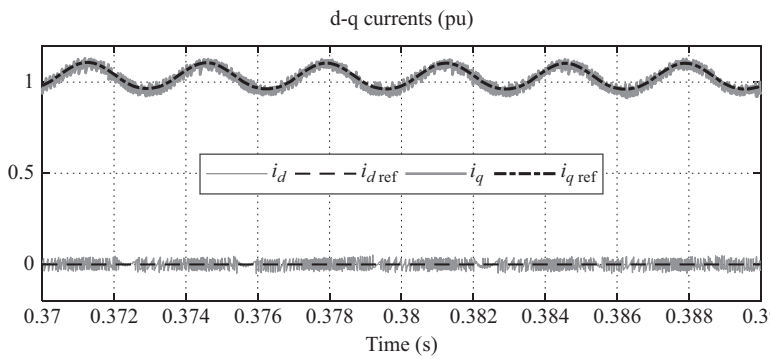


Figure 7.16 Reference and actual currents in d–q frame

7.6 Control of BLDCM in high-speed region

7.6.1 Operation in high-speed region

In many applications such as electric vehicles, tool machines, wide speed range (beyond the rated speed) is required. Above the rated speed, because the power of a BLDCM is a limit determined value, the torque decreases inversely proportional to the motor speed.

Figure 7.17 shows the typical characteristics of a motor drive in the base-speed and high-speed regions. Conventional drive system cannot operate well in the power limit region due to voltage saturation, if no additional special control technique is applied. Although Figure 7.17 is common for any kind of motors, the phenomena of saturation can be explained easily for the BLDCM.

To expand the speed range of a drive, it is common to weaken the existing field. For the separately excited DC motor, as the motor has separate windings for the flux-producing and torque-producing currents, it is very easy to control this motor above rated speed by decreasing the flux in keeping the applied voltage at its rated value. For a vector-control induction motor (IM) drive, flux-weakening operation can be realized by decreasing the *d*-axis (flux-producing) current. For a vector-control PMSM drive, the field of PM can be weakened by introducing a negative *d*-axis current ($I_d < 0$) [13]. For a BLDCM with conventional control, the flux-weakening operation is not a matter of acting on *d*-axis current as compared to other AC motors, because the vector control is not applicable to this kind of motor as mentioned previously.

PWM technique is used to control the applied voltage of BLDCM. Operating at rated speed, the power switches are turned on 120 electrical degrees each half cycle, so the applied voltage attains its rated value. This is the maximal applied

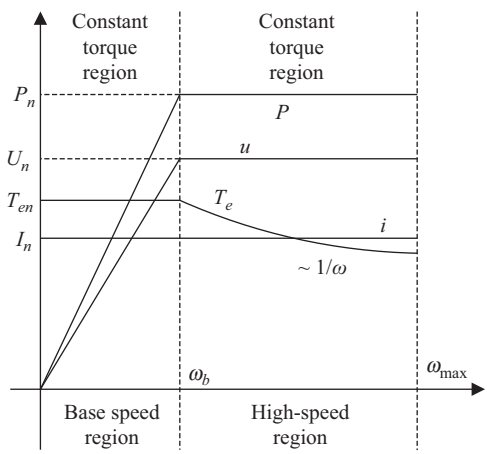


Figure 7.17 Various control variables in functions of motor speed

voltage for a BLDCM. The voltage equation for each phase of the motor (7.3) can be expressed again in general form as

$$u = Ri + L\frac{di}{dt} + e \tag{7.23}$$

Because the applied voltage is limited, if the motor current is large enough to satisfy the load torque, the EMF cannot increase to a higher value. EMF is directly proportional to the motor speed, so the motor speed cannot be developed. Similarly, if we want the motor to operate at a higher speed, the output torque of the motor cannot be developed as required.

7.6.2 Phase-advance approach to expand the speed range of BLDCM

In literature, we can find the so-called phase advance technique to solve the problem of high-speed operation for BLDCM [14–19]. The main idea of this approach can be explained as follows [14]. There are two types of electromotive forces in the phase winding of a BLDCM. One is called BEMF, e, which is induced by the magnet field of the rotating of the PM. Another one is called transformer electromotive force (TEMF), $L(di/dt)$, which is induced by the transformer action of the time-varying stator current in the phase windings. Below the rated speed, BLDCM is controlled conventionally, the phase current is in phase with the phase EMF. When operating above the rated speed, the phase-current leads the phase BEMF. Thus, the TEMF is utilized to counteract the BEMF. This is equivalent to the flux-weakening for the DC motor drive. There is a corresponding advance angle for every given reference speed. The locus of these points is the "phase advance curve." Chan *et al.* proposed in [14] that the value of "advance angle" is governed by an approximate linear relationship with the motor speed. In fact, the "phase advance curve" is not a straight line, but a complicated curve. In the latter work in 1998, Chan *et al*. proposed an algorithm which is called "adaptive searching trajectory" to determine the corresponding advance angle [15]. This algorithm increases the complicatedness of the BLDCM drive. Beside [14,15], other techniques in phase advance approach have been investigated. Lawler *et al*. identified several limitations of the phase advance approach. The phase advance approach is especially sensitive to the motor inductance that must be larger than a threshold value to maintain motor current within rated value when operating at rated power and high speed [16]. If the motor inductance is low, additional cooling will be necessary for the motor and inverter components and the current rating of the inverter will have to be increased. Lawler *et al*. also proposed an inverter topology and control scheme which is called dual-mode inverter control [16]. With this control scheme, the range of motor inductance is widened. An analytical expression of phase advance is given in [17], which can be considered as an improvement of [14,15], when the winding resistance is not negligent.

The "phase advance approach" technique can be easily integrated into the conventional control schema by adding an angle θ_0, as shown in Figure 7.18.

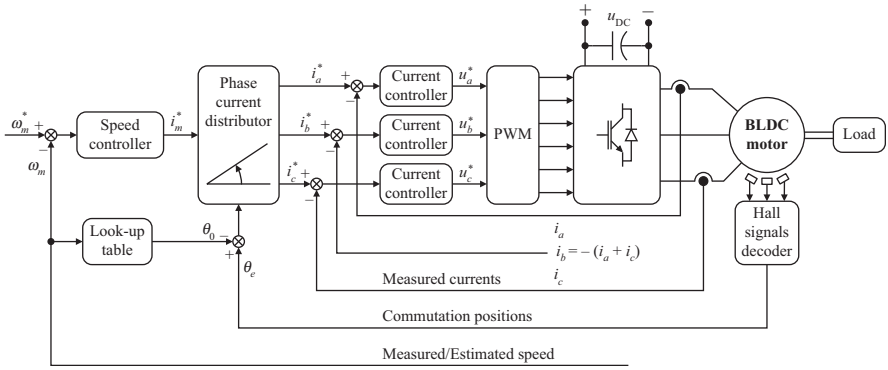


Figure 7.18 Conventional BLDCM drive system with phase-advance for high-speed operation

7.6.3 Pseudo-vector control for high-speed range of BLDCM

The PVC approach presented in Section 7.5 has the second advantage that is in the high-speed region. The flux-weakening control is possible by inserting a negative d-axis current ($i_d^* < 0$) into the calculation of reference currents. The method of calculating the current reference value on the d-axis, which is an important point of PVC, is explained in the literatures [11,12].

The d-axis current calculation in Figure 7.19 is calculated in accordance with the following expression:

$$i_d^* = -\left|\frac{T_e^*}{k_T}\right| \sin\left(\arccos\left(\frac{\omega_b}{\omega_m}\right)\right) = -\left|i_m^*\right| \sin\left(\arccos\left(\frac{\omega_b}{\omega_m}\right)\right) \tag{7.24}$$

This PVC approach is given either by (7.25) if no field-weakening control is realized ($i_d^* = 0$) or (7.26) if the field-weakening control is realized ($i_d^* < 0$).

$$\begin{cases} i_q^* = \dfrac{2}{3} \cdot \dfrac{T_e{}^* \omega_m}{e_q} \\ i_d^* = 0 \end{cases} \tag{7.25}$$

$$\begin{cases} i_q^* = \dfrac{(2/3) \cdot T_e{}^* \cdot \omega - e_d \cdot i_d^*}{e_q} \\ i_d^* = -\left|i_m^*\right| \sin\left(\arccos\left(\dfrac{\omega_b}{\omega_m}\right)\right) \end{cases} \tag{7.26}$$

In (7.27), a stator current i_s^* is given in term of d-axis current reference i_d^* and q-axis current reference i_q^*.

$$i_s^* = \sqrt{i_d^{*2} + i_q^{*2}} \tag{7.27}$$

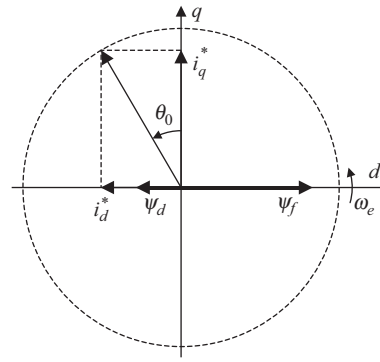


Figure 7.19 Diagram illustrating a vector relation between current reference i_d^* and i_q^*

The trajectory of the stator current i_s^* is the cycle with the radius equal rated value, therefore (7.28) holds

$$i_s^* = \frac{2}{3} \cdot \frac{T_e^* \cdot \omega_m}{e_q} = \frac{2}{3} \cdot \frac{k_T \cdot i_m^* \cdot \omega_m}{e_q} \tag{7.28}$$

7.6.4 Simulation results for high-speed operation using PVC

The operation of the dive in high-speed region was examined. In the test, the speed change command was applied at $t = 0.35$ s, from 1 to 1.3 pu. The flux weakening algorithm was executed by injecting a negative current I_d (7.26) to the PVC block in Figure 7.11. The speed evolution, currents of three phases and the torque are shown in Figure 7.20.

The currents of three phases are shown in Figure 7.21 in a smaller time scale. The reference current of one phase (phase a) and the actual ones are given in Figure 7.22. As is shown, the current waveform is no longer trapezoidal. The pick in current waveform is originated from the added negative current I_d into the system (7.26).

The currents in d–q frame are shown in Figure 7.23, where the operation in high-speed region is clearly demonstrated, in the way that the current i_d is negative, and i_q is decreased due to a smaller load torque applied in high-speed region (see also Figure 7.20).

The effect of the negative current i_d is explicitly proven by the flux trajectory in Figure 7.24, for two modes of operation: with rated speed and at high speed. A noteworthy feature is that the flux trajectory when the motor operates above the base speed is smaller than that under base-speed region. It demonstrates that the flux-weakening control is performed in BLDCM. For the motor with larger inductance, the effect of flux weakening is even more pronounced.

Figure 7.25 shows the relationship between the current and EMF of one phase (phase a). Compared with Figure 7.13, the current is advanced to EMF in this case.

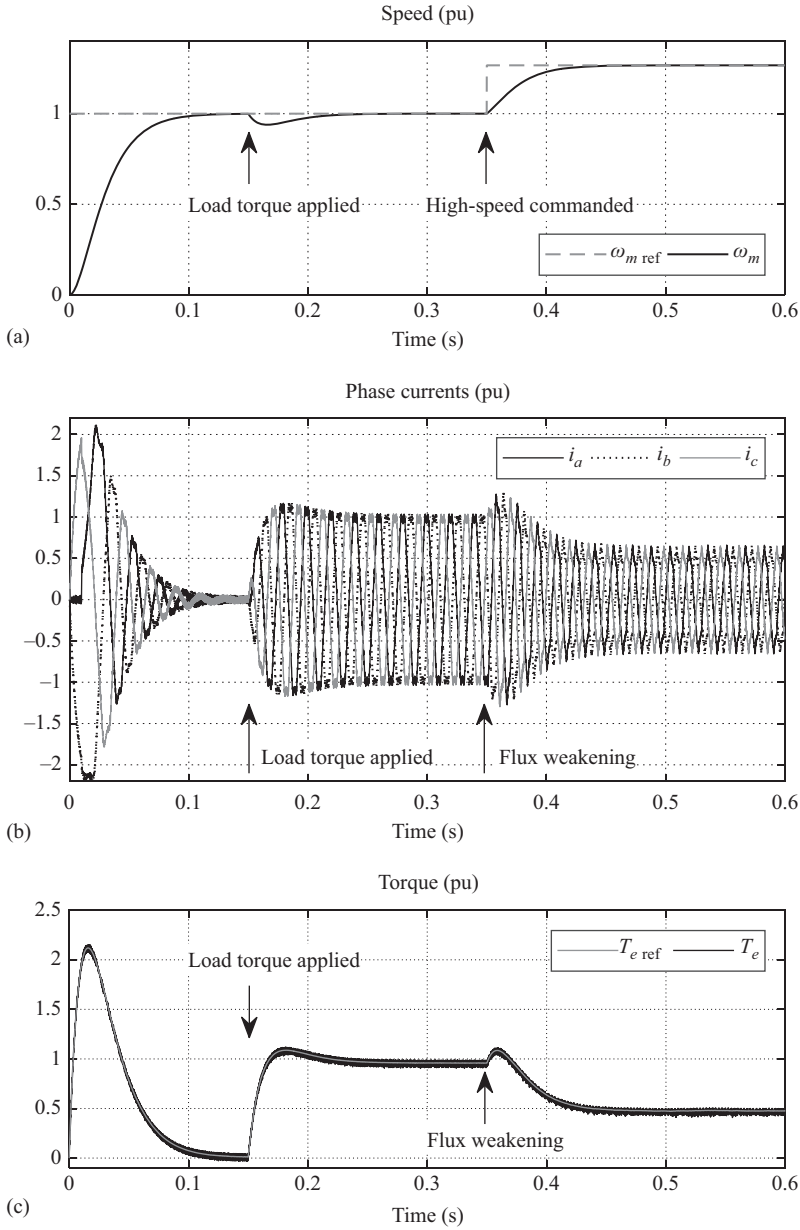


Figure 7.20 Performance of PVC in starting, rated speed and high-speed region: (a) speed, (b) phase currents, (c) torque

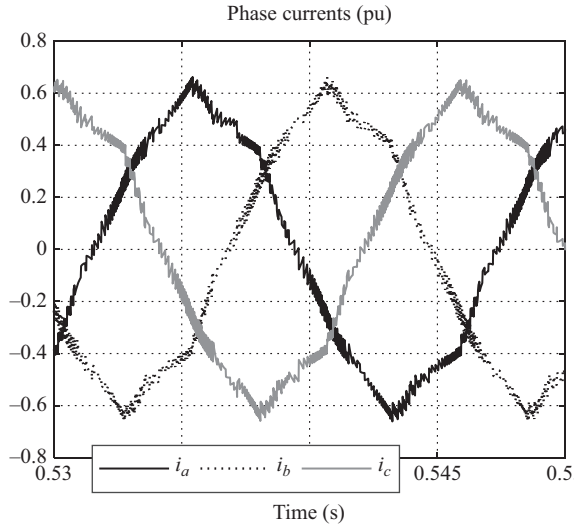


Figure 7.21 Phase currents in high-speed operation

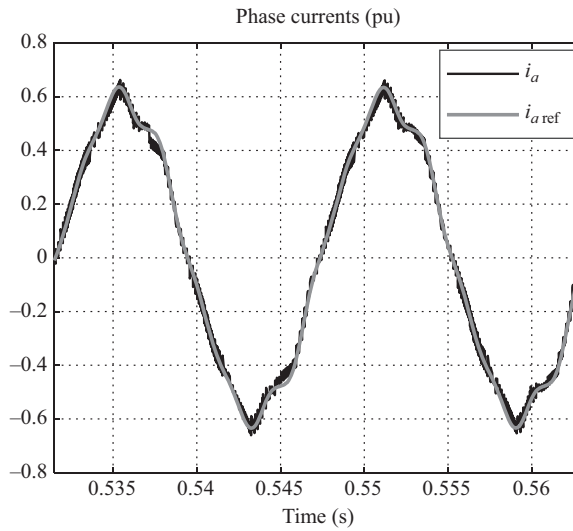


Figure 7.22 Reference and actual currents of one phase

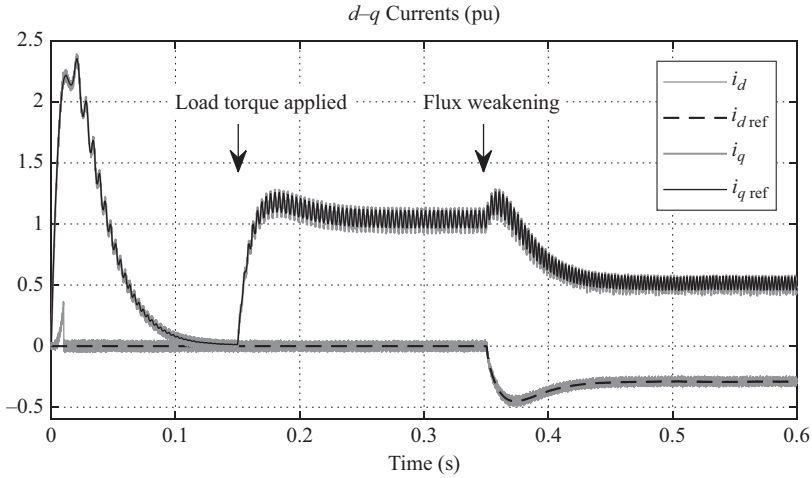


Figure 7.23 d–q-Axis currents

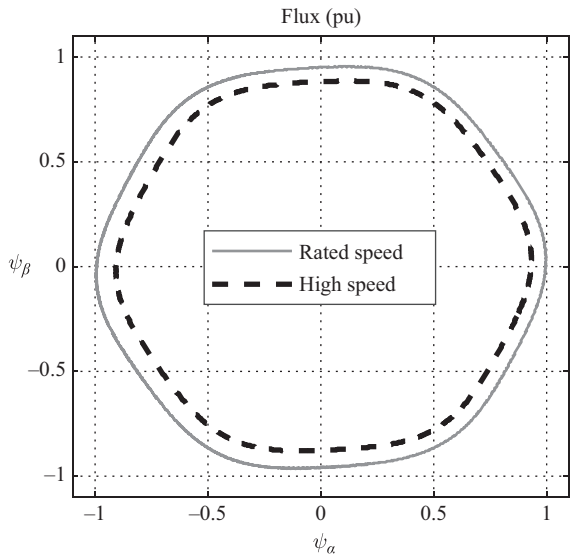


Figure 7.24 The flux trajectory (ψ_α–ψ_β) using PVC for rated speed and high-speed operation

It is to say that injecting a negative current i_d is equivalent to the advancing angle in the conventional control. This interesting remark confirms the physical insight of flux-weakening techniques for BLDCM and the advantages of PVC over the conventional control technique for BLDCM drives.

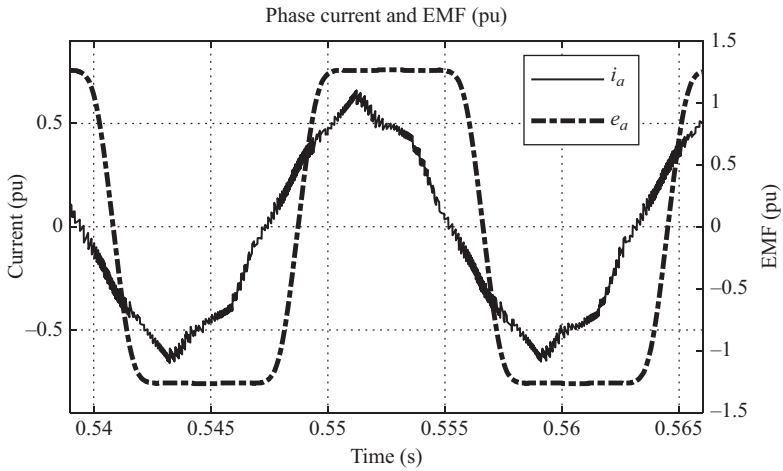


Figure 7.25 Current and EMF of one phase (phase a)

7.7 Summary

Because of the simplicity in construction and in control, BLDCMs are found in a wide range of applications. This kind of motor suffers, however, a serious drawback in the torque ripple, due to sharp communications every 60° electrical. Various efforts have been made to reduce the torque ripple. Phase advance approach is a common practice for controlling the motors above the base speed.

The working principle of the motor has been illustrated using the motor and electronics commutator association, in accordance with Hall-effect sensors sequences. The mathematical modeling of the motor has been carried out. The practical block diagram of three-phase motor has been built for the simulation purpose. Control of the BLDC drive was performed in MATLAB/Simulink environment and the analysis of torque ripples has been provided.

The PVC was presented to improve the performance of the BLDCM drives. The vector-control principle in *d–q* synchronously rotating frame is utilized for the generation of current references only, while the motor currents were controlled, as usually for PM trapezoidal type motors, by individual phase-current control in the stationary *a–b–c* frame. The performance of the PVC has been tested and the results have been compared with those of the conventional phase-current control method. The great improvement in torque ripple reduction has been obtained. By using PVC, the flux weakening operation was also possible, instead of the "phase advance" technique in the conventional control.

List of symbols

m	Number of phases
p	Number of pole-pair

u_a, u_b, u_c	Phase voltages
i_a, i_b, i_c	Phase currents
e_a, e_b, e_c	Phase EMFs
R_a, R_b, R_c	Phase resistances
L_a, L_b, L_c	Phase inductances
M_{ab}, M_{bc}, M_{ca}	Mutual inductance between two phases
P_e	The electrical power
T_e	Torque developed at motor shaft
ω_m	Rotor angular velocity
T_L	Load torque
J	Inertia of rotor and coupled shaft
s	Differential operator
τ	Electrical time constant
θ_e	Electrical rotor position
k_e	EMF constant
ω_e	The electrical angular velocity
I_m	Amplitude of current
E_{LL}	The line-to-line EMF
k_t	Torque constant
ω_{m0}	No-load speed
$\Delta\omega_m$	The speed change
i_d^*, i_q^*	Reference current
T_e^*	Reference torque
i_s^*	Reference stator current

Glossary of terms

Electronic commutator	The voltage source inverter used for switching of the concerned windings as per rotor magnet position. This replaces the mechanical commutator-brush arrangement, making the machine a brushless one
Torque ripple	The peak to peak ripple in the motor torque which is assumed to be constant
Pseudo-vector control	The vector control method used for non-sinusoidal waveforms by taking the EMF information and reference phase currents in *d–q* frame
Hall-effect sensors	The sensors placed in stator for position sensing of rotor magnets using Hall effect

References

[1] J. R. Hendershot Jr and T. Miller, Design of Brushless Permanent-Magnet Motors, Magna Physics Publishing and Clarendon Press, Oxford, 1994.

[2] B. K. Bose, *Modern Power Electronics and AC Drives*, Prentice Hall, Upper Saddle River, NJ, 2002.

[3] P. Pillay and R. Krishnan, "Modeling, simulation, and analysis of permanent-magnet motor drives. II. The brushless DC motor drive," *IEEE Transactions on Industry Applications*, vol. 25, no. 2, p. 274–279, 1989.

[4] R. Carlson, M. Lajoie-Mazenc and J. Fagundes, "Analysis of torque ripple due to phase commutation in brushless DC machines," *IEEE Transactions on Industry Applications*, vol. 28, no. 3, p. 632–638, 1992.

[5] H. Le-Huy, R. Perret and R. Feuillet, "Minimization of torque ripple in brushless DC motor drive," *IEEE Transactions on Industry Applications*, vol. 22, p. 748–755, 1986.

[6] J. Holtz, "Identification and compensation of torque ripple in high-precision permanent magnet motor drives," *IEEE Transactions on Industrial Electronics*, vol. 43, no. 2, p. 309–320, 1996.

[7] T. M. Jahns and W. L. Soong, "Pulsating torque minimization techniques for permanent magnet AC motor drives – a review," *IEEE Transactions on Industrial Electronics*, vol. 43, no. 2, p. 321–330, 1996.

[8] S. I. Park, T. S. Kim, S. C. Ahn and D. S. Hyun, "An improved current control method for torque improvement of high-speed BLDC motor," in *Applied Power Electronics Conference and Exposition (APEC), Eighteenth Annual IEEE*, 2003.

[9] Y. Liu, Z. Q. Zhu and D. Howe, "Direct torque control of brushless DC drives with reduced torque ripple," *IEEE Transaction on Industry Applications*, vol. 41, no. 2, p. 599–608, 2005.

[10] H. Lu, L. Zhang and W. Qu, "A new torque control method for torque ripple minimization of BLDC motors with un-ideal back EMF," *IEEE Transactions on Power Electronics*, vol. 23, no. 2, p. 950–958, 2008.

[11] C. Ta and S. Endo, "Motor and Drive Control Device Therefor". USA Patent US7339346B2, 2008.

[12] C. Ta, "Pseudo-vector control – an alternative approach for brushless DC motor drives," in *IEEE International Electric Machines and Drives Conference (IEMDC)*, 2011.

[13] S. Morimoto, Y. Takeda, T. Hirasa and K. Taniguchi, "Expansion of operating limits for permanent magnet motor by current vector control considering inverter capacity," *IEEE Transactions on Industry Applications*, vol. 26, no. 5, p. 866–871, 1990.

[14] C. C. Chan, J. Z. Jiang, W. Xia and K. T. Chau, "Novel wide range speed control of permanent magnet brushless motor drives," *IEEE Transactions on Power Electronics*, vol. 10, p. 539–546, 1995.

[15] C. C. Chan, W. Xia, J. Z. Jiang, K. T. Chau and M. L. Zhu, "Permanent magnet brushless drives," *IEEE Industry Application Magazine*, vol. 4, no. 6, p. 16–22, 1998.

[16] J. S. Lawler, J. M. Bailey, J. W. McKeever and J. Pinto, "Extending the constant power speed range of the brushless DC motor through dual-mode inverter control," *IEEE Transactions on Power Electronics*, vol. 19, no. 3, p. 783–793, 2004.

[17] B. Nguyen and C. Ta, "Phase advance approach to expand the speed range of brushless DC motor," in *International Conference on Power Electronics and Drive Systems*, 2007.

[18] C. L. Chiu, Y. T. Chen, Y. H. Shen and R. H. Liang, "An accurate automatic phase advance adjustment of brushless DC motor," *IEEE Transactions on Magnetics*, vol. 45, no. 1, p. 120–126, 2009.

[19] J. J. Moon, W. S. Im and J. M. Kim, "Novel phase advance method of BLDC motors for wide range speed operations," in *Applied Power Electronics Conference and Exposition (APEC), Twenty-Eighth Annual IEEE*, 2013.

Chapter 8

Switched reluctance motor drives

Jin-Woo Ahn[1] *and Grace Firsta Lukman*[1]

The concept of switched reluctance motor (SRM) has been widely known for a long time, going back to 1838 when Robert Davidson built one as a traction drive for a train of Edinburgh–Glasgow. The weight of the train was 6 t, and it was operating at 4 mi/h by battery. SRM has the simplest structure among other electrical drives, but it depends heavily on power converter for its operation. Therefore, it has only been recently researched again in the last decade thanks to the development of microprocessor and power electronics, and now it can compete with the commonly used DC and AC motors for industrial applications.

SRM operation relies on the reluctance torque, instead of the continuous torque by rotating magnetic field, so it is necessary to pay attention to the generation of the pulsating torque. Despite having a lot of advantages due to its simple structure, such as low rotor inertia and applicability in harsh environments, SRM is also known for its drawbacks, such as high acoustic noise and vibration, and large torque ripple. However, these problems can be solved or at least minimized through proper design and control methods.

In this chapter, the basic knowledge needed to understand and design an SRM is provided. It is hoped that by reading this, the readers from all levels be able to get deeper comprehension about how to design the proper motor and its controller, solve problems related to the drawbacks, and future prospect of SRM.

8.1 Principle of switched reluctance motor

8.1.1 Operation of SRM

8.1.1.1 Excitation characteristics

The SRM is an electric machine that converts the reluctance torque into mechanical power. Generally, there are two kinds of torque in the electromechanical energy conversion based on the magnetic structure: mutual torque and reluctance torque. Mutual torque is generated in the constant rotating magnetic field by the maximized torque which occurs when excitation energy is applied to both stator and rotor.

[1]Department of Mechatronics Engineering, Kyungsung University, South Korea

On the other side, reluctance torque is caused by the change of reluctance and excitation energy of the magnetic circuit when excitation energy is applied to one side only, stator or rotor. This is due to the characteristics of phase reluctance that gets minimized when the corresponding phase is excited.

Therefore, salient pole shape which changes reluctance as the rotor rotates is required for the utilization of reluctance torque. However, since there is a limit to the geometrical configuration, it is necessary to apply a continuous pulse excitation power for every rotating section. In other words, one pulse excitation is required to create one "stroke" of rotor rotation. Figure 8.1 shows the basic configuration of a doubly salient switched reluctance (SR) drive.

8.1.1.2 Torque generation

In order to obtain the torque expression of the motor, the concept of coenergy W_c' is introduced and the torque equation of the SRM can be obtained as stated below.

The coenergy W_c' of the magnetic circuit of the magnetic structure of the doubly salient SRM is

$$W_c' = \frac{1}{2} i^2 \cdot L \tag{8.1}$$

where i is the current of the phase winding and L is the corresponding inductance. The torque T_e for one phase is the partial derivative of the coenergy for the rotor position angle θ.

$$T_e = \frac{\partial W_c'}{\partial \theta} = \frac{1}{2} i^2 \cdot \frac{dL}{d\theta} \tag{8.2}$$

Here, the generated torque of SRM is proportional to the square of phase current and to the rate of change of the inductance per position angle.

Since torque is proportional to the square of the current, it can be produced regardless of the direction of phase current. However, the sign of the torque varies depending on the slope of inductance, so there will be a negative torque for that particular phase depending on the rotor position. Therefore, in order to eliminate the negative torque, SRM must be switched on and off according to the rotor

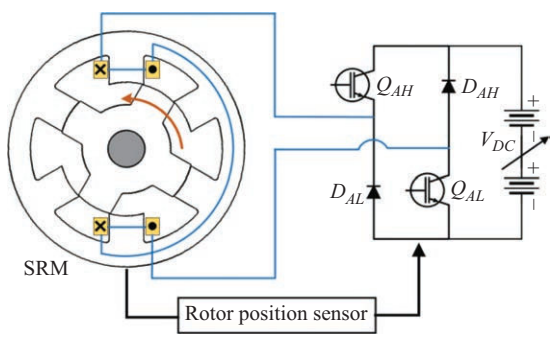


Figure 8.1 SRM drive system

position. Ideal phase current, torque, and inductance profiles for a doubly salient type SRM as shown in Figure 8.2.

As can be seen from Figure 8.2(a), the inductance may increase at $(\theta_s - \theta_1)$, decrease to its minimum value of L_u at $(\theta_2 - \theta_3)$, or constant at $(\theta_1 - \theta_2)$ with respect to the rotor position θ. The maximum value of inductance L_a is reached when a rotor pole pair is aligned with a stator pole pair, and the maximum value of inductance L_u is reached at unaligned position. If a constant excitation current is applied to the phase as shown in Figure 8.2(b), positive torque is generated in the increasing inductance region $(\theta_s - \theta_1)$, and negative torque of the same magnitude is generated at $(\theta_2 - \theta_3)$, just as described in (8.2).

Therefore, in order to produce positive electric torque and prevent the generation of negative torque, it is necessary to acquire rotor position information and perform continuous phase switching excitation accordingly. Figure 8.3 shows a three-phase switching exciter that generates ideal torque by applying switching excitation current to each phase. The output torque T_{out} is generated by the sum of the torques generated by the excitation current of each phase, and it can be calculated as follows:

$$T_{out} = \frac{1}{2} i_a^2 \frac{dL(\theta)}{d\theta} + \frac{1}{2} i_b^2 \frac{dL(\theta - \theta_{st})}{d\theta} + \frac{1}{2} i_c^2 \frac{dL(\theta - 2\theta_{st})}{d\theta} \tag{8.3}$$

where θ_{st} is the rotor stroke angle which can be calculated as $360^\circ/3N_r$ in which N_r is the rotor pole number. Taking a three-phase 6/4 pole SRM as an example, $N_r = 4$ and $\theta_{st} = 30^\circ$.

For actual, nonideal switching excitation, the following points must be taken into account.

1. When switching on exactly in the inductance rising section $(\theta_s - \theta_1)$, the increase of the inductance causes current to be insufficient to produce the required torque, so switching on has to be done before the minimum inductance section to establish a sufficient current.

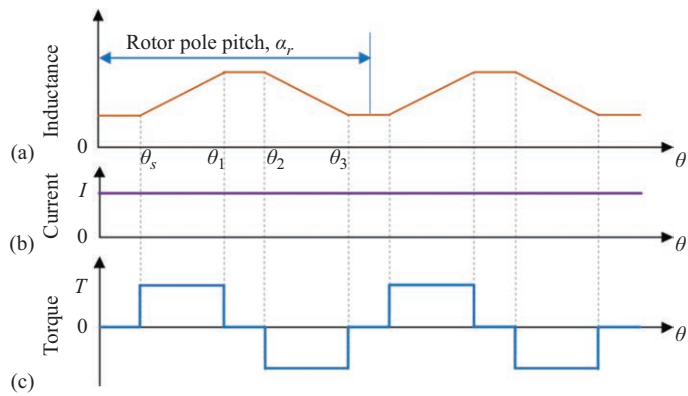


Figure 8.2 Ideal constant excitation profile: (a) phase inductance, (b) phase current and (c) phase torque

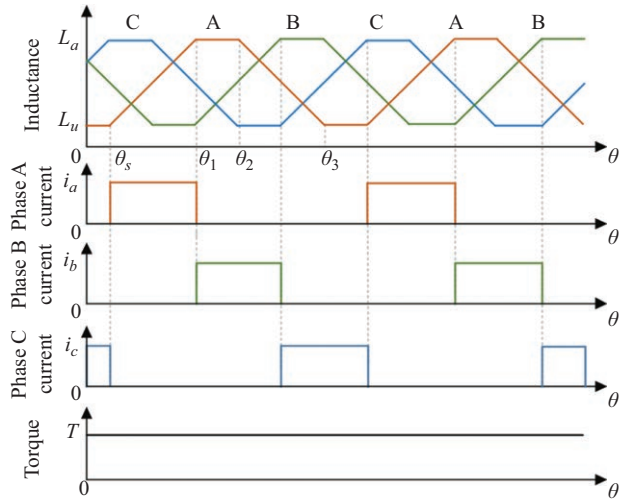


Figure 8.3 Ideal torque generation for switching excitation current

2. When switching off the current, there has to be enough time for it to reach zero before the negative torque region $(\theta_2 - \theta_3)$. The phase current and torque of the actual, nonideal switching excitation are shown in Figure 8.4. The operating characteristics of each section of the rotor position angle in Figure 8.4 are as follows:
   (i) $0 \sim \theta_{\min}$: Minimum inductance section. Switch on is performed in this section to establish a sufficient current.
   (ii) $\theta_{on} \sim \theta_{\min}$: Magnetizing section by applying power to the windings and is known as the advance angle θ_{AD}. The current waveform changes depending on the rotation speed, applied voltage, winding resistance, θ_{AD}, etc. Switching on angle, θ_{on}, is always prior to $\theta_{\min}$.
   (iii) $\theta_{\min} \sim \theta_{\max}$: At $\theta_{\min}$, the leading edge of the rotor pole meets the edge of the stator pole, and the value of inductance increases. As a result, when the maximum value $L_{\max}$ is reached, the maximum constant torque is generated. The equation at this point is

$$V = ri + \frac{d\lambda}{dt} \tag{8.4}$$

where r is the winding resistance and λ is the flux linkage. Assuming that it operates as a constant angular velocity ω and ignores both winding resistance and magnetic nonlinearity of the iron core,

$$V = L\frac{di}{dt} + i\frac{dL}{d\theta}\omega \tag{8.5}$$

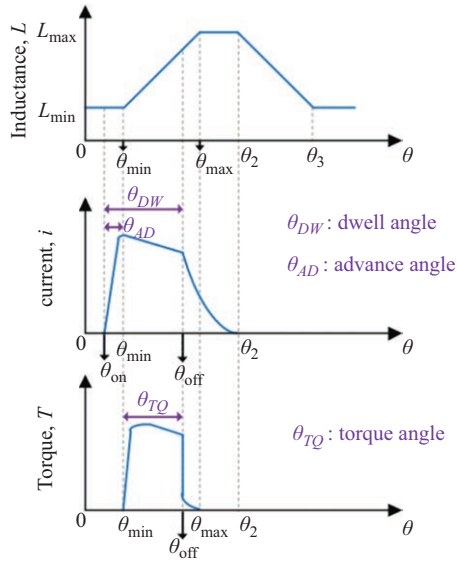


Figure 8.4 Actual torque generation for switching excitation current

At this time, energy flows can be calculated as

$$Vi = \frac{d}{dt}\left(\frac{1}{2}Li^2\right) + \frac{i^2}{2}\frac{dL}{d\theta}\omega \tag{8.6}$$

When SRM operates as a motor, a part of the input is converted to mechanical output $[(i^2/2)(dL/d\theta)\omega]$, and the rest is accumulated as magnetic energy, $[(1/2)Li^2]$. However, when switching on occurs in this section, some of the magnetic energy is returned to the mechanical output and some to the power source.

1. $\theta_{on} \sim \theta_{off}$: This is the section where the inverter switch is turned on. This angle is known as the dwell angle θ_{AD}.
2. $\theta_{\min} \sim \theta_{off}$: The positive torque region is generated by switching, and this angle is called a torque angle, θ_{TQ}.
3. $\theta_{\max} \sim \theta_2$: The inductance is constant at $L_{\max}$, and it causes torque dead zone. This is due to the difference in width between stator and rotor poles, and this region is set to reduce the negative torque in the inductance-decreasing period $(\theta_2 - \theta_3)$.
4. $\theta_2 \sim \theta_3$: The inductance decreases linearly until $L_{\min}$. This section is the demagnetizing section that may generate negative torque. When current flows in this section, energy is returned from the mechanical power to the power source due to the negative torque as well as the magnetically accumulated energy. This is a regenerative action and can be used as braking torque. This is one of the most important features of SRM that enables four-phase operation by instantaneous switching of the circuit.

8.1.2 Characteristics of SRM

SRM has the simplest structure among other electric machines. It comprises a stator with excitation windings and a ferromagnetic salient rotor pole with no windings. The torque generation is based on the tendency of the rotor to be aligned with the excited stator pole pair. The inductance of the stator winding is a function of the angular position of the rotor. Thus, the position of the rotor must be known to effectively give excitation to the windings of each phase to produce torque.

SRMs are classified into two types: singly salient type and doubly salient type. The major feature is that there are neither windings nor permanent magnets on the rotor, and only the stator windings are excited. Therefore, the copper loss of SRM only occurs in stator windings. Because the stator cools effectively faster than the rotor, the motor can be made compact and small for a given rating or capacity.

In order to generate torque, the inductance of the stator winding has to change according to the position of the rotor. Figure 8.5(a) shows a cross section of a non-salient stator with high permeability magnetic material and a two poles rotor.

The above figure shows that the motors are two phased, but it is possible to design more than that. The inductance of a stator phase winding will be maximum when the rotor axis coincides with stator axis and minimum when it is perpendicular or absolutely unaligned. Figure 8.5(b) shows a cross section of a two-phase doubly salient type SRM. Here, there are four stator poles and each pole has a winding. The windings of the opposite poles are connected whether in series or parallel. This type is very similar to Figure 8.5(a) in being two-phase motor with two-pole rotor.

The phase inductance varies from maximum to minimum, from the position where the axis of the rotor coincides with the stator phase axis to where it is perpendicular (assuming the case shown in Figure 8.5). In these two models, the inductance slope varies depending on the shape of the stator, thus making the torque characteristic differs.

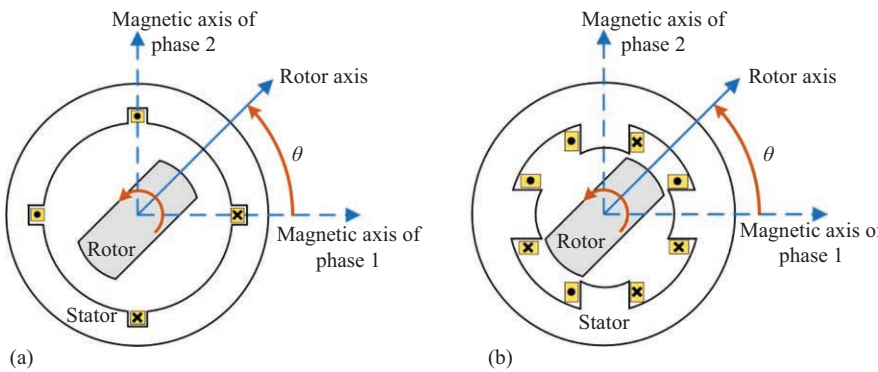


Figure 8.5 SRM cross section: (a) singly salient type and (b) doubly salient type

Because the permeability of the stator and rotor cores is high, if the reluctance can be ignored, the mutual inductance can also be ignored, so the relationship between flux and current becomes very simple. Therefore,

$$\lambda_1 = L_{11}(\theta) = L(\theta) i_i \tag{8.7}$$

$$\lambda_2 = L_{22}(\theta) = L(\theta - 90^\circ) i_2 \tag{8.8}$$

where $L_{11}(\theta)$ and $L_{22}(\theta)$ are the self-inductance of phases 1 and 2. $L(\theta)$ is defined by the angle formed by stator magnetic axis and rotor axis as shown in Figure 8.5. The electromagnetic torque of this system is derived from the concept of coenergy.

$$T = \frac{\partial W'_{fld}(i_1, i_2, \theta)}{\partial \theta} \tag{8.9}$$

In the above equation, the currents i_1 and i_2 are fixed as a constant and are partially differentiated with respect to θ. Using (8.7) and (8.8) and the consideration that the mutual inductance between windings is 0, the coenergy W'_{fld} can be expressed as

$$W'_{fld} = \frac{1}{2} L(\theta) i_1^2 + \frac{1}{2} L(\theta - 90^\circ) i_2^2 \tag{8.10}$$

The torque can be obtained from (8.9) and (8.10).

$$T = \frac{1}{2} i_1^2 \frac{dL(\theta)}{d\theta} + \frac{1}{2} i_2^2 \frac{dL(\theta - 90^\circ)}{d\theta} \tag{8.11}$$

An important characteristic of SRM is shown in (8.11). In the above equation, the torque is proportional to the square of phase current and is independent of its direction. Therefore, the power converter for supplying the phase current can be unidirectional. In other words, it does not require a bidirectional current source. The phase current is turned on and off by a switch such as a transistor or a thyristor. Therefore, since this switch regulates current in one direction only, the power converter is economical and simple in structure, because it requires only half of the switch or any other control devices compared to the bidirectional converter.

Equations (8.10) and (8.11) are useful under the assumption that there is no mutual inductance between each phase. This assumption is valid because the motor is symmetrical as shown in Figure 8.5 (the mutual inductance is 0 if the axes are perpendicular to each other) and if the magnetic material of the rotor and the stator has infinite permeability. However, not all SRMs are symmetrical.

In general, practical SRMs have mutual flux linkage between each phase. Often these conditions are ignored and (8.10) and (8.11) are used to find coenergy and torque.

In some cases, however, this assumption is not usable. In the actual operation, when iron core is saturated by the magnetic flux during operation, the relationship between flux and current is complicated and mutual inductance is produced. Therefore, mutual inductance must be considered.

Although torque can be described such as in (8.9), it is difficult to express it analytically. The relationship between flux, current, and torque of a winding with nonlinear magnetic material can be obtained by numerical analysis. Once the prototype is built, measuring devices must be used to validate various assumptions and approximations during design and to obtain accurate values for actual operation. Let the number of poles of the stator be m and the number of poles of the rotor be n, such machine is called m/n machine.

8.2 Design of switched reluctance motor

Design specification consists of requirements (i.e., torque, speed) and limitations (i.e., temperature rise, supply voltage, and dimensions). Design consists of parameters specifying both motor and controller. It must also include material specification and consider the manufacturing procedure. Sometimes, all dimensions are included in the design procedure. If it is not one of the first things to do when designing is to figure them out. Once the overall dimensions are known, they can be modified for optimization starting from a standard ratio and modify in proportion. By knowing the initial dimensions and then selecting the main parameters one by one, a motor designer can take gradual steps to improve the quality and viability of his design. This process can be done using appropriate analysis software, but most often than not, it still depends on experience. Notable design improvements can continue to be achieved with the repetition of these methods, even in the case of DC motors well known to us.

Accurate and complete design specifications are necessary. Wherever possible, motor designers must compromise to obtain the best design specification. Demanding unnecessary or inappropriate design specifications is also considered as a mistake. For a general example, designing a motor to provide larger than the load requirement. Clients or actual users have to try giving the designer enough information for better design.

The most basic requirements in design specifications are torque, speed, load, and supply voltage. It is also essential to determine whether the motor needs to be bidirectional or whether a braking or generating operation is required. This refers to the four-phase operation in which a motor can operate. Circulation temperature, changes in supply voltage, and other special factors should be included along with any criteria or rules.

SRM has a different operating principle from that of conventional DC or AC motors. This is because the torque generation is based on the reluctance torque rather than mutual torque, and the applied voltage and current also use the pulse wave instead of the sinusoidal wave. Also, phase excitation is performed sequentially, and the operation mode and characteristics are different depending on the number of poles of the stator and the rotor. Therefore, the following points have to be considered when designing an SRM while keeping in mind the basic concepts of existing electric device design.

8.2.1 Selection of pole

The conditions to be satisfied by the number of stator and rotor poles and the arcs are

1. minimization of the mutual inductance mentioned above,
2. "repeatability" of the relative arrangement of stator and rotor poles,
3. minimization of permeance with respect to minimum inductance,
4. self-start capability in both directions, and
5. minimization of switching frequency.

In the case of the number of poles, the following can be known:

$$\mathrm{LCM}(N_s \cdot N_r) = qN_r \tag{8.12}$$

$$\mathrm{LCM}(N_s \cdot N_r) > N_s > N_r \tag{8.13}$$

where N_s and N_r are even numbers, constant q is >2, and LCM is the lowest common multiple. In addition, the following cases can also be known:

$$\min(\beta_r \cdot \beta_s) > \frac{2\pi}{qN_r} \tag{8.14}$$

$$\beta_s \leq \frac{2\pi}{N_r} - \beta_r \tag{8.15}$$

where β_s and β_r are the stator and rotor pole arcs, respectively. Equations (8.12)–(8.15) define the necessary conditions to be satisfied by N_s, N_r, β_s and β_r. However, further consideration is needed to achieve the desired design. Let us first consider the conditions for the possible values of β_s.

$$\beta_s > \beta_r \tag{8.16}$$

$$\beta_{r,\min} = \frac{2\pi}{qN_r} \tag{8.17}$$

$$\beta_{s,\max} = \frac{2\pi}{N_r}\left(1 - \frac{1}{q}\right) \tag{8.18}$$

If $\beta_s < \beta_r$, then

$$\beta_{s,\min} = \frac{2\pi}{qN_r} \tag{8.19}$$

Therefore, the range of β_s is

$$\beta_{s,\max} - \beta_{s,\min} = \frac{2\pi}{N_r}\left(1 - \frac{2}{q}\right) \tag{8.20}$$

Similarly, the range of β_r is

$$\beta_{r,\max} - \beta_{r,\min} = \frac{2\pi}{N_r}\left(1 - \frac{2}{q}\right) \tag{8.21}$$

Therefore, β_s and β_r have the same range. This range increases with increasing q and decreases with increasing N_r. However, at the same time, the above two values in (8.15) must satisfy the following equation:

$$(\beta_r + \beta_s) \leq \frac{2\pi}{N_r} \tag{8.22}$$

The system is schematically shown in Figure 8.6. In this figure, the limit of β_s and β_r combination is represented by the sides of triangle *abc*. The inductance at point *a* (the point at which the iron use is minimized) is dead zone free ($\because \beta_s = \beta_r$). Moving from point *a* toward *b* or *c* along the *ab* or *ac* line, a dead zone starts to appear and the minimum inductance section decreases gradually. When *b* or *c* is reached, the inductance dead zone becomes maximum. Point *c* (just like point *a*) is where the machine has maximum winding space. The winding space at point *b* is zero ($\because$ if $\beta_s = \beta_{s,\max}$, then stator pole arc will be the same as stator pole pitch). The latter case is not physically feasible but keeps in mind that turning β_r closer to $\beta_{r,\min}$ will reduce rotor inertia.

Let us now pay attention to point *d* where $\beta_s = \beta_r = \Phi/2$, where $\Phi = 2\pi/N_r$. At this point, the minimum inductance section and the dead zone disappear. Any point inside the triangle has these characteristics depending on its position. The $\beta_s = \beta_r$ line divides the triangle into two parts: $\beta_s > \beta_r$ and $\beta_s < \beta_r$. As a result from more detailed studies on these design and characteristics constraints, it is known that $\beta_r > \beta_s$ is preferable in practical design. Therefore, the design point must be set inside the triangle of *adc*.

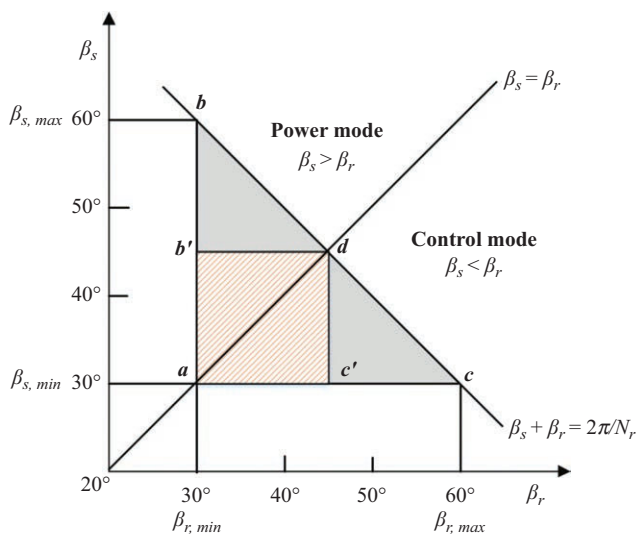


Figure 8.6 Stator and rotor pole selection (6/4 SRM)

Note that in such design, there is a point inside the triangle *adc* (which is symmetrical to the line *ad*), which corresponds to the interchange between rotor and stator pole arc values.

Now, notice the number of rotor poles. Since the instantaneous torque at a certain point is proportional to the slope of the inductance, the permeance corresponding to $L_{\min}$ must be made as small as possible in order to increase the torque. If the air gap due to minor rotor diameter is larger than $d(\Phi - \beta_r)/2$, the inductance becomes dependent on the interpole arc $(\Phi - \beta_r)$.

Therefore,

$$(\Phi - \beta_r)_{\max} = \Phi - \beta_{r,\min} = \frac{2\pi}{N_r}\left(1 - \frac{1}{q}\right) \tag{8.23}$$

Therefore, if N_r is made as small as possible, $L_{\min}$ value decreases. Further study of the above shows the useful combination of numbers for self-starting, bidirectional drive as follows:

- Three-phase motor: $N_s = 6$, $N_r = 4$
- Four-phase motor: $N_s = 8$, $N_r = 6$
- Five-phase motor: $N_s = 10$, $N_r = 4$

8.2.2 Selection of phase number

There are several factors that may affect the selection of phase number, such as reported in [1]:

- Self-starting capability: SRM with phases lower than three may have a torque dead zone which will make the motor unable to self-start.
- Directional capability: The determination of whether it can rotate both clockwise and counterclockwise or just simply unidirectional must be made in the first stage of design.
- Reliability: Higher number of phases increases reliability since a failure of one phase can still be compensated by the rests.
- Cost: Higher number of phases requires a corresponding number of converters and other electrical components such as drivers and logic power supplies.
- Power density: Higher number of phases may lead to a higher power density.

The selection of the phase number, however, is mainly influenced by the required starting torque (and thus the effective value of $dL/d\theta$). There must be an adequate "repeatability" between the change of $L(\theta)$ changes of two phases to obtain the appropriate starting torque at any rotor angle. The proper repeatability is greatly affected by the fringing effect. Fringing effect causes both ends of inductance increasing region to have a rounding part, thus decreasing the $dL/d\theta$ value (in other words, torque). However, useful guidelines for repeatability effects can be inferred from the following ideal $L(\theta)$ changes.

If we define the inductance repeatability ratio of two adjacent phases with respect to the section in which the inductance is changing as K_L, then

$$K_L = \frac{(\theta_1 - \theta_0) - \theta/q}{\theta_1 - \theta_0} = \frac{\min(\beta_r, \beta_s) - 2\pi/qN_r}{\min(\beta_s)} \tag{8.24}$$

If $\beta_s > \beta_r$

$$K_L = 1 - \frac{2\pi}{qN_r} \tag{8.25}$$

8.2.3 Dimensions and parameters

In this section, the general calculations for determining machine physical dimensions are given. Motors with special applications or requirements may not follow these rules, but the concept will be the same.

First, the output torque T can be described as

$$T = kD_r^2 L_{stk} \tag{8.26}$$

where D_r is the rotor diameter in meter and L_{stk} is the stack length of the motor, also in meter. k is the output constant that depends on the application, and its value is shown in Table 8.1.

As explained above, torque is one of the most basic requirements in design specifications. Meanwhile, the stack length is usually predetermined before starting the design. By knowing torque, k, and L_{stk}, D_r can be found. The standard for the ratio of D_r/D_s, where D_s is the stator outer diameter (possibly given), is shown in Table 8.2.

Table 8.1 k *Value per type of motor*

Type of motor	k,**N m**$/m^3$ $(\times 10^3)$
Small, total-enclosed	2–5.5
Integral-hp industrial	5.5–20
High-performance servo	10–40
Aerospace	20–60
Large liquid-cooled	80–200

Table 8.2 Design standard based on pole numbers

Phase	N_s	N_r	D_r/D_s	β_r	β_s
3	6	4	0.3	30°	32°
3	12	8	0.57	16°	15°
4	8	6	0.53	23°	21°

SRM winding is the concentrated type and it has the "end-winding" part due to bending of the coils. The length of end windings is symbolized as L_{et}, and the total length of the motor is expressed as L_e. The relationship is shown below.

$$L_e = L_{stk} + 2L_{et} \tag{8.27}$$

If L_e is set to be $1.2t_s$, then

$$L_e \approx L_{stk} + 2.8t_s \tag{8.28}$$

in which t_s can be calculated as

$$t_s = 2\pi(r_1 + g) \cdot \frac{\beta_r}{360^\circ} \tag{8.29}$$

where r_1 is rotor outer radius and g is the length of air gap between rotor and stator poles at aligned position.

Next is the determination of rotor slot depth, d_r, which is

$$d_r = r_1 - r_0 \tag{8.30}$$

where r_0 is the radius from the center to the outer surface of rotor yoke. It should be at least 20–30 times the length of the air gap to achieve low unaligned inductance, usually set as

$$d_r > \frac{t_s}{2} \tag{8.31}$$

Another parameter is the rotor yoke thickness, y_r. The thickness of the rotor yoke should be sufficient to channel maximum rotor flux without saturation. For two-pole machine, the main flux is divided into two parts, so at least y_r has to be $0.5t_s$. In practical design, 20%–40% is recommended.

$$y_r > 0.7t_r \tag{8.32}$$

Meanwhile, stator yoke thickness, y_s can also be designed similar to y_r, where its value should be at least larger than $0.5t_s$ but in reality, $0.7t_s$ is chosen as minimum point. Thicker stator yoke is necessary to reduce the radial force that happens during excitation between stator pole pairs of the corresponding phase and to strengthen the structure to avoid deformation, which will lead to reduced acoustic noise. However, this action may increase the overall weight and reduce slot winding area, so a proper trade-off is important.

Shaft diameter D_{sh} plays an important role in delivering the output mechanical torque to the load. Based on other parameters calculated above,

$$D_{sh} = D_r - 2(d_r + y_r) \tag{8.33}$$

Shaft diameter D_{sh} plays an important role in delivering the output mechanical torque to the load.

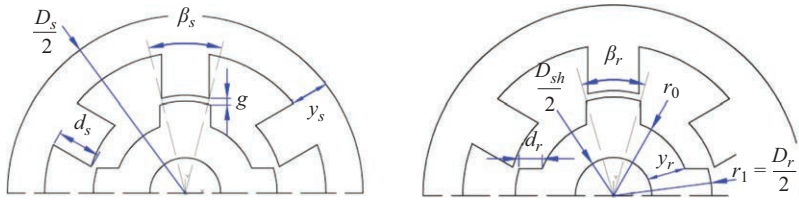


Figure 8.7 Design parameters of SRM

Stator slot depth, d_s, minimizes copper loss and maximizes winding area and is described as

$$d_s = \frac{1}{2}(D_s - D_r - 2(g + y_s)) \tag{8.34}$$

For clearer understanding of these parameters, Figure 8.7 shows all the machine geometry with its variables.

8.3 Control of switched reluctance motor

8.3.1 Power converter

In order to control the current of the stator windings of SRM, many drive circuits are proposed. Cost reduction and performance are usually important in deciding which circuit to use. These two factors, however, are largely conflicting with each other in terms of converter selection.

In other words, converters having one switching element per phase are mainly used for the purpose of minimizing the number of components and mainly used in low-performance systems. Meanwhile, converters with equivalent two-switching components are more commonly used in spite of cost increase because they have better control performance than other converters.

SRM converter topology has some basic requirements, such as

- Each phase should be able to conduct independently of other phases. It means that one phase has at least one switch for motor operation.
- The converter should be able to demagnetize current before it steps into decreasing inductance section. If the machine is operating as a motor, it should be able to excite the phase before increasing inductance section.

In order to improve the performance, such as higher efficiency, faster excitation time, fast demagnetization, high power, fault tolerance, the converter must satisfy some additional requirements. Some of these requirements are listed below:

- The converter should be able to allow phase-overlap control.
- The converter should be able to utilize the demagnetization energy from the outgoing phase in a useful way by either feeding it back to the source (DC-link capacitor) or using it in the incoming phase.

- In order to make the commutation period small, the converter should generate a sufficiently high negative voltage for the outgoing phase to reduce demagnetization time.
- The converter should be able freewheel during the chopping period to reduce the switching frequency. So the switching loss and hysteresis loss may be reduced.
- The converter should be able to support high positive excitation voltage for building up a higher phase current, which may improve the output power of motor.
- The converter should have resonant circuit to apply zero-voltage or zero-current switching for reducing switching loss.

SRM converters are known to be able to have only one component per phase because the torque is independent of current direction. However, there are some problems due to the inductive circuit characteristics of the SRM when using only one switch in the circuit. When the switch is turned off to control the winding current, the circuit must be configured to maintain operation continuity until the current is completely dissipated. Furthermore, it also has to protect the system in the event of a short circuit.

Figure 8.8 shows an asymmetric bridge converter with two switches and diodes per phase. It has three operating modes:

- Mode 1: Both switches are turned on to apply the DC power supply voltage (V_{DC}) to the windings to allow the current to flow.
- Mode 2: Depending on the control method when the winding is excited, one or both of the switches may be turned off to allow current to circulate through one diode, switch and winding, or both switches are turned off so that the current is reduced in the way that energy is returned to the power supply through both diodes.
- Mode 3: Both switches are turned off at the same time for commutation. The current must reach zero or very small before the phase inductance has a negative slope. Otherwise, a negative torque can be generated, which reduces the average torque of the motor and the energy conversion efficiency.

This converter has the best variety of control among the converters for driving SRM. Since the current control of each phase is independent, it is possible to overlap two phases. It is suitable for high voltage and large capacity, also the rated voltage of the switch is relatively low. The disadvantage is that there are two

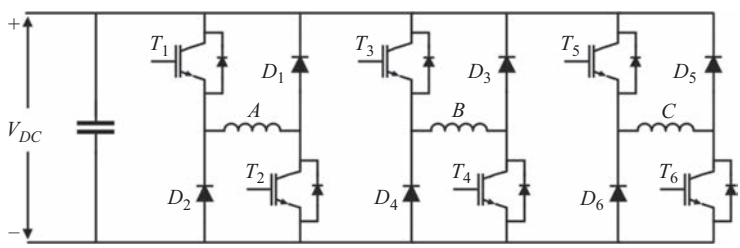


Figure 8.8 Asymmetric bridge converter for three-phase SRM

switches per phase, which leads to the increased number of control and driver circuits, and the drive of the upper level switch must be insulated.

8.3.2 Switching angle control

Figure 8.9 shows the waveform of the excitation current due to the inductance profile and the on switching according to the rotor position. Here, γ is the maximum overlap angle of the stator and rotor poles, which is a small portion of the respective pole arcs. Since β is the starting point of inductance decreasing period, the current should be completely eliminated before β in order to prevent negative torque from being generated, and β is a large portion of the pole arcs of stator and rotor.

As the load changes, the switching angle must be adjusted accordingly to ensure current can produce the appropriate torque.

The control characteristics of the SRM vary according to the voltage waveform, switching signal, and current waveform applied to the phase line. This depends on the phase current waveform for the respective operating speed of the motor. Generally, flat-top shape is suitable for the excited phase current, in consideration of high operating efficiency operation and energy conversion efficiency of the motor. Also, the design of the inverter and the magnetic circuit is based on this. This current value can be obtained by adjusting the switching angle appropriately or by phase current chopping for current limitation. Therefore, the phase current of the motor is generally described based on this flat-top case.

When the motor is operating at a variable speed, two control methods can be used. One is the method of controlling the excitation angle and its interval according to the speed and torque, and the other is the method of limiting the current by chopping in order to control the speed.

When the motor is operating at high speed or heavy load, it is necessary to control the excitation angle (θ_{on} or θ_{AD}) to ensure a sufficient current rise time and to control the conduction time (θ_c or θ_{AD}) depending on the load. In the case of high-speed operation, it has a single pulse current type without current chopping. These phenomena can be illustrated as in Figure 8.10. Figure 8.10(a) and (b) show the before and after of current chopping for low to medium speed operation, in which the current has enough time to build up until the a set reference value. On the other side, the current built up time is usually not enough in high speed operation to produce the required torque. Therefore, instead of limiting the current, ideally the current waveform should be as shown in Figure 8.10(c), which can be achieved

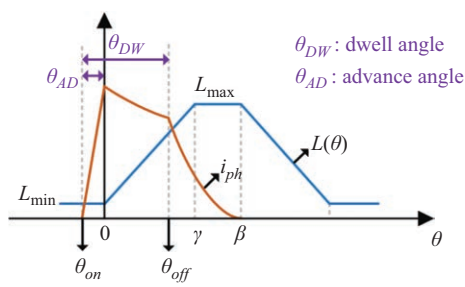


Figure 8.9 Inductance profile and phase current

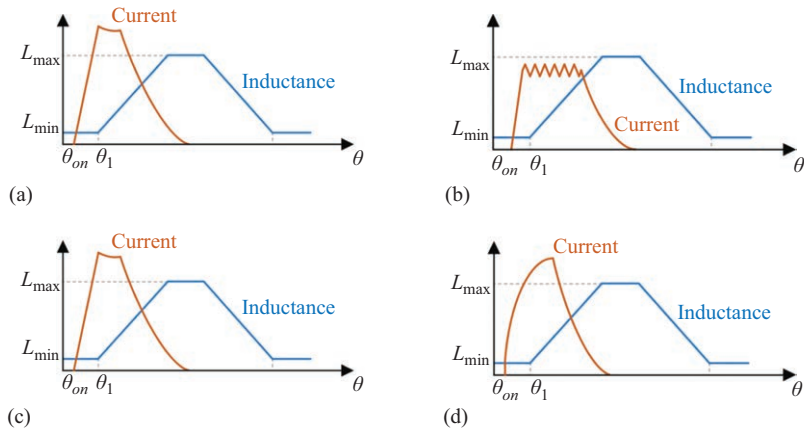


Figure 8.10 Typical phase current waveforms according to rotation speed: (a) and (b) low speed, (c) and (d) high speed

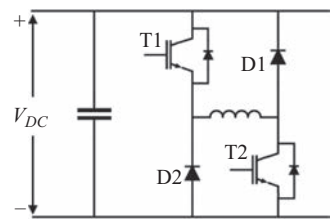


Figure 8.11 Switches for each phase

with single-pulse control. However, in reality, the current waveform tends to shape like that shown in Figure 8.10(d) with no flat-top area. Single pulse control can be achieved by turning on both switches T1 and T2 in Figure 8.11.

When both switches are turned on at the same time, the stored energy in the motor is dissipated through the diodes D1 and D2. At this time, the current flowing in the winding maintains its direction, but the voltage is reversely applied through the diode, so energy decreases rapidly.

Particularly, it should be noted that since the current decay time is long and a considerable amount of current remaining may cause negative torque to be generated, which will affect the efficiency of the drive system. Energy stored in the windings of the motor is returned to the power supply side through the diodes D1 and D2, or partly flows to the next phase.

8.3.2.1 Fixed angle control

A current source excitation method having excellent magnetomotive force characteristics is suitable for SRM magnetization. The current source excitation method is an ideal excitation method in which the generated torque is flat and no negative torque is generated. Moreover, the excitation period can be used as much as possible within a range in which the current does not overlap, so that the mechanical

output can be effectively generated. Therefore, if the phase excitation angle is properly calculated and the appropriate source is excited, the torque and speed can be adjusted. However, in order to obtain a torque characteristic similar to that of the current source, a flat current must flow in a region where the inductance increases. Therefore, voltage and switching angle adjustment of the variable voltage source matching the required speed and load torque must be set.

In order to adjust the excitation voltage and select a fixed switching angle, the voltage must be applied where the inductance increases. This can be done by switching on at the θ_{ON} position in order to let the current required for the torque generation flows. The phase current increases at θ_{ON} and becomes constant when the rotor reaches the $\theta_{\min}$ position. If the electromotive force (EMF) of the motor is equal to the excitation voltage at this time, the current may flow smoothly. The excitation voltage is then removed at the θ_{OFF} position, and a negative voltage is applied to speed up the current reduction. The θ_{OFF} angle is set so that no negative torque is generated during the current-reduction period. At this time, the excitation voltage should be appropriately adjusted according to the required speed and torque of the motor load. Refer to [2] for detailed control methods.

8.3.2.2 Advanced angle control

In the torque generation period, advanced angle control can adjust the leading switching angle variably to establish the flat-top current according to the variable load. In other words, by setting the θ_{AD} to be proportional to the increase of load current as load torque increases, flat-top current can be produced at all times even though the load changes. In the practical application, controlling the advanced angle can be done by measuring load current and using a simple feedback circuit. The relation between torque and current of a phase is shown in Figure 8.12.

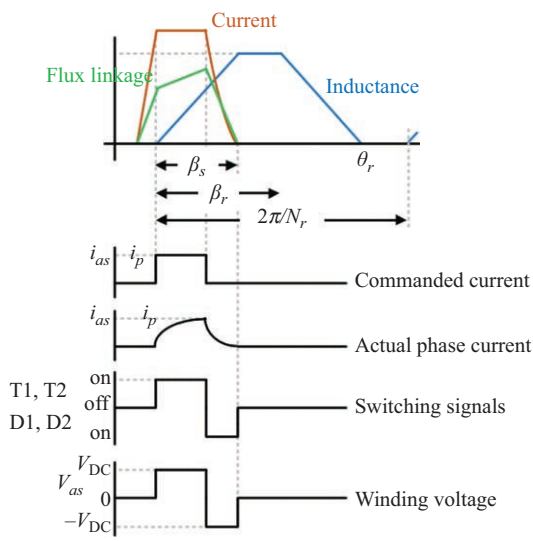


Figure 8.12 Switching angle control method

8.3.2.3 Switch-off angle control

It is necessary to control the advance angle which makes the flat-top current according to the variable load and to control the switch-off angle, θ_{OFF}, appropriately for efficiency improvement. The control of switch off angle can be performed by two ways. First method is by controlling the torque angle, θ_{TQ} (= θ_{MIN} to θ_{OFF}), which is the angular magnitude between the effective torque generation period θ_{MIN} to θ_{OFF}. Second method is by controlling the dwell angle, θ_{DW} (= $\theta_{ON} \sim \theta_{OFF}$).

1. *Constant torque angle control method*
   The torque angle, θ_{TQ}, is the effective interval in which the torque is generated. Regulating the torque angle θ_{TQ} constantly, regardless of the increase or decrease of the load, is equal to making the effective torque interval constant. In a linear condition without magnetic saturation, it is desirable to maximize the θ_{TQ} to the extent that the reducing current does not affect the negative torque, and the maximum output can be maximized while reducing the torque ripple.

   Figure 2.9 shows the current waveform according to the load due to θ_{TQ} constant control. The appropriate advance angle according to the load for making the flat-top current is set and maintained at a constant current, and the switch off is performed while maintaining the full torque angle, θ_{TQ}, irrespective of the load.

   As shown in Figure 8.13, as the load current increases, the saturation point advances and the current rises at the saturation point before switching off. The increased current due to saturation induces an increase of iron loss, and the time taken to extinguish the current becomes longer, which is a factor that lowers efficiency.

   Since the SRM generates torque by the rate of change of inductance, there is a region where the inductance reduces and negative torque is generated. If the load current is so large that the excitation time becomes longer, current may flow in the negative torque region. This induces unstable driving resulting in greater noise generation and lower efficiency. Therefore, in order to suppress the occurrence of negative torque, the maximum load current must be limited, thus limiting maximum output by current limitation.

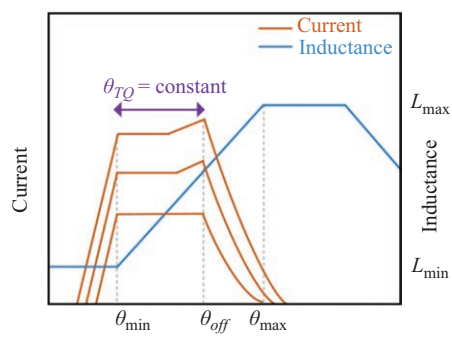


Figure 8.13 Current shape during constant torque angle control

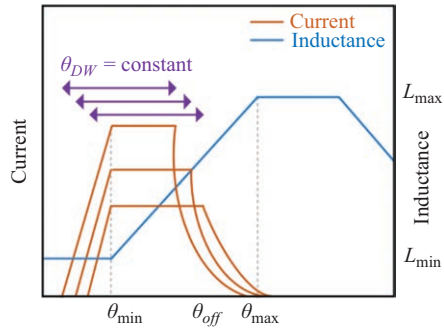


Figure 8.14 Current shape during constant dwell angle control

2. *Constant dwell angle control method*
   The saturation becomes severe as the overlapping portion of the stator and the rotor increases. It is preferable that switching off occurs just before the saturation point since the increasing current may lead to lower efficiency.

   As the load current increases, the saturation point moves forward, so θ_{AD} is adjusted to a large value depending on the load to create a flat-top current phenomenon. Also, at the same time, adjusting the θ_{TQ} to a small value in order to suppress the current rise in the saturation region has an effect of further improving the efficiency.

   The constant control of the dwell angle θ_{DW} is a method of constantly controlling the sum of θ_{DW} by making the increase of θ_{AD} and the decrease of θ_{TQ} constant according to the load current as shown in Figure 8.14.

   The general switching method of SRM is to switch off after a given conduction angle according to the rotor position. If the dwell angle θ_{DW} is kept constant, the advance angle can be adjusted according to the current when controlling the switching angle, which is advantageous in which the switching control program becomes simpler than the θ_{TQ} constant control method in which the θ_{DW} is adjusted variably.

If the dwell angle θ_{DW} is controlled, the switch-off angle θ_{OFF} is advanced in accordance with the increase of the load current, so that the decreasing current does not go into the negative torque region even if the load current increases. Therefore, there is no limitation of the maximum current due to saturation, so the maximum output is larger and stable operation is possible.

8.3.3 Current control

8.3.3.1 Single pulse control

The magnetic flux of the SRM is not constant but must be established from zero at every stroke. This process is controlled by applying the power supply voltage at the zero-crossing angle θ_0 and removing it from the current angle θ_c.

If each phase is powered by a circuit in Figure 8.15, both transistors turn on at θ_0 and off at θ_c. At sufficiently high speeds, voltage and flux linkage, current, and ideal inductance are shown in Figure 8.16. The operation of this type of waveforms is referred to as a single pulse operation. The inductance is obtained based on the assumption that there is no fringing effect, and the cores are having infinite permeability. This inductance is only used as a convenient way to express the waveform corresponding to the rotor position, because it shows directly the amount of overlap between the stator rotor poles involved. The aligned and unaligned positions are also shown in the figure.

The establishment of flux linkages is in accordance with Faraday's law. At a constant acceleration speed, it can be calculated as follows:

$$\Psi_c = \int_{\theta_0}^{\theta_c} \frac{(V_s - Ri)d\theta}{\omega} + \Psi_0 \tag{8.35}$$

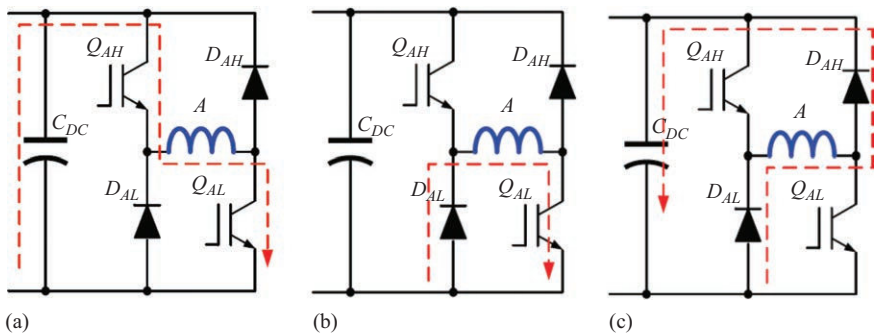


Figure 8.15 Phase excitation of a phase: (a) magnetization, (b) freewheeling, and (c) demagnetization

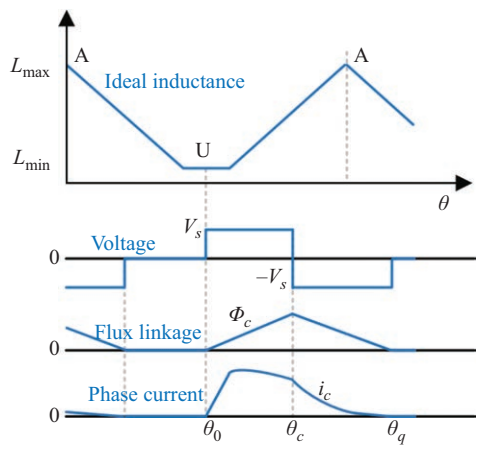


Figure 8.16 Single-pulse waveform

where Ψ_0 is a preexisting flux linkage (usually 0) at θ_0. V_s is the supply voltage, R is the phase resistance, and i is the instantaneous current. The resistance and voltage drop across the controller and power supply are ignored here. Note that Faraday's law describes magnetic flux linkage, not magnetic flux.

In equation [3]

$$\omega\Psi_c = (V_s - V_1)\theta_{DW} \tag{8.36}$$

where $\theta_{DW} = (\theta_c - \theta_0)$ is the dwell angle and V_1 is the average voltage drop caused by the resistor during θ_{DW}. If $Ri \ll V_s$, the flux linkage increases linearly.

During operation of the motor, the magnetic flux must be reduced to zero before the poles separate. Otherwise, the sign of the torque changes and braking torque is generated. To do this, the terminal voltage must be reversed at θ_c. This is usually done by operation of the reflux diode when the transistor is turned off. The angle at which the negative voltage recoils the magnetic flux back to zero at each θ_q is also governed by Faraday's law.

$$0 = \Psi_c + \int_{\theta_c}^{\theta_q} \frac{(-V_s - Ri)d\theta}{\omega} \tag{8.37}$$

This can be written as

$$\omega\Psi_c = (V_s + V_2) \cdot \left(\theta_q - \theta_c\right) \tag{8.38}$$

where V_2 is the average voltage drop due to resistance in the magnetizing period $\left(\theta_q - \theta_c\right)$. When $Ri \ll V_s$, the flux linkage decreases linearly, and rotation is constant, the travel angle is almost equal to the dwell angle and both become Ψ_c/V_s. The total conduction angle including the entire period of establishing and depleting the magnetic flux becomes as follows:

$$\theta_q - \theta_0 = \frac{2\omega\Psi_c}{V_s} \tag{8.39}$$

The highest flux linkage Ψ_c occurs at the rectification angle θ_c.

The entire energizing interval must be within a single pole pitch a_p, where a_p is the rotating angle between two consecutive alignment positions.

$$a_p = \frac{2\pi}{N_r} \tag{8.40}$$

Otherwise, a sawtooth effect will occur with Ψ_0 incrementing for each stroke and continuing with nonzero values. This condition is called continuous excitation. In other words,

$$\theta_q - \theta_{DW} < a_p \tag{8.41}$$

Combining (8.36)–(8.41) to obtain the maximum possible dwell angle,

$$\theta_{DW} < \frac{a_p}{1 + \xi} \tag{8.42}$$

where

$$\xi = \frac{1}{1 + ((V_s - v_1)/(V_s + v_2))} \tag{8.43}$$

If the average resistance voltage drops v_1 and v_2, both have approximately the same fraction p of V_s, then (8.41) and (8.42) become

$$\theta_{DW} < a_p \cdot \frac{(1+\rho)}{2} \tag{8.44}$$

For example, in a symmetrical 6/4 motor, if pole pitch $a_p = 90^\circ$ (360° electrical degrees) and $p = 0.2$, the maximum dwell angle is 54° and the conduction angle is 108°.

In normal SRM, the inductance rising angle is just $a_p/2$. During an inductance period that is ideally reduced, the flux must be zero. This is because the negative or braking torque is generated when the current flows in the section. To avoid this completely, the conduction angle should be limited to $a_p/2$ and the maximum dwell angle is

$$\theta_{DW} < \frac{a_p}{2} \cdot \frac{(1+\rho)}{2} \tag{8.45}$$

If $\rho = 0.2$ in a 6/4 motor, the maximum dwell angle is 27° (108° electrical angle) and the conduction angle is 54°. In practice, a larger dwell angle is used. This is because, during the rising inductance section, the gain at the torque impulse exceeds the small braking torque impulse. This braking impulse usually occurs in low torque/current area (i.e., near and/or unaligned). This condition is shown in Figure 8.16, where the current has a tail that goes beyond the unaligned position. Torque is negative but small during this tail.

In Figure 8.16, the magnetizing angle is in the unaligned position, and the current increases linearly until the poles begin to overlap. The rising inductance generates a counter EMF (back EMF) corresponding to the rising portion of the supply voltage, and this back EMF is equal to V_s when the current waveform reaches the maximum. Subsequently, the back EMF becomes larger than V_s. This is because the flux linkage is still increasing while the speed is constant. The excess of the forward applied voltage becomes minus, and the current begins to decrease. The applied terminal voltage is changed at the commutating point, and the current change ratio is abruptly increased.

At the alignment position, the back EMF is changed to reduce the negative-applied terminal voltage instead of increasing it. Therefore, the current reduction ratio decreases. At this interval, there is a risk that the back EMF increases the power supply voltage and the current starts to increase again. In single pulse operation, the current must be ahead of the several degree alignment position.

Figure 8.16 shows the importance of turning on the supply voltage before the poles begin to overlap. This increases the current to a reasonable magnitude while the inductance is low. If the inductance is nearly constant, there is no back EMF force and the total supply voltage is adequate to increase the current. The dwell

angle can go far beyond the unaligned position at high speeds until before the decreasing inductance section.

8.3.3.2 Chopping control

Chopping is required to control current at low speeds. The simplest operation is to turn on one transistor (T_2 in Figure 8.15) during the interval from θ_0 and θ_c and turn the other switch (T_1) on and off with a fixed duty cycle $d = T_{ON}/T$ at higher frequency. Here, T_{ON} is the on-time and T is the period of the chopper frequency. This form is called soft chopping.

When T_1 is turned on, the voltage V_s is connected to the phase line. When T_1 is off, the winding is shorted through T_2 and D_2. T_1 is called a chopping transistor, and D_2 is a chopping diode. T_2 is a rectifying transistor and D_1 is a rectifying diode. This is because they only change states at the rectification angles of θ_0 and θ_c.

The waveform during soft chopping is shown in Figure 8.17. The average voltage applied to the phase line during the dwell angle is dV_s. When the variable ρ is again used to indicate the average effect of the resistance voltage drop, the flux linkage rise in the dwell period can be set as the fall in the flux linkage during the magnetizing period,

$$\omega\Psi_c = \theta_{DW}(d-\rho)V_s = \left(\theta_q - \theta_c\right)(1+\rho)V_s \tag{8.46}$$

By rearranging this, the total conduction angle becomes

$$\theta_q - \theta_0 = \theta_{DW}\left[\frac{1+d}{1+\rho}\right] \tag{8.47}$$

To prevent continuous energization, θ_{DW} should be restricted to

$$\theta_{DW} < a_p \cdot \frac{1+\rho}{1+d} \tag{8.48}$$

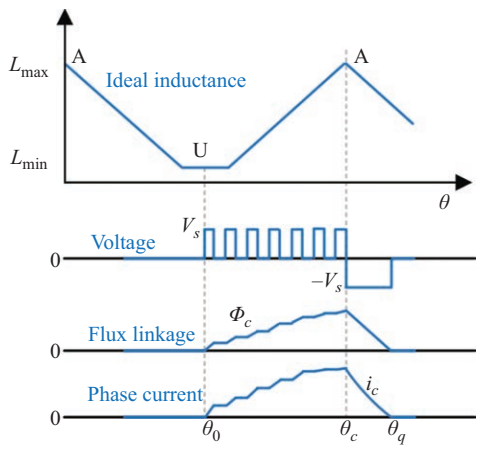


Figure 8.17 Voltage PWM—soft chopping

For example, in a 6/4 motor, $\rho = 0.2$ and $d = 0.5$, the maximum dwell is 72°. θ_{DW} should be limited as follows by completely blocking the braking torque.

$$\theta_{DW} < \frac{a_p}{2} \cdot \frac{1+\rho}{1+d} \tag{8.49}$$

In other words, the absolute maximum, i.e., the 36° dwell in the example, can increase to the maximum value given in (8.47) as the duty cycle decreases.

The same analysis can be performed for the hard chopping shown in Figure 8.18, where both transistors are switched together at a higher frequency. If the switching frequency is kept the same, hard chopping greatly increases current ripple (typically five to ten times). Therefore, it is not preferable as a control method for the operation of the electric motor. However, in a generator or braking operation, it may only be necessary in a possible way to control the current. Some controllers (especially Oultron type controllers) cannot perform soft chopping and always operate with hard chopping. Soft chopping has less noise and less electromagnetic interference. It also reduces the DC ripple current in the power supply and actually reduces the need for a filter capacitor.

In soft and hard chopping, the flux linkage increases as shown in the left hand side of (8.46). Before the overlap starts, the average slope of the current waveform is also almost constant because a linearly increasing flux is applied to a constant inductance. The inductance then increases somewhat linearly, while the flux linkage continues to increase linearly. The current waveform in the voltage pulse width modulation (PWM) does not generate a large current at the pole corner. Also, it works quieter. At the beginning of overlap, not only it can lower current but also can reduce the mechanical impact.

The waveforms in Figures 8.17 and 8.18 show the current angles at the aligned and unaligned positions. This shows that at low speeds, that is, when the chopping

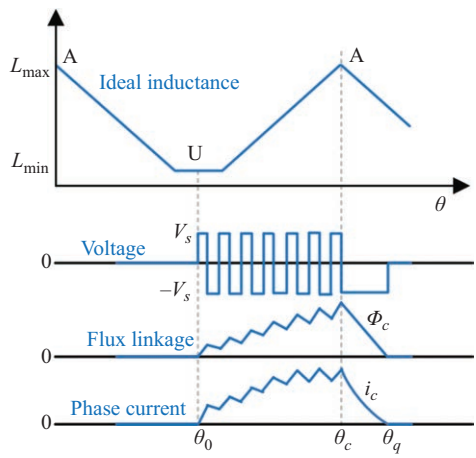


Figure 8.18 Voltage PWM—hard chopping

is the preferred control method, the entire absolute torque range can be used. From (8.46), the ratio of the rising and falling slope of the flux is nearly equal to d, and the flux reduction is small at low duty cycles and delays the current. The pole arc is not expressed in the equation, but it has a great effect on limiting the firing angle and implementing optimal control.

8.3.3.3 Hysteresis control

Figure 8.19 shows a waveform obtained with a hysteretic current regulator whose power transistor is turned on or off as the current is greater or less than the reference current. The instantaneous current is measured using a current transducer with a wide bandwidth and returned to the coupling point. The error is used directly to control the state-of-the-power transistor.

Both soft and hard chopping are possible, but only soft chopping waveform is shown in Figure 8.19. The waveform for hard chopping is similar. As in the case of voltage PWM, soft chopping reduces current ripple and reduces the device required for the filter but is necessary for braking or generator mode operation.

A simple hysteretic controller keeps the current waveform at the hysteresis band between the upper and lower limits. Because the supply voltage is fixed, the switching frequency decreases as the rising inductance of the phase winding turns on. (The rising inductance increases with total inductance.) This can be seen in Figure 8.19.

In Figure 8.19, the waveform in the flux linkage shows a constant flux linkage section when a constant current is being applied to a constant inductance, that is, before the start of pole overlap. Then the inductance increases while the average current is constant and the flux linkage increases with inductance.

The benefits of SRM control methods using current and angle control is provided in Table 8.3.

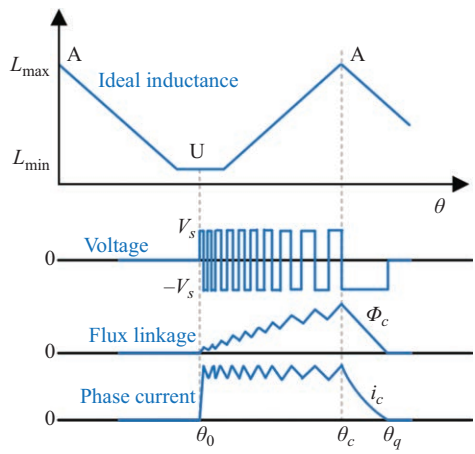


Figure 8.19 Current control—soft chopping

Table 8.3 SRM control methods

	Current control (low speed)	**Angle control (high speed)**
Concept	Back EMF < supply voltage Inductance increase rate is slow Current increase rate is large	Back EMF > supply voltage Inductance increase rate is fast Current increase rate is low
Explanation	Chopping→loss due to switching action Conduction angle decrease→higher torque ripple and acoustic noise In high performance machine (low torque ripple), current overlap method is preferred	Excitation angle is moved forward to allow more current Conduction angle decrease→higher torque ripple, reduced average torque Constant conduction angle→reduced torque ripple and lower acoustic noise

8.3.4 Direct torque control

It is well known that direct torque control (DTC) is an advanced control technology for induction motor developed after vector control. The phases of SRM are excited independently, and the phase current is highly nonlinear instead of sinusoidal waveform; therefore, the theory of conventional DTC for induction motor cannot be directly applied to SRM.

Along with the more detailed research of SRM, some researchers bring the concept of DTC for ac motors into controlling SRM recently [4]. The structure of DTC for SRM is different from that of torque sharing function (TSF) and direct instantaneous torque control (DITC), it resembles that of DTC for AC motors, which incorporates hysteresis controllers for torque and stator flux linkage, respectively.

Amplitude of stator flux vector is controlled to be constant. Torque is controlled by accelerating or decelerating the stator flux. Block diagram of DTC is shown in Figure 8.20.

For a three-phase SRM with asymmetric half-bridge converter, sectors are defined in the following figure, where six voltage vectors are selected optimally (Figure 8.21).

The selection of voltage vectors complies with the following table:

$T\uparrow\ \lambda\uparrow$	$T\uparrow\ \lambda\downarrow$	$T\downarrow\ \lambda\uparrow$	$T\downarrow\ \lambda\downarrow$
V_{k+1}	V_{k+2}	V_{k-1}	V_{k-2}

The advantages and disadvantages of DTC for SRM is described below:

- Advantages:
  - Compared with conventional control strategies such as current chopping control (CCC), high-precision torque feedback control is part of DTC which enables the possibilities of developing high-performance speed controller and position controller.

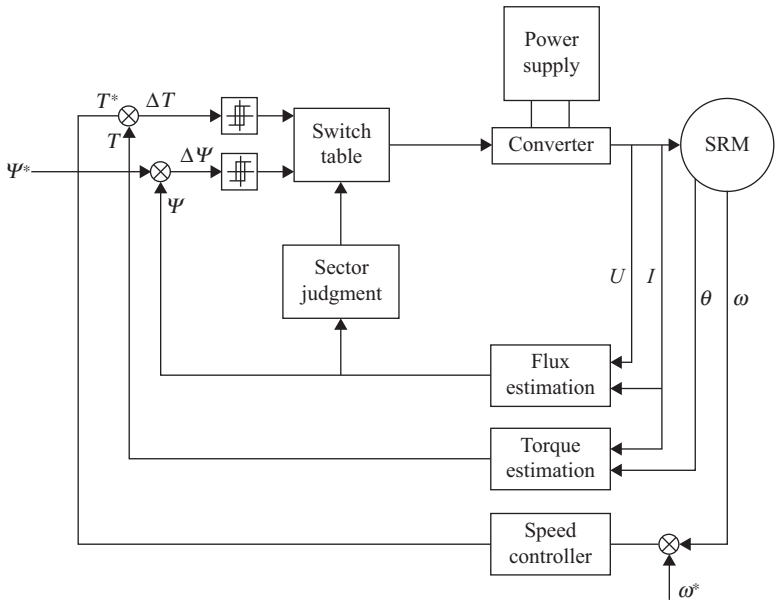


Figure 8.20 Block diagram of conventional DTC

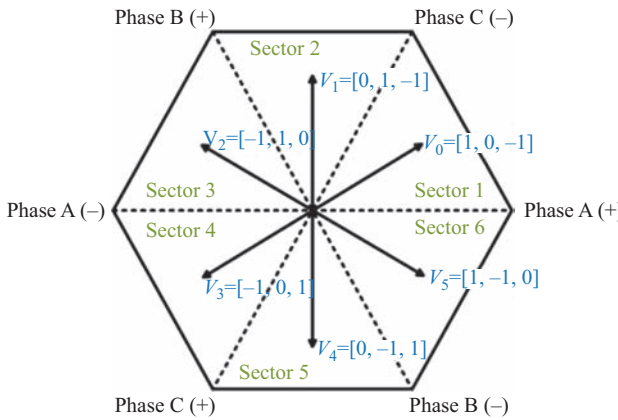


Figure 8.21 Voltage vector selection for a three-phase SRM

– Compared with other instantaneous torque control strategies, such as current-control-based TSF method and current profiling method, where torque-current transformation is required, the torque is directly controlled in DTC. The control strategy possesses the simplicity in implementation by using hysteresis controllers, no predetermined current waveforms required.
– Commutation strategy is also not needed in DTC and the same principle can be applied in any rotor position.

- Disadvantages
  - Unlike induction motor, in order to maintain a constant torque, it is not required to keep a constant amplitude of flux vector for SRM, since at any rotor position, exciting one or at most two phases is enough to reach the required torque, and the excitation of additional phase will only generate negative phase torque and reduce the total output torque [5].
  - High-phase current is required to generate constant flux which increases the copper losses and reduces the efficiency. Compared with other control strategies, it requires longer phase conduction. Besides the absence of current controller in conventional DTC, maximum current which exceeds the system tolerance will occur unexpectedly.

8.4 Modeling of switched reluctance motor

8.4.1 Equivalent circuit

Next, we examine the energy flow from the circuit equations. The equivalent circuit for SRM can be consisting of resistance and inductance with some condition. For the sake of simplicity, the effects of magnetic saturation, fringing flux around the pole corners, leakage flux, and the mutual coupling of phases are usually not considered.

When exciting the magnetic circuit of the SRM, the equivalent circuit for one phase is shown in Figure 8.22. When the applied voltage is V, the phase current is i, the winding resistance is R, and the magnetic flux professor is λ, the voltage equation is shown in (8.4). Also, when the motor rotates at a constant speed ω, the counter EMF $d\lambda/dt$ is as follows:

$$\frac{d\lambda}{dt} = L\frac{di}{dt} + i\frac{dL}{d\theta}\omega \tag{8.50}$$

where $\omega = d\theta/dt$. The first term on the right side of (8.50), which is $L \cdot (di/dt)$, is the reactive voltage due to the current change, and the second term on the right side, which is $i(dL/d\theta)\omega$, is the speed EMF due to the inductance change. Here, the energy flow is given by the following equation:

$$Vi = Ri + \frac{d}{dt}\left(\frac{1}{2}Li^2\right) + \frac{1}{2}i^2\frac{dL}{d\theta}\omega \tag{8.51}$$

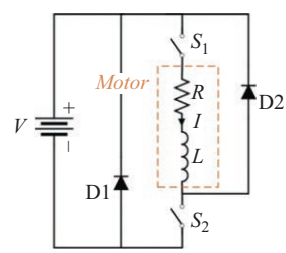


Figure 8.22 Per-phase equivalent circuit

When SRM operates as an electric motor, the input energy supplied from the power source is composed of magnetic energy $((1/2)Li^2)$ and mechanical output $(1/2)i^2(dL/d\theta)\omega$, with the exception for the resistance loss, Ri. Therefore, when the switch is closed during the period of increasing inductance, some of the input energy supplied from the power supply side is converted to mechanical output and the rest accumulates in the magnetic circuit. Also, when the switch is opened in this section, some of the accumulated magnetic energy is converted into mechanical energy and the rest is returned to the power source side.

If the current flows in the section where the inductance remains constant at the maximum value, there is no mechanical output and the input energy is accumulated as magnetic energy. When current flows in the section where the inductance decreases, negative torque generates energy from the mechanical power source to the power source side. This is the regenerative operation of SRM.

8.4.2 Current waveform representation

Since the power source is a voltage source (although it is switched from positive, negative, or zero value), the current is determined by the effective resistance, the counter EMF, and the inductance of the phase winding. All these values change as the rotor rotates. Back EMF and inductance also change with current due to magnetic saturation.

The waveform in the flux linkage should be the integral of $(V - Ri)$. By knowing the flux linkage, the current can be determined from the magnetization curve (Figure 8.23). It is calculated as follows.

$$\Psi = \Psi(i, \theta) \tag{8.52}$$

When Ψ and θ are known, the nonlinear algebraic solution of (8.52) can be used to find the current in these curves. The sequence of dependence is voltage→flux→current.

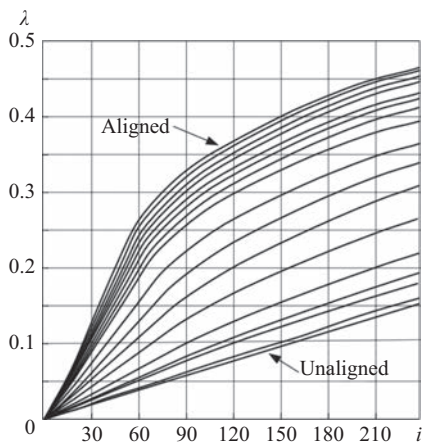


Figure 8.23 Magnetizing curve and flux-linkage curve

Torque and loss can be calculated after finding the current and the flux linkage waveform. (In order to calculate the iron loss in detail, the magnetic flux density waveform shall be obtained from the flux waveform of all parts of the machine.)

At low speeds, the motor does not have enough impedance or back-EMF to limit the current. There are two main measures for this: closed-loop current regulation and voltage PWM, which are described in the previous section and both have soft and hard chopping.

Depending on the state of the power transistor, the power supply voltage applied to the phase line may also be varied. A truth table defining the applied voltage as a function of the switch state is given in Table 8.4.

In the A state (conduction in both transistors), the voltage equation is as follows:

$$V_s - 2v_T - 2r_T i = \omega \frac{d\Psi}{d\theta} + Ri \tag{8.53}$$

where v_T is the fixed voltage drop across each transistor, r_T is the resistance of each transistor, R is the phase resistance, i is the phase current, and Ψ is the phase flux linkage. Most power devices can be modeled by parameters v_T and r_T (mainly IGBTs, MOSFETs, and bipolar transistors). If, as usual, the resistance and v_T are small, this equation is simplified as follows:

$$V_s = \omega \frac{d\Psi}{d\theta} \tag{8.54}$$

This is a derivative of (8.35). If V_s is constant, the flux linkage Ψ increases linearly with the rotor position θ as shown in Figure 8.16. This condition is maintained for $\theta_0 < \theta < \theta_c$.

In θ_c both transistors are off and the voltage equation is

$$-V_s + 2v_d = \omega \frac{d\Psi}{d\theta} + Ri \tag{8.55}$$

where v_d is the forward voltage drop across each energizing diode. Again, if v_d and phase resistance are small, this equation is simplified as follows:

$$-V_s = \omega \frac{d\Psi}{d\theta} \tag{8.56}$$

Table 8.4 Truth table of the applied voltage

State	T1	T2	D1	D2	V
A	1	1	0	0	V_s
B	1	0	0	1	0
C	0	1	1	0	0
D	0	0	1	1	$-V_s$

This is the differential form of (8.37), and after the commutation ($\theta > \theta_c$), the flux decreases linearly.

After integrating the voltage equation, the current waveform should be determined from the flux versus position waveform. Probably the fastest way to do this is the precise analysis method published by Ray and Davis in [6]. In this method, the magnetization curve is represented by the ideal inductance of the trapezoidal linear shape shown in Figure 8.2, while saturation and fringing are ignored. Therefore, the magnetization curve has the general form of Figure 8.24(a). This greatly simplifies the magnetization curve (ignoring both the large saturation at the yoke and the local saturation at the overlapping pole corner), but it shows the important shape of most current waveforms, especially in the development of the controller structure. Also, it makes physical analysis easy.

For accurate result, the magnetization curves must be modeled to include significant physical analysis of major saturation at the yoke and of local saturation near the overlapping poles. In practice, the most preferred form of the magnetization curve is closer to Figure 8.24(b) than 8.24(a). A far more significant effect is the fringing field near the overlapping pole corner. Moreover, this makes the approach based on marking the magnetization curve as it delineated. The basic way to do this is given in [7].

Figure 8.16 shows a typical single pulse current waveform. In this example, θ_0 matches the unaligned position where the phase inductance is small and only changes slowly. As a result, the current increases at a constant rate of approximately $di/d\theta$. If the inductance is equal to the unaligned inductance L_u in the waveform of this part and the resistance is neglected, the increase ratio for the rotor is approximately

$$\frac{di}{d\theta} = \frac{V_s}{\omega L_u} \tag{8.57}$$

When the rotor and stator begin to overlap, the phase inductance begins to increase sharply. Because $\Psi = \Psi(i, \theta)$,

$$\frac{d\Psi}{dt} = \frac{\partial \Psi}{\partial i}\frac{di}{dt} + \omega \frac{d\Psi}{d\theta} = L\frac{di}{dt} + e \tag{8.58}$$

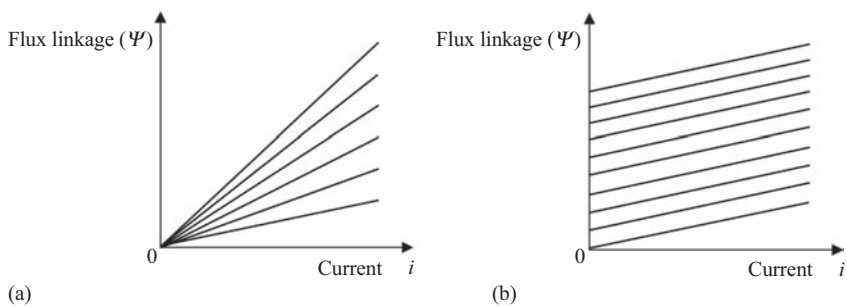


Figure 8.24 Magnetization curve: (a) non-saturated motor and (b) ideal saturated motor

where L is the nonincreasing inductance (the slope of the magnetization curve at θ location). Also, e is the back EMF. In SRM, e depends on the phase current and is 0 when the phase current is zero. This is in contrast to permanent magnet (PM) brushless motors in particular, in which e is independent of the phase current. If the magnetization curve has the ideal shape in Figure 8.24(b) and is uniformly spaced over θ, e will be constant throughout the torque region between alignment and misalignment. In practice this is not possible, but it can be substantially constant for the effective angular region (usable torque range) if the phase current is constant.

A more detailed insight into the back EMF can be obtained from a non-saturated motor with $e = i\omega dL/d\theta$. This shows that the EMF is proportional to the phase current according to the rotor position if the phase inductance is trapezoid, as in the ideal condition. If the phase current is constant and the back EMF is constant and I is equal to the rated current, then the speed at $e = V_s$ is called the base speed [8].

8.4.3 *Torque waveform representation*

In practice, not all *ei* terms in a motor are changed mechanically, since some are stored in magnetic fields. The worst case is the case of a non-saturated motor. In this case, the air gap power is as follows (ignoring the resistance):

$$P_{gap} = T\omega = \frac{1}{2} i^2 \frac{dL}{d\theta} \omega \tag{8.59}$$

And the ratio of energy stored in the magnetic field is

$$iL\frac{di}{dt} + \frac{1}{2} i^2 \frac{dL}{d\theta} \omega \tag{8.60}$$

The addition of (8.59) and (8.60) is $i\omega d\Psi/d$. Less than half of the air gap voltage is being converted to mechanical power. Although only the instantaneous torque and power are described, the maximum energy ratio of the average non-saturated motor to the area of the energy-conversion diagram is

$$E_{\max} = \frac{\gamma - 1}{2\gamma - 1} \tag{8.61}$$

when $\gamma = 10$, it becomes 0.47. The maximum energy ratio for the ideal saturated motor in Figure 8.25 is almost 1, but the energy ratio of a well-designed motor is usually around 0.6–0.7.

The magnetic saturation, which produces the ideal magnetization curve of Figure 8.25, is local magnetic saturation at the overlapping pole corners. This is a required characteristic because it maintains a fixed magnetic flux density at the nested pole corner. This is such that when the rotor pole passes by the stator pole, the flux rotor increases linearly with rotor position, as is in a PM brushless motor. Large magnetic saturation of the magnetic circuit portion away from the air gap is not always desirable. This is because it does not contribute to keeping the magnetic flux density constant in the overlapping region but absorbs the magnetostatic force only.

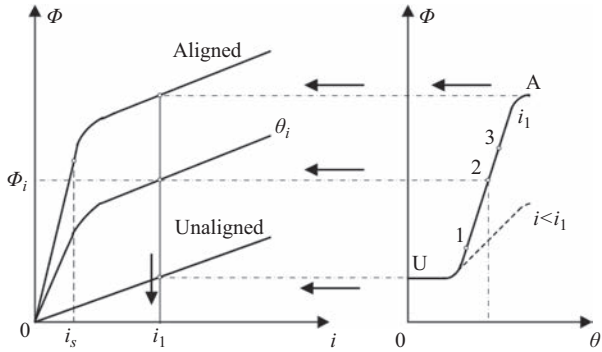


Figure 8.25 Modeling of magnetization curve

Local saturation is beneficial, but it is also necessary that the magnetic flux density it takes up is high and it has the smallest possible i_s current. This implies that a high permeability and saturation flux density B_s are required in the iron core. In normal electrical iron cores, B_s is about 1.7 T.

Harris proposed that the maximum torque generated at the start of overlap when such magnetic flux density values are present is

$$T_{peak} = B_s r_1 L_{stk} \cdot 2N_p i \tag{8.62}$$

where N_p is the number of turns per pole (two stator poles per phase), r_1 is the inner radius of the stator, and L_{stk} is the stack length.

The Harris formula is a simple way to calculate the peak torque available for a given SRM. In a previously published paper, Harris and Sykulski [9] showed that linear changes in force (torque generation) between overlapping poles are valid over a wide range of magnetomotive force. The torque waveform can be computed in (8.9), which is done using the cubic interpolation of the precomputed set of coenergy curves with continuous differentiation at constant current or by the method described in [10].

8.4.4 SRM control system

A block diagram of the SRM with closed loop speed control system is shown in Figure 8.26. The structure of the controller is similar to AC or DC drive. The SRM is shown as a block with an input current and an output torque. Here, the current is a phase current, which can be controlled within a certain range because the current is not a pure DC or AC component and the current varies with speed and load. It is necessary to control the shape of the current to minimize the torque ripple. The velocity error is the difference between the reference velocity and the fed-back current, and it is obtained from the speed transducer connected to the load or motor. In Figure 8.26, the velocity error amplifier produces the pulse-train of the duty cycle by chopping the power transistor at a fixed frequency. This pulse regulation is used to control voltage, instead of current.

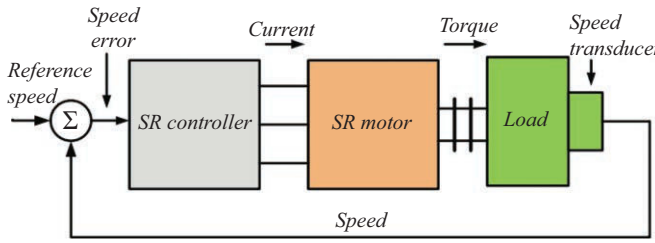


Figure 8.26 Closed-loop speed control system

However, the input to the current limiter is used to turn off the transistor when the current exceeds a certain value.

The SRM is capable of four quadrant operation (forward/reverse direction, positive/reverse torque). In the case of servo control, it is possible to perform a smooth reverse rotation with lower torque ripple, faster dynamic response, higher safety, and operating speed. In the control without the servo device, continuous control of the firing angle is required to optimize the characteristics of the drive with small change in speed.

DC commutator and brushless DC motors have advantages in control because the torque is proportional to the current. AC induction motors and PM synchronous motors with field-oriented control require the characteristics of DC motors. In theory, this is possible because the DC motor equations can be converted to the AC motor equations by reference frame transformations (*dq*-axis transformation).

Conventional SRM does not have *dq*-axis transformation applied and the rule of vector control is not used. Therefore, when four quadrant operation and servo operation are required, control can be performed by real-time control of high-speed operation directly according to phase current and voltage. The relationship between torque, current, speed, and firing angle are nonlinear and it varies depending on a function of speed and load.

The design of a typical SRM controller is shown in Figure 8.27. The current waveform is controlled to reduce torque ripple, and nonlinear characteristics were compensated to obtain constant torque/current. The controller in Figure 8.26 uses a single-chip microcontroller.

In the figure, the output of the SRM and the block of power electronic circuit are torque, the input is the point angle and the angle θ_0 and θ_c. It is assumed here that a current regulator capable of current control is included. This diagram contains the integration circuit of the torque and velocity equations from which the speed and rotor position can be known. The rotor position is sensed by the encoder (or resolver), and the velocity is obtained by a digital algorithm.

The speed of the calculated digital value is compared with the command speed and the error (proportional, integral gain) is input to current regulator that produces a command current signal (i^*).

If the current speed exceeds the reference speed, four quadrant operation is performed so that the motor can generate the braking torque in the servo drive.

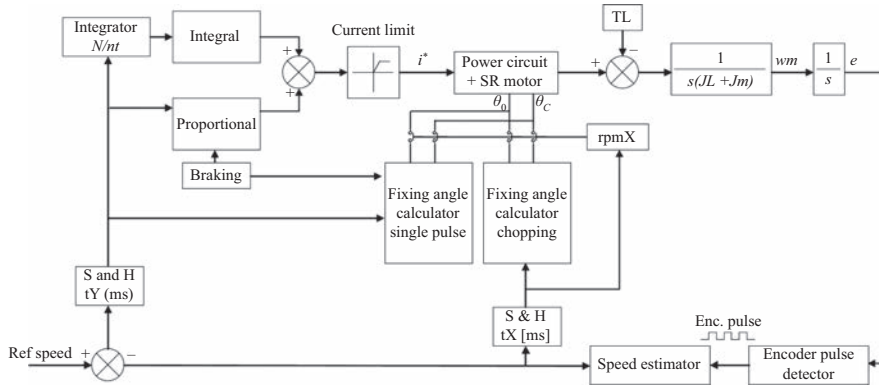


Figure 8.27 Four quadrant control

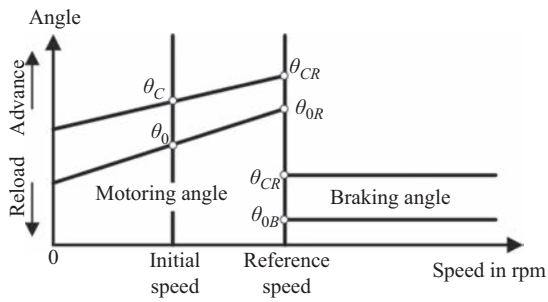


Figure 8.28 Change of excitation angle according to speed

However, in general variable speed control, it is not necessary because it is sufficiently reduced by the load torque.

The current to make the braking torque should be kept at a finite value even if the excitation angle is delayed. The braking torque is a nonlinear function of current and excitation angle, just like the electric torque.

The braking torque is created by the instantaneous change of excitation angle. As shown in Figure 8.28, the excitation angle (θ_0, θ_c) can be known at the initial speed. As the speed increases, the excitation angle advances until the reference speed is reached. At this speed, the excitation angle is the maximum value of the advance angle (θ_{0R} and θ_{cR}). The excitation angle is earlier than the extinction angle (where reduction happens). If the current speed exceeds the reference speed (command speed), the excitation angle is delayed until the preset θ_{0B} and θ_{cB} angles to generate braking torque. The braking torque is controlled by the current controller, which is based on the speed error. At this time, the speed is low enough to control the current. Because this control is not possible for braking at high speed, it is possible to adjust the braking angle by the speed error.

In motoring mode, it is controlled at high speed by current control, but it is sensitive or unstable. Excitation angle control should be used to control the torque. The mapping of the excitation angle is determined by the velocity or velocity error, but this is a nonlinear and complex procedure. Because the nonlinearity dynamometer test is difficult, it is possible to find the optimum angle of excitation by repeatedly searching for the error. This procedure is performed by mathematical simulation.

SRM is mainly controlled by adjusting the advance angle and the applied voltage. Among them, the control of the current degree is performed by a constant conduction angle control method, a variable conduction angle control method, a constant torque angle control method according to a predetermined algorithm according to the speed–torque characteristic of the load. In this method, the magnitude and waveform of the mmf current change corresponding to the change of load.

Because SRM has a nonlinear characteristic and its current waveform changes a lot, it is difficult for the controller to adapt to the load change. Therefore, the speed fluctuation appears and induces torque pulsation, which makes stable operation impossible. This unstable operation has a disadvantage which makes the operation control method become complicated because a supplemental control method needs to be adopted, such as applied voltage control. In other words, this type of operation lacks the flexibility to cope with fluctuations in load torque in a robust manner.

8.4.5 *Example designs of control scheme*

It has been explained in the previous sections that generally there are two types of control that one can use in driving SRM: switching angle control and current control, the control schemes of which are going to be discussed here.

Switching angle control scheme designed for high-speed SRM is shown in Figure 8.29. There are two controllers involved: current and speed controller. Speed controller block is just a simple proportional integral (PI) control that gives output of current reference based on the speed error. The current output from speed controller is limited below allowable value. Sensor will give the actual current value to give the error to the current controller. Then the current can be controlled

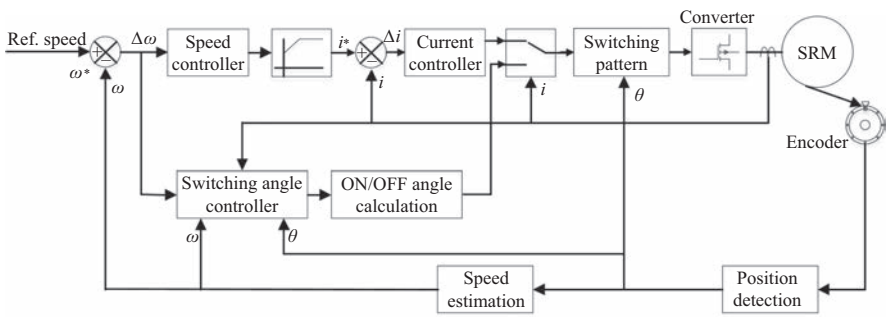


Figure 8.29 Switching angle control scheme

to get the flat-top shape by once again implementing PI control, for simplicity. PI method can be changed to any other method by one's choice. Output of current controller is command voltage for PWM generator.

As the name suggests, there is a separate block to determine the switching angle based on the rotation speed and rotor position. The turn on angle calculation is proposed by Bose *et al.* as presented in [11], while the turn of angle is computed based on turnoff angle theory proposed by Gribble *et al.* as follows:

$$\theta_{on} = \theta_{pos} - 6\frac{L_u N_m}{V_{DC}} i \tag{8.63}$$

$$\theta_{off} = \theta_a - \theta_m \left(-\alpha + \sqrt{\alpha^2 + \frac{24i(1-x)N_m}{R_{ua} V_{DC} \theta_{pos}} i} \right) \tag{8.64}$$

$$R_{ua} = R_u - R_a \tag{8.65}$$

$$\alpha = \frac{R_a}{R_{ua}} \tag{8.66}$$

where R_a and R_u are reciprocals of the aligned (L_a) and unaligned (L_u) inductance, N_m is speed in rpm, V_{DC} is DC link voltage, x is constant usually between 0.6 and 0.7, i is the phase current, and θ_{pos} is rotor position.

On/off angle calculator block in Figure 8.29 used actual encoder index pulses and estimated speed to determine turn-on and turn-off angle. However, in the modeling method, these index pulses can be mathematically calculated by understanding the concept given in Figure 8.30 [12]. To obtain high performance, the point at which current reaches to desired current value should match with rising point of inductance.

In practical application, the encoder is connected to rotor shaft mechanically. So, angle θ_0 from falling edge of index pulse to rising point of inductance is already given. The time to shift from falling edge of index pulse to rising point of inductance is

$$t_0 = \frac{\theta_0}{\omega} \tag{8.67}$$

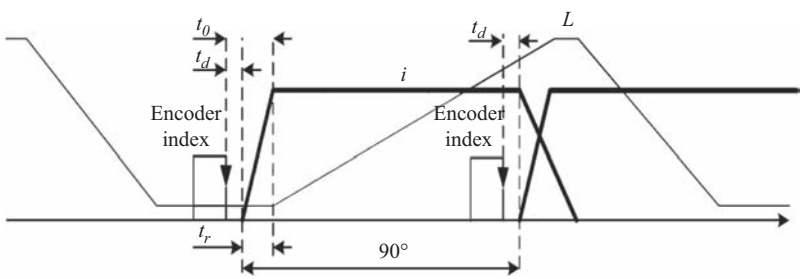


Figure 8.30 Turn-on and turn-off determination

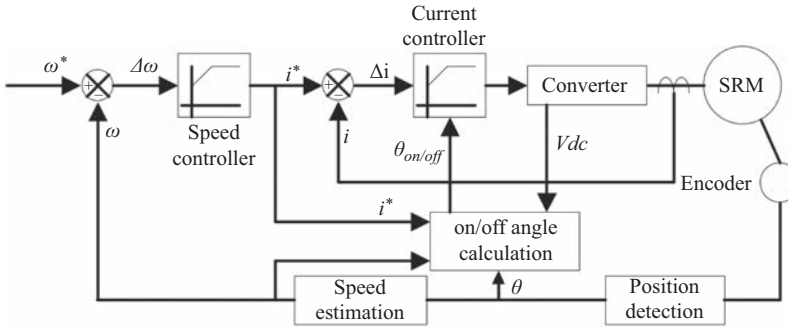


Figure 8.31 Current control scheme

When rotor is located at unaligned position and the stator winding resistance is negligible, the time to build up current from 0 to desired current value is

$$t_r = \frac{L_u \times I_{desired}}{U} \tag{8.68}$$

From Figure 8.30, time delay from falling edge of index pulse to turn-on position is determined from (8.67) and (8.68).

$$t_d = t_0 - t_r \tag{8.69}$$

Dwell angle should be kept constant to produce continuous torque without producing negative torque region. Therefore, after every time delay t_d from falling edge of index pulse, phase commutation should occur.

Unlike high-speed operation where excitation angle needs to be changed, low speed operation is simpler and current control alone is sufficient to operate the motor. The most apparent difference between those two is the existence of switching angle controller block in the diagram. Figure 8.31 shows the current control scheme for low-speed SRM.

The majority of the controller parts is the same, implementing the well-known PI controller that receives speed error as input and gives output as current reference which is then limited below certain value. Then current error value will be calculated and the current regulation happens at the current controller block to get the flat-top shape current, which will give high-performance output.

8.5 Emerging applications

SRM is simple in its construction. Windings are found only on the stator and the rotor merely comprises ferromagnetic core laminations. Researcher used this structure as an advantage to implement the motor usually as high-speed drive, due to its relatively low rotor inertia. Moreover, it is also considered to be of low cost

compared to other electric machines. However, it has some major drawbacks in terms of high acoustic noise and vibration because of its operating nature. Because of this, SRM is mainly used in appliances that are already considered noisy. In this section, some applications of the motor will be described. It can be seen that through various design methods, SRM can have a wide range of utilization which is why it is gaining more interest and rapid development.

8.5.1 Home appliances

8.5.1.1 Vacuum cleaner

A British inventor, Sir James Dyson, revealed what was claimed as the fastest motor in the world which is a small SRM. The announcement was made in 2009 and it was considered a breakthrough at that time. The motor only measures 55.8 mm in diameter and weights around 139 g. This developed motor was dubbed DDM (Dyson digital motor) 2 and was originally meant to be used in DC31 handheld vacuum cleaner with the capability to run at the speed of 104,000 rpm [13,14]. DDM2 was a single-phase, two-pole SRM, as can be seen in Figure 8.32.

8.5.1.2 Food blender

Commercial appliances always require trade-offs between performance and cost. Among a variation of motor types, there is one type that is quite popular for commercial applications: universal motors. As the name suggests, universal motors work with either AC or DC power supply, and it has a simple structure. Moreover, no electric power drive is required, so the weight and cost can be reduced, which is an important factor in industry and business. However, universal motors suffer from problems as listed below:

- Short lifespan due to the wear of carbon brushes and commutator (maintenance is needed).
- High sensitivity to moisture and dust especially if it is electrically conductive. Applications in extreme environment may require an extra cost for protection.
- "Limited" power to weight ratio. The speed range is limited due to the commutator and rotor windings. The motor can run above the rated speed, but at the expense of significantly reduced commutator lifespan.



Figure 8.32 Structure of Dyson digital motor

- Moderate dynamic characteristics, mainly due to the high rotor inertia. Although high acceleration is seldom needed, rapid braking is a requirement for some application. The motor is able to brake, but it needs additional switchgear (a reversing switch for either stator or rotor winding and eventually facilities to initially magnetize the motor). For a controlled or well-defined braking operation, a costly electronic control is necessary.

These problems are basically caused by the brush and commutator in universal motor. Therefore, replacing it with a brushless drive may solve the problem and here is where SRM plays its role. To compete with the low-cost universal motors, an effective way is to use unipolar drives instead of bipolar drives by reducing the number of switches in converter. Single-phase SRMs suit the unipolar excitations by nature and have been involved in many studies as an effective low-cost drive system [15,16].

The proposed hybrid single-phase SRM in [17] uses permanent magnets due to the dead-torque zone problem which can be found in SRM with phases lower than three. Hybrid is given to the name since it does not follow the conventional structure of SRM that utilizes no permanent magnets. However, the rotor still has considerably low inertia since the magnets are located on the stator only. If the rotor stops in this dead zone, then it is impossible to self-start the motor because no torque can be produced in the region. This phenomenon is illustrated in Figure 8.33.

Other than implementing permanent magnets to "park" the rotor, giving it initial starting position, the rotor is also designed to create a nonuniform air gap to improve the output torque of the motor. For the purpose of blending both soft and hard items, more consideration into starting torque was put into design process. The rated speed of the motor is 18,000 rpm and the rated load is set to 0.4 N m. The rotor comprises two sections: salient section and nonuniform section the detail of which can be seen in Figure 8.34.

The stator is 78 mm long and 58 mm wide. The stack length is 30 mm. The prototype of the proposed hybrid SRM is shown in Figure 8.35.

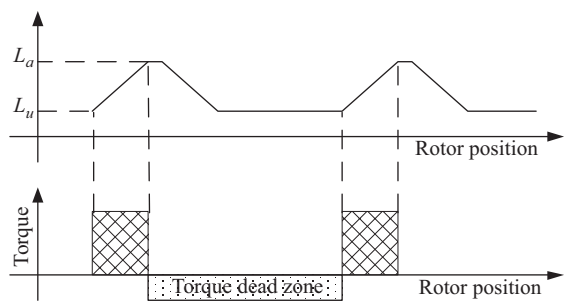


Figure 8.33 Torque dead zone in a single-phase SRM

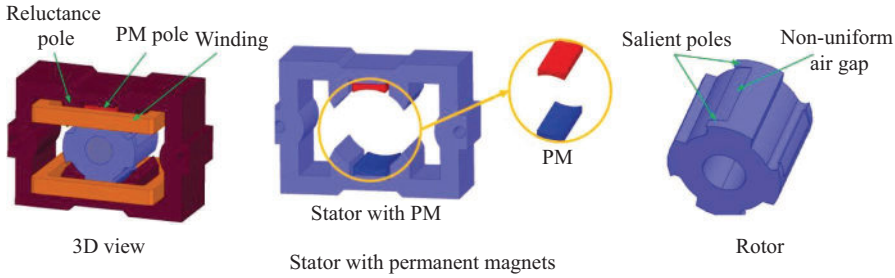


Figure 8.34 Structure of hybrid SRM [17]

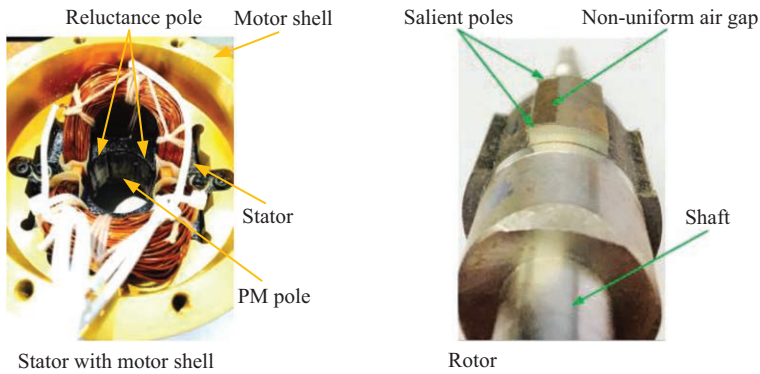


Figure 8.35 Hybrid SRM for blender [17]

8.5.2 Industrial applications

8.5.2.1 Air blower

Another application that can benefit from having SRM as its driving machine is an air-blower. The literature in [12] proposed an optimized design of a two-phase 4/2 poles SRM. Similar to single-phase type, the conventional structure of a two-phase SRM has a torque dead zone. However, it is not as large as single-phase, thus the utilization of permanent magnets is not required. To be noted, phases lower than three also lacks the ability to rotate both clockwise and counterclockwise, so a preset direction is necessary in the design process.

In order to solve the torque dead zone problem, nonuniform air gap and wide rotor pole arc are implemented. Reducing air gap is the cause of increase of inductance, hence it results in increase of output torque and vice versa. Based on this concept, rotor air gap was modified. As for the pole arc, due to the commutation, if it is too large, then negative torque region may be produced, but if it is too narrow, then the torque dead zone may still exist. It is important in order to produce continuous torque.

The final rotor shape after optimization is shown in Figure 8.36. The comparison between conventional 4/2 SRM before the optimization and the proposed structure is given in Figure 8.37. Torque of the propose rotor shape is much better than conventional type. Even though the maximum torque is much reduced, it still got the same average torque. This is due to the high ripple in conventional structure, which can be calculated as:

$$T_{ripple} = \frac{T_{\max} - T_{\min}}{T_{avg}} \tag{8.70}$$

Moreover, the dead zone is also eliminated so that the motor has the capability to self-start.

Prototype for this motor is presented in Figure 8.38. The rated speed for the proposed motor is 30,000 rpm with 0.2 N m of rated torque. The outer diameter of the motor is only 80 mm with the stack length of 30 mm.

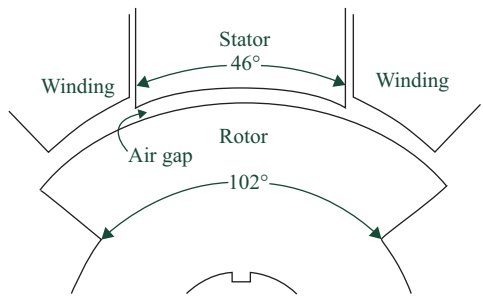


Figure 8.36 Optimized rotor shape of a 4/2 SRM [12]

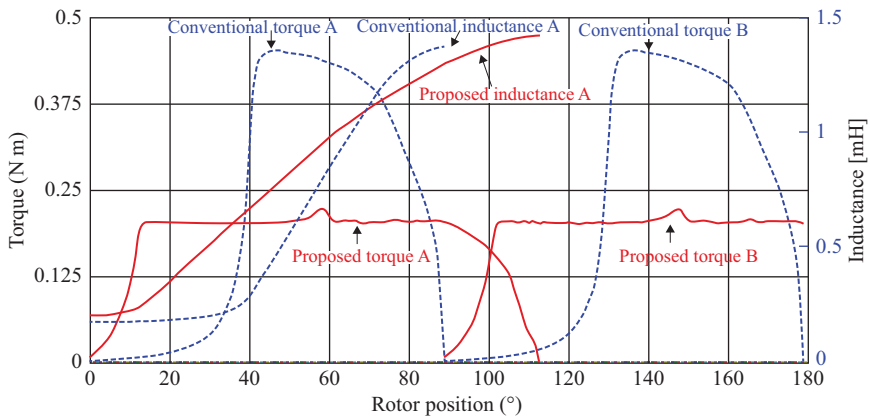


Figure 8.37 Torque and inductance of the proposed versus conventional rotor shape [12]



Figure 8.38 Prototype 4/2 SRM [12]: (a) stator (b) rotor (c) assembled SRM

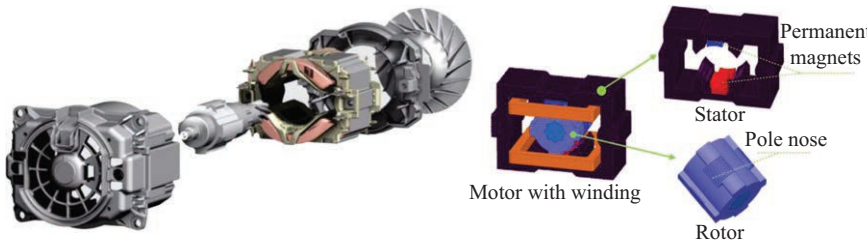


Figure 8.39 SRM structure for hammer breaker (Hilti) [19]

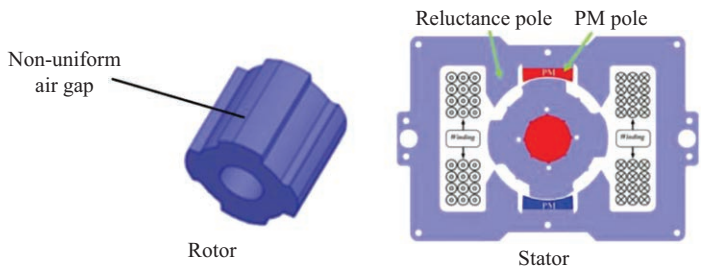


Figure 8.40 Design of proposed motor [19]

8.5.2.2 Hammer breaker

Hilti company is reportedly to use SRM in its hammer breaker products, such as found in Hilti TE 700-AVR, TE 1000-AVR, TE 1500-AVR, and TE 3000-AVR which is claimed to be maintenance-free for life. The structure of the motor is shown in Figure 8.39, with the details about it presented in [18].

However, the proposed motor in [19] is complicated due to the shape and position of permanent magnets and the existence of "pole nose" of the rotor. Therefore, another structure is proposed in [20] which is simpler to manufacture and have similar but slightly higher efficiency than that of Cyrano's. The proposed HSRM (hybrid SRM) adopted rotor with nonuniform air gap and is comparatively easy to stack (Figures 8.40 and 8.41). Both motors were designed to rotate at the

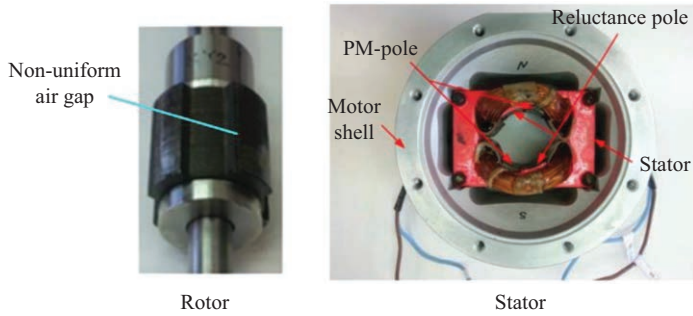


Figure 8.41 Prototype SRM [19]

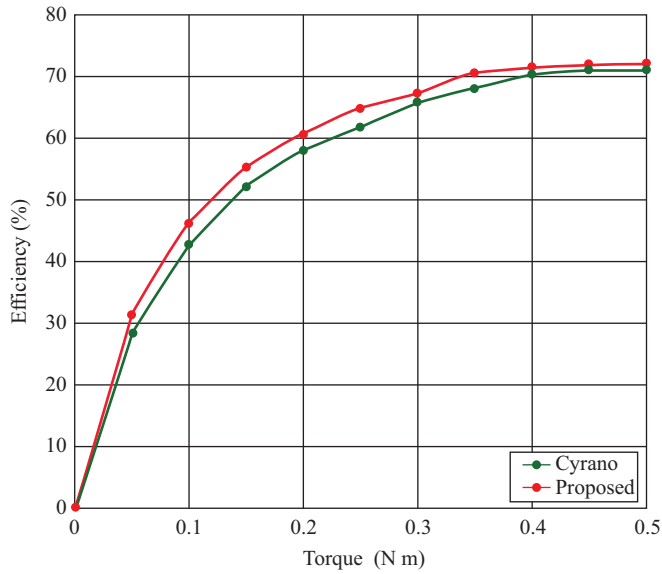


Figure 8.42 Efficiency of HSRM [19] (upper line) and cyrano-motor (lower line) [18]

rated value of 18,000 rpm with 0.4 N m of rated torque. The comparison of efficiency comparison between [18] and [19] is shown in Figure 8.42.

8.5.3 Electric vehicle application

8.5.3.1 Traction motor

In recent years, electric vehicle (EV) is starting to gain more interest due to the increasing problems of environmental pollution and energy crisis. It is considered as the future for a sustainable automobile industry. In order to provide power as much as the internal combustion engine (ICE) in conventional vehicle does, a

high-performance, high-efficiency electric motor is required. However, these high-end technologies usually adopt permanent magnets machines, which in theory have high torque and power density compared with those that are magnet-less. This may create a problem in the future since the supply of permanent magnets is limited, and it adds additional costs in manufacture process.

NEDO projects in Japan have started the development of rare-earth-free motors that has to be competitive in size, power density, and efficiency to the ones with magnets. Literatures in [20,21] reported of such development by designing a 18/12 SRM that matches the performance of permanent magnet synchronous machine (PMSM) of the same size. The pole selection is based on the assumption that more pole will result in higher torque, while sacrificing the possible maximum rotating speed. Also, with the structure of SRM that relatively has short end-winding length, the actual stack length of the core can be made longer, compared to PMSM, thus increasing the output. The outer diameter of the machine is 269 mm with 156 mm of stack length, while the target output torque is 400 N m. Moreover, by utilizing a super-core material of 10JNEX900 for the cores, the efficiency reaches up to 95% at 3,000 rpm. The material has extremely low iron loss, with thickness of 0.1 mm.

The proposed SRM is targeted to be used in Toyota Prius which is a type of hybrid EV that uses both ICE and electric motor. The structure and prototype of the motor is shown in Figure 8.43.

8.5.3.2 Electric supercharger

Automotive industry always opts for lighter and faster vehicles along with better fuel efficiency. Turbochargers were developed to provide more air to the ICE for acceleration boost, propelled by the exhaust gas of the engine itself. Although it is considered efficient due to the use of exhaust gas, the system suffers from a delay, or "turbo lag" when there is not enough exhaust gas, especially at low rpms. Because of this, superchargers were developed. Conventional superchargers are powered by the engine by a belt, but it tends to decrease ICE efficiency and thus, along with the development of power electronics, electric superchargers (ESCs) were invented.



Figure 8.43 Prototype SRM for traction [21]

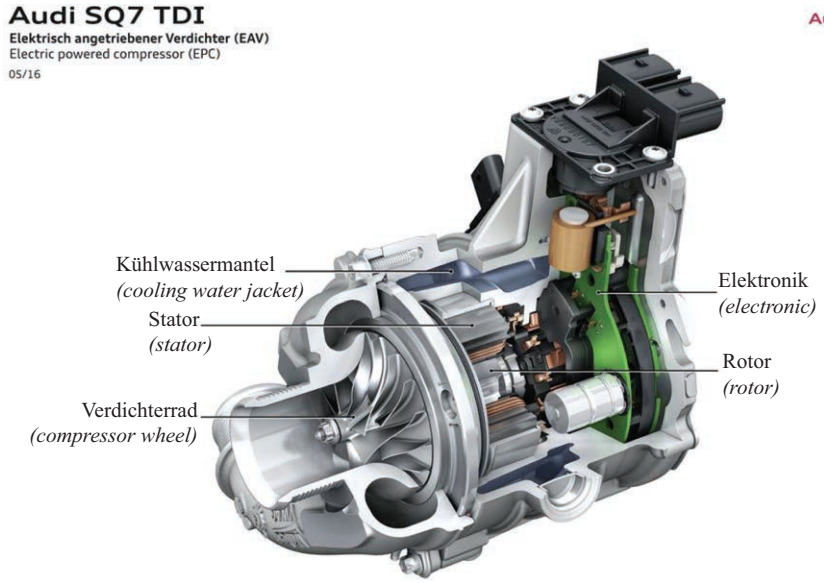


Figure 8.44 Electric supercharger system

It is reported that an ESC with SRM as its electric motor was commercially used in Audi SQ7. The motor's maximum speed is 70,000 rpm. The input voltage is 48 V from battery, and it is able to produce up to 7 kW of maximum power. This is possible thanks to the low inertia of the rotor, with a fast response speed within 350 ms from idle to maximum speed [22]. The cut-off drawing of the system is shown in Figure 8.44 as seen in official Audi website.

8.6 Summary

This chapter provides comprehensive analysis of the SRM drive, starting with machine inductance waveform, the required current waveform, its converter and shaft-interfacing requirements for speed and current control. This chapter is also supplemented with several examples of emerging application in drives for appliances and EVs.

List of symbols

W_c'	The coenergy
i	Phase winding current
L	Phase winding inductance
T_e	Torque generated by the phase winding current
θ	Rotor position angle

θ_{st}	Rotor stroke angle
N_r	Rotor pole number
r	Winding resistance
λ	Flux linkage
ω	angular velocity
θ_{DW}	Dwell angle
θ_{AD}	Advance angle
θ_{TQ}	Torque angle
N_s	Number of stator pole
$\beta_s\ \beta_r$	Stator and rotor pole arcs
D_r	Rotor diameter
L_{stk}	Stack length of the motor
L_{et}	Length of end windings
L_e	Total length of the motor
r_1	Rotor outer radius
g	Length of air gap between rotor and stator poles at aligned position
d_r	Rotor slot depth
r_0	Radius from center to outer surface of rotor yoke
y_r	Rotor yoke thickness
y_s	Stator yoke thickness
D_{sh}	Shaft diameter
θ_{on}	Control the excitation angle
θ_c	Control the conduction time
θ_{OFF}	Switch off angle
Ψ_0	Preexisting flux linkage
V_s	Supply voltage
R	Phase resistance
a_p	Pole pitch
V	Applied voltage
λ	Magnetic flux professor
$d\lambda/dt$	Counter electromotive force
v_T	Voltage drop across each transistor
r_T	Resistance of each transistor
θ	Rotor position
v_d	Forward voltage drop across each energizing diode
L_u	Unaligned inductance
L	Nonincreasing inductance

e	Back EMF
N_p	Number of turns per pole
r_1	Inner radius of the stator
L_{stk}	Stack length
i^*	Command current signal

Glossary of terms

Coenergy	The energy in a machine responsible for production of torque
Dwell angle	The duration for which the inverter is kept on

References

[1] Ramu K. *Switched Reluctance Motor Drives: Modeling, Simulation, Analysis, Design, and Application*. CRC Press, Boca Raton, FL, 2001.

[2] Ahn J. W. *Switched Reluctance Motor (Korean)*. Osung Media, Seoul, 2004.

[3] Nasar S. A. 'DC switched reluctance motor'. *Proceedings of the IEEE*. vol. 116. no. 6. pp. 1048–1049. 1969.

[4] Cheok A. D. and Fukuda Y. 'A new torque and flux control method for switched reluctance motor drives'. *IEEE Transactions on Power Electronics*. vol. 17. no. 4. pp. 543–557. 2002.

[5] Sau S., Vandana R. and Fernandes B. G. 'A new direct torque control method for switched reluctance motor with high torque/ampere'. *IECON 2013 – 39th Annual Conference of the IEEE Industrial Electronics Society*. Vienna. 2013. pp. 2518–2523.

[6] Ray W. F. and Davis R. M. 'Inverter drive for doubly salient reluctance motor; its fundamental behaviour, linear analysis, and cost implications'. *IEE Journal on Electric Power Applications*. vol. 2. pp. 185–193. 1979.

[7] Hendershot J. R. 'Short flux paths cool SR motors'. *Machine Design.* pp. 106–111. September 1989.

[8] Miller T. J. E. 'Converter volt-ampere requirements of the switched reluctance motor drive'. *IEEE Transactions on Industry Applications*. vol. IA-21. pp. 1136–1144. 1985.

[9] Harris M. R. and Sykulski, J. K. 'Simple method for calculating the peak torque of a switched reluctance motor: a computational investigation'. *COMPEL – The International Journal for Computation and Mathematics in Electrical and Electronic Engineering*. vol. 11. no. 1. pp. 193–196. 1992.

[10] Miller T. J. E. 'Nonlinear theory of the switched reluctance motor for rapid computer-aided design.' *IEE Proceedings B – Electric Power Applications*. vol. 137. no. 6. pp. 337–347. 1990.

[11] Miller T. J. E. *Electronic Control of Switched Reluctance Machines*. Newnes, Oxford. 2001.

[12] Khoi H. K. M. *Design and Control of a High Speed 4/2 SRM for Blower Application*. Master thesis, Dept. of Mechatronics Eng., Kyungsung University, Busan, South Korea, 2010.
[13] Bush S. *Dyson vacuums 104,000 rpm brushless DC technology* [online]. 2009. Available from https://www.electronicsweekly.com/market-sectors/power/dyson-vacuums-104000rpm-brushless-dc-technology-2009-06/ [Accessed 29 April 2018].
[14] Brandon J. *Dyson's new vacuum driven by the fastest motor ever* [online]. 2009. Available from https://www.popsci.com/gear-amp-gadgets/article/2009-06/dysons-new-vacuum-driven-fastest-motor-ever [Accessed 29 April 2018].
[15] Stephenson J. M. *Switched reluctance motors*. US Patent. No. 5548173. August 1996.
[16] Lurkens P. *Single-phase reluctance motor adapted to start in a desired direction of rotation*. US Patent. No. 5428257. June 1995.
[17] Jeong K.-I., An Y.-J. and Ahn J. W. 'Design and characteristics comparison of single-phase hybrid switched reluctance motors (Korean)'. *Presented at KIEE Spring Conference*. Wonju-si, Korea. 2018.
[18] Torok V. *Electric motor with combined permanent and electromagnets*. US patent. No. 5345131, September 1994.
[19] Jeong K. I., Lee D. H. and Ahn J. W. 'Performance and design of a novel single-phase hybrid switched reluctance motor for hammer breaker application'. *2017 20th International Conference on Electrical Machines and Systems (ICEMS)*. Sydney, NSW. 2017. pp. 1–4.
[20] Chiba A., Takano Y., Takeno M., *et al.* 'Torque density and efficiency improvements of a switched reluctance motor without rare-earth material for hybrid vehicles'. *IEEE Transactions on Industry Applications*. vol. 47. no. 3. pp. 1240–1246. 2011.
[21] Chiba A., Kiyota K., Hoshi N., Takemoto M. and Ogasawara S. 'Development of a rare-earth-free SR motor with high torque density for hybrid vehicles'. *IEEE Transactions on Energy Conversion*. vol. 30. no. 1. pp. 175–182. 2015.
[22] Dima. *Valeo's electric supercharger targeted for 2015–16 production SAE International* [online]. 2014. Available from http://electrical-cars.net/interesting/valeo-s-electric-supercharger-targeted-for-201516.html [Accessed 30 April 2018].

Chapter 9

Direct torque control of AC machines

Rahul Kanchan[1]

Direct torque control (DTC), although introduced later than the classical field oriented control (FOC), established itself for primary choice in demanding applications where fast torque requirements are necessary. The FOC is based on decoupling control principle to mimic dc motor current control, which involves coordinate transformations and flux- and torque-producing currents controllers. The basic principle of the DTC is to directly control the motor flux vector along the predetermined trajectory at the predetermined speed. Any deviation in the actual motor flux from the reference trajectory is detected by set of hysteresis controllers, which directly select appropriate switching vector in such that the deviation is minimized. The DTC principle simplifies the drive control structure by eliminating the coordinate transformations and proportional–integral (PI) current controllers. The PI controllers are replaced by simple hysteresis comparators. Whereas, the pulse width modulation (PWM) modulator is replaced with simple switching tables that are simply implemented as lookup tables, eliminating any need of modulation dwell time calculations. With this approach, DTC directly generates the command signals for inverter phases. The flux vector orientation is done in stationary reference frame, thus eliminating need for speed/position sensors. The ultimate result of this simplification enables to obtain faster dynamic response as compared to classical FOC controllers.

The basic theory behind DTC was introduced by Depenbrock in 1984 [1–3] through the patent filed in Germany and the United States under the name Direct Self-Control (DSC). At the same time, Takahashi and Noguchi introduced similar technique under the name DTC independently in Japan [4]. Although both the methods are based on direct control of stator flux vector along the predetermined trajectory, the flux vector trajectory is circular in DTC and hexagonal for DSC. Due to its simple control structure, it was adapted immediately in the industrial product chain of one of the largest drive manufacturers "ABB," which created even more curiosity in this technology [5,6]. The topic has been heavily researched over the years and there have been many improvements suggested to the original DTC control structure suggesting further performance improvements, many adaptations to other motor types, grid-side converter control applications have been proposed. Still, the basic concept of DTC has remained the same.

[1]Department of Electrical Systems, ABB Corporate Research Center, Sweden

This chapter introduces the basic principles behind DTC concept in connection with torque control of induction motors. First, the motor torque expression has the function of stator flux and rotor flux of the motor. This is used to illustrate effect of applying different inverter voltage vectors on the magnitude of motor flux and developed torque. The central control structure of DTC is then introduced, with detailed description of each building block. The later part of the chapter looks at promising improvements that have been proposed over the years to improve the performance of the DTC control and gives short summary of industrial adaptations of DTC technology.

9.1 Induction motor model

The induction motor model used in further analysis in this chapter is shown in Figure 9.1.

The stator and rotor voltage equations of the induction motor in terms of space vectors in a stationary reference frame is represented as

$$\begin{aligned} \overline{u}_s &= \bar{i}_s r_s + \frac{d\overline{\psi}_s}{dt} \\ 0 &= \bar{i}_r r_r + \frac{d\overline{\psi}_r}{dt} \end{aligned} \tag{9.1}$$

where

$$\begin{aligned} \overline{\psi}_s &= l_s \bar{i}_s + l_m \bar{i}_r \quad l_s = \mathrm{l}_{ls} + l_m \\ \overline{\psi}_r &= l_r \bar{i}_r + l_m \bar{i}_s \quad l_r = \mathrm{l}_{lr} + l_m \end{aligned} \tag{9.2}$$

The torque produced is be written in terms of stator flux and current quantities as

$$T_e = \frac{3}{2} p \, \overline{\psi}_s \otimes \bar{i}_s \tag{9.3}$$

Stator flux equation can be rewritten as

$$\begin{aligned} \overline{\psi}_s &= l_s \bar{i}_s + \frac{l_m}{l_r}(\overline{\psi}_r - l_m \bar{i}_s) \\ &= \frac{l_\sigma}{l_r} \bar{i}_s + \frac{l_m}{l_r} \overline{\psi}_r \end{aligned} \tag{9.4}$$

where $l_\sigma = l_s l_r - l_m^2$.

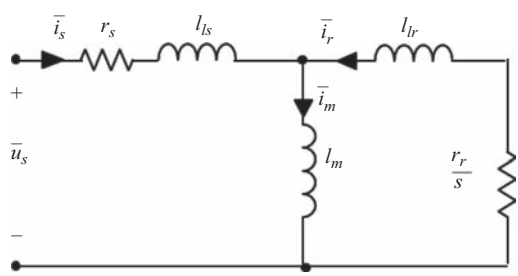


Figure 9.1 Steady-state equivalent circuit representation of induction motor

Similarly, rotor flux can also be expressed in terms of stator flux and currents

$$\overline{\psi}_r = \frac{l_r}{l_m}\overline{\psi}_s - \frac{l_\sigma}{l_m}\bar{i}_s \tag{9.5}$$

From (9.4), the stator current can be rewritten as

$$\bar{i}_s = \frac{l_r}{l_\sigma}\overline{\psi}_s - \frac{l_m}{l_\sigma}\overline{\psi}_r \tag{9.6}$$

The torque equation thus can be represented in terms of stator and rotor flux, by substituting $\bar{i}_s$ from (9.6) is written as below:

$$T_e = \frac{3}{2}p\frac{l_m}{l_\sigma}\overline{\psi}_s\overline{\psi}_r \tag{9.7}$$

Converting into polar coordinates, the torque equation in terms of flux magnitude and angle can be represented as

$$T_e = \frac{3}{2}p\frac{l_m}{l_\sigma}\psi_s\psi_r \sin\theta_{sr} \tag{9.8}$$

where θ_{sr} is angle between stator and rotor flux.

The dynamics between stator and rotor flux can be represented in terms first order delay with rotor time constant τ_r and total leakage factor σ.

$$\psi_r = \frac{l_m/l_s}{1 + s\sigma\tau_r}\psi_s \qquad \text{where } \sigma = \frac{l_\sigma}{l_s l_r},\ \ \tau_r = \frac{l_r}{r_r} \tag{9.9}$$

Thus, the any transient change in stator flux is propagated to rotor flux with an equivalent transient time constant $\sigma\tau_r$.

Neglecting stator voltage drop in the stator voltage equation in (9.1), the transient change in stator flux is

$$d\overline{\psi}_s \cong \overline{u}_s\, dt \tag{9.10}$$

For very short interval Δt, this can be represented as

$$\overline{u}_s\Delta t = \Delta\overline{\psi}_s \tag{9.11}$$

This can be graphically represented as shown in Figure 9.2. Application of voltage vector $\overline{u}_s$ for time interval Δt results in stator flux ψ_s change by $\Delta\psi_s$. The direction of change of ψ_s is dependent upon application of voltage vector. This is the underlying principle of DTC. It is possible to increase or decrease the stator flux by application of voltage vector of appropriate amplitude and direction. The voltage vector V_s shown in Figure 9.2 advances stator flux by an angle $\Delta\theta_{sr}$. The incremental changes $\Delta\psi_s$ and $\Delta\theta_{sr}$ are dependent upon the direction and duration of applied voltage vector. The incremental torque expression under this condition can be represented as

$$\Delta T_e = \frac{3}{2}p\frac{l_m}{l_\sigma}(\psi_s + \Delta\psi_s)\psi_r \sin\Delta\theta_{sr} \tag{9.12}$$

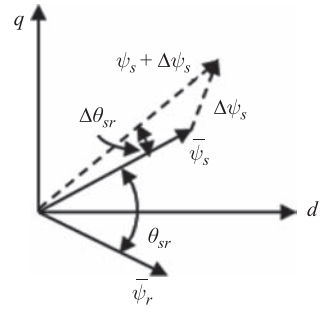


Figure 9.2 Representation of stator and rotor flux in stationary coordinates

9.2 Two-level inverter voltage vector representation

The electrical schematic of two-level converter fed induction motor drive is shown in Figure 9.3(a). Each phase is supplied with a pair of power switches, which are switched complementary to each other, can connect the machine phase winding to either positive or negative dc rail of the converter. This is described graphically as "1" or "0" for machine phase connection to positive or negative dc rail, respectively. Depending upon the status of connection of inverter poles, a combined machine voltage vector is defined as

$$v_s = v_{as} + v_{bs} \cdot e^{j(2\pi/3)} + v_{cs} \cdot e^{j(4\pi/3)} \tag{9.13}$$

where machine phase voltages can be derived in terms of inverter pole states as S_a, S_b and S_c.

$$\begin{aligned} \begin{bmatrix} v_{as} \\ v_{bs} \\ v_{cs} \end{bmatrix} &= \frac{1}{3} \begin{bmatrix} 2 & - & - \\ - & 2 & - \\ - & - & 2 \end{bmatrix} \begin{bmatrix} v_A \\ v_B \\ v_C \end{bmatrix} \\ &= u_{dc} \frac{1}{3} \begin{bmatrix} 2 & -1 & -1 \\ -1 & 2 & -1 \\ -1 & -1 & 2 \end{bmatrix} \begin{bmatrix} S_a \\ S_b \\ S_c \end{bmatrix} \end{aligned} \tag{9.14}$$

Depending upon the states of inverter legs, in total eight different machine phase voltage vectors can be derived, their magnitude as well as orientation forms a hexagonal voltage vector space which can be divided into six distinct sectors, referred as "active voltage vectors" as shown in Figure 9.3(b). Two voltage vector combinations result into zero voltage across machine phases and thus are located at the center.

Now, referring to equation (9.11), the incremental flux vector $\Delta\overline{\psi}_s$ can have six different orientations depending upon which inverter voltage vector has been applied.

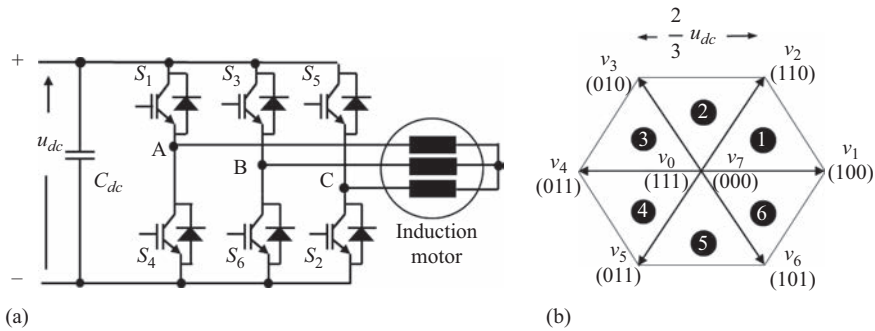


Figure 9.3 Two-level converter fed induction motor drive: (a) electrical schematic and (b) converter voltage vectors

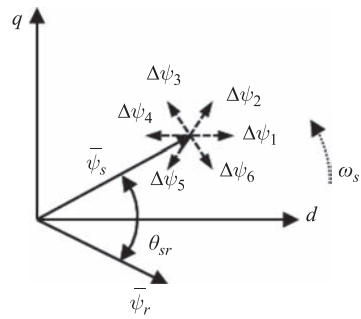


Figure 9.4 Stator flux movement direction on application of different inverter voltage vectors

Assuming that the current flux vector is located in sector 1, the six possible orientations of incremental flux $\Delta\overline{\psi}_s$ are shown in Figure 9.4.

The voltage vectors 1, 2 and 6 result in increase in flux magnitude while 3, 4 and 5 result in decrease in flux amplitude. Similarly, the incremental torque ΔT_e can be derived for all voltage vectors using equation (9.12). As a result, voltage vectors 2 and 3 result in positive torque increment while 5 and 6 result in negative torque increment. The effect of voltage vectors 1 and 4 on torque is dependent on if the voltage vector is lagging or leading the flux vector. The application of zero vectors does not change the flux orientation but results in decrease in torque due to advanced rotor flux during this time. In summary, each voltage vector has different impact on motor torque and stator flux which is also function location of the original stator flux vector. This analysis can be represented in more general form for any sextant k as shown in Table 9.1 for anticlockwise direction of rotation. However, the sextant definition is as shown in Figure 9.5, which is different from the sector designations used earlier in Figure 9.3.

Table 9.1 Effect of voltage vectors on stator flux and motor torque in sextant k

Voltage vector	v_k	v_{k+1}	v_{k+2}	v_{k+3}	v_{k+4}	v_{k+5}	v_z
Flux	↗↗	↗	↘	↘↘	↘	↗	0
Torque	?	↗	↗	?	↘	↘	↘

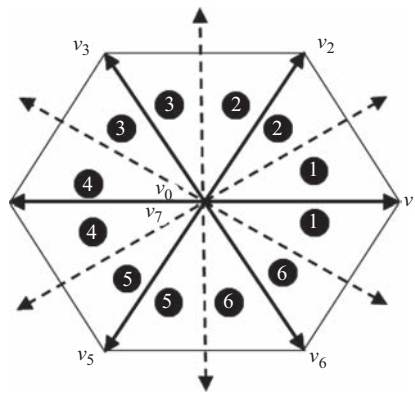


Figure 9.5 Sextant definition for two-level converter configuration

9.3 DTC control principle

The general control schematic of the DTC controller is described in Figure 9.6. It also represents a most likely structure of external speed and flux controller, which can be common to other control schemes also. The speed control loop consists of a PI type controller which generates appropriate torque reference signal T_e^* by comparing reference speed with actual speed. External control loop also consists of some form of flux controller which generates the flux reference signal depending upon operating conditions of the drive.

The main distinguishing feature of the DTC is the internal torque control loop, which consists main building blocks, namely flux comparator, torque comparator, optimal switching logic and a robust motor model. The measured or mostly estimated values of flux and torque in motor model are compared with their reference values in respective flux and torque comparators to generate flux and torque error. The torque and flux comparator process this error to derive flux/torque increase or decrease command. The optimal switching logic acts on these commands to directly generate switching signals S_a, S_b and S_c for the inverter legs. Operation of each of these blocks is explained in below subsection. DTC scheme does not need a complex coordinate transformation or decoupling of the nonlinear terms, which are

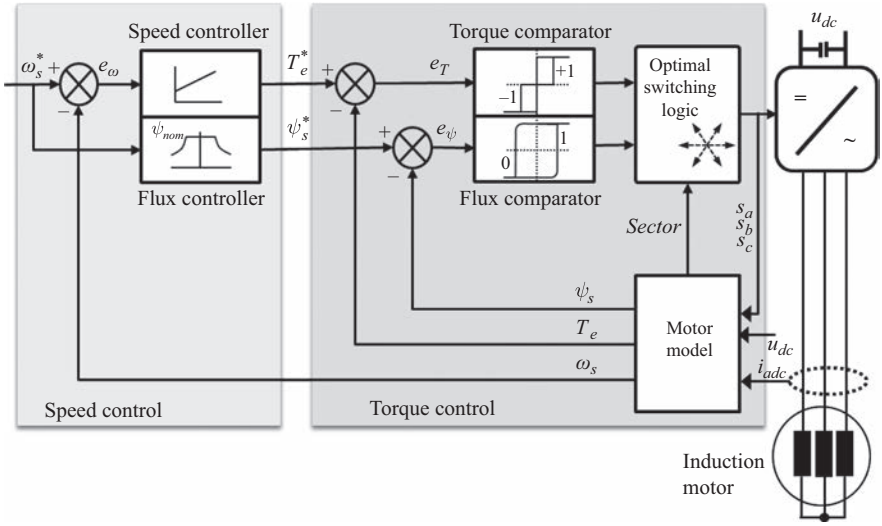


Figure 9.6 Block schematic of direct torque controller (DTC)

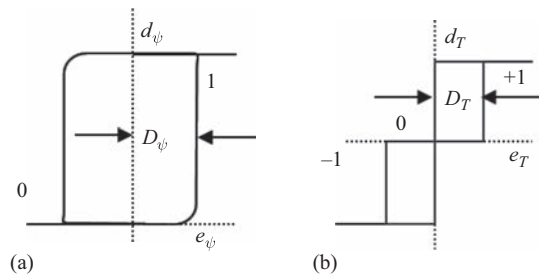


Figure 9.7 Flux and torque comparators

needed in traditional FOC structure. The flux and the torque are either measured or mostly estimated using an adaptive motor model.

9.3.1 Flux and torque comparator

The flux comparator is simple two-level hysteresis comparator, which generates the output d_ψ depending relation between flux error e_ψ and hysteresis band D_ψ. This can be mathematically represented as

$$\begin{aligned} d_\psi &= 1 \quad \text{if } e_\psi > D_\psi; \\ &= 0 \quad \text{if } e_\psi < -D_\psi \end{aligned} \tag{9.15}$$

where d_ψ value of 0 indicate that increase in flux is required, while 1 corresponds to decrease in flux value is required (Figure 9.7(a)).

Whereas the torque comparator is a three-level hysteresis (Figure 9.7(b)), the mathematical expression for torque comparator is

$$\begin{aligned}
&\text{if } e_T > 0,\\
&\{\\
&\quad \text{if } e_T > D_T,\ d_T = 1\\
&\qquad \text{else}, d_T = 0\\
&\}\\
&\text{else}\\
&\{\\
&\quad \text{if } e_T < -D_T,\ d_T = -1\\
&\qquad \text{else},\ d_T = 0\\
&\}
\end{aligned} \tag{9.16}$$

9.3.2 Optimum switching vector selection

The logical signals d_T and d_ψ are input to optimum selection logic, which analyzes the requirements on torque and flux changes and accordingly selects the inverter voltage vector, which will effect such change as per the analysis summarized in Table 9.1. The optimum vector selection logic is summarized in Table 9.2.

Thus, DTC block directly selects inverter voltage vector which satisfies the demands from external speed and flux controllers. The changes in the voltage vectors only occurs when either the flux or torque errors increase beyond the respective hysteresis bandwidths.

9.3.2.1 Treatment during starting up of the drive

During the starting of the drive, the initial flux in induction motor is zero. Thus, the drive needs to build the stator flux before it can generate any torque to accelerate

Table 9.2 Optimum voltage vector selection

		Sextant—k						***Effect***	
d_ψ	d_T	***1***	***2***	***3***	***4***	***5***	***6***	***Flux***	***Torque***
1	1	2	3	4	5	6	1	↗	↗
	0	0	7	0	7	0	7	↗	–
	−1	6	1	2	3	4	5	↗	↘
0	1	3	4	5	6	1	2	↘	↗
	0	7	0	7	0	7	0	↘	–
	−1	5	6	1	2	3	4	↘	↘

Table 9.3 Optimum voltage vector selection during starting up

		Sextant—k						***Effect***	
d_ψ	d_T	***1***	***2***	***3***	***4***	***5***	***6***	***Flux***	***Torque***
1	0	*1*	*2*	*3*	*4*	*5*	*6*	↗	–

the motor to the reference speed. In this situation ($d_T = 0$ and $d_\psi = 1$), the second row which only consists of zero vectors cannot be used and active vectors which can build stator flux at maximum rate must be switched. These are nothing but the active vector central to each sextant. The second row in Table 9.1 is replaced with active vectors encompassing respective sextants during this situation (Table 9.3).

9.3.3 Motor model

The adaptive motor model forms the core of the DTC architecture, its main function is to compute and feedback the actual values of control variables to the DTC controller. The most general form of the motor model estimates the motor torque, stator flux and sextant information from the measured motor current, dc link voltage and the switching vector information. Since the DTC controller directly works in stationary reference frame, the flux determination is done by integrating the stator voltage by neglecting stator resistance drop. This assumption produces errors during low speed or starting up condition, when the stator voltage drop is significantly comparable to applied voltage. Along with the stator flux and torque estimation, the motor model also gives the stator flux sextant information which is required for correct selection of switching vectors in switching tables. The overview of different types of estimators is separately discussed in next section.

Figure 9.8 shows the typical stator flux movement in first quadrant. When the hysteresis band is larger, as shown by dashed circles in Figure 9.8(a), the flux vector undergoes lesser changes resulting into lower switching frequency. But when the flux hysteresis band is lowered, the flux vector undergoes larger amount of switching transitions as shown in Figure 9.8(b). The other aspect of DTC is that the switching frequency is not constant, and it varies within a frequency interval. In one way, this is good since it can dampen particular frequencies causing quieter drive operation. Figure 9.8 also shows the movement of rotor flux vector, which is much smoother as compared to stator flux vector, due to the transient time constant as described in (9.9).

The further improvements in the DTC are proposed to improve torque ripple, estimation of feedback variables, constant switching frequency operation, etc. Still the core of its operation is still same “classical DTC” with flux and torque comparators as described above.

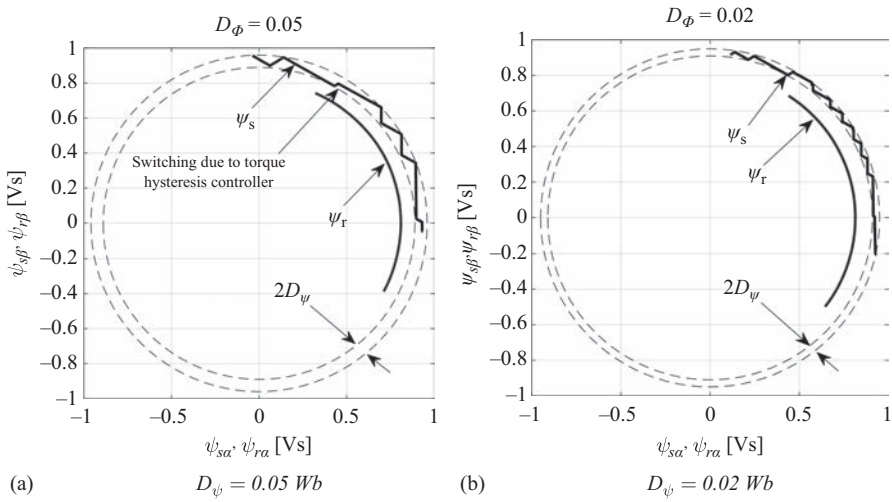


Figure 9.8 Stator and rotor flux vector trajectory

9.4 Flux estimation approaches

This section describes operating principles of some of the widely used flux estimation techniques. Since DTC controller directly controls machine stator flux and torque without any need of coordinate transformation, it is straightforward to estimate the control variables in stationary reference frame. The easiest method is directly integrating the stator voltage equation (9.1) to obtain the stator flux vector. The flux estimator based on this principle is referred as *stator-model-based* or *voltage-model-based* estimators in literature.

$$\overline{\psi}_s = \int (\overline{u}_s - \overline{i}_s r_s) dt \tag{9.17}$$

Although the concept is very simple, the practical implementation is very difficult to obtain accurate integral of voltage terms due to inaccuracies like dc drifts and noise introduced by current, voltage sensing circuits, stator winding resistance variation owing to temperature changes, discrete domain implementation of integration, etc. At low frequencies, the voltage drop in power electronics switches is also significant which must be taken into consideration while designing the flux estimator. This section describes some practical techniques to overcome some of the above issues associated with flux estimation.

9.4.1 Use of low-pass filters

The simplest approach is to replace the perfect integrators in (9.17) with low-pass filter to overcome problem of dc drift and initial value setting of pure integrators (Figure 9.9).

$$\widehat{\psi}_s = \frac{1}{s + \omega_{lp}} (\overline{u}_s - \overline{i}_s r_s) \tag{9.18}$$

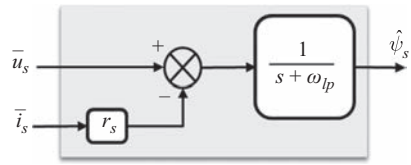


Figure 9.9 Open-loop flux estimation with low-pass filters

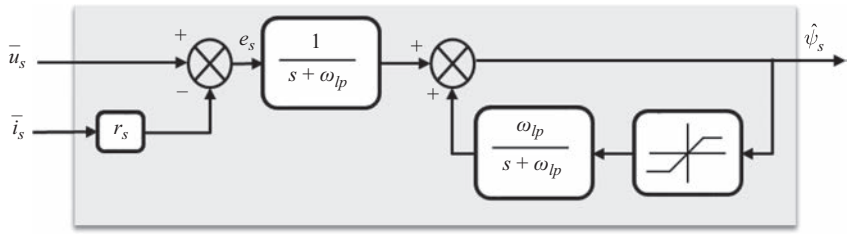


Figure 9.10 Flux estimation with saturable feedback

where ω_{lp} is chosen suitably to provide low cutoff frequency which does not affect the integration in wide speed range.

The low-pass filter functions as pure integrator for frequencies above corner frequency of filter. But at lower than corner frequencies, this approach introduces magnitude and phase errors. Thus, stable operation depends on correct choice of corner frequency of low-pass filter. Also, due to open-loop structure, it is susceptible to drift problems unless suitable closed loop compensation is used.

9.4.2 Flux estimation with feedback

Further improvement has been proposed as shown in Figure 9.10, and its mathematical expression can be represented as

$$\begin{aligned} \widehat{\psi}_s &= \frac{1}{s+\omega_{lp}} e_s + \frac{\omega_{lp}}{s+\omega_{lp}} \widehat{\psi}_s \\ e_s &= (\overline{u}_s - \overline{i}_s r_s) \end{aligned} \tag{9.19}$$

The first term is as before in (9.17), which represents low-pass filter implementation of the original integral term with the corner frequency of ω_{lp}. The second term acts as compensation for the errors introduced by the nonideal implementation of the integrator action. For stator frequencies higher than corner frequency, the gain of the feedback block is almost zero, and thus, the estimator functions as simple low-pass filter as before. But for stator frequencies below corner frequency, the feedback block acts in such a way that the integrator will not be driven into saturation with correct setting of the saturation block in feedback path. With the setting adjusted to the actual flux amplitude, the estimated flux is adjusted up or

down to either positive or negative value of actual flux due to the dc bias present in the input. Essentially, the dc bias in the output is removed much faster than the open-loop estimator. The flux estimator is thus immune to the dc drift or saturation problems. The correct level of flux in saturation block is essential for its correct operation.

In another approach as shown in Figure 9.11, the difficulty of correctly setting the saturation limit is overcome by transforming the estimated flux into polar form to obtain its magnitude and angle information. Then magnitude feedback is then limited to reference flux before converting back into Cartesian format and fed back as compensation. The distortion due to saturation block in Figure 9.10 is eliminated. The algorithm still suffers from the problem of setting right saturation level in amplitude limiter. The algorithm is suitable where the motor flux is rather fixed to nominal flux during motor operation.

Another improvement to flux estimator, making it suitable for variable flux operation, is shown in Figure 9.12. The flux estimator relies on the principle of orthogonality between stator flux and back EMF. A compensation signal $\widehat{\psi}_c$ is

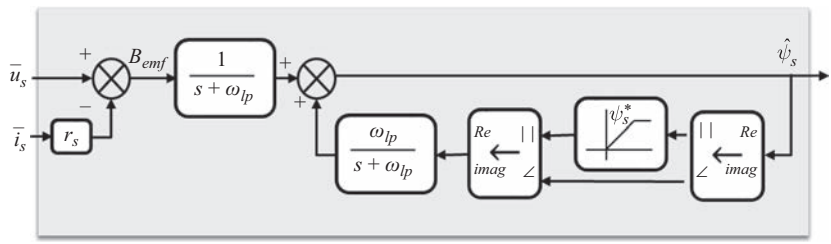


Figure 9.11 Flux estimation using modified amplitude limiter

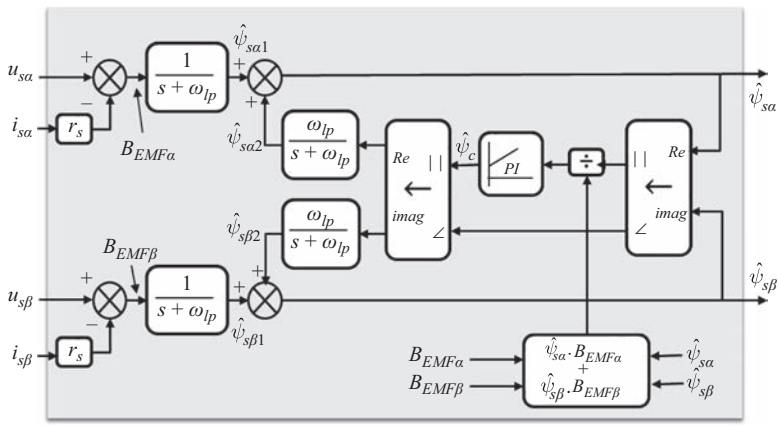


Figure 9.12 Flux estimator based on orthogonality of stator back EMF and flux [7]

generated using a quadrature detector wherein it consists or scalar product calculator followed by a PI regulator. The output of PI regulator can be described as

$$\widehat{\psi}_c = \left(k_p + \frac{k_i}{s}\right)\left(\frac{\widehat{\psi}_{s\alpha} \cdot B_{EMF\alpha} + \widehat{\psi}_{s\beta} \cdot B_{EMF\beta}}{|\widehat{\psi}_s|}\right) \tag{9.20}$$

Ideally when the ideal conditions prevail, there is orthogonal relationship between back EMF and stator flux, and the output input to PI regulator is zero. This condition is lost due to improper initial values or dc bias in input signals to estimator. The PI regulator generates an output $\widehat{\psi}_c$ such that the estimated flux moves toward its actual value. The estimator block easily overcomes the problem of earlier propositions and adequately tracks the varying input flux conditions. Still, the flux estimator suffers from two major drawbacks. First, the PI controller tuning affects the speed and accuracy with which the flux estimator adapts to varying flux conditions. Second, due to the presence of absolute flux in the denominator of the scalar product, the estimator shows instability at zero flux levels and shall be supplemented with limits on lower values of absolute minimum values in the denominator.

Another simplified flux estimator is proposed in [8] which is based on the theoretical analysis presented in [9]. The estimation procedure is based on the principle that the scalar product between estimated value of stator flux and stator current along with direction of change of estimated stator flux can be used to derive a correction signal to be used as compensation signal similar to the flux estimators described above. A modification to the original scheme is suggested in [8] to use scalar product of back EMF and estimated flux, thus revealing similar scheme as in Figure 9.12. The schematic of the flux estimator based on this principle is shown in Figure 9.13.

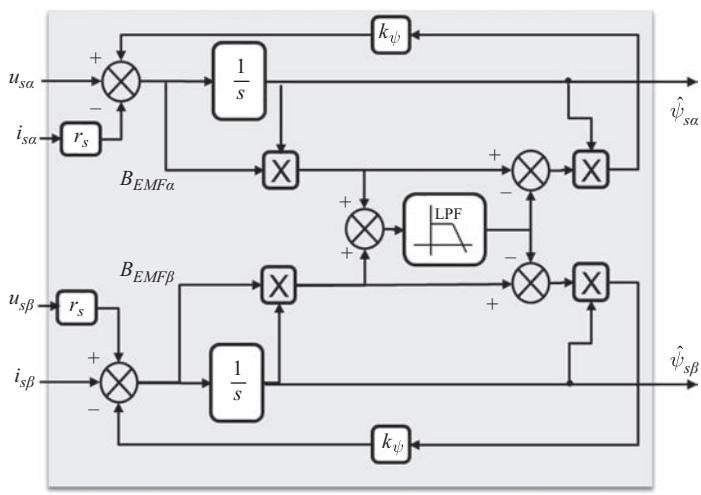


Figure 9.13 Stator flux estimation based on scalar product correction method [8]

The scalar product is high-pass filtered revealing the derivative of the back EMF–flux product which is then fed back to the inputs of back EMF calculation through a gain coefficient k_ψ. The flux estimator is simpler as compared to the one presented in Figure 9.12. Still the correct feedback gain need to be evaluated by trials.

The only machine parameter required in the estimator is stator resistance r_s. The winding resistance is not constant but varies with temperature. The resistance value affects signal $\bar{i}_s r_s$ entering at the input of low-pass filter. When the magnitude of applied voltage very low, which is the case at lower speeds, the error in stator resistance creates significant error in the flux estimation. Thus, although simple, accurate and robust at higher stator frequency, the voltage-model-based flux estimators suffer due to two main problems: the integration problem at low frequencies and sensitivity to stator resistance variation.

9.4.3 *Application of hybrid flux estimators*

Another class of flux estimators makes use of "current model," which is mostly used in indirect rotor FOC schemes. One possible application of this principle which does not rely on the rotor speed feedback is shown in Figure 9.14. The estimator is based on stator flux estimation using "voltage model," which is described earlier and deriving a compensation term using another rotor flux observer operating in rotating coordinates [11]. The advantages of such schemes are that the current model is helpful in assisting the voltage model at low or zero frequencies since it is independent operating frequency. While, at higher stator frequency, the voltage-model-based flux estimation has required accuracy [12]. The compensation signal is generated based on stator flux generated from both models which in turn generates the rotor flux angle for correct transformation between stationary and rotating reference frames for current model. The only drawback of this model is now the stability of the estimator is also dependent on rotor time constant, thus making it susceptible to changes in rotor resistance and inductance parameters. Also there can be several derivatives of flux estimators based on this

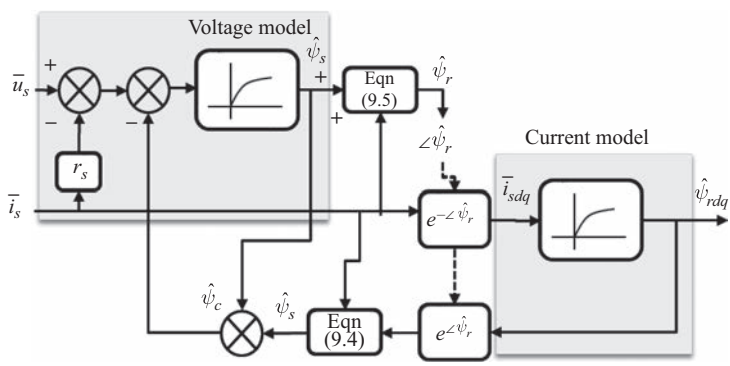


Figure 9.14 Flux vector observer based on voltage model compensated by current model [11]

principle. Simple and robust estimators are possible if the rotor speed is known but then the speed sensorless operation characteristics of DTC drive is lost.

9.4.4 Other methods for estimation of stator flux

The machine flux can also be estimated using full order or reduced order observers. The flux observers work on comparison of the machine input–output relationship with the model of the machine to generate a correction signal. The correction mechanism is used to tune the model of the system such that the model output follows the actual outputs of the drive.

The basic principle of stator observers is shown in Figure 9.15. For the given plant or process characterized by system states x, input u and output y, the plant dynamics can be expressed as

$$\begin{aligned} \dot{x} &= F\,x + G\,u \\ y &= H\,x \end{aligned} \tag{9.21}$$

The full order model of the plant can be constructed, having similar behavior as plant itself.

$$\begin{aligned} \dot{\hat{x}} &= F\,\hat{x} + G\,u \\ \hat{y} &= H\,\hat{x} \end{aligned} \tag{9.22}$$

Then the state observer can be constructed using the outputs from plant and plant model such that the corrected model of the plant can be described as

$$\dot{\hat{x}} = F\,\hat{x} + G\,u + L(y - H\,\hat{x}) \tag{9.23}$$

This is the most common form of the state observer. The feedback gain L is designed such that the required dynamics of the system is achieved.

The states of the systems combinations of stator and rotor flux or current quantities depending upon how the motor model is defined. Due to direct relationship between machine flux and current variables, it is possible to describe

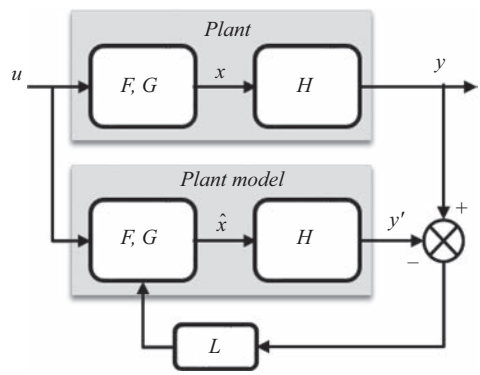


Figure 9.15 Principle of state observers

machine dynamics in terms of stator and rotor fluxes, or stator currents and rotor flux, which is more common in indirect rotor flux-oriented vector control schemes or in terms of stator flux and stator currents which is easier to use for DTC control purposes [10]. Use of stator flux $\overline{\psi}_s$ and stator currents $\bar{i}_s$ as observer's states lets us to obtain the compensation signal by direct comparison with measured stator currents (Figure 9.16) [10].

$$\begin{aligned} \frac{d\overline{\psi}_s}{dt} &= -j\omega_k\overline{\psi}_s - \mathrm{r}_s\bar{i}_s + \overline{u}_s \\ \bar{i}_s + \tau'_{sr}.\frac{d\bar{i}_s}{dt} &= -j(\omega_k - \omega)\tau'_{sr}\bar{i}_s + \frac{1}{r_{sr}}\left(\frac{1}{\tau_r} - j\omega\right)\overline{\psi}_s + \frac{1}{r_{sr}}\overline{u}_s \end{aligned} \tag{9.24}$$

The coefficients of (9.23) can be obtained from machine parameters. The design of observer follows the control system theory where the observer poles are more chosen to be more dynamic without causing any undesirable instability, irrespective of operating speed. Due to closed loop structure, flux observers exhibit robustness to machine parameter variations. The errors caused by drift in actual parameters can be easily compensated by the closed loop structure of observer.

Other forms of flux observers include more robust Kalman or extended Kalman filters which eliminate the need of knowing rotor speed and even it is possible to include machine parameter estimation as a part of observer block. The other topics related to flux estimation like model reference adaptive systems are covered in FOC section of the book and will not be discussed here.

9.4.5 Speed-sensorless operation

One of the main requirements of the motor drives nowadays is to eliminate the need of speed or position sensor. The FOC, which is performed in rotating

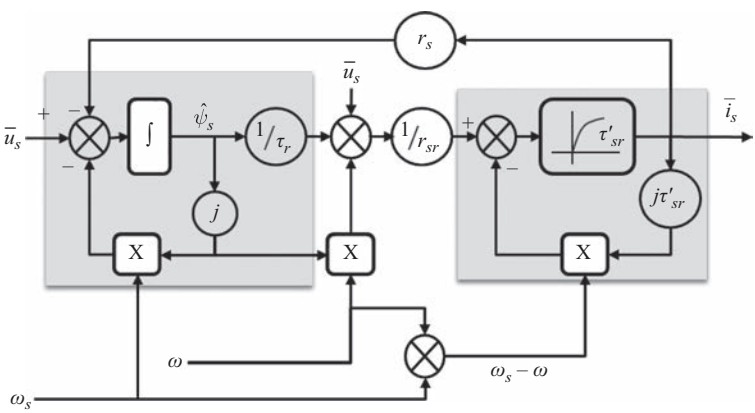


Figure 9.16 Machine representation in terms of $\overline{\psi}_s$ and $\bar{i}_s$ as system states [10]

coordinate system, requires rotor angle information for transformation from stationary to rotating reference frame, which necessitates the use of speed sensor or speed estimation algorithms to make the control scheme sensorless. But DTC scheme is inherently sensorless since it does not involve coordinate transformations. It is thus possible to obtain simple control structure as compared to FOC, unless the flux estimation involves the information about rotor speed. In such situations, the various approaches which have been devised for estimation of speed or position can be equally applied to DTC control methods. These techniques have been well researched in literature in connection with FOC and good summary can be found in [13].

9.5 Simulation of DTC control

An induction motor drive is simulated in MATLAB®/Simulink® simulation environment using Simscape™ Power Systems™ blockset. The specialized toolbox provides component libraries for modeling and simulating electrical power systems, including three-phase machines, electric drives and basic power system components. This eases the task of building the simulation model for electric drives using inbuilt component libraries as well as control component libraries. The induction motor used in simulation is a 15-kW, 1,485-rpm induction motor. The ratings and parameters of induction motor are given in Table 9.4.

The schematic of the simulation model is shown in Figure 9.17. The simulation is performed for analyzing system behavior to step input of speed reference at 0.05 s and nominal torque command is applied at 0.3 s and again removed at 0.5 s. The simulation results presented in Figure 9.18 corresponds to hysteresis band amplitude $D_\psi = 0.05$. Figure 9.18(d) shows the flux vector movement during the interval when the torque step is applied ($t = 0.29$–0.32 s). The same simulation is again performed with $D_\psi = 0.02$, and results are presented in Figure 9.19, where the flux ripple is significantly lower as compared to earlier simulation with larger hysteresis bandwidth (Figure 9.18(b)). Nevertheless, the rotor flux ψ_r in Figures 9.18 and 9.19 is much smoother as described earlier.

Table 9.4 Induction motor rating and parameters

Rating		Parameters	
Nominal power (kW)	15	Stator resistance (Ω)	0.2147
Nominal voltage (V)	400	Stator leakage reactance (Ω)	1.09
Nominal current (A)	28.8	Magnetizing inductance (mH)	64.19
Nominal pf	0.85	Rotor resistance (Ω)	0.2205
Nominal speed	1,485	Rotor leakage reactance (mH)	1.09
Nominal torque (N m)	97.2	Moment of inertia (kg m^2)	0.102
Nominal frequency (Hz)	50	Friction factor (N m s)	0.00951

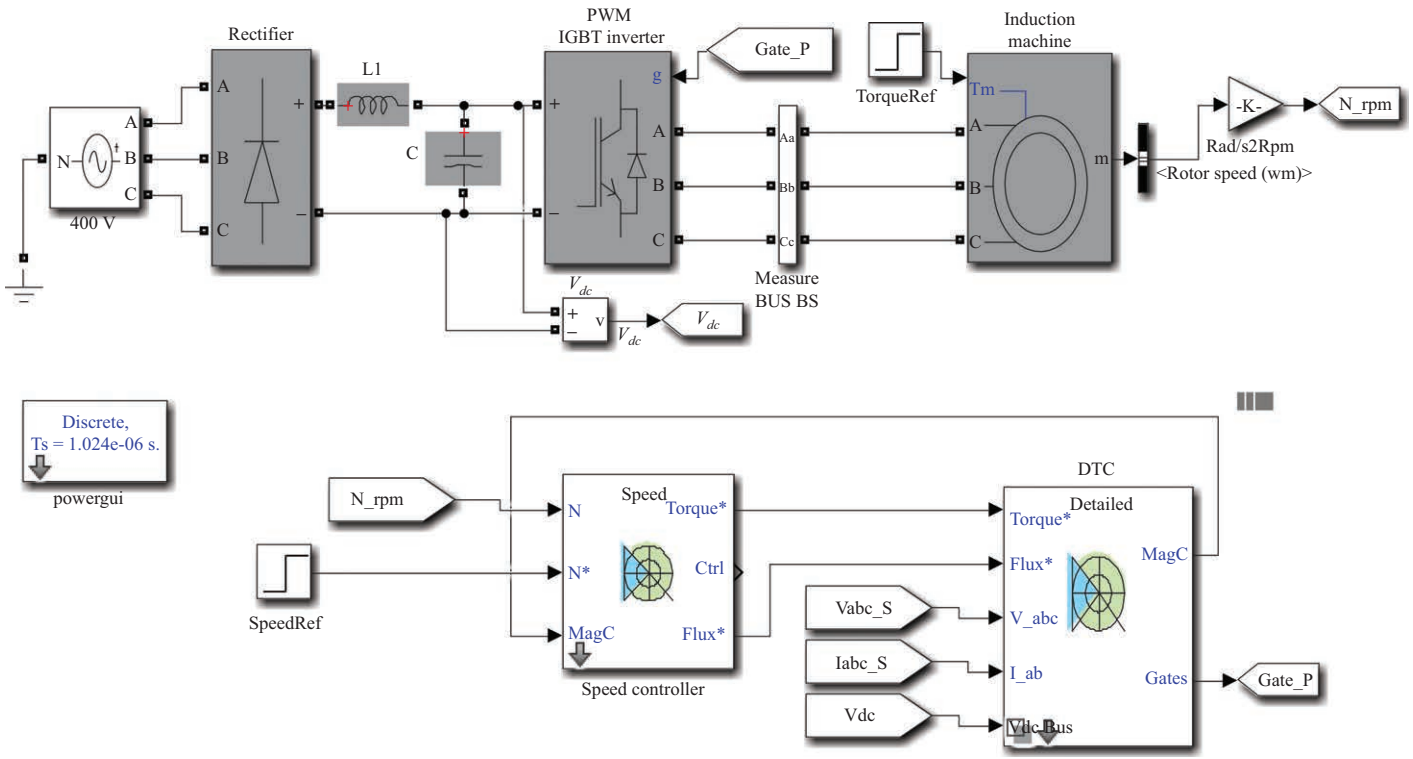


Figure 9.17 Simulink model of induction motor drive using DTC controller

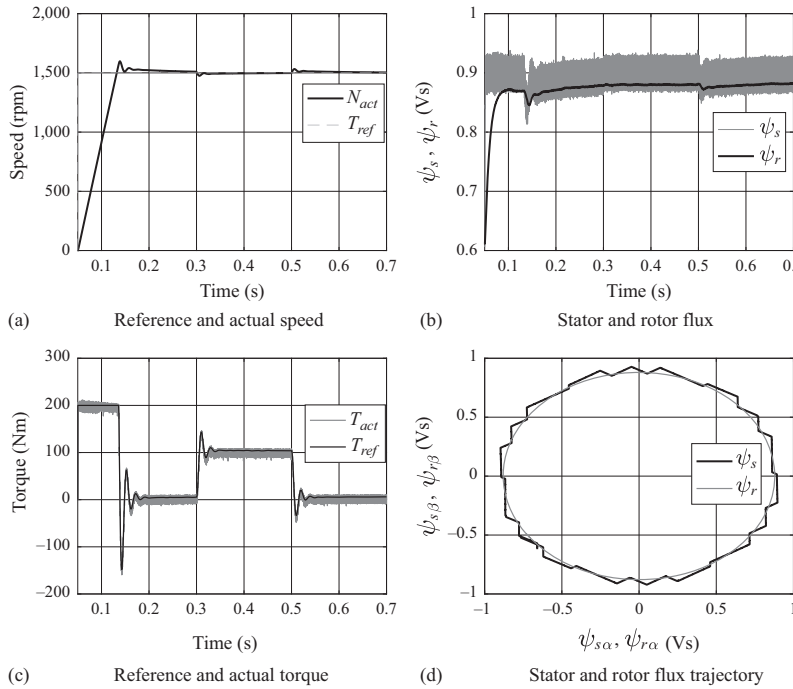


Figure 9.18 Simulation response of DTC controller, $D_\psi = 0.05$

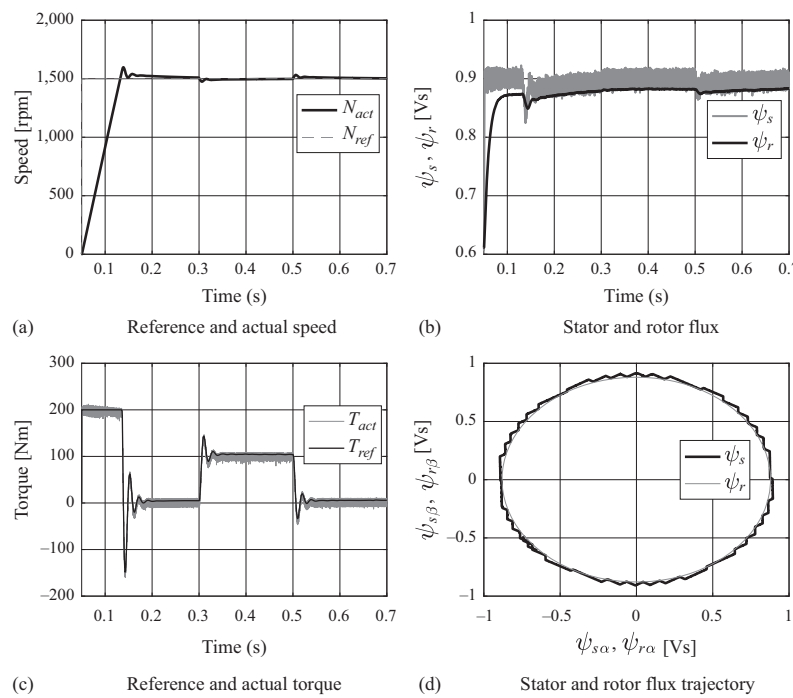


Figure 9.19 Simulation response of DTC controller, $D_\psi = 0.02$

9.6 Performance enhancement of classical DTC scheme

The distinctive advantage of DTC scheme is high dynamic performance as compared to the FOC schemes. The absence of coordinate transformations as well as PI regulators results in superior torque dynamic. The control implementation does not need any voltage modulator making the implementation much simpler than field oriented controllers.

Apart from these benefits, the classical DTC also presents some shortfalls. The drive can exhibit problems during startup when the motor flux is absent and need to be handled with substitution of zero voltage vectors as described earlier. The major limitation is variable the switching frequency and inherent torque and flux ripple. There has been research into overcoming some of these limitations and improve the performance of classical DTC scheme. This section presents an overview of these techniques and compares its performance with classical DTC.

9.6.1 Reduction in torque and flux ripple using alternate switching tables

A straightforward approach to reduce the torque and flux ripple is to reduce the hysteresis bands, but this will eventually lead to increase in switching frequency leading to increase in switching losses of the power devices. So, there must be a compromise made between the allowed torque ripple and maximum allowable switching frequency. The lower limit of the hysteresis bands also comes from the cycle times possible with microcontrollers since they must be able to respond and detect any violations in the hysteresis bands. Alternate strategies involve redesigning the switching tables by re-sorting the voltage vectors which apply short or large torque or flux changes by using multilevel comparators. Another variation in the switching tables can be brought using alternate definitions of sextants as shown in Figure 9.20.

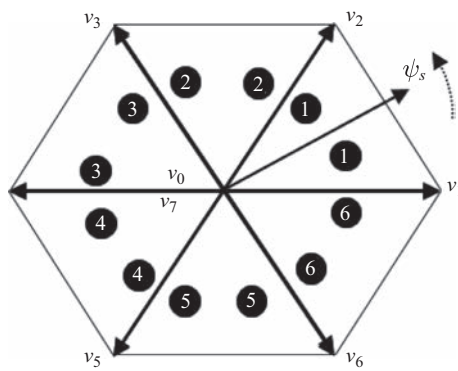


Figure 9.20 Sextant definition for two-level converter configuration

In this case, the effect of voltage vectors v_{k+2} and v_{k+5} on flux amplitude is unknown while the impact on torque changes is evident as summarized in Table 9.5. The other vectors v_k, v_{k+1}, v_{k+3} and v_{k+4} can be used to for different combinations of flux and torque errors in this sextant. A new switching table with modified vectors based on above observation can be described together with new sextant definition. A new set of switching vectors, as shown in Table 9.6, can be built together with new sextant definition based on above observation.

In the above schemes, the impact of v_{k+2} and v_{k+5} on flux amplitude is unknown, whereas in classical DTC, there are always two voltage vectors of v_k and v_{k+3} whose impact on torque amplitude is not known. It is possible to combine these facts to devise a 12-sector strategy as shown in Figure 9.21.

It can be seen that the impact of voltage vectors adjacent to the particular sector is rather lower compared to other voltage vectors. This makes it possible to define voltage vectors having small impact on torque and lead to definition of multiple-band hysteresis for torque comparators. A new set of switching table, as shown in Table 9.7, can be constructed based on above two observations. Here $+\delta T$ and $-\delta T$ indicate small torque change for which the hysteresis band can be chosen suitably.

Table 9.5 Effect of voltage vectors on stator flux and motor torque in sextant k

Voltage vector	v_k	v_{k+1}	v_{k+2}	v_{k+3}	v_{k+4}	v_{k+5}	v_z
Flux	↗	↗	?	↘	↘	?	0
Torque	↘	↗	↗	↗	↘	↘	↘

Table 9.6 Optimum voltage vector selection with modified sextant definition

		Sextant—k						***Effect***	
d_ψ	d_T	***1***	***2***	***3***	***4***	***5***	***6***	***Flux***	***Torque***
1	1	2	3	4	5	6	1	↗	↗
	0	0	7	0	7	0	7	↗	–
	−1	1	2	3	4	5	6	↗	↘
0	1	4	5	6	1	2	3	↘	↗
	0	7	0	7	0	7	0	↘	–
	−1	5	6	1	2	3	4	↘	↘

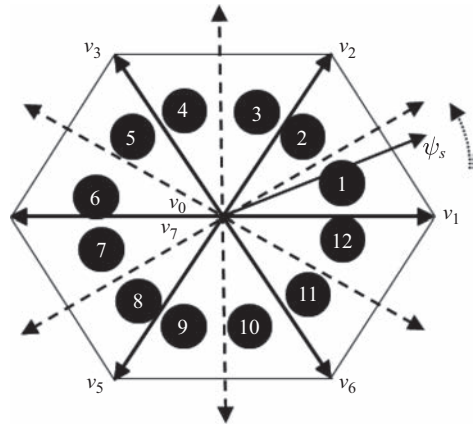


Figure 9.21 Modified DTC with 12 sextant definition

Table 9.7 Optimum voltage vector selection with modified sextant definition

		Sextant—k											
d_ψ	d_T	***1***	***2***	***3***	***4***	***5***	***6***	***7***	***8***	***9***	***10***	***11***	***12***
1	1	2	3	3	4	4	5	5	6	6	1	1	2
	$+\delta T$	2	2	3	3	4	4	5	5	6	6	1	1
	$-\delta T$	1	1	2	2	3	3	4	4	5	5	6	6
	-1	6	1	1	2	2	3	3	4	4	5	5	6
0	1	3	4	4	5	5	6	6	1	1	2	2	3
	$+\delta T$	4	4	5	5	6	6	1	1	2	2	3	3
	$-\delta T$	7	5	0	6	7	1	0	2	7	3	0	4
	-1	5	6	6	1	1	2	2	3	3	4	4	5

9.6.2 DTC-SVM control [11]

Lascu proposed improvement to the classical DTC to overcome the problem of flux and torque ripple with a new type of control structure. This scheme is named as DTC-SVM as it realizes torque and flux comparators combined with SVM. The proposed scheme uses the flux and torque comparators as in classical DTC, but its output is fed to fixed switching frequency PWM modulator for generation of switching vectors. Thus, this strategy exhibits advantages of both DTC control in maintaining fast-torque dynamics and low-torque ripple due to constant switching frequency PWM modulator. The proposed scheme utilizes the flux estimator described in Figure 9.14 and an model reference adaptive control (MRAC) structure for estimation of rotor speed. Unlike the classical DTC

scheme that uses switching tables, the DTC-SVM contains two PI controllers for flux and torque control. The output from flux and torque regulators are $d-q$ voltage reference signals to space vector modulator. The proposed scheme can result into much lower torque and thus current ripple, which can also improve the flux, torque and speed estimator performance (Figure 9.22).

The performance of DTC-SVM can be compared with the classical DTC in simulation model described earlier in Figure 9.17. The simulation results with SVM-DTC controller are presented in Figures 9.23 and 9.24 for 3 and 8 kHz, respectively. The stator flux vector trajectory is much smoother compared to the response with classical DTC. It becomes even smoother with higher switching frequency, which can be only limited by microcontroller cycle time capability and switching losses of power converter. At 8-kHz switching frequency, both stator flux vector and rotor flux vector are sinusoidal.

9.6.3 Predictive torque control

The predictive control schemes work on principle of predicting the future direction of movement of system variables using appropriate system model and analyzing the impact of the all available switching voltage vectors on the course of system behavior. The impact of each voltage vector is evaluated and compared using cost function, and the best voltage vector that minimizes the future states is selected for next switching interval [14]. The basic control structure is shown in Figure 9.25 which consists of motor model for estimation of motor variables, prediction model and cost-function-based optimizer, which optimizes the control variables but directly generating suitable switching commands to the inverter. The main

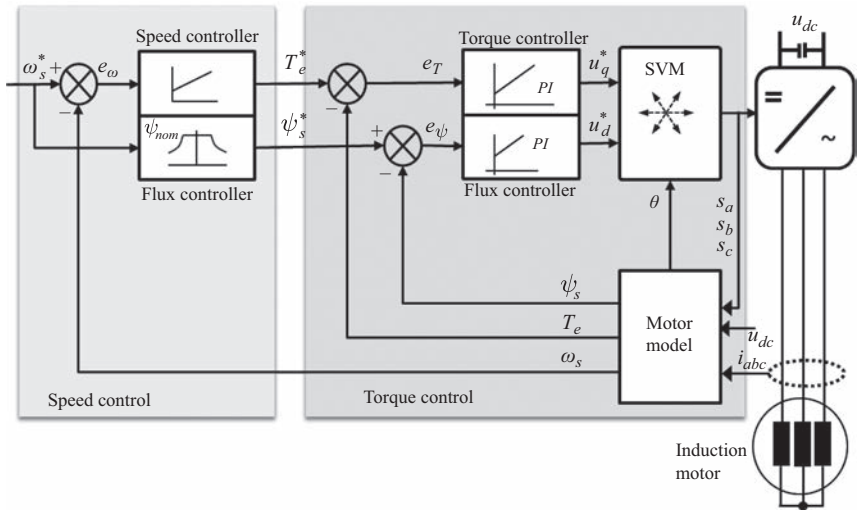


Figure 9.22 Block schematic of DTC-SVM

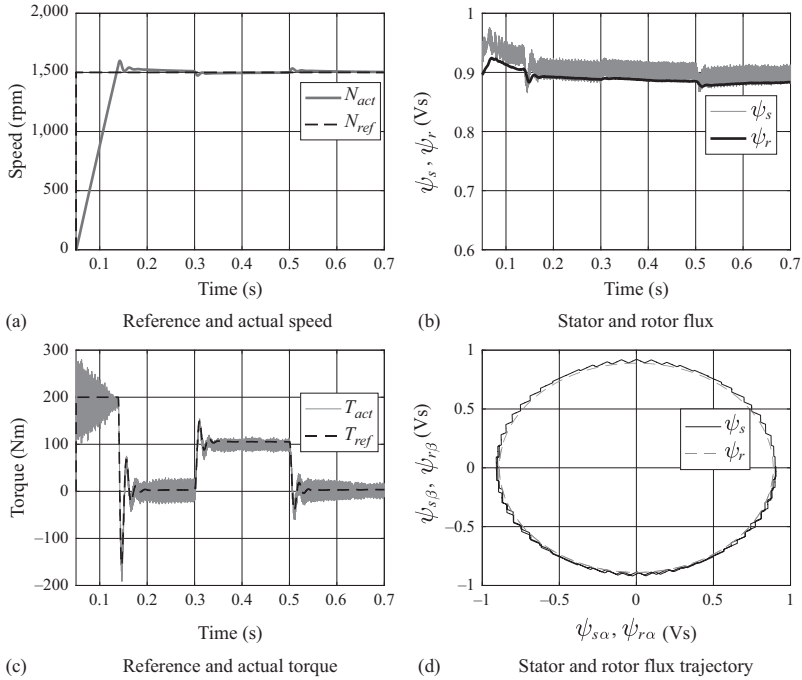


Figure 9.23 Simulation response of DTC-SVM controller, $F_{sw} = 3$ kHz

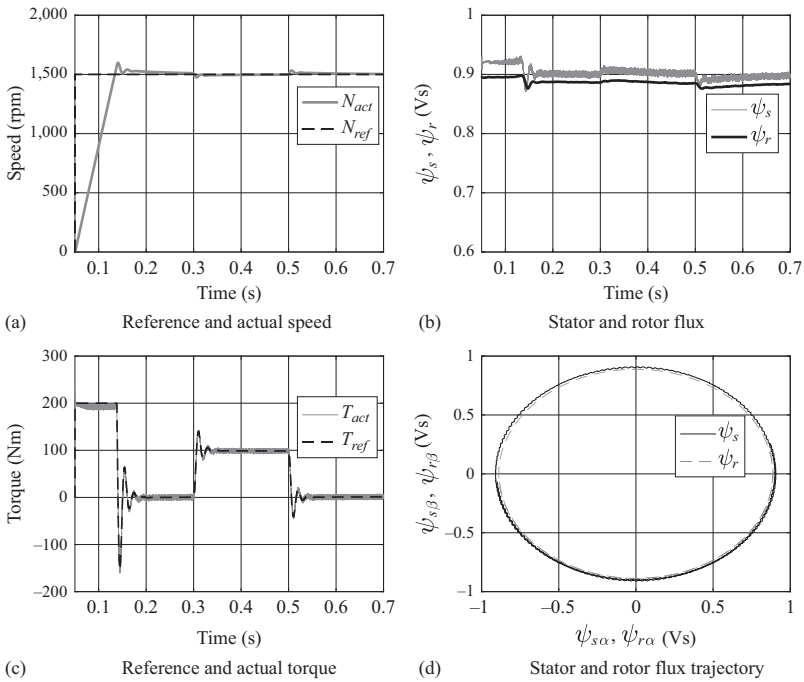


Figure 9.24 Simulation response of DTC-SVM controller, $F_{sw} = 8$ kHz

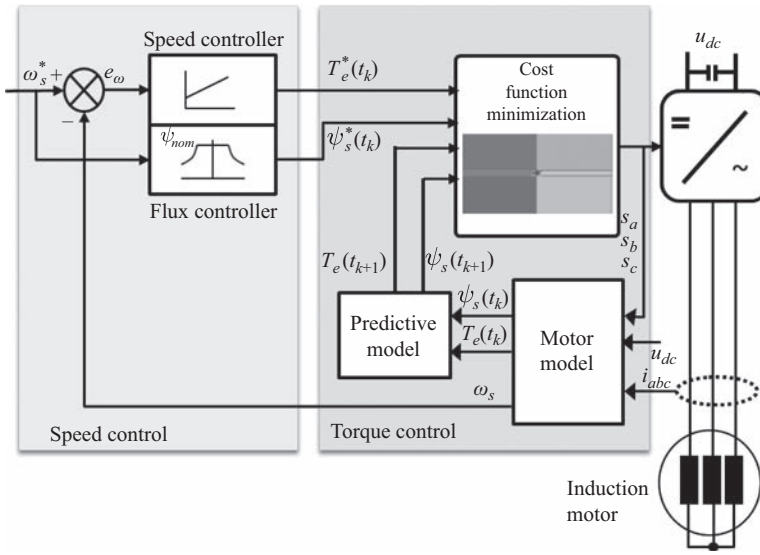


Figure 9.25 Block schematic of model predictive torque control of induction motor

variation comes from the prediction model which can predict the behavior of the system in next switching intervals, and it has major influence on the overall system complexity and computational needs for evaluation of the available switching states. Still, there have been interesting attempts in literature to implement the predictive DTC in simpler way than DTC schemes and having better performance compared to classical DTC schemes [14].

The major drawbacks of such schemes are computation efforts as predictive DTC schemes must compute the cost function for every switching state possibility for each time step. The simpler applications are when the converter in question is only two-level converter, in which it is only seven different vectors for which the computations need to be performed. But the increase in computation efforts for multilevel converters is exponential and thus impractical from implementation point of view. In such situation, the computational efforts can be greatly reduced if the computations can be performed for only selected switching combinations [14].

The computational efforts also increase exponentially when the prediction horizon (number of future predictions) or control horizon (number of future switching steps) is larger than 1 and in such situations also zoning algorithms like branch and bound schemes, which can filter the number of switching states for cost function evaluation, have been proposed for successful implementation of predictive DTC schemes.

9.7 Direct torque control of synchronous motors

DTC operates on direct control of stator flux with the feedback parameters determined from monitoring stator voltage and current quantities. As there is not much dependence on rotor variables, unless the stator variables estimator need it, the DTC strategy can be easily extended to other motor types like permanent magnet synchronous motors (PMSM) (permanent magnet, synchronous reluctance, field wound) as well as switched reluctance motors [15]. The initial attempts were already reported in 1990 [16,17], and several adaptations were reported later to extend the developments in DTC-IM field to PM motors. Still, there are some distinct differences when it comes to DTC of PM motors. First, since there is always existence of magnet flux, there is no need of starting flux buildup, which makes the DTC implementation easier as compared to induction motors. In principle, all types of DTC schemes—classical DTC, SVM-DTC or predictive DTC—have been successfully applied to permanent magnet motor and synchronous reluctance motors (SynRMs).

The classical DTC scheme is implemented for surface-mounted PMSM in [18], it basically utilizes same switching tables as used for induction motor. The fixed-frequency (SVM-based) DTC schemes have been also proposed for PMs. These schemes are based on the model of PMSM which is used to calculate most suitable voltage vector during next switching interval, which is then realized by using space vector PWM. There have been many proposals on how to calculate the most appropriate voltage vector depending upon depth of model and computational complexity of PMSM [19,20]. Again, the model of the PMSM is successfully used to determine the torque trajectory during the next switching interval and an optimal voltage vector can be evaluated which can keep this trajectory under the required bound. A predictive-type controller is proposed, based on this principle in [21] for PMSM. Optimization of flux and torque ripple has been considered in DTC for PMSM [22]. It is possible to predict the time interval by which the flux vector will reach the hysteresis boundary. This is mainly determined by the initial amplitude of flux vector, applied voltage vector amplitude. If the sampling interval is larger this time interval, the flux vector would have already gone outside the hysteresis bound when the next sample is taken. To avoid this, the voltage vector can be switched only for time duration by which flux vector will reach the hysteresis boundary, followed by another vector which turns flux vector in opposite direction. Such duty-cycle-based approach can result into much lower torque ripple than the classical DTC [23].

9.8 Industrial adaptation of DTC schemes

The first commercial drive ACS600 based on speed sensorless DTC principle was introduced by ABB for low-voltage industrial applications in 200–690 V range. The product offering was intended for demanding torque applications like servo drives as well as general purpose industrial applications like pumps, fans conveyors, compressors, etc. The drive offered advantages to the customer by removing the necessity of speed tachometer or encoder. The block schematic of the ABB DTC

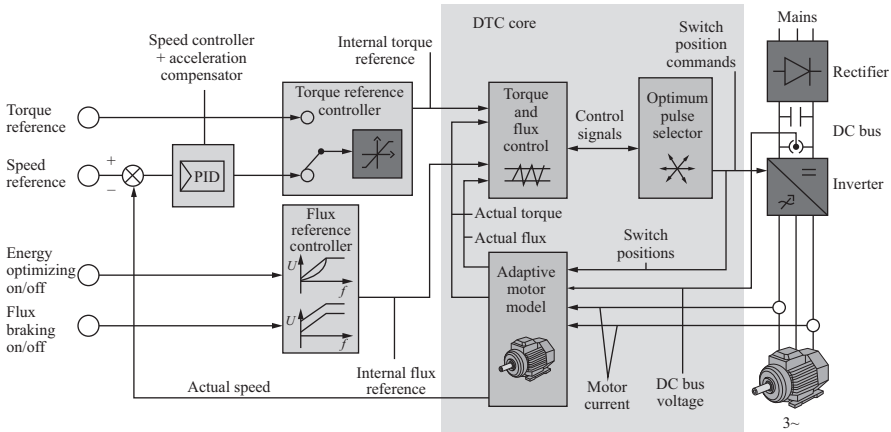


Figure 9.26 DTC control structure in ABB ACS850 drive [8] [Reproduced: courtesy ABB]

control being executed at cycle time of 25 ms is shown in Figure 9.26; the control structure is very similar to the back schematic introduced in Figure 9.6, which directly controls stator flux and developed torque. The drive consists of current sensors in two phases, dc link bus voltage sensor and together with the switching states, the other motor variables are estimated in the adaptive motor model. The voltage drops in semiconductor switches and dead time effects have been adapted into the motor model for accurate estimation of motor variable during operating conditions, especially at low stator frequencies. The claimed torque response is 1–2 ms below 40 Hz compared to 10–20 ms for vector controlled drives. The claimed steady-state speed accuracy be in the range of 10% of motor slip frequency, which comes to 0.1%–0.3% for drive ratings over wide power range. The drive can still supply 100% torque under these operating conditions. Thus, right from its introduction, ABB drive has been proven superior for fastest torque response over wider frequency range, torque linearity which is essential for precision speed applications and dynamic speed accuracy for highly dynamic torque applications.

The recently launched newer generation of ABB drives called ACS880 drives (Figure 9.27) are enhanced with many advancements, which makes it suitable for variety of applications which were not covered by earlier series of ABB drives. The newer digital signal processor (DSP) hardware and improved software architecture has made it possible to achieve shorter execution times of complex control algorithms, adaptive motor models as well as online motor parameter adaptation.

The most lucrative feature among other is that now the ABB DTC drives can support variety of motor types, including PMSM and SynRMs. ABB SynRM plus ACS880 drive packages are now considered top of the line products in terms of meeting the requirements of international energy efficiency regulations. The SynRMs exhibit high torque-to-weight ratio, reducing the overall footprint of motor drive, and together with superior variable speed capability of ACS880 drives, the performance



Figure 9.27 ABB ACS880 drive [Reproduced: courtesy ABB]



Figure 9.28 ABB SynRM-ACS880 drive package for general purpose applications [Reproduced: courtesy ABB]

of the complete package is much superior over wider speed–torque range as compared to induction motor drives. The drive has built in software algorithms for estimation of motor variables, identification of motor parameters, position detection algorithms for smooth startup and auto tuning of motor models, etc. The combination of two optimized motor and drive products offers excellent control performance in general purpose and well as dynamic torque applications (Figure 9.28).

The ability of ACS880 to supply motor torque near zero speed is superior to earlier drives as demonstrated in Figure 9.29 [8]. Similarly, the performance of speed estimators and torque stability for other motor types with ACS880 drive is equally

comparable to the drive performance with induction motor types as shown in Figure 9.30.

ABB has also introduced DTC technology in multilevel converter topologies in medium-voltage applications. ABBs ACS1000 MV drives are based on three-level topology with IGCT switches, which are perfect for medium-voltage high-power applications. The DTC technology, which was originally introduced in LV drives, is then optimized for three-level converter operation and low-loss control of output LC filter. This has enabled ACS1000 offer fast, accurate control from zero to rated speed similar to LV drives. The latest offering in MV drive product family is

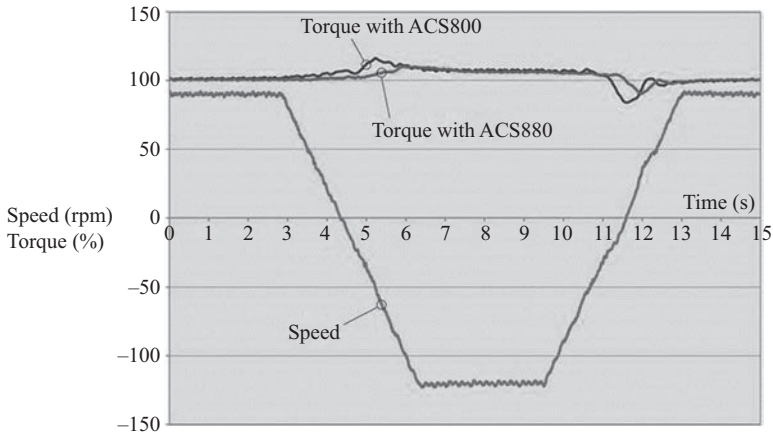


Figure 9.29 Comparison of torque stability of ACS880 with earlier drives [8] [Reproduced: courtesy ABB]

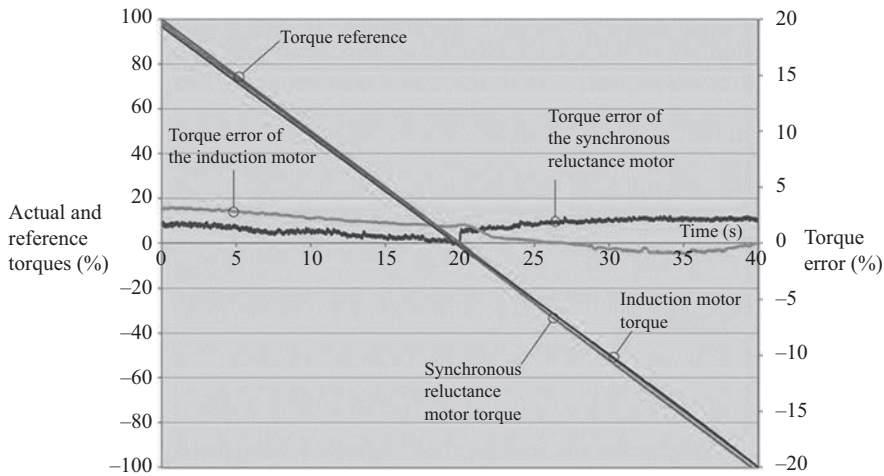


Figure 9.30 Comparison of torque accuracy for induction and SynRM [8] [Reproduced: courtesy ABB]

ACS5000/6000 and recently introduced ACS2000, which are based on five-level ANPC configuration. The DTC technology has been successfully extended to these multilevel drive configurations with power ratings from 250 kW to 50 MW range and voltage ratings from 2.3 to 15 kV range. The complete MV drive portfolio maintains highest torque and speed control performance ever achieved in medium voltage AC drives (Figures 9.31 and 9.32).



Figure 9.31 ABB ACS 2000 MV drive based on five-level ANPC technology [Reproduced: courtesy ABB]

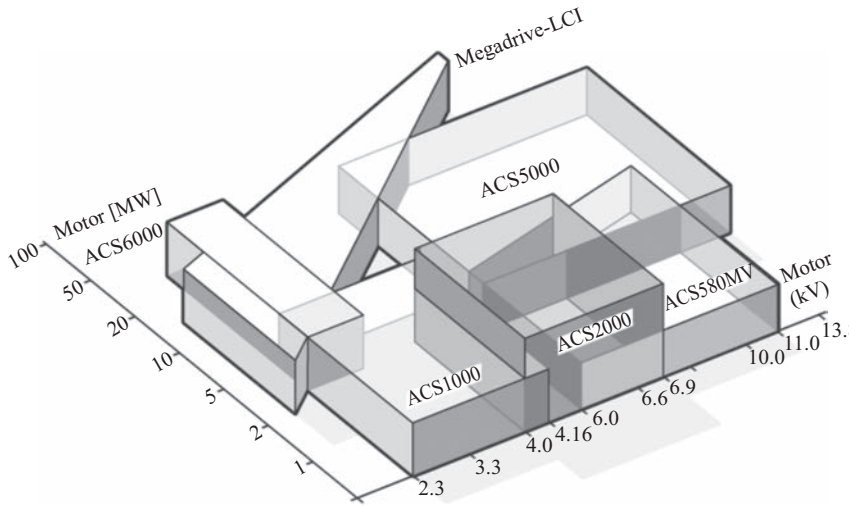


Figure 9.32 ABB medium voltage drive portfolio with DTC control at its core [Reproduced: courtesy ABB]

9.9 Summary

The DTC technology has been steadily developed for induction motors initially and now in a mature stage where its adaptation in commercial products has been accepted by industry. The development focus is now toward adaptation of DTC into complex applications requiring special motor types and drive topologies. The various technology areas are special machines for high-speed applications and multiphase machines with more than three-phase windings. There are attempts to extend DTC strategies for advanced drive topologies like matrix converters, multilevel converter topologies, integrated line side converter control. The complexity in such topologies is coming from increased number of voltage vector combinations, which are available for switching, and thus, decision-making can be a complex and time-consuming process. This is typical situation in even more complex multilevel converter fed multiphase machine architecture where the number of voltage vector combinations rises exponentially with machine phase and converter voltage levels.

List of symbols

θ_{sr}	Angle between stator and rotor flux
τ_r	Rotor time constant
σ	Leakage factor
u_s	Voltage vector
Δt	Time interval
ΔT_e	Incremental torque
e_ψ	Flux error
D_ψ	Hysteresis band
ω_{lp}	Provide low cutoff frequency
x	States
u	Input
Y	Output

Glossary of terms

Direct torque control	The control of torque directly through flux control
Space vector modulation	Modulation of voltage space vector to achieve the desired switching of voltage source converter

References

[1] Depenbrock M., "Direct Self-Control of the Flux and Rotary Moment of a Rotary-Field Machine", *US patent application* US4678248, 1987.

[2] Depenbrock M., "Direct self-control (DSC) of inverter-fed induction machine", *IEEE Trans. Power Electron*., vol. 3, pp. 420–429, 1988.
[3] Baader U. and Depenbrock M., "Direct self-control (DSC) of inverter fed induction machine: A basis for speed control without speed measurement," *IEEE Trans. Ind. Appl.*, vol. 28, pp. 581–588, 1992.
[4] Takahashi I., Noguchi T., "A new quick-response and high-efficiency control strategy of an induction motor", *IEEE Trans. Ind. Appl.*, vol. 22, no. 5, pp. 820–827, 1986.
[5] Tiitinen P., Pohjalainen P. and Lalu J., "The next generation motor control method—Direct torque control, DTC", *in Proc. EPE Chapter Symp*., Lausanne, Switzerland, 1994.
[6] Jääskeläinen E., Pohjalainen P., "DTC—A motor control technique for all seasons", ABB whitepaper, Available online at https://library.e.abb.com/public/0e07ab6a2de30809c1257e2d0042db5e/ABB_WhitePaper_DTC_A4_20150414.pdf.
[7] Hu J. and Wu B., "New integration algorithms for estimating motor flux over a wide speed range", *IEEE Trans. Power Electron*., vol. 13, no. 5, pp. 969–977, 1998.
[8] Bolognani S., Peretti L. and Zigliotto M., "Online MTPA control strategy for DTC synchronous-reluctance-motor drives", *IEEE Trans. Power Electron.*, vol. 26, no. 1, pp. 20–28, 2011.
[9] Luukko J., Niemela M. and Pyrhonen J., "Estimation of the flux linkage in a direct-torque-controlled drive", *IEEE Trans. Ind. Electron*., vol. 50, no. 2, pp. 283–287, 2003.
[10] Holtz J., "The representation of AC machine dynamics by complex signal flow graphs," *IEEE Trans. Ind. Electron.*, vol. 42, no. 3, pp. 263–271, 1995.
[11] Lascu C., Boldea I. and Blaabjerg F., "A modified direct torque control for induction motor sensorless drive", *IEEE Trans. Ind. Appl.*, vol. 36, pp. 122–130, 2000.
[12] Jansen P. L. and Lorenz R. D., "A physically insightful approach to the design and accuracy assessment of flux observers for field oriented I.M. drives", *IEEE Trans. Ind. Appl.*, vol. 30, pp. 101–110, 1994.
[13] Holtz J., "Sensorless control of induction machines—With or without signal injection?", *IEEE Trans. Ind. Electron.*, vol. 53, no. 1, pp. 7–30, 2006.
[14] Linder A. and Kennel R., "Direct model predictive control—A new direct predictive control strategy for electrical drives", *in Proc. Eur. Conf. Power Electron. Appl*., Dresden, Germany, Sep. 2005, pp. 1–10.
[15] Buja G. S. and Kazmierkowski M. P., "Direct torque control of PWM inverter-fed AC motors – A survey", *IEEE Trans. Ind. Electron.*, vol. 51, no. 4, pp. 744–757, 2004.
[16] French C. and Acarnley P., "Direct torque control of permanent magnet drives", *IEEE Trans. Ind. Appl.*, vol. 32, no. 5, pp. 1080–1088, 1996.
[17] Zhong L., Rahman M. F., Hu W. Y. and Lim K. W., "Analysis of direct torque control in permanent magnet synchronous motor drives", *IEEE Trans. Power Electron.*, vol. 12, no. 3, pp. 528–536, 1997.

[18] Zolghadri M. R., Guiraud J., Davoine J. and Roye D., "A DSP based direct torque controller for permanent magnet synchronous motor drives", *in Conf. Rec. IEEE 29th Annual Power Electronics Specialists Conference (PESC'98)*, vol. 2, May 17–22, 1998, pp. 2055–2061.

[19] Swierczynski D. and Kazmierkowski M. P., "Direct torque control of permanent magnet synchronous motor (PMSM) using space vector modulation (DTC-SVM) – Simulation and experimental results", *in Conf. Proc. IEEE 28th Annual Conference of the Industrial Electronics Society (IECON'02)*, vol. 1, Nov. 5–8, 2002, pp. 751–755.

[20] Tang L., Zhong L., Rahman M. F. and Hu Y., "A novel direct torque control scheme for interior permanent magnet synchronous machine drive system with low ripple in torque and flux—A speed-sensorless approach", *IEEE Trans. Ind. Appl.*, vol. 39, no. 6, pp. 1748–1756, 2003.

[21] Pacas M. and Weber J., "Predictive direct torque control for the PM synchronous machine", *IEEE Trans. Ind. Electron.*, vol. 52, no. 5, pp. 1350–1356, 2005.

[22] Adam A. A. and Gulez K., "A new sensorless hysteresis direct torque control algorithm for PMSM with minimum torque ripples", *COMPEL*, vol. 28, no. 2, pp. 437–453, 2009.

[23] Rodriguez J., Pontt J., Silva C., Cortes P., Ammann U. and Rees S., "Predictive direct torque control of an induction machine", *in 11th International Power Electronics and Motion Control Conference EPEPEMC*, 2004.

This page intentionally left blank

Chapter 10

Direct torque control of PM synchronous motor drives

Muhammed Fazlur Rahman[1] *and Dan Xiao*[1]

10.1 Introduction

This chapter describes the direct torque control (DTC) technique for permanent magnet synchronous motors/machines (PMSMs). The DTC technique has evolved much since mid-1980s when a less complex, cheaper and potentially faster method of torque and flux control than the pre-existing rotor flux-oriented vector control (RFOC/VC) for induction machines first emerged [1–7]. The DTC technique is based on closed-loop regulation of torque and stator flux linkage obtained from estimators using voltage vectors and currents in the stator reference frame and the machine model. Drive dynamics under DTC control is as fast and can be faster than that under RFOC/VC in which rotor position sensing is used for exercising control in the rotor reference frame [3,4]. This chapter starts with a brief review of the context of these developments, including the underlying theory (which had existed prior) and methods that have been used to apply DTC to PMSMs. Some comparative evaluations are included that may help researchers and engineers to further develop the method and apply it to high-performance PMSM drives in various applications.

It was shown by Depenbrock [1] and Takahashi [2] almost simultaneously in mid-1980s that estimation of torque and stator flux can be obtained from the machine terminal currents and voltages, and the machine model with good accuracy. The machine terminal voltages can be found from the knowledge of the switching states of the inverter and the DC-link voltage. The developed torque and stator flux could then be placed under control loops (such as hysteresis or other controllers) to achieve high dynamic response. These methods do not require coordinate transformations, high-resolution speed and position sensors, and PWM current controllers. Direct torque control (DTC)—Takahashi's designation—has now been widely accepted.

In the following sections, a brief recount of the underlying rotor flux-oriented control (RFOC) structure for interior PMSMs (IPMSMs) is given in order to

[1]School of Electrical Engineering and Telecommunications, The University of New South Wales, Australia

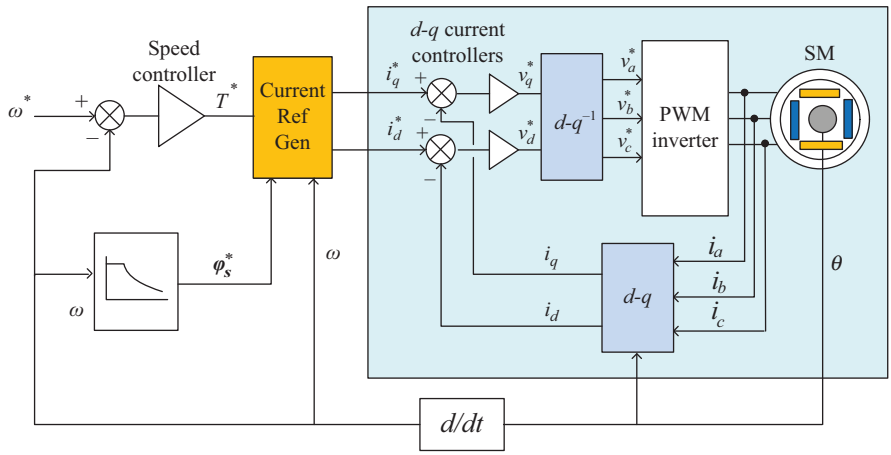


Figure 10.1 The RFOC structure for PMSM

explain the context in which the DTC technique stands (see Figure 10.1). This is followed by a fuller description of DTC techniques for the PMSMs that have evolved to date. Experimental results on performances of DTC of PMSMs under these schemes are included to clarify how these techniques perform.

10.1.1 The PMSM model and RFOC

The RFOC of the IPMSM is based on transformation of machine voltages and currents to and from rotor *dq* coordinates, the *d*-axis of which is fixed and therefore aligned with rotor flux [3]. For this machine, there is the added complication that the developed torque is determined by both i_q and i_d, as indicated by (10.1), when rotor has saliency.

$$T_{\text{dev}} = \frac{3P}{2}\left[\varphi_f i_q + \left(L_d - L_q\right) i_q i_d\right] \quad \text{for the motor with rotor saliency} \tag{10.1}$$

$$T_{\text{dev}} = \frac{3}{2} P \varphi_f i_q \quad \text{for the motor without rotor saliency} \tag{10.2}$$

where

$$\varphi_d = L_d i_d + \varphi_f, \quad \varphi_q = L_q i_q \tag{10.3}$$

and φ_f is the rotor flux linkage with *d*-axis of stator winding. The stator voltages in *d*- and *q*-axes are the following:

$$v_d = R i_d + L_d \frac{di_d}{dt} - \omega_e L_q i_q \tag{10.4}$$

$$v_q = R i_q + L_q \frac{di_q}{dt} + \omega_e \left(L_d i_d + \varphi_f\right) \tag{10.5}$$

The current reference generator selects appropriate references for i_q and i_d, according to speed and certain limiting requirements for current and terminal voltage values, and for flux-linkage values at high speed when the stator flux linkage is weakened. These are called current trajectories.

10.1.2 Current control trajectories for PMSM [8,9]

It can be shown that for the fastest dynamic response is obtained when the current references for i_d and i_q are selected from (10.6), subject to the limit given by (10.7).

$$i_d = \frac{\varphi_f}{2(L_q - L_d)} - \sqrt{\frac{\varphi_f^2}{4(L_q - L_d)^2} + i_q^2} \tag{10.6}$$

$$I_s = \sqrt{i_q^2 + i_d^2} \leq I_{sm} \tag{10.7}$$

The i_q reference is obtained from the output of the speed controller which gives the torque reference. The i_q–i_d trajectory for the maximum torque per ampere (MTPA) characteristic, according to (10.6), is indicated by the MTPA trajectory in Figure 10.2. It is bounded by the current limit circle given by (10.7).

10.1.3 Field weakening under voltage limit

A PMSM may be driven at higher than its base speed corresponding to its pole numbers and base frequency using field weakening (FW). The inverter input DC-link voltage V_{dc} at the base speed, the rated V_{dc}, must be appropriate so that with rated load, the peak line-line AC voltage is not higher than V_{dc}. The motor speed can be

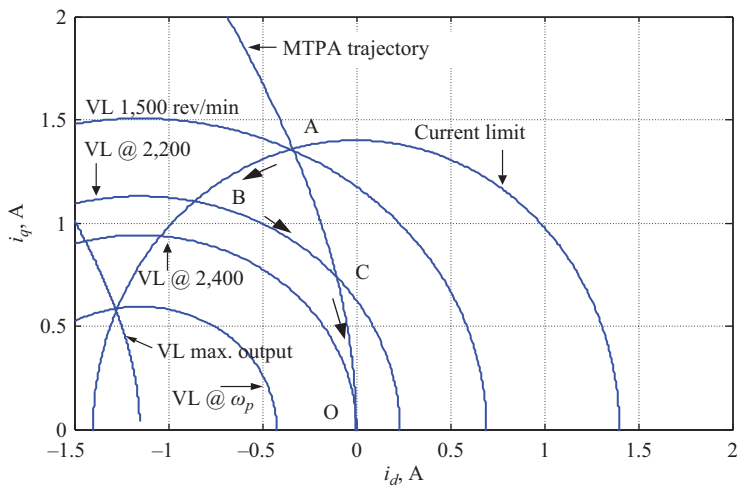


Figure 10.2 The MTPA and FW trajectories for the machine of Table 10.1

higher than base speed by using FW, i.e., by using negative *d*-axis current. At a steady operating speed, the terminal voltage given in the rotor *dq* reference frame must also be subject to limit given by (10.8), for negligible stator resistance *R*.

$$V_s = \sqrt{v_d^2 + v_q^2} = \sqrt{\left(\omega L_q^2 i_q^2\right) + \left(\omega L_d i_d + \omega \varphi_f\right)^2} \leq V_{sm} \tag{10.8}$$

The limiting i_q–i_d trajectory for each speed is an ellipse, as also indicated in Figure 10.2. With RFOC, PWM current controllers in the *d*- and *q*-axes, augmented with speed-dependent terms indicated in (10.4) and (10.5), regulate currents through the machine according to the references which follow the MTPA and FW trajectories indicated by (10.6)–(10.8). Figure 10.2 indicates the optimal control trajectories when an IPMSM is driven under maximum current limit I_{sm} (the MTPA characteristic—trajectory OA) and under the maximum voltage limit V_{sm} trajectory at several speeds (the voltage limit ellipses with weakened φ_d by establishing negative i_d) on the i_d–i_q plane. The blue line in Figure 10.3(a) indicates trajectory following along the maximum current and voltage limit trajectories as speed is increased beyond the base speed of 1,500 rev/min with FW for the machine of Table 10.1. Figure 10.3(b) shows i_d and i_q currents and speed responses as the machine is driven along the optimum trajectories when it is accelerated from 0 to 2,300 rev/min, which includes operation in the FW or constant-power speed range (CPSR).

Such dynamic and steady-state performances are the benchmarks which DTC techniques are expected to match or surpass. The reader is expected to be familiar with the foregoing (10.1)–(10.8), which result from *dq* analyses and rotor flux orientation of the PMSM. References [1–6] are suitable for this.

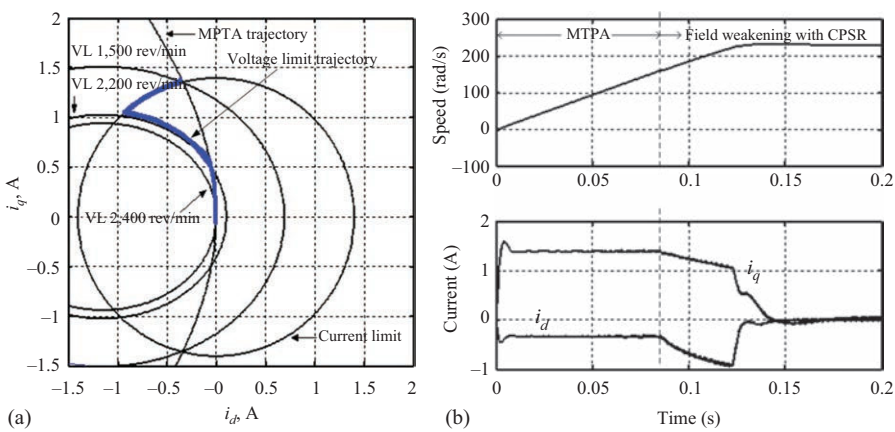


Figure 10.3 (a) Control trajectories and (b) dynamic responses of a PMSM with MTPA and FW trajectory following

Table 10.1 Parameters of the PMSM for Figures 10.2 and 10.3

Number of pole pairs	P	2
Stator resistance	R	18.6 Ω
Magnet flux linkage	φ_f	0.447 Wb
d-axis inductance	L_d	0.3885 H
q-axis inductance	L_q	0.4755 H
Phase voltage	V	240 V
Phase current	I	1.4 A
Base speed	ω_b	1,500 rev/min
Rated torque	T_b	1.95 N-m
Crossover speed	ω_c	2,400 rev/min

10.2 DTC for PMSM

The RFOC scheme described in Section 10.1 assumes that stator inductances and magnet flux linkages are sinusoidal functions of rotor position. These are not strictly true. Furthermore, the magnet flux linkage is a function of rotor temperature. These are not taken into account in the RFOC controller. PWM current controllers also limit torque response dynamics. The DTC scheme overcomes these limitations by estimating the machine developed torque and flux linkage from measurement of machine voltages and currents by using the machine model and by controlling the errors in these variables within defined boundaries by using two comparators. The basic structure of the DTC for any AC machine is indicated in Figure 10.4, in which the torque reference T^* and stator flux-linkage reference φ_s^* are available from the speed controller. The estimated values of these quantities are obtained from the machine model using measured stator currents and the DC-link voltage. These are then regulated by closed-loop controllers, which may be hysteresis comparators. Stator flux linkages can be obtained, in the simplest form, by integrating the back electromotive force (emf), as in (10.9):

$$\boldsymbol{\varphi_s}(t) = \boldsymbol{v_s}t - R\int \boldsymbol{i_s}dt + \boldsymbol{\varphi_s}\Big|_{t=0} \tag{10.9}$$

where $\boldsymbol{\varphi_s} = \sqrt{\varphi_\alpha^2 + \varphi_\beta^2}\angle\tan^{-1}\left(\frac{\varphi_\beta}{\varphi_\alpha}\right)$ and $\boldsymbol{v}_s = \begin{bmatrix} v_\alpha & v_\beta \end{bmatrix}^T$ and $\boldsymbol{i_s} = \begin{bmatrix} i_\alpha & i_\beta \end{bmatrix}^T$.

The non-sinusoidal distributions of stator inductances and the magnet flux with position and the dependence of the latter to temperature variation are automatically included in this computation. The basic principle of DTC is to directly select the voltage vectors to be applied to the machine in the next switching interval according to the differences between the reference and actual (estimated) values of the torque and stator flux linkage, as indicated in Figure 10.4. The stator flux-linkage and torque estimator (FTE), in their simplest form, is indicated in Figure 10.5, in which two integrators are used to integrate the machine back emfs in

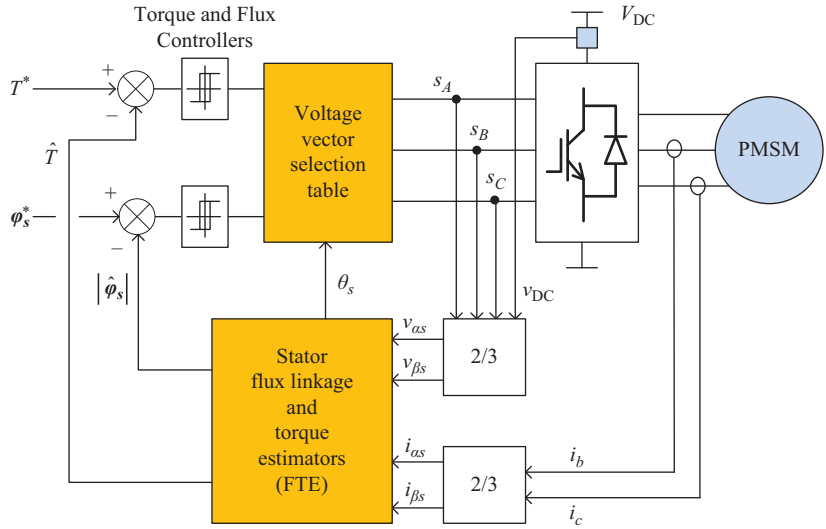


Figure 10.4 Switching table-based DTC with hysteresis controllers for torque stator flux linkage

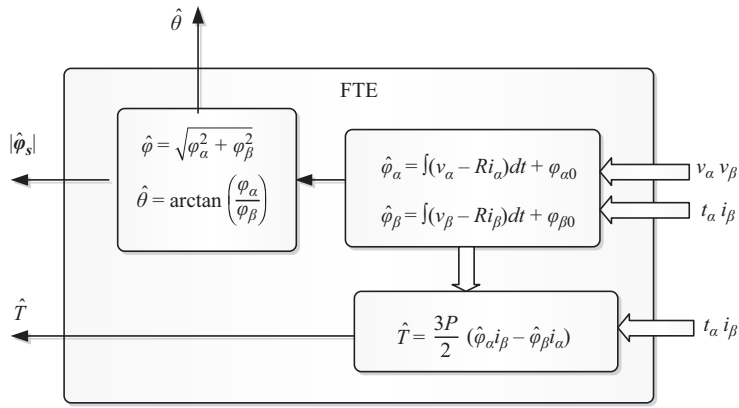


Figure 10.5 An open-loop stator FTE using simple integrators

the stator $\alpha\beta$ frame to obtain the stator flux space vector $|\hat{\varphi}_s|$ and its special angle $\hat{\theta}$. It should be noted here that computations leading to the estimation of torque and flux linkage take place in the stator reference frame and do not require coordinate transformations to rotor or other reference frames using rotor speed or position feedback signals. Thus the DTC for a PMSM has the advantages of less parameter dependence (except for stator resistance) and fast torque response compared to RFOC which employs PWM control in the rotor reference frame via coordinate transformations, and there is no requirement for a rotor position sensor.

The DTC of IPMSM motors is based on the spatial vector relationships of stator flux linkage, rotor flux linkage, stator current and stator voltage. The different reference frames used for analyzing the performance of an interior permanent magnet (IPM) motor are shown in Figure 10.6. The stationary reference frame is denoted as the $\alpha\beta$ frame, in which the α-axis is aligned with the stationary axis of phase A winding. All stator currents and voltage measurements are conducted in this frame. The *dq* reference frame is the rotor reference frame in which the *d*-axis is aligned with the rotor flux linkage. The third frame is aligned with the stator flux-linkage vector and is shown as the *xy* frame in Figure 10.6. The angle between the stator flux vector φ_s and the rotor flux vector φ_f is known as the load angle δ.

The torque developed by an IPM machine is also given by (10.10) in terms of the stator and rotor flux linkages:

$$T = \frac{3P\varphi_s}{4L_dL_q}\left[2\varphi_f L_q \sin\delta - \varphi_s(L_q - L_d)\sin 2\delta\right] \tag{10.10}$$

where

L_d, L_q: direct and quadrature inductance, H;
T: electromagnetic torque, N-m;
P: number of pole pairs; and
φ_s and φ_f: stator and rotor magnet flux linkage, respectively.

It can be seen from (10.10) that the torque is a function of the load angle δ for a fixed stator flux linkage φ_s. Typical T–δ characteristic of an IPMSM is plotted in Figure 10.7 for different values of stator flux linkage. For different values of φ_s, there exists a maximum load angle δ_m that corresponds to maximum developed torque T, as indicated by the red dots in Figure 10.7. The load angle δ, which should never be allowed to exceed δ_m, can be regulated by controlling the phase angle θ_s of the stator flux linkage.

Feedback signals for developed torque T and stator flux linkage λ_s can be obtained from a stator FTE, which also provides information on one of the six 60°

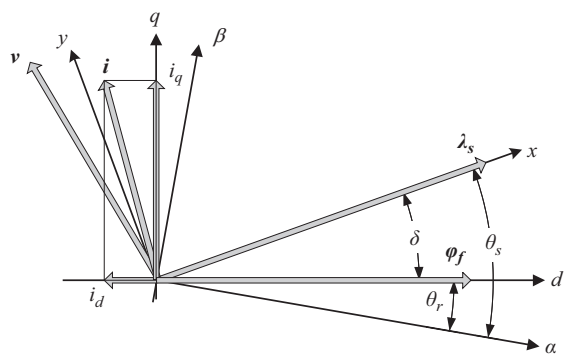


Figure 10.6 Quadrature rotor, stator and stator flux reference frames of a PMSM

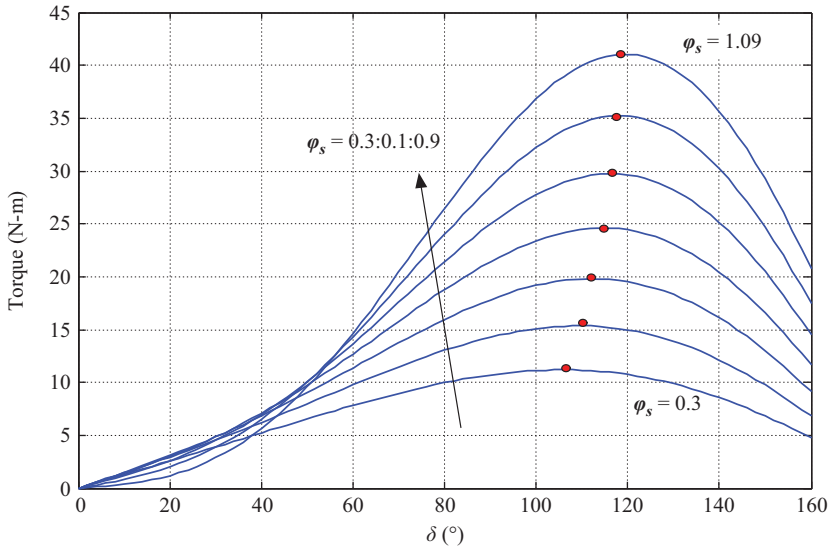


Figure 10.7 Torque T, stator flux linkage φ_s and δ angle characteristics of a PMSM

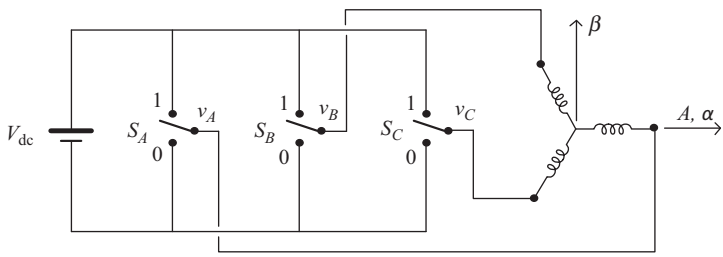


Figure 10.8 A two-level VS inverter for AC motor drive

regions θ_1–θ_6 in which the stator flux linkage occurs during each switching interval of the controllers as shown in Figure 10.10 [10]. Based on these and the state of the comparator outputs, the most appropriate of the eight voltage vectors from a two-level VS inverter, in order to achieve the desired torque and flux-linkage transitions, is selected. Figure 10.8 and Table 10.2 show the circuit and the available voltage vectors for a two-level inverter.

These voltage vectors can also be expressed as

$$\boldsymbol{v_s}(S_a, S_b, S_c) = \frac{2}{3} V_{\text{dc}} \left(S_a + S_b e^{j\frac{2}{3}\pi} + S_c e^{j\frac{4}{3}\pi} \right) \tag{10.11}$$

Table 10.2 Available voltage vectors from a two-level VSI

V_1	V(100)
V_2	V(110)
V_3	V(010)
V_4	V(011)
V_5	V(001)
V_6	V(101)
V_7	V(000)
V_8	V(111)

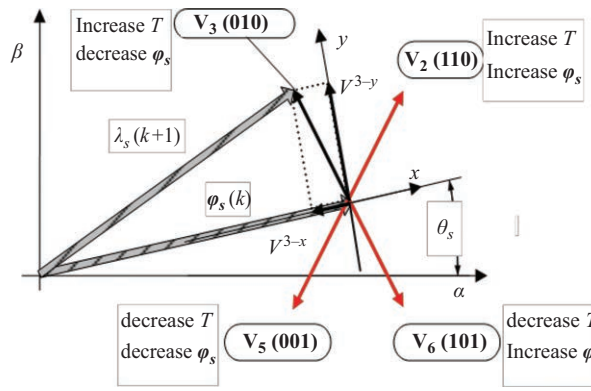


Figure 10.9 Torque- and flux-producing components of a projected voltage vector V_3

The stator flux linkage can be found by integrating the applied voltage vector minus the voltage drop on the stator resistance using (10.9), as shown in (10.3)–(10.5).

The tip of the stator flux-linkage vector φ_s moves in the same direction as the applied voltage vector, an example of which is shown in Figure 10.9, where voltage vector V_3 is applied. The distance which the stator flux-linkage vector moves is determined by the duration and amplitude of the voltage space vector. The amplitude of the applied vector is proportional to the DC bus voltage of the inverter and can be regulated by applying a set of appropriately modulated voltage space vectors. The speed at which the stator flux linkage rotates is determined by the sequence of application of the voltage space vectors. Hence, the rotational speed of the stator flux-linkage vector and its amplitude can be controlled by selecting appropriate voltage vectors.

Figure 10.10 shows how the stator flux vector may be moved as the voltage vectors of Table 10.2 are switched for rotation in the counterclockwise (CCW) direction of rotation. Table 10.3 gives values of the v_α and v_β voltages for each voltage vector that is applied.

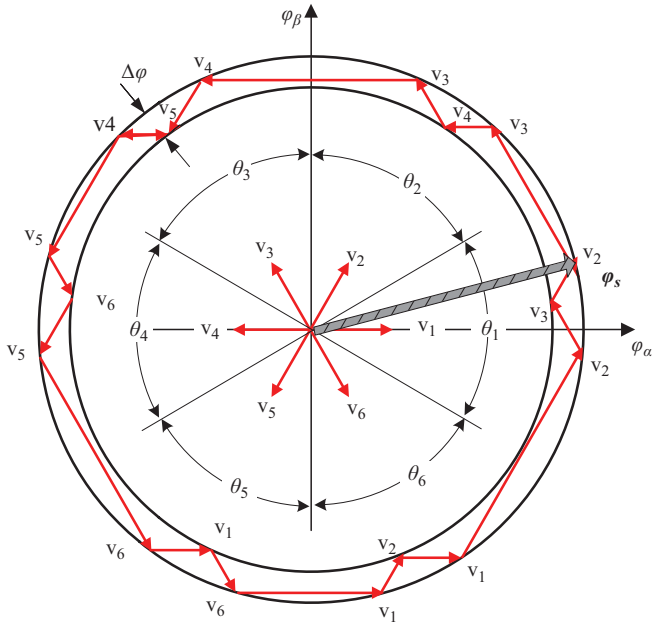


Figure 10.10 Rotation of the stator flux vector by selection of voltage vectors

Table 10.3 The αβ components of the nonzero voltage vectors

	$\mathbf{V_0}$	$\mathbf{V_1}$	$\mathbf{V_2}$	$\mathbf{V_3}$	$\mathbf{V_4}$	$\mathbf{V_5}$	$\mathbf{V_6}$	$\mathbf{V_7}$
v_α	0	$2/3V_{dc}$	$1/3V_{dc}$	$-1/3V_{dc}$	$-2/3V_{dc}$	$-1/3V_{dc}$	$1/3V_{dc}$	0
v_β	0	0	$\sqrt{3}/3V_{dc}$	$\sqrt{3}/3V_{dc}$	0	$-\sqrt{3}/3V_{dc}$	$\sqrt{3}/3V_{dc}$	0

10.2.1 Voltage space vector selection [10,11]

The voltage vector plane is divided into six sectors, θ_1–θ_6, each having an active vector in the middle as shown in Figure 10.10. In each sector, two adjacent vectors are selected in order to minimize the switching frequency. For example, voltage vectors V_3 and V_4 are chosen to increase or decrease the amplitude of $\boldsymbol{\varphi_s}$ when it is in sector θ_2 and rotating in the CCW direction. For clockwise (CW) rotation, vectors V_1 and V_6 are chosen when $\boldsymbol{\varphi_s}$ is in sector θ_2. By selecting appropriate voltage vectors, the amplitude and direction of $\boldsymbol{\varphi_s}$ can be regulated. Figure 10.10 also shows how different voltage vectors are selected to keep $\boldsymbol{\varphi_s}$ within a hysteresis band (between the inner and outer circles) for rotation in the CCW direction.

The widths of bands of the two hysteresis controllers determine the time duration of the applied voltage vectors and therefore the switching frequency. Smaller bandwidths will result in higher switching frequencies. Smooth torque response can be obtained if the bandwidths for stator flux and torque are chosen to be about 5% and 15% of the rated stator flux linkage and the rated torque,

respectively. This statement is based on the fact that torque and stator flux-linkage control will not be limited by the sampling frequency. The band between the two circles represents the hysteresis band within which the stator flux linkage is maintained. When the switching frequency is high and hysteresis band is small, the tip of the flux trajectory becomes a smooth circle.

Reversal of the rotational direction of φ_s is produced by application of the voltage vectors in the opposite direction. For instance, when φ_s is in region θ_1 in Figure 10.10 and rotation in the CW direction is desired, voltage vector pairs V_5 and V_6 are selected. The effect of application of the zero voltage vectors V_0 and V_7 has different implications for induction and synchronous machines. For a squirrel-cage induction machine, the rotor voltages are always zero, so the application of zero stator voltage vectors leads to stopping of further rotation of φ_s. This is not so for the PMSM, in which the rotor flux linkage φ_f continues to rotate with the rotor, resulting in rotation of $\boldsymbol{\lambda}_s$ even when zero voltage vectors V_0 and V_7 are applied. The zero voltage vectors may thus be utilized in reducing torque and flux ripples, and for controlling the torque, especially when the PMSM rotates at a high speeds, where the developed torque can be significantly changed by movement of the rotor flux during the short duration of a sampling period.

In order to select the voltage vectors for controlling the amplitude of the stator flux linkage, the voltage vector plane is divided into six sectors of 60° each, θ_1–θ_6, as shown in Figure 10.10. In each sector, only one of four adjacent voltage vectors may be selected to keep the switching frequency to a minimum. One of four voltage vectors may be selected to increase or decrease the amplitude of φ_s or to increase and decrease the torque. For instance, voltage vectors V_2 and V_3 are chosen to increase or decrease the amplitude of φ_s when it is in region θ_1 and is rotating in CCW direction. Voltage vectors V_5 and V_6 are chosen when φ_s is in region θ_1 and rotates in the CW direction. In this way, the amplitude of φ_s can be adjusted in amplitude and direction as required by choosing the proper voltage vectors. Table 10.3 shows how the voltage vectors are selected for keeping the amplitude of φ_s within a hysteresis band when φ_s is rotating in the CCW direction. The hysteresis band in φ_s is the difference in radii $\Delta\varphi_s$ of the two circles in Figure 10.10.

The eight voltage vectors for controlling the torque and stator flux linkage, as in Table 10.4, are used for two directions of operation of the drive. Variables φ and τ are the outputs of the two hysteresis controllers for stator flux linkage and torque,

Table 10.4 Voltage vectors selection table for flux linkage and torque control under DTC using active and zero voltage vectors

		θ					
φ	T	θ_1	θ_2	θ_3	θ_4	θ_5	θ_6
Increase φ_s	Increase T	V_2 (110)	V_3 (010)	V_4 (011)	V_5 (001)	V_6 (101)	V_1 (100)
	Reduce T	V_8 (111)	V_7 (000)	V_8 (111)	V_7 (000)	V_8 (111)	V_7 (000)
Reduce φ_s	Increase T	V_3 (010)	V_4(011)	V_5 (001)	V_6 (101)	V_1 (100)	V_2 (110)
	Reduce T	V_7 (000)	V_8 (111)	V_7 (000)	V_8 (111)	V_7 (000)	V_8 (111)

respectively. $\varphi = 1$ implies that the estimated flux linkage is smaller than the reference value, and a flux increasing vector should be chosen and vice versa. The same is true for torque, with τ for torque control. θ_1–θ_2 represent the region number defined in Figure 10.10, which indicates the approximate position information of stator flux linkage in a resolution of 60° electrical in the $\alpha\beta$ reference frame.

10.2.2 Stability criteria for DTC

For a surface PMSM for which $L_d = L_q = L_s$ and $\delta_m = \pm\frac{\pi}{2}$, it can be shown that for the fastest response of torque, the i_y components of stator current is given by (10.12), in reference to Figure 10.6:

$$\begin{aligned} T &= \frac{3P}{2}\varphi_s i_y \\ i_y &= \frac{1}{L_s}\varphi_f \sin\delta \end{aligned} \tag{10.12}$$

Thus, for the highest torque dynamics, angle δ must be controlled within $\delta_{\mathrm{m}} \leq \pm\frac{\pi}{2}$, regardless of the value of λ_s.

For the IPMSM, it can be shown that for the fastest response of torque, the i_y components of stator current is given by (10.13), in reference to Figure 10.6:

$$\begin{aligned} T &= \frac{3P}{2}\varphi_s i_y \\ i_y &= \frac{3P\varphi_s}{4L_d L_q}\left[2\varphi_f L_q \sin\delta - \varphi_s\left(L_q - L_d\right)\sin 2\delta\right] \end{aligned} \tag{10.13}$$

Equation (10.13) also implies that the developed torque may not always increase monotonically with the angular displacement δ for a PMSM with saliency for different values of λ_s. When torque is controlled by placing the stator flux linkage vector ahead or behind of the rotor flux-linkage vector by a suitable angle δ, two requirements must be fulfilled, namely,

A. $$\varphi_s < \frac{L_q}{L_q - L_d}\varphi_f \tag{10.14}$$

so that $|T|$ always increases with increase of $|\delta|$, and

B. $\delta < \delta_m$, where,

$$\delta_{\mathrm{m}} = \cos^{-1}\left\{\frac{1}{4}\left(\frac{a}{\varphi_s} - \sqrt{\left(\frac{a}{\varphi_s}\right)^2 + 8}\right)\right\}, \quad \text{where } a = \frac{\varphi_f L_q}{L_q - L_d} \tag{10.15}$$

so that the limiting load angle δ_m is not exceeded. When $\delta > \delta_m$, torque will decrease with increase of δ, and the operation will be unstable.

The variation of the limiting δ_m, with respect to φ_s, is indicated in Figure 10.11.

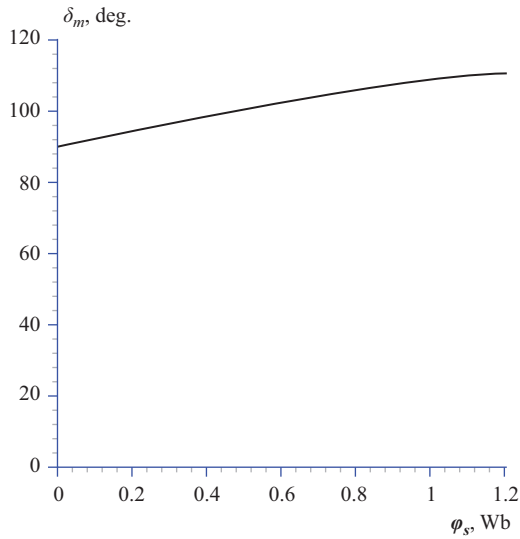


Figure 10.11 The limiting δ_m values versus φ_s for the PMSM of Table 10.1

10.2.3 Torque and flux linkage control of a PMSM by applying voltage vectors

Control of torque using φ_s according to 10.13, 10.14 and 10.15 is straightforward. This is done by selecting the voltage vectors of Table 10.4. However, the voltage vector selection Table 10.4 does not lead to good control of torque, unlike the DTC for induction machines. Because the stator flux linkage is also determined by the rotor flux and the rotation of the rotor, variation of φ_s at low speed can be slow because of slow movement of rotor. In order to overcome this shortcoming for PMSMs, the voltage vector selection Table 10.5 is more appropriate, in which the stator flux linkage is rotated opposite to the direction of motion in order to allow d to reach limiting values more quickly.

Note that zero voltage vectors are not selected when the motor runs at low speed. When the motor runs at a reasonably high speed, the use of Table 10.4 may not affect the torque dynamics appreciably, while reducing the ripples in torque and total harmonic distortion (THD) in motor current waveforms.

In order to select the voltage vectors for torque stator flux control, two hysteresis controllers are used in the classical DTC. The hysteresis band for the torque controller is symmetric around the vertical axis. The torque hysteresis band delta is ΔT_b. The hysteresis band for stator flux linkage is not symmetrical around the flux axis, because the amplitude of the stator flux is always positive. These bands are indicated in Figure 10.12. When ΔT is greater than $\Delta T/2$, $\tau = 1$, and torque has to be increased and vice versa. When ΔT is within the band of $\pm\Delta T/2$, the selected voltage vectors remain unchanged. The same is true for $\Delta\varphi_s$, except that $-\Delta\varphi_s/2$ becomes zero.

Table 10.5 The switching table for inverter for a PMSM

		ϕ					
ϕ	τ	θ_1	θ_2	θ_3	θ_4	θ_5	θ_6
$\phi = 1$	$\tau = 1$	V_2 (110)	V_3 (010)	V_4 (011)	V_5 (001)	V_6 (101)	V_1 (100)
	$\tau = 0$	V_6 (101)	V_1 (100)	V_2 (110)	V_3 (010)	V_4 (011)	V_5 (001)
$\phi = 0$	$\tau = 1$	V_3 (010)	V_4 (011)	V_5 (001)	V_6 (101)	V_1 (100)	V_2 (110)
	$\tau = 0$	V_5 (001)	V_6 (101)	V_1 (100)	V_2 (110)	V_3 (010)	V_4 (011)

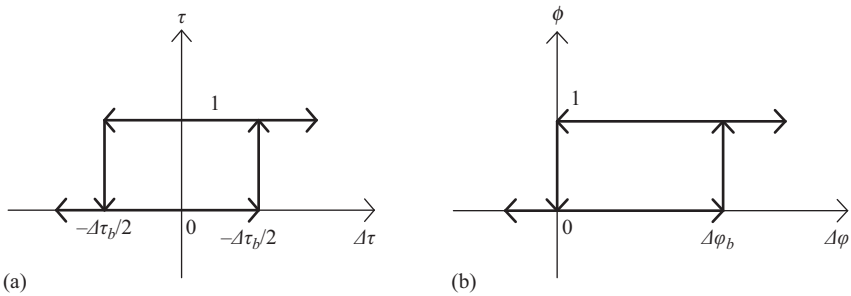


Figure 10.12 The torque and stator flux hysteresis bands in DTC: (a) torque controller and (b) stator flux-linkage controller

Simulation results of torque and flux responses when the IPMSM of Table 10.1 is driven under linear ramp speed references are shown in Figure 10.13. The sampling period used is $T_s = 10$ μs. It is clearly seen that torque and flux linkage are controlled very well with high dynamics comparable to the RFOC counterpart.

When the sampling period is increased to 100 μs, which is what can be easily achieved with a microcontroller or a digital signal processor (DSP), the simulated dynamic responses of torque for the motor of Table 10.1 are shown in Figure 10.14; however, the torque and flux ripples increase, as shown in Figure 10.14. Clearly, the torque and flux ripples increase because of the longer sampling interval used.

Dynamic responses of torque obtained for the motor of Table 10.1 when driven with RFOC and DTC are shown in Figure 10.15. The DTC response is faster than that for the RFOC, due to the proportional and integral (PI) controllers, axes transformation and PWM control used in the RFOC.

Because of the hysteresis torque and flux controllers, the switching frequency of the inverter is variable. Furthermore, the ripple in the torque and flux linkage can also be high unless very high sampling and switching frequency are employed. The torque and flux ripples of DTC drive of the PMSM in Table 10.1 for zero hysteresis bands for torque and flux controllers and for $T_s = 75$ and 125 μs are shown in Figure 10.16(a) and (b), respectively. Clearly, the sampling frequency affects the torque and flux ripples substantially. These are some of the limitations of the DTC technique (the basic DTC) described earlier in this section.

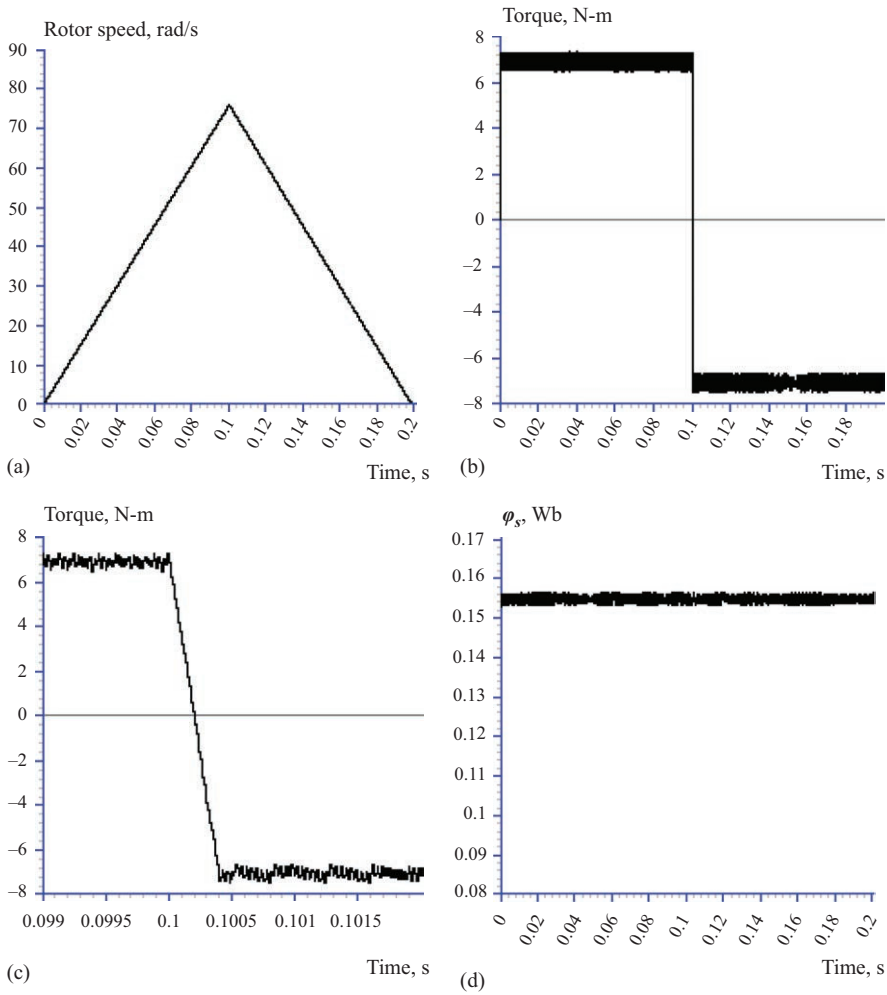


Figure 10.13 Simulation results of DTC for PMSM drive using Table 10.5: $T_s = 10$ μs. (a) Speed response, (b) torque response, (c) torque reversal and (d) amplitude of the stator flux linkage

10.3 DTC with fixed switching frequency and reduced torque and flux ripple

In order to employ fixed-frequency switching of the inverter, say at 10 kHz, and reduce the torque and flux ripples two schemes that use the space vector modulator (SVM) technique [12,13]. Both schemes employ an SVM to achieve fixed-frequency switching of the inverter, at the same time retaining the inherent advantages of the DTC in not using any coordinate transformation and current controllers.

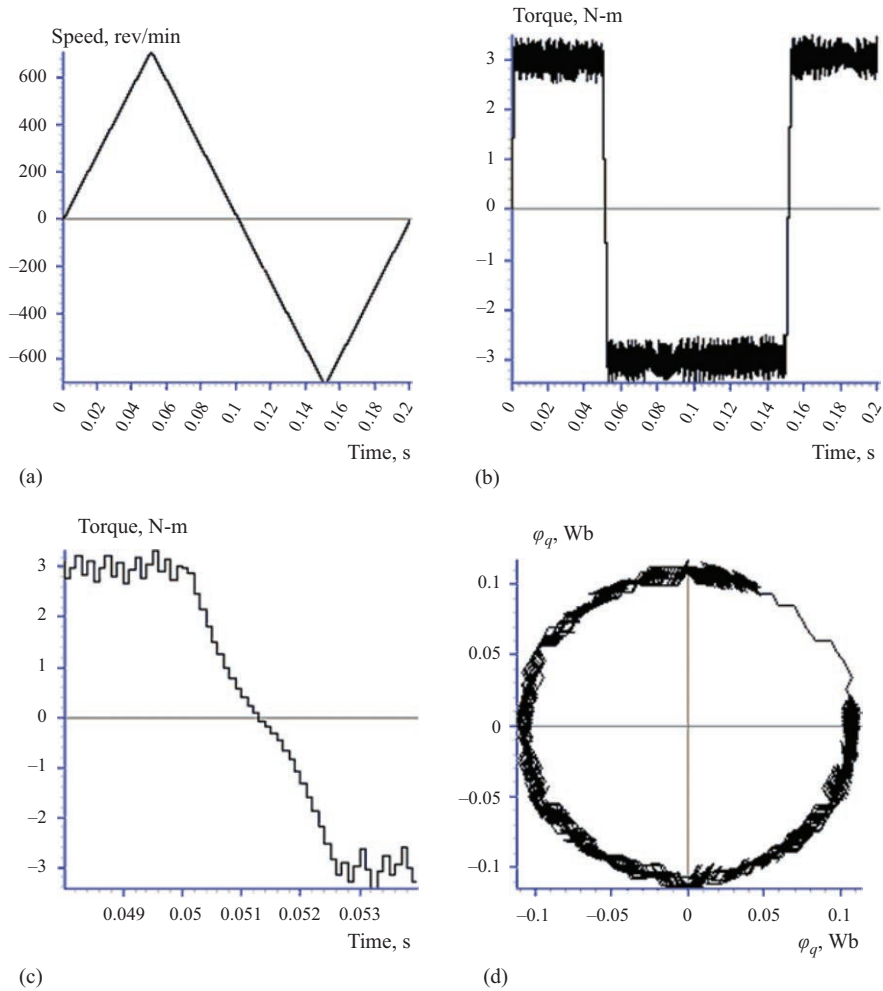


Figure 10.14 Simulation results of DTC for PMSM drive using Table 10.5: $T_s = 100$ μs. (a) Speed response, (b) torque response, (c) torque reversal and (d) locus of the stator flux linkage

The method of [12] uses one PI regulator following the speed controller torque error is obtained and utilizes a reference flux vector calculator (RFVC) as shown in Figure 10.17(a).

The discrete form of stator voltage equations of a PMSM motor can be written as (10.16) in the stator reference frame. T_s is the sampling interval, $\boldsymbol{\varphi_s}$ is the stator flux-linkage vector and $\boldsymbol{i}$ is the stator current vector. $\boldsymbol{v_k}$ is the required voltage vector for the flux linkage to reach the reference flux-linkage vector (φ_k^*) at the end of the next sampling interval. The selection rule of voltage space vectors is based on the error vector, not on the region of flux-linkage vector. For example, if the error flux-linkage vector $\Delta\boldsymbol{\varphi_k}$ is between the vectors of V_1 and V_2, V_1 and V_2 are selected to adjust the error vector such that the error vector is fully compensated.

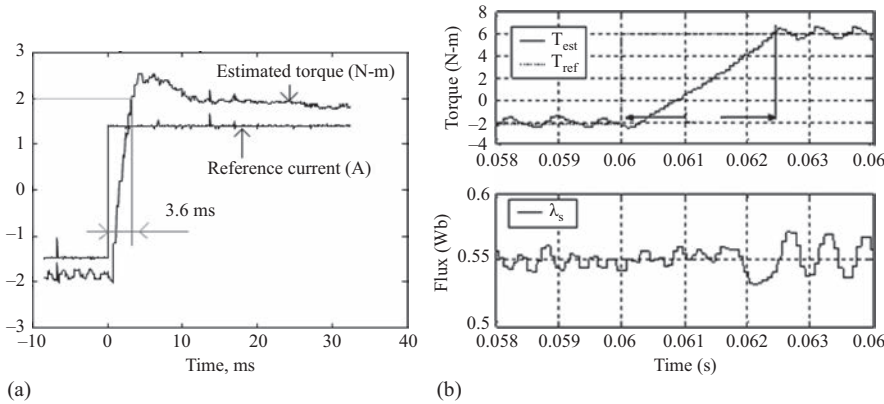


Figure 10.15 Dynamic response of torque for the motor of Table 10.1 under (a) RFOC and (b) DTC; $T_s = 100\ \mu s$

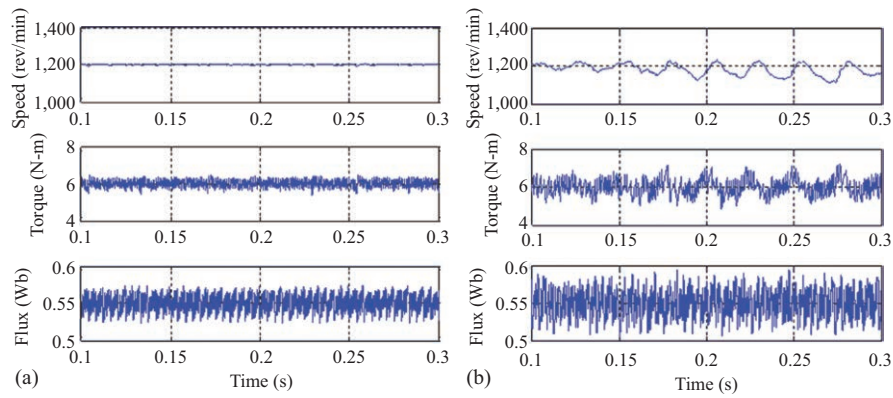


Figure 10.16 Variation of torque and stator flux linkage ripples with sampling period. (a) $T_s = 75$ s and (a) $T_s = 125$ s

The calculation of the durations (T_1, T_2 and T_0) of voltage vectors are given by (10.17)–(10.19) according to the SVM principle, as indicated in Figure 10.18.

$$\boldsymbol{v}_k = \frac{\Delta\boldsymbol{\varphi_s}}{T_S} = \left(\frac{\varphi_s^*(k) - \hat{\varphi}_s(k-1)}{T_S}\right) + R\boldsymbol{i}_{k-1} \tag{10.16}$$

$$T_1 * |V_1| + \frac{1}{2} * T_2 * |V_2| = |\Delta\varphi_k| * \cos\theta \tag{10.17}$$

$$T_2 * |V_2| * \frac{\sqrt{3}}{2} = |\Delta\varphi_k| * \sin\theta \tag{10.18}$$

$$T_1 + T_2 + T_0 = T_S \tag{10.19}$$

In the scheme of [13], illustrated in Figure 10.19, a variable structure controller replaces the PI controller and RFVC. In this scheme, the control objectives are to

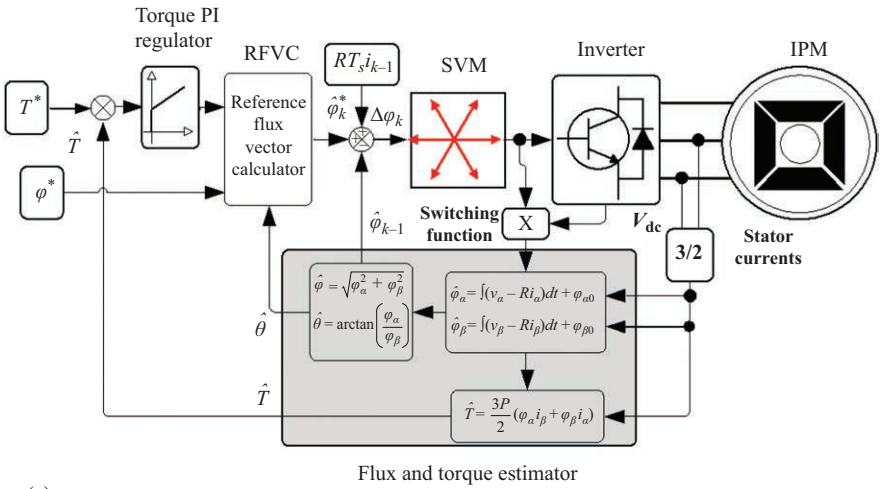


Figure 10.17 (a) DTC controller with RFVC and SVM and (b) RFVC

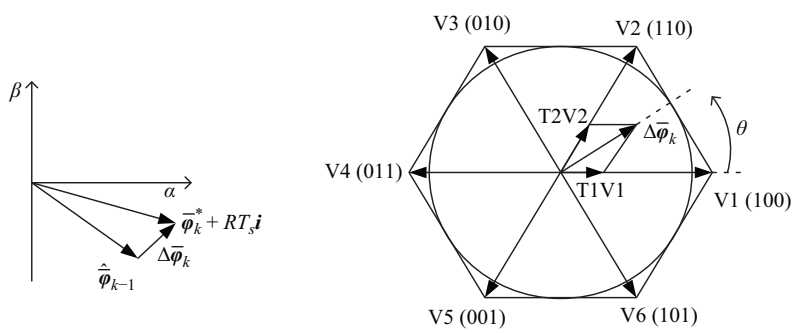


Figure 10.18 SVM with error voltage calculator for elimination of $\Delta\varphi_k$

force torque and flux-linkage errors, e_T and e_φ, along desired trajectories or the switching surface, $S = [\,S_1 \quad S_2\,]^T$, where

$$S_1 = e_T(t) + K_1 \int_0^t e_T(\tau)d\tau - e_T(0) \tag{10.20}$$

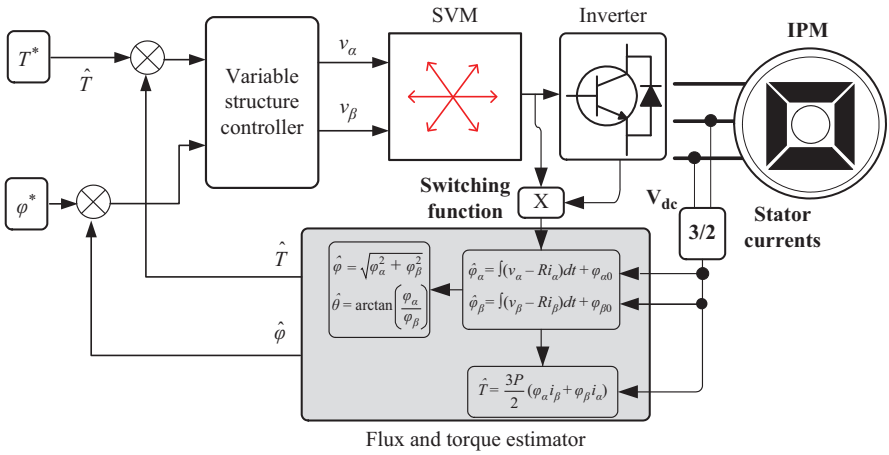


Figure 10.19 Torque and stator flux-linkage control using variable structure controller

$$S_2 = e_\varphi(t) + K_2 \int_0^t e_\varphi(\tau)d\tau - e_\varphi(0) \tag{10.21}$$

where $e_T = T_{\text{ref}} - T$ and $e_\varphi = \varphi_{\text{ref}} - \varphi$ are the errors between the references and the estimated values of torque and square of flux $\varphi = {\varphi_\alpha}^2 + {\varphi_\beta}^2$. K_1 and K_2 are positive control gains. When the system states have reached the sliding manifold and stay on the surface, then we have $S_1 = S_2 = \dot{S}_1 = \dot{S}_2 = 0$.

The derivatives of S are equal to zero, which gives

$$\frac{d}{dt}e_T = -K_1 e_T \tag{10.22}$$

$$\frac{d}{dt}e_\varphi = -K_2 e_\varphi \tag{10.23}$$

In order for the derivatives of the errors e_T and e_φ to converge to zero, K_1 and K_2 need to be positive constants and are chosen according to the desired system dynamics as the amplitudes determine the convergence rates of error dynamics. The design task is then reduced to enforcing sliding mode (SM) in the manifolds $S_1 = 0$ and $S_2 = 0$ with discontinuous stator voltage space vectors. The proof of stability of this scheme via Lyapunov approach is fully described in [13]. Torque and flux ripple performances of the PMSM motor of Table 10.6 under RFVC and VS controllers are shown in Figure 10.20(a) and (b), respectively. Clearly the ripples are much reduced compared to the basic DTC. The ripples in the stator currents, shown in Figure 10.21(a) and (b) for the two schemes, show most of the ripples confined around the fixed switching frequency corresponding to $T_s = 150$ μs.

The transient responses of torque under the two schemes are comparable to the response under basic DTC without SVM. These responses are shown in Figure 10.22(a) and (b). The RFVC is slightly slower than the VS and basic DTC, because of the PI controller used.

Table 10.6 Parameters of the IPM Motor IPMSM-II

Number of pole pairs	P	2
Stator resistance	R	5.8 Ω
Magnet flux linkage	φ_f	0.533 Wb
d-axis inductance	L_d	0.0448 H
q-axis inductance	L_q	0.1024 H
Phase voltage	V	132 V
Phase current	I	3 A
Base speed	ω_b	1,260 rev/min
Crossover speed	ω_c	1,460 rev/min
Rated torque	T_b	6 N-m
Rated power	P_r	1 kW

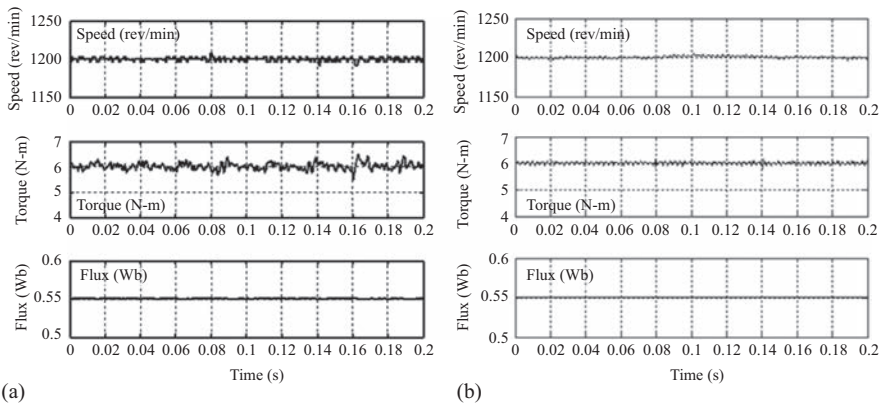


Figure 10.20 Steady-state torque and flux linkage under (a) RFVC-DTC and (b) VS-DTC, for operation at 1,200 rev/min with full load

10.4 Closed-loop flux and torque estimation

The FTE in the foregoing sections uses simple integrators in the stator $\alpha\beta$ reference frame. These estimators are prone to error due the following reasons:

1. the inaccuracy of the integrator equation as a result of drift due to offsets in the measurements of the inverter supply voltage V_{dc} and the stator current sensors,
2. dead times employed in the inverter switches and diode and voltage drops across the switches,
3. variation in stator temperatures due to temperature.

Because of these factors, accuracy of estimations of flux linkage and torque become poor at low speed when the fundamental input voltage to the machine and the back emf are small. With integrator-based FTE, the DTC performance deteriorates

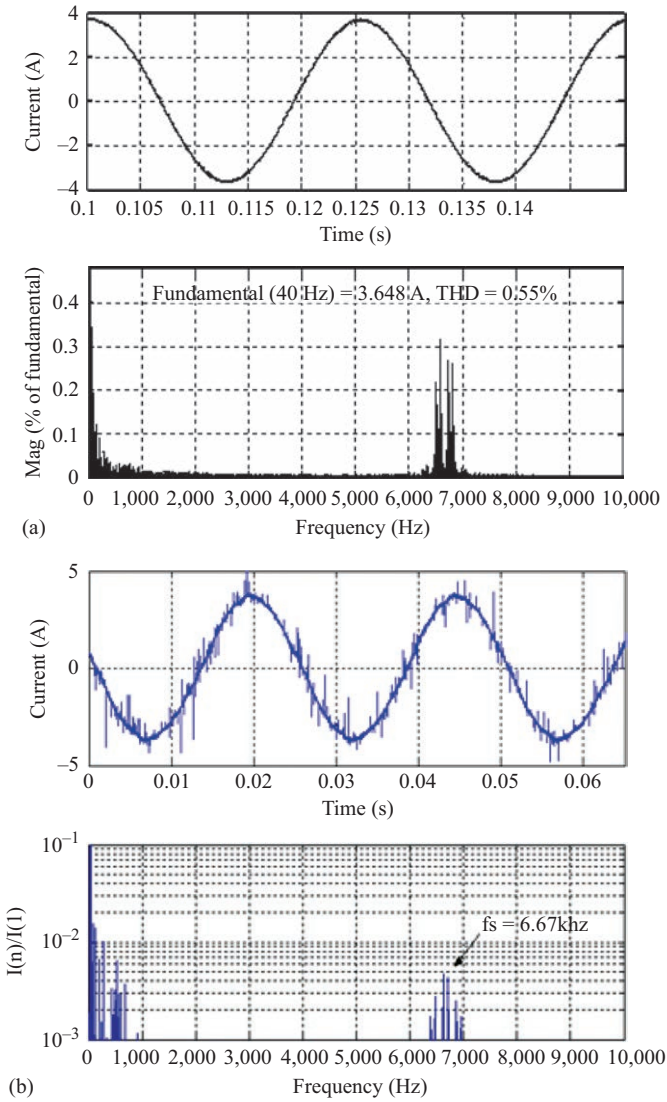


Figure 10.21 Steady-state phase current of the (a) PI-DTC and (b) VS-DTC and its spectrum at 1,200 rev/min with full load and $T_s = 150\ \mu s$

unacceptably at less than 10% of the base speed for a PMSM, leading to instability below this speed. In order to overcome the lack of accuracy of the FTE due to the abovementioned issues, closed-loop observers have been used. One of such closed-loop observers employs an SM observer [14,15] which has very good robustness and stability properties. A brief account of this stator flux observer is given in the following. In this method, both stator $\alpha\beta$ and estimator rotor dq frames are utilized in

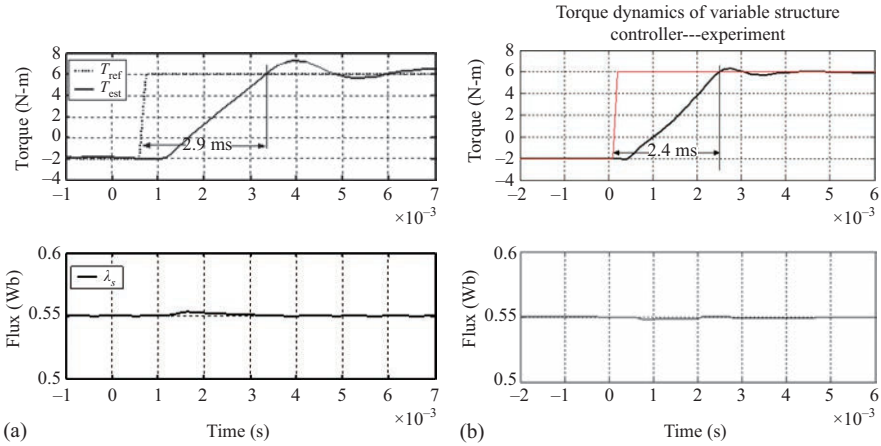


Figure 10.22 Dynamic torque and flux linkage under (a) RFVC-DTC (b) VS-DTC, for operation at 1,200 rev/min when torque reference changes from −2 to 6 N-m (full load)

order to remove the speed dependency of the observers that operate in only one of these frames.

$$\begin{pmatrix} \dot{\hat{\varphi}}_d \\ \dot{\hat{\varphi}}_q \end{pmatrix} = \begin{pmatrix} -\dfrac{\hat{R}}{L_d} & \hat{\omega}_{re} \\ -\hat{\omega}_{re} & -\dfrac{\hat{R}}{L_q} \end{pmatrix} \begin{pmatrix} \hat{\lambda}_d \\ \hat{\lambda}_q \end{pmatrix} + \begin{pmatrix} v_d \\ v_q \end{pmatrix} + \begin{pmatrix} \dfrac{R\varphi_f}{L_d} \\ 0 \end{pmatrix} + KS + \boldsymbol{\Phi}\ \text{sign}(S) \tag{10.24}$$

$$\begin{pmatrix} \hat{i}_d \\ \hat{i}_q \end{pmatrix} = \begin{pmatrix} \dfrac{1}{L_d} & 0 \\ 0 & \dfrac{1}{L_q} \end{pmatrix} \begin{pmatrix} \varphi_d \\ \varphi_q \end{pmatrix} - \begin{pmatrix} \dfrac{\varphi_f}{L_d} \\ 0 \end{pmatrix} \tag{10.25}$$

where superscript $\hat{}$ denotes estimated values and $\boldsymbol{K}$ and $\boldsymbol{\Phi}$ are the feedback gains of the observer. The sliding surface is defined by the stator current errors:

$$\boldsymbol{S} = \begin{pmatrix} S_1 \\ S_2 \end{pmatrix} = \begin{pmatrix} i_d - \hat{i}_d \\ i_q - \hat{i}_q \end{pmatrix} = \begin{pmatrix} \dfrac{1}{L_d} & 0 \\ 0 & \dfrac{1}{L_q} \end{pmatrix} \begin{pmatrix} \varphi_d - \hat{\varphi}_d \\ \varphi_q - \hat{\varphi}_q \end{pmatrix} \tag{10.26}$$

The flux estimation error dynamics is given by

$$\begin{pmatrix} \dot{\tilde{\varphi}}_d \\ \dot{\tilde{\varphi}}_q \end{pmatrix} = (A - KC) \begin{pmatrix} \tilde{\varphi}_d \\ \tilde{\varphi}_q \end{pmatrix} + \tilde{\omega}_{re} \begin{pmatrix} \tilde{\varphi}_d \\ -\tilde{\varphi}_q \end{pmatrix} - \tilde{R} \begin{pmatrix} \dfrac{\tilde{\varphi}_d - \varphi_f}{L_d} \\ \dfrac{\tilde{\varphi}_q}{L_q} \end{pmatrix} - \boldsymbol{\Phi}\ \text{sign}(\boldsymbol{S}) \tag{10.27}$$

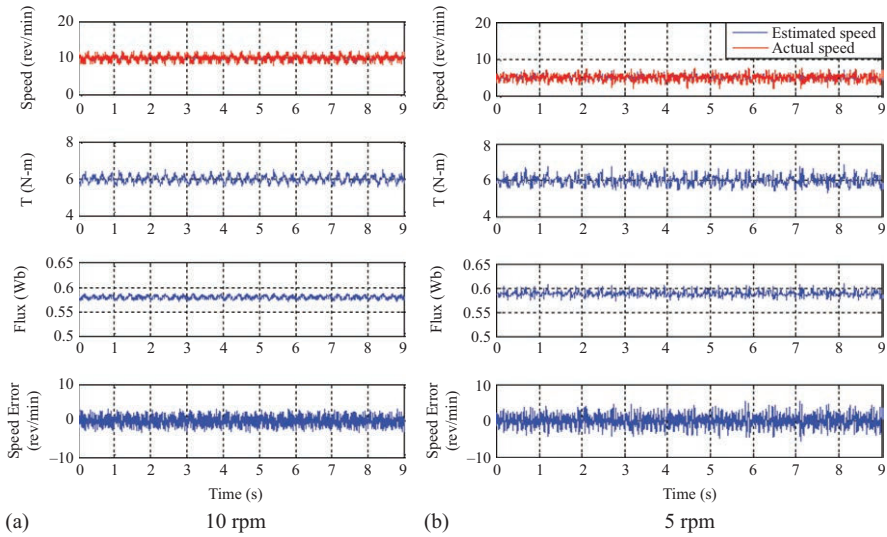


Figure 10.23 Steady-state torque and flux under SM observer at very low speeds, under full-load torque

$$A = \begin{pmatrix} -\dfrac{R_s}{L_d} & \hat{\omega}_{re} \\ -\hat{\omega}_{re} & -\dfrac{R_s}{L_q} \end{pmatrix}; \quad C = \begin{pmatrix} \dfrac{1}{L_d} & 0 \\ 0 & \dfrac{1}{L_q} \end{pmatrix} \tag{10.28}$$

The stability and robustness of this observer are available in [15,16]. The stator resistance R is also estimated within this observer.

Figure 10.23 shows torque and flux ripples when the PMSM is operated at very low speeds (10 and 5 rev/min). Torque and flux ripples are higher at 5 rev/min, as expected. These ripples are much smaller due to higher accuracy of the SM observer when the drive is operated at 1,200 rev/min, as shown in Figure 10.24. The dynamic responses of torque and flux when speed reference speed changes between −20 and +20 rev/min, as shown in Figure 10.25, are also satisfactory.

10.5 Control trajectories with DTC [10,11]

The foregoing sections have analyzed the DTC technique for a PMSM and its performance in the steady-state and dynamic conditions. The control trajectories defined by (10.7) and (10.8) must also be followed under this scheme with direct control of torque and flux linkage. This means that torque and flux-linkage references T^* and φ^* which are output of the speed controller must also satisfy the I_{sm} and V_{sm} limits while operating along the MTPA and FW trajectories derived in Sections 10.1.2 and 10.1.3 and indicated in Figure 10.3(a) and (b).

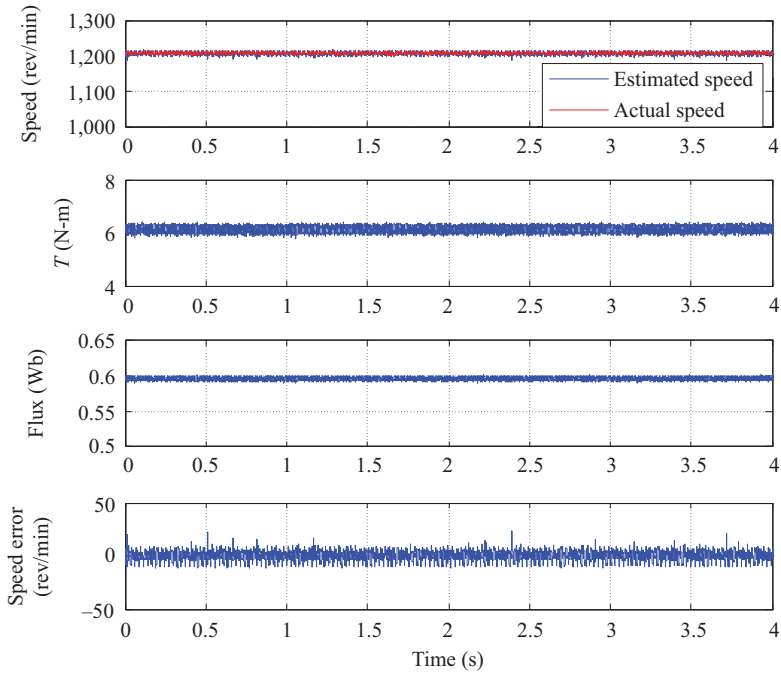


Figure 10.24 Steady-state torque and stator flux linkage under SM observer at 1,200 rev/min with full load

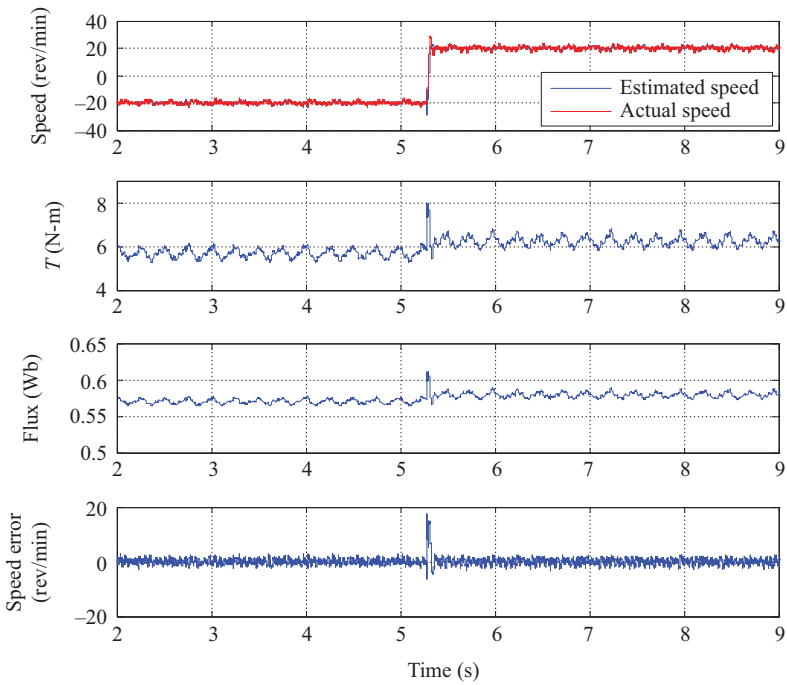


Figure 10.25 Dynamic response of the DTFC drive with SM observer for flux estimation from −20 to +20 rev/min with full load

It should be noted that for each i_d–i_q pair defined by the MTPA and FW trajectories in the i_d–i_q plane, there exist corresponding T, φ_s and δ values in (10.29)–(10.31).

$$T = \frac{3p}{2}\left[\varphi_f i_q + (L_d - L_q) i_q i_d\right] \tag{10.29}$$

$$\varphi_s = \sqrt{\left(\varphi_f + L_d\, i_d\right)^2 + \left(L_q\, i_q\right)^2} \tag{10.30}$$

$$\delta = \tan^{-1}\left(\frac{L_q\, i_q}{\varphi_f + L_d\, i_d}\right) \tag{10.31}$$

10.5.1 The MTPA trajectory under DTC

For the MTPA trajectory, using (10.6) and (10.30), the flux-linkage and load angle trajectories are given by

$$T = \frac{3}{2} P\left[\varphi_f + (L_d - L_q) i_d\right]\sqrt{i_d^2 - \frac{\varphi_f}{L_q - L_d} i_d} \tag{10.32}$$

$$\varphi_s = \sqrt{\varphi_f^2 - \left(\frac{L_d^2}{L_q - L_d} + L_q - L_d\right)\varphi_f\, i_d + \left(L_d^2 + L_q^2\right) i_d^2} \tag{10.33}$$

$$\delta = \tan^{-1}\left(\frac{L_q}{\varphi_f + L_d\, i_d}\sqrt{i_{\mathrm{d}}^2 - \frac{\varphi_f}{L_{\mathrm{q}} - L_{\mathrm{d}}} i_d}\right) \tag{10.34}$$

The relationships among φ_s, δ and positive torque T for a PMSM are shown in Figure 10.13. For negative torque, φ_s remains the same and δ becomes negative.

As shown in Figure 10.26, both the amplitude and angle of φ_s increase with the increase in torque. When torque is zero, angle d is also zero, and the stator flux is

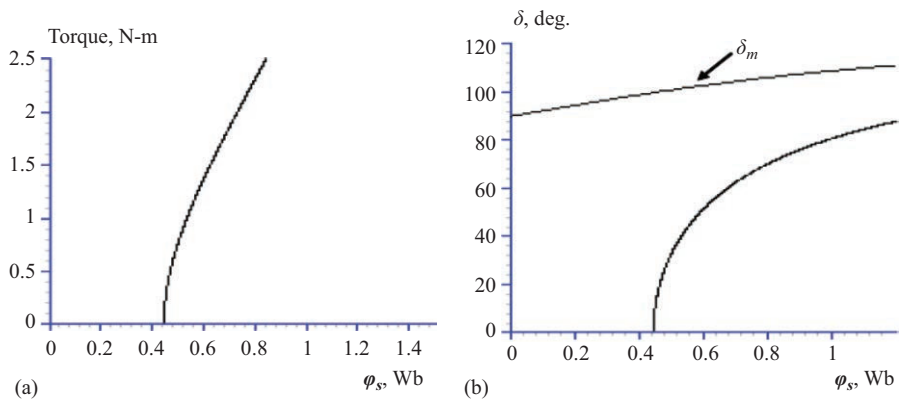


Figure 10.26 Torque and δ as a function of the amplitude of stator flux linkage for the MTPA trajectory

equal to the rotor flux. As is also shown in this figure, the load angle δ cannot exceed δ_m with the MTPA control when the torque is limited below the maximum torque the motor can produce.

Also, according to (10.29), if two of the three variables, namely T, φ_s and δ, are known, the third one is uniquely determined. Provided the torque is known, MTPA control is achieved if the amplitude or the angle of the stator flux is determined from the MTPA trajectory of Figure 10.26, which can be stored in a lookup table [10]. For DTC, it is obvious that the torque and the amplitude of the stator flux linkage, rather than its angle, should be controlled. When the torque and φ_s are controlled in this way, the angle δ will be automatically controlled and it will not exceed δ_m.

10.5.2 Current and voltage trajectories in the T-λ_s plane

Similar to the trajectory control described in Sections 10.1.2 and 10.1.3, the maximum current and voltage constraints of the motor/inverter have to be also taken into account under DTC when the motor operates in the constant-torque (i.e., below base speed) and FW regions (above base speed) [11]. The current and voltage constraints are rewritten in (10.35) and (10.36), respectively:

$$|i_d| = \sqrt{I_{sm}^2 - i_q^2} \tag{10.35}$$

$$|v_d| = \sqrt{V_{sm}^2 - v_q^2} \tag{10.36}$$

From (10.32), (10.33) and (10.35), the current limit trajectory in the T-λ_s plane can be plotted as shown in Figure 10.27.

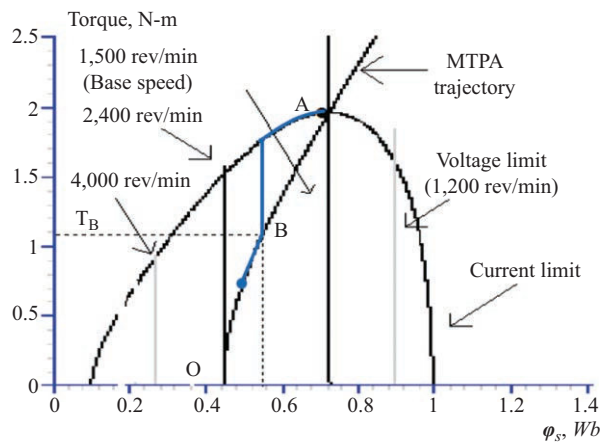


Figure 10.27 MTPA, current limit and voltage limit trajectories with DTC

Because the stator voltage is proportional to the product of the rotational speed and the amplitude of the stator flux linkage, if the stator resistance is neglected,

$$V_s = \omega_r \varphi_s \tag{10.37}$$

where ω_r is the rotational speed of the stator flux linkage.

The maximum voltage trajectories for a motor can be determined by each (i_d, i_q) pair and speed, and by using steady-state voltage (10.4) and (10.5). From (10.36), the maximum voltage limit for each speed is a vertical line (if voltage drop in stator resistance is neglected), as indicated in Figure 10.27. As speed increases, these lines move to the left as is also indicated.

The current limit is satisfied if T and φ_s are controlled on and below the current limit trajectory. The intersection of the current limit and MTPA trajectories is at A in Figure 10.27, which corresponds to the operating point with the maximum torque and current with MTPA. For operation below the base speed, torque and flux references should be selected along OA. Below base speed, the voltage limit trajectories are to the right of the MTPA OA. Therefore, there is no requirement here to control the amplitude of the stator flux linkage φ_s to satisfy the voltage limit.

As the rotor speed increases, the voltage limit trajectories move to the left of the intersection point A and the stator flux will have to be reduced in order to satisfy the voltage limit requirement. For operation above base speed, the trajectory to the right of A is selected. Part of this trajectory can be load dependent—it can be along the MPTA, i.e., along OA if the load torque is below the torque represented by the MTPA trajectory or along the current limit and voltage-limited FW trajectories if it is higher [10].

10.5.3 Performance of PMSM under DTC with trajectory following

The trajectory following of a PMSM with wide FW or CPSR range is indicated in Figure 10.28. The motor is accelerated from zero speed under MTPA. Current reaches limiting value before speed reaches base speed. Current limit and voltage trajectories are followed from 1,500 along intersections of the current limit and voltage limit trajectories. As the drive reaches its reference speed, torque reference from the speed controller reduces and the drive finally settles the desired speed.

10.6 Summary

This chapter gives an account of the DTC technique for PMSMs. It starts with the context of its development and compares its performances with benchmarks from the RFOC which uses a high-resolution speed/position sensor mounted on the shaft to enable control in the rotor reference from via coordinate transformations. Dynamic performances of a PMSM under DTC were compared with performances under RFOC for the same machine, inverter and operating conditions for operation at speed above 10% of the base speed where DTC can work well with flux and torque estimations based on integration of back emf. Performance limitations at lower speed due to the inaccuracies inherent in the simple

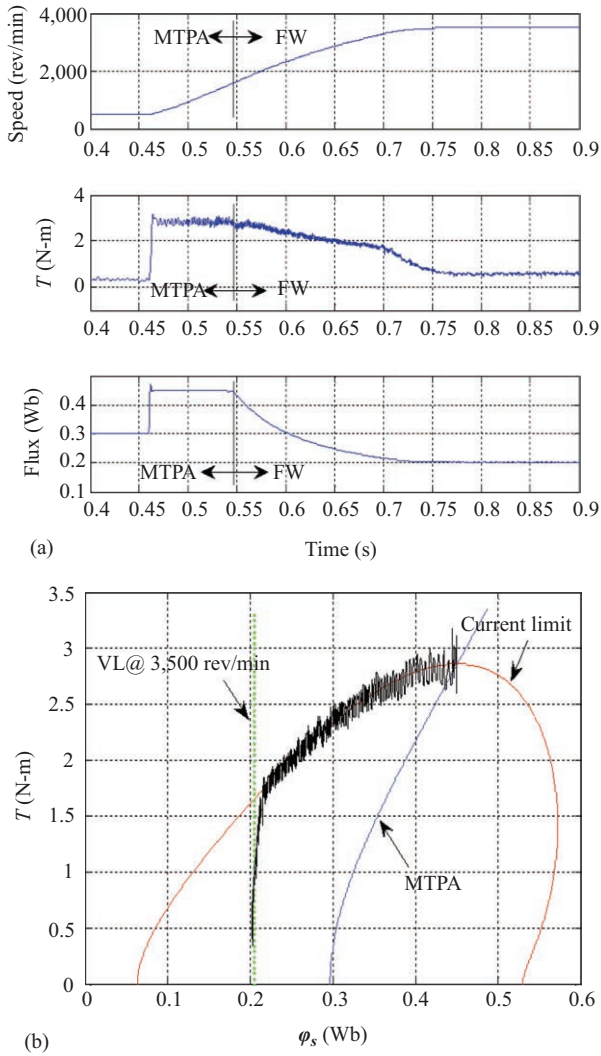


Figure 10.28 (a) Dynamic responses of torque, flux linkage and speed of a four-pole PMSM over a wide-speed range and (b) MTPA and FW trajectories following under DTFC under current and voltage limits

integrator-based FTE and limitations of the variable and low-frequency switching of the basic DTC were brought out. It was shown how SVM technique has allowed fixed-frequency switching. The usefulness of a closed-loop SM flux observer for delivering much higher accuracy flux and torque estimation, resulting in very low-speed operation, was also shown. Finally, the incorporation of optimum torque and flux control trajectories that operate the machine within its maximum current/torque and voltage limits below base speed and in the FW region under DTC was also described.

List of symbols

φ_f	Rotor flux linkage
P	Number of pole pairs
R	Stator resistance
L_d	d-axis inductance
L_q	q-axis inductance
V	Phase voltage
I	Phase current
ω_b	Base speed
T_b	Rated torque
ω_c	Crossover speed
T^*	Torque reference
φ^*_s	Stator flux-linkage reference
$\boldsymbol{\varphi_s}$	Stator flux vector
$\boldsymbol{\varphi_f}$	Rotor flux vector
δ	Load angle
P_r	Rated power
T_b	Rated torque
ω_r	Rotational speed

Glossary of terms

Current trajectories	Current references selected by the current reference generator according to requirements
Rotor flux-oriented control	Control of motor speed and torque using current and voltage vectors

References

[1] M. Depenbrock, "Direct self-control (DSC) of inverter-fed induction machines," *IEEE Transactions on Power Electronics*, vol. 3, no. 4, pp. 420–429, 1988.

[2] I. Takahashi and T. Noguchi, "A new quick response and high efficiency control strategy of an induction motor,'' *IEEE Transactions on Industry Applications*, vol. IA-22, no. 5, pp. 820–827, 1986.

[3] B.K. Bose, *Power Electronics and Drives*, Prentice Hall, Upper Saddle River, NJ, 1982.

[4] S. Sul, *Control of Electric Machine Drive Systems*, IEEE Press and Wiley, Piscataway, NJ, 2011.

[5] I. Boldea and S.A. Nasar, *Electric drives*, CRC Press, Boca Raton, FL, 2016.

[6] T.G. Habetler, F. Profumo, M. Pastorelli and L.M. Tolbert, Direct Torque Control of Induction Machines Using Space Vector Modulation, *IEEE Transactions on Industry Applications*, vol. 28, no. 5 1992.

[7] C. Lascu, I. Boldea and F. Blaabjerg, "A modified direct torque control (DTC) for induction motor sensorless drive,'' *IEEE Transactions on Industry Applications*, vol. 36, no. 1, pp. 122–130, 2000.
[8] T.M. Jahns, "Flux-weakening regime operation of an interior magnet synchronous motor drive,'' *IEEE Trans. on Industry Applications*, vol. IA-23, no. 4, pp. 681–689, 1987.
[9] S. Morimoto, M. Sanada and Y. Taketa, "Wide-speed operation of interior permanent magnet synchronous motors with high-performance current regulator,'' *IEEE Trans. on Ind. Appl*., vol 30, no. 4, pp. 920–926, 1994.
[10] L. Zhong, M.F. Rahman and W.Y. Hu, "Analysis of direct torque control in permanent magnet synchronous motor drives,'' *IEEE Transactions on Power Electronics*, vol. 12, no. 3, pp. 528–536, 1997.
[11] M.F. Rahman, L. Zhong, K.W. Lim, "A direct torque controlled interior magnet synchronous motor drive incorporating field weakening,'' *IEEE Transactions on Industry Applications*, vol. 34, no. 6, pp. 1246–1253, 1998.
[12] L. Tang, L. Zhong, M.F. Rahman and Y. Hu, "A novel direct torque controlled interior permanent magnet synchronous machine drive with low ripple in flux and torque and fixed switching frequency,'' *IEEE Transactions on Power Electronics*, vol. 19, no. 2, pp. 346–354, 2004.
[13] Z. Xu and M.F. Rahman, "Direct torque and flux regulation for an IPM synchronous motor drive using variable structure control approach,'' *IEEE Transactions on Power Electronics*, vol. 22, no. 6, pp. 2487–2499, 2007.
[14] Z. Xu and M.F. Rahman, "An adaptive sliding stator flux observer for a direct torque controlled IPM synchronous motor drive," *IEEE Transactions on Industrial Electronics*, vol. 54, no. 5, pp. 2398–2406, 2007.
[15] G. Foo and M.F. Rahman, "Direct torque control of an IPM synchronous motor drive at very low speed using a sliding mode stator flux observer,'' *IEEE Transactions on Power Electronics*, vol. 25, no. 4, pp. 933–942, 2010.
[16] D. Xiao and M.F. Rahman, "Sensorless direct torque and flux controlled IPM synchronous machine fed by matrix converter over a wide speed range,'' *IEEE Transactions on Industrial Informatics*, vol. 9, no. 4, pp. 1855–1867, 2013.

General reading on DTC

[1] D. Casadei, F. Prpfumo, G. Serra and A. Tani, "FOC and DTC: two viable schemes for induction motors torque control,'' *IEEE Transactions on Power Electronics*, vol. 17, no. 5, pp. 779–787, 2002.
[2] G.S. Buja and M. Kazmierkowoski, "Direct torque control of PWM inverter-fed AC motors – a survey,'' *IEEE Transactions on Industrial Electronics*, vol. 51, no. 4, pp. 744–757, 2004.
[3] M. Kazmierkowski, L.G. Franquelo, J. Rodriguez, M.A. Perez and J.I. Leon, "High-perfromance motor drives,'' *IEEE Industrial Electronics Magazine*, vol. 5, no. 3, pp. 6–26, 2011.

Chapter 11

Matrix converter-driven AC motor drives

Dan Xiao[1] and Muhammed Fazlur Rahman[1]

The matrix converter (MC) is an AC–AC power converter topology. The MC topologies are classified into two types: direct MC (DMC) and the indirect MC (IMC) [1]. The IMC topology is composed of a rectifier with six bidirectional switches (BDSs) and a conventional voltage source inverter (VSI) [2,3]. The large energy storage elements are eliminated from the intermediate DC-link in this topology. The DMC consists of a matrix of fully controlled BDSs which directly connect any output phase to any input phase without using any DC-link or energy storage elements. A variable output voltage of a desired magnitude and frequency can be generated by modulating the gating pulses of BDSs in the MC [4–6].

This chapter mainly focuses on direct torque control (DTC) for MC-driven interior permanent magnet synchronous machine (IPMSM) drive. First of all, it gives a brief overview on the fundamentals of MC followed by the implementation of BDSs for MC. Two current commutation strategies based on input voltage sign and output current direction, respectively, are presented in this chapter. Some other practical issues of MC are also discussed in this chapter, in terms of input filter design and overvoltage protection. Different modulation strategies for MC are briefly reviewed in this chapter. Among these methods, the indirect space vector modulation (SVM) is demonstrated by considering the MC as a two-stage converter, rectifier and inverter stages. The open-loop and closed-loop input power factor (IPF) compensation schemes are presented followed by the DTC schemes for MC drives.

In the conventional DTC for MC drives, the IPF of the MC and the torque and stator flux of the motor are regulated with three hysteresis comparators, respectively. An improved DTC scheme is presented in this chapter. It allows great reduction of input current harmonics without sacrificing the output performance or increasing the complexity of the system. Combination of DTC with indirect space vector modulation (ISVM) for MC can solve the associated problems with hysteresis DTC scheme, such as high torque and flux ripples, high input/output harmonics and variable switching frequency. In the direct torque and flux control (DTFC), closed-loop control of both torque and stator flux is realized on the stator flux

[1]School of Electrical Engineering and Telecommunications, University of New South Wales, Sydney, Australia

reference frame. The DTFC for the MC employs ISVM to synthesize the required input current and output voltage vectors. Experimental verification has been carried out, confirming the effectiveness of each DTC scheme and the performance improvement of the DTFC-ISVM scheme.

IMC-driven motor drives are discussed in the last part of the chapter. The modulation scheme and indirect rotor flux-oriented control (IRFOC) of induction machine drive are presented in this part.

11.1 Matrix converter

The general MC is defined as a single-stage converter which consists of a matrix of $m \times n$ BDSs to directly connect an m-phase voltage source to an n-phase load. Typically, a 3×3 MC, as shown in Figure 11.1, has attracted the highest practical interest as it connects a three-phase voltage source, a standard AC mains, to a three-phase load, a standard motor. The purpose of this section is to give a brief review of the main aspects concerning three-phase-to-three-phase MC operation and basic issues of this topology. It is worth noting that this direct input–output connecting configuration by a 3×3 matrix of BDSs is just one of the possible MC topologies [7–9].

11.1.1 Fundamentals of MC

The relationships between input and output quantities can be expressed as (11.1) and (11.2), where each element in the instantaneous transfer matrix represents the status of each BDS of the MC.

$$\begin{bmatrix} v(t)_{o,A} \\ v(t)_{o,B} \\ v(t)_{o,C} \end{bmatrix} = \begin{bmatrix} S(t)_{aA} & S(t)_{bA} & S(t)_{cA} \\ S(t)_{aB} & S(t)_{bB} & S(t)_{cB} \\ S(t)_{aC} & S(t)_{bC} & S(t)_{cC} \end{bmatrix} \begin{bmatrix} v(t)_{in,a} \\ v(t)_{in,b} \\ v(t)_{in,c} \end{bmatrix} \tag{11.1}$$

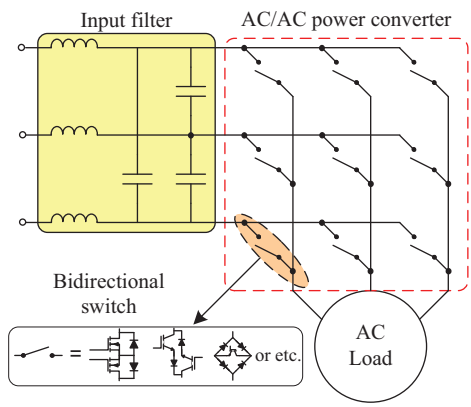


Figure 11.1 Power circuit of three-to-three-phase MC

$$\begin{bmatrix} i(t)_{in,a} \\ i(t)_{in,b} \\ i(t)_{in,c} \end{bmatrix} = \begin{bmatrix} S(t)_{aA} & S(t)_{aB} & S(t)_{aC} \\ S(t)_{bA} & S(t)_{bB} & S(t)_{bC} \\ S(t)_{cA} & S(t)_{cB} & S(t)_{cC} \end{bmatrix} \begin{bmatrix} i(t)_{o,A} \\ i(t)_{o,B} \\ i(t)_{o,C} \end{bmatrix} \partial \tag{11.2}$$

where $S_{iJ} = \begin{cases} 1, \text{switch } S_{iJ} \text{ closed} \\ 0, \text{switch } S_{iJ} \text{ open} \end{cases} (i = a, b, c; J = A, B, C).$

Since MC is a voltage-fed system at the input and a current-fed at the output, the following two requirements must be fulfilled at any time expressed as (11.3): no short circuit between input terminals and no open circuit on the output terminals. Therefore, an output must be connected all the time to one and only one of the input terminals to avoid output current interruption and short circuit between input phases.

$$S_{aJ} + S_{bJ} + S_{cJ} = 1 \tag{11.3}$$

Generally, the digital control algorithm is executed in every sampling period which is normally the same as switching period. Therefore, the instantaneous mathematic model is not applicable to digital control, and the turn-on time of each BDS in each sampling period should be found out by the modulation strategy. Considering that the switching frequency is much higher than the frequencies of input and output, the relationships between input and output quantities of the MC can be described with a low-frequency transfer matrix as (11.4) and (11.5). $m_{iJ}(t)$ is the duty cycle of BDS S_{iJ}, defined as $m_{iJ}(t) = T_{iJ}/T_S$. All the modulation strategies aim to find the solutions to this low-frequency transfer matrix in the MC mathematic model.

$$\begin{bmatrix} v(t)_{o,A} \\ v(t)_{o,B} \\ v(t)_{o,C} \end{bmatrix} = \begin{bmatrix} m(t)_{aA} & m(t)_{bA} & m(t)_{cA} \\ m(t)_{aB} & m(t)_{bB} & m(t)_{cB} \\ m(t)_{aC} & m(t)_{bC} & m(t)_{cC} \end{bmatrix} \begin{bmatrix} v(t)_{in,a} \\ v(t)_{in,b} \\ v(t)_{in,c} \end{bmatrix} \tag{11.4}$$

$$\begin{bmatrix} i(t)_{in,a} \\ i(t)_{in,b} \\ i(t)_{in,c} \end{bmatrix} = \begin{bmatrix} m(t)_{aA} & m(t)_{aB} & m(t)_{aC} \\ m(t)_{bA} & m(t)_{bB} & m(t)_{bC} \\ m(t)_{cA} & m(t)_{cB} & m(t)_{cC} \end{bmatrix} \begin{bmatrix} i(t)_{o,A} \\ i(t)_{o,B} \\ i(t)_{o,C} \end{bmatrix} \tag{11.5}$$

where $m_{aJ} + m_{bJ} + m_{cJ} = 1$ and $0 \le m_{iJ} \le 1 \quad (i = a, b, c; \quad J = A, B, C)$.

11.1.2 Implementation of MC

11.1.2.1 BDS realization

A BDS, also called four-quadrant switch, has to be capable of conducting current and blocking voltage in both directions. Unfortunately, there are no such devices available so far. Consequently, discrete unidirectional semiconductor devices have to be used to construct suitable four-quadrant switch. Figure 11.2 shows different BDS configurations using discrete devices. The diode-bridge (DB) BDS composed of one active device at the center of a single-phase DB requires only one gate driver

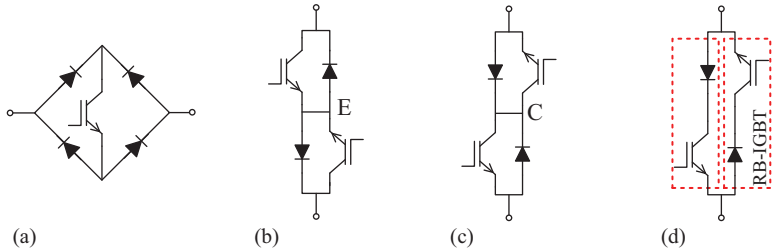


Figure 11.2 Typical BDS arrangements: (a) DB BDS, (b) CE BDS, (c) CC BDS, and (d) RB-IGBT BDS

with one isolated power supply, but its conduction losses are higher than other arrangements. Moreover, some advanced commutation strategies are not allowed with only one controllable device per BDS [10]. The common emitter (CE) and common collector (CC) BDSs consist of two active devices and two diodes connected in antiparallel as shown in Figure 11.2(b) and (c). The diodes are included to provide the reverse blocking capability. The CC and CE arrangements allow independent control of the current direction, and it is more flexible to perform the current commutation between input phases with these two configurations. Compared to the DB arrangement, the conduction losses are reduced since less number of devices conduct current at any one time. Using the active devices with reverse voltage block capability, such as reverse blocking IGBT (RB-IGBT) [11–13], can reduce the total number of devices in the converter, eliminating two antiparallel diodes from each BDS.

In regard to the gate driver circuit, the CE BDS MC requires nine isolated gate drive power supplies. The CC and RB-IGBT arrangements only require six isolated power supplies. However, the CE arrangement is much easier to make a modular structure with only one isolated gate drive power supply per BDS. It may be better for compact design of high-power MCs. In practice, the operation with only six isolated supplies is generally not viable due to the stray inductance of input and output bus bars for the CC and RB-IGBT arrangements.

Integrated power module leads to a very compact converter. The circuit layout is improved and the stray inductance is minimized. A few manufacturers offered commercial power modules for MC applications as shown in Table 11.1. These range from individual BDSs to three-phase-to-single-phase modules to entire three-phase-to-three-phase converters. The first all-in-one matrix module was developed by EUPEC/Infineon [14]. Many experimental and demonstration projects used this CC full three-phase-to-three-phase module rated at 35 A and 1,200 V as the basis for the MC [15,16]. It offers a very high level of integration and power density. Fuji Electric developed three-phase-to-three-phase MC modules based on RB-IGBT arrangement in order to reduce the on-state loss of BDSs by eliminating on-state loss of series-connected diodes.

Since Venturini first presented the modulation strategy for MC operation in 1980 [17], the MC technology has been widely studied [1–16]. Through the

Table 11.1 Commercial integrated power modules for matrix converter [6]

Ratings	Part no.	Arrangement	No. of BDSs	Manufacturer
600 V/100 A	18MBI100W-060	RB-IGBT	9	Fuji
600 V/200 A	18MBI200W-060	RB-IGBT	9	Fuji
1,200 V/100 A	18MBI100W-120	RB-IGBT	9	Fuji
1,200 V/50 A	18MBI50W-120	RB-IGBT	9	Fuji
1,200 V/200 A	DIM200MBS12-A	CE	1	Dynex
1,700 V/400 A	DIM400PBM17	CE	1	Dynex
1,700 V/600 A	DIM600EZM17-E000	CE	3	Dynex
1,200 V/50 A	FIO50-12BD	DB	1	Ixys
1,000 V/60 A	IXRH50N100	RB-IGBT	1	Ixys
1,200 V/60 A	IXRH50N120	RB-IGBT	1	Ixys
600 V/300 A	SML300MAT06	CE	3	Semelab
1,200 V/150 A	SML150MAT12	CE	3	Semelab
1,200 V/35 A	FM35R12KE3	CC	9	Eupec/Infineon
1,200 V/60 A	SK60GM123	CE	1	Semikron

continuous R&D efforts, Yaskawa and Fuji Electric Systems have successfully commercialized the MC products at the general drives market [18,19]. Both series are aimed at the high energy efficiency, low harmonics, line regeneration, compact all-in-one unit and solving typical motor drive issues, such as bulky and lifetime-limited DC bus capacitors, bearing currents and common mode currents.

11.1.2.2 Input filter design

Although the MC is regarded as an all-silicon solution to power conversion, due to the elimination of the bulky and expensive DC-link capacitors from conventional indirect frequency converters, it also requires a minimum of reactive components found in the input filter and clamp circuit. However, typically the size of input inductor of an MC will almost always be smaller than that of an equivalently rated PWM converter [6]. The input filter provides a voltage-stiff port to the MC circuit and attenuates the undesired switching harmonics injected into the power supply.

Although multistage filter topology is preferable in order to achieve higher attenuation at the switching frequency, the single-stage LC filter is the best alternative considering cost, size and complexity [20,21]. Figure 11.3 shows several possible configurations of single-stage LC filters. The design of the LC input filter has to take the following requirements into account [4,21].

An input filter has a cut-off frequency lower than the switching frequency of the converter. The resonant frequency of the filter has to be positioned between the fundamental and the switching frequencies, where no unwanted harmonic components exist. This requirement restricts the range of the product of inductance and capacitance.

$$f_n \ll f_0 = \frac{1}{2\pi\sqrt{L_f \cdot C_f}} \ll f_S \tag{11.6}$$

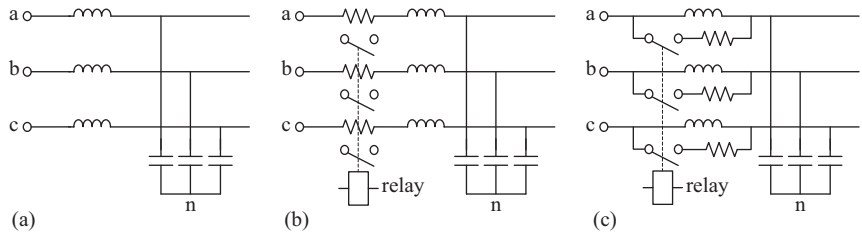


Figure 11.3 Possible single-stage LC filter configurations: (a) simple LC filter, (b) series damping resistors, and (c) parallel damping resistors

where L_f and C_f are the inductance and capacitance of the input filter and f_n, f_0 and f_s are the fundamental frequency of the power supply, resonant frequency of the input filter and switching frequency of the MC, respectively.

The second requirement is to maximize the IPF, cos φ, at the grid frequency for a given minimum output power, $P_{o\,\min}$. Considering an ideal MC and neglecting the voltage drop across the inductor, the displacement angle between the filter input voltage and current is proportional to the filter capacitance as follows:

$$C_{f\,\max} = \frac{P_{o\,\min}}{3\omega_n U_n^2} \cdot \tan\varphi_{\min} \tag{11.7}$$

where $P_{o\,\min}$ is the minimum power level where the displacement angle reaches its limit $\varphi_{\min}$, and U_n and ω_n are the rated input phase voltage and angular frequency of the power grid, respectively.

Therefore, in order to maintain a high IPF in the whole operation region, the capacitor size has to be minimized. The upper limit for the filter capacitance can be found at $P_{o\,\min}$ for a given $\varphi_{\min}$. Although the input displacement factor due to large capacitance can be compensated to unity, the compensation will sacrifice the maximum voltage transfer ratio of MC.

The last but not the least requirement is to minimize the filter inductor voltage drop at the rated current in order to provide the highest output voltage.

$$\frac{\Delta U}{U_n} = 1 - \sqrt{1 - \left(\omega_n \cdot L_f\right)^2 \cdot \left(\frac{I_n}{U_n}\right)^2} = 1 - \sqrt{1 - l_f^2} \tag{11.8}$$

where ΔU is the voltage drop in voltage magnitude due to the input filter inductor and l_f is the filter inductance in p.u. (p.u. $= U_n/\omega_n I_n$). ΔU is the voltage which is not transferred to the output of the MC at any transfer ratio.

The input filter design also has to consider different power density of film capacitors and iron chokes to minimize the volume and weight of the input filter.

$$\frac{S_L}{S_C} = \frac{\omega_n \cdot L_f \cdot I_n^2}{\omega_n \cdot C_f \cdot U_n^2} = \frac{1}{\left(3 \cdot \omega_0 \cdot U_n^2\right)^2} \cdot \left(\frac{P_n}{C_f}\right) \tag{11.9}$$

where S_L and S_C are the installed volt-ampere (VA) in reactive components, $\omega_0 = 2\pi f_0$ and $P_n = 3 \cdot U_n \cdot I_n$, the input active power at unity power factor at rated load.

In order to reduce the level of oscillating energy accumulating in the filter inductor during transients, parallel damping resistors are used to bypass the inductors in practice [22]. Neglecting the resistance of the inductor, the damping factor ζ of the LC filter can be simplified as follows:

$$\zeta = \frac{1}{2R_d}\sqrt{\frac{L_f}{C_f}} \tag{11.10}$$

There is a conflict between the damping factor and filtering performance. The higher the damping factor (the lower the resistance) is, the worse the high-frequency attenuation capability is and the higher the loss is on the damping resistor [22]. The damping factor has to be selected for a compromise solution to both of resonance frequency damping performance and high-frequency harmonic attenuation.

11.1.2.3 Power circuit layout

As discussed in [5], the input of the MC is the voltage-stiff (capacitive) port and the output is the inductive current-stiff port. For a typical three-phase LC input filter, the filter capacitors generally make the voltage-stiff input of the MC. Therefore, it is important that the input filter capacitors need to be properly integrated into the power circuit to achieve safe current commutation between BDSs. As there are nine BDSs connected to the voltage-stiff input port, three for each phase, in the MC circuit, one of solutions with minimized parasitic inductance between the input filter capacitors and the power stage is to connect the capacitor as close as possible to the BDSs as shown in Figure 11.4. As each input connects to three BDSs, a capacitor with the capacitance value $C_f/3$ is connected to each BDS on this phase, totally nine such capacitors for a three-phase MC.

11.1.2.4 Protections

Similar to any other static converters, the MC needs to be prevented from failure under fault conditions. Such faults may result in overvoltage, overcurrent and even short circuit which might be destructive to its semiconductor devices. Overcurrent protection needs to monitor the current by resistor sensing or current transducer. When the detected current reaches the overcurrent protection level, the converter will be immediately shut down by turning off all switches or reducing the motor current to zero by a controlled shutdown, controlling freewheeling states without causing overvoltage [23]. As shown in Figure 11.5, short-circuit protection can be done within the gate drive circuit by detecting IGBT collector–emitter voltage, *Vce*. In case of a short circuit, the saturation voltage will rise and the driver will detect a short circuit. The IGBT is switched off, a short circuit is indicated and converter is forced to shut down. The trip reference level can be adjusted according to the IGBT's transfer characteristic and current rating.

Furthermore, the MC is more sensitive and susceptible to disturbances due to the lack of DC-link energy storage elements and freewheeling paths. An overvoltage

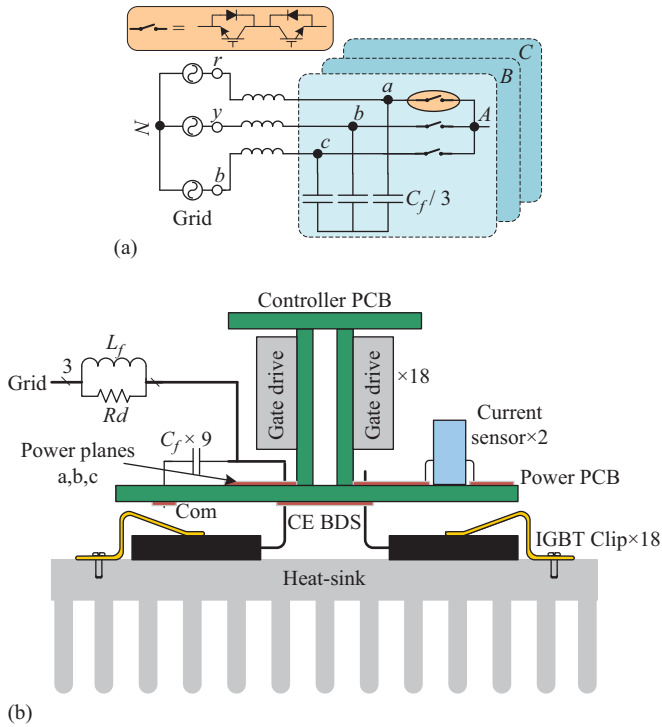


Figure 11.4 (a) Input filter arrangement and (b) power circuit layout of an MC prototype

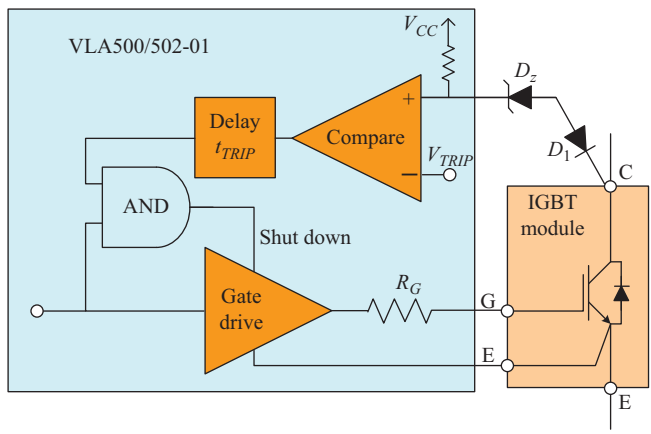


Figure 11.5 Schematic of desaturation-based short-circuit protection

may be caused by such disturbances as voltage spikes due to faulty commutation or parasitic inductance, forced shutdown of the converter due to the overcurrent or short-circuit failure and possible overvoltage originated by input line perturbations. Therefore, protection issues exist in both the grid and the motor side of MC. A straight and simple solution is to connect a capacitor clamp circuit to the input and output terminals via two three-phase fast recovery DBs [24], as shown in Figure 11.6. A new clamp configuration uses six diodes from the BDSs and six extra diodes to achieve the same purpose [25]. But it requires a special arrangement of placing three CE BSDs in the switch matrix with three more isolated power supplies for gate drivers.

An alternative strategy replaces the clamp circuit by varistors to protect each IGBT [26]. Varistors are connected across the terminals at the input and output of the converter, respectively, as shown in Figure 11.7. Bidirectional transient voltage suppressor provides fast clamping action without aging problem of varistors. Since the standoff voltage of a single power Zener diode (see Figure 11.8) nowadays has not reached the voltage levels in many standard industrial applications, this method is suitable for low-voltage stress applications [27].

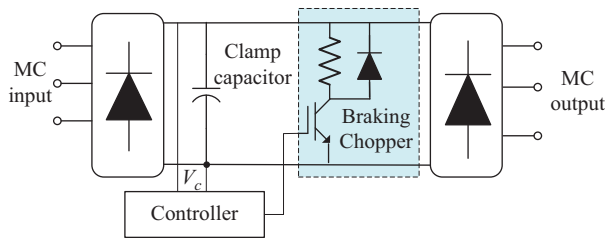


Figure 11.6 Diode clamp circuit for MC

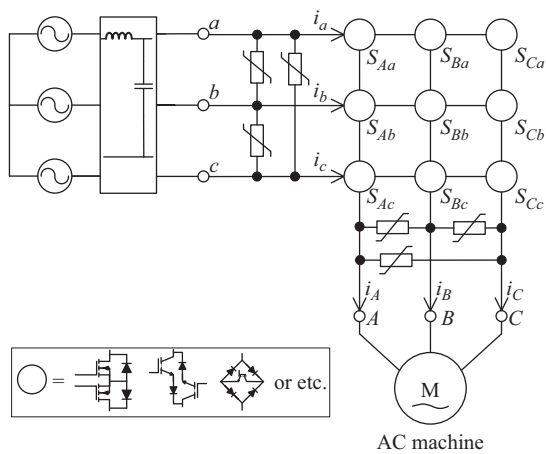


Figure 11.7 Varistor clamp circuit for MC

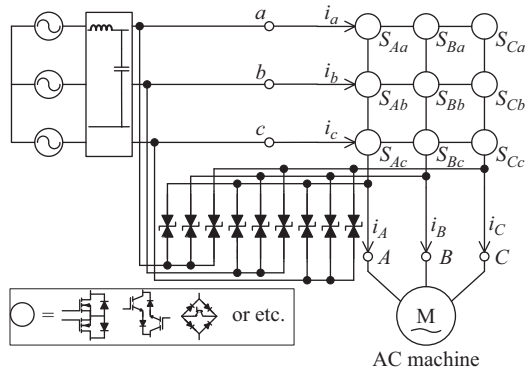


Figure 11.8 Zener diode clamp circuit for MC

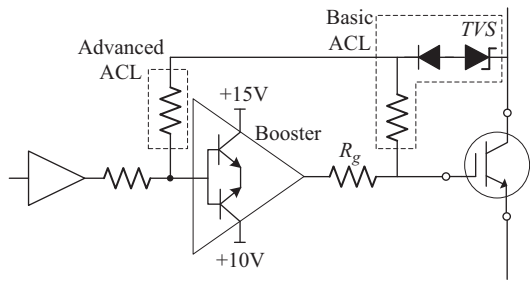


Figure 11.9 Transient voltage suppressor-active clamping circuit for MC

To protect a single IGBT against overvoltage, the gate driver of each IGBT contains an active clamping function as shown in Figure 11.9. If the voltage across the IGBT exceeds the breakdown voltage of the Zener diode, the Zener diode becomes conductive and the gate of IGBT is charged again. The IGBT is driven into its active region in order to dissipate the excess inductive load energy. Since the clamping operation happens only until all IGBTs are off, the losses will not do any harm to the IGBT chip [26].

To ensure a good performance and lifetime of the converter, a combination of both protection strategies is suggested.

A soft shutdown solution without using a clamp circuit has been proposed by adding extra shutdown switching states and paths in the commutation process [23].

11.1.3 Current commutation strategies

According to the modulation algorithm, when output has to be commutated from one input phase to another, two basic rules must be obeyed: one is that input terminals should never be short-circuited and the other is that any output phase must never be open for an inductive load. That means, for each output phase, no two BDSs are switched on at any instant and not all are off at any instant.

Therefore, a reliable current commutation between BDSs is crucial for MCs to operate safely without causing the hazard of a short circuit or a large overvoltage. In order to determine the proper switching sequence of the devices, either input line voltage signs and/or output current directions are required to implement the commutation. According to the information that it relies on, the commutation strategies can be classified into three categories, namely commutations based on current direction, input voltage, and current and voltage signs. The commutation strategies can be also classified according to the number of switching states or the number of step delays involved in each commutation process.

Dead-time commutation and overlap commutation were proposed for the DB arrangement or the real BDS. Either of them requires undesired extra bulky components to minimize the hazard of power circuit, which compromises the volumetric advantage and increases losses of MC [28–30].

To overcome the complexity of the control and realization, common-collector, common-emitter and antiparallel arrangements of two RB-IGBTs have established as the most used BDS configurations [4]. Therefore, the commutation strategies discussed in this section will be applied to these types of configurations. After most of the existing commutation strategies are reviewed, a modified current-direction-based commutation strategy is proposed. The principle of this method is to smoothly switch between four-step and two-step commutations based on a predefined current threshold.

11.1.3.1 Input voltage sign-based commutation

To make it simple, the commutation strategy is explained by considering just two-phase-to-single-phase MC. The two basic requirements, which the commutation has to fulfill at all times, can be visualized in the simplified circuit with two BDS cells across two input lines and one output line of an MC as shown in Figure 11.10(a) and (b). The switches, *SaA2* and *SbA2,* connected to the output line are called positive switches allowing conducting the positive current. The negative current can flow in the switches, *SaA1* and *SbA1,* connected to the input terminals.

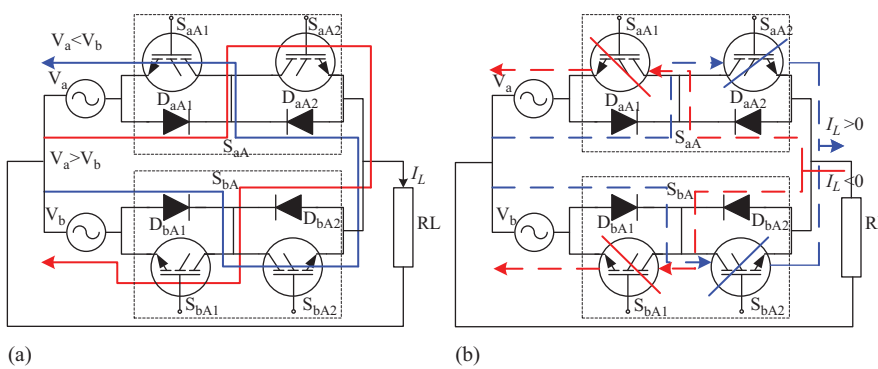


Figure 11.10 Schematic of a two-phase to single-phase MC: (a) Potential short circuit and (b) Potential open circuit

Different commutation techniques have been proposed and implemented in [17,31–34]. In a similar way to a commutation process in a traditional VSI, the "staggered commutation" can be applied to the MC, as there are no natural freewheeling paths in MCs [17]. To achieve this aim, relative magnitudes of input voltages involved in the commutation have to be known in order to determine the switching configuration for each step of the commutation by sensing and comparing the magnitudes of the voltages.

In steady state, both positive and negative switches in the active BDS are turned on, allowing both directions of current flow. In the transition, there are two freewheeling devices turned on within the two commutating BDSs, allowing either positive or negative current flow. In Figure 11.10(b), assuming $V_a > V_b$, negative switch S_{aA1} is a freewheeling device and positive switch S_{bA2} is another freewheeling device. Once the freewheeling devices have been identified, the switching sequential steps for the commutation between any two input lines can be staggered as follows.

The freewheeling switch of the incoming BDS is always turned off at the first step. The non-freewheeling device of the outgoing BDS is switched off at the second step followed by gating the other non-freewheeling device of the incoming BDS at the third step. The load current has now commutated from the outgoing to the incoming phase. Another steady state will be set up after the freewheeling switch of the outgoing BDS is turned off at the last step. The switching diagram is shown in Figure 11.11(a) and (b). The actual output current commutation instant is highlighted in the switching state diagram.

It has to be noted that the identification of freewheeling devices relies on the sign of the voltage rather than that of the output current, but the actual output current commutation takes place either at the second or the third step during the process depending on the output current direction. In the case of commutation from S_{aA} to S_{bA} under positive line voltage, when S_{bA2} is turned on, S_{bA2} and D_{bA1} are reverse biased and block the voltage V_{ab}. The positive current is still carried by S_{aA2}. The current commutation does not commence until S_{aA2} is turned off when the reverse bias ends. If a negative current is required to transfer from S_{aA} to S_{bA}, the load current is fed to V_a through S_{aA1} and D_{aA2} at the first two steps when S_{aA2} is turned off followed by turning on S_{bA2}, because neither of them can carry negative current. But when S_{bA1} is gated at the third step, the transfer of output current takes place because S_{bA1} remains forward biased in the process. In the similar way, the current commutation instants under negative line voltage can be analyzed and found.

A seminatural two-step commutation strategy, based on the input voltage measurement, has been proposed and implemented in [31]. All the devices are kept on except those required to block the reverse voltage. This allows relatively simple commutation of the current between input phases. It is noted that the precise detection of voltage sign at zero crossing of phase-to-phase voltages is critical for this type of communication methods. Poorly selected switching sequence during a commutation will short-circuit the commutating phases [33]. An extra hardware sign detector can be used at the expense of converter cost increase which is not desired. Simply prohibiting a commutation in the critical area leads to distortions in

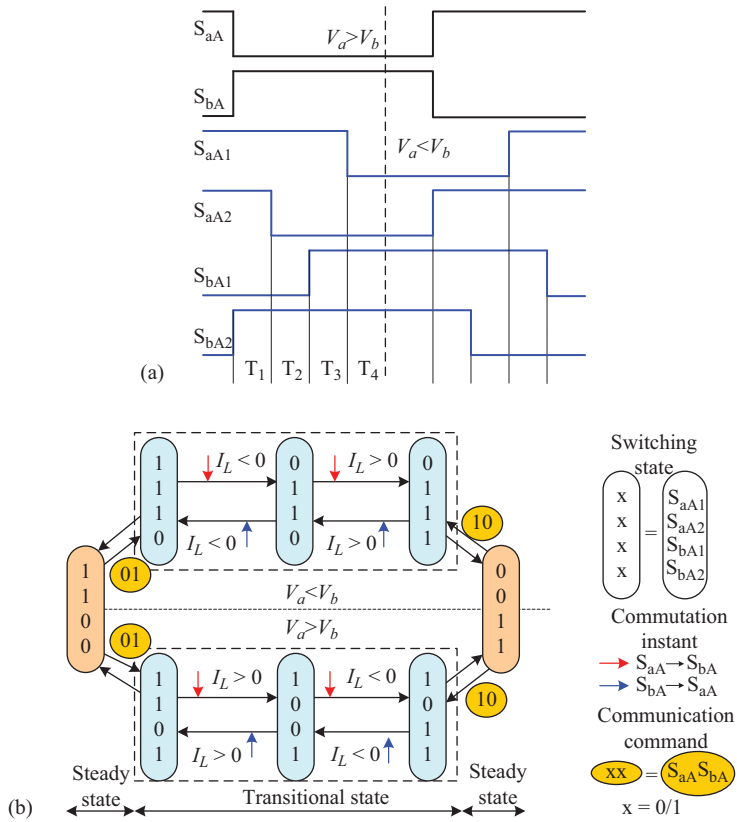


Figure 11.11 Switching diagram of the four-step voltage based commutation strategy between two BDS cells: (a) timing diagram and (b) switching states diagram

the input currents because the expected switching states are not executed. Current direction information can help in most of the cases except the situations in which both signs are unsure. Another effective way is to take the place of a critical sequence by two uncritical sequences. Insertion of two extra uncritical sequences can increase the robustness of the voltage sign-based commutation. However, it increases the number of switching transients in each commutation process and thus the switching losses [33].

11.1.3.2 Current direction-based commutation

A four-step current-controlled commutation was first proposed in [34]. The main difference between this method and the voltage sign-based techniques is that there are no freewheeling paths turned on in this method. The direction of the output current flowing through the commutating BDS is the control object. A simplified commutation circuit shown in Figure 11.10 is helpful to explain this strategy.

In four-step current-based commutation, both of the IGBTs in the active BDS are turned on in steady states to allow both directions of current flow. Figure 11.12(a) shows the timing diagram of two commutations taking place in output current zero-crossing area, where the output current is transferred between BDS S_{aA} and S_{bA}. There are three time delays for the first three steps, since the last turned-on switch would be turned off first in next commutation process. It would not cause any hazard even if it failed to be turned on before the new commutation commenced.

The actual commutation instants are marked in the switching states diagram shown in Figure 11.12(b). It can be seen that they occur either at the second or third step depending on the voltages connected to the two commutating BDSs. The following explanation assumes a positive load current in the direction shown in Figure 11.10(a) and initial steady state that BDS S_{aA} is closed. When a commutation to S_{bA} is required, the current direction is used to determine which device in the active BDS is idle without conducting current, S_{aA1} in this case. S_{aA1} is turned off immediately. After a short time to complete turn-off of S_{aA1}, S_{bA2} is turned on.

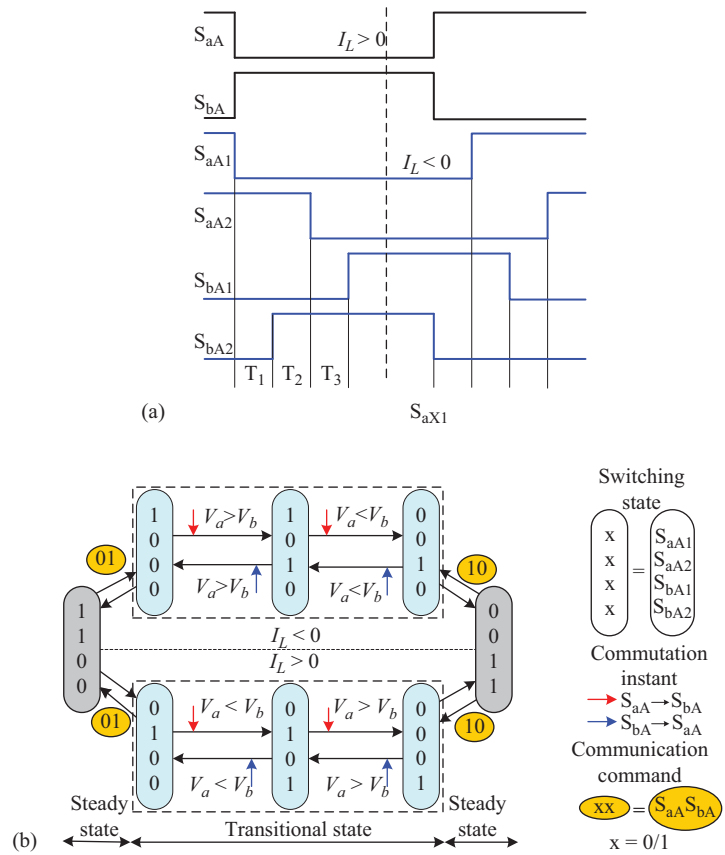


Figure 11.12 Switching diagram of the four-step current direction-based commutation strategy between two BDS cells: (a) timing diagram and (b) switching states diagram

If $V_a < V_b$, the current is transferred from S_{aA2} to S_{bA2} at this point. The turn-on losses occur in S_{bA2} and D_{bA1} during the current commutation, while no switching losses are incurred in BDS S_{aA} due to zero current turn-off of both S_{aA1} and S_{aA2}. It is different from the commutation condition when $V_a > V_b$. The current transfer will take place when the outgoing device S_{aA2} is being turned off instead. And BDS S_{bA} is free of switching losses while turn-off of S_{aA2} incurs losses. At last, the remaining device in the incoming BDS S_{bA1} is turned on to allow current reversal. The delay between each switching event is determined by the device switching characteristics and gate drive propagation delays. The four-step current commutation can be implemented by using D flip-flops and logic gates as shown in Figure 11.13. Switching signals for the BDSs are synchronized to the system clock by using synchronizing D flip-flops. AND gate is taking the synchronized control signal and the inversion of its adjacent signal to prevent any chances of overlapping. The step delay is determined by the period of synchronizing clock signal.

It can be noticed that there are two idle switches operated during the commutation process which create two additional steps. Reduction of the number of steps, i.e. a faster commutation process, can decrease the limit to the minimum switching pulse width and thus the width of the control discontinuity within the linear operating region of the MC. Consequently, two-step commutation strategies have been deemed preferable to four-step commutation strategies due to the improved modulation performance [10].

The basic idea of the two-step current-based commutation is never to operate the non-conducting IGBTs during the commutation process. In steady states, only the carrying current IGBT is closed in the target BDS. There is a potential problem in the critical area where the current is close to zero. It is difficult to get a precise sign of the current without adding additional hardware. One of the solutions is to insert a dead zone at zero-crossing point where no commutation is allowed after turning on the non-conducting IGBT. The current transfers between the two IGBTs of the same BDS without changing the input phase, which is called "inter-switch commutation" [30]. The normal operation is not resumed until the current exceeds this critical area. A small predefined threshold value ΔI_Z determines the width of the inter-switch commutation area. The prohibition of phase commutation within the threshold will degrade output current and voltage to some extent. It is even poorer when the current measurement has a big offset. The communication won't work at the light load when the output current is too small to exceed the threshold. The dead-time commutation can be applied to enhance the threshold commutation. This is not desired because the output current is interrupted during the dead time when the output current threshold value is big in high-rating converters.

The current direction and threshold rely on the accuracy of the current transducer which is necessary in the MC control system. The inter-switch commutation area can be minimized by significantly improved current direction detection with the gate drive level intelligence. The current sign is detected by monitoring the polarity of the voltage drop of each IGBT within every BDS. The dead time is minimized so that breaking a current at the zero crossing does not cause significant overvoltage [4,36].

Although this improved two-step commutation strategy performs fast and safe commutations, it needs to monitor the collector–emitter voltages with gate drive level

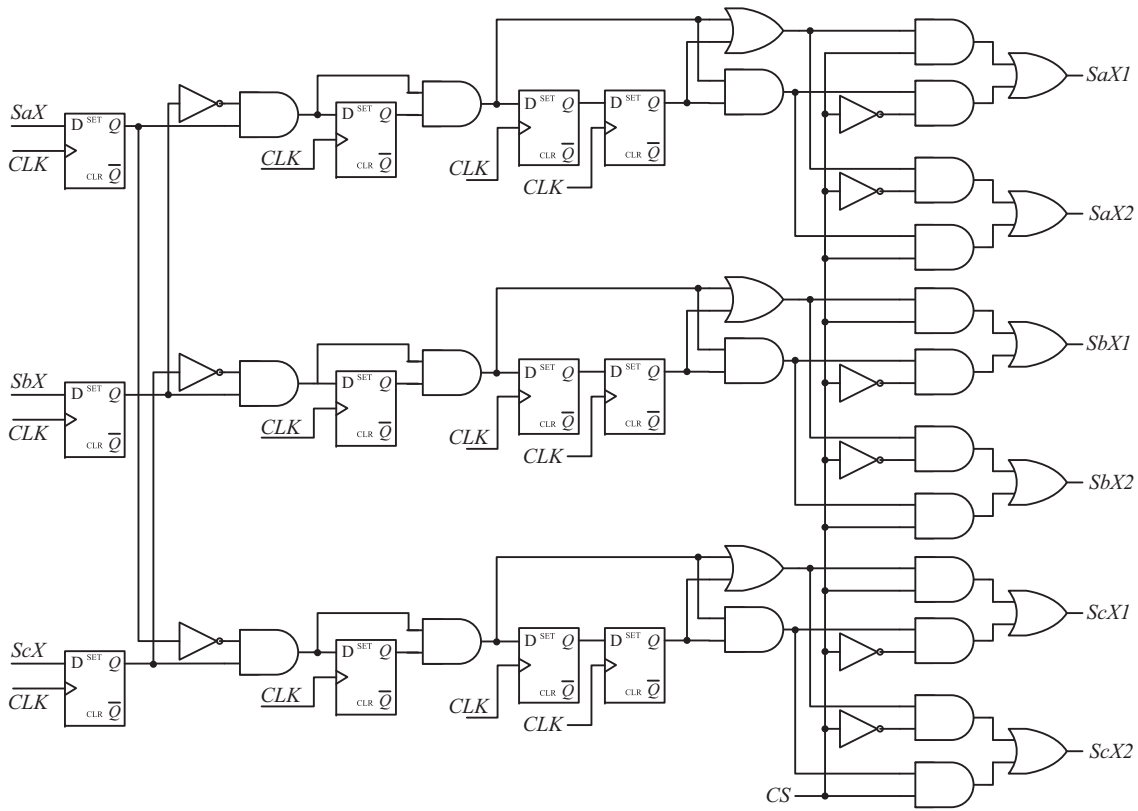


Figure 11.13 Overall circuit of four-step switching sequencer [35]

circuit. It also requires more isolation circuit, like high-speed optocoupler, between the decision unit and current detection unit. It does increase the cost of the converter and the propagation delay of current direction passing in the communication loop.

A hybrid commutation strategy is an extension of the two-step dead-time communication method. It can simply solve the problem incurred by the inter-switch commutation. The normal four-step current commutation is executed within the threshold band ΔI_Z. The two-step commutation is performed when the load current is higher than the threshold. This commutation technique does not need any specially designed hardware for accurate current sign or isolation circuit apart from output current sign and threshold detection circuit which can be easily implemented by adding a comparator into the current measurement circuit. Smaller time delays are set for each step due to less switching time needed to transfer such a small current within ΔI_Z. Since the final switching states for four-step and two-step commutations are different, the transition between the two-step and four-step execution should be taken into account. As shown in Figure 11.14, States "1100" and "0011" are the steady states for four-step and "1000," "0010," "0100" and "0100" for the two-step commutation. There exist the following three cases when the current crosses the boundary of hysteresis band.

Case 1: No commutation is requested during the transition when the current is crossing the boundary. If the absolute value of current is increasing and is about to exceed ΔI_Z, the non-conducting switch of the active BDS is turned off preparing for the two-step commutation. For example, four-step state "1100" is changed to "1000" during the transition if current is higher than ΔI_Z. If the current is decreasing within the bandwidth $\pm\Delta I_Z$, the non-conducting switch S_{aA2} will be turned on for the incoming four-step commutation.

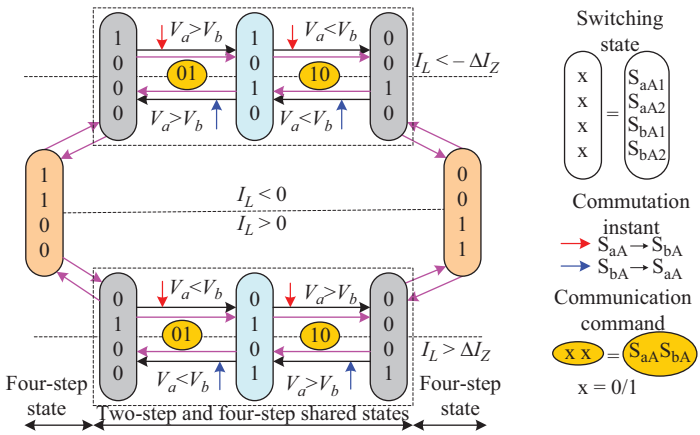


Figure 11.14 Switching diagram of a hybrid commutation based on current direction and threshold

Case 2: Commutation is requested during the transition. The four-step commutation needs to switch to two-step commutation when current is increasing and about to exceed ΔI_Z. The fourth step, turning on the non-conducting device of active BDS, does not need to be executed because the current direction is surely either positive or negative. It becomes a three-step commutation, only the conducting switch turned on. For example, the commutation ends with the third step state "1000" or "0010" if current is positive and bigger than ΔI_Z.

Case 3: Commutation is requested during the transition. The two-step commutation needs to switch to four-step commutation when current is decreasing into the threshold band. An extra step, turning on the non-conducting device of active BDS, must be added at the end of two-step commutation. This allows reverse current to flow as the load current may change the direction before the next four-step commutation request comes. Therefore, a two-step steady state has to change to a four-step steady state. For example, if the current is positive but less than ΔI_Z, state "1100" has to be executed after "1000." The four-step commutation can only start after this extra step.

11.1.4 Modulation techniques

11.1.4.1 Alesina–Venturini (AV) method

This strategy allows the control of the output voltages and IPF based on the duty-cycle matrix approach [37]. The computation of nine duty cycles in the transfer matrix in (11.4) can be expressed in terms of input and target output voltages by the following equation assuming the unity IPF.

$$m_{iJ} = \frac{t_{iJ}}{T} = \frac{1}{3}\left[1 + \frac{2v_i v_J}{V_{im}^2}\right] (i = a, b, c; \quad J = A, B, C) \tag{11.11}$$

where V_{im} is the magnitude of the input voltage, and v_i and v_J represent the specific input voltage and target output voltage, respectively. Considering the constraint $m_{aJ} + m_{bJ} + m_{cJ} = 1$, six duty cycles are calculated by (11.11) in real-time implementation. It is required to measure two line-to-line or phase voltages to calculate the magnitude of the input voltage vector. Typical waveforms of the input/output voltages and currents at the maximum voltage transfer ratio are shown in Figure 11.15.

11.1.4.2 Optimum AV method

An injection of a third harmonic component of input and output voltages in the reference output voltages (11.12) can fit the output voltage within the input voltage envelope with a voltage transfer ratio up to 0.866 [17,31–38].

$$v_J^{opt} = V_{om}\cos[\omega_o t - \beta_J] - \frac{V_{om}}{6}\cos(3\omega_o t) + \frac{V_{om}}{2\sqrt{3}}\cos(3\omega_{in} t) \quad \text{for } k = 1, 2, 3 \tag{11.12}$$

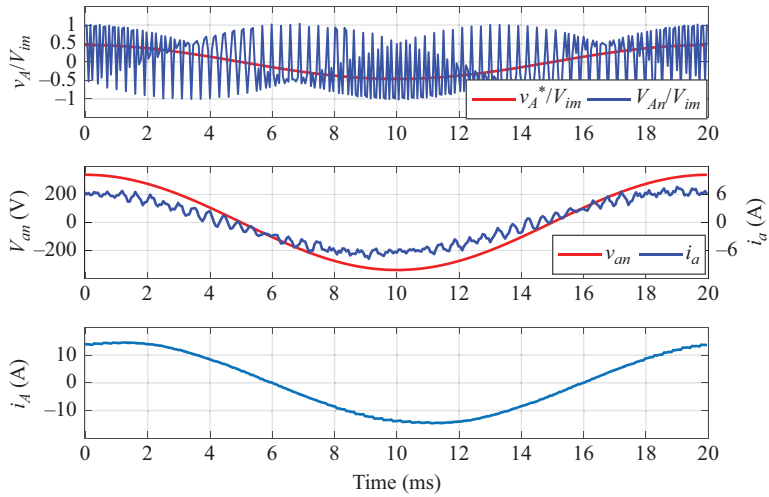


Figure 11.15 Waveforms of AV method at 50 Hz, $q = 0.5$

where V_{om} is the magnitude of the reference output voltage, ω_{in} and ω_o are the angular frequencies of input and output voltages, respectively, and $\beta_J = 0, 2\pi/3, 4\pi/3$ is the phase angle of corresponding output voltage when $J = A$, B and C, respectively.

The formal solution including the input displacement factor control in [17] can be simply described as (11.13) for the real-time application, when the unity IPF is required.

$$m_{iJ} = \frac{t_{iJ}}{T} = \frac{1}{3}\left[1 + \frac{2v_i v_J^{opt}}{V_{im}^2} + \frac{4q}{3\sqrt{3}}\sin(\omega_{in}t - \beta_i)\sin(3\omega_{in}t)\right] \tag{11.13}$$

where $q = V_{om}/V_{im}$ is the transfer ratio and $\beta_i = 0, 2\pi/3, 4\pi/3$ is the phase angle of corresponding input voltage when $i = a, b,$ *and* c, respectively.

It is noted that the IPF is controlled by inserting a phase shift between the measured input voltages and virtual input voltages v_i into (11.13) at the expense of maximum voltage ratio. And the injected third harmonic addition just moves the common point of output voltage waveforms with respect to the neutral point of the input voltage. However, it does not have any effect on the output line-to-line voltages and neither on the load currents since there is no neutral connection between the input and load [4]. Typical waveforms of the input/output voltages and currents are shown in Figure 11.16. The voltage transfer ratio is higher than 0.5. The third harmonics injected in the reference output voltage do not affect the input/output performance of the MC as they are cancelled out by a start-connected load.

11.1.4.3 Scalar modulation methods

The motivation behind scalar modulation is usually given as the perceived complexity of the Venturini method [4]. The active times for the three switches

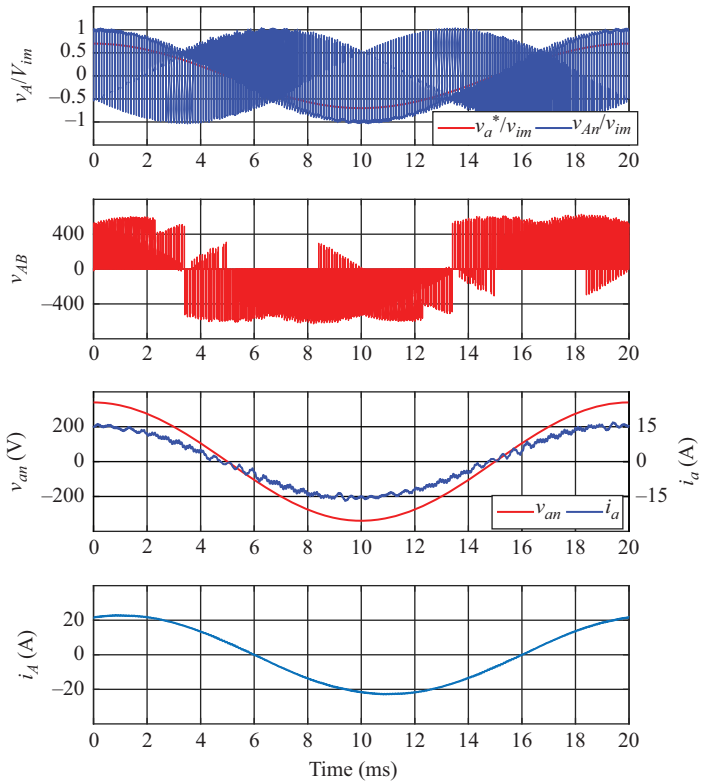


Figure 11.16 Waveforms of optimum AV method at 50 Hz, $q = 0.7$

associated with the required output voltages rely on measuring of instantaneous input voltages and assigning *K–L–M* variable subscripts to the input phases according to the following rules [39,40].

- *Rule 1*: At any instant, assign subscript "*M*" to the input which has a polarity different from the other two.
- *Rule 2*: Assign subscript "*L*" to the smaller (in absolute value) one of the two remaining phases. The third input is assigned by subscript "*K*."

The duty cycles are given by (11.14), and the corresponding output voltage is then expressed by (11.15):

$$m_{LJ} = \frac{(v_J^{opt} - v_M)v_L}{1.5V_{im}^2}, m_{KJ} = \frac{(v_J^{opt} - v_M)v_K}{1.5V_{im}^2}, m_{MJ} = \frac{(v_J^{opt} - v_M)v_M}{1.5V_{im}^2} \quad (11.14)$$

$$v_J = m_{KJ}v_K + m_{MJ}v_M + m_{LJ}v_L \quad \text{for } J = A, B, C \quad (11.15)$$

In the similar way to optimum AV method, common mode addition is superposed over the target output voltage to achieve 0.866 transfer ratio. The modulation duty cycles can also be expressed in the similar form (11.16).

$$m_{iJ} = \frac{1}{3}\left[1 + \frac{2v_i v_J^{opt}}{V_{im}^2} + \frac{2}{3}\sin(\omega_{in}t + \beta_i)\sin(3\omega_{in}t)\right] \tag{11.16}$$

It is noted that the only difference from the AV method is that the last term is prorated with voltage ratio in AV method but fixed at maximum value in the scalar method. The input/output waveforms of MC using scalar modulation are presented in Figure 11.17. The duty cycle difference between scalar and AV optimum methods is illustrated in Figure 11.18.

11.1.4.4 Carrier-based modulation method [41]

The offset duty ratios corresponding to the three input phases are chosen as

$$D_i = |0.5\cos(\omega_{in}t - \beta_i - \varphi_{in})| \tag{11.17}$$

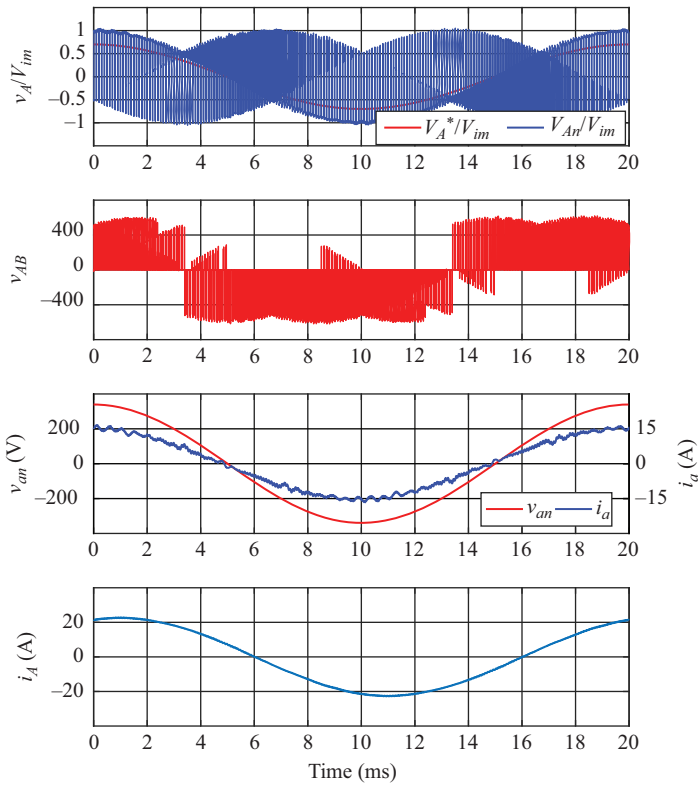


Figure 11.17 Waveforms of Roy's method at 50 Hz, q = 0.7

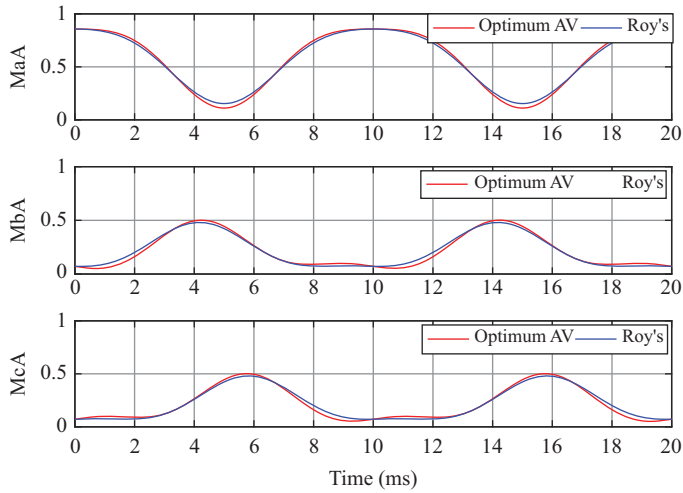


Figure 11.18 The modulation duty cycles for output phase-A in optimum AV and scalar methods (50 Hz, $q = 0.7$)

where φ_{in} is the IPF angle and $\beta_i = 0, 2\pi/3, 4\pi/3$ is the phase angle of corresponding input voltage when $i = a, b$ and c, respectively.

The three-phase modulation indices for output phase $J = A, B, C$ are defined as

$$k_J = k\cos(\omega_o t - \beta_o) \tag{11.18}$$

where k is the amplitude of the modulation indices k_J, $0 \le k \le 0.5$, and β_o is the phase shift of corresponding output phase, respectively.

To fully utilize the input voltage capability, an additional common mode term, $[\max(k_A, k_B, k_C) + \min(k_A, k_B, k_C)]/2$, is added to k_J. The amplitude of k_J will be enhanced from 0.5 to 0.57.

The duty cycles for output phase-$J$are

$$m_{iJ} = D_i + \{k_J - [\max(k_A, k_B, k_C) + \min(k_A, k_B, k_C)]/2\}\cos(\omega_{in} t - \beta_i - \varphi_{in}) \tag{11.19}$$

Considering the constraint that the output phase has to be connected to any of the input phases in any switching cycle, $m_{aJ} + m_{bJ} + m_{cJ} = 1$. Another common-mode duty ratio of $[1 - (D_a + D_b + D_c)]/3$ is added to into D_i. The addition of the common-mode duty ratio injected in all switches will not affect the output line-to-line voltages and input currents.

This carrier-based modulation scheme allows the IPF to be controlled. The duty cycles are affected by the IPF. To have a unity power factor, φ_{in} has to be chosen equal to zero.

Switching signals corresponding to the output phase-A can be obtained by comparing control signals with a triangular carrier using normal PWM strategy as shown in Figure 11.19. The input/output waveforms in Figure 11.20 show that the

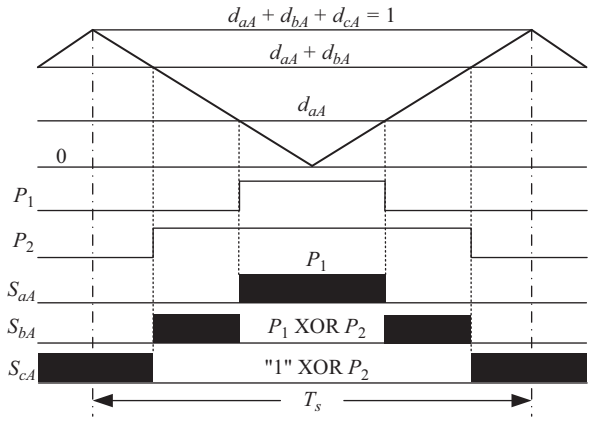


Figure 11.19 Switching signals obtained from a triangular carrier-based PWM

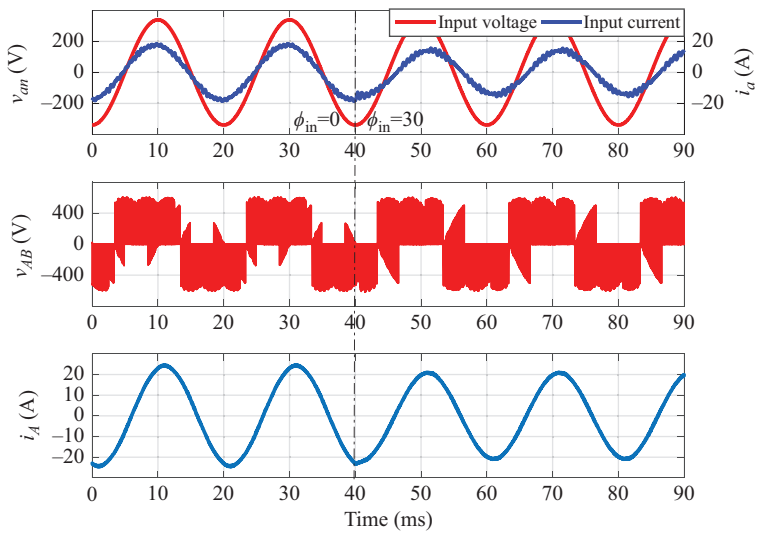


Figure 11.20 Input/output waveforms of MC with carrier-based PWM

displacement angle between the input voltage and current is changed from 0° to 30° lagging immediately after a very short transition.

11.1.4.5 SVM method

Direct SVM

In direct SVM algorithm [42], the instantaneous input current phase angle β_i, as well as the output voltage vector $\bar{v}_o$, is taken as the reference quantity at each sampling period, as shown in Figure 11.21. The control of input displacement

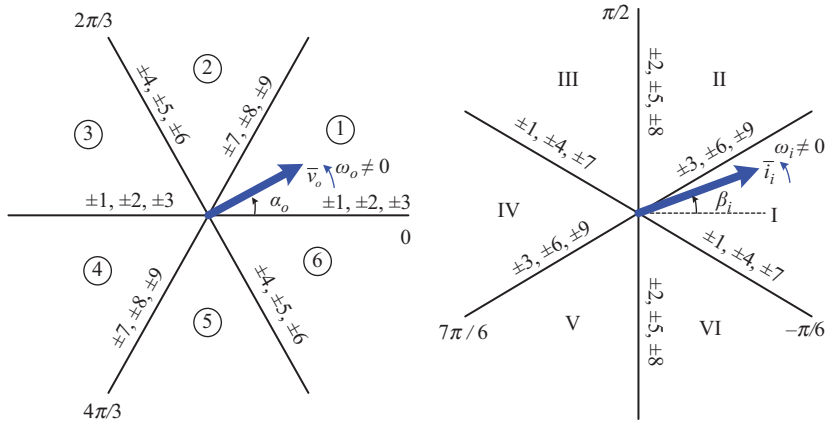


Figure 11.21 Output voltage vectors and input current vectors for direct SVM

factor can be achieved by controlling β_i, as the input voltage phase angle is obtained by the measurement of three-phase voltages.

The duration of the selected switching configurations, known as vector duty cycles, are calculated in (11.20)–(11.24). The vector duty cycles are then assigned to four active and up to three zero configurations selected from Table 11.2. The procedure of converting vector duty cycles into active switching configuration duty cycles is accomplished according to Table 11.3. For instance, sector pair of (I, 1) or (IV, 4) determines that the active switching configurations +9, −7, −3 and +1 are to be used in the synthesis of vectors. Zero configurations are applied to complete the cycle period. There are three zero configurations available in Table 11.2. Different ways to utilize the three zero configurations define different switching patterns, which are characterized by different behaviors in terms of the ripple in input and output quantities.

$$d_1 = \frac{2}{\sqrt{3}} q \frac{\cos(\tilde{\alpha}_o - \pi/3)\cos(\tilde{\beta}_i - \pi/3)}{\cos\varphi_i} \tag{11.20}$$

$$d_2 = \frac{2}{\sqrt{3}} q \frac{\cos(\tilde{\alpha}_o - \pi/3)\cos(\tilde{\beta}_i + \pi/3)}{\cos\varphi_i} \tag{11.21}$$

$$d_3 = \frac{2}{\sqrt{3}} q \frac{\cos(\tilde{\alpha}_o + \pi/3)\cos(\tilde{\beta}_i - \pi/3)}{\cos\varphi_i} \tag{11.22}$$

$$d_4 = \frac{2}{\sqrt{3}} q \frac{\cos(\tilde{\alpha}_o + \pi/3)\cos(\tilde{\beta}_i + \pi/3)}{\cos\varphi_i} \tag{11.23}$$

$$d_0 = 1 - (d_1 + d_2 + d_3 + d_4) \tag{11.24}$$

Table 11.2 Switching configurations of matrix converter used in direct SVM

Switch config.	**A**	**B**	**C**	v_{AB}	v_{BC}	v_{CA}	i_a	i_b	i_c	v_o	α_o	i_i	β_i
+1	a	b	b	v_{ab}	0	$-v_{ab}$	i_A	$-i_A$	0	$2/3 \cdot v_{ab}$	0	$2/\sqrt{3} \cdot i_A$	$-\pi/6$
−1	b	a	a	$-v_{ab}$	0	v_{ab}	$-i_A$	i_A	0	$-2/3 \cdot v_{ab}$	0	$-2/\sqrt{3} \cdot i_A$	$-\pi/6$
+2	b	c	c	v_{bc}	0	$-v_{bc}$	0	i_A	$-i_A$	$2/3 \cdot v_{bc}$	0	$2/\sqrt{3} \cdot i_A$	$\pi/2$
−2	c	b	b	$-v_{bc}$	0	v_{bc}	0	$-i_A$	i_A	$-2/3 \cdot v_{bc}$	0	$-2/\sqrt{3} \cdot i_A$	$\pi/2$
+3	c	a	a	v_{ca}	0	$-v_{ca}$	$-i_A$	0	i_A	$2/3 \cdot v_{ca}$	0	$2/\sqrt{3} \cdot i_A$	$7\pi/6$
−3	a	c	c	$-v_{ca}$	0	v_{ca}	i_A	0	$-i_A$	$-2/3 \cdot v_{ca}$	0	$-2/\sqrt{3} \cdot i_A$	$7\pi/6$
+4	b	a	b	$-v_{ab}$	v_{ab}	0	i_B	$-i_B$	0	$2/3 \cdot v_{ab}$	$2\pi/3$	$2/\sqrt{3} \cdot i_B$	$-\pi/6$
−4	a	b	a	v_{ab}	$-v_{ab}$	0	$-i_B$	i_B	0	$-2/3 \cdot v_{ab}$	$2\pi/3$	$-2/\sqrt{3} \cdot i_B$	$-\pi/6$
+5	c	b	c	$-v_{bc}$	v_{bc}	0	0	i_B	$-i_B$	$2/3 \cdot v_{bc}$	$2\pi/3$	$2/\sqrt{3} \cdot i_B$	$\pi/2$
−5	b	c	b	v_{bc}	$-v_{bc}$	0	0	$-i_B$	i_B	$-2/3 \cdot v_{bc}$	$2\pi/3$	$-2/\sqrt{3} \cdot i_B$	$\pi/2$
+6	a	c	a	$-v_{ca}$	v_{ca}	0	$-i_B$	0	i_B	$2/3 \cdot v_{ca}$	$2\pi/3$	$2/\sqrt{3} \cdot i_B$	$7\pi/6$
−6	c	a	c	v_{ca}	$-v_{ca}$	0	i_B	0	$-i_B$	$-2/3 \cdot v_{ca}$	$2\pi/3$	$-2/\sqrt{3} \cdot i_B$	$7\pi/6$
+7	b	b	a	0	$-v_{ab}$	v_{ab}	i_C	$-i_C$	0	$2/3 \cdot v_{ab}$	$4\pi/3$	$2/\sqrt{3} \cdot i_C$	$-\pi/6$
−7	a	a	b	0	v_{ab}	$-v_{ab}$	$-i_C$	i_C	0	$-2/3 \cdot v_{ab}$	$4\pi/3$	$-2/\sqrt{3} \cdot i_C$	$-\pi/6$
+8	c	c	b	0	$-v_{bc}$	v_{bc}	0	i_C	$-i_C$	$2/3 \cdot v_{bc}$	$4\pi/3$	$-2/\sqrt{3} \cdot i_B$	$\pi/2$
−8	b	b	c	0	v_{bc}	$-v_{bc}$	0	$-i_C$	i_C	$-2/3 \cdot v_{bc}$	$4\pi/3$	$-2/\sqrt{3} \cdot i_C$	$\pi/2$
+9	a	a	c	0	$-v_{ca}$	v_{ca}	$-i_C$	0	i_C	$2/3 \cdot v_{ca}$	$4\pi/3$	$-2/\sqrt{3} \cdot i_B$	$7\pi/6$
−9	c	c	a	0	v_{ca}	$-v_{ca}$	i_C	0	$-i_C$	$-2/3 \cdot v_{ca}$	$4\pi/3$	$-2/\sqrt{3} \cdot i_C$	$7\pi/6$
0_1	a	a	a	0	0	0	0	0	0	0	–	0	–
0_2	b	b	b	0	0	0	0	0	0	0	–	0	–
0_3	c	c	c	0	0	0	0	0	0	0	–	0	–

Table 11.3 Selection of switching configurations for each combination of output and input vector sectors

		Sector of output voltage vector													
		1 or 4					**2 or 5**					**3 or 6**			
Sector of input current vector	I or IV	(I,1) (IV,4)	*+9*	*−7*	*−3*	*+1*	(IV,2) (I,5)	*+6*	*−4*	*−9*	*+7*	(I,3) (IV,6)	*+3*	*−1*	*−6*	*+4*
		(IV,1) (I,4)	*−9*	*+7*	*+3*	*−1*	(I,2) (IV,5)	*−6*	*+4*	*+9*	*−7*	(IV,3) (I,6)	*−3*	*+1*	*+6*	*−4*
	II or V	(V,1) (II,4)	*+8*	*−9*	*−2*	*+3*	(II,2) (V,5)	*+5*	*−6*	*−8*	*+9*	(V,3) (II,6)	*+2*	*−3*	*−5*	*+6*
		(II,1) (V,4)	*−8*	*+9*	*+2*	*−3*	(V,2) (II,5)	*−5*	*+6*	*+8*	*−9*	(II,3) (V,6)	*−2*	*+3*	*+5*	*−6*
	III or VI	(III,1) (VI,4)	*+7*	*−8*	*−1*	*+2*	(VI,2) (III,5)	*+4*	*−5*	*−7*	*+8*	(III,3) (VI,6)	*+1*	*−2*	*−4*	*+5*
		(VI,1) (III,4)	*−7*	*+8*	*+1*	*−2*	(III,2) (VI,5)	*−4*	*+5*	*+7*	*−8*	(VI,3) (III,6)	*−1*	*+2*	*+4*	*−5*
4 active config.			**1**	**2**	**3**	**4**		**1**	**2**	**3**	**4**		**1**	**2**	**3**	**4**

Note: Active switching configurations are shown in italics and sector of output voltage vector is represented in bold.

where $\tilde{\alpha}_o$ and $\tilde{\beta}_i$ are the output voltage and input current phase angles with respect to the bisecting lines of the corresponding sectors, respectively, φ_i is the input current displacement angle and $q = |\bar{v}_o|/|\bar{v}_{in}|$ is the voltage transfer ratio. The following angle limits should be applied in the equations above.

$$-\frac{\pi}{6} < \tilde{\alpha}_o < \frac{\pi}{6}, \quad -\frac{\pi}{6} < \tilde{\beta}_i < \frac{\pi}{6} \quad \textit{and} \quad -\frac{\pi}{2} < \varphi_i < \frac{\pi}{2}$$

Indirect space vector modulation

The motivation behind indirect modulation is to derive a control algorithm for MC from the known PWM strategies for conventional converters. By imaginarily splitting the MC into rectifier stage and inverter stage as shown in Figure 11.22, the input current vector and output voltage vector are synthesized independently and then the two modulation results are combined to complete the modulation for the entire MC [43–45]. In this way, it is easier to understand and implement the modulation algorithm, since the PWM methods for rectifier and inverter are well established. Moreover, it is possible to apply many control algorithms for PWM inverter-fed motors straightway to MC drives with sinusoidal input current and instantaneous IPF control.

The rectifier stage in the equivalent circuit in Figure 11.22 can be assumed to be a stand-alone current source rectifier (CSR) to provide a constant virtual DC-link voltage, U_{pn}, loaded by a DC current, I_{dc}.

Based on the SVM theory, the reference input current vector I_{in}^* is synthesized by two adjacent switching vectors I_γ and I_δ. The input currents are considered constant during a short switching interval T_S which is much shorter than the fundamental frequency of the currents. The active vectors are selected according to the location of the input current vector in the hexagon in a complex plane as shown in Figure 11.22.

The durations of I_γ and I_δ are given as

$$d_\gamma = T_\gamma/T_S = m_C \sin\left(\pi/3 - \theta_{in}^* + \varphi_{in}\right) \tag{11.25}$$

$$d_\delta = T_\delta/T_S = m_C \sin\left(\theta_{in}^* - \varphi_{in}\right) \tag{11.26}$$

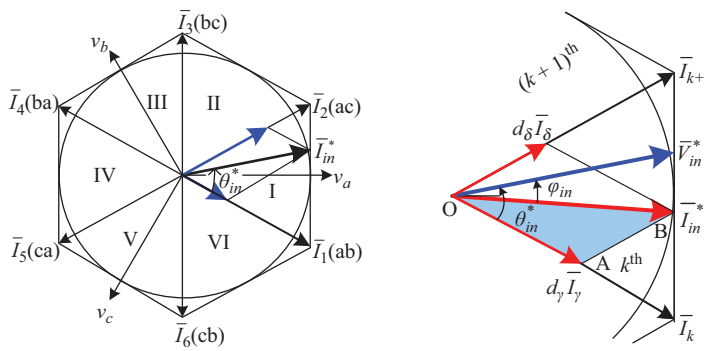


Figure 11.22 Input vector modulation in the rectifier stage using ISVM

where current modulation index $m_C = \left|\bar{I}^*_{in}\right|/I_{DC}$ is between zero and one, and θ^*_{in} is the relative input voltage vector position inside the corresponding sector. The average virtual DC-link current is deduced on the basis that DC power flow is equal to output power at any instant.

It can be seen that the modulation for the entire MC can be deduced by working out the relationship between the output and the DC-link in VSI stage. Considering the inverter part of the equivalent circuit as a conventional voltage supplied inverter by a virtual DC-link. The conventional SVM for VSI is straightway applied to the inverter stage. In the exactly same way as SVM-VSI to synthesize the target output voltage as shown in Figure 11.23, the duty cycles of the adjacent active vectors are calculated by

$$d_\alpha = T_\alpha/T_S = m_V \sin\left(\pi/3 - \theta^*_o\right) \tag{11.27}$$

$$d_\beta = T_\beta/T_S = m_V \sin\left(\theta^*_o\right) \tag{11.28}$$

where θ^*_o is the reference output voltage angle referring to the bisecting line of the corresponding sector.

The averaged virtual DC-link voltage can be found based on the power flow equation since there is no energy storage and ideal switches are assumed in the converter.

$$U_{pn} = \frac{3}{2}\left|\bar{V}^*_{in}\right| m_C \cos(\varphi_{in}) \tag{11.29}$$

where φ_{in} is the input displacement angle between input voltage and current vectors. In order to get a maximum transfer ratio, rectifier stage usually operates the maximum modulation index, i.e. $m_C = 1$. The voltage modulation index defines the desired voltage transfer ratio as

$$m_V = \frac{\sqrt{3}\cdot}{U_{pn}} = \frac{2}{\sqrt{3}}\frac{\left|\bar{V}^*_o\right|}{\left|\bar{V}^*_{in}\right|\cos(\varphi_{in})}, \quad 0 \le m_V \le 1 \tag{11.30}$$

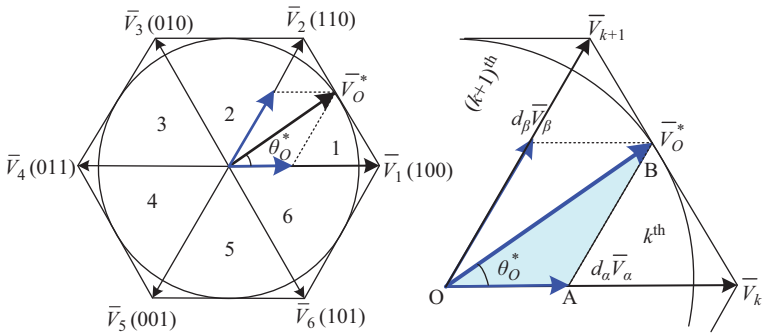


Figure 11.23 Output vector modulation in the inverter stage using ISVM

Under unity IPF, $\cos(\varphi_{in}) = 1$, the maximum voltage ratio $\sqrt{3}/2$ can be obtained when $m_V = 1$.

The required switch states for each voltage and current vector pair can be realized by the proper switching combinations given in Table 11.4. To minimize the number of commutations, the sequence follows a U-shape when the sum of current and voltage sectors is even. Otherwise, an inverted U-shape is followed. For an arbitrary sector location of output and input vectors, the duty cycles of the combined active vectors are now derived from the product of the vector duty cycles in rectifier and inverter stages. Zero vectors are used to complete the sampling period T_S.

$$d_{\alpha\gamma} = d_\alpha \cdot d_\gamma = \frac{2}{\sqrt{3}} \frac{|\bar{V}_o^*|}{|\bar{V}_{in}|} \frac{\sin(\pi/3 - \theta_{in}^* + \varphi_{in})\sin(\pi/3 - \theta_o^*)}{\cos(\varphi_{in})} \tag{11.31}$$

$$d_{\alpha\delta} = d_\alpha \cdot d_\delta = \frac{2}{\sqrt{3}} \frac{|\bar{V}_o^*|}{|\bar{V}_{in}|} \frac{\sin(\theta_{in}^* - \varphi_{in})\sin(\pi/3 - \theta_o^*)}{\cos(\varphi_{in})} \tag{11.32}$$

$$d_{\beta\delta} = d_\beta \cdot d_\delta = \frac{2}{\sqrt{3}} \frac{|\bar{V}_o^*|}{|\bar{V}_{in}|} \frac{\sin(\theta_{in}^* - \varphi_{in})\sin(\theta_o^*)}{\cos(\varphi_{in})} \tag{11.33}$$

$$d_{\beta\gamma} = d_\beta \cdot d_\gamma = \frac{2}{\sqrt{3}} \frac{|\bar{V}_o^*|}{|\bar{V}_{in}|} \frac{\sin(\pi/3 - \theta_{in}^* + \varphi_{in})\sin(\theta_o^*)}{\cos(\varphi_{in})} \tag{11.34}$$

$$d_0 = 1 - d_{\alpha\gamma} - \ d_{\alpha\delta} - d_{\beta\delta} - d_{\beta\gamma} \tag{11.35}$$

It is obvious that the output voltage vector $\bar{V}_o^*$ and the input current displacement angle φ_{in} are known as reference quantities at any cycle period. As it is illustrated

Table 11.4. Sequence of switching combinations in U-shape, N-shape or inversed shapes

		VI aaa		I ccc		II bbb		III aaa		IV ccc		V bbb		VI aaa
		$\bar{I}_1(ab)$		$\bar{I}_2(ac)$		$\bar{I}_3(bc)$		$\bar{I}_4(ba)$		$\bar{I}_5(ca)$		$\bar{I}_6(cb)$		
6	$\bar{V}_1(100)$	abb		acc		bcc		baa		caa		cbb		
1	$\bar{V}_2(110)$	aab		aac		bbc		bba		cca		ccb		
2	$\bar{V}_3(010)$	bab		cac		cbc		aba		aca		bcb		
3	$\bar{V}_4(011)$	baa		caa		cbb		abb		acc		bcc		
4	$\bar{V}_5(001)$	bba		cca		ccb		aab		aac		bbc		
5	$\bar{V}_6(101)$	aba		aca		bcb		bab		cac		cbc		
6														

by Figure 11.22, the control of IPF can be achieved by controlling the phase angle of input current vector since the input voltage phase angle is imposed by the measured supply voltages. Usually, the input current vector is adjusted to lag the input voltage to compensate the effect of the input filter capacitor currents on the IPF.

11.1.5 IPF compensation for MC

An input filter is necessary for an MC system to improve the input current quality with low harmonic components, as well as to provide stiff input voltages to the MC circuit. However, the characteristics of input LC filter make the unity IPF obtained only at high output power level. The IPF at the power supply degrades significantly from the desired unity power factor in the low output power condition.

In order to overcome this problem, the displacement angle between the input current and input voltage of the MC needs to be compensated. Two compensation algorithms will be introduced in this section: open-loop compensation based on the direct calculation of the compensated angle [46] and closed-loop compensation-based proportional and integral (PI) controller [47].

11.1.5.1 Open-loop IPF compensation

The phase shift imposed by the reactive components of input filters can be found from the following basic equations regarding the voltages and currents of power supply and input filter. These equations are derived from an equivalent single-phase model of MC as shown in Figure 11.24.

$$\begin{cases} v_i = v_s - L_f(di_s/dt) \\ i_c = C_f(dv_i/dt) \\ i_s = i_c + i_i \end{cases} \tag{11.36}$$

Considering the fundamental component of the voltages and currents and taking the power supply frequency as the fundamental frequency, ω, the magnitude

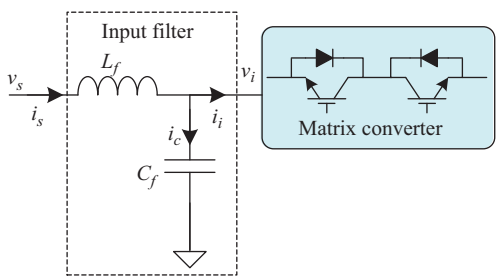


Figure 11.24 Equivalent circuit of a single-phase input filter of MC

and phase angle of the voltage and current of the MC can be obtained as in (11.37). The power supply voltage, $\vec{V}_s$, is used as the reference, and the unity IPF at the power supply is guaranteed by the MC modulation algorithm.

$$\begin{aligned} V_s &= V_s e^{j0} \\ V_i &= V_s - j\omega L_f I_s = \sqrt{V_s^2 + \left(\omega L_f I_s\right)^2} e^{-j\tan^{-1}\left(V_s/\omega L_f I_s\right)} \\ I_i &= \left(1 - \omega^2 L_f C_f\right) I_s - j\omega C_f V_s \\ &= \sqrt{\left(I_s - \omega^2 L_f C_f I_s\right)^2 + \left(\omega C_f V_s\right)^2} e^{-j\tan^{-1}\left[\dfrac{\omega C_f V_s}{I_s - \omega^2 L_f C_f I_s}\right]} \end{aligned} \tag{11.37}$$

From (11.37), $\vec{I}_s$ always leads the input current of the MC, $\vec{I}_i$, with the following displacement angle:

$$\varphi_{in} = \varphi_{i_s/i_i} = \tan^{-1}\left(\frac{\omega C_f}{1 - \omega^2 L_f C_f} \frac{V_s}{I_s}\right) \tag{11.38}$$

This displacement angle is introduced in the MC modulation algorithm in order to achieve a unity IPF operation. From (11.38), the compensated displacement angle depends on three parameters: L and C values of the input filter and the fundamental component of supply current I_s, which varies with the output power level of the MC. Reducing the filter capacitance or increasing the filter inductance can reduce this compensated angle. However, this will result in higher harmonic components in the input current or higher voltage drop across the filter inductor. High output power leads to high IPF as the amplitude of the supply current is increased with the load. To achieve a maximum IPF at the power supply, the MC modulation method must be revised to compensate for the phase shift caused by the input filter. As a result, the input current $\vec{I}_i$ of the MC is imposed to lag the supply voltage $\vec{V}_s$ with a displacement angle φ_{in}. The maximum compensated displacement angle is limited within $\pm\pi/3$ or by the desired voltage transfer ratio so that the duty cycles in the modulation are always between zero and one.

$$\varphi_{in,\,\lim} = \begin{cases} \pm\cos^{-1}\left(2q/\sqrt{3}\right) & \text{if}\left(\sqrt{3}/4 \le q < \sqrt{3}/2\right) \\ \pm\pi/3 & \text{if}\left(0 \le q < \sqrt{3}/4\right) \end{cases} \tag{11.39}$$

where the desired voltage transfer ratio $q = \left|\bar{V}_o^*\right|/|\bar{V}_{in}|$. The maximum voltage transfer ratio of the MC will be reduced to $0.866 \cos \varphi_{in}$ if IPF compensation is employed.

The performance of open-loop IPF compensator is shown in Figure 11.25. It has been tested with a step change of the desired power factor angle from 0° to −45°. The input current to the MC, i_i, lags the corresponding phase voltage in order to achieve the unity power factor at power supply side. A positive compensated

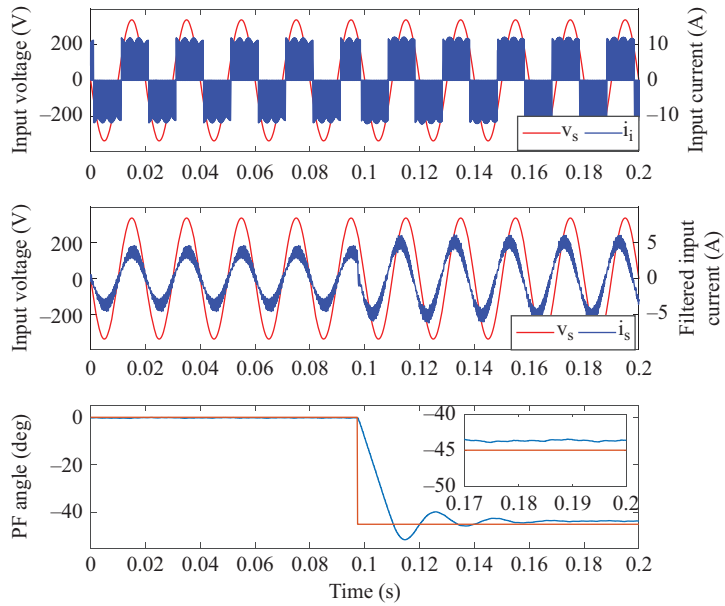


Figure 11.25 Performance of open-loop IPF compensation

displacement angle is imposed to the modulation. In the case of 45° leading power factor operation, the compensated angle is calculated as

$$\varphi_{in} = -\frac{\pi}{4} + \tan^{-1}\left(\frac{\omega C_f}{1-\omega^2 L_f C_f}\frac{V_s}{I_s}\right) \tag{11.40}$$

It is noted that there is steady-state error in the open-loop IPF compensation. This error is increasing with the increase in the reference, 0.5° for PF = 0° and 4° for PF = 0.707 as shown in the figure.

11.1.5.2 Closed-loop IPF compensation

The open-loop compensation algorithm provides a fast response which allows high-IPF achievement. However, the accuracy of this algorithm depends on the parameters of the MC input filter and power supply. A closed-loop compensation algorithm based on a PI controller is proposed to overcome the drawbacks presented in the open-loop method. The closed-loop algorithm is independent of the MC hardware parameters and provides flexible adjustment of the power factor. The required IPF is achieved by properly tuning the PI gains. The power factor control through the closed-loop scheme is thereby more adaptive and accurate than the open-loop manner especially in the applications where unity power factor on the power supply side of matrix rectifier is required when the load changes widely.

The block diagram of the closed-loop control of IPF is shown in Figure 11.26. When the output power of MC changes, a phase shift between the supply voltage and current is generated. An error is generated at the input of the PI controller.

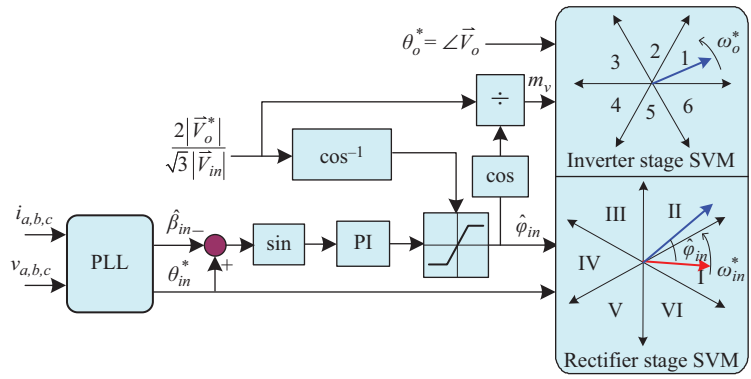


Figure 11.26 Block diagram of closed-loop PI controller for input current displacement angle for ISVM

The <*sin*> function is used to eliminate the error caused by periodic phase angle reset at 2π. The unity power factor at the power supply side of the MC is intrinsically satisfied if the value of $\sin(\theta_{in} - \beta_{in})$is maintained to zero. The output of PI controller is the compensated displacement angle which is imposed on the input current of the MC, $\bar{I}_i$, in the modulation algorithm. The desired voltage transfer ratio determines the saturation point of the PI controller, as described in the open-loop compensation method. The calculation of the actual modulation index needs to consider the compensated displacement angle, φ_{in}.

$$m_V = \frac{2}{\sqrt{3}} \frac{|\bar{V}_o^*|}{|\bar{V}_{in}^*| \cos(\varphi_{in})}, \quad 0 \le m_V \le 1 \tag{11.41}$$

The performance of closed-loop IPF controller is shown in Figure 11.27. With IPF compensation, the supply phase voltage and line current are in phase, which implied by the power factor angle, $(\theta_{in} - \beta_{in})$, in the figure. From 0.8 s when the power factor compensation is disabled, the supply current leads the corresponding phase voltage by 19°. It can be seen from the figure that the amplitude of supply current increases when the power factor is lower than the unity as the output power is kept the same with no change in the output current and output voltage. The closed-loop can achieve a flexible IPF adjustment though the modulation. Figure 11.28 shows the performance of step change of the desired IPF angle from 0° to leading 45°. It can be seen that the input current of MC, i_i, is controlled to lag the input voltage with φ_{in} through the modulation in order to have unity power factor at power supply, whereas it leads the input voltage with $(45° - \varphi_{in})$ when a leading power factor cos 45° is desired. The response time of the closed-loop compensator is 1.4 ms, which is the same as that of the open loop, while the response of the closed-loop compensator settles much faster at the reference with little overshoot in power factor angle. Moreover, the steady-state error is eliminated in the closed-loop scheme.

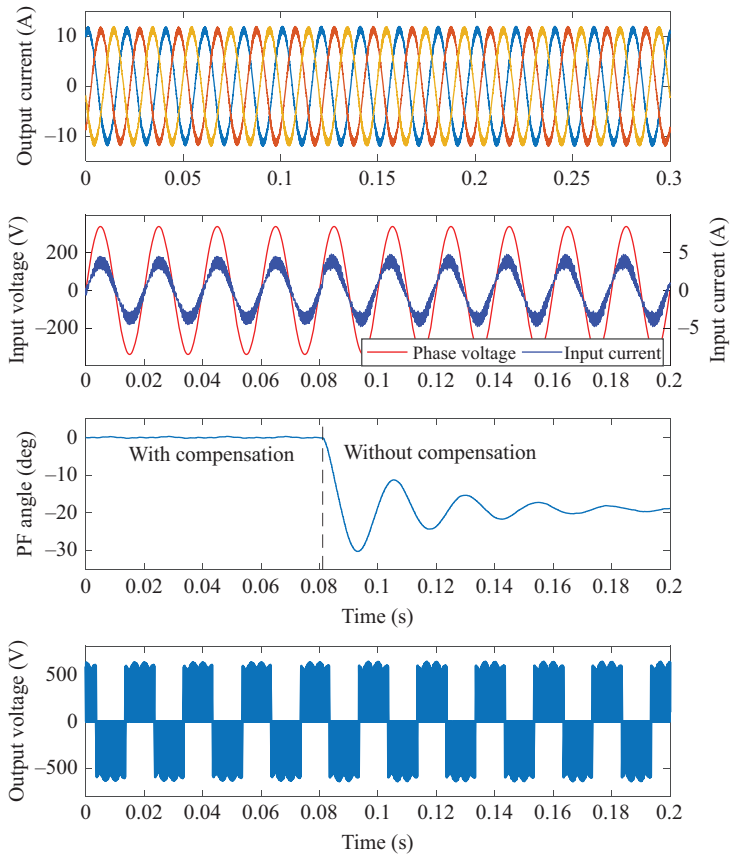


Figure 11.27 Performance of input/output of MC with and without IPFC

11.2 DTC for MC drive

To be better understood, DTC for MC drives will be demonstrated on the basis of DTC for two-level VSI drive. The conventional DTC of IPMSM is based on the following stator flux and torque equations [48,49]:

$$\begin{aligned} \bar{v}_s &= \frac{d\bar{\lambda}_s}{dt} + R_s\bar{i}_s \\ T &= \frac{3P\lambda_s}{4L_dL_q}\left[2\lambda_f L_q \sin\ \delta - \lambda_s(L_q - L_d)\sin\ 2\delta\right] \end{aligned} \tag{11.42}$$

Assuming the voltage drop $R_s\bar{i}_s$ across the stator resistance R_s small to be ignored, the stator flux linkage $\bar{\lambda}_s$ is driven in the direction of the stator voltage vector $\bar{v}_s$ within a short sampling period ΔT.

$$\Delta\bar{\lambda}_s \cong \bar{v}_s\Delta T \tag{11.43}$$

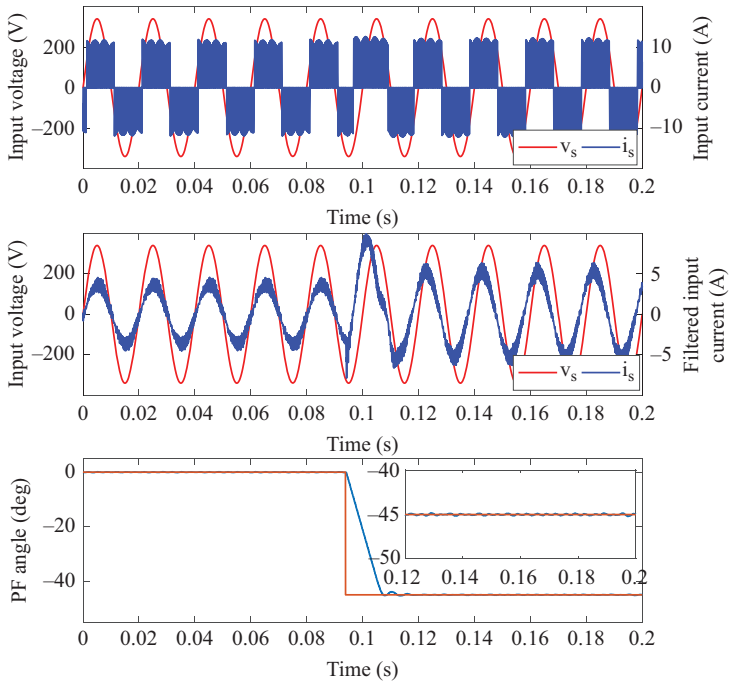


Figure 11.28 Step change of IPF angle from 0° to 45° leading

It implies that the amplitude of the stator flux linkage can be regulated by applying a set of voltage vectors which are radial positive, radial negative, forward positive, forward negative, backward positive, backward negative and zero vectors. The torque can be linearized in a small range of load angle δ as

$$T \approx K_T \delta \tag{11.44}$$

It indicates that the torque is regulated by varying the load angle δ, which is the angle between the stator flux and rotor flux, while the amplitude of the stator flux linkage is kept constant. Since the mechanical time constant is much larger that the electrical time constant, the change in δ is achieved by regulating the speed of the stator flux vector, which in turn is determined by the sequence of the voltage vectors. Consequently, any stator voltage vector determines a torque variation on the basis of two contributions: the variation of the stator flux magnitude and phase angle of stator flux with respect to rotor flux.

Based on the analysis above, the six-vector switching table for torque and stator flux control can be developed as in Table 11.5. C_λ and C_T are the outputs of the flux and torque hysteresis controllers, respectively. $C_\lambda = 1$ implies that the estimated flux is smaller than its reference value and vice versa. The same thing applies to C_T for torque control. Zero vector will be applied when the torque error is within a given hysteresis limits $C_T = 0$. V_0 or V_7 is selected based on the sector of

Table 11.5 Switching table for stator flux linkage and torque control under DTC

C_λ	C_T	θ_1	θ_2	θ_3	θ_4	θ_5	θ_6
$C_\lambda = 1$	$C_T = 1$	$V_2(110)$	$V_3(010)$	$V_4(011)$	$V_5(001)$	$V_6(101)$	$V_1(100)$
	$C_T = 0$	$V_7(111)$	$V_0(000)$	$V_7(111)$	$V_0(000)$	$V_7(111)$	$V_0(000)$
	$C_T = -1$	$V_6(101)$	$V_1(100)$	$V_2(110)$	$V_3(010)$	$V_4(011)$	$V_5(001)$
$C_\lambda = -1$	$C_T = 1$	$V_3(010)$	$V_4(011)$	$V_5(001)$	$V_6(101)$	$V_1(100)$	$V_2(110)$
	$C_T = 0$	$V_0(000)$	$V_7(111)$	$V_0(000)$	$V_7(111)$	$V_0(000)$	$V_7(111)$
	$C_T = -1$	$V_5(001)$	$V_6(101)$	$V_1(100)$	$V_2(110)$	$V_3(010)$	$V_4(011)$

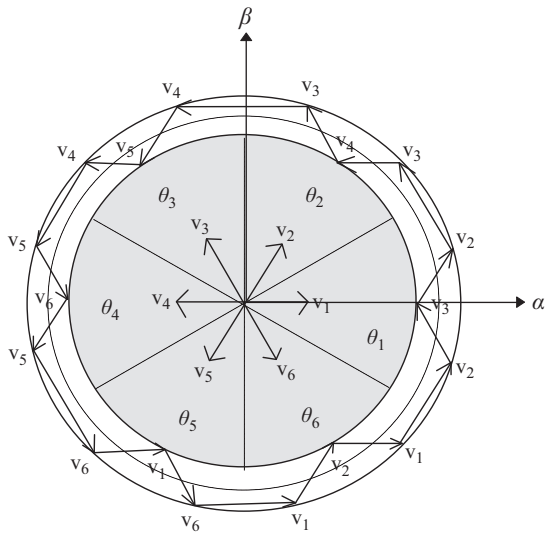


Figure 11.29 Stator flux control by applying appropriate voltage vectors

the stator flux vector. The number of switching times can be minimized in this way. θ_1–θ_6 represent the sectors in which the stator flux vector lies as defined in Figure 11.29. These sectors provide the approximate position information of the stator flux linkage with a resolution of 60° electrical in the stationary reference frame.

The maximum angle $\delta_{\max}$ corresponding to maximum torque occurs when $dT/d\delta = 0$.

$$\delta \leq \delta_{\max} = \cos^{-1}\left(\frac{a - \sqrt{a^2 + 8\lambda_s^2}}{4\lambda_s}\right) \tag{11.45}$$

where $a = \frac{L_q}{L_q - L_d}\lambda_f$.

Furthermore, for stable torque control, the condition that torque increases with increase in load angle δ has to be satisfied. Thus, $dT/d\delta \geq 0$. Let $x = \cos\ \delta$,

$$f(x) = \lambda_f L_q x - \lambda_s (L_q - L_d)(2x^2 - 1) > 0 \tag{11.46}$$

For any, $x \in [\cos \delta_{\max}, 1]$

$$x_1 = \frac{a + \sqrt{a^2 + 8\lambda_s^2}}{4\lambda_s} > 1 \tag{11.47}$$

Solving (11.46) gives us

$$\lambda_s < \frac{L_q}{L_q - L_d}\lambda_f \tag{11.48}$$

Therefore, to ensure a stable DTC of IPMSM drive, the load angle δ and stator flux linkage must be controlled such that (11.45) and (11.48) are satisfied at all times.

11.2.1 DTC of MC drives using three hysteresis comparators

The DTC scheme for MC induction motor drives was initially proposed in [50]. Only one switching configuration is applied to maintain the torque and stator flux error within the hysteresis bands at each sampling time under the constraint of unity IPF.

The MC can be considered as a two-stage converter based on ISVM theory. The principle of the conventional DTC for MC can be considered as a DTC for VSI with a virtual DC-link voltage and a hysteresis control of IPF for a CSR. The DTC for VSI has been explained in the previous section. The virtual DC-bus voltage is generated by the applied input vector in the rectifier stage.

The IPF control is achieved by maintaining the average value of displacement angle close to a desired value, normally to zero for unity power factor. As shown in Figure 11.30, the average value of displacement angle is obtained by applying a low-pass filter (LPF) to the sine value of φ_{in}. The IPF is controlled by controlling the direction of rotation of the input current vector $\bar{I}_{in}^*$. Two fixed input current vectors in each sector have opposite effect on the direction of $\bar{I}_{in}^*$ and thus the displacement angle, φ_{in}. For example, when the input voltage vector $\vec{V}_{in}$ is leading $\bar{I}_{in}^*$ in sector I as shown in Figure 11.31, $\bar{I}_2(ac)$ intends to keep $\bar{I}_{in}^*$ rotating towards $\vec{V}_{in}$. This will decrease φ_{in}. On the contrary, $\bar{I}_1(ab)$ causes $\bar{I}_{in}^*$ to rotate in the opposite direction of $\vec{V}_{in}$, which increases φ_{in}. If the estimated $<\ \sin\ \varphi_{in}\ >$ is positive and output of the comparator $C_\varphi = 1$, $\bar{I}_2(ac)$ will be applied. $\bar{I}_1(ab)$ will be applied when $C_\varphi = 0$. Each applied input current vector in the short sampling period creates a virtual DC-link voltage, which equals to one of the line-to-line voltages. This virtual DC voltage generates any desired active voltage vector for DTC in VSI stage. Combining the voltage vector for VSI-DTC and input current vector for IPF control, a switching table is developed as given in Table 11.6, where j and k are the sector numbers of input voltage vector and stator flux vector, respectively, and i is used to adjust the

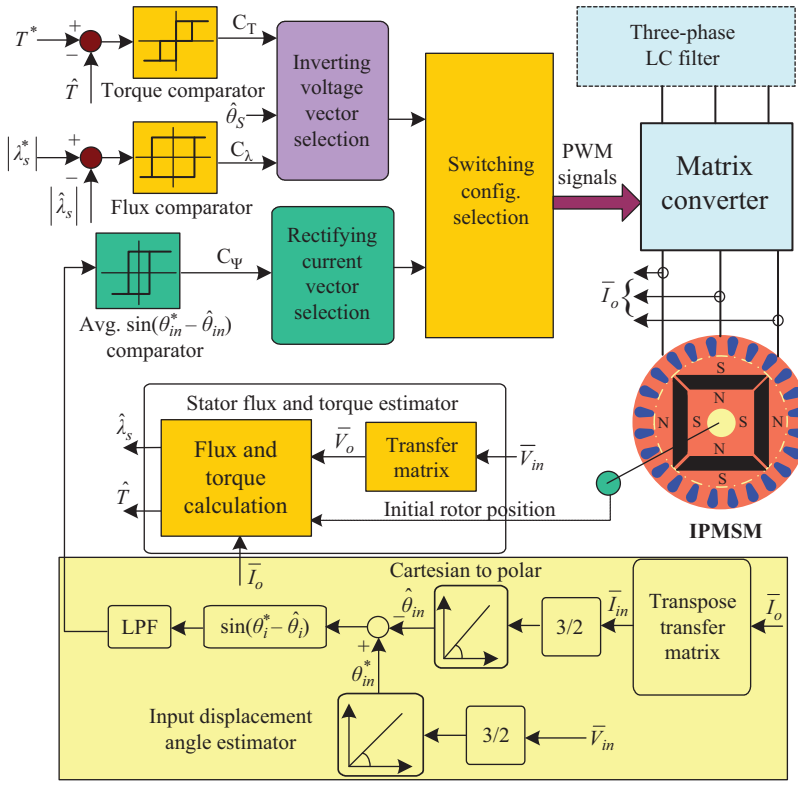


Figure 11.30 Conventional DTC for MC IPMSM drives

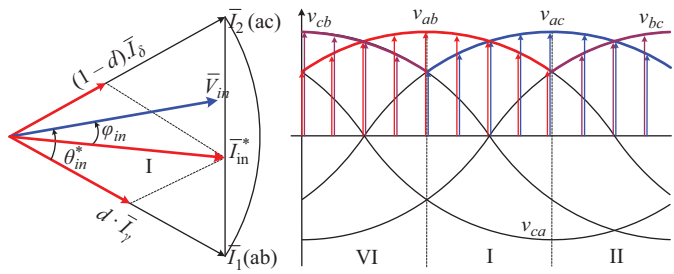


Figure 11.31 Input vectors and their representation in the time domain (d = 0 or 1 for conventional DTC)

vector number in between one and six. One voltage vector is selected for the torque and flux control and one current vector is selected for the IPF control. The switching states corresponding to each of the selected voltage and current vector pairs are determined by the switching configurations of MC given in Table 11.7.

Table 11.6 Switching table for conventional DTC ($i = 0$ or 1; $j = 1 \ldots 6$; $k = 1 \ldots 6$)

$\bar{\lambda}_s$ **in sector** k		**Torque**			$\bar{I}_{in}$ **in sector** j		**Current vector**
		↑	–	↓			
Flux	↑	$\bar{V}_{k+1-6i}$	$\bar{V}_Z$	$\bar{V}_{k+5-6i}$	↑	$\hat{\theta}_{in}$	$\hat{I}_{j+1-6i}$
	↓	$\bar{V}_{k+2-6i}$	$\bar{V}_Z$	$\bar{V}_{k+4-6i}$	↓		$\hat{I}_{j-6i}$

Table 11.7 Switching configurations of matrix converter, indicating the input phase sequences connected to the output phases (A, B and C)

		VI	**I**	**II**	**III**	**IV**	**V**	**VI**
		$\bar{I}_1(ab)$	$\bar{I}_2(ac)$	$\bar{I}_3(bc)$	$\bar{I}_4(ba)$	$\bar{I}_5(ca)$	$\bar{I}_6(cb)$	
6	$\bar{V}_6(101)$	aba	aca	bcb	bab	cac	cbc	
1	$\bar{V}_1(100)$	abb	acc	bcc	baa	caa	cbb	
2	$\bar{V}_2(110)$	aab	aac	bbc	bba	cca	ccb	
3	$\bar{V}_3(010)$	bab	cac	cbc	aba	aca	bcb	
4	$\bar{V}_4(011)$	baa	caa	cbb	abb	acc	bcc	
5	$\bar{V}_5(011)$	bba	cca	ccb	aab	aac	bbc	
6								

The stator currents of the motor and input voltage of the power supply are measured in the drive system while the input currents and the stator voltages are calculated on the basis of the low-frequency transfer matrix of the MC in (11.4) and (11.5). The stator flux is estimated from the integration of the back emf of the machine to avoid requiring continuous position information. The IPF angle is estimated with the knowledge of both input voltage and input current phase angles.

11.2.2 An improved DTC for MCs

The conventional DTC for MC drives selects only one switching configuration to compensate the instantaneous errors in the torque and flux under constraint of unity IPF. The performance of the IPF control determines the input side quality of the MC. The feedback to the IPF controller is the average value of sine calculation ($< \sin \varphi_{in} >$), which is obtained by applying an LPF to its instantaneous value. The low-pass-filtered value does not immediately or fully reflect the status of displacement angle because of the time delay and wave smoothing. This may lead to the wrong hysteresis comparator action and hence selecting the opposite current vector. Furthermore, one of the six fixed input current vectors is kept being applied until the hysteresis comparator changes its output state and/or the sector of input voltage vector changes. The minimum duration of each input current vector is determined by the sampling period rather than the resolution of the digital signal processor (DSP) timer. As a result, the accuracy and resolution of IPF control is low.

This results in distorted input currents with high harmonics scattered around the resonance frequency of the input filter.

In order to overcome the limitation of IPF control in the conventional MC-DTC drive, a modified DTC scheme, as shown in Figure 11.32, is proposed to improve the quality of input currents without compromising the performance of the torque and flux control [51,52]. The fundamental component of the motor terminal voltage is obtained by the measured input voltages and the two given switching states with their durations. The principle of IPF control is presented in Figure 11.31; two adjacent input current vectors applied each sampling period to synthesize the input current vector. The input currents at the power supply are measured in order to implement the closed-loop IPF compensation. The duty cycles of the input vectors are derived from the modulation for the rectifier stage of ISVM. The duty cycles of active and zero vectors in CSR-SVM are calculated as follows:

$$d_k^{svm} = \frac{|\bar{I}_{in}|}{|\bar{I}_k|} \cdot \frac{\sin(60^\circ - \hat{\theta}_{in} + \varphi_{in})}{\cos(\varphi_{in})} \tag{11.49}$$

$$d_{k+1}^{svm} = \frac{|\bar{I}_{in}|}{|\bar{I}_{k+1}|} \cdot \frac{\sin(\hat{\theta}_{in} - \varphi_{in})}{\cos(\varphi_{in})} \tag{11.50}$$

$$d_0^{svm} = 1 - d_k^{svm} - d_{k+1}^{svm} = 1 - \cos(30^\circ - \hat{\theta}_{in} + \varphi_{in}) / \cos(\varphi_{in}) \tag{11.51}$$

where φ_{in} is the displacement angle between the supply voltage and input current of the MC, and $\hat{\theta}_{in}$ is the input voltage vector angle referring to the bisecting line of the corresponding sector k.

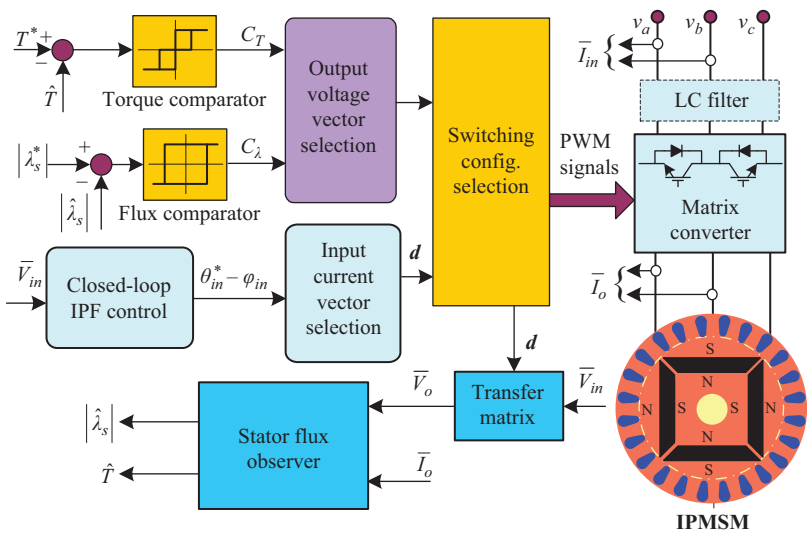


Figure 11.32 An improved DTC for MC IPMSM drive

The duty cycles for two active input current vectors in the proposed DTC can be calculated with (11.52) and (11.53) by prorating the duration of the zero vector to those of active vectors.

$$d_k^{DTC} = d_k^{svm} + \frac{d_k^{svm} \cdot d_0^{svm}}{d_k^{svm} + d_{k+1}^{svm}} = \frac{\sin(60^\circ - \hat{\theta}_{in} + \varphi_{in})}{\cos(30^\circ - \hat{\theta}_{in} + \varphi_{in}) \cdot \cos(\varphi_{in})} \tag{11.52}$$

$$d_{k+1}^{DTC} = d_{k+1}^{svm} + \frac{d_{k+1}^{svm} \cdot d_0^{svm}}{d_k^{svm} + d_{k+1}^{svm}} = \frac{\sin(\hat{\theta}_{in} - \varphi_{in})}{\cos(30^\circ - \hat{\theta}_{in} + \varphi_{in}) \cdot \cos(\varphi_{in})} \tag{11.53}$$

Two switching configurations are applied for different time intervals in each sampling cycle according to the position of the input voltage vector. IPF control described in Section 11.1.5 is also applicable to the modified DTC scheme by involving φ_{in} in the input current vector synthesis. The switching table is given by Table 11.8. The duty cycle d is calculated with the input voltage vector angle, which is also required in the conventional DTC method. The IPF comparator, LPF and the IPF estimator in conventional DTC are all omitted. Therefore, the modified DTC does not increase the complexity of the system but simplifies IPF control.

11.2.3 Experimental results

In order to investigate the performance in both motoring and generating operations, the MC feds a 230 V four-pole 0.97 kW IPMSM mechanically coupled with a permanent magnet DC machine (PMDC). The PMDC machine is used as a dynamometer to load the IPMSM and driven by an H-bridge DC/DC converter. The armature current of DC machine is regulated to carry out a four-quadrant load test. The parameters of the MC prototype, PMDC motor and IPMSM are given in Table 11.9.

The performances of modified DTC and conventional DTC for MC IPMSM drive are compared in Figures 11.33(a)–(d). In the conventional DTC scheme, the average value of IPF is maintained close to zero, 25º displacement angle compensated at 33% rated output power. The low harmonic distortion of the input current is significantly reduced by using the modified DTC, which can be observed from the fast Fourier transform (FFT) traces of the input current. However, the performance of output current is not affected by the new switching pattern used in the modified DTC. It can be observed from the current spectrums that the high harmonic components in the input/output current are scattered from fundamental to

Table 11.8 Switching table for modified DTC, $d = d_k^{DTC}$

$\bar{\lambda}_s$ **in sector** k		**Torque** ($\hat{\omega} > \omega\Delta/\hat{\omega} < -\omega\Delta$)		$\bar{I}_{in}$ **in sector** j	
		↑	↓		
Flux	↑	$\bar{V}_{k+1-6i}/\bar{V}_Z$	$\bar{V}_Z/\bar{V}_{k+5-6i}$	$\hat{\theta}_{in}$	$(1-d)\cdot\bar{I}_{j+1-6i}$
	↓	$\bar{V}_{k+2-6i}/\bar{V}_Z$	$\bar{V}_Z/\bar{V}_{k+4-6i}$		$d\cdot\bar{I}_{j-6i}$

Table 11.9 Parameters of DTC matrix converter IPMSM drive used in this chapter

Switching devices	1,200 V/50 A, 18 × IXER35N120D1	L/L voltage (V)	230
Input filter capacitors of MC	6.6 μF/275 Vac/ph	Line current (A)	3
Input filter inductors of MC	3×1.5 mH/20 A	L/L back EMF (VRMS/kRPM)	136
Parallel damping resistors	3× 47 Ω/5 W	Number of pole pairs	2
Current/voltage transducers	3×LEM LTSR 25-NP3×LEM LV 20-P	Stator resistance (Ω)	5.3
Rated speed of PMDC	1,800 rpm	*d*-axis inductance (H)	0.0448
Rated voltage of PMDC	180 V	*q*-axis inductance (H)	0.1024
Rated current of PMDC	6.9 A	Rotor inertia (kg m^2)	0.001329
Sampling period	50 μs	Rated torque (N m)	6

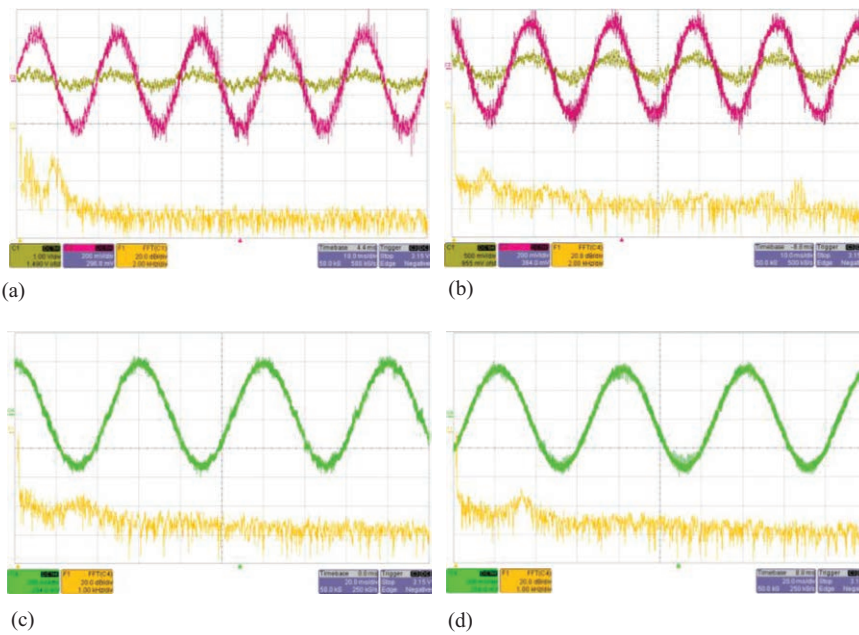


Figure 11.33 Input current (y) and stator current (g) of two DTC schemes with their harmonic spectrums, 20 dB/div, at 500 rpm under rated load. Input voltage and current: (a) 100 V/div,10 A/div; (b) 100 V/div, 5 A/div. Stator current: (c) 2 A/div; (d) 2 A/div

3 kHz and centered around the resonance frequency of the input filter, 1.6 kHz. The variable switching frequency due to the feature of the hysteresis control makes the input filter design difficult, and normally an oversized filter is used.

The input and output performance of the modified DTC MC drive under rated load disturbance is illustrated in Figure 11.34, confirming the inherent bidirectional power-flow capability of the MC. It can be seen from Figure 11.34 that the input current and the corresponding input phase voltage are in phase during the motoring operation while the displacement angle is shifted to 180º during regenerative braking after a short transient process. It implies that the MC is drawing electric power from the AC mains to DC machine and feeding generative power back to the mains with nearly sinusoidal waveforms and at unity IPF. It is noted that both input and stator current waveforms are sinusoidal immediately after the torque reversal command.

11.2.4 DTFC for MC-fed PMSM drives by using ISVM

In the previous section, two hysteresis DTC schemes for MC drives have been presented. Compared with the conventional DTC, the modified DTC scheme features lower harmonic content in the input current, structural simplicity and unity IPF without compromising the merits of DTC, such as fast responses and robustness to parameter variations. However, it possesses several major disadvantages which are summarized as follows:

- high ripples in torque and flux linkage even at high sampling frequency due to the hysteresis control feature and the limited number of voltage vectors available;
- variation of switching frequency dependent on hysteresis bandwidth and operation point;
- relatively high harmonic distortion in input current;

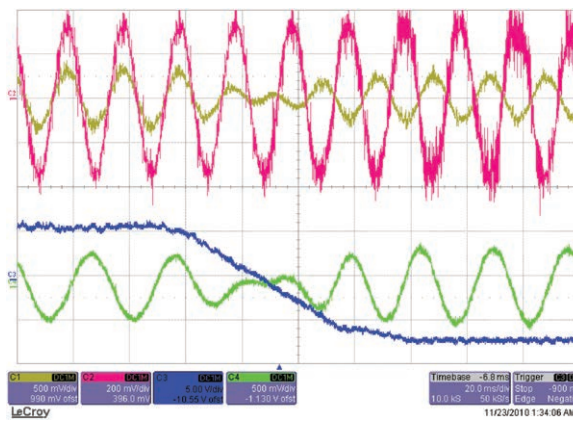


Figure 11.34 Input current (5 A/div), phase voltage (100 V/div), torque (5 N m/div) and stator current (5 A/div) of the proposed DTC with unity IPF compensation at 1,000 rpm under rated load disturbance

- low cut-off frequency of the input filter and consequently big filter capacitance; and
- instability at very low speed and standstill.

To solve the problems above, a DTFC scheme based on ISVM for MC-fed IPMSM drive, as shown in Figure 11.35, is presented in this section. It features low torque and flux ripples, constant switching frequency and sinusoidal input/output currents while maintaining unity IPF and fast dynamics. Independent closed-loop control of both the torque and stator flux linkage is achieved by using two PI controllers. The reference voltage and input current vectors are synthesized by ISVM strategy, which replaces the switching table in the hysteresis DTC schemes. Closed-loop IPF control is feasible and easily implemented in the ISVM strategy.

11.2.4.1 A Mathematical model of IPMSM in the stator flux (*x*-*y*) reference frame

The mathematical model of an IPMSM can expressed in the rotor flux (*d*-*q*) as follows:

$$\begin{cases} v_d = R_s i_d + \dfrac{d\lambda_d}{dt} - \omega_{re}\lambda_q \\ v_q = R_s i_q + \dfrac{d\lambda_q}{dt} + \omega_{re}\lambda_d \end{cases} \tag{11.54}$$

$$\begin{cases} \lambda_d = L_d i_d + \lambda_f \\ \lambda_q = L_q i_q \end{cases} \tag{11.55}$$

$$T = 1.5P(\lambda_d i_q - \lambda_q i_d) \tag{11.56}$$

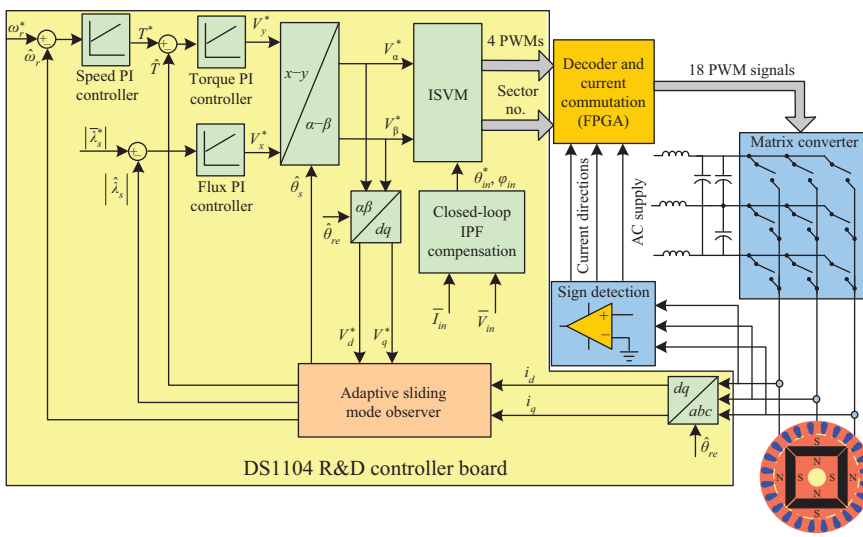


Figure 11.35 Block diagram of the DTFC-ISVM MC IPMSM drive

where i_d, i_q, v_d, v_q, and λ_d, λ_q are the components of current, voltage and stator flux linkage vectors on dq-axes, respectively.

The various reference frames are depicted in Figure 11.36. By using (11.57), (11.54) can be transformed to the x-y reference frame, where the stator flux vector is aligned with x-axis. The proposed DTFC scheme is implemented in x-y reference frame [53,54].

$$\begin{pmatrix} F_x \\ F_y \end{pmatrix} = \begin{pmatrix} \cos\ \delta & \sin\ \delta \\ -\sin\ \delta & \cos\ \delta \end{pmatrix} \begin{pmatrix} F_d \\ F_q \end{pmatrix} \tag{11.57}$$

where δ is the load angle and F represents voltage, current or flux linkage. From (11.54) and Figure 11.36, it can be found that

$$\begin{cases} v_x = R_s i_x + \dfrac{d\lambda_x}{dt} - \omega_S \lambda_y \\ v_y = R_s i_y + \dfrac{d\lambda_y}{dt} + \omega_S \lambda_x \end{cases} \tag{11.58}$$

$$T = 1.5P|\lambda_s| i_y \tag{11.59}$$

Since the stator flux vector is aligned with the x-axis, $\lambda_x = |\lambda_S|$ and $\lambda_y = 0$. Then

$$\begin{cases} v_x = R_s i_x + \dfrac{d\lambda_x}{dt} \\ v_y = R_s i_y + \omega_S \lambda_x \end{cases} \tag{11.60}$$

Substituting (11.59) into (11.60) gives

$$v_x = R_s i_x + \frac{d|\lambda_s|}{dt} \tag{11.61}$$

$$v_y = \frac{R_S T}{1.5P|\lambda_S|} + \omega_S |\lambda_S| \tag{11.62}$$

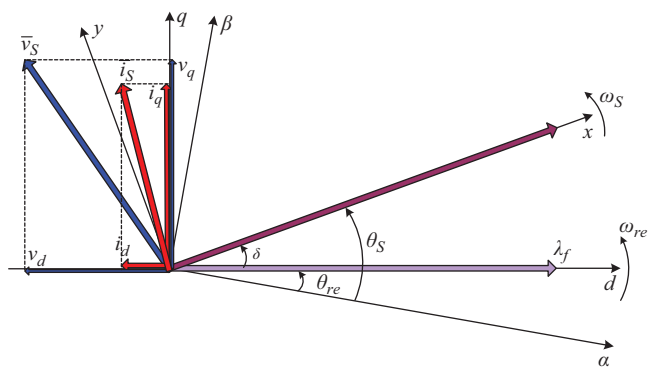


Figure 11.36 The stator and rotor flux linkages in different reference frames

Equation (11.61) shows that the magnitude of the stator flux vector $|\lambda_S|$ can be directly regulated by the x-component of the stator voltage v_x. Similarly, (11.62) reveals the y-component of the stator voltage v_y is qualified to regulate the torque with a feed-forward compensation term $\omega_S|\lambda_S|$, provided that the amplitude of the stator flux $|\lambda_S|$ is maintained constant.

11.2.4.2 Design of the torque and flux PI controllers

With the mathematical models of both the torque and stator flux loops, abundant classical control design methods are readily available. A class of robust control technique called the integral of time multiplied by the absolute of the error (ITAE) criterion [55] is employed in this section. The ITAE criterion is a straight-forward yet effective design tool.

Stator flux PI controller design

By taking Laplace transform both sides and rearranging the terms in (11.61), it gives

$$\lambda_s(s) = \frac{1}{s}[v_x(s) - R_s i_x(s)] \tag{11.63}$$

Considering the voltage drop across the stator resistance $R_s i_x$ as a disturbance in the forward path, the plant model is an integrator whose input and output are the $v_x(s)$ and $\lambda_s(s)$, respectively. A PI controller, as given in (11.64), can be cascaded with the plant model which makes up a typical PI control structure, as shown in Figure 11.37.

$$G_{PI}(s) = \frac{k_{p\lambda}s + k_{i\lambda}}{s} \tag{11.64}$$

Taking the system delay into consideration including the statistical delay of PWM generation and digital signal processing, the open-loop transfer function is altered to (11.65) with an equivalent mathematical model of the delay in the forward path.

$$G_{OL}(s) = \frac{k_{p\lambda}s + k_{i\lambda}}{s^2} e^{-sT_s} \tag{11.65}$$

where T_S is the sampling period. Since T_S is sufficiently small, the delay can be approximated by

$$e^{-sT_s} = 1 - sT_s \tag{11.66}$$

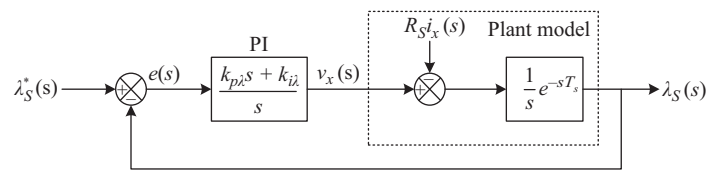


Figure 11.37 Block diagram of the PI-compensated stator flux loop

Substituting (11.66) into (11.65) and ignoring the stator resistance drop, the closed-loop transfer function is given by

$$G_{CL}(s) = \frac{\left(k_{p\lambda}s + k_{i\lambda}\right)e^{-sT_s}}{\left(1 - k_{p\lambda}T_s\right)s^2 + \left(k_{p\lambda} - k_{i\lambda}T_s\right)s + k_i} \tag{11.67}$$

Thus, the closed-loop system is a second-order system whose response is determined solely by the selection of the controller gains. Now, according to the ITAE performance index, the optimum coefficients of the characteristic polynomial of a second-order system are governed by

$$s^2 + 1.4\omega_n s + \omega_n^2 \tag{11.68}$$

where damping ratio $\xi = 0.7$, and ω_n is the natural frequency of the system and can be found by defining the settling time t_s.

$$t_s = \frac{4}{\xi\omega_n} \tag{11.69}$$

The designer has the liberty of dictating the transient performance of the closed-loop flux control system by carefully selecting t_s. Comparing the denominator of (11.67) with (11.68) yields

$$\begin{cases} k_{p\lambda} = \dfrac{\omega_n(1.4 + \omega_n T_s)}{1 + \omega_n T_s(1.4 + \omega_n T_s)} \\ k_{i\lambda} = \omega_n^2(1 - k_{p\lambda}T_s) \end{cases} \tag{11.70}$$

To mitigate the influence of the closed-loop zeros, a pre-filter governed by (11.71) is cascaded in series with the system.

$$G_{PF}(s) = \frac{k_{i\lambda}}{k_{p\lambda}s + k_{i\lambda}} \tag{11.71}$$

Torque PI controller design

Taking Laplace transform and arranging the terms, the torque control equation (11.62) can be expressed as follows:

$$T(s) = \frac{R_s}{1.5P|\lambda_s|}\left(v_y(s) - \omega_s|\lambda_s|\right) \tag{11.72}$$

Consider another expression for the electromagnetic torque with relative to load angle,

$$T = \frac{3P|\lambda_s|}{4L_dL_q}\left[2\lambda_f L_q \sin\ \delta - |\lambda_s|(L_q - L_d)\sin\ 2\delta\right] \tag{11.73}$$

Since the torque operation range is limited within maximum torque, the torque exhibits almost linearity with the load angle within the small operation area.

Their relationship in the small area can be linearized as $T \approx K_T\delta$ with a linearization factor K_T [56].

Differentiating (11.73) both sides with respect to the time yields

$$\frac{dT}{dt} = K_T \frac{d\delta}{dt} = K_T(\omega_s - \omega_{re}) \tag{11.74}$$

where ω_s and ω_{re} are speeds of rotor and stator flux, respectively.

Taking Laplace transform and substituting (11.74) into (11.72) yields

$$T(s) = \frac{K_T\tau}{K_T + \tau s}\left(v_y(s) - \omega_{re}|\lambda_s|\right) \tag{11.75}$$

where $\tau = R_s/1.5P|\lambda_s|$ is a constant. Akin to the stator flux control loop, a PI controller can be cascaded with the plant to achieve closed-loop torque control, as shown in Figure 11.38.

Applying the same analogy as before, the closed-loop transfer function is given by

$$G_{CL}(s) = \frac{K_T\tau\left(k_{pT}s + k_{iT}\right)e^{-sT_s}}{\tau\left(1 - k_{pT}K_TT_s\right)s^2 + K_T\left[1 + \tau\left(k_{pT} - k_{iT}T_s\right)\right]s + k_{iT}K_T\tau} \tag{11.76}$$

Given the identical two degrees-of-freedom design parameters, i.e. ξ and t_s, the controller gains can be selected as follows:

$$\begin{cases} k_{pT} = \dfrac{\omega_n(1.4 + \omega_nT_s) - K_T/\tau}{K_T[1 + \omega_nT_s(1.4 + \omega_nT_s)]} \\ k_{iT} = \dfrac{\omega_n^2(1 - k_{pT}K_TT_s)}{K_T} \end{cases} \tag{11.77}$$

In order to cancel out the closed-loop zero, a pre-filter is inserted in the forward path. Note that a decoupling term $\omega_{re}|\lambda_s|$ is added to the output of the torque PI regulator to alleviate the effect of the disturbance. This can be easily done by calculating the product of the rotor speed and the stator flux magnitude.

Figure 11.39 illustrates the torque dynamics under a unit step reference. The settling time is set to 1 and 3 ms, respectively, which matches the design specification. Likewise, Figure 11.40 illustrates the torque dynamics from 0 to 1 N m. The estimated torque settles at its reference value within the predefined settling time. Thus, the performance of both the flux and torque PI controllers designed with the ITAE criterion is satisfactory.

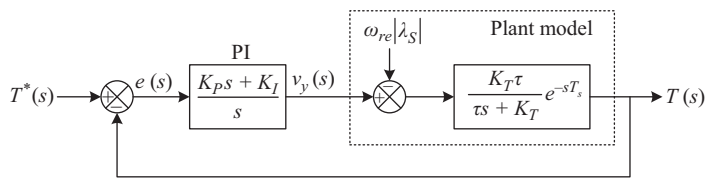


Figure 11.38 Block diagram of a typical PI control structure of flux loop

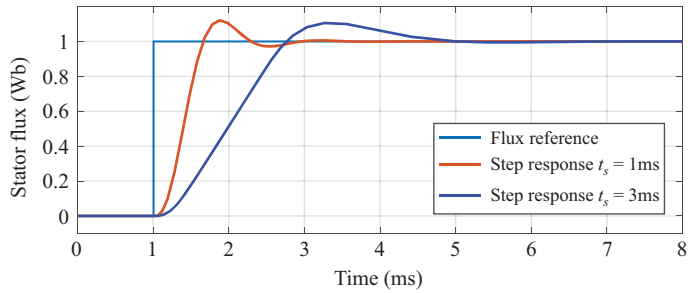


Figure 11.39 Unit step response of stator flux in DTFC with PI controller

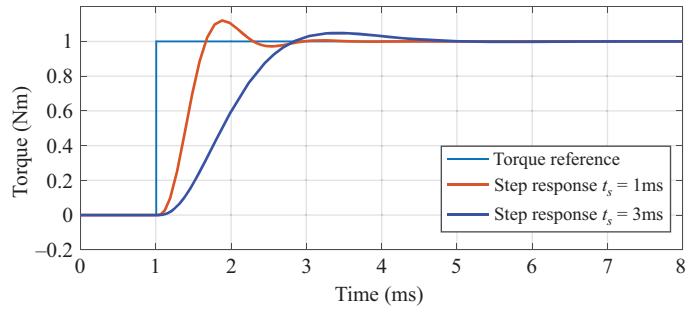


Figure 11.40 Unit step response of torque in DTFC with PI controller

11.2.4.3 Experimental results of DTFC MC drive

The effectiveness and the performance of the DTFC scheme for IPMSM fed by MC have been investigated on the same drive system given in Table 11.9. The sampling frequency is increased to 200 μs and input filter inductance is reduced to 1.0 mH.

The bidirectional power-flow capability of the DTFC MC drive is verified by the full-load disturbance at 1,000 rpm as shown in Figure 11.41. The drive system performs bidirectional power flow naturally without using extra control and modulation strategy. The input and output qualities of the proposed DTFC-ISVM are obviously improved with significantly reduced harmonics and torque ripple in comparison with those of hysteresis DTC schemes. Both input and stator current waveforms are sinusoidal immediately after the step command of a rated torque reversal at high speed. The leading displacement angle due to input filter capacitor is compensated to zero using the closed-loop IPF control strategy. The input current is in phase with the corresponding phase voltage during motoring operation when the speed and torque are both positive. On the other hand, the phase difference between the phase voltage and the current is 180° during regenerative braking when the torque is negative at the same speed.

The input current and stator current waveforms and their corresponding harmonic spectrums at 1,000 rpm with full load are shown in Figure 11.42. It can be noted that the input/output current waveforms of the ISVM DTFC is smoother than

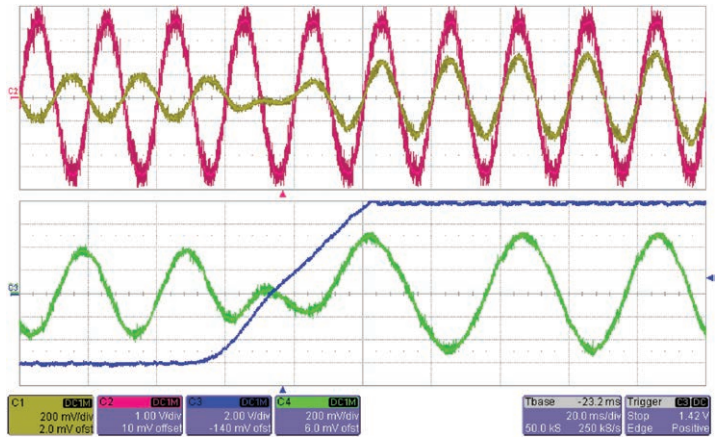


Figure 11.41 Input current (2 A/div), voltage (50 V/div), torque (2 N m/div) and stator current (2 A/div) at 1,000 rpm with full load disturbance

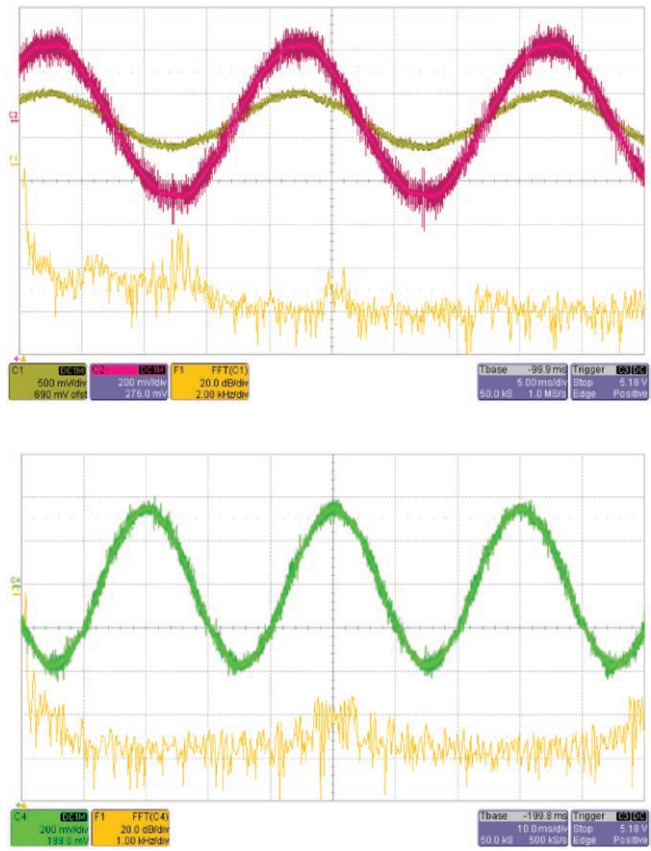


Figure 11.42 Input current (5 A/div), voltage (100 V/div) and stator current (5 A/div) with their harmonic spectrums (20 dB/div), at 1,000 rpm under rated load

the hysteresis DTC scheme. The dominant harmonics in the currents are centered around 5 kHz, which is determined by the sampling frequency of the drive system. This implies, unlike hysteresis DTC, the ISVM DTFC operates at a constant switching frequency, which is the same as the sampling frequency. It results in simple input filter design and consequently optimized size of the input filter.

11.3 IMC-driven AC drives

Figure 11.43 illustrates a modified MC topology, which is known as IMC. It has the same number of switches as DMC and no DC-link capacitor. It is similar to traditional AC/DC/AC converter system which consists of a bidirectional rectifier on the grid side and a conventional VSI on the load side [3]. Consequently, conventional PWM schemes can be employed to regulate the output voltage on VSI side and maintain the DC-link voltage as well as control the IPF on the rectifier side.

11.3.1 Modulation scheme for IMC

11.3.1.1 SVM for rectifier stage

In order to simplify the analysis of the rectifier, the effect of input filter on the grid side is neglected. The modulation scheme is the same as the input vector modulation for conventional MC. Two adjacent active current vectors are applied in each PWM cycle so that the DC-link voltage will be constructed by two of line-to-line voltages. The durations of these two current vectors under unity IPF operation are given as follows:

$$d_\gamma = T_\gamma / T_S = \frac{\sin(60^\circ - \hat{\theta}_{in})}{\cos(30^\circ - \hat{\theta}_{in})} \tag{11.78}$$

$$d_\delta = T_\delta / T_S = \frac{\sin(\hat{\theta}_{in})}{\cos(30^\circ - \hat{\theta}_{in})} \tag{11.79}$$

where $\hat{\theta}_{in}$ is the phase angle within its respective sector of the input voltage vector. The modulated switches, duty cycles of active vectors, and DC-link voltage in each

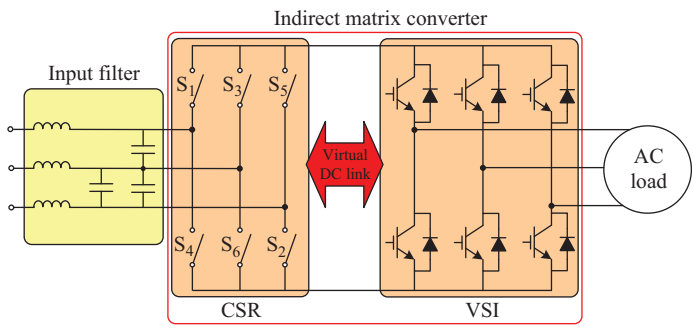


Figure 11.43 Basic topology of IMC

input current sector are given in Table 11.10. The duty cycle for each vector can also be obtained from two of input phase voltages.

11.3.1.2 SVM for inverter stage

Once the PWM sequences of the rectifier have been decided, various PWM methods can be applied to the inverter side, including space vector PWM and sinusoidal PWM. In this section, the seven-segment SVM method will be employed for the inverter side. In the standard seven-segment SVM scheme, the duty cycles of the two active and two zero vectors are determined as follows:

$$d_\alpha = T_\alpha / T_S = \frac{\sqrt{3}\left|\bar{V}_o^*\right|}{\bar{U}_{pn}} \sin\left(\pi/3 - \theta_o^*\right) \tag{11.80}$$

$$d_\beta = T_\beta / T_S = \frac{\sqrt{3}\left|\bar{V}_o^*\right|}{\bar{U}_{pn}} \sin\left(\theta_o^*\right) \tag{11.81}$$

$$d_0 = d_7 = \frac{1}{2}\left(1 - d_\alpha - d_\beta\right) \tag{11.82}$$

where $\bar{U}_{pn}$ is the average DC-link voltage and θ_o^* is the phase angle within its respective sector of the reference output voltage vector.

It can be seen from Table 11.10 that the DC-link is constructed by two line-to-line input voltages. The switching pattern of the inverter stage should be split into two groups. The switching signals can be obtained by comparing control signals with a sawtooth carrier using PWM strategy, as shown in Figure 11.44. Properly arranging the switching sequence in the inverter stage of the IMC can reduce the common-mode voltage [47]. The duty cycle of each vector in the inverter stage is obtained by multiplying duty cycles of rectifier current vectors and inverter voltage vector as follows:

$$d_{\gamma 0} = d_\gamma \cdot d_0; d_{\gamma\alpha} = d_\gamma \cdot d_\alpha; d_{\gamma\beta} = d_\gamma \cdot d_\beta; d_{\gamma 7} = d_\gamma \cdot d_7$$
$$d_{\delta 0} = d_\delta \cdot d_0; d_{\delta\alpha} = d_\delta \cdot d_\alpha; d_{\delta\beta} = d_\delta \cdot d_\beta; d_{\delta 7} = d_\delta \cdot d_7$$

Table 11.10 Modulated switches, duty cycles of active vectors and DC-link voltage

Sector	Input voltage phase angle (θ_{in})	ON switch	Modulated switches and duty cycles (d_γ, d_δ)				DC-link voltage		Average DC-link voltage
I	$[-\pi/6, \pi/6)$	S_1	S_2	$-v_c/v_a$	S_6	$-v_b/v_a$	$-v_{ca}$	v_{ab}	$3V_{im}^2/2v_a$
II	$[\pi/6, \pi/2)$	S_2	S_1	$-v_a/v_c$	S_3	$-v_b/v_c$	$-v_{ca}$	v_{bc}	$-3V_{im}^2/2v_c$
III	$[\pi/2, 5\pi/6)$	S_3	S_4	$-v_a/v_b$	S_2	$-v_c/v_b$	$-v_{ab}$	v_{bc}	$3V_{im}^2/2v_b$
IV	$[5\pi/6, 7\pi/6)$	S_4	S_3	$-v_b/v_a$	S_5	$-v_c/v_a$	$-v_{ab}$	v_{ca}	$-3V_{im}^2/2v_a$
V	$[7\pi/6, 9\pi/6)$	S_5	S_6	$-v_b/v_c$	S_4	$-v_a/v_c$	v_{ca}	$-v_{bc}$	$3V_{im}^2/2v_c$
VI	$[9\pi/6, 11\pi/6)$	S_6	S_1	$-v_a/v_b$	S_5	$-v_c/v_b$	$-v_{bc}$	v_{ab}	$-3V_{im}^2/2v_b$

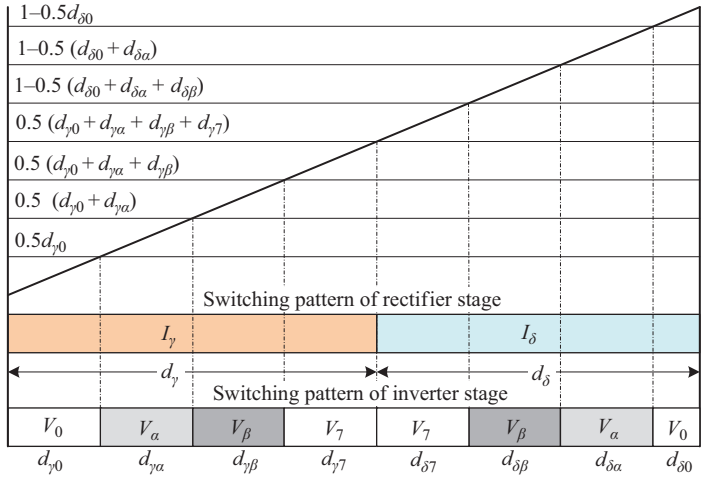


Figure 11.44 Switching pattern of the standard SVM for IMC

11.3.2 Commutation issue for IMC

From Figure 11.44, the rectifier side is commutating only during the inverter side zero vectors, V_0 and V_7. This results in zero DC-link current during commutation on the rectifier side. Therefore, all currents on the rectifier side are zero at any commutation instant. The zero current commutation on the rectifier side largely simplifies the commutating issues always with conventional MCs. In addition, it significantly reduces the switching losses of the rectifier side devices.

11.3.3 Rotor flux-oriented control of induction machine (IM)-driven by IMC

11.3.3.1 Principle of rotor-flux orientation [57–59]

The voltage equations in the synchronously rotating reference frame are

$$\begin{cases} v_{ds} = R_s i_{ds} + \dfrac{d}{dt}(\lambda_{ds}) - \omega_e \lambda_{qs} \\ v_{qs} = R_s i_{qs} + \dfrac{d}{dt}(\lambda_{qs}) + \omega_e \lambda_{ds} \end{cases} \tag{11.83}$$

$$\begin{cases} R_r i_{dr} + \dfrac{d}{dt}(\lambda_{dr}) - (\omega_e - \omega_{re})\lambda_{qr} = 0 \\ R_r i_{qr} + \dfrac{d}{dt}(\lambda_{qr}) + (\omega_e - \omega_{re})\lambda_{dr} = 0 \end{cases} \tag{11.84}$$

and flux linkages are

$$\begin{cases} \lambda_{ds} = L_s i_{ds} + L_m i_{dr} \\ \lambda_{qs} = L_s i_{qs} + L_m i_{qr} \end{cases} \tag{11.85}$$

$$\begin{cases} \lambda_{dr} = L_m i_{ds} + L_r i_{dr} \\ \lambda_{qr} = L_m i_{qs} + L_r i_{qr} \end{cases} \tag{11.86}$$

The rotor currents i_{dr} and i_{qr} cannot be control variables. They can be eliminated from the rotor voltage equations using (11.84).

$$\frac{d\lambda_{qr}}{dt} + \frac{L_r}{R_r}\lambda_{qr} - \frac{L_m}{L_r}R_r i_{qs} + (\omega_e - \omega_{re})\lambda_{dr} = 0 \tag{11.87}$$

$$\frac{d\lambda_{dr}}{dt} + \frac{R_r}{L_r}\lambda_{dr} - \frac{L_m}{L_r}R_r i_{ds} + (\omega_e - \omega_{re})\lambda_{qr} = 0 \tag{11.88}$$

Elimination of transients in rotor flux and the coupling between the two axes occurs when all the rotor flux is in the rotor d-axis. Thus,

$$\lambda_{qr} = 0 \quad \text{and} \quad \left|\vec{\lambda}_r\right| = \lambda_{dr} \tag{11.89}$$

Using (11.89) and (11.90) in (11.87) and (11.88),

$$\omega_e - \omega_{re} = \omega_{sl} = \frac{L_m}{\hat{\lambda}_r}\frac{R_r}{L_r} i_{qs} \tag{11.90}$$

Rotor flux magnitude $\hat{\lambda}_r$ follows i_{ds} slowly,

$$\frac{L_r}{R_r}\frac{d\hat{\lambda}_r}{dt} + \hat{\lambda}_r = L_m i_{ds} \tag{11.91}$$

In steady states, $\hat{\lambda}_r = L_m i_{ds}$. Substituting i_{dr}, i_{qr}, λ_{ds} and λ_{qs} into the torque equation yields

$$T_e = \frac{3P}{2}\frac{L_m}{L_r}\left(\lambda_{dr} i_{qs} - \lambda_{qr} i_{ds}\right) = \frac{3P}{2}\frac{L_m}{L_r}\hat{\lambda}_r i_{qs} \tag{11.92}$$

It is clear from (11.89) and (11.91) that the rotor flux λ_{dr} is determined by i_{ds}, subject to a time delay L_r/R_r. i_{qs}, according to (11.92), controls the developed torque without delay. i_{ds} and i_{qs} are orthogonal to each other and are called the flux and torque-producing currents, respectively. Normally, i_{ds} would remain fixed for operation up to the base speed and it may be reduced to a lower value for field weakening above base speed.

11.3.3.2 Indirect rotor flux-oriented vector control of IM

Based on how the rotor flux is detected and regulated, the flux-oriented control (FOC) for the IM drive can be mainly categorized into two types: indirect and direct schemes. Figure 11.45 summarizes the basic scheme of current control with indirect FOC. In the IRFOC, the slip estimation with measured rotor speed is

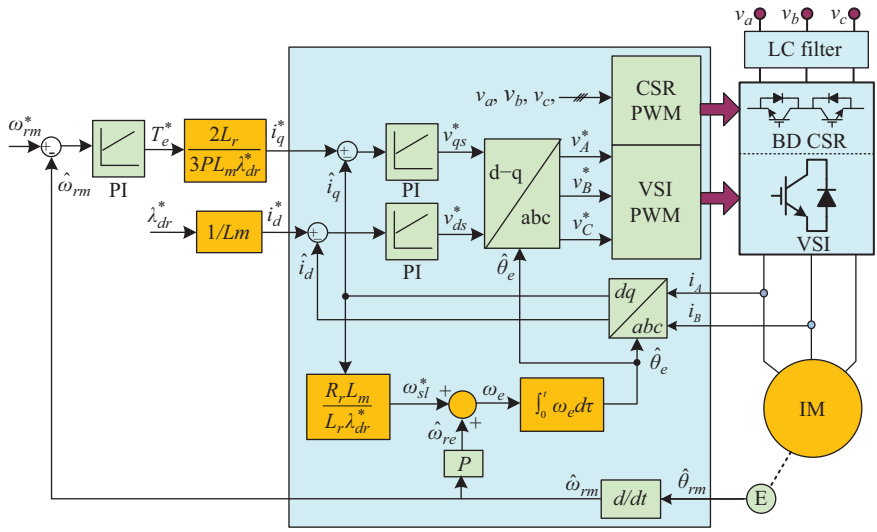


Figure 11.45 Overall block diagram of IRFOC of IM drives using IMC

required in order to compute the synchronous speed. There is no flux estimation appearing in the system. The relationships between torque and i_{qs} given by (11.90) and rotor flux and i_{ds} by (11.91) are used to calculate the current references in the synchronously rotating reference frame using sine and cosine functions of angle θ_e. This angle is obtained as indicated in Figure 11.45. If the orthogonal set of reference rotates at the synchronous speed ω_e, its angular position at any instant is given by

$$\theta_e = \int_0^t \omega_e dt \tag{11.93}$$

A PI controller receives the speed error and generates the reference. This torque reference and the rotor flux reference are used, by means of FOC, to generate the reference currents to the inner control loop. Two independent current controllers in the inner control loop are used to regulate i_{ds} and i_{qs} to their reference values. The compensated i_{ds} and i_{qs} errors are then inverse transformed into the stator *a-b-c* reference frame for obtaining switching signals for the inverter via space vector pulse width modulation (SVPWM) for the VSI stage. The measured input voltages are used for the rectifier stage SVPWM in order to maintain the DC-link voltage as well as to control the IPF.

The performance of the indirect FOC control strategy for an induction machine is shown in Figure 11.46, including the transient response under speed reversal and steady state with full load. It can be observed that the IM drive accelerates under a constant torque (implied by the constant i_{qs} during

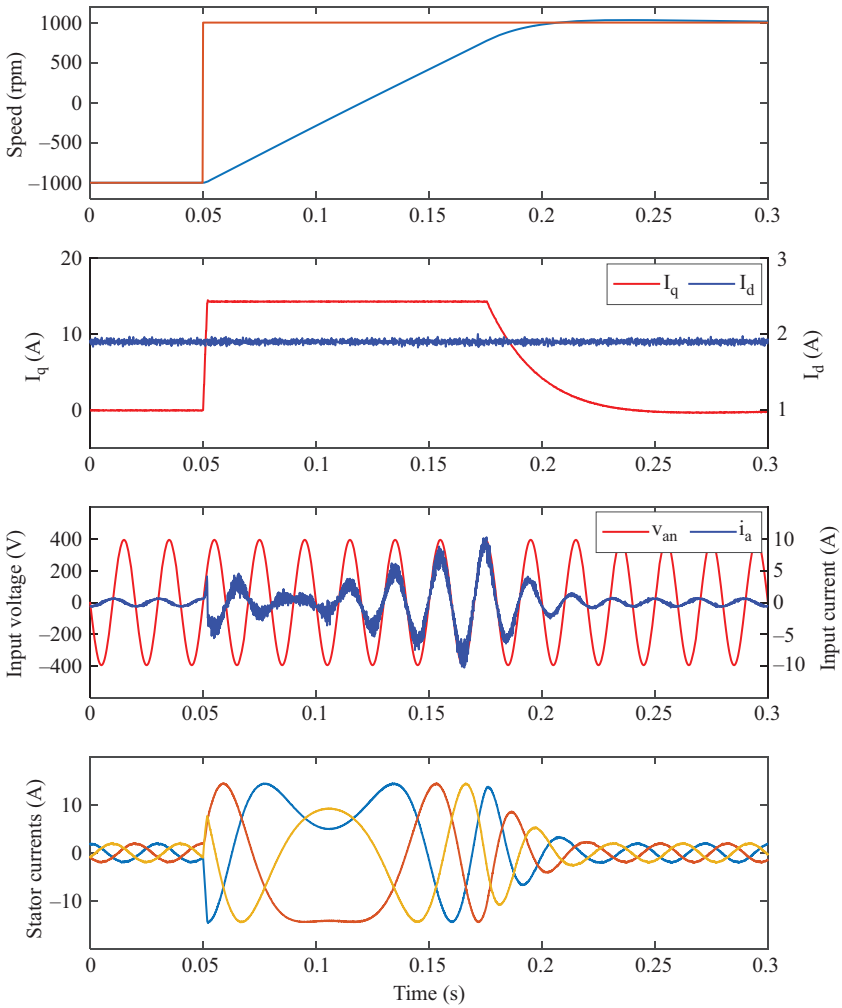


Figure 11.46 Speed reversal for IRFOC strategy using IMC

acceleration) and settles at the final speed with little overshoot in speed. The large overcurrent transients during acceleration are eliminated when the motor almost reaches the speed set point. Obviously, rotor and air-gap fluxes remain constant at all times. During the transient, the amplitude of input current of the IMC increases with the output power of the drive, the product of torque and speed. As shown in Figure 11.47, the unity power factor is obtained only at high output power level due to the effect of input filter capacitor. This effect can be compensated by employing the IPF correction algorithm in the rectifier modulation, as described in Section 11.1.5.

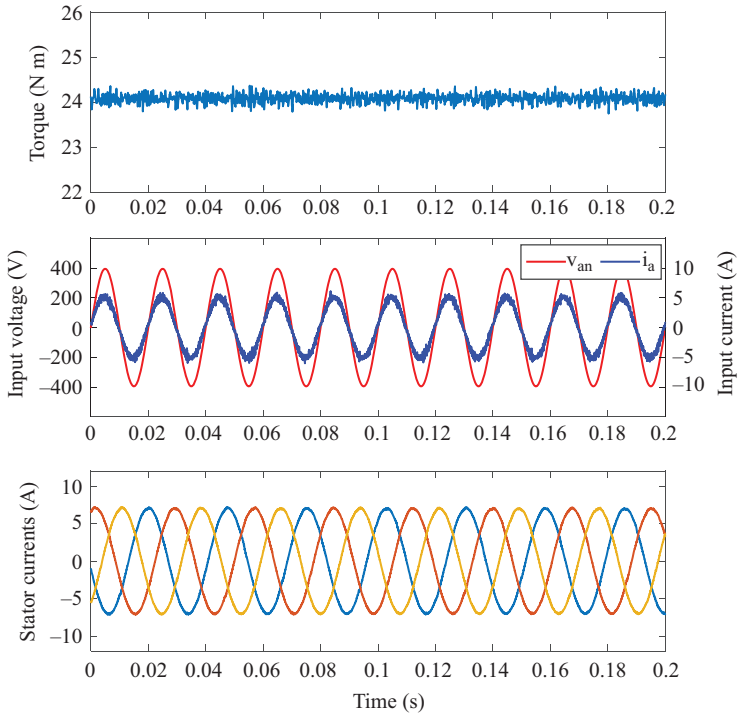


Figure 11.47 Waveforms of torque, input phase voltage, input current and stator currents of the IRFOC IM drive using IMC

11.4 Summary

This chapter has presented the state-of-the-art view in the development of MC AC drives, starting with a brief review on the fundamentals of MCs. Practical implementation issues of MC are discussed in this chapter. The most important practical implementation problem, the commutation between two controlled BDSs, has been solved with the development of highly robust and intelligent multistep commutation strategies. Solutions for overvoltage protection in MC are also discussed in this chapter. The most popular modulation strategies for MCs in the last decade are studied considering the theoretical principles, practical implementations and performances. IPF compensation and control have also been investigated following the ISVM strategy. Closed-loop power factor control is more accurate and robust than the open-loop compensation. It can be easily integrated in the modulation methods by using the displacement angle in the desired input current vector.

This chapter mainly focuses on the DTC for MC-driven IPMSM drives. The principle of DTC schemes for MC drives is based on the DTC principle for VSI drives. The IPF of the MC and the torque and stator flux of the motor are regulated with three hysteresis comparators in the conventional DTC. Input

current harmonics and power factor control have been improved with a modified DTC scheme without compromising the torque and flux control or increasing the complexity of the system. Combination of DTFC with ISVM, DTFC-ISVM, for MC AC drives has solved the associated problems with hysteresis DTC schemes, such as high torque and flux ripples, high input/output harmonics and variable switching frequency. Experimental results have been presented, verifying the effectiveness of DTC schemes and the performance improvement of the DTFC-ISVM scheme.

Finally, the IRFOC of induction motor fed by IMC is studied. The independent modulations applied in the rectifier and inverter stages allow zero-current commutation between BDSs on the rectifier side. It makes the IMC completely free from the complicated commutation issues associated with conventional DMCs.

List of symbols

L_f, C_f	Inductance and capacitance of the input filter
f_n	Fundamental frequency of the power supply
f_o	Resonant frequency of the input filter
f_s	Switching frequency of the matrix converter
$P_{o\ min}$	Minimum output power
φ_{in}	Input power factor angle
k	Amplitude of the modulation indices
β_o	Phase shift
m_c	Current modulation index
d	Duty cycle
i_d, i_q	Components of current
v_d, v_q	Components of voltage
λ_d, λ_q	Components of stator flux linkage
δ	Load angle
T_s	Sampling period
t_s	Settling time
ω_s and ω_{re}	Speeds of rotor and stator flux

Glossary of term

Matrix converter	It is an AC–AC converter consisting of bidirectional switches and does not use any energy storage elements
Indirect space vector modulation	It uses imaginarily splitting the matrix converter into rectifier stage and inverter stage

References

[1] J.W. Kolar, T. Friedli, J. Rodriguez and P.W. Wheeler, "Review of three-phase PWM AC-AC converter topologies," *IEEE Trans. Ind. Electron.*, vol. 58, no. 11, pp. 4988–5006, 2011.

[2] M. Rivera, J. Rodriguez, B. Wu, J.R. Espinoza and C.A. Rojas, "Current control for an indirect matrix converter with filter resonance mitigation," *IEEE Trans. Ind. Electron.*, vol. 59, no. 1, pp. 71–79, 2012.

[3] L.Wei and T.A. Lipo, "A novel matrix converter topology with simple commutation," in *Proc. IAS*, pp. 1749–1754, 2001.

[4] P.W. Wheeler, J. Rodríguez, J.C. Clare, L. Empringham and A. Weinstein, "Matrix converter: a technology review," *IEEE Trans. Ind. Electron.*, vol. 49, pp. 276–288, 2002.

[5] J. Rodriguez, M. Rivera, J.W. Kolar and P.W. Wheeler, "A review of control and modulation methods for matrix converters," *IEEE Trans. Ind. Electron.*, vol. 59, no. 1, pp. 58–69, 2012.

[6] L. Empringham, J.W. Kolar, J. Rodriguez, P.W. Wheeler and J.C. Clare, "Technological issues and industrial application of matrix converters: a review," *IEEE Trans. on Ind. Electron.*, vol. 60, no. 10, pp. 4260–4271, 2013.

[7] J.W. Kolar, F. Schafmeister, S.D. Round and H. Ertl, "Novel three-phase AC–AC sparse matrix converters," *IEEE Trans. on Power Electron.*, vol. 22, no. 5, pp. 1649–1661, 2007.

[8] P. Tenti, L. Malesani and L. Rossetto, "Optimum control of N-input K-output matrix converters," *IEEE Trans. on Power Electron.*, vol. 7, no. 4, pp. 707–713, 1992.

[9] S.M. Ahmed, A. Iqbal and H. Abu-Rub, "Generalized duty-ratio-based pulse width modulation technique for a three-to-k phase matrix converter," *IEEE Trans. Ind. Electron.*, vol. 58, no. 9, pp. 3925–3937, 2011.

[10] P.W. Wheeler, J.C. Clare and L. Empringham, "Gate drive level intelligence and current sensing for matrix converter current commutation," *IEEE Trans. on Ind. Electron.*, vol. 49, no. 2, pp. 382–389, 2002.

[11] S. Bernet, T. Matsuo and T. Lipo, "A matrix converter using reverse blocking NPT-IGBTs and optimized pulse patterns," in *Proc. IEEE PESC/ IEEE Power Electron. Spec. Conf.*, vol. 1, pp. 107–113, 1996.

[12] E. Motto, J. Donlon, M. Tabata, H. Takahashi, Y. Yu and G. Majumdar, "Application characteristics of an experimental RB-IGBT (reverse blocking IGBT) module," *in Conf. Rec. IEEE IAS Annu. Meeting*, 2004, vol. 3, pp. 1540–1544.

[13] C. Klumpner and F. Blaabjerg, "Using reverse-blocking IGBTs in power converters for adjustable-speed drives," *IEEE Trans. Ind. Appl.*, vol. 42, no. 3, pp. 807–816, 2006.

[14] M. Hornkamp, M. Loddenkoetter, M. Muenzer, O. Simon and M. Bruckmann, "EconoMAC the first all-in-one IGBT module for matrix converters," *in Proc. PCIM*, 2001, pp. 1–6.

[15] O. Simon, J. Mahlein, M. Muenzer and M. Bruckmarm, "Modern solutions for industrial matrix-converter applications," *IEEE Trans. Ind. Electron.*, vol. 49, no. 2, pp. 401–406, 2002.

[16] J. Andreu, J. De Diego, I. de Alegria, I. Kortabarria, J. Martin and S. Ceballos, "New protection circuit for high-speed switching and start-up of a practical matrix converter," *IEEE Trans. Ind. Electron.*, vol. 55, no. 8, pp. 3100–3114, 2008.

[17] A. Alesina and M. Venturini, "Analysis and design of optimum-amplitude nine-switch direct ac–ac converters," *IEEE Trans. Power Electron.*, vol. 4, no. 1, pp. 101–112, 1989.

[18] E. Yamamoto, H. Hara, J.K. Kang and H. P. Krug, "Development of matrix converter for industrial applications," Yaskawa White Paper, pp. 1–6, 2007.

[19] I. Sato, A. Odaka, Y. Tamai and H. Mine, "Technologies for practical motor drive system with matrix converter," Fuji Electric Advanced Technology, Ltd, Tokyo, Japan, 2007.

[20] P. Wheeler, H. Zhang and D. Grant, "A theoretical and practical consideration of optimised input filter design for a low loss matrix converter," *Conf. PEVD*, pp. 363–367, 1994.

[21] C. Klumpner, P. Nielsen, I. Boldea and F. Blaabjerg, "A new matrix converter motor (MCM) for industry applications," *IEEE Trans. Ind. Electron.*, vol. 49, no. 2, pp. 325–335, 2002.

[22] H. She, H. Lin, X. Wang and L. Yue, "Damped input filter design of matrix converter," *PEDS'*09, pp. 672–677, 2009.

[23] A. Schuster, "A matrix converter without reactive clamp elements for an induction motor drive system," *IEEE PESC'98*, vol. 1, pp. 714–720, 1998.

[24] J. Mahlein, M. Bruckmann and M. Braun, "Passive protection strategy for a drive system with a matrix converter and an induction machine," *IEEE Trans. on Ind. Eletron.*, vol. 49, no. 2, 2002.

[25] P. Nielsen, F. Blaabjerg and J. Pedersen, "Novel solutions for protection of matrix converter to three phase induction machine," *Conf. rec. Ind. Applicat. 32th Annu. Meeting*, vol. 2, pp.1447–1454, 1997.

[26] J. Mahlein and M. Braun, "A matrix converter without diode clamped overvoltage protection," *in Conf. Proc. IPEMC'2000*, vol. 2, pp. 817–822, 2000.

[27] K. You and F. Rahman, "Over-voltage protection using power Zener diode for matrix converter and matrix-Z-source converter," *2009 International Conference on Power Electronics and Drive Systems (PEDS)*, pp. 193–197, 2009.

[28] C.L. Neft and C.D. Schauder, "Theory and design of a 30-hp matrix converter," *in Conf. Rec. IEEE IAS*, vol. 1, pp. 934–939, 1988.

[29] S. Sunter and J.C. Clare, "Development of a matrix converter induction motor drive," *in Proc. 7th Mediterranean Electrotechnical Conf.*, vol. 2, pp. 833–836, 1994.

[30] R.R. Beasant, W.C. Beattie and A. Refsum, "An approach to the realization of a high-power Venturini converter," *in Conf. Rec. IEEE PESC'90*, pp. 291–297, 1990.

[31] M. Ziegler and W. Hofmann, "Semi natural two steps commutation strategy for matrix converters," *in Conf. Rec. IEEE PESC'98*, vol. 1, pp. 727–731, 1998.
[32] B.H. Kwon, B.H. Min and J.H. Kim, "Novel commutation technique of AC-AC converters," *IEE Proc. Part B*, pp. 295–300, 1998.
[33] J. Mahlein, J. Igney, J. Weigold, M. Braun and O. Simon, "Matrix converter commutation strategies with and without explicit input voltage sign measurement," *IEEE Trans. Ind. Electron.*, vol. 49, no. 2, pp. 407–414, 2002.
[34] N. Burany, "Safe control of four-quadrant switches," *Conf. IEEE IAS*, vol. 1, pp. 1190–1194, 1989.
[35] V. Piriyawong (2007). Design and implementation of simple commutation method matrix converter (Master's thesis). Page 48, Retrieved from CiteSeerX, http://citeseerx.ist.psu.edu/viewdoc/citations;jsessionid=5C9BB0F8B8A004A106508A48DAEDA048?doi=10.1.1.623.14.
[36] L. Empringham, P.W. Wheeler and J.C. Clare, "Intelligent commutation of matrix converter bi-directional switch cells using novel gate drive techniques," *in Proc. IEEE PESC'98*, vol. 1, pp. 707–713, 1998.
[37] M. Venturini, "A new sine wave in sine wave out, conversion technique which eliminates reactive elements," *in Proc. Powercon* 7, pp. E3/1–E3/15, 1980.
[38] A. Alesina and M. Venturini, "Intrinsic amplitude limits and optimum design of 9-switches direct PWM AC–AC converters," *in Proc. IEEE PESC'88*, pp. 1284–1291, 1988.
[39] G. Roy, L. Duguay, S. Manias and G.E. April, "Asynchronous operation of cycloconverter with improved voltage gain by employing a scalar control algorithm," *in Conf. Rec. IEEE-IAS Annu. Meeting*, pp. 889–898, 1987.
[40] G. Roy and G.E. April, "Cycloconverter operation under a new scalar control algorithm," *in Proc. IEEE PESC'89*, pp. 368–375, 1989.
[41] K.K. Mohapatra, P. Jose, A. Drolia, G. Aggarwal, N. Mohan, S. Thuta, "A novel carrier-based PWM scheme for matrix converters that is easy to implement," *IEEE PESC'05*, pp. 2410–2414, 2005, Recife, Brazil.
[42] L. Huber and D. Borojevic, "Space vector modulator for forced commutated cycloconverters," in Conf. Rec. *IEEE-IAS Annu. Meeting*, pp. 871–876, 1989.
[43] L. Huber, D. Borojevic and N. Burany, "Voltage space vector based PWM control of forced commutated cycloconverters," *15th Annual Conf. Ind. Electron. Society IECON'89*, vol. 1, pp. 106–111, 1989.
[44] L. Huber and D. Borojevic, "Space vector modulation with unity input power factor for forced commutated cycloconverters," *Conf. Rec. Ind. Applicat. Society Annual Meeting*, vol. 1, pp. 1032–1041, 1991.
[45] L. Huber; D. Borojevic, "Space vector modulated three-phase to three-phase matrix converter with input power factor correction;" *IEEE Trans. on Ind. Applicat.*, vol. 31, no. 6, pp. 1234–1246, 1995.
[46] H.M. Nguyen, H. Lee and T. Chun, "Input power factor compensation algorithms using a new direct-SVM method for matrix converter," *IEEE Trans. on Ind. Electron.*, vol. 58, no. 1, pp. 232–243, 2011.
[47] K. You, D. Xiao and F. Rahman, "Applying reduced general direct space vector modulation approach of AC–AC matrix converter theory to achieve

direct power factor controlled three-phase AC–DC matrix rectifier," *IEEE Trans. on Ind. Applicat*., vol. 50, no. 3, pp. 2243–2257, 2014.

[48] C. French and P. Acarnley, "Direct torque control of permanent magnet drives," *IEEE Trans. on Ind. Applicat*., , vol. 32, pp. 1080–1088, 1996.

[49] L. Zhong, M.F. Rahman, W.Y. Hu and K.W. Lim, "Analysis of direct torque control in permanent magnet synchronous motor drives," *IEEE Trans. on Power Electron*., vol. 12, pp. 528–536, 1997.

[50] D. Casadei, G. Serra and A. Tani, "The use of matrix converters in direct torque control of induction machines," *IEEE Trans. on Ind. Electron.*, vol. 48, pp. 1057–1064, 2001.

[51] D. Xiao and F. Rahman, "A modified DTC for matrix converter drives using two switching configurations," *Conference Record of EPE '09*, pp. 1–10, 2009.

[52] D. Xiao and M.F. Rahman, "A novel sensorless hysteresis direct torque control for matrix converter-fed interior permanent magnet synchronous motor," *IEEE Power and Energy Society General Meeting, 2010, PES'10*, July 26–29, 2010, Minneapolis, USA.

[53] M. Zelechowski, M.P. Kazmierkowski and F. Blaabjerg, "Controller design for direct torque controlled space vector modulation (DTC-SVM) induction motor drives," *Conference Record of IEEE ISIE '05*, pp. 951–956, 2005.

[54] F. Blaabjerg, M.P. Kazmierkowski, M. Zelechowski, D. Swierczynski and W. Kolomyjski, "Design and comparison direct torque control techniques for induction motors," *Conference Record of EPE '05*, pp. 1–9, 2005.

[55] R.C. Dorf and R.H. Bishop, "Design using performance indices," in *The Control Handbook*, ed. by W.S. Levine, pp. 170–171, Jointly published by IEEE Press, Piscataway, NJ and CRC Press, Boca Raton, FL, 1996.

[56] J. Zhang, Z. Xu, L. Tang and M.F. Rahman, "A novel direct load angle control for interior permanent magnet synchronous machine drives with space vector modulation," *IEEE PEDS'05*, vol. 1, pp. 607–611, 2005.

[57] F. Blaschke, "The principle of field-orientation applied to the transvector closed-loop control system for rotating field machines," *Siemens Review*, vol. 34, 1972.

[58] W. Leonhard, *Control of Electrical Drives*. Springer Verlag, 1996.

[59] P. Vas, *Sensorless Vector and Direct Torque Control*. Oxford University Press, Oxford, New York, Tokyo, 1998.

Chapter 12

An online parameter identification method for AC drives with induction motors

Dhirendran Munith Kumar[1], Hiye Krishan Mudaliar[1], Maurizio Cirrincione[1], and Marcello Pucci[2]

The chapter describes how to implement an online identification method for induction motors within a field-oriented control by using least squares (LS) methods. In particular, it focuses on how to develop the experimental rig by a step-by-step approach, where the different components of the set-up are described to enable readers to have a reference on their own. Attention has been paid both to the connections of the sensors (current, voltage and rotor speed) to the digital signal processing (DSP) of the dSPACE platform and to the construction of the circuits and design of the signal processing part. Experimental results are then presented and discussed to assess the behaviour of the experimental rig with different LS methods to show the flexibility of the test set-up.

12.1 Introduction

Nowadays induction motors (IMs) play a key role in all industry applications because of their cheap cost, robustness and ruggedness and simplicity of construction. They are used both directly supplied by the power grid for simple operations, like pumping, or in innumerable others, if fed by the inverter. Moreover, thanks to the strong progress of power electronics devices, inverter-fed IMs have become easy to control: in particular, the well-known field-oriented control (FOC) or the direct torque control (DTC) have made the decoupled control of flux and current possible, resulting as high performance as those of a DC motor over a wide range of speeds [1,2].

In this respect, the knowledge of the dynamical model of the IM is most important, since it permits highly advanced linear or non-linear control systems to be developed and there is a huge literature in this respect: a good survey is given in [3,4]. However, the IM dynamical model needs a good estimation of the parameters of the motor to achieve a correct control action: e.g. in a rotor flux-oriented control

[1]School of Engineering and Physics, The University of the South Pacific, Fiji
[2]The Institute of Intelligent Systems for Automation of the National Research Council, Italy

drive, an estimation mismatch of the rotor time constant would result in a failure of the control strategy, because of the loss of the correct field orientation.

Nonetheless, the traditional way of estimating the parameters of the motor is by using the classical blocked rotor and no-load tests which present, however, the disadvantages of interrupting the service, since they are carried out offline, giving the values of the parameters in steady-state conditions which can be quite different from those in real-operation conditions. Moreover, the parameters of the machine are time-varying because of heating/cooling (variation of R_s and R_r) and the magnetic saturation (variation of L_m, L_s and L_r).

The above considerations lead to the necessity to have online parameter estimation methods, which converge to the real ones in reasonable time and give unbiased values. There are many ways to retrieve parameters online and a survey can be seen in [4,5]: here it is remembered that these methods are in general classified in "spectral analysis" techniques where the frequency response of injected signals are used, "observation-based techniques" like the extended Luenberger or the Kalman Filter, the Model Reference Adaptive System (MRAS) and finally those based on artificial intelligent techniques, e.g. neural networks, genetic algorithms or fuzzy logic.

All of these methods present some drawbacks: those based on the injection of signals require external equipment to inject the signal and in addition some may suffer from torque pulsations due to high second harmonic. The observation-based method can be computationally very cumbersome, while the MRAS-based ones are highly sensitive to the accurate knowledge of model parameters. Better results are obtainable by using neural networks, but a meaningful test set should be created.

Another way of retrieving the parameters online is by using the least squares (LS) method. With this respect, some methods have been developed, starting from those of [5–11]. These methods generally use the ordinary LS (OLS), often in its recursive form (RLS), and a discussion and thorough presentation of these methods can be found in [4,12–16]. In particular, these methods do not consider the constraints that usually arise when an LS method is used and encounter issues in determining some parameters. In [12], the total LS (TLS) is used in an iterative way that does not need the singular value decomposition (SVD) of the data matrix, thus reducing the computational burden and increasing the accuracy.

This chapter is intended to show how to implement an online parameter estimation method based on LS in an AC drive with IM with FOC. The method proposed is the same as the one presented in [4,12]. Here attention is particularly paid on how to construct physically an experimental rig able to implement the algorithm in a step-by-step approach. Indeed, the chapter is addressed to undergraduate or graduate students to help them to build a suitable experimental rig, tune its controllers, interfacing it with dSPACE and finally implement the least squares (LS), be it OLS or TLS.

The chapter is organized as follows. Section 12.2 presents the essential of the FOC design, Section 12.3 describes how to build the actual electrical drive and interface it with dSPACE, and Section 12.4 explains one way on how the LS method could be applied. Section 12.5 shows and discusses some experimental results in all business areas.

12.2 FOC design

The scheme of the FOC with an IM is shown in Figure 12.1.

12.2.1 Controller tuning

The scheme in Figure 12.1 contains four proportional integrator (PI) controllers for speed, rotor flux linkage and currents in the *x* and *y* directions. The tuning approach for each of the PI loops includes obtaining the Bode plots of the speed, flux and two current loop transfer functions and then using the classical theory for tuning each controller by placing the pole and zero at appropriate locations to obtain desired performance. More details are described in the following.

12.2.1.1 Current loop tuning

The open-loop current transfer function is given by $I_{\mathrm{OL}}(s) = \frac{1}{L_{\mathrm{s}}' s + R_{\mathrm{s}}}$, where OL is the open loop transfer function, s denotes it in the Laplace domain, L_{s}' is the transient stator self-inductance and R_{s} is the stator resistance. The current transfer function can be used to find the parameters of the PI. More specifically, the open-loop gain can be increased to maintain a stability margin over 45°, and a zero is tuned so that the desired bandwidth is obtained.

12.2.1.2 Flux loop tuning

The open-loop flux transfer function is given by $(s) = \frac{L_{\mathrm{m}} R_{\mathrm{r}}}{L_{\mathrm{r}} s + R_{\mathrm{r}}}$, where $L_{\mathrm{m}}$is the three-phase magnetizing inductance, R_{r} is the rotor resistance and L_{r} is the rotor self-inductance. The flux transfer function is used to compute the parameters of the PI.

12.2.1.3 Speed loop tuning

The open-loop speed transfer function is given by $W(s) = \frac{3 L_{\mathrm{m}} p \psi_{\mathrm{r}}}{2 L_{\mathrm{r}} J s}$, where J is the inertia of the IM, ψ_{r} is the rotor flux and p is the pair poles of the IM. Viscous friction has been neglected.

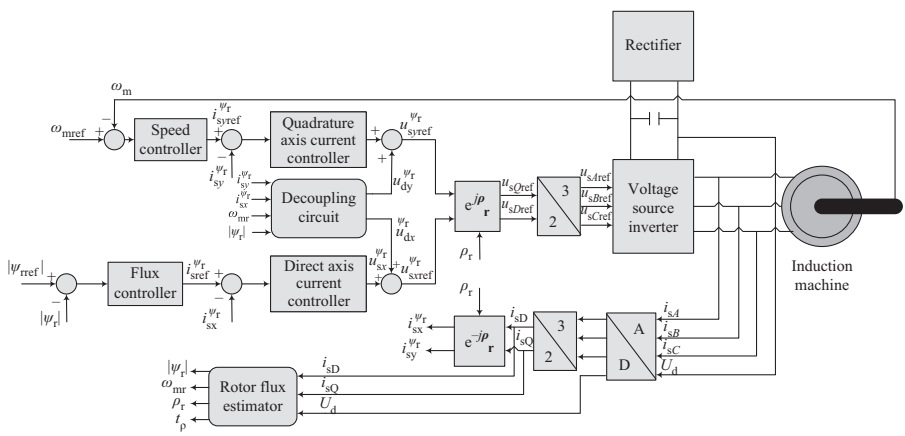


Figure 12.1 FOC scheme

12.3 Description of the test bed

The experimental test bed shown in Figure 12.2 has been developed for implementing the FOC as well as the online parameter estimation LS-based method.

The experimental test bed is made up of the following:

- a three-phase motor with parameters shown in Table 12.1,
- a three-phase VSI (voltage source inverter) of 7.5 kVA from Semikron,

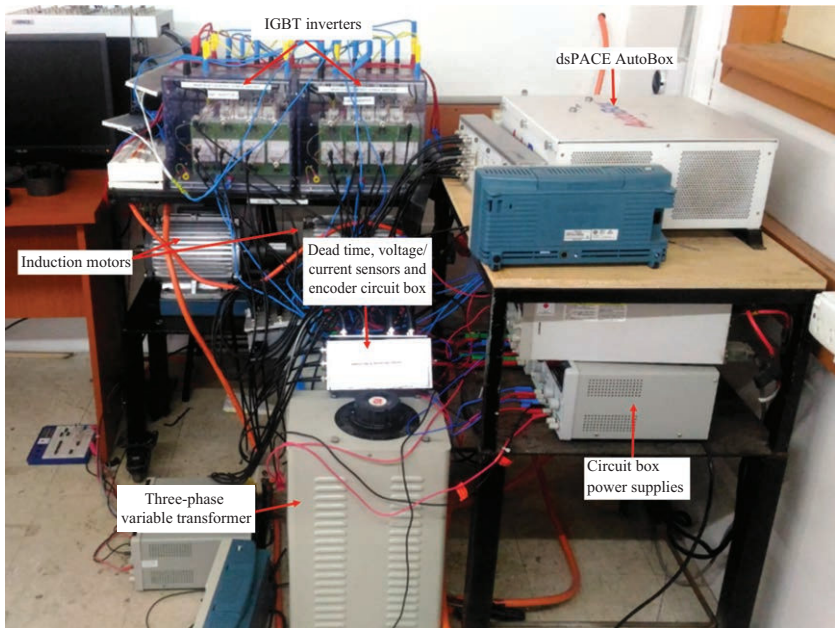


Figure 12.2 Experimental rig

Table 12.1 Parameters of the IM

Rated power [kW]	2.2
Rated voltage [V]	220
Rated frequency [Hz]	50
Pole-pair	2
Stator resistance [Ω]	3.88
Stator inductance [mH]	252
Rotor resistance [Ω]	1.87
Rotor inductance [mH]	252
Three-phase magnetizing inductance [mH]	236
Motor inertia J [kg ·m^2]	0.0089

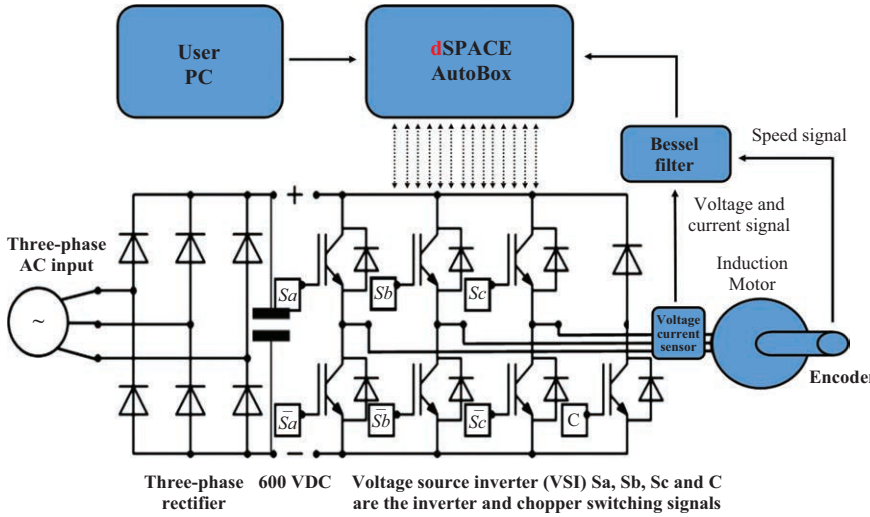


Figure 12.3 Schematics of the experimental rig

- circuit boards with voltage sensors LEM LV 25-P/SP5 and current sensors LEM LA 55-P,
- voltage sensors for the DC-link,
- an electronic card implementing a fourth-order Bessel filter whose cut-off frequency is 800 Hz,
- incremental encoder WDG 58B with 2,500 pulses/round and
- dSPACE **AutoBox** DS1007.

The VSI has been controlled by using a space vector modulation (SVM) with an $f_{PWM} = 5$ kHz, also implemented on the dSPACE. The schematics of the experimental rig is represented in Figure 12.3.

12.4 dSPACE AutoBox

dSPACE AutoBox is generally used for real-time application systems to carry out control experiments and is generally employed for rapid prototyping of electrical drives, development of power trains or advanced driver-assistance systems. For technical details of dSPACE AutoBox, please see Tables A1 and A2 in the appendix.

Before the set-up and configuration of AutoBox, it is important to know the dSPACE hardware connections used for an electrical drive test rig. The general overview of the connections of the dSPACE hardware is shown in Figure 12.4. The PC sends commands to the dSPACE AutoBox processor which sends and receives the control signals from the host to the designated boards. It is important to note that all input and output (I/O) boards can only send and receive signals with a maximum value of 10 V_{DC}.

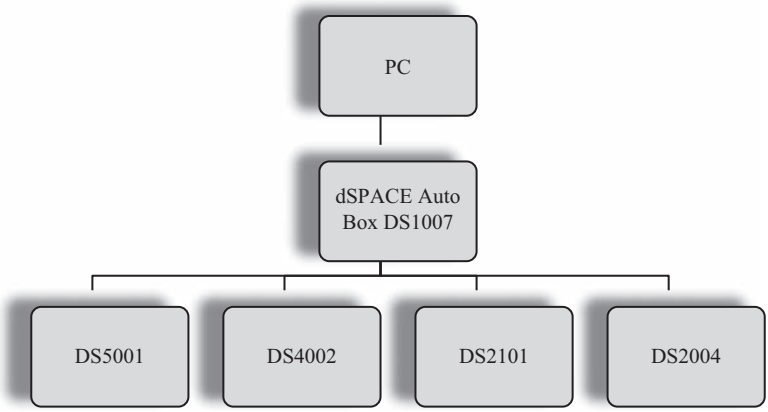


Figure 12.4 General configuration structure

12.4.1 DS1007 PPC processor board

DS1007 is the core of dSPACE AutoBox (see Figure 12.5). It has a great computing power and small I/O processing delays. The board is able to handle high rate of I/O access and has been specifically designed for systems that need high computing power and fast closed-loop rates as is the case of an electrical drive.

12.4.2 DS5001 digital waveform capture board

DS5001 board in Figure 12.6 has been specifically designed to acquire high-frequency pulse width modulation (PWM) signals or position signals. Once the signal has been acquired, the board is able to compute various parameters of the signal, like the frequency, phase shift and duty cycle. In the experimental rig of Figure 12.3, this board is used for the acquisition of the speed of the motor.

In this case, since the output of an incremental rotary encoder is a frequency, the following equation is to be used to compute the actual speed of the motor n in rpm:

$$n = 60f/m \tag{12.1}$$

where f is the frequency in Hz and m is the number of pulses per revolution of the encoder. Figure 12.7 shows how it is implemented in MATLAB®/Simulink®.

12.4.3 DS4002 timing and digital I/O board

DS4002 board in Figure 12.8 has been specifically designed for generating and capturing digital signals. It provides basic functions of conventional digital I/O boards together with features that help perform control tasks. It acquires signals to find their parameters like frequency and phase. It is also able to generate PWM pulses to control gate signals of an inverter.



Figure 12.5 DS1007 board

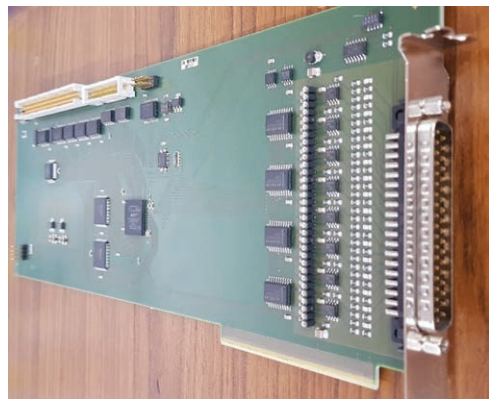


Figure 12.6 DS5001 board

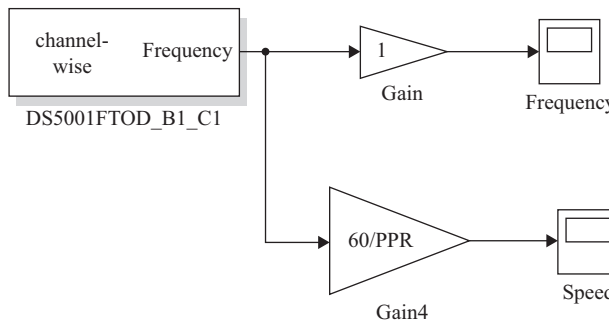


Figure 12.7 Implementation of the DS5001 board on MATLAB/Simulink

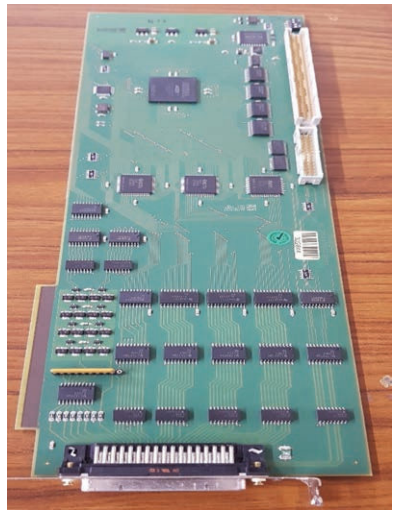


Figure 12.8 DS4002 board

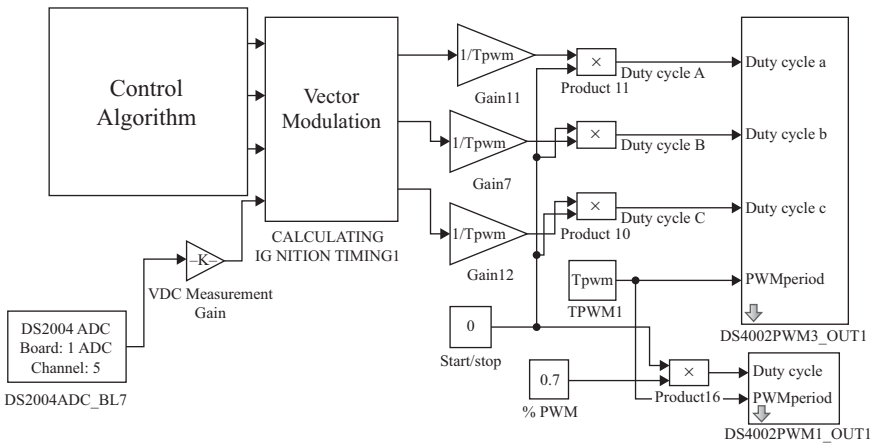


Figure 12.9 DS4002 board used to produce PWM for the gates of the inverter

In case of an electrical drive experimental rig, this board is used for triggering the six gate signals of the two-level inverter. As shown in Figure 12.3, vector modulation techniques are used to produce the switching on and off times using the DS4002 board. It is also used for triggering the chopper of the inverter in case of braking or dissipating excess energy on a load as shown in Figure 12.3. Figure 12.9 shows

how a specific block of DS4002 is used to produce PWM for the gates of the inverter in Simulink environment.

12.4.4 DS2004 high-speed A/D board

This particular board has been specifically designed for fast and precise analog to digital conversion of input signals at high sampling rates (see Figure 12.10). The A/D converter has a resolution of 16 bits. The conversion rate is 800 ns per channel. Having such a high-end specification, the communication overhead is reduced and the overall system performance is improved.

In the case of the electrical drive, the following board is used to acquire the three-phase current signals as well as the DC-link voltage signal. Figure 12.11 shows an example of the data acquisition technique using MATLAB/Simulink environment.

12.4.5 Hardware scheme and interface with dSPACE: I/O boards

The FOC drive has been implemented by using dSPACE, in which the algorithm for the online parameter estimation has also been implemented. In this regard, the whole FOC drive is first developed in MATLAB/Simulink in simulation and then interfaced with dSPACE board channels for I/O. The output signals from dSPACE include the inverter and chopper switching signal for inverter 1, while the input signals to dSPACE include the sensor feedbacks (current and voltages) coming from the three phases and the voltage of the DC-link. The load is given by a twin electrical drive commanded by dSPACE in the same way. Figure 12.4 summarizes the different I/O boards of the dSPACE AutoBox, which will be explained in the following.

The three-phase current and DC voltage feedback acquisition is made via the channels of DS2004 A/D board, while the speed feedback is made via the channel



Figure 12.10 DS2004 A/D board

port of DS5001 digital waveform capture (DWC) board. Both of these boards are used for the feedback of signals to the Control Desk. Moreover, the inverter and chopper switching signals are sent through the DS4002 multi-purpose digital I/O board channels for the insulated-gate bipolar transistor (IGBT) inverter gate trigger and chopper signals. This is schematically shown in Figure 12.12, which shows the designated dSPACE I/O cards with the FOC. However, the user is also required to define the allocated channels and ports that will be used for data acquisition.

The MATLAB/Simulink file with the defined dSPACE I/O channels for hardware is then converted into a *.sdf* file using the Build Command in MATLAB/Simulink environment. The .sdf file generated with MATLAB/Simulink is opened with dSPACE Control Desk for online control of the experimental rig (see Figure 12.13).

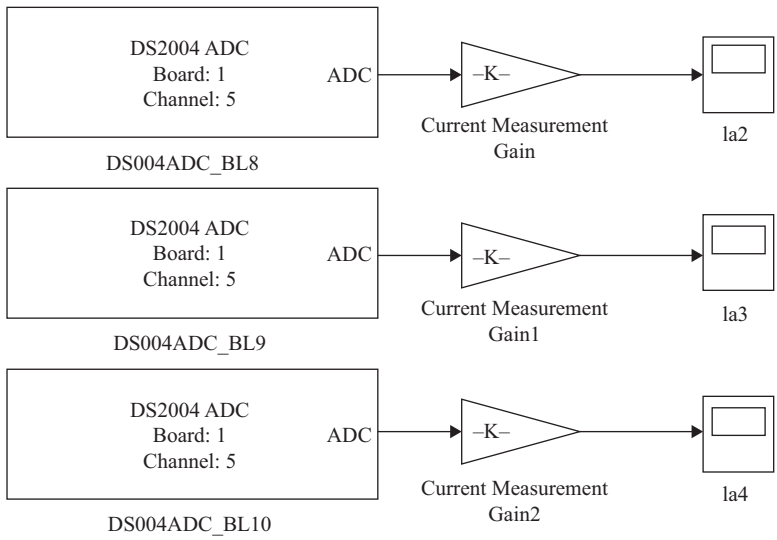


Figure 12.11 Data acquisition with the DS2004 A/D board

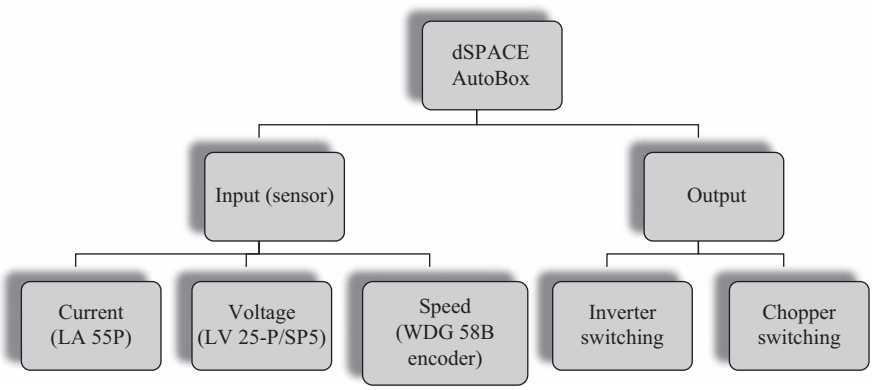


Figure 12.12 dSPACE I/O

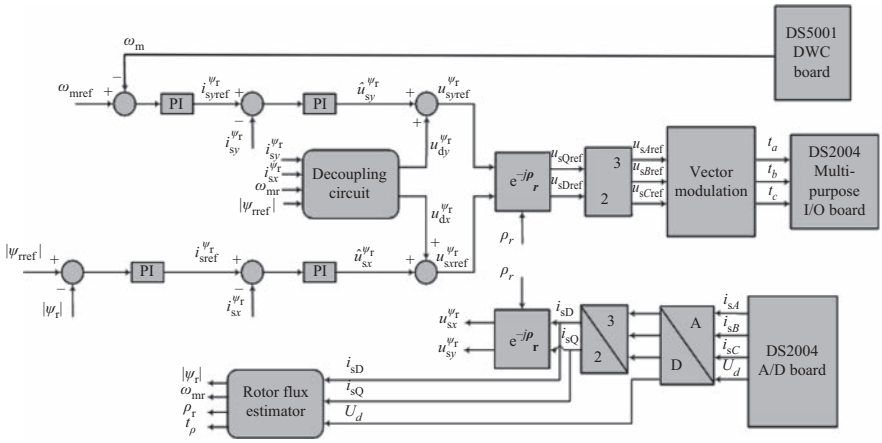


Figure 12.13 Interface with dSPACE I/O

12.5 IGBT inverter

The three-phase IGBT inverter gates are controlled to generate the desired voltage output to control the IM. An IGBT inverter has been used in the test rig because it is able to operate at a high switching frequency and handle the current of the motor.

For this application, the inverter used is SEMITEACH B6U+E1CIF+B6CI, which is a multi-function converter.

Figure 12.14 shows the general connection of the inverter. A three-phase 415 V_{AC} source is connected to the input of the inverter and then converted into 600 V_{DC} by a diode rectifier.

The switching signals $Sa, Sb, Sc, \overline{Sa}, \overline{Sb}$ and $\overline{Sc}$ are created by using the space vector pulse width modulation (SVPWM) technique. The trigger voltage of the inverter is 15 V_{DC} whereas the maximum output from the dSPACE PWM generation board is 10 V_{DC}. Therefore, a suitable amplification circuit is required. In addition, it is important to note that there needs to be a delay in the switch on and off state of the IGBT's in the same column so that Sa and $\overline{Sa}$ will not be switched on/off at the same time. If at any point of time this happens, there would be a short circuit, which could damage the inverter. Thus, a dead time circuit as shown in Figure 12.15 needs to be implemented, providing a dead time of 5 μs.

The switching signal as shown above is first inverted by using the "NOT" gate logic IC-SN7414; for the bottom leg, the input is inverted twice. The inverted PWM signal is then passed through a 1 kΩ resistor and a 270 pF capacitor to reduce the current and to eliminate noise in the signal before entering the differential comparators IC-LM339.

Once passing through the comparator, both the top and bottom signal are then passed through an "AND" gate logic IC-SN7408. Once the appropriate delayed signals are obtained, it is then amplified using the IC-SN7406. This circuit has two outputs given one PWM signal. For a two-level inverter, three of such circuit needs to be made to drive the inverter.

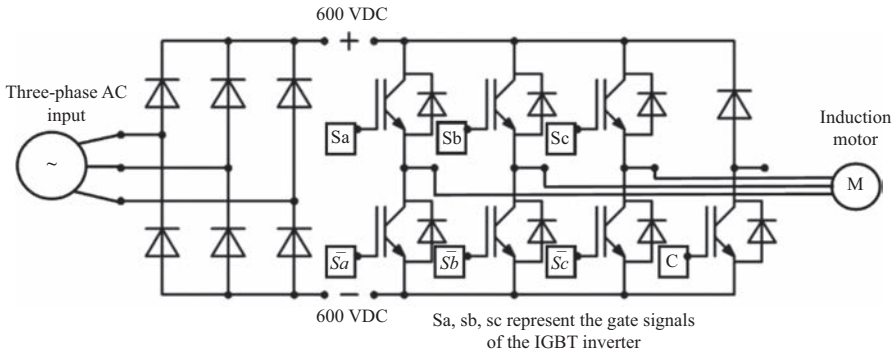


Figure 12.14 Semikron Semitech IGBT inverter

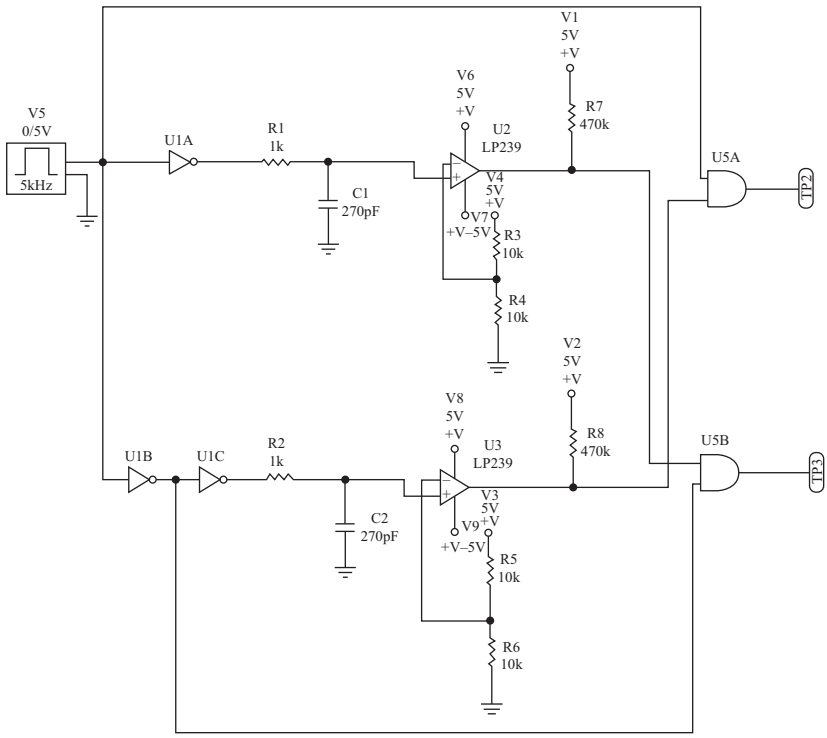


Figure 12.15 Dead time circuit

12.6 Induction motor

For the development of an electrical drive test rig, two motors of the same specifications coupled together have been used. One motor implements the control algorithm while the other implements the load. The motors are twins with a rated steady-state current of 4 A and a power of 2.2 kW. Table 12.1 shows the parameters of the motor after the classical no-load and locked rotor tests.

Afterwards, the next step is to mount the IMs of a flat steel platform, which may vary in shape, size and material, but should be mounted on a rigid surface so that any



Figure 12.16 Motors, platform and coupling

vibration is minimized, otherwise inaccurate data may be acquired. Figure 12.16 shows an example of the platform that is suitable for the mounting the IM. Particular attention should be paid to the alignment of the coupling: misalignment of the motors will result in undesirable effects (harmonics, noise, increase of friction, etc.).

12.7 Sensors of current, voltage and speed

In the following, the configuration of the encoder, the current sensor and the voltage sensors are described.

12.7.1 Encoder configuration

The encoder produces different frequencies at different speeds, and this frequency is used to calculate the speed of the IM rotor shaft according to (12.1). The changing frequency is measured using the dSPACE card DS500 as reported above.

12.7.2 Current sensor configuration

The encoder WDG58B-2500-ABN-I05-K3 has its specific circuit as shown in Figure 12.17. A specific IC DS26LS32CN, quad differential line receiver is used to the output signal of the encoder. The shield is used to avoid harmonics from the surrounding IGBT inverters.

The LA 55P LEM sensor uses Hall effect to measure current in three-phase IM. It is an accurate sensor and highly recommended for AC electrical drive.

The LA 55P current sensor needs a 7 VDC supply and the output is measured across a 100 Ω resistor (see Figure 12.18).

12.7.3 Voltage sensor configuration

The voltage sensor measures the inverter DC-link voltage, and in particular converts the high DC voltage to a significantly small voltage that is used as feedback to the FOC scheme.

The sensor has a high-voltage DC side (±550 V) that uses a high-power resistor to limit the current to 10 mA. DC voltage of the inverter for the load motor tends to increase to +900 VDC when in load operation across 120 kΩ resistor, while the measuring side has a ±12 VDC supply and a 100 Ω resistor (see Figure 12.19).

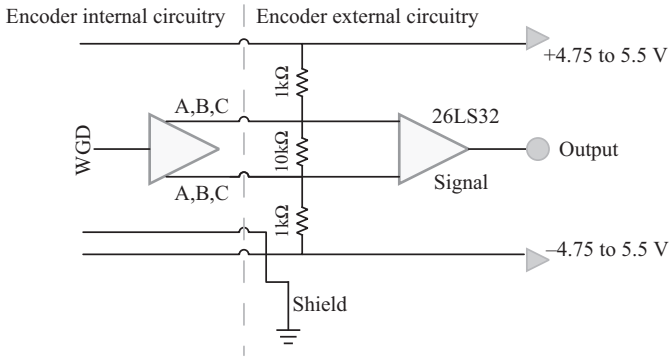


Figure 12.17 Encoder configuration

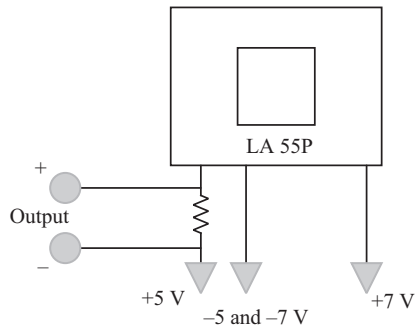


Figure 12.18 Current sensor configuration

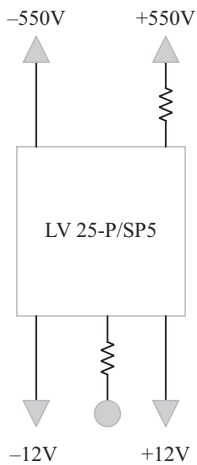


Figure 12.19 Voltage sensor configuration

12.8 Online estimation of the parameters: method and implementation

This part is a summary of the theory of online parameter estimation method presented in [4,12,17].

12.8.1 Description of the method

The IM space-vector equations in the stationary reference frame can be rewritten as follows, if the fundamental assumption that the rotor speed is almost constant, which is valid for standstill, slow transients or in sinusoidal steady state:

$$\begin{pmatrix} \dfrac{di_{\mathrm{sD}}}{dt} & i_{\mathrm{sD}} & \omega_{\mathrm{r}} i_{\mathrm{sQ}} & -\left(\dfrac{du_{\mathrm{sD}}}{dt} + \omega_{\mathrm{r}} u_{\mathrm{sQ}}\right) & -u_{\mathrm{sD}} \\ \dfrac{di_{\mathrm{sQ}}}{dt} & i_{\mathrm{sQ}} & -\omega_r i_{\mathrm{sD}} & -\left(\dfrac{du_{\mathrm{sQ}}}{dt} - \omega_{\mathrm{r}} u_{\mathrm{sD}}\right) & -u_{\mathrm{sQ}} \end{pmatrix} \begin{pmatrix} K_1 \\ K_2 \\ K_{31} \\ K_4 \\ K_5 \end{pmatrix} = \begin{pmatrix} -\dfrac{d^2 i_{\mathrm{sD}}}{dt^2} - \omega_{\mathrm{r}} \dfrac{di_{sQ}}{dt} \\ -\dfrac{d^2 i_{\mathrm{sQ}}}{dt^2} + \omega_{\mathrm{r}} \dfrac{di_{sD}}{dt} \end{pmatrix}. \tag{12.2}$$

This is a matrix equation and the unknowns (K parameters) are defined as follows:

$$K_1 = \frac{1}{\sigma T_s} + \frac{\beta_0}{\sigma}, \quad K_2 = \frac{\beta_0}{\sigma T_s}, \quad K_{32} = \frac{\beta_0}{\sigma}, \quad K_4 = \frac{1}{\sigma L_s}, \quad K_5 = \frac{\beta_0}{\sigma L_s}, \tag{12.3}$$

In this reference frame, it is apparent that a non-linear relationship exists, i.e. given by:

$$K_2 K_4 = K_{31} K_5 \tag{12.4}$$

Moreover, it must be added that from examining (12.3), only some of the five electrical parameters R_s, R_r, L_s, L_r and L_m can be estimated since rotor variables are unknown. Actually, the K parameters can be used only to retrieve four independent parameters:

$$T_r = \frac{K_4}{K_5} \qquad \sigma = \frac{K_5}{k_4(K_1 - K_{31})} \qquad R_s = \frac{K_2}{K_5} = \frac{K_{31}}{K_4} \qquad L_s = \frac{K_1 - K_{31}}{K_5} \tag{12.5}$$

Then L_{m}, L_{r} and R_{r} cannot be retrieved, since no information is available about rotor flux linkages. This means that IMs with same rotor time constant and same $L_{\mathrm{m}}^2/L_{\mathrm{r}}$ will have identical I/O equations.

Equation (12.2) can be solved with an LS method, and the parameters can be retrieved even if the assumption of slowly varying rotor speed is not satisfied.

Remark that (12.2) is composed of two scalar equations that are linearly independent. This has two consequences:

- In sinusoidal steady state, the rank of the matrix is two, so only two parameters can be estimated.
- In non-sinusoidal steady state or during transient, all of the parameters can be estimated, if an LS method is used.

Strictly speaking, the problem under study is to solve (12.2) considering the constraint (12.3), which would give rise to a constrained LS. Moreover, the approximation of slowly varying rotor speed is to be accounted for. This last assumption is not a problem, since LS methods, in particular OLS, solve the LS problem under the assumption that all errors are present in the right term of (12.2). Actually the terms in the matrix are also affected by errors, which would result in the use of TLS techniques. For more details, see [4, Ch. 9]; here only the OLS approach will be dealt with. As for the constraint, since the target is the estimation of the electrical parameters and not the unknowns in (12.2), the use of (12.5) without considering K_2 is preferable. Indeed in this kind of LS approach, the calculation of K_2 is critical: from (12.2), it is apparent that the entries of the second column of the matrix are much smaller than the others, which is the cause of numerical issues in the correct computation of K_2. In conclusion, (12.2) can be computed by an OLS in an unconstrained way. This also gives the advantage of using the huge theory of OLS to study and interpret the solution convergence, the rapidity of convergence, the error, the variance, etc. In all the following, the algorithm which has been used is the OLS in one of its iterative forms. In particular, any LS algorithm can be used with this experimental rig (OLS, DLS, TLS, RLS).

12.8.2 Description and realization of the signal processing system

From inspection of (12.2), the implementation of the online LS parameter estimation requires the following:

- stator current and voltage signals,
- the first and second derivatives of the current signals,
- the first derivative of the stator voltage,
- speed signal and
- anti-aliasing filter.

The anti-aliasing filter is fundamental to cut off all the noise caused by higher harmonics, present in particular in VSI-fed IM, but also if the motor were directly supplied by the grid. This anti-aliasing filter is an analog filter and will permit the subsequent digital processing of the signal, in particular the derivation, which would otherwise amplify high-frequency components. On the other hand, the presence of this filter as well as of the differentiators and further low-pass filters results in distortion and time delays. This can be circumvented by using filters with linear phase, for which the time delay is constant, thus permitting, for each instant

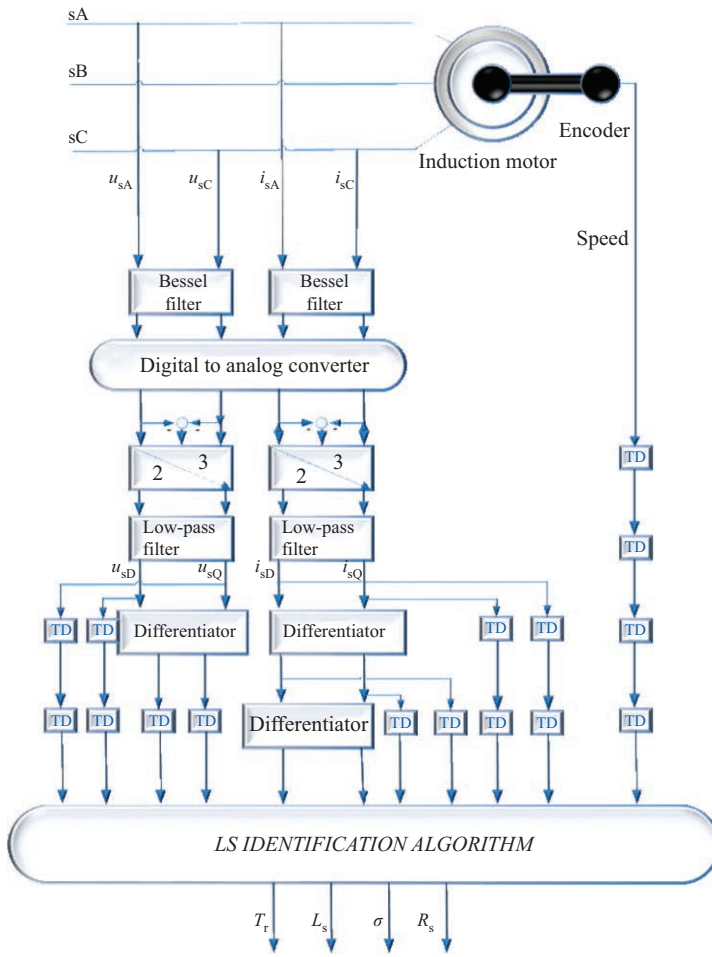


Figure 12.20 Signal processing system [4,12]

of time, to synchronize the signals and respect (12.2). The scheme is shown in Figure 12.20. In the following, each filter is described and discussed

12.8.3 Anti-aliasing filter

The anti-aliasing filter, represented by Bessel filter block in Figure 12.20, is a fourth-order Bessel low-pass filter for the signals from the current sensors and those for the DC-link sensor, after the phase voltages have been reconstructed. Since in this application, the A/D converter has a sampling frequency $f_s = 10$ kHz (or a sampling time $T_s = 100$ μs), all harmonics above 5 kHz are to be cancelled so as to avoid aliasing. Thus, an analog low-pass filter has been designed, in particular a Bessel filter whose phase diagram is almost linear. Figure 12.21 shows the

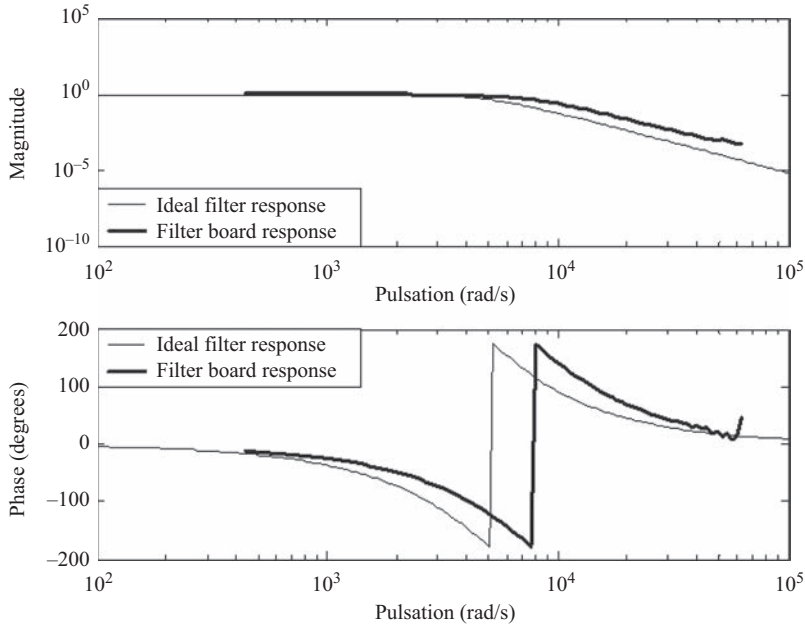


Figure 12.21 Frequency diagram of the low-pass analog Bessel filter (from [4])

frequency diagrams of the designed fourth-order Bessel filter board with 800 Hz as cut-off frequency, and of the ideal filter.

The Bessel filter has been implemented on a board which has six input channels: three-phase voltages and three-phase stator currents coming from the sensor board presented above. It has also six output signals: the three-phase currents and three-phase voltages after filtering. The board is made up of five chips: two chips are operational amplifiers LT1014, each with four inputs and four outputs; the remaining are three chips for filtering. These last three chips are MAXIM® chips (model: MAX274ACNG). The board has a dual supply with four levels of voltages (+15 V, +5 V, −5 V, −15 V) since the operational amplifiers need a +15 V/−15 V supply, and the filter chips require a +5 V/−5 V supply.

The operational amplifiers are used to adapt the signals coming from the sensors compatible with the level of signal required as an input to the filter. The operational amplifiers that process the current signals have a feedback so that the total gain for each is unitary. The operational amplifiers that process the voltage signals have a feedback so that the zero-sequence voltage component (equal to one-third of the voltage sum) is subtracted: this is necessary because the voltages supplied by the VSI have sum which is not null. Figure 12.22 shows the pre-processing circuits. It is noteworthy that each gain of the voltage pre-processor circuits has a gain of one-third.

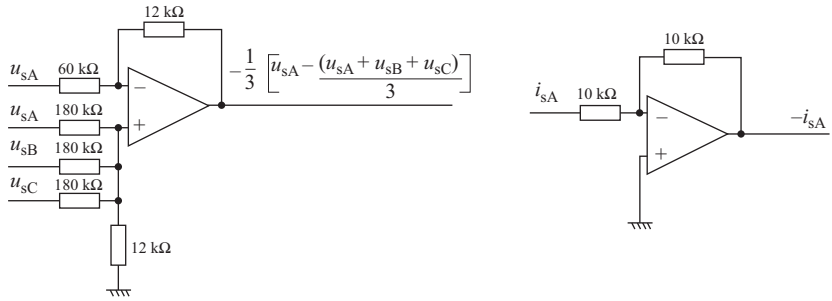


Figure 12.22 Pre-processing of voltage and current signals

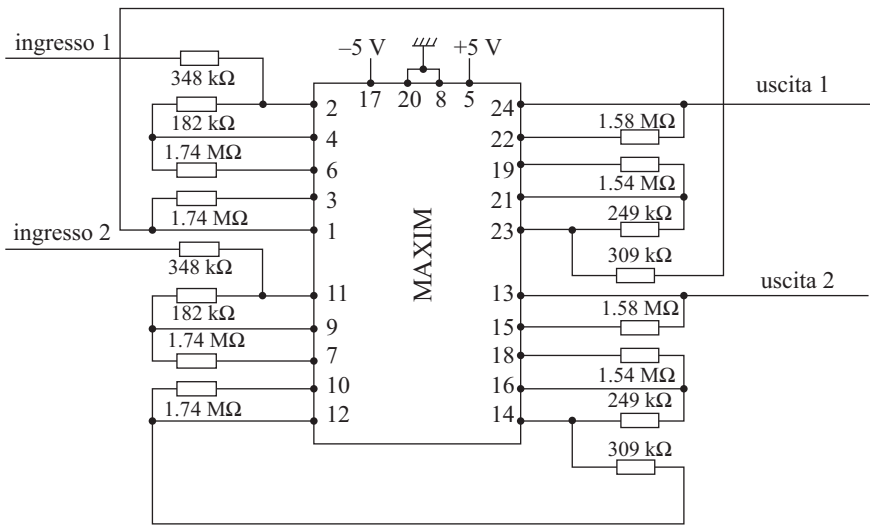


Figure 12.23 Photograph of the fourth-order Bessel filter board

Each MAX274ACNG filter chip is made up of four sections each of which can implement a second-order filter. Since the designed Bessel filter is of fourth order, only two sections have been used (see Figure 12.23). As a whole, three filter chips have been used to process the six input signals. By using the MAXIM® design software the bias resistance have been computed to realize the fourth-order Bessel filter with cut-off frequency of 800 Hz. Figure 12.24 shows the electrical scheme of the bias circuit for the filter and the values of the resistances.

Figure 12.21 shows the frequency response obtained with a suitable instrument, and its comparison with the ideal filter, obtained with MATLAB/Simulink, confirms its validity.

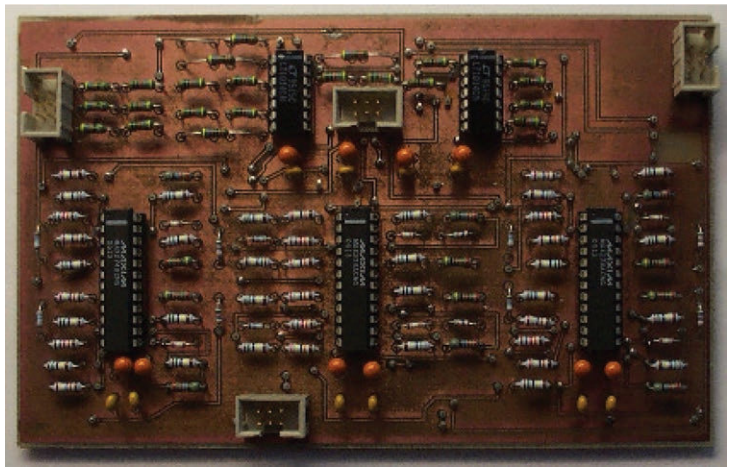


Figure 12.24 Bias circuit for the filter MAXIM®

12.8.4 Digital processing

In Figure 12.20, the digital part is composed of the following:

- an analog-to-digital converter (A/D block in Figure 12.20);
- two FIR low-pass filters to further cancel noise of the stator signals, so as to avoid the following differentiator filters to amplify it;
- three FIR differentiator filters to compute the necessary derivatives as required by (12.2).

The analog-to-digital converter acquires six analog signals with six 16 bit per channel multiplexed in groups of three, and consequently, the percent quantization error, computed as $100/2^{N+1}$, where N is number of bits of the analog-to-digital converter, is 7.6×10^{-4}%. This error is practically negligible with respect to the total percentage error of the acquired signals due to the current and voltage sensors, which is globally of the order of 1%.

The low-pass filters blocks and the differentiator blocks have been designed by using FIR filters so as to have a constant group delay, since they have a linear phase.

The group delay of the Bessel filters and the FIR filters of each block have been computed to obtain the time delays to be used to synchronize the dynamical equations in (12.2) before the LS algorithm implemented on dSPACE processes them. Actually, whenever a stator is processed by any filter, the other unfiltered signals are to be delayed in time and this delay is given by the group delay of each filter, as shown in Figure 12.20.

Figures 12.25 and 12.26 show the frequency responses of the low-pass filter block and the differentiator block presented in Figure 12.20.

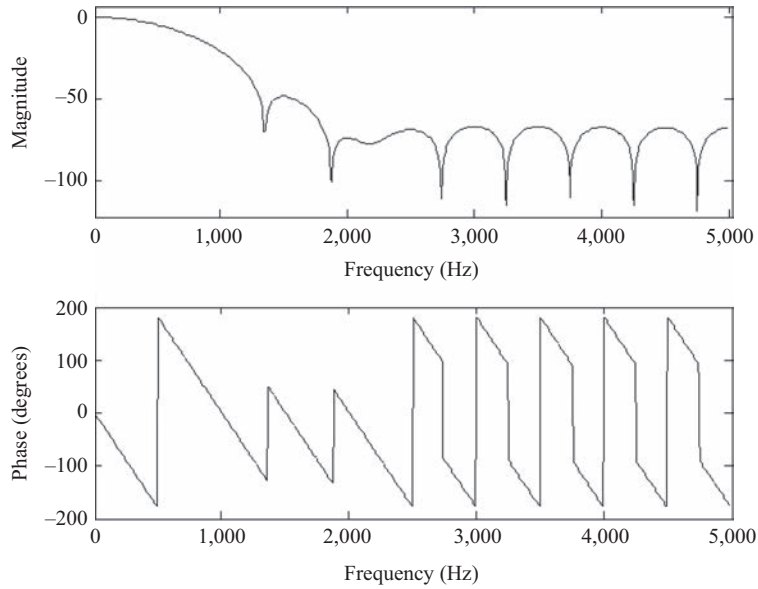


Figure 12.25 Frequency response of F(z)

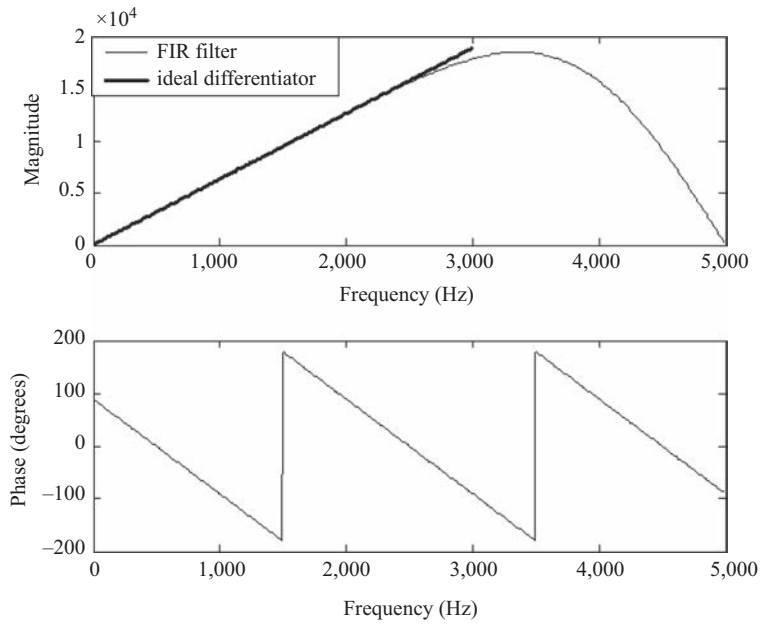


Figure 12.26 Frequency response of D(z)

12.9 Experimental results

The OLS has been applied in its recursive form (RLS) to verify the capability of the experimental rig to retrieve the four parameters of the motor [13]. In particular, a speed transient is given, since it is necessary for the matrix to be fully ranked when (12.2) is solved with LS methods. The experimental test consists in making the FOC follow a speed reference from 0 to 150 rad/s with no load. Figure 12.27 presents the rotor speed as well as the stator currents i_{sD}, i_{sQ}.

Figure 12.28 shows how the computed parameters converge as well as the values obtained with the no-load and blocked-rotor tests (called real values).

Another example is drawn from [17]. In this case, the experimental tests were carried out with several voltage (and correspondingly flux) levels without any torque load: in this way, the motor works with various magnetization levels. Figures 12.29–12.32 show the convergence of the parameters under 55 V, 105 V, 155 V and 220 V, respectively, at the frequency of 50 Hz.

By carrying out several similar tests, the following curves can be drawn (Figure 12.33), giving the dependence of some parameters (L_s and L_m) on the magnetizing status of the machine (in Figure 12.33) as a function of the magnetizing rotor current i_{mr}.

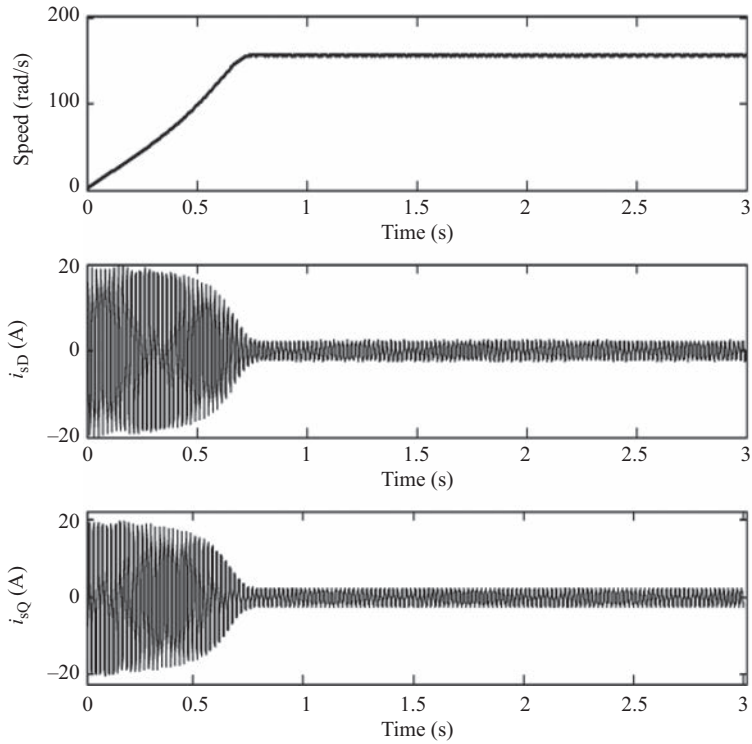


Figure 12.27 Rotor speed and direct and quadrature currents

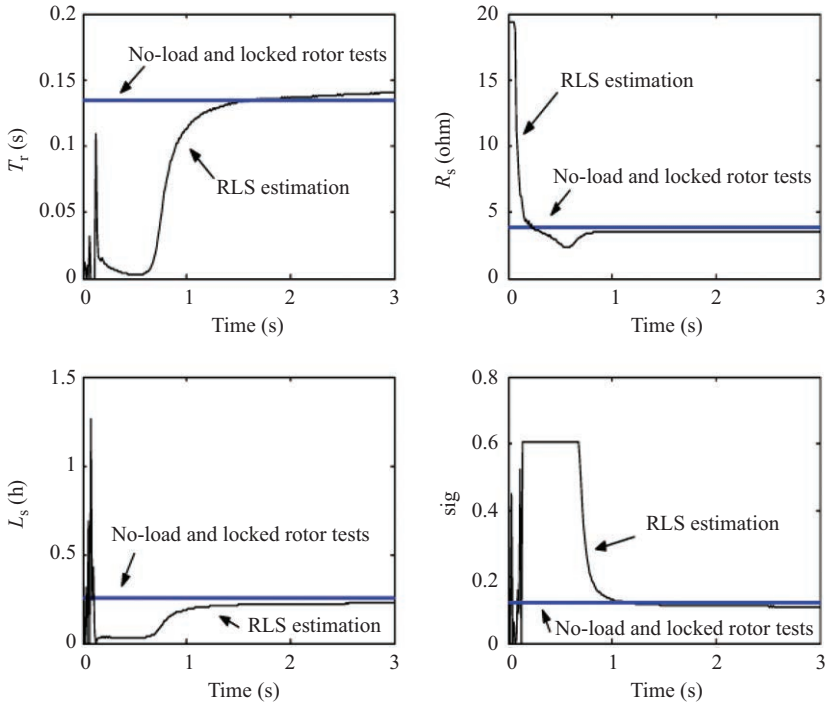


Figure 12.28 Real and estimated motor parameters

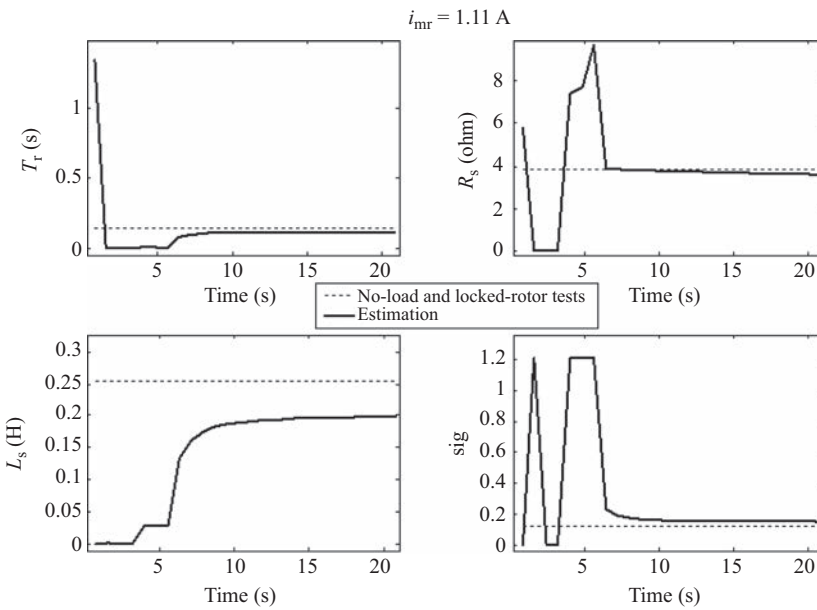


Figure 12.29 Test at 55 V (no load)

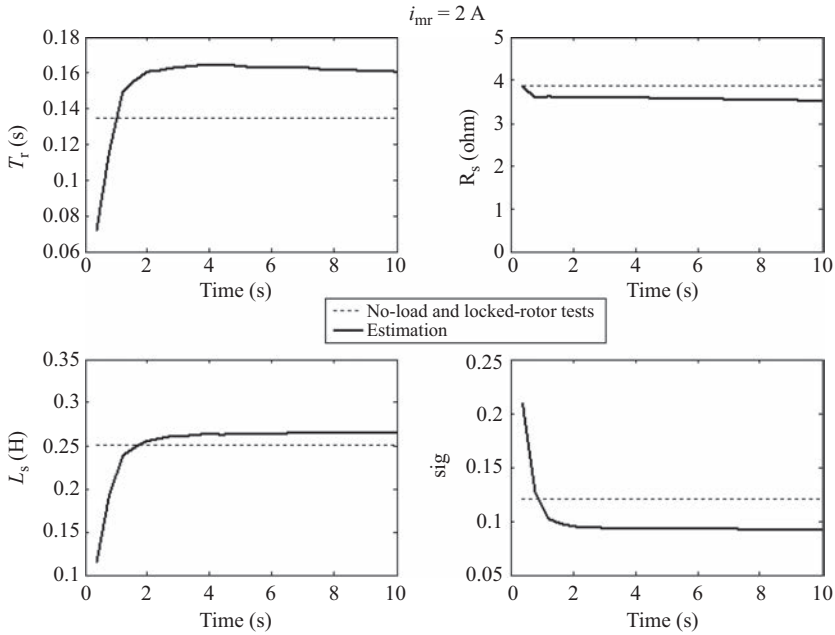


Figure 12.30 Test at 105 V (no load)

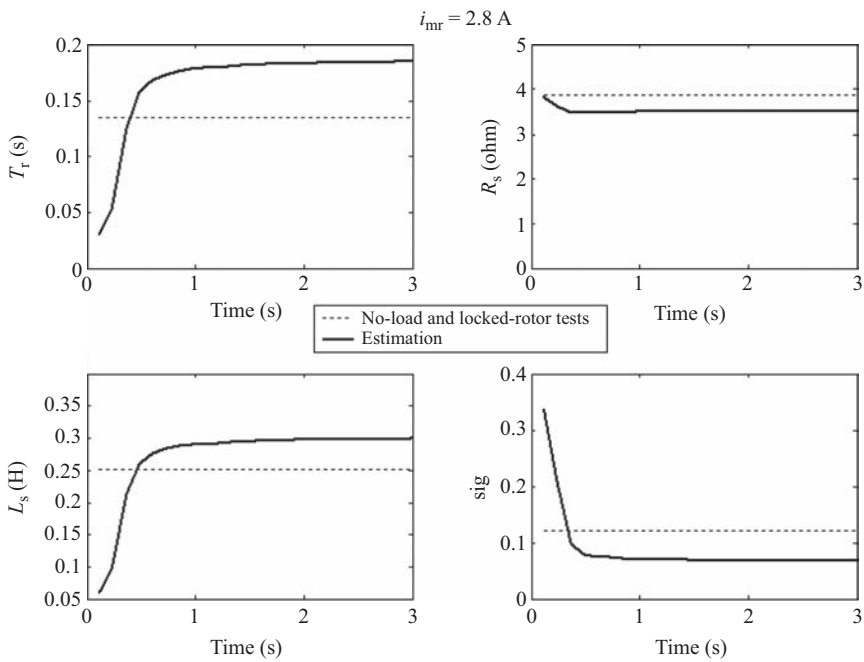


Figure 12.31 Test at 155 V (no load)

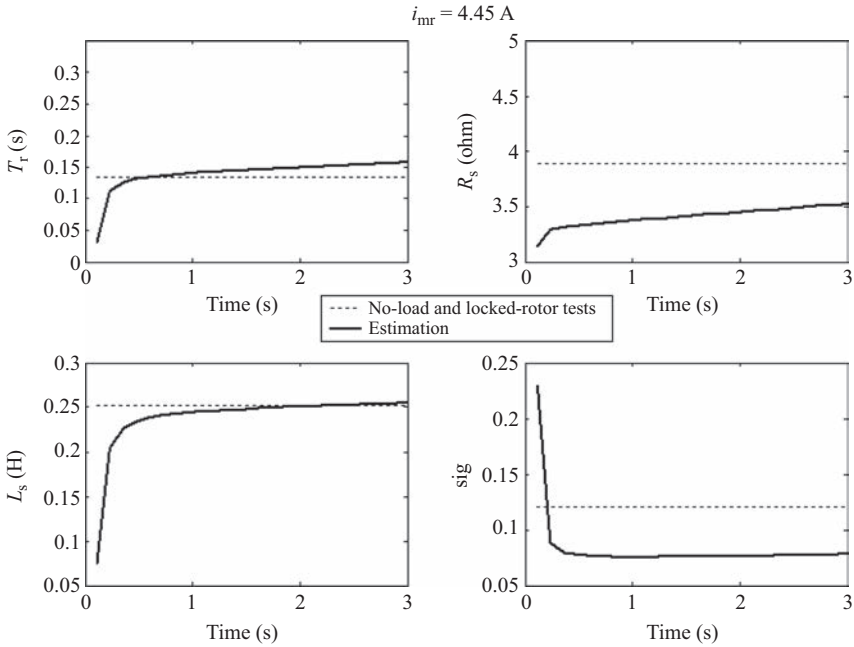


Figure 12.32 Test at 220 V (no load)

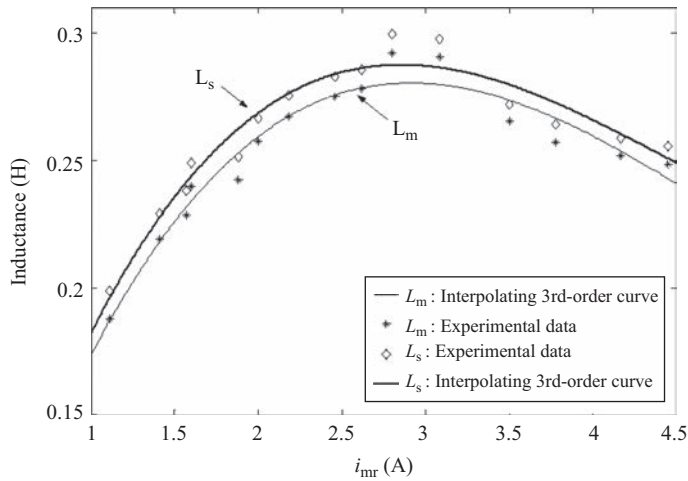


Figure 12.33 Estimated L_s and L_m versus the magnetizing rotor current

12.10 Summary

A test set-up has been developed for the implementation of both an FOC control of an IM and its online parameter estimation. The experimental rig has been explained in a step-by-step way so as to allow its realization straightforwardly. In particular, details on how to connect sensors, boards and A/D converters have been explained in detail. For the online identification techniques, an LS method has been explained for its implementation. The LS permits easily the online parameter estimation by non-invasive real-time measurements of voltages and currents, but requires a suitable signal processing, which has been fully described. Some experimental results have been shown to prove the flexibility of the experimental rig to estimate the parameters also under different magnetic conditions.

Appendix

The I/O pins are shown in Figure A1.

Table A1 IGBT datasheet

Symbol	Conditions	Values	Units
I_{RMS}	No overload	30	A
V_{CES}	IGBT	1,200	V
$V_{CE(SAT)}$	$I_c = 50$ A	2.7(3.5)	V
V_{GES}	$T_{case} = 25(80)$	±20	V
I_c	$T_{case} = 25(80)$	50(40)	A
I_{CM}		100(80)	A
$V_{in(max)}$	Rectifier		
	Without filter	3*480	V
	With filter	3*380	V
	DC capacitor bank		
C_{EQUI}	Total capacitance	1,100/800	V
V_{DCmax}	DC voltage	750	V
Power supply	Driver	0–15	V
	Max per driver	16	mA
Thermal trip	Normal open type	71	Degree Celsius

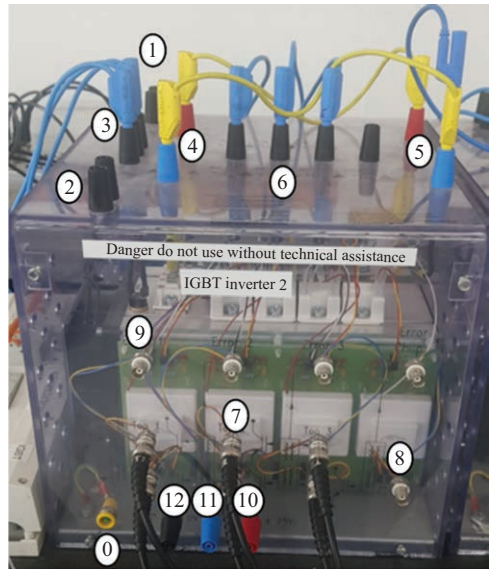


Figure A1 IGBT Semikron Inverter

Table A2 IGBT connection

No.	Type	Function		Max current
0	Grounding panel socket	Earth	0 V	30 A
1	Banana connector 4 mm	Fan power supply	230 V/50 Hz	1 A
2	Banana connector 4 mm	Thermal trip	15 V	5 A
3	Banana connector 4 mm	Rectifier input	230/400 V	30 A
4	Banana connector 4 mm	Dc rectifier	600 VDC	30 A
5	Banana connector 4 mm	DC IGBT inverter inputs	600 VDC	30 A
6	Banana connector 4 mm	AC IGBT + chopper outputs	400 VAC/ 600 VDC	30 A
7	BNC connector	PWM input of inverter	C-MOS logic 0/15 V	1 A
8	BNC connector	PWM input of brake chopper	C-MOS logic 0/15 V	1 A
9	BNC connector	Error output	C-MOS logic 0/15 V	1 A
10	Banana connector 4 mm	15 V driver power supply	15 V	5 A
11	Banana connector 4 mm	0 V driver power supply	15 V	5 A
12	Banana connector 4 mm	Temperature sensor	0–5 V	1 A

List of symbols

$\boldsymbol{u_s}$ $= u_{sD} + ju_{sQ}$. Space vector of the stator voltages in the stator reference frame
$\boldsymbol{i_s}$ $= i_{sD} + ju_{sQ}$. Space vector of the stator currents in the stator reference frame
$\Psi_{r'}$ $= \psi_{rD} + j\psi_{rQ}$. Space vector of the rotor flux-linkages in the stator reference frame
L_s Stator inductance
L_r Rotor inductance
L_m Three-phase magnetizing inductance
R_s Resistance of a stator phase winding
R_r Resistance of a rotor phase winding
ω_r Angular rotor speed (in electrical angles per second)
T_s $= L_s/R_s$. Stator time constant
β_o $= R_r/L_r$. Inverse of the rotor time constant T_r
β $L_m/(\sigma L_s L_r)$
σ $= 1 - L_m{}^2/(L_s L_r)$. Total leakage factor
J Inertia of the IM

Glossary of terms

FOC Field-oriented control
LS Least squares
DTC Direct torque control
MRAS Model Reference Adaptive System
TLS Total least squares
SVD Singular value decomposition

References

[1] P. Vas, *Sensorless Vector and Direct Torque Control*, Oxford Science Publications, Oxford, 1998.
[2] W. Leonhard, *Control of Electrical Drives*, 3rd edition, Springer-Verlag, Berlin, 1997.
[3] R. Marino, P. Tomei, C.M. Verrelli, *Induction Motor Control Design*, Springer-Verlag, London, 2010.
[4] M. Cirrincione, M. Pucci; G Vitale, *Power Converters and AC Electrical Drives with Linear Neural Networks*, Boca Raton: CRC Press, Taylor & Francis Group, 2012.
[5] R.F. Campos, E. Couto, J. de Oliveira, "On-line Parameter Identification of an Induction Motor with Closed Loop Speed Control Using the Least Square Method", *Journal of Dynamic Systems, Measurement and Control*, 139(7), 071010, 2017.

[6] J. Stephan, M. Bodson, "Real-time estimation of the parameters and fluxes of induction motors", *IEEE Trans. on Ind. Appl.*, 30(3): 746–759, 1994.
[7] M. Velez-Reyes, Speed and Parameter Estimation for Induction Motors, MSc Elect. Eng., MIT, Boston (USA), May 1988.
[8] J.L. Zamora, A. Garcia-Cerrada, "Online Estimation of the Stator Parameters in an Induction Motor Using Only Voltage and Current Measurements", *IEEE Trans. on Ind. Appl.*, 36(3): 805–816, 2000.
[9] E. Laroche, M. Boutayeb, "Identification of the Induction Motor in Sinusoidal Mode" *IEEE Trans. on Ener. Conv*., 25(1): 11–19, 2010.
[10] L.A. de S. Ribeiro, C.B. Jacobina, A.M.N. Lima, A.C. Oliviera, "Real-time Estimation of the Electric Parameters of an Induction Machine Using Sinusoidal PWM Voltage Waveforms", *IEEE Trans. on Ind. Appl*., 36: 743–754, 2000.
[11] L.A. de S. Ribeiro, C.B. Jacobina, A.M.N. Lima, "The Influence of the Slip and the Speed in the Parameter Estimation of Induction Machines", IEEE Power Electronics Specialists Conference, PESC 97, 1997, Saint Louis, MO, USA.
[12] M. Cirrincione, M. Pucci, G. Cirrincione, G.A. Capolino, "A New Experimental Application of Least-Squares Techniques for the Estimation of the Induction Motor Parameters", *IEEE Transactions on Industry Applications*, 39(5): 1247–1256, 2003.
[13] M. Cirrincione, M. Pucci, "Experimental Verification of a Technique for the Real-Time Identification of Induction Motors Based on the Recursive Least-Squares", IEEE AMC (7th International Workshop on Advanced Motion Control) 2002, pp. 326–334, 3–5 July 2002, Maribor, Slovenia.
[14] A. Bellini, A. De Carli, M. La Cava, "Parameter Identification for Induction Motor Simulation," *Automatica*, 12(4): 383–386, 1976.
[15] C. Moons, B. De Moor, "Parameter Identification of Induction Motor Drives", *Automatica*, 31(8): 1137–1147, 1995.
[16] H.A. Toliyat, E. Levi, M. Raina, "A Review of RFO Induction Motor Parameter Estimation Techniques", *IEEE Trans. on Energy Conversion*, 18(2): 271–283, 2003.
[17] M. Cirrincione, M. Pucci, G. Cirrincione, G. Capolino, "Constrained Minimisation for Parameter Estimation of Induction Motors in Saturated and Unsaturated Conditions", *Industrial Electronics, IEEE Transactions on*, 52(5): 1391–1402, 2005.

Further References

[1] DS1007 Technical Data Sheet, https://www.dspace.com/en/pub/home/products/hw/phs_hardware/processor_boards/ds1007.cfm
[2] DS5001 Technical Data Sheet, https://www.dspace.com/en/pub/home/products/hw/phs_hardware/i_o_boards/digital_waveform_capture.cfm
[3] DS4002 Technical Data Sheet, https://www.dspace.com/en/pub/home/products/hw/phs_hardware/i_o_boards/generating_and_capturing.cfm
[4] DS2004 Technical Data Sheet, https://www.dspace.com/en/pub/home/products/hw/phs_hardware/i_o_boards/ds2004_high_speed_a_d_board.cfm
[5] Semikron Semitech IGBT Inverter (Data Sheet)

This page intentionally left blank

Chapter 13

Sensorless control of IM drives

Lennart Harnefors[1]

This chapter addresses the fundamental issues of sensorless vector control of induction motor drives. Starting from an historical overview of induction motor control in general, we revisit the two archetypical flux estimators known as the current model and voltage model, as well as their combination into a reduced-order observer. It is demonstrated not only that how speed estimation can be added to the observer but also how the flux estimator can be made inherently sensorless, i.e. the rotor speed no longer appears in the estimator equations. It is shown that all inherently sensorless flux estimators that are based on the reduced-order observer resemble a variant of the voltage model, called the statically compensated voltage model. Finally, theory is developed whereby the coefficients of the inherently sensorless flux estimator can be selected so that stability is obtained for all operating conditions, called complete stability. This includes the low-speed regeneration region where often instability phenomena tend to occur.

13.1 Introduction

Induction motors (IMs) have been manufactured since the 1890s. For decades, they were used mainly in near-constant-speed drives. Fed from a voltage source of constant frequency, their speed could be varied just slightly by changing the slip, e.g. by using a variable external rotor resistance connected by slip rings. The development of the power thyristor enabled the first truly variable-speed IM drives fed by inverters to be constructed in the 1960s, if only in laboratories. Subsequent development of power transistors and effective enough microprocessors for their control – particularly digital signal processors (DSPs) – allowed commercial variable-speed IM drives to become available during the 1980s and 1990s. Today, they are commonplace.

Initially, inverter-fed IM drives were controlled in an open-loop fashion by linearly varying the magnitude and frequency of the imposed stator voltage with the desired speed. The method, called volts-per-hertz control, was found to give sluggish torque response compared to that of a dc motor drive. Remedies for this drawback were found in West Germany in the late 1960s and early 1970s by Hasse [1] and Blaschke [2]. The ideas were developed by Prof. Werner Leonhard

[1]ABB Corporate Research Center, Sweden

and his team at Braunschweig University [3]. Building on the principle of synchronous (dq)-frame modelling of synchronous machines introduced by Park [4], they developed the concept of vector control or field-oriented control. Aligning the dq frame with a flux quantity – generally the stator- or rotor-flux linkage – permits the stator-current component which is aligned with the flux, i.e. the d component, to control the flux level. The current component which is perpendicular to the flux, i.e. the q component, controls the torque. This decouples the control of flux and torque in a fashion similar to a separately magnetised dc motor, thus alleviating the problem of sluggish torque response by keeping the flux constant.

Vector control is complicated by the fact that the flux in an IM is not readily measurable. It has to be *estimated*. The two archetypical flux estimators are the *current model* (CM) and the *voltage model* (VM). They respectively utilise the rotor and stator loops of the dynamic IM model. The VM uses as inputs the stator voltage and the stator current, whereas the CM relies on the stator current and the rotor speed for its flux estimation.

The CM and the VM both can be implemented either in the stationary ($\alpha\beta$) reference frame – which is known as *direct field orientation* (DFO) – or in the dq reference frame – which is known as *indirect field orientation* (IFO). Since DFO uses oscillating variables, field orientation can be achieved without the computation of trigonometric functions. This was an important objective still in the 1980s. The parallel inventions of the similar schemes *direct torque control* (DTC) [5] and *direct self control* (DSC) [6] allowed control-system implementation using relatively simple analog and logic circuitry – an important consideration at a time when effective DSPs were not yet available.

The oscillating variables of DFO cause some difficulties. Another drawback is that the stator frequency is not an explicit variable in the algorithm. The only drawback of IFO is that trigonometric functions, i.e. sine and cosine, have to be computed online. But since modern DSPs have dedicated instructions for this purpose, this is no longer a problem. Consequently, IFO is preferable to DFO in most – if not all – situations.

As mentioned, the VM utilises the stator voltage and current as input signals, but not the rotor speed. A flux estimator which does not use the rotor speed in its equations is known as *inherently sensorless* [7]. Avoiding the use of a speed sensor is advantageous for a number of reasons.

- For a low-power drive, the cost of the speed sensor together with its cabling may be comparable to that of the motor itself.
- In hostile environments, it may be impossible to install a speed sensor.
- Reliability may be impaired, partly due to the risk for sensor malfunction and partly because electromagnetically induced disturbances may be picked up in the cabling.

In both DTC and DSC, it was suggested to use the VM for flux estimation. Thus, both principles are originally inherently sensorless, although later, improvements that involved the CM and speed sensing were proposed [8]. This notwithstanding, a method for estimating the rotor speed in a volts-per-hertz control scheme was suggested as early as 1975 [9] and two different sensorless vector control methods were proposed in 1983 and 1987, respectively [10,11].

The scattered activities on sensorless control, i.e. IM vector control without speed sensing, during the 1980s turned into a tidal wave in the 1990s. The works [12,13] are some of the principal early contributions from that period. The activities which continue to this day – albeit again with lower intensity – have resulted in various methods. Although the proposed schemes may have different properties concerning, e.g. stability, damping, parameter sensitivity and rejection of disturbances, it can never be escaped that they all must originate from the fundamental differential equations that describe the dynamics of the IM. Consequently, many schemes appear to be very different at a first glance, but delving deeper they may be found to be closely related.

Rather than making an overview of the plethora of methods that have been suggested, we in this chapter base all derivations on the classical CM and VM. Their properties together with some needed or useful modifications are reviewed. Fundamentally, the measured speed needs to be replaced by a speed estimate in order for the CM to be utilised in a sensorless IM control system, necessitating speed estimation. The VM requires a modification because it is marginally stable. The proposed modification is called the *statically compensated VM* (SCVM) [14], which alleviates the stability problem of the pure VM.

We then proceed to combine the CM and the VM into a so-called reduced-order observer. It is shown how speed estimation can be added to this observer. As an alternative to adding speed estimation, it is demonstrated how the reduced-order observer can be made inherently sensorless. Interestingly, the reduced-order observer then, for practical purposes, reverts to the SCVM, illustrating one of many interesting analogies between different schemes.

Sensorless IM drives tend to experience stability problems in the regeneration region, which often are difficult to overcome. Ideally, a sensorless IM control system should be such that stability is obtained for all operating conditions, called *complete stability* [15]. The key to obtaining complete stability is to select the gains of the flux and speed estimators analytically – trial-and-error selections are generally not successful. It is shown how the reduced-order observer can be made completely stable.

Finally, the design for complete stability is applied to some special cases, including the CM and the SCVM. It is shown by simulations that stability is obtained with the correct analytical gain selections.

We have attempted to illustrate the theory by adding block diagrams for the derived algorithms where deemed to be helpful (but without adding too much clutter). Yet, the chapter is heavily reliant on equations, and needs to be so, because of the insights gained.

The stability analysis leading up to the design for complete stability may feel difficult to grasp, because it is difficult. Analysing the stability of a sensorless IM control system and finding designs that give complete stability can easily consume months, if not years, of single-minded effort.

One shortcoming of the design for complete stability is that accurate model motor parameters are assumed. Inaccurate parameters may lead to cases of instability, despite the design for complete stability. Although methods for reducing the parameter sensitivity have been proposed (e.g. via online estimation), this is one of the few remaining areas of sensorless control of the IM where still significant new discoveries might be made in the future.

13.2 Essentials of sensorless vector control

13.2.1 IM model and nomenclature

We shall consider the space-vector 'inverse-Γ' model [16], whose equivalent circuit is shown in Figure 13.1. The symbols used here and in the sequel are defined as follows:

$\mathbf{v}_s^s$	Stator-voltage space vector
$\mathbf{i}_s^s$	Stator-current space vector
$\Psi_R^s = \psi_R e^{j\theta}$	Rotor-flux space vector
$\hat{\Psi}_R^s = \hat{\psi}_R e^{j\hat{\theta}}$	Rotor-flux-estimate space vector
$\omega_1 = d\hat{\theta}/dt$	Stator frequency
ω_r	Electrical rotor speed
ψ_{ref}	Rotor-flux-modulus reference
R_s, R_R	Stator and rotor resistances
L_M, L_σ	Magnetising and leakage inductances
$a = R_R/L_M$	Inverse rotor time constant
n_p	Number of pole pairs
K	Space-vector scaling constant

The superscript ^{s} indicates that the variable is expressed in the $\alpha\beta$ frame, whereas the absence of this superscript indicates the dq frame. In the latter case, the components are denoted with the subscripts d and q, e.g. $\mathbf{i}_s = i_d + ji_q$. Notice that, even though ω_1 strictly is the angular stator frequency, we yet call it the stator frequency, for simplicity. The voltage source $j\omega_r\Psi_R^s$ in Figure 13.1 is the rotor electromotive force (EMF), which acts as converter between electrical and mechanical energy (hence, the rotating shaft protruding from the symbol in the figure).

An alternative to the 'inverse-Γ' model is the 'Γ' model [16]. Here, the stator flux $\Psi_s^s = \Psi_R^s + L_\sigma \mathbf{i}_s^s$ is used instead of the rotor flux as complex state variable in addition to the stator current. Identical conclusions can be drawn for the 'Γ'

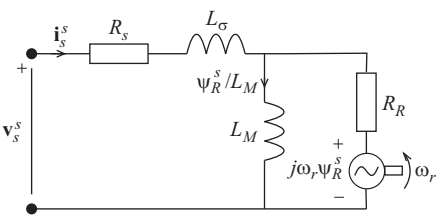


Figure 13.1 Equivalent circuit for the 'inverse-Γ' model of the IM

model, but the equations become somewhat more complicated. On the other hand, the traditional 'T' model, which has two leakage inductances – stator and rotor – is not preferable. This is because it is overparametrised; the two leakage inductances cannot be uniquely identified from the quantities available at the stator terminals.

In the remainder of the chapter it is by 'sensored' and 'sensorless', respectively, meant that ω_r is measured (and the measurement is used in the control system) and not measured, respectively. The rotor flux is assumed never to be measured. Since the slip frequency $\omega_1 - \omega_r$ always is small in absolute terms, it is by 'low speed' implied also that the stator frequency is low, and vice versa.

13.2.2 Dynamic model and principle for vector control

Applying basic circuit laws to the 'inverse-Γ' equivalent circuit, the IM electrical dynamics in the $\alpha\beta$ frame are derived as

$$\begin{aligned} L_\sigma \frac{d\mathbf{i}_s^s}{dt} &= \mathbf{v}_s^s - (R_s + R_R)\mathbf{i}_s^s + (a - j\omega_r)\boldsymbol{\Psi}_R^s \\ &= \mathbf{v}_s^s - R_s\mathbf{i}_s^s - \mathbf{E}^s \end{aligned} \tag{13.1}$$

$$\frac{d\boldsymbol{\Psi}_R^s}{dt} = \underbrace{R_R\mathbf{i}_s^s - (a - j\omega_r)\boldsymbol{\Psi}_R^s}_{\mathbf{E}^s} \tag{13.2}$$

where we shall call $\mathbf{E}^s$ the flux EMF, since its integral gives the rotor flux according to (13.2). The electrical dynamics are given as a second-order state-space system in the complex state variables $\mathbf{i}_s^s$ and $\boldsymbol{\Psi}_R^s$. Since each complex state variable consists of two real-state variables – the real (α) and imaginary (β) parts – the electrical IM model is a fourth-order system in real variables. In addition, the speed ω_r is governed by the mechanical dynamics, which are of order one or higher. The speed interacts non-linearly with the electrical dynamics through the multiplications by ω_r in (13.1) and (13.2), as well as via the relation for the electrical torque

$$\tau_e = \frac{3n_p}{2K^2}\mathrm{Im}\left\{(\boldsymbol{\Psi}_R^s)^*\mathbf{i}_s^s\right\} \tag{13.3}$$

where the superscript * indicates complex conjugate. The full IM dynamics are thus non-linear and of at least order five. Yet, as the mechanical dynamics generally are slower than the electrical dynamics, ω_r can almost always be considered as a parameter. This makes the *uncontrolled* electrical dynamics (13.1)–(13.2) linear. However, when vector control is added, the electrical dynamics again generally become non-linear, as we shall see.

State equations (13.1) and (13.2) interact, i.e. $\mathbf{i}_s^s$ and $\boldsymbol{\Psi}_R^s$ both appear in both equations. Had they been non-interacting, the exponential decay rate (i.e. the open-loop bandwidth) of $\mathbf{i}_s^s$ would have been given by (13.1) as $(R_s + R_R)/L_\sigma$, whereas that of $\boldsymbol{\Psi}_R^s$ would have been given by (13.2) as $a = R_R/L_M$. The inverses are known as the transient and rotor time constants and are typically in the tens-of-millisecond

and hundreds-of-millisecond ranges, respectively; this is because $L_M \gg L_\sigma$. The wide difference between the two time constants indicates that, even though the stator current and the rotor flux interact dynamically, they tend to evolve on different time scales. The slow time scale is that of the flux. In the pioneering research undertaken in the late 1960s and early 1970s, it was found that the key to obtaining fast torque response is to keep the flux constant by means of vector control and vary the torque by controlling the current. Closed-loop current control [17] makes the effective transient time constant even smaller than $(R_s + R_R)/L_\sigma$, often just a few milliseconds or lower.

If the rotor-flux space vector is expressed in polar form as $\Psi_R^s = \psi_R e^{j\theta}$, the *dq*-frame stator current is given by the *dq* transformation

$$\mathbf{i}_s = e^{-j\theta}\mathbf{i}_s^s = i_d + ji_q \tag{13.4}$$

Substitution of $\Psi_R^s = \psi_R e^{j\theta}$ and (13.4) in (13.3) gives

$$\tau_e = \frac{3n_p}{2K^2}\mathrm{Im}\{\psi_R(i_d + ji_q)\} = \frac{3n_p}{2K^2}\psi_R i_q \tag{13.5}$$

showing that the torque becomes proportional to i_q, which therefore is called the torque-producing current component. This component corresponds to the armature current in a dc motor.

Vector control would have been trivial, had the rotor flux been easily measurable. But with very few exceptions, flux measurement is impractical and needs to be replaced by a flux estimator, also known as an observer [18,19], giving a flux estimate $\hat{\Psi}_R^s = \hat{\psi}_R e^{j\hat{\theta}}$. In (13.4), θ is then replaced by $\hat{\theta}$. Accurate flux estimation ideally implies that θ converges to $\hat{\theta}$ (in practice, close to). The drive then performs as if the flux were measured. On the other hand, poor flux estimation results in deteriorating performance, sometimes even instability.

The risk for degraded performance and instability increases greatly if the speed is not measured. However, the main difficulty of sensorless control lies not in speed estimation *per se*, but in accurately estimating the flux without speed measurement. The speed estimator is of secondary importance to the flux estimator and it can even be eliminated by making the flux estimator inherently sensorless, as demonstrated later in the chapter.

Most sensorless schemes involve estimating both flux and speed from the information available at the stator terminals, i.e. voltage and current. Such schemes are always marginally stable for $\omega_1 = 0$, because the magnetising branch then shorts out the rotor branch, cf. Figure 13.1. Speed information is then no longer available at the stator terminals.

This problem vanishes when parasitic effects, such as rotor slot harmonics [20,21] or rotor saliencies [22], can be relied upon for speed estimation. However, the former tends to disappear with skewed rotors, whereas information from the latter is hard to extract, unless the rotor by purpose is made salient [23] (which is usually impractical). Parasitic effects are therefore not considered further here.

13.3 Flux estimation in DFO

In DFO, the flux estimate, which can be expressed in Cartesian coordinates as $\hat{\Psi}_R^s = \hat{\psi}_\alpha + j\hat{\psi}_\beta$, is computed directly in the $\alpha\beta$ frame, based on the dynamic model (13.1)–(13.2). The dq transformation factor can be computed as

$$e^{-j\hat{\theta}} = \frac{(\hat{\Psi}_R^s)^*}{|\hat{\Psi}_R^s|} = \frac{\hat{\psi}_\alpha - j\hat{\psi}_\beta}{\sqrt{\hat{\psi}_\alpha^2 + \hat{\psi}_\beta^2}} \tag{13.6}$$

i.e. sine and cosine of the transformation angle need not be explicitly computed. As mentioned, this was an important objective before the development of effective microprocessors. Figure 13.2 depicts a generic DFO scheme.

In the sequel, some among the most commonly suggested DFO flux estimators are revisited. In this process, it is assumed that the stator current is controlled in a closed loop, such that $\mathbf{i}_s^s$ tracks its reference with a rise time in the millisecond range and with zero static error. In the dq frame, $\mathbf{i}_s = i_d + ji_q$, where i_d and i_q, respectively, are the flux- and torque-producing components. Their references may be adjusted by outer closed loops; i_d by a flux controller, particularly in the field-weakening range, and i_q by a speed controller. These feedback loops are disregarded in the following, however, and the stator current is considered as static. Current control with high bandwidth permits the stator current and its components to be replaced by their respective references in the algorithms for flux and speed estimation, if desired.

13.3.1 Current model

One obvious way of estimating the flux is to simulate (13.2) as

$$\frac{d\hat{\Psi}_R^s}{dt} = \hat{R}_R \mathbf{i}_s^s - (\hat{a} - j\omega_r)\hat{\Psi}_R^s \tag{13.7}$$

where $\hat{a} = \hat{R}_R/\hat{L}_M$ and where it is explicitly noted (by 'hats') that model motor parameters – which are estimates that not necessarily coincide with the true values – must be used. The CM is an open-loop flux estimator, because the true flux Ψ_R^s does

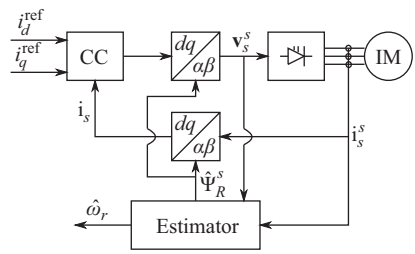


Figure 13.2 DFO vector control system using a combined flux and speed estimator and a synchronous-frame current controller (CC)

not influence the flux estimate; the input signals are the stator current and the rotor speed. With the latter considered as a parameter, (13.7) has a complex pole at

$$p = -\hat{a} + j\omega_r \tag{13.8}$$

(Operator p is used in place of the Laplace-transform variable to avoid confusion with slip s.) Since $|\omega_r| > \hat{a}$ except at low speeds, the CM is in itself a poorly damped system. This must be considered, e.g. in a digital implementation of (13.7). The great benefit of the CM is that, even though the flux estimator itself may be poorly damped, when the flux estimate is used for field orientation, an asymptotically stable control system is obtained for all operating conditions. This holds even when the model parameters deviate significantly from their true values [24]. The main drawback of the CM is its parameter sensitivity, particularly to the rotor resistance, implying slower torque response for larger parameter deviations $R_R - \hat{R}_R$. (The sensitivity to $\hat{L}_M$ is as high, but the magnetising inductance tends to vary less than the rotor resistance, and mainly in the field-weakening region, where the flux is reduced.) For this reason, numerous schemes for rotor-resistance or rotor-time-constant estimation have been proposed over the years, starting with the pioneering work of Garcés [25].

The speed enters (13.7) and must be replaced by its estimate $\hat{\omega}_r$ for a sensorless drive. The speed estimate becomes a function of the estimated flux, which, in turn, indirectly becomes a function of the true flux [7]. A non-linearity is thus introduced in (13.7) when the measured speed is replaced by the estimated speed, which multiplies with the estimated flux

$$\frac{d\hat{\boldsymbol{\Psi}}_R^s}{dt} = \underbrace{\hat{R}_R \mathbf{i}_s^s - (\hat{a} - j\hat{\omega}_r)\hat{\boldsymbol{\Psi}}_R^s}_{\mathbf{E}_c^s} \tag{13.9}$$

Figure 13.3 shows a block diagram of the sensorless CM, where the derivative operator $p = d/dt$ has been introduced.

Making the CM sensorless completely changes the properties relative the sensored CM (13.7), and usually for the worse; the aforementioned excellent stability properties are no longer guaranteed. One benefit is brought as well, though. For reasons that are elaborated on in Section 13.4, the flux estimate becomes insensitive to the rotor resistance (at least in the steady state), obviating the need for rotor-resistance estimation from the standpoint of field-orientation accuracy. Indeed, the rotor resistance and the rotor speed cannot be estimated simultaneously, at least

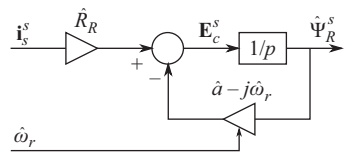


Figure 13.3 Sensorless CM in DFO

not in the steady state and only using information available in the fundamental-wave excitation. This can be deduced from the classical steady-state equivalent circuit. Here, the rotor resistance and the rotor EMF are fused into a resistance R_R/s, where $s = (\omega_1 - \omega_r)/\omega_1$ is the slip [16], implying that they are inseparable as seen from the stator terminals.

13.3.2 Voltage model

The flux EMF can be solved from (13.1) as

$$\mathbf{E}^s = \mathbf{v}_s^s - R_s \mathbf{i}_s^s - L_\sigma \frac{d\mathbf{i}_s^s}{dt} \tag{13.10}$$

This can be combined with (13.2) to form the following flux estimator:

$$\frac{d\hat{\boldsymbol{\Psi}}_R^s}{dt} = \underbrace{\mathbf{v}_s^s - \hat{R}_s \mathbf{i}_s^s - \hat{L}_\sigma \frac{d\mathbf{i}_s^s}{dt}}_{\mathbf{E}_v^s} \tag{13.11}$$

again with model parameters replacing true parameters in the definition of $\mathbf{E}_v^s$. Unlike the CM, ω_r is not present in (13.11), making the VM an inherently sensorless flux estimator [7]. The parameter sensitivity of the VM is low in the medium- and high-speed ranges. The only critical parameter is the stator resistance, but it has impact only at low speeds. The leakage inductance is less critical, as it tends not to vary significantly (and an erroneous value $\hat{L}_\sigma$ has minor impact on the torque).

Usage of the VM was proposed in the pioneering publications on DTC and DSC [5,6], *de facto* making these among the first inherently sensorless IM control schemes.

13.3.3 Statically compensated VM

The VM is marginally stable because it uses open-loop integration [7]: $\hat{\boldsymbol{\Psi}}_R^s$ does not appear on the right-hand side of (13.11). The VM therefore cannot be used as it stands. The standard modification is to add a 'leakage term' to the right-hand side of (13.11):

$$\frac{d\hat{\boldsymbol{\Psi}}_R^s}{dt} = \mathbf{E}_v^s - \alpha_v \hat{\boldsymbol{\Psi}}_R^s \tag{13.12}$$

which in effect replaces the open-loop integration by a low-pass filter

$$\hat{\boldsymbol{\Psi}}_R^s = \frac{1}{p + \alpha_v} \mathbf{E}_v^s \tag{13.13}$$

This results in a flux estimation error. We wish to have a pure integration $1/p$, but we get $1/(p + \alpha_v)$. Thus, even in the ideal case $\hat{R}_s = R_s$ and $\hat{L}_\sigma = L_\sigma$, a steady-state error is obtained, given as

$$\hat{\boldsymbol{\Psi}}_R^s = \frac{j\omega_1}{j\omega_1 + \alpha_v} \boldsymbol{\Psi}_R^s \tag{13.14}$$

This error can be compensated statically by multiplying the SCVM input or output by the inverse of the complex coefficient in (13.14), i.e. $(j\omega_1 + \alpha_v)/(j\omega_1)$. But for a constant α_v, this factor would be singular for $\omega_1 = 0$. The remedy is to vary the filter bandwidth linearly with the stator frequency as $\alpha_v = \lambda|\omega_1|$ (which is known as a 'programmable low-pass filter' [26,27]). The complex compensation gain then becomes

$$\frac{j\omega_1 + \lambda|\omega_1|}{j\omega_1} = 1 - j\lambda_s, \qquad \lambda_s = \lambda\,\mathrm{sgn}(\omega_1) \tag{13.15}$$

The imaginary part of the compensation gain changes sign at $\omega_1 = 0$, but otherwise the real and imaginary parts are both constant. The so obtained flux estimator is called the SCVM [14] and can be expressed in the compact form

$$\hat{\boldsymbol{\Psi}}_R^s = \frac{1 - j\lambda_s}{p + \lambda_s\omega_1}\mathbf{E}_v^s \tag{13.16}$$

The SCVM alleviates the marginal stability of the VM for all stator frequencies but $\omega_1 = 0$, where – recall – all sensorless control systems by necessity are marginally stable. At low stator frequencies, the closed-loop dynamics are sluggish, but the damping improves quickly as $|\omega_1|$ increases, owing to the proportionality of α_v to $|\omega_1|$.

Equation (13.16) looks innocent enough. Yet, one complication is that ω_1 is not an explicit variable, but needs to be computed from the flux estimate. Since the latter can be expressed both in polar and Cartesian forms, as $\hat{\boldsymbol{\Psi}}_R^s = \hat{\psi}_R e^{j\hat{\theta}} = \hat{\psi}_\alpha + j\hat{\psi}_\beta$, we have that

$$\hat{\theta} = \arctan\left(\frac{\hat{\psi}_\beta}{\hat{\psi}_\alpha}\right) \Rightarrow \omega_1 = \dot{\hat{\theta}} = \frac{\hat{\psi}_\alpha\dot{\hat{\psi}}_\beta - \dot{\hat{\psi}}_\alpha\hat{\psi}_\beta}{\hat{\psi}_\alpha^2 + \hat{\psi}_\beta^2} \tag{13.17}$$

Luckily, the flux-component derivatives need not be computed explicitly. Because the flux estimate is obtained by integration, $\dot{\hat{\boldsymbol{\Psi}}}_R^s = \dot{\hat{\psi}}_\alpha + j\dot{\hat{\psi}}_\beta$ can be tapped from the integrator input. Figure 13.4 shows the resulting block diagram, where the upper part

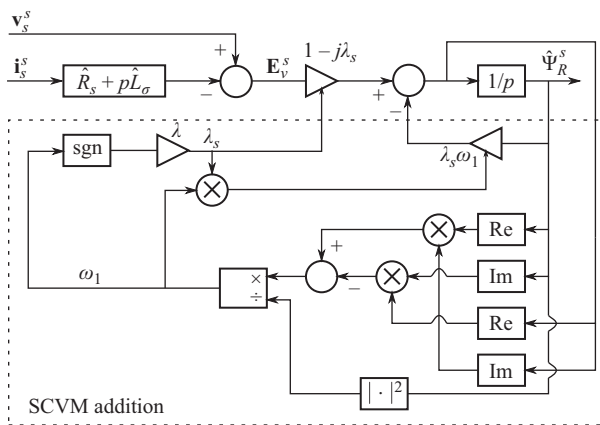


Figure 13.4 VM and SCVM in DFO

represents the pure VM (which is obtained for $\lambda = 0$) and the lower part the SCVM addition. The latter adds complexity due to the need for computing ω_1 and λ_s.

Another issue that needs consideration is that the pure differentiation in the block $\hat{R}_s + p\hat{L}_\sigma$ cannot be implemented perfectly, neither in continuous time nor in discrete time. An Euler discretisation $p \to (1 - q^{-1})/T_s$, where q is the forward-shift operator and T_s is the sampling period, yields a progressively larger error as the stator frequency increases. However, in the same fashion as the compensation gain (13.15), the error can be compensated in the steady state by multiplying the differentiator output with $j\omega_1 T_s/(1 - e^{-j\omega_1 T_s})$ for $|\omega_1| > 0$.

13.3.4 Combination of CM and VM

The CM and the VM are, as mentioned, the archetypical flux estimators. They are, respectively, based on flux-EMF estimation using the rotor and stator loops according to (13.7) and (13.11). Since these equations fully describe the inverse-Γ model of the IM, no other means for flux-EMF estimation are available (at least as long as the fundamental-wave excitation is considered). Still, there are numerous possibilities for how to combine the CM and VM in order to obtain a good flux estimator.

To reiterate, the sensored CM (13.7) is sensitive to the model parameters $\hat{R}_R$ and $\hat{L}_M$ and the sensitivity is the same for all speeds. A stable and well-damped system is always obtained, even for very inaccurate values of the critical model parameters. The VM is sensitive mainly to $\hat{R}_s$, but only at low speeds. The SCVM variant has good damping except in the low-speed region. For a speed-sensored IM drive, one useful approach is therefore to employ a flux estimator that makes a seamless transition from the CM to the VM (SCVM) as the speed increases. This gives fair (but not necessarily good, because of the parameter sensitivity of the CM) dynamic properties in the low-speed region. At higher speeds, good dynamic properties are obtained, owing to the low parameter sensitivity of the VM. There are many suggestions in the literature for how to perform the seamless CV-to-VM (SCVM) transition.

The sensorless CM variant (13.9) has distinctly different properties than the sensored CM (13.7). Chiefly, low-speed stability is no longer guaranteed and $\hat{R}_R$ is no longer critical for the flux estimate. It is therefore not altogether obvious that a good sensorless flux estimator should make a transition from the CM to the VM as the speed increases. Yet, it is beneficial to provide the means for making a combination of the CM and the VM. This is addressed next.

13.3.5 Reduced-order observer

One way – and a simple but yet effective way – of combining the CM with the VM is to augment the sensorless CM (13.9) with feedback of the flux-EMF difference

$$\tilde{\mathbf{E}}^s = \mathbf{E}_v^s - \mathbf{E}_c^s \tag{13.18}$$

which is the difference between the two flux-EMF calculations given in (13.9) and (13.11). The augmentation results in

$$\frac{d\hat{\boldsymbol{\Psi}}_R^s}{dt} = \mathbf{E}_c^s + \mathbf{k}\tilde{\mathbf{E}}^s = \tilde{\mathbf{E}}_v^s + (\mathbf{k} - 1)\tilde{\mathbf{E}}^s \tag{13.19}$$

This is known as a *reduced-order observer* [18]. The observer is reduced in the sense that only one of the two complex state variables, the rotor flux – but not the stator current – is estimated. (Not surprisingly, including also a stator-current estimate would result in a *full-order observer* [18].) Gain $\mathbf{k}$ is complex, so there are two degrees of freedom in the observer design – the real and imaginary parts of $\mathbf{k}$. A flux estimator which makes a seamless transition from the CM to near the VM as the speed increases can be obtained by letting

$$\mathbf{k} = \begin{cases} k\dfrac{|\hat{\omega}_r|}{\omega_\Delta}, & |\hat{\omega}_r| < \omega_\Delta \\ k, & |\hat{\omega}_r| \geq \omega_\Delta \end{cases} \tag{13.20}$$

Parameter k should be selected somewhat smaller than 1, because $k = 1$ would give the pure VM and a marginally stable estimator. The transition from the CM to near the VM is completed when $|\hat{\omega}_r|$ reaches ω_Δ. A flux estimator which is close in spirit to the reduced-order observer is proposed in [28], although it is much more complicated. In this estimator, an 'observer controller' is used to perform the transition from the CM to the VM as the speed increases.

For a sensorless drive, it is not apparent that a selection such as (13.20) is preferable. Gain selection for a sensorless drive requires careful analysis of the flux dynamics. For this purpose, the $\alpha\beta$ frame is inconvenient, because the quantities are statically oscillating. The task of analysing the dynamics is made easier with variables that are constant in the steady state.

13.3.6 Speed estimation

In a sensorless drive, the flux estimator must be augmented with a speed estimator. Whereas flux estimation is a state estimation problem, the consideration of ω_r as a parameter makes speed estimation a parameter estimation – or an *adaptation* – problem [25,29]. For the reduced-order observer, the flux-EMF difference $\tilde{\mathbf{E}}^s$ can be used in an integrating adaptation law [15]

$$\frac{d\hat{\omega}_r}{dt} = \mathrm{Im}\{\mathbf{k}_\omega(\hat{\Psi}_R^s)^*\tilde{\mathbf{E}}^s\} \tag{13.21}$$

where

$$\mathbf{k}_\omega = k_\omega e^{-j\Omega}, \qquad k_\omega > 0 \tag{13.22}$$

is the complex adaptation gain. As for the gain selection for the reduced-order observer, choosing the adaptation gain correctly requires careful analysis. The theory that is developed next gives us the tools for doing so.

Figure 13.5 shows the block diagram for the reduced-order observer with speed estimation. Since the observer gain $\mathbf{k}$ can be a function of $\hat{\omega}_r$, see (13.20), computation of ω_1 is not needed (unlike the SCVM), giving a 'cleaner' implementation.

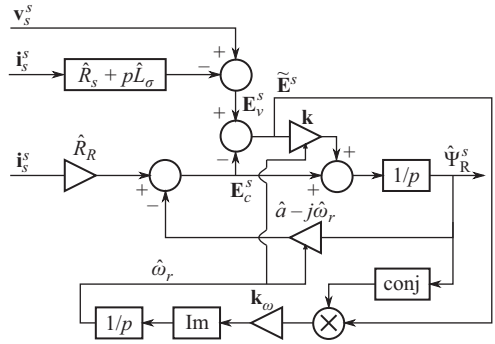


Figure 13.5 Reduced-order observer with speed estimation in DFO

13.4 Flux estimation in IFO

Whereas in DFO the flux estimate is computed in Cartesian coordinates, in IFO polar coordinates are used. IFO was first conceived in the context of the CM. For this reason, it is natural to begin by considering the CM.

13.4.1 Current model

The CM with measured speed, (13.7), can be transformed to the *dq* frame by expressing the flux estimate in polar form as $\hat{\Psi}_R^s = \hat{\psi}_R e^{j\hat{\theta}}$. We obtain

$$\frac{d\hat{\psi}_R}{dt} + j\frac{d\hat{\theta}}{dt}\hat{\psi}_R = \hat{R}_R \mathbf{i}_s - (\hat{a} - j\omega_r)\hat{\psi}_R \tag{13.23}$$

Splitting (13.23) into its real and imaginary parts, with $\mathbf{i}_s = i_d + ji_q$, yields the following relations:

$$\frac{d\hat{\psi}_R}{dt} = \hat{R}_R i_d - \hat{a}\hat{\psi}_R \tag{13.24}$$

$$\frac{d\hat{\theta}}{dt} = \omega_1 = \omega_r + \frac{\hat{R}_R i_q}{\hat{\psi}_R} \tag{13.25}$$

Equation (13.24) shows that ψ_R converges to $\hat{L}_M i_d$ with the model rotor time constant $1/\hat{a}$, so clearly the stator current should be controlled such that

$$i_d = \frac{\psi_{\text{ref}}}{\hat{L}_M} \tag{13.26}$$

Equation (13.25) – which is known as the *slip relation* – shows that the stator frequency equals the rotor speed plus the slip frequency $\hat{R}_R i_q / \hat{\psi}_R$ (the latter which is proportional to the torque).

Unlike DFO, IFO flux estimation is made in the *dq* frame where all quantities are constant in the steady state. This is a benefit. Another benefit is that the stator

frequency is an explicit variable in the control algorithm. Yet another benefit is that poor damping of the estimator itself is much less of an issue. (In fact, even though the estimator proposed in [28] produces an $\alpha\beta$-frame flux estimate, it incorporates a CM which is implemented in the dq frame to avoid poor damping at higher speeds; see (13.8).)

13.4.2 Reduced-order observer

Having considered an IFO implementation of the CM, we now proceed to transform the reduced-order observer (13.19) to the dq frame in a similar way as the CM. This yields

$$\frac{d\hat{\psi}_R}{dt} + j\omega_1\hat{\psi}_R = \mathbf{E}_c + \mathbf{k}\tilde{\mathbf{E}} \tag{13.27}$$

where $\mathbf{E}_c$ and $\tilde{\mathbf{E}} = \mathbf{E}_v - \mathbf{E}_c$ are obtained by dq transformation of (13.9) and (13.11):

$$\mathbf{E}_c = \hat{R}_R\mathbf{i}_s - (\hat{a} - j\hat{\omega}_r)\hat{\psi}_R \tag{13.28}$$

$$\mathbf{E}_v = \mathbf{v}_s - (\hat{R}_s + j\omega_1\hat{L}_\sigma)\mathbf{i}_s - \hat{L}_\sigma\frac{d\mathbf{i}_s}{dt} \tag{13.29}$$

The computation of $\mathbf{E}_v$ involves the derivative of the stator current. But unlike $\mathbf{E}_v^s$, see (13.11), an Euler discretisation does not give a static error, because $\mathbf{i}_s$ – unlike $\mathbf{i}_s^s$ – is constant in the steady state, giving $d\mathbf{i}_s/dt = 0$ statically. Thus, the derivative term in (13.29) may even be dropped without resulting in a steady-state error, although this may slightly degrade the dynamic performance. This is one of several advantages of IFO implementation as compared to DFO implementation.

Equation (13.27) can be split into its real and imaginary parts by expressing all variables in their components as $\mathbf{v}_s = v_d + jv_q$, $\mathbf{i}_s = i_d + ji_q$, $\mathbf{E}_c = E_{cd} + jE_{cq}$, $\mathbf{E}_v = E_{vd} + jE_{vq}$, and $\tilde{\mathbf{E}} = \tilde{E}_d + j\tilde{E}_q = E_{vd} - E_{cd} + j(E_{vq} - E_{cq})$, where for the flux-EMF components we have

$$E_{cd} = \hat{R}_R i_d - \hat{a}\hat{\psi}_R \tag{13.30}$$

$$E_{cq} = \hat{R}_R i_q + \hat{\omega}_r\hat{\psi}_R \tag{13.31}$$

$$E_{vd} = v_d - \hat{R}_s i_d + \omega_1\hat{L}_\sigma i_q - \hat{L}_\sigma\frac{di_d}{dt} \tag{13.32}$$

$$E_{vq} = v_q - \hat{R}_s i_q - \omega_1\hat{L}_\sigma i_d - \hat{L}_\sigma\frac{di_q}{dt} \tag{13.33}$$

Introducing in addition $\mathbf{k} = k_d + jk_q$ now allows (13.27) to be split as

$$\frac{d\hat{\psi}_R}{dt} = E_{cd} + k_d\tilde{E}_d - k_q\tilde{E}_q \tag{13.34}$$

$$\frac{d\hat{\theta}}{dt} = \omega_1 = \frac{E_{cq} + k_q\tilde{E}_d + k_d\tilde{E}_q}{\hat{\psi}_R} \tag{13.35}$$

Equations (13.34) and (13.35) generalise the corresponding equations for the CM; see (13.24) and (13.25). Not surprisingly, for $\mathbf{k} = 0 \Rightarrow k_d = k_q = 0$, they revert to these equations, albeit with $\hat{\omega}_r$ replacing ω_r, since a sensorless drive is assumed. Equation (13.35) therefore may be called a *generalised slip relation* [7].

Equations (13.34) and (13.35) cannot be implemented as they stand, though, because $\tilde{E}_d$ and $\tilde{E}_q$ are both functions of ω_1. This would form an algebraic loop between the left- and right-hand sides of (13.35). The problem can be alleviated by adding a low-pass filter to (13.35). The following alternative to (13.34) and (13.35), expressed in the derivative operator p, is obtained:

$$\hat{\psi}_R = \frac{1}{p}(E_{cd} + k_d\tilde{E}_d - k_q\tilde{E}_q) \tag{13.36}$$

$$\omega_1 = \frac{\alpha_l}{p + \alpha_l}\frac{E_{cq} + k_q\tilde{E}_d + k_d\tilde{E}_q}{\hat{\psi}_R}, \qquad \hat{\theta} = \frac{1}{p}\omega_1 \tag{13.37}$$

The filter bandwidth needs to be selected significantly larger (at least one decade, but often more) than the inverse rotor time constant in order to avoid performance degradation, i.e.

$$\alpha_l \gg \hat{a} \tag{13.38}$$

13.4.3 Voltage model

Even today, it may erroneously be perceived that the CM is the only flux estimator that has an equivalent IFO implementation. The above IFO implementation of the reduced-order observer shows that this is not so. Indeed, *any* DFO flux estimator has an equivalent IFO implementation [7]. Since the VM (13.11) is a special case of the reduced-order observer with $\mathbf{k} = 1$, an IFO implementation of the VM is readily obtained by letting $k_d = 1$ and $k_q = 0$ in (13.34) and (13.35)

$$\frac{d\hat{\psi}_R}{dt} = E_{cd} + \tilde{E}_d = E_{vd} \tag{13.39}$$

$$\frac{d\hat{\theta}}{dt} = \omega_1 = \frac{E_{cq} + \tilde{E}_q}{\hat{\psi}_R} = \frac{E_{vq}}{\hat{\psi}_R} \tag{13.40}$$

A variant including a low-pass filter, which is a special case of (13.36)–(13.37), is obtained as

$$\hat{\psi}_R = \frac{1}{p}E_{vd} \tag{13.41}$$

$$\omega_1 = \frac{\alpha_l}{p + \alpha_l}\frac{E_{vq}}{\hat{\psi}_R}, \qquad \hat{\theta} = \frac{1}{p}\omega_1 \tag{13.42}$$

As the DFO variant, the IFO variant of the VM is marginally stable.

13.4.4 Statically compensated VM

The marginal stability of the IFO variant of the VM can be alleviated by an IFO implementation of the SCVM. Transforming (13.16) to the *dq* frame yields

$$\hat{\psi}_R = \frac{1 - j\lambda_s}{p + j\omega_1 + \lambda_s\omega_1}\mathbf{E}_v \tag{13.43}$$

Next step is to multiply (13.43) by $p + j\omega_1 + \lambda_s\omega_1$ and split the equation into its real and imaginary parts, which results in

$$(p + \lambda_s\omega_1)\hat{\psi}_R = E_{vd} + \lambda_s E_{vq} \tag{13.44}$$

$$\omega_1\hat{\psi}_R = E_{vq} - \lambda_s E_{vd} \tag{13.45}$$

Substituting (13.45) in (13.44) allows the latter to be simplified to $p\omega_1\hat{\psi}_R = (1 + \lambda_s^2)E_{vd} = (1 + \lambda^2)E_{vd}$. Finally, solving for ω_1 in (13.45) and adding a low-pass filter in a similar fashion as previously yields the algorithm

$$\hat{\psi}_R = \frac{\gamma}{p}E_{vd} \tag{13.46}$$

$$\omega_1 = \frac{\alpha_l}{p + \alpha_l}\frac{E_{vq} - \lambda_s E_{vd}}{\hat{\psi}_R}, \qquad \hat{\theta} = \frac{1}{p}\omega_1 \tag{13.47}$$

where in (13.46), $\gamma = 1 + \lambda^2$ for full correspondence to the original DFO variant of the SCVM. However, γ does not necessary have to be selected like that, it can be chosen as seen fit. That is, an additional degree of freedom is allowed by implementing the SCVM in IFO instead of in DFO.

A comparison of (13.41) and (13.42) for the pure VM shows that, in addition to a different gain for the flux-modulus estimation part, in the flux-angle estimation part (i.e. the selection of the stator frequency), now E_{vd} appears (with gain $-\lambda_s$) in addition to E_{vq}. This addition gives the desired stabilising effect.

Since E_{vd} and E_{vq} both are based on the stator loop, described in the $\alpha\beta$ frame by (13.1), they are free of $\hat{L}_M$ and $\hat{R}_R$. This explicitly verifies the claim that the flux estimate of a sensorless IM control system is insensitive to these parameters.

A block diagram for the SCVM in IFO is depicted in Figure 13.6. A comparison to the block diagram for the DFO variant, Figure 13.4, reveals a cleaner

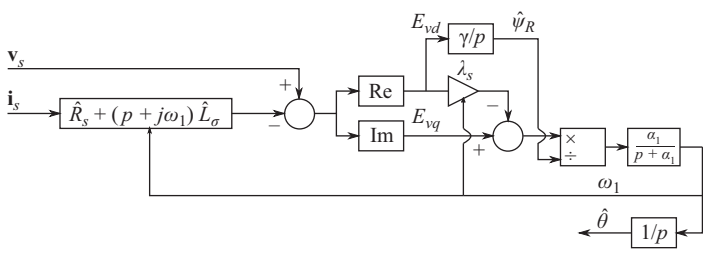


Figure 13.6 SCVM in IFO

implementation. This is because $\hat{\theta}$ is obtained by integrating the explicit variable ω_1, which obviates the computation of ω_1 by differentiation according to (13.17).

13.4.5 Speed estimation

Recall that the VM and the SCVM are inherently sensorless, i.e. they do not use the rotor speed in their equations. This is clearly seen in (13.41)–(13.42). If the CM or the reduced-order observer is used, then speed estimation needs to be added to a sensorless IFO control system. For this purpose, an IFO variant of the DFO speed adaptation law (13.21) can be employed:

$$\frac{d\hat{\omega}_r}{dt} = \mathrm{Im}\{\mathbf{k}_\omega \hat{\psi}_R \tilde{\mathbf{E}}\} \tag{13.48}$$

Guaranteeing the stability of a sensorless drive system is often difficult. Fundamentally though, the adaptation law itself needs to be asymptotically stable. That is, it has to be ascertained that the coefficient for $\hat{\omega}_r$ in the right-hand side of (13.48) is negative. Since $\tilde{\mathbf{E}} = \mathbf{E}_v - \mathbf{E}_c$, where $\mathbf{E}_v$ is free of $\hat{\omega}_r$ and $\mathbf{E}_c = \hat{R}_R \mathbf{i}_s - (\hat{a} - j\hat{\omega}_r)\hat{\psi}_R$ – see (13.28) – it is found that the coefficient for $\hat{\omega}_r$ on the right-hand side of (13.48) is given by $-\mathrm{Im}\{j\mathbf{k}_\omega\}\hat{\psi}_R^2$. With $\mathbf{k}_\omega$ parametrised according to (13.22), this coefficient can be expressed as

$$-\mathrm{Im}\{j\mathbf{k}_\omega\}\hat{\psi}_R^2 = -\mathrm{Re}\{\mathbf{k}_\omega\}\hat{\psi}_R^2 = -k_\omega \hat{\psi}_R^2 \cos\Omega \tag{13.49}$$

So, as long as $\hat{\psi}_R > 0$ and $\mathrm{Re}\{\mathbf{k}_\omega\} = k_\omega \cos\Omega > 0$, adaptation law (13.48) as a stand-alone system is asymptotically stable and $\hat{\omega}_r$ converges exponentially with the rate $k_\omega \hat{\psi}_R^2 \cos\Omega$. But it is thereby by no means guaranteed that the complete sensorless system is stable, establishing that requires further theory development; see Section 13.5.

Equation (13.49) facilitates a simple analytic gain selection. By letting

$$k_\omega = \frac{\alpha_\omega}{\hat{\psi}_R^2 \cos\Omega} \tag{13.50}$$

the exponential convergence rate becomes α_ω. The selections of α_ω and Ω are discussed later in the chapter.

13.4.6 Inherently sensorless reduced-order observer

An alternative to the reduced-order observer with speed adaptation added is to make the reduced-order observer inherently sensorless [30]. This is immediately obtained if consideration is restricted to the VM, i.e. $\mathbf{k} = 1 \Rightarrow k_d = 1, k_q = 0$. But such a restriction is not only undesirable for stability reasons, it is indeed unnecessary to make. In (13.31) it is seen that $\hat{\omega}_r$ appears in E_{cq}, and consequently also in $\tilde{E}_q = E_{vq} - E_{cq}$. The explicit presence of E_{cq} in (13.34)–(13.35) can be eliminated by substituting $E_{cq} = E_{vq} + \tilde{E}_q$, giving

$$\frac{d\hat{\psi}_R}{dt} = E_{cd} + k_d \tilde{E}_d - k_q \tilde{E}_q \tag{13.51}$$

$$\frac{d\hat{\theta}}{dt} = \omega_1 = \frac{E_{vq} + k_q\tilde{E}_d + (k_d - 1)\tilde{E}_q}{\hat{\psi}_R} \tag{13.52}$$

Next step is eliminate also $\tilde{E}_q$. This is more difficult and requires another assumption concerning the speed adaptation law (13.48) in addition to it being asymptotically stable. It is assumed that k_ω is made large enough, so that (13.48) is certain to converge significantly faster than the flux estimate produced by the reduced-order observer. Then, (13.48) can be considered to be in a steady state, i.e. $d\hat{\omega}_r/dt = 0$, as 'seen' from (13.51)–(13.52). That is,

$$\frac{d\hat{\omega}_r}{dt} = \mathrm{Im}\{\mathbf{k}_\omega\hat{\psi}_R\tilde{\mathbf{E}}\} = (\mathrm{Re}\{\mathbf{k}_\omega\}\tilde{E}_q + \mathrm{Im}\{\mathbf{k}_\omega\}\tilde{E}_d)\hat{\psi}_R = 0 \tag{13.53}$$

The general solution to this equation is $\tilde{E}_q = -\mathrm{Re}\{\mathbf{k}_\omega\}\tilde{E}_q/\mathrm{Im}\{\mathbf{k}_\omega\}$. With parametrisation according to (13.22), i.e. $\mathbf{k}_\omega = k_\omega e^{-j\Omega}$, this solution can be expressed as

$$\tilde{E}_q = \xi\tilde{E}_d, \qquad \xi = -\frac{\mathrm{Im}\{\mathbf{k}_\omega\}}{\mathrm{Re}\{\mathbf{k}_\omega\}} = \tan\Omega \tag{13.54}$$

Now, $\tilde{E}_q$ can be eliminated from the estimator equations by substituting (13.54) in (13.51)–(13.52), which yields

$$\frac{d\hat{\psi}_R}{dt} = E_{cd} + (k_d - \xi k_q)\tilde{E}_d \tag{13.55}$$

$$\frac{d\hat{\theta}}{dt} = \omega_1 = \frac{E_{vq} - \left[\xi(1 - k_d) - k_q\right]\tilde{E}_d}{\hat{\psi}_R} \tag{13.56}$$

If in (13.50), α_ω is selected large enough, the reduced-order observer with speed estimation added and the inherently sensorless reduced-order observer have identical behaviour.

13.4.6.1 Inherently sensorless reduced-order observer recast as SCVM

Introducing in (13.55)–(13.56),

$$\lambda_s = \xi(1 - k_d) - k_q \qquad \gamma = k_d - \xi k_q \tag{13.57}$$

and a low-pass filter in the selection of the stator frequency gives the following compact form:

$$\hat{\psi}_R = \frac{1}{p}(\gamma\tilde{E}_d + E_{cd}) \tag{13.58}$$

$$\omega_1 = \frac{\alpha_l}{p + \alpha_l}\frac{E_{vq} - \lambda_s\tilde{E}_d}{\hat{\psi}_R}, \qquad \hat{\theta} = \frac{1}{p}\omega_1 \tag{13.59}$$

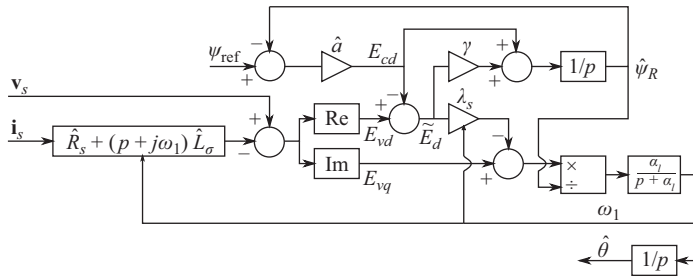


Figure 13.7 Inherently sensorless reduced-order observer recast as the SCVM with injection of E_{cd}

A comparison to the corresponding equations for the SCVM, (13.46) and (13.47), shows a structural similarity. This is the reason for choosing in (13.57) parameter notations identical to those of the SCVM. Indeed, this similarity goes deeper than what is seen at a first glance. From (13.30) and (13.26), we have $E_{cd} = \hat{R}_R i_d - \hat{a}\hat{\psi}_R$ and $i_d = \psi_{\text{ref}}/\hat{L}_M$, respectively, which can be combined to

$$E_{cd} = \hat{a}(\psi_{\text{ref}} - \hat{\psi}_R) \tag{13.60}$$

This results in the block diagram shown in Figure 13.7.

If the model parameters are accurate, then $\hat{\psi}_R$ converges to ψ_{ref}, giving $E_{cd} = 0$. Comparing to Figure 13.6, it is seen that the block diagram in Figure 13.7 reverts to that of the SCVM for $E_{cd} = 0$. The inherently sensorless reduced-order observer and the SCVM are thus, for practical purposes, one and the same thing. (A steady-state error $\psi_{\text{ref}} - \hat{\psi}_R \neq 0 \Rightarrow E_{cd} \neq 0$ is indicative of a detuned model parameter $\hat{L}_M$ and can be used to tune this parameter online.)

13.4.6.2 Inherently sensorless CM

The CM is obtained by letting $k_d = k_q = 0$, for which (13.57) gives $\lambda_s = \xi, \gamma = 0$. Substituting this in (13.58)–(13.59), the reduced-order observer reverts to the CM, but the inherently sensorless variant where $\hat{\omega}_r$ does not appear in the equations. We get

$$\hat{\psi}_R = \frac{1}{p} E_{cd} \tag{13.61}$$

$$\omega_1 = \frac{\alpha_l}{p + \alpha_l} \frac{E_{vq} - \xi \tilde{E}_d}{\hat{\psi}_R}, \qquad \hat{\theta} = \frac{1}{p}\omega_1 \tag{13.62}$$

It is seen that (13.61) is identical to its counterpart (13.24) for the sensored CM, so $\hat{\psi}_R$ always converges to ψ_{ref}; see (13.60). On the other hand, (13.62) is nowhere close to (13.25). Rather, for $\xi = 0$ (13.62) becomes identical to its counterpart (13.42) for the VM. This explicitly shows the previously made claim that the properties of the sensorless CM are distinctly different from those of the sensored CM.

13.4.7 Speed estimation in an inherently sensorless scheme

The beauty of an inherently sensorless IFO scheme is that a speed adaptation law does not have to be used. Speed estimation reduces to the standard slip relation used 'backwards'. With ω_1 given by a generalised slip relation, e.g. (13.59), the speed estimate can be computed using (13.25) as [12]:

$$\hat{\omega}_r = \omega_1 - \frac{\hat{R}_R i_q}{\hat{\psi}_R} \tag{13.63}$$

Here it is seen that $\hat{R}_R \neq R_R$ results in an incorrect slip-frequency estimate and thus a speed estimation error, even in the steady state.

Often, $\hat{\omega}_r$ is fed back to a speed controller, whose output forms the reference for the electrical torque. In turn, the reference for i_q to the current controller is set proportional to this torque reference. This would result in an algebraic loop in (13.63), because the speed controller normally has a proportional part, which creates a direct path from $\hat{\omega}_r$ to the reference for i_q. The problem can be alleviated by augmenting the proportional part of the speed controller with a low-pass filter. Alternatively, the selection of ω_1 of the SCVM, (13.59), can be modified as follows:

$$\hat{\omega}_r = \frac{\alpha_l}{p + \alpha_l}\left(\frac{E_{vq} - \lambda_s \tilde{E}_d}{\hat{\psi}_R} - \frac{\hat{R}_R i_q}{\hat{\psi}_R}\right), \quad \omega_1 = \hat{\omega}_r + \frac{\hat{R}_R i_q}{\hat{\psi}_R}, \quad \hat{\theta} = \frac{1}{p}\omega_1 \tag{13.64}$$

In words, the slip-frequency estimate is subtracted from the input to the low-pass filter, making the output the speed estimate. To this, the slip-frequency estimate is added, forming the stator frequency according to the standard slip relation. Finally, the stator frequency is integrated into the estimate of the rotor-flux angle.

13.5 Design for complete stability

Having considered the reduced-order observer combining the CM and VM, time has now come to find parameter selections whereby complete stability is obtained. This would ideally mean asymptotic stability for all operating conditions. However, as mentioned in Section 13.2.2, a sensorless IM control system is by necessity marginally stable for $\omega_1 = 0$, so this operating point must be exempted.

Guaranteeing complete stability is by far the most challenging task in the design and analysis of a sensorless IM control system, both theoretically and in practice [15]. Particularly, it is difficult to guarantee stability in the regeneration region, i.e. where speed and torque have different signs, and especially at low speeds. Some different instability phenomena may occur; see [31,32] for further information. The most detrimental instability phenomenon is known as *flux collapse*. This results in the motor becoming demagnetised, giving loss of electrical torque and uncontrolled rotation in the direction of the load torque.

The analysis to be presented here involves linear systems theory and the fundamentals of non-linear systems stability theory by means of linearisation. Although the mathematics are not daunting, a chain of several crucial steps is involved. We have done our best to clarify all the steps in enough detail.

To make analysis at all feasible, two assumptions need to be made.

Assumption 1: All model parameters are accurate.

Assumption 2: The inherently sensorless reduced-order observer is used. Alternatively, the gain k_ω is large enough, so that $\hat{\omega}_r$ given by speed adaptation law (13.48) converges much faster than the flux estimate, giving a behaviour similar to that of the inherently sensorless variant.

The analysis consequently accounts for an idealised situation, but it is yet a good start.

Let us begin the analysis process from the very basics by reiterating the flux dynamics (13.2) and the equation for the reduced-order observer (13.19), both in the $\alpha\beta$ frame:

$$\frac{d\boldsymbol{\Psi}_R^s}{dt} = \mathbf{E}^s \tag{13.65}$$

$$\frac{d\hat{\boldsymbol{\Psi}}_R^s}{dt} = \mathbf{k}\mathbf{E}_v^s + (\mathbf{k}-1)\tilde{\mathbf{E}}^s \tag{13.66}$$

where $\tilde{\mathbf{E}}^s = \mathbf{E}_v^s - \mathbf{E}_c^s$. $\mathbf{E}_v^s$ is the flux-EMF estimate of the VM; see (13.11). From Assumption 1 we have that $\hat{R}_s = R_s$ and $\hat{L}_\sigma = L_\sigma$, so (13.11) and (13.1) are identical. Assumption 1 thus allows replacing $\mathbf{E}_v^s$ in (13.66) by the true flux EMF $\mathbf{E}^s$ as given by (13.2). Now, (13.66) can be subtracted from (13.65), giving

$$\frac{d\tilde{\boldsymbol{\Psi}}_R^s}{dt} = (1-\mathbf{k})\tilde{\mathbf{E}}s \tag{13.67}$$

where $\tilde{\boldsymbol{\Psi}}_R^s = \boldsymbol{\Psi}_R^s - \hat{\boldsymbol{\Psi}}_R^s$. Next step is to transform (13.67) to the dq frame as

$$\frac{d\tilde{\boldsymbol{\Psi}}_R}{dt} + j\omega_1\tilde{\boldsymbol{\Psi}}_R = (1-\mathbf{k})\tilde{\mathbf{E}} \tag{13.68}$$

where $\tilde{\mathbf{E}} = \mathbf{E} - \mathbf{E}_c$ and $\mathbf{E}$ is the dq transformation of $\mathbf{E}^s$ as given by (13.2), i.e. $\mathbf{E} = R_R\mathbf{i}_s - (a - j\omega_r)\boldsymbol{\Psi}_R$. Owing to Assumption 1, we have from (13.28) that $\mathbf{E}_c = R_R\mathbf{i}_s - (a - j\hat{\omega}_r)\hat{\boldsymbol{\psi}}_R$, so

$$\tilde{\mathbf{E}} = -(a - j\omega_r)\boldsymbol{\Psi}_R + (a - j\hat{\omega}_r)\hat{\boldsymbol{\psi}}_R = -a\tilde{\boldsymbol{\Psi}}_R + j\omega_r\boldsymbol{\Psi}_R - j\hat{\omega}_r\hat{\boldsymbol{\psi}}_R \tag{13.69}$$

where $\tilde{\boldsymbol{\Psi}}_R = \boldsymbol{\Psi}_R - \hat{\boldsymbol{\psi}}_R$. Then (13.68) is split into its real and imaginary parts. Doing so, we observe that $\tilde{\boldsymbol{\Psi}}_R = \tilde{\psi}_d + j\psi_q$, where $\tilde{\psi}_d = \psi_d - \hat{\psi}_R$ and $\mathbf{k} = k_d + jk_q$. Moreover, $\tilde{\mathbf{E}} = \tilde{E}_d + j\tilde{E}_q$, but Assumption 2 allows us to substitute $\tilde{E}_q = \xi\tilde{E}_d$; see (13.54). This yields

$$\frac{d\tilde{\psi}_d}{dt} = \omega_1\psi_q + (1 + \xi k_q - k_d)\tilde{E}_d \tag{13.70}$$

$$\frac{d\psi_q}{dt} = -\omega_1\tilde{\psi}_d + \left[\xi(1-k_d) - k_q\right]\tilde{E}_d \tag{13.71}$$

From (13.69), $\tilde{E}_d = \mathrm{Re}\{\tilde{\mathbf{E}}\} = -(a\tilde{\psi}_d + \omega_r\psi_q)$. Using (13.57), we identify $1 + \xi k_q - k_d = 1 - \gamma$ and $\xi(1-k_d) - k_q = \lambda_s$, obtaining

$$\frac{d\tilde{\psi}_d}{dt} = \omega_1\psi_q - (1-\gamma)(a\tilde{\psi}_d + \omega_r\psi_q) \tag{13.72}$$

$$\frac{d\psi_q}{dt} = -\omega_1\tilde{\psi}_d - \lambda_s(a\tilde{\psi}_d + \omega_r\psi_q) \tag{13.73}$$

System (13.72)–(13.73) appears to be linear, but because of the selection of ω_1 given by the reduced-order observer; see (13.52), ω_1 becomes a function of the flux components $\tilde{\psi}_d$ and ψ_q. This function may be linearised as

$$\omega_1 = \omega_1^0 + \tilde{\omega}_1(\tilde{\psi}_d, \psi_q) \tag{13.74}$$

where ω_1^0 is the operating point and $\tilde{\omega}_1(\tilde{\psi}_d, \psi_q)$ is the flux-dependent perturbation. However, since $\tilde{\psi}_d = 0$ in the steady state

$$\omega_1\tilde{\psi}_d = \left[\omega_1^0 + \tilde{\omega}_1(\tilde{\psi}_d, \psi_q)\right]\tilde{\psi}_d = \omega_1^0\tilde{\psi}_d + \text{higher-order terms} \tag{13.75}$$

and similarly for $\omega_1\psi_q$. That is, (13.72)–(13.73) can be reduced to a linear system where the flux dependence of ω_1 is neglected and ω_1 is considered as a constant parameter, obviating the need for a notation involving the operating point ω_1^0.

In addition, λ_s and γ may be functions of $\hat{\omega}_r$ and ω_1 and thus in turn of the flux components. But also this impact vanishes when the system is linearised. The gains can therefore be selected as arbitrary functions of $\hat{\omega}_r$ and/or ω_1. Moreover, a gain selection involving ω_r yields the same linearised dynamics if ω_r is replaced by the estimated speed $\hat{\omega}_r$, since $\hat{\omega}_r = \omega_r$ in the steady state, owing to Assumption 1.

Thus, (13.72)–(13.73) can be linearised as the state-space system $\dot{x} = Ax$, with $x = \left[\tilde{\psi}_d, \psi_q\right]^T$ and state matrix

$$A = \begin{bmatrix} -a(1-\gamma) & \omega_1 - (1-\gamma)\omega_r \\ -(\omega_1 + a\lambda_s) & -\lambda_s\omega_r \end{bmatrix} \tag{13.76}$$

This system is obviously asymptotically stable if both eigenvalues of A are in the left half plane. Checking that is done by calculating the characteristic polynomial $\det(pI - A) = p^2 + c_1 p + c_0$, where

$$c_1 = (1-\gamma)a + \lambda_s\omega_r \qquad c_0 = \omega_1[\omega_1 + \lambda_s a - (1-\gamma)\omega_r] \tag{13.77}$$

Asymptotic stability requires that $\{c_1, c_0\} > 0$, but since $c_0 = 0$ for $\omega_1 = 0$, the system will, at best, be marginally stable for zero stator frequency. As previously mentioned, this is by necessity a property of all sensorless IM drives.

To find all completely stabilising parameter selections, let us at first suppose that $\omega_1 \neq 0$. Putting $\gamma = 1 + (\lambda_s\omega_r - l_1)/a$ in (13.77) yields $c_1 = l_1$ – so $l_1 > 0$ is required – and

$$c_0 = \omega_1\left[\omega_1 + \frac{\lambda_s}{a}(a^2 + \omega_r^2) - \frac{l_1\omega_r}{a}\right] \tag{13.78}$$

To make $c_0 > 0$, the expression within the brackets in (13.78) must have the same sign as ω_1. We put it equal to $l_2\omega_1$, $l_2 > 0$, and solve for λ_s. Making the substitution $\omega_r \to \hat{\omega}_r$, which was found to be permitted, yields

$$\lambda_s = \frac{l_1\hat{\omega}_r + (l_2 - 1)a\omega_1}{a^2 + \hat{\omega}_r^2} \qquad \gamma = 1 - \frac{l_1 a - (l_2 - 1)\omega_1\hat{\omega}_r}{a^2 + \hat{\omega}_r^2} \tag{13.79}$$

For $\omega_1 = 0$, we get $c_0 = 0$ and $c_1 > 0$, i.e. marginal stability. So, (13.79) with $\{l_1, l_2\} > 0$ represent all completely stabilising parametrisations.

By equalling (13.57) with (13.79) and solving for l_1 and l_2, the following restrictions for the observer gains result:

$$\begin{aligned} l_1 &= (1 - k_d - \xi k_q)a + (\xi - \xi k_d - k_q)\hat{\omega}_r > 0 \\ l_2 &= \frac{\omega_1 + (\xi - \xi k_d - k_q)a - (1 - k_d - \xi k_q)\hat{\omega}_r}{\omega_1} > 0 \end{aligned} \tag{13.80}$$

This allows the stability properties of any candidate reduced-order observer with gains $\mathbf{k} = k_d + jk_q$ and $\mathbf{k}_\omega = k_\omega e^{-j\Omega}$, k_ω large and $\cos\Omega > 0$ ($\xi = \tan\Omega$), to be assessed. Critical for making $l_2 > 0$ is that the numerator of l_2 is made proportional to ω_1 for small ω_1, thereby lifting the singularity at $\omega_1 = 0$, which otherwise would have the effect that l_2 changes sign when ω_1 does. (It may be noted that the VM, $k_d = 1, k_q = 0$, results in the numerator of l_2 becoming equal to ω_1. But $l_1 = 0$, so the system resulting from usage of the VM is incompletely stable.)

13.6 Examples

The theory for complete stability developed in Section 13.5 is here used in a few design examples, together with their evaluation by simulation.

13.6.1 Inherently sensorless reduced-order observer and SCVM

For an inherently sensorless scheme, gain selections (13.79) should be considered. These gain selections simplify considerably if $l_2 = 1$ and $l_1 = \lambda'(a^2 + \hat{\omega}_r^2)$ are selected. Since l_1 and l_2 thereby become positive for $\lambda' > 0$, the design gives complete stability. A special case which is identical to the parameter selection in [33] is obtained:

$$\lambda_s = \lambda'\hat{\omega}_r \qquad \gamma = 1 - \hat{a}\lambda', \qquad \lambda' > 0 \tag{13.81}$$

where $a \to \hat{a}$ has been substituted, since a is not available in the control system. This is also the parameter selection whereby the SCVM is made completely stable in [34]. That the design for complete stability of the reduced-order observer applies also to the SCVM corroborates the claim made in Section 13.4.6 that the inherently sensorless reduced-order observer and the SCVM for practical purposes are identical.

It may be noted that (13.81) gives a different selection of λ_s than that obtained in the original SCVM design, i.e. $\lambda_s = \lambda \text{sgn}(\omega_1)$; see (13.15). Instead of a step change at $\omega_1 = 0$, a ramping is obtained, giving a smoother behaviour. In addition, the sign change of λ_s occurs at $\hat{\omega}_r = 0$ instead of at $\omega_1 = 0$.

13.6.2 Sensorless CM

Since the sensorless CM uses $\hat{\omega}_r$ in the slip relation, it must be accompanied with a speed adaptation law; see (13.48). If complete stability is desired, the adaptation law must be made fast enough, by selecting the gain modulus k_ω large enough, for Assumption 2 in the stability analysis of Section 13.5 to hold. With k_ω parametrised as in (13.50), $\alpha_\omega \gg \hat{a}$ (e.g. one decade larger) needs to be selected.

Remaining then is to choose the gain angle Ω for complete stability. Using the CM implies putting $k_d = k_q = 0$ in (13.80), resulting in

$$l_1 = a + \xi\hat{\omega}_r > 0 \qquad l_2 = \frac{\omega_1 + \xi a - \hat{\omega}_r}{\omega_1} > 0 \tag{13.82}$$

Suppose that $\Omega = 0$ is selected, in order to maximise the exponential convergence rate of $\hat{\omega}_r$. This gives $\xi = \tan\Omega = 0$, making $l_1 > 0$. On the other hand, $l_2 > 0$ only when $\omega_1 - \hat{\omega}_r$ and ω_1 have equal signs. Since $\omega_1 - \hat{\omega}_r$ is the slip frequency, which is proportional to the torque, stability is lost in the regeneration region where speed and torque have different signs.

Parameters l_1 and l_2 both can be made positive by choosing $\xi a - \hat{\omega}_r = 0 \Rightarrow \xi = \hat{\omega}_r/a$, giving together with (13.50) the following speed-adaptation gain selection:

$$\Omega = \arctan\left(\frac{\hat{\omega}_r}{\hat{a}}\right) \qquad \mathbf{k}_\omega = \frac{\alpha_\omega e^{-j\Omega}}{\hat{\psi}_R^2 \cos\Omega} = \frac{\alpha_\omega}{\hat{\psi}_R^2}\left(1 - j\frac{\hat{\omega}_r}{\hat{a}}\right) \tag{13.83}$$

where $a \to \hat{a}$ has been substituted.

13.6.2.1 Inherently sensorless CM

Let us also have a look at the design for complete stability of the inherently sensorless variant of the sensorless CM. This is obtained by letting $k_d = k_q = 0$ and $\xi = \hat{\omega}_r/\hat{a}$ in (13.57), giving

$$\lambda_s = \frac{1}{\hat{a}} \qquad \gamma = 0 \tag{13.84}$$

Comparing to (13.81), it is seen that the inherently sensorless CM designed for complete stability is obtained as the special case $\lambda' = 1/\hat{a}$. We have thus come full circle by showing that the sensorless CM for practical purposes is a special case of

the SCVM, with the parameter selections (13.84) in (13.46)–(13.47). (Note that (13.46) for $\gamma = 0$ reads $d\hat{\psi}_R/dt = 0$, which implies that $\hat{\psi}_R$ stays constant, but it needs to be initialised to the correct value ψ_{ref}.)

13.6.3 Simulations

An IM with the per-unit (p.u.) parameters $L_M = 2$, $L_\sigma = 0.2$ and $R_s = R_R = 0.05$ is simulated. The model parameters are set as $\hat{L}_M = 1.9$, $\hat{L}_\sigma = 0.19$, $\hat{R}_s = 0.45$ and $\hat{R}_R = 0.04$, i.e. they deviate slightly from their true values. The mechanical dynamics have the inertia $J = 100$ p.u. with negligible viscous damping, and $n_p = 1$. An external load torque τ_l can be added. The base frequency for the p.u. normalisation is set to 50 Hz. Closed-loop speed control, with reference ω_{ref} and feedback of $\hat{\omega}_r$ and with fairly high gain, is used. The output of the speed controller is the reference for i_q, which is saturated so that $\sqrt{i_d^2 + i_q^2} \leq 1$ p.u. at all times. Starting from a situation where the IM is fully magnetised with $\psi_{\text{ref}} = 0.9$ p.u. (giving a stator flux of approximately 1 p.u.), but standing still with zero load torque, the following sequence is executed:

- $t = 0$: ω_{ref} is stepped up to 1 p.u.
- $t = 0.5$ s: τ_l is stepped to -0.5 p.u., implying that the drive enters the regeneration region.
- $t = 1$ s: ω_{ref} is stepped down to 0.1 p.u.
- $t = 1.5$ s: ω_{ref} is slowly ramped down, so that the direction of rotation reverses.

Four simulations are run, as described in the following. In all four resulting figures, the estimated flux $\hat{\psi}_R$ is shown as a dashed curve in the upper subplot in addition to the true flux components.

- **Figure 13.8**: The sensorless CM is used, with $\Omega = 0$ in the speed adaptation law. Instability in the form of growing oscillations results almost immediately. Even before the load-torque step at $t = 0.5$ s, the flux collapses. The simulation is stopped at $t = 1$ s.
- **Figure 13.9**: The sensorless CM is used, with $\Omega = \arctan(\hat{\omega}_r/\hat{a})$ in the speed adaptation law. During the slow rotation reversal, there is a tendency to flux collapse, but stability is regained and the flux converges to $\psi_d \approx \psi_{\text{ref}}$ and $\psi_q \approx 0$. A full flux collapse is obtained for an even more inaccurate $\hat{R}_s$, whereas letting $\hat{R}_s = R_s$ prevents the phenomenon. This demonstrates the sensitivity of the model stator resistance in the low-speed range. Adding online adaptation of $\hat{R}_s$ may therefore be useful. In [30], it is shown how to include such an adaptation law in the stability analysis in order to guarantee complete stability.
- **Figure 13.10**: The SCVM with $\lambda' = 1/\hat{a}$ in (13.81) is used, giving $\lambda_s = \hat{\omega}_r/\hat{a}$ and $\gamma = 0$. This is, in effect, the inherently sensorless variant of the sensorless CM. Indeed, the curves are almost identical to those of Figure 13.8.
- **Figure 13.11**: The original SCVM with $\lambda_s = \lambda\ \text{sgn}(\omega_1)$, $\lambda = 1$ and $\gamma = 1$ is used. Even though this variant of the SCVM is not designed for complete stability, only a slight performance deterioration relative Figure 13.10 can be verified.

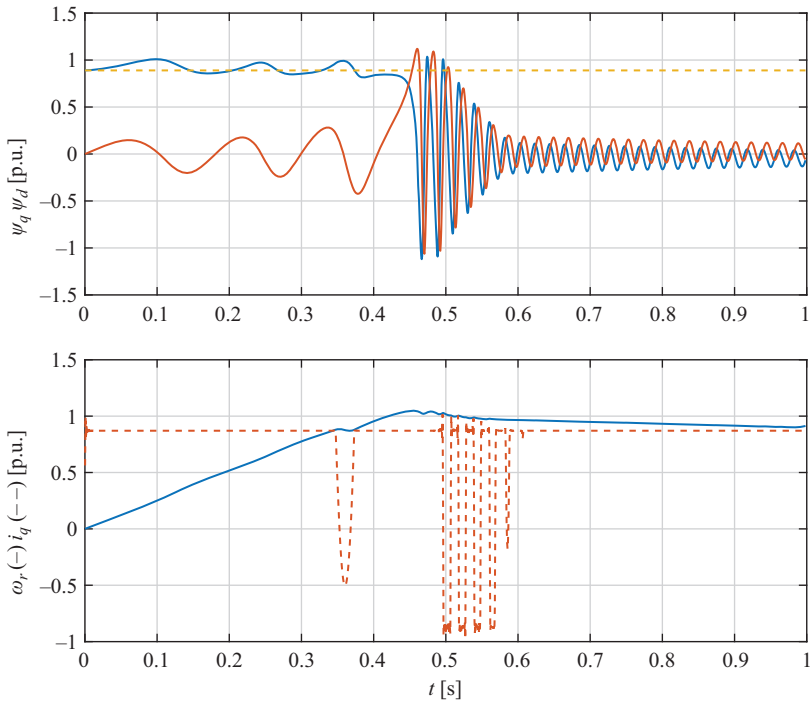


Figure 13.8 Sensorless CM with $\Omega = 0$ *and* $\alpha_\omega = 20\hat{a}$

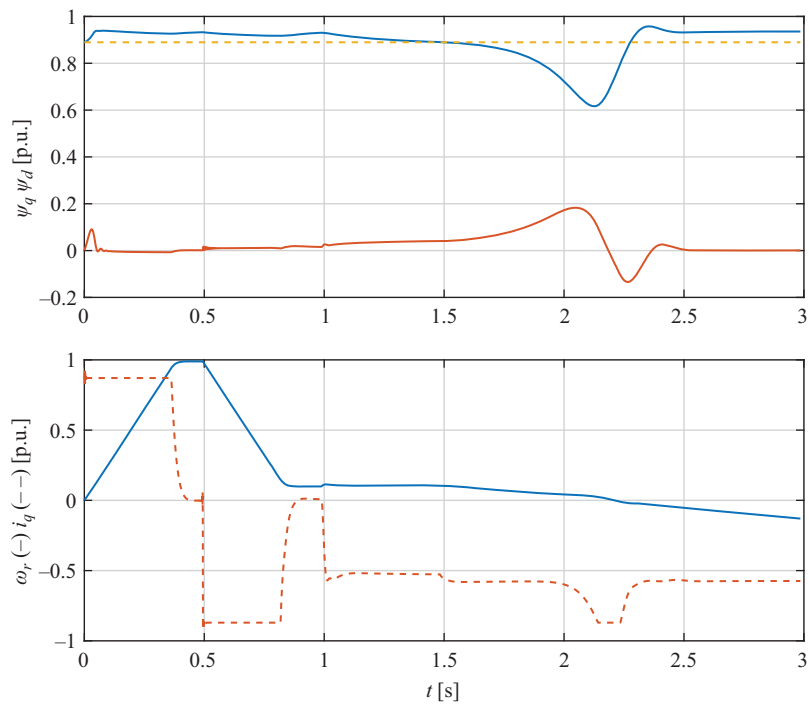


Figure 13.9 Sensorless CM with $\Omega = \arctan(\hat{\omega}_r/\hat{a})$ *and* $\alpha_\omega = 20\hat{a}$

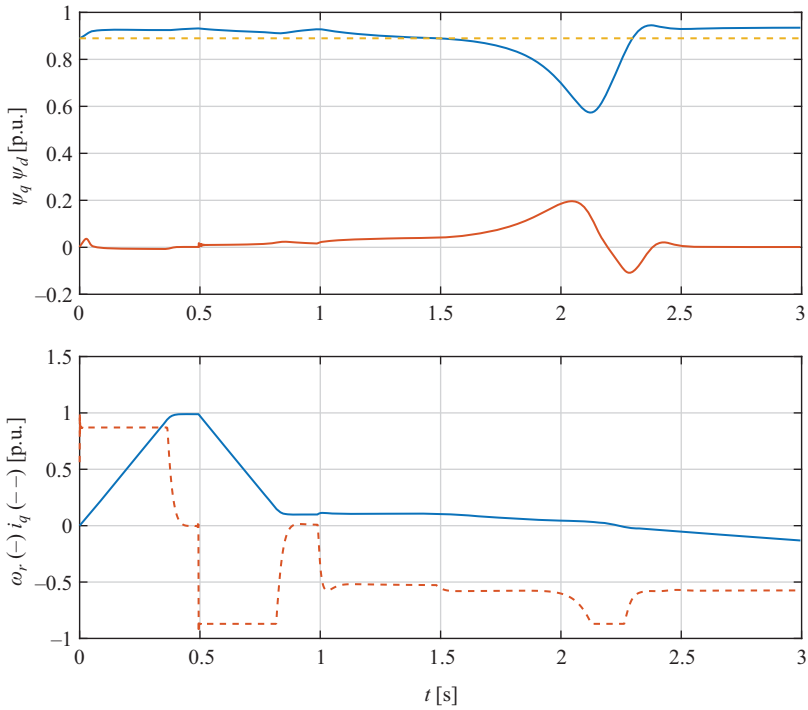


Figure 13.10 SCVM with $\lambda' = 1/\hat{a}$, giving $\lambda_s = \hat{\omega}_r/\hat{a}$ and $\gamma = 0$

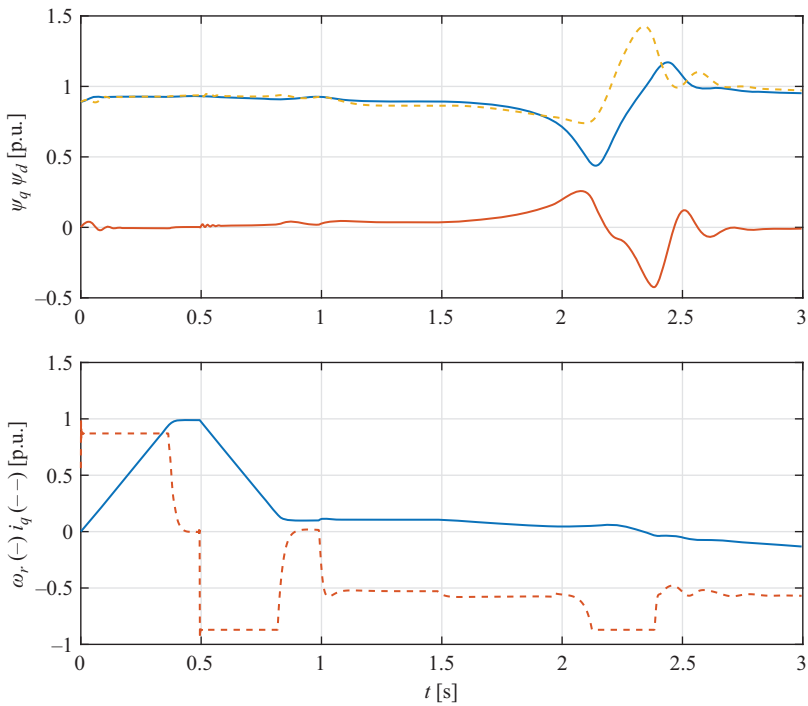


Figure 13.11 SCVM with $\lambda_s = \lambda sgn(\omega_1)$, $\lambda = 1$ and $\gamma = 1$

13.7 Conclusion

We have in this chapter reviewed the topic of sensorless IM control, with focus on IFO-based methods. An interesting observation is that all schemes under consideration for practical purposes can be recast as variants of the SCVM. Although sensorless IM control today is a mature field, there are still some openings for further research. One is the possibility of obtaining complete stability with an estimator based on the instantaneous reactive power, thus eliminating the sensitivity to the stator resistance. As discussed in [32], it is difficult to achieve stability in the regeneration region of such estimators, but some progress has been reported; see [35] and the papers cited therein. Another topic is online adaptation of the rotor resistance (possibly combined with adaptation of the stator resistance). Although the rotor resistance does not affect the field orientation in a sensorless drive, it does affect the accuracy of the speed estimation. Rotor-resistance adaptation for a sensorless drive requires additional excitation in order to work during steady-state conditions; see [36] for a review of the topic and new results.

List of symbols

v_s^s	stator-voltage space vector
i_s^s	stator-current space vector
Ψ_R^s	rotor-flux space vector
Ψ'^s_R	rotor-flux-estimate space vector
ω_1	stator frequency
ω_r	electrical rotor speed
Ψ_{ref}	rotor-flux-modulus reference
R_S,R_R	stator and rotor resistances
L_M,L_σ	magnetising and leakage inductances
α	inverse rotor time constant
n_p	number of pole pairs
K	space-vector scaling constant.
E^s	flux EMF

Glossary of terms

Direct field orientation (DFO)	Estimation of flux using current model (CM) or voltage model (VM) in stationary ($\alpha\beta$) reference frame
Indirect field orientation (IFO)	Estimation of flux using current model (CM) or voltage model (VM) in dq reference frame

Direct self-control (DSC)	Another name of direct torque control (DTC)
Observer	The observer is usually a computer program which provides the estimates of internal stat variables for a given real system

References

[1] K. Hasse, 'Zur Dynamik drehzahlgeregelter Antriebe mit Stromrichter gespeisten Asynchron-Kurzschlußlaufermachinen' (in German), Ph.D. dissertation, Technische Hochschule Darmstadt, Darmstadt, Germany, 1969.

[2] F. Blaschke, 'The principle of field orientation as applied to the new TRANSVECTOR closed-loop control system for rotating-field machines', *Siemens Review*, vol. 39, no. 5, pp. 217–220, 1972.

[3] W. Leonhard, *Control of Electrical Drives*. Berlin: Springer-Verlag, 1996.

[4] R. H. Park, 'Two-reaction theory of synchronous machines generalized method of analysis—Part I', *Trans. Amer. Inst. Electr. Eng.*, vol. 48, no. 3, pp. 716–727, 1929.

[5] I. Takahashi and T. Noguchi, 'A new quick-response and high-efficiency control strategy of an induction motor', *IEEE Trans. Ind. Appl.*, vol. 22, no. 2, pp. 820–827, 1986.

[6] M. Depenbrock, 'Direct self-control (DSC) of inverter-fed induction machine', *IEEE Trans. Power Electron*., vol. 3, no. 2, pp. 420–429, 1988.

[7] L. Harnefors, 'Design and analysis of general rotor-flux-oriented vector control systems', *IEEE Trans. Ind. Electron.*, vol. 48, no. 2, pp. 383–390, 2001.

[8] M. Bertoluzzo, G. Buja and R. Menis, 'A direct torque control scheme for induction motor drives using the current model flux estimation', in *Proc. 2007 IEEE International Symposium on Diagnostics for Electric Machines, Power Electronics and Drives*, pp. 185–190, 2007.

[9] A. Abbondanti and M.B. Brennen, 'Variable speed induction motor drives use electronic slip calculator based on motor voltages and currents', *IEEE Trans. Ind. Appl.,* vol. IA-11, no. 5, pp. 483–488, 1975.

[10] R. Joetten and G. Maeder, 'Control methods for good dynamic performance induction motor drives based on current and voltage as measured quantities', *IEEE Trans. Ind. Appl.,* vol. IA-19, no. 3, pp. 356–363, 1983.

[11] S. Tamai, H. Sugimoto, and M. Yano, M, 'Speed sensor-less vector control of induction motor with model reference adaptive system', in *Conf. Rec. IEEE-IAS Annu. Meeting*, vol. 1, pp. 189–195, *Atlanta*, GA, 1987.

[12] T. Ohtani, N. Takada, and K. Tanaka, 'Vector control of induction motor without shaft encoder', *IEEE Trans. Ind. Appl.*, vol. 28, no. 1, pp. 157–164, 1992.

[13] C. Schauder, 'Adaptive speed identification for vector control of induction motors without rotational transducers', *IEEE Trans. Ind. Appl.*, vol. 28, no. 5, pp. 1054–1061, 1992.

[14] L. Harnefors, M. Jansson, R. Ottersten, and K. Pietiläinen, 'Unified sensorless vector control of synchronous and induction motors', *IEEE Trans. Ind. Electron.*, vol. 50, no. 1, pp. 153–160, 2003.
[15] L. Harnefors and M. Hinkkanen, 'Complete stability of reduced-order and full-order observers for sensorless IM drives', *IEEE Trans. Ind. Electron.*, vol. 55, no. 3, pp. 1319–1329, 2008.
[16] G. R. Slemon, 'Modelling of induction machines for electric drives', *IEEE Trans. Ind. Appl.*, vol. 25, no. 6, pp. 1126–1131, 1989.
[17] L. Harnefors and H.-P. Nee, 'Model-based current control of ac machines using the internal model control method', *IEEE Trans. Ind. Appl.*, vol. 34, no. 1, pp. 133–141, 1998.
[18] G. C. Verghese and S. R. Sanders, 'Observers for flux estimation in induction machines', *IEEE Trans. Ind. Electron.*, vol. 35, no. 1, pp. 85–94, 1988.
[19] H. Kubota, K. Matsuse, and T. Nakano, 'DSP-based speed adaptive flux observer of induction motor', *IEEE Trans. Ind. Appl.*, vol. 29, no. 2, pp. 344–348, 1993.
[20] R. Blasco-Giménez, G. M. Asher, M. Sumner, and K. J. Bradley, 'Performance of FFT-rotor slot harmonic speed detector for sensorless induction motor drives', *IEE Proc.—Electr. Power Appl.*, vol. 143, no. pp. 258–268, 1996.
[21] K. D. Hurst and T. G. Habetler, 'Sensorless speed measurement using current harmonics spectral estimation in induction machine drives', *IEEE Trans. Power Electron.*, vol. 11, no. 1, pp. 66–73, 1996.
[22] J. Holtz, 'Sensorless position control of induction motors—An emerging technology', *IEEE Trans. Ind. Electron.*, vol. 45, no. 6, pp. 840–851, 1998.
[23] P. L. Jansen and R. D. Lorenz, 'Transducerless position and velocity estimation in induction and salient ac machines', *IEEE Trans. Ind. Appl.*, vol. 31, no. 2, pp. 240–247, 1995.
[24] P. De Wit, R. Ortega, and I. Mareels, 'Indirect field oriented control of induction motors is robustly globally stable', *Automatica*, vol. 32, no. 10, pp. 1393–1402, 1996.
[25] L. J. Garcés, 'Parameter adaption for the speed-controlled static ac drive with a squirrel-cage induction motor', *IEEE Trans. Ind. Appl.,* vol. IA-16, no. 2, pp. 173–178, 1980.
[26] B. K. Bose and N. R. Patel, 'A programmable cascaded low-pass filter-based flux synthesis for a stator flux-oriented vector-controlled induction motor drive', *IEEE Trans. Ind. Electron.*, vol. 44, no. 1, pp. 140–143, 1997.
[27] M.-H. Shin, D.-S. Hyun, S.-B. Cho, and S.-Y. Choe, 'An improved stator flux estimation for speed sensorless stator flux orientation control of induction motors', *IEEE Trans. Power Electron*., vol. 15, no. 2, pp. 312–318, 2000.
[28] P. L. Jansen and R. D. Lorenz, 'A physically insightful approach to the design and accuracy assessment of flux observers for field oriented induction machine drives', *IEEE Trans. Ind. Appl.*, vol. 30, no. 1, pp. 101–110, 1994.
[29] K. J. Åström and B. Wittenmark, *Adaptive Control*, *2nd Ed*. Boston, MA: Addison-Wesley Longman.

[30] M. Hinkkanen, L. Harnefors, and J. Luomi, 'Reduced-order flux observers with stator-resistance adaptation for speed-sensorless induction motor drives', *IEEE Trans. Power Electron.*, vol. 25, no. 5, pp. 1173–1183, 2010.

[31] L. Harnefors, 'Instability phenomena and remedies in indirect field oriented control', *IEEE Trans. Power Electron*., vol. 15, no. 4, pp. 733–743, 2000.

[32] L. Harnefors and M. Hinkkanen, 'Stabilization methods for sensorless induction motor drives—A survey', *IEEE J. Emerg. Sel. Top. Power Electron.*, vol. 2, no. 2, pp. 132–142, 2014.

[33] S. Sangwongwanich, U. Nittayatareekul, and P. Magyar, 'Direct speed estimation based on back EMF of induction motors – Its equivalent MRAS representation and stability analysis', in Proc. 10th Eur. Conf. on Power Electron. and Appl., Toulouse, France, Sep. 2003.

[34] L. Harnefors and R. Ottersten, 'Regeneration-mode stabilization of the "statically compensated voltage model"', *IEEE Trans. Ind. Electron.*, vol. 54, no. 2, pp. 818–824, 2007.

[35] A. V. R. Teja, V. Verma, and C. Chakraborty, 'A new formulation of reactive-power-based model reference adaptive system for sensorless induction motor drive', *IEEE Trans. Ind. Electron.*, vol. 62, no. 11, pp. 6797–6808, 2015.

[36] C. Chen and J. Huang, 'Stable simultaneous stator and rotor resistances identification for speed sensorless induction motor drives: Review and new results', to appear in *IEEE Trans. Power Electron*, vol. 33, no. 10, pp. 8695–8709, 2018.

This page intentionally left blank

Chapter 14

Sensorless control of PMSM drives

Gilbert Foo[1], Zhang Xinan[2] and Muhammed Fazlur Rahman[3]

14.1 Introduction

When compared to induction motors, permanent magnet synchronous motors (PMSMs) feature higher torque density, improved efficiency and increased constant power speed range. These distinct advantages have resulted in PMSMs being employed in a myriad of industrial applications. Traditionally, the open-loop V/f control scheme has been the preferred method for PMSM drives owing to its inherent simplicity. Nevertheless, as this method is derived from the steady-state model of the machine and does not rely on any motor feedback information, it offers very poor dynamic performance and is susceptible to external disturbances. Thus, its adoption is limited to applications whose transients are relatively unimportant or occur over long intervals. If high torque and speed dynamic performance is required, the vector control method becomes a necessity.

Unlike the open-loop V/f method, the vector control is derived from the dynamic (*d-q*) model of the PMSM and hence is capable of delivering superior torque and speed dynamic performance. It is not unreasonable to expect a vector-controlled PMSM drive to provide instantaneous torque controllability down to zero speed. The block diagram of the vector control scheme for PMSMs is illustrated in Figure 14.1. From this figure, it can be inferred that the vector control method possesses several salient characteristics – the utilisation of proportional-integral (PI) current controllers, the reliance on the motor model and, most importantly, the requirement of a mechanical encoder for rotor position feedback. In practice, the latter poses several drawbacks such as increased cost and complexity, difficulty of application in hostile and harsh environments, reduced reliability due to additional cabling and susceptibility to electromagnetic interferences (EMIs).

In view of the above-mentioned disadvantages, many researchers have devised creative solutions to enable sensorless operation of the vector control of the PMSM.

[1]School of Engineering, Computer and Mathematical Sciences, Auckland University of Technology, New Zealand
[2]School of Electrical & Electronic Engineering College of Engineering, Nayang Technological University, Singapore
[3]School of Electrical Engineering and Telecommunications, The University of New South Wales, Australia

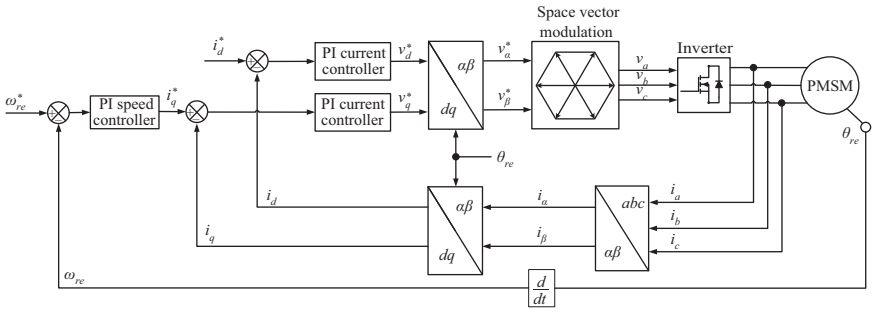


Figure 14.1 Vector control of PMSMs

Instead of relying on the mechanical encoder for position feedback, these methods utilise the existing voltage and current feedback information to estimate the rotor position of the PMSM. The proposed algorithms can broadly be classified into four main categories:

- Open-loop back electromotive force (EMF) estimators [1–3]
- Closed-loop current observers based on advanced models [4–13]
- High-frequency (HF) signal injection-based estimators [14–19]
- Current slope measurement methods [20–22].

The working principle of the open-loop back EMF estimator [1–3] is very straightforward. The rotor flux linkage vector of the PMSM is aligned to the rotor axis. Since the rotor flux linkage is simply the integration of the back EMF, the former and hence the rotor position information can be extracted by estimating the back EMF. A pure integrator is used to perform the estimation and this automatically presents several problems. Any DC-offset present in the measured current or voltage signals will be accumulated by the integrator and will eventually cause it to saturate, rendering the estimator unstable [23–25]. Furthermore, since it is open loop in nature without any correction term, it is very sensitive to variations in the machine parameters, in particular the stator resistance [23]. Moreover, at low speeds, the back EMF is small and the integrator becomes vulnerable to the influence of noise and errors in the measured signals. As an illustration, the output of the PI current controllers is the reference voltage. This is usually taken to be the stator voltage and is used to perform the integration. In reality, the reference voltage is very different from the voltage that appears across the terminals of the PMSM due to inverter non-linear effects such as dead time and forward voltage drop of the power switches [24–26]. At low speeds, this mismatch can be a significant percentage of the actual voltage and consequently, if the integrator uses the reference voltage from the PI current controllers, the estimated back EMF will be erroneous.

While several compensation techniques exist to improve the performance the open-loop integrator, these problems persist in the low-speed region. To further improve the accuracy of the back EMF estimation, closed-loop observers with explicit feedback have been proposed. These observers are generally mathematically complex but all of them possess a similar structure; i.e. they rely on current feedback for enhanced accuracy. The most commonly used closed-loop observer is the model

reference adaptive observer (MRAO) which simultaneously estimates both the stator current and back EMF using the machine model. Speed-adaptive observers can be realised in either the stationary (α-β) [4,5] or rotating (d-q) [6,7] reference frame. In both cases, the estimated current is compared with the measured current and the error signal is then used to improve the accuracy of the estimated quantities. The estimated back EMF is further used to derive the rotor position and speed information. Since the machine model used by the observer is rotor speed dependent, it is paramount that the model is speed-adaptive but this is easily achieved using the estimated rotor speed. In recent years, advanced control theories such as sliding mode control [8–10] and Kalman filter [11–13] have been applied to sensorless control of PMSMs with successful results. The stability, dynamic performance and disturbance rejection qualities of these observers have been proven to be superior to those of the open-loop estimator. Nevertheless, the problems that plague the latter still exist in the closed-loop observer. Its performance degrades precipitously in the very low-speed region, and torque controllability is compromised at typically below 2%–3% of rated speed.

To achieve satisfactory torque control performance at very low speeds including standstill, innovative algorithms based on the anisotropies of the PMSM have been proposed. The saliency or magnetic saturation effects present in the PMSM result in rotor position-dependent inductance variations. These variations are identified by injecting an HF test voltage signal and measuring the corresponding HF currents. Several HF injection methods can be found in the literature. These methods can be classified into rotating vector [14,15], pulsating vector [16,17] and pulse width modulation (PWM) frequency injection [18,19]. The test voltage signal is superimposed onto the fundamental voltage and is usually selected to have a frequency of at least 10 times of the rated frequency to guarantee signal discrimination. Signal processing techniques are then used to extract the rotor position information embedded in the HF current signals. It has been proven experimentally that this method can deliver full-load torque operation even at standstill. However, the necessity of additional HF signals means that increased torque ripples, losses and audible noise are inevitable in the system.

Alternatively, the stator current slope [20–22] can be measured during the application of different voltage vectors by means of large bandwidth current sensors. In a vector-controlled PMSM drive, space vector modulation (SVM) is the preferred PWM technique to synthesise the reference voltage vectors. A total of two active voltage vectors and one zero voltage vector are applied during one switching interval, and their weighted sum is the reference voltage vector. In principle, the current slope can be measured during the application of the zero voltage vector and is again measured when one of the two active voltage vectors is applied. The two measurements are subtracted from each other to eliminate the effects of the stator-resistive drop and back EMF. The residual signal is the current variation due to the stator inductances. Since the inductances vary with rotor position, the current slope can be processed to extract the rotor position information. In this approach, no additional test signal is needed. However, additional hardware and synchronisation issues between the applied PWM and current measurement are its main drawbacks. Furthermore, a minimum non-zero duty cycle for the active voltage vectors must be implemented in the PWM algorithm to ensure that the current variation during the application of the active voltage vector is

captured with sufficient resolution. Nonetheless, this method is capable of providing torque controllability at extremely low speeds including standstill.

Based on the above discussion, this chapter is organised as follows. A brief description of the mathematical model of the PMSM in the stationary (α-β) reference frame from which all the subsequent observers are derived is first presented. The open-loop back EMF estimator is then explained. This is followed by an elaborate analysis of the speed-adaptive observer including its stability criteria and gain selection guidelines. Another closed-loop observer whose speed estimation is independent from the main structure of the observer itself is also provided. Subsequently, the HF signal injection technique and current slope methods are discussed in great detail. Finally, some simulation results are presented to aid the reader in the visualisation of the performance of some of these observers, pertaining to the sensorless control of PMSM drives.

14.2 Mathematical model of the PMSM

The mathematical model of the PMSM in the synchronous rotating (d-q) reference frame can be expressed as

$$\begin{pmatrix} v_d \\ v_q \end{pmatrix} = R_s \begin{pmatrix} i_d \\ i_q \end{pmatrix} + \frac{d}{dt} \begin{pmatrix} L_d & 0 \\ 0 & L_q \end{pmatrix} \begin{pmatrix} i_d \\ i_q \end{pmatrix} + \omega_{re} \begin{pmatrix} -L_q i_q \\ L_d i_d + \lambda_f \end{pmatrix} \tag{14.1}$$

where

v_d, v_q d-q axes components of the stator voltage
i_d, i_q d-q axes components of the stator current
L_d, L_q d-q axes inductance
R_s stator resistance
λ_f permanent magnet flux linkage
ω_{re} rotor speed

The synchronous rotating (d-q) and stationary (α-β) reference frames are depicted in Figure 14.2 and are related by the Park's Transform.

$$\begin{pmatrix} f_d \\ f_q \end{pmatrix} = \begin{pmatrix} \cos\theta_{re} & \sin\theta_{re} \\ -\sin\theta_{re} & \cos\theta_{re} \end{pmatrix} \begin{pmatrix} f_\alpha \\ f_\beta \end{pmatrix} \tag{14.2}$$

where f_d, f_q and f_α, f_β represent the d-q and α-β axes components of the quantity f, respectively, and θ_{re} denotes the rotor position.

Applying Park's Transform in (14.2) to (14.1) yields mathematical model of the PMSM in the stationary (α-β) reference frame.

$$\begin{pmatrix} v_\alpha \\ v_\beta \end{pmatrix} = R_s \begin{pmatrix} i_\alpha \\ i_\beta \end{pmatrix} + \frac{d}{dt} \begin{pmatrix} L_\Sigma + L_\Delta \cos 2\theta_{re} & L_\Delta \sin 2\theta_{re} \\ L_\Delta \sin 2\theta_{re} & L_\Sigma - L_\Delta \cos 2\theta_{re} \end{pmatrix} \begin{pmatrix} i_\alpha \\ i_\beta \end{pmatrix} + \omega_{re}\lambda_f \begin{pmatrix} -\sin\theta_{re} \\ \cos\theta_{re} \end{pmatrix} \tag{14.3}$$

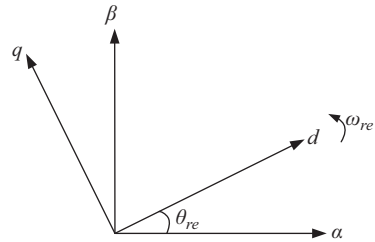


Figure 14.2 The synchronous rotating (d-q) and stationary (α-β) reference frames of a PMSM

where $L_\Sigma = \frac{L_d+L_q}{2}$ and $L_\Delta = \frac{L_d-L_q}{2}$. Rearranging (14.3) as follows,

$$\begin{aligned}
\begin{pmatrix} v_\alpha \\ v_\beta \end{pmatrix} &= R_s \begin{pmatrix} i_\alpha \\ i_\beta \end{pmatrix} + \frac{d}{dt}\begin{pmatrix} L_\Sigma - L_\Delta + L_\Delta(\cos 2\theta_{re}+1) & L_\Delta \sin 2\theta_{re} \\ L_\Delta \sin 2\theta_{re} & L_\Sigma - L_\Delta + L_\Delta(1-\cos 2\theta_{re}) \end{pmatrix} \\
&\quad \begin{pmatrix} i_\alpha \\ i_\beta \end{pmatrix} + \omega_{re}\lambda_f \begin{pmatrix} -\sin\theta_{re} \\ \cos\theta_{re} \end{pmatrix} \\
&= R_s \begin{pmatrix} i_\alpha \\ i_\beta \end{pmatrix} + L_\mathrm{q}\frac{d}{dt}\begin{pmatrix} i_\alpha \\ i_\beta \end{pmatrix} + L_\Delta \frac{d}{dt}\begin{pmatrix} \cos 2\theta_{re}+1 & \sin 2\theta_{re} \\ \sin 2\theta_{re} & 1-\cos 2\theta_{re} \end{pmatrix}\begin{pmatrix} i_\alpha \\ i_\beta \end{pmatrix} \\
&\quad + \omega_{re}\lambda_f \begin{pmatrix} -\sin\theta_{re} \\ \cos\theta_{re} \end{pmatrix} \\
&= R_s \begin{pmatrix} i_\alpha \\ i_\beta \end{pmatrix} + L_\mathrm{q}\frac{d}{dt}\begin{pmatrix} i_\alpha \\ i_\beta \end{pmatrix} + L_\Delta \frac{d}{dt}\begin{pmatrix} 2\cos^2\theta_{re} & 2\sin\theta_{re}\cos\theta_{re} \\ 2\sin\theta_{re}\cos\theta_{re} & 2\sin^2\theta_{re} \end{pmatrix}\begin{pmatrix} i_\alpha \\ i_\beta \end{pmatrix} \\
&\quad + \omega_{re}\lambda_f \begin{pmatrix} -\sin\theta_{re} \\ \cos\theta_{re} \end{pmatrix} \\
&= R_s \begin{pmatrix} i_\alpha \\ i_\beta \end{pmatrix} + L_\mathrm{q}\frac{d}{dt}\begin{pmatrix} i_\alpha \\ i_\beta \end{pmatrix} + (L_\mathrm{d}-L_q)\frac{d}{dt}\begin{pmatrix} \cos\theta_{re} \\ \sin\theta_{re} \end{pmatrix}(\cos\theta_{re} \quad \sin\theta_{re})\begin{pmatrix} i_\alpha \\ i_\beta \end{pmatrix} \\
&\quad + \omega_{re}\lambda_f \begin{pmatrix} -\sin\theta_{re} \\ \cos\theta_{re} \end{pmatrix} \\
&= R_s \begin{pmatrix} i_\alpha \\ i_\beta \end{pmatrix} + L_\mathrm{q}\frac{d}{dt}\begin{pmatrix} i_\alpha \\ i_\beta \end{pmatrix} + (L_\mathrm{d}-L_q)\frac{d}{dt}\begin{pmatrix} \cos\theta_{re} \\ \sin\theta_{re} \end{pmatrix} i_d + \omega_{re}\lambda_f \begin{pmatrix} -\sin\theta_{re} \\ \cos\theta_{re} \end{pmatrix}
\end{aligned} \tag{14.4}$$

Ignoring linearisation errors, (14.4) can be expressed as

$$\begin{aligned}
\begin{pmatrix} v_\alpha \\ v_\beta \end{pmatrix} &= R_s \begin{pmatrix} i_\alpha \\ i_\beta \end{pmatrix} + L_\mathrm{q}\frac{d}{dt}\begin{pmatrix} i_\alpha \\ i_\beta \end{pmatrix} + \omega_{re}(L_\mathrm{d}-L_q) i_d \begin{pmatrix} -\sin\theta_{re} \\ \cos\theta_{re} \end{pmatrix} + \omega_{re}\lambda_f \begin{pmatrix} -\sin\theta_{re} \\ \cos\theta_{re} \end{pmatrix} \\
&= R_s \begin{pmatrix} i_\alpha \\ i_\beta \end{pmatrix} + L_\mathrm{q}\frac{d}{dt}\begin{pmatrix} i_\alpha \\ i_\beta \end{pmatrix} + \omega_{re}\lambda_a \begin{pmatrix} -\sin\theta_{re} \\ \cos\theta_{re} \end{pmatrix}
\end{aligned} \tag{14.5}$$

where $\lambda_a = \left(L_\mathrm{d} - L_q\right)i_d + \lambda_f$ is termed as *active flux linkage* [27–29]. Note that for a surface mounted PMSM, $L_\mathrm{d} = L_q$ and $\lambda_a = \lambda_f$. Conversely, $\lambda_f = 0$ for a synchronous reluctance motor and $\lambda_a = \left(L_\mathrm{d} - L_q\right)i_d$. Thus, λ_a can be viewed as the 'effective' permanent magnet flux linkage of a generic synchronous motor. Now, integrating both sides of (14.5) with respect to time and rearranging yields

$$\begin{pmatrix} \lambda_{a\alpha} \\ \lambda_{a\beta} \end{pmatrix} = \begin{pmatrix} \lambda_\alpha \\ \lambda_\beta \end{pmatrix} - L_\mathrm{q}\begin{pmatrix} i_\alpha \\ i_\beta \end{pmatrix} \tag{14.6}$$

where $\lambda_{a\alpha}$ and $\lambda_{a\beta}$ are the α-β axes components of the active flux linkage, respectively, and are given by

$$\begin{pmatrix} \lambda_{a\alpha} \\ \lambda_{a\beta} \end{pmatrix} = \lambda_a\begin{pmatrix} \cos\theta_{re} \\ \sin\theta_{re} \end{pmatrix} \tag{14.7}$$

Moreover, λ_α and λ_β are the α-β axes components of the stator flux linkage, respectively, and are governed by

$$\begin{cases} \lambda_\alpha = \int (v_\alpha - R_s i_\alpha)dt \\ \lambda_\beta = \int \left(v_\beta - R_s i_\beta\right)dt \end{cases} \tag{14.8}$$

The mathematical model expressed in (14.5)–(14.8) lends itself automatically to the development of the open-loop and closed-loop observers explained hereafter.

14.3 Open-loop back EMF estimator

The rotor position and speed can be obtained from the open-loop estimator as follows. The stator flux linkage is initially estimated from the back EMF according to (14.8):

$$\begin{cases} \hat{\lambda}_\alpha = \int (v_\alpha - R_s i_\alpha)dt \\ \hat{\lambda}_\beta = \int \left(v_\beta - R_s i_\beta\right)dt \end{cases} \tag{14.9}$$

where ^ denotes the estimated quantities. The three-phase stator currents i_a, i_b and i_c are measured and converted into the α-β reference frame via Clarke's Transform.

$$\begin{pmatrix} i_\alpha \\ i_\beta \end{pmatrix} = \begin{pmatrix} 1 & 0 & 0 \\ 0 & \dfrac{1}{\sqrt{3}} & -\dfrac{1}{\sqrt{3}} \end{pmatrix}\begin{pmatrix} i_a \\ i_b \\ i_c \end{pmatrix} \tag{14.10}$$

In contrast, the stator voltages v_α and v_β are derived from the DC-link voltage and switching status of the inverter or alternatively, from the outputs of the PI

current controllers v_d^* and v_q^* and applying inverse Park's Transform:

$$\begin{pmatrix} v_\alpha \\ v_\beta \end{pmatrix} = \begin{pmatrix} \cos\hat{\theta}_{re} & -\sin\hat{\theta}_{re} \\ \sin\hat{\theta}_{re} & \cos\hat{\theta}_{re} \end{pmatrix} \begin{pmatrix} v_d^* \\ v_q^* \end{pmatrix} \tag{14.11}$$

Once the estimated stator flux linkage $\hat{\lambda}_\alpha$ and $\hat{\lambda}_\beta$ are found, the active flux linkage is derived from (14.6):

$$\begin{cases} \hat{\lambda}_{a\alpha} = \hat{\lambda}_\alpha - L_\mathrm{q} i_\alpha \\ \hat{\lambda}_{a\beta} = \hat{\lambda}_\beta - L_\mathrm{q} i_\beta \end{cases} \tag{14.12}$$

The estimated rotor position $\hat{\theta}_{re}$ is then simply obtained by rearranging (14.7):

$$\hat{\theta}_{re} = \tan^{-1}\frac{\hat{\lambda}_{a\beta}}{\hat{\lambda}_{a\alpha}} \tag{14.13}$$

And, the estimated rotor speed $\hat{\omega}_{re}$ is found by differentiating (14.13) and fed through a low-pass filter (LPF) to remove the HF noise:

$$\hat{\omega}_{re} = \frac{d\hat{\theta}_{re}}{dt} \tag{14.14}$$

The estimation position and speed in (14.13) and (14.14), respectively, are then used for Park's transformation and closed-loop speed regulation in the vector control scheme depicted in Figure 14.1. The structure of the open-loop back EMF estimator is graphically shown in Figure 14.3. This estimator has the advantage of being simple. However, in practice, the pure integrator in (14.9) is seldom used due to its susceptibility to DC measurement offsets present in the current and voltage signals. The three-phase currents and DC-link voltage of the PMSM drive are obtained using Hall sensors and operational amplifiers. DC measurement offset due to op-amp non-idealities are inevitable and they change according to thermal conditions. As a consequence, these offsets get accumulated at the integrator output and the flux estimate drift out of bounds. The estimator eventually fails even if a minute dc-offset is present in either the voltage or current channel.

This problem is often mitigated by replacing the pure integrator in (14.9) with an LPF whose cut-off frequency is $\frac{1}{\tau}$. The block diagram of the modified estimator is shown in Figure 14.4. Unlike a pure integrator, the LPF limits the effect of the

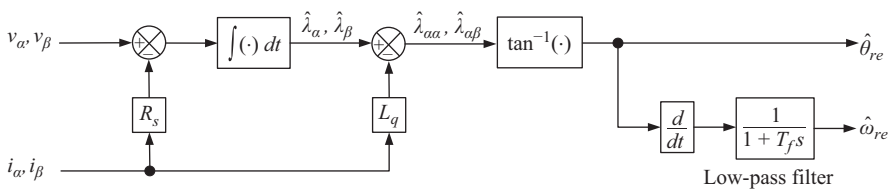


Figure 14.3 Block diagram of the open-loop back EMF estimator

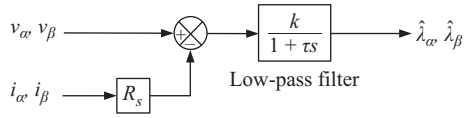


Figure 14.4 Block diagram stator flux linkage observer with the pure integrator substituted by an LPF

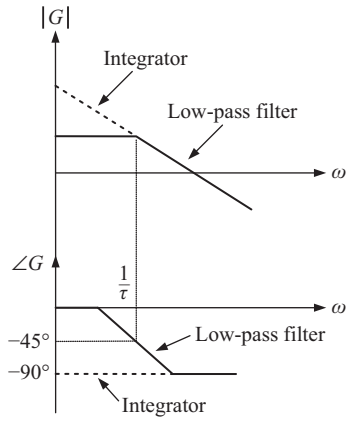


Figure 14.5 Frequency response of the pure integrator and the LPF

dc-offset gain k within reasonable limits at the expense of its frequency response. From the bode diagrams in Figure 14.5, it can be inferred that the LPF mimics the integrator when the operating frequency $\omega \gg \frac{1}{\tau}$. Conversely, the gain and the -90° phase shift of the integrator are lost as the frequencies reduce. If the PMSM drive operates at frequencies below approximately ten times the cut off frequency of the LPF $\left(\omega < \frac{10}{\tau}\right)$, the stator flux linkage estimation in (14.9), and hence, the estimated rotor position and speed in (14.13) and (14.14), respectively, will be erroneous and the stability of the PMSM drive will be jeopardised.

This estimation error is further exacerbated if the effect of inverter non-linearities and stator resistance variations are included. To improve the performance of the sensorless PMSM drive in the lower operating speed range, the closed-loop observers explained in the subsequent section can be utilised instead.

14.4 Closed-loop speed-adaptive observer

By combining (14.5) and (14.7), the PMSM can be represented in state-space form.

$$\begin{cases} \dfrac{d\boldsymbol{x}}{dt} = \boldsymbol{A}\boldsymbol{x} + \boldsymbol{B}\boldsymbol{u} \\ \boldsymbol{y} = \boldsymbol{C}\boldsymbol{x} \end{cases} \tag{14.15}$$

where

$$\boldsymbol{u} = \begin{pmatrix} v_\alpha & v_\beta \end{pmatrix}^T$$
$$\boldsymbol{x} = \begin{pmatrix} i_\alpha & i_\beta & \lambda_{a\alpha} & \lambda_{a\beta} \end{pmatrix}^T$$
$$\boldsymbol{y} = \begin{pmatrix} i_\alpha & i_\beta \end{pmatrix}^T$$
$$\boldsymbol{A} = \begin{pmatrix} -\dfrac{R_s}{L_\mathrm{q}}\boldsymbol{I} & -\dfrac{\omega_{re}}{L_\mathrm{q}}\boldsymbol{J} \\ \boldsymbol{0} & \omega_{re}\boldsymbol{J} \end{pmatrix}$$
$$\boldsymbol{B} = \begin{pmatrix} \dfrac{1}{L_\mathrm{q}}\boldsymbol{I} & \boldsymbol{0} \end{pmatrix}^{\boldsymbol{T}}$$
$$\boldsymbol{C} = \begin{pmatrix} \boldsymbol{I} & \boldsymbol{0} \end{pmatrix}$$
$$\boldsymbol{I} = \begin{pmatrix} 1 & 0 \\ 0 & 1 \end{pmatrix}$$
$$\boldsymbol{J} = \begin{pmatrix} 0 & -1 \\ 1 & 0 \end{pmatrix}$$

Based on the model in (14.15), a full-order closed-loop speed-adaptive observer can be synthesised as follows:

$$\begin{cases} \dfrac{d\hat{\boldsymbol{x}}}{dt} = \hat{\boldsymbol{A}}\hat{\boldsymbol{x}} + \boldsymbol{B}\boldsymbol{u} + \boldsymbol{G}\tilde{\boldsymbol{y}} \\ \hat{\boldsymbol{y}} = \boldsymbol{C}\hat{\boldsymbol{x}} \end{cases} \tag{14.16}$$

where

$$\tilde{\boldsymbol{y}} = \boldsymbol{y} - \hat{\boldsymbol{y}}$$
$$\hat{\boldsymbol{A}} = \begin{pmatrix} -\dfrac{R_s}{L_\mathrm{q}}\boldsymbol{I} & -\dfrac{\hat{\omega}_{re}}{L_\mathrm{q}}\boldsymbol{J} \\ \boldsymbol{0} & \hat{\omega}_{re}\boldsymbol{J} \end{pmatrix}$$
$$\boldsymbol{G} = \begin{pmatrix} g_1\boldsymbol{I} + g_2\boldsymbol{J} \\ g_3\boldsymbol{I} + g_4\boldsymbol{J} \end{pmatrix} \text{ is the gain of the observer.}$$

Note that ^ denotes the estimated quantities and $\hat{\boldsymbol{A}} = \boldsymbol{A} - \tilde{\boldsymbol{A}}$, where $\tilde{\boldsymbol{A}} = \tilde{\omega}_{re}\begin{pmatrix} \boldsymbol{0} & -\frac{1}{L_\mathrm{q}}\boldsymbol{J} \\ \boldsymbol{0} & \boldsymbol{J} \end{pmatrix}$ and $\tilde{\omega}_{re} = \omega_{re} - \hat{\omega}_{re}$.

The state error dynamics can be found by subtracting (14.16) from (14.15):

$$\frac{d\tilde{\boldsymbol{x}}}{dt} = \frac{d}{dt}(\boldsymbol{x} - \hat{\boldsymbol{x}}) = (\boldsymbol{A} - \boldsymbol{G}\boldsymbol{C})\tilde{\boldsymbol{x}} + \tilde{\boldsymbol{A}}\hat{\boldsymbol{x}} \tag{14.17}$$

According to the Popov's hyperstability criterion, the matrix $(\boldsymbol{A} - \boldsymbol{G}\boldsymbol{C})$ must be negative definite. In addition, the non-linear term $\tilde{\boldsymbol{A}}\hat{\boldsymbol{x}}$ must fulfil the condition

$$\int_0^{t_1} \tilde{\boldsymbol{x}}^{\boldsymbol{T}}\tilde{\boldsymbol{A}}\hat{\boldsymbol{x}}\, dt \leq \gamma^2 \tag{14.18}$$

where $\gamma > 0$ and is a constant independent of t_1. The first condition can be fulfilled by carefully selecting the gain of the observer $\boldsymbol{G}$ so that the eigenvalues of $(\boldsymbol{A} - \boldsymbol{GC})$ lie in negative real parts. As an illustration, the poles of the observer can be designed to have identical imaginary parts as the motor poles, but shifted to the left in the complex plane. Rewriting (14.16) in complex form yields

$$\frac{d\hat{\boldsymbol{X}}}{dt} = \hat{\boldsymbol{A}}_{\boldsymbol{c}}\hat{\boldsymbol{X}} + \boldsymbol{B}_{\boldsymbol{c}}\boldsymbol{U} + \boldsymbol{G}_{\boldsymbol{c}}\boldsymbol{C}_{\boldsymbol{c}}\left(\boldsymbol{X} - \hat{\boldsymbol{X}}\right) \tag{14.19}$$

where

$$\begin{aligned}
&\boldsymbol{v} = v_\alpha + jv_\beta \\
&\boldsymbol{i} = i_\alpha + ji_\beta \\
&\boldsymbol{\lambda_a} = \lambda_{a\alpha} + j\lambda_{a\beta} \\
&\boldsymbol{U} = \boldsymbol{v} \\
&\boldsymbol{X} = (\,\boldsymbol{i} \quad \boldsymbol{\lambda_a}\,)^{\boldsymbol{T}} \\
&\boldsymbol{Y} = \boldsymbol{i} \\
&\hat{\boldsymbol{A}}_{\boldsymbol{c}} = \begin{pmatrix} -\dfrac{R_s}{L_\mathrm{q}} & -j\dfrac{\hat{\omega}_{re}}{L_\mathrm{q}} \\ 0 & j\hat{\omega}_{re} \end{pmatrix} \\
&\boldsymbol{B}_{\boldsymbol{c}} = \begin{pmatrix} \dfrac{1}{L_\mathrm{q}} & 0 \end{pmatrix}^{T} \\
&\boldsymbol{C}_{\boldsymbol{c}} = (\,1 \quad 0\,) \\
&\boldsymbol{G}_{\boldsymbol{c}} = \begin{pmatrix} g_1 + jg_2 \\ g_3 + jg_4 \end{pmatrix}
\end{aligned}$$

Thus, the poles of the observer are the roots of the matrix $\left(\hat{\boldsymbol{A}}_{\boldsymbol{c}} - \boldsymbol{G}_{\boldsymbol{c}}\boldsymbol{C}\right)$ which can be found by solving the characteristic equation

$$\begin{aligned}
|\, s\boldsymbol{I} - \left(\hat{\boldsymbol{A}}_{\boldsymbol{c}} - \boldsymbol{G}_{\boldsymbol{c}}\boldsymbol{C}_{\boldsymbol{c}}\right) \,| = s^2 + \left[\left(\frac{R_s}{L_\mathrm{q}} + g_1\right) + j(g_2 - \hat{\omega}_{re})\right]s \\
+ \hat{\omega}_{re}\left[\left(g_2 + \frac{g_4}{L_\mathrm{q}}\right) - j\left(\frac{R_s}{L_\mathrm{q}} + \frac{g_3}{L_\mathrm{q}} + g_1\right)\right] = 0
\end{aligned} \tag{14.20}$$

The poles of the PMSM can easily be found from (14.20) by setting the individual gains $g_1 = g_2 = g_3 = g_4 = 0$. It can be shown that the poles of the PMSM lie at $s = -\frac{R_s}{L_\mathrm{q}}$ and $s = j\omega_{re}$. Let the poles of the observer be

$$s = -\frac{R_s}{L_\mathrm{q}} - k_1 \qquad \text{and} \qquad s = -k_2 + j\hat{\omega}_{re} \tag{14.21}$$

where $k_1, k_2 > 0$. Then, the characteristic equation reduces to

$$\begin{aligned}
|\, s\boldsymbol{I} - \left(\hat{\boldsymbol{A}}_{\boldsymbol{c}} - \boldsymbol{G}_{\boldsymbol{c}}\boldsymbol{C}_{\boldsymbol{c}}\right) \,| = s^2 + \left[\left(\frac{R_s}{L_\mathrm{q}} + k_1 + k_2\right) - j\hat{\omega}_{re}\right]s \\
+ \left[k_2\left(\frac{R_s}{L_\mathrm{q}} + k_1\right) - j\hat{\omega}_{re}\left(\frac{R_s}{L_\mathrm{q}} + k_1\right)\right] = 0
\end{aligned} \tag{14.22}$$

Comparing (14.20) and (14.22) yields

$$\begin{cases} g_1 = k_1 + k_2 \\ g_2 = 0 \\ g_3 = -k_2 L_{\mathrm{q}} \\ g_4 = \dfrac{k_2 L_{\mathrm{q}}}{\mid \hat{\omega}_{re}} \mid \left(\dfrac{R_s}{L_{\mathrm{q}}} + k_1\right) \end{cases} \tag{14.23}$$

Note that the poles in (14.21) have negative real parts, and therefore, the first condition of Popov's hyperstability criterion is satisfied. The gain of the observer $\boldsymbol{G}$ in (14.23) requires the estimated rotor speed $\hat{\omega}_{re}$ which can be derived from the second condition of Popov's hyperstability criterion. Assuming that the estimation errors are small, it can be inferred from (14.6) that

$$\begin{pmatrix} \tilde{\lambda}_{a\alpha} \\ \tilde{\lambda}_{a\beta} \end{pmatrix} \approx -L_{\mathrm{q}} \begin{pmatrix} \tilde{i}_{\alpha} \\ \tilde{i}_{\beta} \end{pmatrix} \tag{14.24}$$

Then, from the second Popov's hyperstability criterion,

$$\begin{aligned} \int_0^{t_1} \tilde{\boldsymbol{x}}^{\boldsymbol{T}} \tilde{\boldsymbol{A}} \hat{\boldsymbol{x}}\, dt &= \int_0^{t_1} \tilde{\boldsymbol{x}}^{\boldsymbol{T}} \begin{pmatrix} \boldsymbol{0} & -\dfrac{1}{L_{\mathrm{q}}}\boldsymbol{J} \\ \boldsymbol{0} & \boldsymbol{J} \end{pmatrix} \hat{\boldsymbol{x}} \tilde{\omega}_{re}\, dt \\ &= \int_0^{t_1} \begin{pmatrix} \tilde{i}_{\alpha} & \tilde{i}_{\beta} & -L_{\mathrm{q}}\tilde{i}_{\alpha} & -L_{\mathrm{q}}\tilde{i}_{\beta} \end{pmatrix} \begin{pmatrix} \boldsymbol{0} & -\dfrac{1}{L_{\mathrm{q}}}\boldsymbol{J} \\ \boldsymbol{0} & \boldsymbol{J} \end{pmatrix} \begin{pmatrix} \hat{i}_{\alpha} & \hat{i}_{\beta} & \hat{\lambda}_{a\alpha} & \hat{\lambda}_{a\beta} \end{pmatrix}^{T} \tilde{\omega}_{re}\, dt \\ &= \left(\frac{1}{L_{\mathrm{q}}} + L_{\mathrm{q}}\right) \int_0^{t_1} \left(\hat{\lambda}_{a\beta}\tilde{i}_{\alpha} - \hat{\lambda}_{a\alpha}\tilde{i}_{\beta}\right) \tilde{\omega}_{re}\, dt \end{aligned} \tag{14.25}$$

Define the speed adaptation law

$$\hat{\omega}_{re} = K_p\left(\hat{\lambda}_{a\beta}\tilde{i}_{\alpha} - \hat{\lambda}_{a\alpha}\tilde{i}_{\beta}\right) + K_i \int_0^t \left(\hat{\lambda}_{a\beta}\tilde{i}_{\alpha} - \hat{\lambda}_{a\alpha}\tilde{i}_{\beta}\right) \tilde{\omega}_{re}\, d\tau \tag{14.26}$$

where K_p, $K_i > 0$. Substituting (14.26) into (14.25) yields

$$\begin{aligned} \int_0^{t_1} \tilde{\boldsymbol{x}}^{\boldsymbol{T}} \tilde{\boldsymbol{A}} \hat{\boldsymbol{x}} dt &= \left(\frac{1}{L_{\mathrm{q}}} + L_{\mathrm{q}}\right) \int_0^{t_1} \left(\hat{\lambda}_{a\beta}\tilde{i}_{\alpha} - \hat{\lambda}_{a\alpha}\tilde{i}_{\beta}\right) \Big[\omega_{re} - K_p\left(\hat{\lambda}_{a\beta}\tilde{i}_{\alpha} - \hat{\lambda}_{a\alpha}\tilde{i}_{\beta}\right) \\ &\quad -K_i \int_0^t \left(\hat{\lambda}_{a\beta}\tilde{i}_{\alpha} - \hat{\lambda}_{a\alpha}\tilde{i}_{\beta}\right) d\tau\Big] dt \\ &= \left(\frac{1}{L_{\mathrm{q}}} + L_{\mathrm{q}}\right) \Big\{-K_p \int_0^{t_1} \left(\hat{\lambda}_{a\beta}\tilde{i}_{\alpha} - \hat{\lambda}_{a\alpha}\tilde{i}_{\beta}\right)^2 dt - K_i \int_0^{t_1} \left(\hat{\lambda}_{a\beta}\tilde{i}_{\alpha} - \hat{\lambda}_{a\alpha}\tilde{i}_{\beta}\right) \\ &\quad \left[\int_0^t \left(\hat{\lambda}_{a\beta}\tilde{i}_{\alpha} - \hat{\lambda}_{a\alpha}\tilde{i}_{\beta}\right) d\tau - \frac{\omega_{re}}{K_i}\right] dt\Big\} \end{aligned} \tag{14.27}$$

The first term on the right-hand side, $-K_p \int_0^{t_1} \left(\hat{\lambda}_{a\beta}\tilde{i}_\alpha - \hat{\lambda}_{a\alpha}\tilde{i}_\beta\right)^2 dt \leq 0$ for all t_1. The second term can be rewritten as

$$-K_i \int_0^{t_1} \left(\hat{\lambda}_{a\beta}\tilde{i}_\alpha - \hat{\lambda}_{a\alpha}\tilde{i}_\beta\right)\left[\int_0^t \left(\hat{\lambda}_{a\beta}\tilde{i}_\alpha - \hat{\lambda}_{a\alpha}\tilde{i}_\beta\right)d\tau - \frac{\omega_{re}}{K_i}\right]dt$$

$$= -K_i \int_0^{t_1} \frac{df(t)}{dt} f(t)dt = -\frac{K_i}{2}\left[f^2(t_1) - f^2(0)\right] \leq \frac{K_i}{2} f^2(0) = \gamma^2 \tag{14.28}$$

where $\gamma = \sqrt{\frac{K_i}{2}} f(0)$ is independent of t_1 and $f(t) = \int_0^t \left(\hat{\lambda}_{a\beta}\tilde{i}_\alpha - \hat{\lambda}_{a\alpha}\tilde{i}_\beta\right)d\tau - \frac{\omega_{re}}{K_i}$. Thus, $\int_0^{t_1} \tilde{\boldsymbol{x}}^{\boldsymbol{T}} \tilde{\boldsymbol{A}} \hat{\boldsymbol{x}} dt \leq \left(\frac{1}{L_q} + L_q\right)\gamma^2$ and the observer expressed by (14.16) with gains in (14.23) is stable. Furthermore, the rotor speed can be estimated from (14.26). On the other hand, the rotor position is found from the estimated active flux linkage in (14.16).

$$\hat{\theta}_{re} = \tan^{-1}\frac{\hat{\lambda}_{a\beta}}{\hat{\lambda}_{a\alpha}} \tag{14.29}$$

The block diagram of the closed-loop speed-adaptive observer is shown in Figure 14.6. In general, this observer delivers improved performance compared to the open-loop integrator but it is still vulnerable to effects to DC-offset and inverter non-linearities. Furthermore, due to its speed-adaptive nature, its low-speed performance is also limited. In digital realisation of the observer, the speed adaptation in (14.26) is usually performed as the last step of the estimation process. Hence, the speed estimate is affected by cumulative errors, noise and delays [30]. When the inaccurate speed value is fed back to the observer in (14.16), the current, active flux linkage and speed estimation gradually worsen. This can easily lead to drive instability especially at low speeds. An alternative is to adopt the speed non-adaptive observer elaborated in the succeeding section.

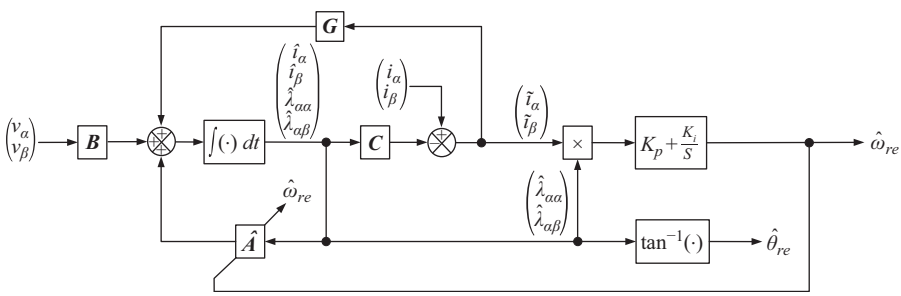


Figure 14.6 Block diagram of the closed-loop speed-adaptive observer

14.5 Closed-loop speed non-adaptive observer

A closed-loop observer independent of rotor speed adaptation [10] can easily be synthesised by incorporating a feedback term to the open-loop estimator in (14.9):

$$\frac{d\hat{\boldsymbol{\lambda}}}{dt} = -\hat{R}_s\boldsymbol{i} + \boldsymbol{v} + \boldsymbol{G}\left(\boldsymbol{i} - \hat{\boldsymbol{i}}\right) \tag{14.30}$$

where

$$\begin{aligned}
&\boldsymbol{v} = \begin{pmatrix} v_\alpha & v_\beta \end{pmatrix}^T \\
&\boldsymbol{i} = \begin{pmatrix} i_\alpha & i_\beta \end{pmatrix}^T \\
&\hat{\boldsymbol{i}} = \begin{pmatrix} \hat{i}_\alpha & \hat{i}_\beta \end{pmatrix}^T \\
&\hat{\boldsymbol{\lambda}} = \begin{pmatrix} \hat{\lambda}_\alpha & \hat{\lambda}_\beta \end{pmatrix}^T \\
&\boldsymbol{I} = \begin{pmatrix} 1 & 0 \\ 0 & 1 \end{pmatrix} \\
&\boldsymbol{J} = \begin{pmatrix} 0 & -1 \\ 1 & 0 \end{pmatrix}
\end{aligned}$$

and $\boldsymbol{G} = g_1\boldsymbol{I} + g_2\boldsymbol{J}$ is the gain of the observer.

Note that ^ denotes the estimated quantities and the estimated stator currents $\hat{i}_\alpha$ and $\hat{i}_\beta$ can be found from the current model of the PMSM:

$$\hat{\boldsymbol{i}} = \boldsymbol{T}^{-1}\left(\hat{\theta}_{re}\right)\boldsymbol{L}^{-1}\boldsymbol{T}\left(\hat{\theta}_{re}\right)\hat{\boldsymbol{\lambda}} + \frac{\lambda_f}{L_d}\begin{pmatrix} \cos\hat{\theta}_{re} \\ \sin\hat{\theta}_{re} \end{pmatrix} \tag{14.31}$$

where $\boldsymbol{T}\left(\hat{\theta}_{re}\right) = \begin{pmatrix} \cos\hat{\theta}_{re} & \sin\hat{\theta}_{re} \\ -\sin\hat{\theta}_{re} & \cos\hat{\theta}_{re} \end{pmatrix}$ and $\boldsymbol{L} = \begin{pmatrix} L_d & 0 \\ 0 & L_q \end{pmatrix}$. Assuming orientation, the stator current error is given by

$$\tilde{\boldsymbol{i}} = \boldsymbol{T}^{-1}\left(\hat{\theta}_{re}\right)\boldsymbol{L}^{-1}\boldsymbol{T}\left(\hat{\theta}_{re}\right)\tilde{\boldsymbol{\lambda}} \tag{14.32}$$

where $\tilde{\boldsymbol{i}} = \boldsymbol{i} - \hat{\boldsymbol{i}}$ and $\tilde{\boldsymbol{\lambda}} = \boldsymbol{\lambda} - \hat{\boldsymbol{\lambda}}$ are the stator current and stator flux linkage error, respectively. The stator flux linkage error dynamics are governed by

$$\frac{d\tilde{\boldsymbol{\lambda}}}{dt} = -\tilde{R}_s\boldsymbol{i} - \boldsymbol{G}\left(\boldsymbol{i} - \hat{\boldsymbol{i}}\right) \tag{14.33}$$

where $\tilde{R}_s = R_s - \hat{R}_s$ is the stator resistance estimation error. Define a Lyapunov candidate function

$$V = \frac{1}{2}\left(\tilde{\boldsymbol{\lambda}}^T\boldsymbol{T}^{-1}\boldsymbol{L}^{-1}\boldsymbol{T}\tilde{\boldsymbol{\lambda}} + \frac{\check{R}_s^2}{\eta}\right) > 0 \tag{14.34}$$

where $\eta > 0$. Assuming that the stator resistance remains constant within one sampling interval,

$$\frac{dV}{dt} = \tilde{\boldsymbol{\lambda}}^{\boldsymbol{T}} \boldsymbol{T}^{-1} \boldsymbol{L}^{-1} \boldsymbol{T} \frac{d\tilde{\boldsymbol{\lambda}}}{dt} + \hat{\omega}_{re} \tilde{\boldsymbol{\lambda}}^{\boldsymbol{T}} \boldsymbol{T}^{-1} \boldsymbol{L}^{-1} \boldsymbol{T} \tilde{\boldsymbol{\lambda}} - \frac{\tilde{R}_s}{\eta} \frac{d\hat{R}_s}{dt} \tag{14.35}$$

Substituting (14.32) and (14.33) into (14.35) yields

$$\frac{dV}{dt} = -\tilde{\boldsymbol{i}}^{\boldsymbol{T}} \boldsymbol{G} \tilde{\boldsymbol{i}} + \hat{\omega}_{re} \tilde{\boldsymbol{i}}^{\boldsymbol{T}} \boldsymbol{T}^{-1} \boldsymbol{J} \boldsymbol{L} \boldsymbol{T} \tilde{\boldsymbol{i}} - \tilde{R}_s \left(i_\alpha \tilde{i}_\alpha + i_\beta \tilde{i}_\beta + \frac{1}{\eta} \frac{d\hat{R}_s}{dt} \right) \tag{14.36}$$

Since $\boldsymbol{G} = g_1 \boldsymbol{I} + g_2 \boldsymbol{J}$, (14.36) can simplified to

$$\frac{dV}{dt} = -\tilde{\boldsymbol{i}}^{\boldsymbol{T}} \boldsymbol{T}^{-1} [g_1 \boldsymbol{I} + \boldsymbol{J}(g_2 \boldsymbol{I} - \hat{\omega}_{re} \boldsymbol{L})] \boldsymbol{T} \tilde{\boldsymbol{i}} - \tilde{R}_s \left(i_\alpha \tilde{i}_\alpha + i_\beta \tilde{i}_\beta + \frac{1}{\eta} \frac{d\hat{R}_s}{dt} \right) \tag{14.37}$$

For global asymptotic stability, $\frac{dV}{dt} < 0$. Hence, the following relationships can be deduced:

$$i_\alpha \tilde{i}_\alpha + i_\beta \tilde{i}_\beta + \frac{1}{\eta} \frac{d\hat{R}_s}{dt} = 0 \tag{14.38}$$

$$-[g_1 \boldsymbol{I} + \boldsymbol{J}(g_2 \boldsymbol{I} - \hat{\omega}_{re} \boldsymbol{L})] < \boldsymbol{0} \tag{14.39}$$

Equation (14.38) ascertains the online stator resistance estimator:

$$\hat{R}_s = -\eta \int_0^t \left(i_\alpha \tilde{i}_\alpha + i_\beta \tilde{i}_\beta \right) dt \tag{14.40}$$

A larger gain η improves the response time of the estimator but may induce unwanted oscillations. As the changes in the stator resistance R_s are caused by thermal effects which have large time constants, a lower value $\eta \approx 1$ usually suffices. Now, the inequality in (14.40) dictates that the matrix $[g_1 \boldsymbol{I} + \boldsymbol{J}(g_2 \boldsymbol{I} - \hat{\omega}_{re} \boldsymbol{L})]$ must be positive definite and can be easily satisfied by appropriate selection of the individual gains g_1 and g_2. Note that the eigenvalues of the matrix $-[g_1 \boldsymbol{I} + \boldsymbol{J}(g_2 \boldsymbol{I} - \hat{\omega}_{re} \boldsymbol{L})]$ dictate the convergence of the observer and are given by the roots of the characteristic equation

$$\begin{aligned} &| \lambda \boldsymbol{I} + [g_1 \boldsymbol{I} + \boldsymbol{J}(g_2 \boldsymbol{I} - \hat{\omega}_{re} \boldsymbol{L})] | = \lambda^2 + 2 g_1 \lambda \\ &\quad + \left[g_1^2 + (g_2 - \hat{\omega}_{re} L_d)(g_2 - \hat{\omega}_{re} L_q) \right] = 0 \end{aligned} \tag{14.41}$$

Without the observer gains ($g_1 = g_2 = 0$), the eigenvalues lie at $\lambda = \pm j \omega_{re} \sqrt{L_\mathrm{d} L_\mathrm{q}}$ and the observer is marginally stable. Shifting these eigenvalues to the left by an amount k to improve the convergence of the observer,

$$\lambda = -k \pm j \hat{\omega}_{re} \sqrt{L_\mathrm{d} L_\mathrm{q}} \tag{14.42}$$

where $k > 0$. Then, the characteristic equation reduces to

$$| \lambda \boldsymbol{I} + [g_1 \boldsymbol{I} + \boldsymbol{J}(g_2 \boldsymbol{I} - \hat{\omega}_{re} \boldsymbol{L})] | = \lambda^2 + 2\lambda \mid \hat{\omega}_{re} \mid s + (k\hat{\omega}_{re})^2 + \hat{\omega}_{re}^2 L_{\mathrm{d}} L_{\mathrm{q}} = 0 \tag{14.43}$$

Comparing (14.41) and (14.43) yields

$$g_1 = k \qquad \text{and} \qquad g_2 = 0 \tag{14.44}$$

Note that while the observer gain $\boldsymbol{G}$ in (14.44) requires the estimated rotor speed information, the observer expressed by (14.30) and (14.31) itself is speed independent. Once the stator flux linkage is estimated in (14.30), the active flux linkage can be found from

$$\begin{cases} \hat{\lambda}_{a\alpha} = \hat{\lambda}_{\alpha} - L_{\mathrm{q}} i_{\alpha} \\ \hat{\lambda}_{a\beta} = \hat{\lambda}_{\beta} - L_{\mathrm{q}} i_{\beta} \end{cases} \tag{14.45}$$

The estimated rotor position $\hat{\theta}_{re}$ is then simply given by

$$\hat{\theta}_{re} = \tan^{-1} \frac{\hat{\lambda}_{a\beta}}{\hat{\lambda}_{a\alpha}} \tag{14.46}$$

And, the estimated rotor speed $\hat{\omega}_{re}$ is found by differentiating (14.46) and fed through an LPF to remove the HF noise.

$$\hat{\omega}_{re} = \frac{d\hat{\theta}_{re}}{dt} \tag{14.47}$$

The block diagram of the closed-loop speed-adaptive observer is shown in Figure 14.7. While this observer is speed independent, its performance is still limited by the accuracy of the measured current and voltage signals as well as the parameters of the PMSM. Hence, there is a lower speed limit for stable operation of the observer. To further improve the performance of the sensorless PMSM drive in the very low-speed region, the non-model-based approach such as the HF signal injection and current slope techniques subsequently explained can be adopted instead.

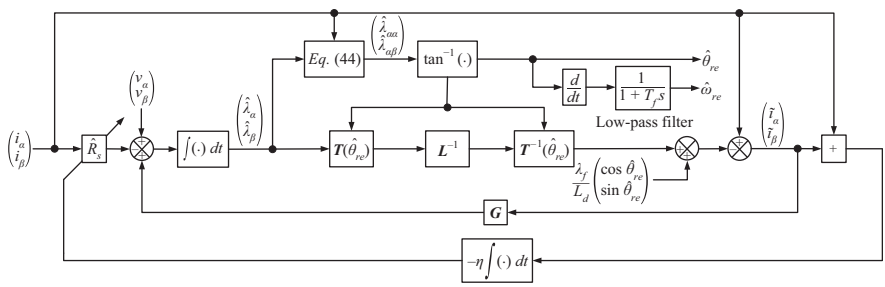


Figure 14.7 Block diagram of the closed-loop speed non-adaptive observer

14.6 HF signal injection

This method entails superimposing an HF voltage signal on the existing fundamental control voltage signals to the terminals of the PMSM and extracting the rotor position information from the resultant HF current signals. Let a carrier voltage signal with amplitude V_c and angular frequency ω_c in (14.48) be injected into the windings of the PMSM [14,15].

$$\begin{pmatrix} v_{\alpha h} \\ v_{\beta h} \end{pmatrix} = V_c \begin{pmatrix} \cos \omega_c t \\ \sin \omega_c t \end{pmatrix} \tag{14.48}$$

where $v_{\alpha h}$ and$v_{\beta h}$ represent the α-β axes components of the injected HF voltage signal. It is paramount that the amplitude V_c be high enough to allow discrimination of the resultant current signals from HF noise. At the same time, it must be low enough such that the available DC-link voltage can be maximally utilised. On the other hand, the carrier frequency ω_c must be high enough to ensure spectral separation between the HF current signals and that of the fundamental excitation. Assuming that the rotor speed is much smaller than the carrier frequency ω_c and the stator resistance is negligible compared to the HF reactances, the resultant HF current signals $i_{\alpha h}$ and $i_{\beta h}$ can be obtained by substituting (14.48) into (14.3):

$$\begin{pmatrix} i_{\alpha h} \\ i_{\beta h} \end{pmatrix} = \frac{V_c(L_d + L_q)}{2\omega_c L_d L_q} \begin{pmatrix} \cos\left(\omega_c t - \dfrac{\pi}{2}\right) \\ \sin\left(\omega_c t - \dfrac{\pi}{2}\right) \end{pmatrix} + \frac{V_c(L_q - L_d)}{2\omega_c L_d L_q} \begin{pmatrix} \sin(\omega_c t - 2\theta_{re}) \\ \cos(\omega_c t - 2\theta_{re}) \end{pmatrix} \tag{14.49}$$

The HF currents in (14.49) consist of two terms. The first term is the positive sequence currents whose amplitude depends on the average inductance of the PMSM and oscillates at the carrier frequency ω_c. Conversely, the second term is the negative sequence with an amplitude proportional to the difference between the *d-q* axes inductances and contains information on the rotor position θ_{re}. This term can be extracted by passing through the measured currents through a band-pass filter with centre frequency ω_c to isolate the HF components $i_{\alpha h}$, $i_{\beta h}$ which are subsequently demodulated according to (14.50):

$$\begin{pmatrix} i^d_{\alpha h} \\ i^d_{\beta h} \end{pmatrix} = \boldsymbol{T}\left(\omega_c t - 2\hat{\theta}_{re} - \frac{\pi}{2}\right) \begin{pmatrix} i_{\alpha h} \\ i_{\beta h} \end{pmatrix} \tag{14.50}$$

where $\boldsymbol{T}\left(\omega_c t - 2\hat{\theta}_{re} - \frac{\pi}{2}\right) = \begin{pmatrix} \cos\left(\omega_c t - 2\hat{\theta}_{re} - \frac{\pi}{2}\right) & -\sin\left(\omega_c t - 2\hat{\theta}_{re} - \frac{\pi}{2}\right) \\ \sin\left(\omega_c t - 2\hat{\theta}_{re} - \frac{\pi}{2}\right) & \cos\left(\omega_c t - 2\hat{\theta}_{re} - \frac{\pi}{2}\right) \end{pmatrix}$ and $i^d_{\alpha h}$ and $i^d_{\beta h}$ signify the α-β axes components of the demodulated HF currents

governed by

$$\begin{pmatrix} i_{\alpha h}^{d} \\ i_{\beta h}^{d} \end{pmatrix} = \begin{pmatrix} \cos\left(\omega_c t - 2\hat{\theta}_{re} - \frac{\pi}{2}\right) & -\sin\left(\omega_c t - 2\hat{\theta}_{re} - \frac{\pi}{2}\right) \\ \sin\left(\omega_c t - 2\hat{\theta}_{re} - \frac{\pi}{2}\right) & \cos\left(\omega_c t - 2\hat{\theta}_{re} - \frac{\pi}{2}\right) \end{pmatrix} \left\{ \frac{V_c\left(L_d + L_q\right)}{2\omega_c L_d L_q} \begin{pmatrix} \cos\left(\omega_c t - \frac{\pi}{2}\right) \\ \sin\left(\omega_c t - \frac{\pi}{2}\right) \end{pmatrix} + \frac{V_c\left(L_q - L_d\right)}{2\omega_c L_d L_q} \begin{pmatrix} \sin(\omega_c t - 2\theta_{re}) \\ \cos(\omega_c t - 2\theta_{re}) \end{pmatrix} \right\}$$

$$= -\frac{V_c\left(L_d + L_q\right)}{2\omega_c L_d L_q} \begin{pmatrix} \sin\left(2\omega_c t - 2\hat{\theta}_{re}\right) \\ \cos\left(2\omega_c t - 2\hat{\theta}_{re}\right) \end{pmatrix} + \frac{V_c\left(L_q - L_d\right)}{2\omega_c L_d L_q} \begin{pmatrix} \cos\left(2\tilde{\theta}_{re}\right) \\ \sin\left(2\tilde{\theta}_{re}\right) \end{pmatrix} \tag{14.51}$$

where $\tilde{\theta}_{re} = \theta_{re} - \hat{\theta}_{re}$ is the rotor position estimation error. The demodulated currents in (14.51) are then low-pass filtered to retain the second term containing the rotor position information. Taking the β-axis component reveals an error signal ε:

$$\varepsilon = LPF\left\{ i_{\beta h}^{d} \right\} = K_\varepsilon \sin\left(2\tilde{\theta}_{re}\right) \tag{14.52}$$

where $K_\varepsilon = \frac{V_c\left(L_q - L_d\right)}{2\omega_c L_d L_q}$. Assuming that the estimation error is small, (14.52) can be approximated by

$$\varepsilon \approx 2K_\varepsilon \tilde{\theta}_{re} \tag{14.53}$$

A PI controller cascaded with an integrator is then used to drive the error in (14.53) to zero and to obtain the estimated rotor position $\hat{\theta}_{re}$. The HF signal injection scheme is depicted in Figure 14.8. Note that the output of the PI controller is the estimated rotor speed $\hat{\omega}_{re}$. The closed-loop system can also be interpreted as the phase-locked loop (PLL) shown in Figure 14.9. The LPF has the transfer function

$$G_{LPF}(s) = \frac{\omega_L}{s + \omega_L} \tag{14.54}$$

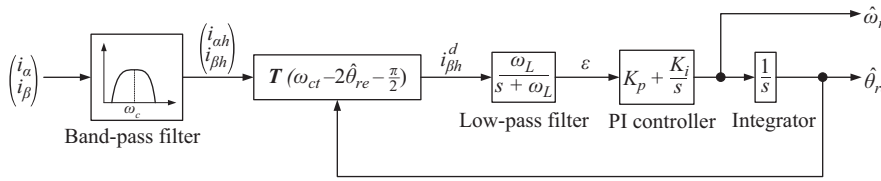


Figure 14.8 Block diagram of the HF signal injection method

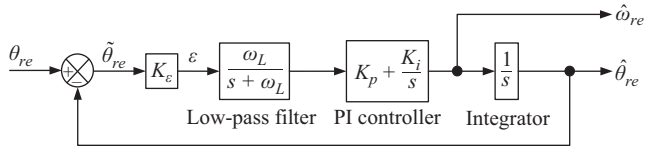


Figure 14.9 PLL for rotor position and speed estimation

where ω_L is the cut-off frequency of the LPF. On the other hand, the transfer function of the PI controller is given by

$$G_{PI}(s) = K_p + \frac{K_i}{s} \tag{14.55}$$

where K_p and K_i are the proportional and integral gains of the controller, respectively. Hence, the closed-loop transfer function of the PLL in Figure 14.9 is

$$T(s) = \frac{\hat{\theta}_{re}(s)}{\theta_{re}(s)} = \frac{2K_\varepsilon\omega_L\left(K_p s + K_i\right)}{s^3 + \omega_L s^2 + 2K_\varepsilon K_p\omega_L s + 2K_\varepsilon K_i\omega_L} \tag{14.56}$$

By selecting the closed-loop poles of $T(s)$ to lie at $s = -\rho$ with multiplicity of 3, where $\rho > 0$, the PI controller gains can be obtained [16]:

$$\begin{cases} K_p = \dfrac{\rho}{2K_\varepsilon} \\ K_i = \dfrac{\rho^2}{6K_\varepsilon} \end{cases} \tag{14.57}$$

Furthermore, the cut-off frequency of the LPF is related to the pole $s = -\rho$ by the following equation:

$$\omega_L = 3\rho \tag{14.58}$$

The HF signal injection method works extremely well at very low operating speeds. However, as the rotor speed increases, it becomes increasingly difficult to separate the HF currents from that of the fundamental frequency and as a result, the effectiveness of this method deteriorates. Thus, it is imperative that the HF signal injection scheme is disabled, and instead, the model-based closed-loop observer is used by the sensorless PMSM drive at high speeds. The former can easily be amalgamated with the closed-loop speed non-adaptive observer discussed in the preceding section to achieve sensorless drive operation over a wide speed range. The block diagram of the combined observer is illustrated in Figure 14.10. The HF signal injection technique provides an additional current error feedback component $\tilde{i}_{\alpha,hf}$, $\tilde{i}_{\beta,hf}$ to the stator flux linkage observer expressed by (14.30).

$$\begin{pmatrix} \hat{i}_{\alpha,hf} \\ \hat{i}_{\beta,hf} \end{pmatrix} = \boldsymbol{T}^{-1}\left(\hat{\theta}_{re,hf}\right)\begin{pmatrix} \dfrac{1}{L_d} & 0 \\ 0 & \dfrac{1}{L_q} \end{pmatrix}\boldsymbol{T}\left(\hat{\theta}_{re,hf}\right)\begin{pmatrix} \hat{\lambda}_\alpha \\ \hat{\lambda}_\beta \end{pmatrix} + \frac{\lambda_f}{L_d}\begin{pmatrix} \cos\hat{\theta}_{re,hf} \\ \sin\hat{\theta}_{re,hf} \end{pmatrix} \tag{14.59}$$

$$\begin{pmatrix} \tilde{i}_{\alpha,hf} \\ \tilde{i}_{\beta,hf} \end{pmatrix} = \begin{pmatrix} i_\alpha \\ i_\beta \end{pmatrix} - \begin{pmatrix} \hat{\tilde{i}}_{\alpha,hf} \\ \hat{\tilde{i}}_{\beta,hf} \end{pmatrix} \tag{14.60}$$

where $\hat{\lambda}_\alpha, \hat{\lambda}_\beta$ is the estimated stator flux linkage obtained from (14.30), $\hat{i}_{\alpha,hf}, \hat{i}_{\beta,hf}$ is the estimated stator current using the HF signal injection method and $\hat{\theta}_{re,hf}$ is the estimated rotor position obtained from the PLL in Figure 14.9. The current error in (14.59) is fed back to the stator flux observer via a speed-dependent observer gain $\boldsymbol{G}_{\boldsymbol{\omega}}$:

$$\boldsymbol{G}_{\boldsymbol{\omega}} = g(\hat{\omega}_{re})\boldsymbol{G} \tag{14.61}$$

where $\boldsymbol{G}$ is the observer gain expressed in (14.30) and (14.43). To ensure a smooth transition between the HF signal injection technique and the model-based observer, the function $g(\hat{\omega}_{re})$ is mathematically defined as

$$g(\hat{\omega}_{re}) = \begin{cases} \omega_T - \hat{\omega}_{re} \mid \hat{\omega}_{re} \mid \leq \omega_T \\ \quad 0 \; otherwise \end{cases} \tag{14.62}$$

where ω_T is the rotor speed at which the HF signal injection is disabled. The function $g(\hat{\omega}_{re})$ is graphically shown in Figure 14.11.

In addition, the amplitude of injected voltage signal in (14.48) is also decreased linearly with rotor speed.

$$V_c = V_{c0} g(\hat{\omega}_{re}) \tag{14.63}$$

where V_{c0} is the amplitude of the injected voltage signal at standstill. In the combined observer, the estimated rotor position $\hat{\theta}_{re}$ and speed $\hat{\omega}_{re}$ used for sensorless control are derived from (14.45) and (14.46), respectively.

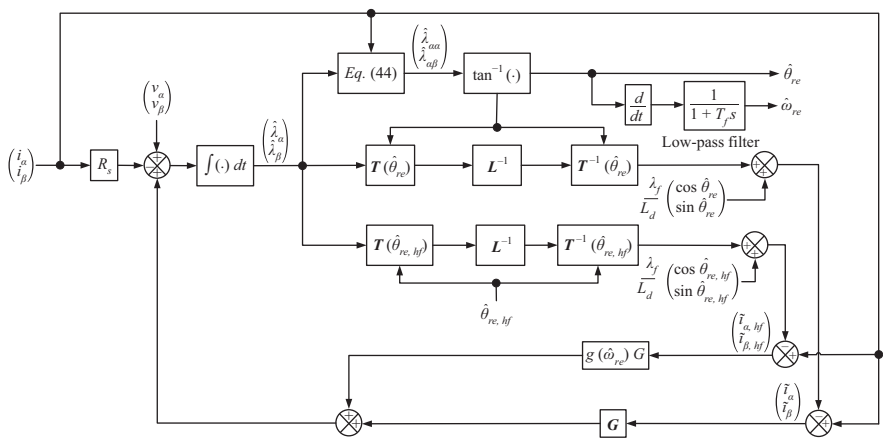


Figure 14.10 Combined HF signal injection and closed-loop speed non-adaptive observer

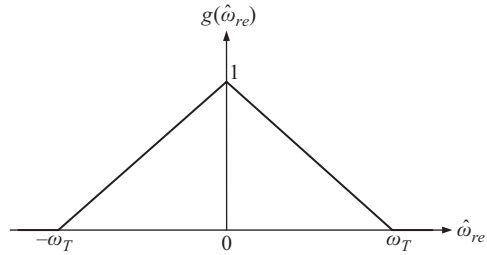


Figure 14.11 Speed-dependent function $g(\hat{\omega}_{re})$

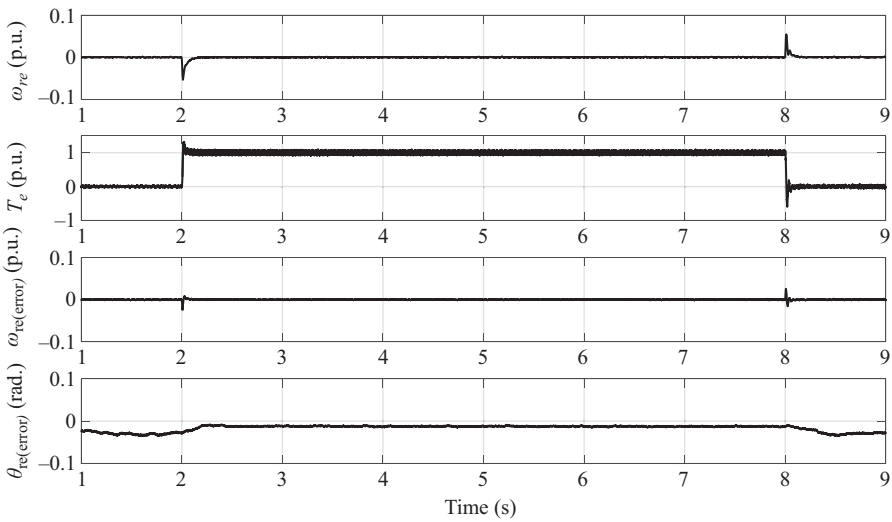


Figure 14.12 Performance of the sensorless PMSM drive with the combined HF signal injection and closed-loop speed non-adaptive observer at standstill due to rated load torque disturbance. The first subplot shows the motor speed while the second subplot illustrates the developed torque. The third and fourth subplots depict the speed and position estimation errors, respectively

The performance of the sensorless PMSM drive with the combined HF signal injection and closed-loop speed non-adaptive observer is investigated in simulation and the results are reported in Figures 14.12–14.14. Figure 14.12 shows persistent zero speed operation while rated load torque is added to the shaft of the motor at $t = 2$s and subsequently removed at $t = 8$s. The sensorless drive is stable without any speed estimation error except during the load transients. Furthermore, the position estimation error is maintained within 0.05 rad. throughout.

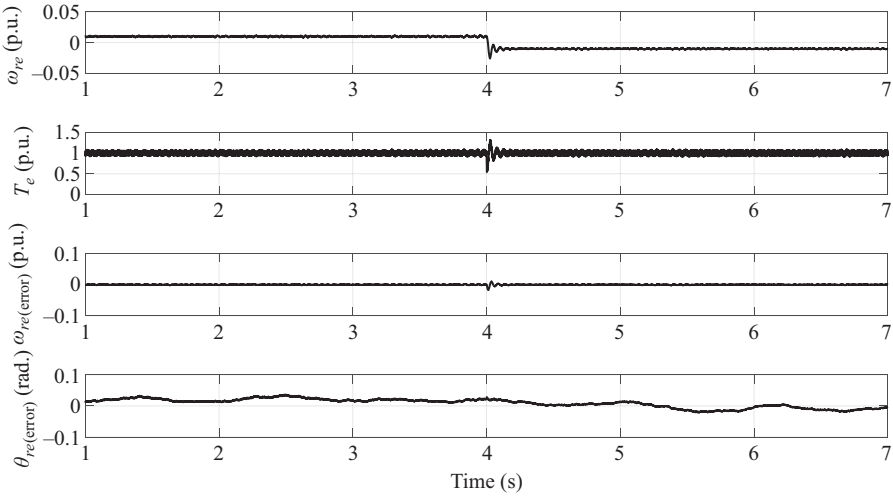


Figure 14.13 Performance of the sensorless PMSM drive with the combined HF signal injection and closed-loop speed non-adaptive observer due to speed reversal from +0.01 p.u. to −0.01 p.u. with rated load torque. The first subplot shows the motor speed while the second subplot illustrates the developed torque. The third and fourth subplots depict the speed and position estimation errors, respectively

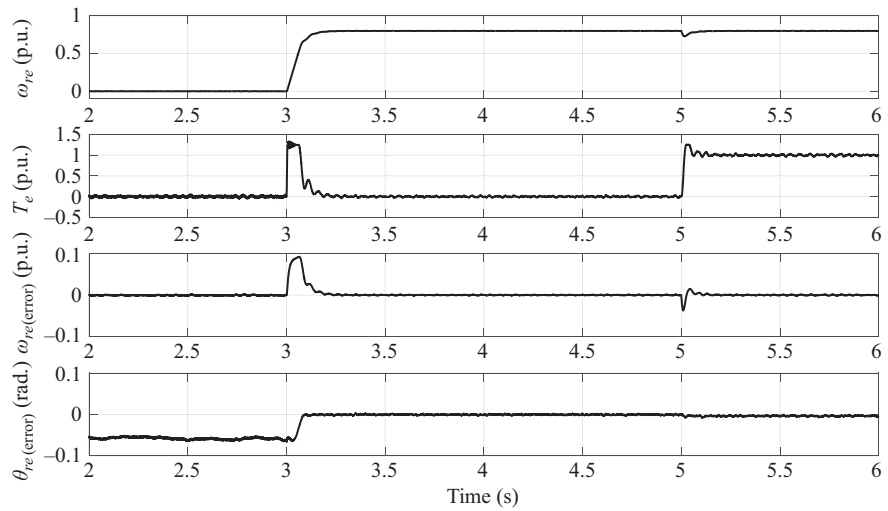


Figure 14.14 Performance of the sensorless PMSM drive with the combined HF signal injection and closed-loop speed non-adaptive observer due to acceleration from standstill to +0.8 p.u. and subsequent rated load torque disturbance. The first subplot shows the motor speed while the second subplot illustrates the developed torque. The third and fourth subplots depict the speed and position estimation errors, respectively

On the other hand, the performance during speed reversal from +0.01 p.u. to −0.01 p.u. at $t = 4$s while driving rated load torque is displayed in Figure 14.13. The drive is also stable during the motoring and regeneration modes and both the speed and position estimation errors are negligible. The crossover between the signal injection and model-based observers can be ascertained from Figure 14.14. In Figure 14.14, the motor is accelerated from standstill to 0.8 p.u. at $t = 3$s with no load. Full-load torque is then added to the shaft of the motor at $t = 5$s. The transition between both methods is smooth and the signal injection is disabled at higher speeds. This is evidenced by the reduction in HF torque ripples at higher speeds. In any case, the stability of the drive is maintained at both low and high speeds with the position estimation error kept within 0.1 rad. Speed estimation error is present during the transients due to the lag effect of the speed filter but quickly converges to zero in steady state.

14.7 Current slope measurement method

In vector-controlled PMSM drives, SVM is the most commonly used PWM method to synthesise the reference voltage vector. In this approach, the weighted sum of two active voltage vectors and one zero voltage vector over one switching period generates the reference voltage vector. Figure 14.15 illustrates an example of the PWM signals for the power switches of phases *a*, *b* and *c* of the inverter during one switching cycle. If the current slope technique is used in conjunction with SVM for sensorless control, it is imperative that the current slope is measured during the application of two distinct voltage vectors within one switching interval, preferably during one active and the zero voltage vector.

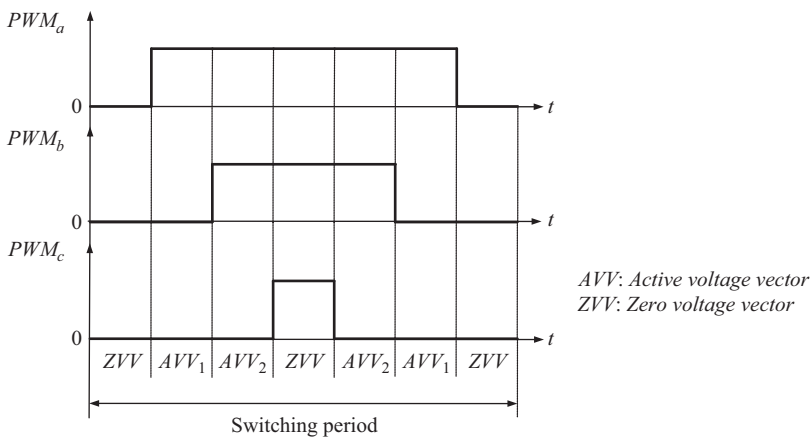


Figure 14.15 Example of the PWM signals for the power switches of phases a, b and c of the inverter under SVM during one switching cycle

Assuming such a method is adopted, according to (14.3), during the application of the active voltage vector $\boldsymbol{v} = \boldsymbol{v_s} = \begin{pmatrix} v_\alpha \\ v_\beta \end{pmatrix}$,

$$\begin{pmatrix} v_\alpha \\ v_\beta \end{pmatrix} = \frac{d}{dt}\begin{pmatrix} L_\Sigma + L_\Delta \cos 2\theta_{re} & L_\Delta \sin 2\theta_{re} \\ L_\Delta \sin 2\theta_{re} & L_\Sigma - L_\Delta \cos 2\theta_{re} \end{pmatrix}\begin{pmatrix} i_\alpha \\ i_\beta \end{pmatrix}\Bigg|_{\boldsymbol{v}=\boldsymbol{v_s}} - R_s\begin{pmatrix} i_\alpha \\ i_\beta \end{pmatrix} + \omega_{re}\lambda_f\begin{pmatrix} -\sin\theta_{re} \\ \cos\theta_{re} \end{pmatrix} \tag{14.64}$$

On the other hand, during the application of the zero vector $\boldsymbol{v} = \boldsymbol{0} = \begin{pmatrix} 0 \\ 0 \end{pmatrix}$, (14.3) can be rewritten as

$$\begin{pmatrix} 0 \\ 0 \end{pmatrix} = \frac{d}{dt}\begin{pmatrix} L_\Sigma + L_\Delta \cos 2\theta_{re} & L_\Delta \sin 2\theta_{re} \\ L_\Delta \sin 2\theta_{re} & L_\Sigma - L_\Delta \cos 2\theta_{re} \end{pmatrix}\begin{pmatrix} i_\alpha \\ i_\beta \end{pmatrix}\Bigg|_{\boldsymbol{v}=\boldsymbol{0}} - R_s\begin{pmatrix} i_\alpha \\ i_\beta \end{pmatrix} + \omega_{re}\lambda_f\begin{pmatrix} -\sin\theta_{re} \\ \cos\theta_{re} \end{pmatrix} \tag{14.65}$$

Assuming that the rotor position θ_{re} remains constant during one sampling interval, subtracting (14.65) from (14.64) yields

$$\begin{pmatrix} v_\alpha \\ v_\beta \end{pmatrix} = \begin{pmatrix} L_\Sigma + L_\Delta \cos 2\theta_{re} & L_\Delta \sin 2\theta_{re} \\ L_\Delta \sin 2\theta_{re} & L_\Sigma - L_\Delta \cos 2\theta_{re} \end{pmatrix}\left(\begin{pmatrix} \frac{di_\alpha}{dt} \\ \frac{di_\beta}{dt} \end{pmatrix}\Bigg|_{v=v_s} - \begin{pmatrix} \frac{di_\alpha}{dt} \\ \frac{di_\beta}{dt} \end{pmatrix}\Bigg|_{v=0}\right) \tag{14.66}$$

where $\begin{pmatrix} \frac{di_\alpha}{dt} \\ \frac{di_\beta}{dt} \end{pmatrix}\Big|_{v=v_s}$ and $\begin{pmatrix} \frac{di_\alpha}{dt} \\ \frac{di_\beta}{dt} \end{pmatrix}\Big|_{v=0}$ are the α-β axes stator current slopes during the active and zero voltage vectors, respectively. According to (14.66), by measuring the slope of the α-β axes stator currents alongside the applied voltage vector within the control cycle, the rotor position can be derived using the recursive least squares (RLS) algorithm. The first row of (14.66) can be alternatively expressed as

$$y = \boldsymbol{A}\boldsymbol{x} \tag{14.67}$$

where

$$y = v_\alpha$$
$$\boldsymbol{A} = \begin{pmatrix} L_\Sigma + L_\Delta \cos 2\theta_{re} & L_\Delta \sin 2\theta_{re} \end{pmatrix}$$
$$\boldsymbol{x} = \left(\begin{pmatrix} \frac{di_\alpha}{dt} \\ \frac{di_\beta}{dt} \end{pmatrix}\Bigg|_{v=v_s} - \begin{pmatrix} \frac{di_\alpha}{dt} \\ \frac{di_\beta}{dt} \end{pmatrix}\Bigg|_{v=0}\right)$$

The coefficients of vector $\boldsymbol{A}$ contains the rotor position information and can be estimated using the RLS algorithm:

$$\boldsymbol{A}(k) = \boldsymbol{A}(k-1) + \frac{\boldsymbol{P}(k-1)\boldsymbol{x}(k-1)}{\lambda + \boldsymbol{x}^{\boldsymbol{T}}(k)\boldsymbol{P}(k-1)\boldsymbol{x}(k)} \times \left(y(k) - \boldsymbol{x}^{\boldsymbol{T}}(k)\boldsymbol{A}(k-1)\right) \tag{14.68}$$

where $\lambda < 1$ is the forgetting factor and k and $k-1$ denote the current and previous control cycles, respectively. $\boldsymbol{P}$ is called the covariance matrix given by

$$\boldsymbol{P}(k) = \frac{1}{\lambda}\left(\boldsymbol{P}(k-1) - \frac{\boldsymbol{P}(k-1)\boldsymbol{x}(k)\boldsymbol{x}^{\boldsymbol{T}}(k)\boldsymbol{P}(k-1)}{\lambda + \boldsymbol{x}^{\boldsymbol{T}}(k)\boldsymbol{P}(k-1)\boldsymbol{x}(k)}\right) \tag{14.69}$$

Since the applied voltage vector y is always known at every time instant and the current slopes $\boldsymbol{x}$ are measurable, the RLS algorithm can be applied in real time to continuously update the coefficients of vector $\boldsymbol{A}$. The same algorithm ought to be applied to the second row of (14.66). Subsequently, the rotor position $\hat{\theta}_{re}$ can be derived from

$$\hat{\theta}_{re} = \frac{1}{2}\tan^{-1}\left(\frac{A_{12} + A_{21}}{A_{11} - A_{22}}\right) \tag{14.70}$$

where A_{11} and A_{12} are the coefficients of vector $\boldsymbol{A}$ found from the RLS algorithm described above. A_{21} and A_{22} are the coefficients of vector $\boldsymbol{A}$ when RLS is applied to the second row of (14.66). It is paramount in this method that proper synchronisation exists between the application of the voltage vector and the measurement of the current slope. In real time, the current slope is obtained by measuring two current samples and calculating the first-order difference when a certain voltage vector is applied, as shown in Figure 14.16.

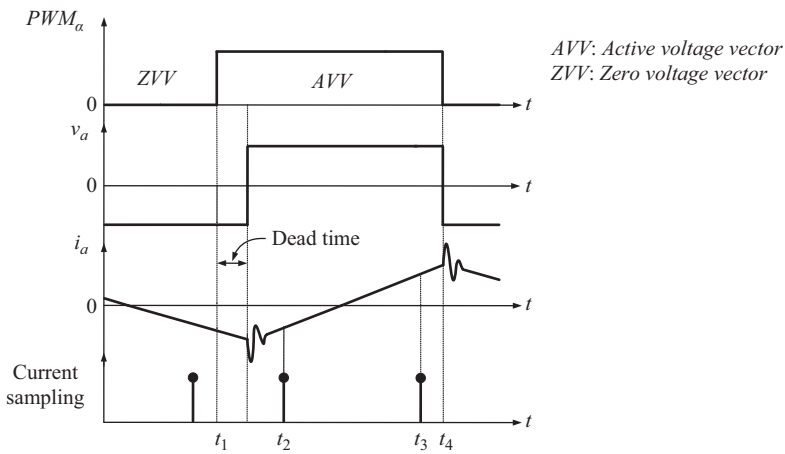


Figure 14.16 Current slope measurement technique

The PWM signal triggers the application of the active voltage vector at time $t = t_1$. The current i_a of phase-a is measured at time $t = t_2$ after a pre-programmed time delay. This time delay must be larger than the sum of the dead time and current transient due the switching action of the inverter, as shown in Figure 14.16. Another current sample is taken at time $t = t_3$ just before the PWM signal goes low at time $t = t_4$. This current measurement instant t_3 can be also programmed in the controller since the falling edge instant t_4 of the PWM signal is always known in advance. The current slope $\frac{di_a}{dt}$ of phase a is then calculated as a first-order difference:

$$\frac{di_a}{dt} \approx \frac{i_a(t_3) - i_a(t_2)}{t_3 - t_2} \tag{14.71}$$

This current measurement method is repeated for phases b and c to obtain the current slopes of those two phases. The α-β axes components of the current slope due to the active voltage vector are then given by Clarke's Transform:

$$\left.\begin{pmatrix} \frac{di_\alpha}{dt} \\ \frac{di_\beta}{dt} \end{pmatrix}\right|_{v=v_s} = \begin{pmatrix} 1 & 0 & 0 \\ 0 & \frac{1}{\sqrt{3}} & -\frac{1}{\sqrt{3}} \end{pmatrix} \left.\begin{pmatrix} \frac{di_a}{dt} \\ \frac{di_b}{dt} \\ \frac{di_c}{dt} \end{pmatrix}\right|_{v=v_s} \tag{14.72}$$

where $\frac{di_b}{dt}$ and $\frac{di_c}{dt}$ are the current slopes of phases b and c, respectively. In the same manner, during the application of the zero voltage vector, the foregoing technique is identically applied to all three phases to obtain the current slopes. Akin to the HF signal injection method, the current slope approach can be merged with the closed-loop speed non-adaptive observer to attain sensorless control over a wide speed range. The block diagram of the resultant observer is depicted in Figure 14.17.

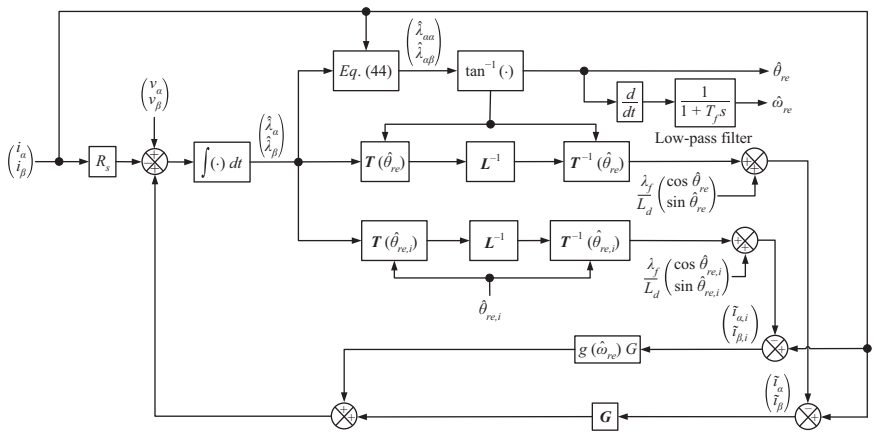


Figure 14.17 Combined current slope measurement and closed-loop speed non-adaptive observer

The current slope method provides the additional current error feedback term $\tilde{i}_{\alpha,i}$, $\tilde{i}_{\beta,i}$ to stabilise the observer at low speeds:

$$\begin{pmatrix} \hat{i}_{\alpha,i} \\ \hat{i}_{\beta,i} \end{pmatrix} = \boldsymbol{T}^{-1}(\hat{\theta}_{re,i}) \begin{pmatrix} \frac{1}{L_d} & 0 \\ 0 & \frac{1}{L_q} \end{pmatrix} \boldsymbol{T}(\hat{\theta}_{re,i}) \begin{pmatrix} \hat{\lambda}_{\alpha} \\ \hat{\lambda}_{\beta} \end{pmatrix} + \frac{\lambda_f}{L_d} \begin{pmatrix} \cos\hat{\theta}_{re,i} \\ \sin\hat{\theta}_{re,i} \end{pmatrix} \tag{14.73}$$

$$\begin{pmatrix} \tilde{i}_{\alpha,i} \\ \tilde{i}_{\beta,i} \end{pmatrix} = \begin{pmatrix} i_{\alpha} \\ i_{\beta} \end{pmatrix} - \begin{pmatrix} \tilde{i}_{\alpha,i} \\ \tilde{i}_{\beta,i} \end{pmatrix} \tag{14.74}$$

where $\hat{i}_{\alpha,i}$, $\hat{i}_{\beta,i}$ is the estimated stator current using the current slope method while $\hat{\theta}_{re,i}$ is the estimated rotor position found in (14.70). The current error in (14.74) is fed back to the stator flux observer through the same speed-dependent observer gain $\boldsymbol{G}_{\boldsymbol{\omega}}$ defined in (14.61).

The performance of the sensorless PMSM drive with the combined current slope measurement and closed-loop speed non-adaptive observer in simulation are shown in Figures 14.18–14.20. Figure 14.18 illustrates the standstill operation with

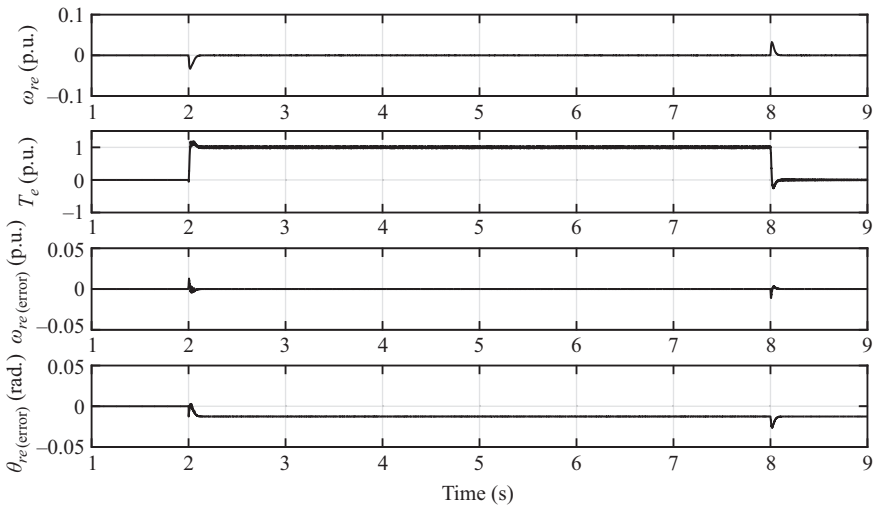


Figure 14.18 Performance of the sensorless PMSM drive with the combined current slope measurement and closed-loop speed non-adaptive observer at standstill due to rated load torque disturbance. The first subplot shows the motor speed while the second subplot illustrates the developed torque. The third and fourth subplots depict the speed and position estimation errors, respectively

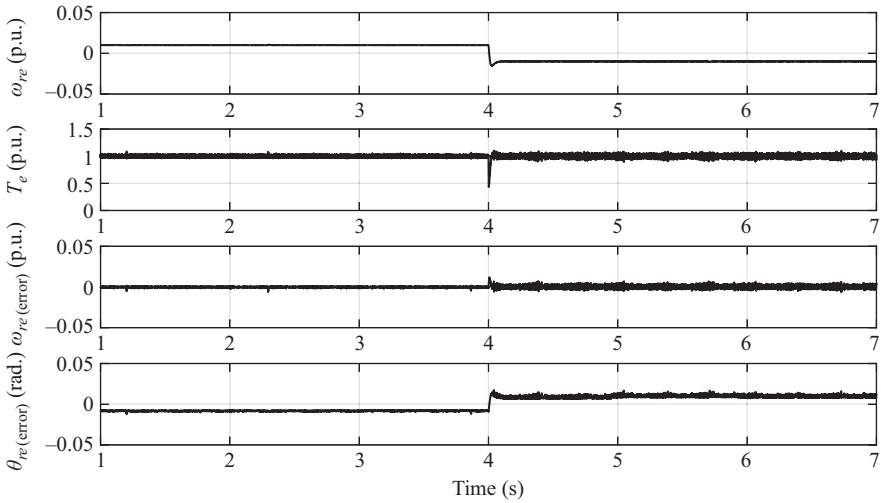


Figure 14.19 Performance of the sensorless PMSM drive with the combined current slope measurement and closed-loop speed non-adaptive observer due to speed reversal from +0.01 p.u. to −0.01 p.u. with rated load torque. The first subplot shows the motor speed while the second subplot illustrates the developed torque. The third and fourth subplots depict the speed and position estimation errors, respectively

rated load torque disturbances. Full load is added to the shaft of the motor at $t = 2s$ and subsequently removed at $t = 8s$. The stability of the drive is maintained without any speed estimation error except during the load transients. Furthermore, the position estimation error is less than 0.02 rad. both during steady-state and transient conditions.

The performance during full-load speed reversal from +0.01 p.u. to −0.01 p.u. at $t = 4$s is shown in Figure 14.19. The drive is also stable during the motoring and regeneration modes and both the speed and position estimation errors are negligible. The motor is accelerated from standstill to +0.8 p.u. at $t = 3$s with no-load in Figure 14.20 to examine the efficacy of the crossover between the current slope measurement, and model-based observer methods can be ascertained from Figure 14.14. The additional feedback from the former is included at low speeds but is disabled at higher speeds. Full-load disturbance is subsequently added to the shaft of the motor at $t = 5$s. In any case, the stability of the drive is maintained throughout with negligible position estimation error. The speed filter introduces speed estimation errors during the speed and load transients but quickly converges to zero in steady state.

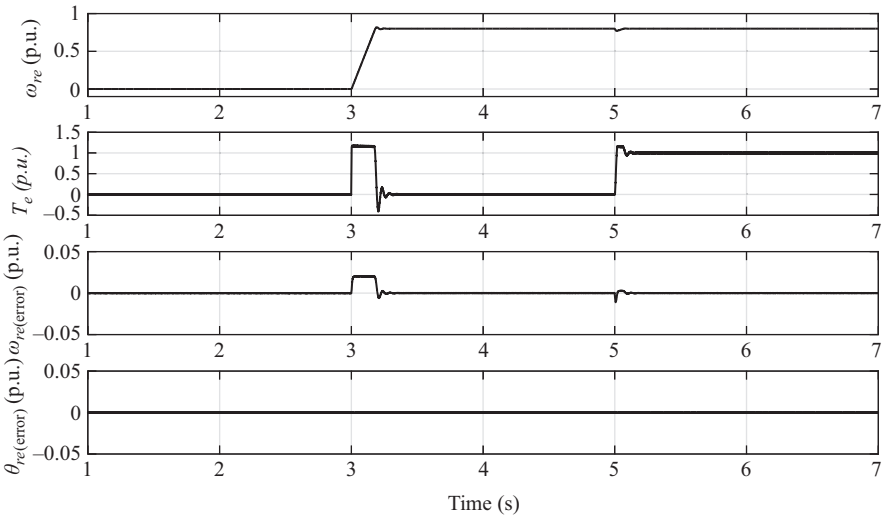


Figure 14.20 Performance of the sensorless PMSM drive with the combined current slope measurement and closed-loop speed non-adaptive observer due to acceleration from standstill to +0.8 p.u. and subsequent rated load torque disturbance. The first subplot shows the motor speed while the second subplot illustrates the developed torque. The third and fourth subplots depict the speed and position estimation errors, respectively

14.8 Summary

This chapter presented several key rotor position and speed estimation methods used in sensorless PMSM drives. Although many estimation techniques exist, they can always be divided into either the model-based and non-model-based approach. The former can be configured in either open loop or closed loop. The open-loop method offers the benefit of being straightforward. The stator flux linkage is simply found by integrating the back EMF of the PMSM, and subsequently, the rotor position is derived from both the stator flux linkage and measured stator currents. Despite its simplicity, it is extremely sensitive to machine parameter variations, current and voltage measurement errors and inverter non-linearities. As such, its accuracy degrades significantly, leading to loss of drive stability in the low-speed region. Its performance can be improved somewhat by incorporating current estimation error feedback, yielding the closed-loop observer. Two classes of closed-loop observers were presented – the full-order speed-adaptive observer and the speed non-adaptive observer. Both observers are more mathematically complex than their open-loop counterpart but provide much improved performance in the low-speed region. Since they still use the mathematical model of the PMSM,

parameter variations, measurement errors and inverter non-linearities still limit their performance. Therefore, they cannot be expected to deliver torque controllability down to zero speed. To circumvent this problem, non-linear effects such as anisotropy in the interior PMSM and magnetic saturation in the surface mounted PMSM can be exploited to provide enhanced rotor position estimation accuracy at very low speeds including standstill. Two methods that take advantage of these properties are the HF signal injection and current slope measurement. In the former, a test voltage signal with a frequency significantly higher than the fundamental frequency is injected into the windings of the PMSM and the resultant current oscillations are measured. It was shown that the rotor position information embedded in the HF currents can be extracted by the application of signal processing techniques. Alternatively, the current slopes can be measured using high bandwidth current sensors to derive the rotor position. It was also proven that the current slopes contain the rotor position information and by using system identification techniques such as the RLS algorithm, the rotor position and, hence, the speed can be estimated. Both methods provide stable full torque operation down to zero speed, but not without their own issues. The signal injection technique induces unwanted torque ripples and audible noise in the system while the current slope measurement approach demands delicate synchronisation between the PWM signals and current measurement. Nevertheless, both these methods have been combined with the closed-loop speed non-adaptive observer to achieve sensorless PMSM drive operation with complete torque controllability over a wide speed range. The simulation results presented prove the veracity of the presented techniques.

List of symbols

υ_d, υ_q	d-q axes components of the stator voltage
i_d , i_q	d-q axes components of the stator current
L_d, L_q	d-q axes inductance
R_s	Stator resistance
$_f$	Permanent magnet flux linkage
ω_{re}	Rotor speed
$_{re}$	Rotor position
$_a$	Active flux linkage
λ_α,λ_β	α-β axes components of the stator flux linkage
ω_T	Rotor speed

Glossary of terms

Sensorless control	The control of a parameter (current, voltage or speed) without using any physical sensor
Estimator	It is another name of the observer

References

[1] L. Tang, L. Zhong, M.F. Rahman and Y. Hu, 'A novel direct torque control for interior permanent magnet synchronous machine drive system with low ripple in flux and torque and fixed switching frequency', *IEEE Trans. Power Electron.*, vol. 19, pp. 346–354, 2004.

[2] M. Mengoni, L. Zarri, A. Tani, G. Serra and D. Casadei, 'Stator flux vector control of induction motor drive in the field weakening region', *IEEE Trans. Power Electron.*, vol. 23, 2008.

[3] D. Casadei, G. Serra, A. Stefani, A. Tani and L. Zarri, 'DTC drives for wide speed range applications using a robust flux-weakening algorithm', *IEEE Trans. Ind. Electron.*, vol. 54, pp. 2451–2461, 2007.

[4] B. Nahid-Mobarakeh, F. Meibody-Tabar and F. Sargos, 'Back EMF estimation-based sensorless control of PMSM: Robustness with respect to measurement errors and inverter irregularities', *IEEE Trans. Ind. Applicat.*, vol. 43, pp. 485–494, 2007.

[5] M. Rashed, P.F.A. MacConnell, A.F. Stronach and P. Acarnley, 'Sensorless indirect-rotor-field-orientation speed control of a permanent magnet synchronous motor with stator resistance estimation', *IEEE Trans. Ind. Electron.*, vol. 54, pp. 1664–1675, 2007.

[6] A. Piippo, M. Hinkkanen and J. Luomi, 'Analysis of adaptive observer for sensorless control of interior permanent magnet synchronous motors', *IEEE Trans. Ind. Electron.*, vol. 55, pp. 570–576, 2008.

[7] B.-H. Bae, S.-K. Sul, J.-H. Kwon and J.-S. Byeon, 'Implementation of sensorless vector control for super-high-speed PMSM of turbo-compressor', *IEEE Trans. Ind. Applicat*., vol. 39, pp. 811–818, 2003.

[8] Z. Xu and M.F. Rahman, 'Direct torque and flux regulation of an IPM synchronous motor drive using variable control approach', *IEEE Trans. Power. Electron*., vol. 22, pp. 2487–2498, 2007.

[9] Z. Xu and M.F. Rahman, 'An adaptive sliding stator flux observer for a direct torque controlled IPM synchronous motor drive', *IEEE Trans. Ind. Electron.*, vol. 54, pp. 2398–2406, 2007.

[10] G. Foo and M.F. Rahman, 'Sensorless direct torque and flux controlled IPM synchronous motor drive at very low speed without signal injection', *IEEE Trans. on Ind*. *Electron*, vol. 57, no. 1, pp. 395–403, 2010.

[11] Z. Xu and M.F. Rahman, 'Comparison of a sliding observer and a Kalman filter for direct-torque controlled IPM synchronous motor drives', *IEEE Trans Ind. Electron.*, vol. 59, pp. 4179–4188, 2012.

[12] S. Bolognani, R. Oboe and M. Zigliotto, 'Sensorless full digital PMSM drive with EKF estimation of speed and position', *IEEE Trans. Ind. Electron.*, vol. 46, pp. 184–191, 1999.

[13] R. Dhaouadi, N. Mohan and L. Norum, 'Design and implementation of an Extended Kalman filter for state estimation of a permanent magnet synchronous motor', *IEEE Trans. Power. Electron.*, vol. 6, pp. 491–497, 1991.

[14] G.-D. Andreescu, C.I. Pitic, F. Blaabjerg and I. Boldea, 'Combined flux observer with signal injection enhancement for wide speed range sensorless direct torque control of IPMSM drives', *IEEE Trans. Energy Conv.*, vol. 23, pp 393–402, 2008.

[15] D. Raca, P. Garcia, D.D. Reigosa, F. Briz and R.D. Lorenz, 'Carrier-signal selection for sensorless control of PM synchronous machines at zero and very low speeds', *IEEE Trans. Ind. Applicat.*, vol. 46, pp. 167–178, 2010.

[16] A. Piippo, M. Hinkkanen and J. Luomi, 'Adaptation of motor parameters in sensorless PMSM drives', *IEEE Trans. Ind. Applicat.*, vol.45, pp. 203–212, 2009.

[17] C. Silva, G.M. Asher and M. Summer, 'Hybrid rotor position observer for wide speed-range sensorless PM motor drives including zero speed', *IEEE Trans. Ind. Electron.*, vol. 53, pp. 373–378, 2006.

[18] S. Kim, J.-I. Ha and S.-K. Sul, 'PWM switching frequency signal injection sensorless method in PMSM', *IEEE Trans. Ind. Applicat*., vol. 48, pp. 1576–1587, 2012.

[19] D. Kim, Y.-Cheol Kwon, S.-K. Sul, J.-H. Kim and R.S. Yu, 'Suppression of injection voltage disturbance for high-frequency square-wave injection sensorless drive with regulation of induced high-frequency current ripple', *IEEE Trans. Ind. Applicat*., vol. 52, pp. 302–312, 2016.

[20] J.-L. Shi, T.-H. Liu and Y.-C. Chang, 'Position control of an interior permanent-magnet synchronous motor without using a shaft position sensor', *IEEE Trans. Ind. Electron.*, vol. 54, pp. 1989–2000, 2007.

[21] R.M.- Caporal, E.B. Huerta, M.A. Arjona and C. Hernandez, 'Sensorless predictive DTC of a surface-mounted permanent-magnet synchronous machine based on its magnetic anisotropy', *IEEE Trans. Ind. Electron.*, vol. 99, pp. 1.

[22] M. X. Bui, D.Q. Guan, D. Xiao and M.F. Rahman, 'A modified sensorless control scheme for interior permanent magnet synchronous motor over zero to rated speed range using current derivative measurements', *IEEE Trans. Ind. Electron.*, vol. 99, pp. 1–1, 2018. (Early Access)

[23] M. F. Rahman, M.E. Haque, L. Tang and L. Zhong, 'Problems associated with the direct torque control of an interior permanent magnet synchronous motor drive and their remedies', *IEEE Trans. Ind. Electron.*, vol. 51, pp.799–809, 2004.

[24] J. Holtz and J. Quan, 'Sensorless vector control of induction motors at very low speed using a nonlinear inverter model and parameter identification', *IEEE Trans. Ind. Applicat*., vol. 38, pp. 1087–1095, 2002.

[25] J. Hu and B. Wu, 'New integration algorithms for estimating motor flux over a wide speed range', *IEEE Trans. Power Electron*., vol. 13, pp. 969–977, 1998.

[26] J.-W. Choi and S.-K. Sul, 'Inverter output voltage synthesis using novel dead-time compensation', *IEEE Trans. Power Electron*., vol. 11, pp. 221–227, 1996.

[27] I. Boldea, M. C. Paicu and G.-D. Andreescu, 'Active flux concept for motion sensorless unified AC drives', *IEEE Trans. Power Electron*, vol. 23, pp. 2612–2618, 2008.

[28] I. Boldea, M. C. Paicu, G.-D. Andreescu and F. Blaabjerg, 'Active flux DTFC-SVM Sensorless Control of IPMSM', *IEEE Trans. Energy Conv.*, vol. 24, pp. 314–322, 2009.

[29] S.-C. Agarlita, I. Boldea and F. Blaabjerg, 'High-frequency-injection-assisted "Active-flux" based sensorless vector control of reluctance synchronous motors, with experiments from zero speed', *IEEE Trans. Ind. Applicat*., vol. 48, pp. 1931–1939, 2012.

[30] C. Lascu, I. Boldea and F. Blaabjerg, 'Comparative study of adaptive and inherently sensorless observers for variable-speed induction motor drives', *IEEE Trans. Ind. Electron.*, vol. 53, pp. 57–65, 2006.

Chapter 15

Predictive torque control of induction motor drive

Muhammed Habibullah[1], Dan Xiao[2], Muhammed Fazlur Rahman[2], and Dylan Dah-Chuan Lu[3]

15.1 Introduction

Model predictive control (MPC) was first introduced in 1960s and received industrial acceptance in the late 1970s [1]. Since then, MPC has become popular for different industrial applications [2–4], especially in the chemical industry, where desired control objectives do not change frequently. This means that the time constant in chemical processes is long enough to undertake the required calculations online and to update the control actions. At that time, MPC was not suitable for dynamic adaptive systems, such as power electronics applications, where the desired control objectives change frequently and hence require a far shorter response time. This is because the speed of available digital signal processors (DSPs) was not high enough to accomplish the necessary calculations within the short control duration. Later, due to the continuous development of DSPs and advancement of semiconductor switches, MPC has spread out in different branches of power electronics, such as converter technologies, energy storage and conversion systems, smart grid, renewable energy conversion and motor drives. MPC for motor drives has drawn much attention from the research community in the last few years [5–17]. The controller can be considered as a well-established technology in the research and development stages [18]. Further, research and development efforts are still required to make this technology available in the industrial and commercial level [18,19].

MPC meets the requirements of modern control systems, such as using plant model and digital control platforms, and allows consideration of many system constraints and restrictions [14]. There are two types of MPC [8,12]: continuous control set MPC (CCS-MPC) and finite control set MPC (FCS-MPC). In CCS-MPC, the controller generates a continuous output for a modulator, and the

[1]Khulna University of Engineering & Technology, Bangladesh
[2]School of Electrical Engineering and Telecommunications, University of New South Wales, Australia
[3]Department of Electrical Engineering, University of Technology Sydney, Australia

modulator generates the switching signals for the inverter to generate the required voltage. Due to the presence of the modulator, the controller yields a constant switching frequency. Conversely, in FCS-MPC, the finite number of control actions available in the system – inverter switching states for motor drives – is evaluated against the desired control objectives. The outputs of the controller are discrete and are directly used to switch the power switches *on/off* in the inverter. The controller yields a variable switching frequency due to the absence of a modulator.

The finite-state predictive torque control (FS-PTC) of motor drives is an FCS-MPC strategy [15,20–24]. In FS-PTC, torque and stator flux are predicted for the finite number of admissible switching states of a voltage source inverter (VSI). The switching state that minimises torque and flux ripple most is chosen as the optimal switching state, and is obtained by actuating a predefined cost function. Several targets, variables and constraints with appropriate weighting factors can be included in the cost function and controlled simultaneously. The selected optimum switching state is applied directly to the inverter to produce the voltage vector to be applied to the motor terminals in the next sampling instant, without requiring an intermediate modulation stage [15]. Another important advantage of PTC is that it has no inner current control loop. As a result, the controller yields fast dynamic response. The advantages of the PTC may thus be summarised as follows:

1. The concept is simple and intuitive.
2. The algorithm is easy to implement.
3. It facilitates the inclusion of system nonlinearities and constraints.
4. Multivariable cases can be controlled simultaneously.
5. It meets the requirements of modern control systems, such as using plant model and digital control platforms.
6. The control algorithm can be modified easily for various applications.

15.2 Comparison between the PTC and classical control strategies (FOC and DTC)

There are two well-established high performance control strategies that exist for AC drives: field orientation control (FOC) [25] and direct torque control (DTC) [26]. FOC was first introduced in the 1970s and it brought a revolution in AC motor control [25]. DTC was introduced in the 1980s and offered a simpler control structure than FOC [26]. Both controllers have been accepted widely in different industrial applications, pushing traditional DC motors towards obsolescence. In the FOC, the stator currents are decomposed into two components: *d*-axis component for flux and *q*-axis component for torque, to realise the behaviour of a separately excited DC machine. Both currents are regulated by two linear proportional-integral (PI) controllers in the synchronously rotating reference frame. A decoupled control of torque and flux is achieved by aligning the *d*-axis with the rotor flux position. Finally, the gate pulses of the inverter are generated using space vector modulation (SVM) to produce the desired voltage vector. The FOC strategy provides good dynamic torque and flux responses with constant switching frequency

Table 15.1 Comparison among FOC, DTC and PTC strategies

Index	FOC	DTC	PTC
Structural complexity	Higher	Lower	Lower
Axis transformation	Yes	No	No
Modulator	Yes	No	No
Parameter sensitivity	Higher	Lower	Higher
Position sensor	Yes	No	No
Switching frequency	Fixed	Variable	Variable
Inclusion of system nonlinearity	Hard	Hard	Easy
Dynamic response	Slower	Faster	Faster
Torque and flux ripple	Lower	Higher	Lower
Current THD	Lower	Higher	Higher
Computational complexity	Lower	Lower	Higher

[27,28]. However, the control structure is complex because of two PI regulators, SVM blocks and axis transformation which requires a high-resolution shaft-mounted speed sensor. Moreover, the robustness of the controller has significant parameter dependency. In contrast, the DTC structure is simpler as it does not have any axis transformation (between the synchronous and stationary frames) and modulation blocks. This control strategy has emerged as an alternative to the FOC strategy [29]. It uses a predefined switching table based on the stator flux position and error signs of torque and flux to select the most appropriate voltage vector for the inverter. The controller provides quick dynamic response. However, the DTC structure includes two hysteresis blocks for controlling torque and flux, which produces more ripple in the torque and flux and variable switching frequency [29]. Research continues on the DTC strategy to reduce these drawbacks and to ensure energy efficient operation of motor drives [30]. On the other hand, PTC has neither modulation nor hysteresis blocks, and is thus a simpler structure compared with the FOC and DTC. The comparison between the classical control and PTC strategies is summarised in Table 15.1.

15.3 PTC System modelling

15.3.1 State-space representation of three-phase systems

State-space representation makes an AC circuit simple to represent and easy to understand and analyse. This study considers a three-phase squirrel-cage induction motor (IM). The IM is supplied from a three-phase AC source. It is well known that the three phases (*a*-*b*-*c*) are located 120° apart in space, as shown in Figure 15.1. They are linearly dependent on each other, which complicates the system model. To simplify the notation of three-phase electrical variables, such as voltage, current and flux, the variables can be modelled adequately using a two-axis reference frame. The two-axis representation of the three-phase system is called 'state-space representation'. This two-axis reference frame may be stationary (α-β) or synchronously rotating

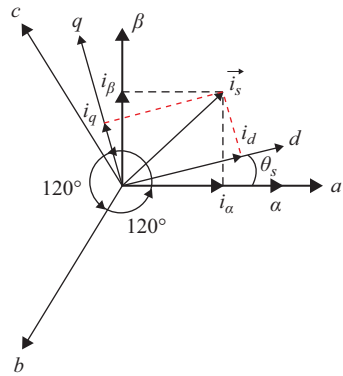


Figure 15.1 State-space two-axis (α-β and d-q) representation of three-phase (a-b-c) systems

(*d-q*), as shown in Figure 15.1. For the state-space representation, the components of a particular variable along *a-b-c* coordinates are projected on *α-β* or *d-q* coordinates. The two coordinates in each reference frame are mutually perpendicular to each other, and linearly independent. This independence makes it possible to control both the flux and torque of an AC machine independently, similar to a separately excited DC machine.

Using the current as an example, the transformation of the *a-b-c* frame to *α-β* frame, which is known as Clarke transformation – is expressed in matrix form as

$$\begin{bmatrix} i_\alpha \\ i_\beta \end{bmatrix} = \begin{bmatrix} 2/3 & -1/3 & -1/3 \\ 0 & \sqrt{3}/3 & \sqrt{3}/3 \end{bmatrix} \begin{bmatrix} i_a \\ i_b \\ i_c \end{bmatrix}$$

Sometimes it is necessary to transform *α-β* frame into a *d-q* frame, especially in vector control (i.e. FOC) design for motor drives. The transformation is called as Park transformation and can be expressed as

$$\begin{bmatrix} i_d \\ i_q \end{bmatrix} = \begin{bmatrix} \cos\theta_s & \sin\theta_s \\ -\sin\theta_s & \cos\theta_s \end{bmatrix} \begin{bmatrix} i_\alpha \\ i_\beta \end{bmatrix}$$

where θ_s is the angle between the *α-β* and *d-q* reference frames, as shown in Figure 15.1. Direct transformation from the *a-b-c* frame to the *d-q* frame (or vice versa) is also used for dynamic modelling of a three-phase system [31].

The current components of i_α and i_β are sinusoidal, as the current vector $\boldsymbol{i}_s$ rotates at a constant speed with respect to the *α-β* frame. In contrast, the i_d and i_q components are normally constant (DC) or piece-wise constant, and are thus linearised. The aforementioned two transformations are equally applicable for voltage and flux, and the transformations are reversible.

The state-space representation of the IM variables in both the α-β and d-q reference frames is as follows:

$$\begin{aligned}
&\text{stator voltage :} && \boldsymbol{v}_s = v_{sa} + jv_{s\beta},\ \boldsymbol{v}_s = v_{sd} + jv_{sq};\\
&\text{rotor voltage :} && \boldsymbol{v}_r = v_{ra} + jv_{r\beta},\ \boldsymbol{v}_r = v_{rd} + jv_{rq};\\
&\text{stator current :} && i_s = i_{sa} + ji_{s\beta}, \boldsymbol{i}_s = i_{sd} + ji_{sq};\\
&\text{rotor current :} && \boldsymbol{i}_r = i_{ra} + ji_{r\beta},\ \boldsymbol{i}_r = i_{rd} + ji_{rq};\\
&\text{stator flux :} && \boldsymbol{\psi}_s = \psi_{sa} + j\psi_{s\beta}, \boldsymbol{\psi}_s = \psi_{sd} + j\psi_{sq};\\
&\text{rotor flux :} && \boldsymbol{\psi}_r = \psi_{ra} + j\psi_{r\beta}, \boldsymbol{\psi}_r = \psi_{rd} + j\psi_{rq}
\end{aligned}$$

15.3.2 Modelling of the IM

The state-space model of a squirrel-cage IM in α-β reference frame can be described by (15.1)–(15.6):

$$\text{Stator voltage equation : } \boldsymbol{v_s} = R_s\boldsymbol{i}_s + \frac{d\boldsymbol{\psi}_s}{dt} \tag{15.1}$$

$$\text{Rotor voltage equation : } 0 = R_r\boldsymbol{i}_r + \frac{d\boldsymbol{\psi}_r}{dt} - j\omega_e\boldsymbol{\psi}_r \tag{15.2}$$

$$\text{Stator flux equation : } \boldsymbol{\psi}_s = L_s\boldsymbol{i}_s + L_m\boldsymbol{i}_r \tag{15.3}$$

$$\text{Rotor flux equation : } \boldsymbol{\psi}_r = L_m\boldsymbol{i}_s + L_r\boldsymbol{i}_r \tag{15.4}$$

$$\text{Electromagnetic torque equation : } T_e = 1.5pIm\left\{\boldsymbol{\psi}_s^*.\boldsymbol{i}_s\right\} \tag{15.5}$$

$$\text{Torque balance equation : } J\frac{d\omega_m}{dt} = T_e - T_l \tag{15.6}$$

where $\boldsymbol{v}_s$ is the stator voltage vector, $\boldsymbol{i}_s$ is the stator current vecto$_r$, $\boldsymbol{i}_r$ is the rotor current vector, $\boldsymbol{\psi}_s$ is the stator flux vector, $\boldsymbol{\psi}_r$ is the rotor flux vector, T_e is the electromagnetic torque, T_l is the load torque, ω_m is the rotor angular speed, ω_e is the rotor angular frequency and p is the number of pole pairs and the remaining parameters are the machine parameters.

The rotor angular frequency ω_e is related directly to the rotor angular speed ω_m by the number of pole pairs p as

$$\omega_e = p\omega_m \tag{15.7}$$

The stator voltage formula in (15.1) shows the relationship among the supplied voltage, stator ohmic drop and stator inductance drop. The inductance drop has two components: stator leakage-inductance drop and back EMF. If the operating speed

is not too low, the ohmic drop is negligible compared with the back EMF; thus, the stator flux is directly proportional to the supplied voltage. This assumption is generally used in the DTC strategy [24]. In this case, an ohmic drop equivalent voltage is injected to the controller at low speed for better accuracy of the controller. As the rotor of a squirrel-cage type is short-circuited itself, the applied voltage at the rotor side is zero, as shown in (15.2). The induced rotor voltage is proportional to the slip (relative velocity between stator flux and rotor speed). Thus, in normal operations under a certain frequency, the induced rotor voltage is maximum at zero speed (slip is equal to 1) and minimum at around synchronous speed (slip is close to 0). By replacing the variable $\boldsymbol{i}_r$ from (15.2) with the variables $\boldsymbol{\psi}_r$ and $\boldsymbol{i}_s$, the modified rotor voltage equation becomes

$$\frac{d\boldsymbol{\psi}_r}{dt} = R_r \frac{L_m}{L_r} \boldsymbol{i}_s - \left(\frac{R_r}{L_r} - j\omega_e \right) \boldsymbol{\psi}_r \tag{15.8}$$

Equation (15.8) is called the rotor current model of the IM, in which $\boldsymbol{i}_s$ and $\boldsymbol{\psi}_r$ are considered as state variables. Generally, the rotor current model is used to estimate the rotor flux. Using (15.3) and (15.4), a relationship is established between the stator and the rotor fluxes as

$$\widehat{\boldsymbol{\psi}}_s = \frac{L_m}{L_r} \widehat{\boldsymbol{\psi}}_r + \sigma L_s \boldsymbol{i_s} \tag{15.9}$$

where $\sigma = 1 - \frac{L_m^2}{L_s L_r}$ is the total leakage factor. Equation (15.9) is used to estimate the stator flux. The symbol '^' in (15.9) is used to indicate the estimated variable.

Some other parameters (not physical) are used frequently in machine modelling for compact expression. These are given in the following:

Rotor coupling factor : $k_r = L_m / L_r$

Equivalent resistance referred to stator : $R_\sigma = R_s + k_r^2 R_r$

Transient stator time constant : $\tau_\sigma = L_\sigma / R_\sigma$

Leakage inductance : $L_\sigma = \sigma L_s$

Rotor time constant : $\tau_r = L_r / R_r$

The electromagnetic torque developed by the motor is estimated using (15.5). The estimated torque quality is dependent directly on the stator current and stator flux and thus on the measurement and estimation, respectively. In PTC, predictions of both the stator flux and stator current are required to predict the torque. Equation (15.1) is employed for stator flux prediction. The stator current is predicted using the equivalent equation of the stator and rotor dynamics of a cage type IM [32]; the expression in compact form is

$$\frac{d\boldsymbol{i}_s}{dt} = -\frac{1}{\tau_\sigma} \boldsymbol{i_s} + \frac{1}{\tau_\sigma R_\sigma} \left\{ \left(\frac{k_r}{\tau_r} - j k_r \omega_e \right) \boldsymbol{\psi}_r + \boldsymbol{v_s} \right\} \tag{15.10}$$

The torque balance in (15.6) is useful for designing a speed controller for motor drives. If the load torque T_l connected with the motor changes, the controller should compensate for any effects on speed. The motor will then spin at the command speed.

15.3.3 Modelling of the inverter

In this study, a two-level VSI (2L-VSI) is considered to produce the necessary voltage vectors. The circuit topology of a 2L-VSI is shown in Figure 15.2. The inverter produces two different levels of voltage, $+V_{dc}$ or $-V_{dc}$, at the output terminals, so called 2L-VSI. The required switching state variables S_x for each phase $x = \{a, b, c\}$ are either logic '1' or '0'. The two switching signals in each phase are complementary. Hence, only one switching signal is generated by the controller. Another switching signal is generated by using logic inversion and dead-time generator circuits. However, because of simplicity, dead-time compensation is not considered in this study. All possible switching states S are shown in Table 15.2. The switching states, in terms of vector for three phases, can be expressed as

$$\boldsymbol{S} = \frac{2}{3}\left(S_a + \boldsymbol{a}S_b + \boldsymbol{a}^2 S_C\right) \tag{15.11}$$

where $\boldsymbol{a} = e^{j2\pi/3}$.

A 2L-VSI produces eight voltage vectors corresponding to eight different state vectors at the output terminals, as shown in Figure 15.3. The voltage vectors generated by the inverter can be defined by

$$\boldsymbol{v} = \frac{2}{3}\left(v_a + \boldsymbol{a}v_b + \boldsymbol{a}^2 v_C\right) \tag{15.12}$$

where v_a, v_b and v_c are phase voltages.

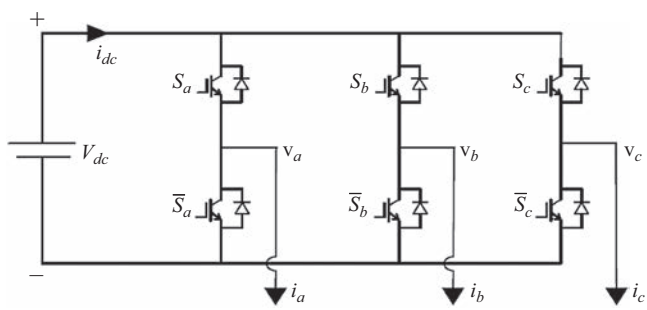


Figure 15.2 Circuit topology of a 2L-VSI showing positive convention for voltages and currents

Table 15.2 Voltage vectors of the 2L-VSI

v_n	$S = [S_a S_b S_c]$	$v = v_\alpha + jv_\beta$
v_0	0 0 0	0
v_1	1 0 0	$2/3V_{dc}$
v_2	1 1 0	$1/3V_{dc} + j\sqrt{3}/3V_{dc}$
v_3	0 1 0	$-1/3V_{dc} + j\sqrt{3}/3V_{dc}$
v_4	0 1 1	$-2/3V_{dc}$
v_5	0 0 1	$-1/3V_{dc} - j\sqrt{3}/3V_{dc}$
v_6	1 0 1	$1/3V_{dc} - j\sqrt{3}/3V_{dc}$
v_7	1 1 1	0

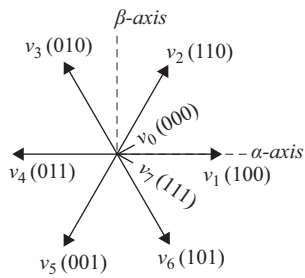


Figure 15.3 Space distribution of all admissible voltage vectors of the 2L-VSI

The voltage vectors can also be expressed in terms of state vectors and the DC-link voltage as

$$v = \boldsymbol{S} V_{dc} \tag{15.13}$$

The inverter is considered as a nonlinear discrete system. The discrete nonlinear voltage vectors, as shown in Table 15.2, are the only control actions in FCS-MPC to drive the motor. With the increase of the number of level of the output voltage of inverter, the discrete number of nonlinear voltage vector increases. For example, the number of control actions for three-level and five-level inverters are $3^3 = 27$ and $5^3 = 125$, respectively.

15.4 Basic structure and working principle of PTC

PTC explicitly uses the model of the inverter and motor. An FS-PTC model comprises two steps: prediction and cost function optimisation, as shown in Figure 15.4. However, the prediction requires a preliminary estimation step. Some variables unavailable (or not reliable) for measurement are estimated in the estimation step.

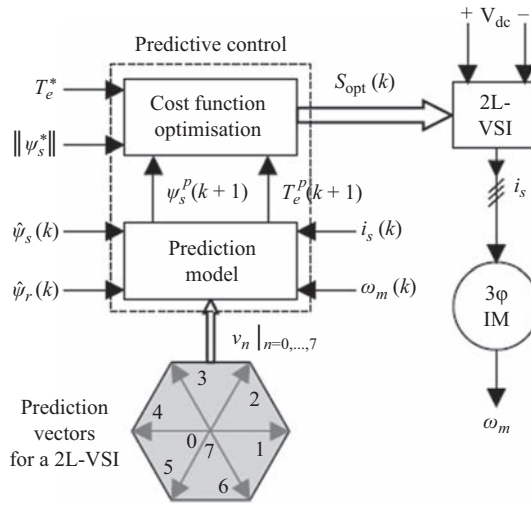


Figure 15.4 FS-PTC scheme for the 2L-VSI-fed IM drive

15.4.1 Estimation

In an FS-PTC system, estimations of stator flux $\widehat{\boldsymbol{\psi}}_s$ and rotor flux $\widehat{\boldsymbol{\psi}}_r$ are required based on the present measurements of stator current $\boldsymbol{i}_s$ and rotor speed ω_m. Conventionally, the rotor current model of the IM as shown in (15.8) is employed to estimate the rotor flux. Then, the simple relationship between the stator and rotor flux is used to estimate the stator flux. The execution frequency of the estimator is the same as that of the controller.

Different discretisation techniques are used in PTC to discretise the system. The most common discretisation techniques are Euler approximation and Taylor series expansion [33]. Incorrect model discretisation introduces errors and degrades the performance of the controller. Using the standard backward-Euler approximation, the estimations of rotor and stator flux in discrete form can be expressed as

$$\widehat{\boldsymbol{\psi}}_r(k) = \widehat{\boldsymbol{\psi}}_r(k-1) + T_s\left[R_r\frac{L_m}{L_r}\boldsymbol{i}_s(k) - \left(\frac{R_r}{L_r} - j\omega_e(k)\right)\boldsymbol{\psi}_r(k-1)\right] \tag{15.14}$$

$$\widehat{\boldsymbol{\psi}}_s(k) = \frac{L_m}{L_r}\widehat{\boldsymbol{\psi}}_r(k) + \sigma L_s\boldsymbol{i}_s(k) \tag{15.15}$$

The estimated electromagnetic torque can then be obtained as

$$\widehat{T}_e(k) = 1.5pIm\left\{\boldsymbol{\psi}_s^*(k).\boldsymbol{i}_s(k)\right\} \tag{15.16}$$

15.4.2 Prediction

The first step of predictive control is performed by predicting the stator flux and torque. PTC may be designed with short or long prediction horizon. Predicting of

control objectives for the next step is called short prediction horizon, and for beyond the next step is called long prediction horizon. MPC with long prediction horizon yields better system's performance and stability than short prediction horizon [34]. However, MPC with long prediction horizon is computationally expensive. Hence, PTC with short prediction horizon is considered in this study.

The selection of variables to be predicted is dependent on the desired control objectives. More numbers of variables mean that the controller requires more calculations. All possible voltage vectors $\{\boldsymbol{v}_0, \ldots, \boldsymbol{v}_7\}$ are evaluated to predict the desired objectives. The stator voltage model of the IM is generally used for stator flux prediction. Using the forward-Euler approximation, the voltage model in discrete time steps can be expressed as

$$\boldsymbol{\psi}_s^p(k+1) = \widehat{\boldsymbol{\psi}}_s(k) + T_s\boldsymbol{v}_s(k) - T_sR_s\boldsymbol{i}_s(k) \tag{15.17}$$

In order to predict the electromagnetic torque, the stator current is also predicted. Hence, the predictions of the stator current discretising (15.10) and then the torque can be expressed as

$$\boldsymbol{i}_s^p(k+1) = \left(1 - \frac{T_s}{\tau_\sigma}\right)\boldsymbol{i}_s(k) + \frac{T_s}{(\tau_\sigma + T_s)}\left[\frac{1}{R_\sigma}\left\{\left(\frac{k_r}{\tau_r} - jk_r\omega_e(k)\right)\widehat{\boldsymbol{\psi}}_r(k) + \boldsymbol{v}_s(k)\right\}\right] \tag{15.18}$$

$$T_e^p(k+1) = 1.5pIm\left\{\boldsymbol{\psi}_s^p(k+1)^*.\boldsymbol{i}_s^p(k+1)\right\} \tag{15.19}$$

15.4.3 Cost function optimisation

The predicted variables are evaluated by a predefined cost function. Generally, in FS-PTC, the cost function includes absolute values of torque error $\left(T_e^* - T_e^p\right)$ and flux error $\left(\left|\boldsymbol{\psi}_s^*\right| - \left|\boldsymbol{\psi}_s^p\right|\right)$. Hence, the cost function can be defined as

$$g = \left|T_e^*(k+1) - T_e^p(k+1)\right| + \lambda_f\left|\left|\boldsymbol{\psi}_s^*\right| - \left|\boldsymbol{\psi}_s^p(k+1)\right|\right| \tag{15.20}$$

where $T_e^*(k+1)$ is the reference torque and $T_e^p(k+1)$ is the predicted torque, $\boldsymbol{\psi}_s^*$ is the reference stator flux (which is always kept constant if field-weakening is not considered) and $\boldsymbol{\psi}_s^p(k+1)$ is the predicted stator flux; k and $k+1$ are the present and next sampling instant. In this study, the weighting factor λ_f sets the relative importance of the stator flux as compared with the torque. Since the sampling time is very small, it is a common practice to assume $T_e^*(k)$ as $T_e^*(k+1)$ [35].

The losses in the inverter are directly proportional to the switching frequency. Hence, the switching frequency should be optimised. For average switching frequency reduction, a switching transition term n_{sw} is included in the cost function and can be defined as follows [14]:

$$n_{sw}(k+1) = \sum_{x=\{a,b,c\}}\left|s_x(k+1)_i - s_x(k)\right| \tag{15.21}$$

where $s_x(k+1)$ is the probable switching state for the next time instant $k+1$, $s_x(k)$ is the applied switching state to the inverter at the time instant k and i is the index of possible voltage vectors $\{\boldsymbol{v}_0, \ldots, \boldsymbol{v}_7\}$. Using the total number of switching transitions $n_{sw}(T)$ over the duration T, the average switching frequency $\overline{f}_{sw}$ per semiconductor switch is calculated by $\overline{f}_{sw} = n_{sw}(T)/12/T$. In the later part of this chapter, the conventional FS-PTC with switching transition term in the cost function is defined as FS-PTC ($\overline{f}_{sw}$).

In order to protect from overcurrent, the cost function g must include another term I_m which is designed based on the maximum current capacity of the stator winding. Therefore, the term I_m can be defined as

$$I_m = \begin{cases} \infty, & if \ \left|i_x^p(k+1)\right| > I_{\max} \\ 0, & \text{otherwise} \end{cases} \tag{15.22}$$

Thus, the complete cost function g for the controller is

$$g = \left|T_e^*(k+1) - T_e^p(k+1)\right| + \lambda_f \left|\left|\boldsymbol{\psi}_s^*\right| - \left|\boldsymbol{\psi}_s^p(k+1)\right|\right| + \lambda_n n_{sw}(k+1) + I_m \tag{15.23}$$

where $\lambda_n$is the weighting factor of n_{sw}. The fourth term I_m does not need a weighting factor. Under normal operating condition, the value of I_m is 0 and thus it has no effect on g. Selecting proper weighting factors for the other three different objectives is a difficult task. The desired system performance may not be achieved due to improper selection of the weighting factors.

The switching state that yields minimum g in (15.23) is stored as an optimal switching state $S_{\text{opt}}(k+1)$, which is used as $S_{\text{opt}}(k)$ in the next sampling instant. The switching state $S_{\text{opt}}(k)$ produces voltage vector $\boldsymbol{v}_{\text{opt}}(k)$ which is applied to the motor terminals at instant k. The algorithm of the FS-PTC is shown in Figure 15.5. A complex loop of prediction and optimisation is apparent; this must be executed for all possible voltage vectors from a power converter.

15.4.4 Limitations of the FS-PTC

The drawbacks of the FS-PTC can be summarised as follows:

1. PTC yields variable switching frequency, since there is no modulator in the control structure.
2. Selecting the weighting factors in the cost function is not an easy task.
3. The control algorithm is computationally expensive, since all voltage vectors are evaluated for the prediction and optimisation loop. The computational burden limits the sampling frequency and, thus, degrades control performance.
4. The controller is highly dependent on the system modelling. Parameter mismatch between the controller and real system (inverter and machine), model discretisation error and sampling errors strongly influence the performance of the controller.

Researchers are currently trying to solve the aforementioned limitations. The computational burden problem of FS-PTC algorithm can be overcome using selected

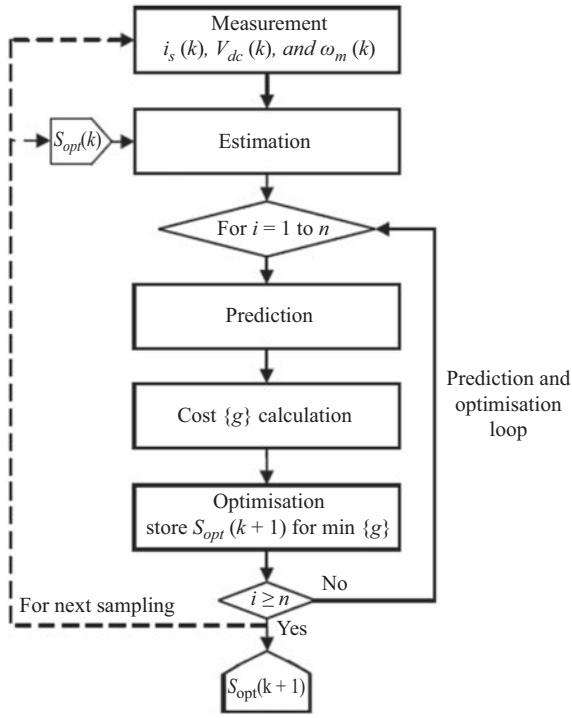


Figure 15.5 FS-PTC algorithm showing the complex prediction and optimisation loop

prediction vectors (SPVs) [36], and the parameter mismatch, model discretisation error and sampling errors are yet to overcome. The structure and principle of SPVs strategy is as follows.

15.5 SPVs-based FS-PTC

The structure of the SPVs-based FS-PTC is similar to the conventional FS-PTC, as shown in Figure 15.6. The main differences are the selection of prediction vectors $\boldsymbol{v}_j$ and the design of cost function, where j may be three values among $n = \{0,\cdots, 7\}$. Conventionally, all voltage vectors of a 2L-VSI are employed for prediction and optimisation. In the SPVs-based FS-PTC, only three – one zero and two active vectors – of the possible eight voltage vectors are evaluated. Thus, the computational complexity is reduced.

15.5.1 Selecting prediction vectors

The selection process of prediction vectors is based on the DTC strategy [26]. The prediction vectors are selected using the present position of the stator flux $\widehat{\boldsymbol{\psi}}_s$ and

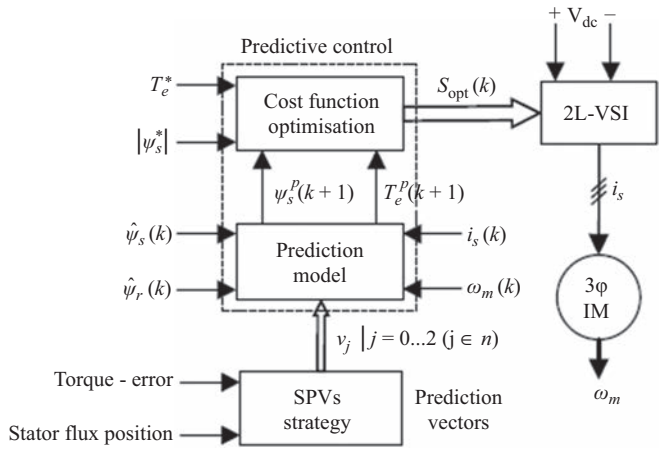


Figure 15.6 FS-PTC using SPVs strategy

the sign of torque error $\delta T_e = \left(T_e^* - \widehat{T}_e\right)$. The position of stator flux $\widehat{\theta}_s$ is estimated as

$$\widehat{\theta}_s = \tan^{-1}\left(\frac{\widehat{\psi}_{\beta s}}{\widehat{\psi}_{\alpha s}}\right) \tag{15.24}$$

We may recall that a 2L-VSI produces six active vectors $\{\boldsymbol{v}_1, \cdots, \boldsymbol{v}_6\}$ and two zero vectors $\{\boldsymbol{v}_0, \boldsymbol{v}_7\}$. In this study, only $\boldsymbol{v}_0$ is considered as the zero vectors in the prediction and optimisation steps, to reduce the computational burden. This assumption is valid as no switching frequency term is included in the cost function, and the effects of $\boldsymbol{v}_0$ and $\boldsymbol{v}_7$ on torque and flux are similar. After optimisation, if the stored optimal voltage vector is a zero vector, then an appropriate zero vector (either $\boldsymbol{v}_0$ or r $\boldsymbol{v}_7$) is selected so that one switching transition occurs. The number of switching transitions is calculated using the applied optimal switching state at time instant k. The space distribution of all voltage vectors in the α-β plane, showing the selection strategy of the prediction vectors, is shown in Figure 15.7. Here, it is apparent that the active voltage vectors change periodically by an angle of $\pi/3$. Accordingly, the α-β plane is divided into six sectors to identify the direction of rotation as

$$(2N-3)\pi/6 \leq \Theta(N) \leq (2N-1)\pi/6 \tag{15.25}$$

where $\Theta(N)$ is the sector with $N = 1, \cdots, 6$.

Let us consider that the stator flux $\widehat{\boldsymbol{\psi}}_s$is rotating in the counterclockwise direction. At a particular instant, different voltage vectors influence the torque and flux differently, and the possible conditions of torque deviation are $\delta T_e > 0$, $\delta T_e < 0$ and $\delta T_e = 0$, and flux deviation are $\delta\psi_s > 0$, $\delta\psi_s < 0$ and $\delta\psi_s = 0$, where $\delta\psi_{\boldsymbol{s}} = \left(|\boldsymbol{\psi}_s^*| - |\widehat{\boldsymbol{\psi}}_s|\right)$. In Figure 15.7, the effects of all active vectors in terms of

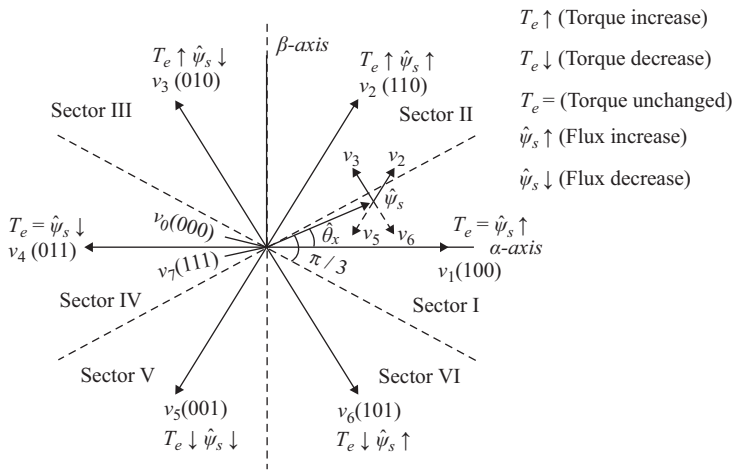


Figure 15.7 Space distribution of all admissible voltage vectors of a 2L-VSI showing the selection strategy of the prediction vectors

increase, decrease or unchanged torque and flux are indicated by the symbols '↑', '↓' and '=', respectively, when the stator flux is located in sector I. These effects on torque and flux are analysed to determine the sign of torque error or flux error. If $\widehat{\boldsymbol{\psi}}_s$ is located in sector I and the torque error $\delta T_e > 0$, then the voltage vectors that satisfy torque increase ($T_e \uparrow$) condition (as shown in Figure 15.7) are selected as prediction vectors. Hence, the possible active prediction vectors are two adjacent forward vectors $\boldsymbol{v}_2$(1 1 0) and $\boldsymbol{v}_3$(0 1 0), which are represented by solid arrows on the tip of the stator flux $\widehat{\boldsymbol{\psi}}_s$, as shown in Figure 15.7. Selecting the two adjacent forward voltage vectors also ensures the possible condition of stator flux deviation $\delta\psi_s > 0$ or $\delta\psi_s < 0$. Similarly, for the same position of stator flux, if $\delta T_e < 0$, the possible active prediction vectors are two adjacent backward vectors $\boldsymbol{v}_6$(1 0 1) and $\boldsymbol{v}_5$(0 0 1). These are represented by dashed arrows on the tip of the stator flux $\widehat{\boldsymbol{\psi}}_s$ in Figure 15.7. Generally, the active vectors are always employed with a zero vector for the IM to reduce the torque and flux ripple effectively. Including a zero vector satisfies the possible conditions of $\delta T_e = 0$ and $\delta\psi_s = 0$. From Figure 15.7, we can see that the active vectors $\boldsymbol{v}_1$(10 0) or $\boldsymbol{v}_4$(0 1 1) might also satisfy the condition $\delta T_e = 0$. However, applying a zero vector is more effective than the active vectors when $\delta T_e = 0$. This is because the stator flux speed should be controlled so it is as slow as possible. Hence, the total number of prediction vectors is three, whereas it is seven (considering one zero vector) in the conventional FS-PTC. A similar analysis is carried out when the stator flux is located in the other sectors. The selected active prediction vectors for all the six sectors are shown in Table 15.3.

It is obvious that if $\widehat{\theta}_s(k-1)$ and $\widehat{\theta}_s(k)$ lie in the same sector and the signs of $\delta T_e(k-1)$ and $\delta T_e(k)$ are same, then maximum of one switching transition is possible between two active vectors, due to the SPVs. Hence, the SPVs strategy also reduces the average switching frequency of the power converter.

Table 15.3 Active prediction vectors dependent on stator flux position $\widehat{\theta}_s(k)$ and torque error δT_e

δT_e \ Θ	I	II	III	IV	V	VI
$\delta T_e > 0$	v_2, v_3	v_3, v_4	v_4, v_5	v_5, v_6	v_6, v_1	v_1, v_2
$\delta T_e < 0$	v_5, v_6	v_6, v_1	v_1, v_2	v_2, v_3	v_3, v_4	v_4, v_5

Table 15.4 Active prediction vectors dependent on stator flux position $\widehat{\theta}_s(k)$ and stator flux error $\delta\psi_s$

$\delta\psi_s$ \ Θ	I	II	III	IV	V	VI
$\delta\psi_s > 0$	v_6, v_2	v_1, v_3	v_2, v_4	v_3, v_5	v_4, v_6	v_1, v_5
$\delta\psi_s < 0$	v_3, v_5	v_4, v_6	v_1, v_5	v_6, v_2	v_1, v_3	v_2, v_4

It is apparent from Figure 15.7 that another switching table based on $\widehat{\theta}_s$ and flux error $\delta\psi_s$ instead of torque error δT_e can be developed. The possible active prediction vectors based on $\delta\psi_s$ for all the six sectors are shown in Table 15.4. However, a relatively lower priority on the stator flux in the cost function must be set compared with the δT_e-based prediction vectors to achieve satisfactory torque and flux performance. This is because the stator flux gets priority over the torque when $\delta\psi_s$-based prediction vectors are considered. Performance in terms of computational burden, torque ripple and flux ripple will be almost similar. However, δT_e-based prediction vectors are considered in this study.

15.5.2 Optimum voltage vector selection

Since two adjacent voltage vectors are selected for the prediction and optimisation, only one switching transition occurs at a particular time instant under a certain condition, as mentioned previously. Hence, the average switching frequency is reduced, and inclusion of the switching frequency term in the cost function is not required for the SPVs-based simplified FS-PTC. This also reduces the computational burden of the control strategy. The cost function used in the SPVs-based simplified FS-PTC is as follows:

$$g = \left|T_e^*(k+1) - T_e^p(k+1)\right| + \lambda_f \left|\left|\boldsymbol{\psi}_s^*\right| - \left|\boldsymbol{\psi}_s^p(k+1)\right|\right| + I_m \tag{15.26}$$

It is obvious that selecting the weighting factors in (15.26) is simpler compared to (15.23) used in the conventional FS-PTC.

In a real-time implementation, the control algorithm calculation time introduces one-step time delay that must be compensated [37]. This is done by two-step-ahead prediction. The predicted stator flux $\boldsymbol{\psi}_s^p(k+1)$ and stator current $\boldsymbol{i}_s^p(k+1)$ are used as the initial states for predictions at time instant $k+2$. To predict $\boldsymbol{\psi}_s^p(k+1)$ and $\boldsymbol{i}_s^p(k+1)$, the optimum voltage vector $\boldsymbol{v}_{opt}(k)$ applied to the motor terminals at the instant k is employed in (15.17) and (15.18), respectively. In this case, for selecting the prediction vectors, $\boldsymbol{\psi}_s^p(k+1)$ instead of $\widehat{\boldsymbol{\psi}}_s(k)$ and $T_e^p(k+1)$ instead of $\widehat{T}_e(k)$ are used to calculate $\widehat{\theta}_s$ and δT_e, respectively. The predictions of the stator flux, stator current and torque at instant $k+2$ can be expressed as

$$\boldsymbol{\psi}_s^p(k+2) = \widehat{\boldsymbol{\psi}}_s(k+1) + T_s\boldsymbol{v}_{opt}(k) - T_sR_s\boldsymbol{i}_s(k+1) \tag{15.27}$$

$$\begin{aligned}\boldsymbol{i}_s^p(k+2) = &\left(1-\frac{T_s}{\tau_\sigma}\right)\boldsymbol{i}_s(k+1) + \frac{T_s}{(\tau_\sigma + T_s)} \\ &\times \left[\frac{1}{R_\sigma}\left\{\left(\frac{k_r}{\tau_r} - jk_r\omega_e(k+1)\right)\widehat{\boldsymbol{\psi}}_r(k+1) + \boldsymbol{v}_{opt}(k)\right\}\right]\end{aligned} \tag{15.28}$$

$$T_e^p(k+2) = 1.5pIm\left\{\boldsymbol{\psi}_s^p(k+2)^*.\boldsymbol{i}_s^p(k+2)\right\} \tag{15.29}$$

As rotor time constant τ_r is much greater than the sampling time T_s and the rotor flux changes slowly compared to the stator flux, it is a general practice to assume $\omega_e(k) = \omega_e(k+1)$ and $\widehat{\boldsymbol{\psi}}_r(k) = \widehat{\boldsymbol{\psi}}_r(k+1)$, respectively.

Hence, to implement the delay compensation scheme [37], the optimum voltage vector is selected by minimising the following cost function:

$$g = \left|T_e^*(k+2) - T_e^p(k+2)\right| + \lambda_f\left||\boldsymbol{\psi}_s^*| - |\boldsymbol{\psi}_s^p(k+2)|\right| + I_m \tag{15.30}$$

15.5.3 Average switching frequency reduction

The selection of only one zero vector, either $\boldsymbol{v}_0$ or $\boldsymbol{v}_7$, with two active vectors for the pre diction and optimisation may increase the average switching frequency. For this reason, if $\boldsymbol{v}_0$ is selected as the optimum voltage vector, an appropriate zero vector, either $\boldsymbol{v}_0$ or $\boldsymbol{v}_7$, is selected in such a way that only one switching transition occurs at a particular time instant. For example, if the applied voltage vector at the time instant k is $\boldsymbol{v}_2(110)$ and the optimum voltage vector actuated for the next time instant $k+1$ is $\boldsymbol{v}_0$, then the switching state '111' is selected instead of '000' as the optimal switching state. Therefore, the state '000' is selected after '100', '010' and '001'; otherwise, '111' is selected as the zero vector.

15.5.4 Overall control structure of SPVs-based FS-PTC

The complete schematic of the SPVs-based simplified FS-PTC is shown in Figure 15.8, which includes four parts: (1) rotor and stator flux estimation; (2) prediction vectors selection; (3) stator flux and torque prediction; and (4) cost

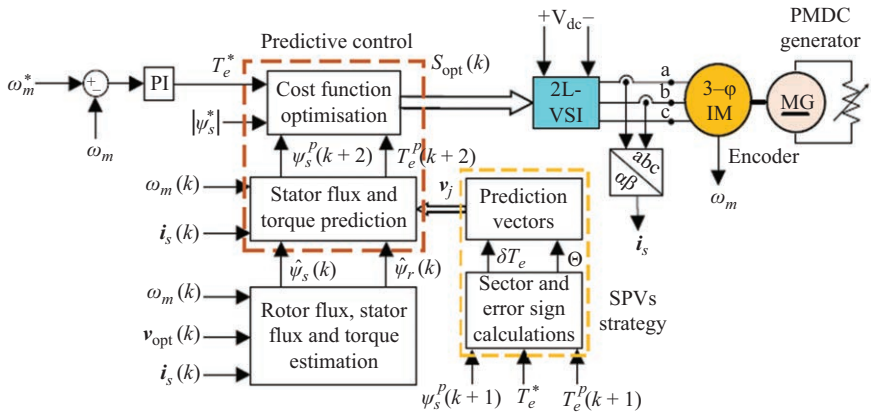


Figure 15.8 Simplified FS-PTC system using torque-error-based SPVs

function optimisation (optimum voltage vector selection). The rotor speed is measured using an encoder mounted on the motor shaft. A PI controller is employed to produce the reference torque, based on the speed error. The speed error is calculated by comparing the measured speed with the command speed. The constant rated stator flux reference is commanded from outside the controller, as field weakening is not considered in this study. Both the aforementioned reference quantities (torque and flux) are used directly in the cost function to actuate the optimum switching state S_{opt} which produces optimum voltage vector.

15.5.5 SPVs-based FS-PTC algorithm

The overall control procedure can be summarised by the following sequences:

Step 1. *Measurement*: Sampling $\boldsymbol{i}_s(k)$, $V_{dc}(k)$ and $\omega_m(k)$.
Step 2. *Apply*: Apply the optimum voltage vector $\boldsymbol{v}_{opt}(k)$ to the motor terminals.
Step 3. *Estimate*: Estimate the rotor flux $\widehat{\boldsymbol{\psi}}_r(k)$ and the stator flux $\widehat{\boldsymbol{\psi}}_s(k)$ using (15.14) and (15.15), respectively.
Step 4. *Predict*: Predict the stator flux $\boldsymbol{\psi}_s^p(k+1)$ stator current $\boldsymbol{i}_s^p(k+1)$ and torque $T_e^p(k+1)$ using (15.17)–(15.19).
Step 5. *Select prediction vectors*: Select the active prediction vectors using Table 15.3.
Step 6. *Predict and calculate cost*: Predict the stator flux $\boldsymbol{\psi}_s^p(k+2)$, stator current $\boldsymbol{i}_s^p(k+2)$ and torque $T_e^p(k+2)$ using (15.27)–(15.29). Then, evaluate the predicted stator flux and torque by calculating the cost using the cost function (15.30). Execute these predictions and cost calculation loop for the selected two active vectors and one zero vector.
Step 7. *Optimise*: Select $\boldsymbol{v}_{opt}(k+2)$ which results minimum g in (15.30) and replace it with an appropriate zero vector if selected $\boldsymbol{v}_{opt}(k+2)$ is a zero vector. Return to Step 1.

15.6 Computational efficiency improvement in the SPVs-based FS-PTC

The execution time of the PTC algorithm is reduced, as the number of prediction vectors is reduced. The simplified algorithm requires additional calculations for the prediction vectors selection (calculations not used in the conventional PTC). However, the calculations are very simple. Therefore, the required extra execution time is much less – 1.28 μs – than the reduced time in the prediction and optimisation steps.

The execution time of the SPVs-based FS-PTC, compared to the conventional FS-PTC, is illustrated in Figure 15.9. Here, the average execution time of the conventional FS-PTC algorithm $\overline{T}_{\text{conventional}}$ without switching transition term in the cost function is 27.68 μs, which is further increased to 30.54 μs if the switching transition term is included in the cost function. The average execution time of the simplified algorithm $\overline{T}_{SPVs}$ is 21.5 μs. Hence, the reduced average execution times with and without switching transition term in the cost function are 30% and 22%, respectively. As the speed control loop is executed in every 2.5 ms, the execution time is increased in every 2.5 ms. Table 15.5 shows a comparison of overall

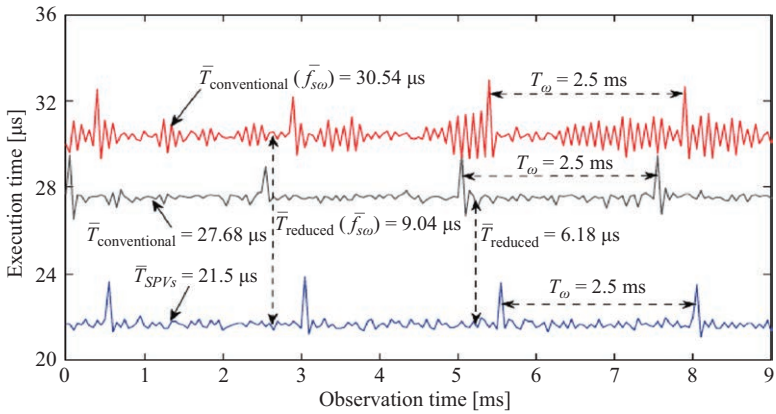


Figure 15.9 Execution times of the SPVs-based FS-PTC and the conventional FS-PTC algorithms

Table 15.5 Overall execution times comparison between the SPVs-based FS-PTC and conventional FS-PTC algorithms

Index	Execution times (μs)		
	FS-PTC	FS-PTC($\overline{f}_{sw}$)	SPVs
Measurement	6.63	6.67	6.64
Estimation	1.60	1.60	1.60
Prediction vectors selection	0.00	0.00	1.28
Prediction and optimisation	26.08	28.94	18.66
Total	38.30	42.20	31.76

execution times. Of course, the execution time is hardware- and (above all) programming-dependent. As the same hardware and programming techniques are used for all cases in this study, the comparison presented here is fair.

15.7 Performance of an IM drive under FS-PTC

In the following, the performance of an IM driven by a two-level inverter and the controller (FS-PTC) described in the earlier section are included. The parameters of the motor on which the FS-PTC technique is applied are given in Table 15.6. A DC machine is used as load on the motor. The specification of the load machine is given in Table 15.7. The parameters of the controller are also included in Table 15.7. The sampling time of the controller is set to 50 μs.

The performance of the control system is measured mainly in terms of stator current THD, torque ripple, flux ripple and average switching frequency. A major effect of harmonic currents in rotating machinery is increased heating due to iron and copper losses at the harmonic frequencies. The harmonic components thus affect the machine efficiency and can also affect the torque developed. Flux variations may produce higher THD in phase current, and torque ripple causes acoustic noise in the system. The switching frequency affects the converter efficiency, because the switching loss in the converter is directly proportional to the switching frequency.

The performance of the SPVs-based FS-PTC is shown along with the two cases of conventional FS-PTC: (1) without and (2) with switching transition term in the cost function. All the voltage vectors $\{\boldsymbol{v}_0 \cdots \boldsymbol{v}_7\}$ are evaluated if switching transition term is considered in the cost function. Otherwise, seven different voltage vectors are evaluated and an appropriate zero voltage vector (either $\boldsymbol{v}_0$ or $\boldsymbol{v}_7$) is then selected, as explained in Section 15.5.3.

Table 15.6 A 1.1 kW, 415 V, 3-ϕ, 50 Hz IM parameter

$R_s = 6.03\ \Omega$	$\psi_{snom} = 1.0$Wb
$R_r = 6.085\ \Omega$	$T_{nom} = 7.4$ N m
$L_s = 0.5192$ H	$N_p = 2$
$L_r = 0.5192$ H	$J = 0.011787$ kg m^2
$L_m = 0.4893$ H	$\omega_m = 1{,}415$ rev/min

Table 15.7 Controller parameters and load specifications

Controller parameters	**DC machine ratings**
$k_p = 0.396$, $k_i = 9.056$	$P = 1.1$ kW
$\lambda_f = 20$ (for SPVs), 30 (for conventional)	$V = 180$ V
$\lambda_n = 0.05$	$I_a = 6.9$ A
$I_{\max} = 5$ A	$\omega = 1{,}800$ rev/min

The followings are presented to show the effectiveness of the FS-PTC algorithms:

1. steady-state behaviour;
2. transient capability of the FS-PTC under rated-speed reversal;
3. average switching frequency;
4. robustness against external rated-load torque disturbance;
5. step rated-torque-transient characteristics;
6. step rated-speed-transient characteristics.

15.7.1 Steady-state behaviour

Figures 15.10 and 15.11 show the steady-state characteristics of the FS-PTC control systems at a speed of 1,000 rev/min with 4.0 N m load torque. It is observed that the torque and flux ripple is marginal. However, the THD of the stator current for the SPVs-based FS-PTC is slightly higher due to lower average switching frequency. The frequency spectra of the stator currents are presented in Figure 15.13(a) and (b), respectively. The average switching frequency for the SPVs-based FS-PTC is lower by 16.62%. Moreover, the frequency spectrum is less distributed over a wide frequency range compared to the conventional FS-PTC. This also confirms the reduction in average switching frequency. To reduce the average switching frequency of the conventional FS-PTC, the switching transition term is included in the cost function. Then, a weighting factor is imposed on the frequency term, provided that the torque and flux ripples are almost similar. The responses of the system and the frequency spectrum of the stator current are presented in Figures 15.12 and 15.13(c),

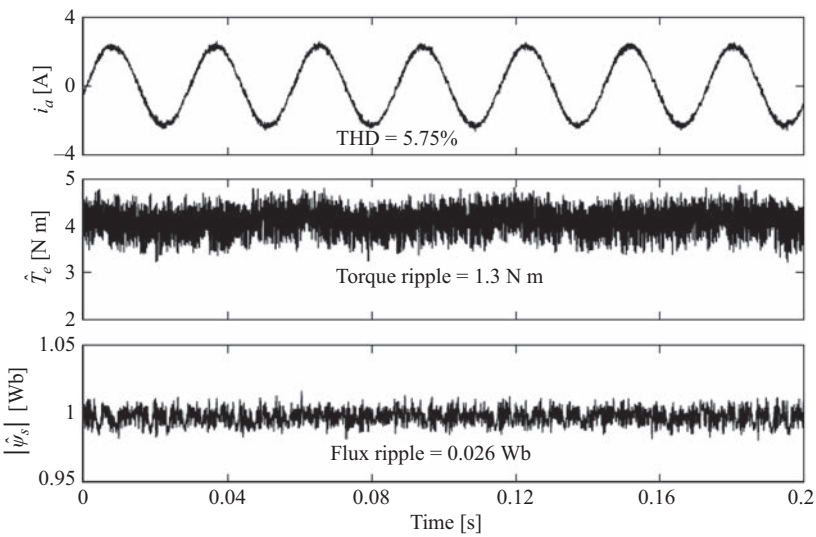


Figure 15.10 Steady-state waveforms of stator current, estimated torque and estimated stator flux at 1,000 rev/min with 4.0 N m load torque for the SPVs-based FS-PTC

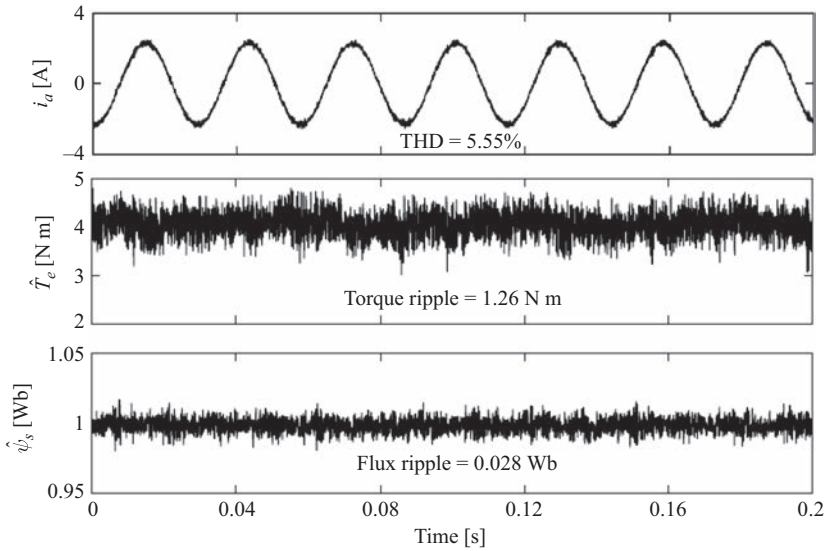


Figure 15.11 Steady-state waveforms of stator current, estimated torque and estimated stator flux at 1,000 rev/min with 4.0 N m load torque for the conventional FS-PTC

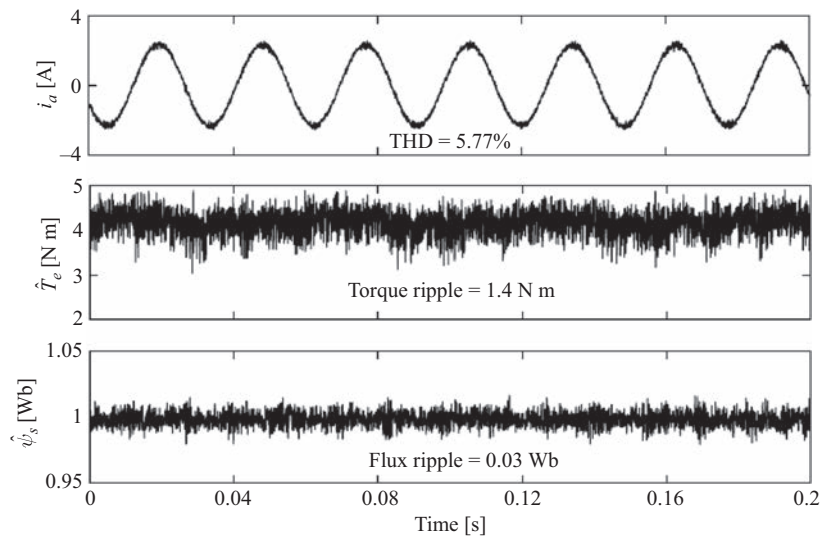


Figure 15.12 Steady-state waveforms of stator current, estimated torque and estimated stator flux at 1,000 rev/min with 4.0 N m load torque for the conventional FS-PTC with average switching frequency reduction

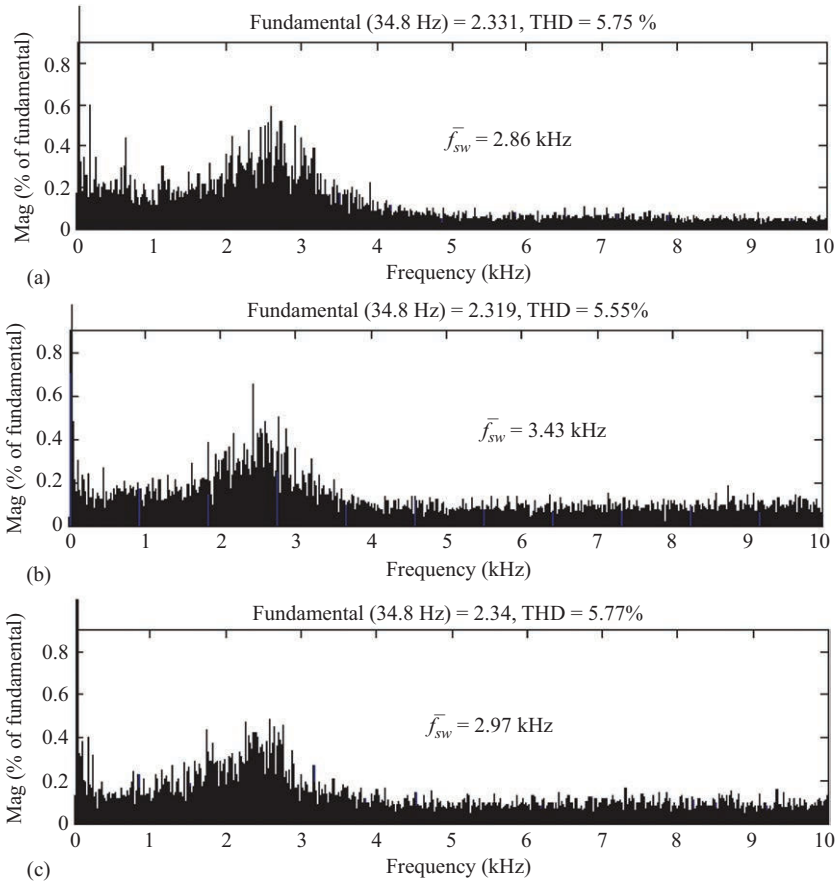


Figure 15.13 Frequency spectra of stator current i_a at 1,000 rev/min using (a) SPVs, (b) conventional algorithm and (c) conventional algorithm with average switching frequency reduction

respectively. Note that the frequency spectra for the FS-PTC are distributed due to the variable switching frequency. Further research on PTC is necessary to keep the frequency spectra in a specified range.

The THD of the stator current is similar to the SPVs-based FS-PTC. However, the average switching frequency is still higher. If a greater weight is imposed on the switching transition term to reduce the average switching frequency further, the torque ripple increases (while keeping the weight of the stator flux error constant). Hence, selecting the weighting factors is a complex task. In this sense, the SPVs-based FS-PTC is simpler compared to the conventional FS-PTC. Table 15.8 summarises the steady-state performance of the FS-PTC systems.

Table 15.8 Quantitative steady-state performance comparison among FS-PTC systems

Index	Conventional	Conventional ($\bar{f}_{sw}$)	SPVs
THD (for i_a) (%)	5.55	5.77	5.75
Torque ripple (N m)	1.26	1.40	1.30
Flux ripple (Wb)	0.028	0.03	0.026
Average Switching frequency (kHz)	3.43	2.97	2.86

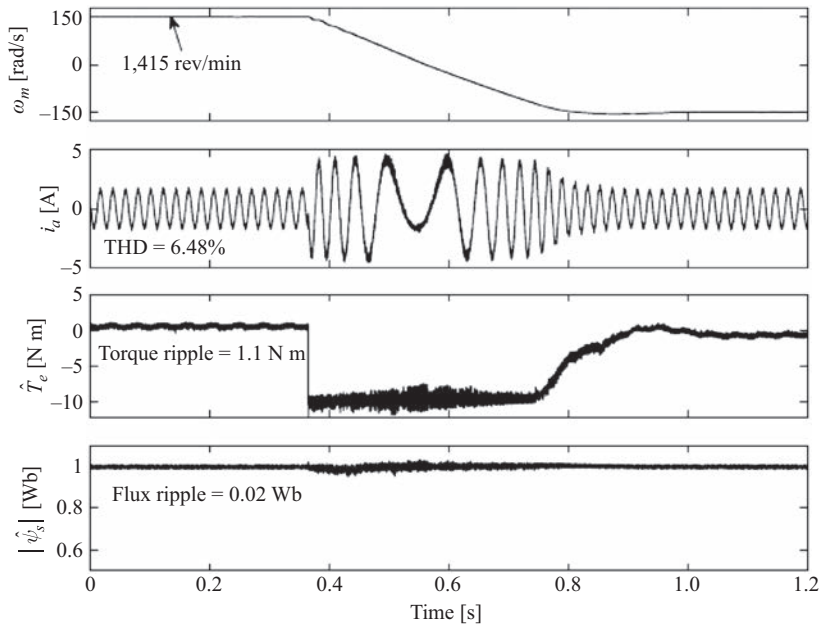


Figure 15.14 Waveforms of speed, stator current, estimated torque and estimated stator flux at no-load torque under rated-speed reversal condition for the SPVs-based FS-PTC

15.7.2 Transient capability under rated-speed reversal

A reverse speed operation of the FS-PTC strategies at rated speed of 1,415 rev/min without load torque (although the DC machine is connected to the fed motor) is shown in Figure 15.14. From top to bottom, the curves are the speed, stator current, estimated torque and stator flux. The stator flux is constant at its rated value of 1.0 Wb. For comparison, same curves are plotted for the all vectors-based FS-PTC, where switching transition term is not included in the cost function, as shown in Figure 15.15. It is seen

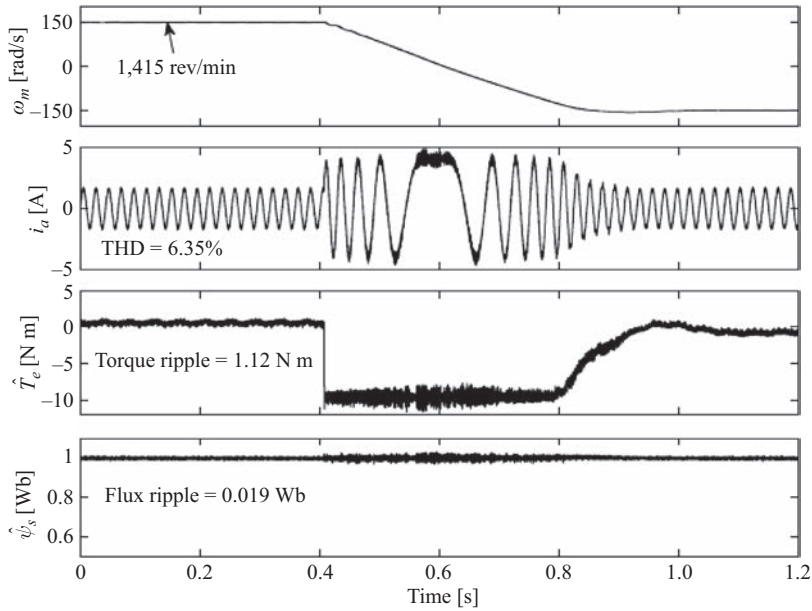


Figure 15.15 Waveforms of speed, stator current, estimated torque and estimated stator flux at no-load torque under rated-speed reversal condition for the conventional FS-PTC

that the performance in terms of the torque and flux ripple is satisfactory. During speed reversal, the ripple is slightly increased for both the SPVs-based FS-PTC and conventional FS-PTC systems. This is because of high current flowing in the stator winding. The THD of the stator current i_a for the simplified FS-PTC is 6.48%, whereas it is 6.35% for the conventional FS-PTC. This slightly higher current THD for the SPVs-based simplified FS-PTC is due to the low average switching frequency. The average switching frequencies are 1.91 and 2.11 kHz for the simplified and conventional control systems, respectively.

From Figure 15.14, it can be noted that a very small dip is present in the stator flux response during speed reversal at time 0.4 s around. This is because the prediction vectors are selected based on the torque error regardless of the stator flux error. During the transient, at a particular position of the stator flux, the voltage vector that produces more torque is selected to reduce the torque error and is applied to the motor terminals. Moreover, the vector producing more torque, in most cases, decreases stator flux and causes flux transient. One possible solution of this problem is to set a higher value of the weighting factor λ_f in the cost function during the transient than the steady-state condition. Another possible solution is to use the stator flux-error-based prediction vectors. In that case, a less priority should be set on the stator flux (small λ_f in the cost function compared to the torque-error-based prediction vectors to achieve satisfactory torque and flux performance).

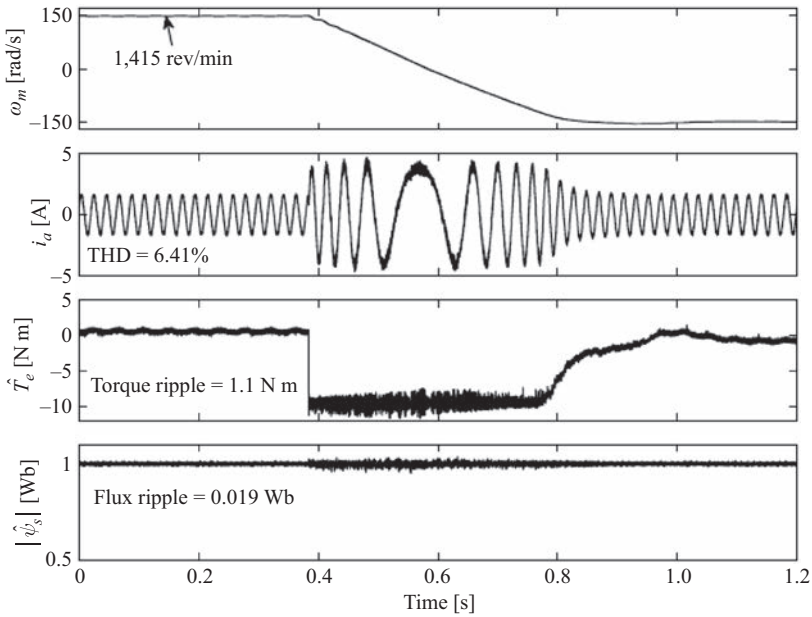


Figure 15.16 Waveforms of speed, stator current, estimated torque and estimated stator flux at no-load torque under rated-speed reversal condition for the flux-error-based FS-PTC

In order to justify the solution mentioned earlier, the flux-error-based prediction vectors are considered. A reverse rated-speed of 1,415 rev/min operation without load torque is illustrated in Figure 15.16. It can be seen that there is no dip in the stator flux response during speed reversal at time 0.4 s around, while the system performance – stator current THD, torque ripple and stator flux ripple – is comparable with the torque-error-based prediction vectors. Hence, the problem can be solved using flux-error-based prediction vectors.

15.7.3 The average switching frequency

Figure 15.17(a) presents the average switching frequencies for the FS-PTC control algorithms at different speeds and load torques. The average switching frequencies are comparable at low and high speeds with 50% or higher of the rated-load torque. The reduction in average switching frequencies for the SPVs-based FS-PTC is significant – maximum 25% of average switching frequency – for the speed range of 400–1,200 rev/min, as can be seen in Figure 15.17(b). The improvement in average switching frequency is also obvious from Figure 15.17(c). However, in the whole operating range of the machine, the variation ranges of average switching frequencies for the FS-PTC strategies are similar (1.58–5.58 kHz for both cases).

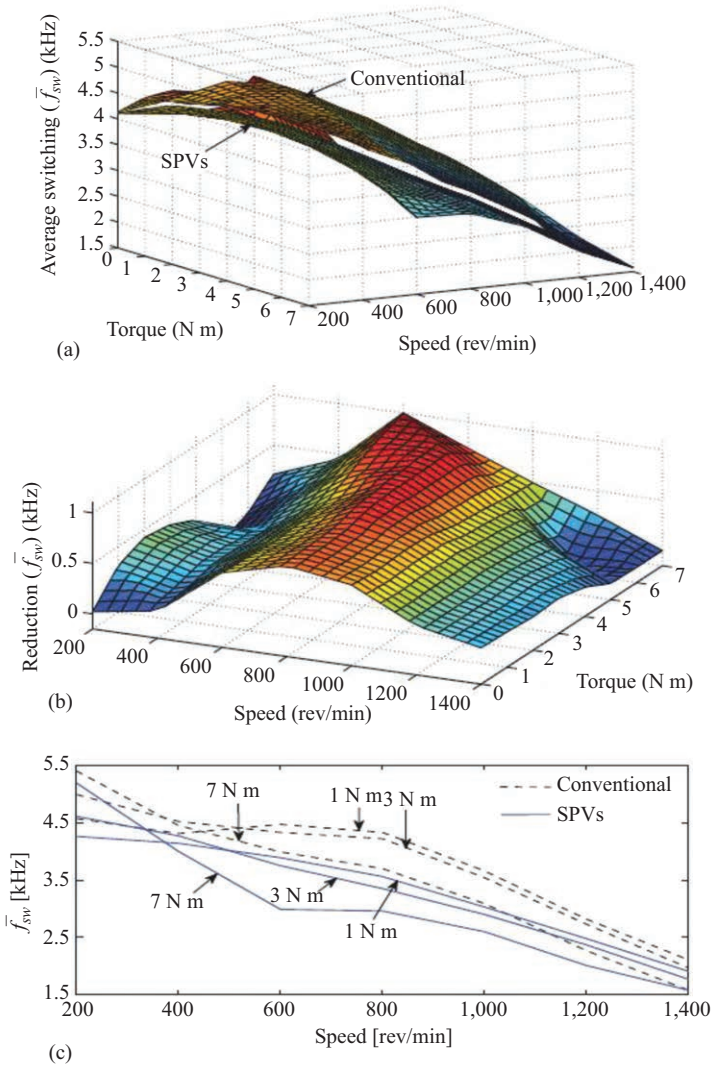


Figure 15.17 (a) Average switching frequencies $\bar{f}_{sw}$ from 200 to 1,400 rev/min with load torque of 0–7 N m; (b) reduction in $\bar{f}_{sw}$; and (c) $\bar{f}_{sw}$ versus speed with torque as parameter

15.7.4 Investigation of robustness against rated-load torque disturbance

Figures 15.18 and 15.19 illustrate the responses to an external rated-load torque disturbance for the FS-PTC algorithms. The load torque, which is dependent on the rotor speed, is suddenly changed from 0 (no-load torque) to 7.4 N m (full-load torque) at 1,000 rev/min. It is observed that stator current THD and the torque and

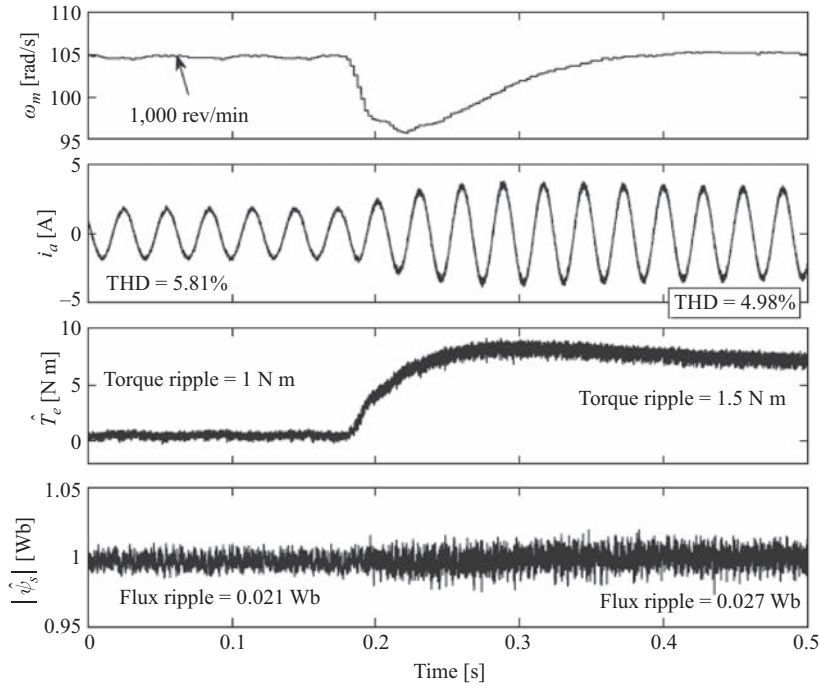


Figure 15.18 Responses to an external rated-load torque disturbance at 1,000 rev/min for the SPVs-based FS-PTC

flux ripple are similar before and after added load. During the load torque change, the stator flux remains constant at its rated value, which ensures decoupled control of the torque and flux. The motor speed returns to its original value within a short time (0.19 s), and the speed responses are identical during load disturbance. The average switching frequencies for the SPVs-based FS-PTC algorithm before and after added load torque are 3.02 and 2.60 kHz, respectively; whereas the average switching frequencies before and after added load torque are 3.67 and 3.09 kHz, respectively, for the conventional FS-PTC algorithm.

15.7.5 Step rated-torque-transient characteristics

Step rated-torque-transient characteristics of the FS-PTC strategies are illustrated in Figure 15.20. A step rated-torque reference of 7.4 N m is commanded. It is seen that the torque rise times for the control algorithms are very close with 0.5 ms versus 0.53 ms, respectively. This means that both control algorithms exhibit fast dynamic responses.

15.7.6 Step rated-speed-transient characteristics

Rated-speed-transient behaviour of the FS-PTC algorithms is presented in Figure 15.21. Similar to the conventional control algorithm, the simplified FS-PTC

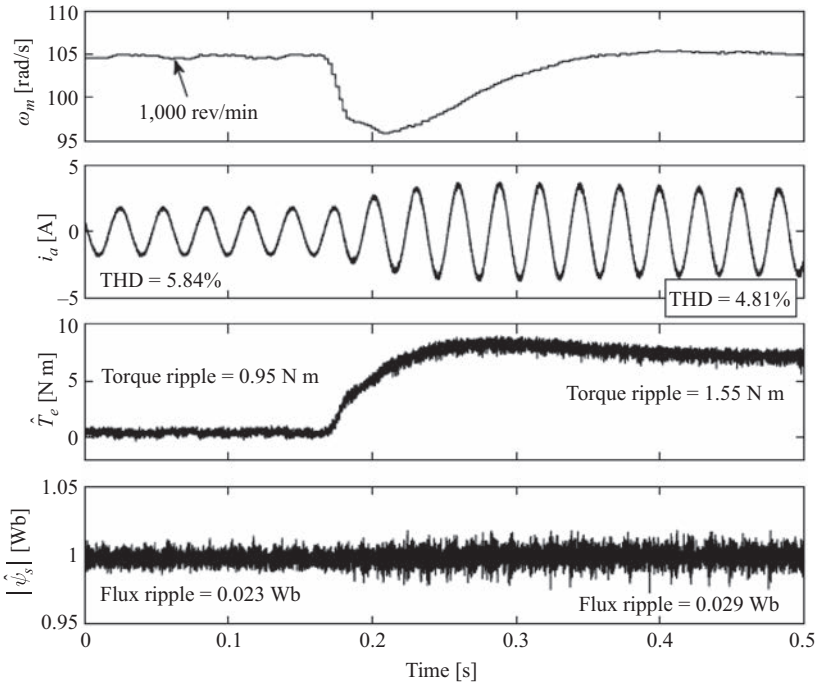


Figure 15.19 Responses to an external rated-load torque disturbance at 1,000 rev/min for the conventional FS-PTC

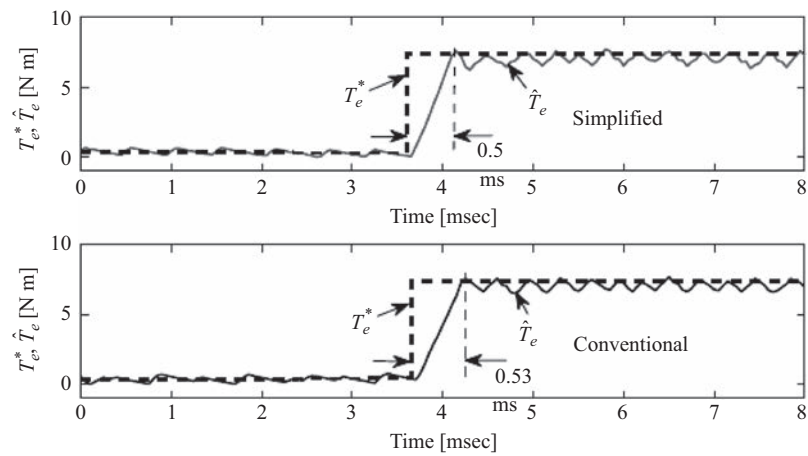


Figure 15.20 Step rated-torque-transient of the FS-PTC algorithms

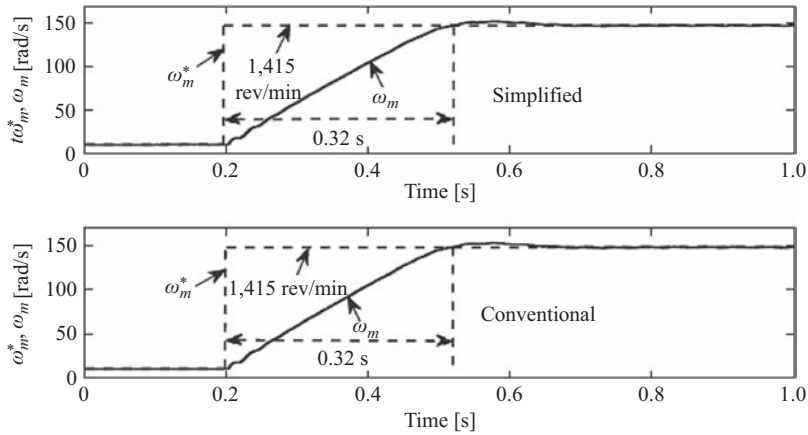


Figure 15.21 Step rated-speed-transient of the FS-PTC algorithms

can track the reference speed accurately without any significant overshoot. The speed rise time is 0.32 s only, which is very short. Hence, the controller tracks the reference speed quickly and accurately.

15.8 Summary

This chapter describes the application of MPC technique to a two-level inverter-driven induction motor. The state-space model of the IM and inverter is discussed. The basic principle of PTC and its application on IM drive are presented in detail. The systematic process of finding the cost function is explained. This process can be used for incorporating other objectives in the cost function if required. The complexity of the PTC algorithm, in terms of computational burden and cost function design, is no longer an issue for a specific objective as shown in this chapter. Experimental results illustrate that FS-PTC algorithm yields good performance in terms of torque and flux ripple, stator current THD, robustness against load torque disturbance, step torque response and step speed response. Further research may be conducted on PTC to minimise parameter mismatch between the controller and the real system, model discretisation error and sampling errors. Stability analysis of PTC under different operating conditions, optimal cost function selection for multi-variable control objectives, cost function optimisation algorithm, frequency spectrum shaping, and increasing prediction and control horizon are also some open topics for research. Research and development efforts on the aforementioned topics are necessary in order to make the controller intelligent and bring this technology to the industrial and commercial level. Currently available control techniques such as DTC allow only a limited number of goals (torque and flux ripple) to be included. The capability of MPC to include many

other objectives such as the machine parameter estimation, dead-time compensation, duty cycle control, efficiency optimisation and more elaborate inverters (multi-level and matrix converters), and the technique of its computational burden reduction clearly shows the possibility of more optimised drive systems in the future.

List of symbols

θ_s	The angle between the α-β and d-q reference frames
v_s	Stator voltage
i_s	Stator current
ψ_s	Stator flux
v_r	Rotor voltage
i_r	Rotor current
ψ_r	Rotor flux
T_Θ	Electromagnetic torque
T_l	Load torque
ω_m	Rotor angular speed
ω_e	Rotor angular frequency
p	Number of pole pairs
σ	Total leakage factor
k_r	Rotor coupling factor
R_σ	Equivalent resistance referred to stator
τ_σ	Transient stator time constant
L_σ	Leakage inductance
τ_r	Rotor time constant
v_a, v_b and v_c	Phase voltages
λ_f	Weighting factor
T_s	Sampling time

Glossary of terms

Decoupled control	Control of two or more parameters independent of each other such as speed and torque
Predictive torque control	The control involving prediction of torque and stator flux for finite number of admissible switching states of a voltage source inverter

References

[1] Garcia C.E., Prett D.M. and Morari M. 'Model predictive control: theory and practice – a survey'. *Automatica.* 1989; 25(3): 335–348.

[2] Maciejowski J.M. *Predictive control with constraints*. Englewood Cliffs, NJ: Prentice Hall, 2002.
[3] Camacho E.F. and Bordons C. *Model predictive control*. London: Springer, 2004.
[4] Goodwin G.C., Seron, M.M. and Dona J.A.D. *Constrained control and estimation – an optimization perspective*. Berlin: Springer Verlag, 2005.
[5] Lee J.H. 'Model predictive control: review of the three decades of development'. *Int. Journal of Control, Automation, and Systems*. 2011; 9(3): 415–424.
[6] Linder A. and Kennel R. 'Model predictive control for electrical drives'. *Proceedings of the Power Electronics Specialists Conference, 2005. PESC'05. IEEE 36th*, 2005, pp. 1793–1799.
[7] Correa P., Pacas M. and Rodriguez J. 'Predictive torque control for inverter-fed induction machines'. *IEEE Trans. on Ind. Electronics*. 2007; 54(2): 1073–1079.
[8] Cortes P., Kazmierkowski M.P., Kennel R.M., Quevedo D. and Rodriguez J. 'Predictive control in power electronics and drives'. *IEEE Trans. on Ind. Electronics*. 2008; 55(2): 4312–4324.
[9] Kouro S., Cortes P., Vargas R., Ammann U. and Rodriguez J. 'Model predictive control—a simple and powerful method to control power converters'. *IEEE Trans. on Ind. Electronics*, 2009; 56(6): 1826–1838.
[10] Cortes P., Ortiz G., Yuz J.I., Rodriguez J., Vazquez S. and Franquelo L.G. 'Model predictive control of an inverter with output LC filter for UPS applications'. *IEEE Trans. on Ind. Electronics*. 2009; 56(6): 1875–1883.
[11] Bolognani S., Bolognani S., Peretti L. and Zigliotto M. 'Design and implementation of model predictive control for electrical motor drives'. *IEEE Trans. on Ind. Electronics*. 2009; 56(6): 1925–1936.
[12] Linder A., Kanchan R., Kennel R. and Stolze P. *Model-based predictive control of electric drives*. Gottingen, Germany: Cuvillier Verlag, 2010.
[13] Geyer T. 'A comparison of control and modulation schemes for medium-voltage drives: emerging predictive control concepts versus PWM-based schemes'. *IEEE Trans. on Ind. Applications*. 2011; 47(3): 1380–1389.
[14] Rodriguez J. and Cortes P. *Predictive control of power converters and electrical drives*. Chichester: Wiley, 2012.
[15] Rodriguez J., Kazmierkowski M.P., Espinoza J.R., *et al.* 'State of the art of finite control set model predictive control in power electronics'. *IEEE Trans. on Ind. Informatics*. 2013; 9(2): 1003–1016.
[16] Vazquez S., Leon J.I., Franquelo L.G., *et al.* 'Model predictive control: A review of its applications in power electronics'. *IEEE Industrial Electronics Magazine*. 2014; 8(1): 16–31.
[17] Kouro S. Perez M.A., Rodriguez J., Llor A.M. and Young H.A. 'Model predictive control: MPC's role in the evolution of power electronics'. *IEEE Ind. Electronics Magazine*. 2015; 9(4): 8–21.
[18] Vazquez S., Rodriguez J., Rivera M., Franquelo L.G. and Norambuena M. 'Model predictive control for power converters and drives: advances and trends'. *IEEE Trans. on Ind. Electronics.* 2017; 64(2): 935-947.

[19] Papafotiou G.A., Demetriades G.D. and Agelidis V.G. 'Technology readiness assessment of model predictive control in medium- and high-voltage power electronics'. *IEEE Trans. Ind. Electronics*. 2016; 63(9): 5807–5815.
[20] Riveros J.A., Barrero F., Levi E., Duran M.J., Toral S. and Jones M. 'Variable-speed five-phase induction motor drive based on predictive torque control'. *IEEE Trans. on Ind. Electronics*. 2013; 60(8): 2957–2968.
[21] Preindl M. and Bolognani S. 'Model predictive direct torque control with finite control set for PMSM drive systems, part 1: Maximum torque per ampere operation'. *IEEE Trans. on Ind. Informatics*. 2013; 9(4): 1912–1921.
[22] Miranda H., Cortes P., Yuz J.I. and Rodriguez J. 'Predictive torque control of induction machines based on state-space models'. *IEEE Trans. on Ind. Electronics*. 2009; 56(6): 1916–1924.
[23] Geyer T., Papafotiou G. and Morari M. 'Model predictive direct torque control—part I: Concept, algorithm, and analysis'. *IEEE Trans. on Ind. Electronics*. 2009; 56(6): 1894–1905.
[24] Papafotiou G., Kley J., Papadopoulos K.G., Bohren P. and Morari M. 'Model predictive direct torque control—part II: Implementation and experimental evaluation'. *IEEE Trans. on Ind. Electronics*. 2009; 56(6): 1906–1915.
[25] Casadei D., Profumo F., Serra G. and Tani A. 'FOC and DTC: two viable schemes for induction motors torque control'. *IEEE Trans. Power Electronics*. 2002; 17(5): 779–787.
[26] Takahashi I. and Noguchi T. 'A new quick-response and high-efficiency control strategy of an induction motor'. *IEEE Trans. on Ind. Applications*. 1986; IA-22(5): 820–827.
[27] Vas P. *Sensorless vector and direct torque control*. New York: Oxford Univ. Press, 1998.
[28] Sul S.-K. *Control of electric machine drive systems*. Piscataway, NJ: Wiley-IEEE, 2011.
[29] Depenbrock M. 'Direct self-control (DSC) of inverter-fed induction machine'. *IEEE Trans. on Power Electronics*. 1988; 3(4): 420–429.
[30] Reza C., Didarul Islam M. and Mekhilef S. 'A review of reliable and energy efficient direct torque controlled induction motor drives'. *Renewable and Sustainable Energy Reviews*. 2014; 37: 919–932.
[31] Ohm D.Y. Dynamic model of induction motors for vector control. Blacksburg, Virginia: *Drivetech, Inc*.,, 2001, pp. 1–10.
[32] Holtz J. 'The dynamic representation of ac drive systems by complex signal flow graphs'. *Symposium Proceedings* in *Industrial Electronics, 1994, ISIE'94*; 1994. pp. 1–6.
[33] Vaclavek P. and Blaha P. 'PMSM model discretization for model predictive control algorithms'. *Proceedings of IEEE/SICE Int. Symp. Syst. Integr.*, 2013, pp. 13–18.
[34] Morari M. and Lee J. H. 'Model predictive control: past, present and future'. *Computers & Chemical Engineering'*. 1999; 23(4/5): 667–682.
[35] Rodriguez J., Kennel R.M., Espinoza J.R., Trincado M., Silva C.A. and Rojas C.A. 'High-performance control strategies for electrical drives: an

experimental assessment'. *IEEE Trans. on Ind. Electronics*. 2012; 59(2): 812–820.

[36] Habibullah M., Lu D.D.-C., Xiao D. and Rahman M.F. 'A simplified finite-state predictive direct torque control for induction motor drive'. *IEEE Trans. on Ind. Electronics*. 2016; 63(6): 3964–3975.

[37] Cortes P., Rodriguez J., Silva C. and Flores A. 'Delay compensation in model predictive current control of a three-phase inverter'. *IEEE Trans. on Ind. Electronics*. 2012; 59(2): 1323–1325.

This page intentionally left blank

Chapter 16

Multiphase machine drives

Radu Bojoi[1] *and Luca Zarri*[2]

16.1 Introduction

Variable-speed AC drives are nowadays based on three-phase electrical machines fed by power electronic converters acting as power interface between the electrical machine and AC or DC power sources. Nevertheless, in the last two decades the multiphase electrical drives have become an interesting alternative for particular applications. However, the application of multiphase drives is still limited, mainly due to their complexity and control that somehow make them more difficult to handle with respect to the conventional three-phase counterparts. Therefore, this work intends to be a useful tool to disseminate the fundamental concepts of multiphase drives to students and application engineers.

16.1.1 Definition of a multiphase drive

An electrical drive is defined as multiphase when the number of phases n of the electrical machine is higher than three ($n > 3$) [1]. The electrical machine is supplied by a multiphase power converter whose commands are generated by a control scheme, implementing a specific control strategy and having as input a torque/speed set point. The most generic schematic block of a multiphase motor drive is depicted in Figure 16.1.

16.1.2 Advantages of multiphase drives

As the power generation and distribution uses the three-phase configuration, the standard AC machines are also three-phase. This is a normal choice and it is not expected to change in the future.

In the past, the variable-speed drives were mainly based on DC machines fed by two-/four-quadrant thyristor converters or on three-phase synchronous machines fed by cycloconverters, while the three-phase induction motors were mainly employed by near-constant speed drives since they were directly connected to the grid.

[1]Dipartimento Energia "G. Ferraris", Politecnico di Torino, Italy
[2]Department of Electric, Electronic and Information Engineering "G. Marconi", Università di Bologna, Italy

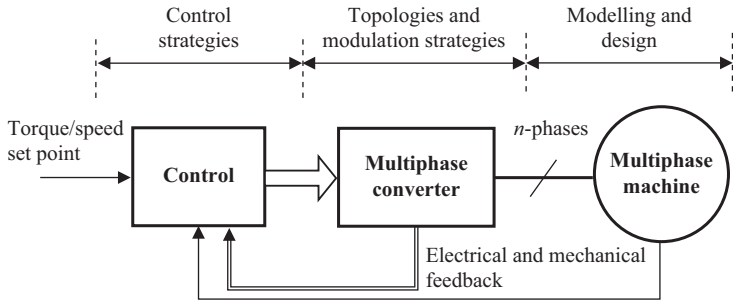


Figure 16.1 Most generic schematic block of a multiphase motor drive

The advent of power electronics and digital microcontrollers after the 1990s allowed an impressive development of inverter-fed variable-speed induction motor drives with the idea of using the same three-phase motor design for cost reasons. Later on, the need for more efficient motor drives led to new three-phase drive solutions based on permanent magnet (PM) machines, using surface mount permanent magnet (SMPM), internal permanent magnet (IPM), synchronous reluctance (SyncRel) and PM-assisted SyncRel rotors.

Independently of the machine technology, the three-phase configuration exhibits two main limitations:

- Given the power level, the phase current can be limited at reasonable levels only by increasing the phase voltage. If the voltage is limited due to the application constraints, the increase in power level would produce a significant increase in the phase currents that would be difficult to manage with the power electronics without special paralleling techniques.
- Limited fault tolerance in case of the fault of one or more phases is the other limitation.

In spite of their increased complexity, the multiphase drives possess several advantages with respect to their three-phase counterparts [1]:

- Lower phase current for the same rated voltage and power due to the power splitting. As example, the use of a six-phase machine halves the phase current with respect to a three-phase machine counterpart and allows using power switches and current sensors of halved rated current.
- Fault-tolerant operation since the multiphase drives can run with one or more open phases due to their redundant structure.
- Reduced root mean square (RMS) current stress of the inverter DC-link input capacitor.
- Inherent multilevel nature of the generated phase voltage.
- Lower torque pulsations, especially for square-wave voltage supply.
- Additional ‘degrees of freedom’ that includes the torque density improvement through harmonic current injection and independent control of series-connected machines.

It is obvious that the advantages of multiphase drives make them particularly interesting in high-power and low-voltage/high-current applications, as well as for safety-critical applications.

16.1.3 A brief history of multiphase motor drives

The power splitting to reduce the phase currents was the main driver to the genesis of the multiphase systems in the 1920s for power generation, when three-phase machine was converted into a six-phase one to overcome the current limit imposed by the circuit breakers of that period [2].

The next attempt was reported after almost five decades in 1969, when a five-phase induction motor drive was investigated in [3]. A few years later (1974), a six-phase induction motor drive with square-wave voltage supply was analysed in [4]; the authors demonstrated that the particular six-phase configuration eliminates the sixth-order torque pulsations that are usually present for a three-phase drive.

The interest for multiphase drives started to grow significantly in the 1990s for marine applications, which adopted the multiphase drives for both ship propulsion and power generation due to obvious advantages given by the power splitting and fault-tolerant features [5].

The evolution of the scientific papers on multiphase drives starting from 1980 up to nowadays is presented in [6], demonstrating an exponential increase of publications covering all aspects regarding the multiphase drives: machine and converter design, modelling and simulation, power converter modulation techniques, drive control strategies and special solutions exploiting the new degrees of freedom. In addition, the literature reports several survey papers [1,5,7–12] that can provide a comprehensive review of the past and recent advancements in this field [13–37].

16.1.4 Applications

The multiphase drives are suitable for high-power applications (MW levels) and low-voltage/high-current applications to exploit the benefits coming from the power splitting and the increased reliability for safety. Therefore, the multiphase drives can be successfully used in transportation electrification and energy production, as shown in Figure 16.2.

1. *Ship propulsion and generation*. The world's first electric warship, UK 'Daring class' Type-45 Destroyer has been put in service from 2007 and it is equipped for the propulsion with two 15-phase, 20 MW, 4.16 kV induction motors fed by pulse width modulation (PWM), insulated gate bipolar transistor (IGBT) inverters. A similar solution employing 15-phase induction motors has been put on service on the all-electric Zumwalt class destroyers for US Navy. Other solutions for propulsion are based on 12-phase machines and 9-phase machines. It is interesting to notice that the preferred solution is the multi-three-phase one that benefits on the modularity of three-phase power electronics.
2. *Aircraft*. Some low power solutions for electrical actuators (such as nose wheel steering for green taxi services or fuel pumps) use six-phase or four-phase motor drives. As far as concerning the power generation, the multiphase

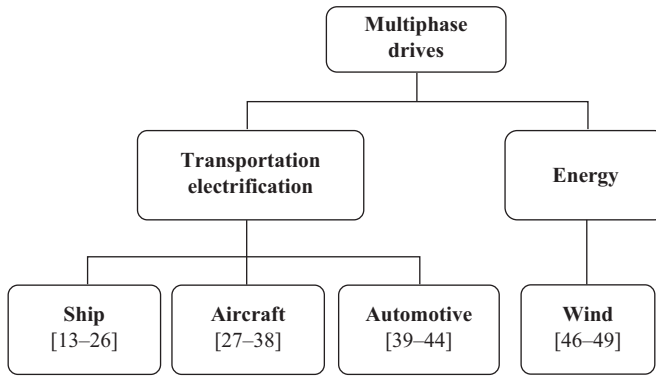


Figure 16.2 Most important applications of multiphase drives along with references

solution is particularly convenient for 28 Vdc generation on small aircrafts or helicopters, where the current per phase can be reduced. The multiphase solution can be also used for power generation at 270 Vdc, typically using brushless three-stage wound rotor synchronous generators.

3. *Automotive and traction*. The penetration of multiphase drives is rather low in automotive applications. This situation is not so surprising since the power levels are of order of hundreds of kilowatts, where the three-phase technology is reliable and cost-effective. However, some attempts have been made for low-voltage systems fed at 48 Vdc, where the power splitting can be successfully used to reduce the power levels. The most popular solution available in production belongs to Robert Bosch Gmbh for a five-phase starter–alternator and a five-phase generator, both with integrated power electronics [44]. The company Hyundai used for a fast elevator a 1.1 MW, 9-phase PM motor drive using a modular multi-three-phase structure, where each three-phase set is fed by a three-phase AC/DC/AC converter with back-to-back configuration [45].
4. *Wind generation*. Although the most part of the solutions for wind energy is based on three-phase doubly fed induction generators, recently some companies decided to go towards direct drive solutions based on multiphase PM generators. Besides the benefits coming from the fault tolerance, the low-speed solutions allow at reducing the complexity or even eliminating the gearbox between the propeller and the generator shaft. As example, the company Gamesa has launched a new series of 5 MW wind turbines based on 12-phase PM generators [46]. The generator has a modular three-phase structure, where each stator winding set is connected to a 1.25 MW three-phase AC/DC/AC converter using two three-phase voltage source converters (VSC) with back-to-back configuration. Once again, it is evident the choice of a multi-three-phase configuration since the modular three-phase power electronic units are already available and can be reused to increase the power level without adopting paralleling techniques [39–49].

16.2 Multiphase electrical machines

Multiphase machines are divided into symmetrical or asymmetrical machines, depending on the electrical displacement between the magnetic axes of two stator adjacent phases. A symmetrical machine has a spatial displacement γ of $360/n$ electrical degrees between the magnetic axes of two consecutive stator phases. As example, a five-phase machine has a spatial displacement γ of 72 electrical degrees between two consecutive stator phases. When the number of phases is an even number or an odd number that is not a prime number, the machine can be seen as m sets having a phases each [8]. Typically $a = 3$ (three-phase sets), $m = 2, 3, 4, 5, \ldots$, and the spatial displacement between the first phases of two consecutive sets is $180/n$ electrical degrees.

As example, an asymmetrical six-phase machine has $m = 2$ three phase sets ($a = 3$) and the spatial displacement between the first phases of the two three-phase sets is 30 electrical degrees. An asymmetrical 12-phase machine has $m = 4$ three phase sets and the spatial displacement between the first phases of two consecutive sets is 15 electrical degrees. Different symmetrical and asymmetrical multiphase machines stator configurations are shown in Figure 16.3.

Undoubtedly, the most employed multiphase machine type is the induction machine (IM), due to its rugged construction and consolidated technology, as well

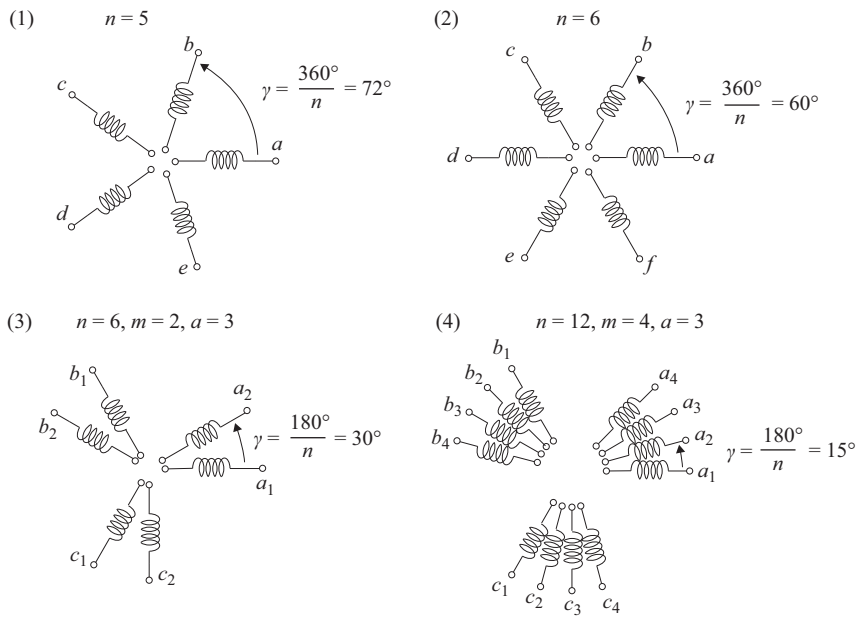


Figure 16.3 Multiphase stator configurations: (1) symmetrical five-phase machine, (2) symmetrical six-phase machine, (3) asymmetrical six-phase machine and (4) asymmetrical 12-phase machine

for its capability to work with square wave supply employing voltage source inverters (VSIs) or current source inverters (CSIs). The other machine types used in multiphase drives are [9] wound rotor synchronous machine, SMPM machine, IPM machine and switched reluctance machine (SRM).

With exception of the IM that are usually designed with distributed windings (DW), the synchronous machines can be designed either with DW or with fractional-slot concentrated windings (FSCW) that are characterized by shorter end-windings length with consequent reduction of Joule losses. Moreover, the FSCW allow obtaining a high phase inductance to limit the current circulation in case of short-circuit faults.

The five-phase and six-phase machine ones are the most employed solutions. The other solutions include 7-phase, 9-phase, 12-phase and 15-phase ones, the last one being very common for ship applications for obvious reasons coming from the high power levels (MW).

The design of multiphase machines follows the basic principles that are normally used for the three-phase machines to obtain an air-gap magnetomotive force (MMF) having a specific harmonic content [50]. If the stator uses DW, it is more convenient to use fully pitched windings to avoid the leakage mutual couplings between phases.

The objective of this section is to provide the basic modelling principles of multiphase machines. In most general case, the model of any multiphase machine in phase time domain contains $4n + 3$ equations, as described in the following:

- n stator electrical equations;
- n rotor electrical equations (only for IMs and for synchronous machines with damper cage);
- n stator magnetic equations representing current-to-stator flux relationship;
- n rotor magnetic equations representing current-to-rotor flux relationship (only for IMs and for synchronous machines with damper cage);
- one equation representing the expression of the electromagnetic torque;
- two mechanical equations; the first one is the mechanical model referred to the machine shaft, the other one is the integral equation of the mechanical speed to get the mechanical rotor position.

The machine model in phase coordinates involves $n \times 1$ vectors representing the phase quantities (voltages, currents and flux linkages) and $n \times n$ matrices of parameters (resistances and inductances). As happens for the three-phase machines, the multiphase machine model can be manipulated to get a model that emphasizes better the flux and torque production variables, so it is better for control purposes. The model manipulation can be performed using two modelling approaches that are described next.

16.2.1 VSD approach

The vector space decomposition (VSD) approach was developed in [51] for an asymmetrical six-phase IM. Later on, the VSD general formulation was given in [1] and [52] for other number of phases.

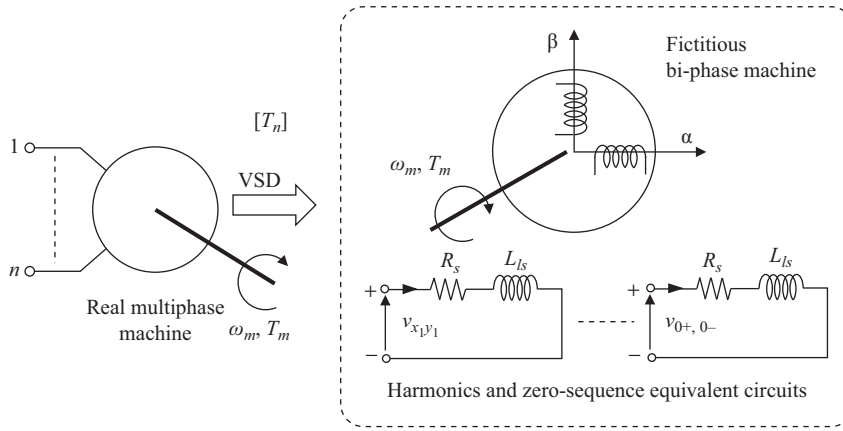


Figure 16.4 Meaning of the VSD approach based on the generalized Clarke transformation using the VSD transformation matrix

The VSD approach decomposes the machine original space, using an $n \times n$ transformation matrix $[T_n]$, into several multiple decoupled subspaces. The main subspace (α,β) contains the flux- and torque-producing current components, while the other subspaces contain harmonics and zero-sequence components with no contributions to the electromechanical energy conversion. The $n \times n$ transformation matrix can be seen as the generalized Clarke transformation applied for multiphase systems to get an equivalent bi-phase machine, as shown in Figure 16.4.

The expressions of the VSD transformation matrices depend on the machine configuration, i.e. symmetrical or asymmetrical. The VSD transformation matrix can be obtained using the procedure from [52] and is briefly described in the following.

16.2.1.1 Symmetrical machines

As shown in Figure 16.3, a symmetrical machine with n phases exhibits a phase propagation angle $\gamma = 2\pi/n$ that defines the following angle $1 \times n$ vector:

$$\theta = [\,0 \quad \gamma \quad 2\gamma \quad .... \quad (n-1)\gamma\,] \tag{16.1}$$

The VSD transformation matrix for symmetrical machines is defined as

$$n = \text{odd} \Rightarrow [T_n] = \sigma \cdot \begin{bmatrix} \cos(\theta) \\ \sin(\theta) \\ \cos(2\theta) \\ \sin(2\theta) \\ ..... \\ \cos(k\theta) \\ \sin(k\theta) \\ \sigma_{zs} \cdot \cos(n\theta) \end{bmatrix}, \quad k < \frac{n}{2} \tag{16.2}$$

$$n = \text{even} \Rightarrow [T_n] = \sigma \cdot \begin{bmatrix} \cos(\theta) \\ \sin(\theta) \\ \cos(2\theta) \\ \sin(2\theta) \\ ..... \\ \cos(k\theta) \\ \sin(k\theta) \\ \sigma_{zs} \cdot \cos(n\theta) \\ \sigma_{zs} \cdot \cos\left(\frac{n}{2}\theta\right) \end{bmatrix}, \quad k < \frac{n}{2} \tag{16.3}$$

where

$$\sigma = \frac{2}{n},\ \sigma_{ZS} = \frac{1}{2} - \text{for the amplitude-invariant form} \tag{16.4}$$

$$\sigma = \sqrt{\frac{2}{n}},\ \sigma_{ZS} = \frac{1}{\sqrt{2}} - \text{for the power-invariant form} \tag{16.5}$$

Different symmetrical multiphase machines, along with their VSD transformation matrix using amplitude-invariant form, are provided in Figures 16.5 and 16.6.

16.2.1.2 Asymmetrical machines

An asymmetrical machine with n phases exhibits a phase propagation angle $\gamma = \pi/n$, as shown in Figure 16.3. Typically, an asymmetrical machine can be seen as a multiple three-phase machine having m three-phase sets. Therefore, the $1 \times n$ vector angle is defined as

$$\theta = \left[0 \quad \frac{2\pi}{3} \quad \frac{4\pi}{3} \quad \gamma \quad \gamma + \frac{2\pi}{3} \quad \gamma + \frac{4\pi}{3} \quad \ldots \quad (m-1)\gamma \quad (m-1)\gamma + \frac{2\pi}{3} \quad (m-1)\gamma + \frac{4\pi}{3}\right] \tag{16.6}$$

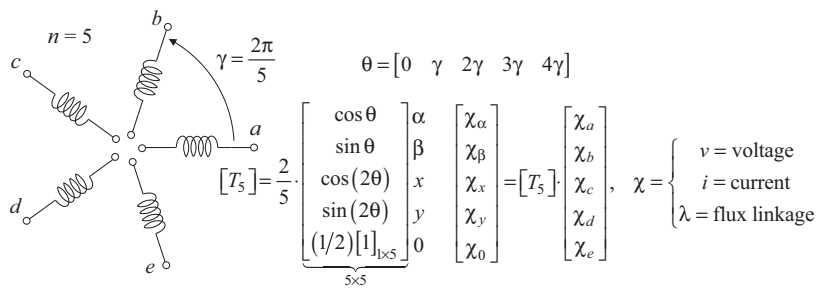


Figure 16.5 Five-phase symmetrical machine and related amplitude-invariant VSD transformation matrix

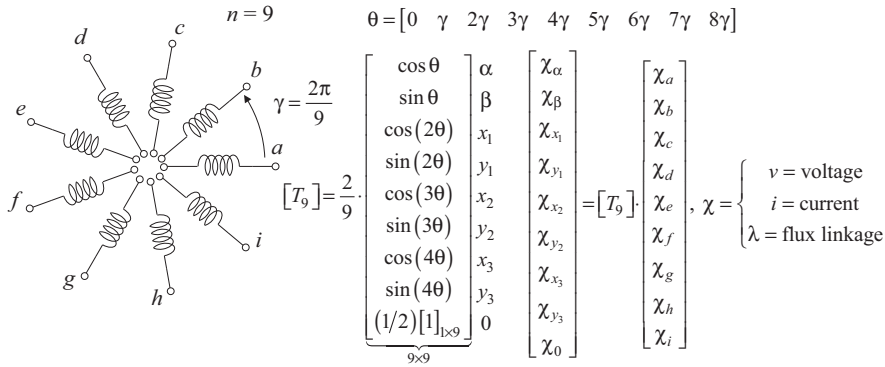


Figure 16.6 Nine-phase symmetrical machine and related amplitude-invariant VSD transformation matrix

The VSD transformation matrix is obtained as

$$[T_n] = \sigma \cdot \begin{bmatrix} \cos(\theta) \\ \sin(\theta) \\ \cos(5\theta) \\ \sin(5\theta) \\ ..... \\ \cos(k\theta) \\ \sin(k\theta) \\ \sigma_{ZS}[ZS] \end{bmatrix}, \begin{matrix} k = 5, 7, 11.. < n \\ k \neq 3i, i \in N \end{matrix}, [ZS] = \begin{bmatrix} \cos(3\theta) \\ \sin(3\theta) \\ ..... \\ \cos(k\theta) \\ \sin(k\theta) \end{bmatrix}, \begin{matrix} k = 3(2i+1) \\ k < n \end{matrix} \tag{16.7}$$

Different asymmetrical multiphase machines along with their amplitude-invariant VSD transformation matrix are provided in Figures 16.7 and 16.8.

16.2.1.3 Features of VSD approach

The VSD approach presents the highest degree of generality as it can be applied for any multiphase machine.

The main subspace (α,β) contains the variables involved in the electro-mechanical energy conversion:

- For five-phase machines, the (α,β) subspace contains the fundamental frequency and time harmonics components of order $10 \cdot i \pm 1, i = 1, 2, ...$(9,11, ...).
- For asymmetrical six-phase machines, the (α,β) subspace contains the fundamental frequency and time harmonics components of order $12 \cdot i \pm 1, i = 1, 2, ...$(11,13, ...).

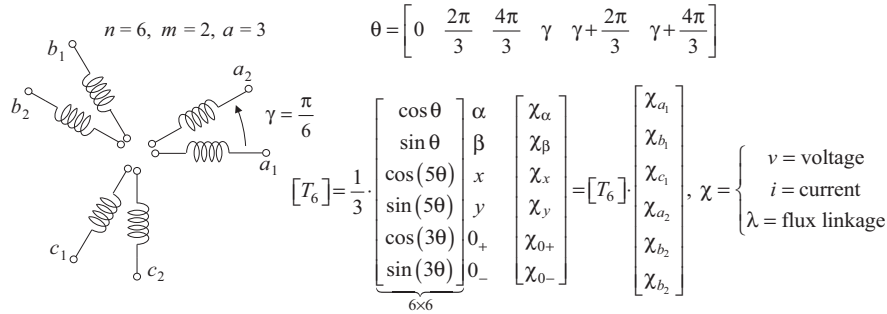


Figure 16.7 Six-phase asymmetrical machine and related amplitude-invariant VSD transformation matrix

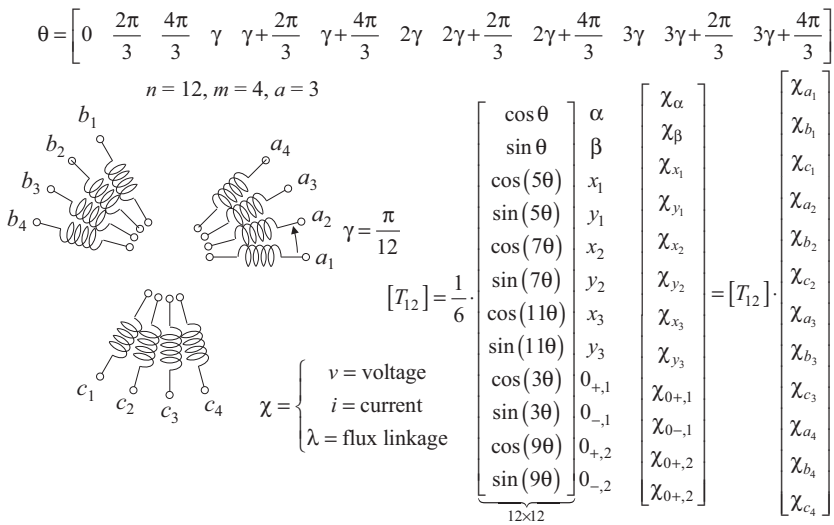


Figure 16.8 Twelve-phase asymmetrical machine and related amplitude-invariant VSD transformation matrix

The (x,y) subspaces contain circulating currents that are not involved in the electromechanical energy conversion, so they are loss-producing components:

- For five-phase machines, the (x,y) subspace contains time harmonics of order $10 \cdot i \pm 3, i = 0, 1, ...(3,7,13)$.
- For asymmetrical six-phase machines, the (x,y) subspace contains time harmonics of order $(12 \cdot i + 6) \pm 1, i = 0, 1, ...(5,7,17,19)$.

The homopolar subspaces contain DC components and additional harmonics:

- For five-phase machines, the homopolar component contains harmonics of order $10 \cdot i \pm 5, i = 0, 1, ...(5,15, \ldots)$.
- For asymmetrical six-phase machines, the zero-sequence subspace contains time harmonics of order $3 \cdot i, i = 1, 3, 5...(3,9, \ldots)$.

In case of balanced operation and ideal supply and machine design, the currents in the (x,y) subspaces should be zero. However, in case of imbalanced operation, the (x,y) subspaces will contain currents at fundamental frequency.

In case of PM machines, if the back-emf voltages are not sinusoidal with harmonics mapped in one of the (x,y) subspaces, then high circulating currents may occur. In this case, the machine control must take care of (x,y) subspaces to cancel the undesired current that would reduce the drive efficiency.

It must be emphasized here that the VSD transformation matrix becomes heavy for machines with a number of phases higher than six.

16.2.1.4 Case study 1: asymmetrical six-phase IM

Under the assumption of having fully pitched stator windings and of neglecting the iron losses, the machine VSD model can be obtained by applying the VSD transformation matrix to the machine model in phase coordinates [53]. Using the complex vector notation, the machine VSD model is described by (16.8).

The equivalent single-phase electrical circuits resulting from the VSD theory are shown in Figure 16.9.

$$
\begin{aligned}
&\bar{v}_{\alpha\beta} = R_s \cdot \bar{i}_{\alpha\beta} + \frac{d}{dt}\bar{\lambda}_{s\alpha\beta} && \bar{\lambda}_{s\alpha\beta} = L_s \cdot \bar{i}_{\alpha\beta} + L_m \cdot \bar{i}_{r\alpha\beta} \\
&\bar{0} = R_r \cdot \bar{i}_{r\alpha\beta} + \frac{d}{dt}\bar{\lambda}_{r\alpha\beta} - j \cdot p \cdot \omega_m \cdot \bar{\lambda}_{r\alpha\beta} && \bar{\lambda}_{r\alpha\beta} = L_m \cdot \bar{i}_{\alpha\beta} + L_r \cdot \bar{i}_{r\alpha\beta} \\
&v_x = R_s \cdot i_x + \frac{d}{dt}\lambda_{sx} && \lambda_{sx} = L_{ls} \cdot i_x \\
&v_y = R_s \cdot i_y + \frac{d}{dt}\lambda_{sy} && \lambda_{sy} = L_{ls} \cdot i_y \\
&v_{0+} = R_s \cdot i_{0+} + \frac{d}{dt}\lambda_{s0+} && \lambda_{s0+} = L_{ls} \cdot i_{0+} \\
&v_{0-} = R_s \cdot i_{0-} + \frac{d}{dt}\lambda_{s0-} && \lambda_{s0-} = L_{ls} \cdot i_{0-}
\end{aligned}
$$

$$
T_e = k_T \cdot p \cdot \left(\bar{\lambda}_{s\alpha\beta} \wedge \bar{i}_{\alpha\beta}\right) = k_T \cdot p \cdot \left(\lambda_{s\alpha} \cdot i_\beta - \lambda_{s\beta} \cdot i_\alpha\right)
$$

$$
k_T = \begin{cases} 3 \text{ - amplitude invariant VSD } [T_6] \\ 1 \text{ - power invariant VSD } [T_6] \end{cases}
$$

$$
\bar{v}_{\alpha\beta} = v_\alpha + j \cdot v_\beta, \quad \bar{i}_{\alpha\beta} = i_\alpha + j \cdot i_\beta, \quad \bar{i}_{r\alpha\beta} = i_{r\alpha} + j \cdot i_{r\beta}
$$

$$
\bar{\lambda}_{s\alpha} = \lambda_{s\alpha} + j \cdot \lambda_{s\beta}, \quad \bar{\lambda}_{r\alpha} = \lambda_{r\alpha} + j \cdot \lambda_{r\beta} \tag{16.8}
$$

where R_s and R_r are the stator and rotor resistances, L_s and L_r are the stator and rotor inductances, L_m is the magnetizing inductance, L_{ls} and L_{lr} are the stator and rotor leakage inductances, ω_m is the rotor mechanical speed, p is the pole-pairs number and k_T is the torque gain depending on the VSD matrix (amplitude invariant or power invariant).

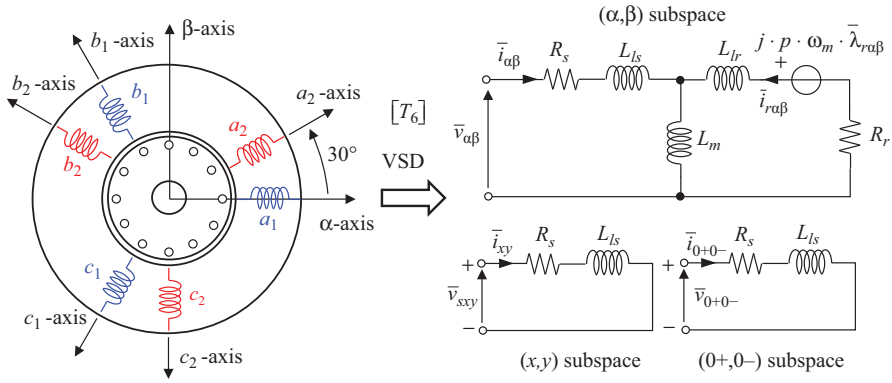


Figure 16.9 Asymmetrical six-phase induction equivalent circuits according to VSD theory

The machine model in (α,β) subspace can be further manipulated to refer it to a rotating (d,q) frame, using the rotational transformation that is the same as the one used for three-phase machines. The rotating (d,q) frame can be defined by the machine stator flux vector or the rotor flux vector, as discussed later in the subsection dedicated to control strategies.

16.2.1.5 Case study 2: asymmetrical IPM machine

An IPM machine exhibits rotor magnetic anisotropy, as the two-pole theoretical machine shown in Figure 16.10. Usually, the rotor d-axis is defined as the North pole axis, using the rule that is normally employed for the SMPM machines.

Assuming fully pitched stator windings, the magnetic model in phase coordinates of a six-phase asymmetrical IPM machine is

$$[\lambda]_{a_1b_1c_1a_2b_2c_2} = L_{ls} \cdot [i]_{a_1b_1c_1a_2b_2c_2} + [M(2\vartheta)] \cdot [i]_{a_1b_1c_1a_2b_2c_2} + [\lambda_m]_{a_1b_1c_1a_2b_2c_2}$$

$$[\lambda]_{a_1b_1c_1a_2b_2c_2} = \begin{bmatrix} \lambda_{a1} \\ \lambda_{b1} \\ \lambda_{c1} \\ \lambda_{a2} \\ \lambda_{b2} \\ \lambda_{c2} \end{bmatrix}, [i]_{a_1b_1c_1a_2b_2c_2} = \begin{bmatrix} i_{a1} \\ i_{b1} \\ i_{c1} \\ i_{a2} \\ i_{b2} \\ i_{c2} \end{bmatrix}, [\lambda_m]_{a_1b_1c_1a_2b_2c_2} = \lambda_m \cdot \begin{bmatrix} \cos(\vartheta) \\ \cos\left(\vartheta - \frac{2\pi}{3}\right) \\ \cos\left(\vartheta + \frac{2\pi}{3}\right) \\ \cos\left(\vartheta - \frac{\pi}{6}\right) \\ \cos\left(\vartheta - \frac{5\pi}{6}\right) \\ \cos\left(\vartheta + \frac{\pi}{2}\right) \end{bmatrix} \quad (16.9)$$

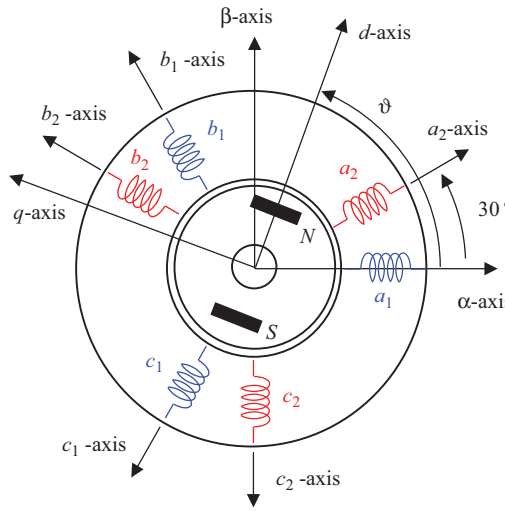


Figure 16.10 Theoretical two-pole asymmetrical IPM machine

where L_{ls} is the stator leakage inductance, $\vartheta = p \cdot \vartheta_m$ is the electrical rotor position, p is the pole-pairs number, ϑ_m is the rotor mechanical position, λ_m is back-emf constant (magnet flux linkage amplitude) and $[M(2\vartheta)]\cdot$ is a 6×6 matrix of stator mutual inductances defined as

$$[M(2\vartheta)] = \begin{bmatrix} M_{S_1S_1} & M_{S_1S_2} \\ M_{S_2S_1} & M_{S_2S_2} \end{bmatrix}, \quad S_1 = a_1b_1c_1, \quad S_2 = a_2b_2c_2$$

$$M_{S_1S_1} = \begin{bmatrix} M_{a_1a_1} & M_{a_1b_1} & M_{a_1c_1} \\ M_{b_1a_1} & M_{b_1b_1} & M_{b_1c_1} \\ M_{c_1a_1} & M_{c_1b_1} & M_{c_1c_1} \end{bmatrix}, \; M_{S_2S_2} = \begin{bmatrix} M_{a_2a_2} & M_{a_2b_2} & M_{a_2c_2} \\ M_{b_2a_2} & M_{b_2b_2} & M_{b_2c_2} \\ M_{c_2a_2} & M_{c_2b_2} & M_{c_2c_2} \end{bmatrix}$$

$$M_{S_1S_2} = \begin{bmatrix} M_{a_1a_2} & M_{a_1b_2} & M_{a_1c_2} \\ M_{b_1a_2} & M_{b_1b_2} & M_{b_1c_2} \\ M_{c_1a_2} & M_{c_1b_2} & M_{c_1c_2} \end{bmatrix}, \; M_{S_2S_1} = \begin{bmatrix} M_{a_2a_1} & M_{a_2b_1} & M_{a_2c_1} \\ M_{b_2a_1} & M_{b_2b_1} & M_{b_2c_1} \\ M_{c_2a_1} & M_{c_2b_1} & M_{c_2c_1} \end{bmatrix} = [M_{S_1S_2}]^t \tag{16.10}$$

The magnetic model can be manipulated by defining M_d as the phase self-inductance when the rotor d-axis is aligned with the phase axis, while M_q as the

phase self-inductance when the rotor q-axis is aligned with the phase axis. Using the M_d and M_q, the following inductances can be further defined:

$$\begin{cases} M_i = \dfrac{M_d + M_q}{2} \\ M_a = \dfrac{M_d - M_q}{2} \end{cases}, \quad M_d < M_q \tag{16.11}$$

The mutual coupling matrices are expressed as

$$[M_{S_1S_2}] = \begin{bmatrix} M_i + M_a \cdot \cos(2\vartheta) & -\frac{1}{2}\cdot M_i + M_a \cdot \cos\left(2\vartheta - \frac{2\pi}{3}\right) & -\frac{1}{2}\cdot M_i + M_a \cdot \cos\left(2\vartheta + \frac{2\pi}{3}\right) \\ -\frac{1}{2}\cdot M_i + M_a \cdot \cos\left(2\vartheta - \frac{2\pi}{3}\right) & M_i + M_a \cdot \cos\left(2\vartheta + \frac{2\pi}{3}\right) & -\frac{1}{2}\cdot M_i + M_a \cdot \cos(2\vartheta) \\ -\frac{1}{2}\cdot M_i + M_a \cdot \cos\left(2\vartheta + \frac{2\pi}{3}\right) & -\frac{1}{2}\cdot M_i + M_a \cdot \cos(2\vartheta) & M_i + M_a \cdot \cos\left(2\vartheta - \frac{2\pi}{3}\right) \end{bmatrix}$$

$$[M_{S_2S_2}] = \begin{bmatrix} M_i + M_a \cdot \cos\left(2\vartheta - \frac{\pi}{3}\right) & -\frac{1}{2}\cdot M_i + M_a \cdot \cos(2\vartheta - \pi) & -\frac{1}{2}\cdot M_i + M_a \cdot \cos\left(2\vartheta + \frac{\pi}{3}\right) \\ -\frac{1}{2}\cdot M_i + M_a \cdot \cos(2\vartheta - \pi) & M_i + M_a \cdot \cos\left(2\vartheta + \frac{\pi}{3}\right) & -\frac{1}{2}\cdot M_i + M_a \cdot \cos\left(2\vartheta - \frac{\pi}{3}\right) \\ -\frac{1}{2}\cdot M_i + M_a \cdot \cos\left(2\vartheta + \frac{\pi}{3}\right) & -\frac{1}{2}\cdot M_i + M_a \cdot \cos\left(2\vartheta - \frac{\pi}{3}\right) & M_i + M_a \cdot \cos(2\vartheta - \pi) \end{bmatrix}$$

$$[M_{S_1S_2}] = \begin{bmatrix} \frac{\sqrt{3}}{2} M_i + M_a \cdot \cos\left(2\vartheta - \frac{\pi}{6}\right) & -\frac{\sqrt{3}}{2}\cdot M_i + M_a \cdot \cos\left(2\vartheta - \frac{5\pi}{6}\right) & M_a \cdot \cos\left(2\vartheta + \frac{\pi}{2}\right) \\ M_a \cdot \cos\left(2\vartheta - \frac{5\pi}{6}\right) & \frac{\sqrt{3}}{2}\cdot M_i + M_a \cdot \cos\left(2\vartheta + \frac{\pi}{2}\right) & -\frac{\sqrt{3}}{2}\cdot M_i + M_a \cdot \cos\left(2\vartheta - \frac{\pi}{6}\right) \\ -\frac{\sqrt{3}}{2}\cdot M_i + M_a \cdot \cos\left(2\vartheta + \frac{\pi}{2}\right) & M_a \cdot \cos\left(2\vartheta - \frac{\pi}{6}\right) & \frac{\sqrt{3}}{2}\cdot M_i + M_a \cdot \cos\left(2\vartheta - \frac{5\pi}{6}\right) \end{bmatrix} \tag{16.12}$$

The application of the amplitude-invariant VSD transformation to the magnetic model yields the following equations in matrix form of the machine model:

$$\begin{bmatrix} \lambda_\alpha \\ \lambda_\beta \end{bmatrix} = \begin{bmatrix} L_{ls} + 3 \cdot M_i + 3 \cdot M_a \cos(2\vartheta) & 3 \cdot M_a \sin(2\vartheta) \\ 3 \cdot M_a \sin(2\vartheta) & L_{ls} + 3 \cdot M_i - 3 \cdot M_a \cos(2\vartheta) \end{bmatrix} \cdot \begin{bmatrix} i_\alpha \\ i_\beta \end{bmatrix} + \lambda_m \cdot \begin{bmatrix} \cos(\vartheta) \\ \sin(\vartheta) \end{bmatrix}$$

$$\begin{bmatrix} \lambda_x \\ \lambda_y \end{bmatrix} = \begin{bmatrix} L_{ls} & 0 \\ 0 & L_{ls} \end{bmatrix} \cdot \begin{bmatrix} i_x \\ i_y \end{bmatrix}$$

$$\begin{bmatrix} \lambda_{0+} \\ \lambda_{0-} \end{bmatrix} = \begin{bmatrix} L_{ls} & 0 \\ 0 & L_{ls} \end{bmatrix} \cdot \begin{bmatrix} i_{0+} \\ i_{0-} \end{bmatrix} \tag{16.13}$$

The complete machine model is obtained by adding the electrical equations and the expression of the electromagnetic torque:

$$\begin{aligned}
\bar{v}_{\alpha\beta} &= R_s \cdot \bar{i}_{\alpha\beta} + \frac{d}{dt}\bar{\lambda}_{\alpha\beta} \\
v_x &= R_s \cdot i_{sx} + \frac{d}{dt}\lambda_{sx} \\
v_y &= R_s \cdot i_{sy} + \frac{d}{dt}\lambda_{sy} \\
v_{0+} &= R_s \cdot i_{0+} + \frac{d}{dt}\lambda_{0+} \\
v_{0-} &= R_s \cdot i_{0-} + \frac{d}{dt}\lambda_{0-} \\
T_e &= k_T \cdot p \cdot \left(\bar{\lambda}_{\alpha\beta} \wedge \bar{i}_{\alpha\beta}\right) = k_T \cdot p \cdot \left(\lambda_\alpha \cdot i_\beta - \lambda_\beta \cdot i_\alpha\right) \\
k_T &= \begin{cases} 3 \text{ - amplitude-invariant VSD } [T_6] \\ 1 \text{ - power-invariant VSD } [T_6] \end{cases} \\
\bar{v}_{\alpha\beta} &= v_\alpha + j \cdot v_\beta, \quad \bar{i}_{\alpha\beta} = i_\alpha + j \cdot i_\beta, \quad \bar{\lambda}_{\alpha\beta} = \lambda_\alpha + j \cdot \lambda_\beta
\end{aligned} \tag{16.14}$$

It is a common practice to refer the machine model to the rotor (d,q) reference frame by using the rotational transformation with the rotor electrical position:

$$[T_{rot}(\vartheta)] = \begin{bmatrix} \cos(\vartheta) & \sin(\vartheta) \\ -\sin(\vartheta) & \cos(\vartheta) \end{bmatrix}, \quad \vartheta = p \cdot \vartheta_m \tag{16.15}$$

The machine model in (d,q) frame results as

$$\begin{aligned}
\begin{bmatrix} v_d \\ v_q \end{bmatrix} &= \begin{bmatrix} R_s & 0 \\ 0 & R_s \end{bmatrix} \cdot \begin{bmatrix} i_d \\ i_q \end{bmatrix} + \frac{d}{dt}\begin{bmatrix} \lambda_d \\ \lambda_q \end{bmatrix} + \omega \cdot \begin{bmatrix} 0 & -1 \\ 1 & 0 \end{bmatrix} \cdot \begin{bmatrix} \lambda_d \\ \lambda_q \end{bmatrix} \\
\begin{bmatrix} \lambda_d \\ \lambda_q \end{bmatrix} &= \begin{bmatrix} L_d & 0 \\ 0 & L_q \end{bmatrix} \cdot \begin{bmatrix} i_d \\ i_q \end{bmatrix} + \begin{bmatrix} \lambda_m \\ 0 \end{bmatrix} \\
L_d &= L_{ls} + 3 \cdot M_d, \quad L_q = L_{ls} + 3 \cdot M_q \\
T_e &= k_T \cdot p \cdot \left(\bar{\lambda}_{dq} \wedge \bar{i}_{dq}\right) = k_T \cdot p \cdot \left(\lambda_d \cdot i_q - \lambda_q \cdot i_d\right) \\
k_T &= \begin{cases} 3 \text{ - amplitude-invariant VSD } [T_6] \\ 1 \text{ - power-invariant VSD } [T_6] \end{cases} \\
\bar{v}_{dq} &= v_d + j \cdot v_q, \quad \bar{i}_{dq} = i_d + j \cdot i_q, \quad \bar{\lambda}_{dq} = \lambda_d + j \cdot \lambda_q \\
\omega &= \frac{d\vartheta}{dt} = p \cdot \omega_m = p \cdot \frac{d\vartheta_m}{dt}
\end{aligned} \tag{16.16}$$

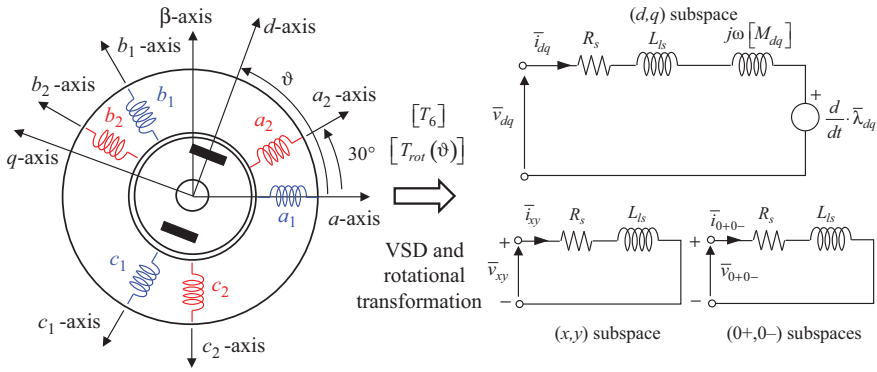


Figure 16.11 Asymmetrical six-phase IPM machine equivalent circuits according to VSD theory and using rotational transformation

The machine equivalent electrical circuits resulting from the amplitude-invariant VSD transformation are shown in Figure 16.11.

16.2.2 Multi-stator approach

The multi-stator (MS) approach is convenient for machines having the number of phases that is multiple of three. This approach has been used for the first time in [4] for an asymmetrical six-phase IM.

The main advantage of this approach is the clear separation of the flux and torque contributions of the single three-phase machine sets. This aspect represents an interesting feature for a modular machine control that deals with independent three-phase inverter units. With respect to the VSD approach where the average currents are controlled, the MS approach allows a direct control of the machine's currents. The MS approach needs a general three-phase Clarke transformation to get the machine model in stationary (α,β) frame. The general three-phase Clarke transformation has its amplitude-invariant form defined as

$$[T_i]=\frac{2}{3}\cdot\begin{bmatrix}\cos(\vartheta_i) & \cos\left(\vartheta_i+\frac{2\pi}{3}\right) & \cos\left(\vartheta_i-\frac{2\pi}{3}\right)\\ \sin(\vartheta_i) & \sin\left(\vartheta_i+\frac{2\pi}{3}\right) & \sin\left(\vartheta_i-\frac{2\pi}{3}\right)\\ 1/2 & 1/2 & 1/2\end{bmatrix},\quad \vartheta_i=k\cdot\gamma,\quad k=0,1,...,m-1 \tag{16.17}$$

The MS approach simplifies significantly the modelling for machines having a large number of phases (>6). That is possible due to the use of simple three-phase Clarke transformations. Given a multiple three-phase machine having *m* three-phase sets, the MS approach will lead to a fictitious multiple bi-phase machine having *m* pairs of windings and *m* zero-sequence circuits, as shown in Figure 16.12.

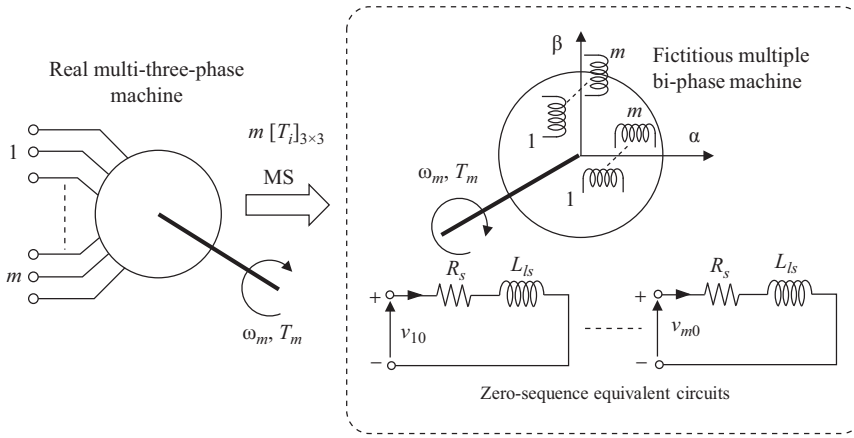


Figure 16.12 Meaning of the MS approach based on multiple modified 3 × 3 Clarke transformation matrices

16.2.2.1 Case study 3: asymmetrical 12-phase IM

For the most general case, the stator consists of m three-phase winding sets, while the rotor is modelled as a three-phase winding.

As described in detail in [9], the (α,β) motor model is obtained as

$$\begin{aligned}
\bar{v}_{k,\alpha\beta} &= R_s \cdot \bar{i}_{k,\alpha\beta} + \frac{d}{dt}\bar{\lambda}_{sk,\alpha\beta}, \quad k = 1,2,...,m \\
\bar{0} &= \frac{R_r}{m} \cdot \bar{i}_{r,\alpha\beta} + \frac{d}{dt}\bar{\lambda}_{r,\alpha\beta} - j \cdot p \cdot \omega_m \cdot \bar{\lambda}_{r,\alpha\beta}, \quad k = 1,2,...,m \qquad (16.18) \\
v_{k0} &= R_s \cdot i_{k0} + \frac{d}{dt}\lambda_{sk0}, \quad \lambda_{sk0} = L_{ls} \cdot i_{k0}, \quad k = 1,2,...,m \\
\bar{\lambda}_{sk,\alpha\beta} &= L_{ls} \cdot \bar{i}_{k,\alpha\beta} + \frac{L_m}{m} \cdot \sum_{z=1}^{m} \bar{i}_{z,\alpha\beta} + \frac{L_m}{m} \cdot \bar{i}_{r,\alpha\beta}, \quad k = 1,2,...,m \\
\bar{\lambda}_{r,\alpha\beta} &= \frac{L_{lr}}{m} \cdot \bar{i}_{r,\alpha\beta} + \frac{L_m}{m} \cdot \sum_{z=1}^{m} \bar{i}_{z,\alpha\beta} + \frac{L_m}{m} \cdot \bar{i}_{r,\alpha\beta}, \quad k = 1,2,...,m \qquad (16.19) \\
T_e &= \frac{3}{2} \cdot p \cdot \sum_{z=1}^{m} \left(\bar{\lambda}_{sz,\alpha\beta} \wedge \bar{i}_{z,\alpha\beta}\right)
\end{aligned}$$

where the circuit parameters correspond to the VSD modelling approach.

The MS approach defines m different stator flux linkage vectors and current vectors. For balanced machine operation, the stator flux vectors should be overlapped, as well as the stator current vectors. The total machine electromagnetic torque is the sum of the contributions of the m stator sets interacting with the three-phase rotor. The equivalent electrical circuits resulting from the MS theory are shown in Figure 16.13.

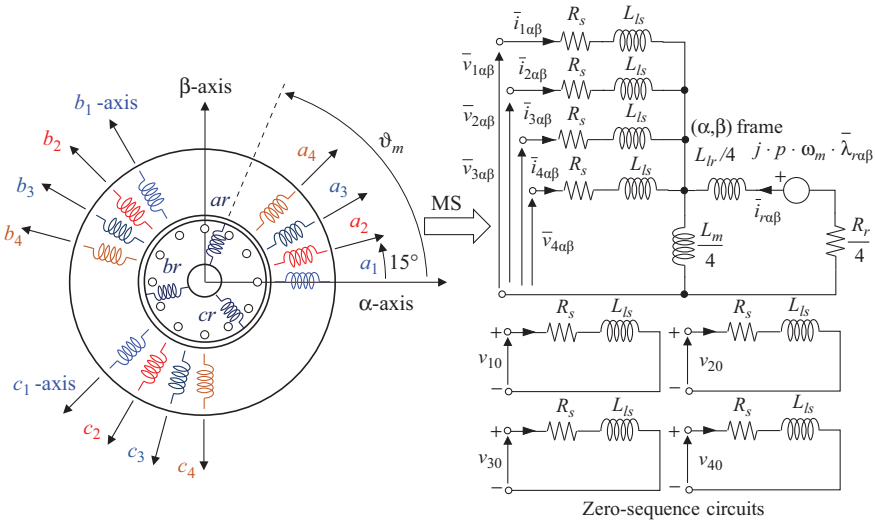


Figure 16.13 Asymmetrical 12-phase IM equivalent circuits according to MS approach

16.2.3 Summary on multiphase machines

The most relevant conclusions regarding the multiphase machines are reported in the following:

- A multiphase machine is an electrical machine with the number of phases n higher than three. A multiphase machine can be either symmetrical or asymmetrical. The most encountered symmetrical machines are five-phase, seven-phase and nine-phase machines. The most employed asymmetrical machines are the 6-phase, 9-phase, 12-phase and 15-phase ones.
- The modelling of a multiphase machine can use the VSD approach or the MS approach. The VSD has general validity, while the MS can be used for machines having a number of phases that is multiple of three.
- The VSD approach decomposes the machine subspace into several decoupled subspaces, divided into three different classes. The first class contains the main fundamental subspace, usually called (α,β), that contains the variables that are involved in the electromechanical energy conversion. The second class is represented by homopolar subspaces, usually called $(0_+, 0_-)$. The last class is specific for the multiphase machines and contains several harmonic subspaces, usually called (x_i,y_i). The VSD needs an $n \times n$ transformation matrix that becomes complicated as the number of phases increases above six.
- For machines with sinusoidal MMF distribution, the lowest order current harmonics that are mapped in the (α,β) subspace are 9th for the five-phase machine, 11th for the asymmetrical six-phase machine. Therefore, the torque ripple is shifted to higher frequencies and consequently has less impact on the mechanical structure.

- The harmonic subspaces contain time harmonics that are not involved in the electromechanical energy conversion. The (x,y) current components are circulating currents that produce additional losses, and for this reason, they must be avoided. As the impedances in the zero-sequence and harmonic subspaces are very low, special care must be taken (e.g. PWM synchronization for all phases) to reduce these circulation currents. A possible problem is encountered for PM machines exhibiting non-sinusoidal back-emf voltages. In this case, the currents in the zero-sequence subspaces must be properly limited through inverter current control.
- The MS approach considers the machine as multiple three-phase machine, where the torque is obtained as the sum of the contributions produced by the individual three-phase stator sets that interact with the rotor. The MS is useful for multiphase drives using a modular structure with three-phase inverter units supplying three-phase stator sets with isolated neutral points. The MS approach needs simple 3×3 transformation matrices, much easier to implement for machines having a number of phases that is higher than 6, i.e. 9, 12, etc.

16.3 Multiphase power converters

16.3.1 Modulation strategies for multiphase inverters

To fully exploit the potential of n-phase motor drives, a general modulation strategy for n-phase VSIs is necessary. Two different methods are usually adopted, i.e. carrier-based PWM [54–68] and space vector modulation (SVM) [69–77].

For three-phase VSIs, the equivalence of these two methods has been proved, and they can be interchangeably used. Conversely, in the case of multiphase VSIs, the carrier-based PWM method seems preferable due to its inherent simplicity because it focuses on the control of each inverter legs independently of the others, whereas SVM selects a switching pattern that involves all the legs of the inverter simultaneously.

A schematic drawing of an n-phase VSI supplying a star-connected balanced load is presented in Figure 16.14.

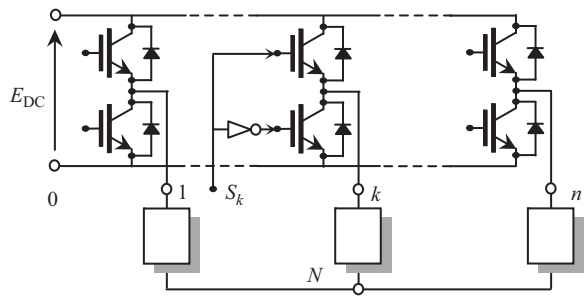


Figure 16.14 Structure of n-phase VSIs

The number n of phases is supposed to be odd for the sake of simplicity. For each inverter leg, the following general relationship can be written:

$$v_{kN} = v_{k0} - v_{N0}, \quad (k = 1, 2, ..., n) \tag{16.20}$$

where v_{kN} and v_{k0} are, respectively, the load and the pole voltages of the kth phase. The space vector representation, applied to (16.20), leads to

$$v_{\text{load},0} = v_{\text{pole},0} - v_{N0} \tag{16.21}$$

$$\bar{v}_{\text{load},\rho} = \bar{v}_{\text{pole},\rho}, \quad (\rho = 1, 3, \ldots, n-2) \tag{16.22}$$

where $v_{\text{load},0}$ and $v_{\text{pole},0}$ are the zero-sequence components of the load and pole voltages, respectively, whereas $\bar{v}_{\text{load},\rho}$ and $\bar{v}_{\text{pole},\rho}$ are the corresponding ρ-th space vectors.

Under the assumption of a balanced load, $v_{\text{load},0}$ is zero, and (16.21) can be rewritten as

$$v_{N0} = v_{\text{pole},0} \tag{16.23}$$

Equation (16.23) shows that the zero-sequence component of the pole voltages defines the potential of the star point v_{N0} and does not affect the load voltages. Also, (16.22) emphasizes that the ρ-th space vector of the load voltages coincides with the ρ-th space vector of the pole voltages.

Let us denote the duty cycles of the inverter legs with m_k ($k = 1, 2, ..., n$), defined as the mean values of the switching signals S_k in each switching period. The duty cycles of the inverter legs must satisfy the following constraints:

$$m_k \in [0,\ 1] \quad (k = 1, 2, ..., n) \tag{16.24}$$

The goal of the modulation technique is to determine how to control the inverter switches so that the mean values of the multiple space vectors $\bar{v}_h$ ($h = 1, 3, \ldots, n-2$) over a switching period T_{SW} are equal to the reference values $\bar{v}_{h,\text{ref}}$ ($h = 1, 3, \ldots, n-2$) of the pole voltages. The multiple space vectors are assumed to belong to the odd-numbered subspaces 1, 3, …, $n-2$, which are related to the corresponding spatial harmonics 1, 3, …, $n-2$ of the air-gap magnetic field in the electric machines.

16.3.2 Pulse width modulation

According to PWM, the problem of modulation can be solved by calculating the duty cycles m_k ($k = 1, \ldots, n$) of each inverter leg as follows [62]:

$$m_k = \frac{1}{E_{\text{dc}}} \left(v_{\text{pole},0} + \sum_{h=1,3,\ldots,n-2} \bar{v}_{h,\text{ref}} \cdot \bar{\alpha}_k^h \right), \quad (k = 1, \ldots, n) \tag{16.25}$$

where E_{dc} is the DC-link voltage,

$$\bar{\alpha}_k = e^{j\frac{2\pi}{n}(k-1)}, \quad (k = 1, \ldots, n) \tag{16.26}$$

and '$\cdot$' is the dot operator, defined as the real part of the product between the first operand and the complex conjugate of the second operand.

Table 16.1 Definition of the zero-sequence voltage for some modulation strategies

SPWM	$v_{0,\text{SPWM}} = E_{\text{dc}}/2$
DPWM-MIN	$v_{0,\text{DPWM-MIN}} = \left(- \min_{k=1,\ldots,M} \sum_{h=1,3,\ldots,n-2} \bar{v}_{h,\text{ref}} \cdot \bar{\alpha}_k^h \right)$
DPWM-MAX	$v_{0,\text{DPWM-MAX}} = \left(E_{\text{dc}} - \max_{k=1,\ldots,M} \sum_{h=1,3,\ldots,n-2} \bar{v}_{h,\text{ref}} \cdot \bar{\alpha}_k^h \right)$
SVPWM	$v_{0,\text{SVPWM}} = \dfrac{v_{0,\text{DPWM-MIN}} + v_{0,\text{DPWM-MAX}}}{2}$
DPWM	$v_{0,\text{DPWM}} = \begin{cases} v_{0,\text{DPWM-MIN}} & \text{if } v_{0,\text{SVPWM}} < E_{\text{dc}}/2 \\ v_{0,\text{DPWM-MAX}} & \text{otherwise} \end{cases}$

In (16.25), the zero-sequence voltage $v_{\text{pole},0}$ is a degree of freedom that the designer can freely choose to optimize the switching losses or the modulation range, thus generating different PWM strategies.

The most common modulation strategies are reported in Table 16.1. The acronyms used for these strategies are the same ones traditionally used for three-phase inverters, which can be considered simpler cases of the generalized techniques adopted for multiphase inverters [78].

Sinusoidal PWM (SPWM) is similar to the traditional sinusoidal PWM, and its reference zero-sequence voltage is always $E_{\text{dc}}/2$.

The zero-sequence voltage of DPWM-MIN is selected so that the minimum duty cycle among $m_1, \ldots, m_n$ is always zero, whereas the maximum duty cycle of DPWM-MAX is always 1. As a consequence, when these strategies are used, in every switching period there is an inverter leg that does not commutate.

The strategy called space vector pulse width modulation (SVPWM) is sometimes called 'symmetric modulation'. This strategy is the generalization for n-phase inverters of the strategy that is commonly used for three-phase inverters.

Finally, discontinuous PWM (DPWM) is a discontinuous modulation, an intermediate strategy between DPWM-MIN and DPWM-MAX. It behaves like DPWM-MAX if the zero-sequence voltage of SVPWM is greater that $E_{\text{dc}}/2$, otherwise it behaves like DPWM-MIN.

Once the duty cycles have been determined, it is possible to generate the inverter switching signals S_k ($k = 1, 2, ..., n$) by comparing the duty cycles m_k ($k = 1, 2, ..., n$), acting as modulating signals, with a triangular carrier signal $c(t)$ having a period T_{sw} and varying in the range [0, 1] (see Figure 16.15).

16.3.3 Voltage limits

The utilization of the DC-link voltage depends on the modulation technique that is used [63,64]. The modulation constraints expressed in (16.24) can be rewritten as

$$m_k - m_i \leq 1, \quad (k = 1, 2, \ldots, n), \quad (i = 1, 2, \ldots, n) \tag{16.27}$$

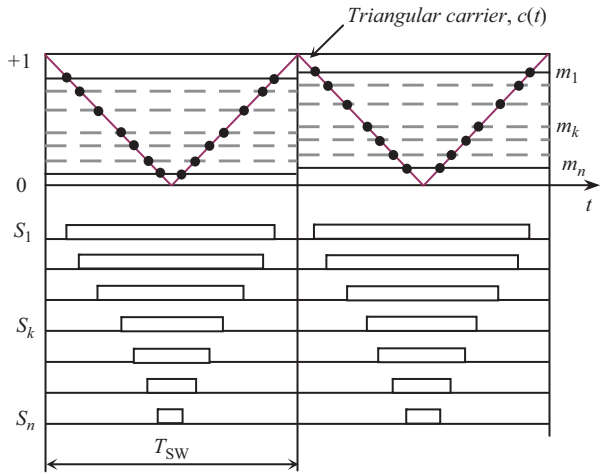


Figure 16.15 Carrier, modulating and switching signals, represented in the particular case of $m_1 > m_2 > \ldots > m_n$

Substituting (16.25) in (16.27), the inequalities can be expressed in terms of voltage space vectors:

$$\sum_{\rho=1,3,\ldots,n-2} \bar{v}_{\rho,\text{ref}} \cdot \left(\bar{\alpha}^{\rho(k-1)} - \bar{\alpha}^{\rho(i-1)}\right) \leq E_{\text{DC}}, \quad (k,i = 1,2,\ldots,n) \tag{16.28}$$

The duty-cycle constraints, given in (16.24), introduce complicated limitations on the admissible values of $\bar{v}_{1,\text{ref}}$, $\bar{v}_{3,\text{ref}}$, ..., $\bar{v}_{n-2,\text{ref}}$ in each switching period. In multiphase inverters, the exact solution of this problem represents a challenging task, because it concerns all the voltage space vectors at the same time. A possible simplification is to consider as variables of the problem only the magnitudes of the space vectors, disregarding the phase angles (i.e. allowing them to assume any value in the range [0,2π]).

Using the polar representation, each voltage vector can be expressed as follows:

$$\bar{v}_\rho = V_{\rho,\text{ref}} e^{j\beta_\rho}, \quad (\rho = 1,3,\ldots,n\ -\ 2) \tag{16.29}$$

Taking into account (16.29), after some manipulations, (16.28) can be rewritten as

$$\sum_{\rho=1,3,\ldots,n-2} 2V_{\rho,\text{ref}} \sin\left[\beta_h - \frac{h\pi}{n}\ (k+i-2)\right] \sin\left[\frac{h\pi}{n}(k-i)\right] \leq E_{\text{DC}} \tag{16.30}$$

The analysis of (16.30), written for each couple (k, i) ($k = 1, 2, ..., n$ and $i = 1, 2, ..., n$), allows determining the voltage limit in an explicit form. Taking the worst case scenario as the reference case allows (16.30) to be rewritten as

$$\sum_{\rho=1,3,\ldots,n-2} 2V_{\rho,\text{ref}} \left|\sin\left[\frac{\rho\pi}{n}(k-i)\right]\right| \leq E_{\text{DC}}, \quad (k,i = 1,2,\ldots,n). \tag{16.31}$$

Due to the inherent symmetry, the constraints (16.31) can be simplified in the following form:

$$\sum_{\rho=1,3,\ldots,n-2} A_{\rho,h} V_{\rho,\text{ref}} \leq E_{DC}, \quad h = 1, 2, \ldots, \frac{n-1}{2} \tag{16.32}$$

where

$$A_{\rho,h} = 2\left| \sin \frac{\pi\rho}{n} h \right| \tag{16.33}$$

If the reference voltage space vectors satisfy (16.32), then it is possible to find a suitable value of $v_{0,\text{pole}}$ that allows the modulating signals to stay in the range [0,1].

From a different perspective, the DC-link voltage that is necessary to synthesize voltage vectors with magnitudes $V_{1,\text{ref}}, V_{3,\text{ref}}, \ldots, V_{n-2,\text{ref}}$ is equal to

$$E_{\text{DC,req}} = \max_{h=1,2,\ldots,\frac{n-1}{2}} \left\{ \sum_{\rho=1,3,\ldots,n-2} A_{\rho,h} V_{\rho,\text{ref}} \right\} \tag{16.34}$$

16.3.3.1 Case study: sinusoidal operating conditions

If the magnitude of voltage vectors $V_{3,\text{ref}}, \ldots, V_{n-2,\text{ref}}$ is zero, it is straightforward to verify that (16.32) leads to the following inequality:

$$E_{\text{DC,req}} = \max_{h=1,2,\ldots,\frac{n-1}{2}} \left\{ \sum_{\rho=1,3,\ldots,n-2} A_{\rho,h} V_{\rho,\text{ref}} \right\} \tag{16.35}$$

Inequality (16.35) is the maximum amplitude of the sinusoidal output voltages that can be achieved with an n-phase inverter. If n is equal to 3 (three phases), then the maximum value of $V_{1,\text{ref}}$ is the well-known value $E_{\text{DC}}/\sqrt{3}$ (about $0.577E_{\text{DC}}$). If n is 5 or 7, the maximum value of $V_{1,\text{ref}}$ decreases, respectively, to $0.526E_{\text{DC}}$ and $0.513E_{\text{DC}}$. When n tends to infinite, the maximum value of $V_{1,\text{ref}}$ goes to $0.5E_{\text{DC}}$.

16.3.3.2 Case study: five-phase inverters

The voltage constraints (16.32) can be rewritten for a five-phase inverter as follows:

$$V_{1,\text{ref}}\ 2\ \sin\left(\frac{\pi}{5}\right) + V_{3,\text{ref}}\ 2\ \sin\left(\frac{2\pi}{5}\right) \leq E_{\text{dc,}} \tag{16.36}$$

$$V_{1,\text{ref}}\ 2\ \sin\left(\frac{2\pi}{5}\right) + V_{3,\text{ref}}\ 2\ \sin\left(\frac{\pi}{5}\right) \leq E_{\text{dc}} \tag{16.37}$$

The corresponding validity domain of $v_{1,\text{ref}}$ and $v_{3,\text{ref}}$ is represented by the shaded area in Figure 16.16.

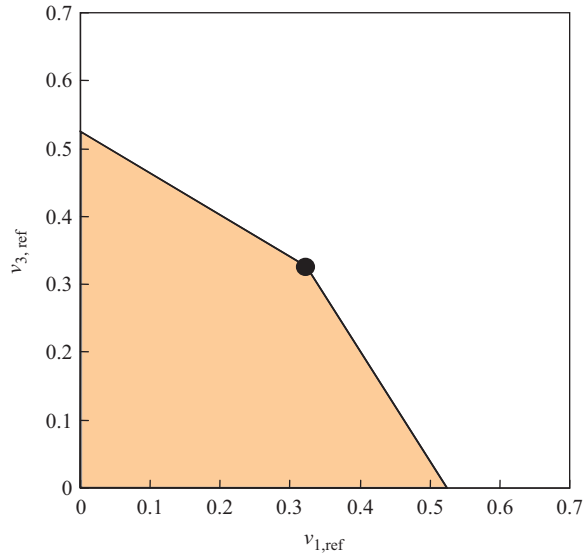


Figure 16.16 Validity domain of $V_{1,ref}$ and $V_{3,ref}$ (in per unit of the DC-link voltage)

16.3.3.3 Case study: seven-phase inverters

The voltage constraints (16.32) can be rewritten for a seven-phase inverter as follows [63]:

$$\frac{V_1}{A}+\frac{V_3}{C}+\frac{V_5}{B} \leq E_{\mathrm{DC}}, \tag{16.38}$$

$$\frac{V_1}{B}+\frac{V_3}{A}+\frac{V_5}{C} \leq E_{\mathrm{DC}}, \tag{16.39}$$

$$\frac{V_1}{C}+\frac{V_3}{B}+\frac{V_5}{A} \leq E_{\mathrm{DC}} \tag{16.40}$$

where

$$A=\frac{1}{2\sin(\pi/7)}\cong 1.152, \quad B=\frac{1}{2\sin(2\pi/7)}\cong 0.640, \quad C=\frac{1}{2\sin(3\pi/7)}\cong 0.513 \tag{16.41}$$

The region of linear modulation can be represented in a three-dimensional space, having $V_{1,\mathrm{ref}}$, $V_{3,\mathrm{ref}}$ and $V_{5,\mathrm{ref}}$ as Cartesian coordinates, arranged so as to form a right-handed coordinate system. Each point of this region has coordinates V_1, V_3 and V_5 that satisfy the inequalities (16.38)–(16.40).

The three constraints (16.38)–(16.40) correspond to three boundary planes that delimit the region of linear modulation. The three conditions (16.38)–(16.40) yield

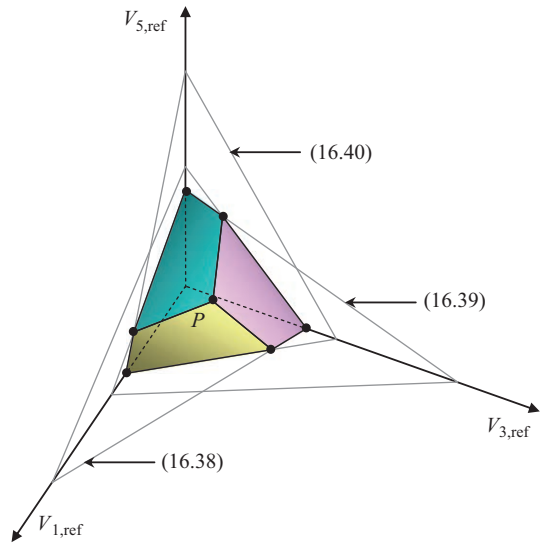


Figure 16.17 Validity domain of $V_{1,ref}$, $V_{3,ref}$ and $V_{5,ref}$ (in per unit of the DC-link voltage)

three planes which are symmetrically placed with respect to the coordinate axes. The planes and the region of linear modulation are shown in Figure 16.17. Point P has a special relevance since the cube having as opposite vertexes P, and the origin of the axes is completely within the region of linear modulation. As a consequence, the operating conditions characterized by $V_{1,\mathrm{ref}} \leq 0.228E_{\mathrm{DC}}$, $V_{3,\mathrm{ref}} \leq 0.228E_{\mathrm{DC}}$ and $V_{5,\mathrm{ref}} \leq 0.228E_{\mathrm{DC}}$ belong to that region.

16.3.3.4 Effect of the zero-sequence component on the power losses

The power losses of an inverter consist of switching power losses and conduction power losses.

If the inverter switches are IGBTs or bipolar junction transistors (BJTs), it turns out that the conduction power losses of multiphase inverters are approximately constant for all modulation strategies as long as the load currents do not change. Consequently, the zero-sequence voltage $v_{\mathrm{pole},0}$ does not affect the total conduction losses but only the switching losses [65]. For example, since DPWM-MAX and DPWM-MIN prevent one branch of the inverter from commutating, their mean switching frequency is lower than that of SVPWM and SPWM, and consequently their switching power losses are expected to be lower.

The switching power losses of an inverter leg are proportional to the instantaneous load current flowing in that leg. Therefore, to minimize the switching losses, it is necessary to avoid the state commutation of the inverter leg that bears the highest current.

Since there are only two basic strategies, DPWM-MIN and DPWM-MAX, that do not change the state of an inverter leg in each switching period, the optimal strategy consists in choosing between DPWM-MIN or DPWM-MAX depending on which of them avoids the commutation of the leg with the highest absolute value of the load current.

To find an analytical formulation of this problem, it is necessary to split the expression (16.25) of each duty cycle m_k in two terms. The first one, m_0, is the zero-sequence component, which is constant for all the phases, whereas the second one, q_k, depends on the multiple space vectors:

$$m_k = m_0 + q_k \tag{16.42}$$

where

$$m_0 = \frac{v_{\text{pole},0}}{E_{\text{DC}}} \tag{16.43}$$

$$q_k = \frac{1}{E_{\text{DC}}} \left(\sum_{h=1,3,\ldots,n-2} \bar{v}_{h,\text{ref}} \cdot \bar{\alpha}_k^h \right) \tag{16.44}$$

If DPWM-MIN is used, then m_0 is so that the lowest duty cycle becomes zero. If DPWM-MAX is used, then m_0 is so that the highest duty cycle becomes one. Let us suppose that $k_{\min}$ and $k_{\max}$ are the indexes of the duty cycles that, respectively, go to zero ($m_{k_{\min}} = 0$) and to one ($m_{k_{\max}} = 1$). Then, the optimal strategy that minimizes the switching losses in every switching period turns out to be the following one:

$$m_0 = \begin{cases} 1 - q_{k_{\max}} & \text{if} \quad |i_{\text{phase},k_{\max}}| > |i_{\text{phase},k_{\min}}| \\ -q_{k_{\min}} & \text{otherwise} \end{cases} \tag{16.45}$$

where $i_{\text{phase},k}$ is the kth load current.

The modulation strategy derived from (16.45) is optimal because it produces the minimum switching losses, whereas the conduction losses are independent of the modulation strategy. This strategy can be considered a generalization for multiphase inverters of the modulation strategy proposed in [78–80] for three-phase inverters. Furthermore, it can be applied to multiphase inverters whatever the number n of phases is (provided that n is odd). In addition, it can synthesize voltage vectors in any d-q plane and is able to fully exploit the DC-link voltage.

If the load currents are assumed sinusoidal and with amplitude I_M, it is possible to calculate the mean value of the total switching losses of the inverter:

$$P_{\text{sw,total}} = nK_{\text{strategy}} f_{\text{sw}} (\tau_{\text{on}} + \tau_{\text{off}} + \tau_{\text{rr}}) E_{\text{dc}} I_M \tag{16.46}$$

where f_{sw} is the switching frequency, K_{strategy} is a coefficient that depends on the modulation strategy, on the number of phases n and the load displacement angle φ, and τ_{on} and τ_{off} are coefficients (with the dimension of time) related to the energy loss process in the IGBTs during turn-on and turn-off, and τ_{rr} is a coefficient (with

Table 16.2 Calculation of the switching losses

Strategy	K_{strategy}
DPWM-MIN or DPWM-MAX	$K_{MM} = \begin{cases} \dfrac{2 - \cos(\phi)\sin\dfrac{\pi}{n}}{\pi} & \text{if } \lvert\phi\rvert < \left(\dfrac{\pi}{2} - \dfrac{\pi}{n}\right) \\ \dfrac{2 + \sin(\lvert\phi\rvert)\cos\dfrac{\pi}{n}}{\pi} & \text{otherwise} \end{cases}$
SPWM or SVPWM	$K_S = \dfrac{2}{\pi}$
DPWM	$K_D = \begin{cases} \dfrac{2}{\pi}\left(1 - \cos(\phi)\left(\sin\dfrac{\pi}{n} - \sin\dfrac{\pi}{2n}\right)\right) & \text{if } \lvert\phi\rvert < \dfrac{\pi}{2} - \dfrac{\pi}{n} \\ \dfrac{2}{\pi}\left(\sin(\lvert\phi\rvert)\cos\dfrac{\pi}{n} + \sin\dfrac{\pi}{2n}\cos(\phi)\right) & \text{otherwise} \\ \dfrac{2}{\pi}\left(1 - \sin(\lvert\phi\rvert)\left(\cos\dfrac{\pi}{2n} - \cos\dfrac{\pi}{n}\right)\right) & \text{if } \lvert\phi\rvert > \dfrac{\pi}{2} - \dfrac{\pi}{2n} \end{cases}$
OPT	$K_{\text{opt}} = \begin{cases} \dfrac{2}{\pi}\left(1 - \sin\dfrac{\pi}{2n}\right) & \text{if } \phi < \dfrac{\pi}{2n} \\ \dfrac{2 - \sin(\phi) - \sin\left(\dfrac{\pi}{n} - \phi\right)}{\pi} & \text{if } \dfrac{\pi}{2n} \le \phi < \dfrac{\pi}{2} - \dfrac{\pi}{2n} \\ \dfrac{2}{\pi}\left(1 - \cos\dfrac{\pi}{2n} + \sin(\phi)\cos\dfrac{\pi}{n}\right) & \text{otherwise} \end{cases}$

the dimension of time) related to the energy loss process of the diodes due to the reverse recovery currents during turn-off.

The coefficient K_{strategy} allows the comparison of the modulation strategies. As long as the values of the DC-link voltage of the output current amplitude and of the switching frequency are the same, greater values of K_{strategy} lead to greater switching losses. Table 16.2 shows the value of K_{strategy} for the most common strategies.

Figure 16.18 shows the behaviour of K_{MM}, K_S, K_D and K_{opt} in the cases $n = 5$ and $n = 7$, respectively.

16.3.4 Space vector modulation

There are several reasons to develop an SVM technique. The main reason is that SVM is well known for three-phase inverters, and it has been integrated in a number of logic devices that can manage the turn-on and turn-off of the inverter switches, such as field programmable gate arrays (FPGAs) and complex programmable logic devices (CPLDs). SVM usually allows an immediate comprehension of the relationships between the features of the modulation strategy and the available degrees of freedom.

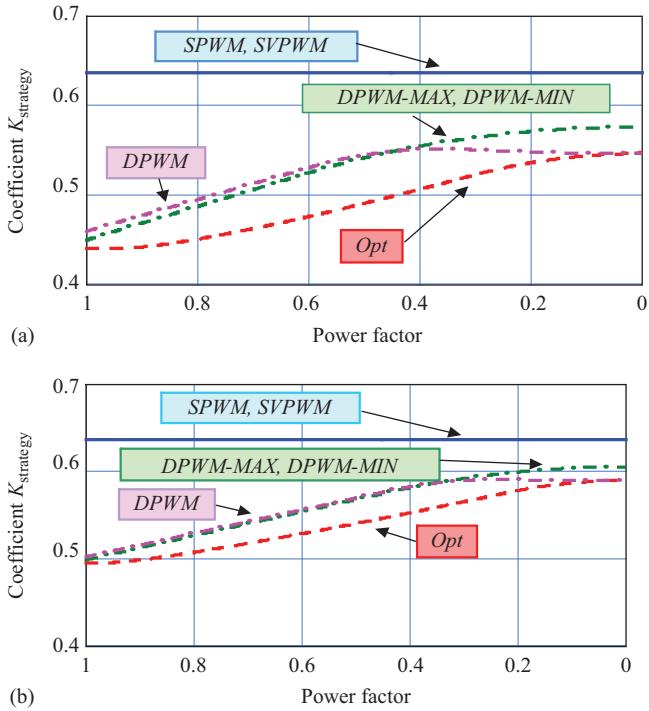


Figure 16.18 Comparison of the coefficient $K_{strategy}$ for strategies SPWM, SVPWM, DPWM-MIN, DPWM-MAX, DPWM and the optimal modulation strategy: five-phase inverter (a) and seven-phase inverter (b)

The research activity for the definition of a general SVM in multiple *d-q* planes has led to some remarkable results.

The first proposals had indeed the merit of demonstrating the feasibility of multiphase drives (in particular five-phase motor drives) but did not exploit all the available degrees of freedom. For example, the SVM techniques proposed in [69–71] require the second voltage space vector to be always zero.

The SVM technique defined in [72] and [73] considered the modulation of the first voltage space vector and allowed also the modulation of the second voltage space vector with small magnitude. Finally, the SVM techniques presented in [74] and [75] can independently synthesize voltage vectors in more than one *d-q* plane, but they cannot ensure to fully utilize the DC input voltage.

General SVM strategies for multiphase inverters are reported in [76,77]. The problem of SVM is solved for multiphase inverters with an odd number of phases by adopting an algorithm based on multidimensional vectors. This approach allows generalizing the SVM used for three-phase inverters and adapting it to multiphase inverters. According to this new approach, the output

voltages of the inverter are represented by a 'multidimensional' vector $\bar{\mathbf{v}}$, which is defined as follows:

$$\bar{\mathbf{v}} = \begin{pmatrix} \bar{v}_1 \\ \bar{v}_3 \\ \dots \\ \bar{v}_{n-2} \end{pmatrix} \tag{16.47}$$

where $\bar{v}_k$ $(k = 1, 3, \dots, n-2)$ are the multiple space vectors. It is worth noting that $\bar{\mathbf{v}}$ is a vector in a $(n-1)$-dimensional space, since $\bar{v}_1, \bar{v}_3, \dots, \bar{v}_{n-2}$ have two scalar components.

The voltage vectors that the inverter can generate can be expressed as a function of the leg state $S_1, S_2, \dots, S_n$, as follows:

$$\bar{v}_\rho = \frac{2}{n}\sum_{k=1}^{n} S_k \bar{\alpha}^{\rho k} \quad \rho = 1, 3, \dots, n-2 \tag{16.48}$$

There are $2^n - 1$ values for each multiple space vector.

The resulting multidimensional vectors can be considered as the edges of the sectors of the multidimensional space. The vectors constituting a multidimensional sector can be expressed as a combination of $n-1$ adjacent multidimensional vectors (i.e. differing one another only in the state of one inverter branch), as follows:

$$\bar{\mathbf{v}} = \delta_1 \bar{\mathbf{v}}^{(1)} + \cdots + \delta_{n-1} \bar{\mathbf{v}}^{(n-1)} \tag{16.49}$$

where $\delta_1, \cdots, \delta_{n-1}$ are positive duty cycles lower than one.

For example, a three-phase inverter has six active vectors that divide the plane in 3! sectors. Similarly, an n-phase inverter has $n(n-1)$ multidimensional vectors that divide the multidimensional space in $n!$ sectors.

Equation (16.49) represents a set of $n-1$ scalar equations, and this is clear if (16.49) is rewritten in terms of multiple space vectors instead of multidimensional vectors, as follows:

$$\begin{pmatrix} \bar{v}_1 \\ \bar{v}_3 \\ \dots \\ \bar{v}_{n-2} \end{pmatrix} = \delta_1 \begin{pmatrix} \bar{v}_1^{(1)} \\ \bar{v}_3^{(1)} \\ \dots \\ v_{n-2}^{(1)} \end{pmatrix} + \cdots + \delta_{n-1} \begin{pmatrix} \bar{v}_1^{(n-1)} \\ \bar{v}_3^{(n-1)} \\ \dots \\ \bar{v}_{n-2}^{(n-1)} \end{pmatrix} \tag{16.50}$$

Given the multidimensional vectors $\bar{\mathbf{v}}^{(1)}, \dots, \bar{\mathbf{v}}^{(n-1)}$, it is possible to find the reciprocal vectors $\bar{\mathbf{w}}^{(1)}, \dots, \bar{\mathbf{w}}^{(n-1)}$ that satisfy the following constraints:

$$\bar{\mathbf{w}}^{(k)} \cdot \bar{\mathbf{v}}^{(k)} = 1, \quad (k = 1, \dots, n-1) \tag{16.51}$$

$$\bar{\mathbf{w}}^{(k)} \cdot \bar{\mathbf{v}}^{(h)} = 0, \quad (h, k = 1, \dots, n-1, h \neq k) \tag{16.52}$$

where the dot product between multidimensional vectors is calculated by summing the result of the dot products of the corresponding multiple space vectors.

Equations (16.51) and (16.52) form a set of $n-1$ linear equations, where the unknown variables are the $n-1$ scalar components of $\bar{\mathbf{w}}^{(k)}$. If the vectors $\bar{\mathbf{v}}^{(1)}, \ldots, \bar{\mathbf{v}}^{(n-1)}$ are linearly independent, this set of equations has one and only one solution.

This procedure can be repeated $n-1$ times, for $k = 1, \ldots, n-1$, thus leading to $n-1$ reciprocal vectors $\bar{\mathbf{w}}^{(1)}, \ldots, \bar{\mathbf{w}}^{(n-1)}$.

The concept of reciprocal vector is well known in vector analysis. Its notion was introduced by the American theoretical physicist, chemist and mathematician Josiah Willard Gibbs in *Elements of Vector Analysis* (Yale University, 1881). The concept of reciprocal vector arises in vector analysis when a vector has to be expressed in a non-orthogonal coordinate system. In order to find the component of the vector, the most natural way is to decompose it along the directions of the tangent vectors, i.e. vectors that have the directions of the coordinate axes. Alternatively, it is possible to use a vector basis composed of normal vectors, i.e. vectors that have directions orthogonal to the coordinate axes. This basis is usually referred as reciprocal basis, and its vectors are named dual or reciprocal vectors.

Roughly speaking, it is possible to say that the concept of reciprocal vector arises from the dualism of 'tangent' and 'normal' vector, which is so frequent in modern geometry and in modern physics.

The usefulness of the reciprocal vectors is evident in the calculation of the duty cycles in (16.49). In fact, each duty cycle can be calculated simply with a dot product, as follows:

$$\delta_k = \bar{\mathbf{v}}_{\mathbf{ref}} \cdot \bar{\mathbf{w}}^{(k)} = \sum_{\rho=1,3,\ldots,n-2} \bar{v}_\rho \cdot \bar{w}_\rho^{(k)}, \quad (k = 1, \ldots, n-1) \tag{16.53}$$

where $\bar{\mathbf{v}}_{\mathbf{ref}}$ is the desired multidimensional voltage vector.

In three-phase inverters, it is well known that carrier-based PWM and SVM are intrinsically equivalent. This equivalence is true also for multiphase inverters and allows an interesting interpretation of the concept of sector used in SVM.

It turns out that the vectors of the multidimensional Sector 1 are those that satisfy the following constraints:

$$m_1 > m_2 > \cdots > m_n \tag{16.54}$$

whereas the other sectors are characterized by a different ordering of the duty cycles of the inverter branches. There are $n!$ different ordering of $m_1, m_2, \ldots, m_n$, hence there are also $n!$ different sectors. If $p(1), \ldots, p(n)$ is a permutation of the leg indexes, so that

$$m_{p(1)} > m_{p(2)} > \cdots > m_{p(n)} \tag{16.55}$$

it is possible to verify that the $n-1$ reciprocal vectors can be expressed in the following form:

$$\bar{\mathbf{w}}^{(k)} = \frac{1}{E_{dc}} \begin{pmatrix} \bar{\alpha}_{p(k)} - \bar{\alpha}_{p(k+1)} \\ \bar{\alpha}^3_{p(k)} - \bar{\alpha}^3_{p(k+1)} \\ \dots \\ \bar{\alpha}^{n-2}_{p(k)} - \bar{\alpha}^{n-2}_{p(k+1)} \end{pmatrix}, \quad (k = 1, 2, \dots, n-1) \tag{16.56}$$

that can be used to find the corresponding duty cycle δ_k with (16.53).

16.3.5 Analysis of the output current ripple

PWM techniques differ in terms of several characteristics, such as the switching losses or the harmonic content of the output voltage. A quality index that is often considered is the ripple of the load currents. To investigate this problem, it is possible to analyse the behaviour of the stator currents over a switching period in a five-phase PWM inverter feeding a five-phase inductive load. Let us denote with $\bar{i}_{1,\text{ref}}$ and $\bar{i}_{3,\text{ref}}$ the desired current vectors flowing through the load, and with $\bar{v}_{1,\text{ref}}$ and $\bar{v}_{3,\text{ref}}$ the corresponding reference voltage vectors. The actual values of the voltage vectors $\bar{v}_1$ and $\bar{v}_3$ differ from the reference ones because of the switching behaviour of the inverter.

The voltage and the current ripple vectors can be defined as follows:

$$\bar{v}_{\rho,\text{rip}} = \bar{v}_{\rho} - \bar{v}_{\rho,\text{ref}}, \quad (\rho = 1, 3) \tag{16.57}$$

$$\bar{i}_{\rho,\text{rip}} = \bar{i}_{\rho} - \bar{i}_{\rho,\text{ref}}, \quad (r = 1, 3) \tag{16.58}$$

where $\bar{i}_1$ and $\bar{i}_3$ are the actual values of the stator current vectors.

The mean values of $\bar{v}_{1,\text{rip}}$ and $\bar{v}_{3,\text{rip}}$ during a switching period T_{sw} are zero, owing to the principle of operation of PWM technique.

Under the assumption of high-frequency ripple components, the following relationships can be determined:

$$\frac{d\bar{i}_{\rho,\text{rip}}}{dt} = \frac{\bar{v}_{\rho,\text{rip}}}{L_{\rho,\text{hf}}}, \quad (\rho = 1, 3) \tag{16.59}$$

where $L_{1,\text{hf}}$ and $\text{L}_{3,\text{hf}}$ are the high-frequency equivalent inductances of the load, respectively, in the α_1-β_1 and α_3-β_3 planes, measured from the inverter output terminals.

The parameter commonly used to represent the distortion of three-phase waveforms is the total RMS value of the ripple over a switching period, or, equivalently, its square value:

$$I^2_{\text{rip,RMS},T_{\text{sw}}} = \sum_{k=1}^{5} i^2_{k,\text{rip,RMS},T_{\text{sw}}} = \frac{1}{T_{\text{sw}}} \int_0^{T_{\text{sw}}} \sum_{k=1}^{5} i^2_{k,\text{rip}}\, dt \tag{16.60}$$

where $i_{k,\text{rip}}$ is the current ripple of the kth phase.

Taking into account the symmetry of the double-sided switching pattern, and introducing the current ripple vectors, (16.60) can be rewritten as

$$I^2_{\text{rip,RMS},T_{\text{sw}}} = \frac{5}{T_{\text{sw}}} \int_0^{T_{\text{sw}}/2} \left(\bar{i}_{1,\text{rip}}\, \bar{i}^{*}_{1,\text{rip}} + \bar{i}_{3,\text{rip}}\, \bar{i}^{*}_{3,\text{rip}} \right) dt \tag{16.61}$$

where the symbol '*' represents the complex conjugate.

Furthermore, the quantities $\bar{i}_{1,\text{rip}}$ and $\bar{i}_{3,\text{rip}}$ can be calculated integrating (16.59) and taking (16.57) into account, as follows:

$$\bar{i}_{\rho,\text{rip}} = \frac{1}{L_{\rho,\text{hf}}} \int_0^t \left(\bar{v}_{\rho} - \bar{v}_{\rho,\text{ref}} \right) d\tau, \quad (\rho = 1, 3) \tag{16.62}$$

Substituting (16.62) in (16.61), after some tedious calculations, gives the following relationship:

$$I^2_{\text{rip,RMS},T_{\text{sw}}}\left(\bar{v}_{1,\text{ref}}, \bar{v}_{3,\text{ref}}, v_{\text{pole},0}\right) = P_2 \left(\frac{v_{\text{pole},0}}{E_{\text{dc}}} \right)^2 + P_1 \left(\frac{v_{\text{pole},0}}{E_{\text{dc}}} \right) + P_0 \tag{16.63}$$

where P_0, P_1 and P_2 are very cumbersome polynomial quantities of T_{sw} (here omitted for saving space) depending on $\bar{v}_{1,\text{ref}}$, $\bar{v}_{3,\text{ref}}$, and their complex conjugates.

Equation (16.63) provides the square of the RMS value of the output current ripple, in each switching period, as a function of the space vectors and the zero-sequence component of the modulating signals. As can be seen, $I^2_{\text{rip,RMS},T_{\text{sw}}}$ is a parabolic function of $v_{\text{pole},0}$.

It can be demonstrated that P_1 and P_2, unlike P_0, do not depend on the ordering of the modulating signals.

The optimal value of $v_{\text{pole},0}$ in each switching period, leading to the minimum output current ripple, can be obtained by solving the following expression:

$$\frac{\partial I^2_{\text{rip,RMS},T_{\text{sw}}}}{v_{\text{pole},0}} = 2\frac{P_2}{E^2_{\text{DC}}} v_{\text{pole},0} + \frac{P_1}{E_{\text{DC}}} = 0 \tag{16.64}$$

After some manipulations, (16.64) furnishes

$$\frac{v_{\text{pole},0,\text{OPT}}}{E_{DC}} = \frac{1}{2} - \frac{\Re_e \left[L^2_{3,\text{hf}} \left(2\bar{v}^2_{1,\text{ref}} \bar{v}_{3,\text{ref}} + \bar{v}_{1,\text{ref}} \bar{v}^{*2}_{3,\text{ref}} \right) + L^2_{1,\text{hf}} \left(\bar{v}^2_{1,\text{ref}} \bar{v}_{3,\text{ref}} + 2\bar{v}_{1,\text{ref}} \bar{v}^{*2}_{3,\text{ref}} \right) \right]}{4\left(L^2_{3,\text{hf}} \left| \bar{v}_{1,\text{ref}} \right|^2 + L^2_{1,\text{hf}} \left| \bar{v}_{3,\text{ref}} \right|^2 \right)} \tag{16.65}$$

As (16.65) emphasizes, the optimal value of $v_{\text{pole},0}$ depends on the values of the high-frequency equivalent inductances of the load.

In the particular case of $L_{1,\text{hf}} = L_{3,\text{hf}}$, (16.65) can be rewritten as

$$\frac{v_{\text{pole},0,\text{OPT}}}{E_{\text{DC}}} = \frac{1}{2} - \frac{3\Re_e \left[\bar{v}^2_{1,\text{ref}}\, \bar{v}_{3,\text{ref}} + \bar{v}_{1,\text{ref}} \bar{v}^{*2}_{3,\text{ref}} \right]}{4\left(\left| \bar{v}_{1,\text{ref}} \right|^2 + \left| \bar{v}_{3,\text{ref}} \right|^2 \right)} \tag{16.66}$$

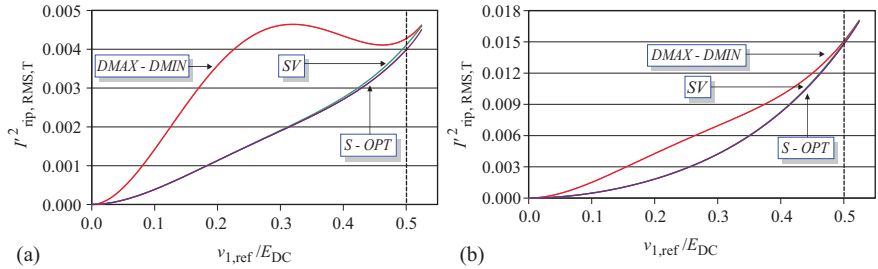


Figure 16.19 Square RMS value (p.u.) of the current ripple in a fundamental period as function of $v_{1,\text{ref}}$. *(a) Case 1.* $\bar{v}_{3,\text{ref}} = 0, KL = 1$. *(b) Case 1.* $\bar{v}_{3,\text{ref}} = 0, KL = 2$

As can be verified, (16.66) shows that SPWM generates the lowest current ripple when $\bar{v}_{1,\text{ref}} \neq 0$ and $\bar{v}_{3,\text{ref}} = 0$, and emphasizes that this result is no longer valid for $\bar{v}_{1,\text{ref}} \neq 0$ and $\bar{v}_{3,\text{ref}} \neq 0$.

A comparison among different modulation strategies, in terms of the square RMS value of the current ripple in p.u. in a fundamental period T ($I'^2_{\text{rip,RMS},T}$), is presented in Figure 16.19.

The RMS value squared of the current ripple in a switching period T_{sw}, expressed in p.u., is obtained as follows:

$$I'^2_{\text{rip,RMS},T_{\text{sw}}} = \frac{I^2_{\text{rip,RMS},T_{\text{sw}}}}{E^2_{\text{DC}}} \frac{L^2_{1,\text{hf}}}{T^2_{\text{sw}}} \tag{16.67}$$

It is worth noting that this quantity is strongly dependent on the parameter $K_L = L_{1,\text{hf}}/L_{3,\text{hf}}$. The value of this parameter depends on the specific inverter load. In multi-motor drives and synchronous motor drives, $K_L = 1$ is a reasonable assumption, whereas in the case of induction motor drives a realistic hypothesis is $K_L = 2$.

16.4 Control of multiphase drives

Depending on the application, the control of high-performance multiphase drives must follow the same specifications imposed to the three-phase counterparts: fast response and zero steady-state errors for the controlled variables: speed, torque, flux and currents.

With respect to the three-phase drives, the multiphase drive control is strongly influenced by the drive configuration. From the literature, the most employed drive configurations are the following:

- conventional multiphase configuration with single neutral point (Figure 16.20);
- multiphase configuration with independent single-phase units (Figure 16.21);
- multiphase configuration with independent three-phase units (Figure 16.22).

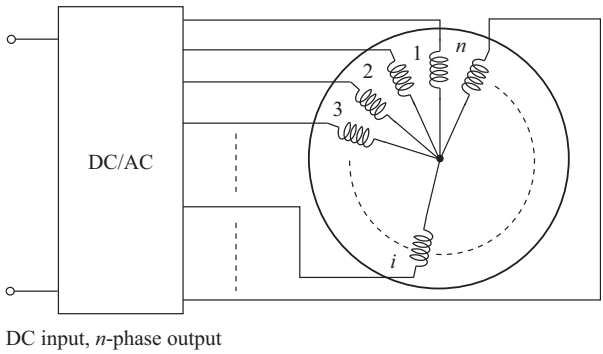


Figure 16.20 Multiphase drive configuration with single machine neutral point

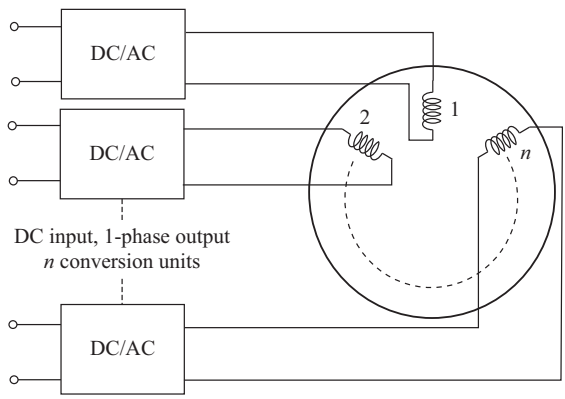


Figure 16.21 Multiphase drive configuration with multiple single-phase units

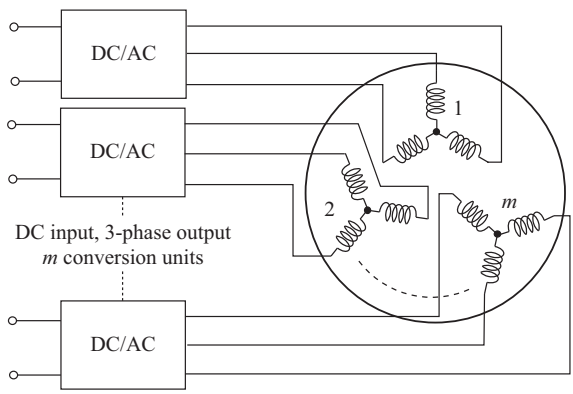


Figure 16.22 Multiphase drive configuration with multiple three-phase units. The disposition of three-phase sets is not the winding spatial distribution

As stated in [81], the machine configuration that uses a single neutral point does not fulfil the requirements of fault-tolerant operation for safety critical applications. The problem can be completely solved when the machine phases are independently fed by a single-phase independent inverter. Another interesting advantage of this solution is the highest voltage utilization of the DC-link for motoring operation, since the maximum peak phase voltage is the DC-link voltage. However, this configuration leads to complicated power electronic structures.

A reasonable compromise between the system complexity and the fault-tolerant operation capability can be obtained with machines having a number of phases that is multiple of three, and the stator consists of independent three-phase sets with isolated neutral points. For this configuration, each three-phase set is supplied by an independent three-phase inverter. This topology is less attractive respect to the previous one from the fault-tolerant point of view. In case of fault, the faulted three-phase set (including the converter) is disconnected from the DC source. However, the power converter can use well-consolidated off-the-shelf three-phase power electronic modules, thus reducing the converter size, cost and design time.

The multiple three-phase configuration usually leads to modular control schemes since the number of independent currents is lower with respect to the multiple single-phase approach. As example, a six-phase machine with two independent neutral points and two three-phase sets will have four independent phase currents. With reference to the VSD modelling approach, that means zero currents in the $(0_+,0_-)$ subspace.

The most generic schematic block of a closed-loop multiphase drive control is shown in Figure 16.23, considering a multiphase inverter with single DC-link. The scheme is valid for synchronous machines and for asynchronous machines as well.

The input is the reference torque or the mechanical speed, depending on the application. In some cases, additional outer loops are included, such as voltage regulation loops for multiphase generators. The measured quantities are the phase currents i_k, the inverter DC-link voltage v_{dc} and the rotor mechanical position ϑ_m. The output of the control are the phase reference voltages v_k^* that are applied to a pulse width modulator to get the inverter switching functions S_k. Alternatively, the control may generate directly the switching function, as happens for some control techniques that are described later in this section.

The most employed multiphase drives control techniques are described in the following subsections.

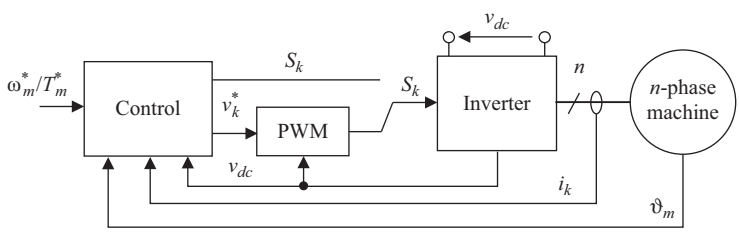


Figure 16.23 General closed-loop control of a multiphase drive

16.4.1 Field-oriented control

The field-oriented control (FOC) applied to the multiphase motor drives uses the same principles applied to the three-phase machines, and it is implemented in a rotating (d,q) reference frame. The FOC aims at regulating the machine currents with an inner current control scheme to get the required torque with a specific machine flux.

For synchronous machines, the d-axis is the electrical rotor position (obtained from the measured mechanical position, as shown in Figure 16.24). For asynchronous machines, the d-axis is usually the position of the estimated rotor flux vector in (α,β) frame, as shown in Figure 16.25. As examples, Figures 16.26 and 16.27 contain two examples for IPM machines and IMs, respectively [82,83].

The torque regulation for an IPM machine needs the generation of the optimal (d,q) current references for maximum torque per ampere operation. At flux weakening, the d-axis current is reduced to keep the command voltage below the maximum inverter voltage, using a voltage controller (Figure 16.26). The minimum d-axis current is limited at the machine characteristic current $(-\lambda_m/L_d)$, while the q-axis current is limited according to the maximum allowed current $I_{\max}$.

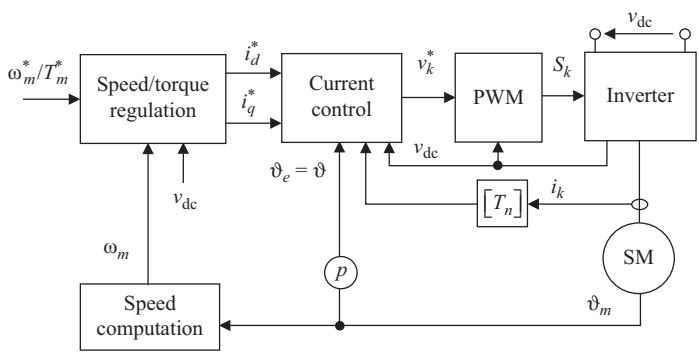


Figure 16.24 Generic FOC of a multiphase synchronous motor drive

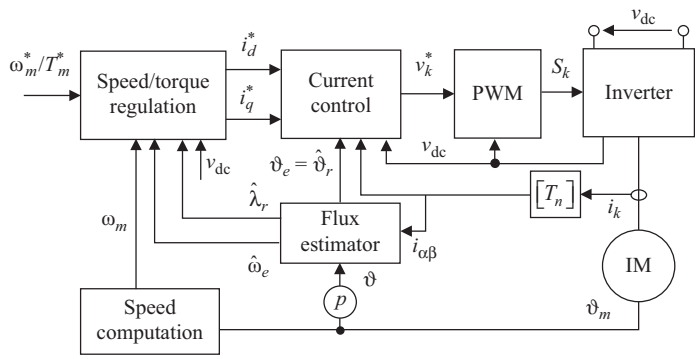


Figure 16.25 Generic direct FOC of a multiphase induction motor drive

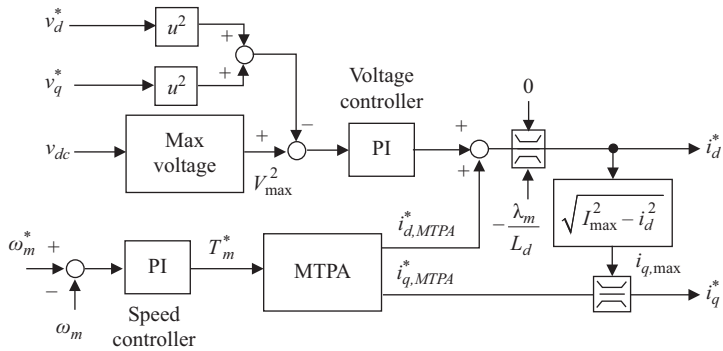


Figure 16.26 Speed regulation for a generic IPM machine

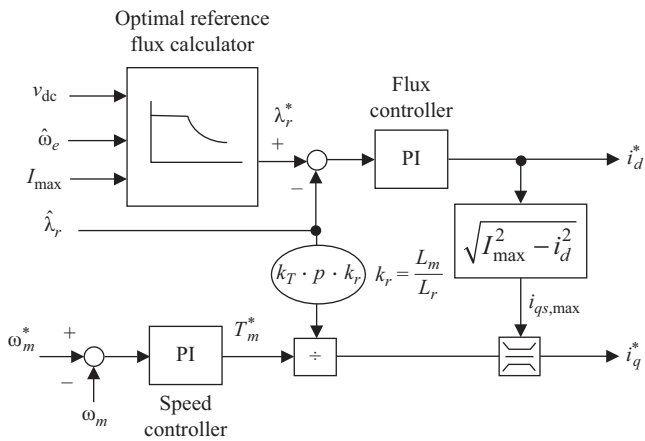


Figure 16.27 Speed regulation for an IM

The torque regulation of an IM is more complicated since it needs an estimation scheme to get the rotor flux vector position $\hat{\vartheta}_e$ in stationary reference frame. One possible solution is to compute the rotor flux position through the slip, using an indirect FOC approach [6,84]. The direct FOC approach uses a flux estimator that provides the rotor flux magnitude $\hat{\lambda}_r$ and its position $\hat{\vartheta}_e$ and electrical speed $\hat{\omega}_e$, as shown in Figure 16.25. The direct FOC exhibits superior dynamic performance with respect to the indirect FOC due to the flux regulation added to the torque regulation, as shown in Figure 16.27. The output of the flux controller is the *d*-axis reference current, while the *q*-axis reference current is computed from the torque reference using the estimated flux and the torque constant that results from the VSD machine model. The reference flux is provided by an optimal reference flux computation block. Below the base speed, the reference flux is constant and equal with its rated value. Above the base speed, the flux is weakened using an optimal strategy, as shown in [83], for maximum torque production.

While the speed/torque regulation scheme of a multiphase machine is similar to the one for a three-phase machine, the current regulation is different due to the existence of multiple subspaces, as shown in Figure 16.28.

Besides the current control in the (*d,q*) frame for torque and flux regulation, additional current regulation blocks must be added to cancel the harmonic currents in the (*x,y*) subspaces and the zero-sequence currents in the (0_+,0_-) subspaces.

At steady-state operation, the (*d,q*) currents are DC quantities, while the (*x,y*) currents are AC quantities. Besides the known harmonics related to these planes, components at fundamental frequency may appear in case of machine asymmetries [85]. Therefore, the current control for the (*x,y*) subspaces and (0_+,0_-) subspaces can be problematic due to the limited performance of proportional-integral (PI) controllers. As the harmonic order of the zero-sequence current is known from the machine configuration, a possible solution is the use of proportional–resonant (P-RES) controllers whose resonant frequency is updated according to the motor frequency [86].

Depending on the machine configuration, some zero-sequence currents can disappear and thus the current control is simplified. As example, an asymmetrical six-phase machine with two isolated neutral points will not have currents in the (0_+,0_-) subspace, so only four current controllers are needed: one pair for the (*d,q*) frame and another one for the (*x,y*) subspace.

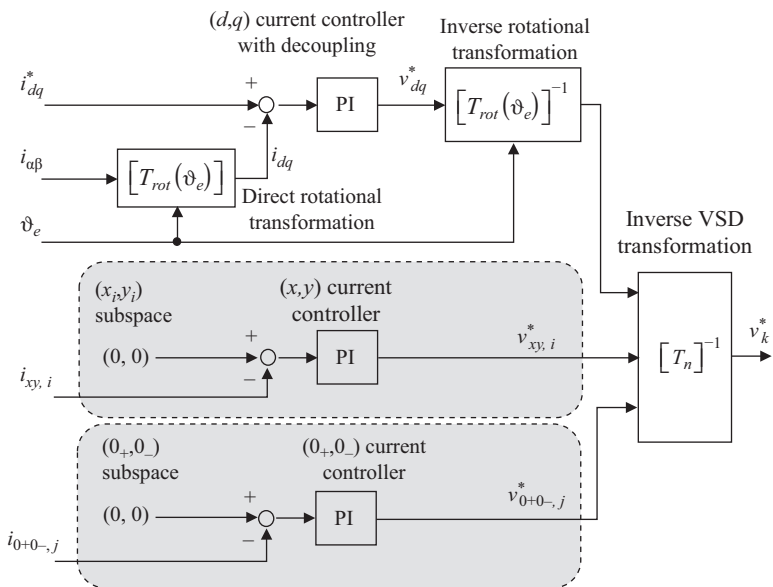


Figure 16.28 Generic current control for multiphase machine

16.4.2 Direct torque control

The direct torque control (DTC) was the main alternative of FOC for the three-phase motor drives. The main goal of DTC is to obtain a fast and robust decoupled control of the stator flux and of the electromagnetic torque without using inner current control loops [87].

With respect to the FOC that is usually implemented in a rotating (d,q) reference frame, the DTC can be implemented in stationary (α,β) frame, so it avoids the direct and rotational transformations. The stator flux and torque are regulated by applying proper voltage vectors provided by the inverter in the (α,β) frame.

From the literature, the DTC solutions for the three-phase machines can be divided into two main groups:

- Direct self control (DSC) and switching-table-based DTC (ST-DTC) techniques: these solutions give variable switching frequency.
- PWM-based DTC (PWM-DTC) techniques: these solutions impose constant inverter switching frequency.

The extension of DTC techniques to the multiphase drives needs a particular analysis due to the existing of the circulating currents in the (x,y) subspaces. Moreover, the number of vectors increases with the phase number due to the increased number of inverter switching states. As a consequence, the application of the DTC to the multiphase drives is often limited to only five-phase and six-phase machines, for which the system complexity is still reasonable. Therefore, hereinafter this subsection will focus mainly on DTC for asymmetrical six-phase induction motors fed by two-level inverters, as shown in Figure 16.29.

The inverter is a switching network of 12 power switches arranged to form 6 legs, where each leg supplies one motor phase. Only one of the power switches of the same leg can operate in the on state to avoid the short circuit of the DC-link, so $2^6 = 64$ switching configurations can be obtained. The machine phase voltages can

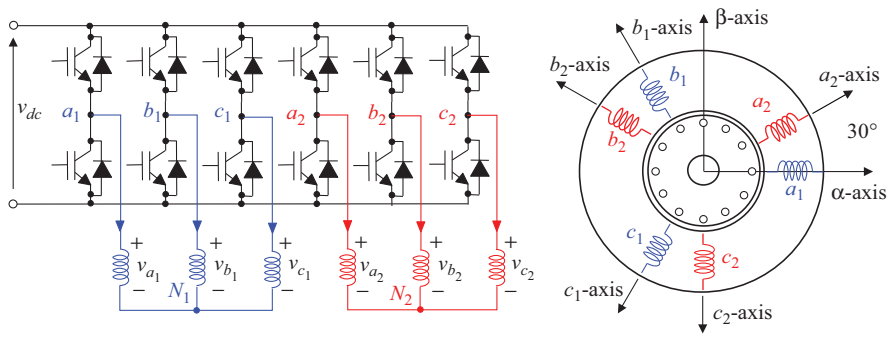


Figure 16.29 Asymmetrical IM with isolated neutral points fed by a two-level six-phase inverter with single DC-link

be computed using the switching function associated to one inverter leg that is defined as

$$\begin{cases} S_j = 1, & \text{if the upper switch is on (lower switch is off)} \\ S_j = 0, & \text{if the upper switch is off (lower switch is on)} \end{cases} \tag{16.68}$$

where $j = a_1, b_1, c_1, a_2, b_2, c_2$.

For the machine having isolated neutral points, the machine phase voltages are separately computed for each three-phase set as

$$\begin{cases} v_i = \left(S_i - \frac{1}{3} \cdot \sum_{k=a_1,b_1,c_1} S_k \right) \cdot v_{\text{dc}} \quad i = a_1, b_1, c_1 \\ v_j = \left(S_j - \frac{1}{3} \cdot \sum_{k=a_2,b_2,c_2} S_k \right) \cdot v_{\text{dc}} \quad j = a_2, b_2, c_2 \end{cases} \tag{16.69}$$

Using the amplitude-invariant VSD matrix transformation for asymmetrical six-phase machines and the matrix form of (16.69), the voltage components in the machine subspaces (α,β), (x,y) and (0_+,0_-) are computed as follows:

$$\begin{bmatrix} v_\alpha \\ v_\beta \\ v_x \\ v_y \\ v_{0+} \\ v_{0-} \end{bmatrix} = \frac{v_{\text{dc}}}{3} \begin{bmatrix} 1 & -\frac{1}{2} & -\frac{1}{2} & \frac{\sqrt{3}}{2} & -\frac{\sqrt{3}}{2} & 0 \\ 0 & \frac{\sqrt{3}}{2} & -\frac{\sqrt{3}}{2} & \frac{1}{2} & \frac{1}{2} & -1 \\ 1 & -\frac{1}{2} & -\frac{1}{2} & -\frac{\sqrt{3}}{2} & \frac{\sqrt{3}}{2} & 0 \\ 0 & -\frac{\sqrt{3}}{2} & \frac{\sqrt{3}}{2} & \frac{1}{2} & \frac{1}{2} & -1 \\ 0 & 0 & 0 & 0 & 0 & 0 \\ 0 & 0 & 0 & 0 & 0 & 0 \end{bmatrix} \cdot \begin{bmatrix} S_{a_1} \\ S_{b_1} \\ S_{c_1} \\ S_{a_2} \\ S_{b_2} \\ S_{c_2} \end{bmatrix} \tag{16.70}$$

As shown in (16.70), no voltage components are generated in the (0_+,0_-) subspace, demonstrating why the machine topology with two separate neutral points is usually preferred.

Considering all the 64 inverter switching configurations, the projections of the normalized voltage vectors (with respect to the DC-link voltage v_{dc}) in the orthogonal subspaces (α,β) and (x,y) are depicted in Figure 16.30.

The decimal numbers in Figure 16.30 show the inverter switching state N whose binary equivalent number gives the values of the switching functions for the inverter legs, considered in the order $a_1b_1c_1a_2b_2c_3$. The inverter provides only 48 independent non-zero vectors and one zero vector to form a 12-sided, 4-layer polygon in each machine subspace. It must be noted that a particular switching combination (as example $N = 36$) will produce a vector in the (α,β) subspace that belongs to the external layer, and another vector (x,y) subspace belonging to the most internal layer.

With respect to the three-phase inverters, where only six non-zero vectors can be used, for the asymmetrical six-phase drives the number of non-zero vectors is significantly higher. As a result, the DSC and the ST-DTC schemes [87–89] should be easily extended to six-phase drives with better results with respect to the three-phase drives. The only problem is the number of non-zero vectors to be used in the (α,β) subspace. A basic DSC scheme for asymmetrical six-phase induction motor drives that uses the vectors of the external layer of the 12-side polygon in the (α,β) subspace is shown in Figure 16.31 [90].

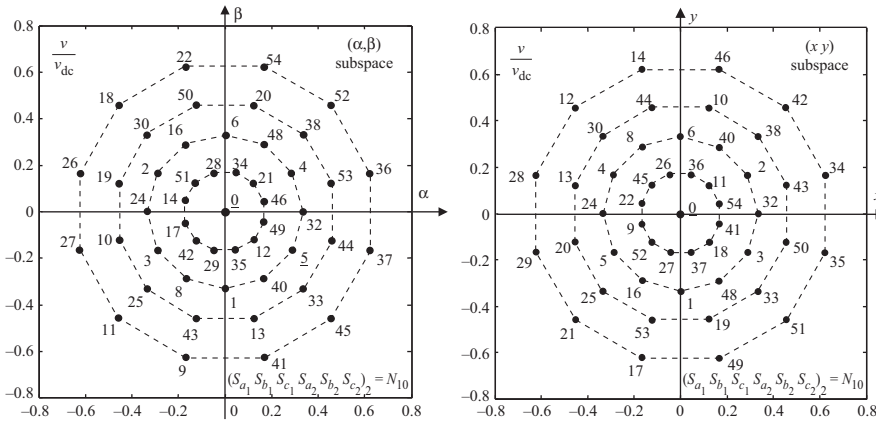


Figure 16.30 Normalized inverter voltage vectors in the (α,β) subspace (left) and in the (x,y) subspace (right)

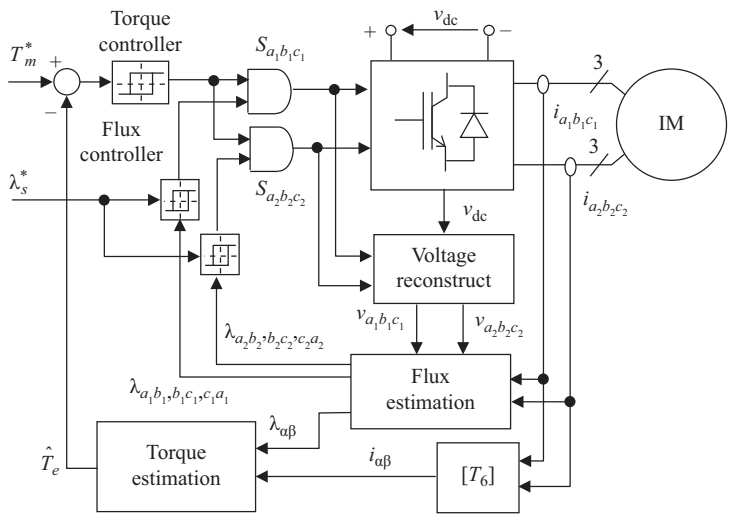


Figure 16.31 Basic DSC for asymmetrical induction motor drive [90]

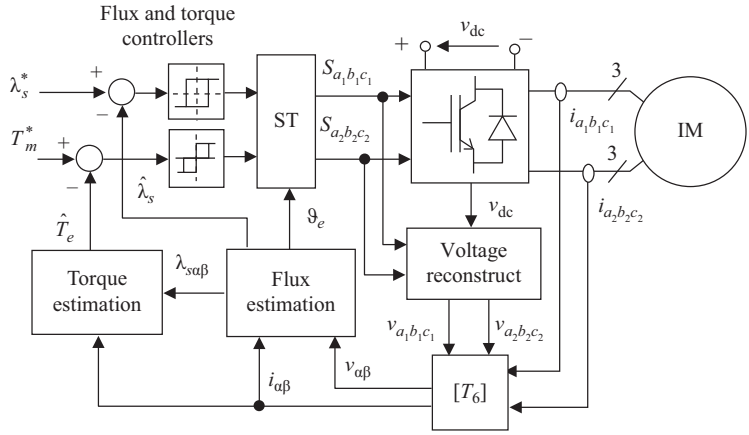


Figure 16.32 Basic ST-DTC for asymmetrical induction motor drive [90]

The basic DSC from Figure 16.31 is simple but large fifth and seventh current harmonics are generated in the (*x,y*) subspace, as demonstrated in [90].

The basic ST-DTC scheme for six-phase induction motor drives is shown in Figure 16.32. Based on the estimated stator flux position, a torque three-level hysteresis regulator and a flux two-level regulator are used to generate the inverter switching functions through an optimal switching table (ST).

The key issue for ST-DTC is the ST design in order to get sinusoidal machine phase currents, by minimizing the circulating current components in the (*x,y*) subspace. Different ST design solutions were discussed and experimented in [91] with good torque and flux regulation performance. It is considered today that the DTC is rather difficult to be implemented for multiphase drives due to the difficulties in limiting the voltage harmonics in the (*x,y*) planes. The problem of the circulation currents can be solved either with constant frequency operation or by using new control solutions, as shown in the next.

16.4.3 Direct flux vector control

The direct flux vector control (DFVC) has emerged as an alternative to FOC and DTC for three-phase motor drives [92]. The DFVC has high degree of generality, and it can be used with either induction or synchronous machines since it is implemented in the rotating (d_s,q_s) reference frame defined by the stator flux vector.

The DFVC can be considered as an evolution of the DTC with the advantage of having constant switching frequency and PWM, while retaining similar benefits in terms of dynamic performance. With respect to the FOC, the DFVC performs better at high speed and flux weakening, since it easily guarantees maximum torque production under current and voltage constraints.

When combined with the MS modelling approach, the DFVC is particularly suitable for multiple three-phase motor drives, employing either induction motors or synchronous motors. Therefore, the DFVC can be considered as a unified control

solution for modular multiple three-phase motor drives shown in Figure 16.16, where each three-phase set is independently controlled.

The DFVC will be analysed in this section for multiple three-phase induction motor drives having m three-phase stator sets. With reference to the MS approach, the DFVC aims at controlling m stator flux vectors in overlapped stator flux frames (d_{sk},q_{sk}, $k = 1,2, \ldots, m$), as shown in Figure 16.33.

The DFVC is implemented in multiple overlapped stator flux frames using the following operating principles:

- The amplitudes of the stator flux vectors λ_{sk} ($k = 1, 2, \ldots, m$) are directly regulated by means of the d_{sk}-axis voltages. Therefore, the d_{sk}-axis becomes a flux axis. The d_{sk}-axis voltage equations are very simple with no q_{sk}-axis coupling terms.

$$\frac{d\lambda_{sk}}{dt} = -R_{sk} \cdot i_{k,ds} + v_{k,ds} \tag{16.71}$$

- The total electromagnetic torque is the sum between the individual contributions of the stator sets:

$$T_e = (3/2) \cdot p \cdot \sum_{k=1}^{m} \left(\lambda_{sk} \cdot i_{k,qs}\right) \tag{16.72}$$

- The torque contribution of one stator winding k set is controlled by regulating the corresponding q_{sk}-axis current ($i_{k,qs}$), using the voltage component $v_{k,qs}$, $k = 1, 2, \ldots, m$. Therefore, the q_{sk}-axis becomes a torque axis. The q_{sk}-axis electrical equations contain coupling terms that are described in detail in [38].
- The maximum torque per volt (MTPV) operation at flux weakening is obtained when the load angles δ_k ($k = 1, 2, \ldots, m$) from Figure 16.33 are equal with 45 electrical degrees. This is equivalent with the machine operation at maximum slip. If the machine is synchronous, then the maximum load angles depend on the rotor design ($\geq$90 electrical degrees).
- The current regulation of q_{sk}-axis allows a straightforward current limitation, as happens for the FOC.

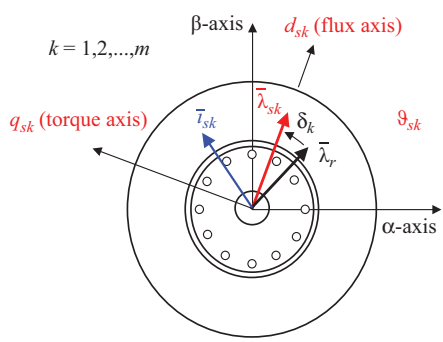


Figure 16.33 Multiple stator flux frames in the DFVC-based MS approach

The DFVC scheme of a generic multiple three-phase IM is shown in Figure 16.34. The DFVC needs a stator flux observer to estimate the individual stator flux vectors $\bar{\lambda}_{sk,k=1-m}$ corresponding to the three-phase stator sets. The stator flux observer provides the position, the amplitude and the speed of the stator flux vectors $\bar{\lambda}_{sk,k=1-m}$. The inputs for the stator flux observer are the reconstructed stator voltages, the acquired currents and the inverter dead-time errors. The inverter dead-time errors are necessary to improve the machine operation at very low speed, and they are provided by the dead-time (DT) compensation block. A detailed description of the flux observer is provided in [38] for a quadruple three-phase IM.

The MS-based DFVC is depicted in Figure 16.35. The current limitation accounts for the maximum inverter current and the maximum allowed load angle [38].

The inner flux-current control for each stator set is obtained with two PI controllers, as depicted in Figure 16.36. To improve the dynamic performance, feedforward terms are added to the outputs of the two controllers. Additional decoupling terms $f^*_{\text{dec},k,qs}$ [38] are also recommended for the q_s-axis current regulation. It must be emphasized here that the two PI controllers can work properly without any feedforward and decoupling terms.

The DFVC combined with the MS modelling approach allows at obtaining the accurate control of multiple three-phase motor drives without the use of $n \times n$ VSD matrices that are difficult to manage when the number of phases is higher than six. The modular DFVC possess the open-fault ride through capability when one or more three-phase inverter units go into fault for different reasons. In this case, the healthy three-phase sets will try to get the same torque by increasing the current within the inverter limits. Some experimental results for a four-pole, 10 kW asymmetrical quadruple three-phase induction motor (Figures 16.37 and 16.38) are shown below to demonstrate this feature. As example, the inverter 2 that supplies

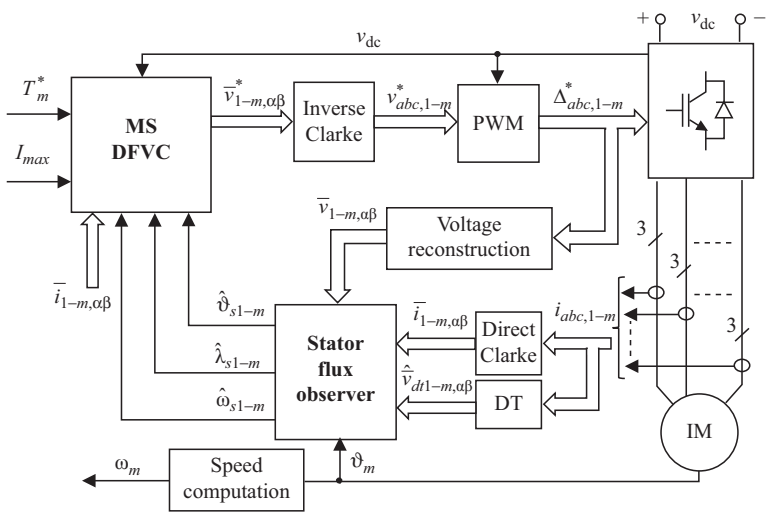


Figure 16.34 DFVC scheme of a generic multiple three-phase IM

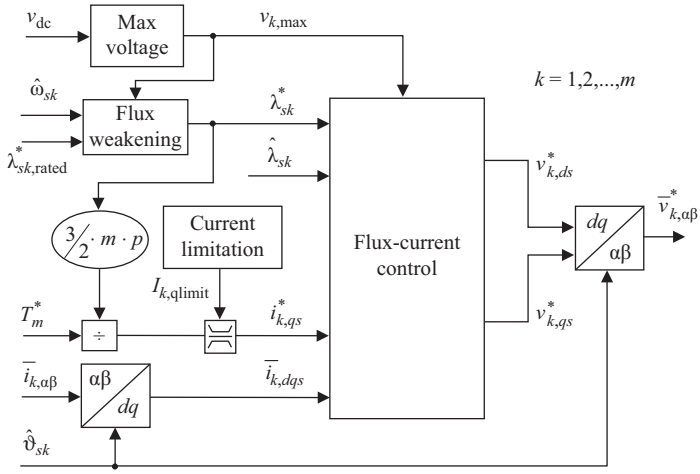


Figure 16.35 DFVC scheme for one three-phase stator set [38]

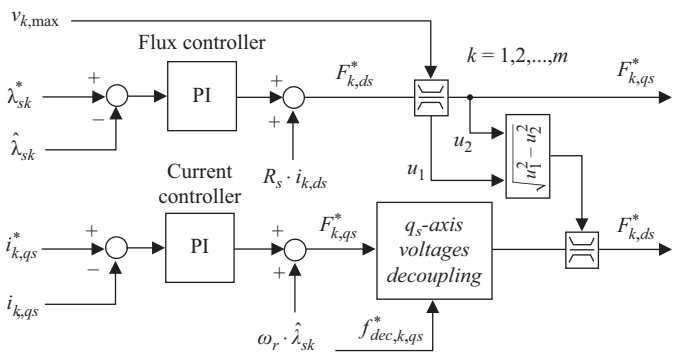


Figure 16.36 Flux and current regulation for one three-phase set

the ($a_2b_2c_2$) set is suddenly shut-off when the machine is working as a generator at negative rated speed (−6,000 rpm) and rated torque (16 N m). The phase currents i_{a1}, i_{a2}, i_{a3} and i_{a4} are shown in Figure 16.37. Without any reconfiguration that is usually needed for fault-tolerant control techniques, the modular DFVC will increase the current for the remaining healthy phase without any issues.

The DFVC keeps running (with lower torque capability) for one or more inverters that are shut-off, as demonstrated in Figure 16.38.

16.4.4 Model predictive control

The model predictive control (MPC) is a known control technique that has emerged for three-phase motor drives as an alternative for the control solutions based on the conventional linear controllers, mainly PI, or on basic nonlinear controllers, such as

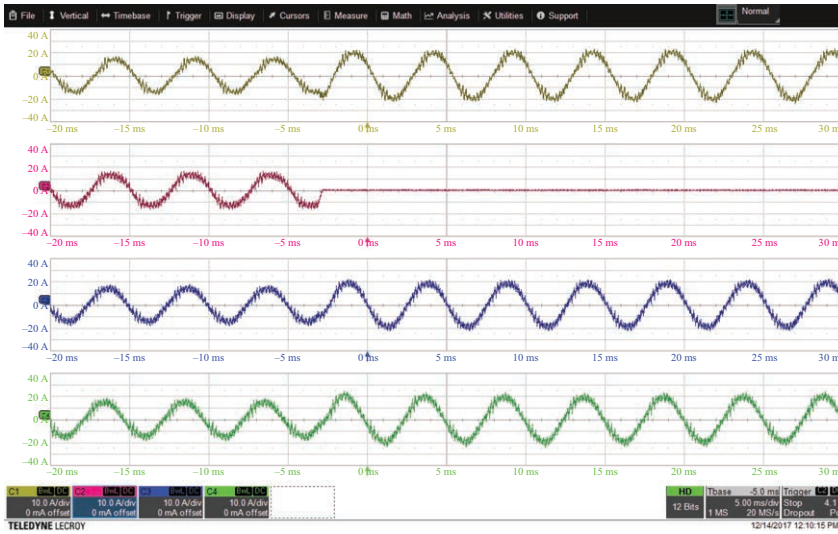


Figure 16.37 Inverter 2 shut-off during generation mode with torque control at −6,000 rpm and with 16 N m (rated torque) [106]. Ch1: i_{a1} (10 A/div), Ch2: i_{a2} (10 A/div), Ch3: i_{a3} (10 A/div), Ch4: i_{a4} (10 A/div), time resolution: 5 ms/div

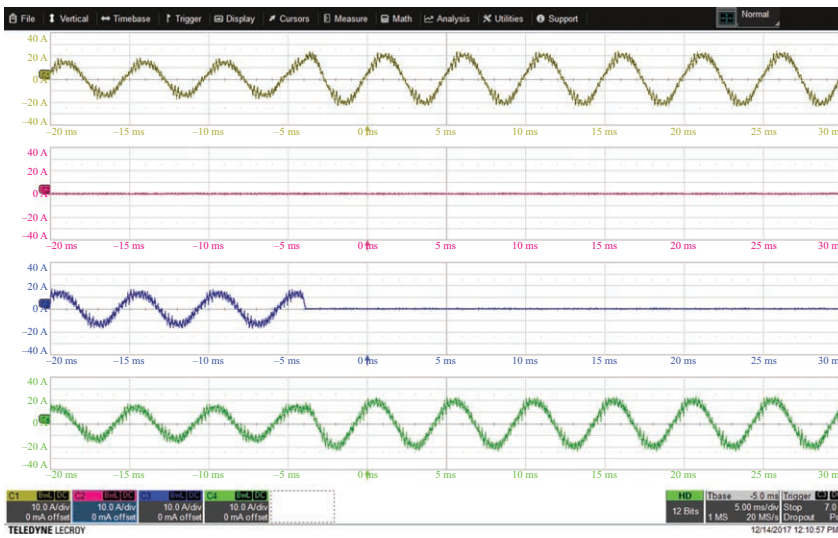


Figure 16.38 Inverter 3 shut-off with inverter 2 already off during generation mode with torque control at −6,000 rpm and with 10 N m [106]. Ch1: i_{a1} (10 A/div), Ch2: i_{a2} (10 A/div), Ch3: i_{a3} (10A/div), Ch4: i_{a4} (10 A/div), time resolution: 5 ms/div

the hysteresis regulators. Although the application of MPC to multiphase drives is rather limited in the real world, the literature contains several attempts that will be addressed in this section.

The MPC is nothing than a different way to get the inverter reference voltages. The main classification of the MPC multiphase schemes depends on the selection method of the reference voltages, resulting into two main categories:

- Finite control set MPC (FCS-MPC) schemes that select the reference voltages among the instantaneous power converter's discrete states. The FCS-MPC provides directly the converter switching functions as they do not need a pulse width modulator. The FCS-MPC imposes variable switching frequency.
- Continuous control set MPC (CCS-MPC) schemes that select the reference voltages among all possible average voltage vectors which the power converter can apply. The CCS-MPC needs a pulse width modulator and imposes a constant switching frequency.

Figure 16.39 contains the most relevant MPC control solutions applied to multiphase drives.

In the FCS-MPC, the reference voltages are selected among the instantaneous power converter's discrete states according to the minimization of a cost function. This operation is quite easy to implement in three-phase FCS-MPC drives where the number of all possible discrete states is only eight for two-level inverters. However, the extension of the FCS-MPC algorithms to multiphase drives is quite complicated as the number of power converter's discrete states increases exponentially. Therefore, the application of FCS-MPC is limited to only five-phase and six-phase motors. The FCS-MPC is divided into the following categories [93–105]:

- FCS-MPC for stationary current control (SCC). Based on the VSD approach, this solution aims at controlling the current in (α,β) frame while keeping to zero the current in the (x,y) subspace.

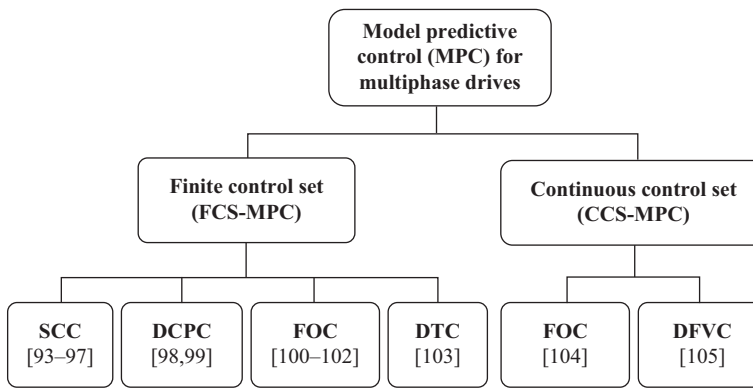


Figure 16.39 Classification of MPC solutions for multiphase drives with references

- FCS-MPC for direct control of phase currents (DCPC).
- FCS-MPC for conventional FOC approach with a cost function aimed at the control of (d,q) currents while minimizing the (x,y) currents.
- FCS-MPC for the DTC approach with a cost function designed for simultaneous stator flux and torque control.

It must be noted that the post-fault operation is not straightforward for the MPC-FCS schemes. Moreover, the current distortion is expected to increase, as some converter states are not available anymore. Another aspect that should be emphasized here is that the literature does not contain an FCS-MPC work that proposes a complete motor control scheme with flux weakening and operation at maximum load angle.

In the CCS-MPC schemes, the reference voltages are computed by using the inverse machine model according with the reference commands and the predicted variables (torque, fluxes and currents). These control schemes use a pulse width modulator and they are executed at constant switching frequency and thus the sampling frequency is also constant and synchronized with the switching frequency. This is an important difference with respect to the FCS-MPC schemes where the switching frequency is variable. The CCS-MPC schemes do not employ any cost function to design, and the number of power converter's discrete states is not so important (conventional PWM strategies are used).

While the FCS-MPC is limited to only the VSD modelling approach, the CCS-MPC can be successfully applied with VSD or with the MS to get modular three-phase control.

The CCS-MPC can provide the torque response in one beat – i.e. it can work in a dead-beat fashion. Moreover, the CCS-MPC completely avoids the distortion of the phase currents with respect to the FCS-MPC schemes. The CCS-MPC can be conveniently implemented either for FOC or for DFVC. As example, Figure 16.40 contains a CCS-MPC applied for DFVC of a multiple three-phase induction motor drive for a modular control [105].

The key block of the CCS-MPC is the model predictive estimator that must predict the stator currents and stator flux vectors at the next sampling time. The dynamic performance is very good. The CCS-MPC scheme has open-phase fault-tolerant ride through capability in case of one three-phase inverter sudden turn-off. Some experimental results for a four-pole, 10 kW asymmetrical six-phase induction motor fed by a 6 kHz inverter are shown next. The phase currents i_{a1} and i_{a2} are shown in Figure 16.41 at rated speed (6,000 rpm and 200 Hz) for fast torque transient from 0 N m up to 24 N m (150% the rated torque).

The phase currents are near sinusoidal with very low distortion, even with a low switching frequency. The same currents are shown in Figure 16.42 for inverter 2 shut-off at steady-state operation at rated speed (6,000 rpm 200 Hz) and 10 N m. It can be noted how the remaining three-phase set keeps working with increase in current to keep constant the reference torque. Complete experimental results, including flux-weakening operation with maximum load angle limitation can be found in [105].

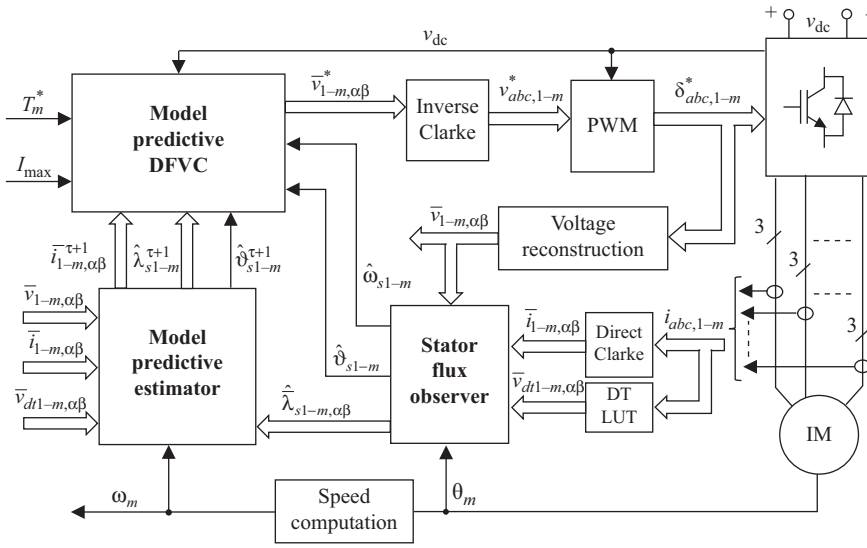


Figure 16.40 Modular DFVC using CCS-MPC for multiple three-phase induction motor drive [105]

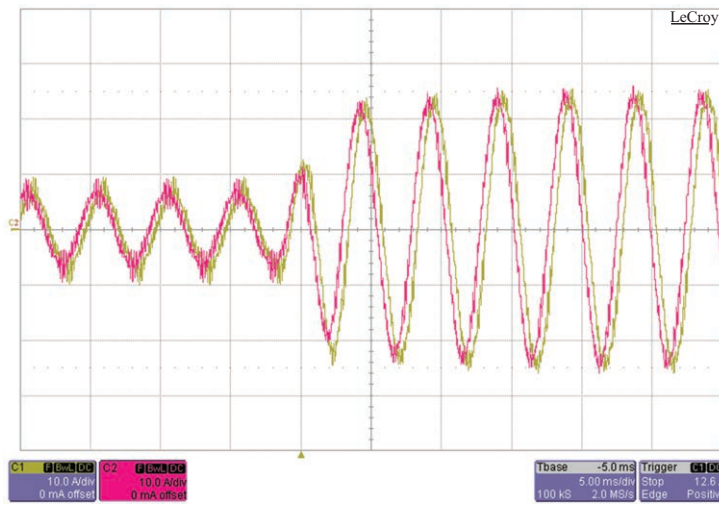


Figure 16.41 Phase currents i_{a1} and i_{a2} at 6,000 rpm (200 Hz) for fast torque transient from 0 N m up to 24 N m (150% rated torque). Ch1: i_{a1} (10 A/div), Ch2: i_{a2} (10 A/div), time scale: 5 ms/div [105]

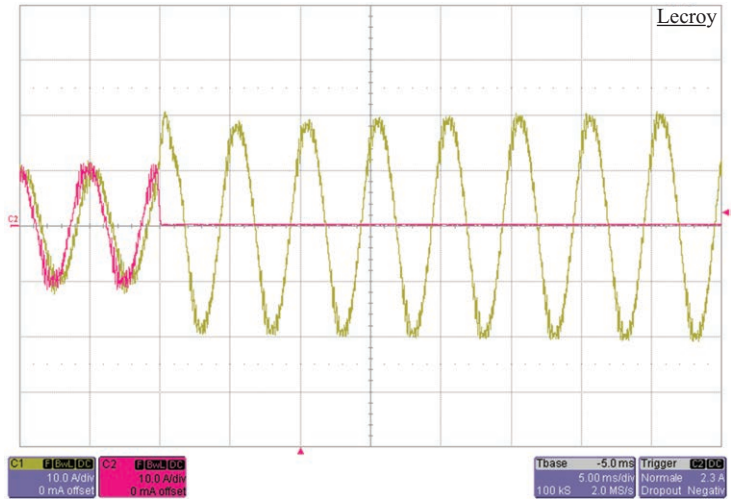


Figure 16.42 Phase currents i_{a1} and i_{a2} at 6,000 rpm (200 Hz) for inverter 2 turn off during steady-state operation at rated speed of 6,000 rpm and 10 N m. Ch1: i_{a1} (10 A/div), Ch2: i_{a2} (10 A/div), time scale: 5 ms/div [105]

16.5 Summary

The most relevant conclusions regarding the control of multiphase drives are the following:

- The multiphase drive configuration influences the control and the fault-tolerant operation. The multiphase motors with single neutral point are not considered as fault tolerant. The best fault-tolerant configuration is the topology that uses machine with isolated phases fed by H-bridge converters. Another fault-tolerant topology is the one that uses multiple three-phase motors having three-phase stator sets with isolated neutral points and fed by independent three-phase inverter units.
- The FOC remains the most employed control solution and it is usually based on the VSD modelling approach. Care must be taken for the current control since the adopted control solution must minimize the current harmonics in the (x_i,y_i) planes. In addition, the VSD approach becomes particularly heavy for multiphase drives with number of phases higher than six.
- The DTC application is rather limited to the five-phase and six-phase drives due to the ST complexity.
- The DFVC is a hybrid control solution between FOC and constant switching DTC since it uses direct flux control and torque current regulation. The DFVC can be considered as a unified approach since it can be easily applied to

synchronous and asynchronous machines. The DFVC combined with the MS modelling approach can be successfully applied for multiple three-phase motor drives to get a modular control structure.

- The FCS-MPC is limited to only five-phase and six-phase machines due to the complexity of the algorithm. The FCS-MPC has been implemented for current control under FOC. The literature does not report complete control solutions working at flux weakening with load angle limitation.
- The CCS-MPC has been implemented for flux and current control under DFVC for asymmetrical six-phase induction motor drives with flux weakening and load angle limitation, as well with open-phase fault operation in case of sudden inverter shut-off.

List of symbols

R_s, R_r	Stator and rotor resistances
L_s, L_r	Stator and rotor inductances
L_m	Magnetizing inductance
L_{ls}, L_{lr}	Stator and rotor leakage inductances
ω_m	Rotor mechanical speed
p	Pole-pairs number
k_T	Torque gain
λ_m	Back-emf constant
f_{sw}	Switching frequency

Glossary of terms

Cycloconverters	The power electronic converters which changes the output frequency in single stage of AC–AC conversion
Vector space decomposition	Splitting the machine original space into *n* subspaces out of which main subspace (α,β) contributes for flux and torque production and others for harmonics, zero-sequence currents, etc.
Discontinuous PWM	The pulse width modulation operated between limits of DPWM-MIN and DPWM-MAX strategies

References

[1] E. Levi, R. Bojoi, F. Profumo, H.A. Toliyat and S. Williamson, 'Multiphase induction motor drives – a technology status review', IET Electr. Power Appl., vol. 1, no. 4, pp. 489–516, 2007.

[2] H. Kim, K. Shin, S. Englebretson, N. Frank and W. Arshad, 'Analytical model of multiphase permanent magnet synchronous machines for energy and transportation applications', IEEE-IEMDC, pp. 172–179, 2013.

[3] E.E. Ward and H. Härer, 'Preliminary investigation of an inverter-fed 5-phase induction motor', Proc. IEE, 1969, 116, (6), pp. 980–984.
[4] R.H. Nelson and P.C. Krause, 'Induction machine analysis for arbitrary displacement between multiple winding sets', IEEE Transactions on Power Apparatus and Systems, vol. PAS-93, no. 3, pp. 841–848, 1974.
[5] R. Bojoi, A. Cavagnino, A. Tenconi, A. Tessarolo and S. Vachetto, 'Multiphase electrical machines and drives in the transportation electrification', 2015 IEEE International Forum on Research and Technologies for Society and Industry Leveraging a better tomorrow (RTSI), pp. 205–212.
[6] M.J. Duran, E. Levi and F. Barrero, 'Multiphase drives: introduction', J. Webster (ed.), Wiley Encyclopedia of Electrical and Electronics Engineering, John Wiley & Sons, Inc., New York, 2017.
[7] Singh, G.K.: 'Multi-phase induction machine drive research – a survey', Electr. Power Syst. Res., vol. 61, pp. 139–147, 2002.
[8] E. Levi, 'Multiphase electric machines for variable-speed applications', IEEE Trans. Ind. Electron., vol. 55, no. 5, pp. 1893–1909, 2008.
[9] R. Bojoi, S. Rubino, A. Tenconi and S. Vaschetto, 'Multiphase electrical machines and drives: a viable solution for energy generation and transportation electrification', 2016 International Conference and Exposition on Electrical and Power Engineering (EPE), pp. 632–639.
[10] E. Levi, 'Advances in converter control and innovative exploitation of additional degrees of freedom for multiphase machines', IEEE Trans. Ind. Electron., vol. 63, no. 1, pp. 433–448, 2016.
[11] F. Barrero and M. Duran, 'Recent advances in the design, modelling, and control of multiphase machines—Part I', IEEE Trans. Ind. Electron., vol. 63, no. 1, pp. 449–458, 2016.
[12] F. Barrero and M. Duran, 'Recent advances in the design, modelling, and control of multiphase machines—Part II', IEEE Trans. Ind. Electron., vol. 63, no. 1, pp. 459–468, 2016.
[13] O. Wasynczuk, P.C. Krause and S.D. Sudhoff, 'Modeling a six-phase electric drive system with a low-speed-reversing control strategy', 1991 Summer Comput. Simul. Conf.
[14] K.S. Smith, R. Yacamini and A.C. Williamson, 'Cycloconverter drives for ship propulsion', Trans. IMurE, vol. 105, pt. 1, pp. 23–52, 1993.
[15] M. Benatmane and T. McCoy, 'Development of a 19 MW PWM converter for U.S. Navy surface ships', Proc. Int. Conf. ELECSHIP, 1998.
[16] F. Terrien, S. Siala and P. Noy, 'Multiphase induction motor sensorless control for electric ship propulsion', PEMD, pp. 556–561, 2004.
[17] L. Parsa and H.A. Toliyat, 'Five-phase permanent magnet motor drives for ship propulsion applications', 2005 IEEE Electric Ship Technologies Symposium, IEEE ESTS 2005 pp. 371, 378, 25–27 July 2005.
[18] T. Ericsen, N. Hingorani and Y. Khersonsky, 'Power electronics and future marine electrical systems', IEEE Trans. Ind. Applicat., vol. 42, no. 1, pp. 155–163, 2006.
[19] S. Castellan, R. Menis, M. Pigani, G. Sulligoi and A. Tessarolo, 'Modeling and simulation of electric propulsion systems for all-electric cruise liners',

IEEE Electric Ship Technologies Symposium, ESTS '07, pp. 60, 64, 21–23 May 2007.

[20] X. Zhang, C. Zhang, M. Qiao and F. Yu, 'Analysis and experiment of multi-phase induction motor drives for electrical propulsion', ICEMS, pp. 1251–1254, 2008.

[21] F. Scuiller, J. Charpentier and E. Semail, 'Multi-star multi-phase winding for a high power naval propulsion machine with low ripple torques and high fault tolerant ability', IEEE-VPPC, pp. 1–5, 2010.

[22] C. Bassi, A. Tessarolo, R. Menis and G. Sulligoi, 'Analysis of different system design solutions for a high-power ship propulsion synchronous motor drive with multiple PWM converters', ESARS, 2010.

[23] G. Sulligoi, A. Tessarolo, V. Benucci, M. Baret and A. Rebora, A. Taffone, 'Modeling, simulation, and experimental validation of a generation system for medium-voltage DC integrated power systems', IEEE Trans. on Ind. Appl., vol. 46, no. 4, pp. 1304–1310, 2010.

[24] A.S. Nanoty and A.R. Chudasama, 'Design of multiphase induction motor for electric ship propulsion', ESTS, pp. 283–287, 2011.

[25] B. Gamble, G. Snitchler and T. MacDonald, 'Full power test of a 36.5 MW HTS propulsion motor', IEEE Transactions on Applied Superconductivity, vol. 21, no. 3, pp. 1083–1088, 2011.

[26] G. Sulligoi, A. Tessarolo, V. Benucci, A.M. Trapani and M. Baret, F. Luise, 'Shipboard power generation: design and development of a medium-voltage dc generation system', IEEE Industry Applications Magazine, vol. 19, no. 4, pp. 47–55, 2013.

[27] B.C. Mecrow, A.G. Jack, D.J. Atkinson, *et al.*, 'Design and testing of a four-phase fault-tolerant permanent magnet machine for an engine fuel pump', IEEE Trans. On Ener. Conv., vol. 19, pp. 671–678, 2004.

[28] G.J. Atkinson, B.C. Mecrow, A.G. Jack, D.J. Atkinson, P. Sangha and M. Benarous, 'Comparison of two different fault-tolerant switched reluctance machines for fuel pump drive in aircraft', IEMDC, 2005.

[29] C. Gerada, K. Bradley, X. Huang, A. Goodman, C. Whitley and G. Towers, 'A 5-phase fault-tolerant brushless permanent magnet motor drive for an aircraft thin wing surface actuator', IEMDC, pp. 1643–1648, 2007.

[30] Z. Sun, J.D. Ede, J. Wang, G.W. Jewell, J.J.A. Cullen and A.J. Mitcham, 'Experimental testing of a 250 kW fault-tolerant permanent magnet generation system for large civil aero-engines', IECEC, AIAA 2007-4829, 2007.

[31] C. Xiaoyuan, D. Zhiquan, P. Jingjing and L. Xiangsheng, 'Comparison of two different fault-tolerant switched reluctance machines for fuel pump drive in aircraft', IEEE-IPEMC, pp. 2086–2090, 2009.

[32] X. Huang, A. Goodman, C. Gerada, Y. Fang and Q. Lu, 'Design of a five-phase brushless DC motor for a safety critical aerospace application', IEEE Trans. Ind. Electron., vol. 59, no. 9, pp. 3532–3541, 2012.

[33] W. Cao, B.C. Mecrow, G.J. Atkinson, J.W. Bennet and D.J. Atkinson, 'Overview of electric motor technologies used for more electric aircraft (MEA)', IEEE Trans. Ind. Electron., vol. 59, no. 9, pp. 3523–3531, 2012.

[34] M. Galea, Z. Xu, C. Tighe, T. Hamiti, C. Gerada and S. Pickering, 'Development of an aircraft wheel actuator for Green Taxing', IEEE-ICEM, pp. 2492–2498, 2014.
[35] M. Rottach, C. Gerada and P.W. Wheeler, 'Design optimisation of a fault-tolerant PM motor drive for an aerospace actuation application', IEEE-PEMD, pp. 1–6, 2014.
[36] C. Gerada, M. Galea and A. Kladas, 'Electrical machines for high performance aerospace applications', IEEE-WEMDCD, pp. 79–84, 2015.
[37] R. Bojoi, A. Cavagnino, A. Tenconi and S. Vaschetto, 'Control of shaft-line-embedded multiphase starter/generator for aero-engine', IEEE Trans. Ind. Electron., vol. 63, no. 1, 2016, pp. 641–652.
[38] S. Rubino, R. Bojoi, A. Cavagnino and S. Vaschetto, 'Asymmetrical twelve-phase induction starter/generator for more electric engine in aircraft', IEEE ECCE 2016, pp. 1–8.
[39] R. Bojoi, A. Cavagnino, M. Cossale, A. Tenconi and S. Vaschetto, 'Design trade-off and experimental validation of multiphase starter generators for 48 V mini-hybrid powertrain', IEEE-IEVC, pp. 1–7, 2014.
[40] S. Sadeghi, L. Guo, H.A. Toliyat and L. Parsa, 'Wide operational speed range of five-phase permanent magnet machines by using different stator winding configurations', IEEE Trans. Ind. Electron., vol. 59, no. 6, pp. 2621–2631, 2012.
[41] Y. Burkhardt, A. Spagnolo, P. Lucas, M. Zavesky and P. Brockerhoff, 'Design and analysis of a highly integrated 9-phase drivetrain for EV applications', IEEE-ICEM, pp. 450–456, 2014.
[42] M.G. Simões and P. Vieira, 'A high-torque low-speed multiphase brushless machine – a perspective application for electric vehicles', IEEE Trans. Ind. Electron., vol. 49, no. 5, pp. 1154–1164, 2002.
[43] A. Bruyere, E. Semail, A. Bouscayrol, F. Locment, J.M. Dubus and J.C. Mipo, 'Modeling and control of a seven-phase claw-pole integrated starter alternator for micro-hybrid automotive applications', IEEE-VPPC, pp. 1–6, 2008.
[44] G. Wolf and N. Pfittzke, 'Five-phase generator', US patent 7,989,996 B2.
[45] E. Jung, H. Yoo, S.-K. Sul, H.-S. Choi and Y.-Y. Choi, 'A nine-phase permanent-magnet motor drive system for an ultrahigh-speed elevator', IEEE Trans. Ind. Applicat., vol. 48, no. 3, pp. 987–995, 2012.
[46] Gamesa Technological Corporation, 'Gamesa 5.0 MW', Oct. 25, 2016, [Online]. Available: http://www.siemensgamesa.com/recursos/doc/productos-servicios/aerogeneradores/nuevas-fichas/catalogo-plataformas-eng.pdf.
[47] I. Gonzalez, M. Duran, F. Barrero, M. Bermudez and H. Guzman, 'Fault-tolerant efficient control of a six-phase induction machine with parallel machine-side converters', IEEE Trans. Power Electron., vol. 31, no. 4, pp. 3068–3079, 2016.
[48] D. Vizireanu, S. Brisset and P. Brochet, 'Design and optimization of a 9-phase axial-flux PM synchronous generator with concentrated winding for direct-drive wind turbine', in Conf. Rec. IEEE IAS Annu. Meeting, Tampa, FL, 2006, pp. 1912–1918.

[49] Z. Xiang-Jun, Y. Yongbing, Z. Hongtao, L. Ying, F. Luguang and Y. Xu, 'Modelling and control of a multi-phase permanent magnet synchronous generator and efficient hybrid 3L-converters for large direct-drive wind turbines', IET Electric Power Applicat., vol. 6, no. 6, pp. 322–332, 2012.
[50] S. Williamson and A.C. Smith, 'Pulsating torque and losses in multiphase induction machines', IEEE Trans. Ind. Appl., vol. 39, no. 4, pp. 986–993, 2003.
[51] Y. Zhao and T.A. Lipo, 'Space vector PWM control of dual three-phase induction machine using vector space decomposition', IEEE Trans. Ind. Applicat., vol. 31, no. 5, 1995, pp. 1100–1108.
[52] I. Zoric, M. Jones and E. Levi, 'Vector space decomposition algorithm for asymmetrical multiphase machines', 2017 International Symposium on Power Electronics (Ee), pp. 1–6.
[53] R. Bojoi, F. Farina, F. Profumo and A. Tenconi, 'Dual three-phase induction machine drives control – a survey', IEEJ Transactions on Industry Applications, vol. 126, no. 4, pp. 420–429, 2006, ISSN: 09136339.
[54] O. Ojo, G. Dong and Z. Wu, 'Pulse-width-modulation for five-phase converters based on device turn-on times', in Proc. of IEEE Ind. Appl. Soc. Annual Meeting IAS, 2006, pp. 627–634.
[55] O. Ojo and G. Dong, 'Generalized discontinuous carrier-based PWM modulation scheme for multi-phase converter-machine systems', in Proc. of IEEE Ind. Appl. Soc. Annual Meeting IAS, 2005, pp. 1374–1381.
[56] N. Bodo, E. Levi and M. Jones, 'Investigation of carrier-based PWM techniques for a five-phase open-end winding drive topology', IEEE Trans. Ind. Electron., vol. 60, no. 5, pp. 2054–2065, 2013.
[57] A. Iqbal, E. Levi, M. Jones and S.N. Vukosavic, 'Generalised sinusoidal PWM with harmonic injection for multi-phase VSIs', in Proc. IEEE Power Electronics Specialist Conference PESC, 2006, pp. 2871–2877.
[58] G. Carrasco and C.A. Silva, 'Space vector PWM method for five-phase two-level VSI with minimum harmonic injection in the overmodulation region', IEEE Trans. Ind. Electron., vol. 60, no. 5, pp. 2042–2053, 2013.
[59] A. Iqbal, E. Levi, M. Jones and S.N. Vukosavic, 'A PWM scheme for a five-phase VSI supplying a five-phase two-motor drive', in Proc. Annual Conference of the IEEE Industrial Electronics Society IECON, 2006, pp. 2575–2580.
[60] Ó. López, J. Álvarez, J. Doval-Gandoy and F.D. Freijedo, 'Multilevel multiphase space vector PWM algorithm', IEEE Trans. Ind. Electron., vol. 55, no. 5, pp. 1933–1942, 2008.
[61] Ó. López, J. Álvarez, J. Doval-Gandoy and F.D. Freijedo, 'Multilevel multiphase space vector PWM algorithm with switching state redundancy', IEEE Trans. on Industrial Electronics, vol. 56, no. 3, pp. 792–804, 2009.
[62] D. Casadei, G. Serra, A. Tani and L. Zarri, 'Multi-phase inverter modulation strategies based on duty-cycle space vector approach', in Proc. of Ship Propulsion and Railway Traction Systems Conference, 2005, pp. 222–229.
[63] D. Casadei, D. Dujic, E. Levi, G. Serra, A. Tani and L. Zarri, 'General modulation strategy for seven-phase inverters with independent control of multiple voltage space vectors', IEEE Trans. Ind. Electron., vol. 23, no. 2, pp. 1921–1932, 2008.

[64] E. Levi, D. Dujic, M. Jones and G. Grandi, 'Analytical determination of DC-bus utilization limits in multiphase VSI supplied AC drives', IEEE Trans. Energ. Convers., vol. 23, no. 2, pp. 433–443, 2008.
[65] L. Zarri, M. Mengoni, A. Tani, G. Serra and D. Casadei, 'Minimization of the power losses in IGBT multiphase inverters with carrier-based pulsewidth modulation', Trans. on Industrial Electronics, vol. 57, no. 11, pp. 3695–3706, 2010.
[66] D. Dujic, M. Jones and E. Levi, 'Analysis of output current ripple rms in multiphase drives using space vector approach', IEEE Trans. on Power Electronics, vol. 24, no. 8, pp. 1926–1938, 2009.
[67] D. Dujic, M. Jones and E. Levi, 'Analysis of output current-ripple RMS in multiphase drives using polygon approach', in IEEE Transactions on Power Electronics, vol. 25, no. 7, pp. 1838–1849, 2010.
[68] D. Casadei, M. Mengoni, G. Serra, A. Tani and L. Zarri, 'A new carrier-based PWM strategy with minimum output current ripple for five-phase inverters', Proceedings of the 2011 14th European Conference on Power Electronics and Applications, Birmingham, 2011, pp. 1–10.
[69] J.K. Kelly, E.G. Strangas and J.M. Miller, 'Multiphase space vector pulse width modulation', IEEE Trans. on Energy Convers., vol. 18, no. 2, pp. 259–264, 2003.
[70] P.S.N De Silva, J.E. Fletcher and B.W. Williams, 'Development of space vector modulation strategies for five phase voltage source inverters', in Proc. IEE Power Electronics, Machines and Drives Conference, 2004, pp. 650–650.
[71] G. Grandi, G. Serra and A. Tani, 'Space vector modulation of a seven-phase voltage source inverter', in Proc. Symposium on Power Electronics, Electrical Drives, Automation & Motion SPEEDAM, 2006, pp. S8-6–S8-13.
[72] A. Iqbal and E. Levi, 'Space vector modulation scheme for a five-phase voltage source inverter', in Proc. of 11th European Conf. on Power Electronics and Applications EPE, 2005, CD-ROM paper 006.
[73] H.M. Ryu, J.H. Kim and S.K. Sul, 'Analysis of multiphase space vector pulse-width modulation based on multiple d-q spaces concept', IEEE Trans. on Power Electronics, vol. 20, no. 6, pp. 1364–1371, 2005.
[74] A. Iqbal and E. Levi, 'Space vector PWM for a five-phase VSI supplying two five-phase series-connected machines', in Proc. of 12th International Power Electronics and Motion Control Conference EPE-PEMC, 2006, CD-ROM paper T2-409.
[75] M. Duran and E. Levi, 'Multi-dimensional approach to multi-phase space vector pulse width modulation', in Proc. of IECON 2006, Paris, France, 7–10 November, 2006, pp. 2103–2108.
[76] A. Lega, M. Mengoni, G. Serra, A. Tani and L. Zarri, 'Space vector modulation for multiphase inverters based on a space partitioning algorithm', IEEE Trans. on Industrial Electronics, vol. 56, no. 10, pp. 4119–4131, 2009.
[77] J. Prieto, F. Barrero, M.J. Durán, S. Toral Marín and M.A. Perales, 'SVM procedure for n-phase VSI with low harmonic distortion in the overmodulation region', IEEE Trans. Ind. Electron., vol. 61, no. 1, pp. 92–97, 2014.
[78] D.G. Holmes and T.A. Lipo, Pulse Width Modulation for Power Converters. New York: Wiley, 2003.

[79] A. Trzynadlowski and S. Legowski, 'Minimum-loss vector PWM strategy for three-phase inverters', IEEE Trans. on Power Electronics, vol. 9, no. 1, pp. 26–34, 1994.
[80] M.C. Cavalcanti, E.R. Cabral da Silva, A.M. Nogueira Lima, C.B. Jacobina and R.N. Cunha Alves, 'Reducing losses in three-phase PWM pulsed dc-link voltage-type inverter system', IEEE Trans. on Industry Applications, vol. 38, no. 4, pp. 1114–1122, 2002.
[81] J.W. Bennet, B.C. Mecrow, D.J. Atkinson and G.J. Atkinson , 'Safety-critical design of electromechanical actuation systems in commercial aircraft', IET Electr. Power Appl., vol. 5, no. 1, pp. 37–47, 2011.
[82] J.-M. Kim and S.-K. Sul, 'Speed control of interior permanent magnet synchronous motor drive for the flux weakening operation', IEEE Trans. Ind. Applicat., vol. 33, no. 1, pp. 43–48, 1997.
[83] S.H. Kim and S.-K. Sul, 'Maximum torque control of an induction machine in the field weakening region', IEEE Trans. Ind. Applicat., vol. 31, no. 4, pp. 787–794, 1995.
[84] D.W. Novotny and T.A. Lipo, Vector Control and Dynamics of AC Drives, Oxford Press, Oxford, 1996.
[85] R. Bojoi, E. Levi, F. Farina, A. Tenconi and F. Profumo, 'Dual three-phase induction motor drive with digital current control in the stationary reference frame', IEE Proceedings, Electric Power Applications, vol. 153, no. 1, pp. 129–139, 2006.
[86] A.G. Yepes, J. Malvar, A. Vidal, O. Lopez and J. Doval-Gandoy, 'Current harmonics compensation based on multiresonant control in synchronous frames for symmetrical *n*-phase machines', IEEE Trans. Ind. Electron, vol. 62, no. 5, pp. 2708–2720, 2015.
[87] I. Takahashi and T. Noguchi, 'A new quick-response and high-efficiency control strategy of an induction motor', IEEE Transactions on Industry Applications, vol. IA-22, no. 5, pp. 820–827, 1986.
[88] M. Depenbrock, 'Direct self-control (DSC) of inverter-fed induction machine', IEEE Transactions on Power Electronics, vol. 3, no. 4, pp. 420–429, 1988.
[89] G. Buja, D. Casadei and G. Serra, 'Direct stator flux and torque control of an induction motor: theoretical analysis and experimental results', Conf. Rec. IEEE IECON, vol. 1, pp. T50–T64, 1998.
[90] R. Bojoi, F. Farina, G. Griva, F. Profumo and A. Tenconi, 'Direct torque control for dual three-phase induction motor drives', IEEE Trans. Ind. Applicat., vol. 41, no. 6, pp. 1627–1636, 2005.
[91] K. Hatua and V.Y. Ranganathan, 'Direct torque control schemes for split-phase induction machines', Conf. Rec. IEEE IAS, vol. 1, pp. 615–622, 2004.
[92] G. Pellegrino, R. Bojoi and P. Guglielmi, 'Unified direct-flux vector control for ac motor drives', IEEE Tran. Ind. Appl., vol. 47, no. 5, pp. 2093–2102, 2011.
[93] F. Barrero, M.R. Arahal, R. Gregor, S. Toral and M.J. Duran, 'A proof of concept study of predictive current control for VSI-driven asymmetrical dual three-phase AC machines', IEEE Trans. Ind. Electron., vol. 56, no. 6, pp. 1937–1954, 2009.

[94] R. Gregor, F. Barrero, S.L. Toral, *et al.*, 'Predictive-space vector PWM current control method for asymmetrical dual three-phase induction motor drives', IET Electric Power Applications, vol. 4, no. 1, pp. 26–34, 2010.
[95] H. Guzman, M.J. Duran, F. Barrero, *et al.*, 'Comparative study of predictive and resonant controllers in fault-tolerant five-phase induction motor drives', IEEE Trans. Ind. Electron., vol. 63, no. 1, pp. 606–617, 2016.
[96] I. Gonzalez-Prieto, M.J. Duran, J.J. Aciego, C. Martin and F. Barrero, 'Model predictive control of six-phase induction motor drives using virtual voltage vectors', IEEE Trans. Ind. Electron., vol. 65 , no. 1, pp. 27–37, 2018.
[97] M. Salehifar, M.M. Eguilaz, G. Putrus and P. Barras, 'Simplified fault tolerant finite control set model predictive control of a five-phase inverter supplying BLDC motor in electric vehicle drive', Electric Power Systems Research, vol. 132, pp. 56–66, 2016.
[98] H. Lu, J. Li, R. Qu, D. Ye and L. Xiao, 'Reduction of unbalanced axial magnetic force in postfault operation of a novel six-phase double-stator axial-flux PM machine using model predictive control', IEEE Trans. Ind. Applicat., vol. 53, no. 6, pp. 5461–5469, 2017.
[99] M. Salehifar and M. Moreno-Equilaz, 'Fault diagnosis and fault-tolerant finite control set-model predictive control of a multiphase voltage-source inverter supplying BLDC motor', ISA Transactions, vol. 60, pp. 143–155, 2016.
[100] C.S. Lim, E. Levi, M. Jones, N.A. Rahim and W.P. Hew, 'FCS-MPC-based current control of a five-phase induction motor and its comparison with PI-PWM control', IEEE Trans. Ind. Electron., vol. 61, no. 1, pp. 149–163, 2014.
[101] M. Cheng, F. Yu, K.T. Chau and W. Hua, 'Dynamic performance evaluation of a nine-phase flux-switching permanent-magnet motor drive with model predictive control', IEEE Trans. Ind. Electron., vol. 63, no. 7, pp. 4539–4549, 2016.
[102] C. Xue, W. Song and X. Feng, 'Finite control-set model predictive current control of five-phase permanent-magnet synchronous machine based on virtual voltage vectors', IET Electric Power Applications, vol. 11, no. 5, pp. 836–846, 2017.
[103] J.A. Riveros, F. Barrero, E. Levi, M.J. Durán, S. Toral and M. Jones, 'Variable-speed five-phase induction motor drive based on predictive torque control', IEEE Trans. Ind. Electron., vol. 60, no. 8, pp. 2957–2968, 2013.
[104] J.L.R. Martinez, R.S. Arashloo, M. Salehifar and J.M. Moreno, 'Predictive current control of outer-rotor five-phase BLDC generators applicable for off-shore wind power plants', Electric Power Systems Research, vol. 121, pp. 260–269, 2015.
[105] S. Rubino, R. Bojoi, S.A. Odhano and P. Zanchetta, 'Model predictive direct flux vector control of multi three-phase induction motor drives', IEEE Trans. Ind. Applicat, vol. 54 , no. 5, pp. 4394–4404, 2018.
[106] S. Rubino, 'High performance control techniques for multiphase edrives', Doctoral Thesis, Politecnico di Torino, Italy, May 2019.

Chapter 17

Fractional-slot concentrated winding machines and drives

Ayman M. EL-Refaie[1]

17.1 Definition of fractional-slot concentrated windings

The classical definition of a concentrated winding is a winding having one slot per pole per phase. This is a standard winding in the case of brushless DC (BLDC) machines with trapezoidal back-electromotive force (EMF) voltage waveforms. This definition has been used in several other references [1,2]. Some researchers refer to such winding configuration as distributed windings having one slot per pole per phase. Figure 17.1 shows an example of such winding configuration in case of a four-pole machine. There are also fractional-slot distributed windings that are typically used to reduce torque ripple and in some cases for ease of manufacturing. Distributed windings can be referred to in general as "overlapping" windings since there is a lot of overlap between the various coils and phases in the end region. The two most common nonoverlapping windings used in PM synchronous machines are 2 slots/pole/phase (typically for brushless AC (BLAC) machines) and as previously mentioned the 1 slot/pole/phase (typically for BLDC machines).

A relatively more recent definition of concentrated windings (even though this type of winding configuration existed for a long time) is a winding concentrated around one tooth [3,4]. These are referred to as "fractional-slot concentrated windings (FSCW)" or "nonoverlapping" windings since there is no overlap between the various coils and phases in the end region (at least in one end of the machine while the other end might have reduced overlap due to the coil connections). Also sometimes "tooth winding" is also used. Using this definition, there are two main categories of FSCW [3,4]. The first category includes designs having concentrated windings and a regular, evenly spaced distribution of slots. The second category includes designs having concentrated windings and slots that are irregularly (i.e., unevenly) spaced.

The first category using evenly spaced stator slots is more popular and more widely used. Within this category, there are two possible winding configurations [3].

[1]Department of Electrical and Computer Engineering, Opus College of Engineering, Marquette University, USA

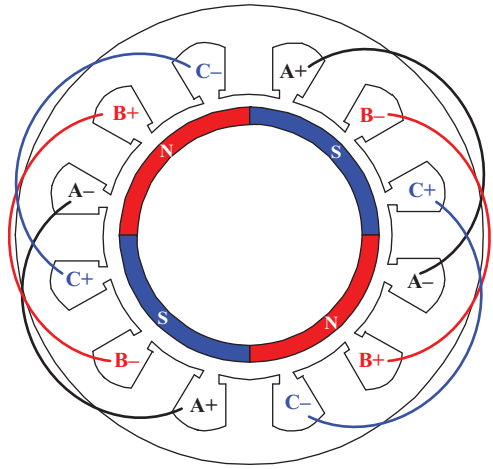


Figure 17.1 Example of concentrated windings having one slot per pole per phase

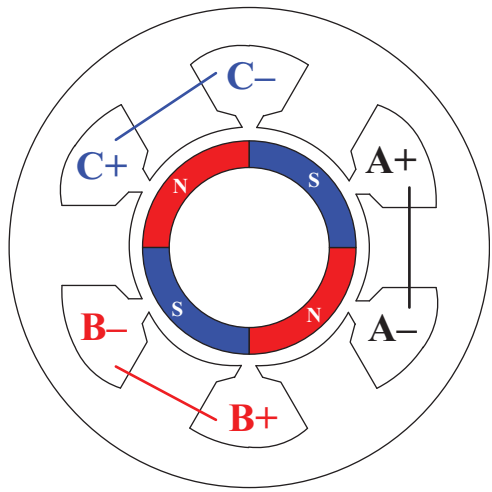


Figure 17.2 Example of SL concentrated windings around one tooth

The first configuration, called single-layer (SL) concentrated windings, has each slot occupied by a coil side of only one phase. This configuration yields a reduced number of coils equal to half the number of stator slots, resulting in simplified designs for manufacturing. An example of this configuration is shown in Figure 17.2 for a four-pole machine. The second configuration is called double-layer (DL) concentrated windings. In this case, two coil sides of the same phase or of two different phases occupy each slot. An example of this configuration is shown

in Figure 17.3 for a four-pole machine. An example of a six-pole machine design having concentrated windings and an irregular distribution of slots is shown in Figure 17.4. Figures 17.5 and 17.6 show actual prototypes of SL and DL windings with regular slot distribution [5].

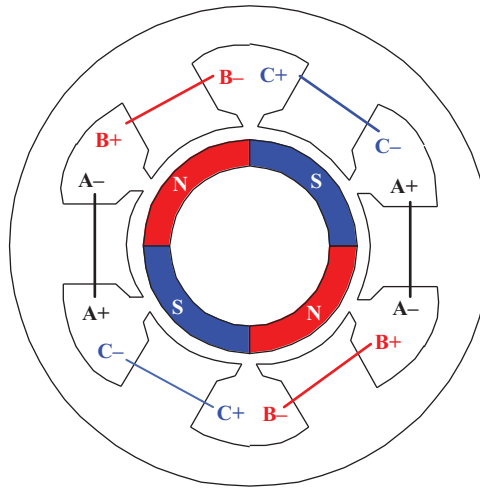


Figure 17.3 Example of DL concentrated windings around one tooth with a regular evenly spaced stator slot configuration

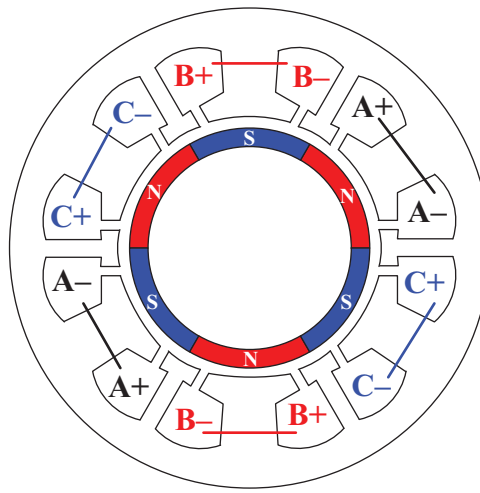


Figure 17.4 Example of concentrated windings around one tooth with an irregular distribution of slots



Figure 17.5 A 12-slot/10-pole design with SL winding [5]

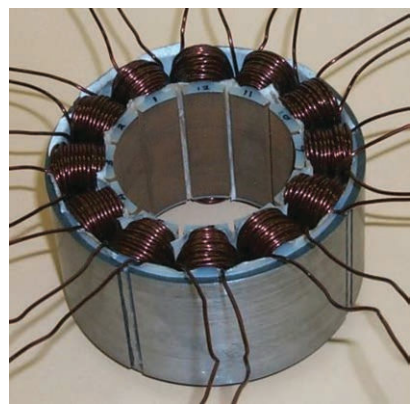


Figure 17.6 A 12-slot/10-pole design with DL winding [5]

17.2 Advantages of using concentrated windings

There are several advantages of using FSCW versus using distributed windings [4,5]. These advantages include the following:

- Significant reduction in the copper volume used in the end region, especially in the case of short axial-length machines. This is clear comparing Figures 17.1 and 17.2. This advantage is also emphasized in Figures 17.7 and 17.8 comparing the end regions of distributed windings and FSCW in the case of a two-pole machine.
- Significant reduction in the Joule losses in the end region due to shorter end turns.

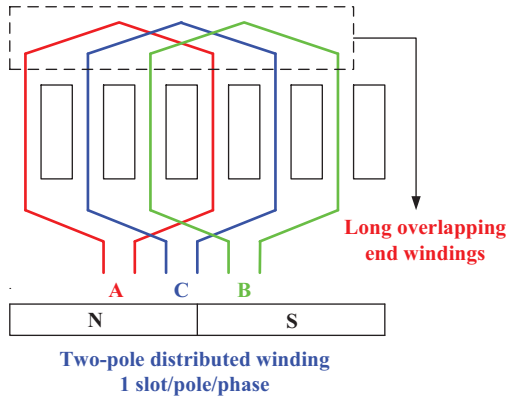


Figure 17.7 Two-pole distributed winding

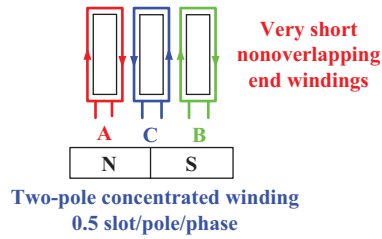
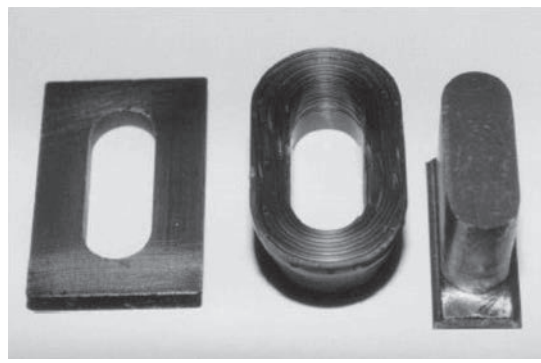


Figure 17.8 Two-pole concentrated winding

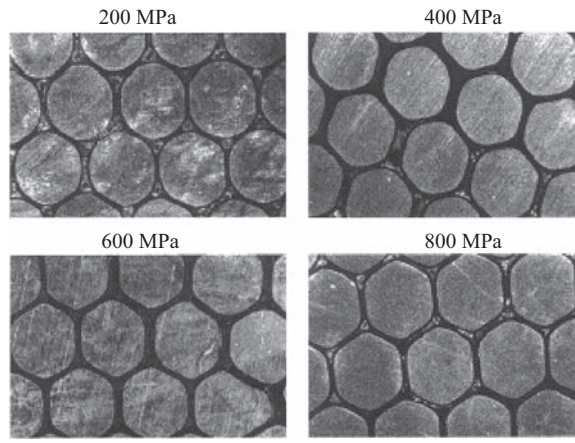
- Potential for improved efficiency compared to distributed windings. This depends on the breakdown of losses between copper and core losses because even though in the case of FSCW there is reduction in copper losses, there could be an increase in core losses in the case of FSWC (especially for high-speed/frequency applications) due to the additional harmonic content as will be discussed later.
- Potential reduction in cost enabled by simplified manufacturing. The ease of manufacturing is further enhanced when the stator can be segmented into separate stator poles. This approach is being pursued with stators made out of conventional steel laminations or soft magnetic composite (SMC) material. Table 17.1 provides a comparison of the various methods of segmenting the stator [6].
- Significantly higher copper slot fill factor (up to 78 %) can be achieved, where slot fill factor is defined as the ratio of the net copper area to the total area of each slot. Such high slot fill factor values have been reported in prototype machines using segmented SMC structures and compressed FSCW [7]. An example of this configuration is shown in Figure 17.9. Similar values of slot fill factor values have been reported in case of segmented laminated stator

Table 17.1 Comparison of various methods for segmenting the stator

	SMC	**Plug-in teeth**	**Joint-lapped core**
Copper slot fill factor	78% with pre-pressed coils	60%–65%	75%
Stator back iron rigidity	Lower rigidity due to segmented back iron	Rigid stator back iron	Lower rigidity due to segmented back iron
Number of pieces and tolerances	2× the number of stator teeth	1× the number of stator teeth	1× the number of stator teeth
Type of stator structure	Solid pieces of SMC	Laminated structures	Laminated structures
Saturation level	Lower saturation level of SMC	Same saturation level as in continuous structures	Same saturation level as in continuous structures



(a)



(b)

Figure 17.9 (a) Manufactured core components and coil [7]. (b) Coil sections resulting from pressing trials [7] (78% fill factor reported)

structures using the "plug-in-tooth" technique [8] shown in Figure 17.10. Also a 75% slot fill factor has been reported using a "joint-lapped core" [9] in Figure 17.11.

- FSCW can be used in the design of modular PM brushless machines with higher numbers of phases to improve fault tolerance [10]. They also can be used in high-phase-number machines to increase the specific torque [11].

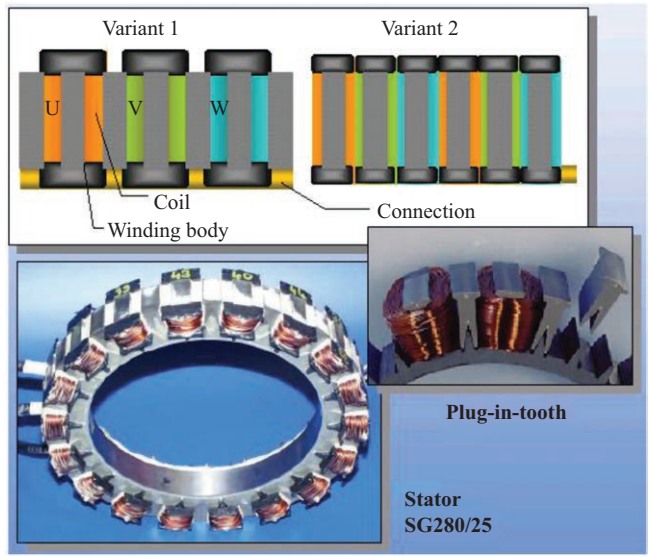


Figure 17.10 Example of stator structure using laminated plug-in-tooth technique [8]

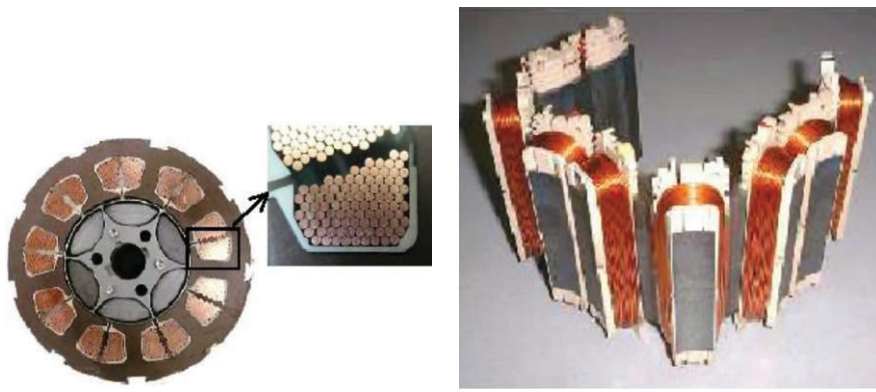


Figure 17.11 (a) Cross section of a joint-lapped core machine [9] (75% fill factor reported). (b) Joint-lapped core after winding [9]

Table 17.2 Comparison of distributed windings and FSCW

	Distributed windings	**FSCW**
Typical copper slot fill factor	35%–45%	50%–65% (if coupled with segmented stator structures)
Stator structure	Continuous laminations	Continuous laminations or segmented structures
End turns	Long overlapping	Short nonoverlapping
Torque-producing stator space harmonic component	Fundamental	In most cases (except for 0.5 slot/pole/phase) a higher-order harmonic

Table 17.2 provides a high-level comparison between distributed windings versus FSCW [6]. Some of the points of comparison will be discussed in more detail in coming sections of this chapter.

17.3 Challenges involved in using FSCW

There are also challenges associated with the application of concentrated windings that must be carefully considered. The key challenge is that spatial magnetomotive force (MMF) distributions in the machine air gap that result from FSCW include significantly more higher-order harmonic contents compared to distributed windings. This can have an impact on

- higher core losses especially in the rotor,
- risks of elevated torque ripple and low winding factors, and
- potential for higher acoustic noise and vibration.

Detailed discussion of the various opportunities and challenges of FSCW is presented in [6].

17.4 Three-phase structures that can support FSCW

For three-phase machines, traditionally FSCW were too often restricted to windings with a shortened pitch of 120 electrical degrees. This corresponds to the designs that have 0.5 slot/pole/phase. Such windings have reduced performance compared to the traditional 1 slot/pole/phase configurations (winding factor of 0.866). The building block of such configurations is shown in Figure 17.12. There are a significant number of three-phase structures that can support FSCW if the number of magnetic poles is increased, making it possible to introduce a fractional number of slots/pole/phase. Several of these slot/pole combinations became very popular and were extensively investigates over the past decade.

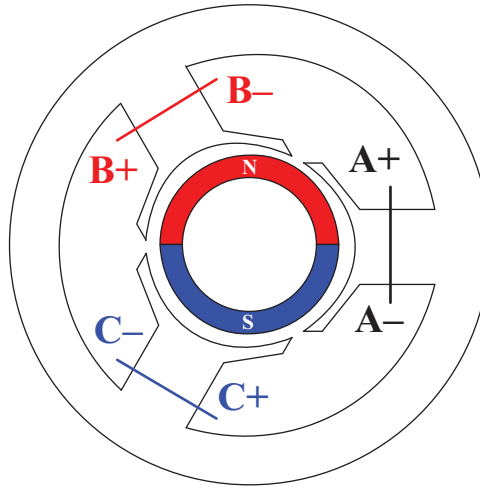


Figure 17.12 Example of FSCW with 1/2 slot/pole/phase

Considering three-phase machines, the candidate combinations of slots and poles that allow the realization of balanced windings are governed by the following condition [3]:

$$\frac{S}{[GCD(S, 2p)]} = 3C \tag{17.1}$$

where S is the number of slots, p is the number of pole pairs, C is a positive integer (1,2,...), and GCD is the greatest common divisor.

The three-phase machines that can be equipped with the most efficient FSCW have numbers of slots/pole/phase less than or equal to 1/2. Table 17.3 summarizes all of the possible combinations of slots and poles that can support concentrated windings [3,4]. Each entry of this table includes the number of slots per pole per phase (q) and the synchronous component winding factor (K_{w1}) associated with the torque-producing spatial MMF component that is electromagnetically coupled with the rotor field.

Winding factor values in the table are surrounded by parentheses when it is possible to artificially increase the winding pitch by extending the tooth tips to collect and concentrate the air gap flux, similar to techniques used with pole pieces in conventional DC or synchronous machines. This situation occurs when the number of slots per pole per phase q is less than 1/3 [3]. For structures that can support SL windings, q is underlined in the table. In these cases, the reduced number of coils ($S/2$) simplifies manufacturing and assembly processes. In [12], this work of identifying feasible slot/pole combinations that can support three-phase FSCW was expanded for higher number of phases.

Table 17.3 Combinations of stator slots (S) and poles (2p) that allow realization of balanced three-phase concentrated windings [3]

S \ 2p	2	4	6	8	10	12	14	16	18	20	22	24
3	1/2 .866	1/4 .866		1/8 (.866)	1/10 (.866)		1/14 (.866)	1/16 (.866)		1/20 (.866)	1/22 (.866)	
6	1.5	1/2 .866		1/4 (.866)	1/5 (.5)		1/7 (.5)	1/8 (.866)		1/10 (.866)	1/11 (.5)	
9		3/4 .617	1/2 .866	3/8 .945	3/10 .945	1/4 (.866)	3/14 (.617)	3/16 (.328)		3/20 (.328)	3/22 (.617)	1/8 (.866)
12	2 .259	1.5		1/2 .866	2/5 .966		2/7 (.966)	1/4 (.966)		1/5 (.5)	2/11 (.259)	
15				5/8 .711	1/2 .866		5/14 .951	5/16 .951		1/4 (.866)	5/22 (.711)	
18			1.5	3/4 .617	3/5 .735	1/2 .866	3/7 .902	3/8 .945		3/10 .945	3/11 (.902)	1/4 (.866)
21				7/8 .538	7/10 .650		1/2 .866	7/16 .870		7/20 .953	7/22 .953	
24		2 .259		1.5	4/5 .588		4/7 .760	1/2 .866		2/5 .966	4/11 .958	

17.5 Comparison of SL and DL configurations

Comparison of SL and DL FSCW has been the focus of several publications [4,5,13]. There are some points of comparison between the SL and DL FSCW configurations that are rather apparent from inspection. In order to assess these differences more accurately, they have to be evaluated in actual machine designs. The following list highlights these differences in a more general and qualitative manner:

- Using two layers per slot requires more insulation, so the slot fill factor is typically less in DL windings compared to SL windings.
- The coil pitch of an SL winding is equal to the slot pitch while the coil pitch of a DL winding is less than the slot pitch. This can be observed in Figure 17.13, where τ_c is the coil pitch and τ_s is the slot pitch.
- The SL winding has almost twice the axial-end winding build (i.e., length) compared to the DL winding. As a result, a DL winding configuration is typically more compact compared to an SL winding configuration.
- Both winding configurations generally reduce the cogging torque amplitude compared to conventional distributed windings that overlap in the end-turn region. A simple explanation for this desirable characteristic can be offered as follows. When half the edges of the north- and south-pole rotor magnets face stator slot openings in a machine with nonoverlapping (FSCW) windings, the remaining pole edges approximately face the centers of the stator teeth,

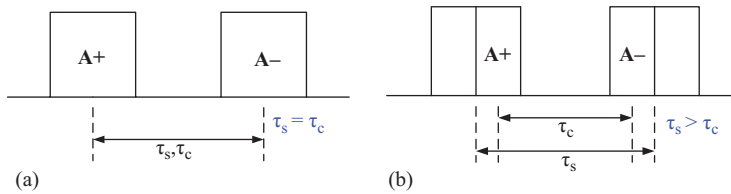


Figure 17.13 (a) Coil pitch of an SL FSCW compared to the slot pitch. (b) Coil pitch of a DL FSCW compared to the slot pitch

reducing the electromagnetic saliency of the stator–rotor structure. For conventional overlapping windings, it is more common to encounter higher levels of electromagnetic saliency, with higher numbers of magnets facing slot openings in some particular rotor positions [14,15].

- SL windings typically produce higher levels of spatial MMF harmonic components in the air gap compared to DL windings, particularly for the subharmonic components. The harmonics contribute extra stator leakage inductance that can be very helpful in some PM machines to reduce the current required for field weakening at elevated speeds in the constant-power region.
- SL windings offer better potential for fault tolerance than DL windings because the phase-to-phase mutual inductance of the stator windings is zero for SL windings with non-salient rotor structures.
- The rotor eddy-current losses are higher for SL windings due to the higher spatial MMF harmonic content in the air gap produced by the SL windings compared to DL windings.

Table 17.4 provides a high-level summary of the key points of comparison between the two types of windings. Since rotor losses have been identified as one of the key challenges of using FSCW as will be discussed later in more detail, there has been several publications that explored going to higher number of winding layers (beyond DL) [16,17] and/or winding configurations that reduce harmonic content in FSCW [18–20]. Some of these proposed winding configurations with a coil pitch that spans two slot pitches and hence they are somewhere between FSCW and distributed windings. In this case, it was shown that there can be significant reduction in harmonic content but at the expense of making the winding configuration more complicated. In [16], the effect of increase in number of winding layers on the winding factors of the torque-producing and the first loss-producing harmonics in FSCW interior PM machines is studied. The optimum slot/pole/phase combinations with a high winding factor for a torque-producing harmonic, but low harmonic content, with four winding layers are identified. An improvement in power density, reluctance torque, efficiency, and torque ripple going from single- to double- to four-layer winding configurations was shown.

In [17], the general theory of the multilayer *m*-phase winding is presented. General rules to design such a type of winding are given. Higher number of phases is included. Different types of machines have been evaluated. It was shown that

Table 17.4 Comparison of DL and SL windings

	DL windings	**SL windings**
No. of coil sides/ slot	2	1
Mutual phase coupling	Significant phase–phase coupling through mutual slot leakage	Very low mutual phase coupling (recommended for fault tolerance)
End turns	Shorter end turns	Longer end turns
Phase inductance	Lower phase inductance due to lower phase leakage inductance	Higher phase inductance due to higher phase leakage inductance (better flux-weakening capability)
Rotor losses	Lower rotor losses mainly due to lower fundamental stator MMF space harmonic component	Higher rotor losses mainly due to higher fundamental stator MMF space harmonic component
Slot/pole combinations	Many slot/pole combinations can support DL windings	Few slot/pole combinations can support SL windings
Ease of manufacturing	More difficult to manufacture since there are 2 coil sides/slot	Easier to manufacture since there is 1 coil side/slot
Synchronous winding factor	Lower	Higher
Back EMF	More sinusoidal	Less sinusoidal

four-layer windings did not show significant improvement in the case of surface PM (SPM) machines. In case of interior PM (IPM) machines, there was significant reduction in torque ripple. In the case of induction machines (IMs), it was shown that four-layer windings make FSCW more feasible even though the torque ripple was fairly high.

17.6 Criteria for choosing the optimum slot/pole combination

As previously discussed, there are several slot/pole combinations that can support three-phase concentrated windings. Criteria for choosing the optimum slot/ combinations will be discussed in this section. In Section 17.4, the synchronous component winding factor K_{w1} was introduced that emerges as an important parameter characterizing each slot/pole combination.

There are two other important parameters that need to be introduced. The first parameter is the lowest common multiple (LCM) of the number of slots and the number of magnetic poles, expressed as $LCM(S, 2p)$. Table 17.5 summarizes the values of this parameter for the various candidate slot/pole combinations listed in Table 17.3.

Table 17.5 Evaluation of LCM(S, 2p) parameter for candidate slot/pole combinations

S \ 2p	2	4	6	8	10	12	14	16	18	20	22	24
3	6	12		24	30		42	48		60	66	
6	6	12		24	30		42	48		60	66	
9		36	18	72	90	36	126	144		180	198	72
12	12	12		24	60		84	48		60	132	
15				120	30		210	240		60	330	
18			18	72	90	36	126	144		180	198	72
21				168	210		42	336		420	462	
24		24		24	120		168	48		120	264	

Table 17.6 Evaluation of parameter K for candidate slot/pole combinations

S \ 2p	2	4	6	8	10	12	14	16	18	20	22	24
3	1	1		1	1		1	1		1	1	
6	2	2		2	2		2	2		2	2	
9		1	3	1	1	3	1	1		1	1	3
12	2	4		4	2		2	4		4	2	
15				1	5		1	1		5	1	
18			6	2	2	6	2	2		2	2	6
21				1	1		7	1		1	1	
24		4		8	2		2	8		4	2	

The second parameter (K) is the ratio of the product of the number of slots and poles to the LCM between the number of slots and the number of the poles, defined as follows:

$$K = \frac{(S * 2p)}{LCM(S, 2p)} = GCD(S, 2p) \tag{17.2}$$

where GCD is the greatest common divisor. Table 17.6 summarizes the values of this parameter K for the various candidate slot/pole combinations listed in Table 17.3.

Based on the entries in Tables 17.3, 17.5, and 17.6 and while considering the nature of the application for which the machine is being designed, the optimum slot/pole combination can be chosen as follows:

1. Choose the combination that has highest value for the synchronous component winding factor (K_{w1}). The rationale is that the average torque developed by a

surface PM machine equipped with concentrated windings and excited by sinusoidal current can expressed approximately as [4,21] follows:

$$T = \frac{1}{4\pi} K_{w1} n_1 n_t S B_{g\ \max} A_g I_{\max} \cos(\gamma)\ [\text{N m}] \tag{17.3}$$

where

K_{w1} is the synchronous winding factor.
n_1 is the number of layers in each slot (1 or 2).
n_t is the number of turns around each tooth.
S is the number of slots.
$B_{g\ \max}$ is the peak value of the no load air gap flux density [tesla].
A_g is the air gap area [m^2].
$I_{\max}$ is the peak phase current [A].

γ is the current angle between the orientation of the stator current vector and the q-axis that is orthogonal to the orientation of the rotor magnet flux linkage vector (electrical radians or degrees).

This equation shows that the winding factor determines the number of effective turns in the stator winding coils. To produce the same torque for lower values of K_{w1} would require either increasing the total number of turns or using higher currents. For the same torque, magnetic loading, and slot fill factor, this will lead to increased copper losses. This gives an important advantage to designs with high values of the winding factor K_{w1}.

It should be emphasized again that when the term "synchronous component" is used, it refers to the torque-producing component of the spatial winding function (i.e., MMF distribution) and not necessarily to the lowest-order Fourier component of the winding function (MMF). In some cases (especially SL winding cases), the lowest-order harmonic component of the spatial winding function does not contribute to average torque production since it is a subharmonic of the main torque-producing component.

2. Choose the combination that has the highest LCM of the number of slots and the number of poles. The reason for choosing the highest LCM value is that the number of cogging torque pulsations or periods (N) per full mechanical rotation is determined by that value [4,14,21].

$$N = LCM(S, 2p) \tag{17.4}$$

Since a higher cogging torque frequency typically indicates lower cogging torque amplitude, it is desirable to select slot/pole combinations with high values of N in order to reduce the cogging torque. In stators with distributed windings and evenly spaced slots, skewing the stator by one slot pitch (as well as other methods to reduce cogging torque) will typically reduce the cogging torque significantly. In the case of concentrated windings, skewing might not be that effective or practical because the choice of fractional slot/pole/phase values leads to large slot pitches. As a result, choosing the right combination of slots and poles is crucial in order to minimize the cogging torque.

3. Choose the combination that has a high even value of K [21,22]. The value of K is important because it is an indication of the symmetry of the machine and, hence, the net radial force that the machine will experience. If the value of K is "1" or any odd integer, this means that the net radial force on the machine is *high (this is typically the case with odd number of stator slots)*. If K is higher than "1" and even, this means that the net radial force on the machine is *low*.

   The net radial force between the stator and rotor comes from two major sources, stator steel to rotor magnet attraction and coil current to magnet interactions. The main radial forces in PM machines under consideration are due to magnet–steel attraction. These can be canceled or reduced by choosing slot/pole combinations that have a value of K higher than unity and even. Symmetric excitation of the coils will reduce or eliminate the remaining radial forces.

   The parameter K actually represents the number of angular rotor positions along the stator air gap periphery where cogging torque reaches peak values at the same time. Values of K that are even numbers indicate that these positions are all diametrically opposite pairs and, hence, the net radial forces on the rotor will be canceled.
4. Depending on the nature of the application for which the machine is being designed, there might be a good reason to prefer using SL windings. A good reason/example is the need for fault tolerance especially in safety critical applications as will be discussed later in more detail. Only some of the slot/pole combinations are compatible with SL windings, as shown previously in Table 17.3.

In addition to the previous four points, there are some general useful guidelines and observations presented in [3] that categorize the various slot/pole combinations based on the number of slots/pole/phase (q). These guidelines are summarized in Table 17.7.

17.7 How to determine the winding layout

After identifying the slot/pole combinations that can support FSCW as well as criteria to choose the "optimum" slot/pole combination, the next step is how to reach the "optimum" winding layout for the chosen slot/pole combination. In [23,24], a method was presented to determine the optimal winding layout for the various slot/pole combinations as well as design FSCW-PM machines based on the stator star of slots. There was another systematic procedure for laying out three-phase FSCW in an optimum way presented in [3], and this will be the focus of this section.

For values below unity, q has to be reduced to a fraction of two nondivisible integers b and c.

$$q = \frac{b}{c} \tag{17.5}$$

A repeatable sequence of 0s and 1s specific to the winding can be derived from this relationship. It is a list of c numbers that characterizes the winding distribution under $c/3$ poles. The structure of the whole machine winding can be derived from a

Table 17.7 Summary of the main features of different categories of balanced three-phase concentrated windings [3]

Slots/pole/phase (q)	Main features
1/2	• Short pitch of 120 electrical degrees • Relatively low performance in case of sinusoidal currents. Low K_{w1} of 0.866 • In case of rectangular currents and smooth rotor with surface PM, no-load back-EMF does not have a flat portion of sufficient width $\geq$ high torque ripple • Used for low-power applications that do not have torque ripple constraints
Between 1/2 and 1/3	• Higher performance compared to $q = 1/2$ • *12-slot, 10-pole design specifically interesting:* $\Rightarrow$ Can support SL winding $\Rightarrow$ Low torque ripple • Low cogging torque
Between 1/3 and 1/4	• For q less than 1/3, it is possible to adjust the width of the tooth tips to a value close to the pole pitch (like horns of the traditional pole pieces in DC or synchronous machines) to increase the magnetic flux linked by the winding, effectively increasing the winding pitch • Can provide high K_{w1} • *12-slot, 14-pole design specifically interesting:* $\Rightarrow$ Can support SL winding $\Rightarrow$ Torque is more sinusoidal $\Rightarrow$ Suitable for sinusoidal currents
Less than or equal 1/4	• More sinusoidal torque but of lower amplitude • In case of rectangular currents, irregular distribution of slots provides higher performance

periodic distribution of the structure under c poles described by three consecutive repeatable sequences if c is an even number. If c is an odd number, this distribution is antiperiodic. The number of 1s in the sequence is equal to b and the number of 0s is equal to b-c. The initial sequence can be described by:

$$\overbrace{\underbrace{000.....0}_{c-b}\,\underbrace{111.....1}_{b}}^{c}$$

For a given structure, the winding with the highest performance can be obtained by the most regular distribution of the 1s among the numbers 0s. An example given at the end of this section will emphasize that this rule is crucial for obtaining the highest synchronous component winding factor K_{w1}.

As an example, consider the case of a three-phase machine with 18 slots and 14 poles:

$$q = \frac{18}{3 * 14} = \frac{3}{7}$$

The following steps show how the whole winding configuration can be obtained:

1. Initial repeatable sequence: 0000111
2. Optimum repeatable sequence: 1010100
3. The optimum sequence is reproduced 3 times: 1010100|1010100|1010100
4. The usual sequence AC′BA′CB′ is assigned to the whole sequence where A′ is the return conductor of conductor A:

1	0	1	0	1	0	0	1	0	1	0	1	0	0	1	0	1	0	1	0	0
A	C′	B	A′	C	B′	A	C′	B	A′	C	B′	A	C′	B	A′	C	B′	A	C′	B

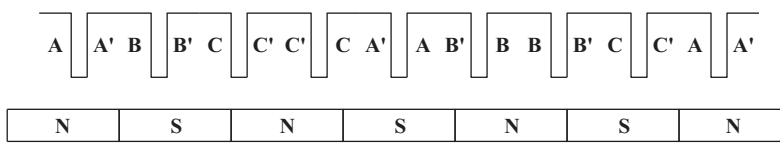
5. The conductors associated with the 1s are selected to form the first layer of the winding. Usually this layer cannot be directly realized to form an SL concentrated winding except for some specific cases identified previously in Table 17.3.

A	B	C	C′	A′	B′	B	C	A

6. The second layer is obtained by shifting the first layer by a tooth or slot pitch and reversing the conductor's direction.

A	B	C	C′	A′	B′	B	C	A	
	A′	B′	C′	C	A	B	B′	C′	A′

7. The final winding layout can be drawn as follows:



To emphasize the importance of developing the most regular distribution of the 1s among the 0s to achieve the optimum repeatable sequence in Step 2, two examples will be considered:

Example 1 For a combination of nine slots and ten poles:

$$q = \frac{9}{3 * 10} = \frac{3}{10}$$

A poor choice for the repeatable sequence in Step 2 would be 1010100000. Following the remaining steps in the procedure described above leads to the following:

1 0 1 0 1 0 0 0 0 0 1 0 1 0 1 0 0 0 0 0 1 0 1 0 1 0 0 0 0 0

A C′ B A′ C B′ A C′ B A′ C B′ A C′ B A′ C B′ A C′ B A′ C B′ A C′ B A′ C B′

A B C C A B B C A

A′ B′ C′ C′ A′ B′ B′ C′ A′

The resulting winding layout is as follows:



and the value of the synchronous component winding factor K_{w1} in this case is *0.4423*.

A much more promising repeatable sequence in Step 2 is 1001001000. Following the remaining steps in the procedure leads to the following:

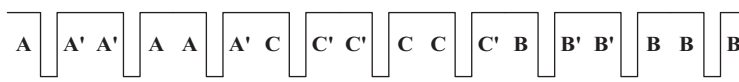
1 0 0 1 0 0 1 0 0 0 1 0 0 1 0 0 1 0 0 0 1 0 0 1 0 0 1 0 0 0

A C′ B A′ C B′ A C′ B A′ C B′ A C′ B A′ C B′ A C′ B A′ C B′ A C′ B A′ C B′

A A′ A C C′ C B B′ B

A′ A A′ C′ C C′ B′ B B′

and the resulting winding layout is as follows:



The synchronous component winding factor K_{w1} in this case is *0.945*, more than twice the previous value. This example makes it clear that choosing the optimum repeatable sequence is crucial for obtaining the highest synchronous winding factor and, hence, the most efficient winding layout. The details of how the winding factor is calculated will be presented in the following section.

Example 2 Consider next a combination of 12 slots and 14 poles:

$$q = \frac{12}{3 * 14} = \frac{2}{7}$$

A poor choice for the repeatable sequence in Step (2) would be 1010000. Following the remaining steps in the procedure described above leads to the following:

1	0	1	0	0	0	0	1	0	1	0	0	0	0	1	0	1	0	0	0	0
A	C′	B	A′	C	B′	A	C′	B	A′	C	B′	A	C′	B	A′	C	B′	A	C′	B

				A		B		C′		A′		B		C						
						A′		B′		C		A		B′		C′				

The resulting winding layout is as follows:



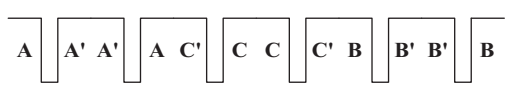
and the value of the synchronous component winding factor K_{w1} in this case is *0.683*.

A much more promising repeatable sequence in Step 2 is 1001000. Following the remaining steps in the procedure leads to the following:

1	0	0	1	0	0	0	1	0	0	1	0	0	0	1	0	0	1	0	0	0
A	C′	B	A′	C	B′	A	C′	B	A′	C	B′	A	C′	B	A′	C	B′	A	C′	B

				A		A′		C′		C		B		B′						
						A′		A		C		C′		B′		B				

The resulting winding layout is as follows:



The synchronous component winding factor K_{w1} in this case is *0.933*, considerably higher than the value with the previous sequence.

In [12], the work presented in [3] was expanded to cover four-, five-, and six-phase configurations. Tables including the winding factors, cogging torque indicators, and net radial force indicators for the various slot/pole combinations have been provided. In addition to these three parameters, a key parameter for choosing the optimal slot/pole combination has been introduced. This parameter is the rotor loss figure of merit (FOM) that helps compare the rotor losses for the various slot/pole combinations on relative basis. The values for the rotor loss FOM have been evaluated for three-, four-, five-, and six-phase designs. Together, all these sets of tables would help a machine designer to converge to the optimal slot/pole combination and number of phases based on his application requirements.

17.8 Calculation of the winding factor

After the winding layout has been determined as described in Section 17.7, the winding factor can be calculated. Three different methods for calculating the winding factor will be presented. Two of these methods can be used for either SL or DL windings while the third can only be used for DL windings. An example illustrating how the three methods can be applied is also presented at the end of this section. This example will show that all three methods lead to identical results.

17.8.1 EMF method

If the EMF phasors ($\bar{E}_i$) of all the winding elements/coil sides are known, the winding factor can be calculated as follows [4]:

$$\overline{Eh}_{phase,pu} = \sum_{Q/3} \overline{Eh}_i \tag{17.6}$$

where

$\overline{Eh}_{phase,pu}$ is the net phase *h*th-order harmonic EMF component in per-unit (phasor sum).
$\overline{Eh}_i$ is the *h*th-order harmonic EMF component phasor in per-unit (p.u.) of the winding element "*i*" that belongs to this specific phase.
Q is the total number of winding elements.

$$Q = S \text{ in case of SL winding} \tag{17.7}$$

$$Q = 2S \text{ in case of DL windings} \tag{17.8}$$

In both cases, we only need to calculate S phasors because, even in the case of DL windings, windings sharing the same slot can be represented by the same phasor.

$$K_{wh} = \frac{\left|\overline{Eh}_{phase,pu}\right|}{Q/3} \tag{17.9}$$

where $Q/3$ is the net phase EMF in p.u. for the special case when all of the winding elements of that phase are lumped together and their EMF vectors are all pointed in the same direction. This is the case for distributed winding with 1 slot/pole/phase. Equation (17.9) can be used to calculate the winding factor for the synchronous (i.e., torque-producing) component as well as any higher-order harmonic or sub-harmonic component. It is important to note that this winding factor includes both the winding distribution and pitch factors.

17.8.2 Winding function method

Another method for calculating the winding factor is to use the winding function [25]. The first step is to calculate the amplitude of the fundamental component (or any other higher-order harmonic) of the actual winding function. This value is equal to the product of the fundamental component (or any other higher-order harmonic) of a rectangular winding function (corresponding to the case when all the phase coils are distributed in a 1 slot/pole/phase configuration) and the winding factor of the winding of interest. Hence, the winding factor can be calculated as follows:

$$K_{\text{wh}} = \frac{N_h}{N_{hbase}} \tag{17.10}$$

where

K_{wh} is the winding function of the hth-order harmonic component.
N_h is the amplitude of the hth-order harmonic component of the actual winding function for the winding of interest.
N_{hbase} is the amplitude of the hth-order harmonic component of the base rectangular winding function for the same number of total turns in a $q = 1$ configuration.

17.8.3 Closed-form expressions

The third method for calculating the winding factor is to use closed-form expressions presented in [26] for fractional-slot windings. The derivations of these expressions have been discussed in detail in [26] and will not be repeated here. In this section, the focus is only to present the end results that can be used for calculating the winding factor. The value of the winding factor for each harmonic is calculated as the product of the corresponding harmonic distribution factor and harmonic pitch factor (i.e., $K_{wh} = K_{dh} * K_{ph}$). *It should be noted that this method is only applicable to DL windings. For SL windings, either the EMF method or the winding function method should be used.*

17.8.3.1 Calculating distribution factor for fractional-slot windings

$$K_{dh} = \frac{\sin(30^{\text{o}})}{N \sin\left(\frac{\alpha_h}{2}\right)} \quad q = \frac{b}{c} \tag{17.11}$$

where

K_{dh} is the distribution factor for the hth-order harmonic component.
q is the number of slots/pole/phase.
b is the numerator of the fraction that fixes the number of slots/pole/phase.
c is the denominator of the fraction that fixes the number of slots/pole/phase.

How to calculate α_h

(i) When c is even,

$$h = \frac{2p}{c}v \quad v = 1, 2, 4, 5, 7.....v_{synchronous} = \frac{c}{2} \tag{17.12}$$

where p is the number of pole pairs.

$$\alpha_h = 2 * d * \alpha_m * v + 180^{\circ} \text{ [elec.degrees]} \tag{17.13}$$

$$\text{where } \alpha_m = \frac{180^{\circ}}{b * m1}\text{[elec.degrees] and } m1 \text{ is the number of phases} \tag{17.14}$$

.

$$d = \frac{m1 * b * P + 1}{c} \tag{17.15}$$

where
d is a number representing the difference between two slots, which correspond to two adjacent vectors of the slot star (the slot star is a star formed of the vectors representing the voltages induced in the various coil sides in all slots).
P is the number of full pole pitches between two adjacent slots, which correspond to two adjacent vectors of the slot star. The smallest integer for which d becomes an integer has to be inserted. $P \geq 1$. *P is odd in case c is even*

(ii) When c is odd,

$$h = \frac{p}{c}v \;\; v = 1, 5, 7, 11, 13..... \; v_{synchronous} = c \tag{17.16}$$

$$\alpha_h = d * \alpha_m * v \quad (P \text{ is even})\text{[elec.degrees]} \tag{17.17}$$

$$\alpha_h = d * \alpha_m * v + 180^{\circ} \quad (P \text{ is odd})\text{[elec.degrees]} \tag{17.18}$$

The previous equations yield the correct signs. If we are only interested in absolute values:

(i) When c is even,

$$K_{dh} = \frac{0.5}{b \cos\left(\frac{d}{b}60v\right)} \tag{17.19}$$

(ii) When c is odd,

$$K_{dh} = \frac{0.5}{b \sin\left(\frac{d}{b}30v\right)} \; (P \text{ is even}) \tag{17.20}$$

$$K_{dh} = \frac{0.5}{b\cos\left(\frac{d}{b}30v\right)} \ (P \text{ is odd}) \tag{17.21}$$

Another way of calculating α_h:

$$\alpha_h = h * d * \alpha_m * \frac{c}{P} \ (P \text{ is even})[\text{elec.degrees}] \tag{17.22}$$

$$\alpha_h = h * d * \alpha_m * \frac{c}{p} + 180^{\circ} \ (P \text{ is odd and } c \text{ is even})[\text{elec.degrees}] \tag{17.23}$$

$$\alpha_h = h * (d * \alpha_m + 180^{\circ}) * \frac{c}{p} \ (P \text{ is odd and } c \text{ is odd})[\text{elec.degrees}] \tag{17.24}$$

17.8.3.2 Calculating pitch factor for fractional-slot windings

$$K_{ph} = \sin\left(\frac{W}{\tau_p}\frac{180}{c}v\right) \ (c \text{ is even}) \tag{17.25}$$

$$K_{ph} = \sin\left(\frac{W}{\tau_p}\frac{180}{2c}v\right) \ (c \text{ is odd}) \tag{17.26}$$

where

K_{ph} is the pitch factor for the hth-order harmonic.
W is the coil width [radians].
τ_p is the pole pitch [radians].

17.8.4 Example of winding factor calculation using three methods

The 12slot/14pole fractional-slot DL concentrated winding is chosen as an example for calculating the winding factor using the three methods introduced in Section 17.8. The calculation of the synchronous harmonic component of the winding factor will be presented in this example. Lower- and higher-order harmonic winding factors can be calculated in a similar way.

17.8.4.1 Using the EMF method

Figure 17.14 shows the optimum winding layout of a 12slot/14pole DL configuration. There are four winding elements for each phase. The goal is to calculate

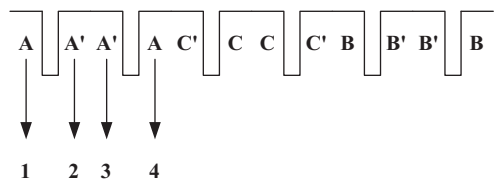


Figure 17.14 Winding layout of 12slot/14pole DL configuration

the winding factor for the synchronous component. The angle γ between two successive slots (the slot pitch in the case of concentrated windings) is 360* 7/12 = 210 elec. degrees.

Voltages of the A phase winding elements in p.u:

$$E7_1 = e^{j(0)}$$
$$E7_2 = -e^{j(210)}$$
$$E7_3 = -e^{j(210)}$$
$$E7_4 = e^{j(60)}$$
$$\sum E7 = 3.2321 + j1.866$$
$$|\sum E7| = 3.7321$$
$$Q = 12$$

Based on (17.53),

$$K_{w7} = \frac{|E7_{phase,pu}|}{Q/3} = \frac{3.7321}{4} = 0.933$$

where K_{w7} is the synchronous winding factor.

17.8.4.2 Using the winding function method

The winding function of the 12slot/14pole DL concentrated winding is shown in Figure 17.15. In this case, it is assumed that each of the two coils/phase has only one turn. The rectangular winding function for the baseline case when the coils are combined into a distributed winding with $q = 1$ is shown in Figure 17.16. In this case, the torque-producing component (synchronous component) is the seventh harmonic component of the winding function. Calculating the amplitudes of the seventh harmonic components of both waveforms leads to the following:

$$N_7 = \frac{1.066284}{\pi}$$
$$N_{7base} = \frac{1.142857}{\pi}$$

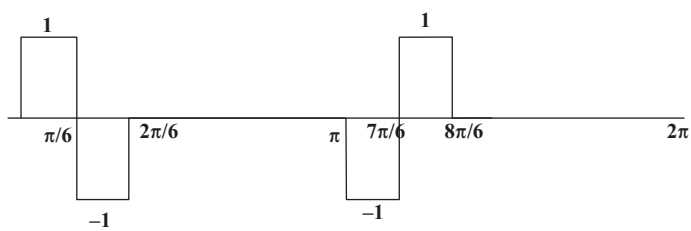


Figure 17.15 Winding function of 12 slot/14 pole DL configuration

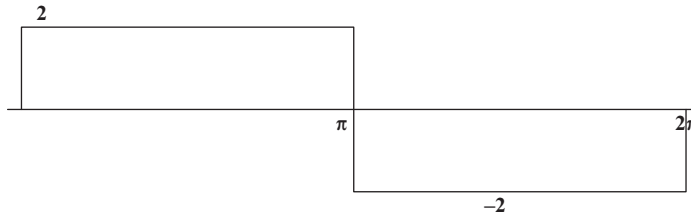


Figure 17.16 Winding function of the rectangular lumped base case

Using (17.54),

$$K_{w7} = \frac{N_7}{N_{7base}} = 0.933$$

It is again emphasised that K_{w7} is the *synchronous* winding factor.

17.8.4.3 Using closed-form expressions

In case of 12 slots and 14 poles,

$$q = \frac{2}{7} \ \therefore b = 2\ c = 7 \text{ (Odd)}$$

Using (17.58),

$$\alpha_m = \frac{180}{2 * 3} = 30^{\circ}$$

Using (17.59),

$$d = \frac{3 * 2 * P + 1}{7} = 1\ P = 1 \text{ (Odd)}$$

Using (17.60),

$$h = \frac{7}{7} v \text{ then} \quad \text{for} \quad h = 7, \quad v = 7$$

Using (17.62), $\alpha_7 = 1 * 30^{\circ} * 7 + 180^{\circ} = 390^{\circ}$.
Using (17.55),

$$K_{d7} = \frac{\sin(30^{\circ})}{2 \sin\left(\frac{390^{\circ}}{2}\right)} = -0.965926$$

Using (17.79),

$$K_{p7} = \sin\left(\frac{210}{180} * \frac{180}{14} * 7\right) = 0.965926$$
$$\therefore K_{w7} = K_{d7} * K_{p7} = -0.933$$

The negative sign in this case has no significance. It can be seen that the three methods yield the same value for the synchronous winding factor, as expected.

17.9 Design and analysis

The design and analysis of FSCW-PM machines is challenging in the sense that the winding configuration deviates significantly for the conventional sinusoidal distribution. The standard *d-q* analysis might not be applicable or accurate in the case of FSCW. This section will cover the key publications addressing the design and analysis of FSCW-PM machines.

Reference [27] represents one of most complete publications summarizing most of the work that has been done regarding the theory and design of FSCW-PM machines.

In [28], a closed-form analytical method for the design and analysis of FSCE SPM machines has been presented. The proposed method is based on analytically calculating the magnetic field in the air gap and building upon this to calculate the various machine parameters and performance on a per-phase basis. The various machine performance aspects have been verified using finite-element analysis (FEA). This approach is suitable for non-salient SPM machines but other analytical approaches were developed for salient IPM machines.

In [29], it was demonstrated that a well-designed magnetic circuit model (MCM) provides a promising method of predicting the cores losses of FSCW-IPM machines that pose special challenges because of their nonlinear electromagnetic characteristics and basic repeating unit that can include several machine poles. Despite the fact that FEA uses a much finer mesh that captures the localized variations in flux density more accurately than the MCM, the permeance models in the MCM are sufficiently good to provide core loss estimates that closely match the FE results under open-circuit operating condition and as well as in the presence of armature reaction.

In [30], it was shown that the FSCW-IPM machine can be designed to achieve appealingly high values of torque and power density, taking advantage of the known advantages of FSCW and IPM machines. This includes the opportunity to design PM machines that are achieving wide ranges of constant-power operation, a valuable feature in some applications. On the other hand, the investigation has also highlighted the fact that FSCW-IPM machines are not generally compatible with achieving high values of magnetic saliency that are required for delivering large contributions of reluctance torque to the total machine torque production. Closer inspection indicates that this conclusion is not that surprising since the wide stator poles that are typical of FSCW configurations serve as spatial low-pass filters that span large angular pitches. In fact, this slot pitch exceeds one full pole pitch when slot/pole/phase is less than 1/3, filtering out magnetic permeance differences along the orthogonal *d*- and *q*-axes.

It is shown that, with increase in saliency, gamma angle at which the maximum torque occurs tends toward 45 degrees, and machine configurations with higher saliency will have higher gamma angle magnitude. Observations made in terms of design with DL winding that had higher saliency when compared to corresponding design with SL winding are seconded in the later section with the help of detailed design torque comparisons. Another set of design comparison is made by changing

the slots/pole/phase while keeping same rotor also indicated that another important conclusion in terms of machines with higher slots/pole/phase value have higher saliency and confirm that wider stator tooth acts as a saliency filter and reduces the resultant saliency.

One of the challenges with IPM machines in general is the separation of the various torque components (reluctance vs. PM torque). This task becomes even more challenging in the case of FSCW-IPM machines due to the presence of all the sub- and super-harmonic components. Several papers tried to tackle this issue.

In [31], alternative techniques for segregating the calculated torque values in FSCW-IPM machines have been investigated. It is shown that the previously established frozen permeability technique does a very good job of predicting the nonlinear effects of saturation on the machine flux linkages, building confidence in the meaningfulness of its resulting PM and reluctance torque component predictions. Unfortunately, the frozen permeability technique is very computation intensive since it depends so heavily on FEA for its execution.

A new modified torque segregation technique based on capturing the effects of the combined q- and d-axis currents in a single saturation variable dependency has been proposed. Predicted PM and reluctance torque values for this new model match the results of the baseline frozen permeability technique very well. It is an appealing alternative because it provides an attractive tradeoff between accuracy and computation time for this torque segregation task as it is necessary to freeze the permeance and perform linear simulations.

In [32], the frozen permeability method has been used to analyze the influence of saturation due to PM, d- and q-axis currents on the different parameters, such as the PM flux linkage, d- and q-axis inductances of fractional-slot PM machines having concentrated windings. The analysis shows that the q-axis PM flux linkage, the influence of d-axis current on the d-axis PM flux linkage, and the cross-coupling effect on the d–q-axis inductance can be neglected in the calculation of the torque speed characteristics of such machines. A proposed partial cross-coupling model has been compared to FEA and experimental results. The proposed model proved to be fairly accurate and a much faster analysis tool.

17.10 Flux weakening

SPM BLAC machines have often been considered to be poor candidates for achieving wide constant power speed range/ratio (CPSR) by means of flux weakening. The principal reason for this will be evident by considering the characteristic current of an SPM machine, defined as

$$I_x \equiv \frac{\Psi_m}{L_d} \text{ [A]} \tag{17.27}$$

where Ψ_m is the RMS flux linkage due to the permanent magnets (PMs) and L_d is the d-axis inductance (which is approximately equal to the q-axis inductance for SPM machines). It is well known that optimal flux weakening, for both SPM and

IPM machines, occurs when the characteristic current I_x equals the rated current I_R [33,34]. The symmetrical three-phase short-circuit current will then be equal to the rated machine current. The inductance of SPM machines is, however, relatively low. Furthermore, if the flux-linkage Ψ_m is reduced, this compromises the torque capability. As a result, the characteristic current tends to be significantly higher than the machine rated current, which severely limits the constant-power, flux-weakening operational range.

However, it was shown in [35] that FSCW-SPM machines have high values of stator leakage inductance (both harmonic leakage and slot leakage), which allows them to achieve a wide CPSR. This type of machine has potential for demanding traction applications requiring wide CPSR, high power density and high efficiency.

In [36], it was shown analytically that the optimal flux-weakening condition could be achieved in SPM equipped with FSCW. FEA validation was provided as well as a design method to achieve this condition. In [37], experimental verification that the optimal flux-weakening condition can be met in SPM machines using FSCW was provided. A 36slot/30pole prototype was built and tested. It was shown that a wide CPSR of ~8:1 could be achieved while achieving a high efficiency above 90% over the entire speed range.

Part of the analysis presented in [36] will be included in this section since it provides a simple and clear explanation of the benefits of FSCW in terms of improving the flux-weakening capabilities of SPM machines. Based on the criteria presented in Section 17.6, the 12slot/14pole and the 12slot/10pole combinations emerge as appealing candidates. These two combinations are the building blocks of two families of designs having numbers of slots/pole/phase (q) of 2/7 and 2/5, respectively. These two combinations are appealing for several reasons including the following: (1) they can support SL windings; (2) they have high winding factor K_{w1} values (0.966); (3) they promise low cogging torque because of their high $LCM(q, 2p)$ values; and (4) their net radial force values should be zero because their K values are even.

In this section, the 12slot/14pole combination with SL winding will be compared to the conventional distributed winding with 1 slot/pole/phase ($q = 1$) which is often used as the benchmark. The analysis will focus on series connection but similar results can be achieved using either series or parallel winding connections. This is expected because the way the coils are connected is just a terminal condition that should not affect the basic performance of the machine. The analytical approach is based on winding functions [25] that provide a very powerful and useful technique for investigating these configurations.

The basic machine stator–rotor repeating unit of the slots per pole per phase (SPP) = 2/7 family has 12 stator slots and 14 rotor magnet poles. (Note that q and SPP are both used to represent the slot/phase/pole parameter.) In order to quantitatively explain why FSCW have potential for improving the flux-weakening capabilities of SPM machines, the 12slot/14pole SL design (SPP = 2/7) will be compared to a distributed 42slot/14pole design (SPP = 1) having the same rotor structure.

The phase "A" winding configuration of both designs is shown in Figure 17.17. It can be seen that there is a significant difference between the two designs. Over the 14 rotor poles, phase "A" of the 12slot/14pole design (designated Winding 1) has

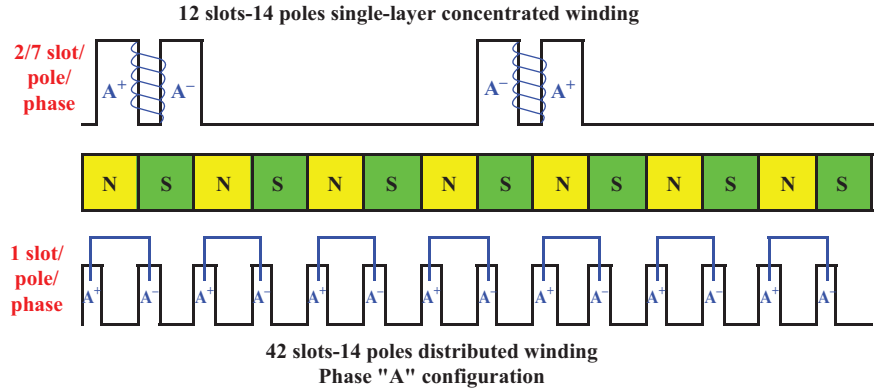


Figure 17.17 Comparison of fractional-slot concentrated (2/7 slot/pole/phase) and distributed full-pitch (1 slot/pole/phase) windings for one phase

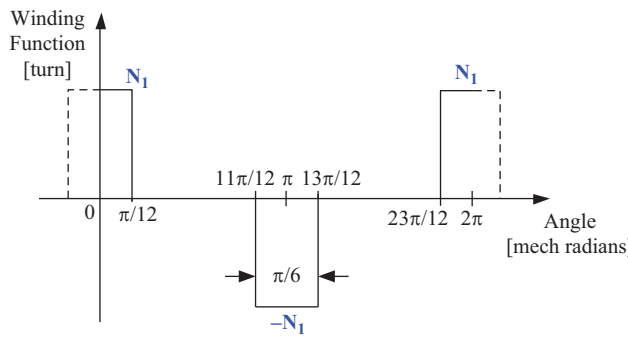


Figure 17.18 Winding function of the 12slot/14pole concentrated fractional-slot winding design (SPP = 2/7)

two coils occupying 4 slots in contrast to 7 coils occupying 14 slots in the case of the 42slot/14pole design (Winding 2).

The goal of this comparison is to show that, for the same magnet flux linkage, the FSCW configuration provides significantly higher phase inductance compared to the distributed winding configuration. By increasing the inductance, the characteristic current is decreased, making it possible to achieve the conditions for optimum flux-weakening operation.

17.10.1 Same magnet flux linkage constraint

The first step is to impose the constraint of equal synchronous component magnet flux linkage for both windings. It is assumed that the 12slot/14pole concentrated winding has N_1 turns/coil while the 42slot/14pole distributed winding has N_2 turns/coil. Plots of the two winding functions are provided in Figures 17.18 and 17.19. All the coils are assumed to be connected in series.

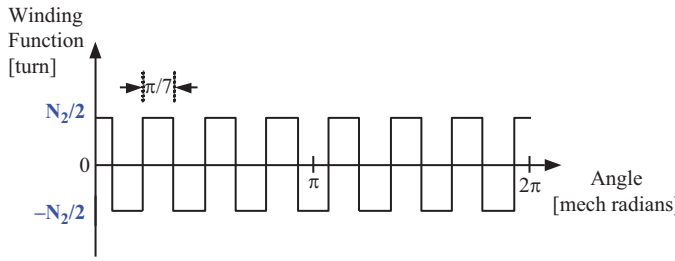


Figure 17.19 Winding function of the 42slot/14pole distributed winding design (SPP = 1)

The magnet flux linkage can be calculated as follows [25]:

$$\Psi_a = r_g l_{eff} \int_0^{2\pi} N_a(\theta) B(\theta) d\theta \text{ [weberturn]} \tag{17.28}$$

where

Ψ_a is the phase "A" magnet flux linkage [weber].
r_g is the air gap radius [m].
l_{eff} is the active length of the machine [m].
N_a is the phase "A" winding function.
B is the air gap magnet flux density [tesla].
θ is the angle along the circumference of the air gap [mechanical degrees].

Since we are interested in the synchronous component magnet flux linkage, only the fundamental component of the B field is considered. It is assumed that both designs have the same rotor structure as shown in Figure 17.16, so the B field is the same in both designs, as follows:

$$B(\theta) = B_{\max} \sin\, p\theta \text{ [tesla]} \tag{17.29}$$

where

$B_{\max}$ is the peak fundamental air gap magnet flux density [tesla].
p is the number of pole pairs.

Applying (17.28) and (17.29) to both windings leads to the following:
For the 12slot/14pole winding,

$$\Psi_1 = 2 r_g l_{eff} \int_{-\frac{\theta_1}{2}}^{\frac{\theta_1}{2}} N_1 B_{\max} \sin(p\theta + 90^o) d\theta = r_g l_{eff} * \frac{4}{p} K_{w1} N_1 B_{\max} \tag{17.30}$$

where θ_1 is p/6, and $K_{w1} = 0.966$ for $q = \text{SPP} = 2/7$ (Refer to Table 17.2)

For the 42slot/14pole winding,

$$\Psi_2 = 2pr_g l_{eff} \int_0^{\theta_2} \frac{N_2}{2} B_{\max} \sin\, p\theta d\theta = r_g l_{eff} * 2N_2 B_{\max} \tag{17.31}$$

where θ_1 is $p/7$, and $K_{w1} = 1.0$ for $q = \text{SPP} = 1$.

Equating (17.30) and (17.31) leads to the following condition for same synchronous component magnet flux linkage in both winding configurations:

$$N_1 = \frac{p}{2K_{w1}} N_2 = 3.623 * N_2 \tag{17.32}$$

17.10.2 Inductance calculations

The self- and mutual-phase inductances for the two windings can next be calculated using the winding functions [25]

$$L_{aa} = \frac{\mu_0 r_g l_{eff}}{g} \int_0^{2\pi} {N_a}^2(\theta) d\theta \text{ [H]} \tag{17.33}$$

$$L_{ab} = \frac{\mu_0 r_g l_{eff}}{g} \int_0^{2\pi} N_a(\theta) N_b(\theta) d\theta \text{ [H]} \tag{17.34}$$

where

L_{aa} is the self-inductance of phase "A" [H].
L_{ab} is the mutual inductance between phases "A" and "B" [H].
μ_0 is the permeability of air [Henry/m].
g is the air gap thickness [m].
L_d is the d-axis inductance [11] $= L_{aa} - L_{ab}$ [H].

The inductances can be evaluated for both windings:
For the 12slot/14pole FSCW,

$$L_{aa} = \frac{\mu_0 r_g l_{eff}}{g} \quad {N_1}^2 \frac{\pi}{3} \qquad L_{ab} = L_{ac} = 0 \text{ [H]} \tag{17.35}$$

$$\therefore L_{d-conc} = \frac{\mu_0 r_g l_{eff}}{g} \quad N_1^2 \frac{\pi}{3} \text{ [H]} \tag{17.36}$$

For the 42slot/14pole distributed winding,

$$L_{aa} = \frac{\mu_0 r_g l_{eff}}{g} \quad N_2^2 \frac{\pi}{2} \; L_{ab} = \frac{Laa}{3} \text{ [H]} \tag{17.37}$$

$$\therefore L_{d-dist} = \frac{\mu_0 r_g l_{eff}}{g} \quad N_2^2 \frac{2\pi}{3} \text{ [H]} \tag{17.38}$$

Combining (17.32), (17.36), and (17.38), the ratio of the *d*-axis inductances for the two windings under the constraint of equal magnet flux linkage can evaluated to be

$$\frac{L_{d-conc}}{L_{d-dist}} = \frac{{N_1}^2}{2{N_2}^2} = 6.56 \tag{17.39}$$

This is a very important result because it indicates that for the same magnet flux linkage, replacing a distributed winding (SPP = 1) with a concentrated fractional-slot winding (SPP = 2/7), increases the *d*-axis inductance by a factor of 6.56. Consequently, the characteristic current of the machine (I_{ch}) is reduced by the same factor, making it much more practical to satisfy the optimum flux-weakening condition of $I_{ch} = I_R$.

It should be noted that the calculated inductances using winding functions only represent the magnetizing and harmonic leakage inductances. The slot leakage and end leakage inductances are not included. It was also shown later that FSCW offer major advantages for increasing the slot leakage component of the machine inductance values [35,36].

17.11 Losses in electrical machines equipped with FSCW

One of the key challenges of using FSCW configurations is the potentially significant increase in various loss components. Such loss components include rotor losses, end losses, and AC losses in the windings, among others. This section will cover what has been done in literature in terms of understanding, evaluating, and potentially reducing these loss components.

17.11.1 Rotor losses

Rotor losses (including magnet losses, rotor core losses, and sleeve losses in case of conductive sleeve) especially at high speeds due to the various sub- and super-space harmonic components inherent to FSCW configurations that are not in synchronism with the rotor come at the top of the list of challenges involved in using FSCW. The main bulk of these losses are due to the subharmonics that can penetrate fairly deep into the rotor.

Several authors investigated the rotor losses with special focus on magnet losses. Effect of both circumferential as well as axial segmentation has been investigated. The effect of various slot/pole combinations and number of phases on rotor losses has been investigated. Losses in conductive retaining sleeves have been investigated. Effect of methods for reducing sleeve losses (including axial segmentation as well copper cladding) has been investigated. This section will cover key publications addressing the various aspects of rotor losses in PM synchronous machines using FSCW.

An analytical model for calculating magnet losses in the case of SPM machines was presented in [38]. This model is powerful as it can account for the effect of peripheral segmentation of the magnets. The model has been used to

evaluate examples of FSCW-SPM machines. This model has been used in [39–41]. It was assumed that the stator current is pure sinusoidal. In [39], it was used to calculate the losses for modular surface PM designs that were introduced in [10,42]. In [40,41], Ishak *et al.* used the model to compare the eddy-current losses in the magnets for both SL and DL winding configurations for both BLDC and BLAC modes of operation. It was shown that the SL winding induces higher eddy-current losses in the magnets due to the higher special harmonic content. Also, it was shown that the induced losses are higher in case of BLDC operation due to the current time harmonic content. It was shown that the effect of magnet curvature on the losses is very small especially in the case of high number of poles. In [43], the model was used to compare the losses for various slot/pole combinations that can support FSCW.

In [44], a general method for evaluating the rotor losses in three-phase FSCW-PM machines was proposed. The effect of the various slot/pole combinations on the rotor losses was investigated. A nonconductive retaining sleeve was assumed.

In [45], a model for calculating eddy-current losses in solid rotor back iron in FSCW-PM machines was presented. Even though the model results did not match well with experimental results, they concluded that the losses in a solid rotor for this type of machines would be unacceptable.

In [46], the effect of axial segmentation on reducing the magnet losses was investigated. A method that is computationally faster compared to a full 3D FEA was presented.

In [47], a method for calculating losses in conducting retaining sleeves of FSCW-SPM machines was proposed. They examined the effect of sleeve axial segmentation and copper cladding on reducing the sleeve losses. They evaluated the sleeve losses for various number of phases and slot/pole combinations.

In [12], as previously mentioned, the effect of number of phases on losses in conducting sleeves of FSCW-SPM machines was examined. A rotor loss FOM was introduced and evaluated for the various slot/pole combinations covering the feasible design space for four-, five-, and six-phase designs.

In [48], an optimal torque control strategy for fault-tolerant PM brushless machines (equipped with FSCW) was proposed. It has been shown that the adoption of a torque control strategy to minimize torque ripple under open-circuit and short-circuit fault conditions may lead to a significant increase in the eddy-current loss in the PMs of such machines.

In conclusion, rotor losses in FSCW-PM machines are typically very significant (especially in the case of SL winding) and the following measures are usually needed to keep the rotor losses at an acceptable level:

1. Rotor back iron needs to be laminated
2. PMs need to be segmented typically on the peripheral and/or axial direction
3. In case a retaining sleeve is needed, nonmetallic sleeves, e.g., carbon fiber, should be used
4. In case of metallic sleeves, axial segmentation of the sleeve and/or shielding (e.g., using copper cladding) will be needed.

17.11.2 End losses

Most of the papers focused on losses in the active portions of the machine. In [49], eddy-current losses in the rotor clamping rings of an FSCW-PM machine were investigated. The loss in rotor nonmagnetic shaft with the option of (i) metallic, (ii) nonmetallic, and (iii) metallic with shielding laminations was also estimated. The study is based on FEA. Desirable slot/pole combinations for different number of phases were investigated. Also, both SL and DL windings were investigated. Experimental results for a three-phase 12 slot/10 pole IPM design (Figures 17.20 and 17.21) were presented in detail. The results confirm that the losses in the rotor clamping rings can be very significant in case of FSCW machines and should not be overlooked during the design phase (up to ~2kW of losses in case of metallic rotor clamping rings).

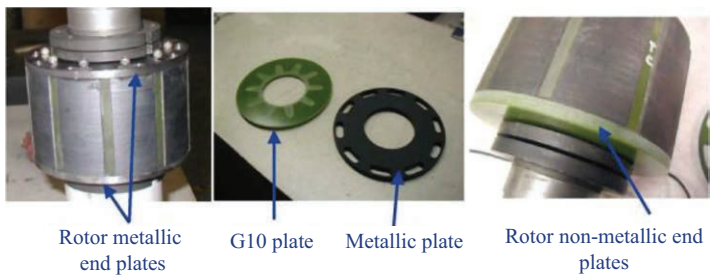


Figure 17.20 Rotor with metallic and nonmetallic clamping rings [49]

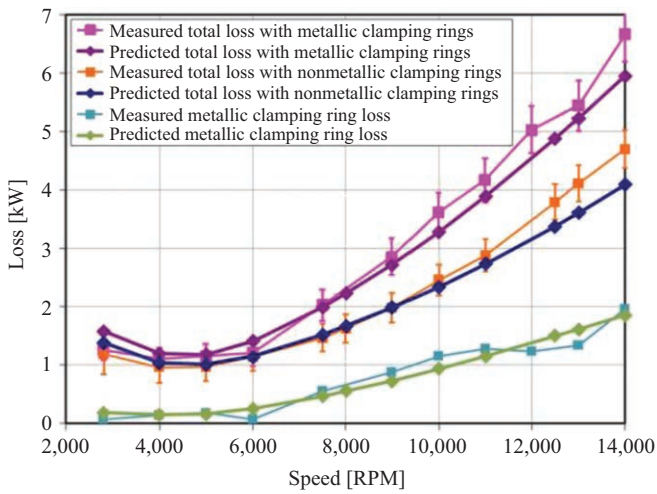


Figure 17.21 Measured and predicted losses at rated load condition with metallic and nonmetallic clamping rings and losses in metallic clamping rings [49]

In [50], the focus has been on losses in the support structure including the frame, clamping rings (magnetic or nonmagnetic), and end shields. Both SL and DL windings have been analyzed. Also, the effect of different number of phases has been investigated. As expected, SL windings produce significantly higher losses compared to DL windings. The lower-order space harmonics contribute most to the losses. The main bulk of the losses are in the end shields (ESs); that is why the axial clearance has a significant impact on reducing the losses. Going to higher number of phases could have a detrimental effect in terms of increasing the losses or increasing the support-structure size and weight along with other dynamics challenges.

17.11.3 AC losses in the windings

Another important loss component that has to be properly accounted for in the case of FSCW (especially due to the fact that most appealing slot/pole combinations have a large number of poles and hence electrical frequencies) is AC losses in the windings. In [51], AC armature losses in FSCW-SPM machines designed for a wide CPSR operation have been investigated. Key conclusions include the following:

- The number of winding layers does not have a significant effect on the AC losses.
- The magnet type has a significant effect on the AC losses since it affects the machine effective air gap and hence the slot leakage flux. As a result, machines using bonded magnets are vulnerable to higher AC losses than machines using sintered magnets.
- Machines with lower pole numbers tend to have lower AC losses compared to the machines belonging to the same family but with higher pole numbers due to the higher excitation frequencies in high-pole-number machines.
- Higher levels of magnetic saturation in the stator tooth tips decreases the AC losses in the conductors because the saturation tends to reduce the effective leakage flux across the slot opening.
- Terminal conditions (series vs. parallel connections) do not have a significant effect on the AC losses provided that the strand size and the current in each strand are not changed.

In [52], thermal analysis of a segmented stator winding design has been presented. A thermal model for a single tooth was developed and supported by tests to identify key heat transfer coefficients. A number of winding assemblies were compared, and the most promising was selected for the final motor prototype. The results from the approach are compared with thermal test results from the complete machine.

17.11.4 Loss reduction

In order to reduce losses in case of FSCW, some novel winding configurations as well as other novel design features have been proposed in literature. In [18], a novel

method for reduction in subharmonics for the FSCW by using winding coils with different number of turns per coil side has been presented. Using the proposed technique, the specific subharmonics can be reduced without influencing the working harmonic. The presented technique is available for different *m*-phases FSCW. Simulation results showed potentially significant reduction in eddy-current rotor losses of more than 60%.

In [19], a new method is presented to simultaneously reduce the sub- and super-harmonics of the 12slot/10pole FSCW MMF. The method is based on doubling the number of stator slots, using two identical winding systems connected in series, and shifted to each other for a specific angle, using stator core with different tooth width and/or using different turns per coil for the neighboring phase coils. It was shown that the new proposed winding topology can have better performances compared to the standard distributed winding. The complexity of winding is less than that of a distributed winding but more than that of a tooth winding. In this concept, the coil pitch is always two slot pitches, which can greatly reduce the end winding length compared to a distributed winding, while being able to achieve better performance than the tooth windings.

In [20], a more general definition and approach for stator shifting (that was presented in [19]) has been presented. This paper investigated a method of cancelation of harmonics in FSCW. The concept of stator shifting is introduced and its effect on the machine performance in terms of the power density, efficiency, torque ripple, and flux-weakening performance was evaluated. It was shown that the concept of stator shifting introduced in FSCW-IPM machines is an effective way of improving the power density and efficiency. The concept is shown to be effective also in improving the saliency and the maximum electromagnetic power available from the machine at higher speeds. The final *optimal shift angle* is identified for each configuration and depends on the slot/pole combination chosen along with the number of layers. Finally, the concept of stator shifting is seen to be more effective in designs with a single subharmonic. In slot/pole combinations with multiple subharmonics, the improvement is curtailed by the effect of these harmonics. The key novelty in the paper is that it explored the effect of shift angle in more general way by scanning a wide range of angles. The paper also highlighted the fact that once high-speed operation under flux-weakening operation is taken into consideration, this can affect the choice of the shift angle in terms of maximizing efficiency at high speeds. Even though an improvement in power density can be seen in IPM machines due to the improvement in saliency, in SPM machines, it is expected that the shifting would reduce the harmonics and hence only reduce the rotor losses but will simultaneously reduce the output power.

In [53], the introduction of nonmagnetic flux barriers in the stator as a means of reducing or even canceling the impact of the lower-order subharmonics has been presented. The proposed geometry as well as the built prototypes is shown in Figures 17.22 and 17.23. The proposed flux barriers can also be combined with axial cooling passages.

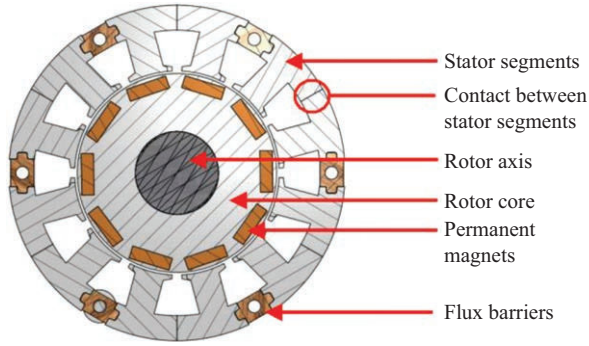


Figure 17.22 Geometry of proposed PM design with flux barriers [53]

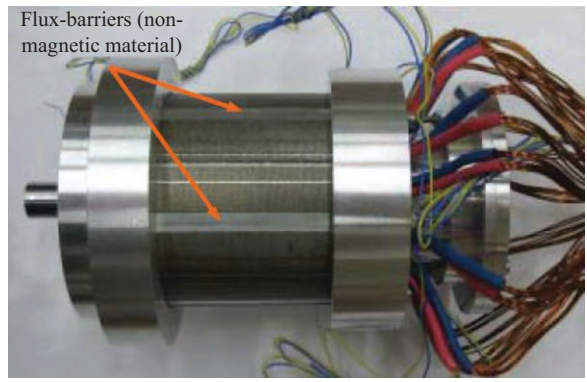


Figure 17.23 Prototype with flux barriers [53]

17.12 Fault tolerance

Fault tolerance is one of the key issues with PM machines in general especially in safety-critical applications. The main reason is that the PMs cannot be de-excited in case of a fault especially in case of a generator that is coupled to a prime mover that cannot be stopped or disconnected in case of a fault, e.g., an aircraft engine.

The key fault-tolerance requirements have been identified in literature as follows:

- Complete electric isolation between phases
- Implicit limiting of fault currents
- Magnetic isolation between phases
- Effective thermal isolation between phases
- Physical isolation between phases
- Higher number of phases.

These requirements can be met by using multiphase SL FSCW where each phase is fed by a single-phase H-bridge power converter. This section will cover the key papers addressing fault tolerance in PM synchronous machines using FSCW configurations.

In [54], some design considerations of fault-tolerant synchronous motors, characterized by a fractional number of slots per pole per phase, were presented. The first advantage of this configuration is a smooth torque because of the elimination of the periodicity between slots and poles. The second one is a higher fault-tolerant capability making the machine able to work even in faulty conditions. However, the fractional-slot configuration presents a high content of MMF harmonics that may cause unbalanced saturation and thus unacceptable torque ripple levels. A method to design fractional-slot motors was illustrated in the paper, including DL and SL windings. The analytical computation is extended to determine the harmonics of MMF distribution. Their effect is highlighted in isotropic as well as anisotropic motors. Finally, some considerations are reported to avoid unsuitable configurations.

In [55,56], post-fault current control strategies of a five-phase PM motor was presented. The analysis covers both the open circuit of one and two phases and the short circuit at the machine terminal of one phase. The proposed control guarantees safe drive operation after any fault occurrence. For the sake of generality, an analytical model has been used to investigate the properties of each post-fault strategy. The results are general, and they apply to PM motor of any power rating. Simulations and experimental results validate the theoretical predictions.

In general, five-phase fault-tolerant PM machines received a lot of attention in literature. Among its key advantages are high torque density, high controllability, reliability, and smooth torque production in case of a fault. Several papers addressed the various design aspects of five-phase fault-tolerant PM machines, power converter topologies as well as post-fault current control strategies for different types of faults [57–59].

In [60], feasible slot and pole number combinations for multiplex two-phase and three-phase fault-tolerant PM machines were analyzed, and their relative merits via a design case study were evaluated. An effective winding short-circuit detection technique based on search coils wound around the stator teeth was also presented, and its performance was assessed. It was shown that the proposed detection technique can reliably detect any type of short-circuit fault under all load conditions.

In [61], a new approach for selecting pole and slot numbers for fault-tolerant PM machines so that there is inherently negligible coupling between phases (regardless of other design detail) was presented. The preferred slot and pole number combinations thereby help to ensure that a fault in one phase does not undesirably affect the remaining healthy phases. Other well-known criteria for fault-tolerant operation, including high phase inductance, also have to be met. It was demonstrated how particular slot and pole combinations can be used to eliminate low pole number armature MMF, thereby reducing the vibration and stray loss present during normal operation.

In [62], the use of PM machine drives in high-performance, safety-critical applications was examined. Likely fault modes were identified, and machine designs were developed for fault-tolerant operation, without severely compromising the drive performance. Fault tolerance was achieved by adopting a modular approach to the drive, with each phase electrically, magnetically, thermally, and physically independent of all others. Power converter requirements were discussed and methods for controlling a faulted phase developed to minimize the impact of a machine or power converter fault.

In [63], the design of a fault-tolerant PM drive based on a 16 kW, 13,000 rev/min, six-phase aircraft fuel pump specification was discussed. A "proof of concept" demonstrator was built and tested, and key parameters were measured. A novel current controller with near-optimal transient performance was developed to enable precise shaping of the phase currents at high shaft speeds. A list of the most likely electrical faults was considered. Fault detection and identification schemes are developed for rapid detection of turn-to-turn faults and power device short-circuit faults. Post-fault control strategies were described, which enable the drive to continue to operate indefinitely in the presence of each fault. Finally, results showed the initially healthy drive operating up to, through and beyond the introduction of two of the more serious faults.

In [64], the design and testing of an aircraft electric fuel pump drive were discussed. The drive is a modular, four-phase, fault-tolerant system, which is designed to meet the specification with a fault in any one of the phases. The motor employed has a PM rotor with the magnets arranged in a Halbach array to maximize the air gap flux density (Figures 17.24 and 17.25). Exceptionally high electric loadings are obtained by flooding the entire motor with aircraft fuel, which acts as an excellent cooling agent. Theoretical results are compared with test results gained in conditions approaching those found in an aircraft. Tests are carried out on the healthy drive and with one of several fault scenarios imposed. The electrical and thermal performance of the drive is assessed, showing how the flooded fuel cooling has excellent performance without introducing significant drag on the rotor.

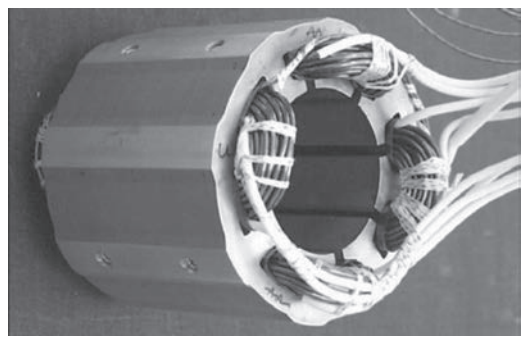


Figure 17.24 Four-phase stator [64]

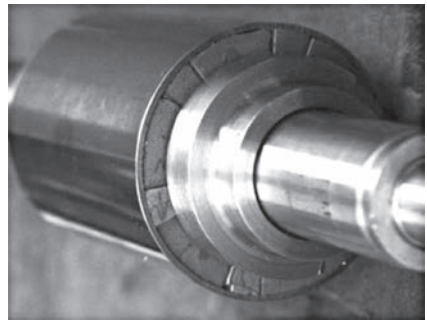


Figure 17.25 Six-pole rotor Halbach array [64]



Figure 17.26 Inside–out embedded PM generator [66]

In [65], the design of a fault-tolerant electric motor for an aircraft main engine fuel pump was discussed. The motor in question is a four-phase fault-tolerant motor with separated windings and a six-pole PM rotor. Methods of reducing machine losses in both the rotor and stator were introduced and discussed. The methods used to calculate rotor eddy-current losses were examined. Full three-dimensional finite-element (FE) time stepping, two-dimensional (2-D) FE time stepping, and 2-D FE harmonic methods were discussed, and the differences between them and the results they produce were investigated. Conclusions were drawn about the accuracy of the results produced and how the methods in question will help the machine designer.

Figure 17.26 shows a fault-tolerant inside–out PM generator [66]. This machine was one of the first PM machines designed targeting primary generation in aerospace (to be embedded inside the engine). The key machine characteristics include. As can be seen, the machine was equipped with SL FSCW. The machine has many unique design details that are included in [66]. A turn–turn fault was introduced, and it was shown that the fault can be detected quickly enough (within 13 ms) and a mitigation scheme applied to reduce fault current from 650 A down to 20 A. This machine pushed the state of the art in terms of PM-fault-tolerant machines, power density, and reliability.

Since the machine phase inductance plays a key role in determining the machine fault currents as well as coupling between the various phases and hence fault tolerance, accurate calculation of the inductance during the design phase is critical. In [67–69], Zhu *et al.* presented an accurate method for calculating inductances of SPM machines with special focus on FSCW configurations.

17.13 Comparison of SPM versus IPM

Even though initially most of the work done on FSCW focused on SPM machines, there has been growing interest and a lot of work was done assessing the use of IPM machines equipped with FSCW. The hope was that FSCW-IPM machines will combine the benefits of the FSCW previously mentioned in addition to the benefits of an IPM rotor in terms of potentially reducing magnet content as well as easier magnet retention compared to SPM machines. This section will focus on the key papers that provided comparison between IPM and SPM machines with FSCW configurations. Table 17.8 provides a high-level comparison of SPM versus IPM machines equipped with FSCW.

In [70], a comparison of FSCW-SPM and FSCW-IPM servomotors was presented. Points of comparison included cogging torque, torque ripple, overload capability, and flux-weakening capability.

In [71,72], the performance of FSCW for low-speed applications was investigated. Comparison of cogging torque, ripple torque, and back EMF for various slot/pole combinations for both SPM and IPM was presented. They concluded that smooth torque production is possible with such winding configurations.

In [73], a comparative analysis and test results performed on three IPM machine designs using FSCW with different saliency ratios was presented. The goal was to identify the flux distribution and thus iron loss effects of using FSCW

Table 17.8 Comparison of SPM versus IPM machines equipped with FSCW

	SPM	**IPM**
Stator structure	Can be segmented or continuous laminations	Can be segmented or continuous laminations
Magnet retention	Metallic or nonmetallic sleeves	Bridges and/or center posts
Flux weakening	FSCW significantly improves flux-weakening capability	Has inherent good flux-weakening capability
Fault tolerance	Improved fault tolerance with FSCW	Improved fault tolerance with FSCW
Rotor losses	Concentrated in retaining sleeve (if metallic) and PMs	Concentrated in rotor laminations and areas of PMs closest to air gap
Reluctance torque	Almost no reluctance torque	Reduced reluctance torque when equipped with FSCW compared to distributed windings

in order to determine the best rotor configuration for the next generation compressor motor for the 42 V car air-conditioning system. It was shown that using FSCW makes the motor more susceptible to iron losses at high speeds. Hence, in order to achieve high efficiency at high speeds, an IPM machine with low q-axis inductance is appropriate as it can reduce iron losses at high speeds. Also, it was shown that using rectangular wires instead of conventional round wires reduces the end-coil region by 15%, and a higher slot fill factor can be achieved. It was shown that using an improved stator tooth configuration where the air gap is larger at the high stress points helps in reducing the vibrations and noise in the machine.

In [74], a comparative analysis of vibration and noise production in surface PM machines and IPM machines equipped with FSCW was presented. A method for reducing the vibrations and noise was proposed by shaping the stator teeth in order to vary the air gap thickness. It was shown that the noise in IPM machines is larger than in surface PM machines. Also, it was shown that the proposed noise reduction method is less effective in the case of IPM machines.

In [75], a comparison between three various rotor structures for a starter/alternator used in a hybrid vehicle and equipped with FSCW was presented. The goal was to achieve high torque density and high efficiency. The three rotor structures under consideration are surface-mounted inset radial and inset tangential PM designs. It was shown that the surface-mounted structure is the most effective in reducing torque ripple.

In [76], the cogging torque reduction in IPM machines in both cases of full pitch overlapping windings and FSCW was investigated. It was shown that by appropriately adjusting the pole-arc to pole-pitch ratio, the optimum ratio for cogging torque minimization that was derived for SPM machines is equally applicable in the case of IPM machines. It was also shown that the cogging torque in case of the FSCW is almost half that in the case of full pitch overlapping windings.

In [77], a detailed comparison of the high-speed operating characteristics of four synchronous PM machines for applications that require wide CPSR was presented. These machines include SPM machines with both distributed windings and FSCW, and two IPM machines with distributed windings. These two versions of the interior PM machine include one with a tight constraint on the machine's back-EMF voltage at top speed and one without this constraint. The target application is an automotive direct-drive starter/alternator requiring a very wide 10:1 CPSR. Detailed comparisons of the performance characteristics of the machines were presented that include important issues such as the back EMF at top speed, machine mass and cost, and eddy-current losses in the magnets. Analytical results were verified using FEA. Guidelines were developed to help designers decide which type of machine is most suitable for high-CPSR applications. Tradeoffs associated with choosing each of these machines were presented.

In [78], a thorough comparison of the converter performance characteristics of three types of synchronous PM machines [77] was presented. Detailed comparisons of the converter performance below and above the base speed were presented. Comparisons include important issues such as the converter switching and conduction

losses, output ripple current, PWM copper and core losses, DC-link current ripple, and bearing currents.

In [79], a comparison of IPM and SPM machines equipped with FSCW and designed for a wide CPSR was presented (Figures 17.27–17.30]). It was shown that both machines can provide high performance and meet several of the very challenging FreedomCar 2020 specifications for traction motors. Two machines, one

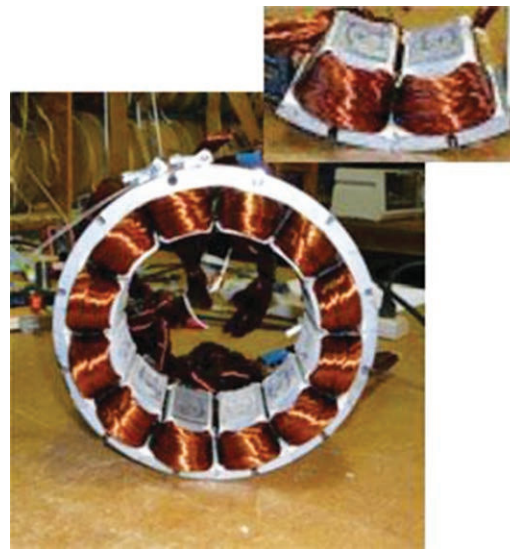


Figure 17.27 Stator of FSCW-IPM design [79]



Figure 17.28 Stator of FSCW-SPM design [79]

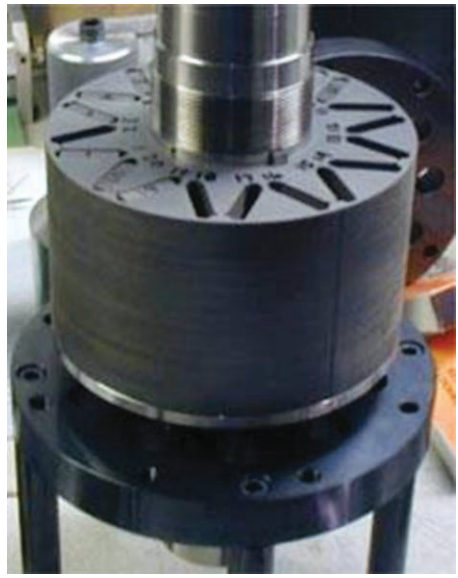


Figure 17.29 Rotor of FSCW-IPM design [79]

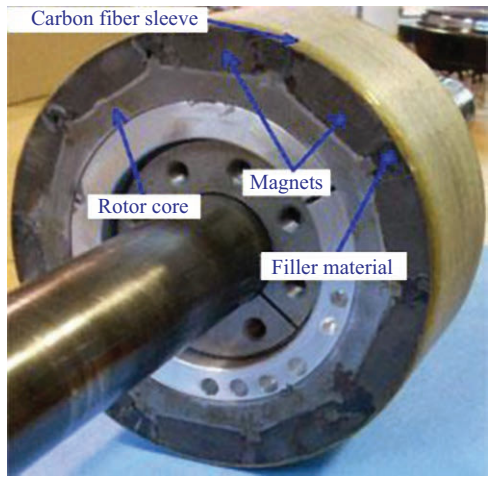


Figure 17.30 Rotor of FSCW-SPM design [79]

IPM and the other SPM, were designed to meet these specifications. The analytical and experimental results for both machines have been compared and the design tradeoffs have been highlighted. Based on the test results of the prototype machines built to date, the 30kW/55 kWpeak, 2,800-14,000-rev/min advanced IPM- and SPM-FSCW machine architectures achieve significant improvements in full-load power density and efficiency compared to the state-of-the-art machines.

17.14 Axial-flux, tubular, and flux-switching machines

The main focus so far has been on radial-flux FSCW-PM machines. Over the last decade, there has been growing interest in other types of PM machines equipped with FSCW. This section will cover the key papers addressing the use of FSCW in other types of machines mainly axial-flux, tubular, and flux-switching machines.

In [80], the design and construction of an axial-flux PM machine (in which the teeth are manufactured from compacted insulated iron powder and the core back is formed from a strip-punched lamination formed, into a circle to grip the teeth) was presented. This new method of construction overcomes the problems associated with punching and winding axial-flux machines formed using index-punched spirally wound laminations (the current state of the art). The construction has been shown to be mechanically stable and rather simple to manufacture. As well as production advantages it offers very high fill factor coils, which can significantly enhance the performance of this type of machine. In [81,82], the design and control of a fault-tolerant seven-phase axial-flux PM machine have been presented.

In [83], an innovative inverter topology for supplying an axial-flux PM machine using FSCW was presented This new topology permits shaping of the inverter output current waveform to be suitably adjusted with respect to the machine back-EMF waveform. This is done by adding a fourth leg or branch to the inverter devoted to controlling the voltage of the neutral point. Improvements in the average torque production have been shown and verified experimentally.

In [84], issues that are pertinent to the design of a linear PM generator for application in a free-piston energy converter were discussed. To achieve the required high power density, high efficiency, and low moving mass, a tubular machine equipped with a modular stator winding and a quasi-Halbach magnetized armature is employed. It was shown that the machine design could be optimized with respect to three key dimensional ratios while satisfying other performance requirements. It was also shown that, when the generator is interfaced to an electrical system via a power electronic converter, both the converter volt-ampere rating and the converter loss should be taken into account when optimizing the machine design. The performance of such a tubular generator is demonstrated by measurements on a ten-pole/nine-slot prototype machine.

In [85,86], analytical models for calculating the various loss components (both on the stator and rotor sides) of tubular modular PM machines were presented.

Another family of machines that continues to have growing interest in literature is the flux-switching/reversal PM (FSPM) machines. There have been a large number of publications addressing different variants as well as design and analysis aspects of FSPM machines. At a high level, this type of machines is comparable to doubly salient PM machines [87]. They have been investigated for various applications [88–90]. Fault-tolerant flux-switching PM machines have been investigated. The same concepts previously covered can be applied to this type of machines including the multiphase approach [91,92].

17.15 Induction machines

After the extensive work that has been done in the area of FSCW PM over the past decade or so, it was a logical step to evaluate the potential of FSCW in other types of machines especially IMs that are still considered the main workhorse for several applications.

In [93], this was the first attempt to quantitatively address the tradeoffs involved in using FSCW in IMs. It focused on squirrel-cage IMs. Based on the analysis results presented, the traditional distributed lap winding is proven to be superior to FSCW in terms of torque production and rotor bar losses for IM applications. The 1/2 SPP shows some promising results in terms of torque production, in addition to significant reduction and simplification of end turns with lower number of coils albeit with more turns/coil (12 slots vs. 48 slots). The penalty is the additional rotor bar losses due to the second and fourth harmonic MMF components. The 2/5 SPP is not promising for torque production. The transient simulation results that simultaneously take into account the effects of all space harmonics and magnetic saturation showed comparable trends compared to the harmonic analysis results. It has also been shown that FSCW tend to have higher torque ripple compared to distributed windings.

In [94], the analysis, design, and tests of a wound-rotor FSCW IM have been presented. An air gap analytical model has been used to evaluate the various slot/pole combinations as well as the number of poles. Higher number of layers (more than two) have been evaluated on both the stator and rotor side. Both two- and four-layer machine prototypes have been built and tested. It has been shown that the four-layer winding exhibits better performance compared to the two-layer one. This is kind of expected due to the reduction in some of the harmonics. Even though the torque ripple is lower compared to the 2 layers, it was still fairly high. This paper showed that potentially there is a path to use FSCW with low-speed high pole-count IM.

17.16 Parasitic effects

Parasitic effects such as noise, vibration, unbalanced magnetic forces, and torque ripple are always a concern when designing electrical machines. These parasitic effects can potentially be higher in FSCW-PM machines due to the additional harmonic contents This section covers sample key papers addressing the parasitic effects in FSCW-PM machines with special focus on vibrations.

In [95], a method for predicting the electromagnetic vibration of PM brushless motors having a fractional number of slots per pole was presented. The method has been validated experimentally. The method has been used to predict the vibration of PM brushless motors having different fractional slot/pole number combinations

In [96,97], the radial force density harmonics and vibration characteristics of three-phase modular PM BLDC machines (in which, the coils that belong to each phase are concentrated and wound on adjacent or alternative teeth) were analyzed.

It was shown that, due to the presence of a large number of low- and high-order space harmonic MMFs, it is more likely that low-frequency modes of vibration are excited in modular machines. Consequently, modular machines are more susceptible to low-frequency resonant vibrations. Experimental results validated the analysis and its findings.

In [98], a general analytical model, formulated in 2-D polar coordinates, to predict the unbalanced magnetic force, which results in PM BLAC and BLDC machines having a diametrically asymmetric disposition of slots and phase windings was developed. It is shown that the unbalanced magnetic force can be significant in machines having a fractional ratio of slot number to pole number, particularly when the electric loading is high. The developed model is validated by FE calculations on nine-slot/eight-pole and three-slot/two-pole machines. In addition, the unbalanced magnetic force has been measured on a prototype three-slot/two-pole machine and shown to be in excellent agreement with predicted results.

In [99], the increase in parasitic effects in FSCW-PM machines was investigated. This includes ripple torque, alternating magnetic fields in the rotor, unbalanced radial forces, and magnetic noise. This paper describes the reasons for the parasitic effects, in which machine topologies are particularly sensitive, and suggests measures in order to reduce their importance. Both traditional and modular concentrated windings are analyzed, as well as DL and SL windings. Measurements on a prototype motor and three commercial servomotors have demonstrated that modular motors are favorable regarding ripple torque minimization.

17.17 Commercial applications and future evolution of research

FSCW-PM machines are used in various commercial applications. This is mainly due to the various advantages covered in the previous sections. This section will provide a sample of the commercial applications where FSCW-PM machines are used.

One of the key areas where FSCW have been significantly adopted is electrical machines for hybrid and electrical vehicles (HEV/EV). The first example is the segmented stator structures with FSCW of the various Honda designs. These designs have significantly high slot fill factor. They use the more traditional 0.5 slot/pole/phase, which has relatively low winding factor of 0.866. The Honda Insight machine is an SPM while the Accord machine is an IPM [6]. Another example is the starter/alternator that was developed by ZF Sachs [8] and shown in Figure 17.10. This design has a plug-in tooth segmented stator structure as previously mentioned. This design is equipped with 2/7 slot/pole/phase, which has high winding factor (0.933 for DL and 0.966 for SL). The key challenge with this winding configuration is the high rotor losses due to the dominant sub- and super-space harmonic components.

Figure 17.31 shows the stator of a Toyota/Aisin FSCW-PM traction motor that was exhibited at EVS 22 (Electric Vehicle Symposium) in Yokohama, Japan [100]. Another good example is the Prius 2010 generator shown in Figures 17.32 and 17.33 [101].



Figure 17.31 Toyota/Aisin motor [100]

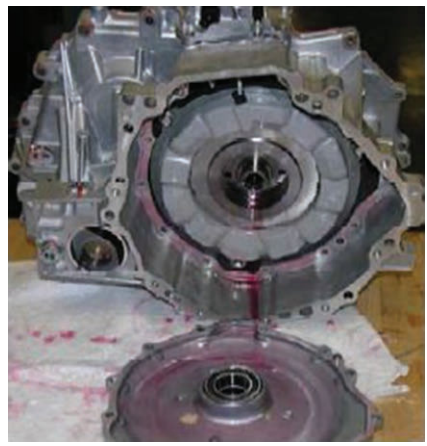


Figure 17.32 Prius 2010 FSCW-PM generator [101]

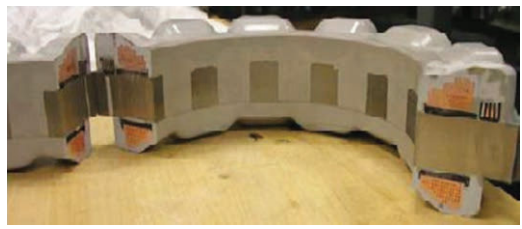


Figure 17.33 Cutout of the Prius 2010 FSCW-PM generator stator winding [101]

The full dimensions and ratings of this machine can be found in [101]. Another key example is "Motor A" in the Chevy Volt's Voltec 4ET50 electric drive system. This machine is mainly used as a generator. This is an FSCW-IPM machine with 24 stator slots and 16 rotor poles (1/2 SPP). The machine has a segmented stator structure as shown in Figures 17.20 and 17.21 and an IPM rotor as shown in Figures 17.34–17.36. More details about this machine can be found in [102].

FSCW-PM machines are also used in home appliances. Whirlpool has commercially made available an inside–out FSCW-PM machine that is used in a washing machine application [6]. FSCW-PM machines are also used in air-conditioning systems. Panasonic has an FSCW-IPM air-conditioner scroll compressor pump motor [6].

FSCW-PM machines are also being considered and evaluated for a wide range of applications, including ship propulsion, wind generators (there are already FSCW-PM wind generators commercially available especially for offshore wind), ocean wave generators, and aerospace applications. FSCW-PM machines are particularly a good fit for marine propulsion and wind applications. Since these are



Figure 17.34 One-tooth assembly of the Voltec motor A [102]



Figure 17.35 Machine A assembly diagram [102]



Figure 17.36 Machine A rotor with the end ring removed to show the magnet arrangement [102]

high-torque, low-speed applications, they lend themselves to a higher number of poles, which is suitable for FSCW. Also, since they are low-speed applications, the higher rotor losses due to FSCW are more manageable compared to high-speed applications.

17.18 Summary

Fractional-slot concentrated-wound AC machines have undergone intensive research and development recently due their compactness, ease of manufacturing and maintenance, and low cost compared to conventional AC machines. Many new applications in appliances, electric traction, and aerospace industries are already possible. These machines pose some control challenges due to the high number of poles, which can be taken advantage of in gearless drives, and the non-sinusoidal nature of its stator MMF. This chapter is focused on the design and performance aspects of the fractional-slot concentrated-wound machines.

List of symbols

S	Number of slots
p	Number of pole pairs
GCD	Greatest common divisor
q	Number of slots per pole per phase
K_{w1}	Synchronous component winding factor
n_1	Number of layers in each slot (1 or 2)
n_t	Number of turns around each tooth

S	Number of slots
$B_{g\ \max}$	Peak value of the no load air gap flux density
A_g	Air gap area
$I_{\max}$	Peak phase current
$\overline{Eh}_{phase.pu}$	Net phase hth-order harmonic EMF component in per-unit (phasor sum)
$\overline{Eh}_i$	hth-Order harmonic EMF component phasor in per-unit (p.u.) of the winding element "i" that belongs to this specific phase
Q	Total number of winding elements
K_{wh}	Winding function of the hth-order harmonic component
N_h	Amplitude of the hth-order harmonic component of the actual winding function for the winding of interest
N_{hbase}	Amplitude of the hth-order harmonic component of the base rectangular winding function
K_{dh}	Distribution factor for the hth-order harmonic component
q	Number of slots/pole/phase
b	Numerator of the fraction that fixes the number of slots/pole/phase
c	Denominator of the fraction that fixes the number of slots/pole/phase
d	Number representing the difference between two slots
P	Number of full pole pitches between two adjacent slots
K_{ph}	Pitch factor for the hth-order harmonic
W	Coil width
τ_p	Pole pitch
K_{w7}	Synchronous winding factor
Ψ_m	RMS flux-linkage due to the permanent magnets
Ψ_a	Phase "A" magnet flux linkage
r_g	Air gap radius
l_{eff}	Active length of the machine
N_a	Phase "A" winding function
B	Air gap magnet flux density
θ	Angle along the circumference of the air gap
B_{max}	Peak fundamental air gap magnet flux density
p	Number of pole pairs
L_{aa}	Self inductance of phase "A"
L_{ab}	Mutual inductance between phases "A" and "B"
μ_0	Permeability of air
g	Air gap thickness
L_d	d-Axis inductance

Glossary of terms

Fractional-slot concentrated windings (FSCW)	It is a winding concentrated around one tooth, so it does not have overlap between the various coils and phases in the end region
Flux weakening	Reduction in main field flux of permanent magnets
Axial-flux machine	The magnetic flux passes the stator or rotor parallel to the shaft axis

References

[1] H.A. Toliyat, T.A. Lipo, and J.C. White, "Analysis of a concentrated winding induction machine for adjustable speed drive applications. Part 1: Motor analysis," IEEE Trans. Energy Conversion, vol. 6, pp. 679–683, 1991.

[2] H.A. Toliyat, T.A. Lipo, and J.C. White, "Analysis of a concentrated winding induction machine for adjustable speed drive applications. Part 2: Motor design and performance," IEEE Trans. Energy Conversion, vol. 6, pp. 684–691, 1991.

[3] J. Cros and P. Viarouge, "Synthesis of high performance PM motors with concentrated windings," IEEE Trans. Energy Conversion, vol. 17, pp. 248–253, 2002.

[4] F. Magnussen and C. Sadarangani, "Winding factors and joule losses of permanent magnet machines with concentrated windings," Proc. of IEEE-IEMDC'03, vol. 1, pp. 333–339, Madison, WI, 2003.

[5] D. Ishak, Z.Q. Zhu, and D. Howe, "Comparison of PM brushless motors, having either all teeth or alternate teeth wound," IEEE Trans. Energy Conversion, vol. 21, pp. 95–106, 2006.

[6] A.M. EL-Refaie, "Fractional-slot concentrated-windings synchronous permanent magnet machines: opportunities and challenges," in IEEE Transactions on Industrial Electronics, vol. 57, no. 1, pp. 107–121, 2010.

[7] A.G. Jack, B.C. Mecrow, P.G. Dickinson, *et al.*, "Permanent magnet machines with powdered iron cores and pressed windings," IEEE Trans. Industry Applications, vol. 36, pp. 1077–1084, 2000.

[8] www.zfsachs.com/dynastart-pc.

[9] H. Akita, Y. Nakahara, N. Miyake, and T. Oikawa, "New core structure and manufacturing method for high efficiency of permanent magnet motors," Rec. of 2003 IEEE Industry Applications Society Annual Meeting, vol. 2, pp. 367–372, Salt Lake City, UT, 2003.

[10] K. Atallah, J. Wang, and D. Howe, "Torque-ripple minimization in modular permanent-magnet brushless machines," IEEE Trans. Industry Applications, vol. 39, pp. 1689–1695, 2003.

[11] H.A. Toliyat, L. Xu, and T.A. Lipo, "A five-phase reluctance motor with high specific torque," IEEE Trans. Industry Applications, vol. 28, pp. 659–667, 1992.

[12] A.M. EL-Refaie, M.R. Shah, R. Qu, and J.M. Kern, "Effect of number of phases on losses in conducting sleeves of high speed surface PM machine rotors," IEEE Industry Applications Society 42nd Annual Meeting, pp. 1522–1529, New Orleans, September 2007.

[13] A.M. El-Refaie and T.M. Jahns, "Impact of winding layer number and magnet type on synchronous surface PM machines designed for wide constant-power speed range operation," in IEEE Transactions on Energy Conversion, vol. 23, no. 1, pp. 53–60, 2008.

[14] Z.Q. Zhu and D. Howe, "Influence of design parameters on cogging torque in permanent magnet machines," IEEE Trans. Energy Conversion, vol. 15, pp. 407–412, 2000.

[15] M. Lajoie-Mazene, J.M. Vinassa, J. Cros, and S. Astier, "Brushless DC motors with low torque ripple," Proc. of Stockholm Power Tech Conference, pp. 87–92, Stockholm, Sweden, June 1993.

[16] P.B. Reddy, A.M. EL-Refaie, and K.K. Huh, "Effect of number of layers on performance of fractional-slot concentrated-windings interior permanent magnet machines," in IEEE Transactions on Power Electronics, vol. 30, no. 4, pp. 2205–2218, 2015.

[17] L. Alberti and N. Bianchi, "Theory and design of fractional-slot multilayer windings," Energy Conversion Congress and Exposition (ECCE), 2011 IEEE, pp. 3112–3119, 2011.

[18] G. Dajaku and D. Gerling, "Eddy current loss minimization in rotor magnets of PM machines using high-efficiency 12-teeth/10-slots winding topology," Electrical Machines and Systems (ICEMS), 2011 International Conference on, pp. 1–6, 2011.

[19] G. Dajaku and D. Gerling, "A novel 24-slots/10-poles winding topology for electric machines," Electric Machines & Drives Conference (IEMDC), 2011 IEEE International, pp. 65–70, 2011.

[20] P.B. Reddy, K.K. Huh, and A.M. EL-Refaie, "Generalized approach of stator shifting in interior permanent-magnet machines equipped with fractional-slot concentrated windings," in IEEE Transactions on Industrial Electronics, vol. 61, no. 9, pp. 5035–5046, 2014.

[21] F. Libert and J. Soulard, "Investigation on pole-slot combinations for permanent-magnet machines with concentrated windings," Proc. of Intl. Conf. on Elec. Mach (ICEM), CD, 2004.

[22] K.F. Konecny, "Compact three-phase permanent magnet rotary machine having low vibration and high performance," U.S Patent 4774428, May 1987.

[23] N. Bianchi, S. Bolognani, and G. Grezzani, "Design considerations for fractional-slot winding configurations of synchronous machines," IEEE Trans. Industry Applications, vol. 42, pp. 997–1006, 2006.

[24] N. Bianchi and M. Dai Pre, "Use of the star of slots in designing fractional-slot single-layer synchronous motors," IEE Proceedings-Electric power Applications, vol. 153, no. 3, pp. 997–1006, 2006.

[25] D.W. Novotny and T.A. Lipo, Vector Control And Dynamics of AC Drives: Calderon Press, Oxford, 1998.

[26] M.M. Liwschitz, "Distribution factors and pitch factors of the harmonics of a fractional-slot winding," AIEE Transactions, vol. 62, pp. 664–666, 1943.
[27] N. Bianchi, M. Dai Pre, L. Alberti, and E. Fornasiero, "Theory and design of fractional-slot PM machines," Tutorial course notes, Industry Applications Society Annual Meeting 2007, New Orleans, 23 Sept., 2007.
[28] A.M. EL-Refaie, T.M. Jahns, and D.W. Novotny, "Analysis of surface permanent magnet machines equipped with concentrated windings," IEEE Trans. Energy Conversion, vol. 21, pp. 34–43, 2005.
[29] J.K. Tangudu, T.M. Jahns, and A. El-Refaie, "Core loss prediction using magnetic circuit model for fractional-slot concentrated-winding interior permanent magnet machines," Energy Conversion Congress and Exposition (ECCE), 2010 IEEE, pp. 1004–1011, 2010.
[30] J.K. Tangudu, T.M. Jahns, and A. El-Refaie, "Unsaturated and saturated saliency trends in fractional-slot concentrated-winding interior permanent magnet machines," Energy Conversion Congress and Exposition (ECCE), 2010 IEEE, pp. 1082–1089, 2010.
[31] J.K. Tangudu, T.M. Jahns, A.M. El-Refaie, and Z.Q.Zhu, "Segregation of torque components in fractional-slot concentrated-winding interior PM machines using frozen permeability," Energy Conversion Congress and Exposition, 2009. ECCE 2009. IEEE, pp. 3814–3821, 2009.
[32] Z. Aza, Z.Q. Zhu, and G. Ombach, "Torque-speed performance analysis of fractional slot PM machines having concentrated windings using alternate methods," Power Electronics, Machines and Drives (PEMD 2012), 6th IET International Conference on, pp. 1–6, 2012.
[33] W. Soong and T.J.E. Miller, "Field weakening performance of brushless synchronous AC motor drives," IEE Proceedings-Electric Power Applications, vol. 141, no. 6, pp. 331–340, 1994.
[34] R.F. Schiferl and T.A. Lipo, "Power capability of salient pole permanent magnet synchronous motor in variable speed drive applications," IEEE Trans. Ind. Appl., vol. 26, pp. 115–123, 1990.
[35] A.M. El-Refaie, Z.Q. Zhu, T.M. Jahns, and D. Howe, "Investigation of winding inductances in fractional slot surface-mounted permanent magnet brushless machines," Proc. of 2008 IAS Annual Meeting, 2–5 Oct., Edmonton, Alberta
[36] A.M. EL-Refaie and T.M. Jahns, "Optimal flux weakening in surface PM machines using concentrated windings," IEEE Trans. Industry Applications, vol. 41, pp. 790–800, 2005.
[37] A.M. EL-Refaie and T.M. Jahns, P.J. McCleer, and J.W. McKeever, "Experimental verification of optimal flux weakening in surface PM machines using concentrated windings," IEEE Trans. Industry Applications, vol. 42, pp. 443–453, 2006.
[38] K. Atallah, D. Howe, P.H. Mellor, and D.A. Stone, "Rotor loss in permanent-magnet brushless AC machines," IEEE Trans. Industry Applications, vol. 36, pp. 1612–1618, 2000.

[39] H. Toda, Z. Xia, J. Wang, K. Atallah, and D. Howe, "Rotor eddy-current loss in permanent magnet brushless machines," IEEE Trans. Magnetics, vol. 40, pp. 2104–2106, 2004.

[40] D. Ishak, Z.Q. Zhu, and D. Howe, "Analytical prediction of rotor eddy current losses in permanent magnet brushless machines with all teeth and alternate teeth windings. Part I: Polar co-ordinate model," Proc. 7th International Conference on Electrical Machines and Systems, ICEMS 2004, CD, 2004.

[41] D. Ishak, Z.Q. Zhu, and D. Howe, "Analytical prediction of rotor eddy current losses in permanent magnet brushless machines with all teeth and alternate teeth windings. Part II: Rectangular co-ordinate model," Proc. 7th International Conference on Electrical Machines and Systems, ICEMS 2004, CD, 2004.

[42] J. Wang, Z.P. Xia, and D. Howe, "Analysis of three-phase surface-mounted magnet modular permanent magnet machines," Rec. of 2nd IEE International Conference on Power Electronics, Machines and Drives (PEMD 2004), vol. 3, pp. 27–32, 2004.

[43] M. Nakano, H. Kometani, and M. Kawamura, "A study on eddy-current losses in rotors of surface permanent magnet synchronous machines," Rec. of 2004 IEEE Industry Applications Society Annual Meeting, vol. 3, pp. 1696–1702, 2004.

[44] N. Bianchi, S. Bolognani, and E. Fomasiero, "A general approach to determine the rotor losses in three-phase fractional-slot PM machines," IEEE International Electric Machines and Drives Conference, IEMDC'07, vol. 1, pp. 634–641.

[45] H. Polinder, M.J. Hoeijmakers, and M. Scuotto, "Eddy-current losses in the solid back-iron of permanent-magnet machines with concentrated fractional pitch windings," The 3rd IET International Conference on Power Electronics, Machines, and Drives, March 2006, pp. 479–483.

[46] J.D. Ede, K. Atallah, G.W. Jewell, J.B. Wang, and D. Howe, "Effect of axial segmentation of permanent magnets on rotor loss of modular brushless machines," Rec. of 2004 IEEE Industry Applications Society Annual Meeting, vol. 3, pp. 1703–1708, 2004.

[47] M.R. Shah and A.M. EL-Refaie, "Eddy current loss minimization in conducting sleeves of high speed machine rotors by optimal axial segmentation and copper cladding," IEEE Industry Applications Society 42nd Annual Meeting, pp. 544–551, New Orleans, September 2007.

[48] J.D. Ede, K. Atallah, J. Wang, and D. Howe, "Effect of optimal torque control on rotor loss of fault-tolerant permanent-magnet brushless machines," IEEE Trans. Magnetics, vol. 38, pp. 3291–3293, 2002.

[49] A.M. El-Refaie, M.R. Shah, J.P. Alexander, S. Galioto, K.-K. Huh, and W.D. Gerstler, "Rotor end losses in multiphase fractional-slot concentrated-winding permanent magnet synchronous machines," Industry Applications, IEEE Transactions on, vol. 47, no. 5, pp. 2066–2074, 2011.

[50] M.R. Shah and A.M. El-Refaie, "End effects in multiphase fractional slot concentrated-winding surface permanent magnet synchronous machines," Energy Conversion, IEEE Transactions on, vol. 25, no. 4, pp. 1001–1009, 2010.

[51] P.B. Reddy, T.M. Jahns, and A.M. El-Refaie, "Impact of winding layer number and slot/pole combination on AC armature losses of synchronous surface PM machines designed for wide constant-power speed range operation," Industry Applications Society Annual Meeting, 2008. IAS '08. IEEE, pp. 1–8, 2008.

[52] R. Wrobel, P.H. Mellor, and D. Holliday, "Thermal modeling of a segmented stator winding design," Industry Applications, IEEE Transactions on, vol. 47, no. 5, pp. 2023–2030, 2011.

[53] G. Dajaku and D. Gerling, "A novel 12-teeth/10-poles PM machine with flux barriers in stator yoke," Electrical Machines (ICEM), 2012 XXth International Conference on, pp. 36–40, 2012.

[54] N. Bianchi, M. Dai Pre, G. Grezzani, and S. Bolognani, "Design considerations on fractional-slot fault-tolerant synchronous motors," in Proc. of 2005 IEEE Intl. Conf. on Elec. Mach. and Drives (IEMDC), San Antonio, TX, CD-ROM, 2005.

[55] N. Bianchi, S. Bolognani, and M.D. Pre, "Strategies for the fault-tolerant current control of a five-phase permanent-magnet motor," IEEE Trans. On Industry Applications, vol. 43, no. 4, pp. 960–970,2007.

[56] N. Bianchi, S. Bolognani, and M.D. Pre, "Design and tests of a fault-tolerant five-phase permanent magnet motor," IEEE 37th Power Electronics Specialists Conference, 2006, PESC'06, 18–22 June 2006 pp. 1–8.

[57] N. Bianchi, S. Bolognani, and M.D. Pre, "Impact of stator winding of a five-phase motor on postfault operations," IEEE Trans. On Industrial Electronics, vol. 55, no. 5, pp. 1978–1987, 2008.

[58] C. Bianchini, E. Fornasiero, T. Matzen, N. Bianchi, and A. Bellini, "Fault detection of a five-phase permanent-magnet machine," IEEE 34th Annual Industrial Electronics Conference, 2008, IECON 08, 10–13 Nov. 2008 pp. 1200–1205.

[59] S. Dwari and L. Parsa, "An optimal control technique for multiphase PM machines under open-circuit faults," IEEE Trans. On Industrial Electronics, vol. 55, no. 5, pp. 1988–1995, 2008.

[60] J. Chai, J. Wang, K. Atallah, and D. Howe, "Performance comparison and winding fault detection of duplex 2-phase and 3-phase fault-tolerant permanent magnet brushless machines," Conference record of the 2007 IEEE Industry Applications Conference 2007, 42nd IAS Annual Meeting, 23–27 Sept. 2007, pp. 566–572.

[61] A.J. Mitcham, A.G. Jack, J.A. Haylock, and J. Coles, "Favourable slot and pole combinations for fault-tolerant PM machines," IEE Proc. -Electr. Power Appl., vol. 151, no.5, pp. 520–525, 2004.

[62] B.C. Mecrow, A.G. Jack, J.A. Haylock, and J. Coles, "Fault-tolerant permanent magnet machine drives," IEE Proceedings-Electric Power Applications, vol. 143, no. 6, pp. 437–442, 1996.

[63] J.A. Haylock, B.C. Mecrow, A.G. Jack, J.A. Haylock, and D.J. Atkinson, "Operation of a fault tolerant PM drive for an aerospace fuel pump application," IEE Proceedings-Electric Power Applications, vol. 145, no. 5, pp. 441–448, 1998.

[64] B.C. Mecrow, A.G. Jack, D.J. Atkinson, *et al.*, "Design and testing of a four-phase fault-tolerant permanent-magnet machine for an engine fuel pump," IEEE Trans. On Energy Conversion, vol. 19, no. 4, pp. 671–678, 2004.

[65] G.J. Atkinson, B.C. Mecrow, A.G. Jack, D.J. Atkinson, P. Sangha, and M. Benarous, "The analysis of losses in high-power fault-tolerant machines for aerospace applications," IEEE Trans. On Industry Applications, vol. 42, no. 5, pp. 1162–1170, 2006.

[66] A. EL-Refaie, M. Shah, and K.-K. Huh, "High power-density fault-tolerant permanent generator for safety critical applications," IEEE Transactions on Industry Applications, vol. 50, no. 3, pp. 1717–1728, 2014.

[67] Z.Q. Zhu, D. Howe, and T.S. Birch, "Calculation of winding inductances of brushless motors with surface-mounted permanent magnets," Proc. International Conference of Electrical Machines (ICEM), pp. 327–332, Paris, 1994.

[68] Z.Q. Zhu and D. Howe, "Winding inductances of brushless machines with surface-mounted magnets," Proc. International Electric Machines and Drives Conference, pp. WB2/2.1–WB2/2.3, 1997.

[69] Z.Q. Zhu, D. Howe, and J.K. Mitchell, "Magnetic field analysis and inductances of brushless DC machines with surface-mounted magnets and non-overlapping stator windings," IEEE Trans. Magnetics, vol. 31, pp. 2115–2118, 1995.

[70] N. Bianchi, S. Bolognani, and G. Grezzani, "Fractional-slot IPM servomotors: analysis and performance comparisons," Proc. of Intl. Conf. on Elec. Mach (ICEM),CD, 2004.

[71] P. Salminen, J. Mantere, J. Pyrhonen, and M. Niemela, "Performance of fractional slot wound PM-motors," Proc. of Intl. Conf. on Elec. Mach (ICEM), CD, 2004.

[72] P. Salminen, M. Niemela, J. Pyrhonen, and J. Mantere, "Performance analysis of fractional slot wound PM-motors for low speed applications," Rec. of 2004 IEEE Industry Applications Society Annual Meeting, vol. 2, pp. 1032–1037, 2004.

[73] H. Murakami, H. Kataoka, Y. Honda, S. Morimoto, and Y. Takeda, "Highly efficient brushless motor design for an air-conditioner of the next generation 42 V vehicle," Rec. of 2001 IEEE Industry Applications Society Annual Meeting, vol. 1, pp. 461–466, 2001.

[74] Y. Asano, Y. Honda, H. Murakami, Y. Takeda, and S. Morimoto, "Novel noise improvement technique for a PMSM with concentrated winding," Proc. 2002 Power Conversion Conference (PCC 2002), vol. 2, pp. 460–465, Osaka, 2002.

[75] S. Cheng, Y. Pei, F. Chai, and S. Cui, "The torque pulsation analysis of a starter generator with concentrated windings based hybrid vehicles," Proc. of IEEE-IEMDC'03, vol. 1, pp. 218–221, Madison, WI, 2003.

[76] Z.Q. Zhu, S. Ruangsinchaiwanich, N. Schofield, and D. Howe, "Reduction of cogging torque in interior-magnet brushless machines," IEEE Trans. Magnetics, vol. 39, pp. 3238–3240, 2003.

[77] A.M. EL-Refaie and T.M. Jahns, "Comparison of synchronous PM machine types for wide constant-power speed range operation," Rec. of the IEEE 2005 Industry Applications Annual Meeting, IAS 2005, Hong Kong, vol. 2, pp. 1015–1022, 2005.

[78] A.M. EL-Refaie and T.M. Jahns. "Comparison of synchronous PM machine types for wide constant-power speed operation: converter performance," IET Electric Power Applications, vol. 1, no. 2, pp. 217–222.

[79] P.B.Reddy, A.M. El-Refaie, K.-K. Huh, J.K. Tangudu, T.M. Jahns, "Comparison of interior and surface PM machines equipped with fractional-slot concentrated windings for hybrid traction applications," Energy Conversion, IEEE Transactions on, vol. 27, no. 3, pp. 593–602, 2012.

[80] A.G. Jack, B.C. Mecrow, G. Nord, and P.G. Dickinson, "Axial flux motors using compacted insulated iron powder and laminations: design and test results," IEEE 2005 International Conference on Electric Machines and Drives, IEMDC 05, 15–18 May 2005 pp. 378–385.

[81] F. Locment, E. Semail, and X. Kestelyn, "Vectorial approach-based control of a seven-phase axial flux machine designed for fault operation," IEEE Trans. On Industrial Electronics, vol. 55, no. 10, pp. 3682–3691, 2008.

[82] F. Locment, E. Semail, X. Kestelyn, and A. Bellini, "Control of a seven-phase axial flux machine designed for fault operation," IEEE 32nd Annual Industrial Electronics Conference, 2006, IECON 06, 6–10 Nov. 2006 pp. 1101–1107.

[83] F. Caricchi, F. Crescimbini, T.A. Lipo, and E. Santini, "Innovative inverter topology for concentrated winding PM motor drives," Rec. of 1992 IEEE Power Electronics Specialists Conference, vol. 2, pp. 964–972, 1992.

[84] J. Wang, M. West, D. Howe, H.Z. De La Parra, and W.M. Arshad, "Design and experimental verification of a linear permanent magnet generator for a free-piston energy converter," IEEE Trans. On Energy Conversion, vol. 22, no. 2, pp. 299–306, 2007.

[85] Y. Amara, J. Wang, and D. Howe, "Analytical prediction of eddy-current loss in modular tubular permanent magnet machines," IEEE Trans. On Energy Conversion, vol. 20, no. 4, pp. 761–770, 2005.

[86] Y. Amara, J. Wang, and D. Howe, "Stator iron loss of tubular permanent magnet machines," IEEE Trans. On Industry Applications, vol. 41, no. 4, pp. 989–995, 2005.

[87] W. Hua, M. Cheng, H. Jia, and X. Fu, "Comparative study of flux-switching and doubly-salient PM machines particularly on torque capability," Rec. of 2008 IEEE Industry Applications Society Annual Meeting, vol. 1, pp. 1–8, 2008.

[88] Y. Cheng, C. Pollock, and H. Pollock, "A permanent magnet flux switching motor for low energy axial fans," Rec. of 2005 IEEE Industry Applications Society Annual Meeting, vol. 3, pp. 2168–2175, 2005.

[89] H. Pollock, C. Pollock, R.T. Walter, and B.V. Gorti, "Low cost, high power density, flux switching machines and drives for power tools," Rec. of 2003 IEEE Industry Applications Society Annual Meeting, vol. 3, pp. 1451–1457, 2003.

[90] C. Pollock, H. Pollock, R. Barron, *et al.*, "Flux switching motors for automotive applications," Rec. of 2005 IEEE Industry Applications Society Annual Meeting, vol. 1, pp. 242–249, 2005.

[91] W. Zhao, M. Cheng, W. Hua, and H. Jia, "A redundant flux-switching permanent magnet motor drive for fault-tolerant applications," Rec. of 2008 Vehicle Power and Propulsion Conference, vol. 1, pp. 1–6, 2008.

[92] A.S. Thomas, Z.Q. Zhu, R.L. Owen, G.W. Jewell, and D. Howe, "Multi-phase flux-switching permanent magnet brushless machine for aerospace application," Rec. of 2005 IEEE Industry Applications Society Annual Meeting, vol. 1, pp. 1–8, 2005.

[93] A.M. El-Refaie and M.R. Shah, "Comparison of induction machine performance with distributed and fractional-slot concentrated windings," Industry Applications Society Annual Meeting, 2008. IAS '08. IEEE, pp. 1–8, 2008.

[94] L. Alberti and N. Bianchi, "Design and tests on a fractional-slot induction machine," Energy Conversion Congress and Exposition (ECCE), 2012 IEEE, pp. 166–172, 2012.

[95] Y.S. Chen, Z.Q. Zhu, and D. Howe, "Vibration of PM brushless machines having a fractional number of slots per pole," IEEE Transactions on Magnetics, vol. 42, no. 10, pp. 3395–3397, 2006.

[96] J. Wang, Z.P. Xia, D. Howe, and S.A. Long, "Vibration characteristics of modular permanent magnet brushless AC machines," 41st IAS Annual Meeting. Conference Record of the 2006 IEEE 41st IAS Annual Meeting Conference, vol. 3, pp. 1501–1506, 2006.

[97] J. Wang, Z.P. Xia, S.A. Long, and D. Howe, "Radial force density and vibration characteristics of modular permanent magnet brushless ac machine," IEE Proceedings – Electric Power Applications, vol. 153, no. 6, pp. 793–801, 2006.

[98] Z.Q. Zhu, D. Ishak, D. Howe, and J. Chen, "Unbalanced magnetic forces in permanent-magnet brushless machines with diametrically asymmetric phase windings," IEEE Transactions on Industry Applications, vol. 43, no. 6, pp. 1544–1553, 2007.

[99] F. Magnussen, and H. Lendenmann, "Parasitic effects in PM machines with concentrated windings," IEEE Transactions on Industry Applications, vol. 43, no. 5, pp. 1223–1232, 2007.

[100] M. Kaizuka, T. Imai, S. Ishikawa, M. Niki, and H. Adachi, "Development of 2005 model year accord hybrid," EVS21, April 2005, Monaco.

[101] http://ecee.colorado.edu/~ecen5017/notes/OakRidge_2010Prius.pdf

[102] K. Rahman, S. Jurkovic, C. Stancu, J. Morgante, and P. Savagian, "Design and performance of electrical propulsion system of extended range electric vehicle (EREV) Chevrolet Voltec," Energy Conversion Congress and Exposition (ECCE), 2012 IEEE, pp. 4152–4159, 2012.

This page intentionally left blank

Index

ABB DTC control 351
ABB SynRM 351–2
AC–DC converters 4, 104–5, 115–18, 121, 132
  single-phase controlled 108–10
  single-phase uncontrolled 110
  three-phase controlled 110
  three-phase uncontrolled 110
ACS880 drives 351–3
active voltage vectors 328, 425, 515, 534–7, 557
adaptive searching trajectory 265
air blower 316–17
aircraft 581–2
Alesina–Venturini (AV) method 406
analogue to digital converters (ADCs) 43, 470
anisotropic magnetoresistive (AMR) effect 40
anti-aliasing filter 466–9
artificial intelligence-based position and speed estimators 178
asymmetrical machines 586–8, 596
axial-flux, tubular, and flux-switching machines 681
axial-flux PM machines 681

back electromotive force (BEMF) 253, 265, 363, 637
back emf-based position estimation technique 176
Bessel filter 467–70
bidirectional switches (BDSs) 11, 389
  realization 391–3
brushless DC motor (BLDCM) drives 245, 637
  construction of 246
  control of, in high-speed region 264
    operation in high-speed region 264–5
    phase-advance approach to expand the speed range 265
    pseudo-vector control for high-speed range 266–7
    simulation results for high-speed operation using PVC 267–70
  modeling of 249
    block diagram of 252
    dynamic model 250–1
    torque-speed characteristic 252–3
  operation principle of 247–8
  phase-current control of 253
    control system configuration 253–4
    simulation results 254–5
  pseudo-vector control of 258
    principle of 258–60
    simulation results and performance comparison 260–3
    system configuration 258
  specific features of 249
  torque ripple analysis and reduction techniques 255–8

carrier-based modulation method 409–11
cascaded structure, tuning of an electric drive using 35–7
cathode ray oscilloscope (CRO) 159
choppers 110–14
Clarke transformation 548, 585, 594–5

Clarke's Transform 518, 537
closed-loop flux-weakening control 235–7
closed-loop IPF compensation 420–1
closed-loop speed-adaptive observer 520–4
closed-loop speed control system 309
closed-loop speed non-adaptive observer 525–7, 532, 538
cogging torque 255, 650
complete stability 481, 483, 500
complex programmable logic devices (CPLDs) 605
concentrated winding (CW) 46, 637
constant back emf (CBE) control 141–2
constant dwell angle control method 294
constant mutual flux linkages (CMFL) control 141
constant-power speed range 46, 54, 216, 362
constant-power–speed ratio 217, 223–4
constant torque angle control method 293
continuous control set MPC (CCS-MPC) schemes 545, 625–6
controlled AC–DC converter-based DC motor drive 116
controller hierarchy for electric drives 3–7
converters for drives 63
  three-phase multilevel inverter 76
    neutral-point voltage control 90–7
    sinusoidal PWM (SPWM) 78–81
    space vector PWM 81–5
    three-level space vector PWM (SVPWM), carrier-based implementation of 86–90
  three-phase two-level inverter 64
    sinusoidal PWM (SPWM) 66–8
    space vector PWM 68–72
    space vector PWM (SVPWM), carrier-based implementation of 72–6
current and voltage model-based sensorless algorithms 177–8
current chopping control (CCC) 301
current control 294
  chopping control 298–300
  hysteresis control 300
  single pulse control 294–8
current controlled pulse width modulator (CC-PWM) 156, 159, 180, 184
current direction-based commutation 401–6
current limit control (CLC) 117–18
current model (CM) 338, 487–9, 491, 493
current-regulated voltage-source (VS) inverter 212
current sensors for electric drive systems 39–41
current slope measurement method 534–40
current source inverters (CSIs) 584
current source rectifier (CSR) 415
current trajectories 233, 235, 361
cylindrical-rotor configuration 139

d-axis "armature reaction" flux linkage 217
d-axis flux linkage 217
DC–DC converters 10, 105–7, 114–15
DC machines, dynamic model of 18–19
DC motor drives 101
  classification of 104–7
  controlled AC–DC converter-based 116
  converters for 107
    choppers 110–14
    DC–DC converters 114–15
    single-phase controlled AC–DC converters 108–10
    single-phase uncontrolled AC–DC converters 110
    three-phase controlled AC–DC converters 110
    three-phase uncontrolled AC–DC converters 110

DC series motor control 131
modeling of DC motor 102–4
performance simulation of 125–31
power quality control and sensor reduction for DC motor drives 121–3
proportional-integral (PI) controller design 120–1
PWM current controller 124
PWM signal generation
for full-bridge converter 125
for half bridge converter 125
for push–pull converter 124
for single switch converters 124
for voltage follower control 124
reference current generator for power quality control 123
uncontrolled AC–DC converter–chopper-based 117–18
uncontrolled AC–DC converter-DC–DC converter-based 118–20
voltage controller 123
decision-making process 147
defuzzification 147–8
demagnetization 288–9, 295
digital control algorithm 391
digital signal processor (DSP) 138, 351, 372, 427, 481, 545
digital signal processor (DSP)-based hardware implementation
of sensorless vector-controlled PMSM drive 184
power circuit of the drive, development of 185
signal conditioning circuits, development of 185
digital signal processor (DSP)-based software implementation
of sensorless vector-controlled PMSM drive 185
estimation of stator flux and position of rotor 185
reference speed input 185
reference winding current generation 186
speed controller 186
speed estimation 186
switching signal generation for voltage source inverter 186
of vector-controlled PMSM drive 157
reference speed input 158
reference winding current generation 158–9
rotor position signals, sensing of 158
speed controller 158
speed sensing 158
switching signal generation for voltage source inverter 159
digital signal processor (DSP)-based vector-controlled PMSM drive 156
power circuit of the drive, development of 157
signal conditioning circuits, development of 157
digital-to-analog converters (DACs) 159
diode-bridge (DB) BDS 391
diode bridge rectifier (DBR) 105
direct field orientation (DFO) 482
flux estimation in 487
combination of current model (CM) and voltage model (VM) 491
current model 487–9
reduced-order observer 491–2
speed estimation 492
statically compensated voltage model (VM) 489–91
voltage model 489
direct flux vector control (DFVC) 620–3
direct matrix converter (DMC) 389
direct self control (DSC) 325, 482, 617
direct torque and flux controls (DTFC) 7
for MC-fed PMSM drives 431
design of the torque and flux PI controllers 434–7
experimental results of DTFC MC drive 437–9

mathematical model of IPMSM in the stator flux (x-y) reference frame 432–4
direct torque control (DTC) 7, 258, 301–3, 325, 359, 482, 617–20
closed-loop flux and torque estimation 378–81
control trajectories with 381
current and voltage trajectories in the T–λ_s plane 384–5
MTPA trajectory under DTC 383–4
performance of PMSM under DTC with trajectory following 385
current control trajectories for PMSM 361
field weakening under voltage limit 361–3
with fixed switching frequency and reduced torque and flux ripple 373–8
flux estimation approaches 334
application of hybrid flux estimators 338–9
estimation of stator flux 339–40
flux estimation with feedback 335–8
speed-sensorless operation 340–1
use of low-pass filters 334–5
induction motor model 326–8
industrial adaptation of 350–4
for MC drive 422–5
improved DTC for MCs 427–9
using three hysteresis comparators 425–7
performance enhancement of 344
DTC-SVM control 346–7
predictive torque control 347–9
reduction in torque and flux ripple using alternate switching tables 344–6
PMSM model and RFOC 360–1
for PMSMs 363–8
stability criteria for DTC 370
torque and flux linkage control of a PMSM 371–3
voltage space vector selection 368–70
principle 329
flux and torque comparator 331–2
motor model 333
optimum switching vector selection 332–3
simulation of 341–3
of synchronous motors 350
two-level inverter voltage vector representation 328–9
discontinuous PWM (DPWM) 599
distributed winding (DW) 46, 584
distribution factor, calculating for fractional-slot windings 657–9
double-layer (DL) concentrated windings 638
doubly salient PM (DSPM) motors 50
DS2004 A/D board 459–60
DS5001 digital waveform capture (DWC) 460
dSPACE AutoBox 455
DS1007 PPC processor board 456
DS2004 high-speed A/D board 459
DS4002 timing and digital I/O board 456–9
DS5001 digital waveform capture board 456
hardware scheme and interface with dSPACE 459–61
DTC-SVM control 346–7
dual-mode inverter control 265
dynamic model
of DC machines 18–19
of induction machines in synchronous reference frame 24
machine inductance and flux linkages 28–9
rotor flux-oriented control (RFOC), conditions for 31–4
voltage, developed power and torque equations 30

synchronous machines in rotor reference frame 19
machine inductance and flux linkages 19–22
rotor flux-oriented control (RFOC) or vector control 23–4
voltage equations 22–3
Dyson digital motor 314

electrical machines, losses in
equipped with FSCW 668
AC losses in windings 671
end losses 670–1
loss reduction 671–2
rotor losses 668–9
electric drive system 64
current sensors for 39–41
elements of 2, 9
speed sensors for 42–5
electric machines and torque–speed (T–ω) boundaries 15–16
electric supercharger 320–1
electric vehicle (EV) 51, 53, 319–21
application 319
electric supercharger 320–1
traction motor 319–20
electromagnetic interferences (EMIs) 513
electromotive force (EMF) 245, 292, 656–7
electronics commutator 246, 271
estimation of stator flux and position of rotor 185
Euler approximation 553–4
extended Kalman filter (EKF) 177, 340

fast Fourier transform (FFT) 429
feedforward vs. closed-loop flux-weakening control algorithms 232–8
field-oriented control (FOC) 57, 142, 309, 605, 614–16
field programmable gate arrays (FPGAs) 605
field weakening controller 116, 155–7
finite control set MPC (FCS-MPC) 545, 625
finite impulse response (FIR) filter 183
finite-state predictive torque control (FS-PTC) 546
induction motor drive under 563
average switching frequency 569–70
robustness against rated-load torque disturbance 570–1
steady-state behavior 564–7
step rated-speed-transient characteristics 571–3
step rated-torque-transient characteristics 571
transient capability under rated-speed reversal 567–9
selected prediction vectors (SPVs)-based 556–63
flux and torque comparator 330–3, 346
flux collapse 500
flux estimation 181
approaches 334
estimation of stator flux 339–40
flux estimation with feedback 335–8
hybrid flux estimators, application of 338–9
speed-sensorless operation 340–1
use of low-pass filters 334–5
flux estimator 181–3, 334, 336–8, 346, 481–2, 486–92, 495, 615
flux linkage and torque estimator (FTE) 363–5, 378–9
flux-switching PM (FSPM) motors 50
flux weakening 663–5
control 230
basic principles of 230–2
feedforward vs. closed-loop flux-weakening control algorithms 232–8
six-step voltage operation for 239
inductance calculations 667–8

range 142
same magnet flux linkage constraint 665–7
food blender 314
electric vehicle application 319
electric supercharger 320–1
traction motor 319–20
industrial applications 316
air blower 316–17
hammer breaker 318–19
fractional-slot concentrated windings (FSCW) 584, 637
advantages of using 640–4
axial-flux, tubular, and flux-switching machines 681
challenges involved in using 644
commercial applications and future evolution of research 683–6
definition of 637–9
design and analysis 662–3
fault tolerance 673–7
flux weakening 663–5
inductance calculations 667–8
same magnet flux linkage constraint 665–7
induction machines 682
losses in electrical machines equipped with 668
AC losses in windings 671
end losses 670–1
loss reduction 671–2
rotor losses 668–9
optimum slot/pole combination, criteria for choosing 648–51
parasitic effects 682–3
single-layer (SL) and double-layer (DL) configurations, comparison of 646–8
surface PM (SPM) versus interior PM (IPM) machines 677–80
three-phase structures that support 644–6
winding factor, calculation of 656
closed-form expressions 658–9
EMF factor 656–7
using closed-form expressions 661
using EMF method 659–60
using winding function method 660–1
winding function method 657
winding layout determination 651–6
fractional-slot concentrated-wound AC machines 12
fractional slot CW (FSCW) 46
fractional-slot windings 657
calculating distribution factor for 657–9
freewheeling 295, 395, 400–1
full-bridge converter
pulse width modulation (PWM) signal generation for 125
full-order observer 492
fuzzy logic control (FLC) toolbox 138, 146
fuzzy pre-compensated PI controller 145–8
decision-making 147
defuzzification 147–8
fuzzification 147
fuzzy logic control 146
fuzzy pre-compensator 146

Gamesa 582
Gray-coded tracks 43

half bridge converter
pulse width modulation (PWM) signal generation for 125
Hall current sensor 39, 175
Hall-effect sensors 245, 247–8, 254–8, 27
hammer breaker 318–19
hard chopping 299–300, 305
Harris formula 308
high-frequency (HF) signal injection 528–34
high-frequency carrier signal injection method for estimation of position and speed 177

high-speed capability curves for surface PM machines 225–7
hybrid electric vehicle (HEV) 53
hybrid flux estimators 338–9
hybrid fuzzy PI controller 148–9

indirect field orientation (IFO) 482
  flux estimation in 493
    current model 493–4
    inherently sensorless reduced-order observer 497–9
    inherently sensorless scheme, speed estimation in 500
    reduced-order observer 494–5
    speed estimation 497
    statically compensated VM 496–7
    voltage model 495
indirect matrix converter (IMC) 389, 439
  commutation issue for 441
  modulation scheme for 439
    SVM for inverter stage 440
    SVM for rectifier stage 439–40
  rotor flux-oriented control of induction machine (IM)-driven by 441
    indirect rotor flux-oriented vector control of IM 442–5
    principle of rotor-flux orientation 441–2
indirect rotor flux-oriented control (IRFOC) 11, 390, 442–5
indirect space vector modulation (ISVM) 389, 415, 431–9
inductance calculations 667–8
induction machine (IM) 583, 682
  dynamic model of, in synchronous reference frame 24
    conditions for rotor flux-oriented control 31–4
    machine inductance and flux linkages 28–9
    voltage, developed power and torque equations 30
induction motor (IM) 326–8, 462–3, 547, 549–51
induction motor (IM) drive, predictive torque control of 545
  basic structure and working principle of PTC 552
    cost function optimisation 554–5
    estimation 553
    limitations of FS-PTC 555–6
    prediction 553–4
  computational efficiency improvement in SPVs-based FS-PTC 562–3
  performance of IM drive under FS-PTC 563
    average switching frequency 569–70
    robustness against rated-load torque disturbance 570–1
    steady-state behavior 564–7
    step rated-speed-transient characteristics 571–3
    step rated-torque-transient characteristics 571
    transient capability under rated-speed reversal 567–9
  PTC and classical control strategies (FOC and DTC), comparison between 546–7
  PTC system modelling 547
    modelling of IM 549–51
    modelling of inverter 551–2
    state-space representation of three-phase systems 547–9
  SPVs-based FS-PTC 556
    average switching frequency reduction 560
    optimum voltage vector selection 559–60
    overall control structure of SPVs-based FS-PTC 560–1
    selecting prediction vectors 556–9
    SPVs-based FS-PTC algorithm 561

induction motor (IM) drives, sensorless control of: *see* sensorless control of induction motor (IM) drives
induction motor (IM) space-vector equations 465
inherently sensorless CM 499, 504
inherently sensorless equations 482
inherently sensorless reduced-order observer recast as SCVM 498–9
input and output (I/O) boards 459–61
input voltage sign-based commutation 399–401
insulated gate bipolar transistors (IGBTs) 246, 395, 397–8, 460–1
integral of time multiplied by the absolute of the error (ITAE) 434
interior permanent magnet (IPM) 202, 365
interior permanent magnet (IPM) machine torque production characteristics 206
  basics of torque production 206–7
  current limit circle 210–11
  impact of magnetic saturation on maximum torque-per-Amp trajectories 211–12
  PMSM torque production characteristics in *dq* current plane 207–10
interior permanent magnet synchronous machine 360, 389, 422, 429, 432
  direct torque control of 365
interior permanent magnet synchronous motor
  and permanent magnet-assisted synchronous reluctance motor (PMaSynRM), comparison of 140
internal permanent magnet (IPM) 236, 580, 584
inter-switch commutation 403
inverse Park transformation 260
"inverse-Γ" model 484–5
inverter, modelling of 551–2
inverter-fed IM drives 481

Kirchhoff's first law 251

light-emitting diodes (LEDs) 43
load perturbation response of sensorless PMSM drive 192–3
low-pass filter (LPF) 334–5, 338, 425

machine inductance and flux linkages 19–22, 28–9
magnetization 51, 295
magnetomotive force (MMF) 584
  distributions 644
  waveform 46
magnet torque and reluctance torque-based classification 139–40
MATLAB®-based model of sensorless vector-controlled PMSM drive 182
  current controlled pulse width modulator (CC-PWM) 184
  flux estimator 182–3
  position and speed estimation 183
  reference winding current generation 183
  speed controller 183
MATLAB-based model of vector-controlled PMSM drive system 152
  power system blockset (PSB) toolbox, modeling using 152
    current controlled pulse width modulator (CC-PWM) 156
    field weakening controller 155
    reference winding current generation 155–6
    speed controller 152–5
MATLAB/Simulink® 260, 460
matrix converter (MC) 389
  current commutation strategies 398
    current direction-based commutation 401–6

input voltage sign-based commutation 399–401
direct torque and flux control (DTFC) for MC-fed PMSM drives by using ISVM 431
design of the torque and flux PI controllers 434–7
experimental results of DTFC MC drive 437–9
mathematical model of IPMSM in the stator flux (*x*-*y*) reference frame 432–4
DTC for MC drive 422–5
improved DTC for MCs 427–9
using three hysteresis comparators 425–7
experimental results 429–31
fundamentals of 390–1
IMC-driven AC drives 439
commutation issue for IMC 441
modulation scheme for IMC 439–40
rotor flux-oriented control of induction machine (IM)-driven by IMC 441–5
implementation of 391
bidirectional switch (BDS) realization 391–3
input filter design 393–5
power circuit layout 395
protections 395–8
input power factor (IPF) compensation for 418
closed-loop IPF compensation 420–1
open-loop IPF compensation 418–20
modulation techniques 406
Alesina–Venturini (AV) method 406
carrier-based modulation method 409–11
optimum AV method 406–7
scalar modulation methods 407–9
SVM method 411–18
maximum efficiency (ME) control 140–1
maximum torqueper-Amp (MTPA) trajectories 23, 140–1, 209–10, 213, 221, 232, 361, 383–4
impact of magnetic saturation on 211–12
maximum torque per voltage trajectory (MTPV) 56–7, 231
MAXIM® design software 469
"mechanically brushless" DC motor 246
metaloxide semiconductor field-effect transistors (MOSFETs) 246
model predictive control (MPC) 545, 623–8
model reference adaptive control (MRAC) 214, 346
model reference adaptive observer (MRAO) 514–15
modern industry and energy usage role of motor drives in 1–3
modulation index 66, 236–7
modulation techniques 406
Alesina–Venturini (AV) method 406
carrier-based modulation method 409–11
optimum AV method 406–7
scalar modulation methods 407–9
space vector modulation (SVM) method 411–18
motor drives, role of
in modern industry and energy usage 1–3
multiphase electrical machines 583–4
multi-stator (MS) approach 594–5
asymmetrical 12-phase IM 595–6
vector space decomposition (VSD) approach 584–5
asymmetrical IPM machine (case study) 590–4
asymmetrical machines 586–7
asymmetrical six-phase IM (case study) 589–90
features of 587–9
symmetrical machines 585–6

multiphase machine drives 579
  advantages of 579–81
  applications 581–2
  brief history of 581
  control of 611–13
    direct flux vector control (DFVC) 620–3
    direct torque control (DTC) 617–20
    field-oriented control (FOC) 614–16
    model predictive control (MPC) 623–8
  definition of 579
multiphase power converters 597
  modulation strategies for multiphase inverters 597–8
  output current ripple, analysis of 609–11
  pulse width modulation 598–9
  space vector modulation (SVM) technique 605–9
  voltage limits 599–601
    five-phase inverters (case study) 601
    seven-phase inverters (case study) 602–3
    sinusoidal operating conditions (case study) 601
    zero-sequence component on power losses 603–5
multi-stator (MS) approach 594–5
  asymmetrical 12-phase IM 595–6
mutual torque 255

NEDO projects in Japan 320
neutral-point-clamped (NPC) three-level inverter 76
neutral-point voltage control
  three-phase multilevel inverter 90–7
Newton's laws of motion
  hierarchical controller scheme from 4
nonoverlapping type: *see* concentrated winding (CW)

observer-based sensorless estimation of position and speed 177
online parameter identification method for AC drives with induction motors 451
  description of the test bed 454–5
  dSPACE AutoBox 455
    DS1007 PPC processor board 456
    DS2004 high-speed A/D board 459
    DS4002 timing and digital I/O board 456–9
    DS5001 digital waveform capture board 456
    hardware scheme and interface with dSPACE 459–61
  experimental results 472–5
  field-oriented control (FOC) design 453
  IGBT inverter 461
  induction motor 462–3
  method and implementation 465
    anti-aliasing filter 467–9
    description and realization of the signal processing system 466–7
    description of the method 465–6
    digital processing 470–1
  sensors of current, voltage and speed 463
    current sensor configuration 463
    encoder configuration 463
    voltage sensor configuration 463–4
open-loop back EMF estimator 514, 516, 518–20
open-loop IPF compensation 418–20
operational amplifiers 468, 519
optimum AV method 406–8
optimum FW (OFW) operating characteristics 228–9
ordinary LS (OLS) 452, 466, 472
output current ripple, analysis of 609–11
overlapping type: *see* distributed winding (DW)

parasitic effects 486, 682–3
Park's transformation 151–2, 179, 183, 260, 548
permanent magnet (PM) 138
permanent magnet (PM) machines 45, 580
  control of the PMSM at deep flux weakening 56–7
  emerging electric machine topologies 47–53
  permanent magnet synchronous machines (PMSMs) with deep flux weakening capability 53–6
  winding topologies, developments in 46–7
permanent magnet (PM) materials 245
permanent magnet-assisted synchronous reluctance motor (PMaSynRM)
  and interior permanent magnet synchronous motor (IPMSM), comparison of 140
permanent magnet DC machine (PMDC) 429
permanent magnet synchronous motors/machines (PMSMs) 16, 56–7, 150–1, 137–8, 201, 245, 320, 350–1, 359
  control of the PMSM at deep flux weakening 56–7
  with deep flux weakening capability 53–6
  design space 227–30
  direct torque control (DTC) of 363–8
    stability criteria for DTC 370
    torque and flux linkage control of a PMSM 371–3
    voltage space vector selection 368–70
  equivalent circuit models 202–6
  flux-weakening control of 230
    basic principles of flux-weakening control 230–2
    feedforward vs. closed-loop flux-weakening control algorithms 232–8
    six-step voltage operation for 239
interior permanent magnet (IPM) 202
IPM machine capability curves 216
  basic principles 216–18
  case 1: $I_{ch}>I_{max}$ 221–3
  case 2: $I_{ch}=I_{max}$ 223–4
  case 3: $I_{ch}<I_{max}$ 225
  high-speed capability curves for surface PM machines 225–7
  PMSM circle diagrams and capability curves 218–21
IPM machine torque production characteristics 206
  basics of torque production 206–7
  current limit circle 210–11
  impact of magnetic saturation on maximum torque-per-Amp trajectories 211–12
  PMSM torque production characteristics in dq current plane 207–10
performance of PMSM under DTC with trajectory following 385
sensorless control of PMSM drives 513
  closed-loop speed-adaptive observer 520–4
  closed-loop speed non-adaptive observer 525–7
  current slope measurement method 534–40
  HF signal injection 528–34
  mathematical model of the PMSM 516–18
  open-loop back EMF estimator 518–20
surface permanent magnet (SPM) 202
vector control of 212
  application of, to SPM and IPM machines 213–15
  principles 212–13
  self-sensing techniques for 215–16

permanent magnet Vernier (PMV) machine 48
phase advance technique 265–6, 271
phase-locked loop (PLL) 529
pitch factor, calculating
  for fractional-slot windings 659
PM brushless DC motor (BLDCM): *see* brushless DC motor (BLDCM) drives
position and speed estimation 183
position estimation 181
power circuit of the drive, development of 157, 185
power quality control and sensor reduction for DC motor drives 121–3
power switch and integrated control devices for drive systems 8–9
power system blockset (PSB) toolbox 138
  modeling using 152
    current controlled pulse width modulator (CC-PWM) 156
    field weakening controller 155
    reference winding current generation 155–6
    speed controller 152–5
predictive torque control (PTC) 347–9, 552
  and classical control strategies (FOC and DTC), comparison between 546–7
  cost function optimisation 554–5
  estimation 553
  limitations of FS-PTC 555–6
  modelling 547
    of IM 549–51
    of inverter 551–2
    state-space representation of three-phase systems 547–9
  prediction 553–4
proportional integral (PI) control 311
proportional-integral (PI) controller 117, 120–1, 143
proportional-integral (PI) feedback control law 254
pseudo-vector control (PVC) 249
  of BLDC motor 258–63, 266–7
pulse-width modulation (PWM) 4, 212, 264, 515, 537, 598–9
  block 37
  current controller 124
  inverter 23
  modeling of PWM current controller 150
  modulator 325
  PWM-DTC techniques 617
  signal generator
    for full-bridge converter 125
    for half bridge converter 125
    for push–pull converter 124
    for single switch converters 124
    for voltage follower control 124
push–pull converter
  pulse width modulation (PWM) signal generation for 124

quadrant operation of a drive and typical load torque 7–8

reduced-order observer 491–2
reference current generator for power quality control 123
reference flux vector calculator (RFVC) 374, 377
reference speed command 120
reference speed input 158, 185
reference stator current, flux component of 149
reference winding current generation 149–50, 155–6, 158–9, 183, 186
reluctance torque 23, 208, 225, 255, 275–6, 282
reverse blocking IGBT (RB-IGBT) 392, 399
Rogowski coil 39, 41
rotor current model of the IM 550

rotor flux-oriented control (RFOC) 7, 23–4, 31–4, 359, 363
PMSM model and 360–1
rotor position signals, sensing of 158
rotor reference frame, dynamics model of synchronous machines in 19
machine inductance and flux linkages 19–22
rotor flux-oriented control (RFOC) or vector control 23–4
voltage equations 22–3
rotor speed 142

saliency ratio 205, 207
scalar modulation methods 407–9
scquirrel cage induction motor (SCIM) 16
selected prediction vectors (SPVs)-based FS-PTC 556
average switching frequency reduction 560
computational efficiency improvement in 562–3
optimum voltage vector selection 559–60
overall control structure of SPVs-based FS-PTC 560–1
selecting prediction vectors 556–9
SPVs-based FS-PTC algorithm 561
self-sensing techniques for vector control drives 215–16
Semikron Semitech IGBT inverter 462
sensorless control 215
sensorless control of induction motor (IM) drives 481
design for complete stability 500–3
direct field orientation (DFO), flux estimation in 487
combination of current model (CM) and voltage model (VM) 491
current model 487–9
reduced-order observer 491–2
speed estimation 492
statically compensated voltage model (VM) 489–91
voltage model 489
essentials of sensorless vector control 484
dynamic model and principle for vector control 485–6
IM model and nomenclature 484–5
indirect field orientation (IFO), flux estimation in 493
current model 493–4
inherently sensorless CM 499
inherently sensorless reduced-order observer recast as SCVM 498–9
reduced-order observer 494–5
speed estimation 497
speed estimation in an inherently sensorless scheme 500
statically compensated VM 496–7
voltage model 495
inherently sensorless reduced-order observer and SCVM 503–4
sensorless CM 504
inherently sensorless CM 504–5
simulations 505–7
sensorless PMSM drive
load perturbation response of 192–3
speed reversal dynamics of 193
starting dynamics of 189–92
steady-state performance of 193
sensorless vector-controlled PMSM drive 179
control circuit, testing of 187
flux estimation 181
MATLAB-based model of 182
current controlled pulse width modulator (CC-PWM) 184
flux estimator 182–3
position and speed estimation 183
reference winding current generation 183
speed controller 183
position estimation 181
power circuit, testing of 187
speed estimation 181
stator voltage estimation 180
winding current estimation 180–1

sensors in drive systems 39
  current sensors for electric drive systems 39–41
  speed sensors for electric drive systems 41–5
shaft-mounted optical speed sensors 43
shaft-mounted position sensors 215
ship propulsion and generation 581
signal conditioning circuits, development of 157
simplified Park's transformation 260
simulation of drive systems 35
  pulse-width modulation block 37
  tuning of an electric drive using a cascaded structure 35–7
  voltage reference amplitude limitation 37
simulink model of induction motor drive using DTC controller 342
Simulink toolbox 152, 183–4
sine-wave PM motor 245–6, 249
single current regulator (SCR) 57
single-layer (SL) and double-layer (DL) configurations, comparison of 646–8
single-layer (SL) concentrated windings 638
single-phase controlled AC–DC converters 108–10
single-phase SRM 315
single-phase uncontrolled AC–DC converters 110, 112
single-stage LC filter 393–4
single switch converters
  pulse width modulation (PWM) signal generation for 124
sinusoidal pulse width modulation (SPWM) 38, 64, 66–8, 599
  three-phase multilevel inverter 78–81
  three-phase two-level inverter 66–8
six-step voltage (SSV) control 141–2, 237, 239
sliding mode controller (SMC) 143–4, 153, 175, 194
slip relation 493
slot per-pole per-phase (SPP) 46
soft chopping 294, 298–300
space vector modulation (SVM) method 38, 373, 411, 439–40, 597, 605–11
  direct SVM 411–15
  indirect SVM 415–18
space vector pulse width modulation (SVPWM) 443, 461, 599
  carrier-based implementation of three-phase two-level inverter 72–6
  three-phase multilevel inverter 81–5
  three-phase two-level inverter 68–72
speed controller 143, 152–5, 158, 183, 186
  comparative study among different 175
  fuzzy pre-compensated PI controller 145–8
    decision-making 147
    defuzzification 147–8
    fuzzification 147
    fuzzy logic control 146
    fuzzy pre-compensator 146
  hybrid fuzzy PI controller 148–9
  proportional integral (PI) controller 143
  sliding mode controller (SMC) 144
speed estimation 181, 186, 492
speed output signal 43
speed reversal dynamics of sensorless PMSM drive 193
speed sensing 158
speed-sensorless operation 340–1
speed sensors for electric drive systems 41–5
square-wave PM motor 245
squirrel-cage induction machine 16, 63, 214
starting dynamics of sensorless PMSM drive 189–92
statically compensated voltage model (SCVM) 483, 489–91

stator flux, estimation of 339–40
stator-model-based estimator 334
stator voltage estimation 180
stator voltages and winding current-based techniques 176–7
steady-state performance of sensorless PMSM drive 193
stochastic filtering-based sensorless estimation of position and speed 177
surface mount permanent magnet (SMPM) 580, 584
surface PM (SPM) synchronous machine 201
surface PM (SPM) versus interior PM (IPM) machines 677–80
surface PM machines, high-speed capability curves for 225–7
switched reluctance machine (SRM) 584
switched reluctance motor (SRM) drives 275
  characteristics of 280–2
  control of 288
    current control 294–300
    direct torque control (DTC) 301–3
    power converter 288–90
    switching angle control 290–1
  design of 282
    selection of phase number 285–8
    selection of pole 283–5
  doubly salient type 280
  emerging applications 313
    electric vehicle application 319–21
    home appliances 314–16
    industrial applications 316–19
  hybrid SRM 315–16
  modeling of 303
    current waveform representation 304–7
    equivalent circuit 303–4
    example designs of control scheme 311–13
    SRM control system 308–11
    torque waveform representation 307–8
  operation of 275
    excitation characteristics 275–6
    torque generation 276–9
  principle of 275
  singly salient type 280
switching angle control 290, 311
  advanced angle control 292
  fixed angle control 291–2
  switch-off angle control 293–4
switching signal generation for voltage source inverter 159, 186
switching-table-based DTC (ST-DTC) techniques 617
symmetrical machines 585–6
synchronous machines, dynamics model of
  in rotor reference frame 19
    machine inductance and flux linkages 19–22
    rotor flux-oriented control (RFOC) or vector control 23–4
    voltage equations 22–3
synchronous motor (SM) drive 137–8
  classification of 138–9
  control techniques for various synchronous speed motors 140–2
  DSP-based software implementation of vector-controlled PMSM drive 157
    reference speed input 158
    reference winding current generation 158–9
    sensing of rotor position signals 158
    speed controller 158
    speed sensing 158
    switching signal generation for voltage source inverter 159
  digital signal processor (DSP)-based vector-controlled PMSM drive 156
    power circuit of the drive, development of 157
    signal conditioning circuits, development of 157

DSP-based hardware implementation of sensorless vector-controlled PMSM drive 184
development of power circuit of the drive 185
development of signal conditioning circuits 185
DSP-based software implementation of sensorless vector-controlled PMSM drive 185
estimation of stator flux and position of rotor 185
reference speed input 185
reference winding current generation 186
speed controller 186
speed estimation 186
switching signal generation for voltage source inverter 186
IPMSM and PMaSynRM, comparison of 140
magnet torque and reluctance torque-based classification 139–40
MATLAB-based model of sensorless vector-controlled PMSM drive 182
current controlled pulse width modulator (CC-PWM) 184
flux estimator 182–3
position and speed estimation 183
reference winding current generation 183
speed controller 183
MATLAB-based model of vector-controlled PMSM drive system 152
power system blockset (PSB) toolbox, modeling using 152–6
permanent magnet synchronous motor (PMSM), modeling of 150–1
pulse width modulator (PSM) current controller, modeling of 150
reference winding current generation, modeling of 149–50
sensorless PMSM drive
load perturbation response of 192–3
speed reversal dynamics of 193
starting dynamics of 189–92
steady-state performance of 193
sensorless vector-controlled PMSM drive 179
flux estimation 181
position estimation 181
speed estimation 181
stator voltage estimation 180
winding current estimation 180–1
sensorless vector-controlled PMSM drive, testing of 186
testing of control circuit 187
testing of power circuit 187
sensor reduction in vector-controlled permanent magnet synchronous motor drive 175
electrical sensor reduction in PMSM drive 179
mechanical sensor reduction techniques in PMSM drive 176–8
vector-controlled PMSM drive system, sensor requirements in 175–6
speed controllers, comparative study among 175
speed controllers, modeling of 143
fuzzy pre-compensated PI controller 145–8
hybrid fuzzy PI controller 148–9
proportional integral (PI) controller 143
sliding mode controller (SMC) 144
vector control (VC) technique, operating principle of 142–3
vector-controlled PMSM drive 159
control circuit, testing of 159–60
load perturbation performance of 166–74

power circuit, testing of 160
speed reversal dynamics of 174–5
starting dynamics of 160–6
voltage source inverter, modeling of 151–2
synchronous motors 139
classifications of 139
synchronous reference frame, dynamic model of induction machines in 24
machine inductance and flux linkages 28–9
rotor flux-oriented control, conditions for 31–4
voltage, developed power and torque equations 30
synchronous reluctance (SyncRel) 580
synchronous reluctance motors (SynRMs) 351
synchronous speed motors
control techniques for 140–2

Taylor series expansion 553
three-level SVPWM, carrier-based implementation of
three-phase multilevel inverter 86–90
three-phase controlled AC–DC converters 110
three-phase multilevel inverter 76
neutral-point voltage control 90–7
sinusoidal pulse width modulation (SPWM) 78–81
space vector pulse width modulation (SVPWM) 81–5
three-level SVPWM, carrier-based implementation of 86–90
three-phase systems, state-space representation of 547–9
three-phase two-level inverter 64
sinusoidal pulse width modulation (SPWM) 66–8
space vector pulse width modulation (SVPWM) 68–72
carrier-based implementation of 72–6
three-phase uncontrolled AC–DC converters 110
thyristor converters 15
time ratio control (TRC) 117–18
tooth-coil winding: *see* concentrated winding (CW)
torque PI controller design 435–7
torque ripple analysis and reduction techniques 255–8
torque–speed (T–ω) boundaries
electric machines and 15–16
T–ω characteristics within 17–18
total harmonic distortion (THD) 371
total least square (TLS) techniques 466
traction motor 319–20
transformer electromotive force (TEMF) 265
tubular switching machines 681
two-level inverter voltage vector 328–9
two-level VSI (2L-VSI) 551

uncontrolled AC–DC converter–chopper-based DC motor drive 117–18
uncontrolled AC–DC converter-DC–DC converter-based DC motor drive 118–20
unity power factor (UPF) control 4, 141

vacuum cleaner 314
variable-speed AC drives 12, 579
variable-speed-drive system 3
variable voltage and variable frequency (VVVF) source 156
vector control (VC) technique, operating principle of 142–3
vector control algorithms 202
vector control drives 63
vector-controlled permanent magnet synchronous motor (PMSM) drive 143, 175
control circuit, testing of 159–60
electrical sensor reduction in 179

load perturbation performance of 166–74
mechanical sensor reduction techniques in 176
artificial intelligence-based position and speed estimators 178
back emf-based position estimation technique 176
current and voltage model-based sensorless algorithms 177–8
high-frequency carrier signal injection method for estimation of position and speed 177
observer-based sensorless estimation of position and speed 177
stator voltages and winding current-based techniques 176–7
stochastic filtering-based sensorless estimation of position and speed 177
permanent magnet synchronous motor (PMSM), modeling of 150–1
power circuit, testing of 160
pulse width modulator (PWM) current controller, modeling of 150
reference winding current generation, modeling of 149–50
sensor requirements in 175–6
speed controllers, modeling of 143
fuzzy pre-compensated PI controller 145–8
hybrid fuzzy PI controller 148–9
proportional integral (PI) controller 143
sliding mode controller (SMC) 144
speed reversal dynamics of 174–5
starting dynamics of 160–6
voltage source inverter, modeling of 151–2
vector control of PM machine 212
application of, to SPM and IPM machines 213–15
principles 212
self-sensing techniques for 215–16
vector duty cycles 412
vector space decomposition (VSD) approach 584–5
asymmetrical IPM machine (case study) 590–4
asymmetrical machines 586–7
asymmetrical six-phase IM (case study) 589–90
features of 587–9
symmetrical machines 585–6
Venturini method 407
voltage, developed power and torque equations 30
voltage controller 123
voltage equations 22–3
voltage follower control
pulse width modulation (PWM) signal generator for 124
voltage limits 599–601
five-phase inverters (case study) 601
seven-phase inverters (case study) 602–3
sinusoidal operating conditions (case study) 601
zero-sequence component on power losses 603–5
voltage model (VM) 489
combination of current model (CM) and voltage model (VM) 491
statically compensated 489–91
voltage-model-based estimator 334
voltage PWM 298–300
voltage reference amplitude limitation 37
voltage source converters (VSC) 582
voltage source inverters (VSIs) 138, 584
modeling of 151–2
voltage space vector selection 368–70

wind generation 582
winding current estimation 180–1
winding factor, calculation of 656
  closed-form expressions 658
    calculating distribution factor for fractional-slot windings 657–9
    calculating pitch factor for fractional-slot windings 659
  electromotive force (EMF) factor 656–7
  example of winding factor calculation using three methods 659
    using closed-form expressions 661
    using EMF method 659–60
    using winding function method 660–1
  winding function method 657
winding layout determination 651–6
winding topologies, developments in 46–7
wound rotor synchronous machine 584

zero configurations 412
zero *d*-axis current (ZDAC) control for the surface PM machine 141
Ziegler–Nichols step response technique 121

Modeling, Simulation and Control of Electrical Drives

Thanks to advances in power electronics device design, digital signal processing technologies and energy efficient algorithms, ac motors have become the backbone of the power electronics industry. Variable frequency drives (VFD's) together with IE3 and IE4 induction motors, permanent magnet motors, and synchronous reluctance motors have emerged as a new generation of greener high-performance technologies, which offer improvements to process and speed control, product quality, energy consumption and diagnostics analytics.

Primarily intended for professionals and advanced students who are working on sensorless control, predictive control, direct torque control, speed control and power quality and optimisation techniques for electric drives, this edited book surveys state of the art novel control techniques for different types of ac machines. The book provides a framework of different modeling and control algorithms using MATLAB®/Simulink®, and presents design, simulation and experimental verification techniques for the design of lower cost and more reliable and performant systems.

About the Editors

Mohammed Fazlur Rahman is Professor and Head of the Energy Systems Group with the School of Electrical Engineering and Telecommunications at the University of New South Wales, Australia. His research interests cover power electronics, motor drives, design of electrical machines with permanent-magnet excitation, and motion control systems. He is a Fellow of the IEEE.

Sanjeet Dwivedi is Senior R&D Control Engineer at Danfoss Power Electronics A/S, Denmark, and former Adjunct Professor with Curtin University Perth, Australia [2016-18]. He holds three international patents. He is a recipient of the Merit Award from Institution of India IE(I) (2006). He was also awarded the 9th Man on the Moon Global Innovation Award of Danfoss (2015) and the IETE-Bimal Bose Award (2017) for outstanding contributions in power electronics and drives. He is a Fellow of the IET and the IEEE.

ISBN 978-1-78561-587-0

9 781785 615870 >

Control, Robotics & Sensors
Energy Engineering

The Institution of Engineering and Technology • www.theiet.org
978-1-78561-587-0